Proceedings of the 8th National Congress on Theoretical and Applied Mechanics, May 28-29, Brussels, Belgium.

ILES of air flow around buildings

D.A. Köse and E. Dick
Department of Flow, Heat and Combustion Mechanics, Ghent University
Sint-Pietersnieuwstraat 41, 9000 Gent – Belgium
E-mail: DemirAli.Kose@Ugent.be, Erik.Dick@Ugent.be

Abstract: **A numerical study of the flow around a cubical building in an atmospheric boundary layer is presented. The Reynolds number of the flow is Re = 4.10^6. Different types of turbulence models, steady state RANS, hybrid RANS/LES and LES, are used and the simulation results are compared to experiments. While in most studies, CFD results are compared with wind tunnel data, in this paper field measurement data are used for comparison. Our objective is to offer an approach to perform simulations on rather coarse grids with moderate computational cost. The outcome is that the Implicit LES (ILES) method is the most accurate for coarse grid simulations. In order to verify the sensitivity of the results to Reynolds number, also simulations of a wind tunnel experiment at Reynolds number 10^5 are done. We show that also for lower Reynolds number, although not optimal, the ILES approach leads to good results.**

Keywords: **ILES, buildings, pressure distribution**

1. INTRODUCTION

Despite the fast increase in computational power, fully resolved ($y^+ < 1$) Large Eddy Simulation (LES) of high Reynolds number flows, such as flows around buildings, is not feasible. In LES, large scales in the flow are resolved while scales smaller than a cut–off length related to the computational cell size are modelled. The influence of the modelled scales on the resolved part of the flow is accounted for by a sub–grid scale model (SGS). The higher the Reynolds number, the higher the amount of grid points needed to adequately resolve the flow. For instance, simulation of the flow around a real size building requires several tens of millions of grid points. Therefore, in practice, RANS models are typically used in the analysis of flows around buildings. RANS models allow much coarser grids because they average flow features over the largest length scale of the turbulence. The drawback is that the flow is represented much steadier than in reality. In particular, flows around buildings are extremely unsteady. Quasi-steady turbulence models are therefore not capable of capturing the main unsteadiness of these flows. Mean velocity profiles, drag and other quantities predicted with RANS models deviate considerable with experimental data [1]. Another option is to use hybrid turbulence models. In such models, the best qualities of RANS (coarse grid, low computational cost) and LES (accuracy) are combined: near walls (e.g. building surface) the hybrid model is in RANS-mode while further away the SGS model is active. Predictions with hybrid models are in better agreement with experimental data than RANS results [2]. However, for reliable predictions, hybrid models require much finer grids than RANS models. For practical use in building flows, the associated computational cost is too high.

In section 2, we describe the different turbulence models that we test. In section 3, we present the results of the flow around a cube in a channel, at relatively low Reynolds number. The aim of this study is to determine which model gives the best velocity and pressure predictions on rather coarse grids. In section 4, the best models are then applied to the flow around a cubical building in an atmospheric boundary layer. The Reynolds number is 6.4 million, based on the building height and the velocity of the approaching flow at building height level. Pressure coefficients on a horizontal and vertical section are available from the measurements [3, 4] and are compared with the simulation results. Finally, in section 5, the results are discussed and conclusions are formulated.

2. TURBULENCE MODELS

Different models are tested. All simulations have been performed with the commercial CFD package FLUENT. Most of the models are standard available in the package.

2.1. Steady RANS models

Standard k–ε model

The transport equations for the turbulence kinetic energy k and dissipation rate ε model are

$$\frac{\partial}{\partial t}(\rho k)+\frac{\partial}{\partial x_i}(\rho k u_i)=\frac{\partial}{\partial x_j}\left[\left(\mu+\frac{\mu_t}{\sigma_k}\right)\frac{\partial k}{\partial x_j}\right]+G_k-\rho\varepsilon$$

and

$$\frac{\partial}{\partial t}(\rho\varepsilon)+\frac{\partial}{\partial x_i}(\rho\varepsilon u_i)=\frac{\partial}{\partial x_j}\left[\left(\mu+\frac{\mu_t}{\sigma_\varepsilon}\right)\right]+C_{1\varepsilon}\frac{\varepsilon}{k}G_k-C_{2\varepsilon}\rho\frac{\varepsilon^2}{k}.$$

G_k is the production of turbulence kinetic energy and is computed consistent with the Boussinesq hypothesis by:

$$G_k=\mu_t S^2,$$

where S is the modulus of the mean rate-of-strain tensor, defined as

$$S\equiv\sqrt{2S_{ij}S_{ij}},$$

with

$$S_{ij}=\frac{1}{2}\left(\frac{\partial u_i}{\partial x_j}+\frac{\partial u_j}{\partial x_i}\right).$$

The turbulent viscosity μ_t is computed from k and ε as

$$\mu_t = \rho C_\mu \frac{k^2}{\varepsilon},$$

where C_μ is constant and equal to 0.09.
The model constants are

$$C_{1\varepsilon} = 1.44,\ C_{2\varepsilon} = 1.92,\ \sigma_k = 1.0 \text{ and } \sigma_\varepsilon = 1.3.$$

k–ω STT model

The transport equations for the k–ω model are

$$\frac{\partial}{\partial t}(\rho k) + \frac{\partial}{\partial x_i}(\rho k u_i) = \frac{\partial}{\partial x_j}\left[\left(\mu + \frac{\mu_t}{\sigma_k}\right)\frac{\partial k}{\partial x_j}\right] + \tilde{G}_k - Y_k$$

and

$$\frac{\partial}{\partial t}(\rho \varepsilon) + \frac{\partial}{\partial x_i}(\rho \varepsilon u_i) = \frac{\partial}{\partial x_j}\left[\left(\mu + \frac{\mu_t}{\sigma_\omega}\right)\right] + G_\omega - Y_\omega + D_\omega.$$

$\tilde{G}_k$ represents the production of turbulent kinetic energy, and is defined as:

$$\tilde{G}_k = \min\left(G_k, 10\rho\beta^* k\omega\right),$$

with G_k computed in the same way as in the k–ε model. β^* is a function of k and ω and contains a compressibility correction.

The term Y_k represents the dissipation of turbulence kinetic energy and is evaluated as

$$Y_k = \rho\beta^* k\omega.$$

G_ω is the production of ω and is given by

$$G_\omega = \frac{\alpha}{\nu_t} G_k,$$

where α is a function of k and ω.

The term Y_ω represents the dissipation of ω and is evaluated as

$$Y_\omega = \rho\beta\omega^2.$$

β^* is a function of k and ω and contains a compressibility correction.

Finally, the turbulent viscosity μ_t is computed as

$$\mu_t = \frac{\rho k}{\omega} \frac{1}{\max\left[\frac{1}{\alpha^*}, \frac{SF_2}{a_1\omega}\right]}.$$

In this expression, F_2 is a blending function, α^* is a function of k and ω, and a_1 is a constant.

2.2. Hybrid RANS/LES models

In the DES approach, the unsteady RANS models are employed in the near-wall regions, while the filtered versions of the same models are used in the regions away from the near-wall.

DES k–ε model

The transport equations for k and ε in the realizable k–ε model are:

$$\frac{\partial}{\partial t}(\rho k) + \frac{\partial}{\partial x_i}(\rho k u_i) = \frac{\partial}{\partial x_j}\left[\left(\mu + \frac{\mu_t}{\sigma_k}\right)\frac{\partial k}{\partial x_j}\right] + G_k - \rho\varepsilon$$

and

$$\frac{\partial}{\partial t}(\rho \varepsilon) + \frac{\partial}{\partial x_i}(\rho \varepsilon u_i) = \frac{\partial}{\partial x_j}\left[\left(\mu + \frac{\mu_t}{\sigma_\varepsilon}\right)\frac{\partial \varepsilon}{\partial x_j}\right] + \rho C_1 S\varepsilon - \rho C_2 \frac{\varepsilon^2}{k + \sqrt{\nu\varepsilon}},$$

where $C_1 = \max\left[0.43, \frac{\eta}{\eta + 5}\right]$ and $\eta = S\frac{k}{\varepsilon}$.

The turbulent viscosity μ_t is computed from

$$\mu_t = \rho C_\mu \frac{k^2}{\varepsilon},$$

where C_μ is no longer constant. G_k is computed the same way as in the standard k–ε model (see section 2.1).

In DES mode, the dissipation term in the equation for k, i.e. ρε, is modified such that

$$Y_k = \frac{\rho k^{\frac{3}{2}}}{l_{des}},$$

where $\ell_{des} = \min\left(\ell_{rke}, \ell_{les}\right)$, $\ell_{rke} = \frac{k^{3/2}}{\varepsilon}$, $\ell_{les} = C_{des}\Delta$ and $\Delta = \max\left(\Delta x, \Delta y, \Delta z\right)$, the maximum grid spacing.
The standard value of C_{des} is 0.65.

DES k-ω STT model

This model is based on the k–ω STT model. The dissipation term of the turbulent kinetic energy is modified such that

$$Y_k = \rho\beta^* k\omega f_{\beta^*}$$

with f_{β^*} defined as

$$f_{\beta^*} = \max\left(\frac{L_t}{C_{DES}\Delta}, 1\right).$$

Δ is the maximum local grid spacing. The turbulent length scale is the parameter that defines this RANS model:

$$L_t = \frac{\sqrt{k}}{\beta^*\omega}.$$

DES k-l model

The k–l one equation model is employed to obtain the turbulent eddy viscosity. For the SGS viscosity the sub-grid scale k_{sgs}–ℓ model of Yoshizawa [5] and Fureby [6] is used.

Mathematically, both models have the same form:

$$\frac{\partial k_T}{\partial t}+\frac{\partial}{\partial x_i}\left(u_i k_T\right)=\frac{1}{\rho}\frac{\partial}{\partial x_j}\left[\left(\mu+\frac{\mu_t}{\sigma_k}\right)\frac{\partial k_T}{\partial x_j}\right]+P_{k_T}-\varepsilon_T .$$

The subscript 'T' is used to identify whether a RANS or a SGS model is used.

P_{k_T} is computed as $P_{k_T}=\mu_T S^2$, and ε_T as $\varepsilon_T=\frac{C_\varepsilon k_T^{3/2}}{\ell_\varepsilon}$.

The turbulent viscosity μ_T is computed as

$$\mu_T=\rho C_\mu \ell_\mu k^{1/2}.$$

The length scales ℓ_μ and ℓ_ε are defined as

$$\ell_\mu=MIN\left(2.4y\left(1-e^{-0.016y^*}\right),\Delta\right),$$

$$\ell_\varepsilon=MIN\left(2.4y\left(1-e^{-0.263y*}\right),\Delta\right),$$

with $\Delta=V^{1/3}$, the cube root of the cell volume, and $y^*=y\frac{\rho k_T^{1/2}}{\mu}$.

In the LES region, C_μ = 0.07 and C_ε = 1.05, while in the RANS region C_μ = 0.09 and C_ε = 1. The DES k-l model had to be programmed with user defined functions (UDF's) since the model is not available in FLUENT.

2.3. LES and implicit LES models

Filtering the Navier-Stokes equations, one obtains

$$\frac{\partial}{\partial x_i}\left(\rho\overline{u}_i\right)=0$$

and

$$\frac{\partial}{\partial t}\left(\rho\overline{u}_i\right)+\frac{\partial}{\partial x_j}\left(\rho\overline{u}_i\overline{u}_j\right)=\frac{\partial\sigma_{ij}}{\partial x_j}-\frac{\partial\overline{p}}{\partial x_j}-\frac{\partial\tau_{ij}}{\partial x_j}.$$

The filtered velocity is denoted by an overbar. σ_{ij} is the stress tensor due to molecular viscosity and τ_{ij} is the sub–grid scale stress defined by $\tau_{ij}=\rho\overline{u_i u_j}-\rho\overline{u}_i\overline{u}_j$.

The sub–grid scale stresses resulting from the filtering operation are unknown, and require modelling. In FLUENT, the sub–grid scale stresses are computed from

$$\tau_{ij}-\frac{1}{3}\tau_{kk}\delta_{ij}=-2\mu_t\overline{S}_{ij},$$

where μ_t is the sub–grid scale turbulent viscosity and $\overline{S}_{ij}$ the rate–of–strain tensor defined by

$$\overline{S}_{ij}=\frac{1}{2}\left(\frac{\partial\overline{u}_i}{\partial x_j}+\frac{\partial\overline{u}_j}{\partial x_i}\right).$$

The sub–grid scale turbulent viscosity has to be modelled. The isotropic part of the sub–grid scale stresses is not modelled but added to the static pressure term.

Standard Smagorinsky–Lilly model

In the Smagorinsky-Lilly model, the eddy-viscosity is obtained from

$$\mu_t=\rho L_S^2\left|\overline{S}\right|,$$

where $\left|\overline{S}\right|\equiv\sqrt{2\overline{S}_{ij}\overline{S}_{ij}}$ and L_S is the mixing length for sub–grid scales, computed using

$$L_S=\min\left(\kappa d, C_S V^{1/3}\right).$$

K is the von Kármán constant, d is the distance to the closest wall, C_S is the Smagorinsky constant equal to 0.1, and V is the volume of the computational cell.

Dynamic Smagorinsky–Lilly model

In this model, the Smagorinsky model constant, C_S, is dynamically computed based on the information provided by the resolved scales of motion [7]:

$$C_s=\frac{1}{2}\left(\frac{L_{ij}\overline{S}_{ij}}{M_{ij}\overline{S}_{ij}}\right),$$

with $L_{ij}=-\widehat{\overline{u}_i\overline{u}_j}+\hat{\overline{u}}_i\hat{\overline{u}}_j$ and $M_{ij}=\Delta^2\left|\hat{\overline{S}}\right|\hat{\overline{S}}_{ij}-\Delta^2\widehat{\left|\overline{S}\right|\overline{S}_{ij}}$.

The caret denotes filtering with a test filter. The numerator can become negative, hence C_s can locally become negative, leading to backscatter, this is transfer of energy from smaller scales to larger scales.

Dynamic kinetic energy SGS model

The dynamic subgrid-scale kinetic energy model in FLUENT replicates the model proposed by Kim and Menon [8]. In this model, a transport equation is solved for the sub–grid scale kinetic energy:

$$\frac{\partial k_{sgs}}{\partial t}+\frac{\partial\overline{u}_j k_{sgs}}{\partial x_j}=-\tau_{ij}\frac{\partial\overline{u}_i}{\partial x_j}-C_\varepsilon\frac{k_{sgs}^{3/2}}{\Delta}+\frac{\partial}{\partial x_j}\left(\frac{\mu_t}{\sigma_k}\frac{k_{sgs}}{\partial x_j}\right).$$

where

$$k_{sgs}=\frac{1}{2}\left(\overline{u_k^2}-\overline{u}_k^2\right).$$

The sub–grid scale eddy viscosity is computed as

$$\mu_t=C_k k_{sgs}^{1/2}\Delta.$$

The model constants C_ε and C_k are determined dynamically.

Implicit LES

In this case, no SGS model is used. This is done by setting the Smagorinsky constant C_S equal to 0. The influence of the unresolved scales on the resolved ones is accounted for by the numerical dissipation of the discretization scheme used. Thereto, a TVD discretization is used. Typically, a bounded central discretization scheme is used.

2.4. Wall model

Instead of using the no–slip boundary condition we impose the wall shear stress at the cube and channel walls in some of the simulations. The stress components are computed using a blending of the viscous τ_w^v and turbulent τ_w^t, expressions for the shear stress. We follow the approach of Popovac and Hanjalic [9]:

$$\tau_w = \tau_w^v e^{-\Gamma} + \tau_w^t e^{-1/\Gamma} = \mu \frac{U_p}{y_p}\left[e^{-\Gamma} + \frac{\kappa y_p^*}{\ln\left(E y_p^*\right)} e^{-1/\Gamma} \right],$$

with the blending function Γ computed as $\Gamma = \frac{0.01\left(y_p^*\right)^4}{1+5y_p^*}$ and $y_p^* = \frac{\rho C_\mu^{1/4} k_p^{1/2}}{\mu} y_p$. The subscript 'p' stands for the centre of the first cell adjacent tot the wall. The wall model is programmed with UDF's.

3. Flow around a surface mounted cube placed in fully developed channel flow

3.1. Computational domain

The geometry consists of a cube placed in a channel. The cube height H is 4 cm. The channel height is 2 times the cube height. The cube is placed at a distance of 3 times the cube height from the inlet of the channel. The channel exit is located 6 cube heights downstream of the leeward side of the cube. The side walls of the channel are at a distance of 3 cube heights left and right of the cube. A side view is given in figure 1. The flow direction is normal to the cube front face.

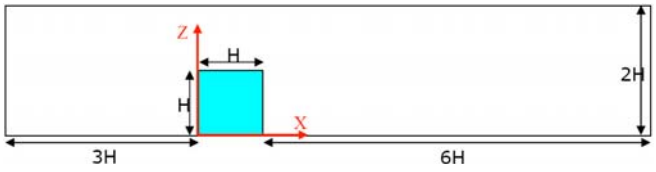

Fig. 1. Cube in channel. Side view of the geometry

3.2. Grid details

The mesh consists of a little more than 270.000 cells. On the cube itself the cell distribution is 15 cells in X and Y directions, 25 in the Z direction. There are 20 cells upstream of the cube and 50 cells downstream of the cube. Near the cube the first adjacent cell centre is at a distance of 4.6 x 10^{-4} m from the cube walls (1.15 % of cube height). A top view of the mesh is given in figure 2.

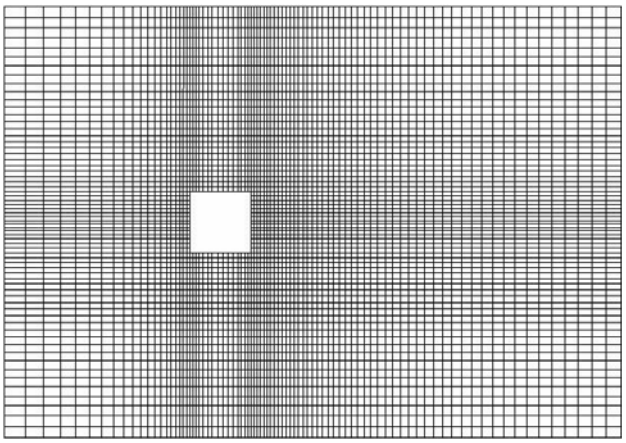

Fig. 2. Cube in channel. Top view of the mesh

3.3. Simulation settings

The Reynolds number of the flow, based on the cube height H and bulk velocity U_b, is Re = 10^5. We take the air density as 1 kg/m^3, bulk velocity U_b as 25 m/s and the molecular viscosity as 10^{-5} kg/ms.

At the inlet of the channel we assume a fully developed turbulent velocity profile. To obtain such a profile we performed a RANS simulation of a turbulent channel flow on the same grid but without the cube placed in it and with periodic inlet and outlet.

Turbulence in the upstream flow is specified with profiles for k and ε. These profiles for k and ε are again taken from the turbulent periodic channel flow simulation.

3.4. Experimental data

Martinuzzi et al. [10] investigated the flow field around surface–mounted, prismatic obstacles with different dimensions. The experimental data obtained from the measurements include the three components of the mean velocity at several upstream and downstream positions. All data have been added to the Journal of Fluids Engineering Data Bank.

3.5. Results

We compare mean stream wise velocity profiles at four locations in the symmetry plane (see figure 3). The focus is on the region in the immediate vicinity of the cube.

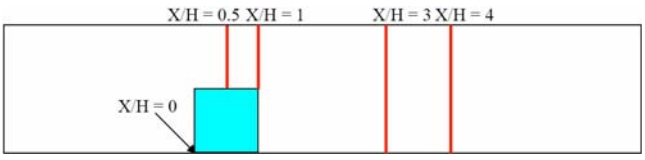

Fig. 3. Cube in channel. Locations in the symmetry plane for velocity profile comparison.

3.5.1. RANS and hybrid RANS/LES

In figure 4, mean velocity profiles at several locations are presented. The plus signs represent the experimental data. The RANS result differs very much from the experimental results. This is also the case for the SST k-ω model (not shown). The hybrid RANS/LES results are good. In particular, the results are very good at all locations with the hybrid version of the SST k-ω model.

In figure 5, we present the results of the hybrid models when the wall model, denoted by WM, is applied. Again, the results of the SST k-ω model are particularly good. Compared to the results without wall model (figure 4), the other hybrid models also benefit from the introduction of a wall model. One has to remark that with the SST k-ω model, FLUENT automatically activates a wall model that is similar to the wall model that we use here, although not identical (enhanced wall function). So, we conclude that the use of a wall model improves considerably the results of hybrid simulations.

3.5.2. LES and ILES

Figure 6 shows the velocity profiles obtained with the LES type of models. At the first two positions the results are very similar for all LES types. Minor differences occur at the positions aft of the cube. Even when the sub–grid scale model is omitted, the differences with the other simulations are very small. Compared to the results of the hybrid RANS/LES with wall model, the results of the LES types differ much more from the experiments. In particular, the difference with the experiments is big at the first position (X/H=0.5). This means that the extent of the recirculation zone at the top of the cube is underpredicted.

3.5.3. Best model for low Reynolds number

The conclusion from the results in figures 4, 5 and 6 is that there is an advantage in using a hybrid formulation. RANS is clearly erroneous due to the impossibility to represent the unsteadiness of the large vortex structures shed by the cube. LES leads to an underestimation of the length of the recirculation zone at the top of the cube. The poor performance of LES has to do with the resolution in wall vicinity. The y^+ value at the centre of the first cell on the cube walls varies from 7 to 115. This value is too big for accurate representation of the near wall zone by LES. Remark that the y^+ value is also too big for RANS simulation without wall model. This explains why the hybrid results benefit from the introduction of a wall model. LES results might also benefit from a wall model. Remark that the wall model described in section 2.4 cannot be used with LES. To make it applicable, we should replace y^* by $y^+ = yu_\tau / \upsilon$. This decreases the numerical stability of the wall model, as it makes the resulting wall shear stress dependent on itself. We could not obtain stable results with such a variant of the wall model for flows with separation zones. Hereafter, we derive a wall model that is practical and numerically stable for LES, but which is limited to large y^+ values.

The conclusion from the comparison is that the DES SST k-ω model with wall model gives the best results.

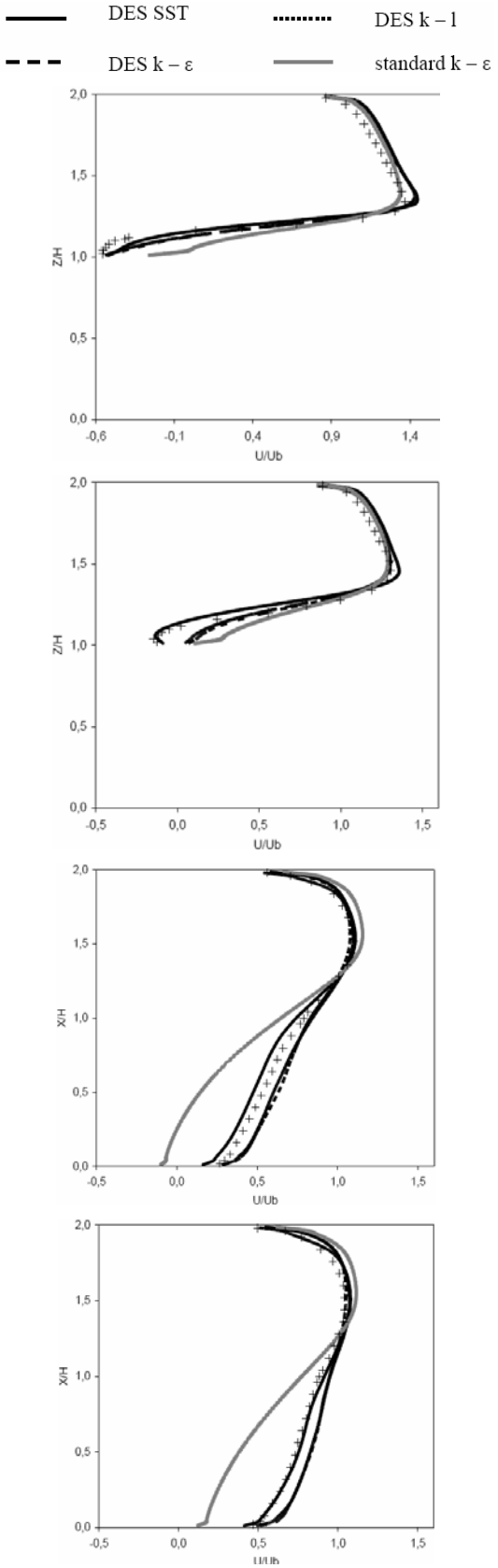

Fig. 4. Cube in channel. Mean streamwise velocity in the symmetry plane at x/H= 0.5, 1.0, 3.0 and 4.0 for RANS and hybrid simulations. Plus signs are experimental data.

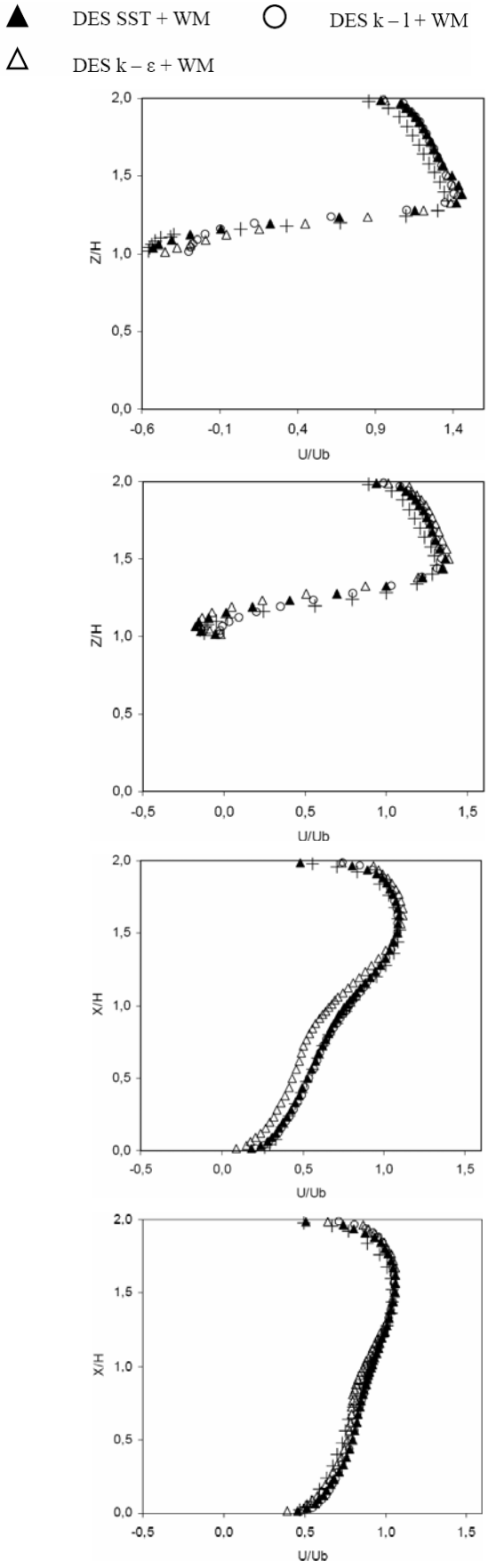

Fig. 5. Cube in channel. Mean streamwise velocity in the symmetry plane at x/H= 0.5, 1.0, 3.0 and 4.0 for hybrid simulations with WM. Plus signs are experimental data.

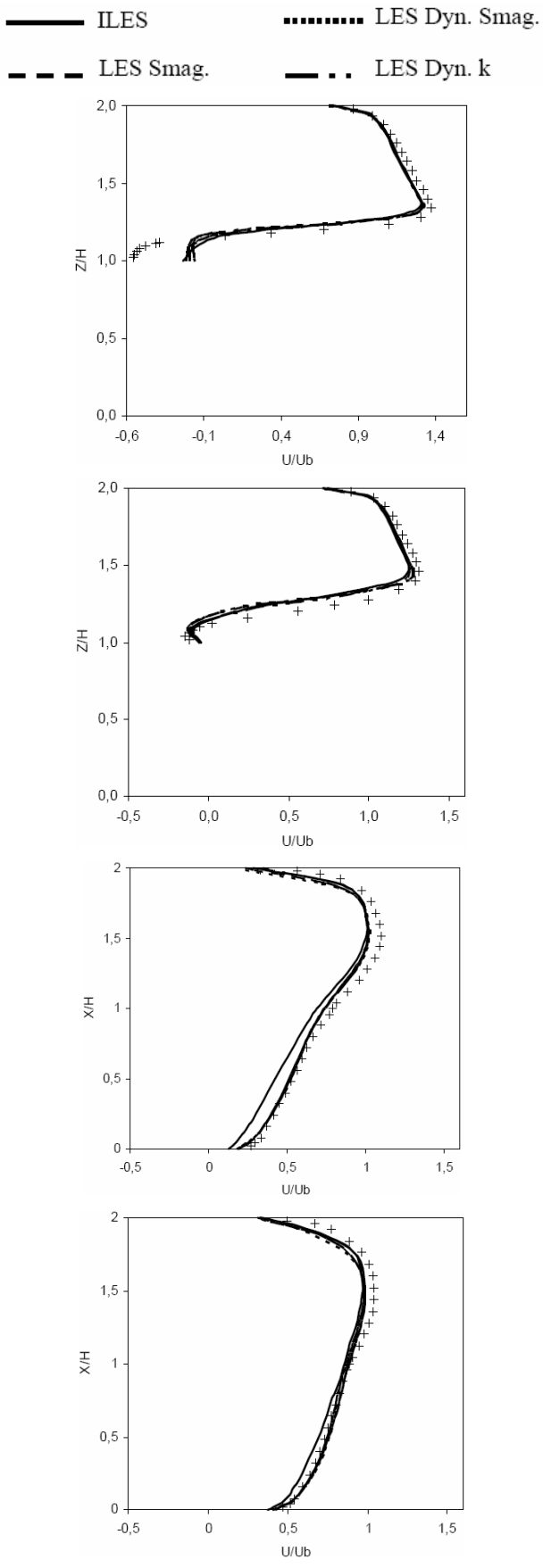

Fig. 6. Cube in channel. Mean streamwise velocity in the symmetry plane at x/H= 0.5, 1.0, 3.0 and 4.0 for LES and ILES. Plus signs are experimental data.

4. FLOW AROUND A CUBICAL BUILDING IN AN ATMOSPHERIC BOUNDARY LAYER (ABL)

4.1. Computational domain

The computational domain extends 10H (H is building height) in streamwise direction, 7H in lateral direction and 5H in height direction. The building is placed at a distance 3H from the inlet of the domain. The side walls are at a distance 3H from the building.

4.2. Grid details

In order to avoid large computational cost, a typical RANS grid (mesh A), sufficiently fine for RANS calculations in steady flow and a second grid, mesh B, but better adapted to LES simulations are used.

Both meshes are structured. Mesh A has a little more than 800.000 cells. The cell distribution on the building walls is 30 cells in all directions, with the first near – wall cell centre at a distance of 0.9cm (the cube height H is 6m). There are 35 cells upstream and in the lateral directions, 45 cells in the Z direction (starting at the top of the cube) and 55 cells downstream (see figure 7).

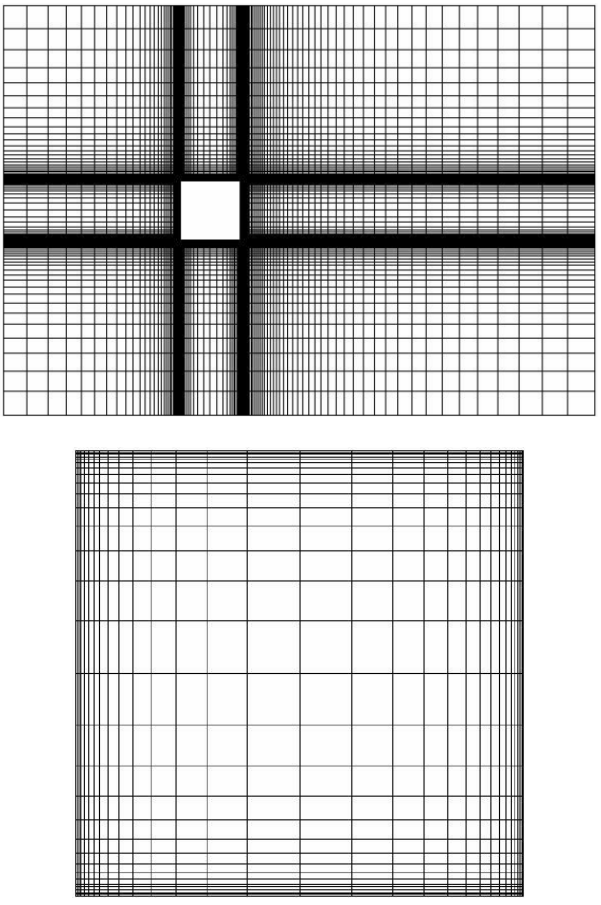

Fig. 7. Cubical building in ABL. View of mesh A (upper) and cell distribution on building top wall (lower)

For mesh B, we started from a coarse mesh and refined it twice in the building vicinity. A refinement consists in splitting a cell into 8 cells with equal size. After two refinements, the grid has approximately 1.2 million cells. The difference between mesh A and mesh B is that the latter has much more cells (a factor of 12) on the building surfaces and is thus better suited to resolve smaller scales (see figure 8).

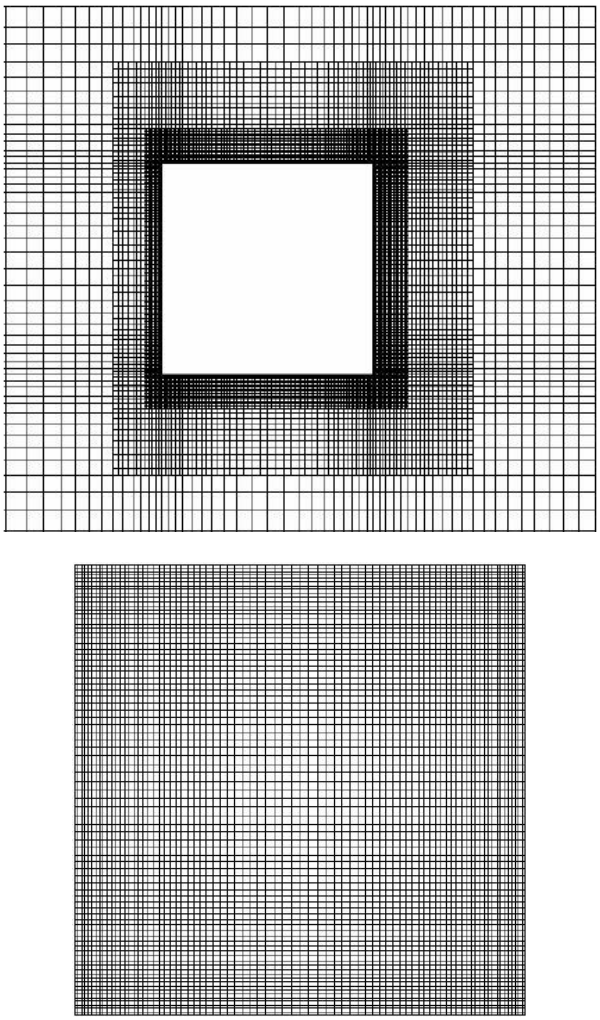

Fig. 8. Cubical building in ABL. Close – up of mesh B (upper) and cell distribution on building top wall (lower)

4.3. Turbulence models used

We have performed simulations with three types of models.

Steady state RANS models

- The standard k – ε model
- The k – ω SST model

Hybrid RANS/LES model

- The DES SST model

We only use one hybrid model since, in section 3, the DES SST model gave the best results.

LES and ILES models

- The Smagorinsky–Lilly model ($C_s = 0.1$)
- ILES (Implicit LES): no SGS model ($C_s = 0.0$)

4.4. Wall model

A wall model based on the log law was derived and used in the ILES simulations instead of the no–slip boundary condition.

Starting from the log law

$$u^+ = \frac{1}{\kappa}\ln\left(Ey^+\right),$$

we can manipulate into

$$e^{\kappa u^+} = E\left(\frac{uy}{\nu}\right)\frac{1}{u^+} = \tau_w E u^+\left(\frac{y}{\mu u}\right),$$

from which follows that

$$\tau_w = \mu\frac{u}{y}\left(\frac{e^{\kappa u^+}}{Eu^+}\right).$$

Once $\frac{e^{\kappa u^+}}{Eu^+}$ is known, the wall shear stress is obtained. Since $\frac{uy}{\nu} = \frac{u}{u_\tau}\frac{y}{\nu}u_\tau = u^+y^+$ we can plot $\frac{e^{\kappa u^+}}{Eu^+}$ for a range of u^+y^+ values and fit a function to the graph. We obtain

$$\frac{e^{\kappa u^+}}{Eu^+} = f\left(u^+y^+\right) = a + b\left(u^+y^+\right)^c,$$

with a = 0.1, b = 0.02057 and c = 0.76879.

Since y^+ is sufficiently high ($> \approx 300$) no blending of the turbulent and viscous expressions for the wall shear stress is done.

The wall model is programmed with UDF's. This wall model is only used in the ILES simulations on both grids.

4.5. Simulation settings

The Reynolds number, based on cube height H and velocity of the approaching flow at cube height, is $Re = 4.1\text{x}10^6$.

At the inlet of the channel we assume a logarithmic velocity profile:

$$U\left(z\right) = 1.194\ln\left(z\right) + 7.38,$$

where z is the spanwise coordinate. This formula was derived from the available data of the approaching flow in the experiment.

Turbulence in the upstream flow is specified with profiles for k and ε or k and ω. The profile for k is derived from the experimental data. Assuming a linear dependence between the turbulence length scale l and the height z (l=2.5z), ε and ω are computed from $\varepsilon = \frac{k^{3/2}}{\ell}$ and $\omega = \frac{\varepsilon}{0.09k}$.

The left and right side walls of the channel are symmetry walls, while the channel outlet and the top of the domain are pressure outlet boundaries. At walls, the no–slip boundary condition is imposed. In the case of ILES we also use the wall model based on the log law.

The momentum, k, ε and ω equations are discretized using a second order upwind scheme (2UP) for the steady state models, while the bounded central difference (BCD) scheme is used in the hybrid and LES simulations. For the pressure-velocity coupling, the SIMPLE algorithm is used.

A time step of 0.01s is used. During every time step iterations are done on until residuals drop below 10^{-4}.

4.6. Experimental data

From the field measurements of Richards and Hoxey [3, 4] we have the properties of the approaching flow: velocities and turbulence intensities. We also have pressure coefficient profiles on a vertical and a horizontal section on the building.

4.7. Results

4.7.1. Mesh A

The numbers -1 to 3 represent the different faces of the building: from -1 to 0: side face, 0 to 1: front face, 1 to 2: top or side face and 2 to 3: back.

Steady state results

The pressure coefficient profiles on the vertical and horizontal sections are shown in figure 9 for the steady state RANS simulations. The steady state predictions are very poor at the top and the side walls of the building. The best agreement with experimental data is at the front. The reason for this discrepancy is that the flow is highly unsteady. Since the RANS models give averaged results, the flow is represented too steady.

HYBRID simulation results

In figure 10, we include the k–w SST RANS results for comparison. The DES–SST results do not differ much from the steady state RANS predictions. Again, the results are poor at the top and side walls. The main reason is that the grid that we use is very coarse. By plotting the relative DES length scale, we see that the LES region is very small and located in the wake of the building. Overall, there is very low LES activity and the simulation is fully RANS in the vicinity of the building. This explains why the hybrid results are almost identical to the RANS results.

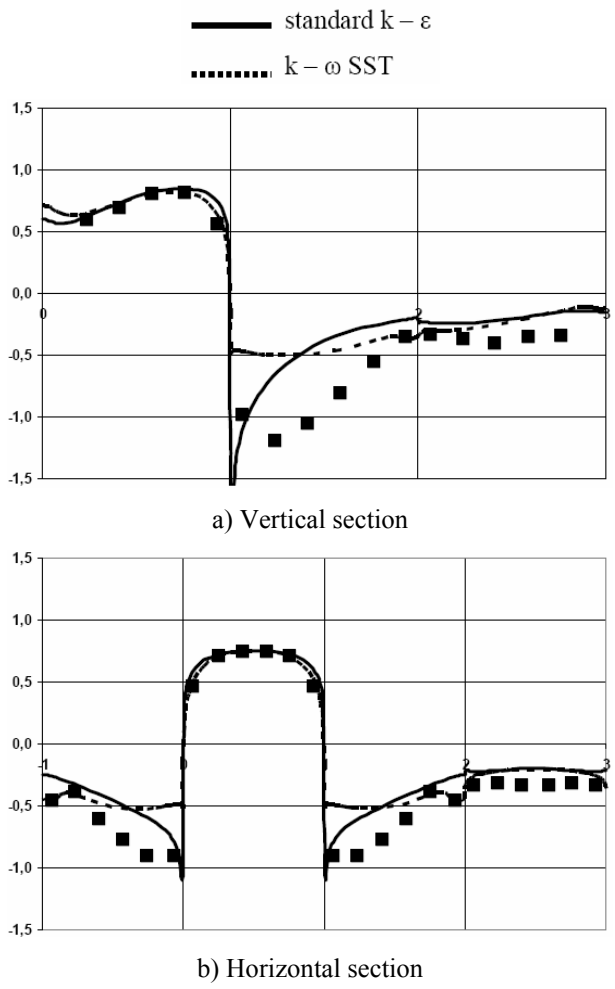

Fig. 9. Cubical building in ABL. Pressure coefficient profiles on the vertical and horizontal sections, RANS results. Black squares are experiments.

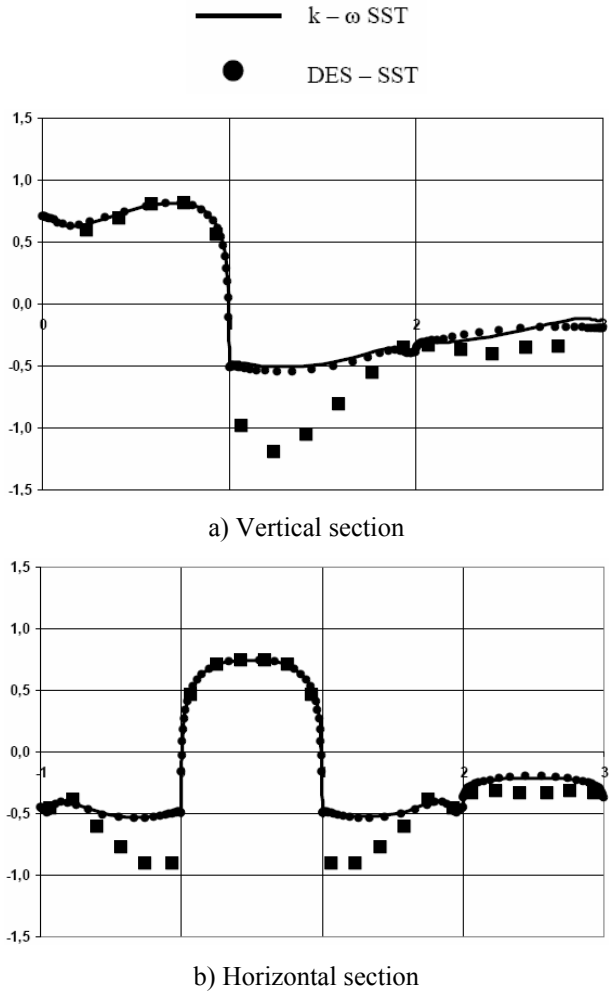

Fig. 10. Cubical building in ABL. Pressure coefficient profiles on the vertical and horizontal sections, HYBRID results. Black squares are experiments.

LES and ILES results

We see on figure 11 that there is almost no difference between the LES and the ILES results, except at the front of the building (vertical section). This means that on the very coarse grid that we use, the SGS model has very little influence. When performing simulations on this grid the SGS model can be omitted.

There is also very little influence of the wall model. With and without wall model, the results are almost the same. We have to remark that, similar as with the hybrid models, FLUENT automatically activates a wall model (enhanced wall function) which is similar, although not identical, to the model that we use.

There is very good agreement with experimental profiles at the front, on the top and at the back of the building. The predictions on the side walls follow the experimental profiles, but there is some deviation. Overall, it is remarkable that we can obtain such good correspondence between ILES results and experiments on a rather coarse grid, which is certainly not fine enough to resolve the small scales.

4.7.2. Mesh B

Since the RANS and hybrid results on mesh A were poor, we did not repeat those calculations on mesh B. Figure 12 shows the results for the LES and ILES.

While we did not observe any difference between ILES with and "without" wall model on mesh A, we see now some influence of the wall model. In particular, at the top and side walls of the building the differences are visible. Remark that FLUENT automatically activates a wall model, if the user does not specify the wall shear stress. Overall, there is no quality difference between our own wall model and that of FLUENT.

We observe that the overall quality of the predictions is not really better on mesh B than on mesh A. This means that both meshes are much too coarse to resolve enough in wall vicinity. The differences in the results are due to the different mesh size in wall vicinity, but there is no conclusion on the best gridding strategy. The observation is that any LES formulation gives good results, taking into account the very coarse grids used.

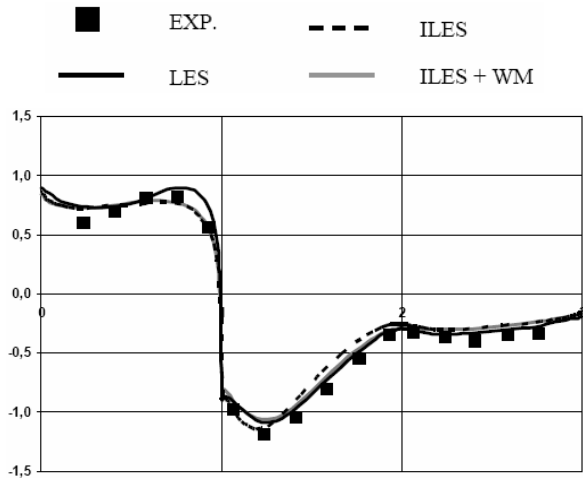

a) Vertical section

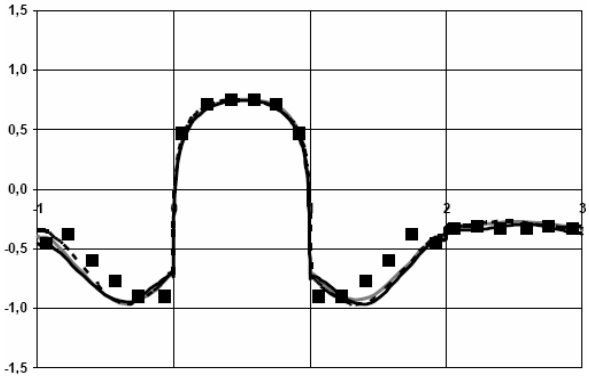

b) Horizontal section

Fig. 11. Cubical building in ABL. Pressure coefficient profiles on the vertical and horizontal sections. LES and ILES results on mesh A.

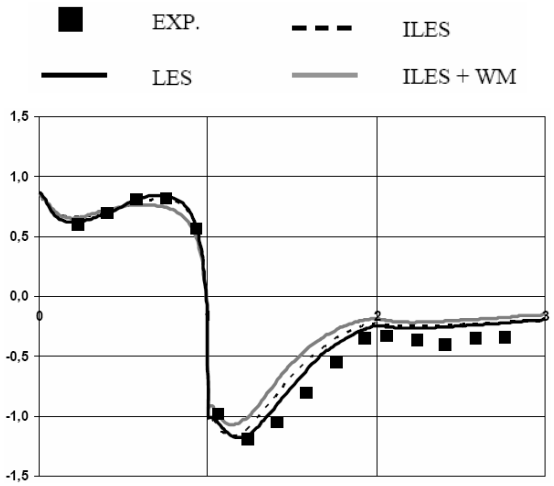

a) Vertical section

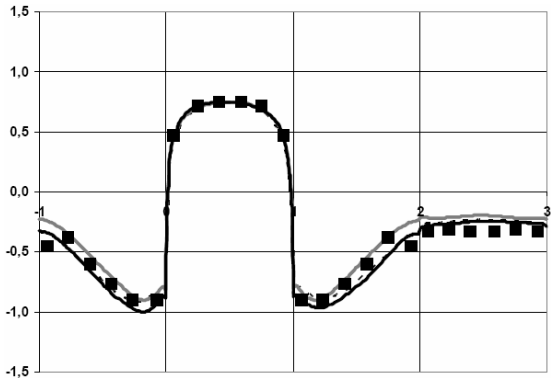

b) Horizontal section

Fig. 12. Cubical building in ABL. Pressure coefficient profiles on the vertical and horizontal sections. LES and ILES results on mesh B.

5. CONCLUSIONS

Based on the results of the wind tunnel experiment, our expectation was that the DES SST model would again perform the best for the cubical building in the atmospheric boundary layer. This is not what we observe. The results of the hybrid RANS/LES simulations are poor and almost equal to the results of the steady state RANS simulations (figures 9 and 10). The main reason for the poor predictions is that the grids which we use are not fine enough for hybrid simulations. Plotting the relative DES length scale reveals that the LES region is very small and is located in the wake of the building. So, there is very low LES activity. One could make use of much finer grids. This would lead to better predictions but at a very large computational cost. This is what we try to avoid here. It is remarkable that we obtain good results on coarse grids with the LES approach. With LES, we also observe only little sensitivity to the quality of the predicted pressure distribution from grid resolution in wall vicinity and from the wall stress calculation method. Clearly, for practical prediction of the pressure distribution on real size buildings, LES is recommended.

ACKNOWLEDGEMENTS

The authors acknowledge the support from the research project ‘Heat, air and moisture performance engineering’ (IWT, contract: HAM SBO 050154)

REFERENCES

[1] Rodi, W., 1997, “Comparison of LES and RANS Calculations of the Flow Around Bluff Bodies”, J. Wind Eng. Ind. Aerodyn., 69–71, pp. 55–75.

[2] Roy, C. J., DeChant, L. J., Payne, J. L., Blottner, F. G., 2003, Bluff-Body Flow Simulations using Hybrid RANS/LES, AIAA Paper 2003-3889

[3] Richards, P.J., Hoxey, R.P., Short, J.L., 2001. Wind pressures on a 6m cube. J. Wind Eng. Ind. Aerodyn. 89 (14–15), 1553–1564.

[4] Richards, P.J., Hoxey, R.P., 2002a, Unsteady flow on the sides of a 6m cube. J. Wind Eng. Ind. Aero. 90 (12), 1855–1866.

[5] Yoshizawa, A., Bridging between eddy–viscosity–type and second order model using a two–scale DIA, 9th Symp. On turbulent Shear Flow, Kyoto, 3, 23.1.1–23.1.6. 1993.

[6] Fureby, C., 1999, Large eddy simulation of rearward–facing step flow, AIAA Journal, Vol. 37, No. 11, 1999.

[7] Lilly, D. K., A proposed modification of the Germano sub–grid scale closure method, 1192, Physics of Fluids, Vol. 4, pp. 633–635

[8] Kim, W.–W., Menon, S., Application of the localized dynamic sub–grid scale model to turbulent wall–bounded flows, Technical Report AIAA–97–0210, American Institute of Aeronautics and Astronautics, 35th Aerospace Sciences Meeting, Reno, NV, January 1997

[9] Popovac, M., Hanjalic, K., 2007, Compound Wall Treatment for RANS Computation of Complex Turbulent Flows and Heat Transfer, Flow, Turbulence and Combustion, Vol. 78, pp. 177–202

[10] Martinuzzi, R., Tropea, C., 1993, The Flow around Surface–Mounted, Prismatic Obstacles Placed in a Fully Developed Channel Flow, Journal of Fluids Engineering, Vol. 115, pp. 85–92

Scale-separation and variational multiscale methods coupled to a stabilized finite element formulation for large eddy simulation of incompressible and turbulent flows

M. Rasquin[12], K.E. Jansen[3], G. Degrez[12]
[1]Université Libre de Bruxelles, Department of Aero-Thermo-Mechanics
CP 165/41, 50 Avenue F. D. Roosevelt, 1050 Brussels - Belgium
[2]von Karman Institute for Fluid Dynamics, Aeronautics and Aerospace Department
72 Chaussée de Waterloo/Waterloosesteenweg, 1640 Rhode-St-Genèse/Sint-Genesius-Rode - Belgium
[3]Rensselaer Polytechnic Institute, Scientific Computation Research Center
Center for Industrial Innovation 7011, 110 Eighth Street, 12180 Troy NY - USA
email: michel.rasquin@ulb.ac.be, jansen@rpi.edu, gerard.degrez@ulb.ac.be

Abstract— **In this study, constant-coefficient-based Smagorinsky models for large eddy simulation of turbulent flows are considered under different formulations. This includes a classical version of the Smagorinsky model and several scale-separation formulations where the resolved velocity field is filtered in order to separate the small turbulent scales from the large ones. From this separation of turbulent scales, the strain rate tensor and/or the eddy viscosity of the subgrid stress tensor is computed from the small scales only. Finally, one variational multiscale (VM) method is analyzed. In addition to the eddy viscosity and strain rate tensor based on the small scales, this VM method implies the projection of shape functions in a subspace related to the small scales These large eddy simulation models are developed within the context a massively parallel $3D$ stabilized finite element code called PHASTA which is able to simulate full $3D$ turbulent and incompressible flows on unstructured meshes. Finally, the relevance of our models is assessed with the large eddy simulation of a fully developed turbulent channel flow under statistical equilibrium. Comparisons in terms of mean velocity and mean shear stresses are performed with a fully resolved direct numerical simulation as a reference.**

Keywords— **turbulence modeling, large eddy simulation, scale-separation methods, variational multiscale method, finite element, channel flow**

I. Introduction

TURBULENCE remains one of the great science and engineering challenges of our day. Challenging applications with turbulent flows range from aerospace to energy to even flow within arteries and respiratory system just to name a few. Because of the non-linear properties of the Navier-Stokes equations which govern the motion of any fluid flow, very few problems of practical interest can be described by analytical means. Experimental studies and new measurement techniques (Laser-Doppler and Particle Image Velocimetry, ...) have given great insight in the understanding of the structure of turbulent flows but these experiments are not always easy to implement for fluid flows of practical interest. Over the last decades, a significant contribution to this progress is due to the development of advanced numerical simulation methods for turbulent flows. Unfortunately, turbulent flows provide a range of scales that is too large to be completely resolved, even on the latest supercomputers available. Consequently, accurate models of turbulent flows are still required to correctly predict their behavior and properties.

II. Turbulence Modeling

Currently, the simulation of turbulent flows can be performed with four different approaches.

- The Direct Numerical Simulation (DNS) where all turbulence length scales and frequencies in the flow are resolved. This approach requires the unsteady Navier-Stokes equations to be solved on highly refined meshes and over a considerable number of small time steps. Therefore, this approach is limited to simple configurations and low Reynolds number applications.
- Large Eddy Simulation (LES) where only the large turbulence length scales are fully resolved whereas smaller ones are accounted for using a subgrid scale model. Computations of flows at higher Reynolds numbers are allowed with LES but the requirements in terms of meshes and time steps remain considerable. Such simulations can be accomplished only by using state-of-the-art numerical methods and supercomputing facilities.
- Reynolds-Averaged Navier-Stokes Simulation (RANSS) where no turbulent motions are resolved. All are modeled, though the mean can be unsteady on time scales clearly smaller than those of turbulence.
- Detached Eddy Simulation (DES), which is basically a LES in regions where it is applicable and a

RANSS elsewhere (e.g. in the boundary layer).
The objective of this work is the development of the promising variational multiscale LES models presented in the next section. Finally, it is thought that the gain of experience in new LES approaches will contribute in the future to the improvement of RANSS and DES models as well, which are the most widespread turbulence models for the computation of most practical engineering problems.

III. Finite Element Formulation

The unsteady and incompressible Navier-Stokes equations are considered in this work. The strong form of the continuity and momentum equations are recalled in Eq. 1

$$\begin{aligned} u_{i,i} &= 0 \\ u_{i,t} + u_j u_{i,j} &= -P_{,i} + \tau_{ij,j} + f_i \end{aligned} \tag{1}$$

where u_i is the i^{th} component of the velocity, P the kinematic pressure (pressure divided by density), f_i the prescribed body force and τ_{ij} the viscous stress tensor given by:

$$\tau_{ij} = \nu \underbrace{(u_{i,j} + u_{j,i})}_{2\,S_{ij}} \tag{2}$$

with ν the kinematic viscosity. The semi-discrete, stabilized, Galerkin finite element formulation of the Navier-Stokes equations implemented in PHASTA is then derived in Eq. 3

$$B(w_i, q\,;\, u_i, P) = 0 \tag{3}$$

with $B(w_i, q\,;\, u_i, P) =$

$$\begin{aligned} &\int_\Omega \{w_i\,(u_{i,t} + u_j u_{i,j} - f_i) + \\ &\qquad w_{i,j}\,(-P\delta_{ij} + \tau_{ij}) - q_{,i} u_i\} dx \\ &+ \int_{\Gamma_h} \{w_i\,(P\delta_{in} - \tau_{in}) + q u_n\} ds \\ &+ \sum_{e=1}^{nel} \int_{\Omega_e} \{\tau_M\,(u_j w_{i,j} + q_{,i}) L_i + \tau_C w_{i,i} u_{j,j}\} dx \\ &+ \sum_{e=1}^{nel} \int_{\Omega_e} \{w_i \widehat{u}_j u_{i,j} + \overline{\tau}\,\widehat{u}_j w_{i,j} \widehat{u}_k u_{i,k}\} dx \end{aligned} \tag{4}$$

In Eq. 3, w_i is the shape function associated to the i^{th} momentum equation, q is the shape function associated to the continuity equation, L_i is the residual of the i^{th} momentum equation, i.e.

$$L_i = u_{i,t} + u_j u_{i,j} + P_{,i} - \tau_{ij,j} - f_i \tag{5}$$

and $\widehat{u}_i = -\tau_M L_i$. The fourth line is the stabilization added to the Galerkin formulation of the incompressible Navier-Stokes equations and the fifth line is the correction of the momentum equations due to stabilization term in the continuity equation. It should be pointed out that integration by parts has been used on the pressure and viscous stress tensor terms. More information about this discretization are available in [1], [2].

IV. Large Eddy Simulation

A. Classical Formulation

In classical LES, the Navier-Stokes equations in Eq. 1 are spatially filtered, leading to Eq. 6.

$$\begin{aligned} \widetilde{u}_{i,i} &= 0 \\ \widetilde{u}_{i,t} + \widetilde{u}_j \widetilde{u}_{i,j} &= -\widetilde{P}_{,i} + \widetilde{\tau}_{ij,j} + \widetilde{f}_i + (\underbrace{\widetilde{u}_j \widetilde{u}_j - \widetilde{u_i u_j}}_{\text{Reynolds stress}})_{,j} \end{aligned} \tag{6}$$

These filtered Navier-Stokes equations govern the motion of the largest and energy-carrying scales of the flow, while the subgrid Reynolds stress term accounts for the effect of the unresolved small scales on the resolved ones. This term gives rise to a closure problem and must be modeled through a subgrid scale model. In practice, for a finite element discretization, the filtering operator $(\widetilde{\cdot})$ is implicit and linked to the resolution of the grid which is not able to capture turbulent scales smaller than a certain characteristic length $\triangle$. Most of the subgrid scale models in use are eddy-viscosity models of the form

$$\widetilde{u}_i \widetilde{u}_j - \widetilde{u_i u_j} = \tau_{ij}^{sgs} = 2\,\nu_t\,\widetilde{S}_{ij} \tag{7}$$

with

$$\widetilde{S}_{ij} = \frac{1}{2}(\widetilde{u}_{i,j} + \widetilde{u}_{j,i}) \tag{8}$$

For the sake of clarity, this implicit filtering operator symbol $(\widetilde{\cdot})$ is dropped in what follows.
ν_t is the turbulent eddy viscosity and several definition have been proposed for this term. One of the most common definitions in use is the Smagorinsky model, where

$$\nu_t = (C_{sgs} \triangle)^2 \sqrt{2\,S_{mn} S_{mn}} \tag{9}$$

C_{sgs} is a constant and $\triangle$ is a characteristic length of the mesh. Lilly [3] evaluated the value of the C_{sgs} constant to 0.18 while Deardorff [4] found that this coefficient must be reduced to 0.1 in the presence of shear.
In addition, it is well known that turbulence features a cascade process by which kinetic energy is transfered from the large turbulent scales to the smaller ones [5].

Below a certain size, the smallest structures are dissipated into heat because of the effect of the viscous term in the Navier-Stokes equations. In the classical formulation of LES models, all the resolved scales are used to model the contribution of the unresolved scales. However, most of the energy exchanges between scales are local [6], [7], which means that the energy of the unresolved scales derives mainly from the energy of the small resolved scales. Scale-separation models use this observation to improve the traditional Smagorinsky model. In practice, they are based on the assumption that the most active subgrid scales are those closer to the cutoff $\triangle$, and that the scales with which they interact the most are those right above the cutoff [8]. An operator $(\bar{\cdot})$ to separate the small resolved scales from the large resolved scales is therefore needed for this kind of model. This operator is illustrated in Eq. 10

$$u^{'} = u - \overline{u} \tag{10}$$

where u is the total velocity field (large and small resolved scales), $\overline{u}$ is the filtered velocity field (large resolved scales) and $u^{'}$ is small-scales resolved field. From Eq. 10, it is possible to compute the eddy viscosity ν_t and the strain rate tensor S_{ij} based either on the small resolved scales or all the scales. Two combinations presented in Eq. 11 and Eq. 12 are tested in the next sections, i.e.

$$\tau_{ij}^{sgs} = 2\,\nu_t^{'}\,S_{ij} = 2\,(C_{sgs}\triangle)^2\sqrt{2\,S'_{mn}S'_{mn}}\,S_{ij} \tag{11}$$

$$\tau_{ij}^{sgs} = 2\,\nu_t^{'}\,S_{ij}^{'} = 2\,(C_{sgs}\triangle)^2\sqrt{2\,S'_{mn}S'_{mn}}\,S_{ij}^{'} \tag{12}$$

On the implementation point of view, this comes down to adding a subgrid term to the momentum equations under the form

$$(w_{i,j}, \tau_{ij}^{sgs})_\Omega = \int_\Omega w_{i,j}\,\tau_{ij}^{sgs} dx \tag{13}$$

One important advantage of these scale-separation models is that the dissipation they introduce through their subgrid scale stress tensor is better controlled compared to their classical version where all the scales are taken into account without any filtering. The main difficulty of these models is to determine the best strategy to filter the resolved velocity field in order to isolate the small resolved turbulent scales in the context of a full 3D computational fluid dynamics code based on a finite element discretization. This will be the subject of Section V.

B. Variational Multiscale Formulation

The philosophy of the variational multiscale models, first introduced by Hughes, Mazzei and Jansen [9] differs significantly from the philosophy of the scale-separation models. As mentioned above, variational multiscale models are based on the decomposition of *both* the weight and solution spaces according to Eq. 14.

$$\begin{aligned} \{w_i, q\} &= \{\overline{w}_i + w_i^{'}, \overline{q} + q^{'}\} \\ \{u_i, P\} &= \{\overline{u}_i + u_i^{'}, \overline{P} + P^{'}\} \end{aligned} \tag{14}$$

The semi-discrete Navier-Stokes equations described in Eq. 4 are therefore split and written for the large resolved scales of the flow on the one hand, and for the small resolved scales of the flow on the other hand. One can therefore writes

$$B(\overline{w}_i, \overline{q}\,;\, \overline{u}_i + u_i^{'}, \overline{P} + P^{'}) = 0 \tag{15}$$

$$B(w_i^{'}, q^{'}\,;\, \overline{u}_i + u_i^{'}, \overline{P} + P^{'}) = 0 \tag{16}$$

where Eq. 15 gives the evolution for the bar field while Eq. 16 gives the evolution for the prime field. One speaks here about a projection of $\{w, q\}$ and $\{u, P\}$ in a subspace related to the small resolved scales.
In the context of a discretization based on truncated Fourier series with n Fourier modes [10], the bar field relates to low wave number modes k up to mode $\overline{n} < n$ while the prime field relates to high wave number modes k with $\overline{n} < k \leq n$. Similarly, in a finite element discretization using a hierarchical basis of order p [11], the bar field is represented by a complete set of hierarchic modes up to an order $\overline{p}$ while the prime field is represented by hierarchic modes of order greater than $\overline{p}$ and up to p .
In any case, a term responsible for the 'rapidly fluctuating' behavior of the small scales appears in Eq. 16 [9], [11]. This term cannot be accurately computed unless very fine resolution in the discretization is used, leading to a direct numerical simulation. Therefore, modelling of this term is required for a large eddy simulation. On the implementation point of view, the effect of this term is accounted for by adding to the small scales equations an eddy viscosity model inspired by the form of the Smagorinsky model. This results in the following term

$$(w_{i,j}^{'}, \tau_{ij}^{sgs})_\Omega = \int_\Omega w_{i,j}^{'}\,\tau_{ij}^{sgs} dx \tag{17}$$

with τ_{ij}^{sgs} inspired from Eq. 12.
It is important to mention that modeling in the variational multiscale formulation is confined to the small scales equations only, which is outlined by $w_{,j}^{'}$ in Eq. 17. Moreover, it is interesting to notice that modeling does not arise due to a closure problem like for

the classical formulation but to the discretization's inability to capture the smallest of the turbulence scales. To conclude this section, the separation of scales is natural in the context of a discretization based on truncated Fourier series or a finite element discretization using a hierarchical basis. It is less obvious within the context of a finite element code based on piecewise linear shape functions only. In Section V, a projection operator is defined for that purpose as well.

V. Filtering and Projection Strategies

In this section, one filter family and one projector are presented in the context of a stabilized linear finite element discretization.

A. Filter

The filter family presented in this subsection derives from the dynamic model for LES [12], [13] and consists in applying a box or a witch hat filter to extract the large scales from the velocity field. This filtering operator F is derived in Eq. 18

$$\overline{f}_k = \frac{\int_{J_k} N_k(x) f(x) dx}{\int_{J_k} N_k(x) dx} \tag{18}$$

where:
- $\overline{f}_k$ is the filtered function $\overline{f}$ (e.g. $\overline{u}$) evaluated at node k;
- J_k is the union of elements which share node k;
- $N_k(x)$ is a weight function associated to node k ($N_k(x) = 1$ leads to the box or top hat filter while $N_k(x) = w_k(x)$ corresponds to the witch hat filter with $w_k(x)$ being the shape function of the finite element formulation at node k).

$f_k^{'}$ is then derived according to $f_k^{'} = f_k - \overline{f}_k$.

It is also possible to apply this filter F recursively, which will result in smoothing more and more the large resolved scales. This filter is therefore not a projector ($F^2(f) \neq F(f)$) and can be used in scale-separation methods only in order to separate the small-scales resolved features from the large ones, but not as part of a variational multiscale model. The effect of the filter is illustrated in Fig. 1 with harmonic functions on a $2D$ structured and regular mesh with 33×33 nodes. In addition to its capacity to separate small and large scales, its smoothness is also to be outlined.

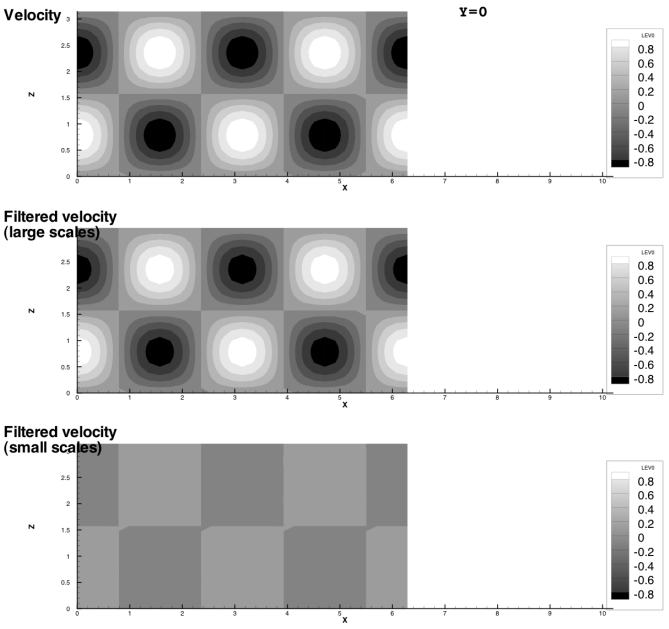

(a) Initial function: $u(x,z) = cos(2x) * sin(2z)$.

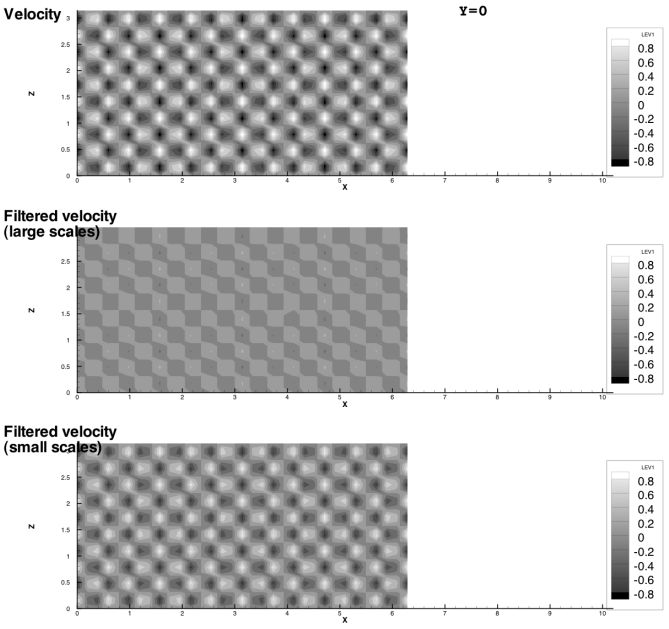

(b) Initial function: $u(x,z) = cos(10x) * sin(10z)$ - Aliasing effect on a 33×33 mesh, which corresponds to a highly fluctuating field at the discrete level.

Fig. 1. Top hat filter - Results for harmonic functions.

B. Projector

The projector P presented in this subsection allows the projection of *both* the velocity field and the shape functions related to the weak formulation of the Galerkin finite element method in a subspace related to the small scales, which is at the core of the variational multiscale approach. This projector, initially described by Koobus and Farhat [14], [15], is based on a node agglomeration procedure to separate *a priori* the scales. For any finite element mesh, a

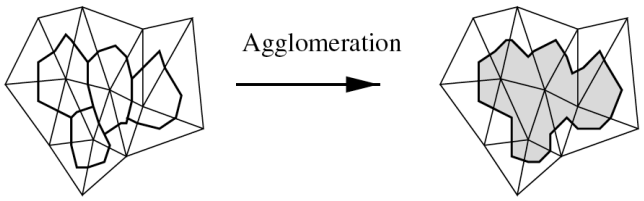

Fig. 2. Unstructured mesh, dual mesh and agglomeration of some nodal cells of the dual mesh into a macro-cell (Koobus and Farhat).

corresponding dual mesh defined by nodal cells can always be derived. These cells can be partitioned and clustered together to form macro-cells according to an agglomeration process. From this process illustrated in Fig. 2, a projection operator for the large scales is derived in Eq. 19,

$$\overline{f}_k = \frac{\sum_{j \in I_k} Vol(C_j) f_j}{\sum_{j \in I_k} Vol(C_j)} \tag{19}$$

where
- $\overline{f}_k$ is the projected function $\overline{f}$ evaluated at node k;
- f_j is the non-projected function f at node j;
- C_j is the nodal cell around node j;
- $Vol(C_j)$ is the volume of cell C_j;
- $I_k = \{j \wr C_j \subset C_{m(k)}\}$;
- $C_{m(k)}$ is the macro-cell containing cell C_k.

The projection of f_k in a subspace related to the small scales is obtained by $f_k^{'} = f_k - \overline{f}_k$.

The effect of this projector is illustrated in Fig. 3 with the same harmonic functions as in Fig. 1. Every aggregate in this $2D$ example has a regular and rectangular shape and includes four nodes. This makes 256 aggregates on the 33×33 mesh used in Fig. 1 and Fig. 3. It can be observed that the separation of scales is less smooth for this projector than for the top hat filter. Indeed, the projector defined in Eq. 19 is based on a discretization and not on an integral. However, its primary objective is achieved, namely the projection of the velocity field in a subspace related to large and small scales. The projector defined in Eq. 19 also verifies $P^2(f) = P(f)$, which is the first condition required for the construction of a variational multiscale model. At this point, this projector can be used in the context of a scale-separation model, like for the top hat or witch hat filter, as illustrated in the next section. However, the projection of the shape functions in a subspace related to the small-scales equations is still needed for a variational multiscale method. Going back to the finite element formulation applied to

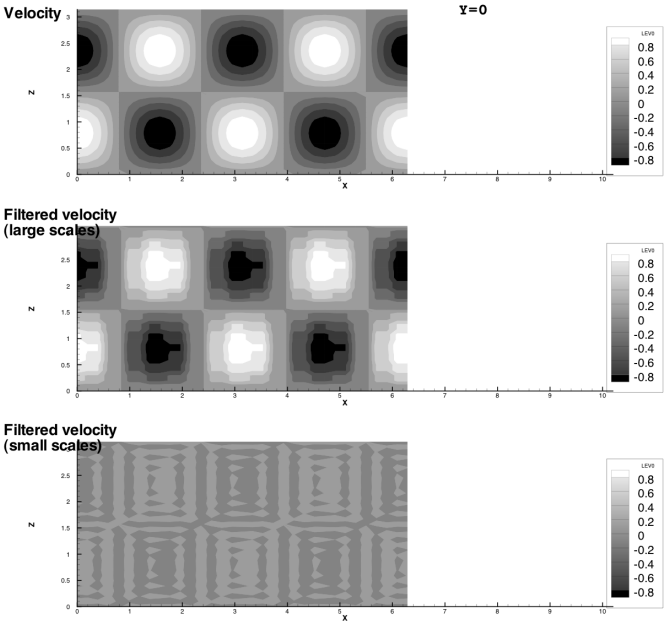

(a) Initial function: $cos(2x) * sin(2z)$.

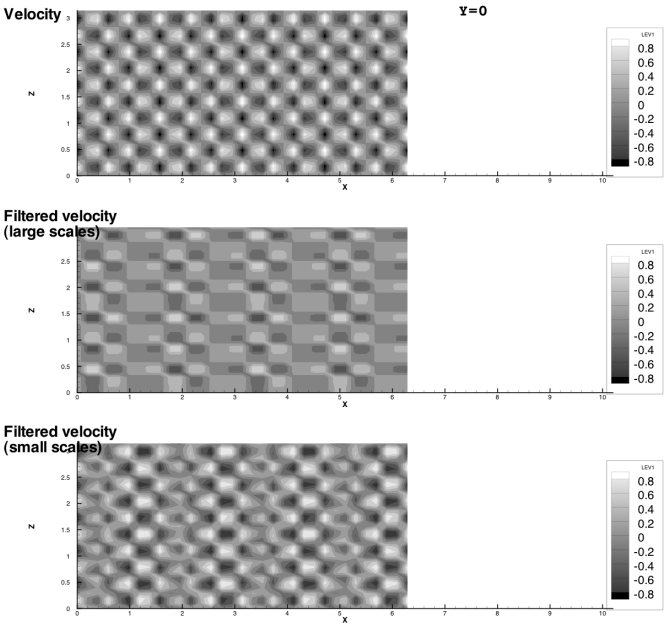

(b) Initial function: $cos(10x) * sin(10z)$ - Aliasing effect on a 33×33 mesh, which corresponds to a highly fluctuating field at the discrete level.

Fig. 3. Aggregation-based projector - Results for harmonic functions.

a mesh with n nodes, the continuous function f (i.e. u or P) can be written as the sum of the value of f at node k weighted by the shape function w_k.

$$f = \sum_{k=1}^{n} w_k f_k \tag{20}$$

It is then natural to write the continuous projected function $\overline{f}$ as

$$\overline{f} = \sum_{k=1}^{n} w_k \overline{f}_k \tag{21}$$

with $\overline{f}_k$ defined in Eq. 19.
After some algebra, one can rewrite

$$\overline{f} = \sum_{k=1}^{n} \overline{w}_k f_k \tag{22}$$

with

$$\overline{w}_k = \frac{Vol(C_k)}{\sum_{j \in I_k} Vol(C_j)} \sum_{j \in I_k} w_j \tag{23}$$

Eq. 23 defines some new interpolation functions $\overline{w}_k$ over the macro-cells $C_{m(k)}$ which are associated to the large-scales equations. Similarly to $f_k^{'}$, the shape functions associated to the small-scales equations is obtained by

$$w_k^{'} = w_k - \overline{w}_k \tag{24}$$

Finally, it is not possible to split the Navier-Stokes equations according to Eq. 15 and Eq. 16 in the context of a piecewise linear finite element code. Therefore, a term $(w_{i,j}^{'}, \tau_{ij}^{sgs})_\Omega$ is directly added to the momentum equation described in Eq. 4.

VI. Results

A. Channel Flow Test Case

Large eddy simulations of the $3D$ unsteady and turbulent channel flow is considered in this work and results are compared with the direct numerical simulation of Kim, Moin and Moser as a reference [16] [17]. The Reynolds number is

$$Re_\tau = \frac{u_\tau h}{\nu} = 392 \quad \text{with} \quad u_\tau = \sqrt{\frac{\tau_w}{\rho}} \tag{25}$$

Computations are performed on a $33 \times 65 \times 33$ mesh. Grid points in the y direction are clustered near the wall via a hyperbolic mapping function [18]. The dimensions of the domain are $L_x = 2\pi$, $L_y = 2h$ ($h = 1$) and $L_z = \pi$. This test case is illustrated in Fig. 4 and the mesh is presented in Fig. 5(a). The grid points in the x and z directions are uniformly spaced while the first grid point in the y direction is positioned at $\Delta y_1^+ = \frac{u_\tau \Delta y_1}{\nu} = 1$. Periodic boundary conditions are applied in the x and z directions while a constant body force term is added in x-momentum of the Navier-Stokes equations in order to force the flow through the channel. This body force control allows the mass flow to vary from time step to time step in such a way that the body force is correctly counterbalanced by the friction at the wall. From a force balance applied to the channel, one gets

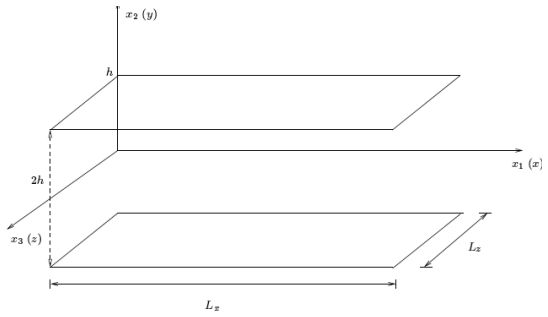

Fig. 4. Sketch of the channel flow.

$$force = \frac{\tau_w}{h} = \rho \frac{(Re_\tau\, \nu)^2}{h^3} \tag{26}$$

An alternative to body force control is mass flow control for which the body force is adjusted at each time step in such a way that the mass flow remains constant. Body force control is straightforward to implement compared to mass flow control but requires in general more time steps before converged turbulence statistics can be obtained. In this study, computations are restarted from fully developed channel flow and turbulence statistics are performed for about sixty flow through times.

B. Turbulence Models

Five configurations of turbulence models have been tested in this work. They all derive from the Smagorinsky model and include

- one classical formulation for which all the resolved scales (small and large) are used to compute both the eddy viscosity and strain rate tensor of the subgrid stress tensor;
- one scale-separation model based on a top hat filter described in Subsection V-A;
- two scale-separation models and one variational multiscale model based on the aggregation projector presented in Subsection V-B .

For the sake of brevity and following the abbreviation rules presented in Table I, these five models are named

- 'SmagoAANP';
- 'SmagoSANP top hat';
- 'SmagoSANP agg', 'SmagoSSNP agg' and 'SmagoSSP agg'.

'AANP' refers to the classical formulation, with all the resolved scales used to compute both the eddy viscosity and strain rate tensor and no projection of

the shape functions. 'SSP' refers to the variational multiscale formulation, with (1) both the eddy viscosity and strain rate tensor computed from the velocity field projected in a subspace related to the small scales and (2) the shape functions projected in a small-scales subspace as well. 'SANP' and 'SSNP' both refer to scale-separation models with the eddy viscosity and strain rate tensor computed according to Table I. Note that there is no difference in the expression of the strain rate tensor and the eddy viscosity between 'SSNP' and 'SSP'. The only difference between these two comes from the difference in the solution.

TABLE I
ABBREVIATIONS FOR LES MODELS SUMMARIZING THE SCALES USED TO COMPUTE THE EDDY VISCOSITY (SMALL OR ALL), THE STRAIN RATE TENSOR (SMALL OR ALL) AND THE SHAPE FUNCTIONS (PROJECTED OR NOT).

	Eddy visc.	Strain tensor	Shape func.
AANP	All: ν_t	All: S_{ij}	No Proj.: w_k
SANP	Small: $\nu_t^{'}$	All: S_{ij}	No Proj.: w_k
SSNP	Small: $\nu_t^{'}$	Small: $S_{ij}^{'}$	No Proj.: w_k
SSP	Small: $\nu_t^{'}$	Small: $S_{ij}^{'}$	Proj.: $w_k^{'}$

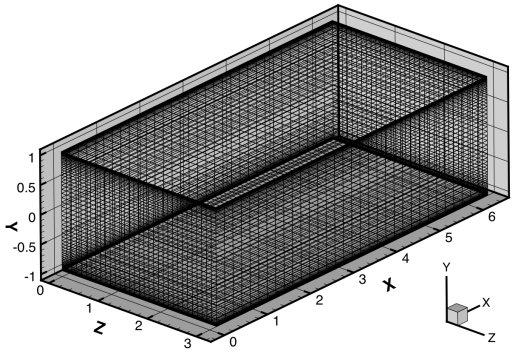

(a) Hexahedral finite elements mesh

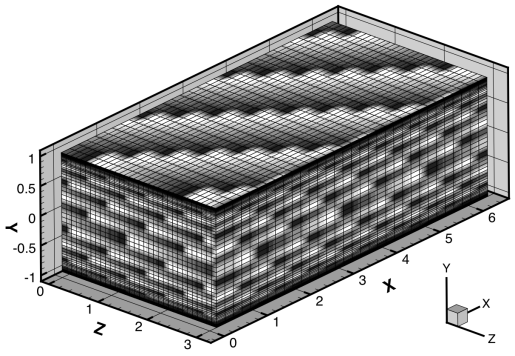

(b) Eight nodes hexahedral aggregates - Each color zone represents an aggregate of nodes

Fig. 5. Mesh and hexahedral aggregates for a $3D$ channel flow.

Similarly to the $2D$ example presented in Fig. 1 and Fig. 3, $3D$ regular and hexahedral aggregates are used for the aggregation projector. These brick-shape aggregates are illustrated in Fig. 5(b).
For all models, the Smagorinsky constant $C_{sgs} = 0.1$ and a Van Driest damping function is used in order to reduce the contribution of the LES subgrid term near the walls. The eddy viscosity becomes thereby

$$\nu_t \Rightarrow \nu_t \left(1 - exp(\frac{-y^+}{A^+})\right)^3 \qquad (27)$$

with

$$y^+ = \left(1 - |\frac{y}{h}|\right)\frac{u_\tau h}{\nu} \quad \text{and} \quad A^+ = 26 \qquad (28)$$

Finally, it should be mentioned that the stabilization parameter τ_M in Eq. 4 has been reduced so that the stabilization terms in Eq. 4 stabilize indeed the piecewise linear finite element formulation but do not play any LES-type model role. Indeed, it is possible to obtain good results with an unresolved stabilized direct numerical simulation of a channel flow just by tuning these stabilization parameters (see [18]).

C. Turbulence Statistics

The eddy viscosity, the stresses and the velocity profiles are analyzed in this subsection. In Fig. 6(a), one can observe that the eddy viscosity of the classical Smagorinsky model ('SmagoAANP') has the same order of magnitude as for the models based on the aggregation projector ('SmagoSANP agg', 'SmagoSSNP agg','SmagoSSP agg') while the scale-separation model based on a top hat filter ('SmagoSANP top hat') leads to a smaller value. However, the lack of smoothness of the aggregation projector is visible, like in Fig 3. The effect of the Van Driest damping is also outlined in Fig. 6(b). Without this near-wall treatment, neither scale-separation models nor variational multiscale models derived from the Smagorinsky model are able to predict correctly the asymptotic behavior of the eddy viscosity near the wall. Indeed, it was observed in this case that ν_t/ν would tend to one near the wall for all the configurations tested in this section.
The viscous stress, Reynolds stress and total stress are plotted in Fig. 7. All models are close to the resolved DNS of Kim, Moin and Moser ('KMM') [16]. The curves of the stabilized unresolved DNS as well as the 'SmagoSSNP agg' and 'SmagoSSP agg' models are even superimposed with the DNS results of KMM. Although they are close, the 'SmagoSANP agg' and

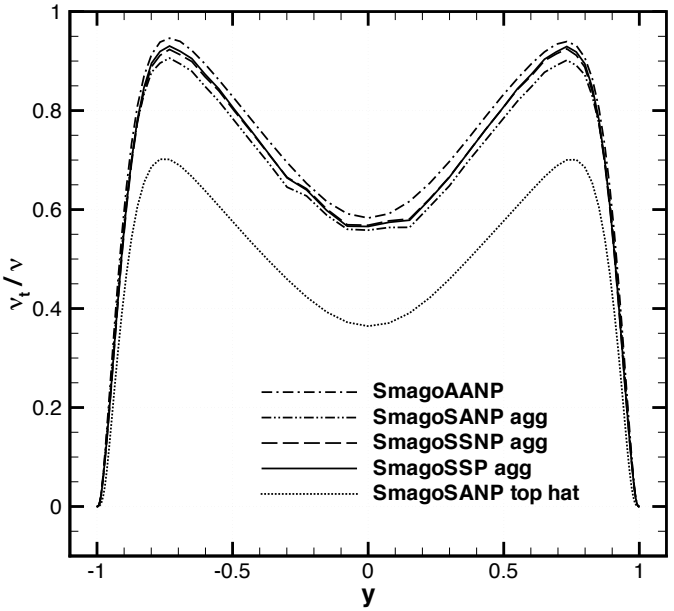

(a) Eddy viscosity profile through the channel flow

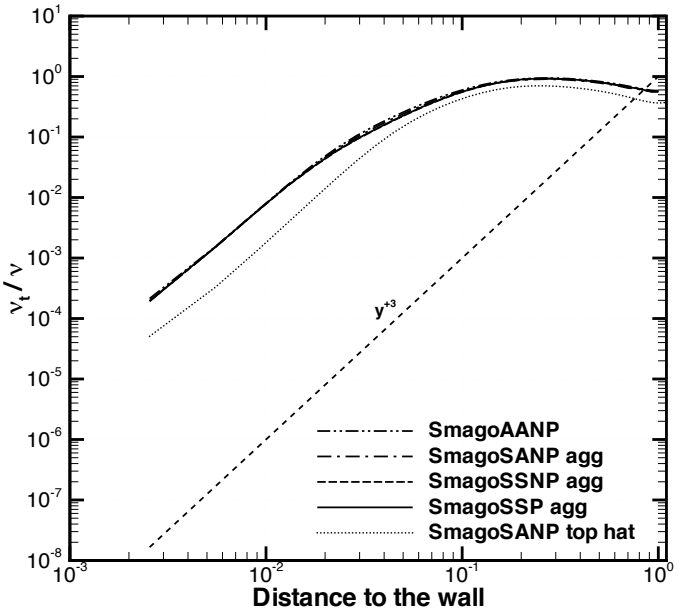

(b) Eddy viscosity profile in the boundary layer

Fig. 6. Mean Eddy viscosity profile.

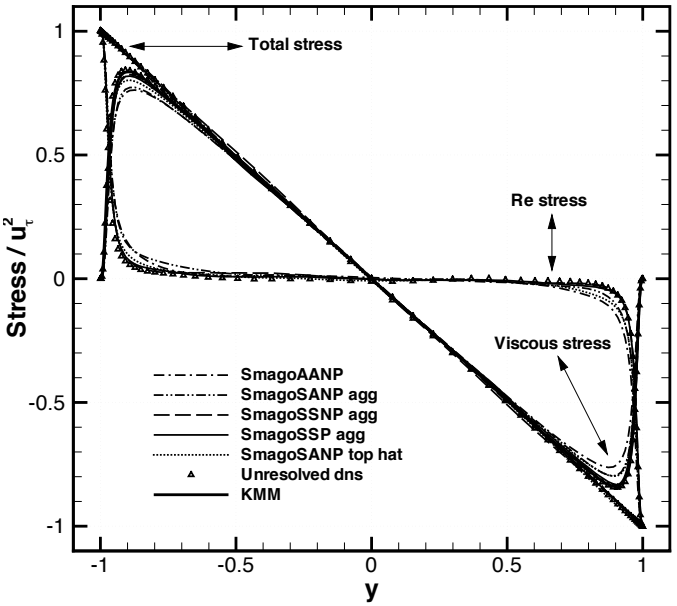

Fig. 7. Viscous stress, Reynolds stress and total stress.

'SmagoAANP' models are the less accurate. This is not surprising since the flow is controlled with a constant body force term, ensuring the correct stress at the wall. In the case of body force control, the relevance of turbulence models is therefore assessed with the analysis of velocity profiles.

Velocity profiles through the channel flow and in the boundary layer are shown in Fig. 8(a) and Fig. 8(b) respectively. Since a body force control is applied, the linear viscous sublayer close to the wall is correctly predicted by the stabilized unresolved DNS and all LES models. Nevertheless, the stabilized unresolved DNS is lacking dissipation while the classical formulation of the Smagorinsky model is on the contrary too dissipative, leading respectively to under and over prediction of the velocity profiles in the buffer and logarithmic layers. The 'SmagoSANP agg' model starts deviating at the beginning of the logarithmic layer. The velocity profiles for the 'SmagoSSNP agg' and 'SmagoSSP agg' are nearly superimposed and start diverging later than the 'SmagoSANP agg' model (namely in the middle of the logarithmic layer) but they are both characterized by some oscillations. These oscillations are clearly due to the aggregates since the wave length of these oscillations coincides with the height of the aggregates in the y direction. The best results have been obtained with the 'SmagoSANP top hat', which correctly predicts the logarithmic layer and starts diverging at the beginning of the wake region. Finally, all these models fail to predict correctly the wake in the middle of the channel, which is usual for LES models applied to the channel flow test case.

D. Notes on the Aggregation Projector

As mentioned in the previous subsection, the shape of the aggregates is an important factor in the aggregation-based variational multiscale method coupled to a piecewise linear finite element discretization. Before using regular brick-shape aggregates as illustrated in Fig. 5(b), a mesh partitioner (METIS pack-

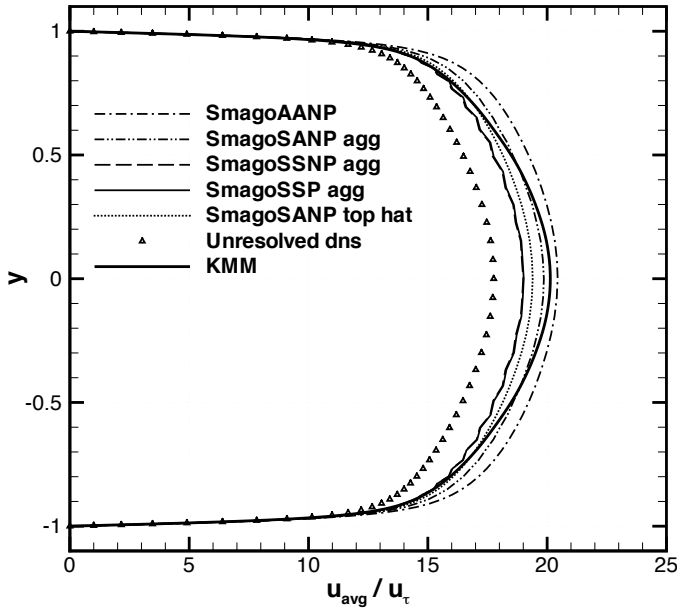

(a) Velocity profile through the channel flow

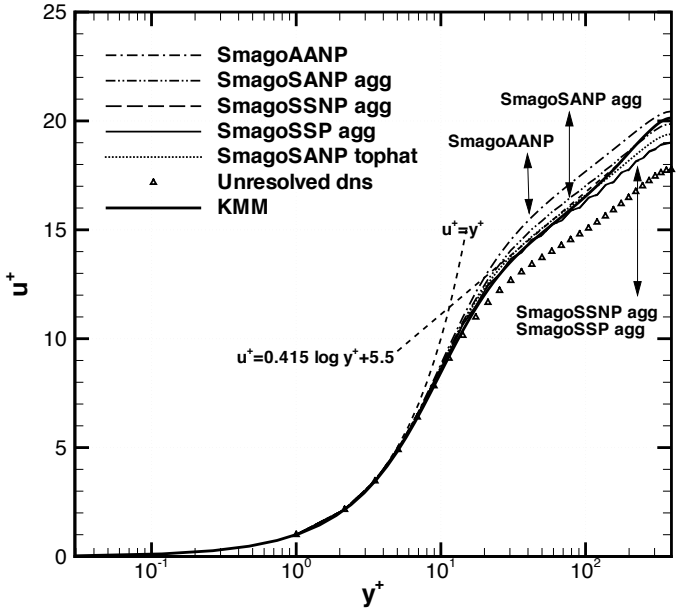

(b) Velocity profile in the boundary layer

Fig. 8. Mean velocity profile.

age) was called to cluster the nodes of the structured hexahedral mesh shown in Fig. 5(a). Most of the aggregates formed with this technique had a $3D$ irregular shape. Some of them had a $2D$ planar shape and were therefore missing the flow features in one direction, leading to divergence of the computation. The three-dimensionality of the aggregates is therefore a key parameter.

Moreover, $3D$ structured brick-shape aggregates seems to leave a signature characterized by spatial oscillations in the turbulence statistics. In order to avoid these oscillations, one solution proposed in this work may consist in choosing randomly at each time-step one aggregation map from a library of different maps. This requires the construction of several aggregation maps instead of one but this may help to avoid the footprint observed in the turbulence statistics. In addition, it should be added here that Koobus and Farhat used the aggregation projector defined in Eq. 19 as part as an unstructured tetrahedral finite volume discretization. It would be interesting to test this method on unstructured tetrahedral finite elements as well and check whether these oscillations are due to the structure of the mesh.

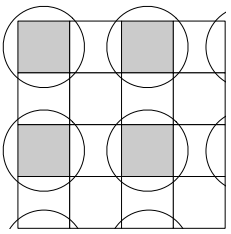

Fig. 9. $2D$ example of a structured mesh (squares: finite elements ; circles: aggregates). Grey finite elements and aggregates own the same nodes, leading to $w'_{,j} = w_{,j}$ in the grey regions.

Finally, no significant difference have been observed between 'SmagoSSNP agg' and 'SmagoSSP agg'. The projection of the shape functions in a subspace related to the small-scales equations does not improve the turbulence statistics in our study. This may be explained again by the structured hexahedral aggregates used in this work. Indeed, $\overline{w}_k$ remains constant for all nodes k that belong to the same aggregate [14]. Since some hexahedral finite elements own exactly the same nodes as some aggregates, $\overline{w}_{,j} = 0$ on these finite elements, leading to $w'_{,j} = w_{,j}$ in Eq. 17. This situation is illustrated Fig. 9. In conclusion, the influence of the projection of the shape functions is less important in the case of structured hexahedral aggregates associated to a structured hexahedral finite element mesh. Again, an unstructured mesh and/or unstructured aggregates may lead to better results.

VII. Conclusions

An aggregation-based variational multiscale (VM) method coupled to a stabilized piecewise linear finite element discretization has been presented in this work for large eddy simulations of turbulent flows. The projector used in the VM method, originally introduced by Koobus and Farhat [14], has shown rela-

tively good results for the channel flow test case. However, some oscillations in the velocity profiles have been observed. These oscillations are thought to be due to the coupling between the structured hexahedral finite element mesh and the structured hexahedral aggregates. Suggestions have been made in Subsection VI-D to remove these oscillations and unstructured meshes might be one answer. Moreover, the importance of the three-dimensionality of the aggregates has also been outlined.

A scale-separation LES model based on a top hat filter has also been implemented. Thanks to this filter, the large and the small resolved scales of the velocity field can be separated. In our particular model, the eddy viscosity is computed from the small scales while the strain rate tensor is based on all the scales. Among all the models tested in this work, this simple LES model has shown the best results so far in terms of velocity profile. No oscillations were observed but unlike the aggregation projector, the top hat filter is not based on a discretization and is therefore much smoother.

In conclusion, variational multiscale methods and their mathematical framework have shown very promising results when coupled to discretizations that naturally lead to a decomposition of the Navier-Stokes equations into large-scales and small-scales equations (finite elements with a hierarchical basis [11], truncated Fourier series [10]). But applying this method in the context of a stabilized piecewise linear finite element discretization still needs some additional developments.

Acknowledgements

The first author is supported by a FRIA fellowship from the French Community of Belgium. As part of this work, an eight months research stay at Rensselaer Polytechnic Institute (RPI) was made possible thanks to a first travelling fellowship granted by the French Community of Belgium. Last but not least, the first author also acknowledges with gratitude the Scientific Computation Research Center (SCOREC) at RPI for its welcome, for its computer resources made available and for its complementary grant.

References

[1] L.P. Franca and S.L. Frey, "Stabilized finite element methods. ii: The incompressible navier-stokes equations," *Computer Methods in Applied Mechanics and Engineering*, vol. 99, no. 209, pp. 233, 1992.

[2] C.H. Whiting and K.E. Jansen, "A stabilized finite element method for the incompressible Navier-Stokes equations using a hierarchical basis," *International Journal for Numerical Methods in Fluids*, vol. 35, no. 1, pp. 93–116, 2001.

[3] D.K. Lilly, "The representation of small-scale turbulence in numerical simulation experiments," in *Proc. IBM Scientific Computing Symposium on Environmental Sciences*, 1967, vol. 195.

[4] J.W. Deardorff, "A numerical study of three-dimensional turbulent channel flow at large Reynolds numbers," *Journal of Fluid Mechanics Digital Archive*, vol. 41, no. 02, pp. 453–480, 2006.

[5] D. Carati, "Large-eddy simulation for turbulent flows: from mathematical foundations to practical applications," *Thèse d'agrégation, Université Libre de Bruxelles*, 2001.

[6] R.H. Kraichnan, "Eddy viscosity in two and three dimensions," *Journal of the Atmospheric Sciences*, vol. 33, no. 8, pp. 1521–1536, 1976.

[7] J.A. Domaradzki, W. Liu, and M.E. Brachet, "An analysis of subgrid-scale interactions in numerically simulated isotropic turbulence," *Physics of Fluids A: Fluid Dynamics*, vol. 5, pp. 1747, 1993.

[8] J. Bardina, J.H. Ferziger, and R.S. Rogallo, "Effect of rotation on isotropic turbulence: computation and modelling," *Journal of Fluid Mechanics Digital Archive*, vol. 154, pp. 321–336, 2006.

[9] T.J.R. Hughes, L. Mazzei, and K.E. Jansen, "Large Eddy Simulation and the variational multiscale method," *Computing and Visualization in Science*, vol. 3, no. 1, pp. 47–59, 2000.

[10] T.J.R. Hughes, L. Mazzei, A.A. Oberai, and A.A. Wray, "The multiscale formulation of large eddy simulation: Decay of homogeneous isotropic turbulence," *Physics of Fluids*, vol. 13, pp. 505, 2001.

[11] K.E. Jansen and A.E. Tejada-Martínez, "An evaluation of the variational multiscale model for large-eddy simulation while using a hierarchical basis.," in *40th AIAA Annual Meeting and Exhibit*, Reno, NV, 2002, number 2002-0283.

[12] M. Germano, U. Piomelli, P. Moin, and W.H. Cabot, "A dynamic subgrid-scale eddy viscosity model," *Physics of Fluids A: Fluid Dynamics*, vol. 3, pp. 1760, 1991.

[13] A.E. Tejada-Martínez and K.E. Jansen, "Spatial test filters for dynamic model large-eddy simulation on finite elements," *Communications in Numerical Methods in Engineering*, vol. 19, pp. 205–213, 2003.

[14] B. Koobus and C. Farhat, "A variational multiscale method for the large eddy simulation of compressible turbulent flows on unstructured meshes—-application to vortex shedding," *Computer Methods in Applied Mechanics and Engineering*, vol. 193, no. 15-16, pp. 1367–1383, 2004.

[15] C. Farhat, A. Rajasekharan, and B. Koobus, "A dynamic variational multiscale method for large eddy simulations on unstructured meshes," *Computer Methods in Applied Mechanics and Engineering*, vol. 195, no. 13-16, pp. 1667–1691, 2006.

[16] J. Kim, P. Moin, and R. Moser, "Turbulence statistics in fully developed channel flow at low Reynolds number," *Journal of Fluid Mechanics Digital Archive*, vol. 177, pp. 133–166, 2006.

[17] R.D. Moser, J. Kim, and N.N. Mansour, "Direct numerical simulation of turbulent channel flow up to Re= 590," *Physics of Fluids*, vol. 11, pp. 943, 1999.

[18] A.V. Trofimova, A.E. Tejada-Martínez, K.E. Jansen, and R.T. Lahey, "Direct numerical simulation of turbulent channel flows using a stabilized finite element method," *Computers and Fluids*, 2008.

Proceedings of the 8th National Congress on Theoretical and Applied Mechanics, May 28-29, Brussels, Belgium.

High-Order Discrete Explicit Filtering for Large Eddy Simulation

Willem Deconinck[1], Clinton P.T. Groth[2], Chris Lacor[1]
[1]Vrije Universiteit Brussel, Department of Mechanical Engineering
Pleinlaan 2-1050 Brussel
[2]University of Toronto Institute for Aerospace Studies
4925 Dufferin Street, Toronto, ON, M3H 5T6
email: willem.deconinck@vub.ac.be

Abstract— **In the context of Large Eddy Simulation (LES) of turbulent flows, there is a current need to compare and evaluate different proposed subfilter-scale (SFS) models so as to assess their suitability for various turbulent flow applications. In order to carefully compare SFS models and compare LES predictions to Direct Numerical Simulation (DNS) results (the latter would be helpful in the comparison and validation of models), there is a real need for a "grid-independent" LES capability. Explicit filtering methods offer one means by which this may be achieved. Advantages of explicit filtering are that it provides a means for eliminating aliasing errors, allows for the direct control of commutation errors, and most importantly allows a decoupling between the mesh spacing and the filter width, which is the primary reason why difficulties arise in comparing LES solutions obtained on different grids having varying resolution.**

This article presents the design and assessment of discrete explicit filters and their application to the prediction of compressible isotropic turbulence prediction on structured grids using high-order finite-volume methods with varying mesh spacing and filter widths.

I. Introduction

The difficulty associated with implicit filtering in LES can be alleviated by performing an explicit filtering operation as a part of the solution process. The explicit filter is applied in physical space using a convolution:

$$\overline{\phi}(x) = \int_{-\infty}^{+\infty} \phi(x') G(x - x'; \bar{\Delta}) \mathrm{dx}' \,, \qquad (1)$$

where G is the filter kernel and $\bar{\Delta}$ the filter width. With explicit filtering the energy in the high frequency portion of the spectrum is damped and it becomes possible to reduce or eliminate the various sources of numerical error that dominate this frequency range [1]. Moreover, explicit filtering allows the filter width to be chosen independently from the mesh spacing. The form of the filter is also known exactly and this allows the direct comparison of LES solutions to experimental or DNS data.

In general, filters do not commute with the discretization scheme when a variable filter width is used [2], so that

$$\left| \frac{\overline{\mathrm{d}\phi}}{\mathrm{dx}} - \frac{\mathrm{d}\overline{\phi}}{\mathrm{dx}} \right| = \mathcal{O}\left(\bar{\cdot}(\S)^{\backslash} \right) \,, \qquad (2)$$

in which n is the order of commutation. To be acceptable, the errors associated with the commutation properties of the filter should be of the same order as the truncation errors associated with the numerical scheme. Implicit filters generally commute only to second order and herein lies the difficulty. When using high-order schemes, it becomes important to use high-order explicit filters that commute up to the desired order of accuracy for simulations having varying filter widths [3]. This can be achieved by imposing the filter moments M^k:

$$M^k(x) = \begin{cases} 1, & k = 0 \,; \\ 0, & k = 1, \ldots, n-1 \,; \\ \text{exists}, & k \geq n \,. \end{cases} \,, \qquad (3)$$

where $M^k(x)$ is defined as

$$M^k(x) = \int_{-\infty}^{+\infty} x'^k G(x - x'; \bar{\Delta}) \mathrm{d}\eta \,. \qquad (4)$$

Analytical explicit filters require the numerical integration of the convolution integral in (1) and generally are therefore inefficient. With discrete explicit filters, the filter kernel G is defined as a weighted summation of dirac functions [4]:

$$G(x_i - x'; \bar{\Delta}) = \sum_{l=-K}^{L} \mathrm{w_l} \; \delta(\mathrm{x}' - \mathrm{x_{i+l}}) \,, \qquad (5)$$

so that (1) can be written as

$$\overline{\phi}_i = \sum_{l=-K}^{L} \mathrm{w_l} \; \phi_{\mathrm{i+l}} \,. \qquad (6)$$

This doesn't require a costly numerical integration procedure and is thus better suited for use in LES. Discrete approaches will be considered herein.

II. High-Order Finite-Volume Scheme

The numerical scheme used is the high-order central essentially non-oscillatory (CENO) Finite-Volume scheme proposed by Ivan et al. [5].

The semi-discrete form of the finite-volume formulation applied to the governing equations for cell (i, j, k) of a three-dimensional multi-block mesh composed of hexahedral computational cells is given by

$$\frac{\mathrm{d}\mathbf{U_{i,j,k}}}{\mathrm{dt}} = -\frac{1}{V_{i,j,k}} \sum_{l=1}^{N_f} \sum_{m=1}^{N_G} \left[\omega\ \mathbf{n_l} \cdot \tilde{\mathbf{F}}_\mathbf{l}\ \mathbf{A_l}\right]_{i,j,k,m} + \mathbf{S_{i,j,k}} \tag{7}$$

where here each cell has $N_f = 4$ faces and a N_G-point Gaussian quadrature numerical integration procedure has been used to evaluate the solution flux through each face. The variable $\mathbf{U_{i,j,k}}$ is the cell-averaged conserved solution state for cell (i, j, k), $V_{i,j,k}$ is the volume of the hexahedral cell, ω is the quadrature weighting coefficient, and A_l and $\mathbf{n_l}$ are the area of the cell face and unit vector normal to the cell face or edge, respectively.

A. Inviscid Flux Evaluation

The numerical fluxes, $\vec{\mathbf{F}} \cdot \mathbf{n}$, at the quadrature points, m, of faces, l, for each cell are determined from the solution of a Riemann problem. Given the left and right solution states, $\mathbf{U_l}$ and $\mathbf{U_r}$, at the quadrature points of the cell interfaces, the numerical flux is given by

$$\vec{\mathbf{F}} \cdot \mathbf{n} = \mathcal{F}(\mathbf{U_l}, \mathbf{U_r}, \mathbf{n}) \tag{8}$$

where the numerical flux F is evaluated by solving a Riemann problem in a direction defined by the normal to the face with initial data $\mathbf{U_l}$and $\mathbf{U_r}$. The left and right solution states, $\mathbf{U_l}$ and $\mathbf{U_r}$, are determined by performing piecewise k-order polynomial solution reconstruction within each computational cell.

B. k-Exact Reconstruction

The evaluation of the coefficients of the reconstructed polynomial requires the least-squares solution of an overdetermined system of linear equations $A\mathbf{x} = \mathbf{B}$, where the coefficient matrix A of the linear system depends only on the mesh geometry and can be calculated in a preprocessing step.

When determining these coefficients it is required that the following conditions be satisfied by the reconstruction procedure: i) the solution reconstruction must reproduce exactly polynomials of degree $N \leq k$; ii) the solution reconstruction must preserve the mean or average value within the computational cell. The latter condition implies that

$$\mathbf{U_{i,j,k}} = \frac{\mathbf{1}}{\mathbf{V_{i,j,k}}} \iiint_{\mathbf{V_{i,j,k}}} \mathbf{u_{i,j,k}}(\mathbf{r})\ \mathrm{dxdydz}\,, \tag{9}$$

where $\mathbf{u}(\mathbf{r})$ is the reconstructed polynomial.

C. Viscous Flux Evaluation

The viscous flux is evaluated in each Gauss-quadrature point and requires both the solution and solution gradient. The flux is taken as the average of the left and right state evaluations.

$$F_v = \frac{1}{2}(F_v(\mathbf{U_l}, \nabla\mathbf{U_l}) + \mathbf{F_v}(\mathbf{U_r}, \nabla\mathbf{U_r})) \tag{10}$$

In this equation $\mathbf{U_l}$ and $\mathbf{U_r}$ are reconstructed in the quadrature points with the k-exact reconstruction. They are reconstructed with one order higher, so that the gradients $\nabla\mathbf{U_l}$ and $\mathbf{U_r}$ are of the desired spatial order of accuracy. However, the number of Gauss-quadrature points is not changed. The fluxes are then integrated over the cell faces using Gauss-quadrature.

III. High-Order Discrete Explicit Filtering

When using a high-order numerical scheme, it becomes important to use high-order explicit filters that commute up to the desired order of accuracy for simulations having varying filter widths. This is the case on non-uniform grids. The class of high-order commuting discrete explicit filters that is assessed and investigated in this work, is based on a linear least squares reconstruction proposed by Haselbacher et al. [6]. This class can be used on both structured and unstructured grids. This explicit filter obtains high-order commutation through approaching the filter by a taylor expansion to the desired order using weighted least squares reconstruction. One equation in this linear system can be written for each cell used in the reconstruction.

$$\phi_i = \overline{\phi}_0 + \sum_{k=1}^{n} \left[\sum_{p_1+p_2+p_3=k} D^k_{p_1,p_2,p_3}\ \Delta x_{0i}^{p_1} \Delta y_{0i}^{p_2} \Delta z_{0i}^{p_3} \right]. \tag{11}$$

In this equation the index 0 indicates the cell-centre of the cell of interest, and index i the cell-centre of a neighbouring cell used in the reconstruction. The coefficients $D^k_{p_1,p_2,p_3}$ are the unknowns of the linear system and are defined as

$$D^k_{p_1,p_2,p_3} = \frac{a_{p_1,p_2,p_3}}{k!} \frac{\partial^k \phi_0}{\partial x^{p_1} \partial y^{p_2} \partial z^{p_3}}\,, \tag{12}$$

where a_{p_1,p_2,p_3} are the trinomial coefficients defined by

$$a_{p_1,p_2,p_3} = \frac{(p_1 + p_2 + p_3)!}{p_1!\ p_2!\ p_3!} \tag{13}$$

Unlike with gradient least squares reconstruction, the cell of interest is not included in the reconstruction stencil, and is treated as an unknown as well.

Solving this system $A\ \mathbf{x} = \mathbf{B}$ results in a filtered variable $\overline{\phi}_0$ at the cell-centre. In this finite-volume context however, what needs to be filtered are cell-averaged values. For high-order schemes the cell-centred and cell-averaged values don't match and special care has to be exercised to the meaning of the coefficients $D^k_{p_1,p_2,p_3}$. However, using the same method to calculate these coefficients as in the k-exact reconstruction described above for the fluxes, ensures that the result is a filtered cell-average.

The reconstruction is only geometry-dependent and can be precomputed. This happens through calculating the pseudo inverse of the coefficient matrix of this system. The vector of unknowns can then be written as

$$\mathbf{x} = \mathbf{A}^{\dagger}\ \mathbf{B} \tag{14}$$

The only unknown of interest in the vector $\mathbf{x}$ is $\overline{\phi}_0$. Hence only the first row of $A^{\dagger}$ is required. This row can be stored and its elements are exactly the discrete filter weights for the cell of interest.

An example of the transfer function of a third-order commutative discrete explicit filter using least squares reconstruction is shown in Figure 1. In this figure κ_Δ represents the grid cutoff wave number, $\kappa_{\bar{\Delta}}$ the filter cut-off wave number, and FGR the filter-grid ratio defined as $\frac{\bar{\Delta}}{\Delta}$ or $\frac{\kappa_\Delta}{\kappa_{\bar{\Delta}}}$.

A. Controlling the Filter-Width

One main difficulty with this class of filters is setting the desired filter-width. By increasing the size of the stencil, the filter-width becomes larger, and the filter will cut off at lower wave numbers. The filter-width furthermore decreases when using a higher-order reconstruction. This is shown in Figure 2. Note that while the physical filter-width increases, the filter cut-off wave number decreases.

It has been proposed by Marsden et al. [3] to use multiple "sub-filters" and combine them with certain weights, which can be optimized to result in a filter with a user-defined filter-width. It has however been found to be difficult to apply this approach to this class of filters, using higher-order reconstruction, as each system of these sub-filter reconstructions requires enough points in the stencil to be overdetermined.

In this work it is proposed to use a weighted least-squares reconstruction for only one main filter. The solution of the least squares reconstruction is then given by

$$\mathbf{x} = (\mathbf{W}\ \mathbf{A})^{\dagger}\ \mathbf{W}\ \mathbf{B}\,, \tag{15}$$

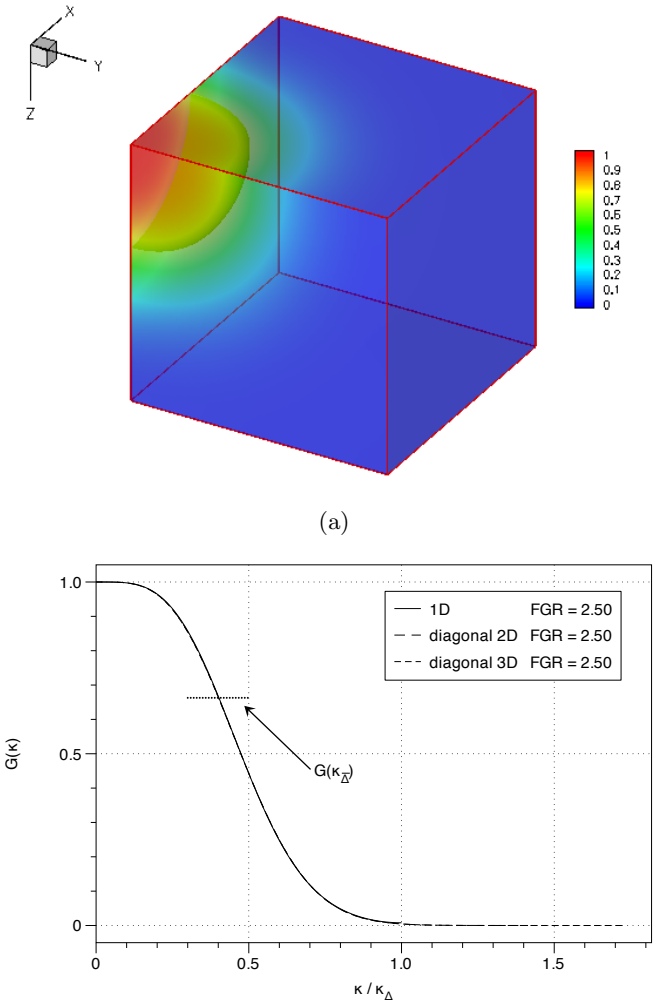

Fig. 1. Transfer function of a discrete explicit filter, with (a) the three-dimensional transfer function and (b) its projection in one dimension. The iso-surface in (a) and horizontal line in (b) denote the value of the transfer function at the filter cut-off.

with W a diagonal matrix of weights. It is not recommended to use an inverse distance or inverse squared distance weighting function as these functions don't allow for an extra user-defined parameter to control the weighting. In analogy to a Gaussian analytical explicit filter, this work proposes the use of a Gaussian distribution for the weighting function:

$$W_i = \sqrt{\frac{6}{\pi\ D^2}}\ \exp\left(-\frac{6\,|\Delta\mathbf{r_{0i}}|^2}{D^2}\right)\,. \tag{16}$$

The parameter D can be tuned so that a desired filter-width is achieved. This is demonstrated in Figure 3. The weighting factor has been chosen to be relative to the mesh spacing to be applicable to multiple mesh sizes.

Apart from allowing the user some control over

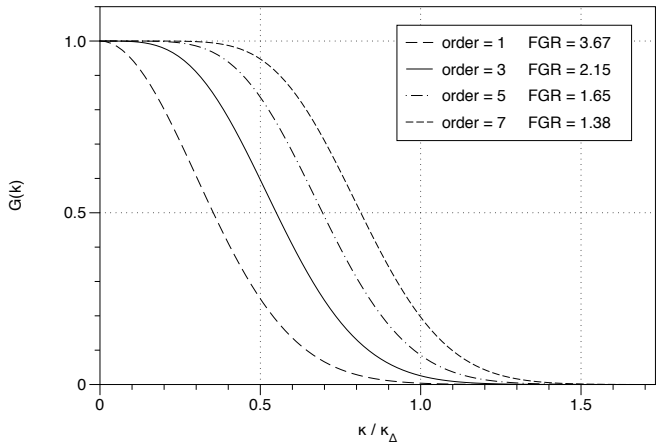

Fig. 2. Transfer functions of the explicit filter changing only the order of reconstruction. FGR is defined as $\bar{\Delta}/\Delta$.

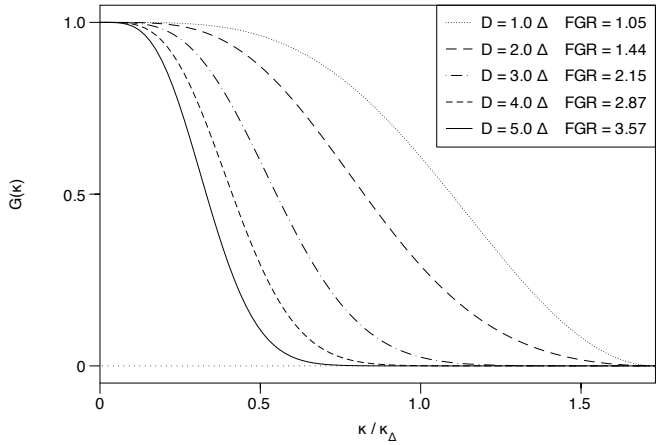

Fig. 3. Transfer functions of a third order explicit filter changing only the parameter D in the Gaussian weighting functions. FGR is defined as $\bar{\Delta}/\Delta$.

the filter-width, this weighting function enhances the shape of the transfer function to become more monotone. As can be observed from Figure 3, the filter-width does not vary linearly with the parameter D. This work proposes to make curve-fits that give the value of the parameter D as a function of the filter-width. This curve-fit is different for every order, and number of rings used in the stencil for the reconstruction.

IV. Implementation of Discrete Explicit Filtering

A. Approach to Explicit Filtering

A number of approaches to explicit filtering exists. The main idea in explicit filtering is to perform filtering with smooth filters in such way that excessive filtering of the results from previous time levels is avoided.

If the approach were to filter the solutions after every time step, one would actually use multiply filtered solutions which leads to excessive damping of the filtered flow solution [7]:

$$\begin{aligned}\bar{U}^{n+1} &= \overline{\bar{U}^n + \Delta t^n \bar{R}^n} \\ &= \overline{\overline{\bar{U}^{n-1}} + \Delta t^{n-1}\overline{\bar{R}^{n-1}}} + \Delta t^n \overline{\bar{R}^n}\end{aligned} \tag{17}$$

A first approach to explicit filtering is to limit the generation of higher frequencies in $\bar{U}^{n+1}$ by filtering the residual $\bar{R}^n$ every time step. This means that both convective and dissipative terms are filtered. As an alternative approach, the idea is to selectively limit the introduction of high frequency content for each term in the governing equations. The only terms that inject higher frequency content in the solution are the non-linear convective terms and the SFS-terms. Lund [7] suggested that by filtering only these terms no additional frequency content is added. Brandt [8] has made a comparison between both approaches to explicit filtering. He found that both approaches only result in small differences, and thus the filtering of the non-linear terms, which generate the high frequency contents in the resolved flow field, seems to be the essential part of explicit filtering.

Comparing the computational cost of filtering the residual however is significantly lower than that of filtering the non-linear terms. This is because the non-linear terms are evaluated in each quadrature point of each cell, and the number of non-linear terms to be filtered can be rather large compared to the number of solution variables.

B. Choice of Filter-Grid Ratio

One of the open questions in the application of discrete explicit filters is the choice of the filter-grid ratio. Ghosal [9] made an analysis on numerical errors in LES of turbulence, as did Chow et al. [10] for more realistic turbulence kinetic energy spectra. They found through applying an explicit filter to a DNS calculation the *exact* SFS-force. Ghosal's results indicate that for a second-order finite-differencing scheme, the truncation error will overshadow the contribution of the SFS-force for a filter-grid ratio of 2. In order for the SFS-force to be significant enough, the filter-grid ratio has to be increased to 4. For a fourth-order spatial discretization scheme, a filter-grid ratio of 2 suffices. In practice, many LES codes use second-order spatial discretization schemes with a filter-grid ratio of unity or at best two. Some of the results of these

LES codes are likely contaminated by significant numerical errors.

Since this work uses a fourth-order numerical scheme, a filter-grid ratio of 2 is used. If a second-order numerical scheme were to be used to resolve the flow field accurately up to the same wave number, a filter-grid ratio of 4 had to be chosen, and hence the grid would have needed to be twice as fine.

C. Choice of CFL number

A fourth-order finite-volume scheme usually requires a low CFL number. The limiting factor comes from the acoustic waves. Increasing the CFL number leads to instabilities originating at high frequencies. It is observed that this instability does not occur when using explicit filtering, as the high frequencies are eliminated by the filtering procedure. The limit of CFL = 1 has been tested with explicit filtering, and shows no difference in solution compared to a lower CFL number. This effect effectively eliminates a large part of the computational expenses associated with the explicit filtering, and might even lead to a slight speedup of the LES calculations.

D. Use of a Secondary Filter

As is apparent from the current application, this method still introduces some high frequency content over time in wave numbers higher than the grid cut-off wave number. This might be because the transfer function might be negative at higher wave numbers or not perfectly zero. A simple solution to this problem is to apply a secondary explicit filter to the actual fully updated solution after a certain number of time steps to remove this build-up. The filter-grid ratio of this filter can be smaller, so that the frequency content of the solution is not affected below the filter cut-off wave number of the primary explicit filter used to filter the residuals.

V. Application of Discrete Explicit Filtering to Isotropic Turbulence Decay

A. Synthetic Turbulent Flow Field

A homogeneous isotropic turbulence field is obtained by initializing a solution domain with Rogallo's random procedure [11], using the model spectrum proposed by Pope [12]. This spectrum has been initialized on a grid with domain dimensions $2\pi \times 2\pi \times 2\pi$ m. This might seem somewhat large for the current application, but the turbulent velocity field is scaled accordingly. These dimensions allow for a better comprehension of the spectral results since the one-dimensional grid cut-off wave number is then a whole number defined as

$$\kappa_\Delta = \frac{N}{2}\frac{2\pi}{D} = \frac{N}{2}\,, \tag{18}$$

with N an even number of cells in one direction, and D the size of the domain in the same direction. The spectrum is constructed so that the specific total kinetic energy $K = 15000$, and the characteristic length scale of the largest eddies $l_0 = \frac{D}{3.2}$. This fixes the other spectrum parameters, which are listed in Table I. This table lists that the Kolmogorov wavenumber κ_η for this spectrum is of the order 10^5 m^{-1}. If one wants to resolve this scale, the mesh requirements would obviously be enormous. This kinetic energy spectrum initialized on a $64 \times 64 \times 64$ grid with periodic boundary conditions. It is shown in Figure 4.

parameter	value	
K	15000	m^2/s^2
u_{rms}	100	m/s
l_0	1.96	m
κ_0	3.2	m^{-1}
l_{11}	0.85	m
ε	$9.36 \cdot 10^3$	m^2/s^3
η	$7.73 \cdot 10^{-6}$	m
κ_η	$8.13 \cdot 10^5$	m^{-1}

TABLE I
Specifics of the Model Spectrum

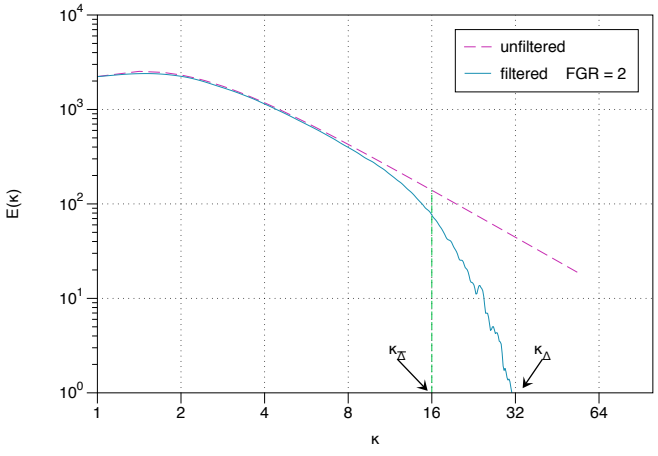

Fig. 4. Application of the used fourth-order explicit filter to the model spectrum on a uniform $64 \times 64 \times 64$ grid. FGR is defined as $\bar{\Delta}/\Delta$.

B. Results and Discussion

In this section a study will be made of 8 different setups. Four types of grids will be considered: a

coarse $64 \times 64 \times 64$ stretched and uniform grid and a fine $32 \times 32 \times 32$ stretched and uniform grid. On these four grids, a Large Eddy Simulation with both implicit and explicit filtering will be performed. Each solution domain is initialized with the filtered synthetic flow field described above. The used SFS-model is the Smagorinsky model with a constant of 0.20.

For the 4 cases on the uniform grids, a study of the turbulent kinetic energy spectrum can be made. Figure 5 and Figure 6 shows these energy spectra after 150ms for respectively the $64 \times 64 \times 64$ grid and the $32 \times 32 \times 32$ grid.

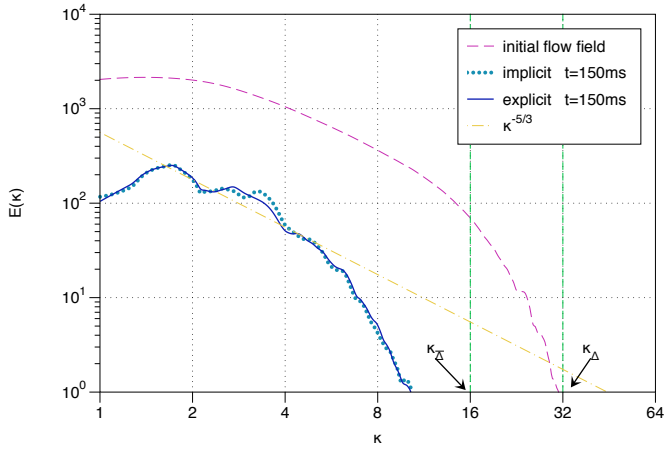

Fig. 5. Turbulent kinetic energy spectra for the uniform $64 \times 64 \times 64$ grid with and without explicit filtering

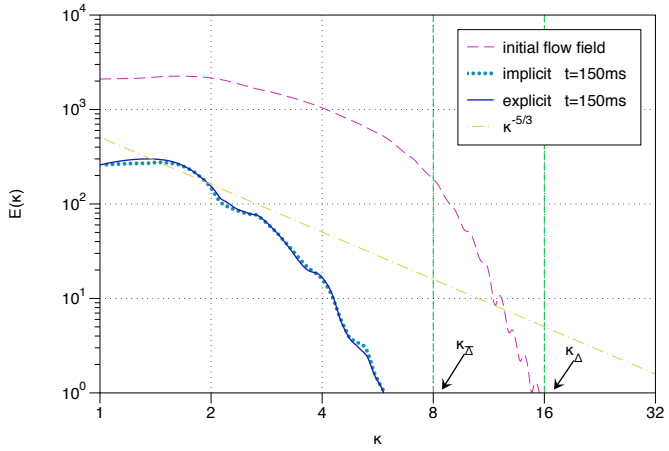

Fig. 6. Turbulent kinetic energy spectra for the uniform $32 \times 32 \times 32$ grid with and without explicit filtering

The energy spectra in Figure 5 follow Kolmogorov's $-5/3$ law closely, as is expected for isotropic turbulence decay. A comparision of the spectra obtained using explicit filtering and implicit filtering shows excellent agreement. This illustrates that the application of the explicit filtering approach does not pollute the results obtained through implicit filtering. These observations can also be made in Figure 6. The numerical scheme seems to be too dissipative and cuts off at wave numbers below the filter-cutoff, so that the importance of the explicit filter is negligible. The main advantage using explicit filtering in this case however is the ability to use a CFL number of 1. In a fourth-order finite-volume scheme, the relative computational cost of applying the explicit filtering is small compared to the overall computational cost. As the CFL number without explicit filtering can be very low in high-order numerical schemes, the advantages of using explicit filtering in this aspect become evident.

Finally a study on non-uniform stretched grids is performed by looking at the decay rate of the total turbulent kinetic energy. The turbulent kinetic energy can be plotted in time to observe the rate of its decay. Figure 7 shows the total turbulent kinetic energy, consisting of the sum of the resolved turbulent kinetic energy and the modelled subfilter turbulent kinetic energy, for all four cases. Again, as is the case when comparing the turbulent kinetic energy spectra for the uniform cases, the implicit filtering cases and explicit filtering cases do not exhibit significant differences. Comparing the two different grids, it can be observed that the total turbulent kinetic energy shows good agreement, although the resolved component of the turbulent kinetic energy is different. This indicates that the SFS-model is capable of modelling the SFS-energy very well. The theoretical asymptotic decay rate is obtained for all 4 cases, showing that the LES calculations are performed correctly, and that using explicit filtering doesn't pollute the solutions obtained by LES with implicit filtering.

VI. Conclusions

This work has attempted to address the issues associated with filtering errors that may arise when using LES with implicit filtering, by considering an explicit filtering approach. A detailed study of a discrete high-order commuting least-squares reconstruction filter has been performed. It has been shown how the filter-width can be controlled using a Gaussian weighting function in the least-squares reconstruction. Although explicit filtering increases the computational cost per time step, larger time steps can be taken without leading to instabilities, thus offsetting a large part of the disadvantages of the incurred higher computational costs of explicit filtering methods. Other test cases have to be performed with more radically

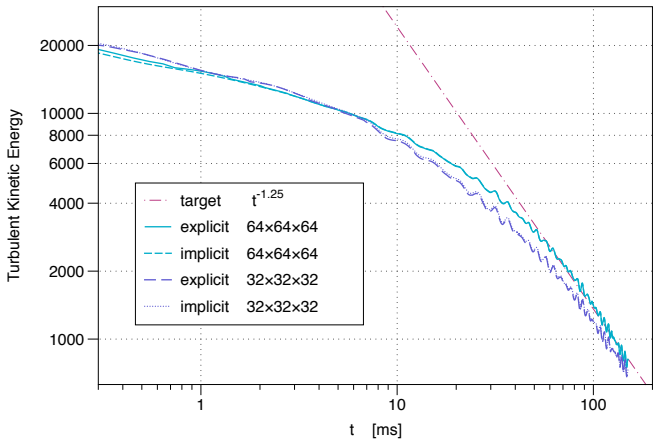

Fig. 7. Turbulent kinetic energy decay of isotropic turbulence on a non-uniform stretched $64\times64\times64$ and $32 \times 32 \times 32$ grid using explicit filtering and implicit filtering.

changing non-uniform grids where the explicit filter has more impact to see a clear advantage in terms of commutation errors.

References

[1] Vasilyev, O. and Lund, T., "A general theory of discrete filtering for LES in complex geometry," *Annual Research Briefs*, Jan 1997.

[2] Berselli, L., Grisanti, C., and John, V., "On commutation errors in the derivation of the space averaged Navier-Stokes equations," *Preprint*, 2004.

[3] Marsden, A., Vasilyev, O. V., and Moin, P., "Construction of Commutative Filters for LES on Unstructured Meshes," *Journal of Computational Physics*, Vol. 175, No. 2, Jan 2002, pp. 584–603.

[4] Sagaut, P. and Grohens, R., "Discrete filters for large eddy simulation," *International Journal for Numerical Methods in Fluids*, Jan 1999.

[5] Ivan, L. and Groth, C., "High-Order Central ENO Finite-Volume Scheme with Adaptive Mesh Refinement," *AIAA Conference*, 2007.

[6] Haselbacher, A. and Vasilyev, O. V., "Commutative discrete filtering on unstructured grids based on least-squares techniques," *Journal of Computational Physics*, Vol. 187, No. 1, May 2003, pp. 197–211.

[7] Lund, T., "On the use of discrete filters for large eddy simulation," *Center for Turbulence Research*, 1997.

[8] Brandt, T., "Study of Large Eddy Simulation and Smagorinsky Model using Explicit Filtering," *36th AIAA Fluid Dynamics Conference and Exhibit*, Jan 2006.

[9] Ghosal, S., "An Analysis of Numerical Errors in Large-Eddy Simulations of Turbulence," *Journal of Computational Physics*, Jan 1996.

[10] Chow, F. and Moin, P., "A further study of numerical errors in large-eddy simulations," *Journal of Computational Physics*, Jan 2003.

[11] Rogallo, R., "Numerical Experiments in Homogeneous Turbulence," *NASA Technical Memorandum*, Jan 1981.

[12] Pope, S. B., *Turbulent Flows*, 2000.

Proceedings of the 8th National Congress on Theoretical and Applied Mechanics, May 28-29, Brussels, Belgium.

Hybrid RANS/LES for impinging jet flows

Slawomir Kubacki[1,2], Erik Dick[1]
[1]Ghent University – Department of Flow, Heat and Combustion Mechanics
St.–Pietersnieuwstraat 41, B-9000 Ghent, Belgium
[2]Czestochowa University of Technology – Institute of Thermal Machinery
Al. Armii Krajowej 21, 42-200 Czestochowa, Poland
email: Slawomir.Kubacki@UGent.be, Erik.Dick@UGent.be

Abstract: **Plane impinging jets with nozzle-plate distances H/B=10 and 9.2 and Re=13500 and 20000 are simulated with k-ω based hybrid RANS/LES models and with a RANS k-ω model. Different ways of substitution of the turbulent length scale by the local grid size in the LES mode of the hybrid RANS/LES model are tested. The results show that the hybrid RANS/LES models, in contrast to the pure k-ω RANS model, give realistic wall shear stress and heat transfer rate along the impingement plate. This is due to ability of the hybrid RANS/LES models to resolve the evolution and break-up of the vortices in the shear layer of the jet, which strongly affects the turbulent flow and convective heat transfer in the stagnation and wall-jet regions.**

Keywords: **plane impinging jet, turbulence modelling, k-ω model, hybrid RANS/LES model.**

I. INTRODUCTION

RANS models present some limitations for simulation of impinging jet flows such as overestimation of the length of the core region (underestimation of the jet expansion) or overprediction of the turbulent kinetic energy production to dissipation ratio in stagnation flow region. On the other hand, LES methods are able to reproduce the large scale structures initiated at the jet exit, their evolution and degradation into smaller eddies. However, since LES aims at resolving the scales of motion responsible for turbulence production, it comes into difficulties in the near-wall region where the size of the eddies is comparable to the Kolmogorov scales, requiring extremely fine grid resolution, approaching that of DNS. In order to alleviate this grid resolution problem in the near-wall region, a hybrid RANS/LES can be applied, where the method acts in RANS mode in the near-wall region and in LES mode in non-equilibrium flow regions away from walls in order to resolve the flow instabilities by comparing the size of the resolved scales to the local grid size Δ.

In present work, the newest version of the k-ω model of Wilcox [1] is applied as a "state-of-the-art" turbulence model. Since the RANS model provides poor description of the flow physics for free jet flows, a hybrid RANS/LES method is constructed in order to resolve the evolution of large scale instabilities in flow regions where the grid density is fine enough (replacing the turbulence length scale by the local grid size). In the near wall regions, the model switches to RANS mode which is known to be adequate for modelling fine scale structures. Three different ways of substitution of the turbulent length scale by the local grid scale are tested. The first method is based on the concept of Strelets [2] where the destruction term in the k-equation of the underlying k-ω SST model was modified in order to unlock the large-scale instabilities in the flow regions where the dynamics of the large scale structures was responsible for the major part of the turbulence production. The approach of Strelets [2] was named Detached Eddy Simulation (DES), according to the assumption that the "detached" eddies are simulated while the "attached" eddies (in thin shear layers) are modelled.

The second way of constructing the hybrid RANS/LES approach is according to Kok et al. [3], where both the destruction term in the k-equation and the definition for ν_t are modified in such a way that in LES mode the Yoshizawa model is recovered [4].

The third approach is according to a proposal of Batten [5]. In [5], a latency factor (or latency function) has been formulated based on the ratio of the products of the turbulent length and velocity scales from the underlying RANS and LES models and it was introduced in the definition of ν_t. In the present work, the latency factor is constructed following the work of Sagaut et al. [6].

Results of simulations of plane impinging jets with nozzle-plate distances H/B=10 and 9.2 and Re=13500 and 20000 (Reynolds number based on slot width B and centreline velocity V_0) are presented and compared to experimental data as well as to LES results of Beaubert and Viazzo [7]. It is demonstrated that the hybrid RANS/LES models are able to reproduce the evolution of the large scale structures initiated at the jet exit and their break-up into smaller scales. Close to the walls and far away from the free jet flow, the model switches to RANS mode, so that most of the turbulence is modelled there.

Overall, excellent results are obtained.

II. STRESS LIMITER OF THE K-ω MODEL FOR HYBRID FORMUATIONS

The new k-ω model of Wilcox [1] reads

$$\frac{Dk}{Dt} = P_k - \beta^* k\omega + \frac{\partial}{\partial x_j}\left[\left(\nu + \sigma^* \frac{k}{\omega}\right)\frac{\partial k}{\partial x_j}\right], \tag{1}$$

$$\frac{D\omega}{Dt} = \alpha \frac{\omega}{k} P_k - \beta\omega^2 + \frac{\partial}{\partial x_j}\left[\left(\nu + \sigma \frac{k}{\omega}\right)\frac{\partial \omega}{\partial x_j}\right] + \frac{\sigma_d}{\omega}\frac{\partial k}{\partial x_j}\frac{\partial \omega}{\partial x_j}, \tag{2}$$

where ν is the kinematic molecular viscosity, k is the turbulent kinetic energy, ω is the specific dissipation rate and $P_k=\tau_{ij}\partial U_i/\partial x_j$, where the components of the modelled stress

tensor are given by $\tau_{ij}=2\nu_t S_{ij} - 2/3k\delta_{ij}$. The turbulent viscosity ν_t is defined by

$$\nu_t = \frac{k}{\tilde{\omega}}, \quad \tilde{\omega} = \max\left(\omega, C_{\lim}\sqrt{\frac{2\bar{S}_{ij}\bar{S}_{ij}}{\beta^*}}\right) \tag{3}$$

with $C_{lim}=7/8$, $\beta^*=0.09$ and $\bar{S}_{ij} = S_{ij} - 1/3\partial U_k/\partial x_k \delta_{ij}$, where $S_{ij}=1/2(\partial U_i/\partial x_j+\partial U_j/\partial x_i)$ are the components of rate of strain tensor. The remaining closure coefficients and auxiliary relations are

$$\alpha = \frac{13}{25}, \quad \beta = \beta_0 f_\beta, \quad \beta_0 = 0.0708, \quad \sigma = 0.5,$$

$$\sigma^* = 0.6, \quad \sigma_{do} = 0.125,$$

$$\sigma_d = \begin{cases} 0 & for \quad \frac{\partial k}{\partial x_j}\frac{\partial \omega}{\partial x_j} \le 0 \\ \sigma_{do} & for \quad \frac{\partial k}{\partial x_j}\frac{\partial \omega}{\partial x_j} > 0 \end{cases}, \qquad f_\beta = \frac{1+85\chi_\omega}{1+100\chi_\omega},$$

$$\chi_\omega = \left|\frac{\Omega_{ij}\Omega_{jk}\hat{S}_{ki}}{(\beta^*\omega)^3}\right|$$

where

$$\Omega_{ij} = \frac{1}{2}\left(\frac{\partial U_i}{\partial x_j} - \frac{\partial U_j}{\partial x_i}\right), \quad \hat{S}_{ki} = S_{ki} - \frac{1}{2}\frac{\partial U_m}{\partial x_m}\delta_{ki}$$

In [8] it was demonstrated that the newest version of the k-ω model is successful for prediction of 2D plane impinging jets at low and moderate nozzle-plate distances (say for H/B<6), whereas a repair is necessary for axisymmetric jets. The ability of the new k-ω model (in contrast to previous versions) to correctly predict the turbulent flow and the convective heat transfer in stagnation flow regions of plane impinging jets is the result of the inclusion of the stress limiter in Eq. (3). In the flow regions characterized by large levels of strain S (e.g. in impingement flow regions), the term $C_{\lim}\sqrt{2\bar{S}_{ij}\bar{S}_{ij}/\beta^*}$ becomes higher than ω in Eq. (3), which makes the production term P_k in Eq. (1) proportional to S instead of being proportional to S^2. For boundary layer flows, the growth of the turbulent shear stress τ is limited in such a way that Bradshaw's assumption is recovered. A similar stress limiter has been implemented in the SST model of Menter [9], but in the SST model the effect of the stress limiter is restricted to the logarithmic and wake parts of the boundary layer, while in the present k-ω model the stress limiter is active everywhere (it can be active in free shear layers). As shown by Durbin [10], a stress limiter can also be derived by imposing realizability constraints. Durbin and Petterson-Reif [11] emphasize that generally a turbulence model will not fulfil the realizability conditions and some changes have to be made in order to ensure realizability. On the other hand, if violation of the realizability constraints is not severe in virtually all cases of interest, the changes to the underlying model can be disregarded. Wilcox [1] emphasizes that the newest version of the k-ω model can serve as the foundation of a more general prescription of the turbulent shear stress. For example, the turbulent shear stress can be obtained with a non-linear eddy viscosity formulation or with a hybrid RANS/LES formulation. It means that the condition (3) can be replaced by any other formulation if an adequate model is available. Our tests showed that for impinging jet simulation with the hybrid RANS/LES methods, the importance of the stress-limiter is small. So for simplicity the stress limiter has been deactivated everywhere, which means that the Eq. (3) is redefined to [12]:

$$\nu_t^{RANS} = \frac{k}{\omega} \tag{4}$$

The reason for doing this is that theoretically a viable subgrid scale model is obtained in the LES mode replacing Eq. (3) by Eq. (4) under the equilibrium condition (the equilibrium condition means that the production is equal to dissipation in the k-equation or simultaneously in both k- and ω-equations). With Eq. (4), the hybrid RANS/LES model reduces to a Smagorinsky-type model under equilibrium condition, if the local grid size Δ is introduced in place of the turbulent length scale L_t. Notice that all hybrid RANS/LES models discussed in the present paper reduce to Smagorinsky-type models under the equilibrium condition. Since the LES mode is active in the free shear layers and in the stagnation flow region, the model is capable of resolving the flow physics there, without necessity of introducing further damping to the modelled shear stress (which will be the case for $C_{\lim}\sqrt{2\bar{S}_{ij}\bar{S}_{ij}/\beta^*} > \omega$ in Eq. 3). As mentioned above, the stress limiter is also neglected in the RANS mode since it has negligible effect on the results presented in near-wall regions.

III. Alternative Methods of Length Scale Substitution in the k-ω Model

Three different ways of substitution of the turbulent length scale by the local grid size are described below when the hybrid RANS/LES functions in LES mode. In the first case, the DES-type formulation of Strelets [2] is implemented by modifying the destruction term in Eq. (1)

$$\beta^* k\omega = \varepsilon \to \max\left(\beta^* k\omega, \frac{k^{3/2}}{C_{DES}\Delta}\right) \tag{5}$$

The constant C_{DES} has been taken from work of Kok et al. [3] namely, $C_{DES}=0.67$. The local grid size Δ is defined by $\Delta=\max(\Delta_x, \Delta_y, \Delta_z)$ where Δ_x, Δ_y, Δ_z denotes the distances between the cell faces in x, y and z directions, respectively. A similar value of the constant C_{DES} has been determined by Yan et al. [13] through simulation of the decay of isotropic turbulence using the k-ω based DES model, namely $C_{DES}=0.7$. Hereafter this model will be called the M1-model.

The second model tested in the present work is the model of Kok et al. [3] where the underlying k-ω model has been used for construction of the "X-LES" approach. In [3], the turbulent length scale has been replaced by the grid size in both ν_t

$$\nu_t = \min\left(\frac{k}{\omega}, \beta^* C_{DES}\sqrt{k}\Delta\right) \tag{6}$$

and the destruction term of the k-equation (Eq. 5).

These modifications result in a model which has a high level of theoretical justification since in LES mode the

Yoshizawa [4] model is recovered. This formulation will be referred as M2-model.

The third model (M3-model) which is studied is based on inclusion of the local grid size only in the definition for ν_t. As shown in [14] [15], the subgrid viscosity can be defined by

$$\nu_t = \beta^* \Delta^{4/3} \varepsilon^{1/3} \tag{7}$$

The RANS-type eddy viscosity can be expressed by

$$\nu_t^{RANS} = \beta^* \frac{k^2}{\varepsilon} = \beta^* L_t^{4/3} \varepsilon^{1/3} \tag{8}$$

According to the kinetic energy cascade, the turbulent kinetic energy is transferred from the largest scales of motion towards smaller and smaller scales approaching that of Kolmogorov size without loss. As a result, a local equilibrium assumption can be formulated equating the dissipation of the small scales to the rate at which the turbulent kinetic energy is transferred from large to small scales. With this assumption, Eqs. (7) and (8) lead to

$$\nu_t = \nu_t^{RANS} \left(\frac{\Delta}{L_t} \right)^{4/3} \tag{9}$$

The term $(\Delta/L_t)^{4/3}$ in Eq. (9) can be interpreted as a damping function which bridges the RANS and LES zones. In order to recover the RANS turbulent viscosity in Eq. (9) for $L_t < \Delta$, the function $(\Delta/L_t)^{4/3}$ is limited by unity according to

$$f\left(\Delta, L_t\right) = \min\left[\left(\frac{\Delta}{L_t} \right)^{4/3}, 1 \right] \tag{10}$$

If the turbulent length scale $L_t=k^{1/2}/(\beta^*\omega)$ is smaller than the local grid size Δ in Eq. (10) (e.g. close to the walls), the model acts in RANS mode. Otherwise, if the turbulent length scale L_t is higher than the local grid size Δ, the turbulent viscosity ν_t^{RANS} is reduced by the function f (Δ, Lt) and ν_t becomes a subgrid viscosity. In the LES zone Eq. (10) together with Eq. (4) reduces to (7).

Table 1 summarizes the definitions of the D_k and ν_t which are used in the M1, M2 and M3 models discussed above.

TABLE I

DISSIPATION TERM D_K IN THE K-EQUATION AND TURBULENT VISCOSITY ν_T FOR MODELS M1, M2 AND M3.

model	D_k	ν_t
M1	$\max(\beta^*k\omega, k^{3/2}/(C_{DES}\Delta))$	k/ω
M2	$\max(\beta^*k\omega, k^{3/2}/(C_{DES}\Delta))$	$\min(k/\omega, \beta^*C_{DES}k^{1/2}\Delta)$
M3	$\beta^*k\omega$	$k/\omega(\Delta/L_t)^{4/3}$

IV. COMPUTATIONAL ASPECTS

Two cases are considered for assessment of the hybrid RANS/LES models presented above. In the first case, the computational domain consists of a rectangular box of length, high and width equal to L=50B, H=10B and W=πB, (for Re=13500) and in the second case the size of computational domain is equal to L=50B, H=9.2B and W=πB (for Re=20000). Figure 1 shows a scheme of the computational domain.

At the inlet to the computational domain (jet exit) an almost flat mean velocity profile was specified according to [16]

$$V(x,0,z) = -V_0\left(1-(2x/B)^{14}\right) \tag{11}$$

As shown in Fig. (2), the profile defined by Eq. (11) agrees well with the experimental data of Maurel and Solliec [17]. The same inlet mean velocity profile was used for both cases.

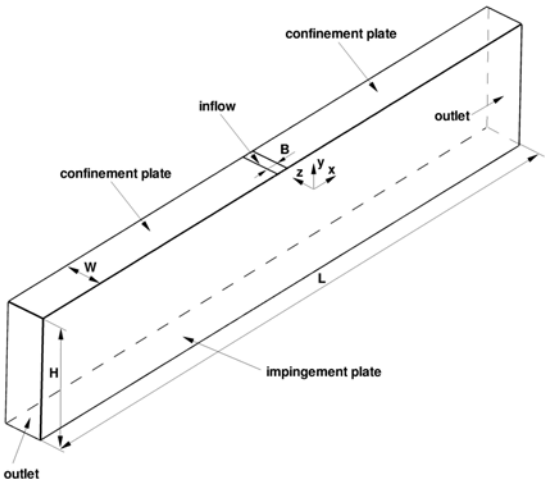

Fig. 1. Scheme of the computational domain.

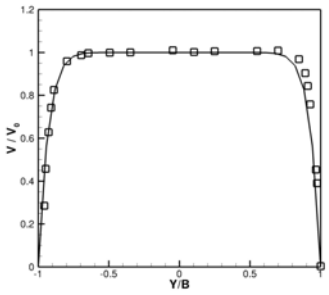

Fig. 2. Profile of the mean v-velocity component imposed at the jet exit. Comparison with the experiments of [17].

As noted in [17], a uniform profile of the fluctuating velocity component can be assumed at the jet exit. In the experiment, the nozzle exit turbulence intensity varied in the range Tu=1.6-2.8% for the case with nozzle-plate distance H/B=10 and Re=13500. For the second case with H/B=9.2 and Re=20000, the turbulence intensity was equal to Tu=1% [18] [19]. The turbulence length scale was not measured. In the present computations, constant profiles of k and ω were specified at the inlet to the computational domain (in both 2-D RANS and hybrid RANS/LES computations) with Tu=2.5% for H/B=10 and Re=13500 and Tu=1.0% for H/B=9.2 and Re=20000 while $l_{t,inlet}$=0.015B (according to Jaramillo et al. [20]). The inlet values of the turbulent quantities were set to $k_{inl}=1.5(Tu*V_0)^2$ and $\omega_{int}=(k_{inl})^{0.5}/l_{t,inl}$, were V_0 denotes the mean velocity in the symmetry plane. In addition to the specified k and ω profiles, the vortex method of Fluent ver. 6.4.7 was used to generate the fluctuations at the jet exit. At the outflow boundaries, pressure outlet boundary conditions were applied with a zero normal gradient condition for the

modelled scalars. At the walls, no-slip conditions were used with the turbulent quantities computed according to Menter [9]

$$k = 0, \quad \omega = 10\frac{6\nu}{\beta_0 (\Delta y)^2}, \tag{12}$$

where Δy is the first point away from the wall. Periodic boundary conditions have been applied in the spanwise z direction.

In the present hybrid RANS/LES computations, the computational grids consists of 140 x 145 x 44 cells (N≈0.9 million) for the first case (H/B=10 and Re=13500) and 140 x 165 x 44 (N≈1 million) for the second case (H/B=9.2 and Re=20000). In the reference LES computations of Beaubert and Viazzo [7] (H/B=10 and Re=13500) the computational mesh consists of 240 x 150 x 64 cells (N≈2.3 million). In the present hybrid RANS/LES simulations the number of grid points has been mainly reduced in the direction tangential to the walls, compared to the LES simulations of Beaubert and Viazzo. The grid points have been clustered towards the walls (in order to fulfil the condition $y^+ \approx 3$) and in the shear layer of the jet, since these are the regions of high velocity gradients. A uniform grid spacing was used in the spanwise z direction.

V. RESULTS

Results of the simulations of plane jets impinging onto a flat plate are presented applying the hybrid RANS/LES models. The results are compared to the experimental data of Maurel and Solliec [17], Asforth-Frost et al. [18], Zhe and Modi [19], Tu and Wood [21], to the LES results of Beaubert and Viazzo [8] and to the 2-D RANS results obtained with the k-ω model.

Fig. (3) shows an instantaneous field of velocity magnitude (top) and an instantaneous field of $f = \min(1, C_{DES}\Delta/L_t)$ in the x-y plane for H/B=10 and Re=13500 obtained with the M1 model. The instantaneous velocity field shows the dynamics of the impinging jet in the LES zone, which roughly corresponds to the values of $f < 1$. As shown in Fig (3, bottom) the RANS zone ($f = 1$) is active close to walls due the grid size Δ being larger than the turbulent length scale L_t. The RANS zone is also active in the middle of the channel at larger distances from the symmetry plane $|x| > 1.5$ (not shown here) where the dynamics of the large scale structures become negligible and the grid becomes too coarse to resolve the flow unsteadiness.

Fig. (4) shows the evidence of counter-rotating longitudinal vortices in the stagnation flow region (at distance X/B=-0.6 from the symmetry plane) for H/B=10, Re=13500. These counter-rotating vortices, also known as Görtler vortices were observed in the stagnation flow region of a plane impinging jet by Sakakibara et al. [22] and Maurel and Solliec [17]. They have been also reproduced in the simulations of Beaubert and Viazzo [7] using the LES technique and in the simulations of Tsubokura et al. [17] using LES and DNS. As mentioned in [21], these vortices appear as an effect of angular momentum instability in flow regions characterized by convex streamline curvature. According to Tu and Wood [21], the Görtler vortices have as effect to lower the wall shear stress τ (lower than the shear stress obtained from the analytical solution of the laminar Hiemenz flow). Correct prediction of the lowering of the wall shear stress by these counter-rotating vortices might be quite important since it counteracts the increase of the wall friction by turbulence coming from the shear layer of the jet.

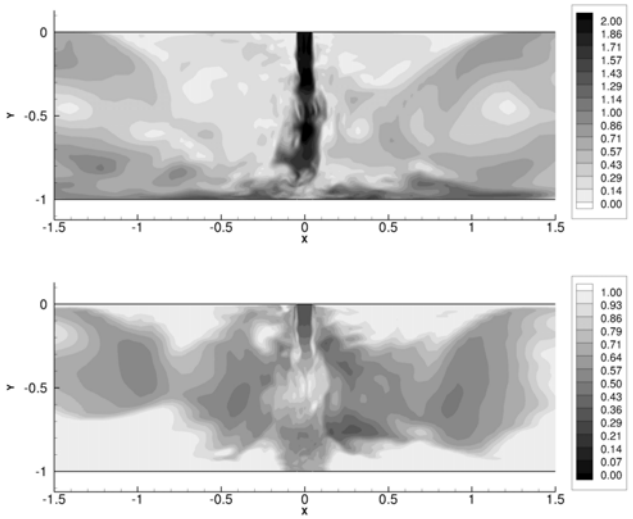

Fig. 3. Contour plots of (top) instantaneous velocity magnitude (in m/s) and (bottom) instantaneous field of $f = \min(1, C_{DES}\Delta/L_t)$ ($f < 1$: LES region, $f = 1$: RANS region) in the x-y plane ($z/B = \pi/2$) for H/B=10, Re=13500.

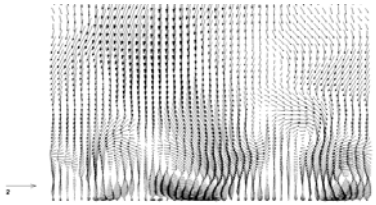

Fig. 4. Counter-rotating vortices close to the impingement plate in the y-z plane at distance x/B=-0.6 (length of the reference arrow is 2 m/s) for H/B=10, Re=13500.

Fig. (5) shows the profiles of mean and fluctuating v-velocity obtained with the different hybrid RANS/LES formulations (M1-model –solid line, M2-model-dashed line, M3-model – dashed dotted line) and the comparison with the experimental data of Maurel and Solliec [17] (symbols), the LES results of Beaubert and Viazzo [7] (solid line together with the symbols) and 2-D RANS results obtained with the k-ω model (dashed-double dotted line). For the hybrid methods, the data have been averaged in time and in the spanwise z direction.

The results obtained with the pure RANS model are erroneous. With RANS, the length of the jet core is strongly overpredicted with respect to the measured value and the value computed by LES and hybrid RANS/LES. As shown in Fig. (5, bottom) the fluctuating velocity component predicted by RANS ($u' = \sqrt{2/3k}$) slightly decays with increasing distance from the jet exit while in reality the fluctuations rise already at Y/B=2. The poor performance of the RANS model is due to its inability to predict turbulence production in absence of velocity gradients in the core of the jet and is also

due to too weak production of turbulent kinetic energy in the shear layer of the jet. This makes the predictions by 2-D RANS for large distance between jet exit and impingement plate very erroneous. Notice that this is in contrast with the good predictions observed for small distance between jet exit and impingement plate [8]. As shown in Fig. (5), the results obtained with the hybrid RANS/LES methods are close to each other and they show good agreement with experimental data and LES. The fluctuating velocity component (v') predicted by the M1 and M2 models has a tendency to rise a bit too fast compared to the experiment and to the LES in the range of (H+y)/B=3-5. In the downstream half of the jet ((H+y)/B =5-10) the agreement between simulations performed with the different hybrid RANS/LES formulations and experiment is excellent. This is slightly in contrast to the LES results of Beaubert and Viazzo [7] which shows much better agreement with the experimental data for (H+y)/B=2-5 than at larger distance from the jet exit. The differences between the hybrid RANS/LES and LES might be due to different inlet conditions (note the uncertainty level in the determination of the turbulence intensity at the jet exit in the experiments of Maurel and Solliec [17] which varied from Tu=1.6 to Tu=2.8%).

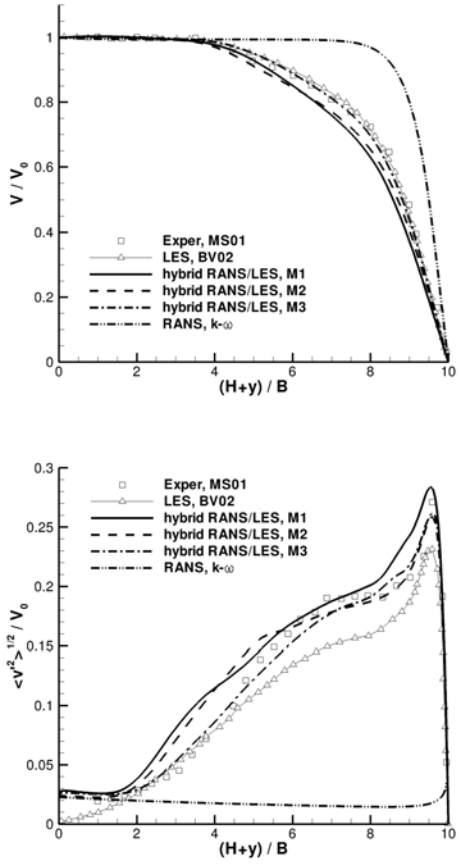

Fig. 5. Mean (top) and fluctuating (bottom) velocity profiles along a symmetry plane for H/B=10, Re=13500. In case of hybrid RANS/LES computations the resolved fluctuating velocity profiles are shown.

Fig. (6) shows the profiles of the skin friction (scaled with $Re_b=b_pV_0/\nu$, where b_p is the half-width of the impingement pressure profile) along the impingement plate. The hybrid RANS/LES results are again compared to experimental data [21] to LES results [7] and to the 2-D RANS results. Note the differences in the nozzle-plate distances and Reynolds number between the experimental data of Tu and Wood [21] and the present results. In [21], the nozzle-plate distances were equal to H/B=8 and 12 (in contrast to H/B=10 applied in the present simulations) and the Reynolds number was equal to Re=11000 (in the present simulations Re=13500). The peak values of $\tau \mathrm{Re}_b^{1/2}/\left(0.5\rho V_0^2\right)$ predicted by RANS are higher than the peak values obtained with the hybrid RANS/LES and LES methods. As discussed above, this is due to overprediction of the length of the core (or underestimation of the jet expansion) using the k-ω model. For this case, the RANS solution agrees very well with LES at larger distances from the symmetry plane (for $x/b_p>2$). The results obtained with the different hybrid RANS/LES formulations show good agreement with the LES results of Beaubert and Viazzo. It is difficult to judge which hybrid RANS/LES formulation gives the best correspondence with the LES. The general tendency is that the peak values of $\tau \mathrm{Re}_b^{1/2}/\left(0.5\rho V_0^2\right)$ around $|x/b_p|=1$ are better reproduced with the hybrid RANS/LES methods than using RANS. The agreement between computed values of $\tau \mathrm{Re}_b^{1/2}/\left(0.5\rho V_0^2\right)$ using hybrid RANS/LES methods, pure RANS and LES is good at larger distances from symmetry plane (at $|x/b_p|>2$).

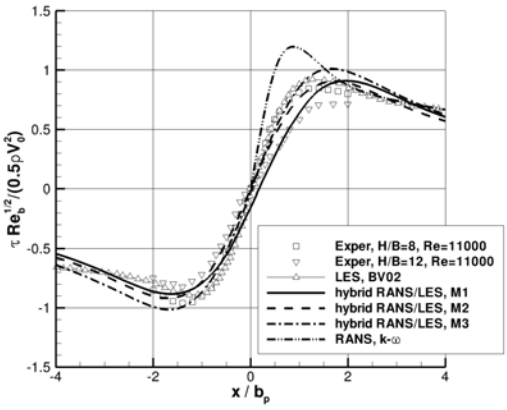

Fig. 6. Distribution of $\tau \mathrm{Re}_b^{1/2}/\left(0.5\rho V_0^2\right)$ along the impingement plate (distance x is normalized by half-width b_p of the impingement pressure profile [21]) for H/B=10, Re=13500.

Fig. (7) shows the resolved Reynolds stress along lines x located at different distances from the jet exit. Similarly to the velocity profiles, the Reynolds stress $\langle u'v'\rangle/(V_0)^2$ was averaged in time and in the spanwise z direction. The results are compared to the experimental data of Maurel and Solliec [17] and to the LES results of Beaubert and Viazzo [7]. At distance y/H=-1/12 from the jet exit (Fig. 7, top) the shear layers begin to develop. The Reynolds stress predicted by RANS has a peak value of $\langle u'v'\rangle/(V_0)^2=0.005$ at x/B=0.5 which is in good agreement with the experimental data. At distance y/H=-0.5 (Fig. 7, bottom) the Reynolds stress is underpredicted by RANS close to the symmetry plane which is due to the eddy-viscosity Boussinesq assumption. At y/H=-

1/12 (Fig. 7, top) the Reynolds stress produced by the hybrid RANS/LES models are much weaker than the Reynolds stress predicted by LES and the differences between the different hybrid RANS/LES implementations are marginal. It means that some of the energy is modelled due to relatively low turbulent length scales originating at the edges of the jet nozzle. The differences between the various hybrid RANS/LES approaches becomes higher at distance y/H=-0.5 (Fig. 7, bottom). All hybrid RANS/LES models slightly overpredict the maximum of $<u'v'>/(V_0)^2$.

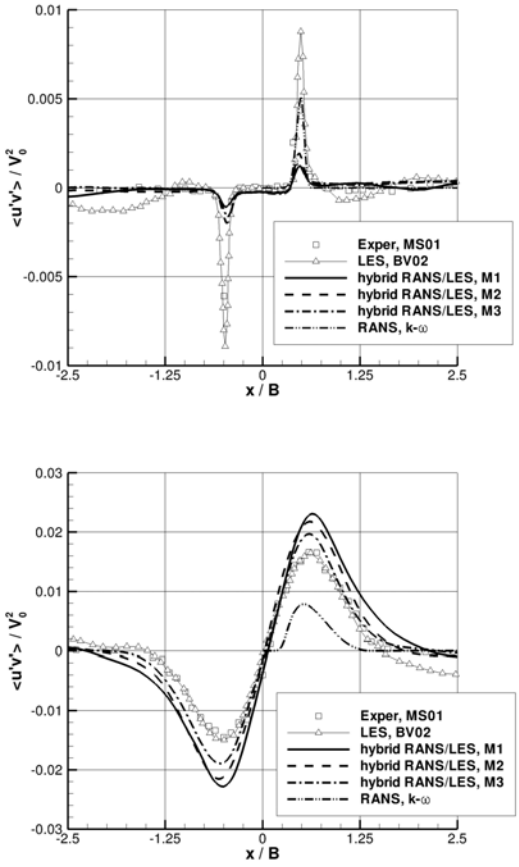

Fig. 7. Evolution of the Reynolds stress $<u'v'>/(V_0)^2$ along X/B at two distances from the jet exit (top) y/H=-1/12, (bottom) y/H=-0.5 for H/B=10, Re=13500.

Fig. 8 shows profiles of computed mean u-velocity components and the comparison with the experimental data of Asforth-Frost et al. [18] and Zhe and Modi [19] along a line perpendicular to the impingement plate at different distances from the symmetry plane for simulation of the plane impinging jet at H/B=9.2 and Re=20000. First of all, quite large differences are visible between the experimental data of Asforth-Frost et al. [18] and Zhe and Modi [19] at distances x/B=1 and x/B=5 (Fig. 8 a and c). As shown in Fig. 8 (a) at distance x/B=1 the mean velocity profile obtained with the pure k-ω model is strongly overpredicted. This is caused by the too slow spreading of the mean velocity profiles in the developing wall jet region into the free stream as a result of too weak turbulence mixing in the shear layer of the jet. It means that the k-ω model is not able to reproduce the near-wall characteristics of the turbulent boundary layer due to ovepredictiion of the length of the jet core. As mentioned above this is a drawback of the eddy-viscosity Boussinesq approximation. With the hybrid RANS/LES methods much better correspondence is obtained with the experimental data than using pure the 2-D RANS model. At distance x/B=2 (Fig. 8 b) the mean velocity profile predicted with the k-ω model again deviates strongly from the experimental data. The best agreement between computed and measured mean velocity profiles is obtained with the M1 model. At x/B=5 (Fig. 8 c) the computational results obtained with both M1 and M2 models are closer to the experimental data of Zhe and Modi [19] than to the experimental results of Asforth-Frost et al. [18] with the M3 model showing the strongest deviations between computations and experiment.

Overall, the best agreement between computations and measurements is obtained with the M1 model. The M2 model gives acceptable results. Highest differences between computed and measured mean velocity profiles are observed with the M3 model.

In order to identify the cause of these differences, contour plots of k are shown in Fig. 9 for all model formulations (M1 model - top, M2 model -middle and M3 model – bottom) in the x-y plane located at z/B=π/2. Note that the M1 model consists of the substitution of the turbulent length scale by the local grid size in the destruction term of the k-equation, the M2 model uses the substitution in the k-equation and in the definition for ν_t (this formulation has a higher level of theoretical justification since in the LES mode the Yoshizawa subgrid scale model is recovered) while the M3 model introduces the grid size only in the definition for ν_t. Interestingly, the instantaneous field of subgrid k obtained with the M1 model (top) is quite similar to the instantaneous field of subgrid k obtained with the M2 model (middle) which gives the impression that both ways of modifying of the k-ω model are nearly equivalent. The instantaneous field of k obtained with the M3 model strongly differs from those obtained with the M1 and M2 models. Much higher levels of modelled turbulent kinetic energy are obtained with the M3 model than using the M1 and M2 formulations due to a different way of modelling of the destruction term in the k-equation (Eq. 1). Note that in LES mode, both the M1 and M2 formulations return the same form of the destruction term in Eq. (1) which is based on the grid size (Eq. 5). This is in contrast to the M3 model which uses the RANS type destruction term. Since the levels of the modelled turbulent kinetic energy obtained with the M1 and M2 models are similar, it means that the different way of computing ν_t in the LES zone (for M1 the definition for ν_t is not modified in the LES zone, while for M2 the definition for ν_t is modified as shown by Eq. 7) has only a secondary effect on the modelled turbulent kinetic energy. This might explain why a stronger spreading of the mean velocity profiles (due to higher turbulent viscosity) was obtained using the M3 model at distances x/B=2 and 5 (shown in Fig. 9 b and c) than applying the M1 and M2 models.

Fig. (10) shows the skin friction coefficient c_f along the impingement plate obtained with the RANS k-ω model and computed with the different hybrid RANS/LES formulations. RANS predicts the skin friction coefficient far too high in the impingement region and also in developing wall jet region. As

mentioned above, this is caused by underprediction of the turbulence mixing in the shear layer of the jet which results in too slow spreading of the mean velocity profiles into the free stream as the flow turns into a wall jet. With hybrid RANS/LES methods much better correspondence between computations and experiment is obtained. The best result is obtained with the M2 model. The peak value of c_f at x/B=2 is slightly overpredicted with all hybrid RANS/LES formulations and only the M1 and M2 models give correct asymptotic behaviour for x/B>8.

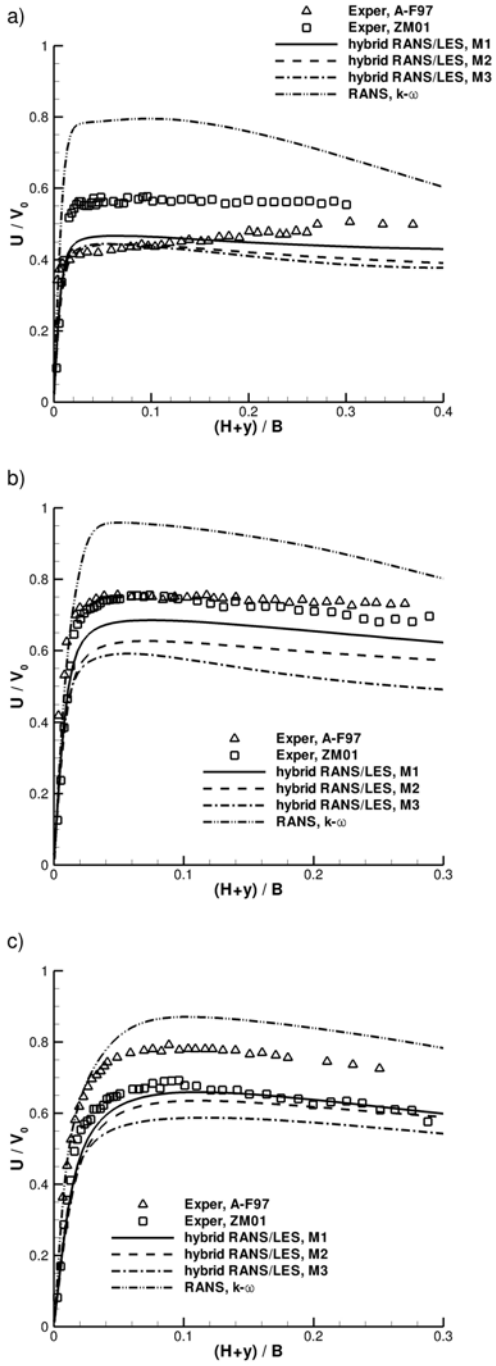

Fig. 8. Variation of the mean u-velocity component along a line perpendicular to the impingement plate at different positions from the symmetry plane a) x/B=1, b). x/B=2, c) x/B=5 for H/B=9.2, Re=20000.

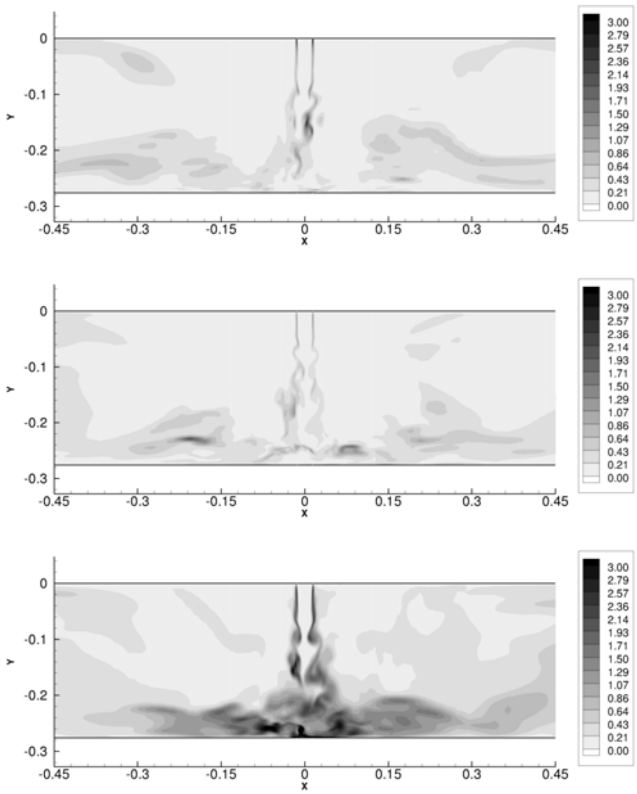

Fig. 9. Instantaneous field of modelled k obtained by (top) M1 model (middle) M2 model and (bottom) M3 model, for H/B=9.2, Re=20000.

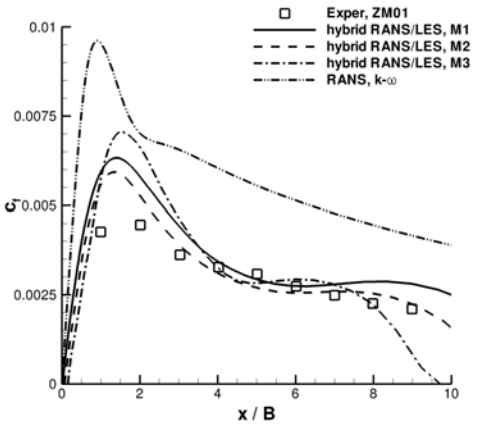

Fig. 10. Distribution of the skin friction coefficient along the impingement plate for H/B=9.2, Re=20000.

Lastly, Fig. (11) shows the distribution of the Nusselt number along the impingement plate and its comparison with the experimental data of Ashforth-Frost et al [18]. RANS is not able to correctly reproduce the monotonic decay of the Nusselt number profile with increasing distance from the symmetry plane (even if the stagnation point Nusselt number is correctly predicted). The M3 hybrid RANS/LES model gives a too high level of the turbulent viscosity in the near-wall region of the developing wall jet which results in overestimation of the heat transfer rates at x/B<6. The other two hybrid RANS/LES formulations (M1 and M2 models)

give the best correspondence between simulations and experiments.

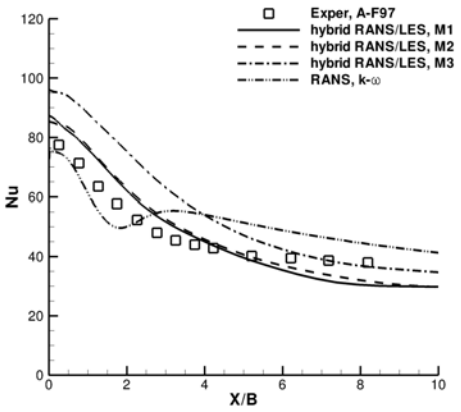

Fig. 11. Distribution of the Nusselt number along the impingement plate for H/B=9.2, Re=20000.

VI. SUMMARY

The performance of hybrid RANS/LES models based on the k-ω model of Wilcox [1] for simulation of plane jets impinging onto a flat plate at high nozzle-plate distances (H/B=10 and 9.2) and moderate Reynolds numbers (Re=13500 and 20000) has been analysed. Different ways of substitution of the turbulent length scale by the local grid size have been tested. For the test case H/B=9.2, Re=20000, the best results have been obtained with the M1 and M2 models. With the M1 model, the local grid size Δ is introduced in the destruction term of the k-equation while for the M2 model the local grid size is introduced in both the destruction term of the k-equation and in the definition for ν_t in LES mode. The M3 model which is based on damping of RANS turbulent viscosity gives a too high level of the modelled turbulent kinetic energy in the free jet and in the stagnation flow regions. The higher level of the turbulent kinetic energy obtained with the M3 model is due to a too much smaller destruction term in the k-equation when switching to the LES mode in the free jet flow region compared to the M1 and M2 models. The M3 model fails to predict the effect of flow acceleration and deceleration in the developing wall jet region at distances x/B=2 and 5, for H/B=9.2 and Re=20000. Too high heat transfer rates along the impingement plate are obtained using the M3 model compared to the experimental data. The M1 and M2 models show good correspondence between computed and measured Nusselt number profiles. For the second case analyzed (H/B=10, Re=13500) all hybrid RANS/LES models gave similar results. It means that this test case (relatively low Reynolds number) is not very critical for assessment of the accuracy of hybrid RANS/LES models. Overall, the M1 and M2 models allow greatly improved impingement flow predictions with respect to the 2-D RANS method and these two formulations are favoured over the M3 model.

ACKNOWLEDGEMENTS

The authors acknowledge the support from the research project 'Novel Multiscale approach to Transport phenomena in Electrochemical Processes' (IWT, contract: MuTEch SBO 040092)

REFERENCES

[1] D.C. Wilcox, *Formulation of the k-ω turbulence model revisited, AIAA Journal,* 46(11), 2008, pp. 2823-2837.

[2] M. Strelets, *Detached Eddy Simulation of Massively Separated Flows*, *AIAA Paper 01-0879*, 39th AIAA Aerospace Sciences Meeting and Exhibit, Reno, Nevada, Jan, 2001.

[3] J. Kok, H. Dol, H. Oskam and H. van der Ven, *Extra-large eddy simulation of massively separated flows*, *AIAA Paper 04-0264*, 42nd AIAA Aerospace Sciences meeting and Exhibit, Reno, Nevada, Jan, 2004.

[4] A. Yoshizawa, *Bridging between eddy-viscosity-type and second-order turbulence models through a two-scale turbulence theory*, Physical Review E, 48 (1), 1993, pp. 273-281.

[5] P. Batten, U. Goldberg and S. Chakravarthy, *LNS-An approach towards embedded LES, AIAA Paper*, 2002-0427, 2002.

[6] P. Sagaut, S. Deck and M. Terracol, *Multiscale and Multiresolution approaches in turbulence*, Imperial College Press, London, 2006.

[7] F. Beaubert and S. Viazzo, *Large eddy simulations of plane turbulent impinging jets at moderate Reynolds numbers, Int. J. Heat Fluid Flow* 24, 2003, pp. 512-519.

[8] S. Kubacki and E. Dick, *Convective heat transfer prediction for an axisymmetric jet impinging onto a flat plate with an improved k-ω model, Int. J. Numer. Methods in Heat and Fluid Flow*, 2008 (to appear)

[9] F.R. Menter, *Two-equation eddy-viscosity turbulence models for engineering applications, AIAA Journal* 32 (8),1994, pp.1598-1605

[10] P.A. Durbin. *On the k-ε Stagnation Point Anomaly. Int. J. Heat Fluid Flow*, 17, 1996, pp.89-90.

[11] P.A. Durbin and B.A. Pettersson-Reif, *Statistical theory and modelling for turbulent flows*, John Willey & Sons Inc., The Atrium, Southern Gate, Chichester, West Sussex, England, 2001.

[12] R.L. Davis and J.F. Dannenhoffer, *Detached-eddy simulation procedure targeted for design, J. of Propulsion Power*, 24(6), 2008, pp.1287-1294.

[13] J. Yan, C. Mocket and F.Thiele, Investigation of alternative length scale substitutions in detached-eddy simulation, Flow, Turbulence and Combustion, 74, (2005) pp.85-102.

[14] C. de Langhe, B. Merci and E. Dick, *Hybrid RANS/LES modelling with an approximate renormalization group. I: model development. J. Turbulence*, 6(13), 2005, pp.1-18.

[15] P. Sagaut, *Large-eddy simulation for incompressible flows*, 3rd edition, Springer, Berlin, 2005.

[16] M. Tsubokura, T. Kobayashi, N. Taniguchi and W.P. Jones, *A numerical study on the eddy structures of impinging jets exited at the inlet, Int. J. Heat Fluid Flow* 24, 2003, pp.500-511.

[17] S. Maurel and C. Solliec, *A turbulent plane jet impinging nearby and far from a flat plate, Exper. in Fluids* 31, 2001 pp.687-696.

[18] S. Ashforth-Frost, K. Jambunathan and C.F. Whitney, *Velocity and turbulence characteristics of a semiconfined orthogonally impinging slot jet, Experimental Thermal and Fluid Science*, 14, 1997, pp.60-67.

[19] J. Zhe and V. Modi, *Near wall measurements for a turbulent impin*ging slot jet, Trans. of the ASME, J. Fluid Eng. 123, 2001, pp.112-120.

[20] J.E. Jaramillo, C.D. Perez-Segarra, I. Rodriguez and A. Oliva, *Numerical study of plane and round impinging jets using RANS models, Numer. Heat Transfer, Part B*, 54, 2008, pp.213-237.

[21] C.V. Tu and D.H. Wood, *Wall pressure and shear stress measurements beneath an impinging jet, Experimental Thermal and Fluid Sci.* 13, 1996, pp.364-373.

[22] J. Sakakibara, K. Hishida and M. Maeda, *Vortex structure and heat transfer in the stagnation region of an impinging plane jet (simultaneous measurements of velocity and temperature fields by digital particle image velocimetry and laser-induced fluorescence), Int. J. Heat Mass Transfer* 40 (13), 1997, pp.3163-3176.

Proceedings of the 8th National Congress on Theoretical and Applied Mechanics, May 28-29, Brussels, Belgium.

Large Eddy Simulation of Pulsed Jet in Crossflow

Axel Coussement[1 2], Olivier Gicquel[1 2] and Gerard Degrez[1]
[1]Department of Aero-Thermo-Mechanics, Université Libre de Bruxelles
Avenue F.D. Roosevelt CP 165/41, 1050 Bruxelles, Belgium
[2]EM2C Laboratory, École Centrale de Paris
Grande Voie des Vignes, 92295 Chatenay-Malabry Cedex, France
email: axcousse@ulb.ac.be

Abstract— **This study quantifies the mixing resulting of a pulsed jet injected in a jet in crossflow configuration. By large eddy simulation computations, it also helps to understand the physical phenomena involved in the formation of the pulsed jet in crossflow. The boundary conditions of the jet inlet were implemented via an NSCBC coupled with a Fourier series development. The signal used to pulse the jet inlet was a square or a sine wave. A new way of characterizing the mixing is introduced with the goal of easily interpreting and quantifying the complicated mixing process involved in pulsed jet in crossflow flow fields. Different flow configurations, pulsed and non-pulsed were computed and compared. This comparison no only allows to characterize the mixing but also to point out some properties of those mixing curves.**

Keywords— **Large Eddy Simulation, Jet in Crossflow, Pulsed Jet in Crossflow, NSCBC**

I. Introduction

Steady jets in uniform crossflow have been investigated by analytical, experimental and numerical approaches in the past 50 years. In addition to being interesting from a theoretical point of view, the jet in crossflow is commonly used in various applications, including V/STOL aircraft in transition flight, turbine film cooling, chimneys, roll control in rockets or fuel mixing in combustion chambers.
For exemple, in a combustion chamber, the mixing of the two flows and the entrainment of the crossflow fluid into the fuel jet can have a critical influence on the size and efficiency of the chamber. This is even more important in high speed combustion, in scramjets for example where ultra-fast mixing is the key to the design of an efficient chamber. This mixing efficiency is also required for pollutant reduction such as NO_x which requires reducing the duration of high-temperature exposure of the combustion gases.
It has long been recognized that jets in crossflow are more efficient mixers than a free jet or a mixing layer [1], [2]. This enhanced mixing is attributed to the counter-rotating vortex pair whose role in the mixing process is explained by Cortelezzi et al. [3]. Experiments of Karagozian et al. [15], Johari et al. [16], [13], [12], Eroglu et al. [14] have shown that one can further improve the mixing by pulsating the jet speed U_j. These experiments have been undertaken in liquid or gaseous phase. For example, Johari et al. [13] who study the penetration of a fully modulated liquid jet in crossflow, show that the maximum penetration occurs at a forcing frequency, f, which corresponds to a jet Strouhal number $St_j \equiv fD/\bar{U}_j = 0.004$ where D is the inner diameter of the jet orifice and $\bar{U}_j$ the temporal mean jet speed. Moreover this maximum penetration occurs at a duty cycle $\alpha = 0.20$, the duty cycle being the ratio between the temporal pulse width and the period of the pulsation. In a latter work, Johari [16] makes a compilation of all the experiments of liquid phase jet in crossflow and finds out general tendencies independent of the jet-to-crossflow momentum ratio $R \equiv \rho_j \bar{U_j}^2/\rho_\infty \bar{U_\infty}^2$ and velocity ratio $J \equiv \bar{U_j}/\bar{U_\infty}$. The work of Karagozian et al. [15] focuses on pulsed jet in crossflow in gaseous phase.
Those works are only experimental and no numerical has been done, to the author's knowledge. In the present work, we will expose the results of present LES computations for the case presented by Karagoian et al. [15]. This particular work was chosen because it involves a gaseous phase jet in crossflow and the flow solver used here doesn't handle easily liquid flows. We will try to easily characterise the mixing of the pulsed jet in crossflow and, of course, the difference in mixing of the pulsed configuration with respect to the steady flow case.

A. Structure of the jet in crossflow

As mentioned before, the mixing properties of the jet in crossflow come from complex three dimensional interactions, most of which were identified in the seventies [4], [5]. Nowadays, lots of investigations have been undertaken to understand the formation and the behaviour of the jet in crossflow flow structures. One can divide the vortical structure of the jet in crossflow into four principal vortices (figure 1).

- The counter-rotating vortex pair (CVP) is the dominant struture downstream of the jet injection point. This structure is generated by the deflection of the jet and is convected by the transverse flow. Experimental studies [6] suggested that the CVP finds its origin in a process of roll up, tilting and folding of the shear layer vortices. This was latter on confirmed by the work of Cortelezzi et al. [3].

• The horseshoe vortex which is due to the adverse pressure gradient just in front of the injection hole. This structure and the vortex-shedding frequency are quite similar to those observed around a solid cylinder [7].
• Shear-layer ring vortices are generated in the boundary layer of the jet orifice and evolve in the flow to generate the CVP [6], [3]. The process involved in the generation of these vortices is a Kelvin-Helmoltz instability in the shear layer when the two streams meet.
• Wake vortices are the least understood. The experiments of Fric et al. [9] suggested that those vortices originate from the wall boundary layer.

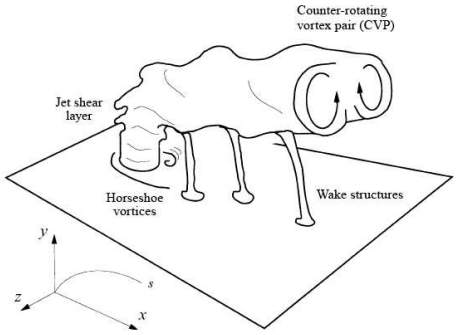

Fig. 1. Structure of steady jet in crossflow

B. Pulsed Jet in Crossflow

Jet unsteadiness strongly impacts the nature of the jet in crossflow. Many experimental studies were undertaken to understand and measure the difference between the steady and pulsed jet in crossflow [10], [11], [12], [13], [14], [15]. By their experimental nature, these studies don't allow to access all the flow variables and, so, deeply understand the physic of this kind of flows. Nevertheless, the work of Johari [16] compiles of all these experiments and by introducing a stroke ratio defined in equation 1 where u_j is the jet velocity at the nozzle exit and A is the nozzle area, it was possible to classify the various flow regimes as a function of the stroke ratio and the duty cycle (figure 2)

$$\frac{L}{d} = \frac{4}{\pi d A} \int_0^{\tau} \int_A u_j \, dA \, dt \tag{1}$$

C. Flow parameters

The flow parameters are derived from the work of Karagozian et al. [15], mostly because by doing that the computation could be compared, at least visually, to some experimental results. The main parameters of the steady jet in crossflow are
• A jet inlet speed of $3.1 m/s$ (U_j)
• A crossflow inlet speed of $1.2 m/s$ (U_∞)
• A nozzle exit diameter of $7.5 mm$

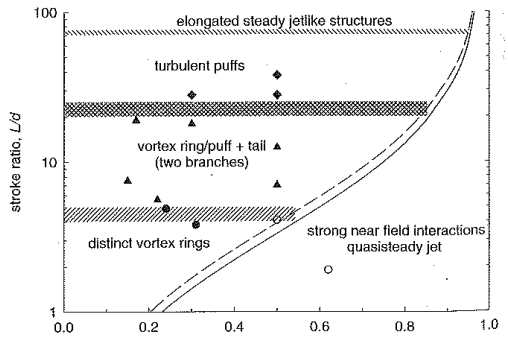

Fig. 2. Structure of steady jet in crossflow by Johari

• Crossflow is composed of pure nitrogen

Different flow cases were computed, table I summarizes all the cases and the flow parameters used. The pulsed computational cases 6, 7 and 8 were chosen so that they have the same rms value as the pulsed signal (≈ 1.7), in this way the same energy is injected in the jet. Moreover, case 2 was chosen because it has the same mean velocity as cases 6 and 8. The other computational cases were chosen to compare the mixing under steady jet conditions and case 1 is the nominal case in the sense that it has the same velocity as the base velocity of the pulsed flow, i.e. the velocity minus the pulsation. Case 6, 7 and 8 will be comparable in terms of energy injected in the jet flow, cases 6, 7 and 2 will be comparable in terms of mass flow. Figure 15 shows instantaneous results for cases 1, 6, 7, 8.

II. Numerical Simulation LES

The Reynolds Averaged Navier Stokes (RANS) and the Direct Numerical Simulation (DNS) stand at both extremes of computational fluid modelling. The first, RANS, tries to model all the scales of turbulence and the other models none of them. The compromise between these two is Large Eddy Simulation (LES) which models only the small scales of turbulence and resolves the large scales. Here an LES approach was used. The first reason for that is obvious : the pulsed jet in crosflow is an unsteady flow. The second reason is related to the jet in crossflow structure which is dominated by large scales of turbulence : the CVP.

To model only the smaller scales of turbulence a filter has to be applied to the Navier-Stokes equations. In the case of compressible flow a Favre filtering [17] is used :

$$\bar{\rho}\widetilde{f}(x,t) = \overline{\rho f(x,t)} = \int_{-\infty}^{\infty} \rho f(x',t) G(x'-x) dx' \tag{2}$$

where ρ is the density, G the filter function and f is a flow parameter : velocity vector, mass fraction of species

TABLE I
COMPUTATIONAL CASES

Case Number	U_∞	U_j	Pulse Type	Pulse Amplitude	Pulse Frequency	Jet Material	R	J
1	$1.2m/s$	$3.1m/s$	no pulse	n.a.	n.a.	nitrogen	6.67	2.58
2	$1.2m/s$	$3.79m/s$	no pulse	n.a.	n.a.	nitrogen	9.975	3.15
3	$6m/s$	$15.5m/s$	no pulse	n.a.	n.a.	nitrogen	6.67	2.58
4	$1.2m/s$	$9.3m/s$	no pulse	n.a.	n.a.	nitrogen	60	7.75
5	$1.2m/s$	$11.55m/s$	no pulse	n.a	n.a.	hydrogen	6.67	9.625
6	$1.2m/s$	$3.79m/s$	sine wave	$2m/s$	$55Hz.$	nitrogen	9.975	3.15
7	$1.2m/s$	$3.1m/s$	$\alpha = 0.15$	$4.6m/s$	$55Hz.$	nitrogen	9.975	3.15
8	$1.2m/s$	$3.1m/s$	$\alpha = 0.60$	$2.25m/s$	$55Hz.$	nitrogen	13.75	3.7

or total energy. By applying this to the Navier-Stokes equations one can find [18]:

$$\frac{\partial \bar{\rho}}{\partial t} + \frac{\partial \bar{\rho}\widetilde{u}_j}{\partial x_j} = 0 \quad (3)$$

$$\frac{\partial \bar{\rho}\widetilde{u}_i}{\partial t} + \frac{\partial \bar{\rho}\widetilde{u}_i\widetilde{u}_j}{\partial x_j} = -\frac{\partial}{\partial x_j}[\bar{P}\delta_{ij} - \bar{\tau}_{ij} - \bar{\tau}^t_{ij}] \quad (4)$$

$$\frac{\partial \bar{\rho}\widetilde{E}}{\partial t} + \frac{\partial \bar{\rho}\widetilde{E}\widetilde{u}_j}{\partial x_j} = -\frac{\partial}{\partial x_j}[\overline{u_i(P\delta_{ij} - \tau_{ij})} + \bar{q}_j + \bar{q}_j{}^t \quad (5)$$

and

$$\bar{\tau}_{ij} = \overline{2\mu\left(S_{ij} - \frac{1}{3}\delta_{ij}S_{kk}\right)} \quad (6)$$

$$\approx 2\mu\left(\widetilde{S}_{ij} - \frac{1}{3}\delta_{ij}\widetilde{S}_{kk}\right) \quad (7)$$

$$\bar{q}_i = -\bar{\lambda}\overline{\frac{\partial T}{\partial x_i}} \quad (8)$$

$$\approx -\bar{\lambda}\frac{\partial \widetilde{T}}{\partial x_i} \quad (9)$$

where

$$\widetilde{S}_{ij} = \frac{1}{2}\left(\frac{\partial \widetilde{u}_j}{\partial x_i} + \frac{\partial \widetilde{u}_j}{\partial x_j}\right) \quad (10)$$

The ideal gas law $\bar{P} = \bar{\rho}\widetilde{rT}$is then added to this system of partial differential equations.

To close the system one must add equations to model $\bar{\tau}^t_{ij}$ and $\bar{q}_j{}^t$ which are the turbulent strain tensor and the turbulent heat flux. To do so, Boussineq's hypothesis is introduced to mimic the subgrid-scale action on the resolved part of the field ;

$$\bar{\tau}^t_{ij} = -\bar{\rho}(\widetilde{u_i u_j} - \widetilde{u}_i\widetilde{u}_j) = 2\bar{\rho}\nu_t\left(\widetilde{S_{ij}} - \frac{1}{3}\widetilde{S_{kk}}\delta_{ij}\right) + \frac{1}{3}\bar{\tau}^t_{kk}\delta_{ij} \quad (11)$$

Then, a subgrid scale viscosity ν_t has to be modelled. Here, the dynamic Smagorinsky model is used [18]

$$\nu_t = (C_s\Delta)^2\sqrt{2\widetilde{S}_{ij}\widetilde{S}_{ij}} \quad (12)$$

where Δ is the filter characteristic length, i.e. the cubic root of the cell volume and C_s is the Smagorinsky constant which is computed to automatically adapt to local flow the conditions .

The turbulent heat flux is modelled using a turbulent Prandtl number.

In the present work the fully compressible, the unstructured grid flow solver AVBP is used. The numerical implementation is based on a finite element discretisation : Taylor- Galerkin (TTGC) and the temporal discretization is an explicit four stages Runge-Kutta. Computations have been performed with a CFL of 0.7

A. Mesh and domain

The figures 3 and 4 show the computational domain. The jet diameter is $D = 7.5mm$. The jet orifice center is located at a distance $A = 4D$ from the inlet of the computational domain, and at a distance $B = 26.6D$ of the outlet. The width, $W = 10.6D$ was chosen to avoid a jet impact on the side boundary.

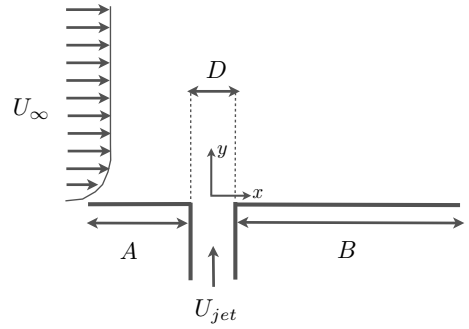

Fig. 3. Computatinal domain side view

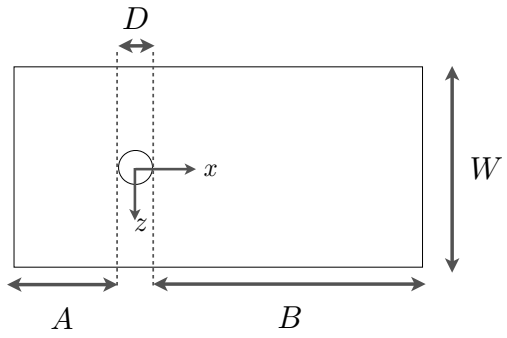

Fig. 4. Computatinal domain up view

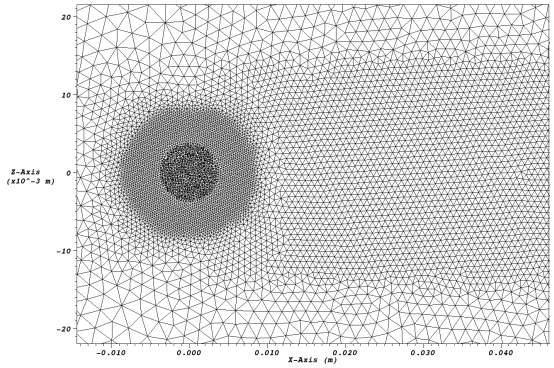

Fig. 6. Mesh up view

The computational grid contains 253495 nodes and 1436506 cells.Thanks to the low speed of both flows, such a number of cells permits to compute a real LES, as it will be explained further. The mesh is refined in the jet pipe and near the mixing zone as shown on figures 5 and 6. This was necessary to correctly capture the physics of the pulsations and the interaction between the crossflow and the pulsation. Indeed, it is recognized that a good description of the flow in that particular region is critical to obtain good results [3]. The order of magnitude of the mesh size, and so the filter size, in that particular region is $\Delta x \approx 100.10^{-6}$.

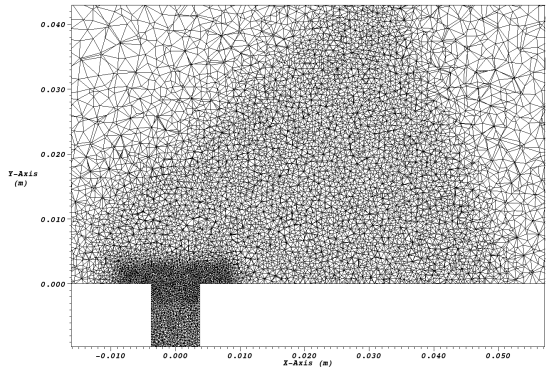

Fig. 5. Mesh side view

One fact that matters in LES is how good is the simulation. This can be expressed in terms of energy : the precision improves when k_{SGS}, which is the sub-grid energy, decrease. Further, when k_{SGS} equals zero, it corresponds to a direct numerical simulation (DNS). If K is defined as the resolved part of the energy one can define the turbulent resolution $M(\underline{x},t)$ (eq 13)

$$M(\underline{x},t) = \frac{k_{SGS}(\underline{x},t)}{K(\underline{x},t) + k_{SGS}(\underline{x},t)} \tag{13}$$

$M = 1$ in the case of RANS simulation and $M = 0$ in the case of DNS. Starting from this, Pope [19] introduced the concept of adaptive LES : the turbulent resolution must be less than 0.2, which corresponds to a resolution of 80%. The parts of the domain in which this criterion is not respected are judged insufficiently resolved. Knowing this, it is possible to judge the quality of the LES simulation by computing this criterion in every point. Evaluating exactly the resolution is fairly impossible, so approximations are made : eq 14 gives an approximation of the resolved part of the kinetic energy and eq 15 gives an approximation of the sub-grid energy. Note that equation 15 was chosen because it overestimates k_{SGS} [18], so that the criterion is more restrictive. $\langle\rangle_T$ denotes the temporal average on a time T and $\widetilde{u}$ is the resolved part of the speed.

$$K(\underline{x},t) \approx 0.5\left(\langle\widetilde{u}^2\rangle_T - \langle\widetilde{u}\rangle_T^2\right) \tag{14}$$

$$k_{SGS}(\underline{x},t) \approx 0.5\langle\tau_{ii}\rangle_T \approx \frac{\langle\nu_t^2\rangle_T}{(C_m\Delta)^2} \tag{15}$$

In equation 15 Δ is the filter size and Cm is an autosimilar function of the turbulence and is defined in equation 16. K_o and A are equal respectively to 1.4 and 0.44. ν_t is the turbulent viscosity, in the case of the flow solver used here it is defined as the sum of the numerical viscosity $\nu_{num}$and the sub-grid viscosity ν_{sgs}. The temporal average was done on one pulsation cycle i.e $T = 1/55$. Only one pulsation was used because the increase in ν_t is mainly due to the pulsation, so that the information contained in a one cycle average is complete enough.

$$C_m = \sqrt{\frac{2}{3}}\frac{A}{\pi K_o^{\frac{3}{2}}} \tag{16}$$

Figure 7 shows the results of the computation of M for case 7. Case 7 was used to compute the criterion because it is the most critical. Indeed, the pulsation is quite abrupt because the pulsation amplitude is the strongest. This will cause a high velocity gradient and so (eq 12) higher sub-grid viscosity.

It is clear that most of the points are in the zone in which $M \leq 0.2$, but some are not. This can be explained by several reasons. First, the computed k_{SGS} was over estimated. It is clear that in the present configurations, large gradients appear : in the zone where the flows meet each other the velocity is changing abruptly, which gives high velocity gradient values. By looking at equation 12 one can see that those gradients produce a high subgrid viscosity. This effect, while being reduced by the dynamic constant, cannot be fully compensated by C_s due to the limitations of the dynamic Smagorinsky model [18]. The final effect is an increase of k_{SGS}.

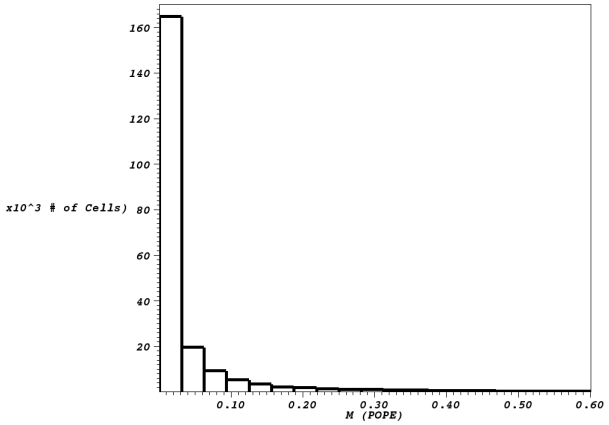

Fig. 7. Number of cell for different values of M, computation case 7

In those zones were the two flows meet, velocity is generally quite low, so that K is also quite low. The final result is an increase of M in some points, especially in the jet-crossflow meeting zone.
Another criteron must be found to be sure that the points at which $M \geq 0.2$ result from the causes explained above. This is done by considering the ratio of the effective viscocity and fluid viscosity [20]. In the case of the flow solver used, AVBP, the effective viscosity $\nu_{eff}$is defined in equation 17 as the sum of the fluid viscosity ν and the turbulent viscosity ν_t. The criterion in this case is that the ratio must be under 10 for a LES, and equal to one in a DNS. As shown in figure 8 the criterion is cleary under 10. Both of the criteria show that the LES is well resolved.

$$\nu_{eff} = \nu + \nu_t \tag{17}$$

B. Boundary Conditions

For pulsed jet configurations, a particular wave shape must be superimposed to the base U_{jet} speed; the boundary conditions for U_{jet} must be time-dependent but still consistent with the physics of the flow. To do so, one can

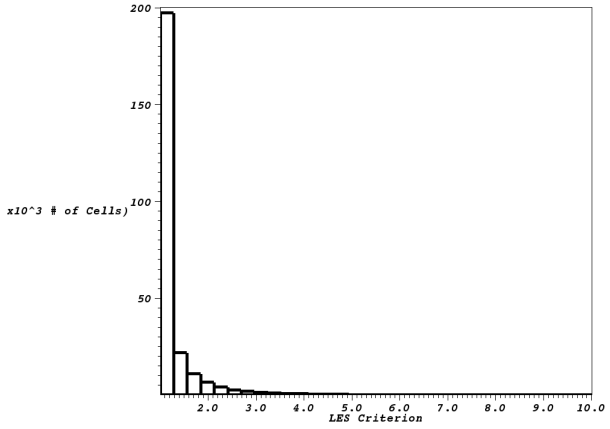

Fig. 8. Number of cells for different values of $\frac{\nu_{eff}}{\nu}$ computation case 7

impose the jet boundary conditions according to the theory of characteristics. Compressible flows are characterized by waves, so that the method of characteristics is the standard approach for controlling the waves crossing the boundary. In viscous flows, the concept of waves is not clearly dened, this dificulty is overcome by imposing others viscous relations as proposed in the NSCBC (Navier-Stokes characteristic boundary condition) method [21].
The NSCBC not only allows to impose a constant boundary condition but also to impose a normal velocity fluctuation at the boundary. This can be done on the only condition that the velocity fluctuation function must be C_1 i.e. the first order derivative must be continuous. So, imposing a pulse signal (figure 9) is impossible because during the rise and the fall of the pulse the derivative is not computable. One way to avoid this is to use a Fourier series (eq 18). Indeed Fourier series are infinitely differentiable and in the case of a pulse wave, coefficients can easily be computed (eq 19, 20, 21). A is the pulse amplitude and α is the duty cycle.

$$v(t) = a_0 + \sum_{n=1}^{\infty} a_n cos(2\pi ftn) + \sum_{n=1}^{\infty} b_n sin(2\pi ftn) \tag{18}$$

$$a_0 = \frac{1}{T}\int_{-T/2}^{T/2} x(t)dt = A.\alpha \tag{19}$$

$$a_n = \frac{2}{T}\int_{-T/2}^{T/2} x(t) cos\left(\frac{2\pi tn}{T}\right) dt = \frac{2A}{n\pi} sin(n\pi\alpha) \tag{20}$$

$$b_n = \frac{-2}{T}\int_{-T/2}^{T/2} x(t) sin\left(\frac{2\pi tn}{T}\right) dt = 0 \tag{21}$$

The number of coefficients taken into account in the code is 10, so that $n = 1, 2 \ldots 10$, for two reasons. First,

such a number of coefficient allows to correctly reproduce a pulsed jet flow field. Second, since it is impossible experimentally to impose a real pulse and since the goal of the simulation is to reproduce experimental results, there is no need to impose something closer to a pure pulsation. Indeed, figure 10 shows the velocity at the jet exit of the experiments of M'Closkey et al.. [15] and it clear that the jet velocity pertubation (dashed line) is not a pure pulsed wave. Part of the work of M'Closkey et al. [15] consisted in designing a device that can impose a pulsation at the jet nozzle exit, by compensating the filter effect of the jet inlet, that's what they called the compensation in figure 10.

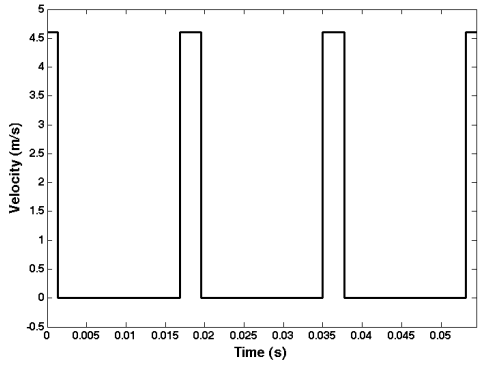

Fig. 9. Pulse signal, $\alpha = 0.15$ and $A = 4.6m/s$

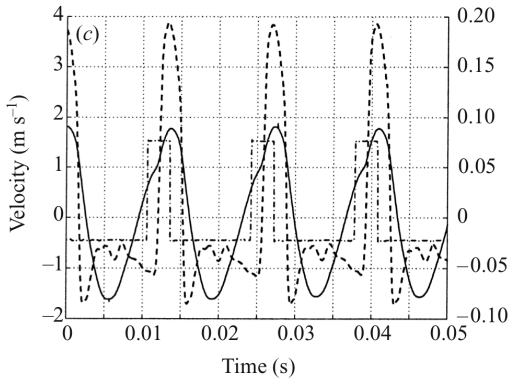

Fig. 10. Actuator signal in Volts (dash-dotted) line, velocity signal at the jet nozzle with compensation (i.e. mean substracted) dashed line and velocity signal at the jet nozzle without compesation at $73.5Hz$ and $\alpha = 0.22\%$

Limiting the Fourier series development to the first 10 coefficients produces the signal showed in figure 11. While it is not exactly identical to the signal showed in figure 10, it will produce the same effects as it is demonstrated later, i.e. the generation of turbulent puffs in the flow.

Figure II-B shows the mean velocity at the jet exit in case 7, which proves that the implementation of the Fourier decomposition of the signal is working. Nevertheless, by comparing figure 11 and II-B it is obvious that the amplitude of the signals is a little bit different. It is well known that the flow in a pipe doesn't have not a flat velocity profile, and the boundary layer also plays a role in changing the velocity profile along with the fact that the flow is unsteady. So the flat velocity profile imposed at the inlet is not the real velocity profile. As a result the mean velocity plotted in figure II-B doesn't have the same amplitude as the profile showed in figure 11. The analysis holds even though the fully-established velocity profile in the pipe differs from a Poiseuille profile for a pulsed flow. Moreover the relaxation coefficients used in the NSCBC further modify the mean velocity at the inlet.

Finally, the boundary conditions are summarized in table II. Note that, in the NSCBC method not only the velocity is imposed at the inlet but also the temperature and the mass fractions along with relaxation coefficients. Since the goal is to simulate a pulsed signal at the inlet, the relaxation coefficient of the velocity is high. In this way, the velocity in the pipe will be as close as possible to the velocity imposed at the inlet. The other relaxation coefficients are chosen low enough, so that they don't perturb the velocity. At the outlet only the pressure is imposed, with low relaxation coefficient to evacuate the acoustic wave as easily as possible. The pipe walls and the plate wall use a non slip wall boundary condition. A slip adiabatic wall boundary condition is enforced on the top and side boundaries. Since the computational domain is big enough, there is no need to impose another type of boundary condition.

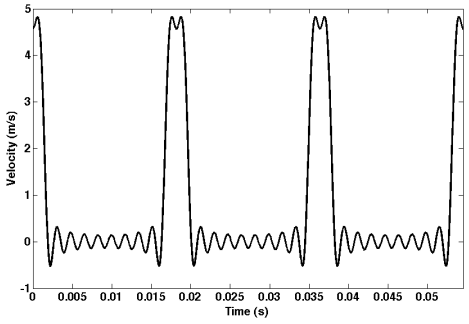

Fig. 11. Pulse signal, $\alpha = 0.15$ and $A = 4.6m/s$ with $n = 10$

III. Simulation Results

A. Steady Jet Solution

To verify the behaviour of the computation in the steady jet configuration, the solution has to be compared with previous studies. Case 1 will be used for that, the velocity ratio in this case is 2.58. This computation will be a bench-

TABLE II
BOUNDARY CONDITIONS RELAX COEFFICIENTS AND FIXED QUANTITIES

Boundary name	Fixed quantities	Relaxation coefficient
Inlet crossflow	$U_{normal}, U_{transversal}, T, Y$	$\sigma_{U_{normal}} = 10000\ \sigma_{U_{transversal},T,Y} = 1000$
Inlet Jet	$U_{normal}, U_{transversal}, T, Y$	$\sigma_{U_{normal}} = 1000\ \sigma_{U_{transversal},T,Y} = 100$
Outlet	P	$\sigma_P = 100$
Jet wall	$q_{wall} = 0, nonslip$	N/A
Bottom wall	$q_{wall} = 0, nonslip$	N/A
Side walls	$q_{wall} = 0$	N/A
Top wall	$q_{wall} = 0$	N/A

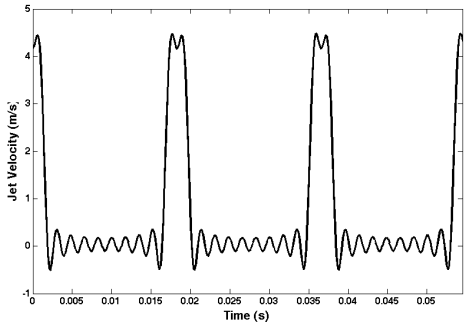

Fig. 12. Mean jet nozzle velocity from LES computation case 7

mark against steady jet experimental results.
To compare with experimental data, the scaling law was used [2]. The scaling law establishes a relation between the position of the locus of the maximum of concentration Y_{cl} and the distance downstream of the jet nozzle. All the coordinates are normalized by JD, the product of the velocity ratio and the jet diameter.

To verify the scaling law, an average field must be used, it is presented in figure 13. A sufficient number of iterations was necessary to get a smooth average field (≈ 200000), the average is computed every 10 iterations. From this average field, the Y_{cl} were extracted and then the equation 22 was applied, the result is showed in figure 14. Both best fit and one third power law have a $A = 1.191$, n for the best fit is 0.325 and the adjusted R-square is 99%. The value of n is similar to the one of the analytical scaling law, which is why the Best fit and one third power law are superposed. The A coefficient differs a little from the literature ([22] [23]. Most of the laws from the literature are established for jet velocity ratio a little bit larger than the ratio of case 1, this could cause difference in mixing. Indeed, in the work of Johari et al. [13] a slight difference is showed between the A coefficient of two jets in crossflow with different velocity ratios, which seems to indicate that the A coefficient depends on the velocity ratio. This could be due to differences in the boundary layer profile or Reynolds number effects, which are known to have an influence in the behaviour of jet in crossflow [3]. Since the flow solver AVBP is known to correctly simulate jet in crossflow [24] no further validations were undertaken.

$$\frac{Y_{cl}}{JD} = A\left(\frac{x}{JD}\right)^n \tag{22}$$

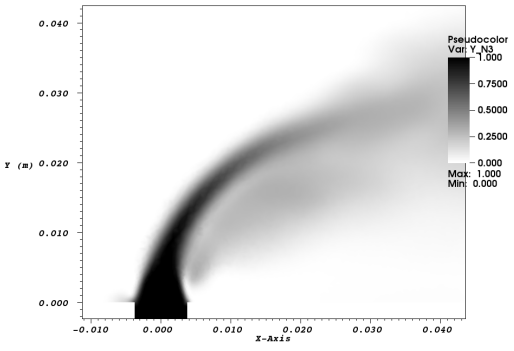

Fig. 13. Average mass fraction of N_3 in section $z = 0$, computation case 1

Numerical simulation permits to access all the variables of the flow with a relative good precision, which is why it complements experimental work. The present work focuses on reproducing one of the experimental cases of M'Closkey et al.. [15], specificaly the $55Hz$ case. Compared to that work, no compensation was used on the input signal because the goal of the compensation was to get rid of the acoustic impedance of the jet flow feed system. Since no flow feed system was modelled, no compensation has to be used.
Figure 15 C must be compared with the work of M'Closkey et al. [15]. Since no mixing, or velocity measurement were made during the experiments, the comparison will only be visual. Figure 16 shows the experimental flow for the equivalent of case 7 in the experiment of M'Closkey et al.. Comparison with figure 15 C shows a good agreement between the experimental and computa-

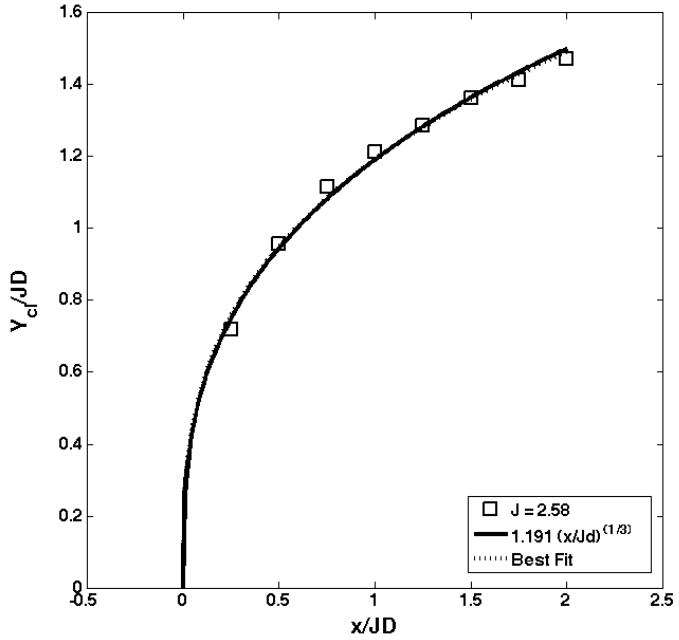

Fig. 14. Normalized penetration of steady jet; solid and dashed curves represent the one-third scaling and the best-fit respectively

tional work.

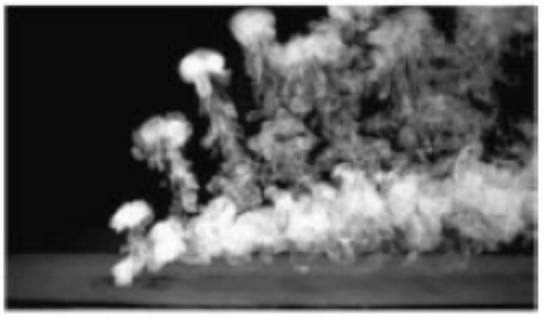

Fig. 16. Experimental pulsed jet in crossflow at $55Hz$, duty cycle 0.15, rms 1.7 from the work of M'Closkey et al.

B. Mixing

In what will follow the jet material will be referenced as N_3 and its concentration as Y_{N_3}. Characterizing the mixing of a steady jet in crossflow is a well known process, but characterizing the mixing of a pulsed flow is more complex. First the jet is unsteady so some kind of mean must be used. Second, if a cross stream-wise slice is observed over time, at some time the concentration of N_3 will be high due to the passage of for example a puff in the slice. At another time the concentration could be zero at the same point because there is no more turbulent puff. Applying a simple average on this kind of flow will result in a false interpretation of the mixing : if at some point the concentration of N_3 of the flow stays 50% of the averaged time at 1 and the rest at 0, the average concentration will be 0.5, which is false : physically, at no time the concentration was 0.5. To avoid this a conditional average has to be used. The conditional average used in the present work is established as follow : for each time sample the domain considered, a surface, is split into smaller surfaces and the integral of the mass flux of N_3, $\dot{m}_{Y_{N_3}}$ is computed over each smaller surface. Then, intervals of N_3 are created $\Delta Y^i_{N_3}$, for each interval the mass flux over the surface is added to the total mass flux of the interval if the mean mass fraction of N_3, $\bar{Y}_{N_3}$ belongs to the interval. The same process is repeated for each time sample and is summarized at figure III-B.

Then, the total mass flux of each interval is averaged over all the time samples. This yields different intervals with a mass flux passing trough each interval. It is still difficult to compare flow with different jet mass fluxes, so the mass flux of each interval is divided by the mean jet mass flux over all the time to normalize the data, the resulting data is named $R = f(\Delta Y^i_{N_3})$. Those data are plotted for case 1 at figure 18 A, which gives the ratio of the jet mass flow at each interval of N_3. A continuous line is plotted because the intervals are small enough to do so, $\Delta Y^i_{N_3} \approx Y_{N_3}$.

Finally, a new curve is deduced from the previous using equation 23, this one gives the percentage of the mass flow of which the concentration is smaller or equal to a certain Y_{N_3} which is noted Y^*. This curve is showed at figure 18 B

$$P_{Y \leq Y^*} = \int_0^{Y*} Y.R.dY \tag{23}$$

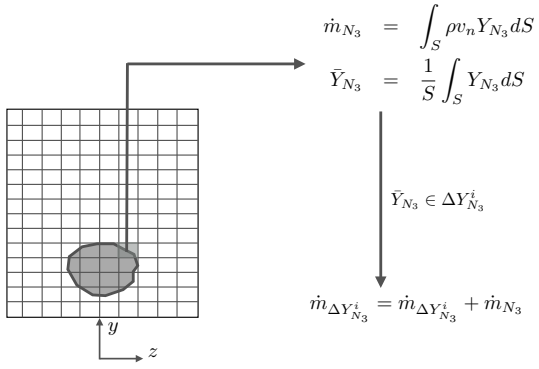

Fig. 17. Scheme of the averaging process : the gray zone represents the zone where the concentration of N_3 is non zero. ρ is the density, $\dot{m}$ is the mass flux, v_n is the velocity normal to the plane and the bar denotes the average

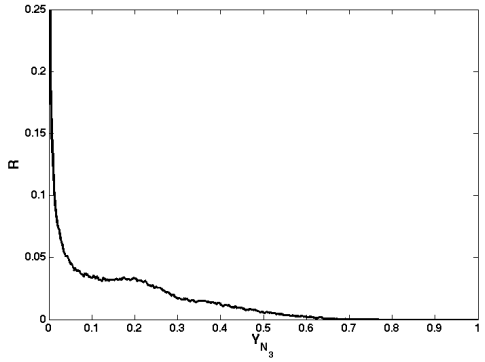

(A)

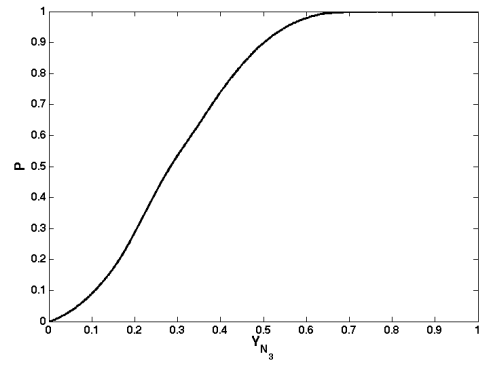

(B)

Fig. 18. A : $R = f(Y_{N_3})$ for case 1, B : $P = f(Y_{N_3})$ for case 1 in a cross stream-wise slice at $x = 3D$

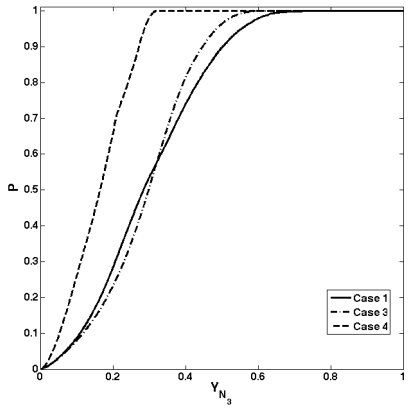

(A)

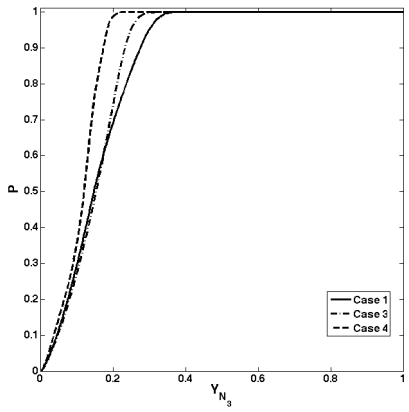

(B)

Fig. 19. A : Comparison of $P = f(Y_{N_3})$ at $x = 3D$, B : Comparison of $P = f(Y_{N_3})$ at $x = 6D$

For all the computational cases, two slices have been done : one at $X = 3D$ and one at $X = 6D$. The conditional averaging process was done over 1300 time samples, so that the conditional means are converged. First a comparison of the steady case is done; at figure 19 A and B case 1, 3 and 4 are plotted. Case 1 and 3 are very close, which is consistent with the work of Smith and Mugal [8] and points out that the steady jet in crossflow scales with the jet velocity ratio. This observation, also shows that the normalization by the jet mean velocity applied during the averaging process seems consistent. The comparison of case 1,3 and 4 also confirms that velocity ratio is a key parameter for the mixing. Nevertheless, the difference in the curves could be attributed to a Reynolds number effect. The comparison between $x = 3D$ and $6D$ show that the general form of the curve stay the same, the case 3 and 1 curves cut each other at more or less the same point, the only difference is that the curve is moved closer to the y-axis, in fact some kind of stretching is applied between the curve at $x = 3D$ and $6D$.

On figure 20 the same curves are plotted for steady cases 1, 2 and 5. Case 5 has the same momentum ratio R as case 1, so that normally the two curves should be superposed, but the hydrogen is very diffusive, so that the difference in the mixing could be attributed to this diffusive effect. At $x = 6D$ the hydrogen jet is already nearly completely mixed, moreover the difference in mixing is clear between case 1,2 and case 5. Note that the same kind of stretching can be observed between $x = 3D$ and $x = 6D$.

To characterize this stretching the mass fraction of N_3 corresponding to $P = 99\%$ and $P = 50\%$ were extracted for all the cases at $x = 3D$ and $x = 6D$ (table III). The ratios of the mass fraction of N_3 at $P = 50\%$ and $P = 90\%$ were computed in the same table, results are plotted in figure 21, which points out the similarity in the ratio between $x = 3D$ and $x = 6D$. It seems that the shape of the curve is related to the jet characteristics. The ratios at $x = 3D$ were plotted as a function of J or R for cases 1 to 8 and no correlation was found, as it can be seen at figure 22. As a conclusion, it seems that this kind of concentration curve depends of the physics of the flow, but not as a classical power law of J or R, which are common in jet in crossflow.

The comparison of the mixing curves of the pulsed jet in crossflow (cases 6 and 7) and a nominal jet in crossflow (case 2) is shown on figure 24. The flows were compared

TABLE III
VALUES OF Y_{N_3} FOR $P = 99\%$ AND $P = 50\%$ AT X=3D AND X=6D FOR ALL THE COMPUTATIONAL CASES

Case	$Y_{P=50\%X=3D}$	$Y_{P=99\%X=3D}$	$Y_{P=50\%X=6D}$	$Y_{P=99\%X=6D}$	$\frac{Y_{P=50\%}}{Y_{P=90\%}}, X = 3D$	$\frac{Y_{P=50\%}}{Y_{P=90\%}}, X = 6D$	R	J
1	28.63	63.13	15.34	33.63	2.205	2.192	6.67	2.58
2	24.12	45.13	11.64	22.38	1.871	1.922	9.975	3.15
3	29.88	54.63	15.37	27.63	1.828	1.797	6.67	2.58
4	16.38	30.63	11.24	20.38	1.869	1.813	60	7.75
5	6.37	19.13	2.62	7.87	3	2.998	6.67	9.625
6	18.12	31.63	10.87	19.38	1.745	1.782	9.975	3.15
7	17.13	44.48	10.13	27.13	2.596	2.678	9.975	3.15
8	21.88	41.63	13.63	24.87	1.902	1.824	13.75	3.7

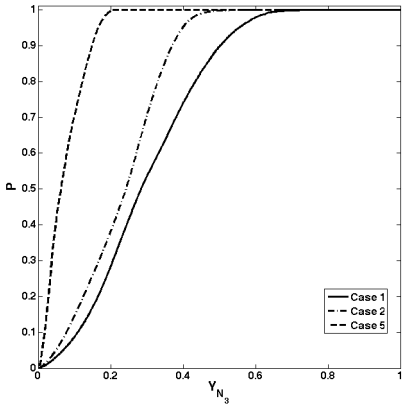

(A)

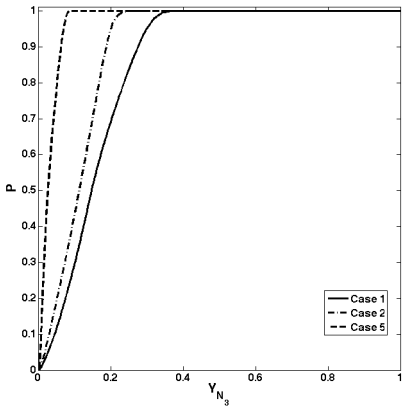

(B)

Fig. 20. A : Comparison of $P = f(Y_{N_3})$ at $x = 3D$, B : Comparison of $P = f(Y_{N_3})$ at $x = 6D$

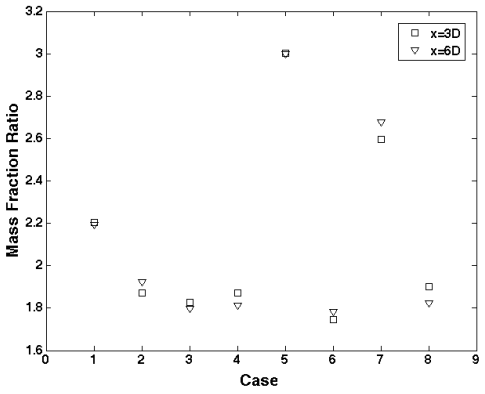

Fig. 21. $\frac{Y_{P=50\%}}{Y_{P=90\%}}$ at $X = 3D$ and $X = 6D$

to case 2 because the three flows configurations have the same mean speed, and cases 6 and 7 have the same RMS value of the pulsation.

For case 7 at $x = 3D$, a enhancement in mixing at low Y_{N_3} is noticed. This could be linked with the conclusion of Johari [13] : the turbulent puff must mix more efficiently that a steady jet in crossflow. A turbulent puff has a concentration decays power law $\propto x^{-3/4}$ while a classical jet in crossflow decay is $\propto x^{-2/3}$. Note that, even with this enhancement, the Y_{N_3} at which $P = 1$ is the same for case 2 and case 7. Further at $x = 6D$ the mass fraction at which $P = 1$ is smaller for case 2 than for case 7. The mixing is, thus, less efficient for a pulsed jet in crossflow, this is due to the perturbation of the jet in crossflow structure by the pulsation. As it can be noticed at figure 23, which represents the instantaneous Q-criterion which corresponds to the flow presented at 15, the flow for case 8 has a much more complicated vortical structure with weaker structures compared to cases 6 and 7, which indicates an influence of the pulsation on the flow. Moreover, case 6 and case 7 present strong coherent vortical structures, due to the strong pulsation, the turbulent puff vortices can be clearly identifed for cases 6 and 7, while cases 1 and 8 present more or less the same flow structure. This is consistent with the analysis of Johari [16], in which it is pointed out that pulsating the jet with a high α results in quasi steady like jet in crossflow (figure 2).

The instantaneous field showed at figure 15 (C) allows to identify two parts in the pulsed jet : a steady like jet and the turbulent puff part. The turbulent puff part produces

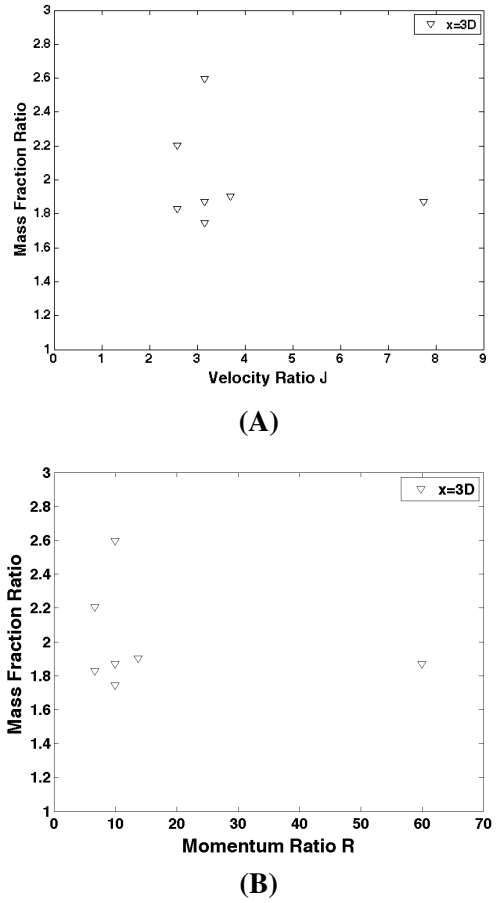

Fig. 22. $\frac{Y_{P=50\%}}{Y_{P=90\%}}$ at $X = 3D$ as a function of : (A) the velocity ratio and (B) the momentum ratio

the low Y_{N_3} mixing enhancement, but the rest of the curve is given by the steady like part. The disturbance of the steady-like part by the pulsation should be the cause of the reduced mixing efficiency at high P values.

The sine pulse (case 6) seems to enhance more generally the mixing, this could be linked to the fact that some kind of turbulent puffs are emitted (15 (C)) . Between those puffs, crossflow material penetrates in the jet, which enhance the mixing. As for case 7 this enhancement vanishes at $x = 6D$, as in the previous case, this could be linked to the perturbation of the steady-like flow structure by the pulsation. The perturbation could reduce the mixing induced by the CVP and so reduce the quantity of crossflow material which is pumped into the jet. This hypothesis still needs to be confirmed by further studies but is consistent with the work of Cortelezzi and Karagozian [3].

Finally, figure 25 compares the three pulsed cases, which have the same rms value for the pulsation but not the same mean jet mass flow. The sinus pulsation gives the best results in term of total mixing i.e value at which $P = 1$. Case 7 is worse on that point but permits to enhance the mixing at low P value. Case 8 is somewhere between the two, which is, in fact, consistent with the form of the signal : a duty cycle of 0.6 is quite close to a sine wave, but the rise and fall between the high speed part and the low speed part of the signal are similar to case 7. Yet, no detached turbulent puffs are observed, which is indicated on the mixing curve by a lack of mixing in the low P value. But, the pulsation still allows to introduce crossflow material in the jet, which, as for the sine wave, gives an overall enhancement in mixing. As a conclusion a sine signal seems to enhance the mixing in the most effective way, nevertheless if a enhancement in mixing at low P values must be obtained a pulse signal with low duty cycle seems to be more recommended.

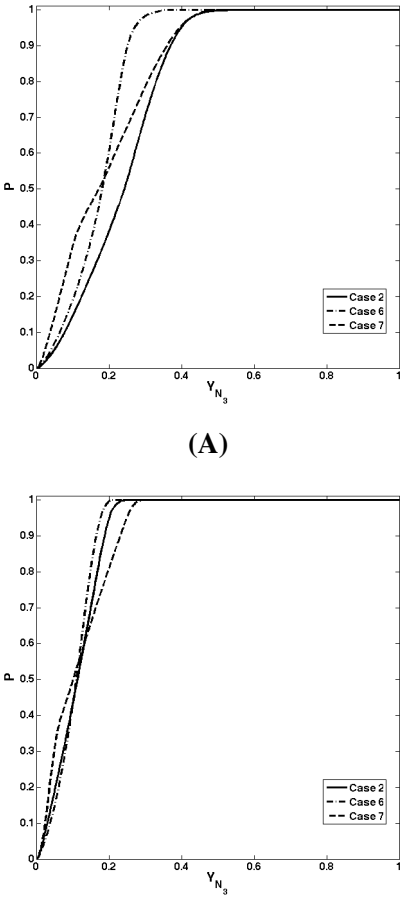

Fig. 24. A : Comparison of $P = f(Y_{N_3})$ at $x = 3D$, B : Comparison of $P = f(Y_{N_3})$ at $x = 6D$

IV. Conclusions

From the results of the present study it can be concluded that pulsating a jet in crossflow does not significantly enhance mixing expressed in terms of the conditional average indicator. This conclusion is in contradiction with the conclusions of previous studies [12], [13], [14], [15], [16]. Nevertheless, those experimental works were conducted

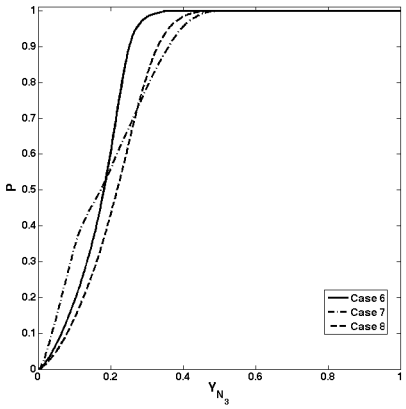

(A)

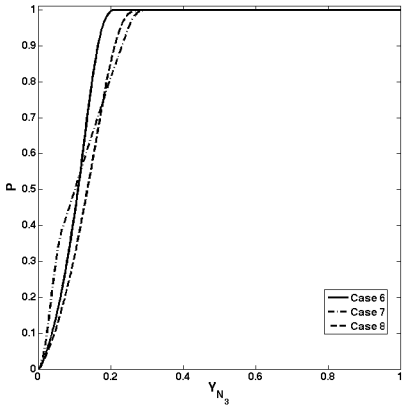

(B)

Fig. 25. A : Comparison of $P = f(Y_{N_3})$ at $x = 3D$, B : Comparison of $P = f(Y_{N_3})$ at $x = 6D$

in water tunnels and with pulse frequencies much smaller than the one used here, which means a lower Womersley number. This could explain the difference : by watching the difference in mixing between case 6 and case 7 and 8, one can tell that a velocity which increases slower, changes the velocity profile at the jet exit and also the mixing behaviour. Further, those experiments focus on the far field mixing, $x \geq 10D$, here the focus was made on the near field mixing. Finally, the mixing was not characterized using the averaging process used here, which makes direct comparison difficult.

The lack of experimental data on pulsed jet in crossflow in gaseous phase have not permitted to validate completely the computation, but the two criteria used for checking the quality of the computation give very good results.

As explained, the quantification of the mixing used here permitted to analyse correctly the mixing of strongly unsteady flow by using conditional averaging. This permitted not only to find out that jet in crossflow seems to have the same P curve shape, at different stream-wise positions but also to show that pulsed jet in crossflow, using a pure pulse signal does not seem to be the best solution for an overall enhancement in mixing. The best enhancement in mixing for low P value, is achieved with a pure pulsed signal and a low duty cycle, but the best overall mixing is realized with a sine wave.

Finally, the next logical step in the study of pulsed jet in crossflow is to apply the conditional averaging process presented here on an experimental case in the near field and the far field, along with numerical investigation of the mixing in the far field. Computations of a pulsed jet in crossflow with the same pulse amplitude but with different duty cycle values should also been done to study numerically the influence of the duty cycle on the mixing, since only the influence of pulse amplitude was studied here.

V. Acknowledgement

The authors wish to thanks the CERFACS CFD Team for developing AVBP, and allowing us to use it. The first author was supported by an FNRS fellowship.

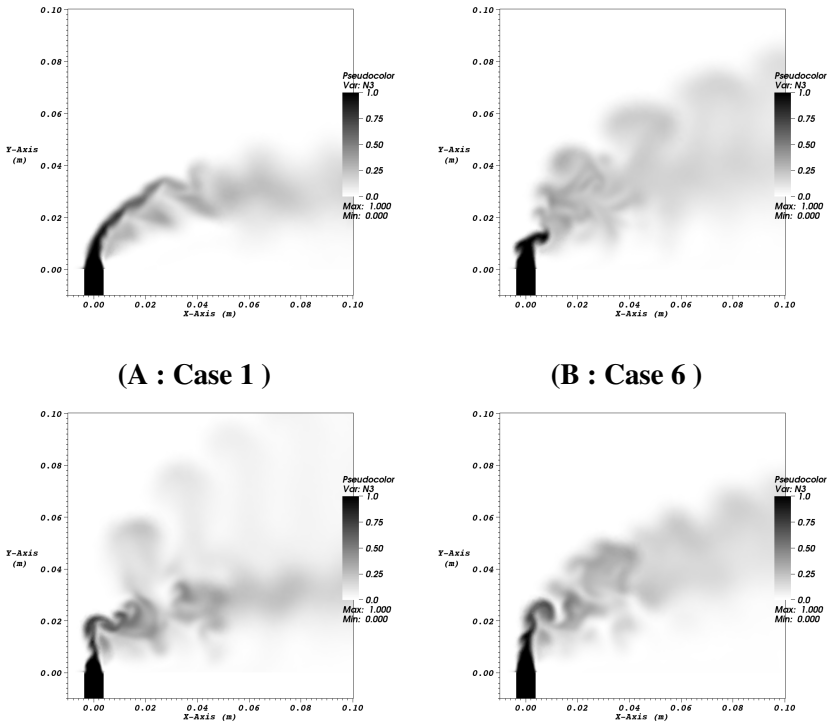

(A : Case 1) **(B : Case 6)**

(C : Case 7) **(D : Case 8)**

Fig. 15. Instantaneous mass fraction of jet inlet gaz (N_3) for four computation case

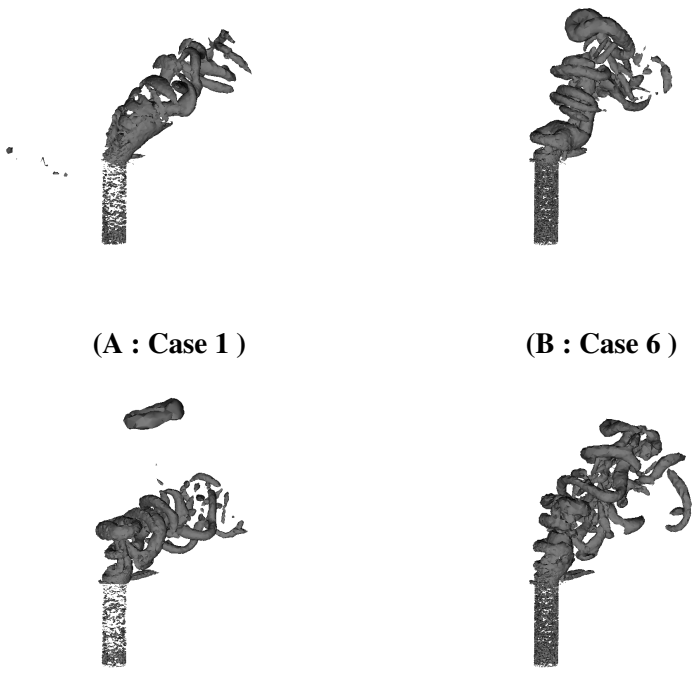

(A : Case 1) **(B : Case 6)**

(C : Case 7) **(D : Case 8)**

Fig. 23. Instantaneous iso Q-criterion surface ($Q-criterion = 7e4$) for four computation cases

REFERENCES

[1] Kamatoni, Y. and Greber, I. *Experiments on a Turbulent Jet in Cross Flow* AIAA Journal, Vol 10, No11, 1972, pp. 1425-1429

[2] Broadwell, J. E. and Breidenthal R. E. *Structure and Mixing of a Transverse Jet in Incompressible Flow* J. Fluid Mech. Vol 148, 1984, pp 405-412

[3] Cortelezzi L. and Karagozian A. R. *On the formation of the counter-rotating vortex pair in transverse jets* J. Fluid Mech. Vol 446, 2001 pp 347-373

[4] Fearn R. and Weston R. *Vorticity associeted with a jet in a cross flow* AIAA Journal, Vol 12, 1974 pp 1666-1671

[5] Kamotani Y. and Greber I. *Experiments on a turbulent jet in cross flow* AIAA Journal, Vol 10, 1972 pp 1425-1429

[6] Kelso R. M. Lim T. T. and Perry A. E. *An experimental study of round jets in cross-flow* J. Fluid Mech. , 306, 1996 pp 111-114

[7] Krothapalli A. Lourenco L. and Buchlin J.M. *Separated flow upstream of a jet in crossflow* AIAA Journal vol 28, Mar 1990, pp 414-420

[8] Smith S.H. and Mungal M.G. *Mixing, structure and scaling of the jet in crossflow* J. Fluid Mech, 357, 1998, pp 83-122

[9] Fric, T.F. and Roshko, A. *Vortical structure in the Wake of a Transverse jet* J. Fluid Mech, 279, 1994, pp 1-47

[10] Wu. J.M., Vakili, A.D. and Yu, F.M. *Investigations of thes Interactring of Nonsymmetric Jets in Crossflow* AIAA Jounral , vol 26 No 8., 1988, pp 940-947

[11] Eroglu A. and Breidenthal, R. E. *Effect of Periodic Distrubances on Structure and Flame Lenght of a Jet in Crossflow* AIAA Paper 91-0317 Jan 1991.

[12] Hermanson, J.C., Wahba, A. and Johari, H. *Duty-Cycle Effects on Penetration of Fully Modulated, Turbulent Jets in Crossflow* AIAA Journal, Vol 36, No 10, 1998, pp 1935-1937

[13] Johari H., Pacheco-Tougas, M and Hermanson, J.C. *Penetration and Mixing of Fully Modulated Turbulent Jets in Crossflow* AIAA Journal, Vol 37, No 7, 1999, pp 842-850

[14] Eroglu A. and Breidenthal, R. E. *Structure Penetration and Mixing of Pulsed Jet in Crossflow* AIAA Journal Vol 39, No 3, 2001 pp 417-423

[15] M'Closkey, R. T., King, J.M. Cortelezzi, L. and Karagozian, A.R. *The actively controlled jet in crossflow* J. Fliud. Mech. 2002 Vol 452 pp 325-355

[16] Johari, H. *Scaling of Fully Pulsed Jets in Crossflow* AIAA Journal, 2006, Vol 44, No11 pp 2719-2725

[17] Favre A. *Statistical Equation for Turbulent Gases* Problems of Hydrodynamics and Continuum Mechanics, Society for Industrial and Applied Mathematics. Philadelphia P.A. 1969, pp 231-266

[18] Sagaut P. *Large Eddy Simulation for Incompressible Flow : An Introduction* 3rd Edition Springer, 2006

[19] Pope S. *Ten question concerning the large-eddy simulation of turbulent flows* New Journal of Physics, 2004 6 35

[20] Naudin A. *Large Eddy Simulation of turbulent combustion with detailed tabulated chemistry* PhD Thesis, 2004 CORIA INSA Rouen

[21] M. Baum, T. Poinsot, D. Thevenin *Accurate Boundary Conditions for Multicomponent Reactive Flows* Journal of Computational Physics, 1994 166 pp 247-261

[22] Niederhaus, C.E. Champagne, F. H. and Jacobs J. W. *Scalar Transport inf a Swirling Transverse Jet* AIAA Journal, 1997, Vol 35, No11 pp 1697-1704

[23] Prire C; *Simulations aux Grandes Echelles : Application au Jet transverse* PhD Thesis, 2005, Edyf, CERFACS

[24] Jouhaud J-C, Gicquel L.Y.M., and B. Enaux *Large-Eddy-Simulation for Aerothermal Prediction Behind a Jet in Crossflow* AIAA Journal, 2007, Vol45, No10, pp2438 - 2447

[25] Majander P., Siikonen T. *Large-eddy simulation of a round jet in a cross-ow* International Journal of Heat and Fluid Flow, 2006, Vol27 pp402415

[26] Andreopoulos J., Rodi W., *Experimental investigation of jets in a crossflow* J. Fliud. Mech. 1984 Vol 138 pp 93-127

[27] Gopalan S., Abraham B. M., Katz J *The structure of a jet in cross-flow at low velocity ratios* Physics of Fluids, 2004 Vol 16 Number 6 pp 2067-2087

Proceedings of the 8th National Congress on Theoretical and Applied Mechanics, May 28-29, Brussels, Belgium.

Bottom friction formulations for free surface flow modeling

Machiels Olivier[1], Erpicum Sébastien[1], Archambeau Pierre[1], Dewals Benjamin[1, 2], Pirotton Michel[1]
[1] Université de Liège – Département ArGEnCo, Unité de recherche HACH
Chemin des chevreuils 1, B52/3 – 4000 Liège
[2] Fond National de la Recherche Scientifique (FRS-FNRS)
email: omachiels@ulg.ac.be, s.erpicum@ulg.ac.be, pierre.archambeau@ulg.ac.be, b.dewals@ulg.ac.be, michel.pirotton@ulg.ac.be

Abstract: **Bottom friction modeling is an important step in river flows computation with 1D or 2D solvers. It is usually performed using empirical laws established for uniform flow conditions or a modern approach based on turbulence analysis.**

Following the definition of the flow validity field of the main friction laws proposed in the literature, an original continuous formulation has been developed. It is suited to model river flows with a high variability of properties (water depth, discharge, roughness…).

The efficiency of this new formulation, theoretically established and numerically adjusted, is demonstrated through various practical applications.

Keywords: **Shallow water, Bottom friction, Empirical laws, Modern laws**

I. Introduction

Shallow Water equations are commonly used to model numerically river flows. Indeed, their only assumption states that the flow velocity component normal to the main flow plane is smaller than the flow velocity components in this plane. This is the case for the majority of river flows where vertical velocity component is negligible regarding the horizontal ones, except in the vicinity of singularities such as weirs for example.

This paper focuses on bottom friction modeling in such mathematical models. This effect is indeed of very high importance for real flow computation despite it is generally evaluated from empirical formulations experimentally determined for ideal uniform flows.

The bottom friction term should represent the whole of the energy losses induced by the friction of the fluid on the rough river bed. It is thus related to the bed characteristics (shape, roughness), to the fluid characteristics (viscosity) and to the flow features (water height, velocity).

The concept of friction slope has been early used to characterize bottom friction. It is an non-dimensional number corresponding to the slope to give to a uniform channel to observe a uniform flow for a given discharge. This concept is at the basis of the first friction laws proposed in the second part of the 18th century by the researchers of the so called "empirical" school. Authors such as Chézy and Manning proposed laws based on experimental results consisting in measuring the friction slope for varied idealized flows in a laboratory flume. A second approach appeared later following works of Prandtl. It provided laws issued from a scientific reasoning on the physics of the shear layer phenomena. It is the "modern" school.

Today, both approaches are used by free surface flow modelers, and these laws are sometimes applied to flow conditions far from those on the basis of which they have been developed.

The aims of the developments presented in this paper were to define the validity fields of varied bottom friction formulations proposed in the literature, and to find a single law usable to describe the bottom friction phenomena for largely variable flow conditions.

II. Main friction laws

The large range of bottom friction formulations proposed in the literature can be divided into two parts: the empirical and the modern approaches.

The first ones have been defined from experimental results in idealized uniform channel and for uniform flows. It's thus important to know the assumptions and the experimental conditions which are at the basis of the formula elaboration.

The second ones are based on theoretical developments related to the physics of the friction phenomena. The structure of these modern formulations is thus more congruent with the laws of fluids mechanics.

The main formulations of these two schools are summarized in this paragraph with the reasoning leading to their elaboration.

A. Empirical laws

The laws of the so called "empirical" school have all been developed on the basis of experimental tests. These tests consisted in measuring the slope to give to a uniform channel to observe a uniform flow [1]. In these flow conditions, the effects of bottom friction are exactly counterbalanced by the gravitational forces. Thus the friction slope is equal to the bottom slope of the channel and simple formulae can be set up to link the channel roughness, the flow variables and the bottom slope. Replacing the bottom slope by the friction slope, the friction effects can be computed for other flow conditions than the uniform ones.

The general form of empirical friction formulations writes:

$$U = \alpha J^{1/2} R_h^{\chi} \qquad (1)$$

It relates the friction slope J to hydraulic and geometric parameters affecting the bottom friction such as U the mean flow velocity, α a friction coefficient and R_h the hydraulic radius. This last parameter reflects the effect of the cross section shape.

The difference between the different friction formulations of the empirical school is in the χ exponent value and in the α coefficient form.

It is important to note that these formulations are not explicitly dependent on the turbulence regime of the flow, despite it is well known this flow state is of great influence on the friction losses.

The first empirical friction law has been proposed by Chézy in 1775 [2], when this engineer had to determine the cross section of channels necessary to provide water to the city of Paris. It writes:

$$U = CJ^{1/2}R_h^{1/2} \tag{2}$$

where C is the roughness coefficient, for which different authors such as Bazin [3], Ganguillet and Kutter [4] proposed formulations function of the shape and the nature of the channel bed.

Another remarkable law is the one developed by Manning in 1919 [5]. It writes:

$$U = \frac{1}{n}J^{1/2}R_h^{2/3} \tag{3}$$

where n is the Manning's coefficient relating the effects of the bottom roughness.

The success of the Manning's formulation is mainly due to the Strickler's relation [6] to define the roughness coefficient. Strickler studied the value of the bottom roughness coefficient K and defined a relation directly related to the size of the roughness elements d.

$$K = \frac{1}{n} = \frac{26}{d^{1/6}} \tag{4}$$

Varied literature sources provide values for K coefficient depending on flow conditions as well as the shape and the nature of channels or rivers beds.

Chézy and Manning-Strickler formulations are the most widely used empirical friction laws. Others exist, based on the same assumptions, such as the laws of Gauckler, Forchheimer, Christen, Hagen and Tillman [1]. They differ only by the exponent of the hydraulic radius in the general formulation (1) (Table I).

TABLE I

VALUE OF χ EXPONENT OF THE HYDRAULIC RADIUS FOR DIFFERENT EMPIRICAL FRICTION FORMULATIONS [1]

Author	χ
Gauckler	0.4
Forchheimer	0.7
Christen	0.625
Hagen	0.714
Tillman	0.7

B.Modern school

At the opposite of the empirical laws, the formulations from the modern school are based on a theoretical reasoning on the physics of the friction phenomena [1].

The developments of the modern school appear one century later than the first empirical development. That is at the start of the 20th century that, under the leadership of Prandtl, many researchers from the University of Göttingen (Germany) developed formulations of a friction coefficient, λ, function of the turbulence of the flow through the Reynolds number Re, and the size of the roughness elements of a pipe, k.

Modern formulations have been initially developed for pressurized flows to determine head losses along a pipe.

The Darcy-Weisbach relation [7] allows to link the friction slope J to the friction coefficient λ:

$$J = \frac{\lambda}{4R_h}\frac{U^2}{2g} \tag{5}$$

where $4\,R_h$ is the equivalent diameter of a channel regarding pressurized flows and g is de gravity acceleration.

The friction coefficient λ evaluation depends on the flow turbulence regime, and thus the Reynolds.

1) Laminar regime

The friction coefficient variation in laminar flows (Re < 5000) has been described by Poiseuille [8]:

$$\lambda = \frac{64}{Re} \tag{6}$$

For this flow regime, the roughness of the pipe has no effects on the flow as it's in laminar conditions.

2) Smooth turbulent regime

In turbulent regime, the effect of the size of the roughness elements on friction depends of the Re value.

Prandtl expressed the variation of the friction coefficient λ for flows on smooth walls in the Prandtl-Von Karman formulation [9]:

$$\sqrt{\frac{1}{\lambda}} = -2\,log\,\frac{2.51}{Re\sqrt{\lambda}} \tag{7}$$

This formulation is a simple function of the state of the fluid such as (6). Indeed, on smooth walls, the size of the roughness elements is negligible compared to the size of the laminar boundary layer.

In the same scope, Blasius [10] proposed an explicit formulation of the friction coefficient for flows on smooth walls:

$$\lambda = \frac{0.3164}{Re^{1/4}} \tag{8}$$

It fits well to Prandtl results for Re lower than 10^5.

3) Rough turbulent regime

The rough turbulent regime is defined by a ratio between the Reynolds number, Re, and the relative roughness, k/R_h. Indeed, more turbulent is the flow, smaller is the laminar boundary layer and more important is the effect of the wall roughness on the flow.

The rough turbulent regime appears when the effects of the roughness are predominant, i.e. for values of the Reynolds number higher than a limit value Re_{Lim} defined by:

$$Re_{Lim} = 2240\,\frac{R_h}{k} \tag{9}$$

For this regime, Nikuradse [11] developed an explicit formulation of the friction coefficient λ function of the relative roughness k/R_h:

$$\sqrt{\frac{1}{\lambda}} = -2\log\frac{k}{14.8R_h} \tag{10}$$

4) Transitional regime

The transitional regime is the regime between the smooth and the rough turbulent ones. Colebrook [12] proposed a formulation of the friction coefficient by combining the Nikuradse (10) and the Prandtl (7) formulations:

$$\sqrt{\frac{1}{\lambda}} = -2\,log\left(\frac{k}{14.8R_h} + \frac{2.51}{Re\sqrt{\lambda}}\right) \tag{11}$$

The implicit character of this equation gives it an uneasily use. It is the reason why different authors tried to find an explicit equivalent formulation, such as Barr [13, 14] and Yen [15]. The second law of Barr provides the best results regarding the Colebrook formulation (11), with less than 1% error on the friction coefficient values:

$$\sqrt{\frac{1}{\lambda}} = -2\,log\left(\frac{k}{14.8R_h} + \frac{4.518\,log\left(\frac{Re}{7}\right)}{Re\left(1 + \frac{Re^{0.52}\left(\frac{k}{R_h}\right)^{0.7}}{76.53}\right)}\right) \tag{12}$$

5) Macro-roughness

Macro-roughness is considered when the size of the roughness elements becomes comparable to the water depth *h*.

$$k_{Lim} = 0.25\,h \tag{13}$$

Developments on macro-roughness are more recent and are directly related to the development of hydrological modeling. They are associated to the modern school because of the similar form of the mathematical formulations.

The formulation of Bathurst [16], developed in 1985, is a reference to study flows on macro-roughness:

$$\sqrt{\frac{1}{\lambda}} = -1.987\,\log\frac{k}{5.15\,h} \tag{14}$$

The formulation of Dubois [17] can also be cited. Based on the same form of Bathurst's law, this formulation takes into account the density *p* of the roughness elements:

$$\sqrt{\frac{8}{\lambda}} = 5.62\,\log\frac{h}{k} + 3.13\,p^{-0.613} \tag{15}$$

In 2D flow modeling, the hydraulic radius R_h is equivalent to the water depth *h*. In the rest of this paper, both expressions will be used similarly.

III. Validity fields of the empirical laws

On the other hand, the empirical laws have not been developed regarding the variation in turbulence regime of real water flows. All of them have been defined in the scope of specific applications and for fixed uniform flow conditions. On the other hand, modern laws take better into account the turbulence regime of the flow but none of them can be applied to the whole flow conditions of real river flows. In this paragraph, the validity field of the main empirical laws is defined regarding the friction losses values provided by the different modern laws depending on the flow turbulence regime.

For laminar flows, the Poiseuille law (6) can be written, using the Darcy-Weisbach relation (5), such as:

$$U = \sqrt{\frac{g\,Re}{8}}\sqrt{JR_h} \tag{16}$$

This equation is similar to the general form of empirical laws. For laminar flow condition:

$$\begin{aligned}\chi &= 0.5\\ \alpha &= \sqrt{\frac{g\,Re}{8}}\end{aligned} \tag{17}$$

Thus, only Chézy's formulation with an adapted value of α can model friction losses in laminar conditions.

In the smooth turbulent regime, Prandtl's law (7) has to be considered. Its implicit form makes the comparison more difficult, but, as the law is independent of the hydraulic radius, the empirical like formulation of equations (5) and (7) is similar to equation (16) and thus χ has to be equal to 0.5 again. Thus, Chézy's formulation is again the only law suited to model friction losses in the smooth turbulent regime.

Blasius formulation can be used to set another empirical like formulation in smooth turbulent regime:

$$U = \sqrt{25.3\,g\,Re^{1/4}}\sqrt{JR_h} \tag{18}$$

In rough turbulent regime, the Nikuradse formulation (10) is a complex function of the hydraulic radius, R_h. Inserted in the Darcy-Weisbach relation (5), the modern law cannot be compared directly with the empirical formulations. This problem can be solved by replacing the logarithm of the relative roughness by its power development. The empirical like formulation of equation (5) and (16) writes then:

$$U = (8g)^{1/2}(Ak)^{-1/2M}\,J^{1/2}R_h^{1/2+1/2M}$$

$$\text{with}\ \begin{cases} A = \dfrac{R_h}{k}\left[-2\log\left(\dfrac{k}{14.8R_h}\right)\right]^{-\ln(10)\log\left(\frac{14.8R_h}{k}\right)} \\ M = \dfrac{\ln(10)}{2}\log\left(\dfrac{14.8R_h}{k}\right) \end{cases} \tag{19}$$

The empirical laws are thus valid for rough turbulent regime if the double equality (20) is satisfied:

$$\begin{cases} \chi = \dfrac{1}{2} + \dfrac{1}{2M} \\ \alpha = \sqrt{\dfrac{8g}{(Ak)^{1/M}}} \end{cases} \tag{20}$$

The first equality can be satisfied for each value of the hydraulic radius exponent χ but for a particular value of the relative roughness k/R_h.

For $\chi = 0.5$, the coefficient *M* value must be infinity. This means that the relative roughness has be 0. So the Chézy's formulation is a limit to the bottom friction evaluation in turbulent regime in case of smooth bed. The formulations with χ value lower than 0.5 are not valid in this specific flow regime.

In the Manning's formulation, with $\chi = 0.667$, the value of *M* has to be 3. That means the bottom friction is correctly

evaluated for a relative roughness equal to 0.037. In this case, the Strickler coefficient is equal to:

$$K = \frac{26.613}{k^{1/6}} \tag{21}$$

This value is very close to the Strickler formulation (4).

For other empirical laws using an exponent χ higher than 0.5, the same calculations can be performed. Each of these laws is thus suited to describe correctly the bottom friction phenomena for a specific value of the relative roughness and a particular form of the α coefficient (Table II).

TABLE II

VALUE OF RELATIVE ROUGHNESS AND COEFFICIENT α FOR A SUITABLE DESCRIPTION OF THE BOTTOM FRICTION EFFECTS IN ROUGH TURBULENT REGIME

Author	χ	k/R_h	α
Christen	0.625	0.005	$31.71/k^{0.125}$
Manning	0.667	0.037	$26.61/k^{0.167}$
Tillman	0.7	0.1	$24.26/k^{0.2}$
Forchheimer	0.7	0.1	$24.26/k^{0.2}$
Hagen	0.714	0.138	$23.51/k^{0.214}$

Considering the whole of the empirical laws, the bottom friction in rough turbulent flows can be correctly evaluated for relative roughness until 0.2. This last value is near the limit of macro-roughness. However, each law considered separately is only valid for a single relative roughness value, and none is thus available for general use.

The same developments as for the Nikuradse's formulation can be performed with the Colebrook's one. However, the coefficients A and M become also a function of the Reynolds number and thus of the state of the flow:

$$A = \frac{R_h}{k\left(-2\log\left(\frac{k}{14.8R_h} + \frac{2.51}{Re\left(A\frac{k}{R_h}\right)^{1/2M}}\right)\right)} \tag{22}$$

$$M = -\log\left(\frac{k}{14.8R_h} + \frac{2.51}{Re\left(A\frac{k}{R_h}\right)^{1/2M}}\right)\ln(10)\left(0.5 + \frac{18.574}{Re\,A^{1/2M}\left(\frac{k}{R_h}\right)^{1/2M+1}}\right)$$

The empirical laws are again valid to predict the bottom friction value if the double equality of equation (20) is verified.

The Chézy's formulation is still a limit for smooth bed and the laws with χ exponent value lower than 0.5 are not valid for transitional regime.

The other empirical formulations are valid for a single value of the relative roughness. However, this value varies with the Reynolds number (Fig. 1).

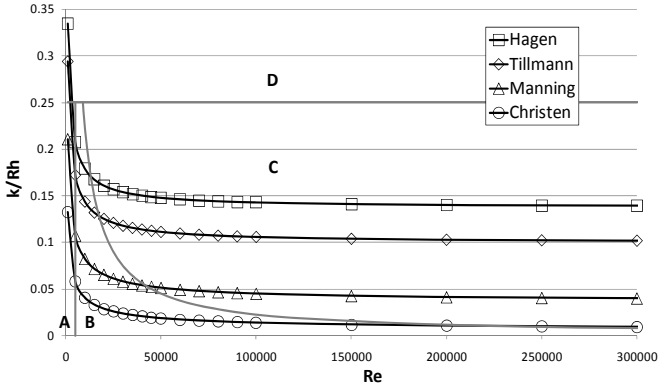

Fig. 1. Value of relative roughness for a correct description of the bottom friction value in transitional regime – B (laminar – A, rough turbulent – C, macro-roughness – D).

As for the rough turbulent regime, the bottom friction value for transitional flows can be correctly evaluated with empirical laws for specific flow condition but none of the laws is of universal application.

Finally, for macro-roughness, the same reasoning can be applied than for the rough turbulent regime. Coefficients A and M are defined such as:

$$A = \frac{h}{k}\left[-1.987\,\log\left(\frac{k}{5.15h}\right)\right]^{-\ln(10)\log\left(\frac{5.15h}{k}\right)} \tag{23}$$

$$M = \frac{\ln(10)}{2}\log\left(\frac{5.15h}{k}\right)$$

They are not a function of the flow regime.

As no empirical law is valid for relative roughness higher than 0.2, none of them is applicable to macro-roughness.

IV. USING FIELDS OF THE FRICTION LAWS

As a result of the study here above, a choice of friction law for modeling could be done depending on the flow conditions (Table III) [18].

When an explicit formulation is available to describe correctly the friction phenomena for particular flow conditions, it has been preferred to the corresponding implicit modern law.

TABLE III

FRICTION LAWS USABLE FOR AN EFFICIENT MODELING OF THE FRICTION PHENOMENA

		Fixed flow conditions	**Variable flow conditions**
Laminar		Chézy or Poiseuille	Chézy or Poiseuille
Turbulent	Smooth	Chézy or Prandtl	Chézy or Prandtl
	Transitional	Empirical laws (ex : Manning)	Colebrook
	Rough	Empirical laws (ex : Manning)	Nikuradse
	Macro-roughness	Bathurst	Bathurst

V. Extension of the empirical laws validity fields

To define more precisely the true validity field of the different empirical friction laws compared to the modern ones, it is necessary to define an acceptable error for friction losses evaluation between both approaches. The following developments consider that an error of 5% is acceptable on the water depth evaluation, defined as:

$$\frac{\Delta h}{h} = \frac{h_{\text{modern}} - h_{\text{empirical}}}{h_{\text{modern}}} \quad (24)$$

For example, considering the Colebrook's formulation, the water depth is computed, using equation (5), as:

$$h_{\text{Colebrook}} = \frac{U^2}{8gJ}\left(A\frac{k}{h}\right)^{-1/M} \quad (25)$$

Regarding the study of the rough turbulent regime, the α coefficient (1) could be expressed as a function of the roughness:

$$\alpha = \frac{B}{k^{\chi-1/2}} \quad (26)$$

where B is a constant parameter.

By extension of this value for all turbulent flows, the water depth computed by the empirical laws can then be evaluated, using the equation (1), as:

$$h_{\text{empirical}} = \frac{U^2}{B^2 J}\left(\frac{k}{h}\right)^{1-2\chi} \quad (27)$$

Using the water depths computed by the Colebrook formulation (25) and by the empirical laws (27) in (24), it is formal that this error is only function of the relative roughness. Validity fields of the friction laws for the description of transitional regime can thus be defined in terms of relative roughness (Table IV) [18].

TABLE IV

VALIDITY FIELDS OF THE PRINCIPAL FRICTION LAWS IN TERMS OF RELATIVE ROUGHNESS

Author	**Validity field (*k/h*)**
Chézy	0
Christen	[0 ; 0.032]
Manning	[0.007 ; 0.1]
Tillman	[0.023 ; 0.29]
Hagen	[0.034 ; 0.38]
Gauckler	No validity
Poiseuille	Only laminar
Prandtl	0
Colebrook	[0 ; 0.1]
Barr	[0 ; 0.1]
Nikuradse	[0 ; 0.1]
Bathurst	[0.1 ; 5.15]

The limit values of these validity fields are actually function of the Reynolds number. However, the variations are negligible for usual values of Reynolds for river flows (Re > 5000).

The higher terms of the validity fields of the Tillman and Hagen laws have been determined by comparison with the Bathurst formulation (14) because they concern macro-roughness.

The limitation of the macro-roughness has been extended to relative roughness of 0.1. It's the results of a comparison, presented in paragraph VII, between modeling results and in situ measurements on river.

Today, the empirical laws of Manning and Chézy are the most widely used formulations for friction modeling. This success comes from their using simplicity and the large existing literature on their parameters values. However, the modern laws are more representative of the physics of bottom friction. Furthermore, explicit forms of the modern laws exist such as the one of Barr (12). The modern laws have thus an important interest for flow modeling.

In practice, other losses, such as these due to the turbulence, are included in the friction term used by most flow solvers. In this case, it is then important to keep in mind that the friction slope J represents not only the bottom friction phenomenon.

VI. Looking for a continuous friction formulation

Regarding the validity fields of the empirical and modern laws (Table IV), it is remarkable that it doesn't exist a single formulation suited to compute friction effects on the wide range of relative roughness encounter in real river flow, where h goes from 0 on the banks to several meters in the channel center with constant roughness height k. However, the k/h ranges of several laws are contiguous such as for example for Colebrook or Barr and Bathurst.

To solve this problem, an original approach has been developed on the basis of the three following statements:

- The Colebrook or Barr formulation is suited to model turbulent flows with relative roughness k/h lower than 0.1.
- The Bathurst formulation is suited to compute friction effect on macro-roughness, i.e. for k/h higher than 0.1.
- But these two formulations are not equal for a relative roughness k/h of 0.1.

Developments have been performed to link continuously these two formulations close to relative roughness k/h equal to 0.1.

Due to its explicit expression, the Barr's formulation has been preferred to the Colebrook one.

To link the laws of Barr (12) and Bathurst (14), a third degree polynomial expression of the relative roughness has been set up:

$$\frac{1}{\sqrt{\lambda}} = A\left(\frac{k}{h}\right)^3 + B\left(\frac{k}{h}\right)^2 + C\left(\frac{k}{h}\right) + D \quad (28)$$

The limits of application range of the different formulations have been choosen to ensure that the relative variation of the λ coefficient stays lower than 0.5 for a water depth variation of 1 cm. This condition allows to ensure the stability of traditional solvers. So, the equation (28) has been developed for k/h values between 0.05 and 0.15.

The parameters A, B, C and D values have been determined to get a continuous variation of λ (same value and tangent)

between the polynomial, the Barr and the Bathurst expressions at each limit of *k/h* range. Parameters *A*, *B*, *C* and *D* have thus to solve the following complex system, depending on *Re*:

$$\text{For } \frac{k}{h} = 0.05 :$$

$$\begin{cases} 3A\left(\frac{k}{h}\right)^2 + 2B\left(\frac{k}{h}\right) + C = \frac{-1.987}{ln(10)\left(\frac{k}{h}\right)} \\ A\left(\frac{k}{h}\right)^3 + B\left(\frac{k}{h}\right)^2 + C\left(\frac{k}{h}\right) + D = -1.987\ log\left(\frac{k}{5.15h}\right) \end{cases}$$

$$\text{For } \frac{k}{h} = 0.15 :$$

$$\begin{cases} 3A\left(\frac{k}{h}\right)^2 + 2B\left(\frac{k}{h}\right) + C = \dfrac{-2\left(\frac{1}{14.8} - \dfrac{0.0413\ log\left(\frac{Re}{7}\right) Re^{0.52}\left(\frac{k}{h}\right)^{-0.3}}{Re\left(1 + \frac{Re^{0.52}(k/h)^{0.7}}{76.531}\right)^2}\right)}{ln(10)\left(\dfrac{4.518\ log\left(\frac{Re}{7}\right)}{Re\left(1 + \frac{Re^{0.52}(k/h)^{0.7}}{76.531}\right)} + \frac{k}{14.8h}\right)} \\ A\left(\frac{k}{h}\right)^3 + B\left(\frac{k}{h}\right)^2 + C\left(\frac{k}{h}\right) + D = -2\ log\left(\dfrac{4.518\ log\left(\frac{Re}{7}\right)}{Re\left(1 + \frac{Re^{0.52}(k/h)^{0.7}}{76.531}\right)} + \frac{k}{14.8h}\right) \end{cases} \quad (29)$$

However, for Reynolds numbers higher than 5000, which characterize most of usual river flows in the range of *k/h* ratio between 0.05 and 0.15, the variation of the parameters values with *Re* is negligible. The final form of the polynomial expression can then been established with constant parameters values:

$$\frac{1}{\sqrt{\lambda}} = 1469.76\left(\frac{k}{h}\right)^3 - 382.83\left(\frac{k}{h}\right)^2 + 9.89\left(\frac{k}{h}\right) + 5.22 \quad (30)$$

and the following expressions can be used to compute continuously the bottom friction effects in rivers or channels whatever the variation of *k/h*:

$$\text{For } \frac{k}{h} \le 0.05 :$$

$$\frac{1}{\sqrt{\lambda}} = -2\ log\left(\frac{4.518\ log\left(\frac{Re}{7}\right)}{Re\left(1 + \frac{Re^{0.52}(k/h)^{0.7}}{76.531}\right)} + \frac{k}{14.8h}\right) \quad (31)$$

$$\text{For } 0.05 \le \frac{k}{h} \le 0.15 :$$

$$\frac{1}{\sqrt{\lambda}} = 1469.76\left(\frac{k}{h}\right)^3 - 382.83\left(\frac{k}{h}\right)^2 + 9.89\left(\frac{k}{h}\right) + 5.22$$

$$\text{For } \frac{k}{h} \ge 0.15 :$$

$$\frac{1}{\sqrt{\lambda}} = -1.987\ log\left(\frac{k}{5.15h}\right)$$

VII. VALIDATION

Two Belgian river reaches have been considered to validate the continuous approach: the Ourthe near the town of Hamoir and the Semois near Membre. These two reaches of 2.6 km and 1.6 km have been selected because of the presence of two water depth measurement stations on both of them. The downstream water depth measurement combined with the discharge measurement provides the necessary boundary conditions for river reach modeling in case of subcritical flow.

The two river reaches have been modeled using the 2D-horizontal flow solver WOLF2D, developed at the University of Liege [19], using different friction laws such as Manning, Barr, Bathurst and continuous formulations, with a 2 x 2 m mesh.

The comparison between the upstream water depths computed using the laws of Barr (12), Manning (3), Bathurst (14) and the continuous formulation (31), and the water depth measurements at the upstream gauging station for different discharges has been used to show the interest of the continuous formulation (Fig. 2 and 3, and Table V).

The computed models, using the different laws named here above, need a comparable calculation time.

The Manning's coefficient *n* has been set up to ensure correspondence with real measurements for the highest discharge. It is equal to 0.025 $s/m^{1/3}$ in the Ourthe and to 0.031 $s/m^{1/3}$ in the Semois. The *k* value for Barr, Bathurst and continuous formulations has been set up to get close of the real measurements as well for the lowest discharge with the Bathurst formulation than for the highest one with the Barr equation. Its value is 0.09 m in the Ourthe and 0.3 m in the Semois.

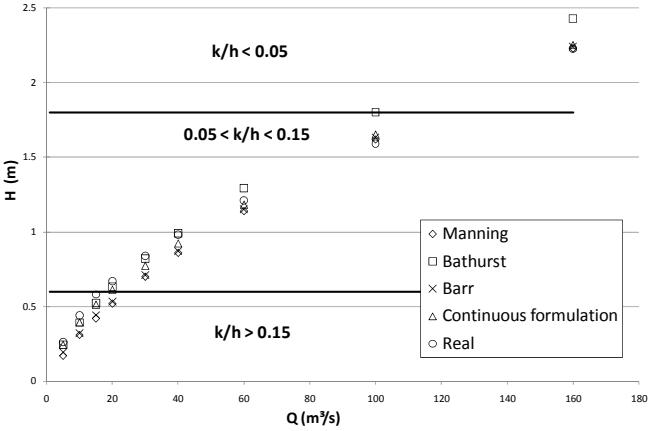

Fig. 2. Computed and measured rating curves in Hamoir on the Ourthe river.

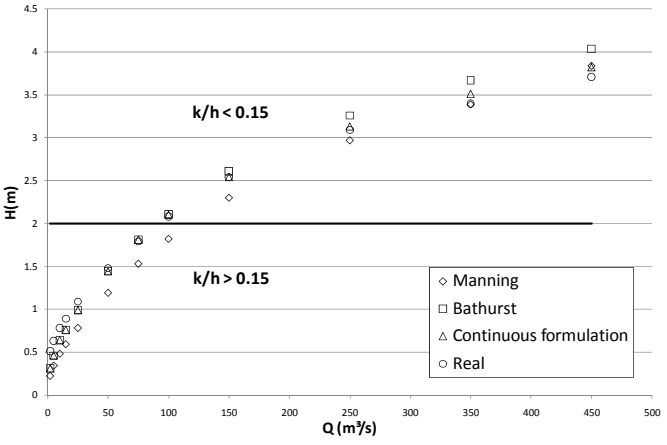

Fig. 3. Computed and measured rating curves in Membre on the Semois river.

TABLE V

MEAN RELATIVE ERROR ON THE REAL WATER DEPTHS (%)

Situation	**Modeling law**	***k/h* <0.05**	**0.05< *k/h* <0.15**	***k/h* >0.15**
Hamoir – Ourthe	Manning	0.9	14.3	30.6
	Barr	1.5	13.1	26.1
	Bathurst	11.1	4.0	9.8
	Continuous formulation	2.3	6.4	10.3
Membre - Semois	Manning	-	5.9	33.9
	Bathurst	-	5.3	15.9
	Continuous formulation	-	1.7	15.9

The water depth is not homogeneous on all the studied river reaches. The *k/h* ratio indicated in the table V is thus the ratio value at the upstream limit of the river reaches, at the center of the cross section. That is the reason why the results provided by the continuous formulation are not exactly equivalent to these provided by the Barr and the Bathurst formulations, respectively for $k/h < 0.05$ and $k/h > 0.15$.

On Ourthe river, for *k/h* ratios lower than 0.05, the water depths computed using the Manning, Barr and continuous formulations are relatively close to the real measurements, when the Bathurst results are further. This expresses well the validity of Barr and continuous formulations for 2D free surface flow with low relative roughness modeling. This also expresses the efficiency of the Manning's formulation for flow conditions near its setting ones. Finally, this shows the limitation of the Bathurst's formulation on low relative roughness.

For *k/h* ratios higher than 0.15, the water depths, provided using the Bathurst and the continuous formulations, are the closest to the real measurements. The important value of the relative error is partially due to the important effect of measurement uncertainty for low water depths. Indeed, the water depth measurements vary of until 5 cm for closed discharge measurements. However, the results show the interest of the Bathurst and the continuous formulation for flow modeling on high relative roughness. They also show the limitations of the Barr formulation for high relative roughness and of the Manning's one when flow conditions move away from its setting conditions.

For intermediary *k/h* ratios, the Bathurst formulation stays attractive when the water depths have a low variability on the river reach such as on the Ourthe river. However, when the water depths are more variable, such as on the Semois river, the continuous formulation becomes more attractive.

VIII. CONCLUSIONS

Friction is a complex phenomenon which has a non negligible influence on the flow characteristics. It is thus necessary to take it into account for a correct flow modeling. Many authors have thus developed friction formulations. But these laws are not always suited to describe the friction phenomenon in the whole range of real varied flow conditions.

In this study, a determination of the different application ranges of the principal laws has been proposed. In parallel, the validity fields of these laws have been calculated in terms of relative roughness to describe correctly usual river flows.

An original friction law has also been developed to fill the lack of a continuous law able to describe the friction phenomenon for the highly variable flow conditions often meet in river flows. This law has been validated by comparison of water depth values on two different rivers in Belgium.

REFERENCES

[1] M. Carlier, *Hydraulique générale et appliquée*, Eyrolles, Paris, 1972.

[2] A. Chezy, *Formule pour trouver la vitesse de l'eau conduite dans une rigole donnée*, Dossier 847 (MS 1915) of the manuscript collection of the École National des Ponts et Chaussées, Paris, 1776. Reproduced in: G. Mouret, *Antoine Chézy: histoire d'une formule d'hydraulique*, Annales des Ponts et Chaussées 61, Paris, 1921.

[3] H. Bazin, *Recherches Expérimentales sur l'Ecoulement de l'Eau dans les Canaux Découverts*, Mémoires présentés par divers savants à l'Académie des Sciences, Vol. 19, Paris, 1865.

[4] E. Ganguillet, W.R. Kutter, *Versuch zur Augstellung einer neuen allgeneinen Furmel für die gleichformige Bewegung des Wassers in Canalen und Flussen*, Zeitschrift des Osterrichischen Ingenieur – und Architecten-Vereines 21, (1) and (2), 1869.

[5] R. Manning, *On the Flow of Water in Open Channels and Pipes*, Instn of Civil Engineers of Ireland, 1890.

[6] A. Strickler, *Beiträge zur Frage der Geschwindigkeitsformel und der Rauhligkeitszahlen für Ströme, Kanäle und geschlossene Leitungen*, Mitt. des Eidgenössischen Amtes für Wasserwirtschaft, Vol. 16, Bern, 1923.

[7] J. Weisbach, J., *Lehrbuch der Ingenieur- und Maschinen-Mechanik*, Braunschwieg, 1845.

[8] J.L.M. Poiseuille, *Sur le Mouvement des Liquides dans le Tube de Très Petit Diamètre*, Comptes Rendues de l'Académie des Sciences de Paris, Vol. 9, 1839.

[9] L. Prandtl, *Über Flussigkeitsbewegung bei sehr kleiner Reibung*, Verh. III Intl. Math. Kongr., Heidelberg, 1904.

[10] H. Blasius, *Das Aehnlichkeitsgesetz bei Reibungsvorga¨ngen*. Z Ver Dtsch Ing 56(16), 1912.

[11] J. Nikuradse, *Strömungsgesetze in rauhen Rohren*, VDI-Forschungsheft, No. 361, 1933.

[12] C.F. Colebrook, *Turbulent Flow in Pipes with particular reference to the Transition Region between the Smooth and Rough Pipe Laws*, Jl Inst. Civ. Engr, No. 4, 1939.

[13] D.I.H. Barr, *Discussion of ''Accurate explicit equation for friction factor.''*, J. Hydraul. Div., Am. Soc. Civ. Eng., 103(HY3), 1977.

[14] D.I.H. Barr, *Solution of the Colebrook–White functions for resistance to uniform turbulent flows*, Proc. Inst. Civ. Eng., 1981.

[15] B.C. Yen, *Channel Flow Resistance : Centennial of Manning's Formula*, Water Resources Publ., Littleton CO, 1991.

[16] J.C. Bathurst, *Flow resistance estimation in mountain rivers*, J. Hydr. Engrg, ASCE, 111(4), 1985.

[17] J. Dubois, *Comportement hydraulique et modélisation des écoulements de surface*, Communication 8, Laboratoire de Constructions Hydrauliques, Ecole Polytechnique Fédérale de Lausanne, 1998.

[18] O. Machiels, *Analyse théorique et numérique de l'influence de la formulation des termes de production et de dissipation dans les équations d'écoulement à surface libre*, Travail de fin d'études, Faculté des Sciences Appliquées, Université de Liège, 2008.

[19] S. Erpicum, P. Archambeau, S. Detrembleur, B.J. Dewals, M. Pirotton, *A 2D finite volume multiblock flow solver applied to flood extension forecasting*, In: P. Garcia-Navarro, E. Playan (Eds), *Numerical modelling of hydrodynamics for water resources*, Taylor & Francis, London, 2007.

Proceedings of the 8th National Congress on Theoretical and Applied Mechanics, May 28-29, Brussels, Belgium.

Advances in one-fluid RANS modeling of concentrated particle-laden flows

Erik A. Toorman[1]
[1]Hydraulics Laboratory, Department of Civil Engineering, Katholieke Universiteit Leuven
Kasteelpark Arenberg 40, 3001 Heverlee – Belgium
email: erik.toorman@bwk.kuleuven.be

Abstract: **Sediment concentrations in open-channel flow reach high values in the viscous sublayer and transient layer above the bottom and modulate the bed roughness due to four-way interaction particle-turbulence interactions. In order to account for these subgrid scale phenomena in 3D numerical sediment transport models for engineering problems in estuaries and coastal areas, a new methodology is proposed consisting of the coupling of a single near-bed layer solved with a low-Reynolds mixing-length model with a low-Reynolds k-epsilon model for the water column above.**

Keywords: **sediment transport, suspension flow, low Reynolds modeling, mixing length, k-epsilon turbulence model**

I. Introduction

Large-scale engineering problems related to sediment transport in estuaries and coastal areas (such as siltation of harbors and waterways or dredged material disposal dispersion) are presently studied more and more with 3D CFD software. These codes basically solve the RANS equations for the suspension, considered as a single fluid with variable density, together with a particle mass balance and a k-ε turbulence closure for the vertical mixing. Historically, these models have emerged from codes for clear water hydrodynamics where the effect of suspended particles on the flow were neglected. But they show a lot of deviation from reality when validated.

There has been much progress in recent years in the understanding and modeling of particle-fluid interactions in suspensions, certainly for very dilute conditions. The much larger scales and concentration levels in nature (>1%) do not allow to apply advanced LES or DNS techniques with Lagrangean particle tracking for two-phase flow. Engineering models for sediment transport can only be improved by redefining the basic equations, by reconstructing the equations from two-phase flow theory to result in a one-fluid formulation which accounts for the particle-fluid interactions, even at high concentrations. At the other hand, the high concentrations and gradients in a thin layer near the bottom, which generate very important apparent bed roughness modulations, require a sub-grid scale modeling approach, because of the very coarse meshes (grid sizes of the order of 1-10 in the vertical and 100-1000 m horizontally) used in these applications for the sake of computing time.

II. Methodology & Results

In order to tackle the problem, two approaches are used in parallel.

A. *Low-Reynolds turbulence models*

At one hand, a coarse grid low-Reynolds model is developed to deal with the near-bottom modulation effects and involves a semi-empirical approach. First, a new low-Reynolds model for a clear fluid over a smooth bottom has been developed based on theoretical considerations and use of DNS data [5]. The new model requires only three empirical damping functions, allowing a complete analytical reconstruction of the various profiles in the wall layer. This study has furthermore validated a previously proposed realizable turbulent time scale formulation [2]: $f_T = (1+\nu/\nu_t)^{1/2}$. It is also confirmed, as suggested in [2], that the damping function f_2 of the dissipation rate term in the RHS of the ε equation should equal f_T^{-1}.

When applied as a PML turbulence closure in a single cell wall layer, and using the analytical solutions at the outer boundary as the near-wall boundary conditions for the low-Reynolds k-ε model, it has been demonstrated that excellent profiles can be computed numerically on one and the same grid for both low and high Reynolds conditions [5] (fig. 1).

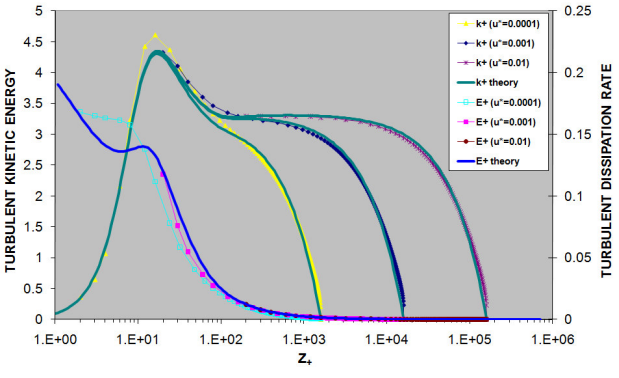

Fig. 1. Computed profiles of k and ε obtained for steady open-channel flow, driven by a constant horizontal pressure gradient, in a 16 meter deep channel on the same grid (100 layers, slightly refined towards the bottom) for three different shear velocities ($u_* = 10^{-4}$, 10^{-3} and 10^{-2} m/s, from low-Reynolds to high-Reynolds range), compared with the analytical low-Reynolds PML solution.

B. *Extension to rough bottoms and suspension flow*

Currently, the low-Reynolds model is being extended for rough bottoms and suspension flow. Experimental and LES data (generated by the VUB) for flow over rough bottoms, as well as experimental data for flume experiments with sand

suspensions show that the non-dimensionalized velocity gradient tends to a constant value at the wall which becomes increasingly smaller than one with increasing roughness or sediment concentration. In order to account for this apparent stretching of the viscous sublayer, it is necessary to increase the viscosity of the fluid. In the case of roughness, this additional viscosity accounts for the subgrid-scale turbulence generated in the vortex shedding eddies between the roughness elements. In the case of suspended particles, it accounts for subgrid scale turbulence generated in the wake of the particles and the granular friction by particle-particle interactions. The empirical closure for the additional viscosity is obtained by inverse modeling of experimental data.

C. One-fluid formulation

At the other hand, a theoretical approach is used to reconstruct the exact conservation equations for the suspension starting from two-phase flow theory. In the one-fluid formulation the suspension RANS equations are obtained by spatial (volumetric or Favre) averaging of the conservation equations of the two phases (fluid and solid) and subsequent (Reynolds) time-averaging. Compared to the traditional NS equations, the following differences can be noticed: variable density and viscosity and extra terms generated by the phase lag between fluid and particles. The closure for the velocity lag and the Reynolds averaging of the corresponding diffusion stress in particular is problematic and requires further study.

An important first result from the study of the two-phase flow equations, is the derivation of a theoretical closure for the turbulent Schmidt number (Sc_t) for steady state dilute turbulent suspension flow [3, 4]:

$$\frac{Sc_t}{Sc_0} = \frac{\left(1+\beta_0 \frac{\nu_t}{w_s k}\frac{\partial k}{\partial z}\right)}{\left(1-\frac{\alpha}{\beta_0 c_\mu}\frac{{w_s}^2}{k}\right)} = \frac{\left(1+\frac{\beta_0 c_\mu}{\alpha}\frac{\tau_t}{w_s}\frac{\partial k}{\partial z}\right)}{\left(1-\frac{\alpha}{\beta_0 c_\mu}\frac{{w_s}^2}{k}\right)} \qquad (1)$$

where: w_s = settling velocity, k = turbulent kinetic energy, ν_t = eddy viscosity, z = vertical coordinate, $Sc_0 = \beta_0^{-1} = 0.7$ = the neutral Schmidt number, $c_\mu = 0.09$ and α = empirical constant (= 0.16-1, based on limited data).

By validation of the individual terms of the turbulent particle flux, it was found that the time scale for the drift flux had to be taken equal to the integral turbulent time scale instead of the particle time scale, which only applies to the gravitational settling flux [3].

D. Non-Newtonian behavior

Thirdly, a new time-dependent non-Newtonian rheological model, based on an earlier version [1], has been implemented into the same code in order to study fluid mud flow behavior and interaction with waves [6]. Future work will integrate the turbulent layer model and the fluid mud layer model into one model to allow the simulation of ocean wave damping by fluid mud as observed in nature.

ACKNOWLEDGEMENTS

This work has been made possible with support from the K.U.Leuven Special Research Fund and the FWO project G.0359.04.

REFERENCES

[1] Toorman, E.A. (1997). Modelling the thixotropic behaviour of dense cohesive sediment suspensions. *Rheologica Acta*, 36(1):56-65.

[2] Toorman, E.A. (1998). A study of modelling (near-wall) turbulence damping. *1st COSINUS Annual General Meeting*, Abstracts, pp.13-18.

[3] Toorman, E.A. (2008). Vertical mixing in the fully-developed turbulent layer of sediment-laden open-channel flow. *J. Hydraulic Engineering*, 134(9):1225-1235.

[4] Toorman, E.A. (2009). Erratum and addendum to "Vertical mixing in the fully-developed turbulent layer of sediment-laden open-channel flow". *J. Hydraulic Engineering*, 135(6) (in press).

[5] Toorman, E.A. (2009). New low-Reynolds mixing-length and k-ε turbulence models for shear flow along smooth walls. (*in preparation*).

[6] Toorman, E.A. (2008). An investigation into the thixotropic wave dissipation potential of fluid mud. *AGU Chapman Conference on Physics of Wave-Mud Interaction.* Book of Abstracts, p.24.

Proceedings of the 8th National Congress on Theoretical and Applied Mechanics, May 28-29, Brussels, Belgium.

Low Mach-number expansion and equilibrium behavior of two-phase granular mixtures

C. Varsakelis, M. V. Papalexandris
Institute of Thermodynamics
Dèpartment de Mèchanique , Universite catholique de Louvain
Place du Levant, B-1348 Louvain-la-Neuve, Belgium
email: christos.varsakelis@uclouvain.be, miltos@uclouvain.be

Abstract— **In this paper we present the Low Mach-number expansion of the two-phase flow model, developed in [1]. This model provides a set of governing equations for compressible flows of two phase granular mixtures, in the absence of chemical reactions, and its derivation is based on the theory of irreversible processes. A suitable non-dimensionalization leads to a system of equations perturbed in terms of the Mach numbers of the two phases, which allows us to obtain the desired expansion. Our approach is thus a generalization of the Low Mach-number expansion of the compressible Navier-Stokes-Fourier equations for single phase flows, [3]. In equilibrium, the model reduces to a highly coupled system of quasi-linear elliptic equations, with the pressure difference between the phases and the granular volume fraction as unknown variables. We present a theoretical analysis of this system of coupled equations and prove the strong dependence of the pressure difference on the volume fraction distribution. The article concludes with the presentation of numerical experiments that are obtained via finite-difference discretization of the equilibrium equations.**

Keywords— **Low-Mach number approximation, granular mixtures, volume fraction, Ladyzhenskaya's decomposition**

I. Introduction

Let us assume that we are given a saturated mixture of an isotropic granular material with approximately spherical grains and an isotropic fluid, in some Lebesgue measurable, convex and bounded domain of $\mathbb{R}^n, n = 2,3$, that the local equilibrium hypothesis is valid [6]. We further assume that the mixture is in absence of chemical reactions and of phase changes. We adopt the model developed in [1] which introduces the volume fractions of the constituents and their spatial gradients as independent thermodynamic variables and consists of the generalized Gibbs equations,

$$T_i = ds_i = de_i - \frac{p_i}{\rho_i^2} d\rho_i - \frac{\beta_i}{\rho_i \phi_i} d\phi_i - \frac{1}{\rho_i \phi_i} \gamma_i \, d\nabla\phi_i, \qquad (1)$$

where $i = s,g$ stands for the solid and gaseous phase respectively and p_i, ρ_i, T_i, ϕ_i stand for the pressure, density, temperature and volume fraction of the i-th phase correspondingly. ψ_i are the Helmholtz free energies, e_i the internal energies, $\beta_i = \rho_i \phi_i \frac{\partial \psi_i}{\partial \phi_i}$ are the configuration pressures representing the elastic, contact forces between the granular grains under compaction. Finally $\gamma_i = 2\rho_i \phi_i \frac{\partial \psi_i}{\partial (\nabla\phi_i \cdot \nabla\phi_i)}$ denote coefficients related to dispersion effects. Since elastic contact forces and dispersion effects are not likely to occur in the gaseous phase [4] we let $\beta_g = \gamma_g = 0$.

The saturation property is expressed by the equation

$$\phi_s(x,t) + \phi_g(x,t) = 1, \text{ a.e. in} \Omega$$

The (multi-dimensional) balance equations for mass, momentum and energy read for the gaseous phase

$$\frac{d\rho_g \phi_g}{dt_g} + \rho_g \phi_g \nabla \cdot \underline{u}_g = 0 \qquad (2)$$

$$\rho_g \phi_g \frac{d\underline{u}_g}{dt_g} + \nabla(p_g \phi_g) = -\nabla(\phi_g \underline{\underline{P}}^v_g) - p_g \nabla\phi_s - \delta(\underline{u}_g - \underline{u}_s) \qquad (3)$$

$$\rho_g \phi_g \frac{d e_g}{dt_g} + p_g \phi_g \nabla \cdot \underline{u}_g = -\phi_g \underline{\underline{P}}^v_g \odot \underline{\underline{V}}^v_g - \nabla(\kappa_g \phi_g \nabla T_g) - h(T_g - T_s) + (-p_g \nabla\phi_s + \delta(\underline{u}_g - \underline{u}_s)) \cdot (\underline{u}_g - \underline{u}_s) \qquad (4)$$

and for the solid phase

$$\frac{d\rho_s \phi_s}{dt_s} + \rho_s \phi_s \nabla \cdot \underline{u}_s = 0 \qquad (5)$$

$$\rho_s \phi_s \frac{d\underline{u}_s}{dt_s} + \nabla(p_s \phi_s) = -\nabla(p^v_s \phi_s) - \nabla(\phi_s \underline{\underline{P}}^v_s) + p_g \nabla\phi_s + \delta(\underline{u}_g - \underline{u}_s) \qquad (6)$$

$$\rho_s \phi_s \frac{d\,(e_s + \psi^c_s)}{dt_s} + p_s \phi_s \nabla \cdot \underline{u}_s = -p^v_s \phi_s \nabla \cdot \underline{u}_s - \phi_s \underline{\underline{P}}^v_s \odot \underline{\underline{V}}^v_s - \nabla \kappa_s \phi_s \nabla T_s + h(T_g - T_s) \qquad (7)$$

where the operator $\frac{d}{dt_i} = \frac{\partial}{\partial t} + \underline{u}_i \cdot \nabla$ stands for the material derivative of the i-th phase, p^v_i, $\underline{\underline{P}}^v_i$ are the bulk viscous pressure and the traceless deviatoric part of the viscous pressure tensor. They arise from the natural decomposition of the viscous pressure tensors of each phase and we observe that $p^v_g = 0$. V^v_i are the traceless deviatoric parts of the deformation tensors $V_i = \frac{1}{2}(\nabla \underline{u}_i + (\nabla \underline{u}_i)^T)$ and κ_i denote the transport coefficients of thermal conductivity. h, δ

are the interfacial heat transfer and drag coefficient respectively. ψ_s^c is the compaction-related part of the solid's free energy, which is equal to the compaction related part of the solid's internal energy. Finally, $\odot$ stands for the Hadamard or component-wise product of two tensors.

We will assume that the interfacial heat transfer coefficient follows the equation

$$h = 6\phi_s \frac{c_p Nu}{Pr d_p^2}\mu_g$$

where d_p is the volume particle's diameter Nu,Pr are the Nusselt and Prandtl number and μ_g is the gaseous phase's shear viscosity coefficient. The above equations are supplemented with the (parabolic along the streamlines) compaction equation

$$\frac{d\phi_s}{dt_s} = \mu_c^{-1}\left(\frac{p_s}{T_s} - \frac{p_g}{T_g} - \frac{\beta_s}{T_s} + \nabla\cdot\left(\frac{\gamma_s}{T_s}\nabla\phi_s\right)\right) \tag{8}$$

were μ_c stands for the dynamic compaction coefficient. In addition we assume,for the shake of simplicity, that the granular material follows the stiffened-gas equation of state, i.e.

$$p_s = -P_\infty + \rho_s T_s R \tag{9}$$

where P_∞ is the "correction pressure and" R is the granular material's constant. Note that all variables used above are in dimensional form.

In this paper we extend the concept of Low-Mach number approximation to such mixtures and we derive the corresponding Low (Zero) Mach number equations.

Moreover, we study the equilibrium problem, as it is predicted by the model under study, both analytically and numerically. The discussion is also supported with representative numerical experiments.

II. Low-Mach number approximation

Let us take into account the exact expressions for $p_s^v, \underline{\underline{P}}_s^v, \underline{\underline{P}}_g^v$ namely:

$$p_s^v = \frac{\gamma_s}{3\phi_s}|\nabla\phi_s|^2$$

$$\underline{\underline{P}}_s^v = \frac{\gamma_s}{\phi_s}\underline{\underline{\Phi}}_s^v - 2\mu_s\underline{\underline{V}}_s^v \tag{10}$$

$$\underline{\underline{P}}_g^v = 2\mu_g\underline{\underline{V}}_g^v \tag{11}$$

where $\nabla\phi_s\otimes\nabla\phi_s = \frac{1}{3}|\nabla\phi_s|^2\underline{\underline{I}} + \underline{\underline{\Phi}}_s^v$ and μ_s, is the shear viscosity coefficient of the solid phase.

We will non-dimensionalize equations 2-9 with the reference variables

$$p_r,\ u_r,\ L_r,\ T_r,\ \rho_r, \mu_r,\ \kappa_r$$

and we will assume that

- $t_r = \frac{L_r}{u_r}$
- $\delta_r = \frac{u_r\rho_r}{L_r}$
- $\beta_r = u_r^2\rho_r$
- $\gamma_r = u_r^2\rho_r L_r^2$
- $h_r = \frac{p_r T_r u_r}{L_r}$
- $\mu_{c_r} = \frac{T_r}{u_r\rho_r L_r}$

Remark II-.1: We observe that the interfacial heat transfer coefficient h_1 is stiff if we assume that solid's grain diameter is order(s) of magnitude smaller compared to L_r i.e. the reference length measure. We will adopt this assumption throughout this paper.

After the calculations we arrive at the following system of equations for the gaseous phase

$$\frac{d\rho_g\phi_g}{dt_g} + \rho_g\phi_g\nabla\cdot\underline{u}_g = 0 \tag{12}$$

$$\rho_g\phi_g\frac{d\underline{u}_g}{dt_g} + \frac{1}{\varepsilon_g}\nabla(p_g\phi_g) = -\frac{1}{Re}\nabla(\phi_g\underline{\underline{P}}_g^v) - \frac{1}{\varepsilon_g}p_g\nabla\phi_s - \delta(\underline{u}_g - \underline{u}_s) \tag{13}$$

$$\rho_g\phi_g\frac{de_g}{dt_g} + p_g\phi_g\nabla\cdot\underline{u}_g = -\varepsilon_g\frac{1}{Re}\phi_g\underline{\underline{P}}_g^v\odot\underline{\underline{V}}_g^v - \frac{1}{PrRe}\frac{\gamma-1}{\gamma}\nabla(\kappa_g\phi_g\nabla T_g) + p_g\nabla\phi_s\cdot((\underline{u}_g - \underline{u}_s)) + \varepsilon_g\delta(\underline{u}_g - \underline{u}_s))\cdot((\underline{u}_g - \underline{u}_s)) - \frac{1}{\varepsilon_g}h(T_g - T_s) \tag{14}$$

and the solid phase

$$\frac{d\rho_s\phi_s}{dt_s} + \rho_s\phi_s\nabla\cdot\underline{u}_s = 0 \tag{15}$$

$$\rho_s\phi_s\frac{d\underline{u}_s}{dt_s} + \frac{1}{\varepsilon_s}\nabla((p_s - p_g)\phi_s) = -\nabla\cdot(\gamma_s\nabla\phi_s\otimes\nabla\phi_s) \tag{16}$$

$$\rho_s\phi_s\frac{de_s}{dt_s} + p_s\phi_s\nabla\cdot\underline{u}_s = -\varepsilon_s p_s^v\nabla\cdot\underline{u}_s - \varepsilon_s\frac{1}{Re}\phi_s\underline{\underline{P}}_s^v\odot\underline{\underline{V}}_g^v - \frac{1}{PrRe}\frac{\gamma-1}{\gamma}\nabla(\kappa_s\phi_s\nabla T_s) + \frac{1}{\varepsilon_s}h(T_g - T_s) - \varepsilon_s\rho_s\phi_s\frac{d\psi_s^c}{dt_s} \tag{17}$$

The compaction equation reads

$$\frac{d\phi_s}{dt_s} = \mu_c^{-1}\left(\frac{1}{\varepsilon_s}\left(\frac{p_s}{T_s} - \frac{p_g}{T_g}\right) - \frac{\beta_s}{T_s} + \nabla\cdot\left(\frac{\gamma_s}{T_s}\nabla\phi_s\right)\right) \tag{18}$$

and the equation state has the form

$$p_s = -P_\infty + \rho_s T(1 + P_\infty) \tag{19}$$

where Re,Pr stand for the Reynold's and Pradtl's number respectively, $\varepsilon_i = \gamma_i M_i^2$, for $i = s,g$ and $M_s = \frac{u_r}{\sqrt{\gamma_s T_r R_s}}, M_g = \frac{u_r}{\sqrt{\gamma_g T_r R_g}}$ stand for the reference Mach numbers of the solid and gaseous phase correspondingly.

The non-dimensionalized equations are obviously perturbed in terms of $\varepsilon_s, \varepsilon_g$, thus, if we assume that

$$M_s, M_g << 1 \Rightarrow \varepsilon_s, \varepsilon_g << 1 \tag{20}$$

one would be tempted to apply the standard perturbation techniques. Note, however, the there is no coupling between the two perturbation parameters, hence, a direct approach will fail.

In order to overcome this, we will assume an a priori functional dependence between $\varepsilon_s, \varepsilon_g$. Perturbation theory, tells us that this relation should be of polynomial type and moreover, since the analysis is asymptotic it suffices to assume a monomial type dependence i.e. $\varepsilon_s = C\varepsilon_g^n, n \in \mathbb{N}\cup\{0\}, C = O(1)$.

A straightforward solution is provided by the mixture itself as follows: Let C_s, C_g denote the speed of sound of the granular and fluid respectively. We can obviously find $C \in \mathbb{R}$, $n \in \mathbb{N}\cup\{0\}$ such as $C_s = CC_g^n$. Having done this we set $\varepsilon_s = C\varepsilon_g^n$.

We note that the degree of the monomial, indicates the incompressibility level that the gaseous phase starts to contribute in the mixture equations, for example if $\varepsilon_s = C\varepsilon_g^2$, the gaseous phases will enter the perturbation modes in the third order of the expansion (incompressibility level). Finally, observe that mixtures that differ only in the coefficient modulo, lead to the same perturbation modes, modulo a constant.

Given a granular material, the monomial functional dependence defines in fact an algebraic equivalence relation among the set of the various gas components. It is therefore, sufficient to work with representatives of each class i.e. in our case we assume that $C = 1$. In this paper we will work with the class of zero degree monomials, $\varepsilon_s = \varepsilon_g$, where the two components contribute to all incompressible modes.

A. The perturbation expansion

Let us now construct the, in general divergent[1], perturbation expansion for each of the unknown functions of the mixture, in terms of $\varepsilon = \varepsilon_s = \varepsilon_g$.

- $p_i = p_i^0 + \varepsilon p_i^1 + O(\varepsilon^2)$
- $\rho_i = \rho_i^0 + \varepsilon \rho_i^1 + O(\varepsilon^2)$
- $T_i = T_i^0 + \varepsilon T_i^1 + O(\varepsilon^2)$
- $u_i = u_i^0 + \varepsilon u_i^1 + O(\varepsilon^2)$
- $\phi_i = \phi_i^0 + \varepsilon \phi_i^1 + O(\varepsilon^2)$
- $e_i = e_i^0 + \varepsilon e_i^1 + O(\varepsilon^2)$
- $p_s^v = p_s^{0v} + \varepsilon p_s^{1v} + O(\varepsilon^2)$
- $\underline{\underline{P}}_s^v = \underline{\underline{P}}_s^{0v} + \varepsilon \underline{\underline{P}}_s^{1v} + O(\varepsilon^2)$
- $\psi_s^c = \psi_s^{0c} + \varepsilon \psi_s^{1c} + O(\varepsilon^2)$

where $i = s, g$ and we have assumed that the perturbation expansions are regular (observe however, that the system of equations is singularly perturbed in terms of $\varepsilon_s, \varepsilon_g$).

[1] In the single phase case the perturbation expansion is weakly convergent. The corresponding analysis for our case is under investigation and it will be the topic of a future work

It is also important to consider the expansion of the non-conservative variables $p\phi_s$, where $p = p_s - p_g$ and $p_g\phi_g$ namely:

$$\begin{aligned} p\phi_s &= (p\phi_s)^0 + \varepsilon(p\phi_s)^1 + O(\varepsilon^2) \\ p_g\phi_s &= p_g\phi_g)^0 + \varepsilon(p_g\phi_g)^1 + O(\varepsilon^2) \end{aligned}$$

On the other hand we have

$$\begin{aligned} p\phi_s &= (p^0 + \varepsilon p^1 + O(\varepsilon^2))(\phi_s^0 + \varepsilon\phi_s^1 + O(\varepsilon^2)) \\ p_g\phi_g &= (p_g^0 + \varepsilon p_g^1 + O(\varepsilon^2))(\phi_g^0 + \varepsilon\phi_g^1 + O(\varepsilon^2)) \end{aligned}$$

The two expansions must be equal, thus after expanding the product and equating the orders of the same magnitude we finally get

$$\begin{aligned} p\phi_s &= p^0\phi_s^0 + \varepsilon(p^0\phi_s^1 + p^1\phi_s^0) + O(\varepsilon^2) \\ p_g\phi_g &= p_g^0\phi_g^0 + \varepsilon(p_g^0\phi_g^1 + p_g^1\phi_g^0) + O(\varepsilon^2) \end{aligned}$$

The main idea behind the Low Mach number approximation is to decompose the compressible solution to the decoupled incompressible modes. If we insert the perturbation expansions into the equation and equate terms of the same magnitude we arrive at the Low or (Zero) Mach number approximation equations

$$T_s^0 = T_g^0, \ \phi_s^0 + \phi_g^0 = 1 \tag{21}$$

$$p_s^0 = p_g^0 = C', \ \phi_s^0 + \phi_g^0 = 1 \tag{22}$$

$$\begin{aligned} h(T_g^1 - T_s^1) =& \rho_s^0\phi_s^0 \frac{d\, e_s^0}{dt_s} + p_s^0\phi_s^0 \nabla\cdot\underline{u}_s^0 \\ &+ \frac{1}{PrRe}\frac{\gamma}{\gamma-1}\nabla\cdot(\kappa_s\phi_s^0\nabla T_s^0) \end{aligned} \tag{23}$$

$$\begin{aligned} h(T_s^1 - T_g^1) =& \rho_g^0\phi_g^0 \frac{d\, e_g^0}{dt_g} + p_g^0\phi_g^0\nabla\cdot\underline{u}_g^0 - p_g^0\nabla\phi_s^0\cdot((\underline{u}_g^0 - \underline{u}_s^0)) \\ &+ \frac{1}{PrRe}\frac{\gamma}{\gamma-1}\nabla\cdot(\kappa_g\phi_g^0\nabla T_g^0) \end{aligned} \tag{24}$$

$$p_s^0 + P_\infty = \rho_s^0 T_s^0 (1 + P_\infty) \tag{25}$$

$$\frac{d\rho_s^0\phi_s^0}{dt_s} = -\rho_s^0\phi_s^0\nabla\cdot\underline{u}_s^0 \tag{26}$$

$$\frac{d\rho_g^0\phi_g^0}{dt_g} = -\rho_g^0\phi_g^0\nabla\cdot\underline{u}_g^0 \tag{27}$$

$$(T_s^1 - T_g^1) = \left(\frac{d\phi_s^0}{dt_s} - \frac{1}{\mu_c T_s^0}(p_s^1 - p_g^1)\right)\frac{\mu_c (T_s^0)^2}{p_s^0} + (\frac{1}{\mu_c}(\frac{\beta^0}{T_s^0} - \nabla\cdot(\gamma_s^0\nabla\phi_s^0)))\frac{\mu_c (T_s^0)^2}{p_s^0} \quad (28)$$

$$\rho_g^0\phi_g^0\frac{d\underline{u}_g^0}{dt_g} = -\nabla((p_g\phi_g)^1) - \delta(\underline{u}_g^0 - \underline{u}_s^0) - \frac{1}{Re}\nabla(\phi_g^0\underline{\underline{P}}^{0^v}_g) \quad (29)$$

$$\rho_s^0\phi_s^0\frac{d\underline{u}_s^0}{dt_s} = -\nabla\cdot(\gamma_s\nabla\phi_s^0\otimes\nabla\phi_s^0) - \nabla(((p_s - p_g)\phi_s)^1) \quad (30)$$

We observe that as in the single phase case, in the momentum equations we recover the gradient of the next mode of the pressure. However, in our case we recover the gradient of the product $p_s\phi_s$, which agrees with the multiphase definition of the momentum equation. Moreover, it may be worth add that we have not assumed anything for the dimension of the problem and our analysis invariant under the choice of the dimension. This is due to the use of the multi-dimensional formulation of the multi-phase balance equations.

This system of equations can solved numerically via a suitable generalization of the algorithm proposed in [2], which studies similar flows in the single phase case.

III. Equilibrium

In equilibrium all the thermodynamic fluxes and forces vanish[1], and therefore, we arrive at the following system of partial differential equations

$$\nabla(p\phi_s) = -\nabla\cdot(\gamma_s\nabla\phi_s\otimes\nabla\phi_s) \quad (31)$$

$$p = \beta_s - \nabla\cdot(\gamma_s\nabla\phi_s) \quad (32)$$

where we use the notation convention $p = p_s - p_g$ and further assume that $p_g = C$. The unknowns are p, ϕ_s, ρ_s, however, since the equation of state is still valid and $T_s = C$ we have $\rho_s = f(p)$, thus, we are left only with two unknowns namely p and ϕ_s. Lat us know fix $n = 2$.

Remark III-.1: We first observe that the system of equations supports the constant solution $\phi_s = C_1, p_s = p_g = C_2$ as an equilibrium solution, which implies that the model captures the equilibrium behavior of homogenous mixtures.

The equilibrium system consists of $n+1$ quasi-linear elliptic equations in terms of ϕ_s. Ellipticity follows from the fact that $\gamma_s \geq 0$ and $\phi_s \geq 0$, while quasi-linearity is obvious.

Since the system is over-determined we cannot guarantee uniqueness of the solutions, assuming existence has been proved, but according to Spenser cohomology theory, we expect the solution's space to be finite dimensional. The interpretation of the above is that our mixture can have multiple-equilibrium distributions, therefore, does not need to be ergodic.

This can be seen more clearly if we assume that we are very close to equilibrium and that convective effects are negligible such that $u \approx 0$. Then the equations (31-32) take the following form[2]:

$$\nabla(p\phi_s) = -\nabla\cdot(\gamma_s\nabla\phi_s\otimes\nabla\phi_s) \quad (33)$$

$$\frac{\partial\phi_s}{\partial t} = p - \beta_s + \nabla\cdot(\gamma_s\nabla\phi_s) \quad (34)$$

which enjoys the consistency property

$$\begin{aligned}&\phi_s \to \phi_s^{eq}\\ &p \to p^{eq} \quad \text{as } t \to t^{eq}\\ &\rho_s \to \rho_s^{eq}\end{aligned}$$

This is a dynamical system and can, therefore, support a variety of equilibrium distributions, depending on its mixing properties and on the choice of the phase space.

The consistency property allows us to numerically approximate the dynamical system instead of the original equilibrium equations, under some suitable modifications of the convergence criteria in order to capture the correct solutions.

A. Coupling complexity and equations of state

The equilibrium equations are strongly coupled in their unknowns. Indeed, if one tries to algebraically manipulate the system so as to isolate one unknown, ends up in circular arguments, since both β_s and γ_s depend on ρ_s, and therefore, by the equation of state on p_s. Since for the simplest form of an equation of state the system is strongly coupled, the complexity of the coupling can only increase if we consider more complicated equations of state.

It is important however, to see that even if one assumes that $\beta_s = k_1\phi_s^2$, $\gamma_s = k_2\phi_s$, $k_1, k_2 \in \mathbb{R}$, i.e. assume that $\rho_s = C$, the equations still cannot be decoupled. The proof of this argument is as follows.

$$\begin{aligned}\nabla(p\phi_s) &= -\nabla\cdot(\gamma\nabla\phi_s\otimes\nabla\phi_s)\\ &= (-\nabla\cdot(\gamma\nabla\phi_s))\nabla\phi_s - \gamma_s H(\phi_s)\nabla\phi_s\end{aligned} \quad (35)$$

where $H(\phi_s)$ stands for the Hessian matrix of ϕ_s. Solving the compaction equation (32) in terms of the elliptic operator and inserting the result to (35) we obtain

$$\nabla(p\phi_s) = (p - \beta_s)\nabla\phi_s - \gamma_s H(\phi_s)\nabla\phi_s$$

Therefore, we have

$$\begin{aligned}\phi_s\nabla p &= -k_1\phi_s^2 - k_2\phi_s H(\phi_s)\nabla\phi_s \Rightarrow\\ \nabla p &= -k_1\phi_s - k_2 H(\phi_s)\nabla\phi_s\end{aligned} \quad (36)$$

[2]This is an alternative way to express the property that the system has memory

Therefore, we need in addition to assume that $p_s = p_g$ in all Ω so as to ensure the de-coupling of the equations.

B. Compatibility criteria and boundary conditions

We first observe that the momentum equation (31) is compatible if and only if

$$-\nabla\cdot(\gamma_s\nabla\phi_s\otimes\nabla\phi_s)\in Ker(curl(.)) \tag{37}$$

i.e. if and only if $curl(-\nabla\cdot(\gamma_s\nabla\phi_s\otimes\nabla\phi_s))=0$ identically.

Let us assume that $-\nabla\cdot(\gamma_s\nabla\phi_s\otimes\nabla\phi_s)\in L^{2,2}(\Omega)$ where $L^{2,2}(\Omega)$ is the usual notation of the space of square integrable 2-dimensional vectorfields. This assumption is consistent with the introduction of the $\nabla\phi_s$ as an independent thermodynamic variable and moreover, let us assume that we are given boundary conditions for ϕ_s of Dirichlet type, for simplicity. It follows that

$$-\nabla\cdot(\gamma_s\nabla\phi_s\otimes\nabla\phi_s)\in L^{2,2}_{curl}(\Omega) \tag{38}$$

where

$$L^{2,2}(\Omega)=L^{2,2}_{div}(\Omega)\oplus L^{2,2}_{curl}(\Omega) \tag{39}$$

stands for the orthogonal Helmholtz decomposition.

By Ladyzhenskaya's decomposition theorem[7] $\tilde{p}=p\phi_s$ is determined uniquely, up to an additive constant, by the following Neummann problem.

$$\nabla\cdot(\nabla\tilde{p})=-\nabla\cdot(-\nabla\cdot(\gamma_s\nabla\phi_s\otimes\nabla\phi_s)),\qquad\in\Omega \tag{40}$$

$$\nabla\tilde{p}\cdot\underline{n}=-\nabla\cdot(\gamma_s\nabla\phi_s\otimes\nabla\phi_s)\cdot\underline{n},\qquad\in\partial\Omega \tag{41}$$

Thus, given boundary conditions for ϕ_s, Ladyzhenskaya's theorem provides us with sufficient boundary compatibility conditions for p.

IV. Numerical approximation

As we have already mentioned we will solve numerically the dynamical system (33-34).

$$\nabla(p\phi_s)=-\nabla\cdot(\gamma_s\nabla\phi_s\otimes\nabla\phi_s)$$

$$\frac{\partial\phi_s}{\partial t}=+p-\beta_s+\nabla\cdot(\gamma_s\nabla\phi_s)$$

and fix Ω, to be in addition a Lipschitz domain of $\mathbb{R}^n$,$n=2,3$. We further assume that we are given compatible boundary conditions $\phi_{|\partial\Omega}, p_{|\partial\Omega}$ and initial conditions p^0,ϕ_s^0 respectively.

We now fix the ingredients:

- Ω is discretized as an equidistant tensor-product staggered grid, with step size Dx
- Spatial differential operators are discretized via central finite difference operators, in order to get second order accuracy.
- Temporal differential operators are discretized via forward finite difference operators, with time step $Dt\leq Dx$.

The numerical method that is used is a combination of a predictor-corrector algorithm and a projection method, which is reciprocal to the standard Cohen projection method widely used for the incompressible Navier-Stokes equations. For our approximation ρ_s is treated as an independent unknown whose values update via the equation of state.

Throughout this section the exponent $*$ stands for the predicted value of a variable, while the exponent $n,n+1$ stands for the corrected value. The numerical method works as follows:

- **Prediction step**

1. The predicted value ϕ_s^* of the volume fraction in the step n is computed via the compaction equation as follows:

$$\frac{\phi_s^*-\phi_s^n}{Dt/2}=\mathrm{Res}(p^n,\phi_s^n,\rho_s^n)=p^n-\beta_s^n+\nabla\cdot(\gamma_s^n\nabla\phi_s^n) \tag{42}$$

2. The predicted value p^* for the pressure is computed by solving "prediction version" of the Neumann problem (40) i.e.

$$\nabla\cdot(\nabla\tilde{p}^*)=-\nabla\cdot(-\nabla\cdot(\gamma_s^*\nabla\phi_s^*\otimes\nabla\phi_s^*)),\qquad\in\Omega \tag{43}$$

$$\nabla\tilde{p}^*\cdot\underline{n}=-\nabla\cdot(\gamma_s^*\nabla\phi_s^*\otimes\nabla\phi_s^*)\cdot\underline{n},\qquad\in\partial\Omega \tag{44}$$

and then dividing by ϕ_s^*. Observe that $\gamma_s^*=\gamma_s(\phi^*,\rho_s^n)$ so technically this would be a semi-prediction value. However, the variation of ρ_s is small and since γ_s enters only the conductivity tensor of the divergence of the tensor product, the dependence on ρ_s is weak and this enables us to accept this value as the predicted one.[3]

3. The predicted value ρ_s^* for the density is computed via the equation of state

$$\rho_s^*=\frac{p_s^*+P_\infty}{1+P_\infty} \tag{45}$$

- **Correction step**

1. The corrected value ϕ_s^{n+1} of the volume fraction in the step $n+1$ is computed via the compaction equation as follows:

$$\frac{\phi_s^{n+1}-\phi_s^n}{Dt/2}=\mathrm{Res}(p^*,\phi_s^*,\rho_s^*) \tag{46}$$

2. The corrected value p^{n+1} for the pressure is computed by solving "correction version" of the Neumann problem (40) i.e.

$$\nabla\cdot(\nabla\tilde{p}^{n+1})=-\nabla\cdot(-\nabla\cdot(\gamma_s^{n+1}\nabla\phi_s^{n+1}\otimes\nabla\phi_s^{n+1})),\ \in\Omega \tag{47}$$

$$\nabla\tilde{p}^{n+1}\cdot\underline{n}=-\nabla\cdot(\gamma_s^{n+1}\nabla\phi_s^{n+1}\otimes\nabla\phi_s^{n+1})\cdot\underline{n},\ \in\partial\Omega \tag{48}$$

[3] In strict formality one should introduce a semi-prediction step for $\tilde{p}$, then compute via the equation of state the ρ_s^* and then compute the prediction value by solving the updated Neuman problem.

and then dividing by ϕ_s^{n+1}.

3. The corrected value ρ_s^{n+1} for the density is computed via the equation of state

$$\rho^* n+1_s = \frac{p_s^{n+1}+P_\infty}{1+P_\infty} \tag{49}$$

- **Convergence test**

In the end of the correction step the algorithm calculates the $l_2(N)$ norm of the difference $\phi_s^{n+1}-\phi_s^n$, where N is the number of grid points, which is equal to

$$\|\phi_s^{n+1}-\phi_s^n\|_{l_2(N)} = \|-\frac{Dt}{2}\mathrm{Res}(p^*,\phi_s^*,\rho_s^*)\|_{l_2(N)} \tag{50}$$

If $\varepsilon << 1$ is the allowed error the algorithm will terminate if

$$\|-\frac{Dt}{2}\mathrm{Res}(p^*,\phi_s^*,\rho_s^*)\|_{l_2(N)} \leq \varepsilon \tag{51}$$

The stability and consistency of the proposed algorithm follow from the classical stability and consistency Lemmas of the finite difference approximation for parabolic and elliptic problems. Thus by Lax's equivalence principle we also obtain convergence.

It is interesting to observe that the numerical method would also work if we had considered the original equilibrium equations (31-32). In this case the method becomes a successive over relaxation (SOR) method and the time evolution parameters are interpreted as pseudo-time steps. However, the approach adopted here gives a physical meaning to the presence of time as parameter and does not only modify the equations for numerical purposes.

V. Numerical experiments

From the various numerical experiments that we performed of pure mathematical interest, we present here an experiment that corresponds to real mixture parameters, a mixture of sand and water. The components of the mixture have been chosen by virtue of the availability of values for β_s, γ_s. In general there exists a lack of experimental data for these values for other materials but sand. The values that we use are adopted from [5].

Parameter values

- Mixture of sand-water in the $[0,0.1]^2$ square
- $\beta_s = 0.02\mathrm{m}^2/\mathrm{s}^2$
- $\gamma_s = 0.04\mathrm{m}/\mathrm{s}^2$
- $\rho_s = 2200\mathrm{kg}/\mathrm{m}^3$
- $\phi_s^0 \approx 0.74$
- $p_g = 1\mathrm{Atm}$
- $T = 1\mathrm{K}$
- $P_\infty \approx 10^3\mathrm{Atm}$

A. Experiments

Experiment 1: Initial guess $\phi(x,y) = 0.74+\sin(x)\cos(0.1-x+\pi/2)\sin(y)\cos(0.1-x+pi/2)$

Experiment 2:Initial guess $\phi(x,y) = 0.7+0.1e(0.1-100x^2)$

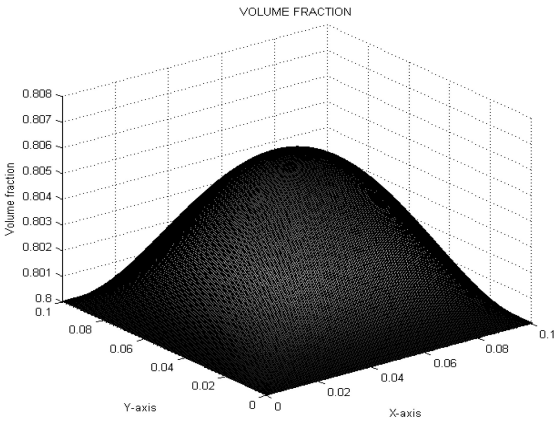

Fig. 1. Volume fraction of experiment 1

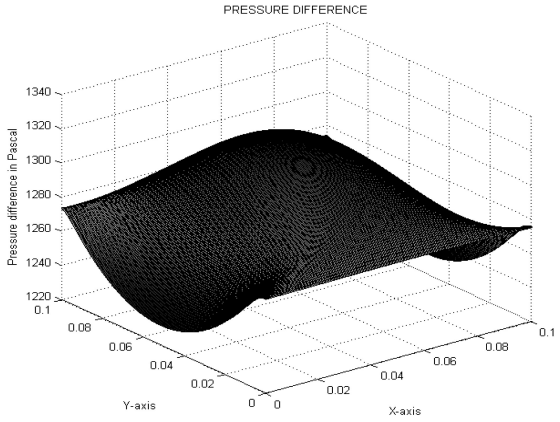

Fig. 2. Pressure difference of experiment 1

VI. Conclusion

In this paper we presented the Low-Mach number approximation equations for a two-phase granular mixture, generalizing the single phase theory to multi-phase flows. Moreover, we examined the equilibrium behavior of such a mixture, both theoretically and numerically, as it is predicted by the model in [1].

Many questions are left open for future discussions. The formal convergence of the perturbation expansion in the Low-Mach number approximation need to be studied in analogy with the single phase case. Global existential theory for the equilibrium equations is also important for the further treatment. Finally, the ergodic study of the dynamical system (33-34) can categorize the initial conditions according to the equilibrium distributions a distinction that can play a major role in the future study of the complete flow in presence of convective and gravitational effects.

References

[1] M. V. Papalexandris, A two-phase for compressible granular flows based on the theory of irreversible processes, , J. Fluid Mech.

(2004), vol. 517, pp. 103-112.

[2] B. Lessani,M. V. Papalexandris, Time-accurate caluclation of variable density flows with strong temperature gradients and combustion, Journal of Computational Physics (2006), vol 212, pp. 218-246.

[3] Ad. Majda, J. Sethian The derivation and numerical solution of the equations for zero mach number combustion, Combust. Sci. Technol. (1985), vol 42, pp. 185-200.

[4] J. B. Bdzil, R. Menikoff, S. F. Son et al, Two-phase modeling of deflagration-to-detonation transition in granular materials: a critical examination of modeling issues, Phys. Fluids (1999), vol 11, pp. 378-492.

[5] S. L. Passman, J. W. Nunziato, P. B. Bailey, Shearing motion of a fluid-saturated granular material, Journal of Rheology (1986), vol 30(1), pp.167-192.

[6] S. R. De Groot & P. Mazur, Nopn-equilibrium Thermodynamics, (1984), Dover

[7] O. Ladyzhenskaya, The Mathematical theory of viscous incompressible flow, (1969), Gordon and Breach

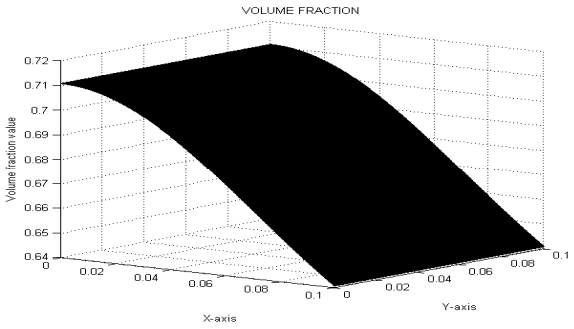

Fig. 3. Volume fraction of experiment 2

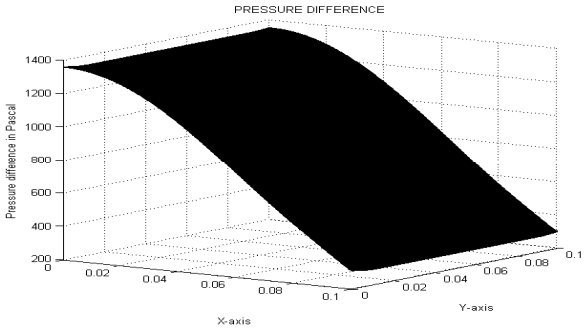

Fig. 4. Pressure difference of experiment 2

Proceedings of the 8th National Congress on Theoretical and Applied Mechanics, May 28-29, Brussels, Belgium.

Pipe flow velocity profiles of complex suspensions, like concrete.

Dimitri Feys[1,2], Ronny Verhoeven[2], Geert De Schutter[1]
[1]Magnel Laboratory for Concrete Research, Department of Structural Engineering, Faculty of Engineering, Ghent University
Technologiepark 904 – 9052 Zwijnaarde - Belgium
[2]Hydraulics Laboratory, Department of Civil Engineering, Faculty of Engineering, Ghent University
Sint-Pietersnieuwstraat 41, 9000 Gent - Belgium
email: Dimitri.Feys@UGent.be

Abstract: **The flow of different suspensions has been studied in literature in order to maximize the transport capacity or to minimize the needed pressure. For concrete, several research projects have been performed, but the question remains if the results for one type of concrete are applicable to another type.**

This paper deals mainly with the flow of self-compacting concrete in pipes. It is shown that the flow of this type of concrete is not influenced by friction between the aggregates, but that the material does not remain homogeneous during the flow. By means of full scale experiments, it is shown that the measured pressure losses are lower than the theoretically calculated pressure losses, due to three effects lowering the viscosity near the wall. The results have been compared with the available literature dealing with traditional concrete, showing some major points of difference. Finally, it is assumed that the velocity profile of concrete in a pipe consists of a plug with uniform velocity in the centre, a lubrication layer with a large velocity gradient near the wall and possibly, a part of the homogeneous concrete also being sheared, depending on the rheological properties and the type of concrete. Unfortunately, no direct velocity profile measuring equipment is available.

Keywords: **Concrete, velocity, rheology, pressure loss.**

I. Introduction

The flow of suspensions, which are liquid materials loaded with solid particles, has been studied for several decades, especially in order to maximize the transport capacities of the carrier liquid, or in order to reduce the pressure needed to transport the suspension [1,2]. The flow of some types of concrete in pipes has been reported in literature, but due to the development of new types of concretes, and due forces of different natures acting on the concrete during flow, it is not certain if the obtained results for one type of concrete can be transferred to another type. This paper will study the flow behaviour in pipes of different concrete types, based on literature and experimental results. In order to distinguish between the different concrete types, suggestions for the velocity profiles will be given, as direct measurements are not yet possible.

In case no particles are present in the suspension, consequently only studying the carrier liquid, the velocity profile can be easily, analytically calculated based on the rheological properties. The addition of particles complicates the situation seriously and analytical solutions are no longer evident to be found. Adding particles can result in two different situations. In the first situation, particles sink to the bottom of the pipe and move much slower than the liquid flowing above, which is better known as bed-flow [1,2]. In the second situation, the particles remain suspended during the flow [1,2]. Only this suspended flow will be described in detail in this paper.

In the next part, concrete will be regarded as a homogeneous suspension and the velocity profile will be calculated based on the rheological properties. Afterwards, the flow behaviour of concrete in pipes will be discussed based on literature and the experimentally obtained results will be described. In the last section, some theoretical modifications to the concrete properties will be proposed in order to approach the experimentally measured pressure losses as well as possible.

II. Concrete – Self-compacting concrete

A. Composition

The composition of concrete can be varied in many different ways, resulting in no real standard composition. Although, it can be roughly estimated that 1 m³ of traditional (vibrated) concrete contains 1300 kg coarse aggregates between 2 and 20 mm (maybe 40 mm), 650 kg of sand, 300 kg of cement and 165 kg of water [3,4].

Self-compacting concrete (SCC) is a rather fluid type of concrete, which does not need any external energy for the removal of air bubbles, and it is able to fill a formwork completely under the acting force of gravity alone. A more detailed description on the difference between traditional and self-compacting concrete will be given in the next section, but a rough composition can be set as follows: 650 kg of coarse aggregates, 850 kg of sand, 350 kg of cement, 250 kg of filler (other fine materials than cement), 165 kg of water and a small amount of superplasticizer, which makes the concrete much more fluid [3].

In any way, whether the concrete is self-compacting or not, it contains around 16.5 vol % of liquid, 1.5 vol % of non-removable air and thus 82 vol % of solid materials, varying in size from 100 nm to 1 cm. As a result, not only the viscosity of the material is modified, but the properties are also influenced by inter-particle forces, inertia and friction. In this paper, the effects of inertia are of no importance for the described results (although it is in other cases) and friction will be discussed separately.

B. Rheological properties

The rheological properties of different concretes have been measured in concrete rheometers and based on the obtained experimental results and literature, a distinction between steady state and transient behaviour will be made. Steady state behaviour corresponds to the situation where all transient

effects have been eliminated and can be regarded as a momentary snapshot of the rheological properties.

1) Steady state properties

The relationship between the shear stress (related to the applied force or pressure) and shear rate (related to the velocity and the geometry) is generally accepted to be of the Bingham type in case of traditional concrete [4]. As a result, a certain stress needs to be exceeded in order to initiate the flow, which is the yield stress, and once the flow has started, an additional stress is needed to accelerate the flow, of which its magnitude is controlled by the viscosity. The Bingham model is shown in equation 1.

In case of self-compacting concrete, a non-linear behaviour has been observed in the experiments, indicating an increase in viscosity with increasing shear rate [5-7]. In this case, the modified Bingham model (eq. 2) [7,8] has been chosen as the most appropriate model to describe the rheological behaviour in steady state.

Equation 1: Bingham model

$$\tau = \tau_0 + \mu \cdot \frac{\partial \gamma}{\partial t} \tag{1}$$

Equation 2: Modified Bingham model

$$\tau = \tau_0 + \mu \cdot \frac{\partial \gamma}{\partial t} + c \cdot \left(\frac{\partial \gamma}{\partial t} \right)^2 \tag{2}$$

where: τ = *shear stress (Pa)*
τ_0 = *yield stress (Pa)*
μ = *viscosity (Pa s)*
$d\gamma/dt$ = *shear rate* (s^{-1})
c = *second order parameter* ($Pa\ s^2$) (> 0)

The main differences between traditional and self-compacting concrete are, apart from the non-linear behaviour, the lower yield stress and higher viscosity in case of SCC [3]. Especially the low yield stress causes the SCC to spread out widely under the force of gravity, while its higher viscosity prevents (or at least slows down) the segregation/sinking of the larger particles [3].

2) Transient behaviour

Due to physical and chemical phenomena which are acting between the cement particles in the concrete, the rheological properties vary in time continuously. Theoretically, the transient behaviour can be divided into three parts: thixotropy, structural breakdown and loss of workability [9].

Thixotropy has a physical nature and is defined as the reversible disruption and rebuilding of connections between the particles. Due to shearing, connections are broken and a larger degree of dispersion is obtained, while due to build-up, more particles get connected. The internal structural state is related to the amount of connections between the particles, resulting in a higher structural state during build-up and a lower structural state due to break down [9,10]. An increase in structural state causes an increase in yield stress and viscosity, and at each shear rate (except at very low shear rates), there exists an equilibrium structural state which is attained when the shear rate is applied during a sufficiently long time [9,10].

At the first contact between cement and water, some chemical reactions occur resulting in some connections between cement particles (other than the thixotropic connections). Due to the hydrodynamic forces induced by shearing, some of these connections can be broken, which is defined as structural breakdown, but during the first 2 – 3 hours of age of the concrete, these chemical connections do not rebuild, at least not at the same rate as the thixotropic connections [9].

Loss of workability is the result of both physical and chemical (at higher ages) connections, which can no longer be broken by the amount of work applied. As a result, the concrete becomes stiffer and finally transforms from a liquid to a strong solid material [9,11].

As can be seen, many phenomena complicate the rheological behaviour of concrete seriously, making it one of the most difficult materials to determine its rheological properties. Currently, the research in this field is still going on, trying to find a practical distinction between the phenomena. In the remaining part of this paper, as it is not easy to distinguish between the thixotropic and the pure structural breakdown, these two effects will be combined in a new definition of structural breakdown [4].

III. FLOW OF HOMOGENEOUS LIQUIDS IN CYLINDRICAL PIPES

The velocity profile of homogeneous liquids in cylindrical pipes can be very easily calculated when the applied pressure or pressure loss, rheological properties of the material and the geometry of the pipe are known. The equilibrium of forces states that the shear stress at the wall must relate to the pressure loss according to equation 3 [12].

Equation 3: Equilibrium of forces

$$\tau_w = \frac{\Delta p_{tot}}{L} \cdot \frac{R}{2} = \Delta p \cdot \frac{R}{2} \tag{3}$$

where: τ_w = *wall shear stress (Pa)*
Δp_{tot} = *total pressure loss over the length L (Pa)*
L = *length of the pipe (m)*
R = *radius of the pipe (m)*
Δp = *pressure loss per unit of length (Pa/m)*

Across the pipe, the shear stress varies linearly from zero in the centre to its maximal value (τ_w) at the wall. This variation of the shear stress is a so-called universal law, meaning it is independent of the rheological properties.

Substituting the shear stress values by the rheological models, like equations 1 and 2, delivers the shear rate distribution across the pipe. For yield stress liquids, the shear rate equals zero in a certain zone of the pipe.

Integrating the shear rate distribution to the pipe radius, with as integration constant the velocity at the wall, which is set at zero due to the no slippage condition, delivers the velocity profile. Figure 1 shows the theoretically calculated velocity profiles for a Newtonian liquid (like water and oil), for a Bingham material (like toothpaste and paint), and a modified Bingham material. Note that for all yield stress materials, a zone of uniform velocity can be observed, which is called the plug.

Further integration of the velocity over the cross section of the pipe delivers the discharge as a function of the pressure loss (or wall shear stress), the rheological properties and the geometry of the pipe. This is shown in equations 4, 5 and 6.

Equation 4: Poiseuille formula

$$Q = \frac{1}{8} \cdot \frac{\pi \cdot \Delta p \cdot R^4}{\mu} \tag{4}$$

Equation 5: Buckingham-Reiner equation

$$Q = \frac{3 \cdot R^4 \cdot \Delta p_{tot}{}^4 + 16 \cdot \tau_0{}^4 \cdot L^4 - 8 \cdot \tau_0 \cdot L \cdot R^3 \cdot \Delta p_{tot}{}^3}{24 \cdot \Delta p_{tot}{}^3 \cdot L \cdot \mu} \tag{5}$$

Equation 6: Extended Poiseuille for modified Bingham

$$Q = \frac{\pi R^3}{840 c^4 \tau_w{}^3} \begin{pmatrix} -\mu^7 + W\mu^6 + 140\mu c^3 \left(\tau_0{}^3 - \tau_w{}^3\right) \\ -2W\mu^4 c(\tau_w + 6\tau_0) + 14\mu^5 c\tau_0 \\ -70\tau_0{}^2 c^2 \mu^3 - 8Wc^3 \tau_w \tau_0 (3\tau_w + 4\tau_0) \\ +2W\mu^2 c^2 \left(3\tau_w{}^2 + 24\tau_0{}^2 + 8\tau_w \tau_0\right) \\ +120Wc^3 \tau_w{}^3 - 64Wc^3 \tau_0{}^3 \end{pmatrix} \tag{6}$$

with: $W = \sqrt{\mu^2 + 4 \cdot c \cdot \tau_w - 4 \cdot c \cdot \tau_0}$

As can be seen, for Newtonian liquids, the Poiseuille formula for laminar flow is obtained (eq. 4) [12,13], and the calculations result in the Buckingham-Reiner equation for Bingham materials [12,14].

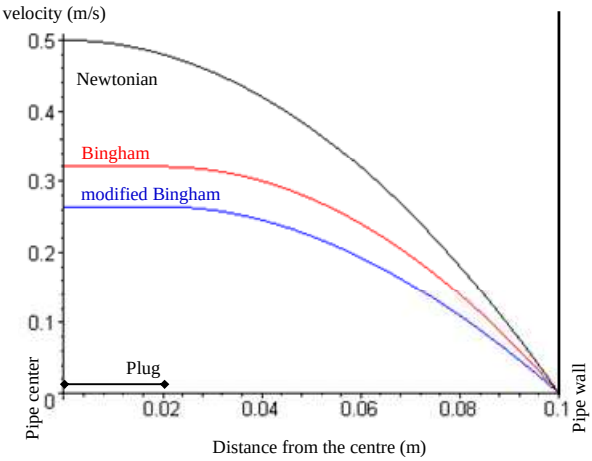

Figure 1: Velocity profile for a Newtonian, Bingham and modified Bingham material. All viscosity parameters equal 10 Pa s, the yield stress equals 20 Pa and c = 0.5 Pa s². The pipe has a radius of 10 cm. Note that in the plug, the velocity is constant for the yield stress materials.

IV. Theoretical Study of the Flow of Concrete in Pipes

Due to the high concentration of solids in concrete, very different flow situations can be obtained with different concrete compositions. In the first section, the theoretical framework will be described, while in the second section, the theory will be applied to different concrete types.

A. Theoretical framework

1) Liquid interactions

The flow of concrete in pipes can be divided into two major classes, depending on the stress transfer inside the concrete [15]. If the stress transfer is of the liquid type, the concrete flows according to the hydrodynamic laws. In a first approach, the principles of section III can be applied in order to describe the flow behaviour of concrete. This case can also be extended to concrete with varying rheological properties across the pipe (see section VI), forming a so-called lubrication layer [15,16] and possibly, an additional velocity component due to slippage can be added [15].

As a result of these liquid type of interactions, the pressure loss per unit of length remains constant along the length of the pipe when disregarding the transient effects and the total pressure evolves linearly with the length of the pipe [17].

2) Solid interactions

The applied pressure during pumping does not only cause the concrete to move in the pipes, but it can also cause the internal water to move inside the concrete [17,18]. In this case, some zones with a low water amount can be created and the stress is transferred by solid interactions between the aggregates. As a result, the hydrodynamic laws of section III can no longer be applied and Coulomb's friction law is valid. The pressure loss at a certain position in the pipe is dependent on the local pressure and as a result, the total pressure decreases exponentially with the length of the pipe [15,17].

Several researchers have shown that these solid interactions cause a much larger pressure loss and that this case must be avoided as much as possible [17]. In case the pump cannot deliver the pressure needed to overcome the frictional stresses, the concrete flow stops and the pipe gets blocked.

B. Application on different concrete types

In literature, a main distinction is made between "pumpable" and "non-pumpable" concretes [15,17]. Although no exact scientific results are available, concrete can be made pumpable by reducing the amount of coarse aggregates and increasing the amount of fines. Also the yield stress must not be higher than a certain value. Pumpable concretes are assumed to move due to the liquid interactions in the cement paste, while non-pumpable concretes suffer more from friction between the aggregates.

Self-compacting concrete is due to its composition already pumpable in any situation. As a result, no problems concerning friction are expected, which has been verified during the full scale tests on 18 different SCC compositions. Nevertheless, friction becomes important during the filling of the pipes with concrete, as the fine materials stick to the wall in order to lubricate the flow and as the coarse aggregates move ahead of the bulk concrete due to inertia caused by the specific pumping action. In this case, a front of aggregates is created in front of the concrete, which can lead to blocking in case the stress transfer is changed from the liquid to the frictional type.

V. Full scale pumping tests with SCC

A. Test setup

In order to execute the full scale pumping tests with SCC, an industrial truck-mounted concrete piston pump has been applied. This type of pump contains two hydraulic cylinders, alternately pushing concrete inside the pipes and pulling concrete from the reservoir. A powerful valve inside the concrete reservoir switches the connection between the pipes and the cylinders, when the pushing cylinder is empty and consequently, the cylinders swap jobs. This specific pump can deliver a discharge which can be varied in 10 discrete steps, between 4 to 5 l/s (step 1) and 40 l/s (step 10).

Figure 2: Truck mounted concrete piston pump.

Figure 3: Loop circuit with a length of 25 m.

Behind the pump, a loop circuit with a total length of around 25 m has been built with steel pipes with an inner diameter of 106 mm and a thickness of around 3 mm. The circuit consisted of a straight, horizontal section with a length of 12 m, a 180° bend and an inclined part. At the end of the circuit, the concrete flows inside a suspended reservoir, equipped with a valve. In normal conditions, the valve is open and the concrete falls back inside the reservoir of the pump. For sampling and discharge calibration, the valve is closed.

The concrete pump and the loop circuit are depicted in figures 2 and 3 respectively.

B. Measurement systems

1) Pressure losses

The pressure losses have been measured by means of two pressure sensors, located in the straight, horizontal section with a separation distance of 10 m. Close to each pressure sensor, three strain gauges have been attached to the outer pipe wall, following the deformation of the pipe, which is related to the local pressure [15]. These strain gauges acted as a back-up in case something happened with the pressure sensor. Both the pressure sensors and all strain gauges are connected with a data acquisition system, registering the output at a rate of 10 measurements per second.

The pressure sensor and strain gauges are depicted in figure 4.

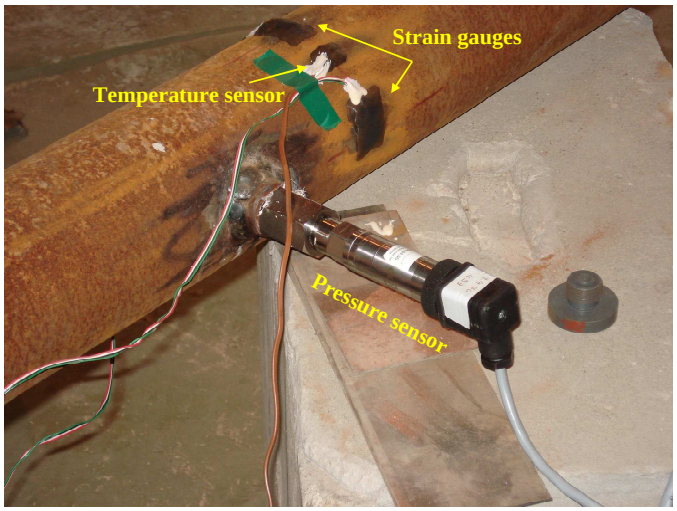

Figure 4: Pressure sensor and strain gauges.

2) Discharge

No direct equipment was available for measuring the velocity or discharge. On the other hand, during the switch of the valve of the pump, a clear pressure drop can be seen in the obtained data files. By measuring the time between two switches of the valve of the pump, the discharge can be easily calculated, knowing that the total contents of 1 pumping cylinder is 83.1 l.

This discharge has been calibrated by pumping the contents of 1 full cylinder inside the suspended reservoir with the valve closed. As this reservoir is attached to the rolling bridge by means of a load cell, the force variation is easily recorded and with known density, the discharge can be easily calculated. This calibration procedure has proven that the applied discharge measuring system delivers accurate results.

As mentioned, no direct measurement equipment has been applied to determine the discharge, although an electromagnetic discharge meter has proven to be useful in case of concrete [15]. Also the above described volumetric discharge calibration could have been performed during all tests, but it was too elaborate to be performed continuously. Specific equipment to measure the velocity profile is on the other hand not yet available for concrete. The only tool able of

non-invasive measuring of the velocity is MRI, but this is too expensive to be applied in concrete research [19].

3) Rheological properties

The rheological properties have been measured with the Tattersall Mk-II rheometer [4,20], by stepwise decreasing the rotational velocity after a pre-shearing period. This procedure has been applied in order to eliminate thixotropy and structural breakdown in the concrete before the measurement [4,9-11]. The rotational velocity and resulting torque have been transformed into fundamental rheological units. Afterwards, if possible, both the Bingham and modified Bingham models have been applied on the results. More information and details on the Tattersall Mk-II rheometer and the measuring and data transformation procedure can be found in [20].

C. Testing procedure

The total amount of concrete needed for the execution of the tests is at least 1.25 m³. As a result, all concretes have been produced in a ready-mix plant and transported to the lab. In normal conditions, the concrete arrived in the lab 45 minutes after its production. The insertion of the concrete took normally 10 minutes and afterwards, the setup was ready for the first test.

A test consisted of pumping the concrete at the five lowest discharges available (steps 1 to 5), for safety reasons, in descending order, while maintaining each discharge step during five full strokes (= 5 full cylinders being pumped). A plot of the upstream pressure during a test can be seen in figure 5, in which clearly the decreases and increases in pressure can be seen due to the change of the valve. In the beginning of the test, the pressure is high, which is due to the high discharge (high Q) and the pressure spikes are close to each other. At the end, the opposite can be seen. At each discharge, the average of the pressure in equilibrium during the five strokes has been calculated.

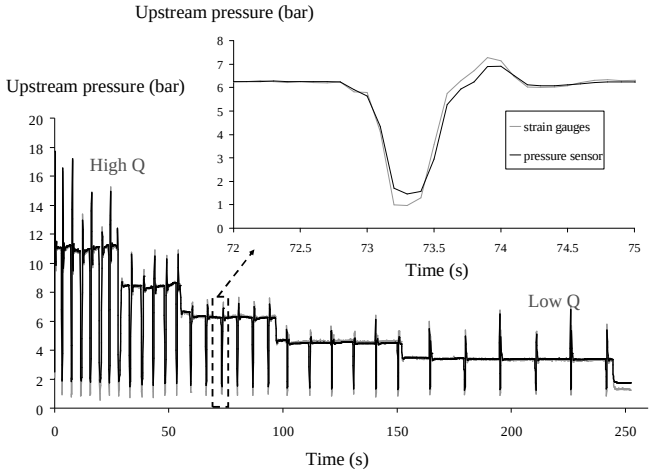

Figure 5: Upstream pressure during a pumping test. The inset shows a detailed evolution of the pressure during the switch of the valve of the pump.

Before each test, a certain amount of concrete is pumped in the suspended reservoir with the valve closed, and a sample is loaded in the rheometer in order to determine the rheological properties simultaneously as the pumping test.

Each 30 minutes, the test has been repeated until the concrete was removed according to the planning.

D. Results

1) Elimination of inaccurate results

The amount of concrete needed for the rheometer test is 12.5 l, which is only 1% of the total amount of concrete available in the circuit. In some cases, serious doubts arose whether the taken sample was fully representative for the total concrete amount. In these cases, the tests have not been taken into account for the further analysis, described in this paper.

Furthermore, due to structural breakdown defined at the end of section 2, the flow resistance of the concrete decreases during the first three pumping tests on the concrete. As the pressure losses have not been determined in equilibrium conditions during the first two tests, these results have been omitted also. As a result, only results from the third test on have been applied in the analysis. Figure 6 shows the pressure loss – discharge curve for a self-compacting concrete (LM 7) and a traditional concrete (TC 1), clearly indicating shear thickening in the first case and perfectly linear behaviour in the second case.

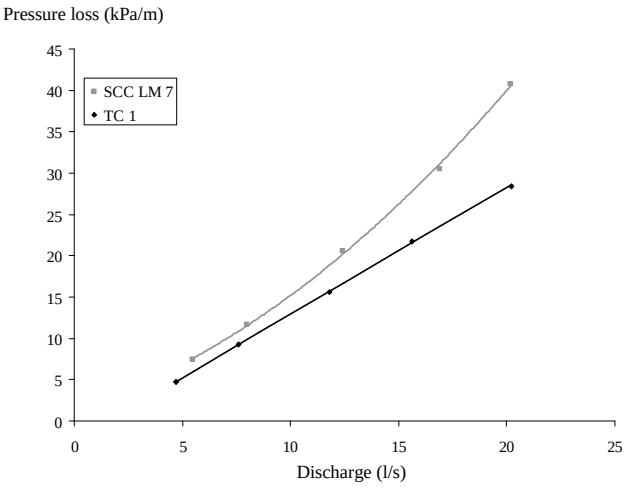

Figure 6: The pressure loss – discharge curve for self-compacting concrete SCC LM 7 (grey) shows non-linear behaviour, while the traditional concrete TC 1 (black) does not.

2) Comparison with theoretical formulae

Based on the obtained rheological properties, both with the Bingham and the modified Bingham model, if applicable, the pressure loss corresponding to each discharge applied has been determined with equations 5 and 6. In this first approach, the concrete was assumed to be homogeneous over the cross section of the pipe. When defining the prediction ratio as the ratio of the theoretical pressure loss to the experimental pressure loss, values between 2 and 5.5 in case of the Bingham model, and 4 and 10.5 in case of the modified Bingham model have been obtained. These values are too high to be attributed to measurement inaccuracies, and as a consequence, some effects must cause lower pressure losses, which will be discussed in the next section.

VI. Heterogeneous concrete flow

As no direct velocity profile measurements are currently possible, an estimation of three effects, being the geometrical wall effect, structural breakdown and dynamic segregation, which all cause a decrease in the pressure loss, will be given in this section. Only for the geometrical wall effect, some approximate calculations are given, as a lot of inaccuracies are encountered. For the other effects, their influence will only be described qualitatively.

A. Geometrical wall effect

1) Principle

The principle of the geometrical wall effect is quite simple: the aggregates cannot penetrate a rigid boundary, in this case the pipe wall, creating a layer with a lower concentration of aggregates in this region. As it has been described in literature, a lower concentration of aggregates induced lower rheological properties [9].

2) Mathematical description

In order to incorporate the geometrical wall effect into a mathematical model, the same principles of section III will be applied. The shear stress distribution remains linear, as it is a universal law, but due to the varying concentration of aggregates, the rheological properties vary across the pipe. At a distance larger than $d_{max}/2$ from the wall, with d_{max} corresponding to the maximal aggregate size (16 mm in our case), the rheological properties are assumed to remain constant. This "unaffected zone" will be reflected as the bulk concrete in this section. When approaching the wall, the yield stress and viscosity are assumed to decrease linearly from their value in the bulk concrete, to the values of the composing cement paste (= cement + water + filler + superplasticizer) at the wall. As the rheological properties of the cement paste have not been measured, a value equal to 1/100 of the values for the concrete have been chosen. The shear thickening parameter c of the modified Bingham model has a somewhat more complicated evolution, described in detail in [20]. Figure 7 shows the assumed evolution of the Bingham parameters yield stress and viscosity, and of the modified Bingham parameters yield stress and c across the pipe.

Note that the average of the rheological properties calculated over the cross section of the pipe corresponds to the measured values in the rheometer, as due to the presence of ribs in the latter case, the geometrical wall effect is prevented to influence the measurements.

Based on these new rheological properties, the shear rate and velocity profiles can be calculated, which are shown in figure 8. As can be clearly seen in case of the Bingham model, a large velocity gradient is present near the wall, indicating the existence of a lubrication layer. For the modified Bingham model, this velocity gradient is not so clearly visible, due to the very large importance of the shear thickening near the wall.

Unfortunately, due to the large mathematical complexity, no theoretical formulae for the velocity and discharge are available.

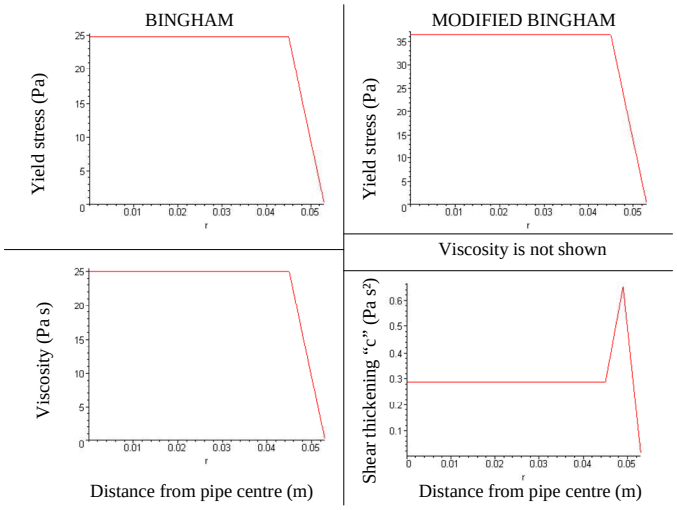

Figure 7: Evolution of Bingham yield stress and viscosity (left) and modified Bingham yield stress and shear thickening parameter "c" (right), for SCC LM 7, test 3. The values measured in the rheometer were: $\tau_0 = 21.25$ Pa, $\mu = 21.42$ Pa s (Bingham) and $\tau_0 = 31.22$ Pa, $\mu = 16.73$ Pa s, $c = 0.367$ Pa s² (modified Bingham).

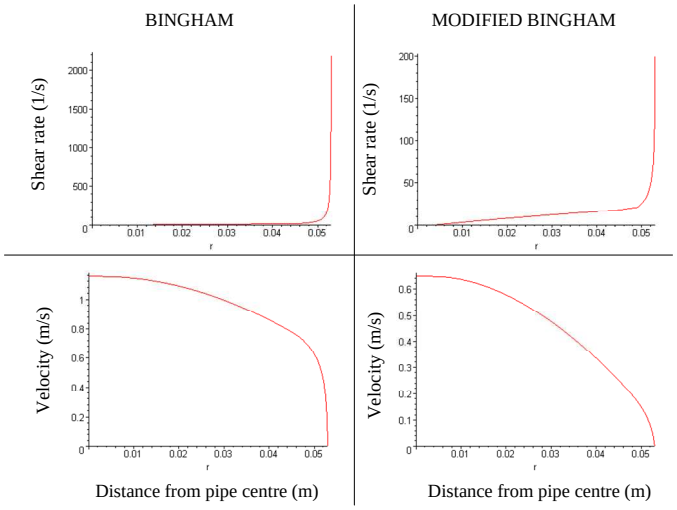

Figure 8: Shear rate (top) and velocity (bottom) profile in case the Bingham (left) or the modified Bingham (right) model have been applied to the concrete. The results correspond to the rheological properties shown in figure 7 and an applied pressure loss of 20.57 kPa/m.

3) Prediction ratio

When applying this new theoretical model, the prediction ratio decreases to 0.6 (but mostly larger than 1) to 2 for the Bingham model, and to 2 to 9 for the modified Bingham model. As a result, when neglecting shear thickening in the concrete, the pressure losses in straight sections can be almost perfectly predicted (within a factor 2).

On the other hand, as shown in figure 9, a shear thickening effect must be present in the pumped SCC. When considering the Bingham model, it can be seen that the prediction ratio decreases with increasing discharge, indicating the presence of shear thickening. On the other hand, as the prediction ratio increases with increasing discharge for the modified Bingham model, it can be concluded that the shear thickening in the pipes is not as large as measured in the rheometer. As a result,

the calculated velocity gradient will be too small and a smaller prediction ratio can be obtained, if the correct shear thickening can be determined.

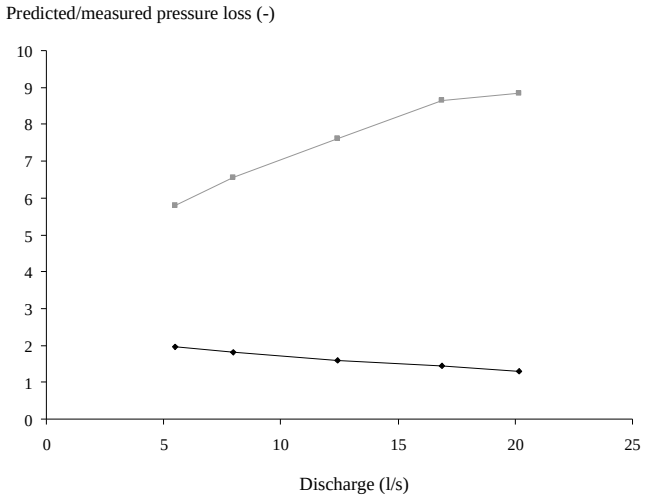

Figure 9: Prediction ratio as a function of discharge shows a decrease with increasing discharge in case of the Bingham model (black) and an increase with increasing discharge for the modified Bingham model (grey), indicating the existence of some shear thickening during pumping, but not as large as measured in the rheometer.

4) Shortcomings

Although this new model is delivering quite good results, it has a lot of shortcomings, making it currently impossible to estimate the other effects.

- As it has been mentioned before, the sampling of the concrete induces a large error. Although the most doubtful results have been omitted, no real certainty exists about how representative each sample is.
- The rheological properties have been measured in the Tattersall Mk-II rheometer and are compared to the pumping results. In se, this is a kind of comparison between two (concrete) rheometers, which induces differences. As it is not certain that the Tattersall rheometer delivers the correct values, this type of error will influence the results.
- Extrapolating rheological curves is a very dangerous task, as the rheological behaviour can change depending on the shear rate interval. The maximal shear rate applied in the rheometer is around 15/s, while in the pipes, when not considering the geometrical wall effect, the maximal shear rate must be equal to 35/s to 45/s. This is probably the reason why the shear thickening is not as large in the pipes as in the rheometer. On the other hand, 15/s is a very large shear rate in a concrete rheometer, endangering the accuracy of the measurement technique considerably. Increasing the maximal shear rate in a concrete rheometer is not easy.
- The calculations have been performed with a linear evolution of all rheological properties, as any more complex variation complicates the analytical calculations significantly. On the other hand, the linear evolution of these properties is probably not correct, as they should evolve according to the Krieger-Dougherty (or equivalent) equation [21,22]. Also the variation of shear thickening should be studied in more detail.
- Due to the lack of equipment, staff, time and an extracting procedure for the measurement of the rheological properties of cement paste, values have been assumed, which induces a new error.

As can be seen, the new model still has a lot of issues to overcome, which are needed in order to quantify the other effects.

B. Structural breakdown

As mentioned in the second section when dealing with the transient rheological behaviour of concrete, the (equilibrium) internal structural state decreases with increasing shear rate. As the material in the vicinity of the wall is sheared at larger shear rates than in the centre, this part of the concrete has to become even more fluid. Although quantification of this effect is very difficult to perform, it has to occur according to the theory.

C. Dynamic segregation

Dynamic segregation is defined as the movement of coarse aggregates away from zones with higher shear rates [4,15]. In fact, this effect would amplify the results of the geometrical wall effect. Although it can be doubted whether it occurs in case of self-compacting concrete, it has been proven to occur in case of traditional concrete [15].

As traditional concrete has a higher yield stress than SCC, it would mean that for a certain pressure loss, the material would move very slowly, or not at all, due to a very large plug. In order to flow more easily, the concrete itself creates a kind of lubrication layer of mortar in the vicinity of the wall. In case of traditional concretes with a rather high yield stress, all shearing occurs in this lubrication layer and the bulk concrete moves forward as a plug at uniform velocity in the pipe.

D. Combination of effects

Whether one of these effects occurs separately, or in a combination with the others, all effects cause a decrease in viscosity in the vicinity of the wall, increasing the shear rate, the velocity gradient and consequently, increasing the discharge at equal pressure loss.

In general, the velocity profile of concrete flowing through a pipe is composed of three parts:

- A plug in the centre
- A large velocity gradient in the vicinity of the wall
- A smaller velocity gradient in between

In case of high yield stress concretes, the plug can be that large that it causes the velocity gradient in the bulk concrete to disappear. Depending on the rheological properties and the type of concrete, the magnitude of the lubrication layer near the wall can vary significantly.

VII. CONCLUSIONS

Based on the rheological properties of a liquid suspension, the theoretical relationships between pressure loss and discharge can be easily calculated if the material remains homogeneous.

The flow of concrete in pipes can occur in two different regimes: the flow can be dominated by liquid interactions, providing the possibility to apply the derived theoretical formulae, or it can be dominated by friction between the aggregates, increasing the pressure needed and possibly leading to blocking.

Self-compacting concrete is a much more fluid concrete type, with a lower yield stress than traditional concrete and a lower amount of coarse aggregates. As a result, the flow of this concrete type is expected to be dominated by liquid interactions.

Full scale pumping tests on self-compacting concrete have shown that the material does not remain completely homogeneous in the pipe. Several effects create a less viscous material layer near the wall increasing the velocity gradient and total discharge at equal pressure loss.

An attempt has been made in order to incorporate the geometrical wall effect into the theoretical calculations, and although promising results have been obtained, a lot of shortcomings still need to be handled.

Structural breakdown causes theoretically a decrease in rheological properties in the zones with high shear rates, which is near the wall. Unfortunately, a practical quantification of this effect is currently very difficult.

Dynamic segregation has been described as the effect enabling the movement of high yield stress traditional concrete, but it is not expected to have such a large effect on the flow of self-compacting concrete.

As a general conclusion, one can state that the velocity profile of concrete flowing through a pipe is composed of three parts:

- a plug in the centre of the pipe due to the yield stress
- a part of the bulk concrete in the centre which is sheared, if the yield stress is not too high
- a lubrication layer with a large velocity gradient, of which the magnitude and properties depend on the rheological properties and the type of concrete.

As can be seen in this paper, a lot of uncertainties still exist on this topic and further research is certainly needed in order to better understand the movement of concrete in pipes. Only in this way, measures can be taken in order to optimize the concrete transport an to increase energy savings during placing.

ACKNOWLEDGEMENTS

The authors would like to acknowledge the Research Foundation in Flanders (FWO-Vlaanderen) for the financial support of this project and the technical staff of both the Magnel and Hydraulics laboratory for the preparation and execution of numerous tests.

REFERENCES

1 Brown N.P., Heywood N. I, *Slurry Handling, Design of Solid-Liquid Systems*, Elsevier Applied Science, London, 1991.

2 Coussot P., *Mudflow Rheology and Dynamics*, Balkema, Rotterdam, 1997.

3 De Schutter G., Bartos P., Domone P., Gibbs J., *Self-Compacting Concrete*, Whittles Publishing, Caithness, 2008.

4 Tattersall G.H., Banfill P.F.G., *The rheology of fresh concrete*, Pitman, London, 1983.

5 de Larrard F., Ferraris C.F., Sedran T., Fresh *concrete: A Herschel-Bulkley material*, Mat. Struct. **31** (1998), 494-498.

6 Heirman G., Vandewalle L., Van Gemert D., *An analytical solution of the Couette inverse problem for shear thickening SCC in a wide-gap concentric cylinder rheometer*, J. non-Newt. Fluid Mech. **150** (2008), 93-103.

7 Feys D., Verhoeven R., De Schutter G., *Fresh self compacting concrete: a shear thickening material*, Cem. Conc. Res. **38** (2008), 920-929.

8 Yahia A., Khayat K.H., *Analytical models for estimating yield stress of high-performance pseudoplastic grout*, Cem. Conc. Res. **31** (2001), 731-738.

9 Wallevik J.E., Rheological properties of cement paste: *Thixotropic behavior and structural breakdown*, Cem. Conc. Res. **39** (2009), 14-29.

10 Roussel N., *A thixotropy model for fresh fluid concretes: Theory, validation and applications*, Cem. Conc. Res. **36** (2006), 1797-1806.

11 Wallevik J.E., *Rheology of particle suspensions, Fresh concrete, mortar and cement paste with various types of lignosulphonates*, Ph-D dissertation, The Norwegian University of Science and Technology, Trondheim, 2003.

12 Macosko C.W., *Rheology Principle, measurements and applications*, Wiley-VCH, New-York, 1994.

13 Poiseuille J.L.M., *Recherches expérimentales sur le mouvement des liquides dans les tubes de très-petits diameters*, CR Acad. Sci. Paris. **11** (1840); 961-967, 1041-1049.

14 Buckingham E., *On plastic flow through capillary tubes*. Proc. Am. Soc. Testing Mat. **21** (1921), 1154–1161.

15 Kaplan D., *Pumping of concretes*, Ph-D dissertation (in French), Laboratoire Central des Ponts et Chausées, Paris, 2001.

16 Thrane L.N., *Form filling with self-compacting concrete, Ph-D dissertation*, Danish Technological Institute – Technical University of Denmark, Copenhagen, 2007.

17 Browne R.D., Bamforth P.B., *Tests to establish concrete pumpability*, ACI-Journal **74** (1977), 193-203.

18 Ede A.N., *The resistance of concrete pumped through pipelines*, Mag. Conc. Res. **9** (1957), 129-140.

19 Jarny S., Roussel N., Rodts S., Bertrand F., Le Roy R., Coussot P., *Rheological behavior of cement pastes from MRI velocimetry*, Cem. Conc. Res. **35** (2005), 1873-1881.

20 Feys D., *Interactions between rheological properties and pumping of self-compacting concrete*, Ph-D dissertation, Ghent University, Ghent, 2009.

21 Krieger I.M., *Rheology of monodisperse lattices*, Adv. Coll. Interface Sc. **3:2** (1972), 111-136.

22 Mahaut F., Chateau X., Coussot P., Ovarlez G., *Yield stress and elastic modulus of suspensions of noncolloidal particles in yield stress fluids*, J. Rheol. **52** (2008), 287-313.

Proceedings of the 8th National Congress on Theoretical and Applied Mechanics, May 28-29, Brussels, Belgium.

Investigation on the influence of various sediment-fluid coupling approaches to the flow and sediment transport

Widera Patryk[1], Lacor Chris[1]
[1]Department of Mechanical Engineering, Vrije Universiteit Brussel
Pleinlaan 2, 1050 Brussels - Belgium
email: patryk.widera@vub.ac.be, chris.lacor@vub.ac.be

Abstract— **The present paper investigates influence of the sediment concentration to the flow in the closed channel at $Re_\tau = 180$. The computational methodology is based on Large Eddy Simulation (LES). The fluid-sediment coupling is obtained by affecting fluid density, fluid viscosity and sediment settling velocity, hence the sediment transport is assumed to be four-way coupled. Comparison has shown strong influence of sediment, also at low concentrations. Additionally, nonlinearity in variation of sediment transport parameters in function of increasing sediment concentration have been noticed.**

Keywords— **Large Eddy Simulation, Channel flow, Sedimentation, Four way coupling**

I. Introduction

An understanding of the mechanics of sediment-fluid coupling on small and large flow scales is important in a variety of ecological, geophysical and industrial fluid mechanical problems. In particular, the ability to predict sediment concentrations including two and four way coupling effects in a channel with rough bed is essential in erosion and sediment transport problems. Based on the previous experience in sediment transport modeling (Widera et al. 2008), it is known that for small flow scales Large Eddy Simulation seems to be the best approach, that combines high accuracy (compared to RANS) and relatively short computational time (compared to DNS). Apart of this, the unsteady LES gives the opportunity to compare advanced flow and sediment transport parameters (i.e. resolved and modeled fluctuations). The LES solution gives also some insight into the relation between the sediment and fluid diffusion ratio, which is not very well known yet, but it is one of the most important parameters in sedimentation modeling.

II. The numerical model

The LES equations for incompressible flow are obtained by filtering the incompressible Navier-Stokes equations and can be formulated as

$$\frac{\partial \bar{\rho}}{\partial t} + \frac{\partial \bar{\rho}\tilde{u}_i}{\partial x_i} = 0 \tag{1}$$

$$\frac{\partial \bar{\rho_m}\tilde{u}_i}{\partial t} + \frac{\partial \bar{\rho_m}\tilde{u}_i\tilde{u}_j}{\partial x_j} = -\frac{\partial \bar{p}}{\partial x_i} + \frac{\partial}{\partial x_j}[\mu\left(\frac{\partial \tilde{u}_i}{\partial x_j} + \frac{\partial \tilde{u}_j}{\partial x_i}\right) - \tau_{ij}] + F \tag{2}$$

where $\bar{u}_i$, $\bar{u}_j$ where $(i, j = 1, 2, 3)$ are the filtered velocity components, $\bar{p}$ is the filtered pressure, ν the fluid kinematic viscosity and F is the driving force. τ_{ij} in equation (2) is the subgrid scale (sgs) stress defined as:

$$\tau_{ij} = \bar{\rho}(\widetilde{u_i u_j} - \tilde{u}_i\tilde{u}_j) \tag{3}$$

This term is unknown and has to be modeled, see section III.

Note that, although the code is incompressible (meaning there is no coupling between pressure and density), the density which is mixture density can vary as it is proportional to the sediment concentration. The varying density requires the use of a Favre filtering operator. The Favre filtered value of any quantity ϕ is denoted as $\tilde{\phi}$ and defined as:

$$\tilde{\phi} = \frac{\overline{\rho\phi}}{\bar{\rho}} \tag{4}$$

where the '-' symbol represents the filter operator.

Due to increasing sediment concentration, especially in regions next to the bottom, the suspension density is also increasing which can cause additional turbulence damping and can also change fluid inertia effects. In this work, the suspension density is calculated using the following equation

$$\rho_m = \rho_s\tilde{C} + \rho_w(1 - \tilde{C}) \tag{5}$$

where ρ_w is the clear fluid density, ρ_s is the sediment density and C represents the sediment concentration. Note that equation (5) implies a coupling between the sediment and the fluid.

The filtered sediment phase equation is given by

$$\frac{\partial \bar{\rho}_s\tilde{C}}{\partial t} + \frac{\partial \bar{\rho}_s[(\tilde{u}_j - v_s\delta_{j3})\tilde{C}]}{\partial x_j} = \frac{\partial}{\partial x_j}(D\frac{\partial \tilde{C}}{\partial x_j} - C_j) \tag{6}$$

where $\tilde{C}$ is the Favre filtered sediment concentration, δ_{j3} is the Kronecker delta, D is the sediment diffusion and C_j is the subgrid scale sediment flux given by

$$C_j = \bar{\rho}(\widetilde{C u_j} - \tilde{C}\tilde{u}_j) \tag{7}$$

III. Modeling of the LES subgrid scale terms

Many sgs models are available in the literature, see Sagaut (1998) for an overview. In the present application the WALE model is used Nikoud (1998). It is preferred over the Smagorinsky model (1963), which gave less good results for the present testcase, see also Ghorbaniasl et al. (2009). The WALE model is formulated as

$$\tau_{ij} - \frac{1}{3}\delta_{ij}\tau_{kk} = -2\mu_{sgs}(\tilde{S}_{ij} - \frac{1}{3}\tilde{S}_{mm}\delta_{ij}) \tag{8}$$

$$\mu_{sgs} = \bar{\rho_m}C_w\triangle^2|\tilde{S}_w| \tag{9}$$

where

$$|\tilde{S}_w| = \frac{(\tilde{S}^d_{ij}\tilde{S}^d_{ij})^{\frac{3}{2}}}{(\tilde{S}_{ij}\tilde{S}_{ij})^{\frac{5}{2}} + (\tilde{S}^d_{ij}\tilde{S}^d_{ij})^{\frac{5}{4}}} \tag{10}$$

with

$$\tilde{S}^d_{ij} = \frac{1}{2}(\tilde{g}^2_{ij} + \tilde{g}^2_{ji}) - \frac{1}{3}\delta_{ij}\tilde{g}^2_{kk} \tag{11}$$

and

$$\tilde{S}_{ij} = \frac{1}{2}\left(\frac{\partial \tilde{u}_i}{\partial x_j} + \frac{\partial \tilde{u}_j}{\partial x_i}\right) \tag{12}$$

The tensor $\bar{g}^2_{ij}$ is given by

$$\tilde{g}^2_{ij} = \frac{\partial \tilde{u}_i}{\partial x_k}\frac{\partial \tilde{u}_k}{\partial x_j} \tag{13}$$

where C_w is the WALE coefficient and $\triangle$ the filter width.

Various approaches are proposed in the literature to model the sgs sediment fluxes, e.g. Chumakov and Rutland (2004), Chumakov and Rutland (2005), Cabot and Moin (1993). In the present paper the classical gradient hypothesis is used because of its simplicity and because of previous good experience with this model, Lessani (2003).

$$C_j = -D_{sgs}\frac{\partial \tilde{C}}{\partial x_j} \tag{14}$$

with the sgs diffusion defined as

$$D_{sgs} = \bar{\rho_s} C_q \triangle^2 |\tilde{S}_w| \tag{15}$$

where C_q is a model constant.

The constants C_w and C_q appearing in the models can either be chosen as constant or calculated via the dynamic procedure of Germano et al. (1991)). In the present application the dynamic procedure was used both for C_w and C_q based on the formulation of Lilly (1992), see also Lessani (2003). This makes the approach free of any tuning constant.

IV. The coupling methods

Coupling effects in the present model are based on the basic physical properties of a suspension, i.e., a fluid medium with varying viscosity, varying density and varying settling velocity. The varying viscosity model uses the approximation of Toda and Furuse (2006) defined as

$$\mu_m = \mu_f[\frac{1 + 0.5\kappa\tilde{C} - \tilde{C}}{(1-\kappa\tilde{C})^2(1-\tilde{C})}]; \kappa = 1 + 0.6\tilde{C} \tag{16}$$

The settling velocity model is based on the Stokes law defined as

$$v_{scf} = \frac{1}{18}\frac{(s-1)gD_s^2}{\nu} \tag{17}$$

where $s = \rho_s/\rho$. Additionally, to incorporate the effects of the sediment concentration the Stokes settling velocity which is valid only in clear fluid is corrected by the equation of Van Rijn (1993)

$$v_s = (1 - 2.1\tilde{C})(1 - 0.75\tilde{C}^{0.33})v_{scf} \tag{18}$$

V. Test case description

As it was mentioned, sediment transport in turbulent flow in closed channel is chosen as test case. The domain size is $Lx = 4\pi\delta$, $Ly = 2\delta$ and $Lz = 4/3\pi\delta$, where $h = 2\delta = 0.04$ and consist of $32 \times 48 \times 32$ cells.The nondimensionalized cell size in streamwise, vertical and spanwise direction are $\triangle x^+ = 67$, $\triangle y^+ = 0.8 - 17$ and $\triangle z^+ = 22$, respectively. For spatial discretisation, the second order central finite volume scheme and for the time discretization low storage four-stage second order Runge-Kutta scheme was used.

The boundary conditions for fluid are assumed to be no-slip wall at top and bottom of the domain and periodical in streamwise and spanwise direction. The boundary conditions for sediment phase at the bottom and the top surface are based on the zero flux condition

$$v_s\tilde{C}\bar{\rho}_m + D_t\frac{\partial \tilde{C}}{\partial y} = 0 \tag{19}$$

where $D_t = D + D_{sgs}$ is the sediment diffusivity. Note that the laminar diffusivity D is assumed here to be identical as the laminar viscosity i.e. $D = \mu$, i.e. the laminar Schmidt number is assumed to be one. In the streamwise and spanwise directions periodic boundaries are imposed.

VI. Results

A. Mixture phase

In this section results of simulations will be presented. The research on the coupling effects is currently in progress. The results shown are therefore to be considered as preliminary. As first, mixture phase will be described and the sediment phase afterwards.

In figure 1, we compare results for the mean streamwise velocity. As can be clearly seen, the sediment concentration has strong influence to the flow field. The mean velocity of low concentrated mixture is reduced about 1.5% comparing with the clear fluid case. For the high concentrated case, the mean velocity drop is already about 10%. This clearly indicate the nonlinearity of velocity drop in function of rising sediment concentration. Figures 2, 3 and 4 presents the rms values of stream-

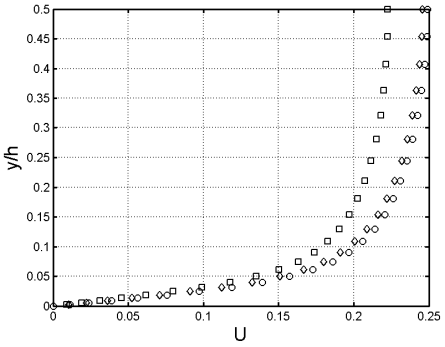

Fig. 1. The streamwise velocity profiles.

wise, vertical and spanwise velocity fluctuations, respectively. The LES data are compared with DNS of Moser et al. (1999). The rms values of streamwise velocity fluctuations overshooting the DNS data about 28%. However, this difference seems to be usual for low-Re flow simulation performed on coarse mesh. The effect of sediment influence can be noticed by the increased fluctuation in the flow center, i.e. $y/h = 0.5$. It is interesting to note that rms values of streamwise velocity are non-symmetrical along the channel center axis. This is due to the sediment concentration, and its influence to the mixture density and viscosity. The rms values of vertical and spanwise velocities presented in

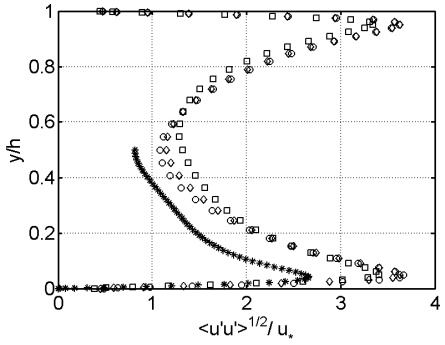

Fig. 2. Rms values of streamwise velocity fluctuations compared with DNS data (* symbol).

figure 3 and figure 4 shows similar response for increasing concentration as the streamwise ones. It is clearly noticeable that velocity fluctuations are increasing in center of the channel in function of increasing sediment concentration. However, it is interesting to note that rms values of the vertical velocity fluctuations are not decreasing in the boundary layer region, as it is for streamwise and spanwise fluctuations. The drop of rms values

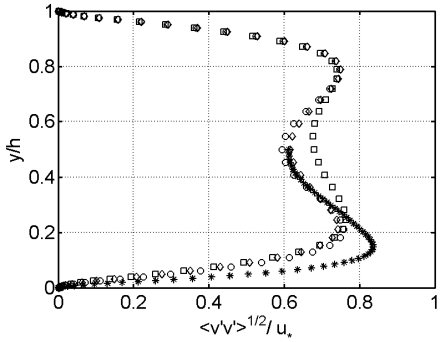

Fig. 3. Rms values of vertical velocity fluctuations.

of spanwise velocity fluctuations in the bottom region can also be noted in figure 4. Comparing coupled and not coupled fluids, it is clear that rms values are lower in the boundary region for mixtures and higher for not coupled fluid. However, it is interesting that the rms value for mixture is increasing (in function of concentration) in the center of the flow (as in figure 2). This is probably due to the increased density and viscosity of mixture. The varying properties of mixture (density and viscosity) is causing increased shear forces in the flow and due to that better mass transfer between the highly turbulent boundary layer and less turbulent flow center. Variation of viscosity in function of sediment concentration is presented in figure 5. As it is shown, maximum increase of viscosity is located near the bottom and it is about 6% higher than in the clear fluid (for low concentrated case) and 28% for high concentrated mixture. The averaged values of mixture viscosity are, 3% for low concentrated case and about 14% for high concentrated case. Sediment influence can also be noted in plot with subgrid-scale results (figure 6), which shows ratio of the modeled and laminar viscosity. As it is expected (from the rms data of velocity fluctuations), the subgridscale mixture fluctuations increasing in function of in-

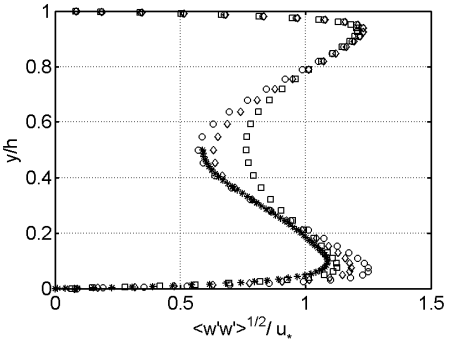

Fig. 4. Rms values of spanwise velocity fluctuations.

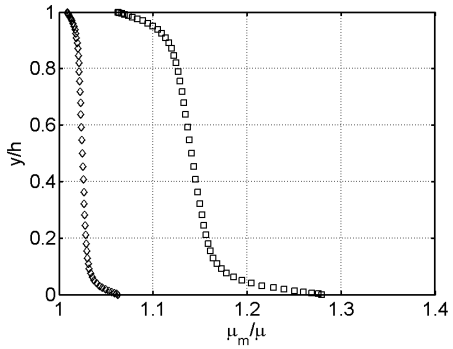

Fig. 5. Ratio between mixture and clear fluid dynamic viscosity.

creasing sediment concentration in the channel center, and they are decreasing in the boundary layer region. This is an effect of increased resolved velocity fluctuations in the channel center.

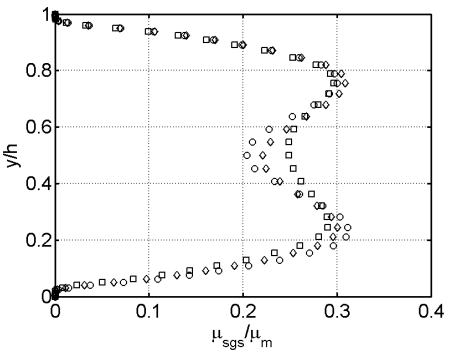

Fig. 6. Ratio between sgs and clear fluid viscosity, for low and high concentrated case.

B. Sediment phase

Distribution of sediment concentration for all cases is compared to the theoretical Rouse profile. The Rouse profile (equation 20) is used to plot profile of the sediment concentration in steady, uniform channel flows and is derived based on the assumption of the parabolic eddy diffusivity. It has been validated with laboratory observations in the limits of low sediment concentration and small particle size. The Rouse equation is defined

as follows:

$$C_s = C_a \left[\frac{y(h-y_a)}{y_a(h-y)} \right]^{-P} \tag{20}$$

where $y_a = 0.5y/\lambda_w$ is the reference height where the sediment reference concentration C_a is sampled, P is the Rouse parameter ($P = v_s/\kappa u_* \beta$) where κ denotes the Von Karman coefficient and $\beta = 0.95$ is the correction coefficient which represents relationship between sediment diffusion and mixture viscosity.

Results of sediment concentration for low sedimented mixture are presented in figure 7 and for high sedimentation in figure 8. As can be seen, already small sedimentation is modifying the vertical sediment concentration profile. The main responsible for modification of the sediment concentration profile are mixture viscosity and density. Due to increase of the viscosity and density sediment buoyancy force is increasing, which leads to decrease of settling velocity and increase of sediment volume in developed flow, see figure 7.

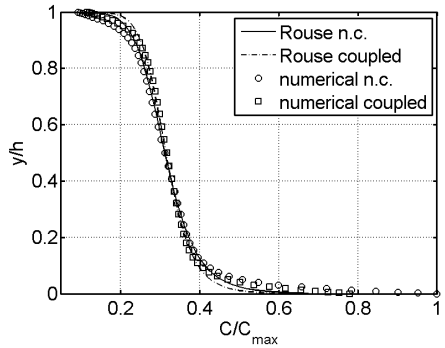

Fig. 7. Sediment concentration profile, low concentration case.

Very similar sediment concentration modification can be noted in figure 8, where difference between not coupled and coupled sediment solution is better visible. It is also interesting to note, that increased sediment amount in developed flow implies that the sediment concentration at the bottom is getting smaller (assuming constant sediment volume in domain - zero sediment flux at boundaries). This means, the bottom shear forces which are generated by suspended sediment can get smaller in flow with higher turbulence level.

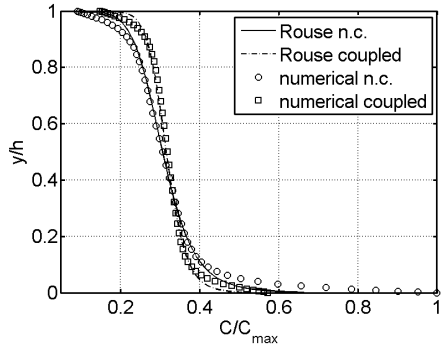

Fig. 8. Sediment concentration profile, high concentration case.

Profiles of rms values of sediment fluxes in streamwise, vertical and spanwise direction are presented in figure 9. , figure 10. and figure 11., respectively.

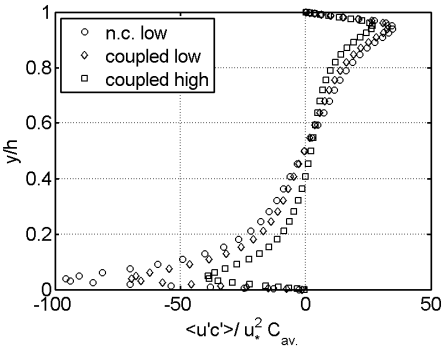

Fig. 9. Rms values of streamwise sediment fluctuations.

Rms results are scaled with the clear fluid case friction velocity and average sediment concentration. As can be seen, the highest rms value of the sediment fluxes is located in bottom boundary layer. It is interesting to note, that drop of the rms value is not linear in function of sediment concentration. Rms value for low concentrated mixture is about 30% smaller than in not coupled case, while in high concentrated case it is about 60% smaller. This means, drop of the rms value is only twice as high as for the low concentrated case, while the sediment concentration is about 5 times higher.

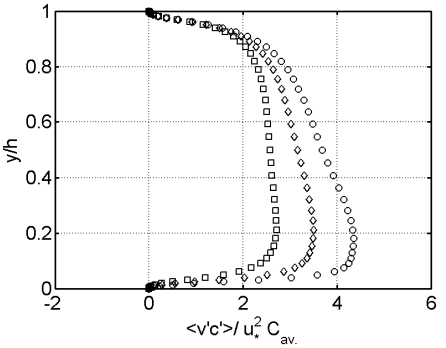

Fig. 10. Rms values of vertical sediment fluctuations.

Similar results might be noted in figure 10. Drop of the rms value of vertical sediment fluxes is two times higher for the high concentrated mixture than for the low concentrated one. This confirms previous results, see figure 9. It is also interesting to note, that increased sediment concentration in mixture implies that the vertical sediment fluxes across the channel are more uniform, i.e. difference between rms value at $y/h = 0.2$ and $y/h = 0.8$ is smaller for high concentrated mixture.

Comparing vertical rms values with the streamwise ones, it is possible to note that the total drop of sediment fluxes is smaller in vertical direction, in function of increasing sedimentation.

As it is expected, results of spanwise rms values are not changing in function of increasing sediment volume, see figure 11.

VII. Conclusions

To estimate influence of coupled model to the sediment and the flow solution, obtained results are compared with theoretical

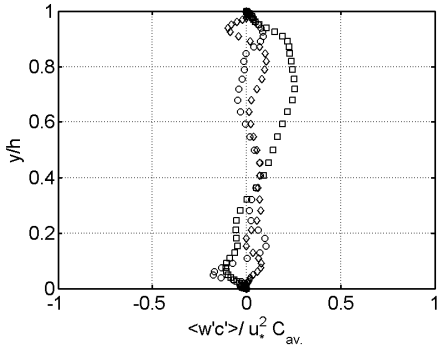

Fig. 11. Rms values of spanwise sediment fluctuations.

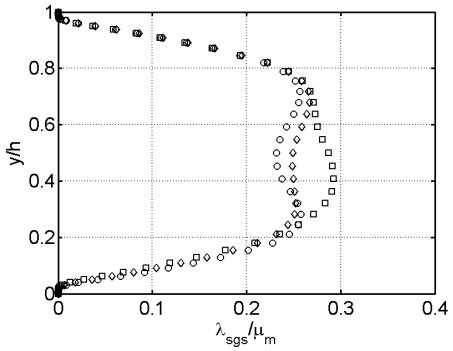

Fig. 12. Ratio between subgrid-scale flux and clear fluid viscosity.

concentration profile based on the Rouse assumption. Results confirmed sediment influence to the flow, its characteristics and sediment transport itself. As it has been presented, the sediment concentration can have a major influence to the flow field. Obtained results explicitly showed that also low sediment concentration is able to have meaningful influence on the flow field and sediment transport. Sediment is responsible for damping of velocity fluctuations, increase of density and viscosity of the mixture. It has been noted that increase of sediment concentration led to increase of rms value of velocity fluctuations in the center of the flow. This is probably due to varying viscosity and density, which are increased in case of suspended sediment. This results in enlarged shear stress and increased momentum transfer towards channel center. Additionally, it has been shown that increasing sediment concentration in domain is influencing symmetry of rms values across the channel (wall normal direction). It has also been noted, that, when the sediment volume in mixture was increasing, the more unsymmetrical rms values of velocity fluctuations were obtained. Performed investigation proved also usefulness of the eulerian methodology for low sediment concentrated suspensions. Ongoing work is extending the model with the inclusion of the additional effects due to the velocity-lag between fluid and solid movement, which should allow simulations at even higher concentrations, as encountered in nature. Based on this, it will be possible to improve existing large scale sediment transport models (e.g. models based on the RANS approach), perform more accurate large scale simulations and with higher sediment concentration.

ACKNOWLEDGMENTS

This research was partially funded by Flemish Science Foundation (FWO) under contract G.0359.04. This support is gratefully acknowledged.

REFERENCES

[1] Cabot W. & Moin P., *Large Eddy Simulation of scalar transport with the dynamic subgrid scale model*, in Book: *Large eddy simulation of complex engineering and geophysical flows.* by Galperin B. and Orszag S., Cambridge University Press, pp. 141-158, 1993

[2] Chumakov S. and Rutland Ch., *Dynamic structure models for scalar flux and dissipation in LES*, AIAA, Vol. 42, 2004

[3] Chumakov S. and Rutland Ch., *Dynamic structure subgrid-scale models for large eddy simulation*, International Journal for Numerical Methods In Fluids, Vol. 47, 2005

[4] Germano M., Piomelli U., Moin P. and Cabot W.H., *A dynamic subgrid-scale eddy viscosity model*, Physics of Fluids A, Vol. 3(7), pp. 1760-1765, 1991

[5] Ghorbaniasl Gh., Widera P. and Lacor Ch. *Quality of dynamic variational multiscale models on distorted grids*, Journal of Turbulence, accepted for publication, 2009

[6] Lessani B., *Large Eddy Simulation of Turbulent Flows,Application to Low Mach Number and Particle-Laden Flows*, PhD Thesis, Vrije Universiteit Brussel, Brussels, Belgium, 2003

[7] Lilly D.K., *A proposed modification of the Germano subgrid-scale model*, Physics of Fluids A, Vol. 4(3), pp. 633-635, 1992

[8] Moser R. D., Kim J. and Mansour N. N., *Direct numerical simulation of turbulent channel flow up to* $Re_\tau = 590$., Physics of Fluids, 11, pp.943-945, 1999

[9] Muste M., Yu K., Fujita I. and Etterna R., *Two-phase versus mixed-flow perspective on suspended sediment transport in turbulent channel flows*, Water Resources Research, 41, 2005.

[10] Sagaut P., *Large eddy simulation for incompressible flows: an introduction*, Springer-Verlag Berlin Heidelberg, Scientific Computation serie, 1^{st} edition, ISBN 3-540-67890-5, ISSN 1434-8322, 1998

[11] Toda K. and Furuse H., *Extension of Einstein's viscosity equation to that for concentrated dispersions of solutes and particles*, Journal of Bioscience and Bioengineering, 102(6),524-528, 2006.

[12] Van Rijn L., *Sediment transport, part 2: suspended load transport*, 110(11), 1431-1456,1984.

[13] Van Rijn L., *Principles of sediment transport in rivers, estuaries and coastal seas*, ISBN:Part I+II: 978-90-800356-9-0, Aqua Publications, Netherland, 1993.

[14] Widera P., Toorman E. and Lacor Ch., *Large eddy simulation of sediment transport in open-channel flow*, Journal of Hydraulic Research (accepted in 2008).

[15] Widera P., Ghorbaniasl G. and Lacor Ch., *Study of the sediment transport over flat and wavy bottom using Large Eddy Simulation*, submitted to Journal of Turbulence.

Proceedings of the 8th National Congress on Theoretical and Applied Mechanics, May 28-29, Brussels, Belgium.

Simulation and design of flapping wings for a Micro Air Vehicle

K. Evers[1,2], D.Vandepitte[1], D.Reynaerts[1]
[1]Department of Mechanical Engineering, Katholieke Universiteit Leuven
Celestijnenlaan 300 B, B-3001, Heverlee – Belgium
[2]Department of Industrial Sciences and Technology, Katholieke Hogeschool Brugge-Oostende
Zeedijk 101, B-8400 Oostende – Belgium
email: kenny.evers@khbo.be, dirk.vandepitte@mech.kuleuven.be, dominiek.reynaerts@mech.kuleuven.be

Abstract: **This paper reports the first steps in a research project that aims to design and develop a high payload flapping-wing MAV. As the wings provide both lift and thrust for a flapping-wing aircraft, a thorough study and understanding of flapping-wing aerodynamics is essential. Therefore, in the first part of this paper a mathematical model using an unsteady potential method is developed. The second part lists the main results that follow from the simulations. A number of guidelines for the further MAV wing design are deduced.**

Keywords: **micro air vehicle, ornithopter, flapping wings, unsteady panel code, wind tunnel tests**

I. Introduction

The possible applications of small unmanned air vehicles, commonly called Micro Air Vehicles (MAVs), vary from search-and-rescue to surveillance missions. Present-day MAVs, however, generally lack the capability of carrying a significant payload, which restricts their field of applications. Amongst the different types of MAVs, flapping-wing MAVs deserve special attention. Flapping wings enhance manoeuvrability and allow flight in a wide range of forward velocities, including hover.

II. Aerodynamic modelling of flapping wings

A. Choice of model type

Flapping-wing MAVs can fly in a wide range of flight conditions, from fast forward flight to hover. Ideally, the aerodynamic model should be able to simulate either case. Yet, there are certain issues which may complicate the modelling process. Firstly, a choice needs to be made between 2D and 3D-models.

Due to the three-dimensional nature of a wing's flapping motion, a 3D-model seems indispensable. However, the goal is not to simulate the flow around flapping wings as accurately as possible, but to develop an engineering tool to perform quick calculations to aid the MAV wing design. Therefore, the long computer time which is usually associated with these 3D-calcuations, would certainly discourage such use. Hence, the choice was made for a two-dimensional unsteady potential code, which solves relatively quickly.

B. Model discrepancies

Obviously, this aerodynamic model can only crudely approximate the conditions of a real flapping wing.

Firstly, the two-dimensional nature of the model implies that it can only simulate a 2D-airfoil kinematic. Hence, in the model a two-dimensional airfoil heaving motion will stand in for the wing's three-dimensional flapping motion. Consequently, no tip effects are incorporated in the calculations.

Secondly, the model only deals with rigid airfoils whereas real wing prototypes may display a pronounced elastic deformation during one flapping cycle. To deal with this effect, the airfoil heaving motion is combined with a pitching motion around the leading edge. It is important to notice that for a real wing this pitching motion results in a passive way due to inertial effects and flow forces. In the model, however, this pitching motion is a kinematic which needs to be imposed explicitly.

These discrepancies immediately point out the strengths and restrictions of the model. This model will probably serve well as a qualitative design tool to provide guidelines and to predict tendencies in order to enhance lift and thrust of a flapping wing. After all, the physics of three-dimensional and two-dimensional flows are not inherently different, so tendencies derived for 2D-airfoils will highly probably still apply for 3D-wings. Yet, it will be hard to relate individual numerical values of lift and thrust coefficients given by the model to lift and thrust forces of a real wing. Consequently, the model is not suitable for use as a quantitative design tool.

C. Development and testing of a linear vortex element model

Most unsteady panel codes use a discrete vortex distribution on the airfoil. In order to simulate the more difficult hover case, however, a higher order potential method is preferred. In a first attempt, a potential method was developed based on the work of Lebental [1]. He presented a two-dimensional inviscid, unsteady panel code that uses a time-marching approach along with a freely convected trailing-edge wake to model flow around flapping airfoils.

An airfoil is discretised into *N* panels with a linear vorticity distribution γ_1 to γ_{N+1}. At each time step k a constant vorticity wake element $\gamma_{TE}(k)$ is shed at the trailing edge. This results in *N+2* unknowns. Tangential flow is prescribed at the centre of each panel, giving *N* equations. An unsteady Kutta condition that imposes zero pressure difference across the chord is applied at the trailing-edge, resulting in one additional equation. The conservation of circulation completes the set of equations. Due to the non-linear nature of the unsteady Kutta condition, the resulting set needs to be solved in an iterative way. A Newton method is used.

The described model assumes fully attached flow at the leading-edge. Yet, leading-edge vortex shedding appears to be important in flapping-wing lift creation, especially when the forward flight speed is reduced. Therefore, the model was expanded to include leading-edge separation by imposing an unsteady Kutta condition at the leading-edge. Consequently, at each time step k a constant vorticity wake element $\gamma_{LE}(k)$ is also shed at the leading edge. Figure 1 shows schematically the discretisation of the airfoil along with its wakes.

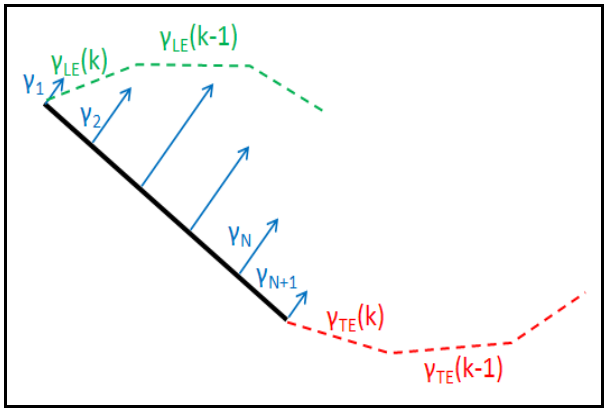

Fig. 1. Airfoil at time step k with linear vorticity distribution (blue arrows). The leading-edge wake (green) and trailing-edge wake (red) consist of constant vorticity elements.

Lebental performed a number of convergence tests for the case of fully attached flow, giving a good agreement between model output and test results. However, it is equally important to test the model for a case for which separation at the leading-edge is abundant. Therefore, an additional convergence test was carried out to check the model behaviour in such a case. A blunt object in a normal flow generates a Kármán vortex street, which is similar to the vortices shed by a flapping wing. Additionally, the normal flow past a flat plate is very well documented. Hence, this can serve as a test case for the model. If the model performs well for this test case, there is a strong indication that the model captures correctly the most important effects associated with leading-edge separation.

For the simulation 50 airfoil panels and 100 time steps per period were used, over a total of 10 periods. Figure 2 shows the model's visualisation of the wakes. The drag coefficient, expressed as a negative thrust coefficient, is shown in Figure 3. As can be seen from this figure, there are two contributions to the drag coefficient. The blue dashed line is a contribution associated with the airfoil circulation and will be referred to as the static contribution. The green dashed line is a contribution due to fluid acceleration and will be referred to as the dynamic contribution. For the case of a flat plate in a normal flow, the mean value of the dynamic contribution is approximately zero. Hence, the main contribution to the mean drag coefficient is static. Averaging over cycles 5 to 10, a mean value of 1.77 is found for the drag coefficient. Experimentally, a drag coefficient equal to 1.98 is observed [4].

The frequency of vortex shedding can be expressed in a dimensionless quantity as the Strouhal number. For a flat plate at 90 degrees angle of attack a Strouhal number of around 0.18 is experimentally found [4], whereas simulations give a Strouhal number of approximately 0.167, again averaged over cycles 5 to 10. Consequently, the model relative error of the mean drag coefficient and the Strouhal number is -10.6% respectively -7.2% for this test case. It should, however, be mentioned that these results may slightly vary depending on the number of airfoil panels and the chosen time step.

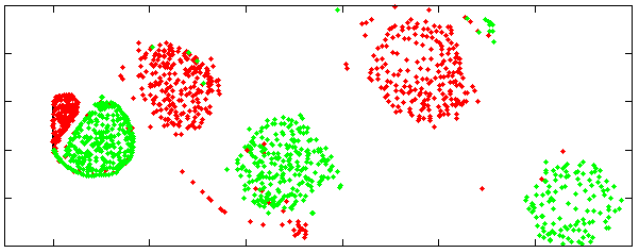

Fig. 2. Model's visualisation of a Kármán vortex street behind a flat plate in a normal flow. The units on both axes are equally spaced spatial coordinates.

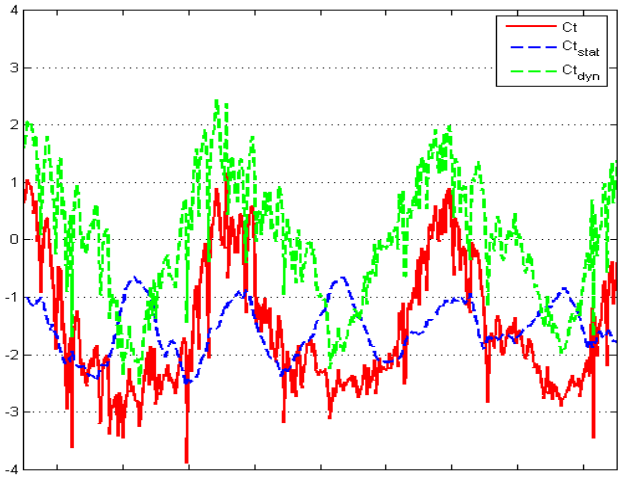

Fig. 3. Drag coefficient in function of time, expressed as a negative thrust coefficient, of a flat plate at 90 degrees angle of attack for a model with linearly varying bound vorticity. The results of cycles 5 to 7 are shown. The blue dashed line is the static contribution, the green dashed line is the dynamic contribution. The red line shows the sum of both.

Nonetheless, this model has an important drawback. The non-linear nature of the Kutta conditions negatively influences the model's robustness. For oscillatory airfoil motions, the flow in the vicinity of the leading edge changes violently during the transitions from upward to downward motion and vice versa. During these flow reversal phases, the iterative Newton method may not converge at times. Especially when the forward flight speed is strongly reduced, i.e. near-hover conditions, convergence issues arise.

It can be concluded that converence problems prevent solutions in near-hover conditions, which ironically are the conditions were this model should outperform lower order methods. In the next subsection such a lower order method is developed which benefits from linear equations and, consequently, higher robustness.

D. Development and testing of a discrete vortex element model

A discrete vortex model was developed, based on the work by Katz and Platzer [2]. Zdunich et al. [3] already developed a similar model as part of the Mentor project. The bound vorticity on the airfoil is now modelled using discrete point vortices.

Clearly, a discrete vorticity distribution is less accurate than a linearly varying vorticity distribution, which makes this model not appropriate to simulate (near-)hover conditions. However, for the discrete vorticity distribution the Kutta conditions are already satisfied and need not to be stated explicitly. Therefore, this model yields a linear set of equations which can be solved by a matrix inversion. This adds significant robustness to the model. The airfoil discretisation for this model can be seen in figure 4. The same convergence test was also performed for this discrete vortex model. The drag coefficient of the flat plate is shown in figure 5. Again, for the simulation 50 airfoil panels and 100 time steps per period were used, over a total of 10 periods.

When comparing figures 3 and 5, it is clear that the discrete vortex model yields less smooth instantaneous force coefficients than the linearly varying vortex model. The mean drag coefficient for this model, averaged over cycles 5 to 10, is 2.21 and the Strouhal number is 0.156. So, the model relative errors are respectively +10.5% and -13.3%. Again, these results may vary slightly depending on the number of airfoil panels and the number of time steps per period.

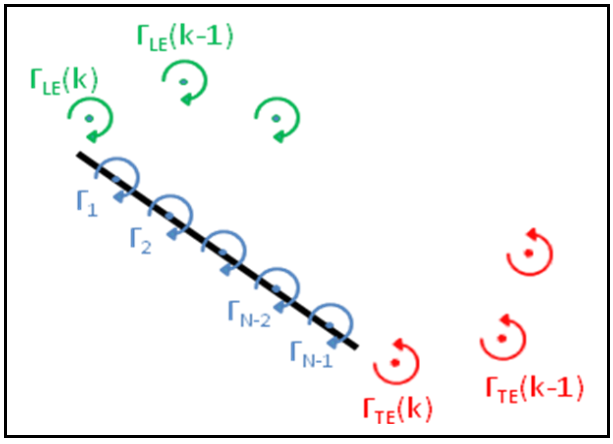

Fig. 4. Airfoil at time step k with discrete vorticity distribution (blue arrows). The leading-edge wake (green) and trailing-edge wake (red) consist of discrete point vortices.

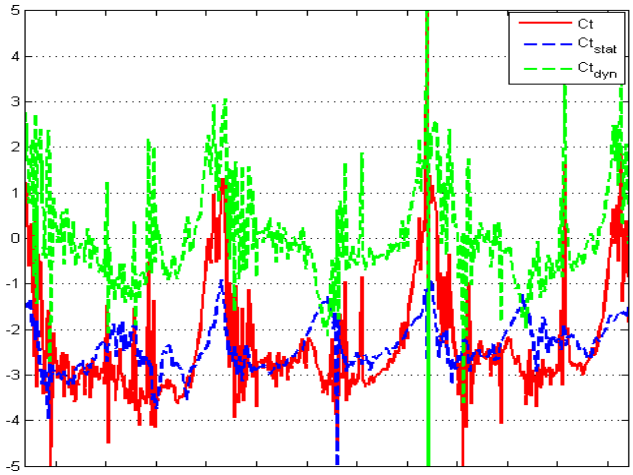

Fig. 5. Drag coefficient in function of time, expressed as a negative thrust coefficient, of a flat plate at 90 degrees angle of attack for a model with discrete bound vortices. The results of cycles 5 to 7 are shown. The blue dashed line is the static contribution, the green dashed line is the dynamic contribution. The red line shows the sum of both.

E. Comparison of both models

Aside from the smoothness of the model output, the results of this simple convergence test are inconclusive to determine which model is best. Both models give results that are in reasonable agreement with empirical data of a flat plate in a normal flow.

In theory, the linear vortex element model should outperform the discrete vortex element model for oscillatory airfoil motions, especially in (near-)hover conditions. Convergence issues, however, counteract this advantage. Thus, the discrete vortex element model will be used for further simulations as its good robustness is a clear asset for an engineering tool.

III. Model Results

A. Flapping frequency

The flapping frequency, or the non-dimensional Strouhal number, strongly influences the energy efficiency of the flapping cycle. Taylor et al. [5] showed that the Strouhal number for natural flyers seems to be constrained to the narrow range of 0.2-0.4 as this corresponds to the highest power efficiency. Yet, most MAVs flap at much higher frequencies, corresponding to Strouhal numbers of around 1. This results from the fact that present-day MAV wings do not generate sufficient lift and thrust to support the MAV weight at this optimal working point. Therefore, in all further simulations, a Strouhal number of 1 will be used.

B. Thrust force and heaving-pitching phase lag

Both heaving and pitching motion are modelled as a sinusoidal function with frequency equal to the flapping frequency. However, there may be a phase lag between heaving and pitching motion. To determine the optimal

phase difference Δ between heaving and pitching motion, a series of simulations with different values for Δ was performed. Figure 6 shows schematically the possible values for Δ. For these simulations 50 airfoil panels and 100 time steps per period were used, over a total of 10 periods. The heaving amplitude was chosen equal to the airfoil chord length, and the pitching amplitude is 20°. Figure 7 shows for all simulations the thrust coefficient, averaged over cycles 5 to 10. As the mean angle of attack over one period is zero, there is no significant lift created by these airfoil motions.

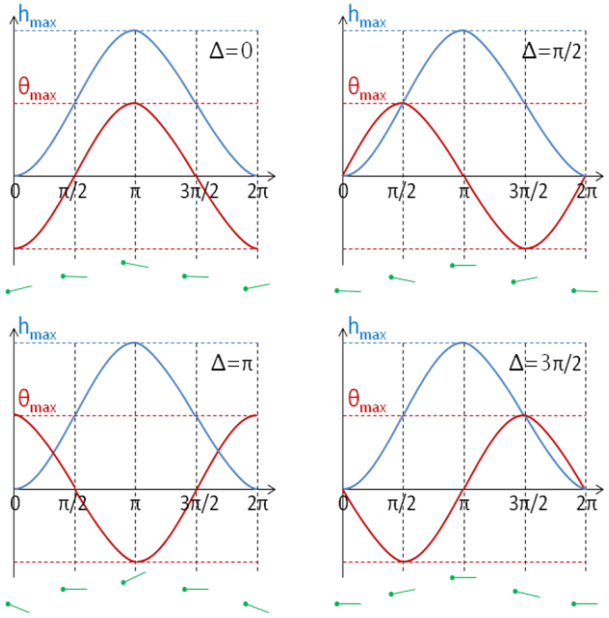

Fig. 6. Four different values of the phase lag Δ between heaving motion (blue) and pitching motion (red). The green lines represent the airfoil at each step of the cycle.

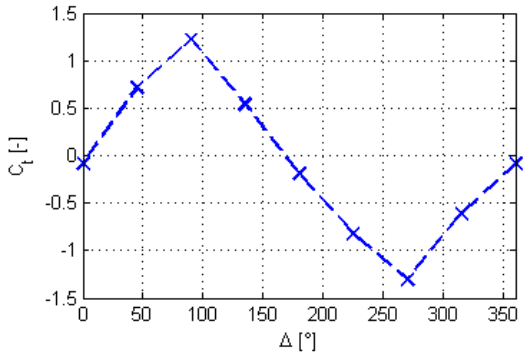

Fig. 7. Mean thrust coefficient of a combined heaving and pitching motion with heaving amplitude equal to the airfoil chord, and pitching amplitude equal to 20° and for different values of the phase difference between heaving and pitching motion.

The results in figure 7 clearly show that a phase lag between heaving and pitching motion of 90° yields maximum thrust force. This can be achieved in a passive way by constructing a wing out of a flexible membrane and a stiff leading edge. The wing stiffness can be further manipulated by adding one or more stiff elements to the wing surface in order to optimise the elastic deformation.

In a next step, a series of simulations was performed for pitching amplitudes going from 0 to 45°. The simulation conditions remain the same as in the previous case. Additionally, a phase lag Δ of 90° is now used (and in all further simulations). Figure 8 shows an approximately linear relationship between pitching amplitude and thrust coefficient, favouring high pitching amplitudes. This result again stresses that the wings should be highly flexible around the leading-edge, allowing passive pitching.

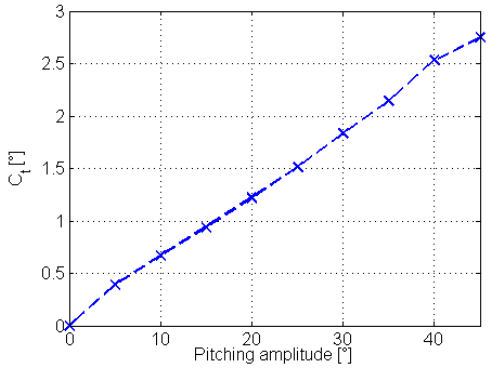

Fig. 8. Mean thrust coefficient of a combined heaving and pitching motion for various values of the pitching amplitude. The heaving amplitude equals the chord length.

C. Lift force

The airfoil kinematics from the previous subsection do not generate a mean lift force. In order to add lift, the airfoil can be placed under a mean angle of attack. According to Sheldal and Klimas [6], a flat plate positioned under a constant angle of attack yields a non-zero mean lift coefficient (and also a non-zero drag coefficient). A series of simulations of an airfoil placed under a constant angle of attack is carried out, and the results are compared to the results of Sheldal and Klimas. This is shown in figure 9.

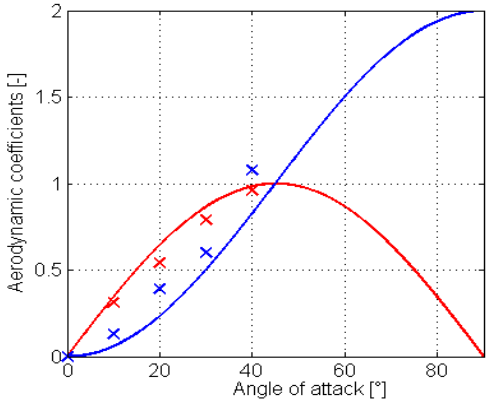

Fig. 9. Lift (red) and drag (blue) coefficient of a flat plate positioned under various angles of attack. The solid lines show the results of Sheldahl and Klimas. The red and blue markers are simulation results.

Subsequently, a similar series of simulations was performed but this time a heaving and pitching motion was superimposed on the constant angle of attack. The heaving amplitude is again taken equal to the airfoil chord length, the pitching amplitude is 20°. As in the previous simulations, 50 airfoil panels and 100 time steps per period were used. The results are presented in figure 10. It is clear that now the drag coefficient becomes negative, i.e. a thrust coefficient, due to the combined pitching and heaving motion. The lift coefficient, however, does not increase significantly compared to the case of a constant angle of attack. A low angle of attack (close to zero) yields the highest thrust coefficient but almost no lift force. When the angle of attack approaches 45°, the lift coefficient becomes maximum whereas the total thrust coefficient drops due to the increased airfoil drag. Hence, it seems optimal to fly at a moderate angle of attack of around 20°-30°. At this point the lift is already sufficiently high and the airfoil drag is still acceptable.

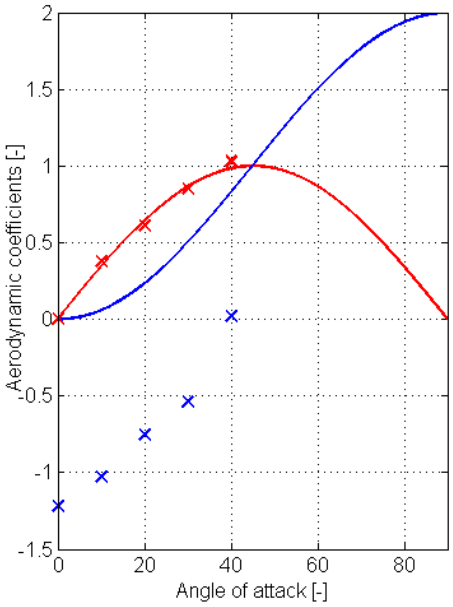

Fig. 10. Lift (red) and drag (blue) coefficient of a flat plate positioned under various angles of attack with a superimposed pitching and heaving motion. The red and blue markers are simulation results of mean lift and drag coefficients respectively. The solid lines represent the results of Sheldahl and Klimas (no heaving and pitching motion).

IV. Conclusion

The first part of this paper presented two 2D mathematical models using an unsteady potential code to model the flow around a flapping airfoil with leading-edge separation. One model used constant vorticity elements for the wakes and linearly varying vortex elements for the bound vorticity. This model should be more accurate, especially in (near-)hover conditions but convergence problems counteract this advantage. The second model uses discrete point vortices to model both bound and free vortices. This model has an excellent convergence due to its linear set of equations. Both models were able to predict within 15% of accuracy both the drag coefficient and the Strouhal number of the flow around a flat plate in a normal flow.

The simulation results provide a number of guidelines for the further MAV wing design. Firstly, there should be a lag between heaving and pitching motion of a quarter period. This can be achieved passively by constructing a wing out of a flexible membrane and a stiff leading edge. Secondly, the thrust coefficient increases in an approximately linear way with the pitching amplitude. This again indicates that the wing should be highly flexible around the leading edge. Finally, the wings should be positioned under a mean angle of attack of around 25° to generate sufficient lift, without sacrificing much of the thrust.

References

[1] S. Lebental, *Optmization of the aerodynamics of small-scale flapping aircraft in hover*, partial Ph.D. thesis, Duke University, 2008.

[2] J. Katz and A. Plotkin, *Low-speed aerodynamics*, 2nd ed., Cambridge Universisty Press, Cambridge, 2001.

[3] P. Zdunich, D. Bilyk, M. MacMaster and D. Loewen, *Development and testing of the Mentor flapping-wing micro air vehicle*, Journal of Aircraft, Vol. 44, No. 5, Sept.-Oct. 2007, pp. 1701-1711.

[4] C. Tropea, A. Yarin and J. Foss, *Springer handbook of experimental fluid mechanics*, Springer, Berlin, 2007.

[5] G. Taylor, R. Nudds and A. Thomas, *Flying and swimming animals cruise at a Strouhal number tuned for high power efficiency*, Nature, 425, 2003, pp. 707-711.

[6] R. Sheldahl and P. Klimas, *Aerodynamic characteristics of seven symmetrical airfoil sections through 180-degree angle of attack for use in aerodynamic analysis of vertical axis wind turbines*, Sandia National Laboratories, Tech. Rep., 1981.

Proceedings of the 8th National Congress on Theoretical and Applied Mechanics, May 28-29, Brussels, Belgium.

Air-oil separation devices for aircraft engine lubrication systems

Amélie Ruelle[1] and Johan Steimes[1], François Gruselle[1], Patrick Hendrick[1]
[1]Université Libre de Bruxelles, Aero-Thermo-Mechanics Department
CP165/41, Avenue F.D. Roosevelt 50, B-1050 Brussels, Belgium
Email: aruelle@ulb.ac.be, jsteimes@ulb.ac.be, fgrusell@ulb.ac.be, phendrick@ulb.ac.be

Abstract— **The current environmental and economical issues lead most of the technological sectors to review their behavior towards energy consumption. Within the framework of the aeronautical industry, the aim is not only to reduce the specific fuel consumption of aircraft, but also the oil consumption. Currently, a lot of research is performed towards this reduction, and a part of the solution is a renewal of the propulsion system. To help the aircraft engine companies to go through this evolution, the auxiliary equipments also have to be adapted to those new propulsion systems. This involves the development of new cooling and lubrication solutions. This paper will focus on the separation of air and oil in the lubrication system and on the reduction of the oil consumption. It will also present the current technologies, the solutions chosen to reach the goals and the numerical challenge of two-phase flow simulations.**

Keywords— **Aeronautics, Aircraft Lubrication, Two-phase flows**

I. Introduction

NOWADAYS , multiphase flows are more and more studied, whether it is in the area of computational fluid dynamics or experimental studies. This interest occurs because many applications use multiphase flows. Therefore, with the current ecological and economical pressures, the topic of multiphase separation is showing an increasing potential. Separators able to extract one phase from another are used in multidisciplinary areas, like the extraction of oil with cylindrical cyclone separators [1], in oil refining with horizontal gravity separators [2] , in pipes going to pumps used in the nuclear area [3], in air separation for two-stage to orbit launchers [4] or in lubrication areas like aircraft lubrication systems [5].

It is in this last area that our work will find its place. Lubrication systems of classic aircraft engines are composed of oil feeding system and scavenge systems. The presence of air in the bearing chambers causes the presence of an air-oil mixture in the scavenge system. In order to ensure good performance for the oil pumps, the air has to be separated from the oil. A good separation process also rejects lesser oil into the atmosphere. Moreover, the next generation of turbofans have to reduce their specific fuel consumption, and this reduction goes through an improvement of the lubrication systems. That is why the ATM department is studying a lot of different concepts to separate the air-oil mixture.

A rotating separator, that also acts as a pumping system, is currently studied and is already at his third prototype testing. Solutions are also considered to replace the current separation systems, by a Vortex separator or by some more simple separators like plate separators, ... There are two ways to study those concepts: Computational Fluid Dynamics (CFD) or experimental studies. Both ways are currently evaluated. In this paper, we present the test benches developed for the rotating separator and the vortex separator. Those benches are now running with water and air, as the water at ambient temperature has almost the same viscosity as the oil used in turbofans. The measurement techniques are also discussed. A multiphase flow CFD method is also presented.

II. Rotating separator test-bench and visualizations

THE ATM department is developing an innovative system to pump and separate a two-phase flow that could be used for many applications where there is a need of extracting a phase of a multiphase flow, before the flow goes through a pump. This includes oil extraction, flow in nuclear pumps, and flows in aircraft gas turbine engine lubrication systems. The separation is performed in the first part of the machine, which is axial. The separated flow goes then into a centrifugal part that ensures the pumping function. The separation uses the same forces as the ones acting in the vortex separator, which is discussed later on. To support this development a test bench was built at the ATM laboratory.

A. Test bench

The application needs to have a two-phase flow at the entrance of the separator. The bench is, therefore, providing a water/air mixture, in different proportions. The mixing chamber receives on one side air from a compressor and on the other side water from a tank. The flow rates are fixed by hand valves. The mixing chamber's output is then connected to the prototype. The exits of the separator are then forwarded to measurement apparatus. The water outlet, for example, is redirected to a visualization cell. Figure 1 shows a sketch of the separator test bench.

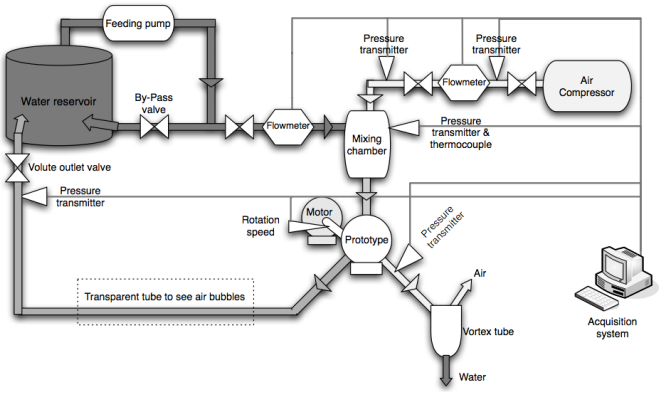

Fig. 1 The rotating separator test bench.

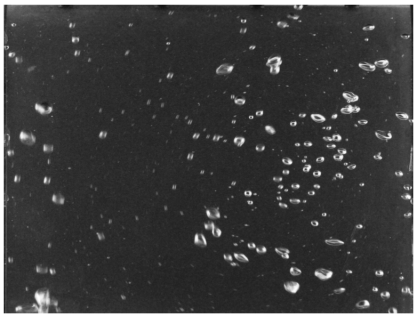

Fig. 3 The visualization cell results.

B. Visualizations

A visualization test cell is still in development at the ATM department. The flow coming from the exit of the separator goes through a plexiglas tube that is designed with a cross section tacking into account the flow velocity and the cell thickness and width. The background is made of white sheets of paper illuminated by lights. In future works, a negatoscope is going to be used for the visualization. The first tests were performed using a webcam but the results were not satisfactory, as the bubbles are too fast to be captured with the frame rate of a webcam. With a digital camera the results are more concluding. A program is then used to compute the surface and volume of the air bubbles. Those datas are used to compute the volume fraction of air in the water and so, the separation efficiency. Figure 2 shows the test cell and Figure 3 a picture obtained from this cell.

Fig. 2 The visualization cell.

III. Vortex test bench

At this stage of the study, the performance of the rotating separator are very good, but in non-stationary phases, one of the exit can have a large increase in the air or oil flow. Also, it can appear in future developments that one of the outlets of the rotating separator is not efficient enough. Therefore it is interesting to see the performance of a separator that would be located after the rotating separator. At this stage of the study, the separator is a, well known, vortex separator. A vortex separator works in a very simple way: the centrifugal forces acting because of the tangential inlet separate the water and the air [6]. The air goes in a counter-vortex flow through the vent located at the top of the separator, while the water leaves through the lower exit and falls into the oil tank. This separator is cylindrical with a tangential inlet of 50mm and made of plexiglass. The exit is composed of gaps located all around the bottom of the separator. An interesting point of this prototype is that we can change the length of the vent tube and the length of the cylindrical separation room, as it is well known that those two parameters are of big importance in the performance of the separator [6] [7].

A. Adaptation of the test bench

With the available theoretical models, it is difficult to estimate in a quick way performance of a vortex separator if it does not fit into the scope of the empirical correlations developed for other vortex separators. The Bart, Muschelknautz, Meissner and Loffler , ... models, which are compared in [8], are not easily connected to the reality of gas-liquid flows for which you do not exactly know the kind and size of the air bubbles (stratified flow, bubbly flow, ... [9]).

CFD simulations, already performed on two-phase flow vortex separators ([10] [11]) are also not easy. This is why we decided to, at first, perform experimental tests that would be the fastest way to get results, as we had an already built vortex separator and the test bench of the rotating separator. This vortex separator is designed for much higher water and air flows than the rotating separator. Therefore, a pump going up to $180\frac{m^3}{h}$ and installed next to the rotating separator test bench is used. The same air compressor is used, but as it is limited to 10 bars, we

can only provide the desired air flow during short periods of time. This makes the test campaign challenging, as everything has to be done quickly. This is made easier by the Labview program that gets all the entrance data's like the pressure, the flow, the temperature, ... automatically. The outlet of the water tank is then redirected to a plexiglas tube where we can see if there are still some air droplets left. A view of the vortex separator, its tank and a part of the test bench is showed on Figure 4.

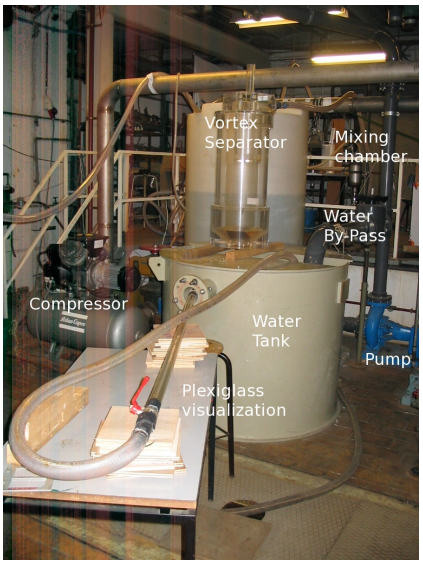

Fig. 4 The vortex separator test bench.

B. *First results*

Previous results showed that the separator, for an air-water ratio of $3,9$ and with an inlet of $50mm$, has $99,9\%$ of the air leaving the separator through the vent tube. The $\frac{air}{water}$ ratio at the tank outlet is about $0,061$. So it is a very good way to separate a flow at that ratio.

Measurements in multiphase flow are not an easy matter. One could use settling techniques as an easy way to measure how much air there is at the water outlet of the separator. But, this is not easily implemented in our separator, as there are not enough air droplets in the flow to see a decrease of the water level in the settling vessel. The test results mentioned earlier were possible by filling the settling vessel during 50 minutes. In our installation we can only provide the desired air flow during 1 minute, so this technique is not really appliable. This is one of the reasons why the visualization technique is currently studied at the ATM department.

The visualization cell has to be adapted to be used in this case, as the flow is quite different in speed and quantity. For those reason, we used a visual check of the tank outlet and, for the first tests, the flow goes through a plexiglas tube where we can see the air droplets. The air-water flow is coming from the rotating separator previously discussed. This means that it is plugged on one of the rotating separator outlets and that it will receive a lot of air, or a lot of water. The goal of those tests is thus to see how the vortex separator reacts with low and high ratios.

While the separator's tank is being filled, the test bench goes through a non-stationary state were a lot of air is expulsed through the outlet, as can be seen on Figure 5. Once

Fig. 5 Plexiglass visualization during the start of the tests.

a stationary state is achieved, visual checks at the plexiglass tube show a good separation during a couple of seconds. There are only a few, and very small, air bubbles leaving through the exit. After this short period of time, a vortex is created in the water remaining in the tank, as can be seen on Figure 6. This vortex is responsible of an important increase of the air flow at the water outlet. The air comes straight from the free surface of the water in the tank, to the exit, through the center of the vortex tube. An improvement for the next test sessions would consist in the installation of a plate above the outlet, to prevent the apparition of this vortex.

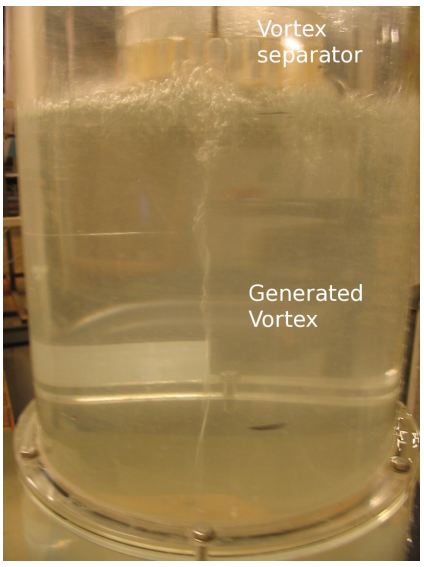

Fig. 6 The vortex created in the separator tank.

IV. Other technologies

THE cyclone, or vortex separator, presents a good separation efficiency and is used in a lot of applications. Nevertheless, its geometry complicates the integration in a closed volume, like an engine oil tank. In terms of fabrication and machining facility, it can be interesting to explore which other technology can realize the same separation function between liquid and gas. Especially, we are interested in a non-moving structure that realizes the separation quickly and in a minimum space requirement.

If we look through the literature, information can be found in different sectors as petroleum, nuclear, automobile, etc. [12]. The natural gas buoyancy can be exploited by increasing residence time allowing gas to escape the mixture [13]. This is the principle of settling tank used in petroleum industry [14]. Besides, at high temperature, decrease of liquid viscosity, convection forces and gas bubbles expansion enhance gas buoyancy. Separation is then promoted. However, introduction of residence time used in this way would lead to a growth of the volume requirements for the oil tank. Another solution to promote gas buoyancy is the use of baffles [15]. Different kinds of baffles are found in the literature: horizontal, vertical, curved. The horizontal baffles create a funnelled path for the incoming flow; this one is then slowed down and gas bubbles can rise up by buoyancy. In general, the end of the baffle is immersed into the tank to avoid re-mixture [15]. In the same idea, the vertical baffles decelerate and spread the incoming gas-liquid mixture to let the gas escape via buoyancy [15]. Curved plates, as shown in Figure 7, are called momentum breaker devices [16]. The multiphase fluid entering in the tank is then rudely slowed down and separation occurs : gas with liquid drops goes in the upper part and liquid is diverted in the lower part of the tank [13].

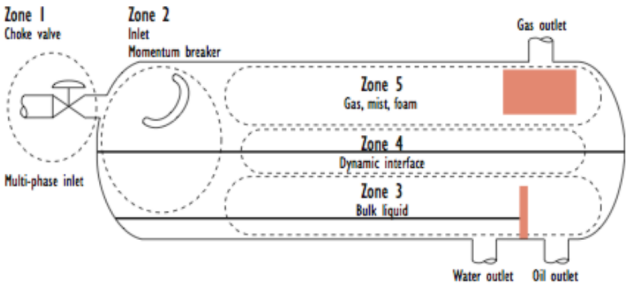

Fig. 7 Horizontal Vessel Separator [17].

In the petroleum industry, other configurations can be employed, as shown in Figure 8 taken from [18]. It can be seen that a vertical baffle is used as an inlet diverter. This one is placed just in front of the inlet section: it deflects the incoming flow and diffuses its momentum to favour gas/liquid separation. After that, a horizontal degassing baffle provides separation between gas stream and liquid volume. This baffle avoids re-mixture by protecting the liquid surface from disturbance in the inlet section and gives a supplementary residence time for the separation of gas bubbles by buoyancy [18].

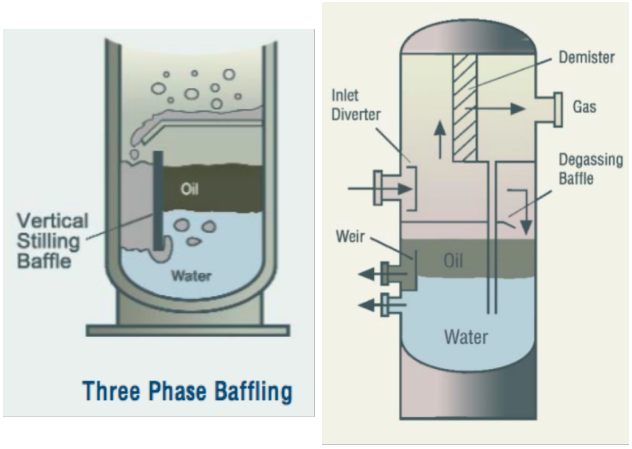

Fig. 8 Vertical Crossflow Separator [18].

The employed technology depends of the ratio between the gas and liquid volumes. The previous technologies concern liquid flow containing gas bubbles, but in a lot of applications there are also gas flows with a low quantity of liquid [19]. This kind of flow can be the separated gas entraining removal liquid droplets. Typically, for those flows, a demister is used [20]. It consists on a coalescer media, for example a suite of undulating plates (see Figure 9), which deflect the air flow path and hold back the liquid droplets, due to their higher density. By coalescence effect, this mesh type structure transforms the mist into bigger droplets that go down with gravity [21]. For bubbles smaller than 15 µm, metal foam or fibreglass can also be used as coalescer media [21]. The crossing velocity of the flow characterizes the separation efficiency and is limited by the re-circulation of bubbles after coalescence [21].

Fig. 9 Coalescing Media [18].

V. Numerical Simulations

TWO-PHASE flow simulations are a topic in development, with the aim of representing in a more realistic way the complex forces interacting between liquid and gas molecules. As briefly shown before, multiphase flows are present in many engineering devices. The design of these devices is enhanced by the prediction of some flow characteristics using numerical simulations [22]. In the separation context, simulations would help to gain a better understanding of the hydrodynamic interactions between the bubbles and the separation devices presented previously. The CFD computation will be performed with the CFD software Fluent/Ansys.

We present the main equations describing the fluid movement and bubbles definition, as used in CFD software tools. We consider an incompressible fluid flow, which is completely filled with a substance of one phase (liquid) and the other phase (gas) is only available as bubbles. They are called progressive interface flows and the methods explained here to model the interface deformation are called interface capturing [23]. These methods can also be used to represent stratified, slug and plug flows, and other interaction phenomenon as fragmentation and coalescence [24]. They are limited to the prediction of interface which scale is larger than the mesh resolution. An example of computations by Level Set method can be seen on Figure 10.

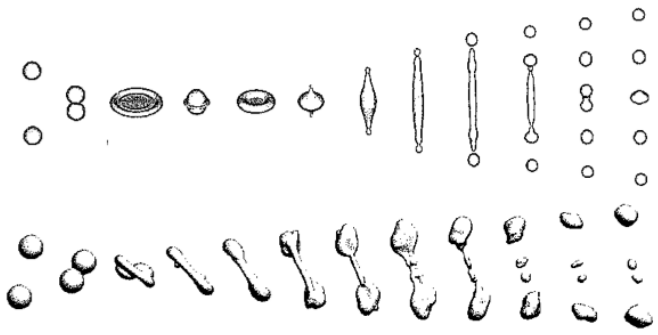

Fig. 10 Example of computation by Level Set method - bubbles collision [24].

We will focus on problems with fixed mesh and more particularly on purely eulerian methods of front capturing that constitute the Volume of Fluid method and the Level Set method. We do not consider neither heat transfer nor phase change.

In both cases, the velocity field computation of two-phase flows is performed by numerical solution of only one Navier Stokes equation (1) associated to a continuity equation (2) to describe the fluid movement [24]:

$$\rho\left(\frac{\delta u_i}{\delta t}+u_j\frac{\delta u_i}{\delta x_j}\right)=-\frac{\delta p}{\delta x_i}+\frac{\delta}{\delta x_j}\left(\mu\left(\frac{\delta u_i}{\delta x_j}+\frac{\delta u_j}{\delta x_i}\right)\right)+f_{\gamma,i}+\rho g_i \tag{1}$$

$$\frac{\delta u_j}{\delta x_j}=0 \tag{2}$$

where u is the velocity field, p the static pressure, and $f_{\gamma,i}$ is an equivalent force representing the surface tension forces.

To perform the interface capturing with the volume of fluid method, a scalar variable function $\psi(x,t)$ represents the volume fraction of one phase in the mesh. It is defined by the resolution of its advection equation (3) in the velocity field calculated by equations (1) and (2) [24].

$$\frac{\delta\psi}{\delta t}+u_j\frac{\delta\psi}{\delta x_j}=0 \tag{3}$$

The physical characteristics of the fluid ρ and μ are localized and instantaneous variables that can be expressed by an average of each phase characteristic, weighted by the volume fraction of the two fluids [24]. The volume fraction computed could be seen as an average presence rate in each cell: cells with volume fraction equal to 1 or 0 are only full of one phase, and the other cells are cut by the numeric interface [24]. An interface reconstruction method is then used, based on this volume fraction and on the normal to the interface linked to the volume fraction field. The VOF method presents a good mass conservation [24].

The Level Set method also involves a scalar variable $\psi(x,t)$ which is called level set function, which is continuous and continuously derivable [24]. This function has no real physical representation; its transport is governed by the advection equation 3 and the function is chosen in a way that the surface $\psi(x,t)=0$ is the interface. It could for example be a signed distance to the interface [23]. Thus, this method does not need an interface reconstruction. Another advantage is the easy determination of the derivatives but the mass conservation is not always performed when the bubble boundaries are strongly twisted [24].

VI. Conclusions and Future Works

THIS paper has treated the topic of multiphase flows and, in particular, the gas-liquid separation technologies. Nowadays, the most encoutered separation device is the cyclone separator. Its separation is quite efficient but in some cases, like in aircraft oil tanks, they present some difficulties of integration in a small and closed volume, that leads to an increase of cost production. The main concern of this paper was to indentify and present alternatives to this classical separator.

A first explored device is a rotating separator that groups the pumping and separating functions. This prototype is already well elaborated and the first tests showed a good efficiency in liquid quality but improvements have still to be done for the air outlet. In this context, the cyclone separator has thus been tested with flow rates and gas/liquid ratios conditions similar to those at the outlet of the rotating separator. In this unusual gas/liquid ratio, we shall see if the separation function is as efficient as in normal conditions. The first test results showed that the cyclone separator seems to be a viable solution, but the test sequence has still to be improved. The point was also made on measurement techniques, as our air flow rate doesn't allow to use the simple settling techniques, and the first results of a visualization measurement method were presented.

This paper also focused on more simple separation technologies as plates and baffles and some solutions were presented. The first steps of numerical simulation were also presented in the paper. Indeed, they will help to get a better understanding of the interaction between bubbles and the separator structure.

In future works, the challenge will be to find out if such devices can deliver performance that are as good as the ones of the cyclone separator. This design research will be done with the help of test benches but also with numerical simulations. An another part of the work will look for improvement or a more fundamental re-degisn of the vortex separator to look out if it can replace the separation function of the rotating separator.

REFERENCES

[1] G.E. Kouba, O. Shoham, and S. Shirazi,, "Design and performance of gas liquid cylindrical cyclone separators", in *7th International Conference on Multiphase Production*, pp. 307-327, Cannes, France, 1995.

[2] J. J. Brunsmann, J. Cornelissen and H. Eiler, "Improved Oil Separation in Gravity Separators", in *Journal of Water Pollution Control Federation*, Vol. 24, No. 1, pp. 44-55, January 1962.

[3] V. Dostal and M. Takahashia, "Modeling and optimization of steam dryer for removal of lead-bismuth droplets ", in *Progress in Nuclear Energy* Volume 50, Issues 2-6, pp. 631-637 March-August 2008.

[4] D. Bizzarri and P. Hendrick, Ngendakumana P. and G. Heyen "Experimental Study Of An In-flight Air Separation Device, in *13th AIAA International Conference on Space Planes and Hypersonic Systems and Technologies*, Capua, Italy, 16-20 May 2005.

[5] A. Linke-Diesinger, *Systems of Commercial Turbofan Engines*, Springer Berlin Heidelberg, 2008.

[6] A.C. Hoffmann an L.E. Stein, *Gas Cyclones and Swirl Tubes: Principles, Design, and Operation*, 2nd ed., Springer-Verlag Berlin, 2008.

[7] L. Wang, *Theoretical Study of Cyclone Design*, PhD Thesis, Texas A&M University, Tulsa, Texas, 2004.

[8] C. Cortés and A. Gil "Modeling the gas and particle flow inside cyclone separators", in *Progress in Energy and Combustion Science*, Issue 33, pp. 409-452, 2007.

[9] C.E. Brennen, *Fundamentals of Multiphase Flow* Cambridge University Press, 2005.

[10] S. M. Mousavian and A. F. Naja, *Numerical simulations of gas-liquid-solid ows in a hydrocyclone separator*, Springer-Verlag, 2008.

[11] A. Mainza, M. Narasimha, M.S. Powell, P.N. Holtham and M. Brennan , Study of ow behaviour in a three-product cyclone using computational uid dynamics, in *Minerals Engineering* Volume 19, Issue 10, pp. 1048-1058, August 2006.

[12] Sogefi Filter Division, *La sparation des gaz de Blow-By*, www.sogefifilterdivision.com/site/docs_wsw/RUB_10182/gaz-carter-2008.pdf, 2009.

[13] E. Hansen, "Separation offshore survey - Design/Redesign of Gravity Sparators'", in *Exploration and production: the oil and gas review*. 2006

[14] A.F. Sayda and J. H. Taylor, Modeling and control of three-phase gravity separators in oil production facilities, in *n Proc. American Control Conference*, New York 11-13 July 2007.

[15] D.J. Aslin, Eaton Copr., "Monitoring bearing and gear failures in aircraft gas turbine engines, part 2 : Removing air and wear debris particles from the scavenge lube mixture'", in *Sensors Magazine*, November 2001.

[16] J. L. Tapias, *Pipe separator and T junctions'*, PhD Thesis, Cranfield University, Cranfield, England, United Kingdom, 2007.

[17] FMC Technologies, "Subsea system'", http://www.fmctechnologies.com/ 2009.

[18] Natco Group Technologies, http://www.natcogroup.com/, 2009.

[19] E. Schmidt, "Dust Separation", in *Ullmann's Encyclopedia of industrial chemisty* Januaray 2008.

[20] T. Austrheim, *Experimental Characterization of High-Pressure Natural Gas Scrubbers*, PhD Thesis, University of Bergen, Bergen, Norway, 2006.

[21] P.F.R. Cusack, P. Hennessey and M. Neuman, "Demystifying the selection of mist eliminators", in *Chemical Engineering* Nov-Dec 1993.

[22] A.N. Kochevsky, *Possibilities of Simulation of Fluid Flows using the Modern CFD Software Tools*, Sumy State University, Sumy, Ukraine, September 2004.

[23] E. Marchandise, *Simulation of three-dimensional two-phase flows: coupling of stabilized finite element method with a discontinuous level set approach*, PhD Thesis, Universit Catholique de Louvain, Belgium, December 2006.

[24] B. Oesterlé, *Ecoulements multiphasiques: des fondements aux méthodes d'ingnierie*, Lavoisier, Paris, 2006.

Proceedings of the 8th National Congress
on Theoretical and Applied Mechanics,
May 28-29, Brussels, Belgium.

Wind tunnel investigation of the stall flutter oscillations of a bridge deck

T. Andrianne[1], G. Dimitriadis[2]
[1,2]Department of Aerospace and Mechanical Engineering, University of Liège
Chemin des chevreuils 1, 4000 Liège – Belgium
email: t.andrianne@ulg.ac.be, gdimitriadis@ulg.ac.be

Abstract: ***Torsional Stall Flutter (TSF) is a one degree of freedom, self-excited phenomenon induced by the periodic separation/re-attachment of the flow around a body. The present paper proposes an experimental investigation of TSF on a bridge deck. A section model free to oscillate in torsion is tested in a low-speed wind tunnel. Static and dynamic tests are performed to enable a complete interpretation of the phenomena involved. For low airspeeds, the Karman vortex shedding excites the structure, resulting in small oscillations at the vortex shedding frequency. For high airspeeds, the deck undergoes Limit Cycle Oscillations (LCO) due to the TSF phenomenon. Nevertheless the Karman vortex shedding excitation is still present and appears in the measured forces signals. Peaks and troughs in the lift coefficient are detected for each pitching period. They are interpreted as the separation/re-attachment of the flow around the deck. The large amplitudes motion of the deck undergoing TSF reduces the amplitude of the aerodynamic lift coefficient.***

Keywords: **Nonlinear Aeroelasticty, Stall flutter, Bridge**

I. Introduction

Civil engineering structures, especially bridge decks have received particular attention concerning their aerodynamic and aeroelastic behavior since technological progress led to slender and flexible structures [1], [2].

Even though modern bridge decks are becoming more and more streamlined, the flow field remains separated around most of the deck surface, even at zero angle of attack of the wind on the structure. Therefore, bridge decks are considered as bluff bodies from the aerodynamic point of view. Add-ons, such as security railings and wind shields, placed on the upper side of the deck prevent any type of attached flow over it [3].

The complex behavior of the separated airflow around a body creates fluid-structure interactions that can lead to nonlinear aeroelastic phenomena.

Generally the aeroelastic effects taken into account in bridge engineering are classified in three main categories [1]:

- Vortex-shedding;
- Galloping: Including Across wind galloping and Wake galloping;
- Flutter;

The Flutter class can be further subdivided into: classical two degree of freedom flutter, torsional flutter (with attached flow), panel flutter (typically applied to bridge elements) and single degree of freedom flutter. The latter type treats detached flows for vertical flexion and torsion degrees of freedom.

The present work proposes an experimental analysis of the one-degree of freedom stall flutter applied to a generic bridge deck. The torsional degree of freedom is analyzed and the aeronautical term Torsional Stall Flutter (TSF) is used to describe the phenomenon.

Two types of tests have been carried out: static and dynamic. The combination of the static and dynamic tests results allowed the study of the TSF phenomenon in isolation from the other aeroelastic effects. The main characteristics of TSF are highlighted through the analysis of the motion of the deck (torsional frequencies and amplitudes) and through the aerodynamic forces induced by the oscillating stalled flow field around the body.

II. Stall Flutter Phenomenon

Stall flutter is a motion-dependant phenomenon, characterized by flow separation and reattachment over the surface of the body at least once during an oscillation period. This complex flow field is responsible for large variations of the aerodynamic loading acting on the structure. The interaction between this aerodynamic loading and the restoring forces of the structure leads to self-excited motions such as Limit Cycle Oscillations (LCO).

The resulting LCO is a non-linear motion characterized by its oscillation frequency and amplitude. Different types of LCOs may exist because of the non-symmetric shape of the bridge's deck and its sharp angles. The source of non-linearity in the TSF phenomenon is aerodynamic only.

Investigations of stall flutter started in the early 1950's for propeller blades [4], [5]. Further analyses were carried out on compressor blades of gas turbines and on helicopter blades [6]. Stall flutter has also been investigated for space reentry vehicles, [7] and wind turbines, [8].

Torsional stall flutter has long been associated with dynamic stall. Dynamic stall is defined as the abrupt loss of lift and pitching moment acting on a body undergoing imposed high amplitude oscillations, following the shedding of a powerful vortex at the leading edge. Torsional stall flutter is a self-excited oscillation caused by the interaction of the dynamic stall phenomenon with a flexible structure that has at least a torsional degree of freedom.

Recently, experimental studies of airfoils by Li and Dimitriadis [9] identified two types of motion induced by Torsional Stall Flutter on a symmetric wing section: symmetric LCOs and asymmetric LCOs. Symmetric LCOs

were caused by a classical TSF mechanism whereas asymmetric LCOs were the result of the interaction of static torsional divergence with dynamic stall. Experimental investigations by Poirel [10] studied the effect of the Reynolds number on a pitching airfoil. Interesting observations are made about the type of flow separation that can cause the wing oscillations.

An analytical study of the stall flutter phenomenon was undertaken by Sarkar and Bijl [11] among others. In their work they use a semi-empirical model of the aerodynamic forces during stall, developed experimentally by Onera [12].

Furthermore, vortex particle methods have been used to simulate detached flows around moving bodies by a number of researchers (e.g. Spalart [13]). These 2D models, linked to a structural model render possible the investigation of simple 2D bodies undergoing TSF. This method was recently implemented for the study of bridge decks by Taylor and Vezza [14].

III. Experimental set-up

The present experiments were carried out in the wind tunnel of University of Liège. This atmospheric wind tunnel can reach airspeeds up to 65m/s in closed loop configuration. The rectangular test section measures 1.8m in width by 1.5m in height. The level of turbulence of the incoming air is below 0.5%. All tests were carried out without adding turbulence in the oncoming flow field.

A. Bridge model and supporting system

A generic bridge is studied in the present work (**Fig. 1**). It is composed of a trapezoidal beam supporting the traffic deck. Wind screens are added to both sides of the bridge. The equivalent porosity of these screens is 42%.

The model is a section type model. It is 0.317m wide by 1.2m long, fitted with end-plates to approximate two-dimensional flow around the structure (**Fig. 2**).

The section model is supported by a structure allowing static and dynamic tests. The structure was designed following the principle developed by Sarkar [15]. An aluminum axis passes through the plane of symmetry of the bridge deck, supported by two bearings. The center of this axis lies 2.7cm below the upper surface.

Static tests were performed using force and torque sensors. The model was statically restrained and lift, drag and pitching moment were measured.

The dynamic tests were performed by allowing a pitch degree of freedom, restrained by springs. The supporting system allows heave, in-plane and pitch motion. In the present work, only the motion of the pitch degree of freedom was free.

The pitch restoring force was provided by two extension springs and a lever arm clamped to the pitch axis of the deck. Two lever arms of different lengths were used (0.39m and 0.50m). The corresponding identified modal parameters were:

- Low Stiffness (LS) case: 2.12 Hz / 1.6%
- Higher Stiffness (HS) case: 2.70 Hz / 1.8%

The polar moment of inertia of the bridge deck around the pitch axis is 0.15kgm^2/m.

B. Measurements

Forces and torques measurements of the airflow on the structure were performed using traction/compression sensors and a torque sensor. Force and moment response signals were recorded for periods of 10 seconds. Motion measurements were carried out using PCB accelerometers with an operating frequency range from 0 to 300Hz and an acceleration range from 0 to 20g. Airflow measurements were performed using a one-component hotwire probe. For all measurements, the acquisition rate was set to 1kHz.

IV. Results

A. Static results

The aerodynamic coefficients of lift, drag and pitching moment were measured for angles of attack varying between -14° and +30°. The airflow velocity was set to 20m/s for each angle of attack. The pitching moment was defined positive nose up.

Fig. 3 presents the variation of C_L, C_D and C_M with the angle of attack. The slope of the curve of C_L is positive up to and angle of attack of 5°. From 5° to 16°, it is negative and the value of C_L abruptly falls from 0.5 to 0 for higher angles of attack. From 20° to 30°, the lift coefficient increases slightly to positive values.

The drag coefficient C_D has a maximum value of 0.58 for an angle of attack of 14°. The C_D is relatively flat; to a first approximation it could be said that C_D remains unaffected by the angle of attack.

The pitch coefficient C_M increases from -14° to 0° but remains approximately constant from 0° to 30°.

B. Strouhal identification

The Strouhal number was measured at several angles of attack of the deck. The deck was fixed in the flow field and a hotwire probe was placed one chord downstream of the trailing edge. The probe measured the variation of the streamwise component of the velocity. The measured signal was further analyzed in the frequency domain to identify periodic phenomena in the wake of the static deck. The wind tunnel airflow velocity was set to 23m/s for each angle of attack.

Fig. 4 presents the variation of the Strouhal number for angles of attack varying between -10° and +10°. The difference between the Strouhal numbers at -10° and 10° reaches 24%. It can be explained by the modification of geometry, impacting the behavior of the flow around the deck, which in turn affects the vortex shedding process.

The definition of the Strouhal number ($St = f\,D\,/\,U$) gives an estimation of the shedding frequencies for different airspeeds. This estimation considers that the effect of the Reynolds number on the Strouhal number is weak. This assumption is realistic for bluff-bodies with sharp edges, especially in the narrow Reynolds number range considered in this study (1.2e10^5 to 4e10^5).

The estimation of these frequencies will be used further to explain observations made in the pitch response signals measured during the dynamic tests.

C. Dynamic results

The dynamic experiments comprised two main aspects. First the effect of the stiffness was studied by measuring the pitch motion of the deck only at various airspeeds. Then, for the lower stiffness set-up, the motion and the aerodynamic forces acting on the deck were measured simultaneously and analyzed.

The rotation of the deck around its pitch axis was measured by accelerometers. As a consequence the centre of the oscillations, i.e. the pitch angle around which the oscillations were centered could not be measured: accelerometers cannot measure static deflections. Nevertheless, it was possible to estimate the oscillation centers by equating the restoring forces of the springs and the static aerodynamic torques, using the static results of section A. The results presented in the following section take into account this estimated static deflection. The initial angle of attack of the bridge deck relative to the incoming horizontal airflow was set to zero for all the tests.

Fig. 5 presents the maxima and minima of the pitch oscillations of the deck with the lowest stiffness for several airflow velocities. The airspeed was initially 0m/s, increased to 19.1m/s, reduced to 6m/s and finally again increased to 19.1m/s.

From 0m/s to 13.4m/s (A to C in **Fig. 5**), very small oscillations around the static angle of deflection were observed. This static angle was 4.5° at 13.4m/s. When the airspeed reached 14.7m/s (point D), the deck suddenly started a large oscillating pitch motion between -5° and +15° around an equilibrium position of +5°. The airspeed was subsequently increased up to 19.1m/s (point E) while the oscillation amplitudes remained approximately constant around the corresponding static deflection angles. The airspeed was then reduced from 19.1m/s to 6.8m/s (point E to G) and the amplitude of oscillation did not change significantly. When the airspeed was set to 6.3m/s the deck suddenly stopped its large amplitude motion (point B). The airspeed was again increased and only small amplitudes were observed up to point H. When airspeed reached 12.8m/s (point I), the deck suddenly started to oscillate as described above at point D. While the amplitudes of oscillation recorded during the two occurrences of the phenomenon were very similar, the pitch oscillation onset airspeed was different, i.e. 14.7m/s the first time and 12.8m/s the second. It can be concluded that the onset mechanism for these oscillations is quite complex.

Branch ABC is a decaying motion branch. The static deflection is due to the static aerodynamic pitching moment. Having said that, the motion on this branch features a small amplitude motion whose origins are presented in the following section.

Branches GFE and G'F'E' are stable LCOs. This self-excited motion is due to the dynamic stall phenomenon occurring when the pitching angle reaches large values. For the maximal airspeed imposed in the wind tunnel, the deck oscillates between E and E' in a motion centered around a positive pitch value. For lower airspeeds the oscillation are centered around a smaller pitch angle and the LCO is nearly symmetric around the zero pitch axis.

Fig. 6 shows clearly that at airspeeds between 6 and 14m/s two types of motion are possible: decaying response or LCO. The motion that the structure will follow depends on the initial conditions. As the pitch angle is increased from 0^o, the response levels are very low and the bridge remains on the decaying response motion (plot (a) in **Fig. 6**). When a particular value of the airspeed is reached (a bifurcation airspeed, around 13-14m/s), the motion suddenly switches to LCO (plot (b) in **Fig. 6**). Then, as the airspeed is decreased, the structure is already on the LCO branch and therefore remains on it (plot (c) in **Fig. 6**) until a secondary bifurcation airspeed of 6m/s is reached, at which point the response reverts to decaying (plot (d) in **Fig. 6**).

Nonlinear dynamics theory requires that the stable LCO branch and the stable decaying motion branch must be separated by a branch of unstable LCOs. This unstable branch links point C and H to G and G' and causes the dependence on initial conditions and the hysteretic behavior of the pitch oscillation amplitude. This branch was not identified experimentally during the wind tunnel tests described here; this identification will be undertaken in the course of future experiments.

1) Effect of the pitch stiffness

The pitch oscillation behavior of the high stiffness set-up is qualitatively equivalent to the low stiffness set-up. Both amplitude results are presented in **Fig. 7**. At point A, the airspeed was 6m/s and the deck oscillated very weakly around the static angle for each stiffness set-up. When the airspeed exceeded point B, the low stiffness set-up started suddenly a large oscillation motion, as described above. For this airspeed, the high stiffness set-up was still at rest and no motion was observed. When the airspeed was further increased (exceeding point B') the high stiffness deck started to oscillate between -15° and 20°. This behavior was reasonable, since the restoring torque applied by the springs was higher and more energy was needed to destabilize the system.

Nevertheless the amplitude of oscillation of the high stiffness set-up is higher than that of the low stiffness set-up. This observation has not been explained yet.

Fig. 8 shows the evolution of the frequency of the LCO motion of the deck with airspeed. Both stiffness set-ups are presented. It can be observed that the frequencies match the natural frequencies of the pitch degree of freedom for each stiffness set-up and are rather constant with airspeed.

2) Aerodynamic forces and motion of the deck

The variations of the lift and drag forces were measured simultaneously with the pitch response of the bridge deck for the low stiffness set-up. The main drawback of equipment used for these simultaneous measurements was the need to use pneumatic bushes to allow stiction-free force measurement. These bushes induce a certain amount of flexibility in the structure, resulting in a small degree of freedom in heave. This low amplitude motion was not measured. It should be mentioned that the aerodynamic pitching moment around the pitch axis could not be measured since the pitch degree of freedom was set free.

Fig. 9 presents the maximal and minimal oscillating pitch values measured for this set-up. Three points corresponding to

three airspeeds and behaviors of the deck are selected and analyzed below.

Point A represents a decaying motion condition. The pitching oscillations around the static equilibrium pitch angle (1.5°) are small as shown by the black curve in **Fig. 10**. Nevertheless high variations of lift and drag coefficients are observed for this airspeed. The upper plot in **Fig. 10** represents 3 seconds of measurement of the pitching angle, lift and drag coefficients. The aerodynamic coefficients are multiplied by 10 to fit on the same plot with the pitching angle. One can observe a beating phenomenon without periodicity. The lower plot of **Fig. 10** is a zoom on a section of the upper one, showing the obvious in-phase variations of lift and drag coefficients. The main frequency component in the lift and drag signals is 14.0Hz. This frequency is far from the natural frequency in pitch of the system (2.12Hz). The excitation responsible for these forces variations is aerodynamic but different from the stall flutter phenomenon observed in the previous sections. The structure is excited by the periodic ejection of vortices in the wake and around the deck section. The Strouhal number was measured to be 0.16 for zero angle of attack of the deck (see **Fig. 4**). According to the definition of the Strouhal number, one can estimate the frequency of vortex shedding. Using a characteristic cross-dimension (D) of 0.1m and the airspeed at point A, 9.7m/s, one finds an estimated frequency of 15.5Hz. It can be conclude that oscillations of the aerodynamic forces are due to the shedding of small vortices behind the bridge deck; these oscillatory aerodynamic forces result in very low amplitude oscillations of the bridge in bridge. It can be theorized that this low amplitude bridge motion is due to the damping of the structure and to the low energy level of the small vortices shed in the flow field.

Point B sits on the stable LCO characterized by pitch angles varying between -7° and 15° at an airspeed of 12.5m/s. The upper plot of **Fig. 11** presents 3 seconds of measurement of the pitch angle, lift and drag coefficients (multiplied by 10). The pitching frequency is 2.1Hz, equal to the natural frequency of the pitch degree of freedom of the deck. The lift and drag signals contain two frequency components, one at the pitch oscillation frequency and one at the vortex shedding frequency. It is interesting to note that the lift and drag signals are not totally repeatable, each cycle is slightly different, although the main frequency components are the same. In order to observe the average the aerodynamic forces in a more deterministic manner, the lift and drag signals were period-averaged, based on the period of the pitch oscillations. These period-averaged signals are presented in the lower plot of **Fig. 11**.

The first important observation is the presence of global peaks in the signals of C_L and C_D during the upstroke motion of the deck, before the maximal pitching angle. Both C_L and C_D decrease abruptly to their minimum values when the pitching angle reaches its maximum. During the down stroke motion the aerodynamic coefficients increase to stabilized values and the phenomenon repeats itself at the next pitching cycle. This high amplitude motion at the pitch oscillation frequency is characteristic of TSF. The time-delay between the displacement and the forces acting on the structure is due to the complexity of the stall and re-attachment processes. This complexity can also explain the low repeatability of the measured force signals.

Second observation concerns the frequency content of the aerodynamic signals. The upper plot of **Fig. 11** shows the periodic sequence of peaks and troughs repeated for each pitching oscillation. It also shows a higher frequency component in the signals. The corresponding frequency is 14.1Hz and it can be attributed to the vortex shedding phenomenon, as explained for point A. Using the definition of the Strouhal number to estimate the frequency of vortex shedding leads to 20Hz when considering St = 0.16 corresponding to the zero angle of attack. But the deck is pitching between -10° and 15° and the Strouhal definition may provide a rough estimation of the range of frequencies of vortex shedding. From the available data, the Strouhal numbers for -10° and 15° are 0.16 and 0.11 respectively. The frequencies range spreads then from 13.7Hz to 20Hz, which includes the 14.1Hz frequency component observed in the aerodynamic force signals.

Point C sits on the stable LCO where the deck oscillates between -12° and 14°. The corresponding airspeed is 7m/s. The pitching frequency is 2.1Hz, identical to the pitching frequency at point B. The shape of the aerodynamic coefficients signals is similar to the shape obtained at B, but peaks and troughs do not occur at the same time. Peaks of C_L and C_D occur just before the maximal pitching angle while troughs occur just after the maximal pitching angle.

The amplitudes of oscillation of C_L and C_D around their central values are the same for points B and C. The aerodynamic coefficients varying with time can be linked to the measured instantaneous pitching angles. The classical representation of the lift coefficient versus angle of attack of the structure is presented in **Fig. 13**. It shows the static lift coefficient identified in the first part of the study and the dynamic lift coefficients from the bridge deck free to pitch.

Concerning the dynamic lift coefficients, the decaying and very small amplitudes oscillations (decaying motion branches) are plotted with red circles. Each circle corresponds to one airspeed value between 6m/s and 10m/s. In this range of airspeeds the effect of the Reynolds number is weak as it can be observed on the figure. Recall that for sharp-edged bluff bodies, the effect of the Reynolds number on the aerodynamic coefficients is not predominant since the behavior of the boundary layer is dictated by the sharp geometry of the body. The corresponding mean angle of attack is 1.7° and the mean lift coefficient is 0.76. These values fit well with the C_L curve indentified during static experiments.

The lift coefficients measured during large amplitude LCO motions are plotted in black in **Fig. 13**, for one selected airspeed corresponding to point B from **Fig. 9** (v = 12.5m/s). The period-averaged oscillating lift coefficient measured at this condition is plotted against pitch angle. It can be seen that the dynamic lift oscillation occurs around the static lift coefficient curve. The maximal and minimal values of the dynamic C_L are 2.1 and -1.2 respectively. This represents a ratio of 2.7 between the dynamic and static maximum lift coefficient. This order of magnitude between the dynamic and the static maximum C_L has often been reported for airfoil experiencing stall flutter [16].

The maximum amplitudes of the lift coefficients of points A, B and C of **Fig. 9** are comparable. These coefficients vary

between -2.5 and 3 for the three points. Nevertheless the lift coefficient signals of points B and C have an additional frequency component corresponding to the pitching oscillation of the deck. This results in an attenuation of the lift coefficients, transforming the periodic signal of point A (**Fig. 10**) to signals like those recorded at points B and C (**Fig. 11** and **Fig. 12**) where the maximum and minimum amplitudes are only reached near peaks and troughs of the pitch oscillation. These maxima and minima are separated by a lower amplitude, higher frequency oscillation component. This component is characterized by a frequency around 15Hz and, for example, lift coefficient oscillation amplitudes around 2. The co-existence of these two frequency components demonstrates the difference between the TSF oscillations of streamlined and bluff bodies. For streamlined bodies, such as wings and wing sections, the airflow is completely attached over part of the TSF cycle. Dynamic stall occurs as a result of the shedding of a large vortex at the leading edge, once or twice per cycle (depending on whether the oscillations are symmetric or asymmetric), [17].

On this bridge structure, the boundary layer is never fully attached. Even when the bridge is kept static, there are large areas of separation and the flow around the bridge oscillates, shedding vortices into the wake. Once the TSF oscillations begin, the shedding of vortices continues at roughly the same non-dimensional frequency (Strouhal number). The difference is that now some of the vortices shed during a cycle are much stronger than others. The strongest vortex is shed just before the maximum pitch angle is reached. This vortex is the bluff body equivalent of the leading edge vortex that causes dynamic stall in airfoil sections. It is suspected that part of the energy of all the other vortices shed over a cycle is absorbed by this dominant vortex. Flow visualization experiments are required in order to confirm this assertion.

V. Conclusions

This paper investigates experimentally the behavior of a bridge deck free to oscillate in pitch. The objective is to study the TSF phenomenon that occurs due to the complex interaction between the stalled flow field and the pitch motion of the deck.

The analysis of the motion of the deck revealed the existence of both decaying and LCO motions. Decaying motion is observed for low airspeeds when the deck starts initially from rest. It can be accompanied by a very low amplitude oscillation around the static deflection angle, at the vortex shedding frequency. The LCO motion is a large amplitude motion, centered on the static deflection angle. This LCO is observed at higher airspeeds and presents a hysteresis loop: when the airspeed is reduced below the LCO onset airspeed, the large amplitude motion persists. It stops when the airspeed is reduced quite a bit further. The unstable LCO branch that must link the stable LCO and decaying motion branches has not been measured experimentally and will be the subject of further investigations.

The effect of the torsional stiffness of the deck on the TSF has been studied and it was observed that:

- the onset of the phenomenon is delayed when increasing the stiffness;
- the oscillation amplitudes are higher for higher torsional stiffness. This phenomenon has not been explained yet.
- the TSF oscillation occurs at the natural frequency of the pitch degree of freedom (i.e. depends on the pitch stiffness).

The simultaneous measurements of the aerodynamic forces and acceleration response of the structure allowed the observation of several interesting phenomena. As the aerodynamic pitching moment was not measured, the discussion presented in this work is based on the lift and drag forces only.

When starting from rest, the structure oscillates with very small amplitudes and a frequency imposed by the vortex shedding process.

For higher airspeeds, the deck jumps to the stable large amplitude LCO and the lift coefficient possesses two main frequency components:

- a frequency component corresponding to the vortex shedding process, as for the small amplitudes motion.
- a lower frequency component equal to the bridge deck's pitching oscillation frequency. The ejection of major vortices when high amplitudes are reached can be interpreted as peaks and troughs in the lift and drag coefficient signals.

The amplitudes of the lift coefficient of the deck undergoing small oscillations motion due to Karman vortex shedding or large oscillations motion due to TSF are comparable. The proposed explanation is that the large amplitude motion breaks the harmonic ejection of vortices and reduces the aerodynamic forces applied to the deck.

In conclusion, this paper presents preliminary results and conclusion about TSF oscillations on a model of a bridge deck based on a set of experimental data. Further experimentation is required in order to fully describe the phenomenon. Several interesting aspects for further work have already been identified, including the estimation of the position of the unstable LCO branch and, thus the complete visualization of the bifurcation that gives rise to TSF oscillations. Furthermore, flow visualization of the flow around the bridge deck performing LCOs will shed light on the exact mechanism of vortex shedding and the formation of the dominant vortex once per cycle.

VI. Figures

Fig. 1. Generic bridge deck model.

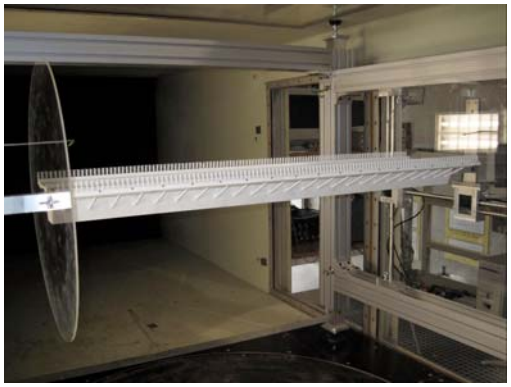

Fig. 2. Experimental set-up in wind tunnel.

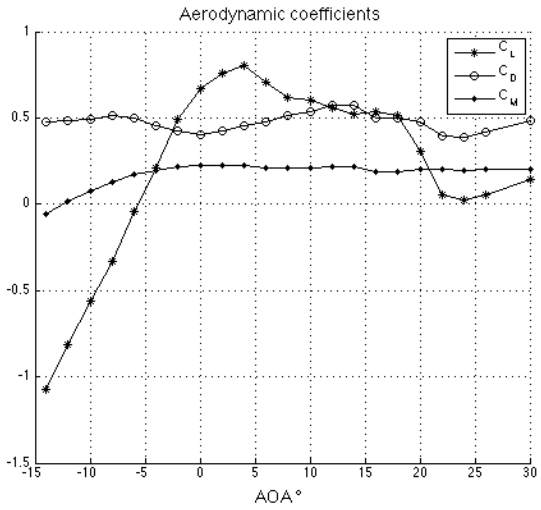

Fig. 3. Aerodynamic coefficients of the bridge deck.

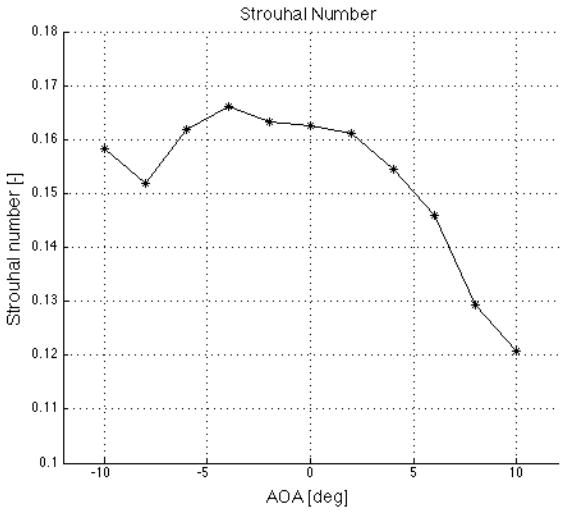

Fig. 4. Strouhal number for different angles of attack.

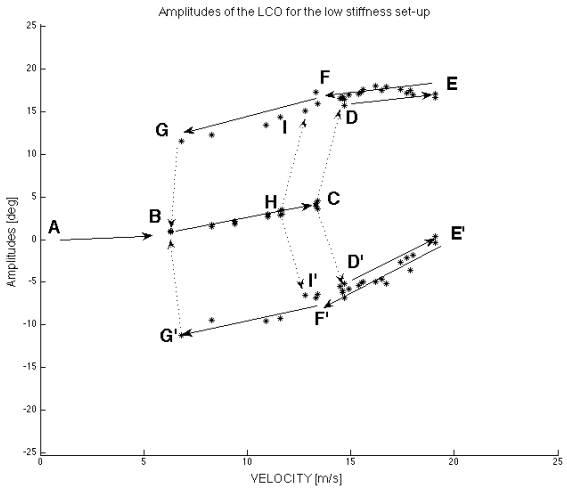

Fig. 5. LCO amplitudes for the low stiffness set-up.

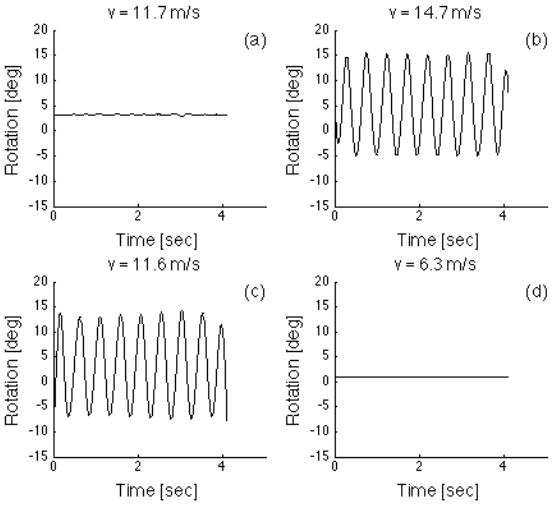

Fig. 6. Time signals (low stiffness set-up).

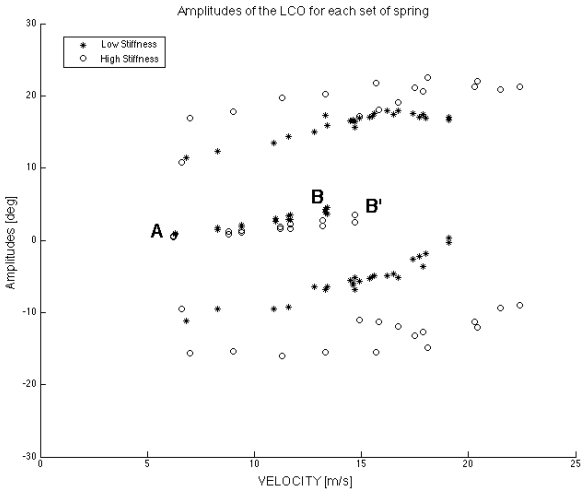

Fig. 7. LCO amplitudes for both set-ups.

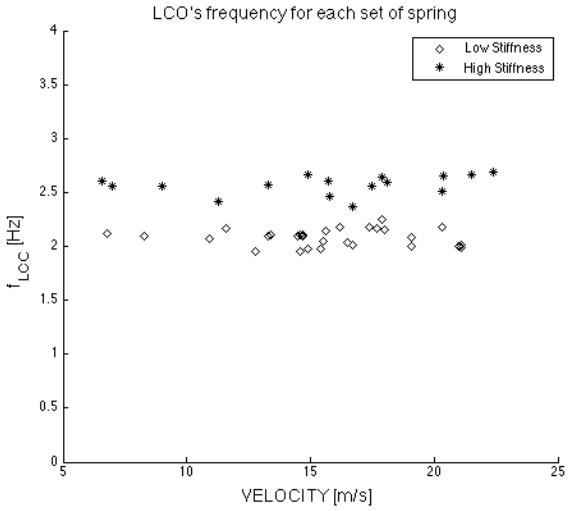

Fig. 8. LCO frequencies for both set-ups.

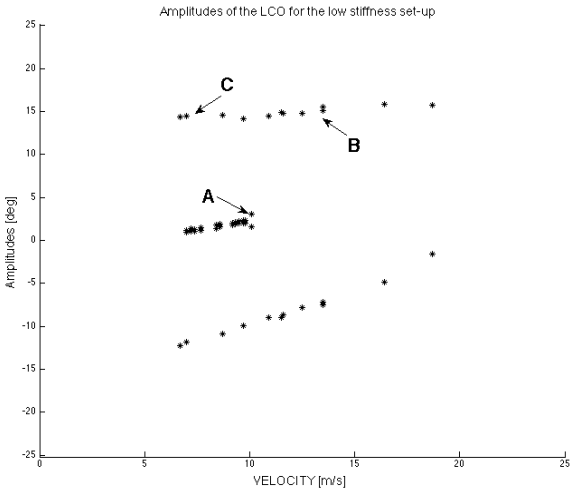

Fig. 9. LCO amplitudes.

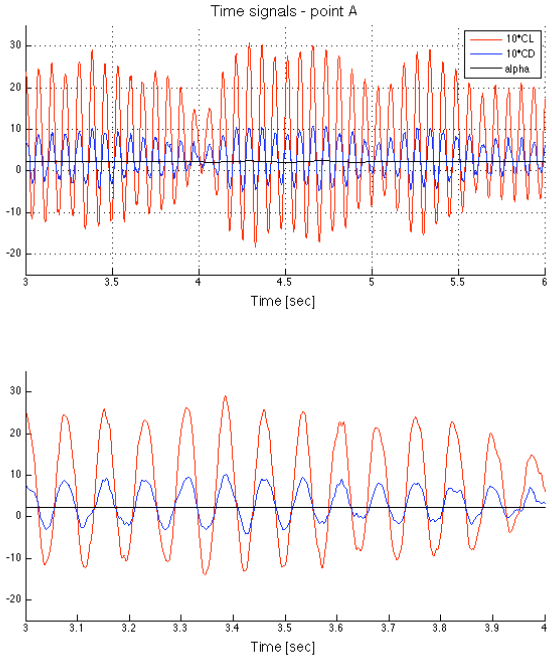

Fig. 10. Point A from Fig. 9.

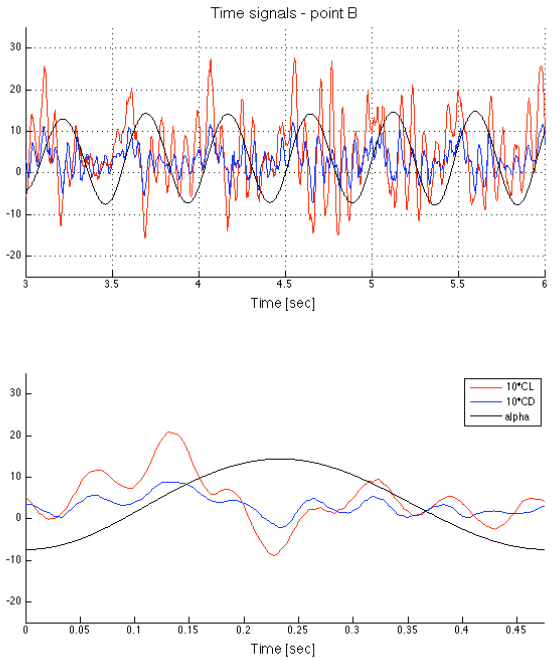

Fig. 11. Point B from Fig. 9.

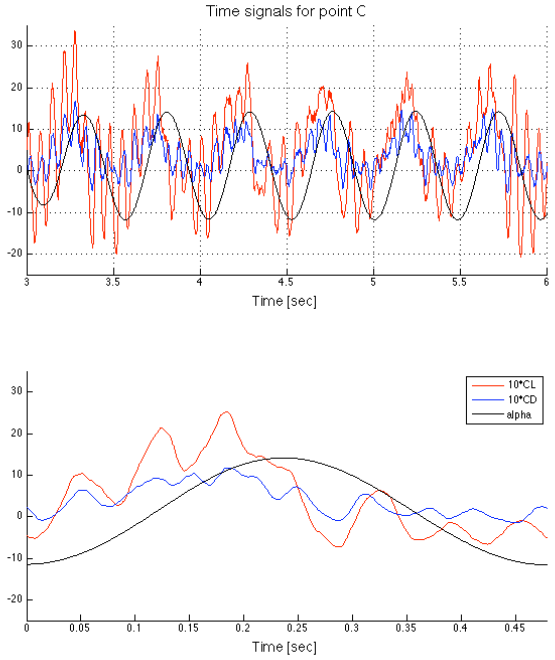

Fig. 12. Point C from Fig. 9.

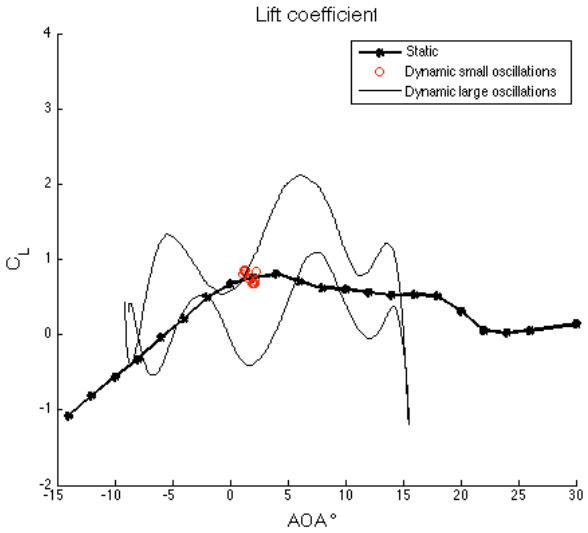

Fig. 13. CL versus AOA

REFERENCES

[1] Simiu, E., Scanlan, R.H., "Wind Effects on Structures: Fundamentals and Applications to Design", third Ed. Wiley, New York, 1996.

[2] Scanlan, R.H., “Developments in low-speed aeroelasticity in the civil engineering field”, AIAA Journal, vol. 20, n°6, 839-844, June 1982.

[3] Bartoli, G., Righi, M., “Flutter mechanism for rectangular prisms in smooth and turbulent flow”, Journal of wind engineering and industrial aerodynamics 94 (2006), 275-291.

[4] Theodorsen, T., Regier, A.A., “Effect of the lift coefficient on propeller flutter”, NACA Wartime Report, July 1945, n° L5F30.

[5] Baker, I.E., "The Effects of Various Parameters, Including Mach Number, on Propeller-Blade Flutter with Emphasis on Stall Flutter", NACA RML50L12b, 1950; reissued as NACA TN 3357, Jan. 1955.

[6] Crimi, P. "Analysis of helicopter rotor blade stall flutter", Journal of Aircraft, vol 11, n°7, July 1974.

[7] Ericsson, L.E., Reding, J.P., “Stall-flutter analysis” Journal of aircraft, vol. 10, n°1, 5-13, January 1973.

[8] Chaviaropoulos, P.K., "Flap/lead–lag aeroelastic stability of wind turbine blade sections.", Wind Energy 2, 99–112, 1999.

[9] J. Li and G. Dimitriadis, "Experimental study of stall-induced LCOs of free-vibrating wing", CEAS International Forum on Aeroelasticity and Structural Dynamics, Stockholm, Sweden, 2007.

[10] D. Poirel, Y. Harris, A. Benaissa, "Self-sustained oscillations of a NACA0012 airfoil at low-to-moderate Reynolds numbers", Journal of Fluids and Structures 24 (2008) 700-719.

[11] Sarkar, S., Bijl, H., “Nonlinear aeroelastic behavior of an oscillating airfoil during stall-induced vibration”, Journal of fluids and structures 24 (2008) 757-777.

[12] Tran, C.T., Petot, T., "Semi-empirical model for the dynamic stall of airfoils in view of the application to the calculation of responses of a helicopter blade in forward flight." Vertica 5, 35–53, 1981.

[13] P.R. Spalart, "Vortex methods for separated flows", NASA TM, NASA, June 1988.

[14] Taylor, I.J., Vezza, M., “A numerical investigation into the aerodynamic characteristics and aeroelastic stability of a footbridge” Journal of fluids and structures 25 (2009) 155-177.

[15] Sarkar, P.P., Chowdhurya A.G, Gardnerc T.B., "A novel elastic suspension system for wind tunnel section model studies", Journal of wind engineering and industrial aerodynamics 92 (2004), 23-40.

[16] Francis, M.S. and Keesee, J.E., "Airfoil dynamic stall performance with large amplitude motions.", AIAA Journal, 23(11):1653–1659, 1985

[17] Dimitriadis , G. and Li, J., "Bifurcation behavior of an airfoil undergoing stall flutter oscillations in a low speed wind tunnel", submitted to AIAA Journal, July 2008

Proceedings of the 8th National Congress on Theoretical and Applied Mechanics, May 28-29, Brussels, Belgium.

Simulation-based Sensitivity Analysis of a Mach 4.5 Mixed-Compression Intake

Hiromasa Kato[1], Keiichi Ito[1], and Ingrid Lepot[1]
[1]Multidisciplinary Optimization Group, Cenaero,
Rue des Frères Wright 29, 6041 Gosselies
email: hiromasa.kato@cenaero.be

Abstract— **A sensitivity analysis of a supersonic mixed-compression intake of a variable-cycle turbine-based combined cycle (TBCC) engine is presented. The TBCC engine is designed to power a long-range Mach 4.5 transport capable of antipodal missions studied in the framework of an EU FP6 project, LAPCAT. The nominal intake geometry was designed using DLR abpi cycle analysis program by taking into account various operating requirements of a typical mission profile. The intake consists of two movable external compression ramps followed by an isolator section with a bleed channel. The compressed air is then diffused through a rectangular-to-circular subsonic diffuser. A multi-block Reynolds-averaged Navier-Stokes (RANS) solver with Srinivasan-Tannehill equilibrium air model was used to compute the total pressure recovery and mass capture fraction. While RANS simulation of the nominal intake configuration provides more realistic performance characteristics of the intake than the cycle analysis program, the intake design must also take into account in-flight uncertainties for robust intake performance. In this study, we focus on the effect of geometric uncertainties on the pressure recovery and mass capture fraction, and propose a practical approach to simulation-based sensitivity analysis. The method begins by constructing a light-weight analytical model, a radial-basis function (RBF) network, trained via efficiently sampled RANS simulation results. Using the RBF network as the response surface approximation, stochastic sensitivity analysis is performed using the analysis of variance (ANOVA) technique by Sobol. This approach makes it possible to perform a generalized multi-input-multi-output sensitivity analysis based on high-fidelity RANS simulation. The resulting Sobol's influence indices allow the design engineer to identify dominant parameters as well as the degree of interaction among multiple parameters, which can then be fed back into the design cycle.**

Keywords— **Sensitivity analysis, surrogate modeling, ANOVA, mixed-compression intake, RANS**

I. Introduction

IN the framework of LAPCAT, an EU FP6 Project, several propulsion system concepts to power long-range (anti-podal) civil transport missions are studied. One of them is a variable-cycle turbine-based combined cycle (TBCC) engine. The mixed compression intake system was designed for the TBCC engine in the previous studies. [1] [2] The nominal intake geometry was designed using DLR abpi cycle analysis program by taking into account various operating requirements of a typical mission profile. It is made up of three external compression ramps, two of them movable, followed by an isolator section with bleed channel. The compressed air is then diffused through a rectangular-to-circular subsonic diffuser. The primary performance measures of supersonic intakes are total pressure ratio and mass capture ratio. In this study, a multi-block Reynolds-averaged Navier-Stokes (RANS) solver with Srinivasan-Tannehill equilibrium air model is used to compute total pressure recovery and mass capture fraction.

While numerical simulations of the intake flowfield yield performance with greater accuracy, one of the concerns from a systems analysis point of view is the verification of mass estimate of the intake system, in particular against uncertainties when one takes into account in-flight perturbations of the intake walls. Thus, a more important question is rather the feasibility of the proposed intake layout both from aerodynamics and structural points of view. On the aerodynamics front, there is the issue of startability and stability. On the structural front, a proper mass estimate is needed to ensure that the compression layout is realizable within the mass budget allowed for the intake system. In this study we focus on the sensitivity of the intake performance under geometric uncertainties/perturbations, which can be later used to justify the mass estimation allotted for the intake structure.

The approach taken in this study for the sensitivity analysis is based on high-fidelity direct numerical simulations of the perturbed configurations, rather than a simplified model as is often the case. The method begins by constructing a light-weight analytical model, a radial-basis function (RBF) network, trained via adaptively sampled RANS simulation results. Using the RBF network as the response surface approximation, stochastic sensitivity analysis is performed using analysis of variance (ANOVA) technique by Sobol.

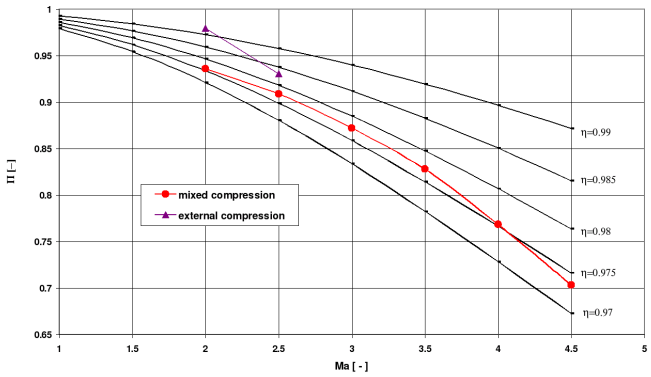

Fig. 1. Air-Intake pressure recovery of LAPCAT-M4 3ramp-mixed compression intake according to abpi-calculation and intake-efficiency.

This approach makes it possible to perform a generalized multi-input-multi-output sensitivity analysis based on high-fidelity RANS simulation. The resulting Sobol influence indices allow the engineer to identify dominant parameters as well as the degree of interaction among multiple parameters, which can then be fed back into the design cycle.

II. Preliminary Air Intake Design

The nominal configuration of the intake system was designed previously by using DLR abpi cycle analysis program as reported in [1]. The detailed mass estimate was also performed and presented in [2]. The variable-cycle engines, four in total with two engines on each wing, are all fed by the two dimensional mixed compression ramp intake system. The compression system consists of three external ramps, two of them (i.e. except the first ramp) movable, followed by two cowl ramps, finally connected to an isolator section whose purpose is to stabilize the terminal shock before the flow is diffused by a rectangular-to-circular diffuser. DLR abpi analysis found the cruise point pressure recovery of around 70% at Mach 4.5 as can be seen from Fig. 1 (taken from [1]).

III. Sensitivity Analysis

This section describes the methodology for analyzing sensitivity of the problem whose characteristics is obtained by a series of computer simulations.

In sensitivity analysis, one tries to identify, quantitavely as well as qualitatively effects of perturbations in the input parameters on the outputs. The steps for stochastic sensitivity analysis are as follows

1. Generate samples of geometric perturbation by design of experiments (DoE).
2. Run flow simulation at each sample location, and evaluate the intake performance.
3. Train RBFN using the database of the input (perturbation) and the output (performance) samples.
4. Analyze the first-order sensitivity indices (Sobol indices).

A. Design of Experiments

Design of experiments (DoE) is a procedure in which the experimenter tries to capture as best as possible the behavior of the problem at hand using as few as possible number of experiment runs. In the current context, the experiment is deterministic computer simulations, therefore the objective is to use a DoE technique to efficiently capture the output of the simulations. A set of numerical simulation samples are then used to construct a surrogate model. The sampling algorithm used in this study is based on the Latin Hypercube Sampling (LHS) method. It is a stochastic sampling strategy and one of its advantage is that it does not depend on the problem dimensions. The fact that any sampling density can be chosen has an important practical benefit, where the problem dimension, i.e. the number of design parameters, far exceeds that which can be reasonably treated by more conventional sampling techniques.

LHS is a technique based on the property of Latin square, in which no collision of values happens in any dimension. When generalized to arbitrary dimensions, it is called Latin Hypercube. LHS can be relatively easily implemented by generating a series of permutated sample locations for each dimension in a unit hypercube of N dimensions, and then scaling the sample locations to the corresponding parameter scales. A table of 5 samples for a two dimensional problem sampled by LHS is depicted in Fig. 2. Here, the sampled points have all unique locations in any given direction, i.e. there is no collision of parameter values in X1 nor X2 axes.

B. Surrogate Model

The objective of running numerical simulations at all the sample points generated by DoE is to construct a closed form expression of the intake performance. This function is then used as the performance predictor in the subsequent sensitivity analysis. This is accomplished by approximating the performance figures (output) for arbitrary perturbations (input). For this approximation, a form of neural network called Radial Basis Function Network (RBFN) is employed.

The RBF network is a linear neural network model with one layer of hidden units, schematically depicted

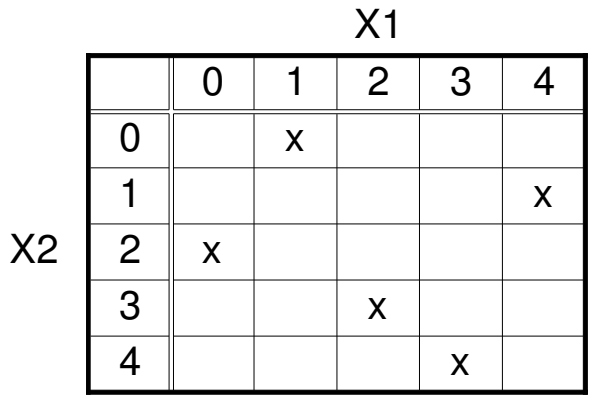

Fig. 2. Latin-hypercube sampling in two dimensions

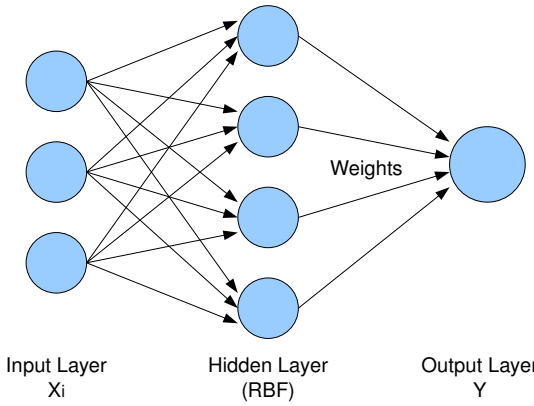

Fig. 3. Radial Basis Function Network

in Fig. 3, and is written as

$$y = \sum_{i=1}^{N} w_i \rho_i \left(\|\mathbf{x} - \mathbf{c_i}\| \right) \tag{1}$$

where $\mathbf{x}$ is the input vector, ρ_i the Radial Basis Function, w_i the weight vector, and y the output. Among various forms of RBF kernel, popular ones include the Gaussian

$$\rho \left(\|\mathbf{x} - \mathbf{c}\| \right) = \exp \left(-\frac{(\mathbf{x} - \mathbf{c})^2}{r^2} \right)$$

and multiquadrics

$$\rho \left(\|\mathbf{x} - \mathbf{c}\| \right) = \frac{\sqrt{r^2 + (\mathbf{x} - \mathbf{c})^2}}{r}$$

where $\mathbf{c}$ is the center of the RBF, r the radius. The multiquadrics is used in this study.

A set of numerical samples obtained in the DoE act as the training sample set, providing input-output pairs for which the function response is to be estimated.

C. Assessment of Surrogate Model Quality

As the sensitivity analysis, the detail of which is described in the following section, is carried out on the surrogate model, it is imperative that the model predicts the intake performance as accurately as possible. The easiest way of validating the quality of the surrogate model is to create another set of accurate simulation samples (validation samples) and measure the discrepancy between the validation samples and the surrogate model prediction. Obviously this is prohibitive in terms of computational requirements as it means that we would have to run many more simulations just for validation which will not be used in the training of the surrogate model. This is a dilemma as we have extra samples which we can use to further improve the surrogate model, yet will be thrown away.

The Leave-One-Out procedure [3] is a way to estimate the accuracy of a surrogate model without the need for creating extra data for validation. If we create a data set with n sampled points, $n-1$ samples are used in training a surrogate model and k-th sample point is left out in the training process. The output value at the k-th sample point is then estimated with the metamodel and compared with that of the dataset. We do this with all the n sample points ($k = 1, ..., n$), and we obtain a set of estimated output (with Leave-One-Out) and the true output. The two output set can be statistically analyzed for error estimation and so on.

For a sample set of input-output pairs, where x_i and y_i denote input and output respectively and N is the number of samples. Given a set of all the samples X

$$X = \{x_i : i = 0, ..., N\}$$

we define another set with k-th sample left out

$$X^k = \{x_i : i = 0, ..., N; i \neq k\}$$

A surrogate model, f^k, is then trained using the set X^k.

$$y = f^k(x)$$

We evaluate this surrogate model at the k-th sample point which was left out in the training, then we have

$$\hat{y}^k = f^k(x_k)$$

Repeating this process N times for $k = 1, ..., N$, we obtain a set of k pairs of true values and predicted values.

$$\{(y_k, \hat{y}^k) : k = 1, ..., N\}$$

If we plot this set, a perfect surrogate model would yield a straight line since $y_k = \hat{y}^k$. Otherwise, there

will be errors between the true value y_k and the predicted value $\hat{y}^k$. Here, one can employ a simple linear correlation between y_k and $\hat{y}^k$, denoted customarily by R which for a perfect surrogate model $R = 1$. The closer the value of R is to 1, the better the surrogate model is.

D. Analysis of Variance (ANOVA)

Consider a deterministic model $y = f(X)$ where $X = (x_1, x_2, \ldots, x_n)$ is a vector of n input variables and y is the model output. $f(X)$ can be decomposed into a form referred to as high dimensional model representation.

$$\begin{aligned} f(X) &= f_0 + \sum_i f_i(x_i) + \sum_{i<j} f_{ij}(x_i, x_j) \\ &\quad + \sum_{i<j<k} f_{ijk}(x_i, x_j, x_k) + \ldots \end{aligned} \tag{2}$$

This decomposition of the function is not unique as the lower order can be selected arbitrarily and the highest order term can be written as the difference between $f(X)$ and the lower order terms. However, if the average of each of the term in the summands of the right hand side of equation (2) is set to zero and f_0 is set to be a constant, the expression is proven to be unique. The terms are given as the following.

$$f_i(x_i) = E(y|x_i) - E(y) \tag{3}$$

$$\begin{aligned} f_{ij}(x_i, x_j) &= E(y|x_i, x_j) \\ &\quad - f_i(x_i) - f_j(x_j) \end{aligned} \tag{4}$$

$$\begin{aligned} f_{ijk}(x_i, x_j, x_k) &= E(y|x_i, x_j, x_k) \\ &\quad - f_{ij}(x_i, x_j) - f_{ik}(x_i, x_k) \\ &\quad - f_{jk}(x_j, x_k). \end{aligned} \tag{5}$$

The first order sensitivity index for variable x_i is given by

$$S_i = \frac{V[E(y|x_i)]}{V(y)}, \tag{6}$$

and if we calculated the indices to the highest order, we have

$$\sum_{i=1}^{n} S_i + \sum_{i=1}^{n} \sum_{j=i+1}^{n} S_{ij} + \ldots + S_{ij\ldots n} = 1. \tag{7}$$

The numerator in equation (6) means "variance of expected value of y given x_i", the denominator is the "total (unconditional) variance".

For a statistician or a scientist who is trying to reduce the amount of error incurred in the output y due to the error in the input variable (or measurement) x_i, this measure would give the relative importance of the variable in driving the output uncertainty. He/she would fix x_i and let other variables vary in the range of their estimated errors. This would give $E(y|x_i)$ and repeat this process with different values of x_i within its error bounds to get $V[E(y|x_i)]$. The same process can be applied to the analysis of the sensitivity of surrogate models constructed from deterministic simulation models. Instead of input errors, the variables are swept through the domain of interest with x_i fixed. We can compute its average and change x_i to a next value until enough x_i values are tried out in the domain of interest. Then, the variance of the obtained averages would give the numerator of equation (6). The denominator can be obtained by a random sampling in the domain of X and computing the variance of their corresponding y s.

The virtue of this method is that it takes all the nonlinearities and interactions into account as compared to "one variable at a time" way of sensitivity analysis. More over, even if we conduct the sensitivity analysis only to the first order, we will always have an idea of what remains unexplained by calculating $1 - \sum_{i=1}^{n} S_i$.

Following the discussion above, we now formulate the way to compute the first order sensitivity indices. As before,we express a surrogate model with n-dimensional input space as

$$y = f(x_1, x_2, \ldots, x_n). \tag{8}$$

The total variance is therefore

$$\begin{aligned} D &= \underset{X \in R^n}{V}(f(X)) \\ &= \int_{X \in R^n} f^2(x_1, x_2, \ldots, x_n)\, dx_1 dx_2 \ldots dx_n - f_0^2. \end{aligned} \tag{9}$$

The multidimensional integral of Eq. 10 can be computed using the Monte Carlo Integration. Similarly the following equation gives the $E(y|x_i)$.

$$\begin{aligned} f_i(x_i) &= \int_1 \int_2 \ldots \int_{n-1} f(x_1, x_2, \ldots, x_n) \\ &\quad dx_1 dx_2 \ldots dx_{i-1} dx_{i+1} \ldots dx_n - f_0 \end{aligned} \tag{10}$$

Again, the integration is performed using the Monte Carlo method, but this time x_i is held constant. By doing this multiple of times, we can conduct the next integration to obtain $V[E(y|x_i)]$.

$$D_i = \underset{x_i}{V}(f_i(x_i)) = \int_{x_i} f_i^2(x_i)\, dx_i \tag{11}$$

Then, the first order sensitivity indices are given as

$$S_i = \frac{D_i}{D}. \tag{12}$$

TABLE I
COMPARISON OF INTAKE PERFORMANCE

	Pressure recovery	Mass capture ratio
DLR abpi	71%	85%
Cenaero	66%	77%

Two parameters need to be set in the course of the computation of indices. The first one is the number of samples to compute the Monte Carlo integration in equations (10) and (11), and the second one is how many x_i s to calculate in equation (11). We refer the first number as n_{samp} and the second number as n_{pts} respectively. The right numbers are problem dependent. Experience tells us that

$$n_{samp} = 1000 \sim 10000 \quad (13)$$
$$n_{pts} = 50 \sim 300 \quad (14)$$

are usually adequate.

IV. 3-D Flowfield Analysis of the Redesigned Intake.

3-D flow field over the redesigned intake has been computed on a mesh consisting of 2 million nodes approximately. The multiblock structured RANS flow solver uses the curve fits for the thermodynamic and transport properties of equilibrium air with vibrational excitation. [7] [8] The one-equation turbulence model of Spalart-Allmaras was used for fully turbulent flows over the intake. Table I compares the performance parameters between DLR abpi simulation and the 3-D RANS analysis of the redesigned intake (marked as Cenaero). The total pressure recovery is based on the mass averaged total pressure behind the terminal shock.

Figure 4 shows Mach number distribution on the planes cut normal to the flow direction as well as on the side wall which reveals that there are significant 3-D effect caused by the side wall. The flow pattern inside the isolator exhibits complex interaction as the vortical structure caused by the side wall external edge passes through the corner between the cowl and the side wall.

V. Intake Performance Sensitivity Analysis

The stochastic perturbation to the intake geometry is now applied to investigate the effects on the intake performance, namely total pressure recovery and mass capture ratio. The perturbation is applied to the two external movable ramps, cowl wall, and the isolator

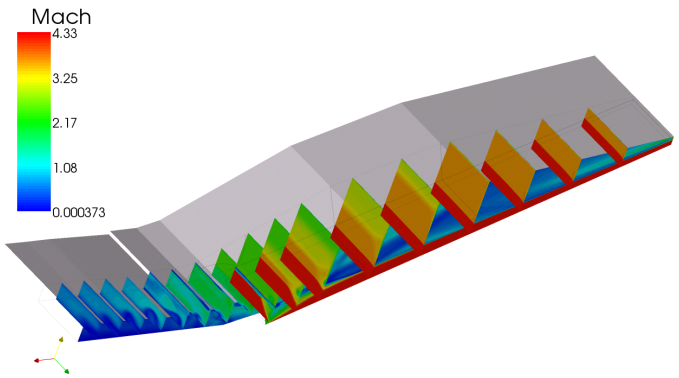

Fig. 4. Side-wall and transverse cuts showing Mach number distribution.

ceiling, as shown in Fig. 5. The extent of perturbation is set to 2cm for external ramp walls and 1cm for isolator walls. The walls are perturbed by applying sinusoidal curves to the nominal geometry as shown in Fig. 5.

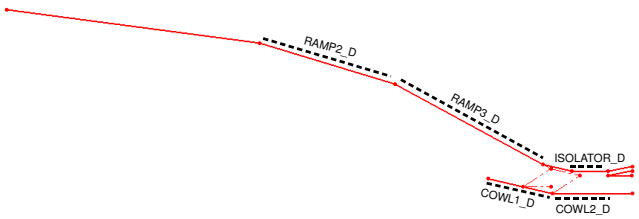

Fig. 5. Perturbed walls.

Firstly a set of sample points are generated by the LHS technique. The 3-D projection of the samples is shown in Fig. 6. Note that the perturbation is applied simultaneously in all five dimensions and that Fig. 6 shows merely a visualizable representation of sample distribution.

In the sample set, each sample point represents an intake geometry. The intake performance is then computed for each geometry by running a full RANS simulation as done in the previous section. The result of this RANS campaign is the distribution of intake performance fluctuations due to the geometry perturbations. The 2-D plot of fluctuations in total pressure and mass flow rate just behind the terminal shock is shown in Fig. 7, which shows approximately 4% and 2% fluctuations in mass flow rate and total pressure.

Although Fig. 7 gives an idea of the magnitude of performance fluctuation, it would be even more insightful to investigate, among all the perturbed walls, which perturbed wall affects the performance most. Doing a naive sampling-based sensitivity analysis di-

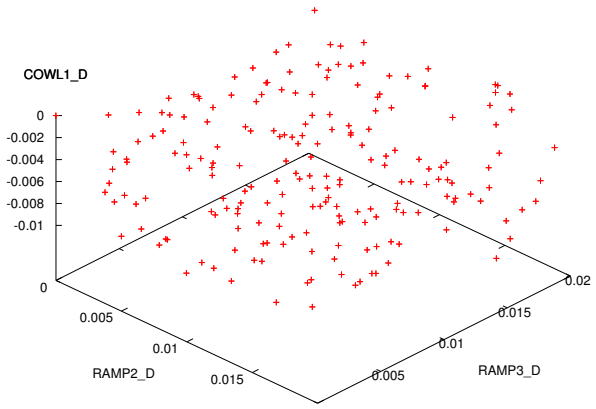

Fig. 6. LHS samples.

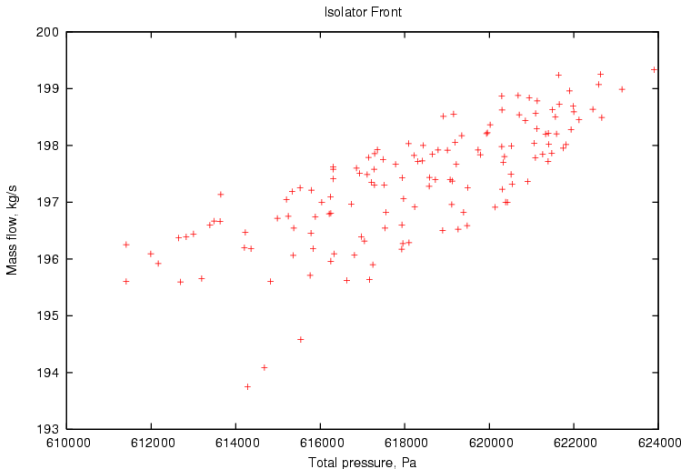

Fig. 7. Total pressure and mass flow fluctuation due to geometry perturbation.

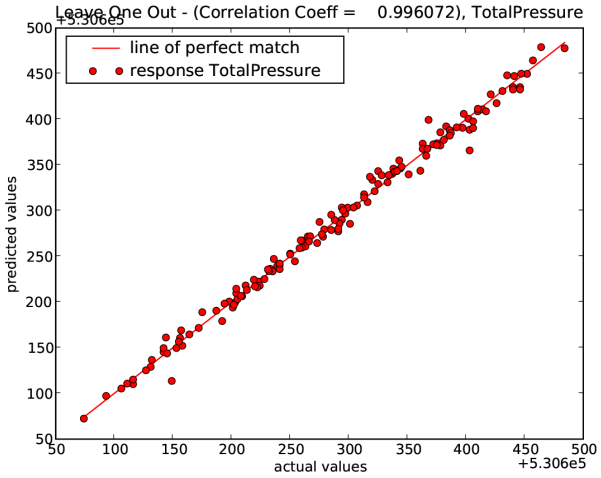

Fig. 8. Leave-one-out correlation analysis of the surrogate model for total pressure.

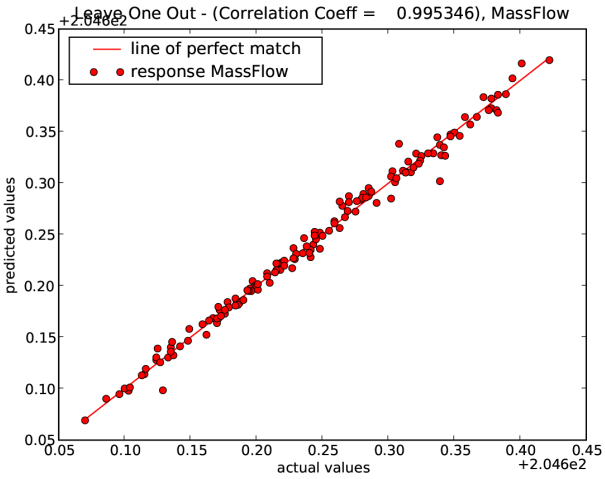

Fig. 9. Leave-one-out correlation analysis of the surrogate model for mass flow rate.

rectly on a computationally heavy simulation such as the RANS code is not practical. Therefore we first build a surrogate model, a function which is far lighter than the simulation code, which would map the perturbation input to the performance output. Thus, using the sample set as the training data set, we build an RBFN model as described in Section III-B.

As the accuracy of sensitivity analysis depends on the quality of the surrogate model, we test its quality by the LOO procedure as described in III-C. Figures 8, 9, and 10 show the correlation plot for the outputs, total pressure, mass flow rate, and mass-averaged Mach number respectively. The correlation coefficients, R, are all above 0.99, which indicate that the RBFN model trained by the LHS sample set is of very high quality. Therefore we accept this surrogate model to be an approximation sufficiently accurate for capturing the behavior of the intake performance.

Now that the confidence on the quality of the surrogate model is confirmed quantitatively, stochastic sensitivity analysis can be applied on the surrogate model to extract the measure of influence of each parameters on the intake performance response. Following the procedure described in Section III-D, Sobol's indices are computed.

Figures 11 and 12 show the pie charts indicating the degrees of parameter influence on the performance in terms of total pressure recovery and mass flow rate. The influence index marked as *2nd order* shows that there is little interaction among the parameters, as it represents only a few percent of the total sensitivity. This means that the perturbation applied on a given wall influences the performance more or less independently of the perturbations applied on other walls. On the other hand, the perturbations on the upper and

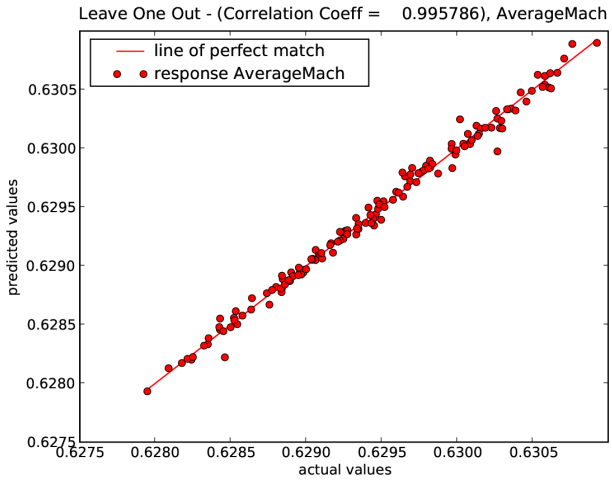

Fig. 10. Leave-one-out correlation analysis of the surrogate model for mass-averaged Mach number at the probe plane.

lower walls of the isolator (those marked as *COWL2_D* and *ISOLATOR_D*) represent the dominant parameters affecting the intake performance, followed by the third external ramp (*RAMP3_D*) and the cowl interior wall (*COWL1_D*), each contributing about 10%. Therefore, the designer of the intake can identify and prioritize these components to be emphasized in the overall design of the intake, for instance in its mass estimation.

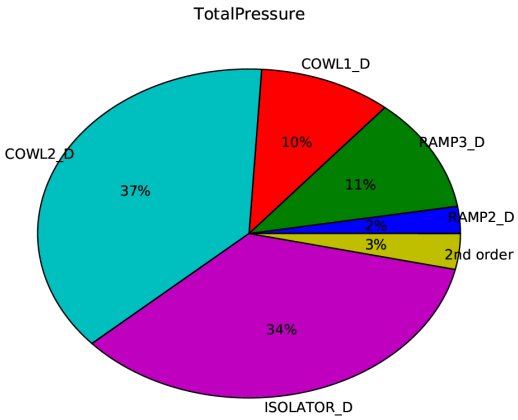

Fig. 11. ANOVA on total pressure.

VI. Conclusion

A sensitivity analysis based on high-fidelity numerical simulations, aided by an efficient sampling and surrogate modeling techniques, was applied to the performance sensitivity analysis of a supersonic mixed-compression intake system under arbitrary geometric perturbations. The detailed sensitivity structure of the intake performance was revealed thanks to the application of a stochastic ANOVA analysis using Sobol indices. The essence of the presented technique lies in the attention paid specifically to capture the nonlinearity of the problem. This is reflected in the choice of methodologies at every step of the sensitivity analysis. The first component is the RANS simulations which served as the basis of performance prediction which captures more nonlinear flow physics than a simplified model often used in this type of analysis. The second is the black box approach used in the surrogate modeling. The last is the use of stochastic ANOVA. These choices, when combined together, lead to the practical engineering tool which achieves a better balance of both nonlinear physics and rapid turn-around time of the analysis.

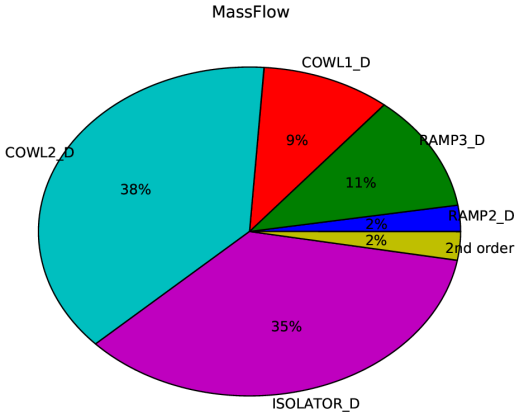

Fig. 12. ANOVA on mass flow rate.

Acknowledgments

This work was performed within the "Long-Term Advanced Propulsion Concepts and Technologies" project investigating high-speed airbreathing propulsion. LAPCAT, coordinated by ESA-ESTEC, is supported by the EU within the 6th Framework Programme Priority 1.4, Aeronautic and Space, Contract No. AST4-CT-2005-012282. Further info on LAPCAT can be found on `http://www.estec.esa.int/techresources/lapcat`.

References

[1] Martin Sippel, Keiichi Okai, Hiromasa Kato, and Apurva Kumar, "Preliminary definition of a tbcc propulsion system for a mach 4.5 supersonic cruise airliner," in *18th International Symposium on Air Breathing Engines*, 2007.

[2] Martin Sippel and Keiichi Okai, "Component analysis of

tbcc propulsion for a mach 4.5 supersonic cruise airliner," in *2nd European Conference for AeroSpace Sciences (EUCASS)*, 2007.

[3] Martin Meckesheimer, Andrew J. Booker, Russell R. Barton, and Timothy W. Simpson, "Computationally inexpensive metamodel assessment strategies," *AIAA Journal*, vol. 40, no. 10, pp. 2053–2060, 2002.

[4] Karen Chan, Andrea Saltelli, and Stefano Tarantola, "Sensitivity analysis of model output: Variance-based methods make the difference," in *Proceedings of the 1997 Winter Simulation Conference*, 1997, pp. 261–268.

[5] European Commission, Joint Research Centre of Ispra, Italy, "A cookbook for applying sensitivity analysis in practical cases of modeling," http://sensitivity-analysis.jrc.ec.europa.eu/tutorial/index.asp.

[6] I. M. Sobol, "Global sensitivity indices for nonlinear mathematical models and their Monte Carlo estimates," *Mathematics and Computers in Simulation*, vol. 55, pp. 271–280, 2001.

[7] S. Srinivasan, J. C. Tannehill, and K. J. Weilmuenster, "Simplified curve fits for the thermodynamic properties of equilibrium air," NASA-CR 181245, 1986.

[8] S. Srinivasan, J. C. Tannehill, and K. J. Weilmuenster, "Simplified curve fits for the transport properties of equilibrium air," NASA-CR 178411, 1987.

Proceedings of the 8th National Congress on Theoretical and Applied Mechanics, May 28-29, Brussels, Belgium.

Micromechanical modeling of elasto-plastic composites: numerical assessment of mean-field schemes

L. Brassart, I. Doghri, L. Delannay
Université catholique de Louvain, Department of Mechanical Engineering
Av. Georges Lemaître 4 - 1348 Louvain-la-Neuve
email: laurence.brassart@uclouvain.be

Abstract— **This work focuses on the applicability of mean-field approaches to predict the effective behavior of composites made of an elasto-plastic matrix reinforced by hard inclusions. General loading conditions (non-monotonic, non-proportional) are considered, which requires a history-dependent scheme. Moreover, a particular attention is paid to the prediction of the stress developed within the inclusions. Recent models including short range particle/matrix interactions and second moments of the stress and strain fields are presented and assessed against direct finite element computation of representative cells containing a random arrangement of inclusions.**

Keywords— **Mean-field homogenization, Multiscale, Self-consistent, Multiphase metals**

I. Introduction

THE problem of predicting the effective properties of composite materials can be efficiently addressed by mean-field (MF) approaches. Their relatively low computational cost (as compared to full-field finite element (FE) simulations) allows the micro/macro transition to be performed at each Gauss point in a large scale simulation. Except for the simplest ones, the upper and lower bounds due to Voigt and Reuss, these methods rely on the "equivalent inclusion" concept, whose solution for linear elastic behavior is provided by Eshelby's seminal work. Extending these schemes to elasto-plastic materials is an active research field. In particular, several important issues have to be addressed by nonlinear MF approaches, namely: linearization of the constitutive response, definition of comparison materials, use of first and/or second moments of the fields, computation of Eshelby's or Hill's tensors.

We focus on *incremental* MF models, which are suited for path-dependent behavior. Such models rely on comparison materials having a fictitious, uniform, instantaneous stiffness, to which linear schemes (written in rate form) may be applied. For instance, the incremental Mori-Tanaka scheme [1] sucessfully predicts the macroscopic stress-strain response of elasto-plastic composites [2]. However, the modeling tends to underestimate the average inclusions response when these are significantly stiffer than the matrix [2]. This can be attributed to short range interactions taking place at particle/matrix interfaces, which are overlooked by the MF model. Intra-phase fluctuations of the fields are also neglected in a first-order homogenization procedure. Nevertheless, it is emphasised that the equivalent inclusion hypothesis remains acceptable for the modeling of elasto-plastic composites with relatively low reinforcement volume fraction [3].

In this work, we aim to improve the phase predictions by proposing an alternative treatment of intraphase strain heterogeneity. The benchmark is a two-phase steel made of an elasto-plastic matrix reinforced by linear elastic inclusions. Strain heterogeneities are introduced in the matrix modeling through the use of a multisite model that captures short range interactions at particle matrix interfaces. Direct FE computation of representative cells are performed in order to verify the predictions of the proposed model.

II. Model description

Most MF schemes rely on the equivalent inclusion concept: each reinforcing phase is modeled by a single, ellipsoidal inclusion embedded in an infinite medium, characterized by a reference, uniform tangent operator. Phase interactions are taken into account in a simplified way, through the choice of the material properties that are given to the surrounding medium. These models focus on long-range interactions. Alternatively, multisite approaches focus on short-range interactions, assuming that every inclusion interacts with its direct neighbourhood. These models were initially developed for the prediction of texture evolution in deformed polycrystalline aggregates [4], [5], [6].

The proposed model [7] aims to enrich the MF scheme with short-range effects through a multisite modeling of particle-matrix interactions. In particular, the ALAMEL model [6] is used. This model considers stacks of two subregions lying on either sides of a planar interface separating two phases labelled I and II. Macroscopically prescribed deformation is achieved on average over the two subregions, while some strain relaxation mostly through shear is allowed, so that displacement continuity and stress equilibrium are satisfied.

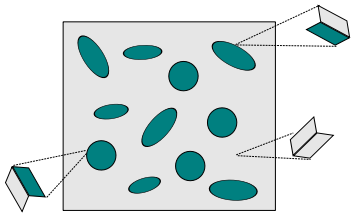

(a)Model microstructure

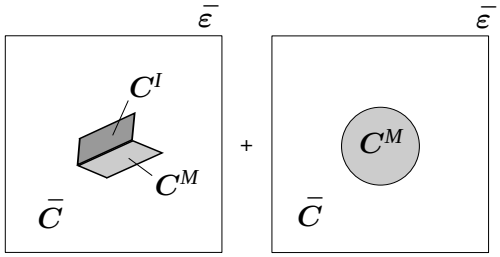

(b)Self-consistent model

Fig. 1. (a) Model microstructure of the two-phase composite and (b) schematic representation of the coupled mean-field/multisite approach. A self-consistent assumption is used to determine the strain partitioning among the pseudo-grains.

The model microstructure of the composite consists of zones made of the matrix material which are ”far enough” from the interfaces and others which are close to interface and where short-range interactions are predominant (Figure 1(a)). The latter are modeled by a large number of two-phase ”pseudo-grains”, whose interface normals are chosen to be statistically representative of the phases topology. In every stack, one subregion takes the material properties of the inclusions, and the other the properties of the matrix. In addition, it is assumed that the region of the matrix that is far from interfaces may be treated as a supplementary pseudo-grain with uniform properties. Finally, a self-consistent assumption is used to determine the strain partitioning between all pseudo-grains. In order to deal with non-monotonic loading paths, a Hill-type incremental formulation is adopted. The self-consistent assumption combined with the multisite approach is depicted in Figure 1(b).

III. Results and Conclusions

The model is applied to a two-phase steel made of elastic martensite inclusions embedded in a ferritic elasto-plastic matrix. The predictions of the proposed model are compared to reference results provided by FE computations on a representative unit cell consisting of a prismatic box containing a random dispersion of about 30 inclusions, see Figure 2. Predictions of other incremental MF approaches (without short range effects) are also presented for comparison. Figure 3 shows the average stress of the inclusion during an uniaxial traction test for a composite with 15% of inclusions. As expected, the multisite features allow to raise the stress level in the inclusions as compared to classical MF methods, namely the Mori-Tanaka and self-consistent incremental models. In particular, the multisite model provides the best fit during the first half of the loading. Then, it overestimates the inclusion stress.

Several modifications could improve the present model. One could change the ratios of subregions within a stack, or the pseudo-grain shape. In order to better capture the slope of the reference curve, one could also use a Mori-Tanaka scheme to determine the strain partitioning among pseudo-grains.

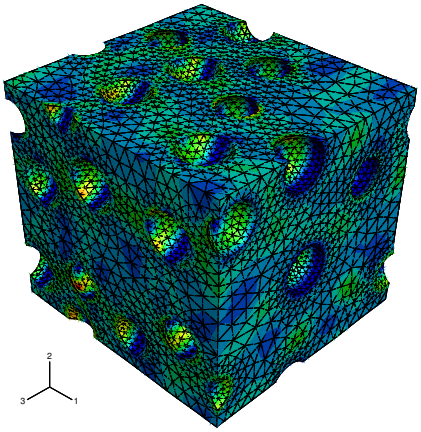

Fig. 2. FE computation is performed on periodic unit cells containing thirty randomly dispersed inclusions. Elements belonging to the inclusions are not shown.

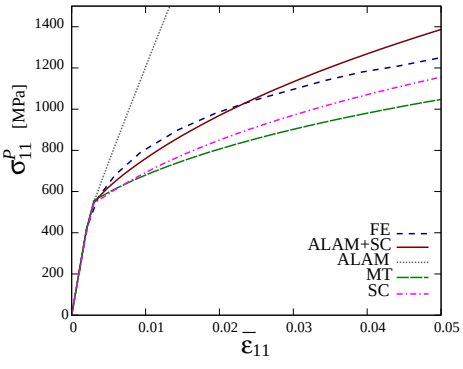

Fig. 3. Average stress in the inclusions as a function of the macroscopic strain for a DP steel with 15% of inclusions. ALAM+SC refers to the combination of the multisite approach with a self-consistent scheme, in ALAM, a Voigt scheme is used, SC refers to a classical, two-phase self-consistent scheme and MT to the Mori-Tanaka scheme.

ACKNOWLEDGMENTS

L. Brassart and L. Delannay are mandated by the National Fund for Scientific Research (FNRS, Belgium). The authors gratefully acknowledge O. Pierard for providing the tools for microstructure generation. Computing facilities were made available through contract FRFC-2.4502.05 with FNRS.

REFERENCES

[1] I. Doghri and A. Ouaar. Homogenization of two-phase elasto-plastic composite materials and structures: Study of tangent operators, cyclic plasticity and numerical algorithms. *Int. J. Solids Struct.*, **40**, 1681-1712, (2003).

[2] L. Delannay, I. Doghri and O. Pierard. Predictions of tension-compression cycles in multiphase steel using a modified incremental mean-field model. *Int. J. Solids Struct.*, **44**, 7291-7306, (2007).

[3] L. Brassart, L. Delannay and I. Doghri. Coupling of Mori-Tanaka model with a finite element analysis of the single inclusion problem for the homogenization of elasto-plastic composites. *In preparation*, (2009).

[4] R. A. Lebensohn and G. A. Canova. Self-consistent approach for modelling texture development of two-phase polycrystals: application to titanium alloys. *Acta Mater.*, **45**, 3687-3694, (1997).

[5] P. Van Houtte, S. Li, M. Seefeldt and L. Delannay. Deformation texture prediction: from the taylor model to the advanced lamel model. *Int. J. Plasticity*, **21**, 589-624, (2005).

[6] L. Delannay, M. A. Melchior, J. W. Signorelli, J.-F. Remacle and T. Kuwabara. Influence of grain shape on the planar anisotropy of rolled steel sheets - evaluation of three models. *Comp. Mater. Sci.*, **45**, 739-743, (2009).

[7] L. Brassart, I. Doghri and L. Delannay. Self-consistent modeling of DP steel incorporating short range interactions. Proceedings of ESAFORM 2009, Twente.

Proceedings of the 8th National Congress on Theoretical and Applied Mechanics, May 28-29, Brussels, Belgium.

Finite element modelling of the material behaviour of glass fibre textile reinforced cementitious composite

Tine Tysmans[1], Sigrid Adriaenssens[2], Jan Wastiels[3]
[1, 2, 3] Department of Mechanics of Materials and Constructions, Vrije Universiteit Brussel
Pleinlaan 2, 1050 Brussels – Belgium
email: tine.tysmans@vub.ac.be, sigrid.adriaenssens@vub.ac.be, jan.wastiels@vub.ac.be

Abstract: **The application of glass fibre textile reinforced cementitious composites (GTRC) in doubly-curved shells has numerous advantages over other widely-used materials for free form shapes. In this paper, the suitability of different material models - available in the finite element programs Ansys and Abaqus - for the modelling of glass textile reinforced cementitious composites is evaluated. The use of the concrete smeared crack model in Abaqus for the description of the material response of glass fibre textile reinforced Inorganic Phosphate Cement is validated by means of comparison of a finite element model of a uniaxial and biaxial tension-tension test with experimental results.**

Keywords: **textile reinforced cementitious composite, material modelling, finite element model, shell, smeared cracking**

I. INTRODUCTION

Modern architecture tends towards impressive shapes with three-dimensional curvature. With this evolution, the demand for suitable materials for durable, structurally efficient and (fire)safe free form building applications arises. The most common materials used for three-dimensional forms are membranes, steel-reinforced concrete and the recently more frequently used fibre reinforced plastics. However, all three of these materials have their disadvantages for application in free form shells.

Membranes allow for very light and freeform shapes, but exhibit problems of acoustics, fire-safety and insulation. The necessary membrane prestress requires moreover strong anchorage and increases the total weight and the amount of material used.

Fibre reinforced plastics also allow for free forms, applying them as faces in sandwich panels. This composite system leads to lightweight and stiff but relatively thick structures. For their application in buildings, a fire retardant resin has to be used, which increases the cost significantly and does not lead to fire safe behaviour. An underlying steel framework is usually needed to carry the loads to the foundations.

When properly designed, structurally efficient and slender steel-reinforced concrete shells can be made to cover large spans. The form freedom of steel-reinforced concrete shells is however limited due to the practical difficulties in positioning and shaping the steel reinforcement bars. The high cost associated with placing the reinforcement makes freeform steel reinforced concrete shells an uneconomical solution. Another disadvantage of using steel reinforcement is the necessity of a concrete cover, which causes an increased dead weight and shell thickness (the minimal concrete cover on both sides amounts to minimally three centimetres, depending on the exposure coefficient [1]).

Textile reinforced cementitious composites (TRC) can eliminate some of the disadvantages inherent to steel-reinforced concrete, without losing the advantages. The reinforcement diameter is three orders of magnitude smaller, which eases the manufacturing of doubly-curved shells. When using dense fibre mats instead of short fibre bundles, a high reinforcement ratio and thus high tensile capacity can be achieved, while steel reinforcement can be eliminated. When using only a noncorrosive reinforcement such as glass fibres, the concrete corrosion cover can be omitted and the self weight of the shell decreased. Consequently, thin and fire-resistant small span shells with strongly varying curvature can be built [2].

In order to design and analyse complex-shaped doubly-curved glass fibre textile reinforced cementitious composite (TRC) shells, finite element analyses are necessary: Analytical formulas for the force distribution and critical buckling load are only available for certain shell shapes and are often a simplification of the real stress pattern, assuming only normal forces while neglecting the bending moments occurring in shells. Moreover, when designing with TRC, the nonlinear material behaviour should be taken into account. Finite element modelling software facilitates the calculation of the actual stress pattern in shells, considering the TRC nonlinear mechanical response. When using new materials like TRC, a large amount of effort is invested in implementing the appropriate material modelling. Safe, stable and material efficient TRC shell design must take into account the specific material behaviour of TRC [3]: The constitutive behaviour of TRC is different in tension and compression. In compression, the material can be assumed to behave linearly elastic. In tension, TRC behaves highly nonlinear as a result of cracking of the cementitious matrix and frictional fibre-matrix interaction. In this paper, the possibilities of modelling this behaviour in a commercially available finite element modelling package such as Abaqus and Ansys are reviewed, in general as well as specifically for application in shell design. Consequently, the smeared crack model in Abaqus is validated experimentally. The findings in this paper can also be used as a guideline to model other cementitious composites exhibiting a similar behaviour.

II. Glass fibre textile reinforced cementitous composite: material behaviour

A. TRC composite: material choices

This paper focuses on modelling a cementitious composite consisting of an Inorganic Phosphate Cement (IPC, [4]) matrix, and dense randomly oriented E-glass fibre mats impregnated by the hand lay-up technique to allow for high fibre volume fractions. Glass fibres are economical relative to other types of fibres considering their mechanical properties, and can be added in large amounts. E-glass fibres are cheaper than alkali-resistant glass fibres, but are chemically damaged by the alkalinity of most cementitious matrices. Therefore Inorganic Phosphate Cement (IPC) was chosen as matrix. IPC, developed at the Vrije Universiteit Brussel, has a neutral pH after hardening and facilitates a durable cementitious composite with E-glass fibres. Previous research has indeed shown that the strength loss with time of E-glass fibres embedded in the IPC-matrix is negligible [5]. Moreover, the rheology of the fresh IPC-matrix allows much higher fibre volume fractions (up to 20%) compared with Ordinary Portland Cement fine tuned mortars.

B. Glass fibre textile IPC: uniaxial behaviour

The constitutive behaviour of GTR-IPC under compression is mainly determined by the cementitious matrix and is approximately linear elastic. Its behaviour in tension however is highly nonlinear. Figure 1 shows the stress-strain curve of a 500 mm x 75 mm x 5 mm, 20 fibre volume percent GTR-IPC specimen under increasing tensile load. The test is displacement-controlled (2 mm/min) and performed by an Instron 5885 universal test machine. Strain measurements are executed with a 50 mm double averaging clip-on extensometer.

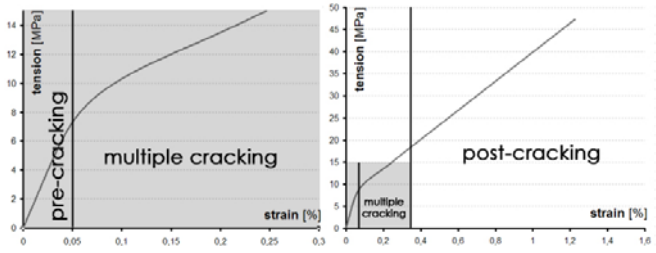

Fig. 1. Experimental stress-strain behaviour of 20 vol.% GTR-IPC under uniaxial tensile load

Three phases can be determined in the tensile behaviour of GTR-IPC ([6]):

- Stage I: pre-cracking. At the beginning of loading, the stiffness of the uncracked composite is determined by the "law of mixtures" for linear elastic composites and is equal to the Young's modulus in compression. Since the volume fraction of the glass fibres is 20%, the stiffness in this first stage is mainly determined by the matrix.

- Stage II: multiple cracking. When exceeding the tensile strength of the IPC matrix, the first cracks appear. At the crack face, the whole tension force has to be carried by the reinforcement. As the amount of fibres is larger than the critical fibre volume fraction, the acting load can be carried and the composite does not fail. As the tension force increases, additional cracks occur: due to the frictional bond between filaments and cementitious matrix, forces are transferred in the IPC matrix until its tensile strength is reached again. The cracking distance and the crack width are determined by the properties of the reinforcement, the bond characteristics between reinforcement and matrix, and the tensile failure strain of the matrix.

- Stage III: post-cracking. In this stabilised crack pattern stage, no further cracks occur. As the load increases, the filaments are strained further until their strength is reached. Failing of the specimen can however also happen as a result of fibre pull-out.

C. The stochastic cracking model

The stochastic cracking model (Cuypers et al. [7]) has been developed to describe the nonlinear tensile behaviour of GTR-IPC and has been validated previously with numerous experimental data. This model is based on the theory of crack formation over a certain stress range and describes stochastic introduction of cracking by means of a 2-parameter Weibull function. The experimental stress-strain data of the 20 fibre volume % GTR- IPC specimens are fitted to this stochastic cracking model and thus reduced to a 2-parameter dependency. Figure 2 shows that the resulting curve fits the experiment well.

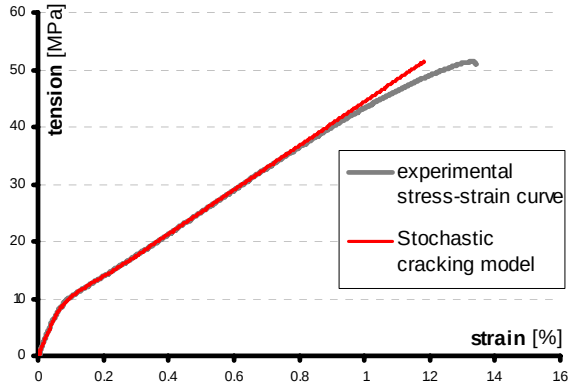

Fig. 2. Experimental stress-strain behaviour of 20 fibre vol.% GTR-IPC and fit to stochastic cracking model

This stochastic cracking model is used to implement the nonlinear tensile behaviour into the finite element program Abaqus. A numerical advantage of using this model over the experimental data is that the model curve does not show any noise and stress is continuously increasing with strain.

III. Finite element material models: selection

A. selection criteria

In this first step, a set of available material models in Ansys 11.0 and Abaqus 6.7.1 which qualify for the modelling of GTRC is selected, and their (dis)advantages are discussed.

The selection criteria are defined as follows:

(1) capacity to implement different constitutive behaviour in tension and compression,

(2) ability to implement nonlinear tensile behaviour,

(3) possible application of these material models on shell and solid elements.

B. Selected material models

Many nonlinear material models exist in commercially available finite element programs, however most are designed for metals and assume the same constitutive behaviour in tension and compression. Criterion 1 significantly reduces the number of appropriate models for TRC. Table 1 gives an overview of models that fit the first two criteria, and the elements onto which they can be assigned. Both Anisotropic and Cast Iron models are typical metal plasticity models. The extended Drucker-Prager model is mostly used to model frictional materials, which are typically granular-like soils and rock, but is also applied to polymeric and composite materials. The concrete models in Abaqus are aimed at steel-reinforced concrete, but can also be used for plain concrete. In what follows, the selected models are discussed more into detail: focus is put on the type of yield surface, the plasticity modelling, the element types onto which they can be assigned and the (dis)advantages of their application in TRC shell design.

TABLE I

CAPACITIES OF PLASTICITY MODELS IN ANSYS AND ABAQUS

Model name	**Crit. 1**	**Crit. 2**	**Elements**
Ansys models			
Anisotropic	✓	bilinear	Link, beam, plane, shell, solid
Cast Iron	✓	✓	Plane (not plane stress), solid, solid shell
Extended Drucker-Prager	✓	✓	Plane (not plane stress), solid
Abaqus models			
Cast Iron	✓	✓	Any stress-displacement element besides plane stress (no shell)
Extended Drucker-Prager	✓	✓	(generalized) plane strain, axisymmetric, plane stress, solid
Concrete	✓	✓	Beam, shell, solid

C. The Anisotropic model

The Ansys anisotropic plasticity option (ANISO, [8]) uses a generalized Hill potential theory and accounts not only for differences in yield strengths in orthogonal directions, but also for differences in yield strengths in tension and compression by using a modified Hill's yield criterion. Hill's criterion is an extension to the von Mises yield criterion to account for the anisotropic yield of the material (see figure 3).

Only bilinear material response can be modelled with the ANISO option (see figure 3). As can be seen on figure 1, the uniaxial tensile material response of TRC can be simplified to a bilinear curve without losing much accuracy. The intersection between the two linear curves with different E-modulus however does not correspond to the actual inflection point of the curve where TRC cracks and becomes plastic. For biaxial (or multiaxial) stress state applications such as TRC shells, the yield criterion must coincide with the actual uniaxial plasticity point and the ANISO model is therefore less applicable to the modelling of the IPC behaviour.

The model can be applied to link, beam, plane, shell and solid elements.

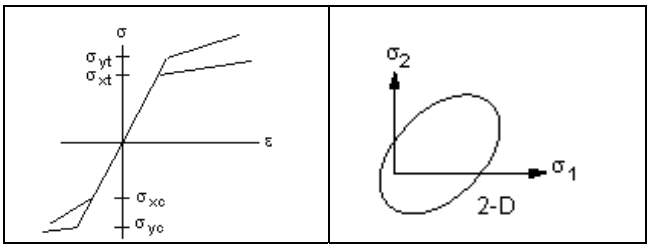

Fig. 3. Stress-strain behaviour and 2D yield surface for the Anisotropic plasticity model (ANISO) in Ansys [8]

D.The Cast Iron plasticity model

The Cast Iron plasticity option in Ansys (CAST, [8]) or Abaqus ([10]) is designed to model grey cast iron, which exhibits markedly different inelastic behaviour in tension and compression. The yield surface combines the von Mises and the Rankine criterion to describe the different behaviour in tension and compression. In tension, the yielding is pressure-dependent and the Rankine maximum stress criterion is used. In compression, the behaviour is pressure independent and the von Mises yield criterion is used.

The model provides elastic-plastic behaviour with different yield strengths, flow, and hardening in tension and compression (see figure 4). An advantage of the model is that the Poisson coefficient can be different for the elastic and the plastic behaviour, as is the case for TRC (ν = 0.3 before cracking and reduction to 0.1 after cracking for randomly oriented glass fibre reinforced IPC [9]). The initial elastic behaviour is isotropic, and is the same in tension and compression as for TRC, and is thus no limitation of the model when applied to TRC.

The model can be applied to solid elements, plane elements which are not plane stress, and solid shells in Ansys. In Abaqus, the model can be used with any stress/displacement element other than elements for which plane stress is assumed (shell, plane stress continuum and membrane elements). The model can also be used for beams and trusses. For general

applications, this Cast Iron plasticity model could offer an interesting material modelling approach. However it can not be applied to general shell elements, only to solid shells (in Ansys) or continuum shells (in Abaqus). The thickness of the latter is determined by the geometry of the structure like for solid elements, but their kinematic and constitutive behaviour is similar to shell elements. Contrarily to shell elements, the geometry is thus not defined by a reference surface with thickness defined through section properties. This limitation is a serious disadvantage in the initial shell design stage; a new model must be build for every change in thickness. The model can however be apt for the final analysis of a TRC structure.

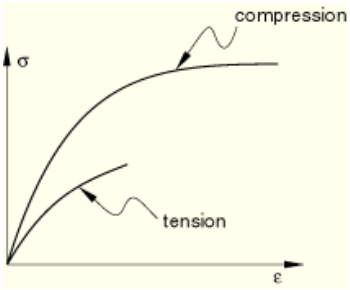

Fig. 4. Stress-strain behaviour for the Cast Iron model in Ansys or Abaqus ([8], [10])

E. The Extended Drucker-Prager model

The Drucker-Prager material model is designed for granular (frictional) materials such as soils, rock, concrete, ceramics and other pressure dependent materials. The model is used to model materials in which the compressive yield strength is greater than the tensile yield strength, such as polymers and TRC composites. The yield surface is a circular cone which corresponds to the outer apices of the hexagonal Mohr-Coulomb yield surface and is thus less conservative (see figure 5).

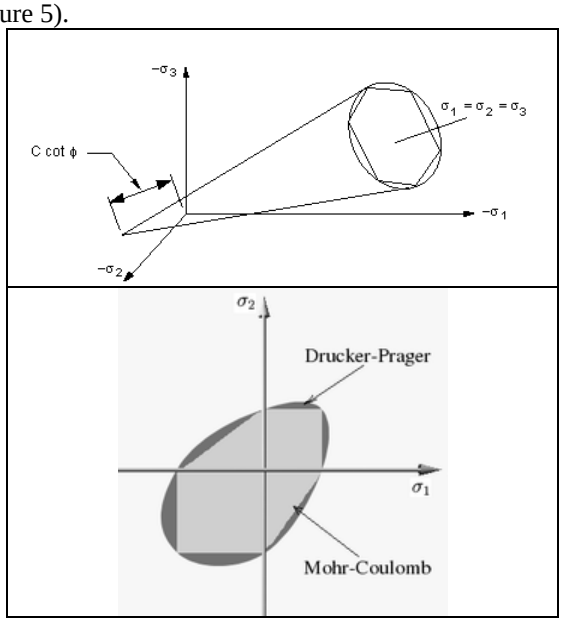

Fig. 5. Drucker-Prager and Mohr-Coulomb yield surface in 3D stress field and plane stress

The Drucker-Prager model in Ansys and Abaqus ([8], [10]) assumes the material response to be elastic – perfectly plastic: The yield surface does not change with progressive yielding and there is no hardening rule. The TRC stress-strain behaviour in tension after cracking can thus not be included in the model.

The Extended Drucker-Prager models in Ansys and Abaqus however do allow a material to harden isotropically. The yield criteria are based on the shape of the yield surface in the meridional plane. In this plane, the yield surface can have a linear, hyperbolic or a general exponent form [10]. Experimental data must be available in terms of cohesion and friction angle, or triaxial test data must be available to calibrate the model.

A multilinear stress- plastic strain post-cracking behaviour can be inserted in the model. The model can be coupled with a linear elastic model, which has the same E-modulus in tension and compression to model the initial linear elastic behaviour of TRC in tension, and the total linear elastic assumed behaviour of TRC in compression.

The Extended Drucker-Prager (EDP, [8]) model in Ansys can only by applied to plane elements which are not plane stress and solids but not to shell or solid shell elements, which makes the model less interesting for its application in finite element shell design. The Extended Drucker-Prager model in Abaqus can be applied to plane strain, generalized plane strain and axisymmetric elements, solids, but also to plane stress elements like shells.

F. The concrete models in Abaqus

Three different concrete models exist in Abaqus: the Smeared Crack model (Abaqus/Standard), the Brittle Cracking model (Abaqus/Explicit) and the Concrete Damaged Plasticity model (available in both Abaqus/Standard and Abaqus/Explicit). The models are designed for steel-reinforced concrete, but can also be implemented to model plain concrete or other quasi-brittle materials, and have naturally the possibility to model different behaviour in tension and compression.

All three concrete models can be applied to beam, shell and solid elements (beam, shell, plane stress, plane strain, generalized plane strain, axisymmetric and three-dimensional elements).

1. The smeared crack concrete model

The smeared crack model in Abaqus/Standard is intended for applications in which the concrete is subjected to essentially monotonic straining. The model must be coupled to a linear elastic model to describe the linear elastic behaviour of TRC in compression and initially in tension. An independent crack detection surface determines if a point fails by cracking (figure 6). This failure surface is a linear relationship between the equivalent pressure stress, p, and the Mises equivalent deviatoric stress, q. Figure 6 also shows the yield surface of concrete in compression. Figure 7 shows the plane stress yield and crack surface. This surface can be fitted to experimental data by the definition of four failure ratios:

- The ratio of the ultimate biaxial compressive stress to the ultimate uniaxial compressive stress.
- The absolute value of the ratio of the uniaxial tensile stress at cracking to the ultimate uniaxial compressive stress.

- The ratio of the magnitude of a principal component of plastic strain at ultimate stress in biaxial compression to the plastic strain at ultimate stress in uniaxial compression.
- The ratio of the tensile principal stress at cracking, in plane stress, when the other principal stress is at the ultimate compressive value, to the tensile cracking stress under uniaxial tension.

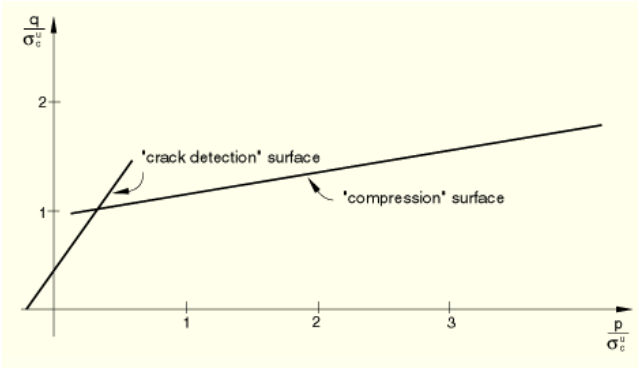

Fig. 6. Crack detection and yield surface

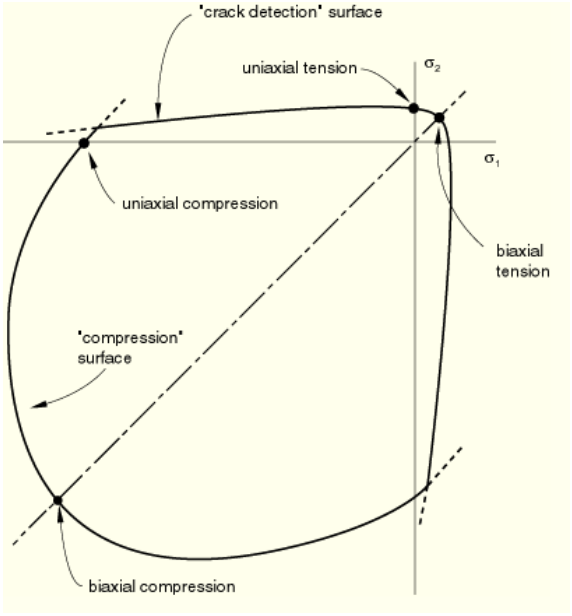

Fig. 7. Plane stress yield and crack surface

In the post-cracking phase, the smeared crack model is originally aimed to describe the strain softening due to the interaction between the steel bars and the concrete. However, tension stiffening with an increasing post-failure stress-strain relation – like for TRC- can also be modelled with the smeared cracking model.

The concrete model is a smeared crack model in the sense that it does not track individual cracks. Constitutive calculations are performed independently at each integration point of the finite element model. The presence of cracks enters into these calculations by affecting the stress and material stiffness associated with the integration point.

2. The brittle cracking model in Abaqus/Explicit

The brittle cracking model is intended for applications in which the concrete behaviour is dominated by tensile cracking and compressive failure is not important. In compression, the material response is assumed to be linearly elastic, and plasticity can not be modelled. This assumption is however a good approximation for the compressive behaviour of TRC and thus not a restriction.

Crack initiation in tension is detected by the simple Rankine criterion (see figure 8, [10]): a point cracks if the maximum principal tensile stress exceeds the material's tensile strength. Post-cracking behaviour of TRC can be inserted by a post-failure stress-strain relation. The brittle cracking model follows the same principle as the smeared crack model: cracks are not tracked, but constitutive calculations are performed at each integration point and 'cracks' affect the stress and material stiffness of that point.

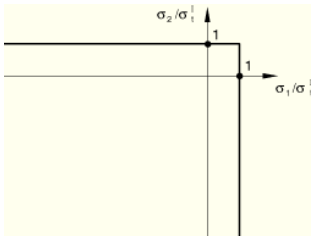

Fig. 8. Rankine criterion in plane stress ([7])

Abaqus/Explicit is a dynamic analysis program. Quasi-static solutions can be obtained however by applying a load slowly enough and hereby eliminating any significant inertia effects (an example of a quasi-static solution in Abaqus Explicit of a steel-reinforced concrete shell modelled with the brittle cracking model can be found in [11]).

3. The concrete damaged plasticity model

The concrete damaged plasticity model in Abaqus/Standard and Abaqus/Explicit is based on the assumption of scalar (isotropic) damage and is designed for applications in which the concrete is subjected to arbitrary loading conditions, including cyclic loading. The model takes into consideration the degradation of the elastic stiffness induced by plastic straining both in tension and compression. The model also accounts for stiffness recovery effects under cyclic loading.

The yield surface is created based on following parameters, which need to be determined experimentally:

- Dilation angle in the p–q plane.
- Flow potential eccentricity: The eccentricity defines the rate at which the hyperbolic flow potential approaches its asymptote.
- The ratio of initial equibiaxial compressive yield stress to initial uniaxial compressive yield stress.
- The ratio of the second stress invariant on the tensile meridian to that on the compressive meridian at initial yield for any given value of the pressure invariant p such that the maximum principal stress is negative.
- Viscosity parameter, used for the visco-plastic regularization of the concrete constitutive equations in Abaqus/Standard analyses.

The nonlinear tensile response after crack initiation of TRC can be inserted by a post-failure stress-strain relation in

tension. A plastic behaviour in compression can also be defined when required. The damaged plasticity model does not track individual cracks either, but follows the principle of the smeared crack model.

G. FE-material model for TRC:

All models described above have the general capacity to describe the nonlinear and anisotropic (in tension and compression) response of textile reinforced cementitious composites. To apply a material model in TRC shell design however, different aspects of the material models must be considered. First of all, the use of shell elements instead of solids leads to a better computational efficiency and is therefore preferred. Moreover, the determination of the minimum shell thickness is more straightforward when only having to adapt the shell thickness. Secondly, shells are loaded by biaxial stress fields, and thus the model's yield/cracking surfaces must correspond well to experiments. Finally, experimental data must be available to calibrate and validate the material model. Therefore, the concrete smeared crack model is evaluated to be the most appropriate model for TRC shell design. In the remainder of this report, the validity of the smeared crack model for TRC material modelling is tested by firstly simulating a uniaxial tensile test in the finite element model Abaqus and checking convergence, and secondly by comparing a FE model of a biaxial tension-tension test to a physical biaxial experiment on a TRC cruciform specimen.

IV. Uniaxial tensile test on GTR-IPC: Simulation in Finite element model

The smeared crack model in Abaqus can model nonlinear uniaxial tensile behaviour after crack initiation, but is initially destined to model strain softening which reaches zero stress at ten times the crack strain [10]. GTR-IPC however exhibits an increasing stress-strain behaviour and moreover over a relative large strain domain: Cracking of the 20 fibre vol% is initiated at approximately 5 MPa or 0.038 % strain while failure occurs at more than 50 MPa or 1.18 % strain. In order to check the applicability of the smeared crack model for this different constitutive behaviour of GTR-IPC than it was designed for, simple uniaxial tension of a thin plate was simulated in Abaqus.

A thin rectangular plate of 200 mm width and 2.2 mm thickness (same as the thinnest zone of the biaxial test specimen, see paragraph V) is subjected to a uniaxial line load (shell edge load) at both sides. Ever increasing loads are applied, augmenting with steps of 2.5 kN total applied load. 20*20 four node linear thin shell elements with six degrees of freedom per node (S4R) and nine integration points per section are used. The stochastic cracking fitting on an experimental tensile test (see figure 2) is implemented in the smeared crack model.

Due to the simple geometry of the specimen, the stresses corresponding to the applied loads can easily be determined. These stresses are plotted in function of the strains obtained with the finite element model and compared to the implemented experimental stress-strain behaviour in figure 9. It can be concluded that the smeared crack model converges and can properly be used to model the highly nonlinear tensile stress-strain behaviour of GTR-IPC for thin plates.

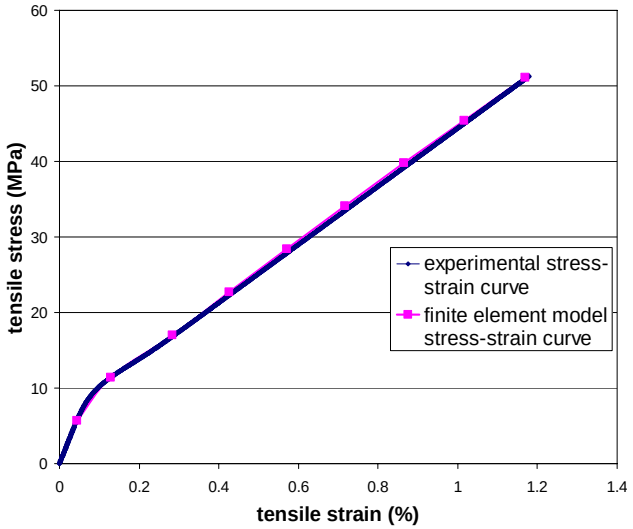

Fig. 9. Comparison of smeared crack modelled and experimental uniaxial tensile stress-strain behaviour

V. Biaxial tensile-tensile test on GTR-IPC: Finite element model and experimental verification

A. Experimental Setup

The biaxial tension-tension test is performed on cruciform specimens in a test set up at the MeMC laboratory at the Vrije Universiteit Brussel, which has been specifically designed for biaxial tests (see figure 10, [12]). The plane biaxial test device uses servo-hydraulic actuators for the application of the loads, which represents a very versatile technique. Four independent actuators (two per loading direction) are used in order to avoid second order effects: when only one actuator per loading direction would be used, the centre of the specimen would move, causing one side of the specimen to bend and resulting in undesired asymmetric strains. The experimental set-up used by the authors consists of four actuators with a close-loop servo control using the measured loads as feedback system that allows the centre of the specimen to stand still. The device has a maximum capacity of 100 kN in both directions and is restricted to tensile loads. No cylinders with hydrostatic bearings were used in the set-up: failure or slip in one arm of the specimen would result in sudden radial forces that could seriously damage the servo-hydraulic cylinders and load cells. To prevent this damage to the testing equipment to occur, hinges are used to connect the specimen to the load cells, and the servo-hydraulic cylinders to the test frame. Using four hinges in each loading direction results in an unstable situation in compression and consequently only tensile loads can be applied.

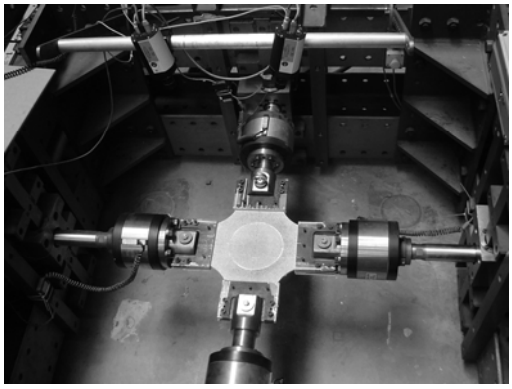

Fig. 10. Biaxial test set up

The geometry of the test specimen is shown in Figure 11. The cruciform specimen is build up out of 3 plates: one full cruciform plate, and two plates with a hole of diameter 200 mm. All three plates have a fibre volume fraction of 20 % and a thickness of 2.2 mm. The three plates are glued together with epoxy glue (Araldite AW 136 H + hardener HY 994) to form the cruciform specimen with reduced thickness of 2.2 mm in the centre. The specimen is fixed with four clamps of 50 mm depth, using the same epoxy glue. Bolting is excluded as a connection method as it would damage the specimen and could cause premature failing in the clamps. As the connection is glued, the applied force can assumed to be uniformly distributed over the length of the clamp.

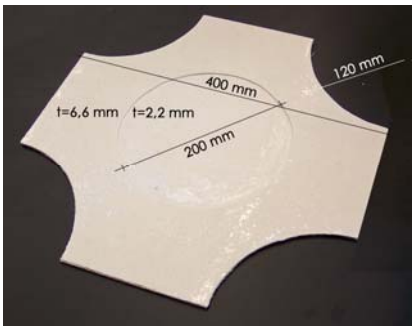

Fig. 11. Geometry cruciform specimen

The specimen is loaded with a force ratio of 1/1 at a speed of 5 kN/min (load controlled). Strains in the midpoint of the cruciform specimen should thus be equal in both principal strain directions. Strain measurements are carried out with Digital Image Correlation, a full-field measuring technique which can be used to retrieve the deformation field of the specimen. A speckle pattern is applied on the top surface of the specimen. Images are taken every 1.2 seconds. By comparing the images in deformed and undeformed state, the deformation field can be obtained. Starting from these data, the strain distribution is calculated over the whole specimen surface at every 0.1 kN. This surface measuring technique allows one to see a possible asymmetrical distribution of the strains before failing, contrarily to measures with strain gauges. These asymmetrical strain distributions can occur due to imperfections of the test specimen or asymmetry of the test set up.

B. Finite element model

Due to the ill definition of the load bearing area of the biaxial specimen, stresses (and thus theoretical strains) in the biaxially loaded zone cannot be calculated from the experimentally applied loads. Therefore only the comparison of the experimental strains, in function of the applied load, with the strains from the finite element model in Abaqus (version 6.7-1) allows validation of the smeared crack model. This comparison will show not only the capacity of the smeared crack model to simulate biaxial crack initiation and post-cracking behaviour, but will also evaluate whether the uncoupled stiffness behaviour assumed in the FE model is valid or whether there is an influence of stresses and cracks in one direction on the material stiffness in the perpendicular direction.

The geometry of the cruciform specimen is inserted as a surface with varying thickness and with 50 mm shorter arms (as this part of the arms is in the clamps during testing). Four node linear thin shell elements with six degrees of freedom per node (S4R) and nine integration points per section are used. The displacement of the four edges is prevented in the vertical z-direction. The tensile force is uniformly applied at the edges as a shell edge load in steps of 2.5 kN. Self weight can be neglected in the model as it is much smaller than, and moreover perpendicular to the applied biaxial loads.

To describe the material response of TRC, initially a linear elastic model is used, with an E-modulus of 13.2 GPa and a Poisson-coefficient of 0.3. For the crack initiation and post-cracking behaviour, the concrete smeared crack model was used. The uniaxial experimental data (see figure 2), fitted on to the stochastic cracking model ([7]), are inserted in this model. The uniaxial tensile cracking stress is put to 5 MPa according to the uniaxial tensile test (see figure 2) and is used to calculate the second failure ratio (the absolute value of the ratio of the uniaxial tensile stress at cracking to the ultimate uniaxial compressive stress). For the other failure ratios, the default values are used. These values are of no importance for the simulation of the tension-tension test. In the future however, tension-compression biaxial experiments should be executed to calibrate the fourth failure ratio, describing the cracking surface when compression occurs in the perpendicular direction. In the doubly-curved shells that will be designed, this is the most occurring stress state. The other failure ratios, describing the compressive yield surface, are of no importance for the shell design, as in practice stresses will be limited to the linear elastic stage of the cementitious composite in compression.

Figure 12 shows the distribution of the maximum principal strains for the modelled biaxial specimen, under a total load of 20 kN/direction. The model shows equal strains of 0.234 % in the centre point of the specimen. This corresponds to principal stresses of 22.3 MPa. The discontinuity at the boundary of the two different plate thicknesses results in stress concentrations, which result in large strain concentrations due to the nonlinear tensile behaviour. According to the model, it is expected that the specimen will fail at this circle boundary, before achieving its failure strength in the centre point of the specimen.

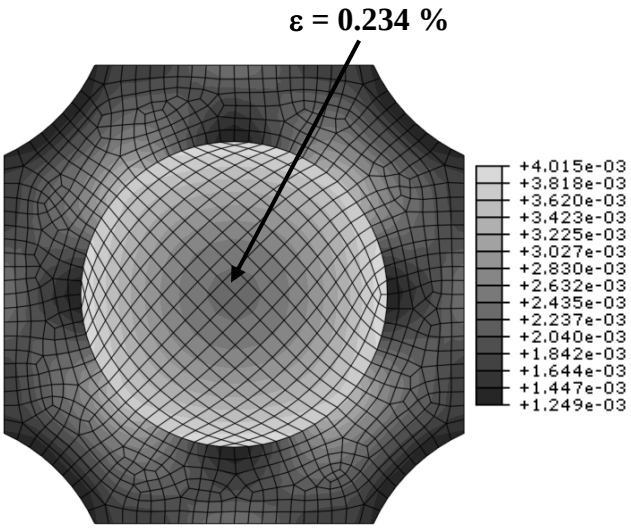

Fig. 12. Maximum principal strain distribution in the cruciform specimen under biaxial load of 20 kN/direction according to finite element model

C.Experimental results and comparison with FEM model

The experimental distribution of the maximum principal strain, observed with DIC under a tensile load of 20 kN per direction, is shown in Figure 13.

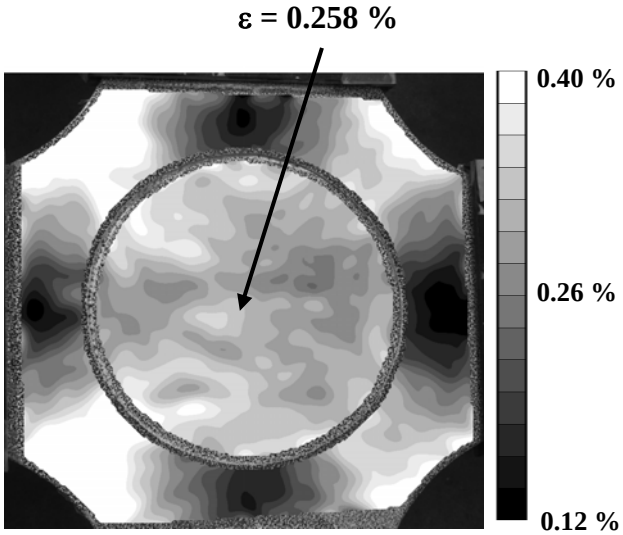

Fig. 13. Experimental maximum principal strain distribution in the cruciform specimen under biaxial load of 20 kN/direction, observed with DIC.

The experimental and FEM strain distribution correspond well. With DIC, no strain values could be obtained near the edges and the thickness change boundary, so additional local measurements (i.e. strain gauges) have to be taken to validate the model, more specifically the stress concentrations at the thickness change edge. Figure 13 also shows that the experimental strain distribution is not fully symmetric, as a result of the inherent material and geometric imperfections of the GTR-IPC specimen.

From the strain data obtained every 0.1 kN with DIC, a force-strain curve is extracted for the first and second principal strain in the centre point of the cruciform specimen (Figure 14). Theoretically both principal strains should be equal and this is approximately the case as can be seen in figure 14. Both curves can be compared with the force-strain data points that can be extracted from the finite element model. Due to convergence problems in the FEM- model, the model curve is limited up to 40 kN. Figure 14 clearly demonstrates that model and experimental data have the same trend line, that the 'cracking' initiation point corresponds well between model and experiment and that the smeared crack model can simulate appropriately the post-cracking behaviour of TRC in biaxial tension-tension.

Figure 14 also demonstrates that cracks in one direction have no influence on the stiffness in the perpendicular direction, as the experimental post-cracking stress strain curve agrees well to the FEM stress-strain curve using the uniaxial experimental data for the smeared crack model.

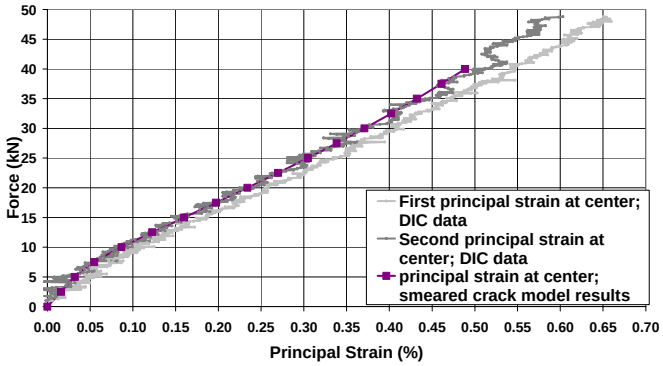

Fig. 14. Force-Principal Strain diagram of biaxial test up to failure and comparison with finite element model results.

VI. Conclusion

This paper provides a good overview of the material models - existing in the finite element programs Abaqus and Ansys - that can be used to model textile reinforced cementitious composites, and of their (dis)advantages. Specifically for the application in TRC shell design, the concrete smeared crack model in Abaqus was selected as most appropriate model. This model was validated by simulating a uniaxial tensile test in the finite element model Abaqus and checking convergence, and by comparing a FE model of a biaxial tension-tension test to a physical biaxial experiment on a TRC cruciform specimen.

Acknowledgements

This research is financially supported by the Fund for Scientific Research in Flanders, Belgium (FWO), through a scholarship for the first author.

References

[1] European Committee for Standardisation (CEN). *Eurocode 2: Design of Concrete Structures – Part 1-1: General rules and rules for buildings: 4: Durability and cover to reinforcement.* CEN, April 2004.

[2] T. Tysmans, S. Adriaenssens, H. Cuypers, J. Wastiels, *Numerical Analysis of Textile Reinforced Concrete Shells with Double Curvature.* Selected for special publication Composites Science and Technology, doi: 10.1016/j.compscitech.2008.09.021.

[3] T. Tysmans, H. Cuypers, S. Adriaenssens, J. Wastiels and O. Remy. *Design of TRC saddle shells, part B: Influence of material nonlinearity.* Presented at the Challenges for Civil Construction 2008 Conference, April 16-19, 2008, Porto.

[4] EP 0 861 216 B1. *Inorganic Resin Compositions, Their Preparation And Use Thereof.*

[5] Cuypers H, Wastiels J, Van Itterbeeck P, De Bolster E, Orlowsky J, Raupach M. *Durability of glass fibre reinforced composites experimental methods and results*. Composites Part A: applied science and manufacturing 37, 2006, pp. 207-215.

[6] Brameshuber W. *Textile Reinforced Concrete: State of the art Report* of RILEM Technical Committee 201-TRC, Aachen, Germany, 2006, pp. 29-35, 135-147.

[7] Cuypers H, Wastiels J. *Stochastic matrix-cracking model for textile reinforced cementitious composites under tensile loading.* Materials and Structures 39; Oct 2006, pp. 777–786.

[8] Ansys 11.0 Documentation

[9] Cuypers Heidi. *Analysis and Design of Sandwich Panels with Brittle Matrix Composite Faces for Building Applications*. Ph.D. Thesis, Vrije Universiteit Brussel, Belgium, Department of Mechanics of Materials and Constructions. November 2001.

[10] Abaqus version 6.7 Documentation: *Abaqus Analysis User's Manual, Abaqus Analysis Theory Manual.*

[11] Abaqus version 6.7 Documentation: Abaqus Example problems Manual; 1.1 Static and Quasi-static stress analyses; *1.1.5 Collapse of a concrete slab.*

[12] Smits A., Van Hemelrijck D., Philippidis T.P., Cardon A. *Design of a cruciform specimen for biaxial testing of fibre reinforced composite laminates.* Composites Science and Technology 66(2006), pp. 946-975.

Michromechanical modeling of composite materials with coupled Viscoelastic-Viscoplastic behaviour.

B. Miled, I. Doghri, L. Delannay
Université Catholique de Louvain
Centre for Systems Engineering and Applied Mechanics (CESAME)
4, Av. G. Lemaître, B-1348 Louvain-la-Neuve, Belgium

email:{bilel.miled, issam.doghri, laurent.delannay}@uclouvain.be

Predicting the impact resistance of short glass fibre-reinforced polyamides is needed in new industrial applications. Our objective is to propose a model which takes account of both the statistical distribution of the fibre orientations and the coupled viscoelastic-viscoplastic behaviour of the surrounding polyamide matrix.

A constitutive model for the matrix is developed which couples linear viscoelasticity and viscoplasticity into a unified set of equations suitable for multi-axial deformation. The model follows the concept of strain decomposition into viscoelastic and viscoplastic strain components. Adjustable parameters in the stress-strain relations are found by fitting the experimental data. The model includes the effects of strain rate and strain hardening.

We develop mean-field homogenization (MFH) models, which are based on assumed relations between average strain fields in each phase, and represent a very cost-effective scale-transition method. However, we also conduct direct finite element (FE) analysis of representative volume elements (RVEs) to analyse the influence of various structural parameters of the reinforced composite, such as the shape and the volume fraction of the fibre, on the macroscopic mechanical response.

We present a general time-discrete linearization procedure for rate-dependent material models, which is developed for viscoelastic-viscoplastic constitutive models. This new formulation leads to an incremental constitutive relation in the time domain which is form-similar to linear thermo-elasticity, and linear mean-field homogenization models can then be used, the other issues –besides linearization- have been resolved.

Both the theory and numerical algorithms have been developed, and numerical simulations are presented. Direct F.E. analyses of RVEs are also carried out in order to verify the predictions of the proposed MFH methods.

References

[1] Klompen E, Constitutive modelling of long and short term behaviour. PhD thesis, University of Eindhoven, 2005.
[2] Tervoort T.A, Smit R.J.M, Brekelmans W.A.M, Goevart L.E. A constitutive equation for the elasto-viscoplastic deformation of glassy polymers. Mech Time-Dep. Mat, 1:269-291, 1998.
[3] Colak O, Modeling deformation behavior of polymers with viscoplasticity theory based on overstress. International Journal of Plasticity, 21:145-160, 2005.
[4] Doghri I, Adam L, Bilger N. Mean-field homogenization of elasto-viscoplastic composites based on a general incrementally affine linearization method, 2008.
[5] Doghri I. Mechanics of deformable solids. Linear, nonlinear, analytical and computational aspects. Springer, Berlin. 2000.

A natural neighbour approach of linear elasticity, elastoplasticity and fracture mechanics based on Fraeijs de Veubeke variational principle

***Li Xiang[1,2], Serge Cescotto[1], Laurent Duchêne[1]**

1 ArGEnCo department, Liège University, Belgium
2 Dalian University of Technology, P. R. China
Email: Xiang.Li@ulg.ac.be

I. INTRODUCTION

In the present paper, we use a new approach of the natural neighbour method based on the Fraeijs de Veubeke (FdV) functional [1]. It is developed for linear elasticity [2], elastoplasticity [3] and for linear fracture mechanics. It uses separate discretizations of the displacements, stresses, strains and support reactions. It is shown that, in the absence of body forces, the derivatives of the nodal shape functions are not required. In addition the numerical calculation of integrals over the area of the domain is avoided: the only area integrals that have to be computed have analytical expressions. This constitutes an advantage over classical meshless and finite elements methods.

II. FRAEIJS DE VEUBEKE FUNCTIONAL FOR LINEAR ELASTICITY

For a 2D elastic solid A with a boundary $S = S_t \bigcup S_u$, the FdV functional writes:

$$\Pi(u_i, \varepsilon_{ij}, \Sigma_{ij}, r_i) =$$

$$\int_A W(\varepsilon_{ij})dA + \int_A \Sigma_{ij}\left[\frac{1}{2}\left(\frac{\partial u_i}{\partial X_j} + \frac{\partial u_j}{\partial X_i}\right) - \varepsilon_{ij}\right]dA$$

$$- \int_A F_i\, u_i\, dA - \int_{S_t} T_i\, u_i\, dS + \int_{S_u} r_i(\tilde{u}_i - u_i)dS$$

where u_i is the displacement field, Σ_{ij} is the stress field, ε_{ij} is the strain field, $\tilde{u}_i$ are displacements imposed on the part S_u of the solid Boundary, r_i are the surface support reactions on S_u, T_i are the surface tractions imposed on S_t, F_i are the body forces and $W(\varepsilon_{ij})$ is the strain energy density.

In the natural neighbour method [4], the domain contains *N* nodes (including nodes on the domain contour) and the *N* Voronoi cells corresponding these nodes are built.

The discretization is based on those Voronoi cells and not on finite elements.

The following hypotheses are made: the assumed strains ε_{ij} and stresses Σ_{ij} are constant over each Voronoi cell, the support reactions r_i are constant over the supported cell edges and the assumed displacements u_i are interpolated by:

$$u_i = \sum_{J=1}^{N} \Phi_J\, u_i^J ,$$

where Φ_J is a Laplace interpolant [5] and u_i^J is the displacement of node *J* corresponding to the Voronoi cell *J*.

Despite of the rich initial discretization, the method eventually leads to a system of equations of the classical type $[M]\{q\} = \{\tilde{Q}\}$ with $[M]$ a symmetric matrix, $\{q\}$ the set of unknown nodal displacements and $\{\tilde{Q}\}$ equivalent nodal forces.

A number of patch tests and other numerical examples show that the method allows solving problems involving nearly incompressible materials without locking.

With this formulation, in absence of body forces, the derivatives of the nodal shape functions are not required and numerical calculation of integrals over the area of the domain is avoided: only integral son the contours of the Voronoi cells are needed which can be performed by a classical Gauss integration scheme.

III. NON LINEAR MATERIALS

The previous method is extended to materially non linear problems from the variational equation:

$$\delta\Pi(\dot{u}_i, \dot{\varepsilon}_{ij}, \Sigma_{ij}, r_i) = \int_A \sigma_{ij}\, \delta\dot{\varepsilon}_{ij}\, dA$$

$$+ \int_A \Sigma_{ij}\left[\frac{1}{2}\left(\frac{\partial \delta\dot{u}_i}{\partial x_j} + \frac{\partial \delta\dot{u}_j}{\partial x_i}\right) - \delta\dot{\varepsilon}_{ij}\right]dA$$

$$+ \int_A \delta\Sigma_{ij}\left[\frac{1}{2}\left(\frac{\partial \dot{u}_i}{\partial x_j} + \frac{\partial \dot{u}_i}{\partial x_j}\right) - \dot{\varepsilon}_{ij}\right]dA$$

$$- \int_A f_i\, \delta\dot{u}_i\, dA - \oint_{S_t} T_i\, \delta\dot{u}_i\, dS$$

$$+ \int_{S_u} \delta r_i(\tilde{\dot{u}}_i - \dot{u}_i)dS - \int_{S_u} r_i\, \delta\dot{u}_i\, dS = 0$$

in which the constitutive stresses are obtained by integration of a system of equations of the type:

$$\dot{\sigma}_{ij} = f_{ij}(\sigma_{ij}, q_{ij}, \dot{\varepsilon}_{ij}) \quad ; \quad \dot{q}_{ij} = h_{ij}(\sigma_{ij}, q_{ij})$$

with q_{ij} a set of internal variables.

In such a case, a step by step procedure with Newton-Raphson iterations is needed for the solution. The most important result of this development is that the advantages mentioned in the linear case (no integration over the domain area, no need for the derivatives of the Laplace interpolant, final equation system of the classical type) are preserved throughout the iteration process. This is true no matter the non linear constitutive equation (elasto-plastic, elasto-visco-plastic, …) and no matter the time integration scheme used to integrate this constitutive equation. It remains also valid if the consistent tangent iteration matrix is computed analytically.

IV. LINEAR FRACTURE MECHANICS

In order to extend the method to linear fracture mechanics problems, a special cell called "Linear Fracture Mechanics Voronoi Cell (LFMVC)" is created at the crack tip

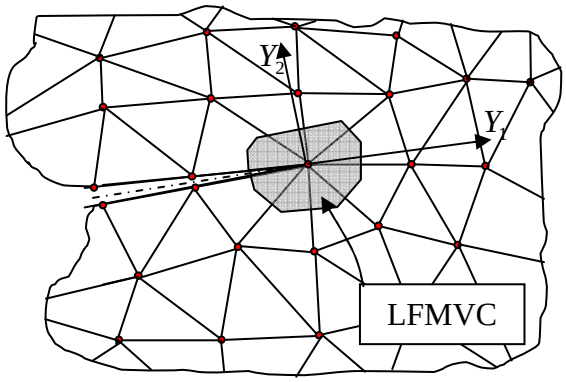

in which the discretization is the following one:

The assumed displacements v_i are interpolated in the local frame (Y_1, Y_2) by the Laplace interpolant as in ordinary Voronoi cells: $v_i = \sum_{J=1}^{N} \Phi_J v_i^J$ where v_1, v_2 are the components of the displacement at a point in the LFMVC with respect to (Y_1, Y_2).

The assumed stresses are interpolated in the local frame (Y_1, Y_2) by: $\{P\} = \{P^O\} + \{P^F\}$

with $\{P^F\} = K_{\Sigma 1}\{H_1\} + K_{\Sigma 2}\{H_2\}$,

$$\{H_1\} = \frac{1}{\sqrt{2\pi r}} \cos\frac{\theta}{2} \begin{Bmatrix} 1 - \sin\frac{\theta}{2} \sin\frac{3\theta}{2} \\ 1 + \sin\frac{\theta}{2} \sin\frac{3\theta}{2} \\ \sin\frac{\theta}{2} \cos\frac{3\theta}{2} \end{Bmatrix}$$

$$\{H_1\} = \frac{1}{\sqrt{2\pi r}} \begin{Bmatrix} -\sin\frac{\theta}{2}(2 + \cos\frac{\theta}{2} \cos\frac{3\theta}{2}) \\ \cos\frac{\theta}{2} \sin\frac{\theta}{2} \cos\frac{3\theta}{2} \\ \cos\frac{\theta}{2}(1 - \sin\frac{\theta}{2} \sin\frac{3\theta}{2}) \end{Bmatrix}$$

where r and θ are the polar coordinates in the local frame.

$K_{\Sigma 1}$ and $K_{\Sigma 2}$ are stress intensity coefficients.

The assumed strains are interpolated in the local frame (Y_1, Y_2) by: $\{\gamma\} = \{\gamma^O\} + [D]\{P^F\}$

where $[D]$ is the inverse of Hooke's elastic tensor.

In absence of body forces, only integrals on the area of the LFMVC have to be computed but they can be calculated analytically. On the other Voronoi cells, the advantages mentioned for the linear elastic case are preserved.

REFERENCES

[1] FRAEIJS de VEUBEKE, BM. Diffusion des inconnues hyperstatiques dans les voilures à longerons couplés. *Bull. Serv. Technique de l'Aéronautique* 1951 N° 24, *Imprimerie Marcel Hayez, Bruxelles.*

[2] S.CESCOTTO, LI X., A natural neighbour method for linear elastic problems based on Fraeijs de Veubeke variational principle, Int. J. Num. Meth. in Eng, 2007; **71**:1081-1101

[3] LI X. , S.CESCOTTO, B. ROSSI, A natural neighbour method for materially non-linear problems based on Fraeijs de Veubeke variational principle, *Acta Mecanica Sinica* (in press)

[4] CUETO E., SUKUMAR N, CALVO B, CEGONINO J and DOBLARE M. Overview and recent advances in natural neighbour Galerkin methods. *Archives of Computational Methods in Engineering 2003*; **10**, 4:307-384.

[5] BELIKOV VV., IVANOV VD, KONTOROVICH VK, KORYTNIK SA, SEMONOV AY. The non Sibsonian interpolation: A new method of interpolation of the values of a function on an arbitrary set of points. *Computational Mathematics and Mathematical Physics 1997*, **37**(1): 9-15

Blast wave attenuation process by shock absorbing material

Croquet Vincent[1], Ndambi Jean Marie[1], Vantomme John[1]
[1]Department of Mechanical Engineering, Royal Military Academy
Renaissancelaan 30, 1000 Brussels – Belgium
email: vincent.croquet@rma.ac.be, jmndambi@rma.ac.be, john.vantomme@rma.ac.be

Abstract: **A shock wave generated during an explosion process can cause several damages to persons and buildings. The nature and the seriousness of this damage depends on the pressure and impulse levels; it is thus of high importance to reduce as much as possible those levels. With this aim, protective materials can be put in front of building walls in such a way that the walls are not loaded beyond the material compressive strength. The choice of the optimal shock absorbing material and thickness can be done using the Hansen movement equations and its analytical and numerical solutions. Based on this model, the paper studies the evolution of the displacement with time respectively, for different combinations of materials (horizontal sandwich paper, metal cans, polyurethane, vertical sandwich paper) and charges (1kg to 5kg), for several weights of caps (1kg, 7.8kg, 15kg), for different material surfaces (0.5 to 10 m²) and for several material thicknesses (1m to 3m). The results show that the use of horizontal sandwich paper allow to increase the explosive charge until 2.5kg equivalent TNT without reaching the material saturation whereas other materials are already saturated. Similarly, an increase of the hat weight allows delaying the saturation process. The simulations made with several thicknesses also show the horizontal sandwich paper as the material reaching the last the saturation. This is a first step in the design of a shock wave absorbing layer in function of blast load scenarios.**

Keywords: **blast wave, attenuation process, absorbing material**

I. INTRODUCTION

The objective of this project is to study the damping possibilities of the shock wave induced by a detonating agent. The typical case consists in comparing the effect of the shock on an unprotected wall to a protected one. Several materials (polyurethane, vertical sandwich paper, horizontal sandwich paper, can assembly) and dimensions will be studied in the aim to maximize the attenuation and this taking into account the environmental geometrical constrains. Schematic views of both situations are presented in figure 1.

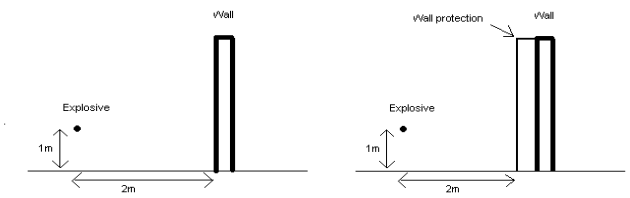

Fig. 1. Schematic view of unprotected and protected wall

II. MATERIAL CHOICE

A. Introduction

The damage nature and seriousness depend on the pressure and impulse level. In the way to optimize the shock absorbing potential, it is interesting to use the material behind its ultimate compressive limit. This practically means that the material isn't totally compacted and that the material transmits less effort in comparison to a case it will be totally rigid. The deformation value is then lower than ϵ_d and the constrain remains at a σ_0 value as shown in figure2.

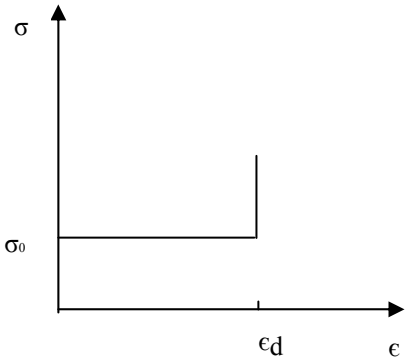

Fig. 2. Constrain evolution vs. deformation

In the aim to compare the aforementioned materials, the Hansen movement equation (cf. Paragraph B) and its analytical solution were implemented in Matlab. Results of the implementation shows the displacement evolution of the material vs. time and allow thus to estimate which materials are totally compressed (saturation) or not. Several cases will be treated to show the influence of the material, the hat (metallic part which distributes uniformly the shock on the material) weight, the material thickness (distance charge-material fixed or variable). Non saturated cases will be highlighted in a summary table.

B. The Hansen equations

The Hansen movement equation is done by the following expression:

$$\left[1+\frac{\varphi_f A}{M_1 \varepsilon_D}\right]\ddot{u}+\frac{\varphi_f A}{M_1 \varepsilon_D}\dot{u}^2+\left(\sigma_0-p(t)\right)\frac{A}{M_1}=0 \quad (1)$$

where

- u is the displacement ;
- ρ_f is the polyurethane density ;
- A is the PUR surface ;
- M_1 is the hat weight ;

- ϵ_d is the PUR strain ;
- σ_0 is the PUR stress behind the wave front ;
- p(t) is the pressure evolution vs time :

$$p(t) = p_0(1 - \frac{t}{t_0}), t \le t_0$$

$$p(t) = 0, t > t_0$$

with

- p_0 the initial pressure ;
- t_0 the positive phase duration.

The solution of equation (1) can be found analytically [2]:

$$\frac{u}{\varepsilon_D l} = 0, \quad t \le 0 \text{ where } \frac{p_0}{\sigma_0} \le 1 ;$$

$$\frac{u}{\varepsilon_D l} = -m + \sqrt{m^2 + 4\xi\left\{\left(1 - \frac{\sigma_0}{p_0}\right)\left[\frac{t}{t_0}\right]^2 - \frac{1}{3}\left[\frac{t}{t_0}\right]^3\right.} ,$$

$$0 < t \le t_0 \text{ and } \frac{p_0}{\sigma_0} > 1 ;$$

$$\frac{u}{\varepsilon_D l} = -m + \sqrt{m^2 + 4\xi\left\{-\frac{1}{3} + \left[\frac{t}{t_0}\right] - \frac{\sigma_0}{p_0}\left[\frac{t}{t_0}\right]^2\right.}$$

$$, t_0 < t \le \frac{1}{2}\frac{p_0}{\sigma_0}t_0 \text{ and } \frac{p_0}{\sigma_0} > 2 ;$$

$$\frac{u}{\varepsilon_D l} = -m + \sqrt{m^2 + \xi\left\{\frac{p_0}{\sigma_0} - \frac{4}{3}\right.}, \quad t > \frac{1}{2}\frac{p_0}{\sigma_0}t_0 \quad \text{and}$$

$$\frac{p_0}{\sigma_0} > 2 .$$

where

- $m = \frac{M_1}{M_0}$;
- $\xi = \frac{I}{M_0 P_0 \varepsilon_D l}$ with $I = \frac{1}{2} p_0 t_0 A$ and $P_0 = p_0 A$;
- M_0 is the PUR density;
- l is the PUR thickness.

C. *Influence of the material*

The implementation has been done with material dimensions of 1m high, 1m breadth and 1m thickness; an explosive charge disposed at 2m distance from the protective wall and 1m from the ground, a hat weight of 7.5kg.

We observe that for 1kg equivalent TNT, all kind of material are usable (no saturation); the material presenting the lowest σ_0 value will thus be preferred. For 2kg equivalent TNT, the choice is restraint to polyurethane and horizontal sandwich paper. For 2.5kg equivalent TNT, only the horizontal sandwich paper allows to avoid the saturation. Above this last weight, any abovementionnated materials allow to avoid the saturation process. Non saturated cases (X) are presented in table I.

TABLE I

	vertical sandwich paper	can assembly	PUR	Horizontal sandwich paper
1kg eq.TNT	X	X	X	X
2kg eq.TNT			X	X
2.5kg eq.TNT				X
3kg eq.TNT				
4kg eq.TNT				
5kg eq.TNT				

Some results are presented in figure 3.

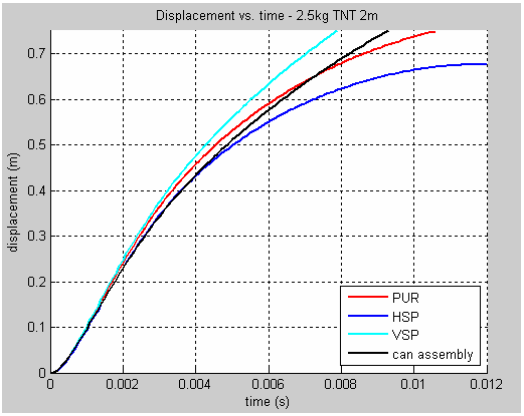

Fig. 3. Evolution of the displacement vs. time

D. *Influence of the hat weight*

The implementation has been done with: PUR material, material dimensions of 1m high, 1m breadth and 1m thickness; an explosive charge disposed at 2m distance from the protective wall and 1m from the ground and a hat surface of 1m².

We observe that for 1kg and 2kg equivalent TNT, all hat weight are usable. For 2.5kg, the choice is restraint to a 15 kg hat weight. Above this quantity, the use of the three hat weight lead to saturation; it will thus be necessary to increase the hat weight. Generally, we can say that whatever the explosive charge, an increase of the hat weight lead to a decrease of the displacement value. This can be explained by using the formula F=m*a where F represents the force, m the mass and a the acceleration. During the explosion process, a

force equilibrium occurs between the damping material and the hat.

Considering the force constant, a mass reduction then lead an acceleration increase, thus to a speed acceleration and thus to a displacement increase.

Non saturated cases (X in the table) are presented in table II.

TABLE II

	M=1kg	M=7.5kg	M=15kg
1kg eq.TNT	X	X	X
2kg eq.TNT	X	X	X
2.5kg eq.TNT			X
3kg eq.TNT			
4kg eq.TNT			
5kg eq.TNT			

Some results are presented in figure 4.

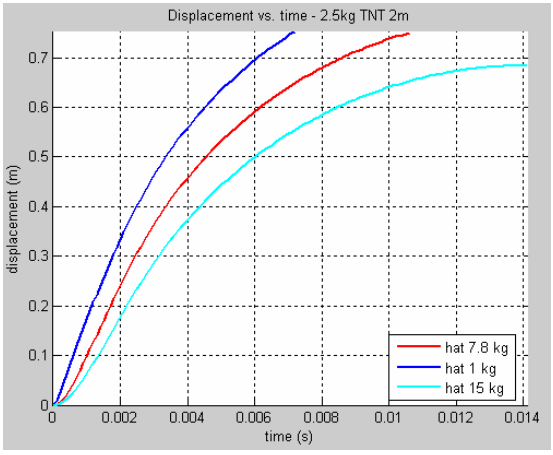

Fig. 4. Evolution of the displacement vs. time

E. Influence of the material thickness

The implementation has been done with PUR material, material dimensions of 1m high, 1m breadth and variable thickness; an explosive charge disposed at 2m distance from the protective wall, 1m from the ground and a hat weight of 7.5kg.

1) Distance charge-material fixed (future building)

For a 1m thickness (l parameter), any material reach the saturation if the charge is 1kg equivalent TNT. For a 2kg charge, only the polyurethane and the horizontal sandwich paper don't sature; and for a 2.5kg charge, only the horizontal sandwich paper doesn't sature. Above this charge, all materials reach the saturation.

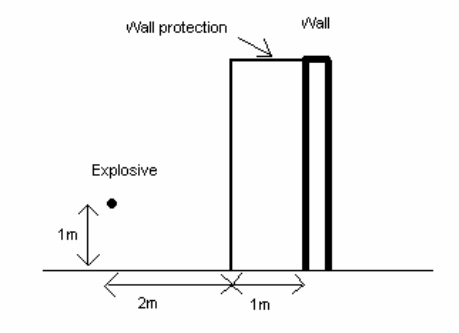

Fig. 5. Protected wall d=2m l=1m

Some of the results are presented in figure 6.

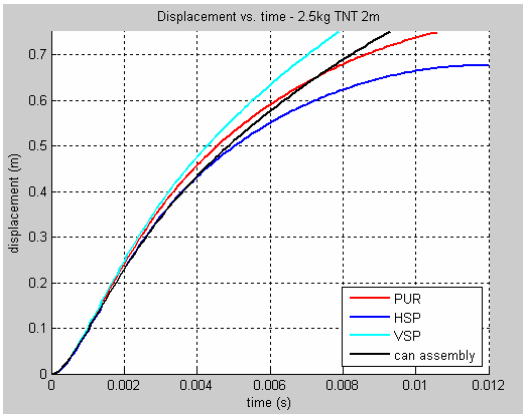

Fig. 6. Evolution of the displacement vs. time

For a 2m thickness, any material reach the saturation as still as the charge remains lower or equal to 2.5kg. For a 3kg charge, only the polyurethane and the horizontal sandwich paper don't sature; and for a 4kg charge, only the horizontal sandwich paper doesn't sature. Above this charge, all materials reach the saturation.

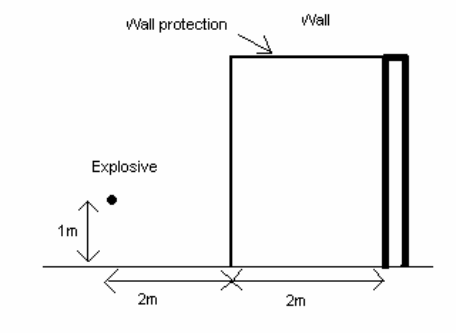

Fig. 7. Protected wall d=2m l=2m

Some of the results are presented in figure 8.

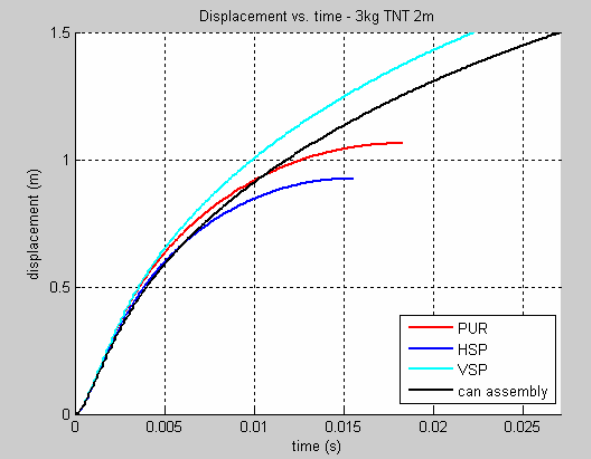

Fig. 8. Evolution of the displacement vs. time

For a 3m thickness, any material reach the saturation as still as the charge remains lower or equal to 3kg. For a 4kg and 5kg charge, only the polyurethane and the horizontal sandwich paper don't sature.

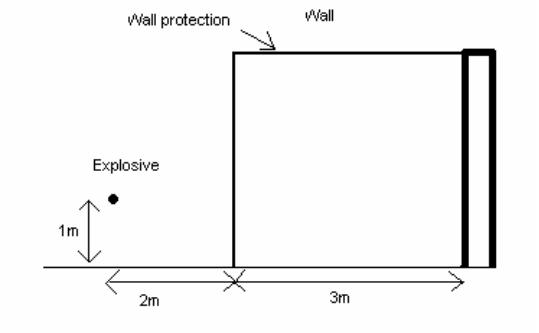

Fig. 9. Protected wall d=2m l=3m

Some of the results are presented in figure 10.

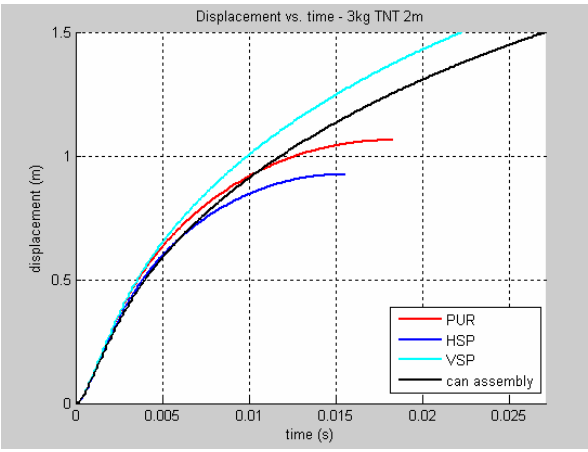

Fig. 10. Evolution of the displacement vs. time

Non saturated cases are presented in table III.

TABLE III

	l=1m d=2m	l=2m d=2m	l=3m d=2m
1kg eq.TNT	SPH/PUR/ SPV/C	SPH/PUR/ SPV/C	SPH/PUR/ SPV/C
2kg eq.TNT	SPH/PUR	SPH/PUR/ SPV/C	SPH/PUR/ SPV/C
2.5kg eq.TNT	SPH	SPH/PUR/ SPV/C	SPH/PUR/ SPV/C
3kg eq.TNT	/	SPH/PUR	SPH/PUR/ SPV/C
4kg eq.TNT	/	SPH	SPH/PUR
5kg eq.TNT	/	/	SPH/PUR

SPH: sandwich paper horizontal, PUR: polyurethane, SPV: sandwich paper vertical, C: can assembly, l: material thickness, d: distance explosive-wall

2)Distance charge-material variable (existing building)

For a 1m thickness (th parameter) (cf.figure10), any material reach the saturation as still as the charge remains lower or equal to 4kg. For a 5kg charge, only the polyurethane and the horizontal sandwich paper don't sature.

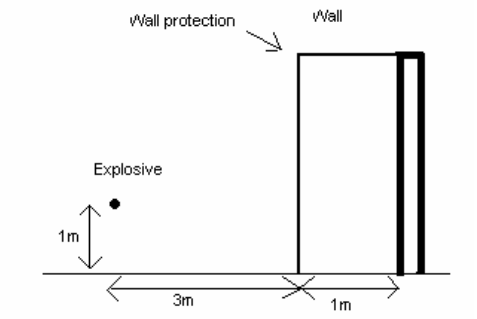

Fig. 11. Protected wall d=3m l=1m

Some of the results are presented in figure 12.

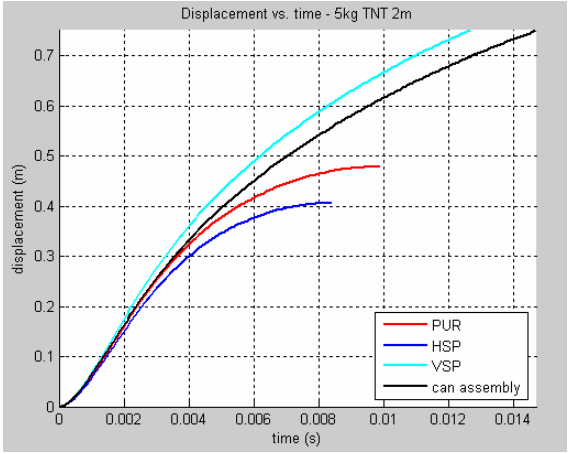

Fig. 12. Evolution of the displacement vs. time

For a 2m thickness, any material reach the saturation as still as the charge remains lower or equal to 2.5kg. For a 3kg

charge, only the polyurethane and the horizontal sandwich paper don't sature; and for a 4kg charge, only the horizontal sandwich paper doesn't sature. Above this charge, all materials reach the saturation.

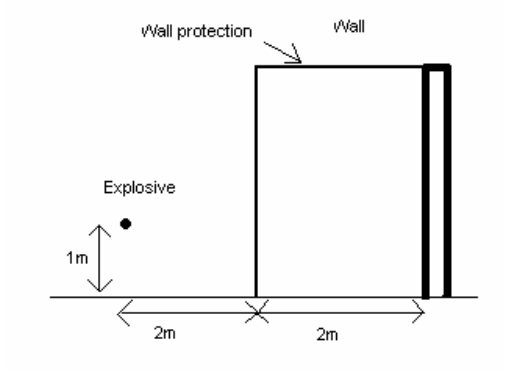

Fig. 13. Protected wall d=2m l=2m

Some of the results are presented in figure 14.

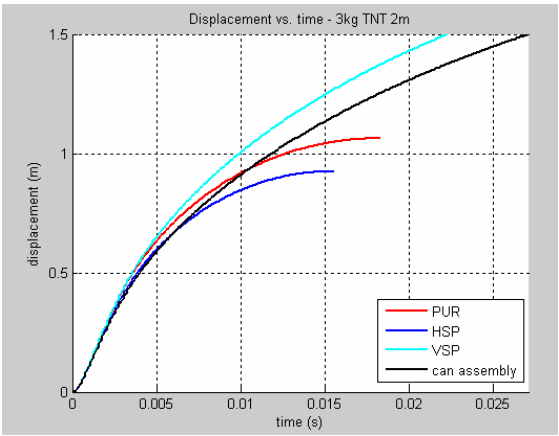

Fig. 14. Evolution of the displacement vs. time

For a 3m thickness, any material reach the saturation as still as the charge remains lower or equal to 1kg. Above this charge, only the polyurethane and the horizontal sandwich paper don't sature.

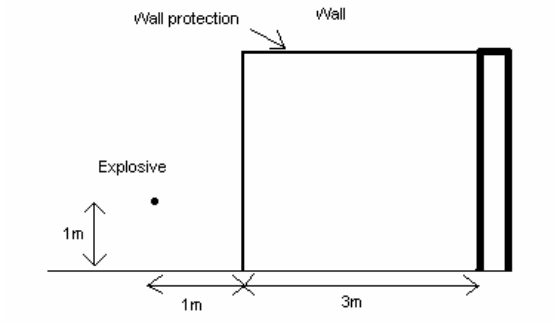

Fig. 15. Protected wall d=1m l=3m

Some of the results are presented in figure 16.

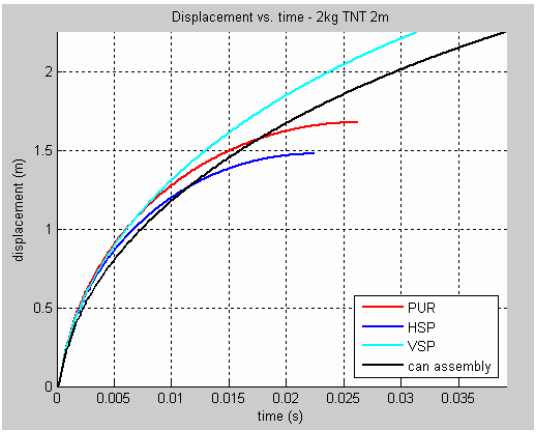

Fig. 16. Evolution of the displacement vs. time

Non saturated cases are presented in table IV.

TABLE IV

	l=1m d=3m	l=2m d=2m	l=3m d=1m
1kg eq.TNT	SPH/PUR/ SPV/C	SPH/PUR /SPV/C	SPH/PUR/ SPV/C
2kg eq.TNT	SPH/PUR/ SPV/C	SPH/PUR /SPV/C	SPH/PUR
2.5kg eq.TNT	SPH/PUR/ PV/C	C SPH/PUR/ SPV/C	SPH/PUR
3kg eq.TNT	SPH/PUR/ SPV/C	SPH/PUR	SPH/PUR
4kg eq.TNT	SPH/PUR/ SPV/C	SPH	SPH/PUR
5kg eq.TNT	SPH/PUR	/	SPH/PUR

SPH: sandwich paper horizontal, PUR: polyurethane, SPV: sandwich paper vertical, C: can assembly, l: material thickness, d: distance explosive-wall

F. Influence of the hat surface (constant hat weight)

The implementation has been done with 1kg equivalent TNT charge, PUR material, material dimensions of 1m high, 1m breadth and 1m thickness; an explosive charge disposed at 2m distance from the protective wall, 1m from the ground and 7.5 kg hat weight.

We observe that for a hat surface equal to the material surface, the different materials don't reach the saturation. The influence appears for the PUR since a surface ratio of 3 and for the SPH since a ratio of 3.5.

Non saturated cases (X) are presented in table V.

TABLE V

Surfaces ratio	vertical sandwich paper	can assembly	PUR	Horizontal sandwich paper
"1:1"	X	X	X	X
"2:1"			X	X
"3:1"			X	X
"4:1"				X
"5:1"				

III. CONCLUSION

The use of protective materials disposed in front of the building walls is optimized when the wall are not loaded beyond the materials compressive strength. The choice of the optimal shock absorbing material and thickness can be done using the Hansen movement equations and its analytical and numerical solutions. The result of the simulations show that the use of horizontal sandwich paper allow to increase the explosive charge until 2.5kg equivalent TNT without reaching the material saturation whereas other materials are already saturated. Similarly, an increase of the hat weight allows delaying the saturation process. The simulations made with several thicknesses also show the horizontal sandwich paper as the last one reaching the saturation and thus being the most appropriate to protect walls.

REFERENCES

[1] D. W. Hyde ; *CONWEP : Conventional Weapons Effect-Collection of conventional weapons effects calculations from the equations and curves of TM 5-855-1,* "Fundamentals of Protective Design for Conventional Weapons", 1992.

[2] Hanssen, A.G., Enstock, L., Langseth, M., *Close –range blast loading of aluminum foam panels, International Journal of Impact Engineering*, 27, 593-618, 2007.

[3] De Wolf, K., Lecompte, D., Vantomme, J., Pequet, E., Rustema, R., Borgers, J., *Blast wave mitigation capacity of a can assembly part I: experimental results*, International Journal of Impact Engineering, 2007.

Proceedings of the 8th National Congress on Theoretical and Applied Mechanics, May 28-29, Brussels, Belgium.

Determination of the material damping ratio in the soil using the half-power bandwidth method

S. A. Badsar, M. Schevenels, and G. Degrande
Department of Civil Engineering, K.U.Leuven
Kasteelpark Arenberg 40, B-3001 Leuven, Belgium
e-mail: sayedali.badsar@bwk.kuleuven.be

Abstract— **This paper presents a technique for the determination of the material damping ratio of shallow soil layers. It is based on the Spectral Analysis of Surface Waves (SASW) test. The technique is an alternative to existing methods, where the damping ratio is determined from the spatial decay of the Rayleigh wave. These methods are based on the hypothesis that the response of the soil in the SASW test is due to a single mode surface wave. Therefore, the resulting attenuation curve can become erroneous when higher modes contribute to the soil's response. Moreover, in these methods, the estimate of the attenuation curve is based on an estimate of the geometric spreading function. The latter is computed using the shear wave velocity of the soil, which is determined by inversion of the experimental dispersion curve. Errors in the experimental dispersion curve and in the inversion procedure lead to an erroneous geometric spreading factor and, consequently, experimental attenuation curve. In the proposed technique, the wave field recorded in the SASW test is transformed to the frequency-wavenumber domain by means of a discrete approximation to the Hankel transformation. The resulting (experimental) spectrum exhibits peaks corresponding to the Rayleigh modes. The peak corresponding to the fundamental Rayleigh wave is identified and used to determine the experimental dispersion and attenuation curves and, subsequently, the soil profile. The dispersion curve is derived from the peak's position, while the attenuation curve is derived from its width, using the half-power bandwidth method. In this technique there is no need for calculating the geometric damping. The occurrence of higher Rayleigh modes does not affect the attenuation curve associated with the fundamental Rayleigh wave, as higher modes appear as separate peaks in the f-k spectrum and do not interfere with the peak corresponding to the fundamental Rayleigh wave. The method is applied to data collected from a test site Lincent in Belgium.**

Keywords— **Material damping, Attenuation, Rayleigh waves, Half-power bandwidth, In-situ tests, Shear modulus.**

I. Introduction

THE The Spectral Analysis of Surface Waves (SASW) method aims to determine the dynamic shear modulus and the material damping ratio of shallow soil layers. It is based on an in situ experiment where Rayleigh waves are generated by means of an impact hammer, a falling weight, or a hydraulic shaker. The resulting wave field is recorded by a number of sensors at the soil's surface and used to determine the dispersion and attenuation curves of the soil. An inverse problem is solved to identify the corresponding soil profile.

The SASW method has been utilized in different applications over the past couple of decades. It has been used to investigate pavement systems [14], to assess the quality of ground improvement [2], to determine the thickness of waste deposits [9], and to identify the dynamic shear modulus [12], [13] and the material damping ratio [5], [10], [16] of shallow soil layers. The shear wave velocity and material damping ratio are important for the calculation of vibrations in the free field or in buildings due road or rail traffic, industrial machinery, and construction activities.

In order to determine dynamic soil properties, both in situ and laboratory methods have been used in the literature. Laboratory measurements like resonant column or torsional shear tests are often used to determine properties of cohesive soils, but for non-cohesive soils, there is a risk of sample disturbance. Although laboratory tests are useful for parametric studies of soil properties [16], in situ tests preserve the natural status of the soil and avoid sample disturbance. Moreover, a larger volume of the soil is examined when performing in situ tests, avoiding a bias in the results due to local variations of the properties.

Borehole techniques are well known for in situ determination of soil properties. These techniques have a good resolution at large depths compared to surface wave methods. On the other hand, surface wave methods have the same range of operating frequencies as the frequency range of interest in the ground vibration analysis, and they are non-invasive tests to save time and money [20].

The surface wave methods established by Lai [10] and Rix et al. [16], and extended by Foti [5], to determine the material damping ratio, are based on the hypothesis that the response of the soil in the SASW test is due to a single surface wave [11]. If multiple surface waves contribute to the response (e.g. due to the high stiffness contrast or the inclusion of a softer layer), this assumption does not hold and the resulting attenuation curves are affected. Moreover, in these methods, the estimate of the attenuation curve is based on an estimate of the geomet-

ric spreading function. The latter is computed using the shear wave velocity of the soil, which is determined by inversion of the experimental dispersion curve. Errors in the experimental dispersion curve and in the inversion procedure (e.g. due to the non-uniqueness of the problem) lead to an incorrect estimate of the geometric spreading factor and, consequently, the experimental attenuation curve.

In this paper, an alternative method for the determination of the material damping ratio is proposed, using the half-power bandwidth method. The half-power bandwidth method has originally been developed in the field of structural dynamics to determine the modal damping ratio of a structure from the width of the peaks in the structure's frequency response function. It is applied to the frequency-wavenumber content of the soil's response in this research.

This paper is organized as follows: section 2 elaborates the f-k analysis using the half-power bandwidth method. In section 3, the method is used to determine the soil properties of a test site in Belgium.

II. f-k ANALYSIS USING THE HALF-POWER BANDWIDTH METHOD

An alternative method to determine the dispersion and attenuation curves is presented. This method is based on the peaks in the f-k spectrum $\tilde{H}^{\mathrm{E}}_{zz}(k_r,\omega)$. The spectrum is calculated by transforming the transfer function $\hat{H}^{\mathrm{E}}_{zz}(r,\omega)$ to the frequency-wavenumber domain according to the procedure proposed by Forbriger [3]. This procedure is similar to a classical slant stack analysis [17], but the Fourier transformation is replaced by a Hankel transformation. In this way, the cylindrical symmetry of the problem is properly accounted for. The f-k spectrum of the response is defined as:

$$\tilde{H}^{\mathrm{E}}_{zz}(k_r,\omega)=\int_0^{\infty}\hat{H}^{\mathrm{E}}_{zz}(r,\omega)J_0(k_r r)\,r\,dr \tag{1}$$

where a tilde above a variable denotes its representation in the frequency-wavenumber domain and $J_0(k_r r)$ is the zeroth order Bessel function of the first kind. Equation (1) is approximated by truncation of the integral at $r=r_M$ (the position of the farthest receiver) and the discretization of the integration domain between $r=0$ and $r=r_M$. In order to mitigate the effect of the truncation of the integration domain, an exponential window $\hat{w}(r,\omega)$ is applied to the data in the frequency-space domain. The application of an exponential window can be considered as the introduction of artificial damping, resulting in a higher spatial attenuation of the surface waves. The window $\hat{w}(r,\omega)$ is applied for each frequency ω independently and defined as:

$$\hat{w}(r,\omega)=e^{-\hat{A}_{\mathrm{art}}(\omega)r} \tag{2}$$

The exponent $\hat{A}_{\mathrm{art}}(\omega)$ is chosen so that:

$$\frac{|\hat{w}(r_{\max},\omega)\hat{H}^{\mathrm{E}}_{zz}(r_{\max},\omega)|}{|\hat{w}(r_{\min},\omega)\hat{H}^{\mathrm{E}}_{zz}(r_{\min},\omega)|}=q \tag{3}$$

where $r_{\min}$ and $r_{\max}$ denote the positions of the nearest and the farthest receiver, respectively. For frequencies ω where equation (3) results in a negative exponent $\hat{A}_{\mathrm{art}}(\omega)$, this exponent is set equal to zero. The application of the window ensures that the amplitude ratio of the response at the farthest and the nearest receiver does not exceed a value q. A value $q=10^{-4}$ has been used here to avoid overestimation of the attenuation coefficient at the low frequencies.

Following Forbriger [3], the Bessel function $J_0(k_r r)$ in equation (1) is replaced by a zeroth order Hankel function $H_0^{(1)}(k_r r)/2$ to account for the fact that the wave field only consists of outgoing waves. The following approximation is thus obtained:

$$\tilde{H}^{\mathrm{E}}_{zz}(k_r,\omega)=\frac{1}{2}\sum_{j=1}^{M}\hat{H}^{\mathrm{E}}_{zz}(r_j,\omega)H_0^{(1)}(k_r r_j)\hat{w}(r_j,\omega)r_j\Delta r_j \tag{4}$$

where M is the number of receivers, r_j is the source-receiver distance for receiver j, and $\Delta r_j=r_j-r_{j-1}$. The transfer function $\hat{H}^{\mathrm{E}}_{zz}(r,\omega)$ is normalized at each frequency to the corresponding maximum value.

The half-power bandwidth is defined as the width of the peak $\Delta\omega$ where the magnitude of the frequency response function is $1/\sqrt{2}$ times the peak value [1]. For a weakly damped single degree of freedom system, the half-power bandwidth equals (figure 1):

$$\Delta\omega=2\xi\omega_{\mathrm{res}} \tag{5}$$

where ω_{res} is the resonance frequency. This procedure can be generalized to multi-degree of freedom systems with widely spaced resonance frequencies.

The half power bandwidth method is also applicable to the representation of the response in the frequency-wavenumber domain. At every frequency ω, the half-power bandwidth $\Delta k(\omega)$, defined as the difference $k_2(\omega)-k_1(\omega)$ between the wavenumbers $k_1(\omega)$ and $k_2(\omega)$, is equal to (figure 2):

$$\Delta k(\omega)=2\xi(\omega)k_{\mathrm{res}}(\omega) \tag{6}$$

with $\xi(\omega)$ a frequency dependent damping coefficient and $k_{\mathrm{res}}(\omega)$ the wavenumber where the response is maximum:

$$k_{\mathrm{res}}(\omega)=\frac{k_2(\omega)+k_1(\omega)}{2} \tag{7}$$

Introducing the linear relation $\alpha^{\mathrm{E}}_{\mathrm{R}}(\omega)=\xi(\omega)k_{\mathrm{res}}(\omega)$ between the damping coefficient $\xi(\omega)$ and the attenuation coefficient $\alpha^{\mathrm{E}}_{\mathrm{R}}(\omega)$ into equation (6), the following expression

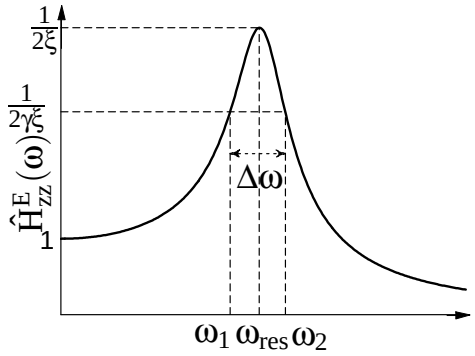

Fig. 1. half-power bandwidth method.

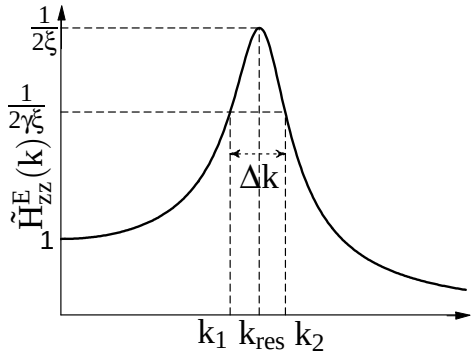

Fig. 2. half-power bandwidth method in the wavenumber domain.

is obtained for the attenuation coefficient $\alpha^E_R(\omega)$:

$$\alpha^E_R(\omega) = \frac{k_2(\omega) - k_1(\omega)}{2} \tag{8}$$

In order to avoid mixing of adjacent peaks, it is suggested to use a larger scale factor γ than $1/\sqrt{2}$ to ensure that the calculated attenuation coefficient $\alpha^E_R(\omega)$ corresponds to the picked peak:

$$\alpha^E_R(\omega) = \frac{k_2(\omega) - k_1(\omega)}{2\sqrt{\gamma^{-2} - 1}} \tag{9}$$

A value of $\gamma = 0.99$ is used in this paper.

In this alternative approach, the occurrence of multiple Rayleigh modes does not affect the attenuation curve of either the fundamental or the dominant Rayleigh wave, as all modes appear as separate, non-interfering peaks in the frequency-wavenumber spectrum. Moreover, the experimental attenuation curve is derived directly from the experimental data, avoiding the use of a (possibly incorrect) estimate of the soil's shear wave velocity.

III. Test site in Lincent

The method discussed in the previous sections is applied to data collected at a site in Lincent, Belgium, next to the HST line L2 between Brussels and Liège. Several Seismic Cone Penetration Testing (SCPT) and SASW tests have been performed on this site. In preparation of the construction of the high speed railway track, borings and cone penetration tests have been carried out. The borings reveal the presence of a silt top layer with a thickness of about 1.2 m, followed by a fine sand layer reaching to a depth of 3.2 m and a sequence of very stiff layers of arenite and clay [6], [7]. The depth of the ground water table has been monitored from August 1993 to July 1997. It exhibits seasonal fluctuations between 6.0 m to 12.2 m, with an average value of 10.4 m [6].

The most recent SCPT tests on the site in Lincent have been performed in May 2003 [6], [7]. These tests have allowed for the determination of the shear wave velocity up to a depth of 6 m: it increases almost linearly from 160 m/s at 1 m depth to 280 m/s at 6 m depth. Accounting for the seasonal fluctuations of the soil properties at this site, these results correspond well to the SASW results. The material damping ratio has also been derived from the SCPT tests [8], resulting in a highly uncertain value that varies between 0.00 and 0.06.

The most recent SASW test on the site in Lincent has been performed in February 2008 [18]. Use has been made of 104 receivers, located up to 104 m from the source. In order to filter out the background noise, 100 hammer impacts on a 40 cm $\times$40 cm $\times$8 cm aluminum foundation are averaged. The averaged time history of the vertical displacement $u^E_z(r,t)$ at the surface is shown in figure **??**.

A Hankel transformation is applied to the experimental transfer function $\hat{H}^E_{zz}(r,\omega)$ to give the f-k spectrum $\tilde{H}^E_{zz}(k_r,\omega)$ (figure 3). Using the relation between the phase velocity and the wavenumber $C^E_R(\omega) = \omega/k^E_R(\omega)$, the vertical axis in figure 3 is shown in terms of the phase velocity instead of the wavenumber. The fundamental dispersion curve between 15 Hz and 70 Hz is clearly visible in this figure. Below 15 Hz, the accuracy of the transfer function $\hat{H}^E_{zz}(r,\omega)$ and, consequently, the frequency-wavenumber spectrum $\tilde{H}^E_{zz}(k_r,\omega)$ is too low for a reliable estimation of the dispersion curve $C^E_R(\omega)$. The largest wavelength λ_{Rmax} that can be measured is 15 m. Following Foti [4], the maximum depth that can be investigated with this wavelength is $\lambda^E_{Rmax}/3$. This allows for the determination of the soil properties up to a depth of about 5 m. Above 70 Hz, the trace of the first dispersion curve disappears. Theoretically, the highest frequency where the dispersion curve $C^E_R(\omega)$ can be estimated is determined by the distance between two adjacent receivers. The smallest wavelength that can be measured with 1 m distance between ad-

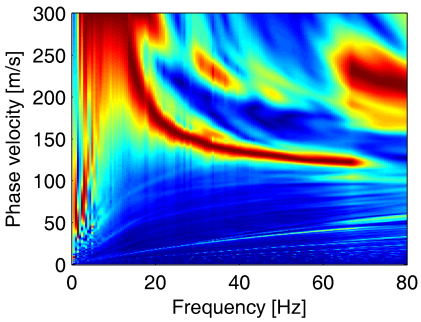

Fig. 3. The experimental transfer function $\tilde{H}_{zz}^{E}(C_R, \omega)$ measured at the site in Lincent.

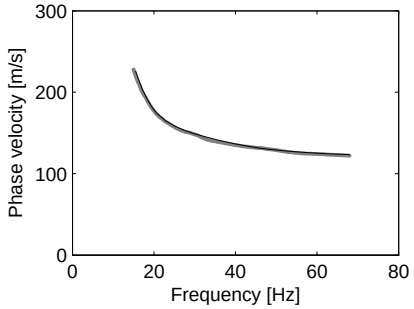

Fig. 4. The experimental (gray line) and identified (black line) dispersion curve.

jacent receivers equals 2 m. In the high frequency range (i e. larger than 75 Hz), the wavelength of the Rayleigh wave is smaller than 2 m. This gives rise to spatial aliasing, resulting in unreliable data that can not be used to determine the dispersion curve $C_R^E(\omega)$. Comparison of the dispersion curve measured in February 2008 (figure 3) with the dispersion curves obtained from previous SASW tests [15] shows that the soil properties at the site in Lincent exhibit seasonal fluctuations, resulting in a variation of about 10 % in the shear wave velocity near the surface.

Figure 4 shows a smooth experimental dispersion curve derived from the spectrum presented in figure 3. The ElastoDynamics Toolbox (EDT) [19] for Matlab is used to calculate the theoretical dispersion and attenuation curves. A

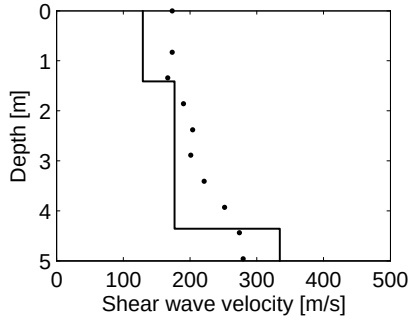

Fig. 5. The identified shear wave velocity profile, compared with the SCPT results (black dots).

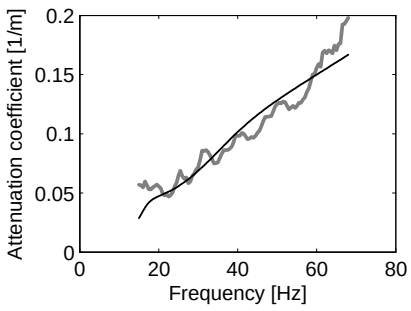

Fig. 6. The original (gray line) and identified (black line) attenuation curve.

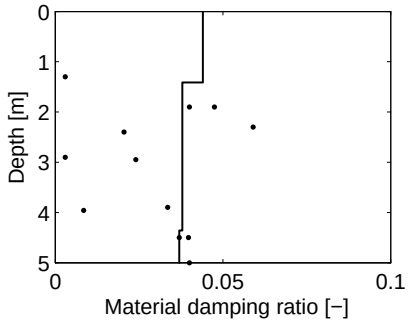

Fig. 7. The identified material damping ratio profile, compared with the SCPT results (black dots).

perfect match is observed in figure 4 between the experimental dispersion curve and the dispersion curve corresponding to the identified shear wave velocity profile. The identified shear wave velocity profile is close to the SCPT results as shown in figure 5. The experimental and identified attenuation curves are presented in figure 6. The identified attenuation curve results in the identified material damping ratio profile shown in figure 7. It is observed that the results of the SCPT are scattered around the current results.

IV. CONCLUSION

The half-power bandwidth method is successfully applied to the frequency-wavenumber content of the soil's response, in order to determine the material damping ratio. The position of the peak in the f-k spectrum is used to calculate the experimental phase velocity, while the width of the peak is used to determine the experimental attenuation coefficient. The technique has been used to determine the soil properties of a test site in Lincent, Belgium. The results agree with SCPT results.

ACKNOWLEDGMENTS

The results presented in this paper have been obtained within the frame of the project G.0595.06 "In situ determination of material damping in the soil at small deformation ratios", funded by the Research Foundation - Flanders

and the project OT/05/41 ”A generic methodology for inverse modeling of dynamic problems in civil and environmental engineering”, funded by the Research Council of K.U.Leuven. The second author is a postdoctoral fellow of the Research Foundation - Flanders.

REFERENCES

[1] A.K. Chopra. *Dynamics of structures*. Pearson Prentice Hall, Upper Saddle River, NJ, third edition, 2007.

[2] V. Cuellar and J. Valerio. Use of the SASW method to evaluate soil improvement techniques. In *Proceedings of the 14th international conference soil mechanics and foundation engineering*, pages 461–464, 1997.

[3] T. Forbriger. Inversion of shallow-seismic wavefields: I. Wavefield transformation. *Geophysical Journal International*, 153(3):719–734, 2003.

[4] S. Foti. *Multistation methods for geotechnical characterization using surface waves*. PhD thesis, Politecnico di Torino, 2000.

[5] S. Foti. Using transfer function for estimating dissipative properties of soils from surface-wave data. *Near Surface Geophysics*, 2:231–240, 2004.

[6] L. Karl. *Dynamic soil properties out of SCPT and bender element tests with emphasis on material damping*. PhD thesis, Universiteit Gent, 2005.

[7] L. Karl, W. Haegeman, and G. Degrande. Determination of the material damping ratio and the shear wave velocity with the Seismic Cone Penetration Test. *Soil Dynamics and Earthquake Engineering*, 26(12):1111–1126, 2006.

[8] L. Karl, W. Haegeman, G. Degrande, and D. Dooms. Determination of the material damping ratio with the bender element test. *Journal of Geotechnical and Geoenvironmental Engineering, Proceedings of the ASCE*, 134(12):1743–1756, 2008.

[9] E. Kavazanjian, M.S. Snow, C.J. Poran, and T. Satoh. Non-intrusive Rayleigh wave investigations at solid waste landfills. In *Proceedings of the first international congress on environmental geotechnics*, pages 707–712, Edmonton, 1994.

[10] C.G. Lai. *Simultaneous inversion of Rayleigh phase velocity and attenuation for near-surface site characterization*. PhD thesis, Georgia Institute of Technology, 1998.

[11] C.G. Lai, G.J. Rix, S. Foti, and V. Roma. Simultaneous measurement and inversion of surface wave dispersion and attenuation curves. *Soil Dynamics and Earthquake Engineering*, 22(9-12):923–930, 2002.

[12] G. Lombaert, G. Degrande, J. Kogut, and S. François. The experimental validation of a numerical model for the prediction of railway induced vibrations. *Journal of Sound and Vibration*, 297(3-5):512–535, 2006.

[13] S. Nazarian and M.R. Desai. Automated surface wave method: field testing. *Journal of Geotechnical Engineering, Proceedings of the ASCE*, 119(7):1094–1111, 1993.

[14] S. Nazarian and K.H. Stokoe II. Nondestructive testing of pavements using surface waves. *Transportation Research Record*, 993:67–79, 1984.

[15] L. Pyl and G. Degrande. Determination of the dynamic soil characteristics with the SASW method at a site in Lincent. Report BWM-2001-02, Department of Civil Engineering, K.U.Leuven, August 2001. STWW Programme Technology and Economy, Project IWT-000152.

[16] G.J. Rix, C.G. Lai, and A.W. Spang Jr. In situ measurement of damping ratio using surface waves. *Journal of Geotechnical and Geoenvironmental Engineering, Proceedings of the ASCE*, 126(5):472–480, 2000.

[17] N. Ryden and C.B. Park. Fast simulated annealing inversion of surface waves on pavement using phase-velocity spectra. *Geophysics*, 71(4):49–58, 2006.

[18] M. Schevenels, S.A. Badsar, and G. Degrande. Application of the SASW method for the determination of stiffness and damping parameters of soils. International Seminar on Interaction Soil-Railway Track for High Speed Trains, Lisbon, Portugal. Invited lecture, September 2008.

[19] M. Schevenels, S. François, and G. Degrande. EDT: An ElastoDynamics Toolbox for MATLAB. *Computers & Geosciences*, 2009. Accepted for publication.

[20] S. Yoon. *Array-Based Measurements of Surface Wave Dispersion and Attenuation Using Frequency-Wavenumber Analysis*. PhD thesis, Georgia Institute of Technology, 2005.

Proceedings of the 8th National Congress on Theoretical and Applied Mechanics, May 28-29, Brussels, Belgium.

A new stress-strain model for linepipe steels in strain-based design

Stijn Hertelé[1], Wim De Waele[2], Rudi Denys[2]
[1]FWO Flanders aspirant – Ghent University – Department of Mechanical Construction and Production – Laboratory Soete
[2]Ghent University – Department of Mechanical Construction and Production – Laboratory Soete
Sint-Pietersnieuwstraat 41 – 9000 Gent
email: stijn.hertele@ugent.be, wim.dewaele@ugent.be, rudi.denys@ugent.be

Abstract: **In this study a new six-parameter stress-strain model for modern pipeline steels is proposed. In finite-element analyses for strain-based design, these steels have often been described using the Ramberg-Osgood equation and similar expressions, but have proven to show a more complex behaviour in reality.**

The proposed model is based on the Ramberg-Osgood equation, to which a second strain hardening coefficient is added. It was validated by investigating least-squares curve-fits on a set of previously conducted tensile tests of contemporary pipeline steels. More specifically, the improvement towards Ramberg-Osgood was investigated by means of a least-squares performance parameter and visual assessment of the obtained model curves.

As regards the investigated tensile tests, the developed stress-strain expression was found to accurately describe continuously yielding steels, often providing significantly better results than Ramberg-Osgood. It is concluded that the proposed expression might be a step forward towards an improved quantitative description of pipeline steels in finite-element analyses of a strain-based design. To achieve this, further work should be conducted on the prediction of suited model parameters.

Keywords: **Strain-based design, pipeline steels, stress-strain relationship, Ramberg-Osgood**

I. Introduction

Pipelines can be subjected to significant plastic deformations during installation and operation. Possible causes of these deformations are earthquakes in the case of on-shore pipelines, and bending during installation in the case of off-shore pipelines [1]. Strain-based design concerns the structural response of welded pipelines to those imposed displacements. A strain-based assessment predicts pipeline failure or leakage, and is therefore of great economical and environmental importance.

Finite-element modelling is a commonly applied analysis technique in the field of strain-based design. An important required input is the stress-strain relationship describing the mechanical behaviour of the pipeline material. Indeed, the shape of the pipe metal's post-yield response has a significant effect on the achievable plastic strain of the pipeline [2]. Therefore, an accurate stress-strain description is needed over the entire strain range.

In finite-element analyses, the stress-strain relationship of a material is often represented by a model curve. This allows the material to be described quantitatively by means of model parameters, and consequently enables the execution of parametric studies. A well known constitutive law is the Ramberg-Osgood equation, which is commonly applied for metals because of its simplicity and its ease of use in finite-element software. Ramberg-Osgood describes the strain hardening behaviour during plasticity by means of a power law with one constant exponent [3]. Along with other similar single-exponent power-law hardening equations, it has also been widely used to model pipeline steels in strain-based design [1][4][5][6][7].

However, previous research has shown that modern pipeline steels should be characterised by two different strain hardening exponents, depending on the strain level [8]. Therefore, the currently applied single-exponent stress-strain models are not suited to accurately describe those steels.

This article presents a new stress-strain model, specifically developed for modern pipeline steels. It is based on the Ramberg-Osgood equation, but has two different strain hardening exponents instead of one. A series of experimental data has been used to investigate the possibilities of the proposed model, in comparison to the Ramberg-Osgood model. The results suggest that, in contrast to Ramberg-Osgood, the presented model can very accurately describe the full-range stress-strain behaviour of pipeline steels. This constatation is most pronounced for steels with a continuous yielding behaviour.

II. Background: the Ramberg-Osgood model

In 1943, Ramberg and Osgood presented a constitutive law that expresses the total true strain ε as a function of the true stress σ, as follows [3]:

$$\varepsilon = \frac{\sigma}{E} + p\left(\frac{\sigma}{\sigma_p}\right)^n \tag{1}$$

In this equation, σ_p is the material's proof stress corresponding to the plastic strain p. It has become common practice to use the 0.2% proof stress [9], as it is often seen as an equivalent yield stress. The stress-strain relationship then takes the form:

$$\varepsilon = \frac{\sigma}{E} + 0.002\left(\frac{\sigma}{\sigma_{0.2}}\right)^n \tag{2}$$

As can easily be seen, Eq. (2) (to which shall be referred as the 'Ramberg-Osgood model' in what follows) is characterised by merely three model parameters: an elasticity modulus E, the 0.2% proof stress of the model curve $\sigma_{0.2}$ and an exponent n. This exponent determines the rate of strain hardening, and is consequently called the 'strain hardening exponent'. There are several methods to determine suitable values for E, $\sigma_{0.2}$

and n for a specific experimental stress-strain curve, two of which are described here.

A first approach is applying a least-squares curve-fit of the model equation to the experimental data. This method requires an iterative calculation with a large number of datapoints and is therefore rather time-consuming. However, least-squares curve-fitting generally leads to an optimal solution. Hence, it is ideal in order to thoroughly investigate the possibilities of the model.

A second approach is to estimate the model parameters by means of stress-strain characteristics. Since this method does not require knowledge of the entire dataset, it is more practical to use. For the specific case of Ramberg-Osgood, E and $\sigma_{0.2}$ can be determined as the experimentally obtained values of elasticity modulus (E_0) and 0.2% proof strength ($R_{p0.2}$). To determine n, again there are two different approaches. Firstly, if a good approximation of the model to the experimental stress-strain curve is required in the small-scale yielding area (i.e. at the onset of yielding, just after the elastic area), the exponent can be estimated using the experimental 0.01% and 0.2% proof stresses $R_{p0.01}$ and $R_{p0.2}$ [10][11][12]:

$$n = \frac{\ln\left(\frac{0.2}{0.01}\right)}{\ln\left(\frac{R_{p0.2}}{R_{p0.01}}\right)} \tag{3}$$

Eq. (3) ensures that the Ramberg-Osgood model exactly matches the experimental stress-strain curve at the 0.01% and the 0.2% proof stress. However, the agreement can be dramatic for larger strains with this choice for n, see Figure 1.

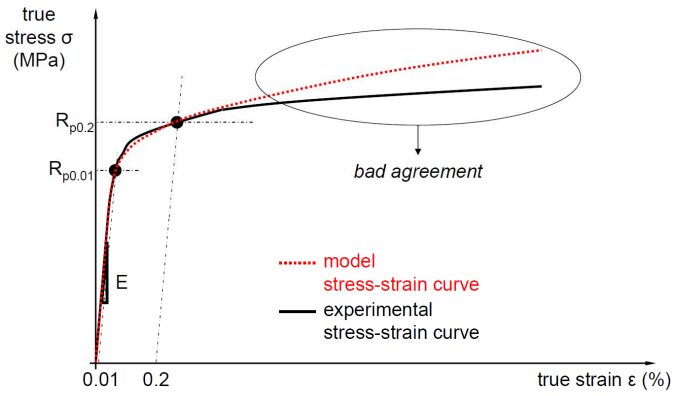

Fig. 1. Experimental stress-strain curve versus Ramberg-Osgood model using Eq. (3) (not to scale).

Alternatively, an acceptable approximation over the entire strain range may be desired. In that case, it is better to apply a relation based on the experimental 0.2% proof stress $R_{p0.2}$, the true value of ultimate tensile strength R_m and the plastic part of the true uniform elongation uEL_p (expressed in %) [4][9]:

$$n = \frac{\ln\left(\frac{uEL_p}{0.2}\right)}{\ln\left(\frac{R_m}{R_{p0.2}}\right)} \tag{4}$$

Figure 2 illustrates that Eq. (4) results in a model curve that intersects the experimental stress-strain curve at the 0.2% proof stress and the ultimate tensile strength. The agreement is globally good, but can be locally poor in the small-scale yielding area.

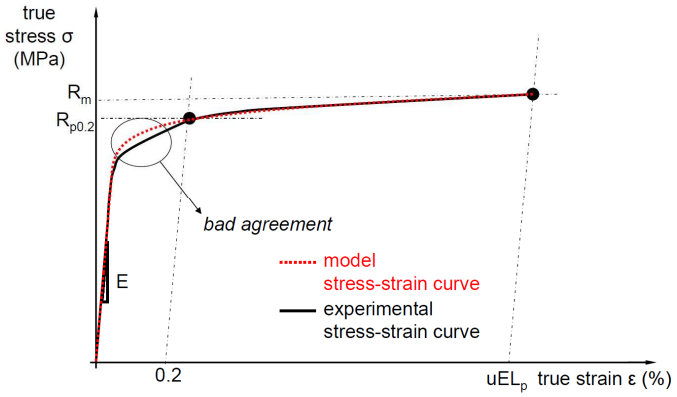

Fig. 2. Experimental stress-strain curve versus Ramberg-Osgood model using Eq. (4) (not to scale).

The Ramberg-Osgood equation was originally designed for aluminium alloys. Later, it proved to be a suitable model for some conventional steels too. However, some metallic materials tend to show a more complex tensile behaviour. Well-documented is the category of stainless steels, which are often impossible to accurately describe with one constant strain hardening exponent for the entire strain range [10][11][12][13][14]. The example of stainless steels indicates the general necessity of a critical pre-analysis to guarantee that Ramberg-Osgood is an appropriate model for the investigated material.

III. The New Stress-Strain Model

For the case of high strength steels, the degree of non-linearity is the result of a complex interaction between material composition, heat treatment, and level of cold work [15]. Two facts play a significant role in this consideration. Firstly, modern micro-alloyed pipeline steels are produced with the TMCP (‘*T*hermo *M*echanical *C*ontrolled *P*rocess’) rolling process, which leads to a very fine microstructure. As a consequence, a rather high ratio of yield strength to (engineering) ultimate tensile strength ($R_{p0.2}/R_m^e$) is typically achieved. This results in a reduced strain hardening effect, which distinguishes TMCP steels from conventional steels in terms of stress-strain behaviour. Secondly, the pipe production process (e.g. cold working due to UOE pipe forming, thermal treatment due to anti-corrosion coating [16]) further complicates the shape of the stress-strain curve.

Denys et al. [8] pointed out that the strain hardening behaviour of high-strength pipeline steels can be divided into

two separate regions: small-scale yielding and extensive yielding. Since Ramberg-Osgood has only one strain hardening exponent, it cannot accurately describe this so-called 'double n'-behaviour. Obviously, an improved new model must not show this restriction.

Because of the simplicity of the Ramberg-Osgood expression, Eq. (2) was taken as a starting point for the new model. Considering the 'double n'-behaviour of pipeline steels, the following constraints were put forward regarding the shape of the model curve:

- In the small-scale yielding area (at the onset of yielding), a Ramberg-Osgood equation with a first strain hardening exponent n_1 should be followed. This curve is further called RO_1.
- In the extensive yielding area (large strains, up to the uniform elongation *uEL*), the curve should follow Ramberg-Osgood with a second strain hardening exponent n_2, possibly translated over a certain strain value. This curve is further called RO_2.
- Between these two yielding areas there should be a transition zone, where the shape smoothly changes from RO_1 to RO_2. This curve is further called $RO_{1\to2}$.

An analytical consideration of the constraints mentioned above led to the following piecewise definition of the proposed model:

$$\varepsilon = \begin{cases} \mathrm{RO}_1(\sigma) & \sigma \le \sigma_1 \\ \mathrm{RO}_{1\to2}(\sigma) & \sigma_1 < \sigma \le \sigma_2 \\ \mathrm{RO}_2(\sigma) & \sigma_2 < \sigma \end{cases} \tag{5}$$

The transition between different sub-equations is determined by two model parameters, σ_1 and σ_2. The sub-equations are defined as follows (stresses are expressed in MPa, strain is dimensionless):

$$\mathrm{RO}_1(\sigma) = \frac{\sigma}{E} + 0.002\left(\frac{\sigma}{\sigma_{0.2}}\right)^{n_1} \tag{6a}$$

$$\begin{aligned} \mathrm{RO}_{1\to2}(\sigma) = {} & \frac{\sigma}{E} + 0.002\left(\frac{\sigma}{\sigma_{0.2}}\right)^{n_1} \\ & + 0.002\frac{\sigma-\sigma_1}{\sigma_2-\sigma_1}\cdot\left[\left(\frac{\sigma}{\sigma_{0.2}}\right)^{n_2} - \left(\frac{\sigma}{\sigma_{0.2}}\right)^{n_1}\right] \\ & - \frac{0.002}{\sigma_2-\sigma_1}\cdot\left[\frac{\sigma^{n_2+1}-\sigma_1^{n_2+1}}{(n_2+1)\cdot\sigma_{0.2}^{n_2}} - \frac{\sigma^{n_1+1}-\sigma_1^{n_1+1}}{(n_1+1)\cdot\sigma_{0.2}^{n_1}}\right] \end{aligned} \tag{6b}$$

$$\mathrm{RO}_2(\sigma) = \frac{\sigma}{E} + 0.002\left(\frac{\sigma}{\sigma_{0.2}}\right)^{n_2} - \Delta\varepsilon \tag{6c}$$

The introduction of a translation term $\Delta\varepsilon$ in the extensive yielding area was necessary to ensure continuity at the point $\sigma = \sigma_2$. It is defined by:

$$\Delta\varepsilon = \frac{0.002}{\sigma_2-\sigma_1}\cdot\left[\frac{\sigma_2^{n_2+1}-\sigma_1^{n_2+1}}{(n_2+1)\cdot\sigma_{0.2}^{n_2}} - \frac{\sigma_2^{n_1+1}-\sigma_1^{n_1+1}}{(n_1+1)\cdot\sigma_{0.2}^{n_1}}\right] \tag{7}$$

The model has six independent parameters, all of which are easily interpretable: E, $\sigma_{0.2}$, n_1, n_2, σ_1 and σ_2. First, the parameters E and $\sigma_{0.2}$ have the same physical meaning as in the Ramberg-Osgood model. Next, n_1 and n_2 are two strain hardening exponents that characterize the nature of the 'double n'-behaviour. Finally, σ_1 and σ_2 are the stresses that define the intervals of application of the different sub-equations. Figure 3 provides a graphical overview of the new model and its six parameters. Comparing Eqs. (6a) and (6c) with Eq. (2), it can be easily seen that the shape of the new stress-strain equation describes a Ramberg-Osgood curve for small-scale yielding and for extensive yielding.

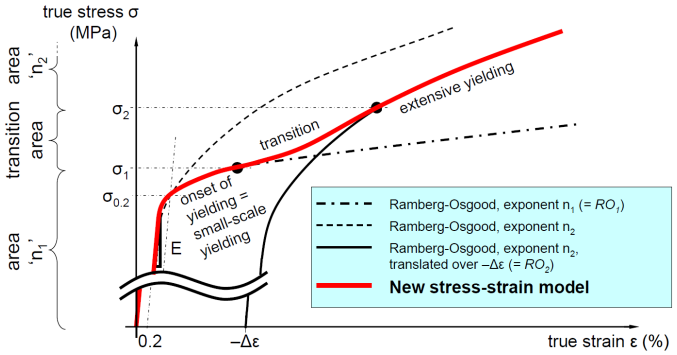

Fig. 3. A graphical overview of the proposed model and its model parameters.

IV. Experimental Validation

A. Experimental data

In order to qualify the obtained expression, it has been evaluated using a set of 58 experimental stress-strain curves of contemporary pipeline steels, all of which are strength grade API 5L X70 [17] (specified minimum yield strength 482 MPa). These data were obtained from standard tensile tests, previously conducted at Laboratory Soete of Ghent University.

There is a great diversity regarding the shapes of the investigated stress-strain curves. This is firstly illustrated in Figure 4, showing three fundamentally different experimental curves. Both steels with a discontinuous yielding behaviour (e.g. curve (a)) and steels with a continuous yielding behaviour (e.g. curves (b) and (c)) were included. Also, a broad spectrum of yield-to-tensile ratio was covered in the analysis. Defined as the ratio between the 0.2% proof stress $R_{p0.2}$ and the engineering value of the ultimate tensile strength R_m^e, it ranged from 0.77 to 0.94. The effect of $R_{p0.2}/R_m^e$ can be seen in Figure 4, by comparing curve (b) ($R_{p0.2}/R_m^e$ = 0.94) with curve (c) ($R_{p0.2}/R_m^e$ = 0.77).

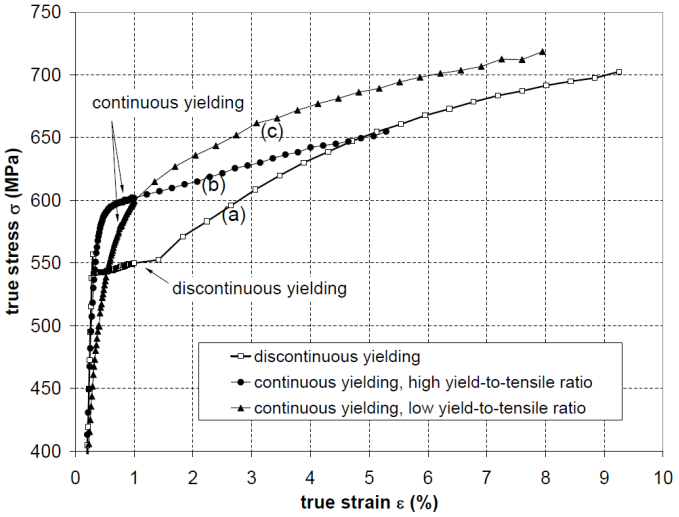

Fig. 4. An illustration of the different possibilities as regards the strain hardening behaviour of pipeline steels.

Secondly, even between steels with a similar yield-to-tensile ratio $R_{p0.2}/R_m^e$, significant differences in the shape of the stress-strain curve can be observed. Figure 5 illustrates this for two experimental curves with a $R_{p0.2}/R_m^e$-value of approximately 0.857. Here already, it may be interesting to note that for these curves, the ultimate tensile strength R_m^e is reached at similar strain values (which can be identified as the strain at the upper right point of the curves). Consequently, there is a recognizable correspondence not only for $R_{p0.2}/R_m^e$, but also for *uEL*. Thus, application of Eq. (4) would result in similar values for the strain hardening exponent *n* for both curves, and therefore a similar Ramberg-Osgood model shape.

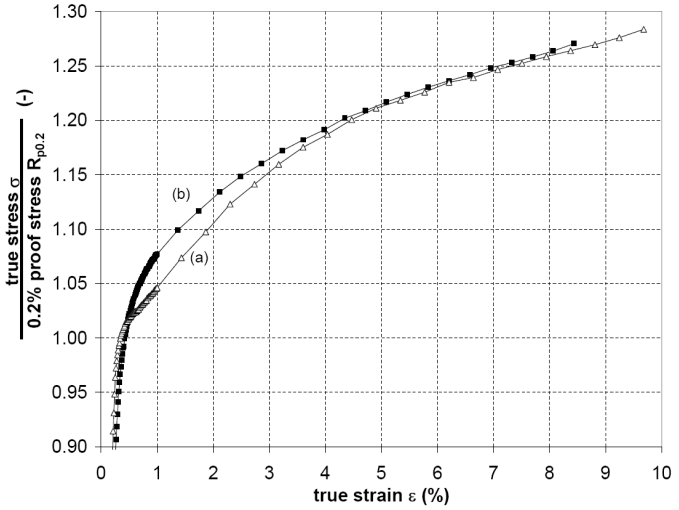

Fig. 5. Two tensile tests with a similar yield-to-tensile ratio and uniform elongation, but nevertheless a different shape.

An interesting way to represent stress-strain curves is in a double logarithmic diagram. As can be derived from Eqs. (6a) and (6c), the slope of the stress-strain curve in such a plot should be 1 in the elastic area, $1/n_1$ in the small-scale yielding area and $1/n_2$ in the extensive yielding area. Figure 6 illustrates this for the case of n_1 being greater than n_2. However, the case of n_1 being smaller than n_2 was also observed to be possible.

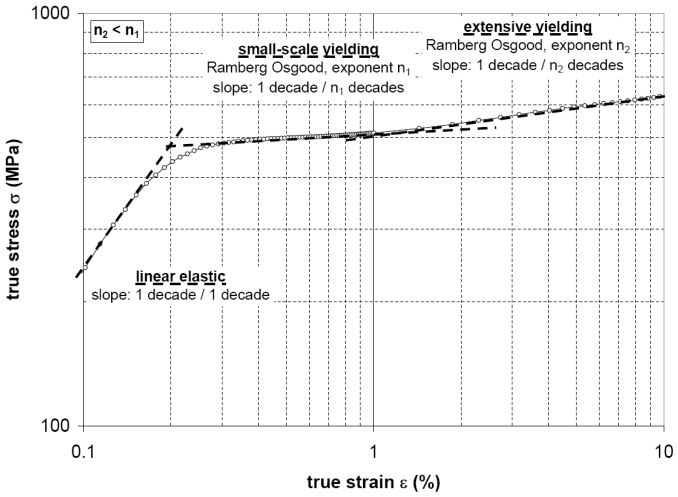

Fig. 6. Experimental double logarithmic stress-strain curve, with n_1 greater than n_2.

B. Preprocessing

All tensile test results were equally preprocessed. Firstly, the part of the curve after occurrence of the ultimate tensile strength was removed. In strain-based design, namely, necking of the test specimen is considered as a limit state. That is exactly what happens when the ultimate tensile strength is achieved, so the remaining part of the stress-strain curve is of no relevance.

Secondly, the measured values of stress and strain (the so-called 'engineering' values, σ^e and ε^e) were transformed to true stress and strain values (σ and ε), using the following well known conversion formulae:

$$\varepsilon = \ln\left(1+\varepsilon^e\right) \tag{8}$$

$$\sigma = \sigma^e \cdot \left(1+\varepsilon^e\right) \tag{9}$$

From these equations, the relationship between true and engineering values of uniform elongation (respectively *uEL* and uEL^e, in %) and ultimate tensile strength (respectively R_m and R_m^e) can be derived:

$$uEL = 100 \cdot \ln\left(1+uEL^e/100\right) \tag{10}$$

$$R_m = R_m^e \cdot \left(1+uEL^e/100\right) \tag{11}$$

The experimental stress-strain curves often contained many thousands of datapoints. Analyses on datasets of that size would have been extremely time-consuming. Therefore, they were finally simplified to a reduced but still sufficient set of 100 datapoints by means of interpolation. Eighty of these datapoints were taken in the strain interval [0% - 1%], because that area shows the biggest change in stress-strain behaviour (transition from elastic to plastic).

C. Analysis

After preprocessing, the actual analysis was carried out. Model parameters of the Ramberg-Osgood equation (E, $\sigma_{0.2}$,

n) and the new model (E, $\sigma_{0.2}$, n_1, n_2, σ_1, σ_2) were calculated for every tensile test as explained hereafter.

For the Ramberg-Osgood model as well as for the new model, E was first calculated from the experimental data using the true stresses at 0.01% and 0.15% total true strain:

$$E = \frac{\sigma(\varepsilon = 0.15\%) - \sigma(\varepsilon = 0.01\%)}{0.0015 - 0.0001} \qquad (12)$$

Indeed, these stresses are not yet plastic for API 5L X70 steel, and therefore representative of the proportionality between stress and strain in the elastic zone.

After E, the other model parameters were determined separately for Ramberg-Osgood and the new model. As regards the determination of $\sigma_{0.2}$ and n for the Ramberg-Osgood model, three alternatives were investigated, the last of which differs fundamentally from the first two. First, $\sigma_{0.2}$ was given the value of the experimental 0.2% proof stress $R_{p0.2}$, and n was determined by Eq. (3). Next, $\sigma_{0.2}$ was determined analogously, but Eq. (4) was used for n instead of Eq. (3). Finally, $\sigma_{0.2}$ and n were simultaneously determined by a least-squares curve-fitting of the model to the reduced set of 100 datapoints. As regards the new model, no equations are available yet to estimate all parameters properly. Therefore, only curve-fitting was applied to determine the 'optimal' values for $\sigma_{0.2}$, n_1, n_2, σ_1 and σ_2.

In the field of optimization techniques, least-squares curve-fitting is determining the parameter set $\vec{\theta}^*$ that minimizes the *RMS*-value (an abbreviation for '*R*oot *M*ean *S*quare') of a dataset (x_i, y_i), $i = 1 \ldots n_{data}$ towards a model function $f(x, \vec{\theta})$ (x being the argument, $\vec{\theta}$ being the multi-dimensional parameter set). This *RMS*-value is defined as follows:

$$RMS(\vec{\theta}) = \sqrt{\frac{1}{n_{data}} \cdot \sum_{i=1}^{n_{data}} \left(y_i - f(x_i, \vec{\theta}) \right)^2} \qquad (13)$$

Since in our case, *RMS* has the dimension of strain, it is expressed in %. The closer *RMS* approaches zero, the better the model equation represents the experimental curve. In other words, the *RMS*-value after curve-fitting is a quantitative measure for the quality of the model for each tensile test.

To calculate the least-squares curve-fits of the Ramberg-Osgood model and the new model to the experimental data, the iterative Levenberg-Marquardt algorithm [18] was used. This algorithm yields accurate results after a limited number of iterations, starting from an initial estimation $\vec{\theta}_o$ of the optimal parameter set. However, one needs to be critical about the result. If $\vec{\theta}_o$ is badly chosen, i.e. far away from the optimal parameter set $\vec{\theta}^*$, there is a possibility that the Levenberg-Marquardt algorithm leads to a local minimum of *RMS* instead of the absolute minimum. In that case, the result is not the optimal but a suboptimal parameter set (see Figure 7, illustrating the problem in one dimension). Therefore, several curve-fits with different initial parameter estimates were performed for every tensile test. Further, all calculated curve-fits were visually assessed afterwards to check if the model curve closely approximated the experimental curve. If not, more curve-fits with other initial parameter estimates were performed. Finally, the best fit was chosen for further analysis.

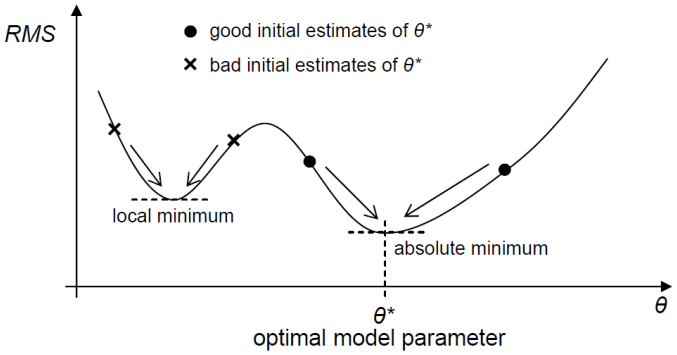

Fig. 7. Illustration of good and bad initial estimates of the optimal parameter set, using the Levenberg-Marquardt algorithm for least-squares curve-fitting.

V. Results

A. Ramberg-Osgood, with parameters determined using tensile test characteristics

As regards the Ramberg-Osgood model, the validity of Eqs. (3) and (4) was verified by visual inspection of the corresponding model curves. A representative result is shown in Figure 8. As can be seen, especially Eq. (3) yields an unacceptable result for this example. This is due to a low value of $R_{p0.01}$, a phenomenon which was also observed in a large amount of other investigated tensile tests. Hence, Eq. (3) appears to be unsuited for pipeline steels.

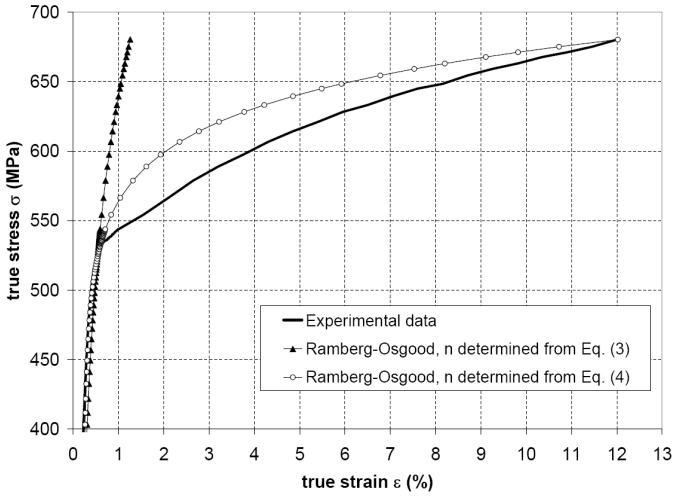

Fig. 8. An example of 'bad' Ramberg-Osgood approximations, using Eqs. (3) and (4).

Although better than Eq. (3), Eq. (4) also seems to be unsatisfactory. The approximation is more accurate for larger strains, because the model curve with this formula always intersects the experimental data at the maximum strain. For smaller strains, however, the representation of the curve is of

very poor quality. This was observed in a large number of the analysed tests. Therefore, also using Eq. (4) is questionable for pipeline steels.

B. Least-squares curve-fits of Ramberg-Osgood and the new model

The curve-fits of Ramberg-Osgood and the new model were assessed in two ways.

On the one hand, the fits of both models were compared in terms of their *RMS*-value for all tensile tests. The result is summarized in Figure 9, from which two important constatations can be made. First, it can be seen that all obtained *RMS*-values are lower for the new model than for the Ramberg-Osgood model, because all points on the figure are located beneath the 1:1 line. More specifically, the average *RMS*-value for the new model was about 45 percent of that calculated for the Ramberg-Osgood model. Numerical values are summarized in Table I. Thus, the new model generally seems to describe the mechanical behaviour of pipeline steels in a more realistic manner. Next, it was observed (see Figure 9 and Table I) that the *RMS*-values for Ramberg-Osgood as well as the newly proposed model are higher for curves with discontinuous yielding than for curves with continuous yielding. This suggests that both models are better at representing continuously yielding steels.

TABLE I

AVERAGE *RMS*-VALUES OBTAINED BY LEAST-SQUARES CURVE-FITTING

	Ramberg-Osgood	new model
all tests	0.149%	0.067%
continuous yielding only	0.117%	0.045%
discontinuous yielding only	0.305%	0.172%

On the other hand, the quality of the curve-fits was visually assessed. This allowed to intuitively qualify the obtained *RMS*-values. Figure 10 displays two example curves: one with continuous yielding, and one with discontinuous yielding. They have been deliberately chosen, because the *RMS*-values of their curve-fits approximately equal the average values of Table I. Curve (a) clearly shows that, in contrast to Ramberg-Osgood, the newly proposed model can very accurately describe continuously yielding curves.

However, curve (b) indicates that, albeit better than Ramberg-Osgood, the new model is not capable of reproducing the experimental curve in the case of discontinuous yielding.

VI. DISCUSSION

The results of this study indicate that the developed model is a significant improvement to the Ramberg-Osgood equation as regards the stress-strain behaviour of modern pipeline steels that exhibit continuous yielding behaviour. This follows from a comparison of the obtained *RMS*-values of both models, as well as the visual assessment of all curve-fitted model curves. Note that the newly developed model is nothing more than an extension of Ramberg-Osgood. Indeed, setting n_2 equal to n_1 in Eqs. (6a), (6b) and (6c) reduces Eq. (5) to a Ramberg-Osgood curve with strain hardening exponent $n = n_1$ (= n_2). Hence, every Ramberg-Osgood curve can also be described by the new model. This explains why not a single investigated tensile test produced a higher *RMS*-value for the new expression than for Ramberg-Osgood.

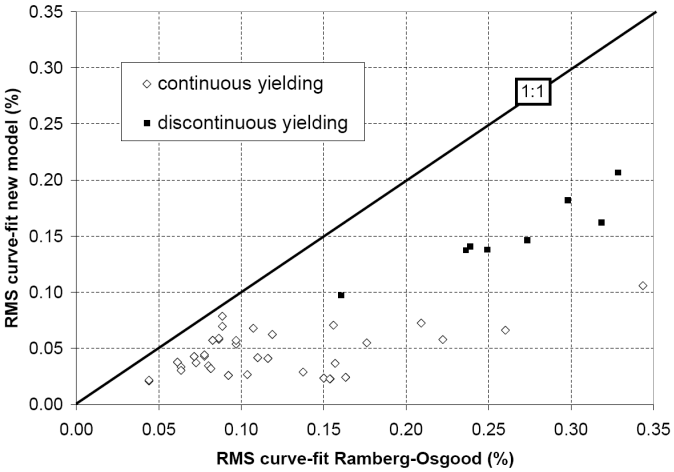

Fig. 9. *RMS*-values of all obtained curve-fits, compared for Ramberg-Osgood and the developed model.

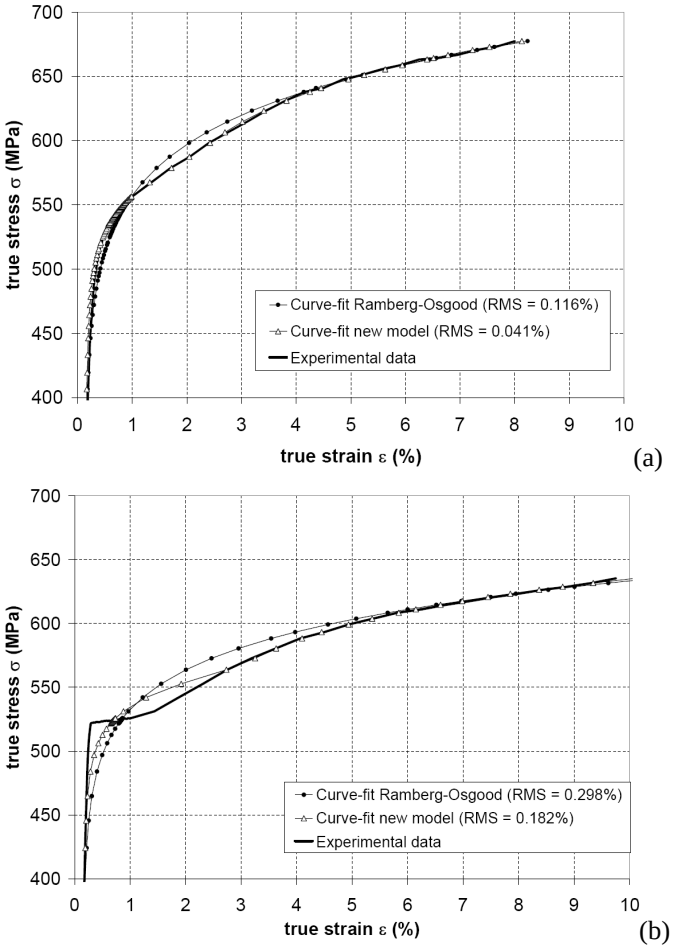

Fig. 10. Examples of curve-fitted experimental stress-strain curves. (a): continuous yielding; (b): discontinuous yielding.

The new model is better than Ramberg-Osgood because it contains two independent strain-hardening exponents: one for the onset of yielding (n_1) and one for extensive yielding (n_2). This constatation is in accordance with previous research of Denys et al. [8], who recognized the possible 'double n'-behaviour of high-strength pipeline steels. The developed model is a mathematical translation of the ideas explained in their work.

If the Ramberg-Osgood equation is nevertheless used, its parameters should be calculated by curve-fitting. The usage of tensile characteristics to calculate the parameters proved to give possibly unacceptable results, for the case of Eq. (3) as well as Eq. (4).

The presence of two strain hardening exponents in the new model largely increases the possibilities regarding the model curve shape. This is illustrated in Figures 11(a) and 11(b). These figures respectively represent curves (a) and (b) in Figure 5. Looking at Figure 11(a), it can be clearly seen that the new model takes the shape of the experimental curve over the entire strain range, whereas this is not the case for the Ramberg-Osgood model. The latter can only produce good approximations if the shape of the experimental curve can be characterised by one strain hardening exponent, as is the case in Figure 11(b).

Despite the good results obtained for continuously yielding steels, the developed model was very hard to properly fit with discontinuous curves. However, it should be mentioned that probably not all curve-fits were optimal for that category. Indeed, as can be easily understood, a good agreement would in the case of discontinuous yielding require n_1 to approach infinity. In that limit case, the *RMS*-value becomes very sensitive to slight parameter variations. Consequently, *RMS* reaches very high values in close vicinity to the optimal parameter set, making it more difficult to find initial estimates that lead to this optimum. Therefore, the proposed model seems unsuited to easily describe discontinuously yielding steels.

Notwithstanding the current limitation to continuously yielding steels, the development of the model could be a first step towards a better description of pipeline steels in terms of tensile behaviour. So far, the model has only been tuned by means of the complex and time-consuming method of least-squares curve-fitting. Further work is required in order to determine relations that can predict suitable model parameters using easily measureable tensile test characteristics, such as $R_{p0.2}$ and $R_{p0.2}/R_m^e$. Moreover, other API 5L strength grades should be investigated to study the possible influence of the grade on these predictive relations. Once this has been achieved, it will be possible to describe the entire stress-strain behaviour of pipeline steels by means of only a limited number of tensile test characteristics.

VII. Conclusions

A new stress-strain model has been developed, in order to describe the mechanical behaviour of modern high-strength pipeline steels. It is suited for strain-based applications, which require an accurate representation of the stress-strain relationship over the entire strain range up to the event of necking.

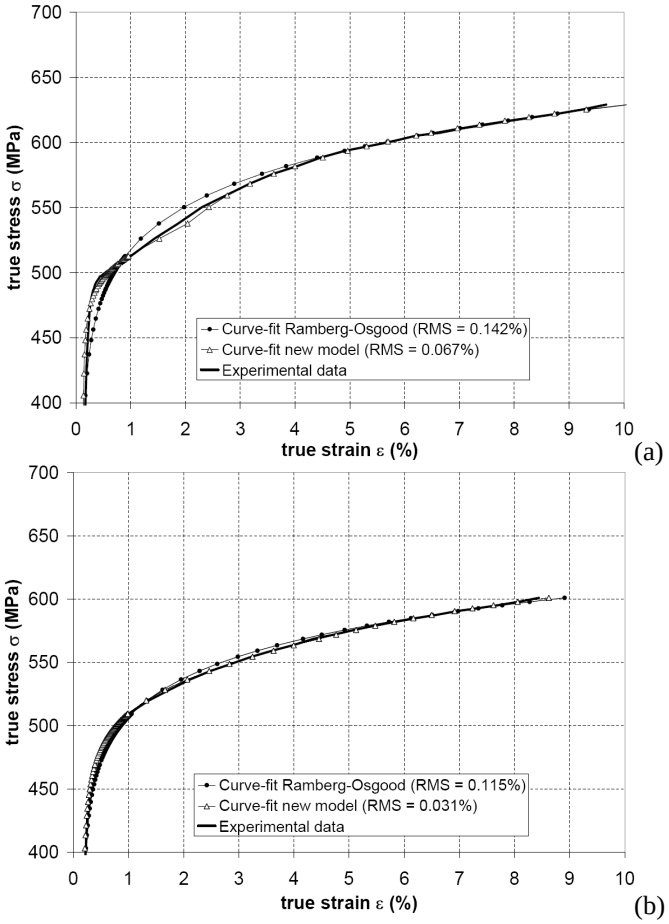

Fig. 11. Illustration of the possibilities of the new model compared to Ramberg-Osgood. (a): curve with distinct 'double n'-behaviour; (b): curve that can be characterized by one strain hardening exponent.

The model is an extension of the Ramberg-Osgood equation. It contains two strain hardening exponents, which can be independently varied. In total, there are six parameters: E, $\sigma_{0.2}$, n_1, n_2, σ_1, σ_2.

Analyses on a set of API 5L X70 steels showed that, in the case of continuously yielding steels, the proposed expression can be significantly more accurate than the original Ramberg-Osgood equation. However, discontinuously yielding steels were difficult to describe with the developed model, because it was far from trivial to find suited initial estimations of the optimal parameter set.

It is believed that the development of the proposed model can be a first step towards an improved quantitative description of continuously yielding steels in strain-based design, in terms of model parameters instead of an entire stress-strain curve.

Acknowledgments

The author would like to acknowledge the FWO (Fonds voor Wetenschappelijk Onderzoek) – Flanders for its financial support.

REFERENCES

[1] H. Bratfos, *Use of strain-based ECA for the assessment of flaws in pipeline girth welds subjected to plastic deformations*, Proc. Int. Conf. on Application and Evaluation of High-Grade Linepipes in Hostile Environments, Yokohama, Japan, 2002.

[2] R. Denys, *Interaction between material properties, inspection accuracy and defect acceptance levels in strain based pipeline design*, Safety, Reliability and Risks Associated with Water, Proceedings of the NATO Advanced Research Workshop on Safety, Reliability and Risks Associated with Water, Oil and Gas Pipelines, ISBN 978-1-4020-6525-5, Alexandria, Egypt, 2007.

[3] W. Ramberg and W.R. Osgood, *Description of stress-strain curves by three parameters*, Technical Note No. 902, National Advisory Committee For Aeronautics, Washington DC, 1943.

[4] A. Liessem, G. Knauf and S. Zimmerman, *Strain Based Design – What the Contribution of a Pipe Manufacturer Can Be*, Proc. 17th Int. Offshore and Polar Engineering Conf., Lisbon, Portugal, 2007.

[5] P.J. Budden, *Failure assessment diagram methods for strain-based fracture*, Engineering Fracture Mechanics, Vol. 73, pp. 537 – 552, 2006.

[6] K.R. Jayadevan, E. Østby and C. Thaulow, *Fracture response of pipelines subjected to large plastic deformation under tension*, International Journal of Pressure Vessels and Piping, Vol. 81, pp. 771 – 783, 2004.

[7] Y.Y. Wang, W. Cheng, M. McLamb, D.J. Horsley, J. Zhou and A. Glover, *Tensile strain limits of girth welds with surface-breaking defects – Part 1: An analytical framework*, Proc. 4th Int. Conf. on Pipeline Technology, Ostend, Belgium, pp. 235 – 250, 2004.

[8] R. Denys, P. De Baets, A. Lefevre and W. De Waele, *Material tensile properties in relation to the failure behavior of girth welds subject to plastic longitudinal strains*, Proc. Int. Conf. on Application and Evaluation of High-Grade Linepipes in Hostile Environments, Yokohama, Japan, pp. 159 – 172, 2002.

[9] N. Huh, Y. Kim and K. Yoon, *Influence of Ramberg-Osgood fitting on the determination of plastic displacement rates in creep crack growth testing*, Fatigue and Fracture of Engineering Materials and Structures, Vol. 30, No. 4, pp. 277 – 286, 2007.

[10] K. Rasmussen, *Full-range stress-strain curves for stainless steel alloys*, Journal of Constructional Steel Research 59, pp. 47 – 61, 2003.

[11] W.M. Quach, J.G. Teng and K.F. Chung, *Three-stage Full-Range Stress-Strain Model for Stainless Steels*, Journal of Structural Engineering, Vol. 134, No. 9, September 2008.

[12] K. Abdella, *Inversion of a full-range stress-strain relation for stainless steel alloys*, International Journal of Non-Linear Mechanics, Vol. 41, pp. 456 – 463, 2006.

[13] L. Gardner and D.A. Nethercot, *Experiments on stainless steel hollow sections – Part 1: Material and cross-sectional behaviour*, Journal of Constructional Steel Research, Vol. 60, pp. 1291 – 1318, 2004.

[14] E. Mirambell and E. Real, *On the calculation of deflections in structural stainless steel beams: an experimental and numerical investigation*, Journal of Constructional Steel Research, Vol. 54, pp. 109 – 133, 2000.

[15] L. Gardner and M. Ashraf, *Structural design for non-linear metallic materials*, Engineering Structures, Vol. 28, pp. 926 – 934, 2006.

[16] D. Duan, J. Zhou, B. Rothwell, D. Horsley and N. Pussegoda, *Strain aging effects in high strength line pipe materials*, Proc. 17th Int. Pipeline Conf., Calgary, Alberta, Canada, 2008.

[17] API 5L Specification for Line Pipe, 44th edition, October 2007.

[18] D. Marquardt, *An Algorithm for Least-Squares Estimation of Nonlinear Parameters*, SIAM Journal on Applied Mathematics 11, pp. 431 – 441, 1963.

Behaviour of Expanded Metal Sheets under Shear Loading

Phung Ngoc Dung[1], André Plumier[2]
[1]Department of Construction, Hanoi Architectural University, Viet Nam
KM N°10, Nguyen Trai Street, Ha Noi, Viet Nam
[2]Department of Structural Engineering, University of Liege
1, Chemin des Chevreuils, B-4000 Liège
Email : Dung.PhungNgoc@student.ulg.ac.be, A.Plumier@ulg.ac.be

ABSTRACT

Theoretical study of expanded metal shear panel (EMSP) has shown that EMSP is to be useful in the seismic retrofitting of buildings. Although this product has merit of strength and ductility, it is only used for filters in electrical applications or for the protection of machines (worker's safety) or buildings (anti-intrusion) and it is seldom used for structural applications. There is no guidance existing to help the engineers determine the mechanical properties or to indicate in which field of the structures this product can be used. With the aims at providing some quantitative data and insight for these purposes, this paper describes and compares the results of 16 static and static cyclic experiments of 4 types of expanded metal material in small-scale. These experiments provide useful information. The behaviour of expanded metal sheets (EMSs) is very ductile under monotonic shear loading and stable under quasi-static-cyclic shear loading.

Keyword: Expanded Metal, Cyclic behaviour, Cyclic Tests, Hysterical Loops.

I. INTRODUCTION

Expanded metal is a truss made from metal sheet by cuttings, cold-stretching and flattening [1]. Cuttings and cold-stretching a metal sheet becomes a three-dimension structure. It becomes a two-dimension sheet by flattening. There is neither interlacing nor welding in the elaboration process. An expanded metal sheet (EMS), as shown in Figure 1, has many rhomb-shape stitches. Each rhomb-shape stitch has four bars which are exactly the same dimensions and is geometrically characterized by four diagonal lengths – LD, CD (outer diagonal length), LD_{in}, CD_{in} (inner diagonal length), by the width – A and by the thickness of the bar - B. These dimensions are illustrated in Figure 2.

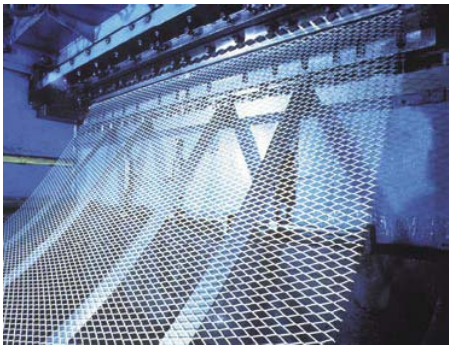

Figure 1 – Fabrication of expanded metal sheets

There are two types of expanded metal product, that is, a normal or standard type and a flattened type. In the normal type, rhomb-shape stitches are connected together by overlapping at the end of each bar. In contrast, there is no overlap between stitches in flattened type. They are continuously connected together to form a completely flattened sheet.

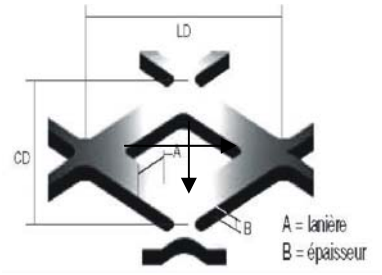

Figure 2 – An expanded metal rhomb-shape stitch

At the moment, expanded metal material is mainly used for filters, in electrical applications or for the protection of machines (worker's safety) or anti-intrusion fences for buildings…etc. Because there are no calculation and mechanical criteria for these types of material, it is seldom used in structural applications.

Some additional considerations have to be taken into account when working with expanded metal. The manufacture of expanded metal truss is not a "refined" technique: tolerances, due to cuttings and cold stretching, are sometimes very large: manufacturers indicate up to 10% on diagonals and bars dimensions. In the same order of ideas, sections of bars are not always perfectly rectangular and, when expanded metal trusses are loaded, some stress concentrations surely occur at the ends of the cuttings. In some cases, tolerances up to 50% have been measured on the section of the bars between the profile catalogue and the real section [1], [2].

The theoretical study of Etienne Pecquet [2] on monotonic behaviour of expanded metal sheets showed that under shear forces EMS behaves like two bands, which are compression and tension bands corresponding to the two diagonals of the sheet. More particularly, in one rhomb-shape stitch under shear forces, there are always two bars subjected to tension forces and the other two subjected to compression forces. Because the thickness of bars, which is also the thickness of EMS, is very small in comparison to the dimension of the sheet, the EMS is always globally buckled under a low shear force. Due to early global buckling, the compression effects on either the overall behaviour of EMS or the local behaviour of bars are always neglected and the EMS work with one tension band developed in post-buckled stages. Assuming that EMS works only in post-buckled stages, a lot of monotonic numerical simulations have been performed on different sizes of sheets, and with different commercial expanded metal profiles. An analytical model has also been developed for EMS under monotonic shear loadings.

Under monotonic loadings, the diagonal tension field actions provide a resistance which can be adequate for lateral resisting systems. However under cyclic loadings equivalent to seismic loadings, the behaviour of EMSs may be different. To provide some quantitative data on behaviour of EMSs, this paper describes 16 tests on four expanded metal profiles: 8 experiments on monotonic loadings and 8 experiments on cyclic loadings.

This experimental study is a part of a research aiming at characterizing the expanded metal material product for structural application, particularly for retrofitting reinforced concrete frames against earthquakes.

II. REVIEW OF PREVIOUS RESEARCH

In the stages 2005-2008 of the Macro Mousses Project, research work has been done by Etienne Pecquet at University of Liege. One part of the research was about mechanical behaviour of EMSs under monotonic shear loadings. In that study, two approaches, which are analytical models, in-plane and extended-plate models, and numerical simulations, are used and compared to results of experiments on the monotonic behaviour of EMSs under shear loading. Mechanical properties and stress-strain relationship of an expanded metal bar are shown in Table 1 and after doing many tests in tension.

Plane beam elements are used in the in-plane analytical model to determine elastic stiffness of EMSs, the section resistance with the interaction between axial and flexural stresses and the in-plane buckling of individual bars being taken into account.

The extended-plate model, allowing the out of plane instabilities, has been applied for the EMSs as the beam webs with adapting concepts of resistant sections and flexural stiffness of the sheets.

Numerical simulations, performed with FINELG, have used 3D beam elements. Each bar of the truss was modelled as one 3D beam element having seven degrees of freedom at each node. First critical analysis has been performed to obtain global instabilities and initial imperfections and then full nonlinear step by step analysis have been performed.

An analytical model has been adjusted to represent the monotonic behaviour of EMSs. Because of early buckling, the contribution of the sheet to the overall resistance before buckling is always neglected. After buckling a tension band develops along the diagonal direction of the sheets and the sheets work as a rectangular diagonal bar with a certain section area related to the dimensions and types of expanded material. The proposed resistance of a sheet made by expanded metal profile CDxLDxAxB is expressed by:

$$V = 0,27.l_{dia}.\alpha.B.f \qquad \text{(Exp. 1)}$$

Where: V – shear resistance of the sheet
l_{dia} – diagonal length of the sheet
B – Thickness of the sheet – the dimension B of the bar
f – Stress generated in the equivalent diagonal bar

$$\alpha = \frac{A}{l_{bar}} = \frac{A}{\sqrt{\left(\frac{LD - LD_{in}}{2}\right)^2 + \left(\frac{CD - CD_{in}}{2}\right)^2}}$$

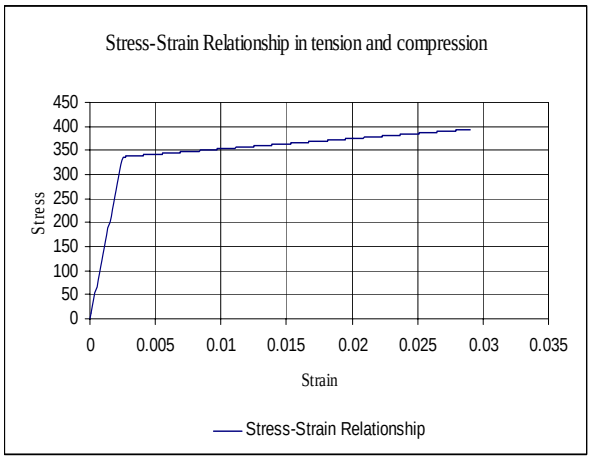

Figure 3 – Stress-strain relationship of an expanded metal bar

III. DESIGN OF EXPERIMENTS

In order to assess the real behaviour of the EMSs and to compare it to the results of numerical simulations, several considerations had to be taken into account.

First, the experiments have to be designed so that it is possible to reach to ultimate shear resistance of existing commercial expanded metal profiles. For that, all components of experiments are capacity designed to the ultimate shear resistances of all EMSs, as determined by the proposed analytical model [2].

Second, the tests should set forward which one, among two types of EMSs, normal and flattened types, is the most suitable for structural applications.

Third, dimensions of testing sheets have to be taken into account. The standard commercial dimensions of EMSs are approximately about 1250mm x 3000mm. At this stage of the study, it was not necessary to test with the EMS's dimensions greater than commercial dimensions, though the test sheets should have enough stitches of expanded metal truss to obtain the global behaviour of the EMS including not only the resistance but also the instability phenomenon.

Fourth, aiming at obtaining pure shear behaviour of EMSs, the test would be designed so that shear forces from the machine is entirely transmitted to the sheets.

Having accounted for all those considerations, the experiments have been designed. Figure 4 presents the test set up with one of expanded metal panel and the testing boundary frame: the overall dimensions correspond to the centre lines of the framing members, that is a width of 800mm and a length of 1200mm. The EMSs have dimensions about 695x1095mm.

Figure 5 gives a global view of the frame for shear tests in the configuration of the biggest dimensions.

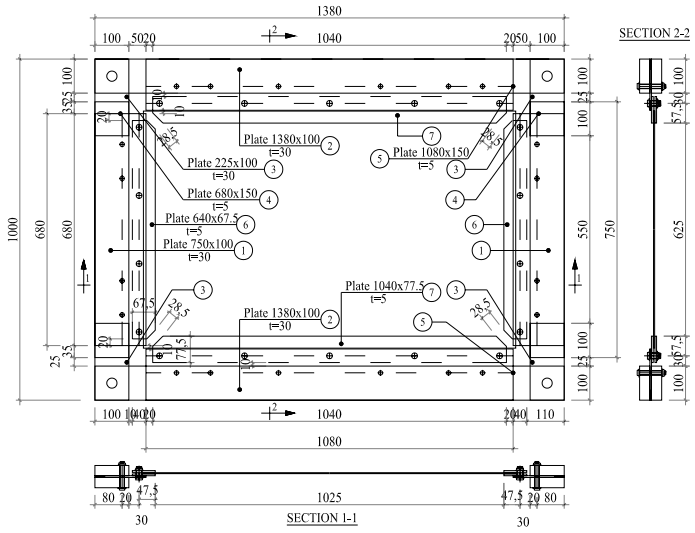

Figure 4– Overall sketch of testing frame

Because the testing frame components are connected together by hinges, the forces which act on the testing frame along diagonal direction are equivalent to the forces acting on the expanded metal sheet. And these forces can be divided into a horizontal and a vertical component. When the axial force is applied at one end of the diagonal, the hinges at the other end of the diagonal freely move. As shown on Figure 6, the axial force on the diagonal of the frame is equivalent to the application of a direct shear force.

The testing machine and the measurement devices are chosen accordingly to the estimated maximum responses of the expanded metal sheets.

Figure 5 – Global view of the frame for shear tests

IV. DETAILS OF SPECIMENTS

Details of all testing specimens are given in Table 2.

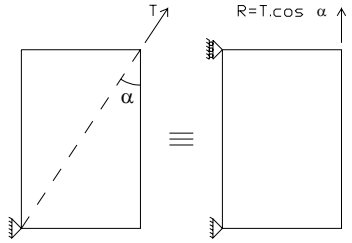

Figure 6 – Loadings on the frame

V. TEST PROCEDURES

Monotonic Test

Monotonic test mainly aims at comparing the ultimate shear forces which have been determined by numerical simulations with test results. In addition many properties of specimens are evaluated to provide data for cyclic test phase such as: monotonic force-displacement curve, conventional limit of elastic range: F_y^+-conventional yielding force and e_y^+-corresponding displacement, and initial stiffness of specimen. The forces acting on the expanded metal specimens are monotonically increased until a complete failure of the specimens will be clearly observed. The displacements which correspond to each step of monotonically increasing forces are recorded simultaneously. Forces and displacements are directly measured by measurement devices which have been attached along to the diagonal of specimens.

Cyclic Test

Cyclic testing procedure is based on the recommendation of ECCS – 1986 [3] (European Convention for Constructional Steelwork). Cyclic testing phase is divided into two stages. A first stage is a monotonic test used to define the parameters of the cyclic test. A second stage is to test EMS specimens in cyclic loadings. First stage procedures are listed in Table 3.

Second stage could start after having the results from the first stage. In this stage, the EMS specimens will be pulled and pushed successively in many cycles. The tests are run with control displacements. The testing procedure of this stage is presented in Table 4.

Table 1 – Mechanical properties of an expanded metal bar

Initial Stiffness – Modulus E_1(MPa)	Yield Stress (MPa)	Yield Strain (%)	Strain Hardening Modulus (E_t) (MPa)	Ultimate Strain (%)	Ultimate Stress (MPa)
134000	337	0.0025	2139	0.029	393

Table 2 – Details of all testing specimens

Specimens	Types	LD (mm)	CD (mm)	A (mm)	B (mm)	Erection Directions
1	Flattened	51	27	3.5	3.0	LD parallel to short side of the testing frame
2	Flattened	51	27	3.5	3.0	CD parallel to short side of the testing frame
3	Flattened	86	46	4.3	3.0	LD parallel to short side of the testing frame
4	Flattened	86	46	4.3	3.0	CD parallel to short side of the testing frame
5	Normal	51	23	3.2	3.0	LD parallel to short side of the testing frame
6	Normal	51	23	3.2	3.0	CD parallel to short side of the testing frame
7	Normal	86	40	3.2	3.0	LD parallel to short side of the testing frame
8	Normal	86	40	3.2	3.0	CD parallel to short side of the testing frame

Table 3 – Calibrating monotonic tests

Step	Descriptions
1	Evaluating the tangent at the origin of the Force-displacement curve; it gives a tangent modulus $E_t^+ = \tan(\alpha_y^+)$
2	Locating the tangent that has a slope of $\frac{E_t^+}{10}$
3	Defining the level of F_y^+ which is the intersection of the two tangents
4	Determining the value of e_y^+ which is the displacement corresponding to that intersection

Table 4 – Cyclic testing procedures

Steps	Applied displacements in tension	Applied displacements in compression	Number of cycles
1	$e_y^+/4$	$e_y^-/4$	1
2	$2^* e_y^+/4$	$2^* e_y^-/4$	1
3	$3^* e_y^+/4$	$3^* e_y^-/4$	1
4	e_y^+	$-e_y^+$	1
5	$2^* e_y^+$	$-2^* e_y^+$	3
>=6	$(2+2n)e_y^+$	$-(2+2n)e_y^+$	3

VI.EXPERIMENTAL OBSERVATIONS

Monotonic Test Phase

General features:

Under monotonic loadings, the behaviour of all testing specimens can be divided into an elastic stage and a plastic stage. The elastic range starts from the beginning of a test until reaching yield displacement. These yield deformations of all specimens range from 0.85mm (0.12% drift) to 1.17mm (0.18% drift) as shown in Table 5. Beyond the elastic range, all the EMSs perform plastic deformations until attaining ultimate displacements. During the plastic deformations the section area of bars reduces and the slope of force-displacement curves decreases.

There are four couples of two similar tested EMSs in eight testing specimens. In a couple, the expanded metal profile is the same. They are different in the way of setting up to the testing frame as shown in Table 2. Because of this difference, the values of yield displacements, yield force, ultimate displacements and ultimate shear force of each specimen in each couple are slightly different.

In all the specimens, there are some discrete positions which have had visible out-of-plane deformations. These initial buckling deformations are different in each specimen. They

become clearer after rather low shear forces are applied. The shapes of buckling waves, as shown in Figure 7, are the same for all testing EMSs. Although the sheets are prone to global buckling, there is no buckle of individual bar observed from the beginning to the end of the test.

Figure 7 – Buckling shape after testing of specimens

The first broken bars observed in all tests are located at the diagonal corners opposite to the force application points of the testing frame. The section areas of these bars clearly decrease before being broken. In spite of the fact that some bars are broken, the sheets keep carrying shear forces. It is also observed that after each bar is broken the shear force is suddenly reduced and then increased until the sheets are completely broken. The broken bars first appear at the corners of the testing frame, then spread gradually to the centre of the sheets.

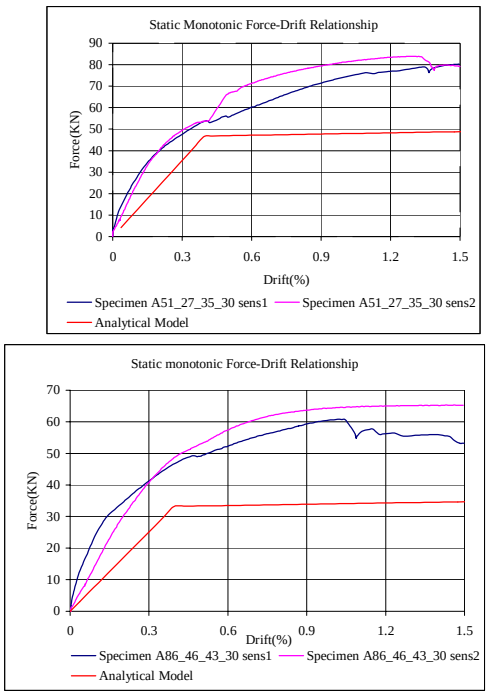

Figure 8 – Force–drift curve in monotonic tests of flattened types and analytical model

All the tests are stopped because EMSs have been largely deformed. There is no failure either at the weld connections between the expanded metal sheets and the plates or at the bolt connections between sheet-plates and intermediate-plates.

Particular features:

Out of the two material types of tested specimens, the normal type buckles more rapidly than the flattened type. The shear forces causing buckling in normal type specimens are lower than in flattened types. In each expanded metal type, the ultimate shear forces are proportional to the section area of bars and inversely proportional to the voids of the sheets. The initial stiffness of normal types is much lower than that of flattened types.

Although ultimate shear forces in normal type specimens are less than those in flattened types, the corresponding displacements in normal types are much greater than that in flattened types. Apparently, normal type specimens are more ductile than flattened type specimens. Ductility factors of normal types are twice greater than those of flattened types.

Figure 8 and Figure 9 show the relationships between forces and drifts in monotonic tests in comparison with the analytical model of two expanded metal types.

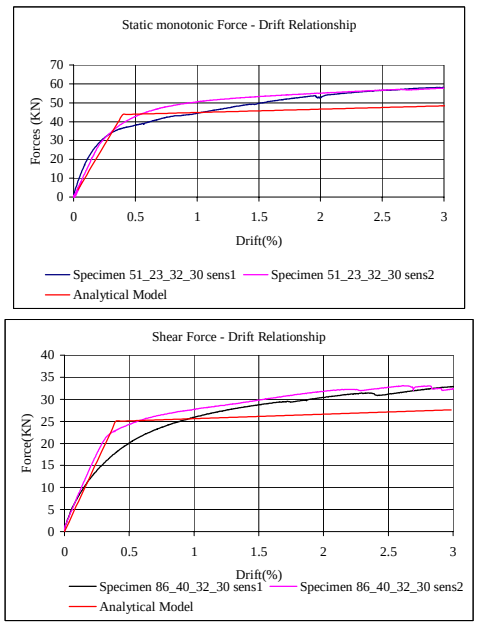

Figure 9 – Force–drift curves in monotonic tests of normal types and analytical model

Cyclic Test Phase

General features:

All specimens behave elastically in first four cycles until reaching a yield displacement which is also nearly the same as the yield displacements in monotonic tests. In the elastic range, the behaviour of all specimens is not completely symmetric. Beyond elastic ranges when the displacements become larger the hysteric loops are more symmetric.

Initial out of plane deformations are observed in all specimens before testing. In some specimens, these phenomena become clearer after low shear forces are applied to the sheets. Out of plane deflections of the sheets become larger in successive cycles.

In monotonic tests, there is no instability of individual bar. However, in cyclic tests, instability phenomena of bars are clearly observed in all specimens in the plastic range. In addition, the section areas of all the buckled bars are reduced visibly.

Like in monotonic tests, all first broken bars, as shown in Figure 10, are located at four corners of the testing frame and before being broken their section areas are considerably reduced. It is also observed that the crack directions in all cyclic tests start at four corners and then progress to the centre of the sheets to form four crack lines. It is worth noting that, in almost all cyclic tests, the maximum shear force is attained on the cycle on which the first broken bars have appeared.

During first four cycles, the behaviour of the EMSs is linear. From fifth cycle to the end of the tests the shapes of hysteretic behaviour of the EMSs are stable S-shapes. Hysteretic loops in all specimens are characterized by strong pinching. Pinching effects are due to the global instabilities of the EMSs, which cause large degradation in stiffness of the sheets. Like in monotonic tests, tension bands are developed in sheets in every cycle. In addition, because of the pinching effects, before redeveloping new tension band the stiffness of the sheets is approximately equal to zero in the other diagonal. From the beginning to the end of the tests, there has been no failure either at the weld connections between the expanded metal sheets and the sheet-plates or at the bolt connections between sheet-plates and intermediate-plates.

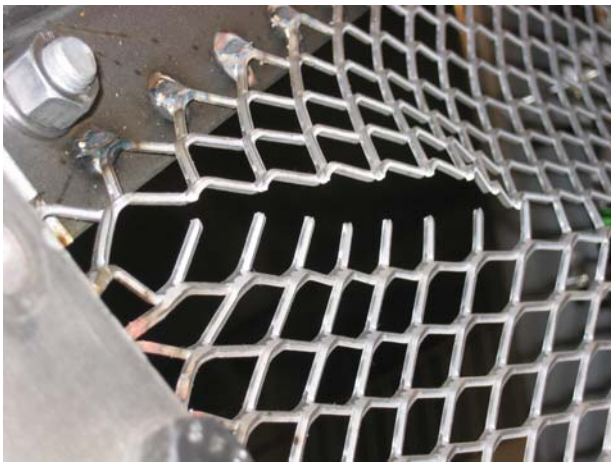

Figure 10 – Crack line and broken bars

Particular features:

In monotonic tests, if two specimens have the same profiles but they are different in the way of setting up to the testing frame, their behaviour is not much different. In cyclic tests, their behaviour is very similar in first four cycles. It means that in these cycles, the sheets are in elastic ranges. However, in the plastic range, particularly when reaching the ultimate shear forces or the maximum displacements which are corresponding to ultimate shear forces in monotonic tests, some specimens behave quite differently. The ultimate shear forces and number of hysteretic cycles are quite different from one specimen to another.

As shown in Table 7 and Table 8, the number of cycles in hysteretic behaviour of flattened expanded metal types and the energy which is dissipated are greater than that of normal types.

It is also observed that out of plane deformations at failure of normal type specimens are much greater than those of flattened specimens.

As shown in

Figure **11** and Figure 12, pinching effects on the hysteretic behaviour are much larger for normal type specimens than for flattened type specimens.

VII. SUMMARY OF OBSERVATIONS

An experimental test program has been carried out on small scale of un-stiffened expanded metal sheet test specimens. The main objectives of the tests was to calibrate the simple analytical model for monotonic shear loading that has been proposed by Etienne Pecquet [2] and to study the hysteretic behaviour of expanded metal sheets subjected to shear.

In both monotonic and cyclic phases of the tests all sheets have buckled at very low shear forces. Some of the specimens (specimens 7 and 8) were globally buckled before testing. Furthermore it was observed that normal types of EMSs, including specimen 5, 6, 7 and 8 (profiles: 51_23_32_30 and 86_40_32_30), buckle more easily than flattened types, which are specimens 1, 2, 3 and 4 (profiles: A51_27_35_30 and A86_46_43_30).

The first broken bars observed in both monotonic and cyclic phases of tests are located near one of four corners, then develop to the centre of the sheets. Additionally it is easy to observe that the broken bars are the bars working in tension. There is no bar being locally buckled in monotonic tests. However, in all cyclic tests, many bars have been buckled before being broken. Moreover, in almost cyclic tests, the maximum shear forces have been attained on the cycle on which first broken bar has been observed.

The maximum shear forces of EMSs in monotonic tests are dependent on the voids of the sheets. With nearly the same voids, ultimate shear forces of flattened type specimens are much greater than those of normal types. Nevertheless, it is observed that maximum displacements of flattened types are much less than those of normal types and the ductility of normal types are much greater than that of flattened types.

The hysteretic loops of all specimens are S-shaped due to pinching effects, but they are stable. The displacement ductility of all specimens is largely different, ranging from 10 to 20. Pinching effects on all specimens due to yielding in tension and to buckling in compression caused the degradation of stiffness of the sheets. In cyclic tests, pinching effects are clear in successive cycles beyond the elastic range. In addition, the magnitude of the buckling deformations and deterioration in stiffness of sheets are increased correspondingly.

In all specimens in cyclic test phases, the stiffness of the sheets is approximately equal to zero during the inversion of force.

Table 5 – Monotonic test results

Specimens	Yield force (KN)	Yield displacement (mm)	Yield Drift (%)	Initial Stiffness (KN/mm)	Ultimate shear force (KN)	Ultimate displacement (mm)	Ultimate Drift (%)
1	33.4	1.0	0.14	33.4	78.9	9.4	1.35
2	32.2	1.0	0.14	32.2	83.7	8.7	1.25
3	27.9	0.85	0.12	32.8	60.8	7.1	1.02
4	25.9	1.17	0.17	22.1	65.0	8.3	1.2
5	27.3	1.3	0.18	21.0	60.6	25.7	3.7
6	18.0	0.9	0.13	20.0	57.5	20.3	2.9
7	9.3	0.93	0.13	10.0	31.3	15.6	2.24
8	10.2	0.93	0.13	11.0	32.3	15.7	2.26

Table 6 – First four cycle results

Specimens	Monotonic yield force (KN)	Monotonic yield displacement (mm)	Monotonic yield Drift (%)	Forces at fourth cycle (KN)	Displacements at fourth cycle (mm)	Drift at fourth cycle (%)
1	33.4	1.0	0.14	30.4	1.01	0.15
2	32.2	1.0	0.14	31.1	1.02	0.15
3	27.9	0.85	0.12	20.2	0.88	0.13
4	25.9	1.17	0.17	24	1.10	0.15
5	27.3	1.3	0.18	23.4	1.01	0.15
6	18.0	0.9	0.13	19.0	1.00	0.15
7	9.3	0.93	0.13	10.1	1.20	0.17
8	10.2	0.93	0.13	11.0	1.29	0.19

Table 7 – Cyclic testing results at displacements corresponding to ultimate forces in monotonic tests

Specimens	Monotonic ultimate shear force (KN)	Corresponding displacement (mm)	Corresponding drift (%)	Corresponding shear force (KN)	Displacements at relatively corresponding to monotonic test (mm)	Corresponding drift (%)	Number of cycles (cycles)
1	78.9	9.4	1.35	56.0	9.8	1.41	23
2	83.7	8.7	1.25	74.0	9.7	1.40	14
3	60.8	7.1	1.02	42.5	8.7	1.30	20
4	65.0	8.3	1.2	43.3	9.3	1.34	11
5	60.6	25.7	3.7	15.5	20.9	3.0	32
6	57.5	20.3	2.9	40.5	20.4	3.0	12
7	31.3	15.6	2.24	23.2	14.5	2.1	11
8	32.3	15.7	2.26	28.9	14.5	2.1	14

Table 8 – Maximum shear forces in cyclic tests and corresponding displacements

Specimens	Cyclic ultimate shear forces (KN)	Cyclic corresponding displacements (mm)	Cyclic corresponding drifts (%)	Number of cycles (cycles)
1	71.6	8.3	1.2	20
2	-75.6	-16.9	2.4	16
3	-48.2	-20.2	2.9	26
4	-49.3	-14.8	2.1	13
5	-48	-7.3	1.1	14
6	-45	-7	1.0	10
7	27	9.3	1.33	8
8	-28	-10.8	1.56	12

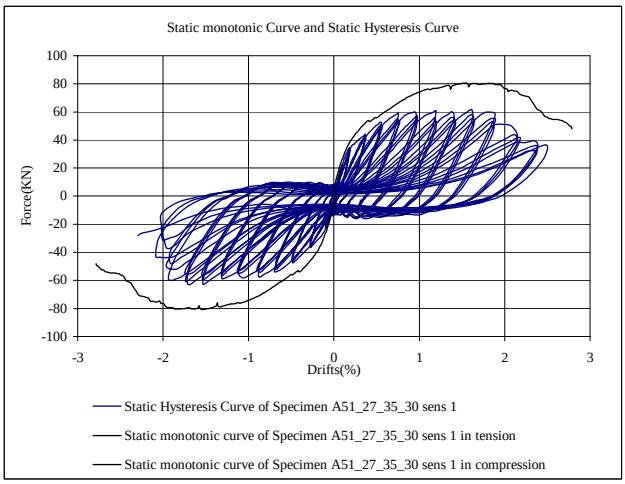

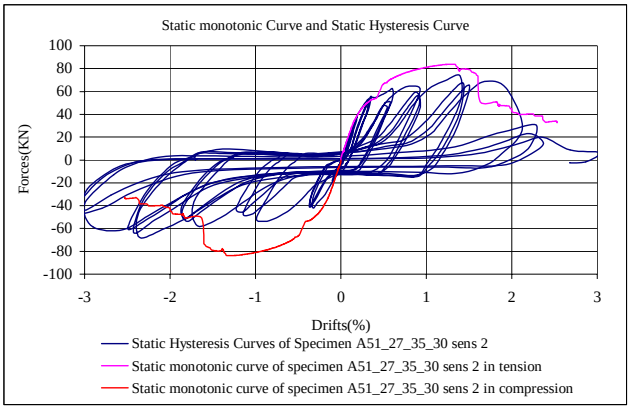

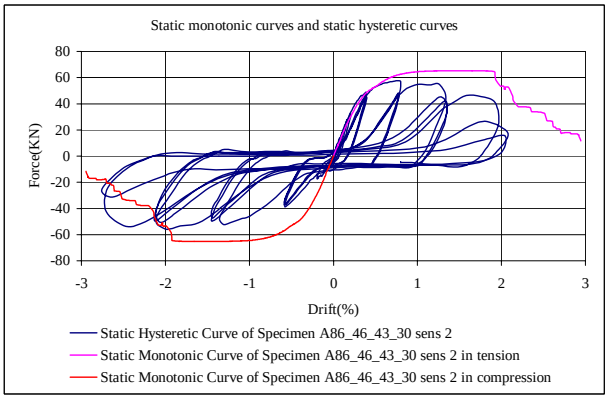

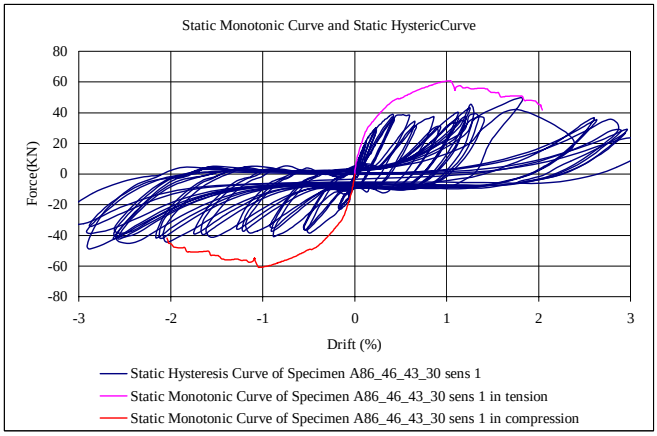

Figure 11 – Hysteretic behaviour of flattened type specimens.

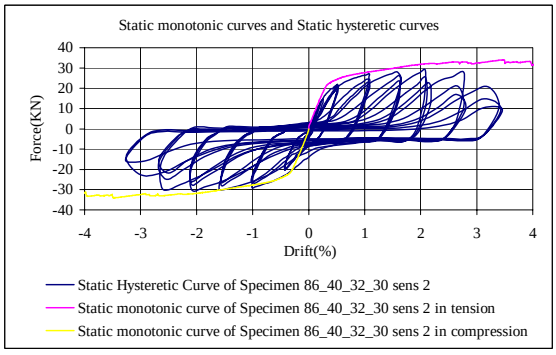

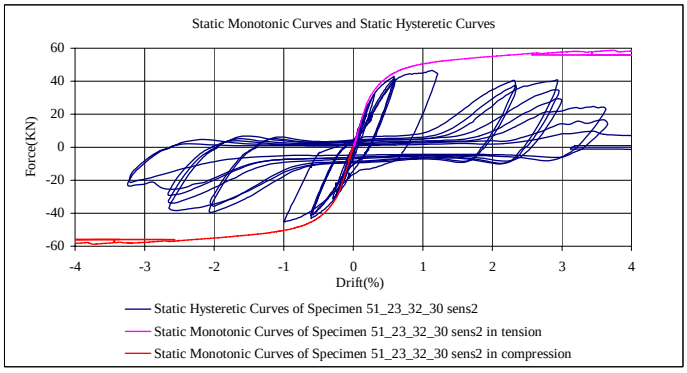

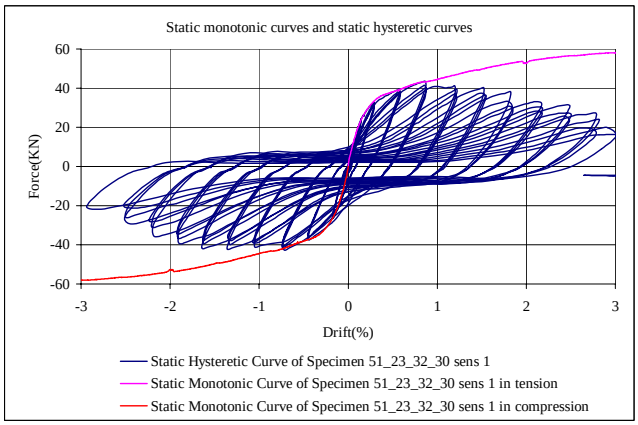

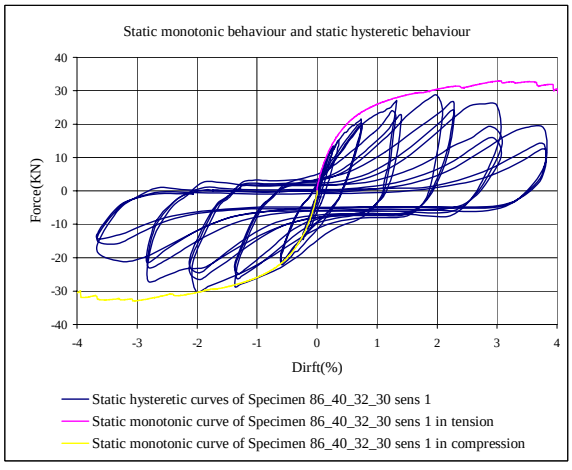

Figure 12 – Hysteretic behaviour of normal type specimens.

VIII. CONCLUSIONS

1. The correlation between the analytical model and monotonic tests varies largely different. In some cases, the analytical model much underestimates the real behaviour of the EMSs. It may be that only one tension band for the monotonic behaviour of the sheets is not enough. The sheets might work in more than one tension band.
2. Because under rather low shear forces the sheets are globally buckled, the contribution of compression diagonal to the resistance of sheets can be neglected.
3. The degradation in stiffness of the sheets due to pinching effects results in a smaller enclosed area under the hysteretic curve and, therefore, a lower amount of energy absorbed by the system during successive cycles.
4. The deflection required to redevelop the tension field is based on the yielding displacements experienced by the sheets on the previous cycles.

IX.PERSPECTIVES

The results of the experiments in small scale specimens described above do not fit in all cases with numerical model and/or analytical formula proposed [2]. This may be due to detrimental effects of weld connections. Furthermore, until now no proposal for hysteretic behaviour of expanded metal material under shear loading has been made.

The next steps of the research on expanded metal material are

1. To improve the analytical model proposed by the study of Etienne Pecquet.
2. To make numerical simulations on expanded metal sheets from small dimension to large dimension of the sheets under cyclic loading and seismic excitations; the simulation should represent the hysteretic behaviour of expanded metal sheets.
3. To make additional cyclic tests in small-scale using other solution for the connection, such as epoxy, glue or butt weld in order.
4. To realise additional tests on large scale expanded metal panel and to check the hysteretic behaviour obtained from the numerical simulations in that case.
5. To model reinforced concrete structures with and without expanded metal shear panels (EMSP).

ACKNOWLEDGEMENTS

This research has been made possible thanks to funding from the French Community of Belgium – Macromousse Project and to a funding of the Socialist Republic of Viet Nam.

REFERENCES

1. Métal Déployé Belge s.a, ‘Le catalogue Métal Déployé’, édition 10/2003

2. E. Pecquet, S.Cescotto, ‘Mechanical behaviour of expanded metal sheets: critical and ultimate loads of square and rectangular sheets loaded in shear’, 7th National Congress on theoretical and Applied Mechanics, May 2006.

3. ECCS 1986 - Recommended Testing Procedure for Assessing the Behaviour of Structural Steel Elements under Cyclic Loads

Proceedings of the 8th National Congress on Theoretical and Applied Mechanics, May 28-29, Brussels, Belgium.

Modeling of preloaded threaded pipe connections

Jeroen Van Wittenberghe, Patrick De Baets, Wim De Waele
Department of Mechanical Construction and Production, Ghent University
St.-Pietersnieuwstraat 41, 9000 Ghent – Belgium
email: jeroen.vanwittenberghe@ugent.be, patrick.debaets@ugent.be, wim.dewaele@ugent.be

Abstract: **In this paper a modeling method to perform parametric studies on preloaded threaded connections is presented. The method uses a non-linear 2D axisymmetric finite element model, and is illustrated by a parametric study of an API Line Pipe connection. The method was used to quantify the influence of the coefficient of friction, the wall thickness of pin and box and the box recess length of the connection.**

Keywords: **parametric study, threaded pipe connection, finite element model, API Line Pipe**

I. Introduction

A. Outline

Threaded pipe connections are used to join pipelines as an alternative for welding and in applications where pipes should be frequently coupled and uncoupled. The connections consist of a male and female part, called respectively pin and box. To maintain a sealed and secure connection while being subjected to external variable loads, they are commonly preloaded. This can be done by using conical connections and tightening the pin and box with a specified torque, called 'make-up' torque. This make-up torque is different for every connection type and size. Due to the combination of the preload and external loads, together with the thread geometry, a complex multiaxial stress distribution develops over the connection.

The stress distribution depends on the coupling's geometrical parameters like pipe dimensions and thread type, but is also influenced by the contact interaction properties of the material of the connection. Resulting stress concentrations can initiate fatigue cracks and cause a premature failure of the connection. According to Griffin et al [1] the highest stress concentration under axial load can be expected at the last engaged thread (LET) of the pin.

The influence of the different geometrical and contact parameters on the connector's applicability and service life are not well known. In this study a newly developed program is presented that can be used to perform parametric finite element (FE) studies on threaded pipe connections. After a general introduction on FE modeling of threaded connections, the structure of the program will be presented. In the subsequent sections, the results of a parametric study on a preloaded API Line Pipe threaded connection are discussed.

B. Modeling of Threaded Connections

The simulation of threaded connections is characterized by two non-linearities. Firstly, high local stresses can appear, exceeding the material's yield strength even during the make-up stage. Hence, non-linear elastic-plastic material models are necessary. Secondly, surface interactions together with small sliding between pin and box result in non-linear contact behavior.

Starting from the 1980's the finite element method is used to model threaded connections. Since the computational performance of the computers in that time was rather limited, it was not possible to model full non-linear 3D models. Hence, hybrid models [2, 3] and 2D axisymmetric models [4] were used. With the hybrid modeling techniques, the global load distributions over the threads is analytically calculated and local stresses are determined using 2D axisymmetric finite element models of only a few threads. Results from both techniques were validated by photoelastic experiments. With increasing computing power, the hybrid method was completely abolished to use 2D axisymmetric models with finer meshes. Mid 1990's, more complex material models were introduced to model elastic-plastic material behavior [5-7] and better contact interaction properties were defined to allow sliding of the threads [8].

Nowadays threaded pipe connections are still commonly modeled using 2D axisymmetric finite element models with elastic-plastic material behavior and contact interaction of the threads [1, 9-13]. Despite the vast performance increase of computers over the last decades, full 3D models of threaded couplings still require very long calculation times due to the high number of nodes in the contact analysis. In addition to this, due to their complexity and multiple contacting surfaces, full 3D models tend to be less stable and to diverge from a solution more easily. Performed 3D simulations are generally simplified by using linear elastic material properties and using very coarse meshes [14], resulting in inaccurate stress distribution and useless stress concentration factors. Generally much more precise results can be obtained with 2D axisymmetric models. The disadvantage of the 2D simulations is that they neglect the helical shape of the threads and the runout region. However, it was shown by Chen and Shih [15] in the analysis of bolts and more recent by Zhong [16] for threaded pipe connections, that the results of 2D axisymmetric models are in good agreement with the results of accurate time-consuming full 3D models.

Defining correct contact interactions requires accurate knowledge about the interaction properties, like the coefficient of friction (COF), of the contacting interface. However, a variety of values for the COF are used. In ISO 10407-1 [17] values for the COF are specified between 0.06 and 0.14, mentioning a typical value of 0.08 when thread compounds are used. Guangjie et al [11] even use a lower value of about 0.02. In experimental studies friction values between 0.06 and 0.09

were obtained by Ertas et al [18] for tests on pipeline steel with different thread compounds and Santus et al [13] measured values of 0.15 during torsion tests on full scale threaded connections. As will be shown further, this variation of the coefficient of friction has a significant influence on the thread opening of the connection and correct values for the COF should be used.

II. Modeling Strategy

To be able to perform parametric studies to simulate the influence of different parameters on the connection's behavior, a new modeling method was developed using a combination of Matlab® R2008a and Abaqus® 6.8-1. This method was entitled *ThreadGen*© and its structure is illustrated in Fig. 1.

The input of the program consists of the connection's geometrical parameters, loading conditions, material and contact properties together with parameters concerning the numerical analysis like mesh size.

During the first stage of the program, a Matlab® program generates the coordinates of the connection geometry based on the connection input. These coordinates are then processed to generate two Python scripts that can be run by Abaqus® (*Connection.py* and *ConnectionResult.py*). Another Matlab® program generates a script *ConnectionOutput.m* that contains the data necessary to process the generated numerical results.

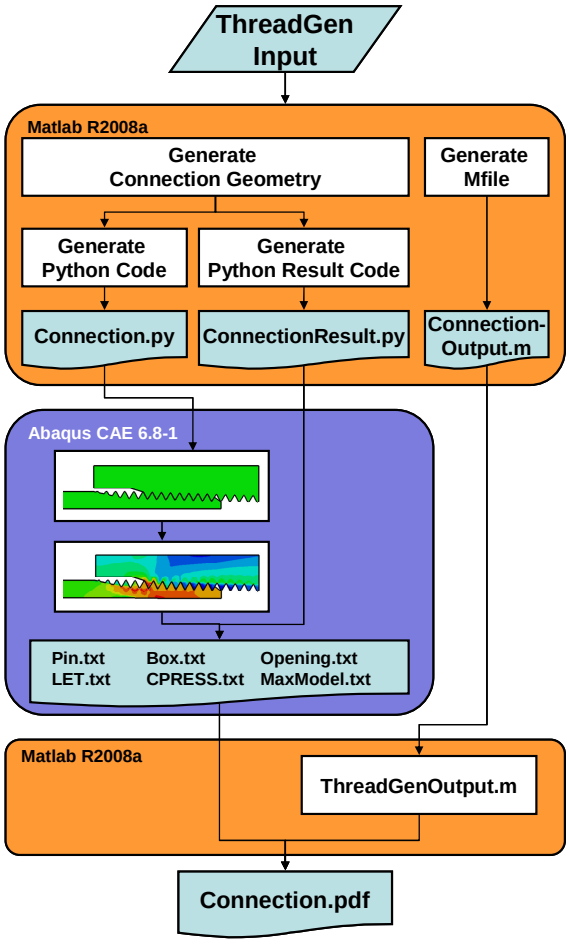

Fig. 1: Structure of the parametric program ThreadGen©

During the second stage, the Python scripts are run in Abaqus®. The script *Connection.py* generates the model geometry together with material, interaction, loading and mesh properties. The model is then analyzed and the second Python script *ConnectionResult.py* is run, which processes the results and selects the relevant data from the finite element simulations and generates specific output as txt-files and images.

In the final stage the output data is processed again by Matlab® to generate a pdf-document summarizing the selected results. This is done by the script *ThreadGenOutput.m* which uses the earlier generated script *ConnectionOutput.m*. The generated results in the txt-files can also be used for further detailed analysis.

When performing parametric studies multiple variations of a connection can be easily simulated by generating a batch of input scripts in the first stage. During the second stage, all connections are then automatically simulated and processed. In the third stage the generated output files are processed automatically.

III. Finite Element Model

A. Model Geometry

ThreadGen© was used to perform a parametric study on an API Line Pipe connection. The standard connection according to API 5B specifications [19] is shown in Fig. 3 and consists of a female box that connects the threaded ends (called "pin") of two pipes. For the numerical model, only the section in the dashed rectangle is used. The resulting model is shown in Fig. 3. The modeled connection has a nominal size of 4", which corresponds to a pin with outside diameter of 114.3 mm and wall thickness of 6.0 mm. The box has an outside diameter of 132.1 mm and total length of 114.3 mm. The unthreaded pipe body of the pin has a length of 100 mm to eliminate boundary effects when an external tensile stress is applied at its free end.

The script to generate the connection geometry is built in such a way that the geometric parameters like pin diameter and wall thickness, box wall thickness, number of engaged threads and thread dimensions - thread pitch and height - can be easily adjusted. In this way all standard connection sizes and a wide range of modifications can be easily generated.

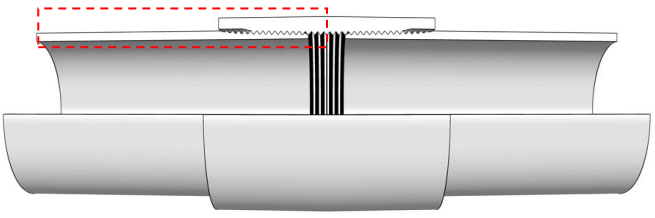

Fig. 2: Section view of an API Line Pipe Connection

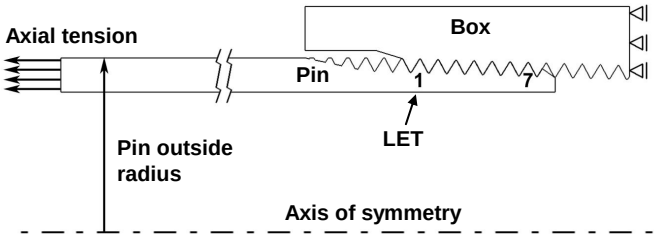

Fig. 3: 2D axisymmetric model of the API Line Pipe connection

The mesh of the FE model was determined through a mesh optimization study and is illustrated in Fig. 4. For the standard 4" connection, the pin consists of 14111 and the box of 5670 linear quadrilateral CAX4R elements. The global mesh size for both pin and box is 1 mm. A finer mesh with seed size 0.2 mm was used in the threads of the box. Since the box is a more rigid component than the pin, the box thread surfaces serve as the master elements in the contact analysis. The mating pin thread surfaces are defined as the slave elements and have an even finer mesh. To be able to study the local stress distribution, the thread roots of the pin are seeded with fifteen elements. The resulting mesh details of the standard API Line Pipe connection are shown in Fig. 5. Note that to avoid sharp edges at the thread crest and root a fillet was applied with a radius of 0.05 mm.

A multi-linear elastic-plastic material model with kinematic hardening for API grade B steel is used. This is the standard material for this type of connection. The model uses a Young's modulus of 208 GPa and a Poisson coefficient of 0.3. The material's yield strength is 241 MPa. The ultimate tensile stress value (true stress) is 521 MPa, the corresponding elongation is 23%. All values correspond to the properties of API steel grade B as specified by API 5L [20].

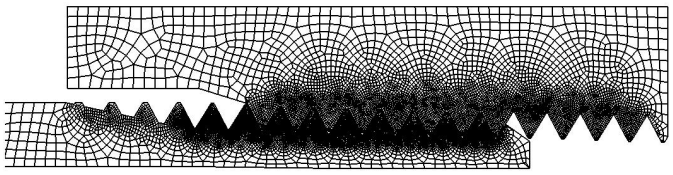

Fig. 4: Mesh of the FE model

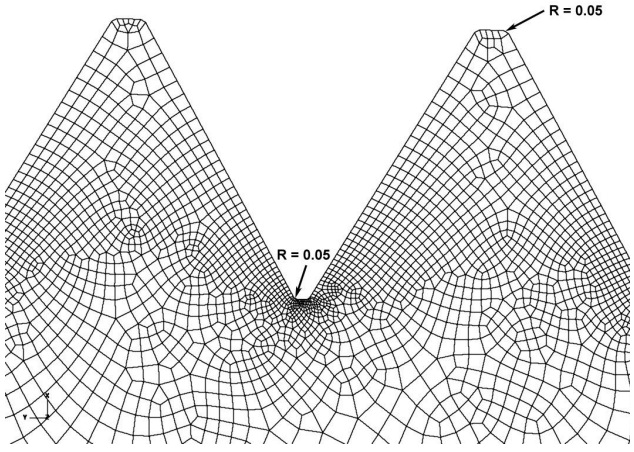

Fig. 5: Detailed mesh around thread root of the pin

B. Analysis of the standard connection

The analysis is carried out in two consecutive steps. In the first step the make-up of the connection is simulated by applying a certain radial overlap between pin and box in the model. This overlap corresponds to the number of make-up turns specified in API spec. 5B. The thread surfaces are then brought into contact using the interference fit option in Abaqus®. During the second step an additional axial tensile stress is applied, as shown in Fig. 3. The magnitude of this stress should be lower than the stress corresponding to the connection's pull-out strength, that can be estimated from the empirical formulas given by Clinedinst [21]. For the considered connection a value of 373 kN is calculated for the pull-out strength. This corresponds to a uniform axial tensile stress of 183 MPa in the pipe body of the pin. Since the thread opening increases drastically at loads near thread pull-out, the calculations tend to diverge from a stable solution. For this reason the applied axial tensile stress is limited to 150 MPa.

The resulting von Mises equivalent stress distribution for both calculated steps is shown in Fig. 6. Note that the stresses in the pin are very high and are close to the material's yield strength even in the make-up stage. When the axial load is applied, the highest stress concentration appears at the root of the last engaged thread of the pin (indicated by the arrow in Fig. 6b). This corresponds to the results obtained by Griffin et al [1] for the analysis of well casing connections and by Dvorkin and Toscano [9] for other API connections.

In Fig. 7 and Fig. 8 the different stress components are shown for the make-up stage and with an additional external load of 150 MPa. From these figures it can be seen that for both load steps, the high von Mises stresses are mainly the result of hoop stresses and axial stresses. Radial and shear stresses are low apart from some local effects around the last engaged thread of the pin.

The acting hoop stresses in the pin have a negative sign, which indicates compressive stresses while the hoop stresses in the box are positive, being tensile stresses. In the thread runout region of the pin, the axial stresses are compressive at the inside wall of the pin and axial tensile stresses appear at the outside. This is the consequence of bending of the pin due to make-up deformation. A similar situation appears at the box recess region. This is the unthreaded extension at the left side of the box. Due to make-up this recess tends to bend causing the axial stress gradient at that location.

The maximum acting von Mises equivalent stress is 425 MPa, which corresponds to a stress concentration factor of 2.83 relative to the applied axial tensile stress of 150 MPa. The stress concentration is mainly composed of axial and hoop tensile stresses. The compressive hoop stress in the pin is reduced due to the axial tensile stress.

The stress concentration at the last engaged thread of the pin is caused by the non uniform load distribution of the axial load over the different threads. This distribution, as a percentage of the total load, is shown in Fig. 9, thread number 1 corresponds to the LET of the pin, as shown in Fig. 3.

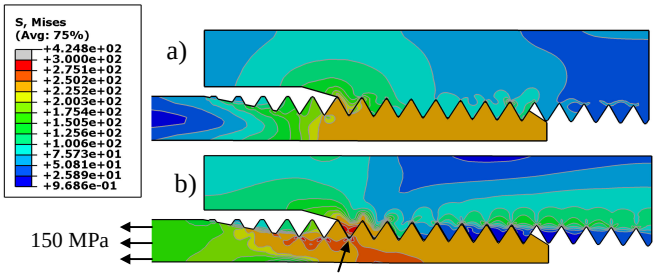

Fig. 6: von Mises stress distribution a) at make-up; b) with an external axial tensile stress of 150 MPa

At an external tensile stress of 100 MPa, the LET carries 47% of the total load. The thread after the LET, which is not fully engaged (thread 0 in Fig. 9), carries a negative load which is a compression caused by the bending of the pin during make-up. When the external stress is increased to 150 MPa, the LET starts to bend, transmitting part of its load to the other threads. Additionally, with this load, the threads will start to slide over each other, creating an opening between the threads and eliminating the compressive load on thread 0. This way the load carried by the LET is reduced to 36% of the total load.

The opening between the threads, however, is highly undesirable since the fluid inside the pipe can find its way out through the created helical path.

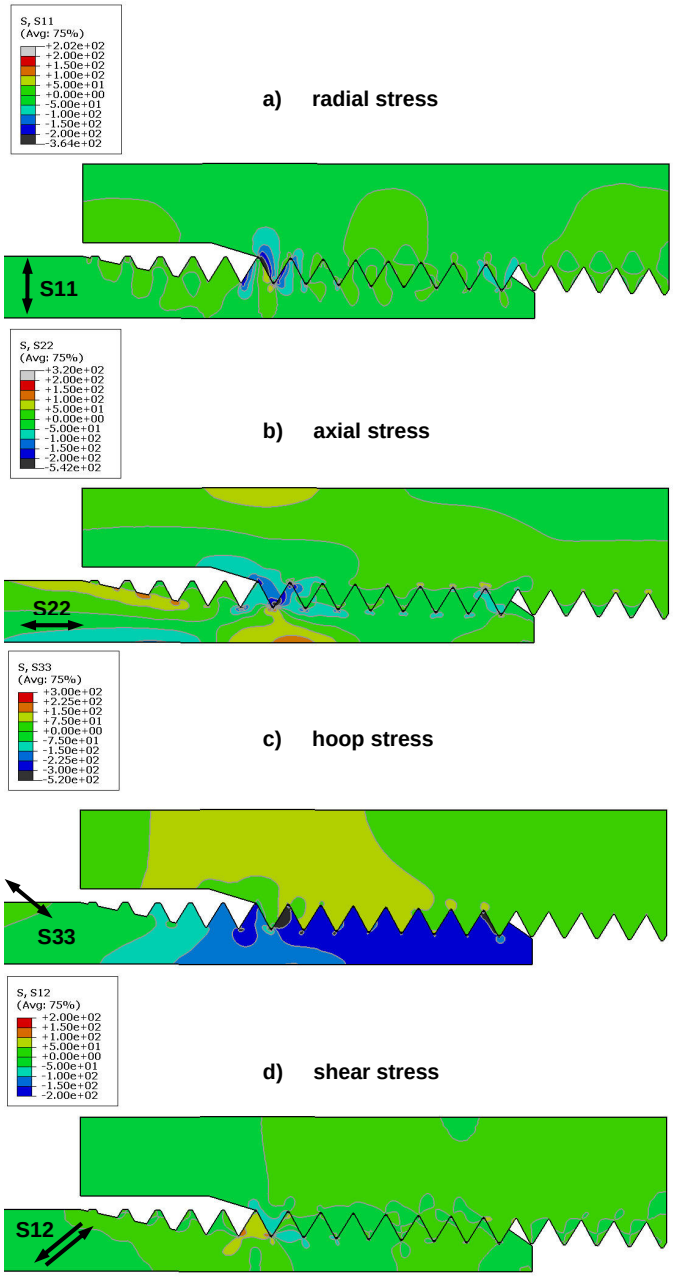

Fig. 7: Stress components at make-up

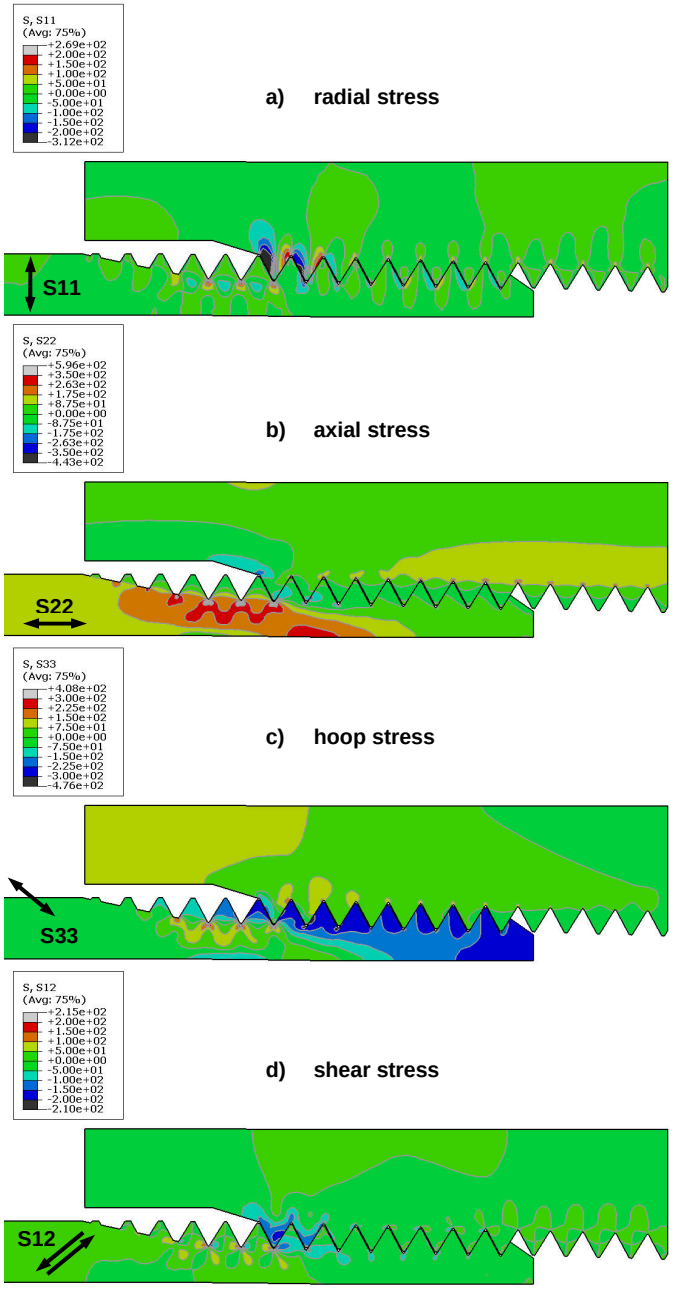

Fig. 8: Stress components with an additional axial load of 150 MPa

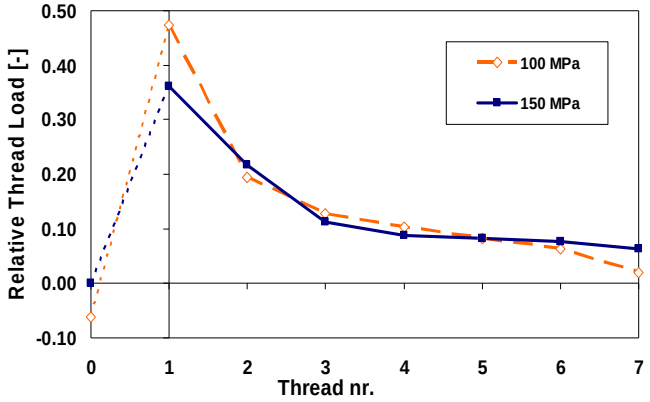

Fig. 9: Thread load distribution (numbering as in Fig. 3)

IV. Parametric Study

A. Performance Parameter

It is known from Newport [3] that changing the hoop stiffness of pin or box affects the load distribution over the threads. The exact correlations and the effect on the overall behavior of the connection, however, remain unknown.

To study the influence of changes in COF, pin and box wall thickness and box recess length, a parametric study was carried out. To evaluate the results of this study, a performance parameter P is introduced, see Eq. 1:

$$P = \frac{1}{O_n} \cdot \frac{1}{TL_n} \tag{1}$$

The performance parameter combines the inverse of the normalized thread opening O_n, as an indication for the sealability of the connection, with the inverse of the normalized thread load at the last engaged thread of the pin TL_n, as a measure for the static and fatigue strength of the connection. This way the parameter encloses the two basic requirements that should be met during its service life.

The normalized opening O_n is defined as the ratio between the value of the opening of the connection with a certain modification and the value of the opening of the standard API Line Pipe connection (0.093 mm) at an external axial stress of 150 MPa and with a COF of μ = 0.12, see Eq. (2):

$$O_n = \frac{O_{mod\,ified\_connection}}{0.093mm} \tag{2}$$

As will be shown in Fig. 10, the thread opening starts to increase after a certain external axial stress is exceeded. For this reason the normalized opening O_n is defined at the highest applied external stress of 150 MPa. At this stress, however, the LET is bent and the load distribution over the threads has changed. This is why the normalized thread load TL_n is defined at a lower external axial stress of 100 MPa where the load distribution is more representative for the overall behavior of the connection.

The normalized thread load TL_n is the ratio between the thread load at the LET of the pin of the connection with a certain modification and the standard API connection at an external axial stress of 100 MPa (47%), see Eq. (3).

$$TL_n = \frac{TL_{mod\,ified\_connection}}{47\%} \tag{3}$$

The parameters O_n and TL_n are defined relative to the values of the standard API Line Pipe connection, therefore the value of the performance parameter P equals 1 for the standard connection. A value of $P > 1$ implies an improved performance relative to the standard connection, while $P < 1$ implies a performance decrease. In the following paragraphs the performance parameter will be used to quantify the effects of parametrical changes on the behavior of the connection.

B. Results

1) Influence of the coefficient of friction

By changing the coefficient of friction as the only parameter during a series of simulations it was found that the thread opening due to external loading is highly dependent on the value of the COF. Even when the COF is kept between the values mentioned previously, the behavior of the connection changes significantly, as can be seen from Fig. 10.

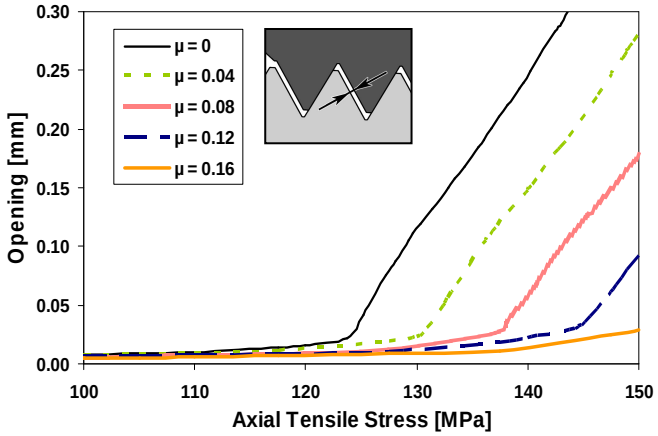

Fig. 10: Influence of the coefficient of friction on the thread opening

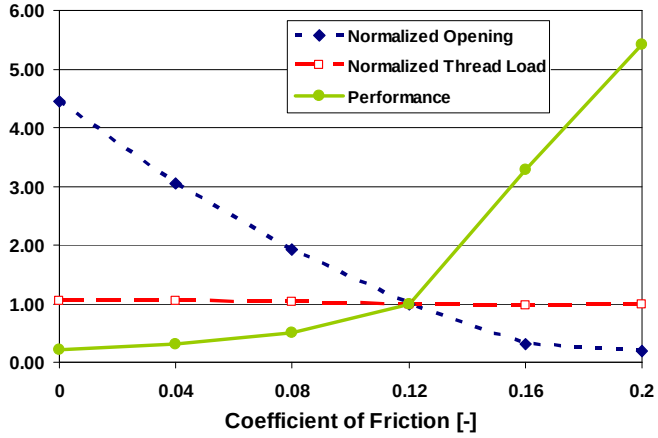

Fig. 11: Influence of the coefficient of friction on the connection parameters

The opening is defined as the perpendicular distance between the thread flanks, and varies for an external tensile stress of 150 MPa between 0.03 mm when μ = 0.16 and 0.41 mm for the frictionless situation. At low values of the COF, the thread opening starts to increase at a lower external load than when a higher COF is used.

From this it can be seen that accurate knowledge of the COF is necessary to model threaded connections. In a previous study by the authors [22], the COF was determined experimentally for an API Line Pipe connection. A value of μ = 0.12 was obtained, which is used as the standard value for the COF throughout the subsequent simulations.

Despite the important influence on the thread opening of the connection, a change in COF has no important effect on the stress and load distribution of the connection, as shown in Fig. 11. For this reason the performance parameter *P* increases with increasing coefficient of friction. As a remark it is noted that increasing the friction between pin and box can be undesirable in some cases because of the higher torque necessary for make-up. Additionally, thread grease or thread compounds are necessary to avoid galling damage that can occur during make-up due to high friction. The performance parameter, however, does not take this phenomenon into account.

2) Box wall thickness variation

When the wall thickness of the box is increased, this component becomes more rigid. This means that the deformation of the box during make-up will be smaller and lower tensile hoop stresses will appear as is illustrated in Fig. 12 (the hoop stresses are taken at outside wall of the box). This means that, for the same number of make-up turns, the pin will have to deform more. For the standard connection, the engaged threads of the pin are yielding at make-up. A further increase in plastic deformation, for the connection with the increased box wall, does not change the pin hoop stress significantly. But in the runout region of the pin, which does not yield at make-up, the magnitude of the compressive hoop stresses are increased due to the higher box stiffness. When the box wall is decreased, box stresses increase and pin stresses decrease in the runout region. The influence of the box wall thickness on the axial stress and von Mises equivalent stress is completely similar.

When the connection is loaded, it can be seen from Fig. 13 that a thinner box results in a lower thread load on the LET of the pin. However, due to the higher deformation of the pin, the opening will be larger. The increased opening dominates the thread load reduction giving a decreased overall performance *P*. Increasing the box wall thickness gives an increased performance (up to 6% for a 6mm wall thickness increase). This is only due to the reduced thread opening, the thread load does not increase with a wall thickness larger than the standard value, although the hoop stress in the runout region of the pin is higher.

Only a box wall thickness increase results in a connection with a better performance. However, this would mean a heavier, more expensive coupling and hence is not desirable.

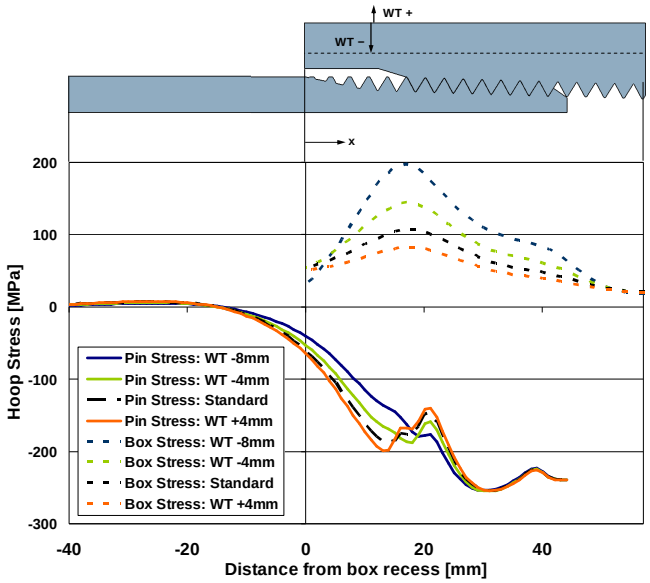

Fig. 12: Hoop stress at the inside wall of the pin and the outside wall of the box at make-up for different values for the box wall thickness.

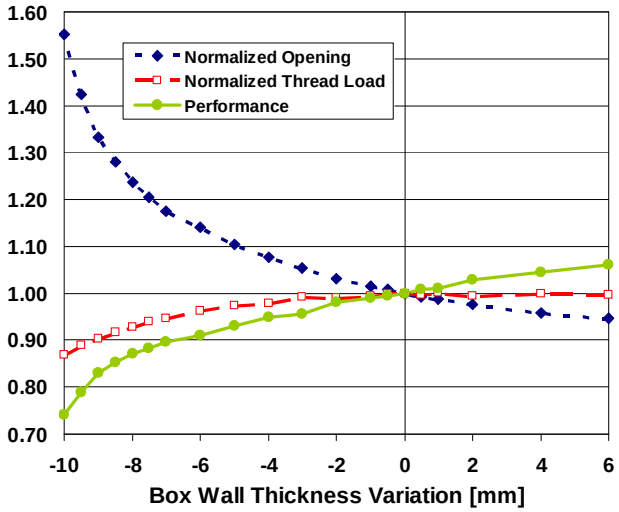

Fig. 13: Influence of the box wall thickness on the connection parameters

3) Pin wall thickness variation

Instead of decreasing the box wall, the pin wall could be increased to get the same change in stiffness between pin and box. As can be seen from Fig. 14, a pin wall thickness increase results in an increased box hoop stress and a decreased compressive hoop stress in the runout region of the pin at make-up.

When an external axial load is applied, it can be seen that both the thread load at the LET of the pin and the thread opening decrease with increasing pin wall thickness. Hence the performance parameter increases with increasing pin wall thickness. Note that an increased wall thickness of the pin, means that the total force on the connection is increased since the external applied axial stresses are kept constant at 100 MPa and 150 MPa.

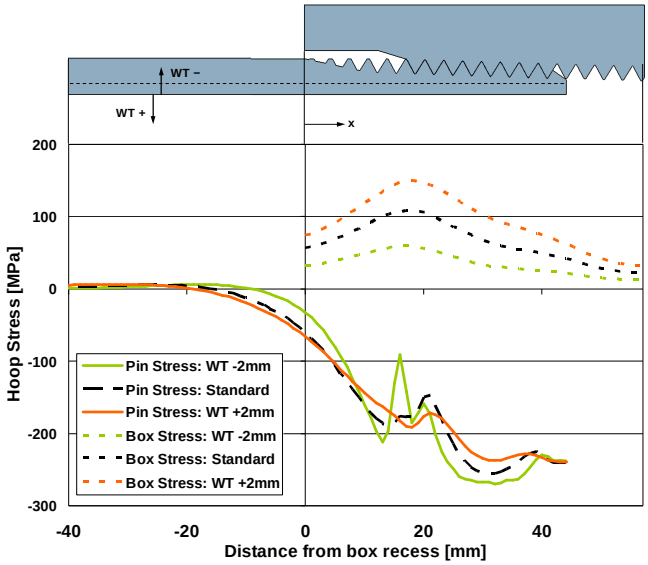

Fig. 14: Hoop stress at the inside wall of the pin and the outside wall of the box at make-up for different values for the pin wall thickness.

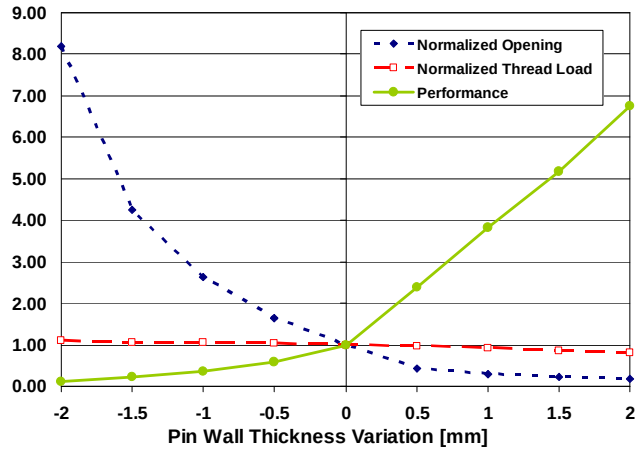

Fig. 15: Influence of the pin wall thickness on the connection parameters

4) Recess length variation

As is discussed in paragraph III.B, bending of the recess causes a raised axial stress in the box. For this reason, the recess length was changed during the parametric study. From Fig. 16 it can be seen that reducing the recess length results in a higher maximum value of the hoop stress in the box and reduces the hoop stress in the runout region of the pin. As can be expected from the previous results, this creates a reduction in thread load on the LET of the pin together with an increased opening. In Fig. 17 results for connections with a reduced recess length, together with varying wall thickness are shown. It can be seen that decreasing the recess length increases the connection's performance until a maximum is reached after which the performance will decrease. With a reduced box wall thickness, this maximum appears for a smaller value of the recess reduction.

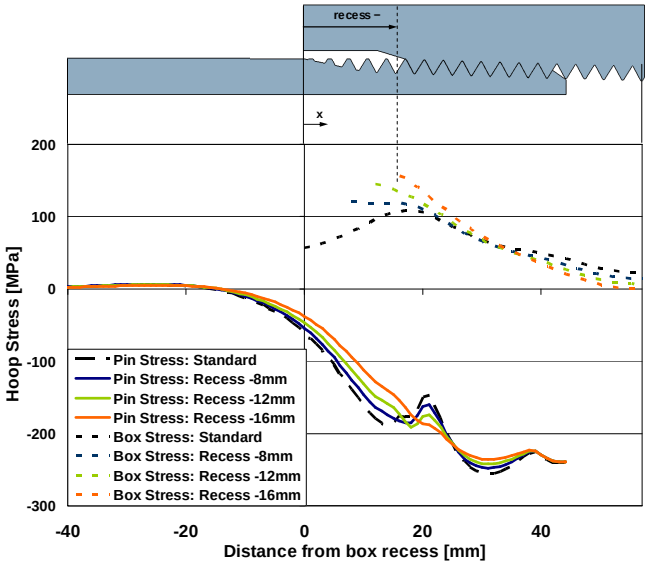

Fig. 16: Hoop stress at the inside wall of the pin and the outside wall of the box at make-up for different values of the box recess length.

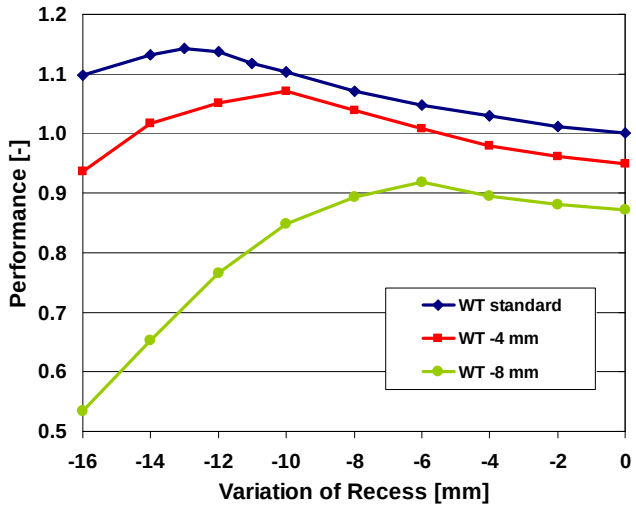

Fig. 17: Influence of the box recess length and wall thickness on the connection performance

For any recess reduction, an additional decrease of the box wall thickness does not result in an increased connection performance, which corresponds to the results obtained for the connections where the box wall thickness was altered. The best result is obtained for a box with standard wall thickness and a recess reduction of 13 mm.

V. Conclusions

A new modeling method, entitled *ThreadGen*©, to perform parametric studies on threaded connections has been presented. The modeling strategy and the used non-linear 2D axisymmetric finite element model were discussed. The modeling method was illustrated by a parametric study of an API Line Pipe threaded connection.

A performance parameter was defined, combining strength and sealability parameters to quantify the influence of the

coefficient of friction, pin and box wall thickness and recess length. It was shown that accurate knowledge about the coefficient of friction between the threads is necessary to obtain reliable results.

Improved performance was obtained for a pin with increased wall thickness, reducing the box wall thickness is not desirable. Additionally an optimal value for the box recess length was found, different from the standard size.

ACKNOWLEDGEMENTS

The authors would like to acknowledge the financial support of the BOF fund (B/04939) of the Ghent University-UGent and of the FWO Vlaanderen (3G022806).

REFERENCES

[1] Griffin, R.C., Kamruzzaman, S., Strickler, R.D., *Casing Drilling Drill Collars Eliminate Downhole Failures,* Offshore Technology Conference, Houston, Texas, USA, May 2004.

[2] Glinka, G., Dover, W.D., Topp, D.A., *Fatigue assessment of tethers*, Institution of Mechanical Engineers Conference, Proceedings nr. C135/86, pp. 187-198, 1986.

[3] Newport, A., *Stress and fatigue analysis of threaded tether connections*, PhD Thesis, University College London, 1989.

[4] Assanelli A.P., Dvorkin, E.N., *Finite-Element Models of OCTG Threaded Connections*, Computers & Structures, 47(4), pp. 725-734, 1993.

[5] Dvorkin, E. N., Assanelli, A. P. and Toscano, R. G., *Performance of the QMITC Element in Two-Dimensional Elasto-Plastic Analysis*, Computers & Structures, 58(6), pp. 1099-1129, 1996.

[6] Assanelli, A.P., Xu, Q., Benedetto, F., Johnson, D.H., Dvorkin, E.N., *Numerical/experimental analysis of an API 8-round connection*, Journal of Energy Resources Technology-Transactions of the ASME. 119(2), pp. 81–88, 1997.

[7] Curley, J.A., Prinja, N.K., *Failure Investigation of an offshore drilling* component, Abaqus Users' Conference, pp. 1-14, Chester, UK, May 1999.

[8] MacDonald, K.A., Deans, W.F., *Stress analysis of drillstring threaded connections using the finite element method*, Engineering Failure Analysis, 2(1), pp. 1-30, 1995.

[9] Dvorkin, E.N. and Toscano, R.G., *Finite element models in the steel industry, Part II: Analyses of tubular products performance*, Computers and Structures, 81(8-11), pp. 575–594, 2003.

[10] Kristensen, A.S., Toor, K., Solem, S.I., *Finite Element analysis of jar connections: modeling considerations*, Journal of Structural Mechanics: Special issue for the 18th Nordic Seminar on Computational Mechanics, pp. 1-4, Helsinki, Finland, 2005.

[11] Guangjie, Y., Zhenqiang, Y., Qinghua, W., Zhentong, T., *Numerical and experimental distribution of temperature and stress fields in API round threaded connection*, Engineering Failure Analysis, 13(8), pp. 1275–1284, 2006.

[12] Bertini, L., Beghini, M., Santus, C. and Baryshnikov A., *Fatigue on drill string conical threaded connections, test results and simulations*, 9th Int. Fatigue Congress, Atlanta, USA, 2006.

[13] Santus, C., Bertini, L., Beghini, M., Merlo, A., Baryshnikov, A., *Torsional strength comparison between two assembling techniques for aluminium drill pipe to steel tool joint connection*, International Journal of Pressure Vessels and Piping, 86(2-3), pp. 177-186, 2009.

[14] Ribeiro Plácido, J.C., Valadão de Miranda, P.E., Netto, T.A., Pasqualino, I.P., Miscow, G.F., de Carvalho Pinheiro, B., *Fatigue analysis of aluminum drill pipes*, Materials Research, 8(4), pp. 409-415, 2005.

[15] Chen, J.J., Shih, Y.S., *A study of the helical effect on the thread connection by three dimensional finite element analysis,*" Nuclear Engineering and Design, 191(2), pp. 109–116, 1999.

[16] Zhong, A., *Thread Connection Response to Critical Pressures*, Abaqus Users' Conference, pp. 690–706, Paris, France, May 2007.

[17] ISO 10407-1, *Petroleum and natural gas industries – Drilling and production equipment – Part 1: Drill stem design and operating limits*, 2004.

[18] Ertas, A., Cuvalci, O., Carper, H.J., *Determination of Friction Characteristics of J-55 OCTG Connections Lubricated with Environmental Safe Thread Compound*, Tribology Transactions, 42(4), pp. 881-887, 1999.

[19] API Specification 5B, *Specification for Threading, Gauging and Thread Inspection of Casing, Tubing and Line Pipe Threads (U.S. Customary Units)*, American Petroleum Institute, fourteenth edition, 1996.

[20] API Specification 5L, *Specification for Line Pipe*, American Petroleum Institute, forty-second edition, 2000.

[21] Clinedinst, W.O., *Joint Strength Formulas for API Threaded Line Pipe*, API Circular PS-1533, 1976.

[22] Van Wittenberghe, J., De Baets, P., De Waele, W., Van Autrève, S., *Numerical and Experimental Study of the Fatigue of Threaded Pipe Couplings*, accepted at the Contact and Surface Conference, Algarve, Portugal, to be published in June 2009,.

Proceedings of the 8th National Congress on Theoretical and Applied Mechanics, May 28-29, Brussels, Belgium.

Combined experimental-operational modal testing of a bow-string footbridge

Edwin Reynders[1], Guido De Roeck[1]
[1]Katholieke Universiteit Leuven, Department of Civil Engineering
Kasteelpark Arenberg 40, B-3001 Leuven, Belgium
email: edwin.reynders@bwk.kuleuven.be, guido.deroeck@bwk.kuleuven.be

Abstract— **A recent development in Operational Modal Analysis (OMA) is the possibility to use measured, artificial forces as an addition to the unmeasured, ambient excitation. This combined experimental-operational or OMAX approach (Operational Modal Analysis with eXogenous forces), requires special system identification algorithms, that take both the ambient and the forced excitation into account. The ambient excitation is not considered as noise, as it is in Experimental Modal Analysis (EMA), but as a valuable yet unmeasured part of the excitation, so that the ratio between forced and ambient excitation can be much lower than in classical EMA testing. The modes that are (partly) excited by the measured forces can be scaled in an absolute way, e.g., to unity modal mass. The combined modal testing of footbridges is explored for a bow-string footbridge with spans of** 75.2m **and** 30.3m**. The modal parameters (eigenfrequencies, damping ratios, mode shapes and modal scaling factors), obtained from a combined vibration test, are compared with the ones obtained from other modal tests and from a finite element model. The comparison demonstrates the feasibility of using small, cheap, and practical actuators for OMAX testing of footbridges, as opposed to the heavy, expensive, and impractical actuators such as electromechanical or hydraulic shakers that usually have to be used for EMA testing of civil engineering structures.**

Keywords— **structural mechanics, operational modal analysis, exogenous inputs, combined vibration testing**

I. Introduction

Due to the continuous economical demand for a more efficient use of structural materials and due to important improvements in design and manufacturing methods, the slenderness and span length of bridges in general and footbridges in particular have increased significantly during the last decades. Lightweight, slender structures are, however, more sensitive to dynamic loads and therefore more likely to be the subject of human comfort problems, such as frequent perception of excessive vibrations, or structural problems, such as fatigue or flutter. As a result, the susceptibility of footbridges to vibrations has become an important design issue. The experimental verification of the design values, in particular the modal parameters such as eigenfrequencies, damping ratios, mode shapes, and modal scaling factors, is essential for design validation, so for guaranteeing the safety and serviceability of the structure. Damping and boundary conditions may depend on the vibration amplitude. Therefore, it is important that the experimental determination of the modal parameters of the structure "as built" is performed in normal operational conditions, i.e., around the operating point. This belongs to the domain of operational modal analysis (OMA).

In operational modal analysis, the dynamic response of a structure to the operational forces is measured. From the response, the modal parameters are extracted using output-only system identification methods. A disadvantage of the OMA approach is that the mode shapes can not be scaled in an absolute sense, e.g. to unity modal mass, unless a second measurement is performed with adding or removing a significant amount of mass to or from the structure [10]. This is rather cumbersome for heavy structures such as (foot)bridges [9]. Another disadvantage of OMA is that the frequency content of the ambient excitation is usually narrow banded, and as a result only a limited number of modes can be extracted from the ambient data with high quality.

Therefore, there is an increasing interest towards operational modal analysis with exogenous inputs (OMAX) [4], where an artificial force is used in operational conditions and a system model is identified that takes both the artificial and the operational forces into account. The main difference between OMAX and the traditional experimental modal analysis (EMA) approach from mechanical engineering [5], [8], [3] is that the operational forces are included in the identified system model: they are not considered as noise but as useful excitation. As a consequence, the amplitude of the artificial forces can be equal to, or even lower, than the amplitude of the operational forces. This is of crucial importance for the modal testing of civil engineering structures, since it allows the use of excitation devices that are small and practical when compared to the actuators that are needed for EMA testing such as electromechanical or hydraulic shakers, which are heavy and difficult to transport.

In this paper, OMAX testing of footbridges is explored for a steel arch footbridge at Wetteren, Belgium. It has a large span of 75.2m and a short span of 30.3m. The footbridge was subjected to three OMAX tests: using a drop weight system, an impact hammer, and a pneumatic artificial muscle (fig. 1).

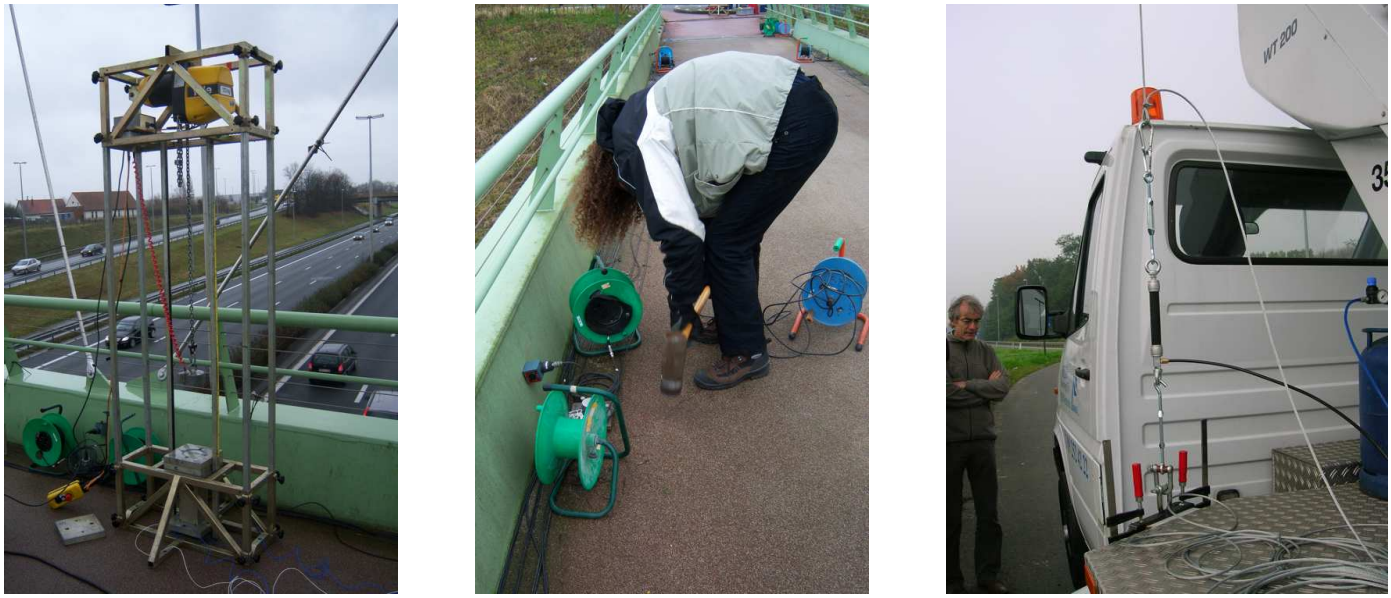

Fig. 1. Actuators used for combined modal testing of the Wetteren footbridge: a drop weight system (left), an impact hammer (center), and a pneumatic artificial muscle (right).

The text is organized as follows. First, the choice of actuators for combined modal testing is briefly discussed. Then, the formulation of a system model that takes both the ambient and the forced excitation into account, is treated, and it is explained how such a model can be identified from measured data using subspace identification. Next, the combined modal testing of the Wetteren footbridge is discussed thoroughly, and the results are compared to the values obtained from other modal tests and from a finite element model. The paper ends with the conclusions drawn from the tests.

II. Excitation sources

Table I contains a comparative overview of the properties of four possible actuators for the combined modal testing of footbridges and the ever present ambient excitation. It is clear that the choice of the type of actuator depends on the criteria that are of major concern for a specific application.

If the cost of testing and the ease of installation are critical, the use of shakers can be excluded since they are not very cost-effective [7]. If a specific excitation signal is needed, such as a multisine, a (periodic/burst) random signal, or a swept sine, and a maximum force amplitude of several kN is sufficient, the use of a pneumatic artificial muscle (PAM) could be considered as an alternative for a shaker, since its investment cost is smaller. However, since a PAM can only exert tension forces, it has to be mounted between the bridge deck and a fixed anchor point beneath the bridge, which means the installation time and cost are still quite high. PAMs have originally been designed for application in robotics. The idea of using them for bridge testing, as well as the development, originated recently from the Acoustics and Vibration Research Group of Vrije Universiteit Brussel [2].

A cheap, fast and easy-to-install drop weight system was developed at the Structural Mechanics division of K.U.Leuven [7]. To control the amplitude of the generated impact force, both the mass (up to 120kg in steps of 10kg) and the drop height (up to 1m), can be adjusted. An electromagnet is used for lifting and dropping the mass. The frequency content of excitation can be influenced by adjusting the settings of the damper on which the mass falls. With this system, even eigenfrequencies below 1Hz can be excited easily [12]. The drop weight system can be considered as a larger and more controllable version of the classical impact hammer, which, due to the low maximum force, is only feasible for combined modal testing of moderately short footbridges. When continuously repeated impacts during a certain period of time are required, an impact hammer requires a lot of manpower. This is not the case for the drop weight system, where the power for lifting the mass is provided by a small electric motor.

III. Subspace identification for combined vibration tests

Suppose that a total of n_o outputs (accelerations, velocities, displacements, strains, ...) and n_i forces are measured and that the measured outputs are grouped in a vector $\boldsymbol{y}(t) \in \mathbb{R}^{n_o}$ and the measured forces in a vector $\boldsymbol{f}(t) \in \mathbb{R}^{n_i}$. In this section, it is shown a system model that takes both the ambient and the forced excitation into account can be

TABLE I
COMPARISON OF EXCITATION SOURCES. THEIR PROPERTIES ARE ASSESSED FROM VERY FAVORABLE (++) OVER NEUTRAL (0) TO VERY UNFAVORABLE (−−).

criterion	ambient	shaker	drop weight	hammer	PAM
investment cost	++	−−	+	+	+
installation cost	++	−−	+	++	−
power consumption	++	−−	+	++	0
low-frequency excitation	++	0	+	−	0
high-frequency excitation	−	++	+	+	+
modal scaling factors	−−	++	++	+	+
controlled amplitude	−−	++	++	0	++
controlled signal	−−	++	0	−	++
maximum amplitude	−	++	++	−	0

constructed and identified from the measured data.

When the structure is linear elastic and has general viscous damping, its spatial discretization with finite elements yields the following system of ordinary differential equations:

$$\boldsymbol{M}\frac{d^2\boldsymbol{u}(t)}{dt^2}+\boldsymbol{C_2}\frac{d\boldsymbol{u}(t)}{dt}+\boldsymbol{K}\boldsymbol{u}(t)=\boldsymbol{B_2}\boldsymbol{f}(t)+\boldsymbol{B_3}\boldsymbol{e}(t),$$

where $\boldsymbol{M}$, $\boldsymbol{C_2}$ and $\boldsymbol{K}$ are the mass, damping, and stiffness matrices, respectively, $\boldsymbol{e}(t)$ is the vector with the ambient nodal forces, $\boldsymbol{u}$(t) is the vector with nodal displacements, $\boldsymbol{B_2}$ and $\boldsymbol{B_3}$ are selection matrices and t denotes the time. The finite element equations can be rearranged into a continuous-time state space model, that has the advantage of containing only first order derivatives:

$$\frac{d\boldsymbol{x}(t)}{dt}=\boldsymbol{A_c}\boldsymbol{x}(t)+\boldsymbol{B}_{c1}\boldsymbol{f_t}+\boldsymbol{B}_{c2}\boldsymbol{e}(t), \tag{1}$$

where

$$\begin{aligned}\boldsymbol{x}(t) &= \begin{bmatrix}\boldsymbol{u}(t)\\ \frac{\boldsymbol{du}(t)}{dt}\end{bmatrix} \qquad \boldsymbol{A_c}=\begin{bmatrix}\boldsymbol{0} & \boldsymbol{I}\\ -\boldsymbol{M}^{-1}\boldsymbol{K} & -\boldsymbol{M}^{-1}\boldsymbol{C}_2\end{bmatrix}\\ \boldsymbol{B}_{c1} &= \begin{bmatrix}\boldsymbol{0}\\ \boldsymbol{M}^{-1}\end{bmatrix}\boldsymbol{B_2} \qquad \boldsymbol{B}_{c2}=\begin{bmatrix}\boldsymbol{0}\\ \boldsymbol{M}^{-1}\end{bmatrix}\boldsymbol{B_3}.\end{aligned}$$

$\boldsymbol{x}(t)$ is called the state of the structure. If $\boldsymbol{y}(t)$ contains some linear combination of nodal accelerations, velocities or displacements, it can be written as

$$\begin{aligned}\boldsymbol{y}(t) &= \boldsymbol{C_a}\frac{d^2\boldsymbol{u}(t)}{dt^2}+\boldsymbol{C_v}\frac{d\boldsymbol{u}(t)}{dt}+\boldsymbol{C_d}\boldsymbol{u}(t)\\ &= \left[\boldsymbol{C_d}-\boldsymbol{C_a}\boldsymbol{M}^{-1}\boldsymbol{K} \quad \boldsymbol{C_v}-\boldsymbol{C_a}\boldsymbol{M}^{-1}\boldsymbol{C_2}\right]\boldsymbol{x}(t)\\ &\quad \boldsymbol{C_a}\boldsymbol{M}^{-1}\boldsymbol{B_2}\boldsymbol{f}(t)+\boldsymbol{C_a}\boldsymbol{M}^{-1}\boldsymbol{B_3}\boldsymbol{e}(t)\\ &= \boldsymbol{C}\boldsymbol{x}(t)+\boldsymbol{D}\boldsymbol{f}(t)+\boldsymbol{D_e}\boldsymbol{e}(t),\end{aligned} \tag{2}$$

where $\boldsymbol{C_a}$, $\boldsymbol{C_v}$ and $\boldsymbol{C_d}$ are selection matrices.

When the forces $\boldsymbol{f}(t)$ and $\boldsymbol{e}(t)$ can be approximated with some function that is piecewise constant during each discrete time step Δt, the following discrete-time state-space model of the structure is obtained:

$$\boldsymbol{x}_{k+1} = \boldsymbol{A}\boldsymbol{x_k}+\boldsymbol{B}\boldsymbol{f_k}+\boldsymbol{B_e}\boldsymbol{e_k} \tag{3}$$

$$\boldsymbol{y_k} = \boldsymbol{C}\boldsymbol{x_k}+\boldsymbol{D}\boldsymbol{f_k}+\boldsymbol{D_e}\boldsymbol{e_k} \tag{4}$$

where

$$\begin{aligned}\boldsymbol{A} &= e^{\boldsymbol{A_c}\Delta t}\\ \boldsymbol{B} &= (\boldsymbol{A}-\boldsymbol{I})\boldsymbol{A_c}^{-1}\boldsymbol{B}_{c1}\\ \boldsymbol{B_e} &= (\boldsymbol{A}-\boldsymbol{I})\boldsymbol{A_c}^{-1}\boldsymbol{B}_{c2}.\end{aligned}$$

An eigenvalue decomposition of $\boldsymbol{A}$ yields the undamped eigenfrequencies f_{udi} and the damping ratios ξ_i:

$$\boldsymbol{A}\boldsymbol{\psi_i}=\lambda_i\boldsymbol{\psi_i}, \quad \lambda_{ci}=\frac{\ln\lambda_i}{\Delta t}, \quad f_{udi}=\frac{|\lambda_{ci}|}{2\pi}, \quad \xi_i=\frac{-\lambda_{ci}^R}{|\lambda_{ci}|},$$

where $|\bullet|$ denotes amplitude and λ_{ci}^R denotes the real part of λ_{ci}. The mode shapes $\boldsymbol{\phi_i}$ can be obtained using $\boldsymbol{C}$:

$$\boldsymbol{\phi_i}=\boldsymbol{C}\boldsymbol{\psi_i}$$

How the mode shapes $\boldsymbol{\phi_i}$ can be scaled to unity modal mass in order to obtain the mass-normalized mode shapes $\boldsymbol{\varphi_i}$, is explained in detail in [13].

Since $\boldsymbol{f}(t)$ and $\boldsymbol{e}(t)$ are band-limited, a modal model reduction of (3-4), where only the modes that are excited, are retained, can be performed [13].

When performing vibration measurements, the number of ambient forces acting on the structure (i.e., the length of $\boldsymbol{e_k}$) is usually unknown. Therefore, the term $\boldsymbol{B_e}\boldsymbol{e_k}$ in (3) is replaced by a single vector $\boldsymbol{w_k}\in\mathbb{R}^n$. Moreover, a vector which contains the output measurement noise $\boldsymbol{y_k^N}$ is added to the right hand side of (4), whereupon the term $\boldsymbol{D_e}\boldsymbol{e_k}+\boldsymbol{y_k^N}$ is replaced by $\boldsymbol{v_k}\in\mathbb{R}^{n_o}$. As a result, (3-4) changes into

$$\begin{aligned}\boldsymbol{x}_{k+1} &= \boldsymbol{A}\boldsymbol{x_k}+\boldsymbol{B}\boldsymbol{f_k}+\boldsymbol{w_k}\\ \boldsymbol{y_k} &= \boldsymbol{C}\boldsymbol{x_k}+\boldsymbol{D}\boldsymbol{f_k}+\boldsymbol{v_k}.\end{aligned}$$

This state-space model has only one free parameter: the system order n. The model can be obtained from the measured data with the reference-based combined deterministic-stochastic subspace identification method [13].

IV. The Wetteren footbridge

The construction of a new roundabout at the N42 national road on top of the E40 highway at Wetteren, Belgium, created a potentially dangerous situation for cyclists and pedestrians due to the numerous approaches to and exits from the highway. In order to separate the bicycle track and the footpath completely from the road traffic, a new footbridge was built to the west of the roundabout in 2003 (fig. 2). This steel bridge has two spans, a short one of 30.33m and a large one of 75.23m. At the largest span, the bridge is of the bow-string type, with an inclination of 13.78° of the bows.

Fig. 2. Footbridge in Wetteren, Belgium, viewed from the south side.

Before the modal tests were performed, a detailed finite element model of the bridge was made in ANSYS. The beams and bows were modeled with Timoshenko beam elements (BEAM188), the cables, which are stainless steel bars with diameters between 27 and 30mm, with truss elements (LINK8), and the steel plates of the bridge deck with shell elements (SHELL63). The model shows that for most of the mode shapes, there is a strong interaction between the bows and the bridge deck, which makes these mode shapes truly three-dimensional. The first two modes consist mainly of lateral deformation of the bows while the bridge deck remains relatively undeformed.

An OMA test was performed on October 10, 2007, followed by an OMAX test one day later. For the OMAX test, a commercially available PAM (DMSP-20 from Festo) was used as actuator (fig. 1). In both tests, 72 degrees of freedom (DOFs) where measured in 5 setups: the vertical and horizontal acceleration of the bridge deck at 44 and 23 locations, respectively, and the out of plane acceleration of the bows at 5 locations (fig. 3). Because of the large amount of traffic at the highway under the bridge, monitoring the inclined bows safely is difficult in practice. Therefore, only the out of plane accelerations at the four bow lower ends and at one higher point on a bow were measured. On January 18, 2008, two other OMAX tests were performed. For the first test, the actuator was a drop weight system releasing continuously a mass of 30kg from a height of 20cm (fig. 1). In this test, 33 accelerations were measured in 2 setups. For the second test, a hammer was used to produce continuously repeated impact forces (fig. 1), and 20 accelerations were measured in a single setup.

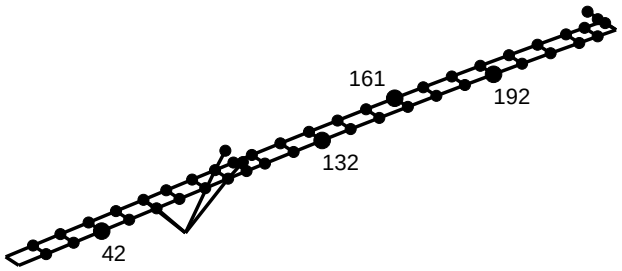

Fig. 3. Measurement grid at the Wetteren footbridge: 3D view from the south side. Each sphere indicates a measurement point. The numbered points appear in the text.

The drop weight, the PAM, and the impact hammer produced a vertical force at nodes 132, 192, and 42, respectively (fig. 3). Fig. 4 shows the power spectral density (PSD) values for the applied forces in the first setup of each test. As a swept logarithmic sine between 0.1 and 10Hz was chosen as force signal, the PAM force drops above 10Hz. The force level for the repetitive hammer impacts is clearly lower than for the PAM and the drop weight. It should be noted that for the PAM and the drop weight, much higher force levels can be achieved if necessary, by using a larger muscle [1] or increasing the mass and drop height, respectively. Since the use of an impact hammer for combined modal testing is treated extensively in the next section, the repetitive hammer impact data will not be considered in the remainder of this section.

Fig. 5 shows the vertical acceleration PSD at point 161 (fig. 3) The distances from this point to both the PAM and the drop weight driving points are equal. The vibration levels for the PAM data are significantly higher than for the other data between 4 and 8Hz. The vibration levels for the drop weight data are significantly higher than for the other data from 15Hz on. At the other frequency intervals, the vibration levels for the OMAX tests are not significantly

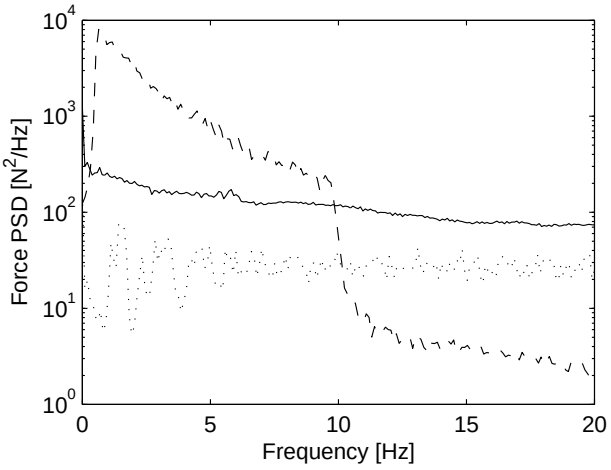

Fig. 4. Wetteren footbridge: Force PSD values (full line: drop weight; dashed line: PAM; dotted line: hammer).

higher than the vibration levels for the OMA test. This clearly illustrates the combined experimental-operational nature of the OMAX tests that have been performed.

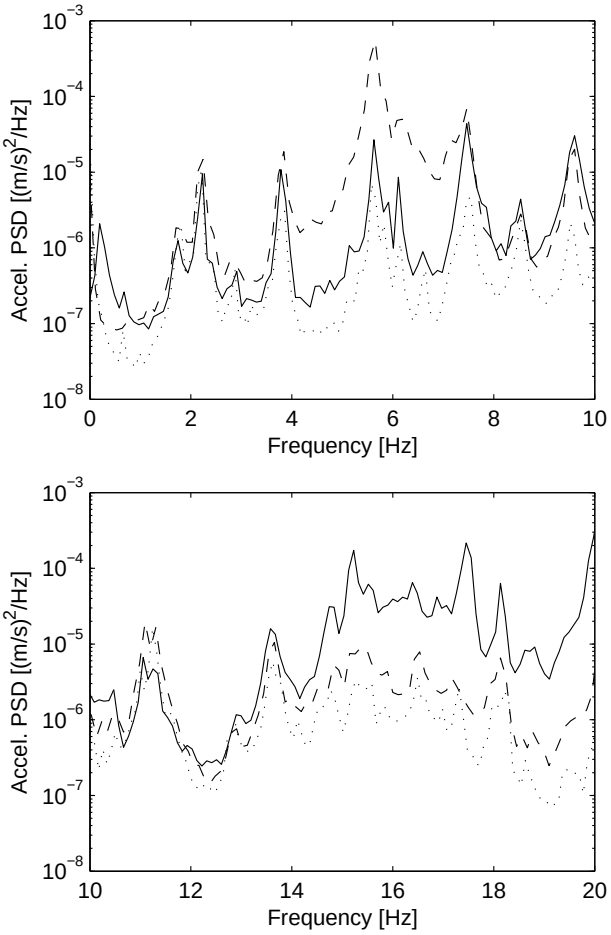

Fig. 5. Wetteren footbridge: Acceleration PSD values at midspan (full line: drop weight; dashed line: PAM; dotted line: only ambient excitation).

The measured signals were digitally low-pass filtered with an eighth-order Chebychev Type I filter with a cutoff frequency of 20Hz in both the forward and the reverse direction to remove all phase distortion, and then re-sampled at 50Hz. Subsequently, the signals were high-pass filtered with a fourth-order Butterworth filter with a cutoff frequency of 0.2Hz, again in both the forward and the reverse direction. From the data, the modal properties have been extracted using the CSI/ref algorithm [13] for the OMAX tests, and the SSI-data/ref algorithm [11] for the OMA test. The block Hankel matrix was constructed with two times 40 and 30 block rows for CSI/ref and SSI-data/ref, respectively. The seven channels that are common to all setups were used as reference channels. A model order range from 2 to 200 in steps of 2 was chosen for the construction of the stabilization diagrams.

Table II provides a comparative overview of the results obtained with the ambient, drop weight, and PAM data. Since normal modes are expected, i.e. the phase difference between the coefficients of the mode shapes is 0° or 180°, the modal phase collinearity (MPC) [6] is a good validation parameter to assess the quality of the mode shapes. An MPC value of 1 indicates a perfect normal mode, an MPC value near 0 a highly complex mode. The MPC values of modes 1,4,8,18,23,25 and 29 are significantly lower for the ambient data than for the OMAX data. This is an indication for less accurate mode shape estimates. Fig. 6 compares some mode shapes, obtained with the ambient and the PAM data. The use of an exogenous force clearly yields smoother mode shapes. For modes 1, this could be expected from the MPC values, but for modes 7 and 27, this is remarkable since the MPC values of both estimates are nearly the same. Other mode shapes, obtained from the OMAX data, are shown in fig 7. Since in the OMAX test with the PAM, more DOFs were measured than in the other tests, only the mode shapes obtained from the PAM data are plotted.

From table II, it is clear that, for most of the modes, the MPC values for the drop weight data are higher than for the PAM data, especially above 6Hz. For some of these modes, there is a corresponding significant difference in damping ratio (modes 1,4,8,9,25 and 29), or even in eigenfrequency (modes 1 and 4), indicating an overall less accurate estimate. For most of the modes, the eigenfrequencies and damping ratios, obtained from both OMAX data sets, correspond very well.

The table also shows the MAC (modal assurance criterion) values between the measured mode shapes $\boldsymbol{\phi}_i$ and the calculated mode shapes $\boldsymbol{\phi}_{FEM,i}$, which are defined as [5]

$$MAC = \frac{|\boldsymbol{\phi}_i^* \boldsymbol{\phi}_{FEM,i}|^2}{|\boldsymbol{\phi}_i||\boldsymbol{\phi}_{FEM,i}|}.$$

TABLE II

OMAX TESTING OF WETTEREN FOOTBRIDGE: COMPARISON OF UNDAMPED EIGENFREQUENCIES f_{udi} AND DAMPING RATIOS ξ_i, OBTAINED FROM THE DROP WEIGHT AND THE PAM DATA USING CSI/REF. THE MAC AND MPC VALUES AS WELL AS THE MSF BETWEEN THE MEASURED MASS-NORMALIZED MODE SHAPES AND THE ONES OBTAINED FROM THE FINITE ELEMENT MODEL, ARE SHOWN AS WELL.

nr.	FEM	ambient			drop weight					pneumatic artificial muscle (PAM)				
	f_{udi} [Hz]	f_{udi} [Hz]	ξ_i [%]	MPC [−]	f_{udi} [Hz]	ξ_i [%]	MPC [−]	MAC [−]	MSF [−]	f_{udi} [Hz]	ξ_i [%]	MPC [−]	MAC [−]	MSF [−]
1	0.739	0.711	2.12	0.80	0.688	0.93	0.99	0.97	$-0.05-0.01i$	0.693	1.05	0.98	0.96	$-0.47-0.21i$
2	1.739	1.671	0.21	1.00	1.678	0.33	0.99	0.95	$-1.13+0.40i$	1.669	0.23	0.99	0.93	$1.79+0.38i$
3		1.769	0.59	0.97	1.775	0.62	0.93			1.758	0.76	0.98		
4	2.363	2.138	1.90	0.80	2.216	0.50	0.99	0.99	$1.59-0.10i$	2.195	0.50	0.99	0.99	$-1.01+0.02i$
5	3.250	3.743	0.76	0.98	3.768	0.61	0.97	0.93	$0.53-0.00i$	3.731	0.55	0.98	0.84	$1.01-0.14i$
6	3.833	3.836	0.67	0.95	3.847	0.58	0.99	0.94	$1.07-0.00i$	3.838	0.49	0.98	0.89	$1.19+0.19i$
7	3.891	4.442	0.56	0.99	4.466	0.77	0.98	0.95	$-1.18+0.02i$	4.480	0.76	0.96	0.91	$0.28+1.36i$
8	3.939	5.143	1.15	0.80	5.187	0.26	0.99	0.95	$0.85-0.02i$	5.154	0.44	0.97	0.92	$1.20+0.14i$
9	6.377	6.111	0.52	0.89	6.126	0.23	0.93	0.92	$-1.02-0.20i$	6.117	0.27	0.99	0.93	$-0.69-0.04i$
10	6.662	6.321	0.73	0.98	6.350	0.78	0.99	0.97	$-0.61+0.32i$	6.321	0.50	0.99	0.96	$-0.10+0.51i$
11	6.991	6.621	0.62	0.98	6.638	0.72	0.98	0.96	$1.21-0.06i$	6.605	0.58	0.99	0.94	$1.21-0.04i$
12		7.209	2.15	0.84	7.287	3.31	0.85			7.238	2.34	0.79		
13	8.028	7.509	0.70	0.84	7.491	0.60	0.89	0.92	$1.10-0.06i$	7.488	0.70	0.88	0.87	$-0.35+0.02i$
14		7.582	1.36	0.88	7.608	1.69	0.97			7.577	1.29	0.93		
15	8.599	8.322	1.18	0.97	8.298	1.24	0.95	0.86	$-1.14-0.00i$	8.307	1.18	0.97	0.88	$-1.24-0.04i$
16		8.556	0.58	0.93	8.587	0.62	0.98			8.565	0.68	0.95		
17		9.570	0.88	0.91	9.605	0.85	0.93			9.565	0.74	0.96		
18	10.395	9.962	1.28	0.87	10.004	1.35	0.96	0.90	$0.14-0.76i$	9.967	1.10	0.94	0.80	$0.32-1.23i$
19	11.397	10.503	0.50	0.96	10.516	0.57	0.97	0.87	$0.92-0.03i$	10.475	0.64	0.97	0.87	$0.99-0.08i$
20	11.864	11.245	0.66	0.97	11.226	0.96	0.96	0.91	$-1.08+0.13i$	11.214	0.78	0.92	0.90	$0.40+1.28i$
21	11.624	11.804	1.71	0.95	11.883	1.97	0.96	0.90	$-0.73-0.05i$	11.821	1.68	0.97	0.88	$0.84-1.17i$
22	13.146	12.739	0.28	0.87	12.777	0.29	0.90			12.728	0.35	0.85	0.80	$0.36-0.00i$
23	13.254	12.896	0.65	0.47	12.900	0.93	0.87	0.94	$-0.90-0.06i$	12.863	0.72	0.65	0.85	$0.48-0.77i$
24	14.479	13.522	0.51	0.86	13.525	0.48	0.83	0.86	$-0.88-0.01i$	13.530	0.72	0.76		
25		13.648	0.60	0.77	13.640	0.42	0.89			13.606	0.39	0.92		
26	15.620	14.809	0.50	0.92	14.842	0.10	0.99	0.92	$-0.94-0.10i$	14.810	0.41	0.95	0.88	$0.03+0.42i$
27		15.225	0.69	0.86	15.223	0.38	0.96			15.213	0.46	0.87		
28	16.648	16.514	0.68	0.97	16.509	0.63	0.97			16.502	0.53	0.96	0.90	$-0.93-0.12i$
29		17.531	0.92	0.72	17.517	0.59	0.90			17.508	0.31	0.90		
30	18.537	17.839	0.26	0.87	17.856	0.26	0.90	0.92	$1.10+0.19i$	17.833	0.28	0.88	0.91	$-0.53+0.02i$

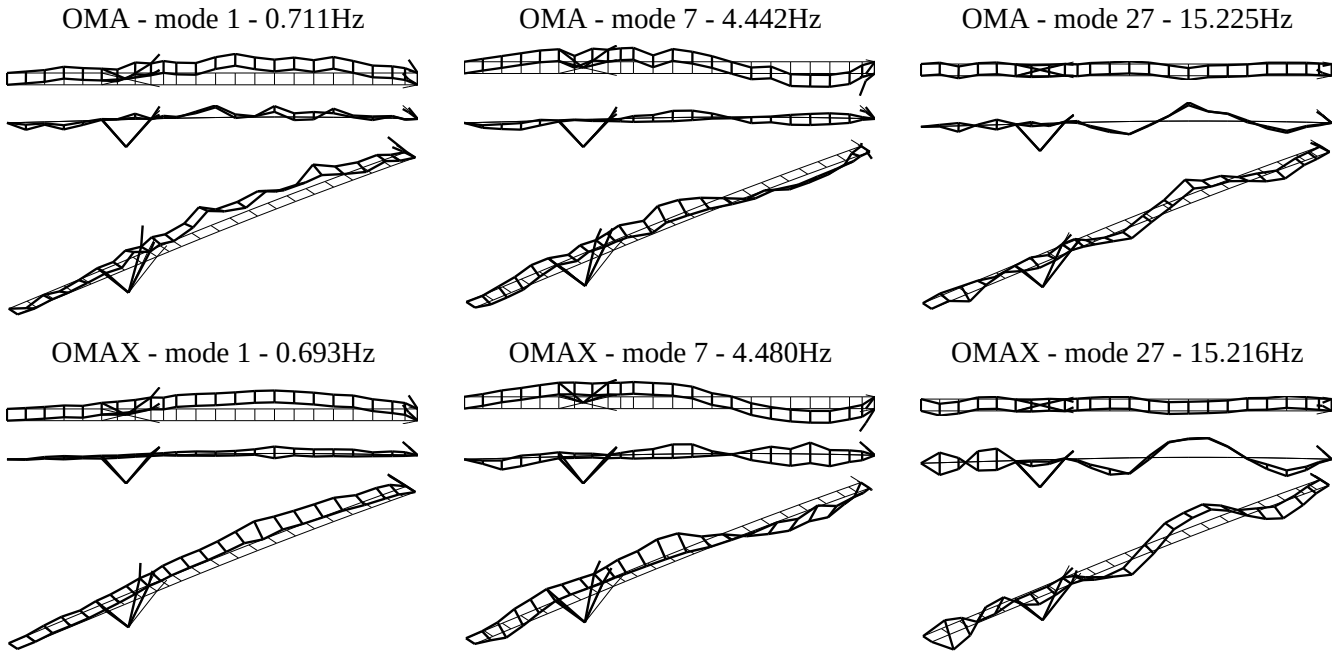

Fig. 6. OMA vs. OMAX testing of Wetteren footbridge: comparison of some mode shapes (top: top view, middle: side view from the southeast side, bottom: three-dimensional view from the south side).

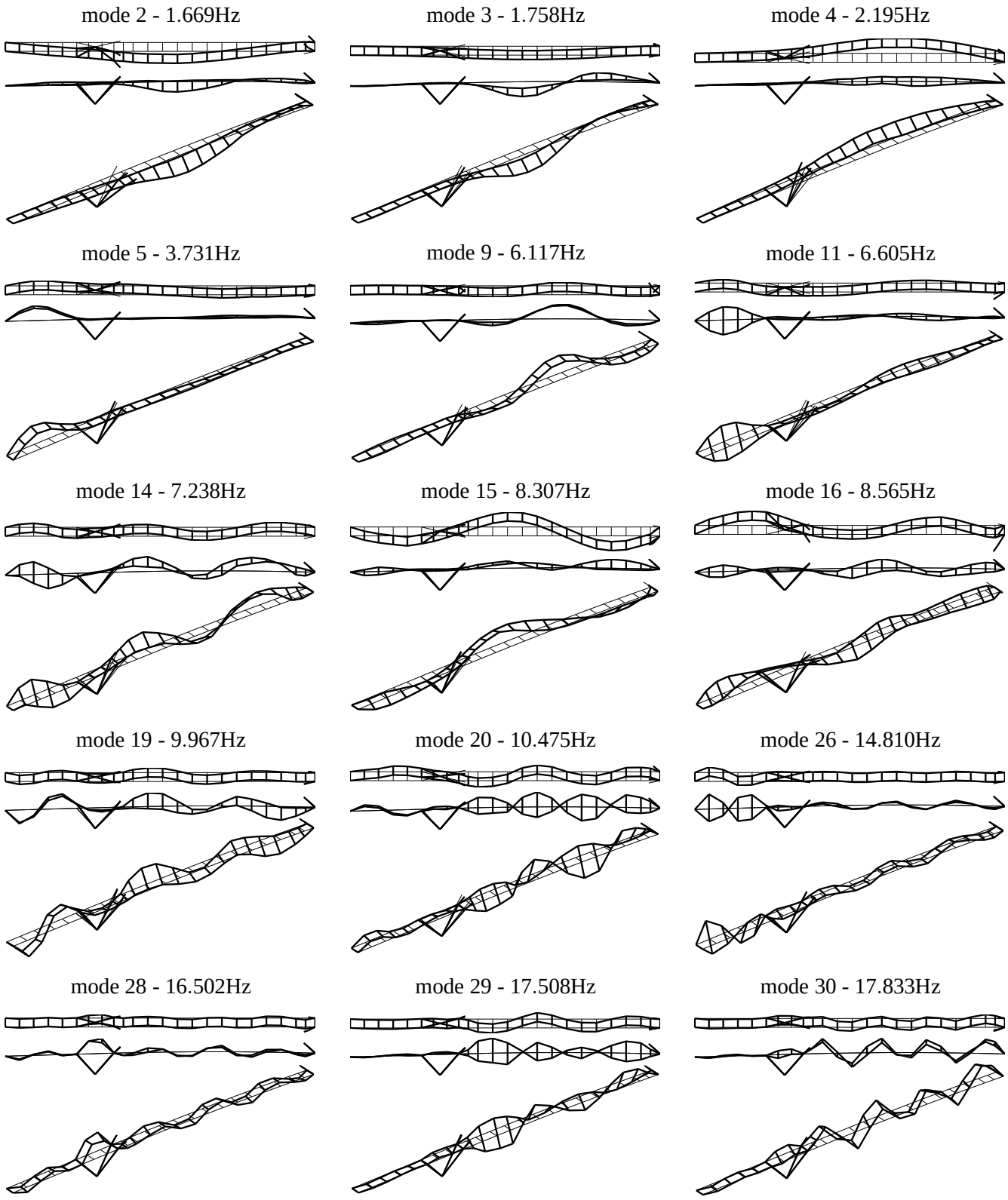

Fig. 7. OMAX testing of Wetteren footbridge: some mode shapes, obtained using CSI/ref (top: top view, middle: side view from the southeast side, bottom: three-dimensional view from the south side).

When the MAC value is unity, both modes are perfectly correlated. When the MAC is zero, both modes are uncorrelated. In the table, the eigenfrequencies, obtained from the finite element model, are given when the MAC value between the calculated mode shape and a measured mode shape exceeds 0.8. In this case, also the modal scaling factor (MSF) between both the measured mass-normalized mode shape $\boldsymbol{\varphi_i}$ and the calculated one $\boldsymbol{\varphi}_{FEM,i}$, defined as [5]

$$MSF = \frac{\boldsymbol{\varphi}_i^* \boldsymbol{\varphi}_{FEM,i}}{|\boldsymbol{\varphi}_{FEM,i}|}, \tag{5}$$

is provided. The MSF gives a least squares estimate of the ratio between both mass-normalized mode shapes. When the MSF is real and close to one, both mass-normalized mode shapes have nearly the same amplitude and phase. Since it only makes sense to calculate the MSF when the corresponding MAC is large [5], the table only shows MSF values when the corresponding MAC exceeds 0.8. For the drop weight data, the real part and the amplitude of the MSF of modes 2,6,7,8,9,13,15,19,20,23,24,26 and 30 lies between 0.8 and 1.2. For the PAM data, this is only the case for modes 4,5,19 and 28.

Since some modes (e.g. modes 1, 2, 4, 8, 22) mainly involve deformation of the bows, sometimes combined with a lateral deformation of the bridge deck, it is not surprising that the MSF for some of these modes (e.g. mode 1) could not be well determined, considering the location and direction of the drop weight and PAM forces. The same holds for modes 5,6,10,11,21 and 26, which mainly involve deformation of the short span. However, since it concerns an OMAX test, the other modal parameters of these modes are accurately determined, thanks to the fact that the operational excitation is taken into account.

V. Conclusions

The capacities of combined modal testing (OMAX testing) of footbridges have been explored in a real-life case study. The steel Wetteren footbridge, whose main span is of the bow-string type, has a very high modal density in the analyzed frequency range $0-18$Hz. Most of the modes show a complex three-dimensional behavior, where the inclined arches interact with the bridge deck. An in-depth comparison with numerical models and OMA test results showed that the modal parameters (eigenfrequencies, damping ratios, mode shapes and modal scaling factors), obtained from the OMAX tests, are of good, sometimes even superior, quality, while the amplitude of the applied forces was of the same level as the amplitude of the operational excitation. This demonstrates the feasibility of using small and practical actuators for modal testing of footbridges.

Acknowledgements

The Wetteren footbridge tests were performed in collaboration with the Industrial Engineering Department of Katholieke Hogeschool Sint-Lieven in Gent, Belgium, and the Acoustics and Vibration Research Group from Vrije Universiteit Brussel in Brussel, Belgium.

References

[1] K. Deckers, T. De Troyer, E. Reynders, P. Guillaume, D. Lefeber, and G. De Roeck. Applicability of low-weight pneumatic artificial muscle actuators in an OMAX framework. In *Proceedings of ISMA2008 International Conference on Noise and Vibration Engineering*, pages 2445–2456, Leuven, September 2008.

[2] K. Deckers, P. Guillaume, D. Lefeber, G. De Roeck, and E. Reynders. Modal testing of bridges using low-weight pneumatic artificial muscle actuators. In *Proceedings of IMAC 26, the International Modal Analysis Conference*, Orlando, FL, February 2008.

[3] D. J. Ewins. *Modal testing*. Research Studies Press, Baldock, U.K., second edition, 2000.

[4] P. Guillaume, T. De Troyer, C. Devriendt, and G. De Sitter. OMAX - a combined experimental-operational modal analysis approach. In P. Sas and M. De Munck, editors, *Proceedings of ISMA2006 International Conference on Noise and Vibration Engineering*, pages 2985–2996, Leuven, Belgium, September 2006.

[5] W. Heylen, S. Lammens, and P. Sas. *Modal analysis theory and testing*. Department of Mechanical Engineering, Katholieke Universiteit Leuven, Leuven, Belgium, 1997.

[6] J.-N. Juang and R.S. Pappa. An eigensystem realization algorithm for modal parameter identification and model reduction. *Journal of Guidance, Control and Dynamics*, 8(5):620–627, 1985.

[7] C. Krämer, C.A.M. de Smet, and B. Peeters. Comparison of ambient and forced vibration testing of civil engineering structures. In *Proceedings of IMAC 17, the International Modal Analysis Conference*, pages 1030–1034, Kissimmee, FL, USA, February 1999.

[8] N.M.M. Maia and J.M.M. Silva. *Theoretical and experimental modal analysis*. Research Studies Press, Taunton, U.K., 1997.

[9] E. Parloo, B. Cauberghe, F. Benedettini, R. Alaggio, and P. Guillaume. Sensitivity-based operational mode shape normalization: application to a bridge. *Mechanical Systems and Signal Processing*, 19(1):43–55, 2005.

[10] E. Parloo, P. Verboven, P. an Guillaume, and M. Van Overmeire. Sensitivity-based operational mode shape normalization. *Mechanical Systems and Signal Processing*, 16(5):757–767, 2002.

[11] B. Peeters and G. De Roeck. Reference-based stochastic subspace identification for output-only modal analysis. *Mechanical Systems and Signal Processing*, 13(6):855–878, 1999.

[12] B. Peeters, J. Maeck, and G. De Roeck. Vibration-based damage detection in civil engineering: excitation sources and temperature effects. *Smart Materials and Structures*, 10(3):518–527, 2001.

[13] E. Reynders and G. De Roeck. Reference-based combined deterministic-stochastic subspace identification for experimental and operational modal analysis. *Mechanical Systems and Signal Processing*, 22(3):617–637, 2008.

An automatic tool for the simplified modelling of discrete cracking phenomena in masonry structures : case study on the Magdalene church in Tournai

Jérôme NOËL, Thierry DESCAMPS, Laurent VAN PARYS
Department of Civil Engineering and Structural Mechanics, F.P.Ms Faculty of Engineering of Mons
Rue de Houdain 9, 7000 Mons - Belgium
email : jerome.noel@fpms.ac.be, thierry.descamps@fpms.ac.be, laurent.vanparys@fpms.ac.be

Abstract— **The Magdalene church in Tournai suffers for a long time various pathologies. This article describes a related numerical study prepared in the department of Civil Engineering and Structural Mechanics at the Faculté Polytechnique de Mons. The analysis is based on full 3D models taking into account the behaviour of soft soils through equivalent springs and the superstructure itself. All the materials involved in the study were assumed to be linear elastic. Some non linearities were introduced, by coupling Matlab and ABAQUS, through an automatic iterative approach likely to simulate a discrete crack propagation process. The obtained results confirm the assumptions of the experts about the influence of underground soil alterations and the observed pathologies may then become better understood. A provisional map of soil qualities has been proposed that could be useful for prescribing future geotechnical investigations.**

Keywords— **FEM, masonry, discrete cracking**

I. Introduction

SINCE the civil authorities have understood the necessity to preserve the old building heritage to be transmitted to the next generations, important budgets are allocated to finance heavy restoration campaigns. Many historical buildings have been forgotten for decades and it is important to understand the behaviour of damaged buildings before that efficient solutions may be proposed for the future.

The engineers, by coupling powerful calculation methods with classical on-site investigations, can precise the structural behaviour of the building. This paper presents an application of such a method, the Finite Element Method, to study the rather complex configuration of the Magdalene church made of interactions between the superstructure and the undergrounds parts (soft soils, etc).

II. The church and its pathologies

THE erection of the Magdalene church in Tournai began during the 13th century. It is characterized by an architecture associated with the transition between romanic and gothic style. The church is recognized as ”Historical Heritage” by the Belgian authorities.

Although some damages are not recent, the church seems to suffer new pathologies affecting some important structural parts (namely the main diaphragm arch) since its abandon in 1965. The structural problems led the civil authorities to install temporary strengthening devices.

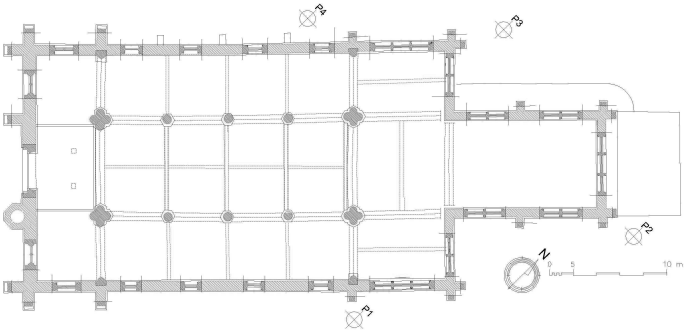

Fig. 1. Plane view of the church

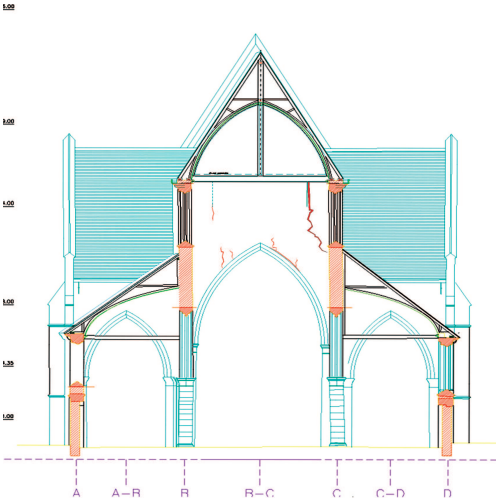

Fig. 2. Outline of the main diaphragm arch’s pathologies

From a local point of view, the observation of disorders shows that pathologies affect the main diaphragm arch (see Fig.2) as well as a set of 2 spans located in the middle part of eastern nave.

From a global point of view, sensitive settlements may be noticed. They affect essentially the external walls of the transept and the western bell tower (see pink line of graphic on Fig.3 and Fig.4). The altitude variations of a stone ribbon all around the church’s walls were taken using an optical level. That ribbon was supposed to have been built horizontally.

III. Preliminary geotechnical campaign

A preliminary geotechnical campaign has been performed. Under the level of the masonry foundations, the quality of soils may be considered as very poor. This could be explained by the fact the church is located along the Escaut River. Nevertheless, the conclusions of the preliminary campaign are based on a limited number of tests that have been performed outside the church as illustrated in Fig.1 (P1, P2, P3 and P4). These did not permit to design a significant repartition map of soils qualities underneath the whole structure.

IV. Finite element modelling of the masonry building

A. Soil model

The soil is modeled with springs that are connected between the estimated level of the bedrock (obtained from the preliminary geotechnical analysis) and the basis of the masonry structure. The stiffness of the springs has been set on the basis of the collected settlement information. An iterative approach has been used : from the comparison between the results of calculations and the trends observed in the reality, the inadequacies are outlined and a modification of stiffness parameters is proposed for the next calculation step.

The iterative process is performed until a correct trend equation between the settlements observed in the model and in the reality is achieved (see Fig.3 and Fig.4).

B. Geometry

The final model used for the computation is composed of three main parts :

- Soft soil : the part under the bottom face of the foundation is modelled by springs made with 8 nodes bricks (compressive strength of the soil - no pressure bulb). The geometrical extension of springs is located directly under the width of external walls and internal pillars.
- Bedrock : the bedrock itself is not included but its particular effect has been taken into account through the length of the springs. The vertical translation of each node at the bottom face of the soft soil has been constrained.
- Superstructure : due to unsatisfying results obtained by previous and more simple methods, a complete 3D model of the superstructure made with 8 nodes bricks has been used. The action of timber frameworks and roof structures has been taken into account through the introduction of equivalent local and distributed loads. The morphology was obtained from a precise topographical survey.

It's important to notice that, although geometrical simplifications were necessary, inertia and cross-section area properties were carefully respected.

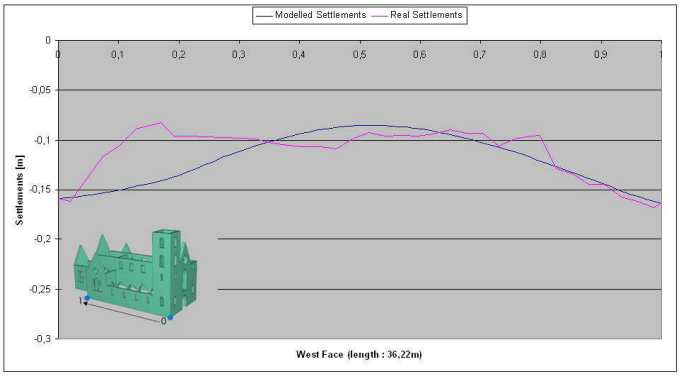

Fig. 3. Modelled and real settlements of the west face

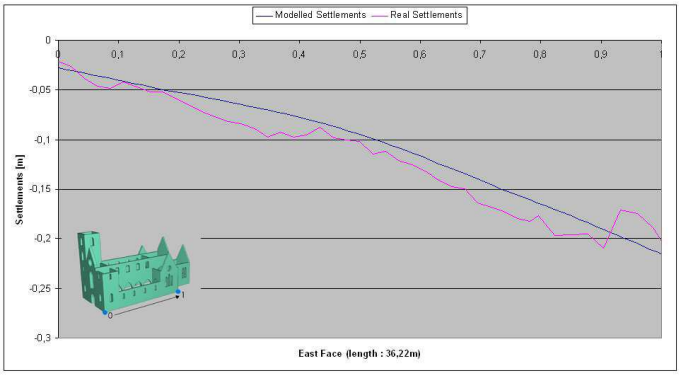

Fig. 4. Modelled and real settlements of the east face

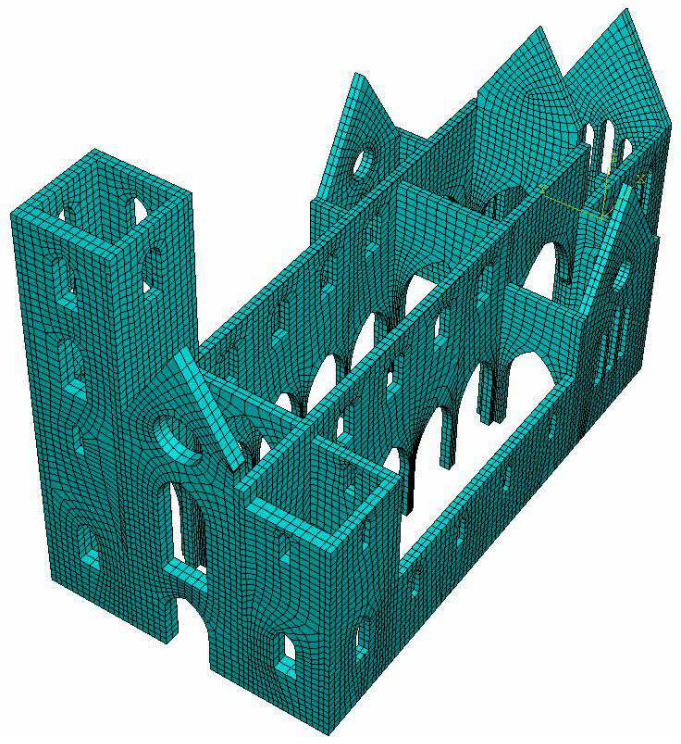

Fig. 5. Meshed model of the superstructure

C. Materials

Due to a lack of knowledge about the characteristics of the walls of the church (no test results were available), we decided to consider each material as homogenous and linear elastic. Of course this kind of behaviour is not very appropriate when applied to masonry structures and soils.

Nevertheless, this assumptions have already been used by recognized specialists like Professor G. Macchi (University of Pavia, Italy) involved in the study of the Pisa Tower (for which soils and masonries were interacting), Professor P. Halleux (University of Brussels, Belgium) engaged in the engineering calculation of the Town hall Tower in Brussels and Professor D. Lamblin (Faculty of Engineering, Mons, Belgium) for several patrimonial studies in Belgium.

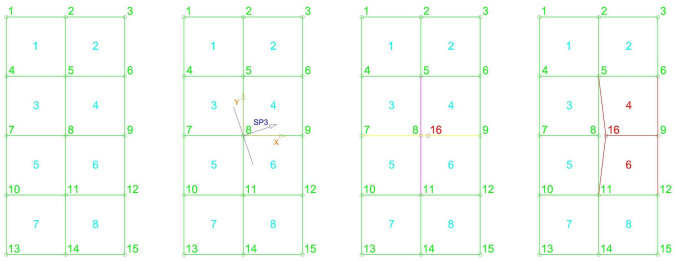

Fig. 6. Steps of the crack initiation process

Moreover, a crack propagation process has been implemented for the masonry model. This is an automatic, discrete and iterative process based on the value of the maximum principal stress and a modified Rankine Criterion : it is assumed that failure occurs when the maximum principal stress σ reaches the uniaxial tension strength σ^+. Actually, the compression strenght is assumed to be infinite. The criterion can then be written as :

$$\infty < \sigma < \sigma^+ \tag{1}$$

Introduncing the dicrete cracking phenomenon consists in modelling the cracks as geometric discontinuities in opposition to the smeared cracking phenomenon for which the caracteristics of the material are modified where the fractures take place.

Actually, both techniques give rather good results for the study of brittle materials, with the smeared cracking model being traditionally far more popular because of its computational conveniance. It may be noticed that discrete cracking model as used in our study have distinct advantages over smeared cracking ones where informations such as detailed cracking path, crack spacing and width are needed.

Initiation of a crack is simulated locally by duplication of one node into two nodes in the model (see Fig.6). On the basis of this new geometry, a new calculation is performed and the propagation of crack is simulated. This process continues until stabilization of the stress state is reached everywhere in the model.

The practical implementation is achieved through a coupling between Matlab and ABAQUS Software. This software detects the node with the highest principal stress and calculates the orientation of the associated vector. This vector reflects the orientation of the real crack plane. As we only depend on the size and orientation of the mesh for the morphology of the crack, we have to determine the modelled crack plane closest to the real one. Then the program duplicates the node in order to create the discrete crack itself. Once those steps are done, a new source file is written (Matlab) and automatically submitted to the computing engine of the finite element software. This last, calculates the stress and displacement fields. The results obtained will be used for the next iteration. For some steps, Matlab has to read the data files provided by ABAQUS. It reads and modifies the source file for introducing the new geometry containing the crack.

In order to validate the results provided by this coupling, we studied the propagation of cracks in a model of a beam composed with a material presenting high compressive strength and rather low tensile strength. We could, then, compare the numeric results with the analytic calculus.

The results show the apparition of a first crack at midspan. It is interresting to see that other cracks are alternatively created on one side and on the other of the first fracture. The cracks evolve until the stabilization of the stress value under the given maximum value.

The total model of the church presents about 65000 nodes and 195000 equations : a reasonable calculation time is a limitation criterion for the geometrical precision and the constitutive law. Although the model can be improved (geometrically and materially), it can give to the problem a good solution with correct understanding of the behaviour of the soil and the superstructure settled on it.

The program gives an overview of the localisation and of the importance of the cracks. Thanks to those results, we could better understand why some reparations were carried out in the past and why the strengthening devices were placed. For instance, nowadays the cracks shown on Fig.8 are not visible but we have the confirmation that those walls had to be repaired.

Moreover, the analyses of those models showed the new repartition of stresses and strains calculated for each step in redundant models.

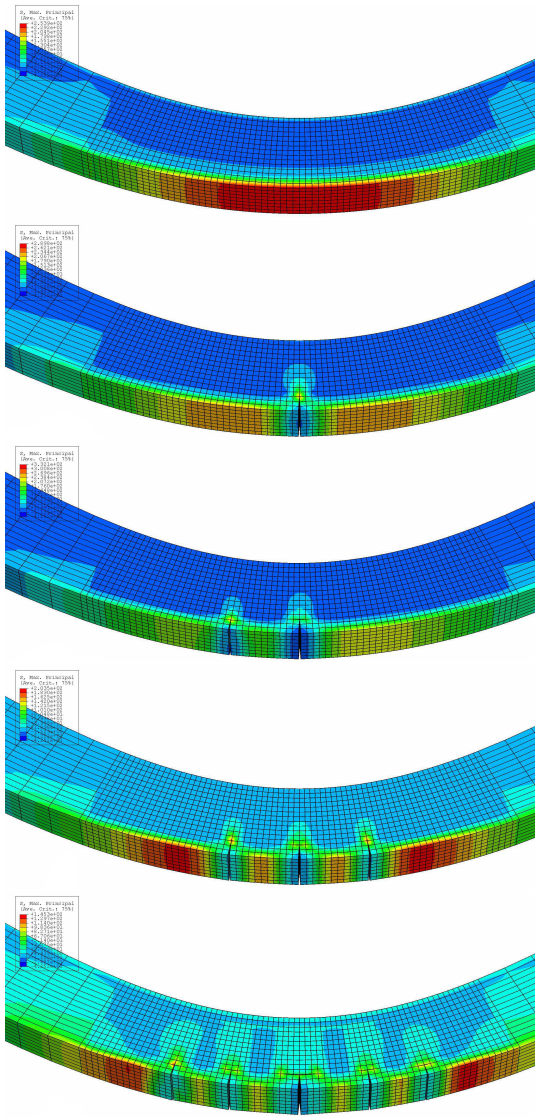

Fig. 7. Overview of the cracking process on a beam submitted to flexion and axial compression

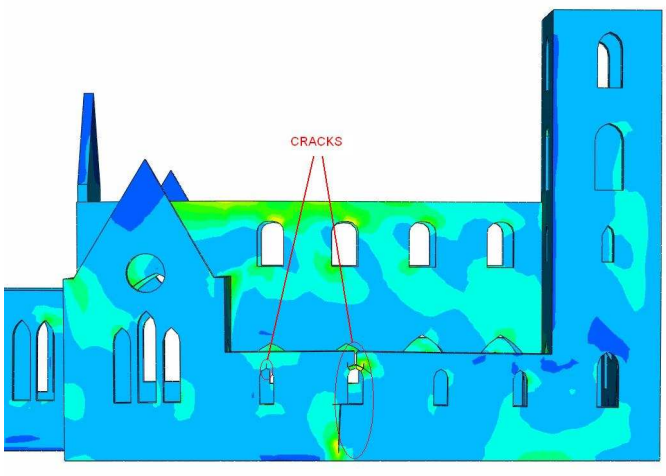

Fig. 8. View of the cracked model of the church

V. Prospects and improvements

ALTHOUGH the results are encouraging, some improvements are needed. The program only works with monopart models which does not allow to deal with models made of different materials for which the tensile resistance varies (e.g. masonry with steel reinforcement). As we only depend on the mesh organisation for the crack orientation, an adaptive mesh during the cracking process would result in taking into account the real crack orientation.

The program provided good results on a beam and for the study of the Magdalene church. The next building to be analyzed is the Our-Lady Cathedral in Tournai which suffers many problems of cracks in its masonry and foundations.

VI. Conclusions

THIS study concerns a finite element analysis performed on a heritage building. It relies on elastic constitutive laws for materials and an automatic discrete iterative cracking process of masonry implemented inside the Matlab environment and piloting an ABAQUS STANDARD solver. Previsions were made about the soil qualities and a map of soil qualities has been proposed that could be useful for prescribing future geotechnical investigations.

Such previsions are important for their consequences on the superstructure. They constitute an efficient and helpful tool for engineers engaged in the preservation of the building.

References

[1] J. NOËL, *Pathologie de l'église de la Madeleine de Tournai*, Master Thesis, F.P.Ms Faculty of Engineering of Mons, Belgium, 2008.

[2] G. MACCHI, *Private communication*, F.P.Ms Faculty of Engineering of Mons, Belgium, 2000.

[3] A. COSTE, *L'architecture gothique : lectures et interpretations d'un modèle*, University of Saint-Etienne, France, 1997.

[4] T. SADOWSKI (ed.), *IUTAM Symposium on Multiscale Modelling of Damage and Fracture Processes in Composite Materials*, Dolny, Poland, 2006.

[5] D. MARTENS & A. VERMELTFOORT, *13th IB^{2}MaC Amsterdam*, Eindhoven University of Technology, The Netherlands, 2004.

Proceedings of the 8th National Congress on Theoretical and Applied Mechanics, May 28-29, Brussels, Belgium.

Operational Transfer Path Analysis

Gert De Sitter, Christof Devriendt, Patrick Guillaume
Vrije Universiteit Brussel, Department of Mechanical Engineering
Acoustics and Vibration Research Group
Pleinlaan 2-1050 Brussel
email: gert.de.sitter@vub.ac.be

Abstract— **One of the tools used to study the NVH behaviour of a system is the Transfer Path Analysis. It aims to identify the operational forces and the propagation paths of the vibrations and is especially interesting in the case when the system is composed of different subsystems. The classical techniques identify the transfer paths when the system is disassembled. This way one eliminates flanking transfer paths. Yet it is very time-consuming and the boundary conditions are not correct anymore. The presented method makes it possible to identify the transfer paths without disassembling the system. The advantages are that the overall testing time is reduced and that the real boundary conditions are present. In this article the theory will be reviewed and it will be validated using data generated by finite element simulations.**

Keywords— **Transfer Path Analysis, operational**

I. Introduction

WHEN one is confronted with an NVH problem, a logical approach is to identify on one hand the NVH sources and on the other hand the contribution of each source to the problem [1], [2]. The contribution of each source will be linked with how the vibrations propagate through the system. One now can have two kinds of situations: either the system is built up from several linked subsystems or this subdivision is not that straight forward.

If the system is not build up from distinct subsystems there will be a common behaviour in all the degrees of freedom. One then should use techniques that exploit this feature, e.g. experimental modal analysis [3], [4], [5]. Using the modal model it is possible to estimate the contributions of the sources. The sources themselves can then be identified by solving the inverse problem [6].

However, if there are several linked subsystems, the vibrations will propagate from the sources through the system following certain transfer paths. Identifying how the sources contribute to the problem comes down to identifying the transfer paths [7], [8], [9], [10]. Such kind of analyses are called: Transfer Path Analysis (TPA), Path Contribution Analysis, ... In this article one will deal with those kind of analyses.

The classical TPA techniques identify the transfer paths by isolating each path. This is possible by disassembling the system [1]. When the system is disassembled, one applies a known force at the location where the subsystem of interest is linked with another subsystem. If one knows the force and the response, one can identify the transfer path. The disassembling is needed to eliminate any flanking paths. This approach has two major disadvantages. First, the disassembling is very time-consuming. Secondly, the boundary conditions are not correct anymore. As all real-world systems are non-linear to a certain extent the system will not be linearised in the correct working points. Note also that during the time that the system is disassembled in most of the cases it probably will not be operational.

In this article a procedure will be described that makes it possible to identify the transfer paths without disassembling the system. This eliminates the two major drawbacks of the classical experimental TPA: the time-consuming disassembling and the wrong boundary conditions. It will be shown that the proposed procedure has another advantage: operational forces are no longer a problem. On the contrary, the more operational forces the better.

In the next section the problem will be stated. This will be followed by a theoretical framework. It will start with a solution for the most simple mechanical case: a 2 degree of freedom system (DOF) with 1 link. Then a system with 2 links will be discussed. After the theoretical section, the procedure will be validated by means of finite element simulations.

II. Problem Statement

Assume a mechanical structure as in Figure 1. It is composed of a clamped lower beam which is connected with an upper beam by three links. Suppose also that there are some unknown operational forces that act on the upper beam. A typical problem could be that the displacement in point X is too large. To solve this problem it would be interesting to know what the forces are in the 3 links and how they contribute to the displacement in point X.

The classical Transfer Path Analyse (TPA) techniques will start with disassembling the system which is very time-consuming. In a second step one applies a known force (or moment) at each link separately. By measuring the responses one is able to estimate the contribution of each transfer path. This is shown in Figure 2. After re-

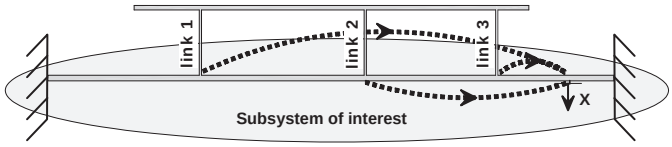

Fig. 1. Problem Statement

assembling again, one can identify the operational forces by solving the inverse problem [11], [12], [13]. Note that after disassembling of the system the boundary conditions of the lower beam could have changed severely which leads to errors. After all, all real world systems are non-linear to a certain extent. So the system will be linearised in working points that do not agree with the operational working points.

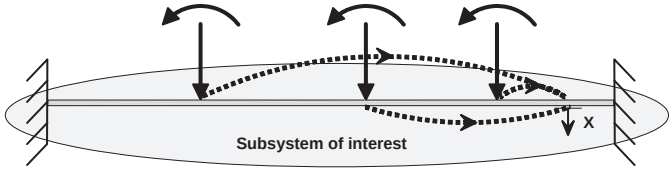

Fig. 2. Identification of 3 transfer paths with classical TPA

It would be interesting if one did not have to disassemble and reassemble the whole system. The question is: 'Is it possible to identify the frequency response function (FRF) between 2 points of an isolated subsystem without disassembling the system?' In other terms: is it possible to eliminate the effects of the upper beam and links? It will be shown that it can be done without disassembling. But then additional measurements will be required at the links. This is shown in Figure 3. The theoretical aspects will be treated more in detail in the next section.

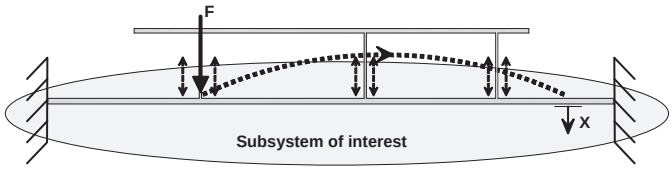

Fig. 3. Identification of the first transfer path with operational TPA

III. Theoretical aspects

A. A system with 2 degrees of freedom

The most simple mechanical structure that consists of 2 linked subsystems is a 2 DOF system (see Figure 4). Suppose that one is interested in the FRF H_{11} between a force F_1 on mass 1 and the response X_1 of mass 1 of the isolated subsystem of interest. So the effects of the linked subsystem have to be eliminated.

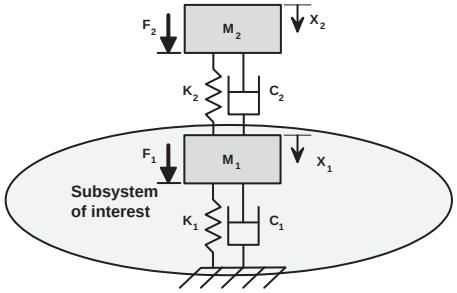

Fig. 4. A 2 DOF system

In Figure 4 M_1, C_1 and K_1 form the subsystem of interest. C_2 and K_2 form the link and M_2 is the linked subsystem. F_2 is an unknown operational force that acts on the mass M_2.

The FRF of the isolated system of interest $H_{11}(s)$ is the FRF of a 1 DOF system, i.e. $H_{11}(s) = (s^2M_1 + s\,C_1 + K_1)^{-1}$. The displacement X_1 of the assembled system equals to:

$$X_1(s) = H_{11}(s)F_1(s) + H_{11}(s)(sC_2 + K_2)(X_2(s) - X_1(s)) \tag{1}$$

This formula forms the basis of OTPA. Because only if there exists an (unknown) operational force $F_2(s)$ which acts on M_2 and only if this force is not fully correlated with the known force $F_1(s)$, the known force $F_1(s)$ and the relative displacement $(X_2(s) - X_1(s))$ are not fully correlated. In this case it is possible to estimate $H_{11}(s)$ using an H_1 estimator with $F_1(s)$ and $(X_2(s) - X_1(s))$ as the references:

$$X_1(s) = H_{11}(s)F_1(s) + G_{11}(s)(X_2(s) - X_1(s)) \tag{2}$$

Note that the less $F_1(s)$ and $(X_2(s) - X_1(s))$ are correlated the better the estimate will be.

A visual representation of this idea is shown in Figure 5. Note that the relative displacement $X_{12} = (X_2(s) - X_1(s))$ should be measured.

Figure 6(a) shows the estimate of H_{11} in the case there is no operational force F_2. As expected, this estimate is wrong. When there is an operational force F_2 that acts on mass M_2 which is not fully correlated with the known force F_1, the OTPA correctly estimates the FRF. This is shown in figure 6(b). Note that both the known force F_1 and the unknown operational force F_2 are white-noise sequences. Because of those uncorrelated forces, the measured FRF of the assembled system which is the FRF between the known force F_1 and the displacement X_1 is noisy too in Figure 6(b).

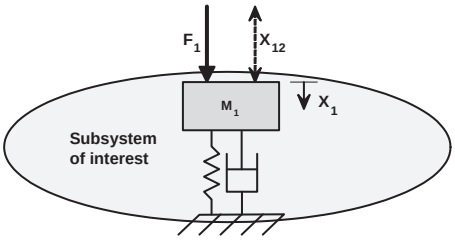

Fig. 5. OTPA of a 2 DOF system: identification of H_{11}

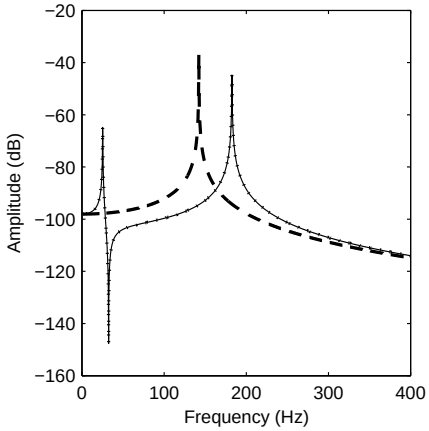

(a) Without an operational force F_2

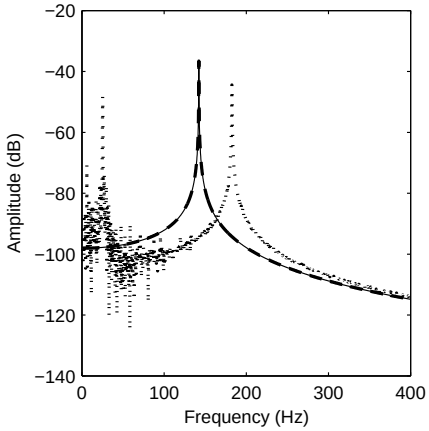

(b) With an operational force F_2

Fig. 6. OTPA of a 2 DOF system: (−−) FRF H_{11} of the isolated subsystem of interest, $(\cdots)$ Measured FRF of the assembled system, (—) OTPA estimate of the FRF of the isolated subsystem of interest

B. A system with 6 degrees of freedom

In this section it will be shown that the OTPA procedure also can be used for structures with multiple links. Suppose that the structure now consists of 6 masses and 2 links as in Figure 7. Suppose also that there can act some unknown operational forces on the masses M_4, M_5 and M_6 and that the transfer path $H_{12}(s)$ between the masses M_2 and M_1 has to be estimated. So the subsystem of interest contains the masses M_1, M_2 and M_3. It can be proved that

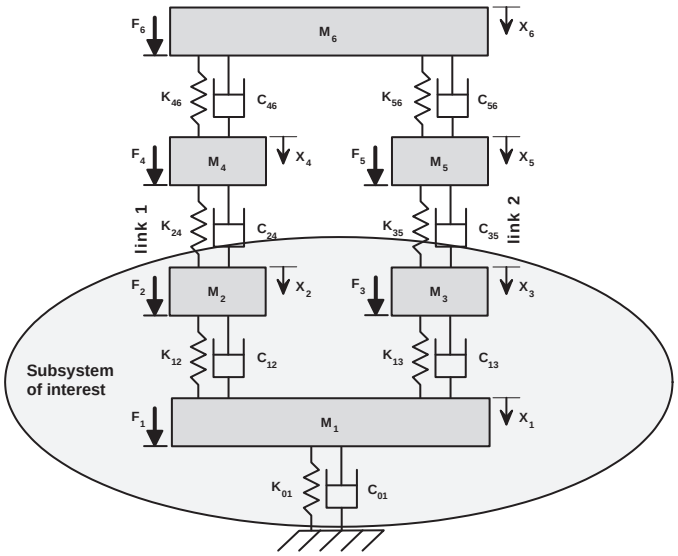

Fig. 7. A 6 DOF system

the displacement $X_1(s)$ can be written as

$$\begin{aligned} X_1(s) = {} & H_{12}(s)F_2(s) + H_{12}(s)(sC_{24}+K_{24})(X_4(s)-X_2(s)) \\ & + H_{13}(s)F_3(s) + H_{13}(s)(sC_{35}+K_{35})(X_5(s)-X_3(s)) \end{aligned} \tag{3}$$

So if one is interested in $H_{12}(s)$ (the FRF of the isolated subsystem of interest), one has to apply a known force $F_2(s)$ at mass M_2. Also one should not apply a force at mass M_3. Now the displacement $X_1(s)$ can be written as

$$\begin{aligned} X_1(s) = {} & H_{12}(s)F_2(s) + G_{12}(s)(X_4(s)-X_2(s)) \\ & + G_{13}(s)(X_5(s)-X_3(s)) \end{aligned} \tag{4}$$

If one is interested in $H_{12}(s)$ of the isolated subsystem of interest, one can apply the H_1 estimator with $F_2(s)$, $(X_4(s)-X_2(s))$ and $(X_5(s)-X_3(s))$ as references. In order to get a correct estimate of $H_{12}(s)$, $(X_4(s)-X_2(s))$, $(X_5(s)-X_3(s))$ and $F_2(s)$ must not be fully correlated. So one needs at least 2 uncorrelated operational forces that act on mass M_4, M_5 or M_6.

This can be visualised as in Figure 8. Note that the relative displacements $X_{24} = X_4(s) - X_2(s)$ and $X_{35} = X_5(s) - X_3(s)$ have to be measured. One can conclude that for every link one needs to measure the relative displacement at that link. Those relative displacements should not be fully correlated which is only possible if the number of uncorrelated operational forces is greater than or equal to the number of measured relative displacements. Note that it is not necessary to know the operational forces.

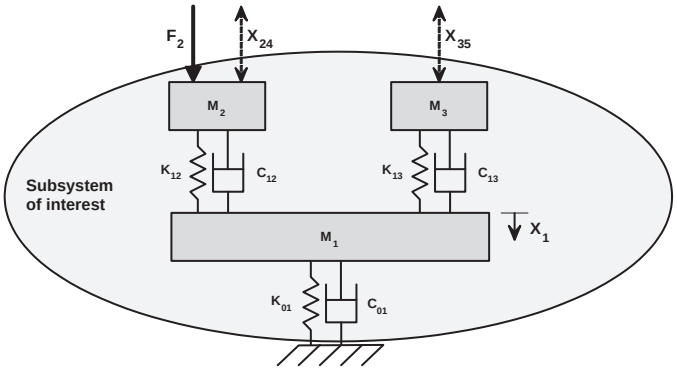

Fig. 8. OTPA of a 6 DOF system: identification of H_{12}

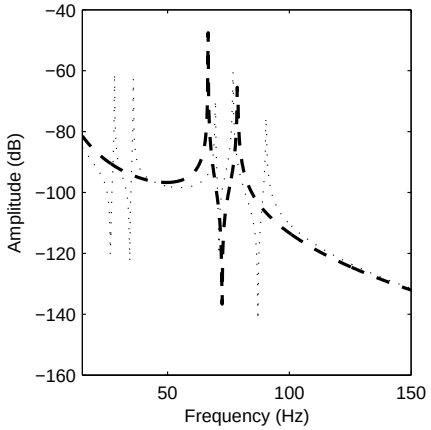

(a) H_{12} of disassembled and assembled system

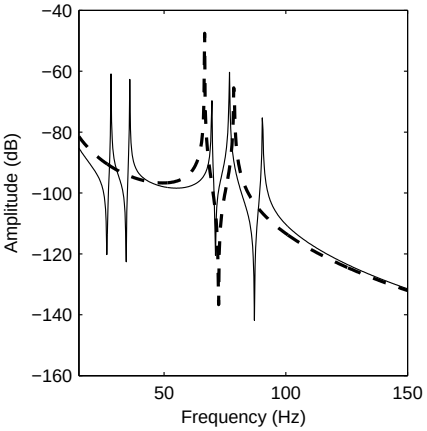

(b) OTPA estimate of H_{12}

Fig. 9. OTPA of a 6 DOF system: without any operational force: (−−) FRF of the isolated system of interest, (···) Measured FRF of the assembled system, (—) OTPA estimate of the FRF of the isolated system of interest

In Figure 9(a) the FRF of interest H_{12} - the FRF of the isolated system of interest - is plotted together with the FRF that would be measured when the system would be assembled. It is obvious that there is a big difference. In this case there are no operational forces applied and this results in a wrong estimate (see Figure 9(b)).

Now 2 uncorrelated operational forces are applied. In Figure 10(a) it can be seen that the FRF that one measures even gets worse because the operational forces act as disturbing noise. But in this case the OTPA estimate is perfect (see Figure 10(b)).

Now one can describe the approach for a general structure with multiple links. First one should identify the isolated subsystem of interest. In a second step one should identify the transfer paths of interest. Each transfer path will have a specific degree of freedom where the force will be applied and a specific degree of freedom where the displacement will be measured. Note that those degrees of freedom always will be within the subsystem of interest (or at the boundary), e.g. in the previous 6 DOF system the known force F_2 has been applied at Mass M_2 and the target displacement was at mass M_1. To estimate a specific transfer path, one should now apply a known force at the force location. At the same time a sufficient set of uncorrelated operational forces should be present at degrees of freedom which are located outside of the subsystem of interest, e.g. in the previous 6 DOF system one needed at least 2 uncorrelated operational forces that acted on mass M_4, M_5 or M_6. Using an H_1 estimator one now can estimate the transfer path of the isolated subsystem of interest. This H_1 estimator will use the known force and the relative displacements at the links as references.

IV. Finite Element Simulations

A. Goal of the simulations

In this section the OTPA method will be validated on the system that already has been described during the problem statement (see Figure 1). It will be tried to identify the first transfer path which is shown in Figure 3. One will also take into account that during a real measurement there are some constraints. In theory one should apply a known force at the interface between the link and the lower beam. But because of the fact that disassembling of the whole system has to be avoided, the known force will be applied at the bottom side of the beam. In the theoretical examples one used relative displacements as references for the H_1 estimator. During real measurements, one will measure the strains using strain gages. Also during real measurements it would be impossible to measure the strains at the interface. So the strains will be measured at 0.5 cm above the lower beam.

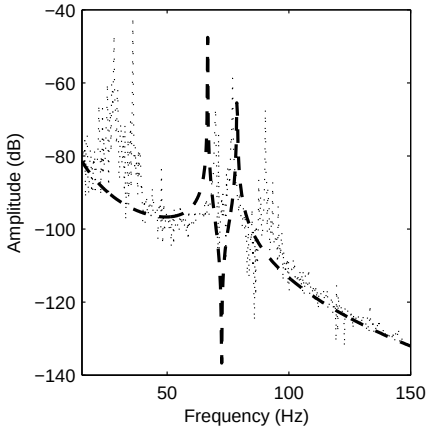

(a) H_{12} of disassembled and assembled system

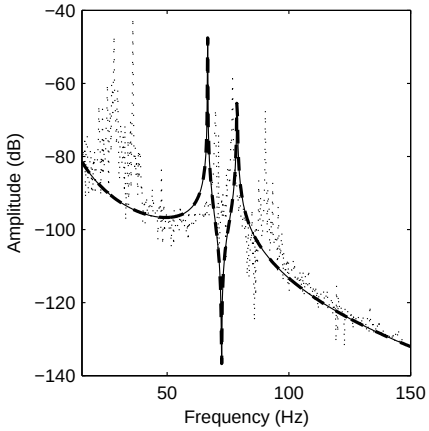

(b) OTPA estimate of H_{12}

Fig. 10. TPA of a 6 DOF system: with 2 operational forces: (−−) FRF of the isolated system of interest, (···) Measured FRF of the assembled system, (—) OTPA estimate of the FRF of the isolated system of interest

B. Simulation Set up

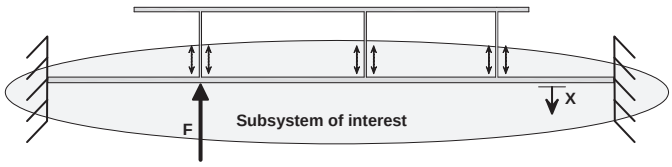

Fig. 11. TPA of a FEM: measured signals

The simulation setup of the 2D structure is shown in Figure 11. On this figure F is the known force and X is the measured response. The lower beam has a length of 86 cm and a thickness of 8 mm. The upper beam has a length of 60 cm and a thickness of 6 mm. The three links have a length of 10 cm and a thickness of 4 mm. The links are located at 23 cm, 48 cm and 68 cm from the left end of the lower beam. The response location is located at 71 cm from the left end of the lower beam. The width of the 2D structure is 1 cm.

Assume that one is interested in how the vibrations propagate from F to X in the isolated system of interest (only the lower beam). To estimate this transfer path, one has to measure the strains in the three links. Since the isolated system of interest only contains the lower beam, the interface at the links should be as close as possible to the lower beam. Because one had to take into account the moments at the links, there were 2 strain measurements for each link. During the simulation 6 unknown forces were used: 3 in the vertical direction (all on the upper beam) and 3 in the horizontal direction (one on each link). The locations of those operational forces are shown in Figure 12. The FEM mesh consisted of 2001 points and 3120 triangular elements. This refined grid was especially needed at the links. This is shown in Figure 13.

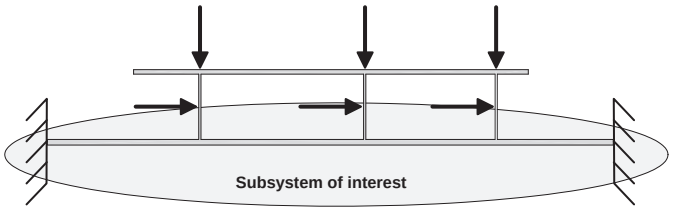

Fig. 12. TPA of a FEM: operational forces

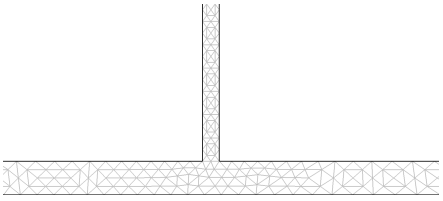

Fig. 13. FEM: grid at a link

C. Simulation results

Because of the fact that one has to take into account the moments 2 strain measurements are needed for each link. Doing this will result in a sufficient set of references. During the simulations there were no unknown forces that acted directly on the target subsystem (i.e. the lower beam). Because of the fact that 6 strain measurements were used, at least 6 unknown uncorrelated forces were needed. And because 6 references and one known force were measured, the H_1 estimator needed 7 data records.

Taken this into account the simulation results were as expected. In Figure 14 the results of the simulation are shown. Figure 14(a) shows that the OTPA method is able to estimate the FRF of the isolated system of interest without disassembling the system. Due to the fact that on real structures one can not measure at the direct interface between the links and the target subsystem there are some minor errors. In fact by moving the strain measurement locations 5 mm away from the link, one assumes that this little part of the link (5 mm) is part of the target subsystem. So this results in a small mass loading. This is also shown in the Figures 14(b) and 14(c). This also shows that for other kinds of links one has to measure the strains as close as possible to the isolated subsystem.

D. Applicability of the method: strain measurement location

The simulation results show that the strain measurement location introduces errors. Therefore it is interesting to simulate some more cases to see how the errors are related to the location. Figure 15 shows the results of different strain measurement locations: 5 mm, 10 mm and 15 mm above the lower beam. On this Figure one sees that the further the strain measurement sensors are located from the link-subsystem interface, the bigger the errors are. The mass loading becomes more important which results in a shift of the poles. This is even more visible if one also adds the plots of the locations: 7.5 mm and 12.5 mm. This is shown in Figure 16(a) and 16(b). It is obvious that it would be bad practice to locate the strain gages far from the interface. In most real cases it should be possible to place the strain gages at 5 mm from the interface. In that case the errors are still acceptable.

V. Conclusions

In this paper a new Transfer Path Analysis Technique has been introduced which can be used in operational conditions. It has the big advantage that no disassembling is needed and that operational forces do not have to be eliminated. On the contrary: the more uncorrelated operational forces that act on the system the better. Compared to the classical techniques this technique is less time consuming and the real boundary conditions are present. It is a technique that can be perfectly used on operational systems.

The theory of the technique has been deducted from simple mechanical models. In the last part of this paper the procedure has been validated on a Finite Element Model.

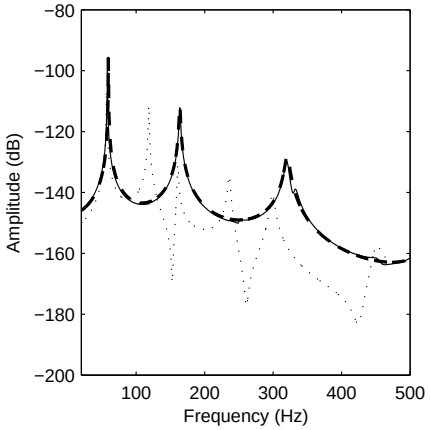

(a) 20Hz - 500 Hz

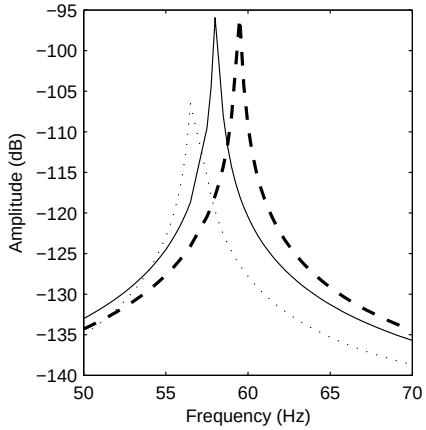

(b) 50Hz - 70 Hz

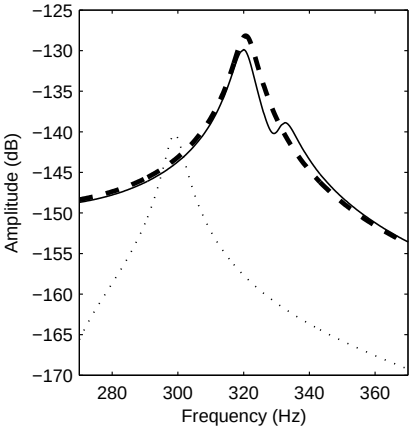

(c) 270Hz - 370 Hz

Fig. 14. TPA of a Finite Element Model: (−−) FRF of the isolated system of interest, (···) Measured FRF of the assembled system, (—) OTPA estimate of the FRF of the isolated system of interest

References

[1] J. Plunt, "Finding and fixing vehicle nvh problems with transfer path analysis," *Sound And Vibration*, vol. 39, no. 11, pp. 12–16, 2005.

[2] H. Van der Auweraer and J. Leuridan, "A new testing paradigm for today's product development process - part 1," *Sound And Vibration*, vol. 39, no. 9, pp. 14–18, 2005.

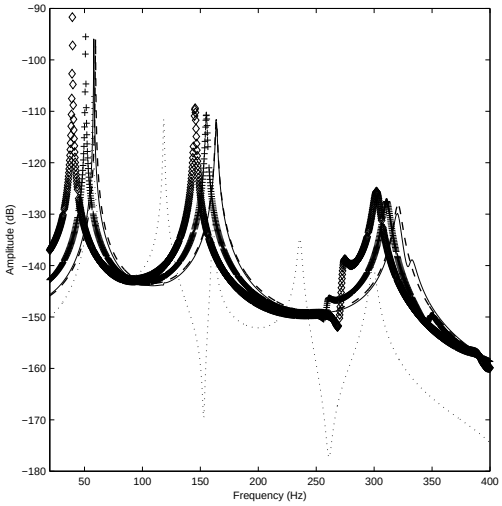

Fig. 15. TPA of a Finite Element Model: Influence of strain measurement location: (−−) FRF of the isolated system of interest, (···) Measured FRF of the assembled system, (—) OTPA estimate with strain measurements at 5 mm from the interface, (+) OTPA estimate with strain measurements at 10 mm from the interface, (◇) OTPA estimate with strain measurements at 15 mm from the interface

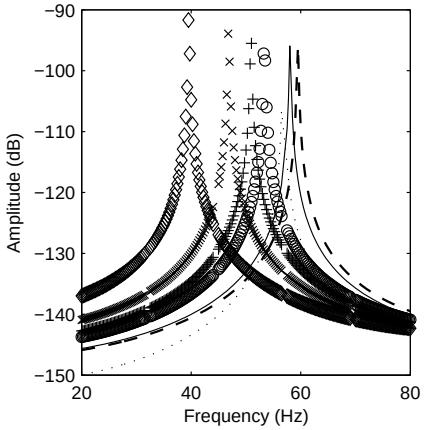

(a) 20 Hz - 80 Hz

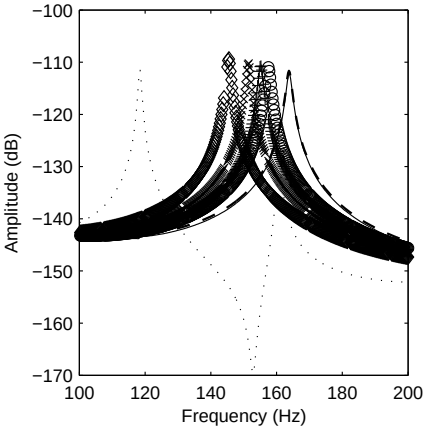

(b) 100 Hz - 200 Hz

Fig. 16. TPA of a Finite Element Model: Influence of strain location: (−−) FRF of the isolated system of interest, (···) Measured FRF of the assembled system, (—) OTPA estimate with strain measurements at 5 mm from the interface, (∘) OTPA estimate with strain measurements at 7.5 mm from the interface, (+) OTPA estimate with strain measurements at 10 mm from the interface, (×) OTPA estimate with strain measurements at 12.5 mm from the interface, (◇) OTPA estimate with strain measurements at 15 mm from the interface

[3] W. Heylen, S. Lammens, and P. Sas, *Modal Analysis Theory and Testing*, Katholieke Universiteit Leuven, Departement Werktuigkunde, 1997.

[4] N. Maia and J. Silva, *Theoretical and Experimental Modal Analysis*, Research Studies Press Ltd., 1997.

[5] D. Ewins, *Modal Testing: Theory, Practice and Application*, Research Studies Press Ltd., 2000.

[6] P. Guillaume, E. Parloo, and G. De Sitter, *Source Identification form Noisy Response Measurements Using an Iterative Weighted Pseudo-Inverse Approach*, Proceedings of the International Conference on Noise and Vibration Engineering (ISMA-2002). 2002.

[7] H. Van der Auweraer, P. Mas, S. Dom, A. Vecchio, K. Janssens, and P. Van de Ponseele, "Transfer path analysis in the critical path of vehicle refinement: The role of fast, hybrid and operational path analysis," *S.A.E. Technical Papers*, vol. 01, no. 2352, 2007.

[8] P. van der Linden, P. Van de Ponseele, and G. Coppens, *Investigation of binaural transfer functions; reciprocity in free field and in-vehicle*, Proceedings of the International Conference on Noise and Vibration Engineering (ISMA-26). 2006.

[9] A. Rust and I. Edlinger, "Active path tracking for vehicle noise source identification," *Sound And Vibration*, vol. 36, no. 2, pp. 14, 2002.

[10] P. Padilha and J.R. Arruda, "Comparison of estimation techniques for vibro-acoustic transfer path analysis," *Shock and Vibration*, vol. 13, no. 4-5, pp. 459–467, 2006.

[11] A. Thite and D.J. Thompson, "The quantification of structure-borne transmission paths by inverse methods. part 1: Improved singular value rejection methods," *Journal of Sound and Vibration*, vol. 264, no. 2, pp. 411–431, 2003.

[12] A.N. Thite and D.J. Thompson, "The quantification of structure-borne transmission paths by inverse methods. part 2: Use of regularization techniques," *Journal of Sound and Vibration*, vol. 264, no. 2, pp. 433–451, 2003.

[13] Y. Kim and P.A. Nelson, "Optimal regularisation for acoustic source reconstruction by inverse methods," *Journal of Sound and Vibration*, vol. 275, no. 3-5, pp. 463–487, 2004.

Proceedings of the 8th National Congress on Theoretical and Applied Mechanics, May 28-29, Brussels, Belgium.

Consideration of the dynamic effects of the bridges due to the passage of train

Kai Liu[1], Guido De Roeck[1], Geert Lombaert[1]
[1]Katholieke Universiteit Leuven, Department of Civil Engineering
Kasteelpark Arenberg 40, B-3001 Leuven, Belgium
email: kai.liu@bwk.kuleuven.be, guido.deroeck@bwk.kuleuven.be, geert.lombaert@bwk.kuleuven.be

Abstract— **Research on dynamic amplifications in bridge response due to the passage of train has been a topic for many years. A number of methods have been developed to consider the dynamic effects of the train loads on the bridge. This paper investigates under which conditions dynamic train-bridge interaction should be considered for the dynamic analysis of a bridge during a train passage. The results of a moving load model are compared to those of an analysis of dynamic train-bridge interaction considering different vehicle models with a varying degree of sophistication. The effect of several parameters related to the train and the bridge is studied. The ratio of the mass of the vehicle and the bridge and the ratio of the natural frequency of the vehicle and the bridge, the train speed are identified as significant factors that determine the effect of dynamic train-bridge interaction on the bridge response.**

Keywords— **dynamic effect, moving load, train-bridge interaction, parametric study**

I. Introduction

The dynamic response of railway bridges under moving trains has been a topic of research interest for many years. The basic quantity to evaluate dynamic effects due to moving traffic on bridges is the Dynamic Amplification Factor (DAF), which represents the increase in the dynamic response with respect to the static one for a single moving load [1]. The dynamic amplification factor, however, does not take into account resonance effects due to repeated loading by a series of axles. The Eurocode 1 [1] specifies under which conditions a dynamic analysis is required.

In the dynamic analysis of the bridge, a moving train is traditionally represented as a series of moving axle loads. Timoshenko [2] developed the classical solution for a simply supported beam subjected to a moving load. An elaborate discussion of beam-structures subjected to moving loads is presented by Frýba [3].

Considerable experimental and theoretical research has recently been performed on train-bridge interaction [4,5,6,7]. In the analysis of dynamic train-bridge interaction, a distinction is made between the subsystems for the train and the bridge. Both subsystems are coupled by the compatibility of displacements and equilibrium of forces at the contact points [8,9,10]. Different vehicle models with a varying degree of sophistication have been developed to account for the dynamic properties of the vehicle. The simplest model for a train is a series of 2 degree-of-freedom(DOF) mass-spring-damper systems that account for the suspension of the vehicle. Chu et al. [11] studied train-bridge interaction with a 3-DOF vehicle model consisting of the car body and wheel-axle sets. A time domain integration method is used to solve the dynamic equations of the coupled train-bridge system. Tan et al. [12] presented a vehicle model that has 7-DOF and is capable of accommodating both roll and pitch modes. The influence of various parameters on the behavior of the coupled system is studied in three numerical examples. Xia et al. [13] proposed a 15-DOF vehicle model and analyzed the passage of the Thalys high speed train on a concrete box-girder bridge in Antoing on the high speed line between Paris and Brussels. The model is validated by comparing the results of computations with in situ measurements.

In the literature, however, it is not very clear in which case a moving load model suffices for the prediction of the bridge response and under which conditions it is necessary to account for the dynamic interaction between the train and bridge. Liu et al. used both approaches for the particular case of the dynamic response of the Sesia viaduct during the passage of the Italian high speed train ETRY500. In this case, both approaches give predictions that are in good agreement with the experimental results [15].

The main purpose of this paper is to provide a better understanding of train induced bridge vibration and to investigate under which conditions dynamic train-bridge interaction analysis should be accounted for. It is organized in the following manner. Section 2 presents the numerical model developed for the analysis. Two methodologies are considered to represent the action of the vehicle on the bridge: (1) a moving load model and (2) a model that takes into account dynamic train-bridge interaction. In section 3, a parametric study is performed to identify the parameters that determine the dynamic response of the bridge.

II. Numerical model

A. Bridge subsystem

When a finite element model of the bridge is used to study its dynamic behavior, the equation of motion of the bridge can be expressed as:

$$\mathbf{M_b}\ddot{\mathbf{V}}_\mathbf{b} + \mathbf{C_b}\dot{\mathbf{V}}_\mathbf{b} + \mathbf{K_b}\mathbf{V_b} = \mathbf{P_b} \qquad (1)$$

where $\mathbf{M_b}$, $\mathbf{C_b}$ and $\mathbf{K_b}$ are the mass matrix, damping matrix and stiffness matrix of the bridge, respectively; $\mathbf{V_b}$, $\dot{\mathbf{V}}_\mathbf{b}$ and $\ddot{\mathbf{V}}_\mathbf{b}$ represent the displacement, velocity and acceleration vectors of the bridge; $\mathbf{P_b}$ is the vector with the external forces.

In the following, the Modal Superposition Method [14] is adopted to solve the equation of motion of the bridge. It is assumed that only the first N_0 modes of the bridge are contributing to the response. The equation of motion of the bridge can be now rewritten as follows:

$$\ddot{\mathbf{q}} + \mathbf{C}_\mathbf{b}^* \dot{\mathbf{q}} + \mathbf{K}_\mathbf{b}^* \mathbf{q} = \mathbf{P}_\mathbf{b}^* \tag{2}$$

where it has been assumed that the eigenvectors are normalized with respect to the mass matrix $\mathbf{M_b}$. The vector $\mathbf{q}$ collects the modal coordinates. The matrices $\mathbf{C}_\mathbf{b}^*$, $\mathbf{K}_\mathbf{b}^*$ and $\mathbf{P}_\mathbf{b}^*$ are defined as follows:

$$\mathbf{C}_\mathbf{b}^*=2\zeta\Omega,\ \mathbf{k}_\mathbf{b}^*=\Omega^2,\mathbf{P}_\mathbf{b}^*=\Phi^\mathrm{T}\mathbf{P_b}$$

where Φ is the $N_0 \times N_{\mathrm{DOF}}$ matrix of eigenvectors and Ω is the $N_{\mathrm{DOF}} \times N_{\mathrm{DOF}}$ diagonal matrix of eigenvalues of the considered modes; The modal damping ratio ζ is assumed to be equal for all considered modes.

B. Train load modeling

The first attempt to represent the action of the vehicle on the bridge is the so-called moving load model, where the train is modeled as a series of moving loads. The force vector $\mathbf{P_b}$ can be written as follows:

$$\mathbf{P_b}(\mathbf{t}) = \mathbf{P_b^{qs}}(\mathbf{t}) = \sum_{\mathbf{i=1}}^{\mathbf{n}} \mathbf{y_i}(\mathbf{t})\mathbf{F_{Gi}} \tag{3}$$

where the superscript *qs* in $\mathbf{P_b^{qs}}(\mathbf{t})$ refers to the fact that only the quasi-static loading of the bridge is accounted for. The vector $\mathbf{y_i}(\mathbf{t})$ is the $N_{\mathrm{DOF}} \times 1$ vector that transfers a moving unit load to nodal loads according to the position of the *i*th axle. The load amplitude F_{Gi} is equal to the weight of the *i*th axle of the train.

To account for the dynamic effect of the train on the bridge, vehicle models with a varying degree of sophistication are considered (figure 1). Vehicle model c is an elaborate model that considers both the vertical motion of the car body and the bogie, while vehicle models a and b are simplified versions of vehicle model c.

In a similar way as for the bridge, the equation of motion of the vehicle can be written as:

$$\mathbf{M_v}\ddot{\mathbf{V}}_\mathbf{v} + \mathbf{C_v}\dot{\mathbf{V}}_\mathbf{v} + \mathbf{K_v}\mathbf{V_v} = \mathbf{P_v^{dy}} \tag{4}$$

where $\mathbf{M_v}$, $\mathbf{C_v}$ and $\mathbf{K_v}$ are the mass, damping and stiffness matrices; $\mathbf{V_v}$, $\dot{\mathbf{V}}_\mathbf{v}$ and $\ddot{\mathbf{V}}_\mathbf{v}$ are the displacement, velocity and acceleration vectors of the vehicle system; $\mathbf{P_v^{dy}}$

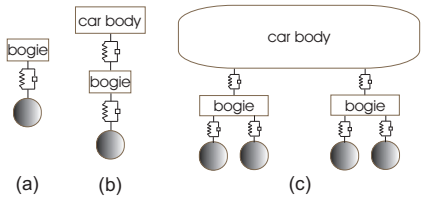

Fig. 1. (a)a 1-DOF (b)a 2-DOF, and (c) a 3-DOF vehicle model for dynamic train-bridge interaction analysis

is the force vector that collects the dynamic force on the vehicle [15].

The coupling of the vehicle and bridge subsystems by the compatibility of the displacements at the contact points is now illustrated for the case of vehicle model c [15]. The equation of motion of the vehicle can be derived from the dynamic force equilibrium (figure 2).

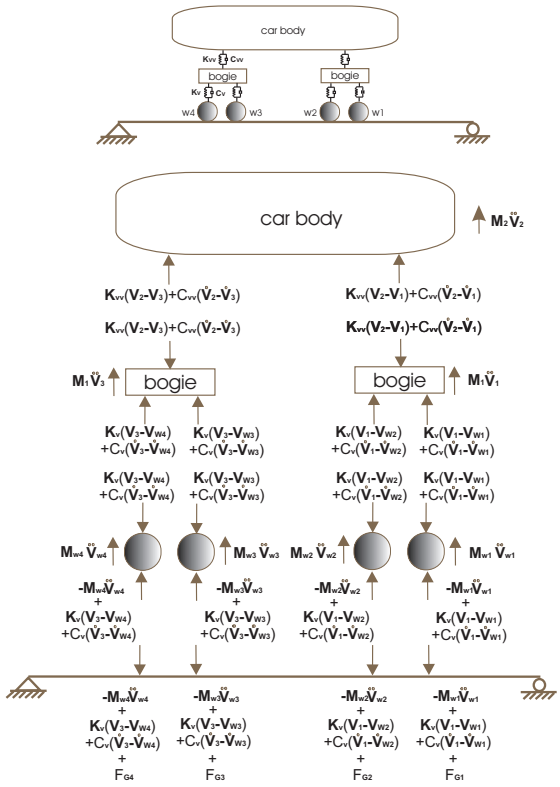

Fig. 2. A simply supported beam subjected to a moving vehicle.

The mass matrix of the vehicle can be expressed as

$$\mathbf{M_v} = \mathbf{diag}[\mathbf{M_1}, \mathbf{M_2}, \mathbf{M_1}] \tag{5}$$

where M_1 and M_2 are the mass of the bogie and the car body, respectively.

The stiffness matrix of the vehicle system is expressed

as:

$$\mathbf{K_v} = \begin{bmatrix} 2K_V + K_{VV} & -K_{VV} & 0 \\ -K_{VV} & 2K_{VV} & -K_{VV} \\ 0 & -K_{VV} & 2K_V + K_{VV} \end{bmatrix} \quad (6)$$

where K_V and K_{VV} are the spring stiffness coefficients of the primary and secondary suspension system, respectively.

The damping matrix is derived from the stiffness matrix by replacing the stiffness coefficients (K_V, K_{VV}) by the damping coefficients (C_V, C_{VV}) of the primary and secondary suspension system.

The displacement vector $\mathbf{V_v}$ is expressed as:

$$\mathbf{V_v} = [\mathbf{V_1}, \mathbf{V_2}, \mathbf{V_3}]^{\mathrm{T}} \quad (7)$$

where V_1 and V_3 are the vertical displacements of the front and back bogie, respectively, while V_2 is the vertical displacement of the car body.

The equations of motion are integrated according to the Newmark-β method with values β=0.25 and γ=0.5 corresponding to the trapezoidal rule [18]. The integration procedure is described more elaborately in Ref. [15].

III. Parametric study

For simply supported bridges, the results of ERRI D214 showed that resonance is unlikely for spans longer than 40 m [16]. This study has been limited however, to the case of simply supported bridges of relatively short span without consideration of transverse effects. The simply supported bridge in Ref. [17] is chosen as the reference case in the present parametric study. The characteristics of the bridge are as follows. The bridge has a length L of 34 m, a mass per unit length m_b=11400 kg/m, a bending stiffness EI=9.92×10^{10} Nm^2, and a modal damping ratio ζ of 2% for all considered modes. The fundamental natural frequency f_b=4.01 Hz.

The train type considered in this study is the Italian ETR500Y high speed train. The main characteristics of the train are listed in Table I. It is composed of a locomotive followed by 8 passenger cars and another locomotive. The length of the locomotive is 19.7 m, while the length of the passenger cars is 26.1 m. The average static axle loads for the locomotives and passenger cars are 176.4 and 112.9 kN, respectively. The natural frequencies of the car body and the bogie can be estimated from the following equations:

$$f_{vc} = \frac{1}{2\pi}\sqrt{\frac{2}{\frac{1}{Kvv}+\frac{1}{2Kv}}} \quad (8)$$

$$f_{vb} = \frac{1}{2\pi}\sqrt{\frac{2Kv+Kvv}{M_1}} \quad (9)$$

The values for K_V and K_{VV} of ETR500Y are used to estimate the frequencies of the car body and the bogie as 0.49 Hz and 4.06 Hz, respectively.

Item	Unit	Locomotive	Passenger car
Mass of the car body (M_2)	kg	55,976	34,231
Mass of the bogie (M_1)	kg	3896	2760
Mass of the wheel set (M_w)	kg	2059	1583
Vertical stiffness of the primary suspension system (K_V)	kN/m	1,792,200	808,740
Vertical damping of the primary suspension system (C_V)	kN·s/m	15,250	7500
Vertical stiffness of the secondary suspension system (K_{VV})	kN/m	472,060	180,554
Vertical damping of the secondary suspension system (C_{VV})	kN·s/m	36,250	16,250
Carriage length (d)	m	19.7	26.1

TABLE I
THE DYNAMIC CHARACTERISTICS OF THE ITALIAN ETR500Y HIGH SPEED TRAIN.

In order to investigate the conditions under which dynamic train-bridge interaction needs to be taken into account, a parametric study is performed. The following dimensionless parameters are defined: the speed parameter α, the frequency parameter κ and the mass parameter γ.

The dimensionless speed parameter α is defined as:

$$\alpha = \frac{v}{f_b d} \quad (10)$$

where v is the train speed, d is the characteristic length of a car and f_b is the fundamental natural frequency of the bridge. The critical speed caused by a long series of regularly spaced axles is reached at α=1. For the Italian high speed train ETR500Y, the characteristic length d=26.1 m, so that with a value of f_b=4.01 Hz for the fundamental natural frequency, the critical speed is reached at 377 km/h.

The dimensionless frequency parameter κ is:

$$\kappa = \frac{f_v}{f_b} \quad (11)$$

where f_v and f_b are the frequency of the vehicle and the first bending frequency of the bridge, respectively. Due to the low value of the natural frequency f_{vc} of the car body, this part of the vehicle is dynamically uncoupled from the bridge. Therefore the natural frequency f_{vb} of the bogie is considered for f_v in equation (13). For the train and the bridge in the current study f_{vb}=4.06 Hz while f_b=4.01 Hz, so that the value of κ is 1.01 in the reference case.

The dimensionless mass parameter γ is defined as:

$$\gamma = \frac{M_v}{M_b} \quad (12)$$

where M_v is the total mass of the train and M_b is the mass of the bridge. With M_v=445544 kg and M_b=387600 kg, the value of γ is therefore 1.1495 in the reference case.

A. *Influence of the speed parameter on the dynamic response of the bridge*

According to Eurocode 1 [1], the frequency range considered in the determination of the maximum deck acceleration should have an upper limit of 30 Hz or 1.5 times the frequency of the first eigenmode of the structural element being considered. The frequency range should at least include the first three modes. For the present bridge with a fundamental natural frequency of 4.01 Hz, the threshold for low-pass filtering is therefore 30 Hz.

Figures 3 and 4 present the dynamic amplification factor DAFu and the maximum vertical acceleration at mid-span, respectively, as a function of the dimensionless speed parameter α. The dynamic amplification factor DAFu is defined as:

$$\text{DAFu}=\frac{u_{dyn}(l/2)}{u_{sta}(l/2)}$$

where $u_{dyn}(l/2)$ is the maximum dynamic displacement and $u_{sta}(l/2)$ is the maximum static displacement at mid-span of the bridge.

For low values of α, there is no significant difference between the different train load models. The difference, however, gets larger when the speed parameter α approaches a value of 1, which corresponds to the resonant speed. In general, the moving load model produces the largest dynamic amplification, while the vehicle models a, b, and c generate a lower dynamic amplification. This is due to the presence of the suspension system which results in a reduction of the contact force applied to the bridge.

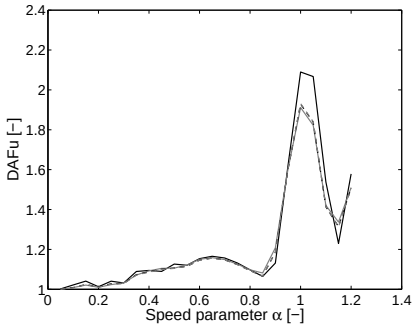

Fig. 3. The dynamic amplification factor DAFu as a function of the dimensionless speed parameter α for the moving load model (solid black line), vehicle model a (solid gray line), vehicle model b (dashed black line) and vehicle model c (dashed gray line).

Figure 5 depicts the acceleration at mid-span in the time domain and frequency domain for a train passage at resonant speed for the moving load model and vehicle model c. In both models, a peak occurs at 4.01 Hz, which corresponds to the first bending frequency of the bridge. A reduction of the peak magnitude is observed when dynamic train-bridge interaction is taken into account.

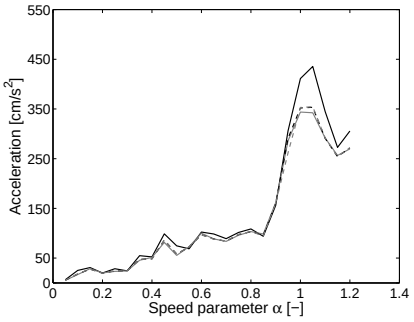

Fig. 4. Maximum vertical acceleration at mid-span as a function of the dimensionless speed parameter α for the moving load model (solid black line), vehicle model a (solid gray line), vehicle model b (dashed black line) and vehicle model c (dashed gray line).

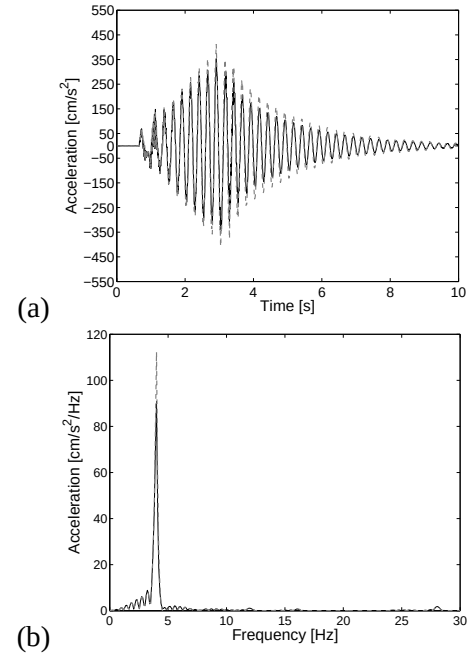

Fig. 5. (a) time history and (b) frequency content of the acceleration at mid-span of the moving load model (dashed gray line) and vehicle model c (solid black line)

B. *Influence of the frequency parameter on the dynamic response of the bridge*

The dynamic train-bridge interaction is affected by the natural frequencies of the two subsystems. In the following, the stiffness of the suspension system is modified to investigate the influence of the frequency parameter κ in the range from 0.1 to 2.0.

Figures 6 and 7 show the dynamic amplification factor

DAFu and the acceleration, respectively, at resonant speed as a function of the frequency parameter κ. When the value of the parameter κ is close to 0, there is a small difference between the moving load model and vehicle models a, b, and c. Due to the low stiffness of the suspension system, the vehicle is dynamically uncoupled from the bridge and the static load is the only component that affects the response of the bridge. In this case, a moving load model satisfactorily represents the vehicle. In the case where the stiffness of the suspension system is relatively high, corresponding to a high value for κ, the train can be represented by a moving mass.

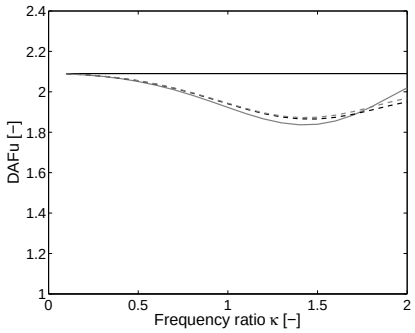

Fig. 6. The dynamic amplification factor DAFu at resonant speed as a function of the dimensionless frequency parameter κ for the moving load model (solid black line), vehicle model a (solid gray line), vehicle model b (dashed black line) and vehicle model c (dashed gray line).

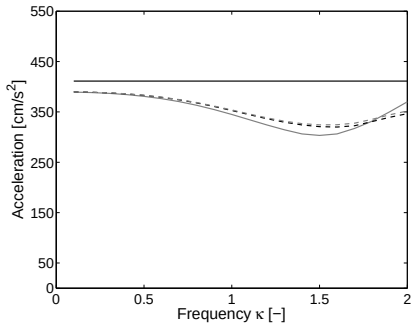

Fig. 7. Maximum vertical acceleration at mid-span at resonant speed versus dimensionless frequency parameter κ for the moving load model (solid black line), vehicle model a (solid gray line), vehicle model b (dashed black line) and vehicle model c (dashed gray line).

C. Influence of the mass parameter on the dynamic response of the bridge

A modification of the vehicle mass changes both the quasi-static force and the dynamic force and therefore affects the dynamic response of the bridge. In this subsection, the response of the bridge to a moving train is considered for different values of the mass parameter γ between 0.1 and 3.

The parameter γ is modified by changing the mass of the vehicle, while the stiffness of the suspension system is adjusted correspondingly to maintain a constant value of 1.01 for the frequency ratio κ.

Figures 8 and 9 show that the dynamic response increases linearly with the increase of the mass ratio γ for the moving load model. For low values of the mass parameter, there is a small difference between the three vehicle models and the moving load model. With an increasing mass ratio, however, dynamic train-bridge interaction becomes more important, and reduces the dynamic amplification factor DAFu. Figure 9 shows that for a mass parameter γ of 3, the acceleration at mid-span is reduced by 32% by dynamic train-bridge interaction.

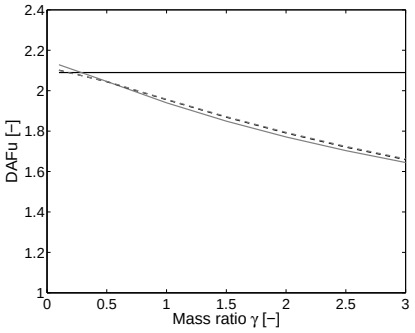

Fig. 8. The dynamic amplification factor DAFu at resonant speed as a function of the dimensionless mass parameter γ for the moving load model (solid black line), vehicle model a (solid gray line), vehicle model b (dashed black line) and vehicle model c (dashed gray line).

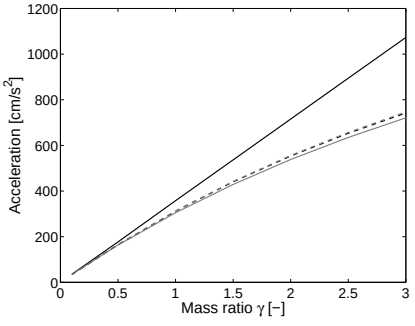

Fig. 9. Maximum vertical acceleration at mid-span at resonant speed as a function of the dimensionless mass parameter γ for the moving load model (solid black line), vehicle model a (solid gray line), vehicle model b (dashed black line) and vehicle model c (dashed gray line).

IV. Conclusions

This study investigates the effect of dynamic train-bridge interaction on the bridge response during a train passage. The influence of several dynamic characteristics of the train and the bridge on the dynamic response of the bridge is studied. The following conclusions can be drawn from this study:

1. The dynamic amplification attains its maximum value at a critical train speed where the passage of a series of regularly spaced axles excites the bridge at its resonance frequency.

2. When the train speed approaches its critical value, dynamic train-bridge interaction results in a lower dynamic response of the bridge as compared to the moving load model. The reduction is larger for the bridge acceleration at mid-span than for the corresponding displacement.

2. When the ratio of the natural frequency of the vehicle and the bridge is much smaller than one, the response of the bridge can be estimated by a moving load model. For an increasing ratio, dynamic train-bridge interaction becomes more important and reduces the dynamic amplification at the critical speed. The largest reduction is found when the natural frequency of vehicle is slightly larger than the natural frequency of the bridge.

3. The results are dependent on the type of vehicle model and it is therefore important to choose a suitable vehicle model in the analysis. Among the vehicle models adopted in the study, vehicle models b and c give the most accurate prediction, while vehicle model a provides a good approximation due to the very low value of the natural frequency of the car body.

4. Dynamic train-bridge interaction is more important for the situation when the ratio of the mass of the vehicle and the bridge is relatively large. When the mass ratio is low, a moving load model is sufficient for the dynamic analysis of the bridge. With an increasing mass ratio, the effect of dynamic train-bridge interaction becomes more important.

Acknowledgements

The research is conducted in the framework of the EC Research Fund for Coal and Steel RTD project RFSR-CT-2006-00032 “DETAILS” (Design for optimal life cycle costs (LCC) of high speed railway bridges by enhanced monitoring systems). The support of the EC is gratefully acknowledged.

References

[1] EN 1990:2002/A1:2005, Eurocode - Basis of structural design, Final Draft. European Committee for standardization. CEN, 2006.

[2] Timoshenko S.P. History of the strength of materials. *D. van Nostrand Co.*, 1953.

[3] L. Frýba. Vibration of solids and structures under moving loads. *Thomas Telford*, 1999.

[4] Y.K. Cheung, F.T.K. Au, D.Y. Zheng, Y.S. Cheng. Vibration of multi-span bridges under moving vehicles and trains by using modified beam vibration functions. *Journal of Sound and Vibration*, 228: 611–628, 1999.

[5] H. Xia, Y.L. Xu, T.H.T. Chan. Dynamic interaction of long suspension bridges with running trains. *Journal of Sound and Vibration*, 237: 263–280, 2000.

[6] C.H. Lee, M. Kawatani, C.W. Kim, N. Nishimura, Y. Kobayashi. Dynamic response of a monorail steel bridge under a moving train. *Journal of Sound and Vibration*, 294: 562–579, 2006.

[7] N. Zhang, H. Xia, W.W. Guo. Vehiclebridge interaction analysis under high-speed trains. *Journal of Sound and Vibration*, 309: 407–425, 2008.

[8] C.W. Kim, M. Kawatani, K.B. Kim. Three-dimentional dynamic analysis for bridge-vehicle interaction with roadway roughness. *Engineering Structures*, 19: 936–944, 1997.

[9] M.K. Song, H.C. Nohb, C.K. Choi. A new three-dimensional finite element analysis model of high-speed trainbridge interactions. *Engineering Structures*, 25: 1611–1626, 2003.

[10] C.H. Lee, C.W. Kim, M. Kawatani, N. Nishimura, T. Kamizono. Dynamic response analysis of monorail bridges under moving trains and riding comfort of trains. *Engineering Structures*, 27: 1999–2013, 2005.

[11] K.H. Chu, C.L. Dhar, V.K. Garg. Railway-Bridge Impact: Simplified Train and Bridge Model. *Journal of the Structural Division*, 105: 1823–1844, 1979.

[12] G.H. Tan, G.H. Brameld, D.P. Thambiratnam. Development of an analytical model for treating bridge-vehicle interaction. Journal of Engineering Structures. *Engineering Structures*, 20: 54–61, 1998.

[13] H. Xia, N. Zhang, G. De Roeck. Dynamic analysis of high speed railway bridge under articulated trains. *Computers and Structures*, 81: 2467–2478, 2003.

[14] Anil K. Chopra. Dynamics of Structures: Theory and Applications to Earthquake Engineering. *Prentice Hall*, 2000.

[15] K. Liu, E. Reynders, G. De Roeck, G. Lombaert. Experimental and numerical analysis of a composite bridge for high-speed trains. *Journal of Sound and Vibration*, 320:201-220, 2009.

[16] ERRI D214 RP9, Railway Bridges for Speed up to 350 km/h; Dynamic loading effects including resonance. Final report. European Railway Research Institute subcommitee D21. 1999.

[17] Raid Karoumi. Response of Cable-Stayed and Suspension Bridges to Moving Vehicles. *PhD thesis*, 1998.

[18] Newmark NM. A method of computation for structural dynamics. *Journal of Engineering Mechanics*, 96: 593–620, 1970.

Proceedings of the 8th National Congress
on Theoretical and Applied Mechanics,
May 28-29, Brussels, Belgium.

Control a Pneumatic Artificial Muscle (PAM) with hysteresis determination

Tri Vo Minh[1], Tegoeh Tjahjowidodo[2], Herman Ramon[3], Hendrik Van Brussel[1]
[1]Mechanical Engineering Department, Division PMA, KULeuven
[2]Flanders' Mechatronics Technology Centre,
Celestijnenlaan 300D, B3001 Heverlee, Belgium
[3]Department of Biosystems, Division of Mechatronics, Biostatistics and Sensors
Kasteelpark Arenberg 30, B3001 Heverlee, Belgium
e-mail: tri.vominh@student.kuleuven.be

Abstract: **In control systems using PAM, most of investigators go directly to deal with inherent hysteresis as an uncertainty. Therefore a number of advanced control algorithms have been developed for PAM control in the last 2 decades. In this paper, a PAM hysteresis is shown as an interpretable part which can be well described by a mathematical model. The proposed model is then implemented in the feed forward path of a feedback control scheme for a single PAM position control. The performance of positioning control shows an effective improvement in transient state. The inevitable characteristics of the nonlinear flow are also discussed later in this paper.**

Keywords: **McKibben-based PAM, hysteresis modeling**

I. INTRODUCTION

PAMs or pneumatic muscles have become a desirable candidate for the development of humanlike robots as well as anthropomorphic devices. The challenge in using such actuator is that it is difficult to control the position precisely. The main source leading to the poor performance in position control is due to the PAM hysteresis. In our research interest, the hysteresis function with non-local memory has been found not only suited for the PAM hysteresis interpretation but also applicable to the PAM position control system.

Recently, more effort has been put into the development of control strategies for PAM, in which the hysteresis was almost leaving as unmodeled parameters and/or disturbances. Meanwhile, a few works has been performed for dealing with hysteresis. Tondu and Lopez [1] introduced Coulomb dry friction model as an additional part to the contracting force in order to increase the accuracy of the static force with hysteresis consideration as well as to explain the nonlinear dynamic behavior due to such a friction. Davis and Caldwell [2] afterwards extended Tondu's hysteresis model by considering deeply the strands' friction. This assessment resulted in a cumbersome mode which has many parameters needed beforehand. Van Damme et al. [4] described hysteresis in Pleated PAM [5] by using Preisach model. However, this modeling approach can not interpret for such a hysteresis with non-local memory. Chou and Hannaford [3] experimentally gave an in-depth description of the hysteretic phenomena in a PAM, such as rate independency, history dependency, but they did not go further to come up with a theoretical foundation. Tri Vo Minh et al. continued Chou's observation and have proved that this kind of hysteresis is comparable to the behavior of the presliding regime in the friction of two contacting surfaces [6].

In the control system regarding to using only one muscle [8-14], the PAM hysteresis was almost always un-modeled and considered as part of the uncertainties of the contracting force model. This shortcoming is proposed to be overcome by using the pole placement methods [8,9,15] neural networks control [17], variable structure control or sliding mode control [18-20], or using a combination of more advanced techniques such as nonlinear PID control [12], adaptive fuzzy model-based control [13], adaptive fuzzy logic siding mode control [16]. A few contribution has been found for controlling a PAM with hysteresis consideration; Hildebrandt et al. introduced the hysteresis model developed in [7] in an inverse model based control algorithm [14], while Balasubramanian and Rattan suggested using an offset for compensating the hysteresis [13].

This paper is organized as follows: a new deterministic approach, in which the hysteresis is characterized and modeled, is presented in section II. Section III describes a new proposed setup and a control scheme as well. Results and discussion are placed in section IV. Section V comes up with conclusion and future work.

II. HYSTERESIS MODELING

A. A similarity of PAM hysteresis to the presiding regime in a mechanical contacting element

As earlier discussed, Chou and Hannaford reported that there are two interesting properties of the PAM hysteresis: history dependency and rate-independency. These key properties show similarities to the pre-sliding regime in mechanical contacting elements, which was characterized by Swevers in [21]. The analogy of the two phenomena: pre-sliding regime in the friction of mechanical contacting elements and hysteresis in a PAM, allows us to use the hysteresis function with non-local memory to model the PAM hysteresis.

The hysteresis function with non-local memory (eq. 1) is used to predict the hysteretic output F_{hys}. In this function, the hysteresis loop is fully characterized by a virgin curve $f(x)$ and the historical value F_m of the lastly reversed point x_m. Sketching of the hysteretic output prediction can be depicted in Fig. 1.

$$F_{hys} = F_m + 2f((x - x_m)/2) \quad (1)$$

Assume that the displacement x has not been moved before, now it starts moving at origin following to the positive direction (to the right hand side). The hysteresis output will take virgin cure value ($y = f(x)$). After arriving at x_m the motion is reversed (velocity changes sign), the system will memorize the last value F_m and the hysteresis output is the sum of this value and the flipped-double-stretched virgin curve '$2f((x - x_m)/2)$'. The behavior is the same when the displacement is reversed after arriving at $x = -x_m$. The last value will be '$-F_m$' and the double stretched virgin curve will be '$2f((x + x_m)/2)$'.

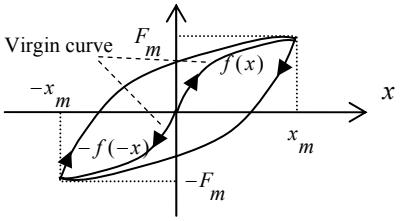

Fig. 1. Sketching of the hysteresis function

B.Modeling hysteresis with non-local memory using Maxwell-slip elements.

Iwan [22] developed a discrete model containing several elements in a parallel connection to capture the hysteresis behavior with non-local memory, in which each contributed element is referred to as a Maxwell-slip element (bottom of Fig.2). One element is mass-less and simply determined by two parameters, namely a stiffness k and a saturation force w [23, 24]. When the element starts to displace from an equilibrium state, it will stick and behave like a linear spring with certain stiffness, k. If the element is continuously displaced, it will reach a maximum output hysteresis force, which is referred to as the saturation force, w. Beyond this state, the elementary hysteresis still keeps the saturation value. By putting several elements (with different parameters of 'stiffness' and 'saturation force') in parallel, the complex behavior of non-local memory hysteresis can be modeled discretely, referred to as Maxwell-slip model.

Assume that the pressure/contraction hysteresis is found. A Maxwell-slip modeling approach can be resembled as shown in Fig. 2. The output pressure at any instant motion of a PAM can be calculated by using the following equation:

$$P_{hys} = \sum_{1}^{n} P_i \quad (2)$$

where n represent a number of elements.

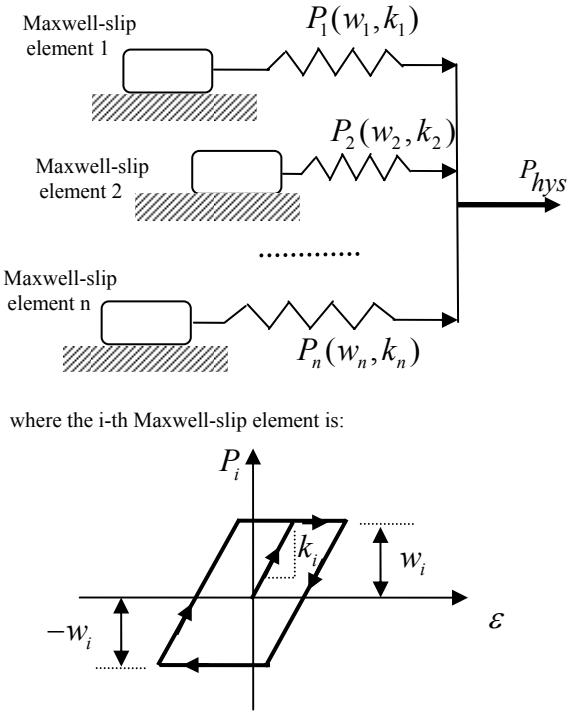

Fig. 2. Modeling hysteresis using the Maxwell-slip model.

With the above analysis, the hysteresis loop is fully characterized by a virgin curve. The key problem now is to find the hysteresis loop, from which the virgin curve will be withdrawn. We have also the Maxwell-slip model approach where the contributed elements to hysteresis can be represented by Maxwell elements. The procedure to identify representative elements can be found in [23, 24], which is briefly given in appendix A.

III.EXPERIMENT SETUP

A.Constrained setup

Constrained setup is a novel setup in PAM study where the hysteresis is assumed to be disappeared. The aim of this experimental setup is to find the empirical model of the contracting force F_{const} without hysteresis. The test muscle is constrained at its two tips, of which one is connected via a force sensor. After being constrained at a certain length, the pressure inside the muscle was increased and, as a result, the contracting force was accordingly increased (see Fig.3).

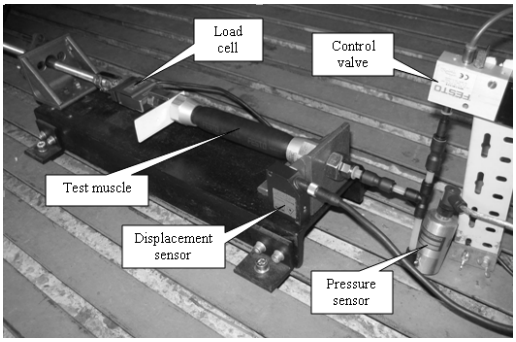

Fig.3. Photo of the constrained test setup.

The achieved model in this case is called 'constrained model', which takes a form as:

$$F_{const} = P\sum_{i=0}^{2} C_i\varepsilon^i + \sum_{j=0}^{3} C_j\varepsilon^j \quad (3)$$

where C_i, C_j are the coefficients of the polynomial function, P is the internal pressure of the muscle, and ε is the contraction ratio defined as the ratio of the difference between the maximum length $l_{\max}$ and the actual length l to the maximum length of the muscle: $\varepsilon = \dfrac{l_{\max} - l}{l_{\max}}$

This model is comparable to the model developed by Hildebrandt et al. [25]. Even though this model is not satisfied our control purpose yet due to no hysteresis presented, we use this model as a base to extract the pressure/length (or pressure/contraction) hysteresis in the isotonic tests. An isotonic test is carried out as the test muscle hangs and moves a certain mass up and down (see Fig.4). The curves of isotonic tests with different masses are shown in Fig. 5. In this figure we can also see the single-line type curves which are reconstructed from the constrained model at the same load.

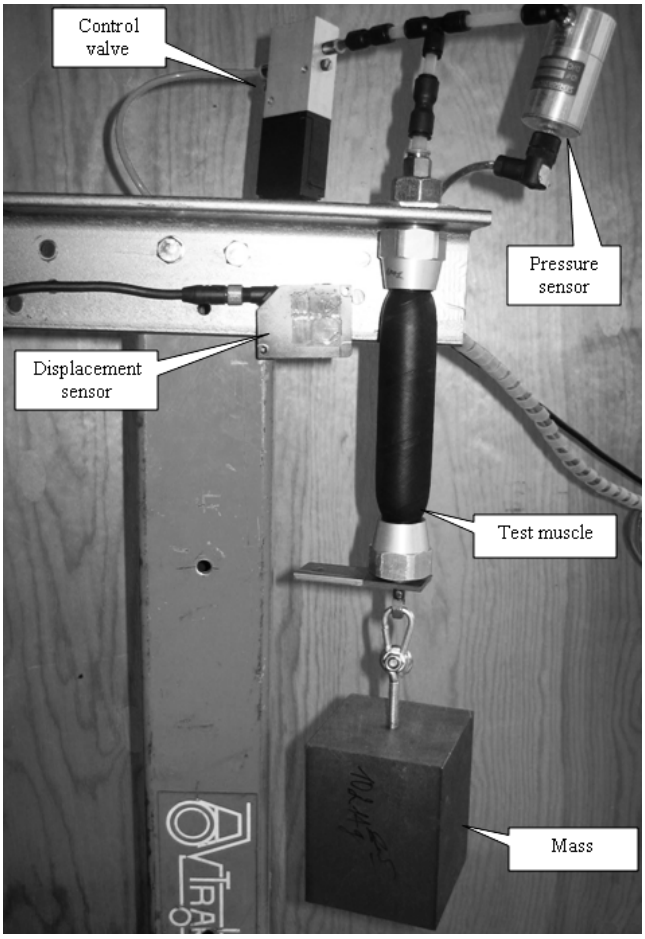

Fig.3. Photo of the isotonic test setup.

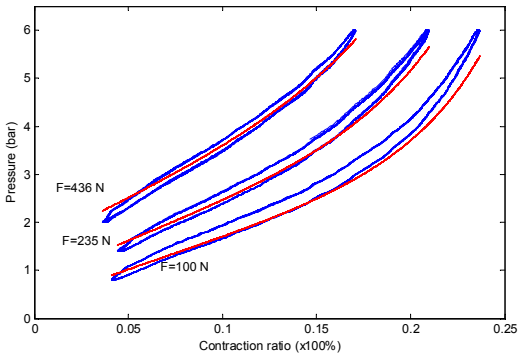

Fig.5. The isotonic test (loop-type curve) at different loads compared to the constrained model (single-line curve).

B.Proposed scheme for single PAM position control

To date, for the plant of a control system with existing hysteresis, the most effective way is found to use a feedforward hysteresis compensation as shown in Fig. 6 [26]. In this scheme, the acquired pressure for the muscle to lift a carrying mass up and down is assumed to be well served. A PI controller is introduced to cope with the nonlinear dynamics of the plant (in this case, a mass-spring system)

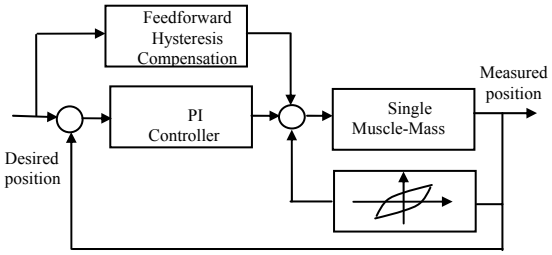

Fig. 6. The proposed control scheme.

IV. RESULTS AND DISCUSSIONS

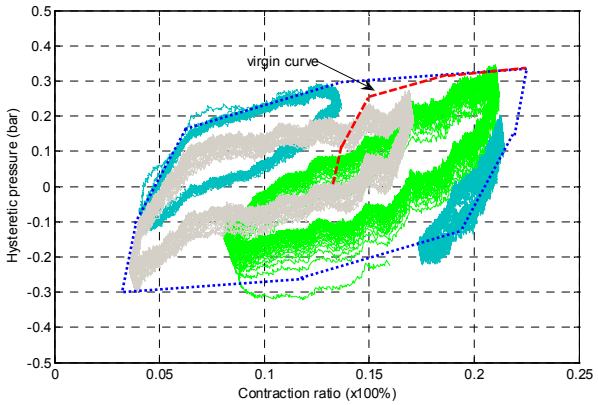

Fig. 7 The extracted hysteresis (resulting from the subtraction of the loop-type curves from single-line curves in fig.5).

Thanks to the constrained model, the pressure/contraction ratio hysteresis during muscle contraction/extension with carrying masses is found. By applying the procedure given in appendix A, the model (i.e a virgin curve) is identified. This model is fed forward to compensating for hysteresis. By this

way, the PAM position control is significantly improved. As we can see in Fig. 8, the oscillation in transient state is removed when the hysteresis compensation is activated. The proposed model takes an action because the stiffness in the transient state is instantly increased by introducing a parallel connection 'springs' as described in the way of how a Maxwell-slip model works (section II.B).

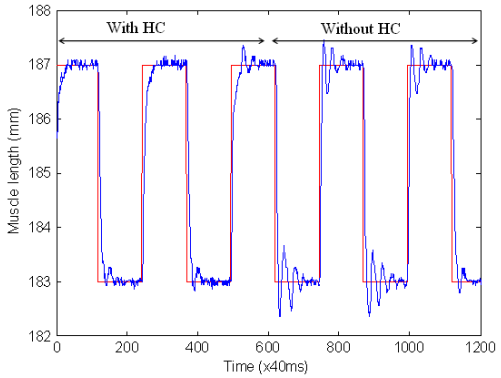

Fig.8. Position control with/without hysteresis compensation

A small overshoot is not completely gone. This can be explained due to the nonlinear flow as shown in appendix B. In fact, the required pressure is served by a pressure regulated system, in which a proportional valve is used as a control element to supply the air mass. No matter what type of the valve is used, the flow function (appendix B, eq. B5, B6, B7) is in the sonic or near sonic stage, where the air mass velocity rises very fast and is independent on flow function but dependent on flow conductance. It means that the small overshoot is inevitable. However, it does not give much effect on the transient response in a single PAM position control.

V. Conclusion/Future Work

The PAM hysteresis has been shown to be modelable based on the hysteresis function with non-local memory. The position control of a single PAM with hysteresis model-based feedforward compensation shows a significant improvement in transient state, which can sequentially improve the bandwidth of the overall system. As in our expectation, the same procedure is going to be resembled in the antagonistic structure, where the pressure difference/angular displace hysteresis is expected to have the same behavior.

Acknowledgements

The authors gratefully acknowledge the DGDC (Directorate-General for Development Cooperation), from the Belgium Government, for awarding a scholarship to the first author and for funding this research.

Appendices

A.Procedure to obtain Maxwell-slip model parameters

As the virgin curve is identified, a piecewise-linearization method can be applied to calculate the representative Maxwell-slip elements. Four segments K_a, K_b, K_c, and K_d are intuitively picked up to represent for four Maxwell-slip elements. Eight parameters qualifying these four elements have to be identified, which consist of four stiffness parameters k_1, k_2, k_3, k_4 and four saturation values w_1, w_2, w_3, w_4. The system of eight equations (eq. A1) is thus established based on a coordinate analysis, where a_1, a_2, a_3, a_4 and b_1, b_2, b_3, b_4 are directly measured in the graph. Solving these equations yields eight parameters. These parameters are later on introduced to the hysteresis model. In the case of pressure/length hysteresis, the predicted output pressure of the model at any PAM position is used to compensate in the position control scheme as shown in Fig.6.

$$
\begin{aligned}
&k_1 + k_2 + k_3 + k_4 = K_a = a_1 / b_1 \\
&k_2 + k_3 + k_4 = K_b = a_2 / (b_2 - b_1) \\
&k_3 + k_4 = K_c = a_3 / (b_3 - b_2) \\
&k_4 = K_d = a_4 / (b_4 - b_3) \\
&w_1 / k_1 = b_1 \\
&w_2 / k_2 = b_2 \\
&w_3 / k_3 = b_3 \\
&w_4 / k_4 = b_4
\end{aligned}
\qquad \text{(A1)}
$$

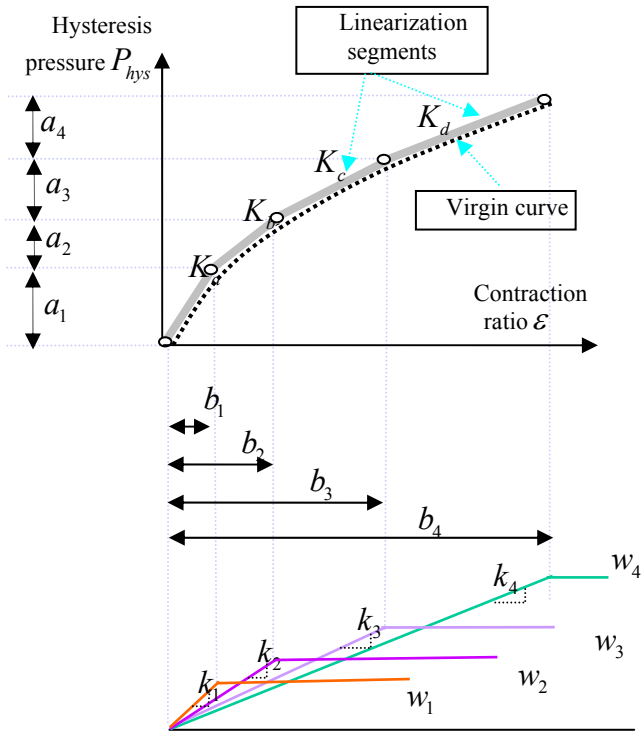

Fig. a1. Calculating parameters for representative Maxwell-slip elements based on virgin curve.

B.Asymmetric flow

Assume that during charging and discharging of the air, the process is in-between the isothermal and adiabatic states. The relationship of the mass of air, the muscle volume and the internal pressure is governed by the polytrophic gas law:

$$P\left[\frac{V}{m}\right]^{\gamma} = const. \quad \text{(B1)}$$

Taking the total differential of equation (B1), one can get:

$$\dot{P}V + \gamma P\dot{V} = \gamma\left(\frac{\dot{m}}{m}\right)PV$$

For an ideal gas, we have also:

$$PV = mRT \quad \text{(B2)}$$

Substituting (B2) into (B1), the building-up pressure can be described by the following equation:

$$\dot{P} = \frac{\gamma}{V}\left(\dot{m}RT - P\dot{V}\right) \quad \text{(B3)}$$

where:

P is the pressure inside the muscle,

V is the volume of the muscle,

m is the mass of air inside the muscle,

γ is the polytrophic exponent,

R is the universal gas constant, and

T is the air temperature inside the muscle.

The muscle volume varies during contraction/extension, thus one can obtain the volume as a function of the contraction ratio as follows:

$$V = \sum_{n=0}^{3} C_n \varepsilon^n \quad \text{(B4)}$$

where:

C_n are the coefficients of the polynomial function.

The mass flow rate through a non-ideal nozzle is governed by the following equation:

$$\dot{m} = P_u C \rho_0 \sqrt{\frac{T_0}{T_1}} \quad \text{if} \quad \frac{P_d}{P_u} \le b \qquad \text{(sonic flow)} \quad \text{(B5)}$$

and

$$\dot{m} = P_u C \rho_0 \sqrt{\frac{T_0}{T_1}} \sqrt{1 - \left(\frac{\frac{P_d}{P_u} - b}{1 - b}\right)^2} \quad \text{if} \quad \frac{P_d}{P_u} \succ b \text{ (subsonic flow)} \quad \text{(B6)}$$

where:

P_u, P_d are the upstream and downstream pressure respectively,

b is the critical pressure ratio,

$\dot{m}$ is the mass flow rate through the nozzle,

C is the flow conductance,

ρ_0, T_0 are the air density and air temperature respectively at standard condition , and

T_1 is the air supply temperature.

Equation (B5 and B6) can be rewritten in short from as the follows:

$$\dot{m} = P_u C \frac{1}{\sqrt{T_1}} \psi\left(\frac{P_d}{P_u}\right) \quad \text{(B7)}$$

where:

$\psi\left(\frac{P_d}{P_u}\right)$ is called the flow function, which is dependent only on the pressure ratio.

REFERENCES

[1] B. Tondu, "Analysis and Modeling of the Dynamic Behavior of the McKibben Artificial Muscle," IFAC Robot Control, Nantes, France, 1997, pp. 315-319.

[2] S. Davis, Darwin G. Caldwell, "Braid Effects on Contractile Range and Friction Modeling in Pneumatic Muscle Actuators," *The International Journal of Robotics Research*, Vol. 25, No. 4, April 2006, pp. 359-369.

[3] C. P. Chou, B. Hannaford, "Static and dynamic characteristics of McKibben pneumatic artificial muscles," *Proc. IEEE Intl. Conf. on Robotics and Automation*, San Diego, CA, May 1994, Vol. 1, pp. 281-286.

[4] Van Damme Michael, Beyl Pieter, Vanderborght Bram, Van Ham Ronald, Vanderniepen Innes, Versluys Rino, Daerden Frank, Lefeber Dirk, "Modeling Hysteresis in Pleated Pneumatic Artificial Muscles," *IEEE International Conference on Robotics, Automation & Mechatronics*, 2008, pp. 471-476.

[5] F. Daerden and D. Lefeber: The concept and design of pleated pneumatic artificial muscles, International Journal of Fluid Power 2(3), 2001, pp.41-50.

[6] Tri Vo Minh, Tegoeh Tjahjowidodo, Herman Ramon, and Hendrik Van Brussel, "Non-local Memory Hysteresis in A Pneumatic Artificial Muscle", *accepted to MED09, Thessaloniki, Greece*

[7] B. Tondu, P. Lopez, Modeling and control of Mckibben artificial muscle robot actuators, IEEE Control Systems Magazine , Vol. 20, No. 2, 2000, pp. 15-38.

[8] D. G. Caldwell, G. A. Medrano-Cerda, and M. J. Goodwin, Braided Pneumatic Actuator Control of a Multi-Jointed Manipulator, IEEE Int.Conf.on Systems, Man & Cybernetics, Le Touquet, France, Oct. 1993, pp. 423-428.

[9] T. Kimura, S. Hara, T. Fujita, and T. Kagawa, Feedback linearization for pneumatic actuator systems with static friction, Control Eng. Practice, v01.5, No.10, 1997, pp. 1385-1394.

[10] D. W. Repperger, K. R. Johnson, C. A. Phillips, Nonlinear Feedback Controller Design of A Pneumatic Muscle Actuator System, Proceedings of the American Control Conference, San Diego, California, June 1999, pp. 1525-1529.

[11] P. Carbonell, Z. P. Jiang, D.W. Repperger, Nonlinear control of a pneumatic muscle actuator: backstepping vs. sliding-mode, Proceedings of the 2001 IEEE International Conference on Control Applications, Mexico, September, 2001, pp. 353-358.

[12] S. W. Chan, J. H. Lilly, D. W. Repperger, and J. E. Berlin, Fuzzy PD+I learning control for a pneumatic muscle, IEEE international conference on fuzzy systems, 2003, pp. 278-283.

[13] K. Balasubramanian, K. S. Rattan, Trajectory tracking control of a pneumatic muscle system using fuzzy logic, Fuzzy Information Processing Society, Annual Meeting of the North American, 2005, pp. 472- 477.

[14] A. Hildebrandt, O. Sawodny, R. Neumann, A. Hartmann, A cascaded tracking control concept for pneumatic muscle actuators, European Control Conference 2003 (ECC03), Cambridge UK, (CDRom), 2003.

[15] G. A. Medrano-Cerda, Colin J. Bowler, and D.G. Caldwell, Adaptive position control of antagonistic pneumatic muscle actuators, IROS, USA, August 1995, pp. 378-383.

[16] J. Schröder, D. Erol, K. Kawamura, and R. Dillmann, Dynamic pneumatic actuator model for a model-based torque controller, IEEE Int Symp. On Computational Intelligence in Robotics and Automation, 2003, pp. 342-347.

[17] P. van der Smagt, F. Groen, K. Schulten, Analysis and control of a rubbertuator arm, Biol. Cybern, Vol. 75, 1996, pp. 433–440.

[18] M. Hamerlain, Anthropomorphic robot arm driven by artificial muscles using a variable structure control, Proc. IEEE Int. Conf. Intelligent Robots Systems, Pittsburgh, PA, Aug. 1995, pp. 550–555.
[19] D. Cai, H. Yamaura, A robust controller for manipulator driven by artificial muscle actuator, Proceedings of the 1996 IEEE international conference on control applications, 1996, pp. 540–545.
[20] J. H. Lilly, L. Yang, Sliding mode tracking for pneumatic muscles actuators in opposing pair configuration, IEEE Transactions on Control Systems Technology, Vol, 13, No. 4, 2005, pp. 550–558.
[21] J. Swevers, F. Al-Bender, C. Ganseman, and T. Prajogo, "An integrated friction model structure with improved presliding behavior for accurate friction compensation," *IEEE Trans. Automat. Contr.*, Apr. 2000, Vol. 45, pp. 675-686.
[22] W. D. Iwan, A distributed-element model for hysteresis and its steady-state dynamic response, Journal of Applied Mechanics, 1966, pp. 893-898.
[23] Tri Vo Minh, Tegoeh Tjahjowidodo, Herman Ramon, and Hendrik Van Brussel, "A new approach to modeling hysteresis in a pneumatic artificial muscle using the Maxwell-slip model", submitted to Focused Section on Anthropomorphism in Mechatronic Systems, IEEE/ASME Transaction on Mechatronics.
[24] Tri Vo Minh, Tegoeh Tjahjowidodo, Herman Ramon, and Hendrik Van Brussel, "Control of Pneumatic Artificial Muscle (PAM) with Model-Based Hysteresis Compensation", accepted to AIM09, Singapore.
[25] A. Hildebrandt, O. Sawodny, R. Neumann, and A. Hartmann, Cascaded control concept of a robot with two degrees of freedom driven by four artificial pneumatic muscle actuators, American control conference, 2005, pp. 680–685.
[26] Wim symens, "Motion and vibration control of mechatronic system with variable configuration and non-linear friction", PhD dissertation, 2004.

Proceedings of the 8th National Congress on Theoretical and Applied Mechanics, May 28-29, Brussels, Belgium.

A powered knee exoskeleton for gait rehabilitation

Pieter Beyl, Pierre Cherelle, Rino Versluys, Innes Vanderniepen, Dirk Lefeber
Robotics & Multibody Mechanics Research Group, Department of Mechanical Engineering,
Vrije Universiteit Brussel, Pleinlaan 2, 1050 Brussels - Belgium
email: pieter.beyl@vub.ac.be, pierre.cherelle@vub.ac.be, rino.versluys@vub.ac.be, innes.vanderniepen@vub.ac.be, dlefeber@vub.ac.be

Abstract— **Research in robot-assisted gait rehabilitation has seen significant improvements in human-robot interaction, thanks to high performance actuator technologies and dedicated control strategies. In this context we propose a combination of lightweight, intrinsically compliant, high power actuators (Pleated Pneumatic Artificial Muscles, PPAMs) with safe and adaptable guidance along a trajectory by means of Proxy-based Sliding Mode Control (PSMC). This paper reports on the development of a gait rehabilitation exoskeleton prototype intended as a platform for the evaluation of design and control concepts in view of improved physical human-robot interaction. The performance of proxy-based sliding mode control as a "robot-in-charge" control strategy is evaluated both in simulation and in experiments on a test setup. Compared to PID control, test results indicate good tracking performance and safe system behavior.**

Keywords— **robot-assisted gait rehabilitation, powered exoskeleton, compliant actuator, proxy-based sliding mode control, human-robot interaction**

I. INTRODUCTION

LOCOMOTION training is considered an effective approach to helping incomplete spinal cord injured subjects recover their walking capabilities [1],[2]. The automation of locomotion training by means of a powered exoskeleton potentially improves training efficacy and rehabilitation outcome [3],[4]. Physiological gait patterns can be produced and adapted with higher accuracy. Automatic monitoring of the patient's progress allows the development of more adequate training schemes. The robotic device relieves strain on therapists, thus enabling longer training sessions and allowing the same number of therapists to supervise more patients.

Several research groups are developing powered exoskeletons for the rehabilitation of gait. The Lokomat (Hocoma AG, Switzerland) is one of the few commercialized step rehabilitation systems and well reported in literature [5],[6]. The Biomechatronics Lab of the University of California has developed several robotic devices (ARTHuR, PAM, POGO) to study automated gait training of spinal cord injured patients [7]. With their LOPES project the Biomechanical Engineering Lab of the University of Twente focuses on task-specific gait training of post-stroke patients [8]. Powered leg exoskeletons are also being developed at for instance the University of Delaware [9], the University of Michigan [10] and the University of Salford [11]. Although the clinical results of automated treadmill training reported in literature are encouraging [12], existing gait rehabilitation devices do suffer from a few limitations and future research faces some important challenges. First of all, most devices do not actively support the ankle joint, which results in poorly constrained and unnatural motion of the foot. Consequently, certain causes of gait dysfunction like dropped foot or spastic foot extension cannot be adequately countered during therapy. Secondly, the use of a suspension system with a harness leads to an unnatural body weight distribution and hinders balance and postural reactions of the patient, required in functional walking. Additionally, due to their actuation system and control approach these robots often lack compliance, which is considered an important prerequisite for safe human-robot interaction [13]. There is a growing tendency towards patient-cooperative control strategies, where, instead of predefined movements being imposed, the patient's intentions and efforts are taken into account [7],[8],[14]. Still, in many cases, either compliant behavior is only built-in on the control level or only partially built-in on the hardware level.

We hypothesize that a device providing full body weight support, active ankle assistance and adaptable compliant behavior, that is both built-in in the actuation system and taken advantage of on the control level, has the potential to improve the quality of automated treadmill training. Our goal is to develop such a device and to meet the aforementioned challenges by means of a special type of actuator: the pleated pneumatic artificial muscle (PPAM) [15]. This actuator is inherently compliant and we believe it will provide the necessary soft touch for a better human-robot interaction. Additionally, the actuator's high pulling force enables the robot to carry the full weight of the patient, without resorting to an overhead suspension system.

Before starting the development of a complete gait rehabilitation robot however, it is sensible to reduce the scale and complexity of the problem in order to identify and address technical problems in an early stage. Therefore the first phase of the project involves the development of a unilateral leg exoskeleton with a PPAM powered knee joint.

This paper reports on the mechanical design of the prototype and a study of control performance. The paper is organized as follows. Section II describes the mechanical design of the prototype. The design specifications are outlined, the dimensioning of the actuators is briefly explained and a description of the mechanical structure is given. In section III the control approach is introduced and control performance is discussed on the basis of simulation results and experiments on a simplified test setup. The final section gives a brief overview of future work and conclusions.

II. MECHANICAL DESIGN

A. Design Specifications

The device consists of a unilateral exoskeleton and a supportive arm. The supportive arm is intended to passively gravity-balance the device to avoid asymmetrical loading of the subject. For the exoskeleton, articulation is required at the ankle, knee and hip, but only the knee joint is to be powered in this stage. The actuation system should provide sufficient knee joint torque to support human gait in walking experiments on a treadmill. As mentioned in the introductory section, the exoskeleton prototype will be a proof-of-concept device, primarily intended for the development and testing of design and control concepts. For this reason, the design has been tailored to the requirements of an average male subject. For the adjustability of the device only small inter-subject variations have been taken into account. The actuation system needs to be dimensioned carefully according to the kinematical and dynamical requirements. Representative Clinical Gait Analysis (CGA) data serves as a first estimate of the required output characteristics [16]. A knee joint range of motion of 90° in flexion is sufficient in normal overground walking. Torque requirements are predominantly determined by the large peak torque occurring at early stance, typically $50Nm$ for an average male subject in normal overground walking [16]. The generated torque is to be transferred to the subject's lower limb avoiding any excessive load or displacement at the interface. To this end, the exoskeleton needs to be fitted properly.

B. Actuator Configuration and Dimensioning

The pleated pneumatic artificial muscle (PPAM) is a lightweight, air-powered actuator that generates linear motion [15]. Its core element is a reinforced pleated membrane that expands radially and contracts axially when pressurized. To obtain a bidirectional rotational actuator, one can configure two single-acting actuators in an antagonistic configuration. The actuator forces can be transferred to the joint in different ways, for instance a pulley-and-belt system (Fig. 1(a)) or a direct connection through fixed levers (Fig. 1(b)). We have chosen a configuration based on a four bar linkage mechanism (Fig. 1(c)), as it combines the advantages of both of the aforementioned configurations, namely compactness and good torque matching.

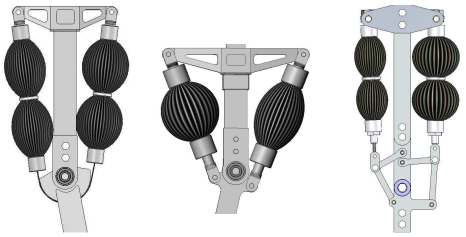

(a) (b) (c)

Fig. 1. Antagonistic configurations of PPAM's driving a robotic joint.(a) Pulley-and-belt connection. (b) Connection through fixed levers. (c) Connection based on four bar linkages.

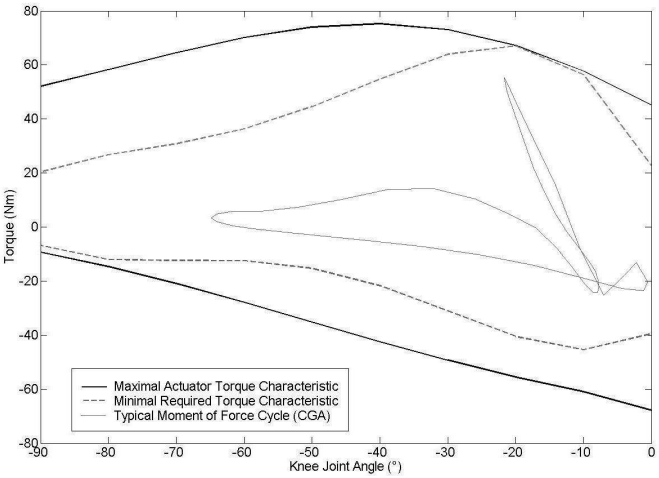

Fig. 2. Torque-angle characteristic of the exoskeleton's knee joint compared to the minimal required characteristic based on CGA data and a typical torque cycle out of CGA data

The output characteristics of the proposed configuration are determined by a large number of design parameters. In order to find an optimal configuration, we have formulated the design problem as an optimization problem with multiple nonlinear objectives and multiple nonlinear constraints. We have used an exhaustive search based optimization approach in order to find a valuable solution that meets the design specifications without recurring to complex optimization techniques. For a detailed description the reader is referred to [17]. Figure II-B shows the maximal knee joint torque characteristic of the selected optimal actuator configuration, compared to the minimal required angle-torque envelope based on CGA data (taking into account inter-subject variability) and to a typical angle-torque cycle out of CGA data for normal walking [16]. Due to design bottlenecks and the fact that the torque-

angle relationship cannot be arbitrarily shaped, the actuator system is overdimensioned in the range corresponding with low PPAM contraction levels and high pulling forces.

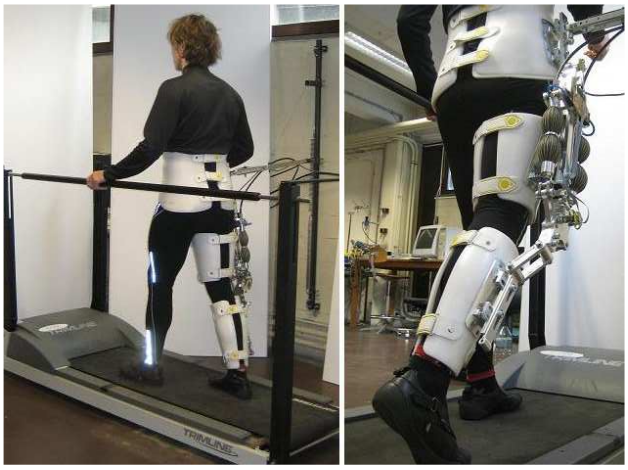

Fig. 3. Lab setup with treadmill, exoskeleton and supportive arm.

C. Exoskeleton Design

Figure 3 depicts the gait rehabilitation exoskeleton in a lab setup for walking experiments. The exoskeleton consists of adjustable hip, thigh, shank and foot links interconnected by hinge joints. Two-piece rigid thermoplastic shells with a foam inlay and Velcro straps provide an adaptable fit at the lower and upper leg and the hip. Their position and orientation with respect to the exoskeleton frame are adjustable by means of slider mechanisms. The actuators are tethered to an external pressurized air supply system with high performance pressure regulating servo valves. Mechanical limiters prevent hyperextension of the knee and flexion angles exceeding 90°. The telescopic supportive arm is connected to the hip link by means of a ball joint. Additionally, the arm can pivot about a horizontal and vertical axis near the supporting wall. A zero free length spring mechanism is incorporated to passively gravity-balance the supportive arm and the exoskeleton [18].

III. CONTROL

A. System Requirements

Since a medical rehabilitation device closely interacts with patients, we consider safety the most important prerequisite. Moreover, due to impaired motor control, muscle weakness and deconditioning, the patient is virtually a slave to the machine during therapy and literally in a vulnerable position. Therefore, safety aspects are to be considered in all stages of design and safety measures should be incorporated on the software level (control) as well as the hardware level.

Thanks to the intrinsic compliance of the actuation system deviations from the target position are allowed and passively counteracted without complex feedback control mechanisms. Obviously this affects tracking performance, however our goal is to achieve functional walking without putting too much emphasis on the accuracy of the gait pattern. We believe the compliant behavior might substantially improve human-robot interaction, especially for patients with spastic hypertonicity of the leg muscles.

Although we aim at a specific target patient group, namely motor incomplete spinal cord injured (SCI) patients, there is a large intersubject variability in terms of for instance residual motor control. Therefore we envisage different control strategies: a trajectory tracking approach (”robot-in-charge”) with compliance adaptation for patients with poor motor control and a force amplification approach (”patient-in-charge”) for specific gait support of patients with sufficient voluntary locomotor capability. Intermediate or hybrid control strategies might be appropriate for patients who do not fit in either end of the spectrum.

The exoskeleton prototype will serve as a test setup for the implementation of these control strategies on a single actuated joint. For the sake of simplicity, the trajectory tracking approach is investigated first. In this context we propose proxy-based sliding mode control, a new control method introduced by Kikuuwe and Fujimoto [19]. It has been demonstrated experimentally in [19] and [20], that it combines good tracking performance with a safe response to large deviations from the target position. The following section briefly explains the general idea behind proxy-based sliding mode control applied to the gait rehabilitation exoskeleton. For a detailed description of the control methodology, the reader is referred to [19].

B. Proxy-based Sliding Mode Control

In proxy-based sliding mode control (PSMC) a proxy or virtual object is simulated, that is connected to the robot’s end-effector by a PID-type virtual coupling. The proxy’s position is controlled by an ideal sliding mode controller in order to track the reference position. In [20] a modified form of PSMC is suggested, so that each robot link is controlled separately instead of solely the end-effector.

Now, let us consider a simplified representation in the sagittal plane of a human leg in swing phase attached to the exoskeleton as depicted in Fig. 4. Assuming an ideal, rigid connection, we model the combined system as a 3 degree of freedom (DOF) serial linkage consisting of a hip link fixed to the reference frame and a thigh, shank and foot link. To simplify the model further we lock the ankle joint so that the foot link is perpendicular to the shank link. This leaves us with a 2 DOF system.

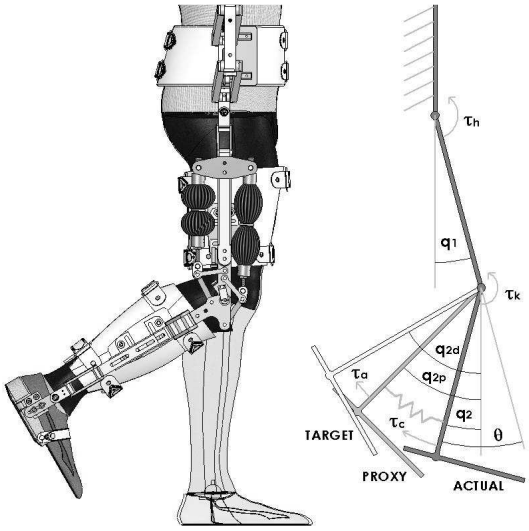

Fig. 4. Serial linkage model (right) of the system (left) consisting of the gait rehabilitation exoskeleton and a human leg in swing phase.

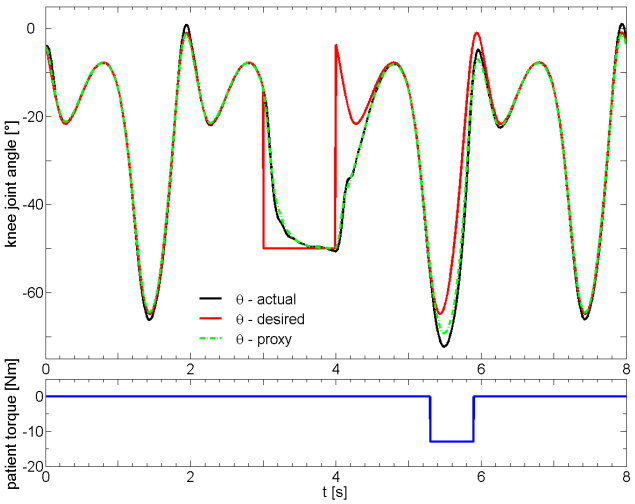

Fig. 5. Simulation results regarding system safety: a step change in the trajectory to -50° @ $t = 3s$ and a virtual patient torque of $-13Nm$ @ $t = 5.25s$ are imposed during tracking.

Returning to PSMC and applying the control method to the powered knee joint, we distinguish the actual position q_2 of the lower leg link, the target position q_{2d} and the position of the proxy q_{2p}, in this case a virtual lower leg link (Fig. 4). The virtual link is attached to the real link by means of a torsional PID-type virtual coupling exerting a torque τ_c. This is also the real torque applied by the actuators to the real link. On the other hand a virtual torque τ_a, the output of a sliding mode controller, is applied to the virtual link in order to track the target link. The response characteristics of the PSMC controller are largely determined by the PID gains for small positional errors, ensuring tracking performance, and in case of large deviations by the sliding mode controller part, ensuring a smooth recovering motion. In fact, PSMC can be seen as an extension to both conventional PID control and sliding-mode control.

C. Simulation

The primary objective of the simulation study is to assess the control performance of PSMC, before proceeding with the experimental validation on the prototype. The dynamical model of the 2 DOF system, described in III-B, is formulated in Eq. (1), with H and C the inertia and centrifugal/coriolis matrix, G the gravitational torque vector, $\tau = [\tau_h - \tau_k, \tau_k]^T$ the vector of net torques acting on each link and $q = [q_1, q_2]^T$ the vector of joint angles. The inertial properties have been estimated by means of CAD software and anthropometric data [21]. In Eq. (2) the pressure dynamics are modeled by a combination of a first-order system, approximating valve dynamics, and the polytropic law linking angular variations to pressure variations inside the PPAMs [22]. Here T_i is a time constant, p_{id} the desired pressure, $V_i(\theta)$ the muscle volume, P_{atm} the atmospheric pressure, n the polytropic coefficient, $\theta = q_2 - q_1$ and $i = 1, 2$.

$$H(q)\ddot{q} + C(q,\dot{q})\dot{q} + G(q) = \tau \tag{1}$$

$$\dot{p}_i = \frac{p_i}{T_i} + \frac{p_{id}}{T_i} - n(p_i + P_{atm})\frac{1}{V_i(\theta)}\frac{dV_i(\theta)}{d\theta}\dot{\theta} \tag{2}$$

Taking into account the force-contraction characteristic of the PPAMs [15] and the kinematics of the configuration, we can formulate the knee joint actuator torque as in Eq. (3), with torque functions m_i, depending on joint angle θ and the design parameters. With the $\Delta p - approach$ [22], controller outputs p_i are reduced to one single output Δp, added to or subtracted from the desired mean pressure p_m. The controller implemented in this simulation is based on an adapted PSMC formulation proposed in [20]. A gravity and inertia compensation term Δp_{ff} are added, which results in the control law stated in Eq. (4). The reader is referred to [20] for the definition of Δp_{psmc} and a detailed description.

$$\tau_{act} = p_1 m_1 + p_2 m_2 = p_m(m_1 + m_2) + \Delta p(m_1 - m_2) \tag{3}$$

$$\Delta p = \Delta p_{ff} + \Delta p_{psmc} \tag{4}$$

In simulation the virtual patient performs a gait like motion with the leg suspended and attached to the exoskeleton. He is assumed to generate the total required power at the hip joint and no power at the actuated knee joint. The required hip and knee joint trajectories are based on CGA data [16]. Since we are mainly interested in the knee joint dynamics at this point, the hip joint kinematics are tracked by a high gain tracking controller. By means of the simulation

model, implemented in MATLAB, we have evaluated the performance of the PSMC controller in case of undisturbed trajectory tracking and in case of large deviations from the target position and perturbations. PID control with gravity and inertia compensation was used as a reference. Figure 5 illustrates safe system behavior in case of PSMC: deviations from the target trajectory, due to for instance high level controller failure or interaction with the patient, are allowed without severe corrections and countered with a slow and smooth recovering motion. These simulation results encouraged experimental validation of PSMC on the prototype.

D. Experiments

TABLE I
TUNED PSMC AND PID CONTROL PARAMETERS

PSMC		PID	
Parameter	Value	Parameter	Value
$K_p[bar/rad]$	3.5	$K_p[Nm/rad]$	120
$K_i[bar/rad.s]$	3.25	$K_i[Nm/rad.s]$	80
$K_d[bar.s/rad]$	0.25	$K_d[Nm.s/rad]$	10
$\lambda[s]$	0.3		
$\Delta p_{lim}[bar]$	0.5		

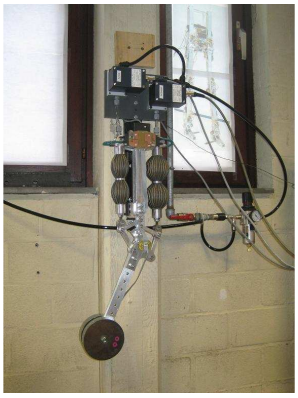

Fig. 6. Simplified 1 DOF test setup for control evaluation.

We have tested PSMC on a simplified test setup with one single (actuated) degree-of-freedom (Fig.6). The inertial parameters of the lower link match those of the exoskeleton's lower leg link combined with estimated body segment parameters. PID control with gravity and inertia compensation was used as a reference for evaluating system behavior. Both controllers were implemented on the setup and tuned on a trial-and-error basis. Table I lists the tuned control parameter values for the PSMC and PID controller. Parameter λ is a time constant that determines the recovery motion in case of large perturbations. Parameter Δp_{lim} limits the output pressure and in this way sets the

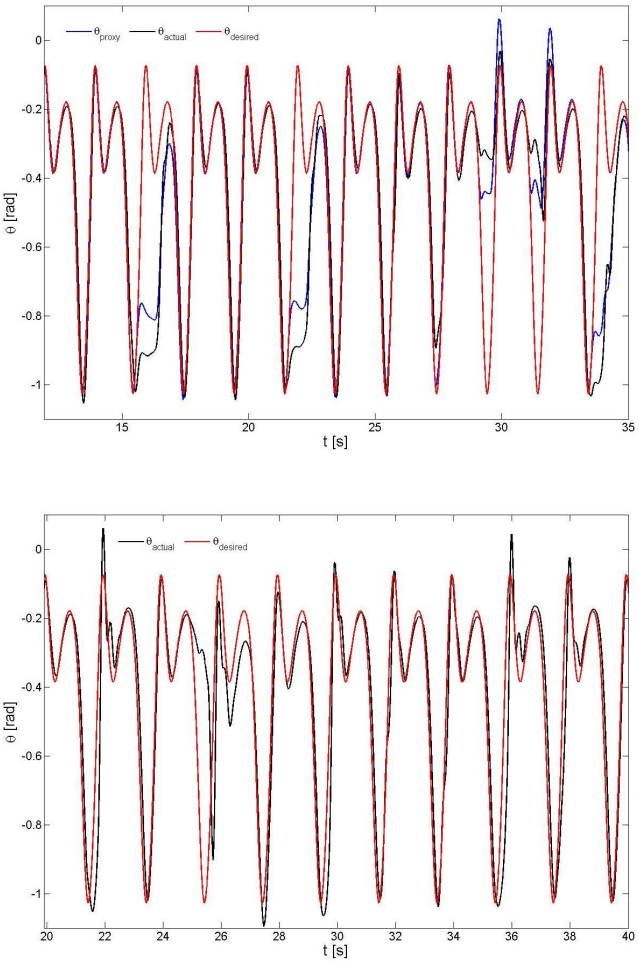

Fig. 7. PSMC (top) and PID (bottom) tracking experiment with manually imposed disturbances: desired, actual (and proxy) trajectories.

transition between the small perturbation response and the large perturbation response. Due to this decoupling relatively higher values can be assigned to the PSMC gains compared to the PID gains, especially the integral gain. PSMC and PID showed comparable undisturbed tracking performance, but as expected very different system behavior in case of external disturbances. In Fig. 7 the desired and actual trajectories are depicted originating from PSMC and PID tracking experiments respectively, during which disturbing forces were being imposed manually. The corresponding desired and actual angular velocities are shown in Fig. 8, the corresponding torque imposed by the actuation system in Fig. 9. In the absence of force sensor measurements, the latter have been estimated by means of muscle pressure measurements and the model in Eq. (3). In case of PID control external torques below the maximal torque output hardly cause any trajectory deviation, whereas large trajectory deviations pro-

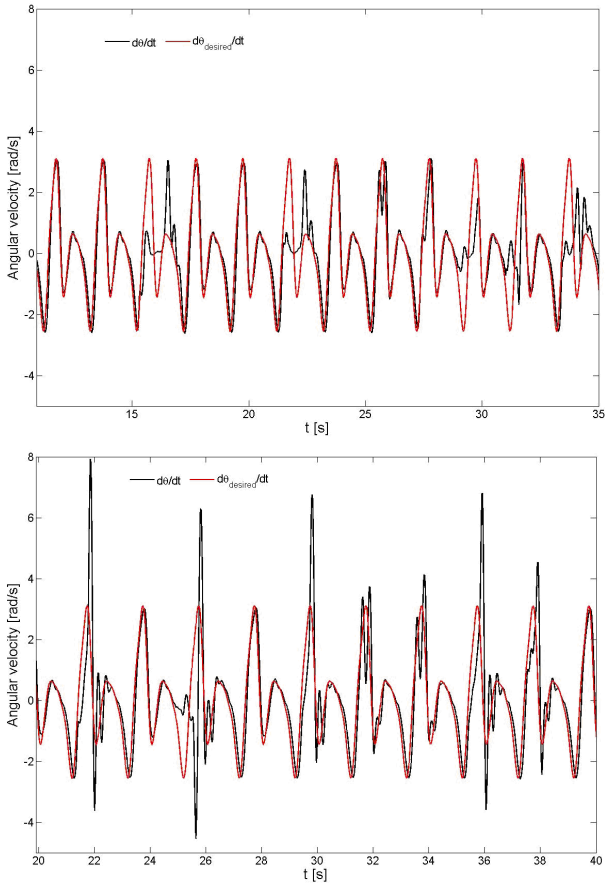

Fig. 8. PSMC (top) and PID (bottom) tracking experiment with manually imposed disturbances: desired and actual angular velocities.

voke high torques and recovery motions with angular velocity values up to 2.5 times the maximal desired value. In view of robot-assisted rehabilitation of gait we consider such behavior not compatible at all with the occurrence of muscle spasms or voluntary muscle activity. In PSMC however the smooth, adjustable recovery motion and adjustable maximal restoring force considerably improve system safety. Thanks to the latter, the actuation system output hardly exceeds the torque imposed during undisturbed trajectory tracking, as can be seen from Fig. 9. These experimental results show the potential of PSMC as a safe "robot-in-charge" control strategy for the gait rehabilitation exoskeleton prototype.

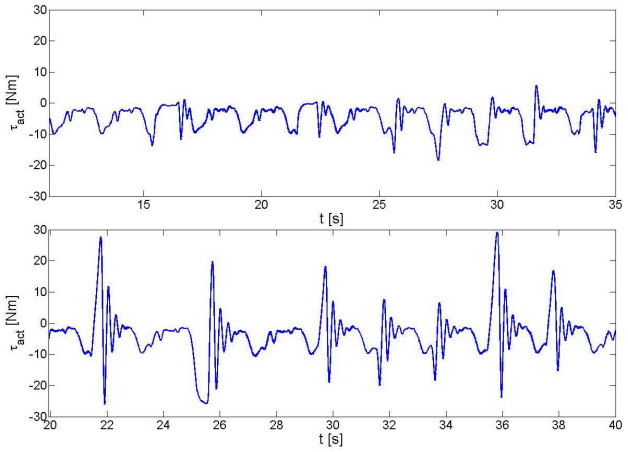

Fig. 9. PSMC (top) and PID (bottom) tracking experiment with manually imposed disturbances: estimated actuation system torque.

IV. CONCLUSIONS AND FUTURE WORK

A gait rehabilitation exoskeleton prototype with a knee joint powered by pleated pneumatic artificial muscles has been developed for the assessment of design and control concepts. The mechanical design process was mainly focused on the optimization of the actuation system. In view of the system's safety requirements and envisaged compliant behavior, we have focused on proxy-based sliding mode control (PSMC) as a trajectory tracking based approach to gait training in SCI patients with poor motor control. Control performance has been explored in a simulation study and in experiments on a test setup, indicating good tracking performance and safe system behavior in comparison with PID control. Next, we will evaluate wearability and control performance of the exoskeleton prototype in treadmill walking experiments with healthy subjects.

ACKNOWLEDGMENTS

This research is funded by a Ph.D grant of the Institute for the Promotion of Innovation through Science and Technology in Flanders (IWT-Vlaanderen). It is supported by a Concerted Research Action, "ALTACRO, Automated Locomotion Training using an Actuated Compliant Robotic Orthosis", funded by the Research Council of Vrije Universiteit Brussel - VUB.

REFERENCES

[1] Wirz M., Colombo G., Dietz V., "Long term effects of locomotor training in spinal humans," *J Neurol Neurosurg Psychiatry*, vol. 71, pp. 93-96, 2001.

[2] Wernig A., Muller S., "Laufband locomotion with body support improved walking in persons with severe spinal cord injuries," *Paraplegia*, vol. 30, no. 4, pp. 229-238, 1992.

[3] Krebs H., Aisen M., Hogan N., "Increasing productivity and quality of care: robotaided neuro-habilitation," *Journal of Rehabilitation Research and Development*, vol. 37, no. 6, pp. 639-652, 2000.

[4] Colombo G., Wirz M., Dietz V., "Driven gait orthosis for improvement of locomotor training in paraplegic patients," *Spinal Cord*, vol. 39, pp. 252-253, 2001.

[5] Colombo G., Jrg M., Schreier R., Dietz V., "Treadmill training of paraplegic patients with a robotic orthosis," *Journal of Rehab Research and Development*, vol. 37, pp. 693-700, 2000.

[6] Jezernik S., Colombo G., Keller T., Frueh H., Morari M., "Robotic Orthosis Lokomat: A Rehabilitation and Research Tool," *Neuromodulation*, vol. 6, no. 2, pp. 108-115, 2003.

[7] Aoyagi D., Ichinose W.E., Harkema S.J., Reinkensmeyer D.J., Bobrow J.E., "A robot and control algorithm that can synchronously assist in naturalistic motion during body-weight-supported gait training following neurologic injury," *IEEE Transactions on Neural Systems and Rehabilitation Engineering*, vol.15, no.3, pp.387-400, 2007.

[8] Veneman J.F., Kruidhof R., Hekman E.E.G., Ekkelenkamp R., Van Asseldonk E.H.F., van der Kooij H., "Design and evaluation of the LOPES exoskeleton robot for interactive gait rehabilitation," *IEEE Transactions on Neural Systems and Rehabilitation Engineering*, vol.15, no.3, pp.379-386, 2007.

[9] Agrawal S. K., Banala S. K., Mankala K., Sangwan V., Scholz J. P., Krishnamoorthy V., Hsu W., "Exoskeletons for gait assistance and training of the motor impaired," *Proc. of the IEEE International Conference on Rehabilitation Robotics*, pp. 1108-1113, 2007.

[10] Ferris D. P., Sawicki G. S., Domingo A. R., "Powered lower limb orthoses for gait rehabilitation." *Topics in Spinal Cord Injury Rehabilitation*, vol. 11, pp. 34-49, 2005.

[11] Costa N., Caldwell D.G., "Control of a Biomimetic "Soft-actuated" 10DoF Lower Body Exoskeleton," *Proc. of the IEEE/RAS-EMBS International Conference on Biomedical Robotics and Biomechatronics*, pp.495-501, 2006.

[12] Wirz M., Zemon D., Rupp R., Scheel A., Colombo G., Dietz V., and Hornby G., "Effectiveness of automated locomotor training in patients with chronic incomplete spinal cord injury: a multicenter trial," *Archives of Physical Medicine and Rehabilitation*, vol. 86, no. 4, pp. 672-680, 2005.

[13] Bicchi A., Tonietti G., "Fast and "soft-arm" tactics [robot arm design]," *IEEE Robotics & Automation Magazine*, vol.11, no.2, pp. 22-33, 2004.

[14] Riener R., Lunenburger L., Jezernik S., Anderschitz M., Colombo G., Dietz V., "Patient-cooperative strategies for robot-aided treadmill training: first experimental results," *IEEE Transactions on Neural Systems and Rehabilitation Engineering*, vol. 13, no. 3., pp. 380-394, 2005.

[15] Verrelst B., Van Ham R., Vanderborght B., Lefeber D., Daerden F., Van Damme M., "Second generation pleated pneumatic artificial muscle and its robotic applications," *Advanced Robotics*, vol. 20, no. 7, pp. 783-805, 2006.

[16] Winter D. A., "The biomechanics and motor control of human gait: normal, elderly and pathological. Second edition," University of Waterloo Press, 1991.

[17] Beyl P., Naudet J., Van Ham R., Lefeber D., "Mechanical design of an active knee orthosis for gait rehabilitation," *Proc. of the IEEE International Conference on Rehabilitation Robotics*, pp. 100-105, 2007.

[18] Rahman T., Ramanathan R., Seliktar R., Harwin W., "A Simple Technique to Passively Gravity-Balance Articulated Mechanisms," *Trans. of the ASME- J of Mechanical Design*, vol. 117, no. 4, pp. 655-658, 1995.

[19] Kikuuwe R., Fujimoto H., "Proxy-based sliding mode control for accurate and safe position control," *Proceedings of the IEEE Int. Conference on Robotics and Automation*, pp. 25-30, 2006.

[20] Van Damme M., Vanderborght B., Van Ham R., Verrelst B., Daerden F., Lefeber D., "Proxy-Based Sliding Mode Control of a Manipulator Actuated by Pleated Pneumatic Artificial Muscles," *Proc. of the IEEE International Conference on Robotics and Automation*, pp.4355-4360, 2007.

[21] *Anthropometric source book, Volume I: Anthropometry for designers*, Webb Associates, 1978, NASA Ref. Pub. no. 1024.

[22] Verrelst B., Van Ham R., Vanderborght B., Vermeulen J., Lefeber D., Daerden F., "Exploiting the Adaptable Passive Behaviour to Influence Natural Dynamics Applied to Legged Robots," *Robotica*, vol. 23, no. 2, pp. 149-158, 2005.

Proceedings of the 8th National Congress on Theoretical and Applied Mechanics, May 28-29, Brussels, Belgium.

Design of SAM, a new fully portable exoskeleton device with local joint control

Pierre Letier, More Avraam, Samuel Veillerette, Mihaita Horodinca, André Preumont
Active Strucures Laboratory,Université Libre de Bruxelles
Av. F.D. Roosevelt 50 CP 165/42, 1050 Brussels - Belgium
email: pierre.letier@ulb.ac.be,scmero@ulb.ac.be

Abstract— **This paper presents the development of SAM, the Sensoric Arm Master, a 7-DOF portable exoskeleton with integrated actuation and sensors. Local joint control, based on an impedance and admittance approach, is implemented to improve performances of the device. Some experiments have been conducted with the system to show the functionality of the exoskeleton device linked to a virtual reality. This system is used also in the frame of the EXOSTATION project aimaing at developing a complete control chain for space haptic teleoperation.**

Keywords— **haptic, exoskeleton, teleoperation, virtual reality, NCTAM 2009**

I. Introduction

HAPTIC devices are used to produce force sensation to the operator either in the case of the teleoperation of a real slave robot or in the field of virtual reality. They enhance the level of immersion compared to a simple visual display. The position of the user is measured by the device's sensors and used to control the robot or interact with virtual objects. Interactions forces are then reflected on the human through actuators.

One family of haptic device is exoskeleton. It consists of an external mechanical structure attached to the body of the operator and following his anatomy. Compared to simple desktop haptic device, the exoskeleton structure allows measuring simultaneously the position of different parts of the body and producing multipoint contacts. Moreover, in the field of haptic rendering, the use of a fully portable/transportable device can be advantageous in specific applications as the operator is not linked to a fixed base. Applications are found in robotic arm teleoperation for space exploration missions or for CBRNE (Chemical, Biological, Radioactive, Nuclear and Explosive) crisis management . The haptic device is usable near the slave robot avoiding transmission delays. An other field is the virtual training in large environments.

Most of the exoskeletons developed until now are grounded [1][2][3][4][5]. This is due to the use of a heavy structure and big DC-based actuators to allow high torque level comparable to the human arm joints capabilities. Most of them are foreseen also for rehabilitation applications for which a high torque level is needed.

Only a few fully portable devices have been reported in the literature. In [6] water cooling is used to allow higher level of current and torque for a given actuator size. In [7], it was envisaged to delocalize the actuators, with bowden-cables, in the back of the operator to reduce the weight carried by the arm. In [8] and [9], the DC actuation is replaced by pneumatic muscle actuators with a better power/weight ratio allowing a low system weight. However, these concepts bring more complexity due to the requirement of annex systems and cable routing. In [10] electric brakes are implemented, making the device light and compact. However the use of brakes can limit the type of sensations that the operator can feel, as the reaction forces from springs.

This paper presents the design of the Sensoric Arm Master (SAM), a new 7-DOF anthropomorphic fully portable exoskeleton. Considering only haptic activities, the specifications in terms of achievable actuation torque can be reduced. As reported in [11] for desktop devices, only 1/20th of the maximum human force level is required to produce a good haptic sensation. Based on this principle, the actuators were selected to fit this level, allowing the design of a light and simple system with on-joint actuation. In the first section, the design of the exoskeleton is described related to the kinematics design, the mechanical structure, the selection of the actuation and sensor technologies. The second section presents different control strategies that have been implemented and tested on the system. Section 3 illustrates the achieved results. Finally, section 4 presents the application of SAM in the frame of the EXOSTATION project aiming at developing a demonstrator for a teleoperation robotic manipulator for the International Space Station.

II. Exoskeleton Design

A. Mechanical Design

SAM consists of a serial kinematics, isomorphic to the human arm (Fig. 1). There are 7 actuated DOF from the shoulder to the wrist, which corresponds to the minimum number of joint allowing full immersion of the operator. The exoskeleton can be adapted to the morphology of the user by a set of 5 sliders located in the various Aluminum links.

The kinematics is chosen to be simple and to maximize the workspace without singularities. As shown in Fig. 2, if 3 orthogonal rotational joints parallel to the refer-

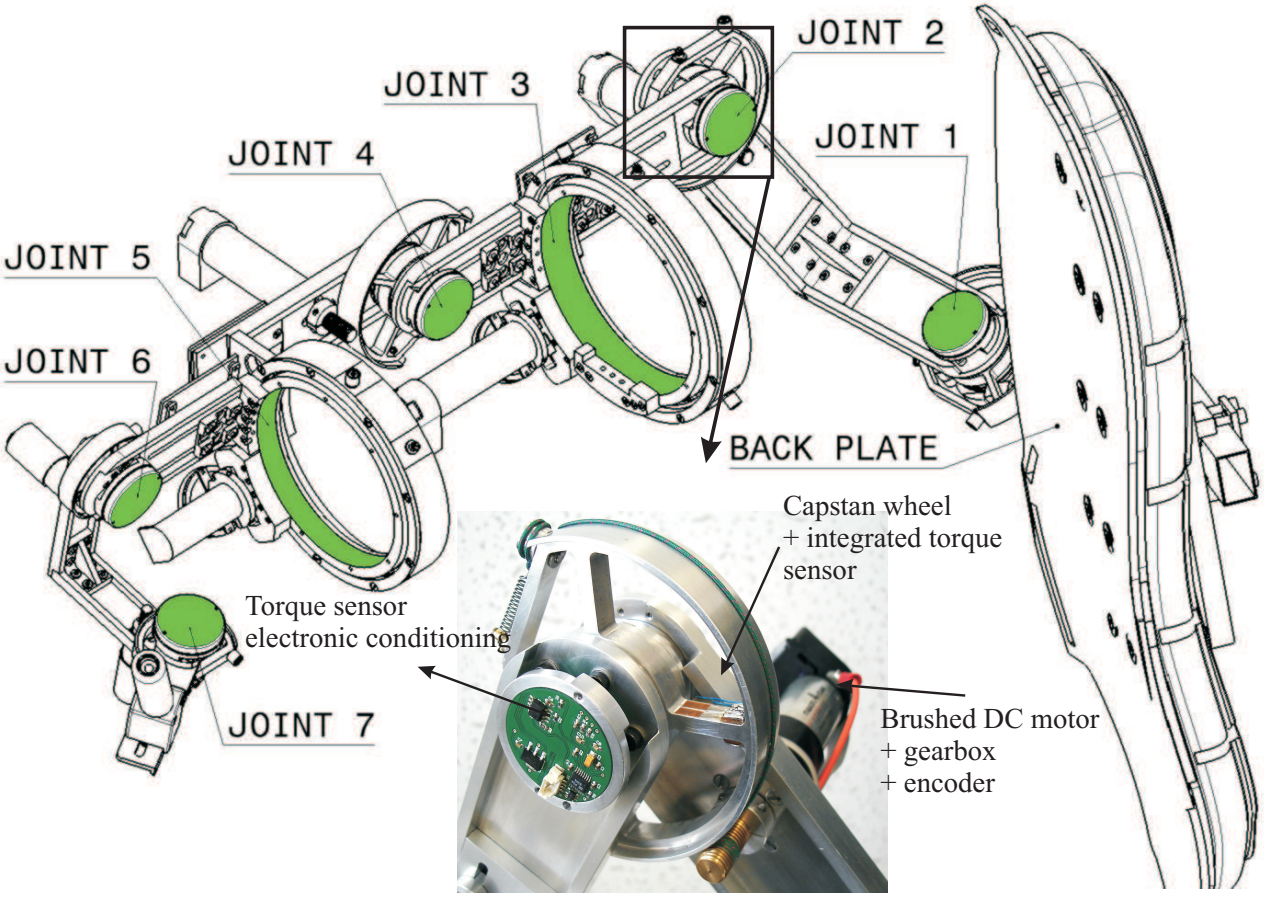

Fig. 1. CAD view of the Sensoric Arm Master (SAM) and joint 2 physical implementation.

ence axis (X,Y,Z) are used to represent the spherical joint of the shoulder, singularities appear in the center of the workspace. In order to move these singularities from the center to the frontier of the workspace, the joint configuration of the shoulder has been modified by two successive rotations, respectively α around Y and β around Z of the inertial reference frame (Fig. 2), to reach the final configuration used in this study. An other singular region exists at the wrist in the initial design. The same method has been used to delocalize the singularity, leading to a rotation of γ of the joint 6.

The exoskeleton is attached to the user body by four points at the back, the upper and lower arm and the hand. The ergonomic dorsal backplate is made from hard plastic and implements the body fastening system. On the arm, shell polypropylene orthesises, with internal foam layers, are used. They allow comfortable fixation and adaptation to different arm diameters.

The final weight of the device is 7kg, including the mechanical structure, the actuators and the on-board electronic. This value allows the operator to use correctly the system, but gravity compensation can improve the comfort.

B. Actuation

Based on the results of a previous study where several actuation technologies were compared [12], each joint is composed of a brushed DC motor coupled with a cable capstan and gearbox with reduction ratio between 3 and 23 depending on the joint. The capstan type reducer, often used in haptic devices, allows zero-backlash transmission as well as low friction at the expense of a low torque/volume ratio. The diameter of the wheel is proportional to the reduction ratio. At the opposite, gearbox presents a good compactness but with a higher level of friction and some backlash. The purpose of combining the two types of reducers is to achieve a high enough torque combined with high compactness, low friction and low backlash transmission. Table I summarizes the selected actuators and the target torque corresponding to 1/20th of the human capabilities for each joint [4][13].

C. Sensors

In order to allow implementing different kind of control strategies, position and force/torque are measured on the exoskeleton. Incremental encoders, located on each actuator, measure the angular position of the joints. A value of

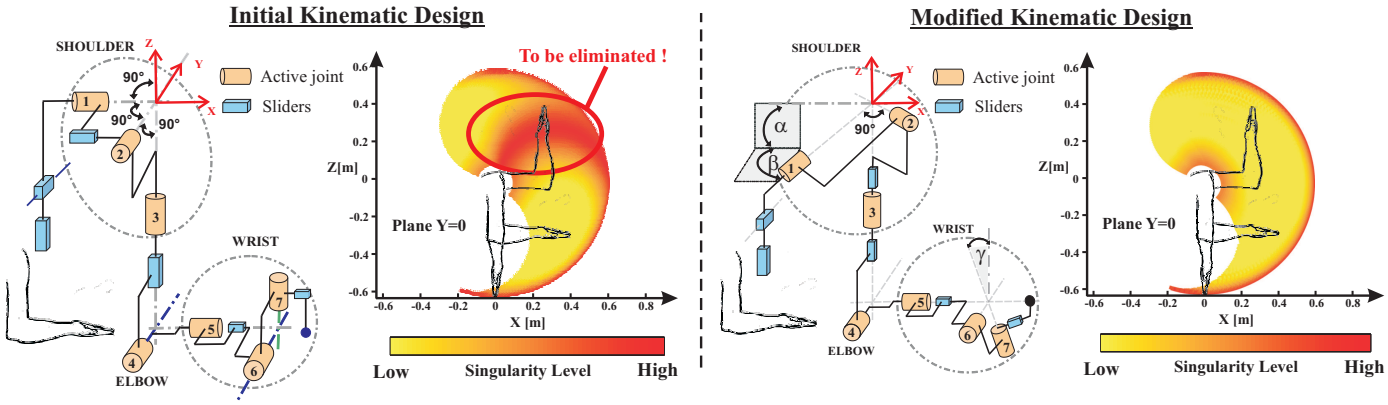

Fig. 2. Influence of the kinematics structure on the singularity level in the plane Y = 0 in front of the operator (theoretical workspace, not considering interactions between body and mechanical parts). The singularity level is based on the evaluation of the condition number (ratio between extreme singular values) of the Jacobian Matrix, considering the 4 first joints and the arm aligned with plane Y =0.

512 pulses/revolution, associated with the reduction ratio, bring a high resolution with good speed measurement capabilities (derived from digital position signal).
Each joint is equipped with a local torque sensor, based on strain gages technology. They measure the deformation of the ribs inside the capstan reducer, through a full Wheatstone bridge. The ribs dimensions define the sensitivity of the torque sensor. They were chosen to resist a torque two times greater than the maximum deliverable torque of the actuators. A local programmable electronic conditioning board amplifies the torque signal and sends it to the controller through a current loop to decrease the noise sensitivity.

III. System Control

In a force feedback teleoperation system, the information of position and force/torque is exchanged between the master and slave devices (virtual or real robot) to control the other side. As they are usually kinematically different, the exchange of information between them has to be done in Cartesian space (with a possible scaling).

A. Impedance Control

There exist two great families of control method, depending on the direction of the information exchange between the master and the slave device. In *Impedance* control (Fig. 3), the position is sent from the Master to control the slave and, at the same time, the force/torque measured on the slave or estimated in the VR is used to control the exoskeleton. The cartesian position of the master is estimated from the joint angular position through the direct kinematics, and the force/torque set-point of the slave (in Cartesian coordinates) is converted into joint coordinates through the Jacobian transpose.
The disadvantage of the plain impedance control strategy is that the operator is sensitive to the friction and inertia of the mechanical system. To alleviate this, a local control is implemented on each joint to reduce friction in free motion (when the slave sends zero force set-point) and at the same time to increase the fidelity and stabilize the arm in contact (when the slave sends a non-zero set-point). This requires a set of force/torque sensors on the joints of the master.
The local joint controller used here is called *hybrid controller* [14]. It consists in the coupling of a torque feedback controller and a feedforward friction compensator. The latter is based on the friction model

$$Model = \tau_c(sign(\dot{\theta}_{m_i})) + b_v\dot{\theta}_{m_i} \quad (1)$$

with τ_c being the Coulomb friction and b_v the viscous coefficient estimated for the joint i. Due to the discontinuity of the model around null speed, instabilities or sticking sensations can appear. For this reason, when the velocity of the joint approaches zero, the controller switches to the torque feedback,

$$H = \tau_{d_i} + K(\tau_{d_i} - \tau_{h_i}) \quad (2)$$

with τ_{d_i} being the joint torque set-point from the Slave or VR, τ_{h_i} the torque measured on the joint and K the feedback gain. Stability considerations limit the feedback gains and thus the level of compensation that can be achieved. However, by switching to the *Model* for higher velocities, a higher value for K can be used. By merging both methods, the Hybrid controller can reduce the disadvantages of each of them. To avoid discontinuous sensations, the switching between the two methods is done by multiplying respectively the *Model* term and the torque

TABLE I
JOINT ACTUATION DESCRIPTION.

Joint	Maximum human torque [Nm]	Torque in daily life [Nm]	Motor type	Gear type	Total reduction ratio	Maximum permanent torque[Nm]	Maximum driver torque [Nm]
1	130	10	Maxon A-max 32	Maxon GP-32C (1:23)	264.5	9.3	14.3
2	120	10	Maxon A-max 32	Maxon GP-32C (1:23)	264.5	9.3	14.3
3	60	3.1	Maxon A-max 26	Maxon GP-26B (1:19)	342	4.8	14.2
4	72	3.8	Maxon A-max 26	Maxon GP-26B (1:19)	218.5	3.1	8.7
5	9	0.4	Maxon A-max 22	Maxon GP-22A (1:19)	299.25	1.3	4.5
6	21	0.38	Faulhaber 2232-024	Faulhaber GP-20/1 (1:3.7)	33.33	0.6	1.73
7	21	0.38	Faulhaber 2232-024	Faulhaber GP-20/1 (1:3.7)	33.33	0.6	1.73

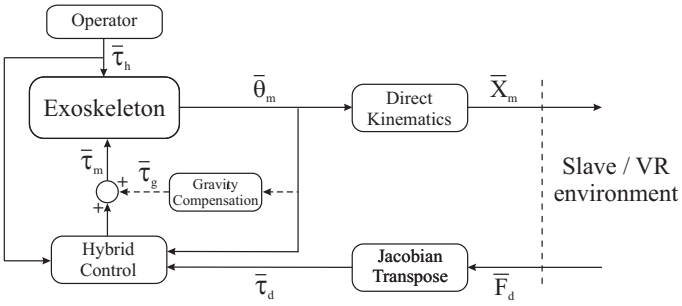

Fig. 3. Impedance type control with hybrid local torque control.

feedback term by the output gain of a *high-pass* and a *low-pass* filter based on the velocity measurement. Finally, a weight compensation torque τ_g, based on the computation from CAD model, can be added to the command torque. It helps to reduce the weight that the user has to carry with his arm. The gravity load is balanced between the arm and the back of the user through the back plate fixations. The motor command for joint i is given by,

$$\tau_{m_i} = Model\frac{|\dot{\theta}_{m_i}|}{\alpha+|\dot{\theta}_{m_i}|} + K(\tau_{d_i}-\tau_{h_i})\frac{\beta}{\beta+|\dot{\theta}_{m_i}|} + \tau_{d_i} + \tau_g \quad (3)$$

with α and β being coefficients to fix the bandwidth of the filters. The setpoint τ_{d_i} is not scaled by the filter's gains to insure torque tracking during contact.

B. Admittance Control

The other family of control method is admittance control. From the master point of view, the exchange of information is done in a opposite way. Generally, the force/torque information measured on the master and the slave (or in the VR) are applied to a virtual device with a given dynamic. The position, velocity and/or acceleration of this device is then used as set-point for the master and the slave. The purpose of this method is to replace the master dynamic (inertia, frictions,...) with that of the virtual device. This can be achieved by using high position control gains.

Depending on the type of force/torque measurement accessible on the master, different types of virtual device can be considered. If a end-point sensor is used, the virtual device is represented by a virtual mass with damping in cartesian space. The cartesian forces measured at the exoskeleton tip and in the slave/VR environment are applied to this mass. Its velocity is then converted in joint velocity set-point with the inverse Jacobian.

If no end-tip force information is available but only local joint torque, as for the presented exoskeleton, the virtual device is then represented by a dynamic model of the exoskeleton arm (Fig. 4). The joint position set-point is estimated by the computation of the inverse dynamic. However the inverse of the mass matrix has to be calculated. To avoid that, here, we use a decoupled model of the arm dynamic. With the hypothesis of small velocity and acceleration (the human is inside the system), we neglect the centrifugal and centripetal contributions and we consider a diagonal mass matrix. Each joint can then be computed independently. The position of joint i of the virtual device will be given by,

$$\ddot{\theta}_{d_i} = \frac{\tau_{h_i} - (J^T F_d)_i - B_i\dot{\theta}_{d_i}}{M_i} \quad (4)$$

with M_i and B_i the selected mass and damping for joint i. These values have to be decreased, as they will fix what the operator will feel. However, their choice is limited by stability considerations. On the master, the motor command is given by,

$$\tau_m = K_{p_i}(\theta_{d_i}-\theta_{m_i}) - K_{d_i}(\dot{\theta}_{d_i}-\dot{\theta}_{m_i}) + \tau_g \quad (5)$$

with K_{p_i} and K_{d_i} the gains of the position controller of joint i. The contribution for gravity compensation can also be

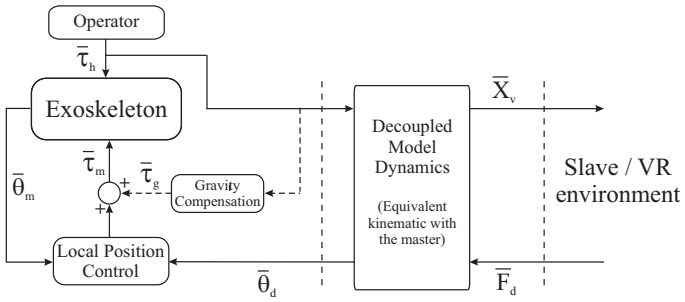

Fig. 4. Admittance type control.

added. It has to be noted that for devices with an end-tip force sensor, the gravity compensation is automatically included in the command.

The advantage of admittance control, compared to impedance control, is the inherent capacity of this method to decrease the dynamic of the system felt by the user (frictions, inertias) to tend to the dynamic of the virtual device (if high enough gains are used in the position controllers). This method is then well suited for high dynamic devices. Moreover a better stability can be presented when contacting hard surfaces in the slave world.

IV. Experiments and results

Experiments have been conducted on SAM exoskeleton (Fig. 5) for the different control methods presented earlier. The master has been used in combination with a simplified VR based on CHAI3D. The control was firstly implemented using the DS1103 dSpace control board coupled with MATLAB SIMULINK. In a second stage, the controller hardware has been replaced by a PC running real-time QNX operating system (ECO) and delocalized electronic boards mounted near the joints on SAM as seen in Fig. 5. ECO implements the communication with the slave system and the control algorithms. All other features are managed by the local boards : PWM generation for the actuators, quadrature encoder, torque sensor and joystick interfaces. Each board is able to drive two joints. They are inter-connected through a 24V power bus and a serial data bus allowing communication rate of 1Khz. ECO is connected to the network through the *Joint Dispatcher*, implemented on a PCI plug-in board. It dispatches global requests from ECO to individual requests for each joint, collects individual answers and merges them for ECO. Each joint controller and the Joint Dispatcher are built around a Microcontroller from Texas Instruments' F281x family. The purposes of this distributed configuration is to limit the size of the actuators and sensors wires, reduce the computation load on ECO and allow using a simple computer to command the whole exoskeleton.

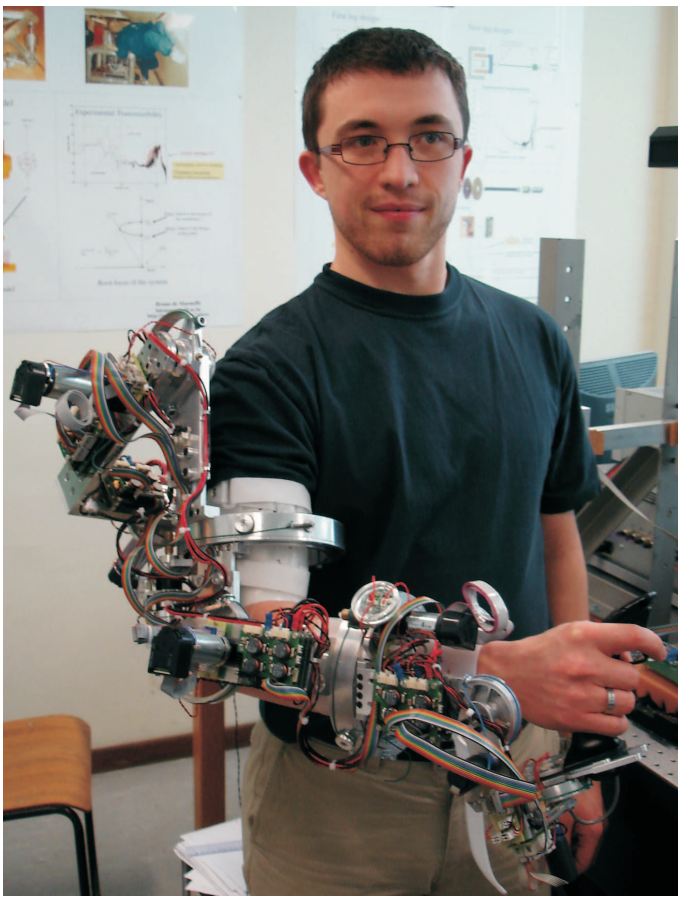

Fig. 5. SAM exoskeleton prototype.

A. Free motion and wall contact

In free motion or when contacting a wall with the slave or in the VR, the hybrid control can help to increase the fidelity and the stability of the contact. Fig. 6 compares the torques measured on joint 2 with and without local hybrid control when contacting a horizontal wall with stiffness $K_{wall} = 50N/m$ (soft contact). Without control we observe a mismatch between the torque set-point and the measured one during the contact. Although the open loop gain is appropriate, this problem comes from sticking phenomenon inside the gearbox when the motor produces high torque with a low velocity. That blocks the position of the user who can apply higher torque without producing motion deeper in the wall and thus without set-point modification. On the other hand, with Hybrid control, a better agreement between the torque set point and the measured one is obtained.

We can observe also a reducing of the friction in free motion when the slave force set point is zero.

According to the application, friction can be added or removed through the model part of the hybrid control. If a higher stiffness has to be simulated, adding friction when a hard contact is detected can help to stabilize the system.

The same experiment has been conducted with the admit-

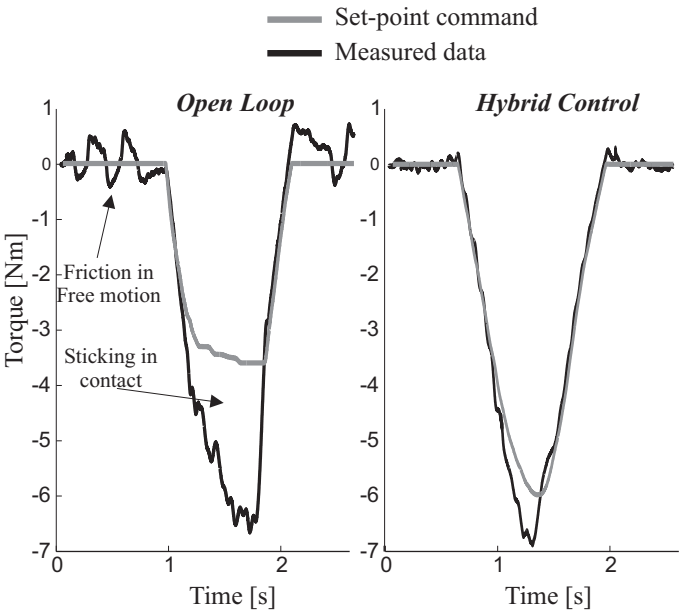

Fig. 6. Comparison of torque set-point and measured torque on joint 2 with open loop and hybrid control when the exoskeleton is contacting an horizontal plane with Kwall = 50Nm (in front of the operator).

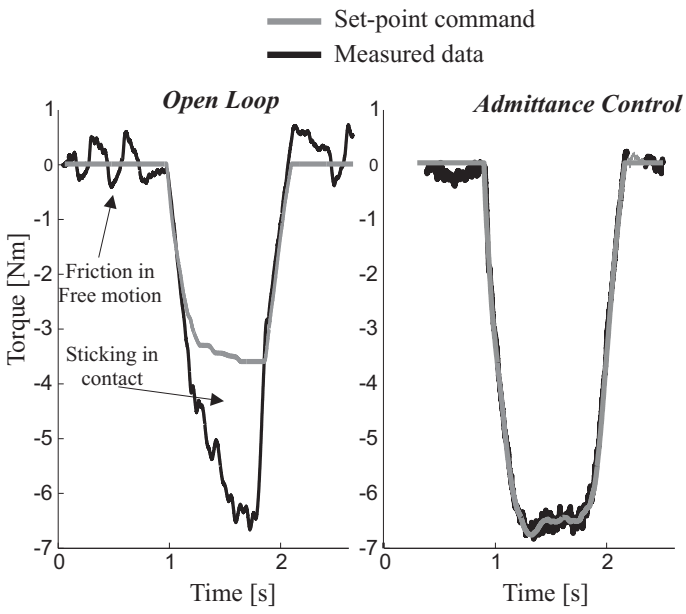

Fig. 7. Comparison of torque set-point and measured torque on joint 2 with open loop and admittance control when the exoskeleton is contacting an horizontal plane with Kwall = 50Nm (in front of the operator).

tance control (Fig. 7). Similar results are obtained in terms of global sensations from the operator side view. A deeper analysis shows that, for the selected parameters, in admittance control, the remain level of friction is slightly greater than hybrid control. At the same time, the follow-up of the slave set-point is better. As said before, the use of admittance control has shown moreover a better stability for high stiffness rendering.

B. Haptic rendering

So far, the results obtained in terms of haptic rendering have been very satisfying. Firstly they show the possibility for SAM to produce enough force to the operator in order to create a sensation of rigid contact. Secondly, several geometrical forms can be presented to the operator. Fig. 8 represents the position of the operator when he follows a sphere in the 3D VR (projection in front plane). We observe a good match between the real position and the virtual object showing that the user feels a spherical shape. During these experiments, the gravity compensation has also been tested. The level of compensation can be selected between 0 and 100%. To reduce the load on the motor (in term of current) and keep some margin for the torque output,we usually select 50% of compensation, which significantly increases the comfort of the operator.

V. Application for Space exploration

SAM exoskeleton has been used in the frame of the EXOSTATION project, an ESA-funded project aiming at developing a complete teleoperated haptic control chain for slave robots in the International Space Station or for planets exploration. Compared to the previous experiments, this system allows the operator who is wearing the exoskeleton, to remotely control a complete virtual slave robot. The slave is following every movement done by the operator and the exoskeleton procures him force-feedback sensations.

The global system is composed of four main components. The first component is the 7-DOF exoskeleton SAM, playing the role of the master robot in the haptic loop. The second component is the exoskeleton controller (ECO) composed of the master controller and local integrated joint controllers, presented earlier. These implement the real-time control strategies and manage the communication links with the slave robot simulator. The system also includes a virtual reality training environment composed of a Slave Simulator and a Visualisation Client. The Slave Simulator is a modular application simulating, on top of ODE (Open Dynamics Engine) a 7-DOF actuated slave arm, cinematically equivalent to SAM. The 3D Visualisation Client, based on OpenGL, allows one to several users to visualize the state of the slave arm and provides a GUI to remotely control the simulator (Fig. 9).

Experiments conducted with this system have shown the ability of the exoskeleton to teleoperate haptically a slave

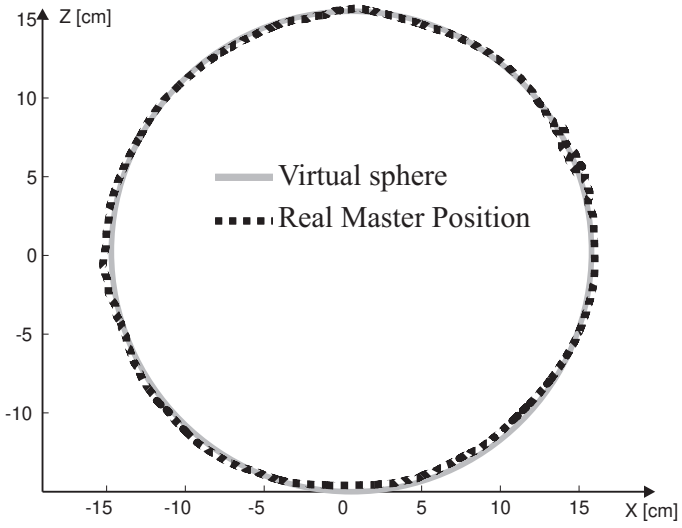

Fig. 8. Shape rendering experiment : comparison of the virtual sphere position and the real exoskeleton end-point position when the user is trying to follow the shape.

robot during specific scenarios as object screening, manipulations, peg int the hole or screwing operations. The next step of this project is the teleoperation of a real slave robot. This project has been conducted in collaboration with two belgian companies : *Micromega Dynamics* (ECO controller) and *Space Application Services* (virtual robot and 3D visualization client)

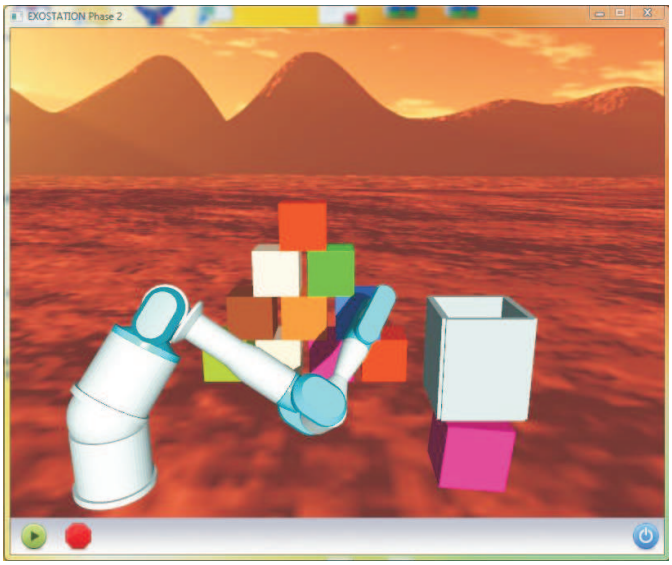

Fig. 9. : 3D Visualisation client representing the slave robot.

VI. Conclusions

This paper has introduced and described a 7-DOF fully portable exoskeleton device with a specific kinematics to avoid singularities in the normal workspace. On each joint a local controller is implemented to reduce friction in free air motion and increase fidelity and stability in contact. It has been shown that the exoskeleton is able to provide high quality 3D haptic rendering when interacting with a simplified Virtual Reality. The use of the local Hybrid control increases significantly the performances of impedance control. An other approach, based on admittance control, has also been presented, showing similar results.

Based on the acquired experience, a new exoskeleton device will be designed, taking into account the use of other materials to decrease the global weight and increase the total structure stiffness. The use of other reducers like harmonic drives will also be investigated. Indeed, although these present a great friction and limit the natural backdrivability of the system, the use of the hybrid or admittance control allow their implementation.

Pictures and videos of the exoskeleton and the EXOSTATION setup can be found on the website : *http:\\www.ulb.ac.be\scmero*.

Acknowledgments

This study is funded by ESA in the framework of a Technology Research Program (contract No. 18408/04/NL/CP) entitled: Control Stations for new Space A and R Applications.

References

[1] T. Nef, M. Mihelji, and R. Riener, "Armin: a robot for patient-cooperative arm therapy," *Medical & Biological Engineering & Computing*, vol. 45, pp. 887–900, September 2007.

[2] A. Frisoli, F. Rocchi, S. Marcheschi, A. Dettori, F. Salsedo, and M. Bergamasco, "A new force-feedback arm exoskeleton for haptic interaction in virtual environments," in *Proc. First Joint Eurohaptics Conference and Symposium on Haptic Interfaces for Virtual Environment and Teleoperator Systems World Haptics 2005*, 18–20 March 2005, pp. 195–201.

[3] J. C. Perry, J. Rosen, and S. Burns, "Upper-limb powered exoskeleton design," vol. 12, no. 4, pp. 408–417, Aug. 2007.

[4] C. Carignan, M. Liszka, and S. Roderick, "Design of an arm exoskeleton with scapula motion for shoulder rehabilitation," in *Proc. th International Conference on Advanced Robotics ICAR '05*, 18–20 July 2005, pp. 524–531.

[5] A. Nakai, T. Ohashi, and H. Hashimoto, "7 dof arm type haptic interface for teleoperation and virtual reality systems," in *Proc. IEEE/RSJ International Conference on Intelligent Robots and Systems*, 13–17 Oct. 1998, vol. 2, pp. 1266–1271.

[6] A. Bin, "Sensory feedback exoskeleton armmaster," December 1995.

[7] P. Letier, A. Schiele, M. Avraam, M. Horodinca, and A. Preumont, "Bowden cable actuators for torque feedback in haptic applications," in *Proc. Eurohaptics 2006 Conference*, July 2006, pp. 251–256.

[8] Sooyong Lee, Sangmin Park, Munsang Kim, and Chong-Won Lee, "Design of a force reflecting master arm and master hand using pneumatic actuators," in *Proc. IEEE International Confer-*

ence on Robotics and Automation, 16–20 May 1998, vol. 3, pp. 2574–2579.

[9] N. Tsagarakis and D. Caldwell, "Development and control of a "soft-actuated" exoskeleton for use in physiotherapy and training," *Autonomous Robots*, vol. 15, pp. 21–33, 2003.

[10] Yoon Sang Kim, J. Lee, Sooyong Lee, and Munsang Kim, "A force reflected exoskeleton-type masterarm for human-robot interaction," *IEEE Transactions on Systems, Man and Cybernetics, Part A*, vol. 35, no. 2, pp. 198–212, Mar 2005.

[11] M. K. O'Malley and M. Goldfarb, "The effect of virtual surface stiffness on the haptic perception of detail," vol. 9, no. 2, pp. 448–454, June 2004.

[12] P. Letier, M. Avraam, M. Horodinca, A. Schiele, and A. Preumont, "Survey of actuation technologies for body-grounded exoskeletons," in *Proc. Eurohaptics 2006 Conference*, 2006, pp. 497–500.

[13] J. Rosen, J. C. Perry, N. Manning, S. Burns, and B. Hannaford, "The human arm kinematics and dynamics during daily activities - toward a 7 dof upper limb powered exoskeleton," in *Proc. th International Conference on Advanced Robotics ICAR '05*, 18–20 July 2005, pp. 532–539.

[14] N.L. Bernstein, D.A. Lawrence, and L.Y. Pao, "Friction modeling and compensation for haptic interfaces," in *Proc. First IEEE Joint Eurohaptics Conference and Symposium on Haptic Interfaces for Virtual Environment and Teleoperator Systems (IEEE)*, Pisa, 2005, pp. 290–295.

Proceedings of the 8th National Congress on Theoretical and Applied Mechanics, May 28-29, Brussels, Belgium.

Dynamic simulation and embedded control of the AMRU 5 hexapod robot

Q. Bombled, O. Verlinden[1]
[1]Faculté Polytechnique de Mons, Department of Theoretical Mechanics, Dynamics and Vibrations (TMDV)
Boulevard Dolez 31 - 7000 Mons
email: quentin.bombled@fpms.ac.be, olivier.verlinden@fpms.ac.be

Abstract— **A complete dynamic model of the six-legged robot AMRU 5 has been established, by means of a multi-body approach in generalized coordinates. It includes gravity and contact ground forces, as well as DC motors and controllers. At an higher level, a gait algorithm has been elaborated to compute the reference joint trajectories sent to the controllers. It works for fixed gait patterns and is composed of a general inverse kinematics algorithm, allowing a completely free motion of the main robot body according to its 6 DOF. It has been successfully implemented on the robot.**

Keywords—**walking robots, gait generation, decentralized control, dynamic model**

I. Introduction

FOR many years, walking robots are a wide challenge for researchers. Even if they are less fast, energetically greedier and more complex at command level than wheeled robots, they have the ability to get over obstacles and to move on unstructured ground. This aptitude makes them potentially interesting to replace the human in hardly tasks like demining, exploration in hostile conditions, nuclear site maintenance or building guard. The gait generation and its adaptation to rough environments (collisions detections, holes, ...) is more than ever a present and relevant topic for engineers. A huge number of walking robots exists, each of them having its own structure and its own usefulness. Two main approaches have been envisaged to make them walking [1] : the first one is called the engineering approach. The leg motion is a consequence of the references computed by a central agent imposing a motion to the main body of the robot. One of the first implementations was on the DANTE II robot, on the occasion of the Alaskan volcano exploration in 1994. Recently, Porta and Celaya [2] worked in this way on LAURON III and GENGHIS robots. The second approach is biologically inspired : initiated by Wilson in 1966 (and still used nowadays), it is based on the insects observation. Global motion of the robot is here a consequence of the leg motions. If a central agent exists, it just arbitrates when conflicts arise. This progressive reflexion allowed to define types of gaits, basic motions of the legs (produced by CPG's for example), structures for control, enhancement of mechanical design for the legs and so on. Parker [3] with cyclic genetic algorithms or Cruse [4] with neural networks, and many other research teams tried to mimic the animal behaviour in different ways on walking machines like HANNIBAL, STIQUITO or TARRY II. Even if these implementations were successful, there are very few complete dynamic models of legged robots. Most of them are purely kinematic. Nevertheless, this kind of model can be greatly useful for selecting and designing the controller. In the following, section II gives details about the dynamic model of AMRU 5. Section III describes the gait algorithm. Section IV presents some results obtained by the dynamic model. Section V outlines the hardware implementation and gives some experimental observations, and finally section VI discusses the results and outlooks.

II. AMRU 5 dynamic model with EasyDyn

A. Description

AMRU 5 (figure 1) is a six-legged robot with 3 degrees of freedom per leg. Initially devoted to demining mission, it has been built by the Royal Military Academy of Belgium, within the framework of the AMRU project (Autonomous Mobile Robot in Unstructured environment). The robot is 30 kg heavy and has an outer diameter of about 1.2 m. Each Degree Of Freedom (DOF) is controlled by a DC motor. The leg is based on a pantograph mechanism actuated by 2 DC motors. Hence, the foot (extremity of the leg) can be moved independently according to a radial and a vertical motion. Tangential motion is allowed by the rotation of the pantograph chassis about a vertical axis.

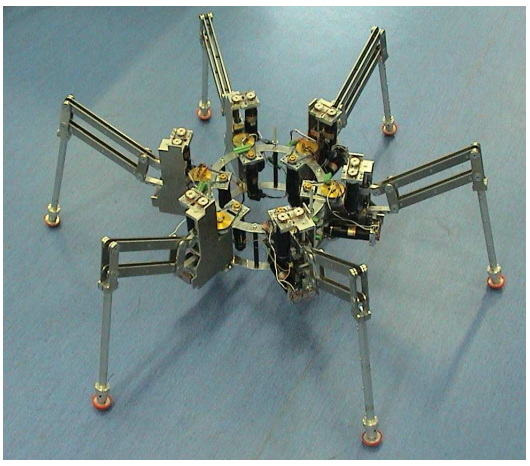

Fig. 1. AMRU 5

B. Multibody model of AMRU 5

The equations governing the dynamic behavior of a multibody system can be written in the following form :

$$\mathbf{M}(\underline{\mathbf{q}}) \cdot \underline{\ddot{\mathbf{q}}} + \underline{\mathbf{h}}(\underline{\mathbf{q}}, \underline{\dot{\mathbf{q}}}) = \underline{\mathbf{g}}(\underline{\mathbf{q}}, \underline{\dot{\mathbf{q}}}, \mathbf{t}) \tag{1}$$

with $\underline{\mathbf{q}}$ a $n_{cp} \times 1$ vector gathering the n_{cp} configuration parameters, $\mathbf{M}(\underline{\mathbf{q}})$ the mass matrix of dimension $n_{cp} \times n_{cp}$, $\underline{\mathbf{h}}(\underline{\mathbf{q}}, \underline{\dot{\mathbf{q}}})$ of dimension $n_{cp} \times 1$ representing the centrifugal and Coriolis forces, and $\underline{\mathbf{g}}(\underline{\mathbf{q}}, \underline{\dot{\mathbf{q}}}, t)$ of dimension $n_{cp} \times 1$, the contribution of applied forces. These equations are built from inertia properties, kinematics and appplied forces, by using the theoretical mechanics laws, for all the bodies composing the robot.

In the case of AMRU 5, figure 2 gives the considered degrees of freedom for leg 0.

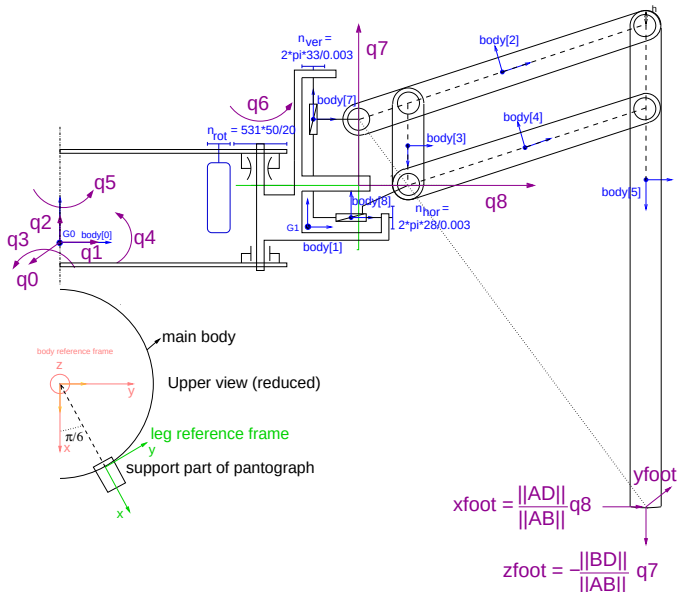

Fig. 2. Kinematic description of the leg 0

The first body is the frame of the robot, which can move freely, and consequently has 6 DOF denoted by $q_0 \dots q_5$. Leg 0 consists of 8 bodies : the pantograph support part `body[1]` which rotates about the vertical axis (q_6), 4 bodies for the pantograph mechanism (`body[2]` to `body[5]`), and 3 bodies for the rotors of the three actuators (`body[6]` to `body[8]`). q_7 is the vertical displacement leading to the up and down motion of the foot z_{foot}, and q_8 is the horizontal displacement resulting in the radial foot motion x_{foot}. (q_6, q_7, q_8) are related to the corresponding rotor position by a reduction ratio $(n_{rot}, n_{ver}, n_{hor})$. The same kinematic description is applicable to the five other legs. To build the set of equations (1), inertia properties of the bodies, applied forces and complete kinematics at position, velocity and acceleration levels are needed. Both inertia properties and applied forces are quite easy to determine. But kinematics in global coordinates is relatively difficult to express by hand. At position level, we use the Homogeneous Transformation Matrices (HTM) to express coordinates of bodies in the global reference frame.

Considering figure 3 : Relative situation of frame j with

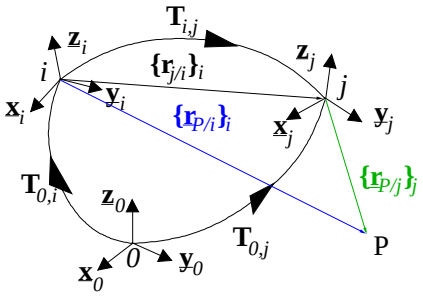

Fig. 3. Homogeneous transformation matrices

respect to the frame i can be described by the HTM

$$\mathbf{T}_{i,j} = \begin{pmatrix} \mathbf{R}_{i,j} & \{\underline{\mathbf{r}}_{j/i}\}_i \\ 0\,0\,0 & 1 \end{pmatrix} \tag{2}$$

where

- $\{\underline{\mathbf{r}}_{j/i}\}_i$ is the coordinate vector of frame j with respect to frame i, projected in frame i;
- $\mathbf{R}_{i,j}$ is the rotation tensor describing the orientation of frame j with respect to frame i.

To express the coordinates of a point P belonging to frame j (of coordinates $\{\underline{\mathbf{r}}_{P/j}\}_j$), in frame i, we can write :

$$\begin{pmatrix} \{\underline{\mathbf{r}}_{P/i}\}_i \\ 1 \end{pmatrix} = \mathbf{T}_{i,j} \cdot \begin{pmatrix} \{\underline{\mathbf{r}}_{P/j}\}_j \\ 1 \end{pmatrix} \tag{3}$$

which is equivalent to

$$\{\underline{\mathbf{r}}_{P/i}\}_i = \{\underline{\mathbf{r}}_{j/i}\}_i + \mathbf{R}_{i,j} \cdot \{\underline{\mathbf{r}}_{P/j}\}_j = \mathbf{T}_{i,j} \circ \{\underline{\mathbf{r}}_{P/j}\}_j \tag{4}$$

The operator $\circ$ of Eq. (4) is introduced for the sake of simplicity. To obtain a complete kinematic description at velocity and acceleration level in global coordinates (that's to say, projected in the frame 0), it can be demonstrated that velocities and acceleration of the center of mass of each body is related to the configuration parameters by :

$$\{\underline{\mathbf{v}}_i\}_0 = \{\mathbf{J}_{Si}\}_0 \cdot \underline{\dot{\mathbf{q}}} \tag{5}$$

$$\{\underline{\boldsymbol{\omega}}_i\}_0 = \{\mathbf{J}_{\omega i}\}_0 \cdot \underline{\dot{\mathbf{q}}} \tag{6}$$

$$\{\underline{\mathbf{a}}_i\}_0 = \frac{d}{dt}\{\underline{\mathbf{v}}_i\}_0 = \{\mathbf{J}_{Si}\}_0 \cdot \underline{\ddot{\mathbf{q}}} + \{\dot{\mathbf{J}}_{Si}\}_0 \cdot \underline{\dot{\mathbf{q}}} \tag{7}$$

$$\{\underline{\dot{\boldsymbol{\omega}}}_i\}_0 = \frac{d}{dt}\{\underline{\boldsymbol{\omega}}_i\}_0 = \{\mathbf{J}_{\omega i}\}_0 \cdot \underline{\ddot{\mathbf{q}}} + \{\dot{\mathbf{J}}_{\omega i}\}_0 \cdot \underline{\dot{\mathbf{q}}} \tag{8}$$

where $\{\mathbf{J_{Si}}\}_\mathbf{0}$ and $\{\mathbf{J_{\omega i}}\}_\mathbf{0}$ are the velocity transformation matrices projected in the global frame 0, and can be deduced from derivative operations on homogeneous transformation matrices. In the following, $\{\}_0$ is omitted for the sake of clarity.

C. EasyDyn library

Building and solving equations of motion is made thanks to the C++ EasyDyn library, developed in the TMDV department ([5]). This library allows the simulation of problems represented by second-order (or first-order) differential equations and, more particularly, multi-body systems. The whole kinematics of all the bodies is computed by means of a MuPAD routine called CAGeM (Computer Aided Generation of Motion), which performs the first and second time derivatives of the position and projects them in the global frame. This script also generates a C++ application file. When launched, it builds equations of motion (1) and integrates them following a Newmark scheme. It also creates a scene for visualisation and a text file with the resulting ($\underline{\mathbf{q}}, \underline{\dot{\mathbf{q}}}, \underline{\ddot{\mathbf{q}}}$). Interest of EasyDyn is double :

- EasyDyn is completely free and open source;
- The C++ application file can be completed by force elements, actuators, controllers and so on : the only condition is that physics has to be described by a first or second-order differential equation.

D. Multiphysics model

D.1 Ground contact forces

We use a visco-elastic contact model for the foot-ground interaction. Visco-elastic normal contact force between a point (foot) and a plane (ground) is calculated as follows (in the direction of the normal vector, see figure 4) :

$$F_n = K_n pen^{p_k} + C_n pen^{p_d} \frac{d\,pen}{dt} \tag{9}$$

where *pen* is the penetration of the contact point (foot of AMRU 5) in the plane (ground), K_n the stiffness coefficient (rigid ground means a high stiffness coefficient, typically $1e6\ N/m^{p_k}$), p_k the exponent of the penetration for the normal elastic force, C_n a damping coefficient relative to the normal contact force, p_d the exponent of the penetration for the normal damping contact force. The tangential friction force is calculated as follows :

$$\underline{\mathbf{F}}_t = -fF_n * \frac{\underline{\mathbf{v}}_g}{v_{glim}} \text{ if } ||\underline{\mathbf{v}}_g|| < v_{glim} \tag{10}$$

$$= -fF_n * \frac{\underline{\mathbf{v}}_g}{||\underline{\mathbf{v}}_g||} \text{ if } ||\underline{\mathbf{v}}_g|| \geq v_{glim} \tag{11}$$

where f is the friction coefficient, v_{glim} the limit slip velocity, and $\underline{\mathbf{v}}_g$ is given by Eq. (12)

$$\underline{\mathbf{v}}_g = \underline{\mathbf{n}} \times (\underline{\mathbf{v}}_{A_{foot/plane}} \times \underline{\mathbf{n}}) \tag{12}$$

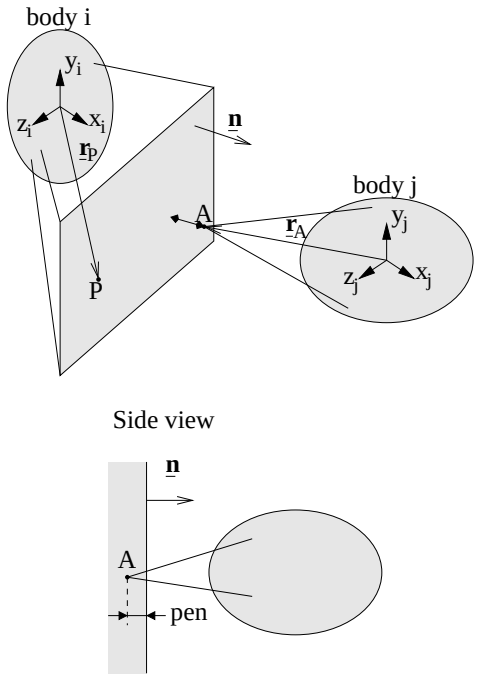

Fig. 4. Principle of ground contact forces computations

D.2 Friction forces

In the pantograph mechanism and in the nut-screw systems, the mechanical backlash is strongly reduced. Therefore, friction forces are really important. We choose the *LuGre* model [6] from university of **Lu**nd and **Gre**noble. More complete than the Coulomb friction, it is very spread thanks to its simplicity and its capacity to model both static and dynamic effects. At very low velocities, it is based on the average deflection z of the contact asperities, sometimes called bristles, while at steady state velocities it is close to the well-known General Kinetic Friction model (Coulomb + viscous friction with Stribeck's effect). Friction force is determined by Eq. (13)

$$F_f = \sigma_0 z + \sigma_1 \frac{dz}{dt} + \sigma_2 v \tag{13}$$

where F_f is the friction force, σ_0 is the contact stiffness and σ_1 the contact damping. A term proportional to the relative velocity between the surfaces, $\sigma_2 v$, can be added to take into account the viscous friction. Average deflection of the bristles, z, is given by :

$$\frac{dz}{dt} = v - \sigma_0 \frac{|v|}{g(v)} z \tag{14}$$

where $g(v)$ models the Stribeck's effect ([6]). This function is positive and depends on many factors such as material properties, lubrication, temperature, ... Investigations have already lead to a rough estimation of the friction parameters, but a better refinement and identification for the six legs is necessary to take friction into account more precisely.

D.3 Motion control

Each actuator drives one and only one degree of freedom thanks to the decoupling of the pantograph mechanism. Then, decentralized control is envisaged, where each loop is a single-input single-output model (figure 5).

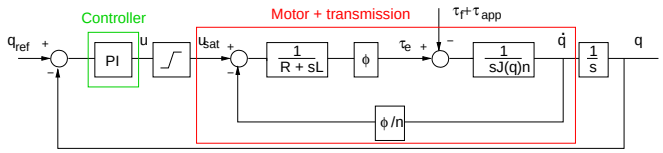

Fig. 5. PI control scheme for a leg

The electrical motor and the transmission model are drawn from the following equations :

$$u = Ri + L\frac{di}{dt} + k_\phi \frac{\dot{q}}{n} \quad (15)$$

$$\tau_e = k_\phi i \quad (16)$$

$$\tau_e = J(q)n^2 \frac{d(\frac{\dot{q}}{n})}{dt} + \tau_{app} + \tau_f \quad (17)$$

where u is the voltage command, i the current, k_ϕ the torque constant of the motor, R the armature resistance and L the inductance. τ_e, τ_f and τ_{app} are respectively the electrical, the friction and the applied torques. Equations are written from the DOF point of view, thus reduction ratio n of the transmission appears, and inertia $J(q)$ is expressed consequently. Discrete PI controller is implemented in the model following the well-known equation (18), which gives the voltage command at time k :

$$u^k = k_p \cdot \varepsilon^k + I^{k-1} + k_i \cdot \Delta t \cdot \varepsilon^{k-1} \quad (18)$$

where k_p and k_i are controller gains, ε is the error signal, I^{k-1} is the integral term at time $k-1$ and Δt is the sample time. To move the robot, the dynamic model needs the joint references for the controller. The latter are given to the model by means of the gait generation algorithm.

III. Gait generation

Gait patterns can be splitted up into two categories :

- *fixed* gait : sequence of leg step is known in advance, therefore it is difficult to deal with rough terrain with obstacles because any interaction with the environment needs a desynchronization of the leg sequence. This kind of gait includes the tripod and forward wave gaits which are the quickest for the six-legged robots.
- *free* gait : several algorithms of free gait exist (see for example [2], [7]). They are able to handle with rough terrains, and leg coordination depends strongly on the interaction with environment, i.e. searching ground and obstacles avoidance.

Presently, we only have position informations on the robot, which leads to the development of a fixed gait algorithm. The free gait needs more sensing capabilities, like force or current sensing. Posture of the robot could also be controlled by minimizing the gap with respect to a reference posture. the robot has to keep its posture parallel to the ground when walking on non-flat surfaces. Again, extra sensors like an inclinometer would help to reach this goal. In section VI, further works are envisaged and details about current sensing and posture control are outlined. Our gait algorithm consists of two steps :

1. An Inverse Kinematics Algorithm (IKA), used to find the joint variables of one leg on the ground for the desired motion of the body;
2. The gait generation itself, which manages the swing and the support phase of the legs.

A. Inverse kinematics

In the following, we assume :

- Tripod gait;
- Rigid and flat ground;
- No slip between ground and feet.

Consider the body and n legs supporting the robot (not necessary 6). We have $6+3\cdot n$ DOF. Because we consider no slip and a point contact, we have 3 constraints per contact. Finally, we find :

$$6_{dof,body} + 3 \cdot n_{dof,leg} - 3 \cdot n_{dof,footcontact} \quad (19)$$

which means that, whatever the number of legs on the ground, there are always 6 DOF for the robot, even if the number of actuators is greater than six. Consequence is that the solution for inverse kinematics is unique, Thus under the previous assumptions, our algorithm is valid for any number of legs (but at least 3) touching the ground. Consider one leg in figure 6 : The actual body position is

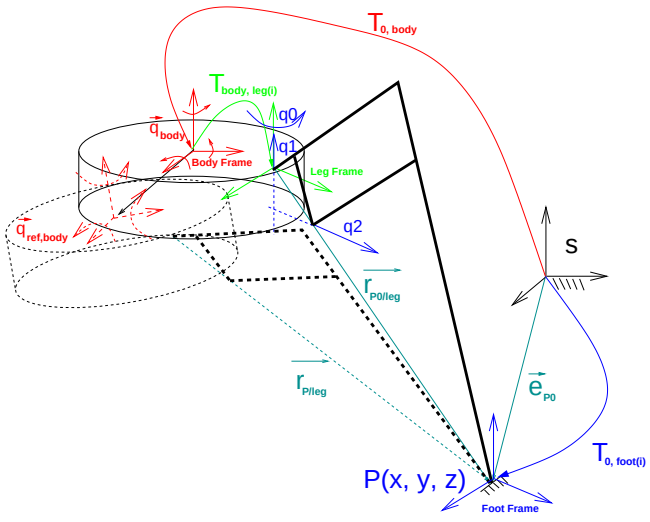

Fig. 6. Inverse kinematics principle

represented in plain line, and the desired position in dotted line. The initial foot position is defined in the local leg reference frame as $\{\underline{\mathbf{r}}_{P0/leg}\}_{leg}$, and in the global reference frame as $\underline{\mathbf{e}}_{P0}$. They are related by Eq. (20) :

$$\{\underline{\mathbf{r}}_{P0/leg}\}_{leg} = (\mathbf{T}_{0,body} * \mathbf{T}_{body,leg})^{-1} \circ \underline{\mathbf{e}}_{P0} \qquad (20)$$

When robot moves, $\mathbf{T}_{0,body}$ is changing with respect to the desired references $\underline{\mathbf{q}}_{ref,body}$. $\mathbf{T}_{body,leg}$ is a constant, proper to the architecture of the hexapod. Because there is no slip of the foot during the motion, $\underline{\mathbf{e}}_{P0}$ is also constant. Once the new $\mathbf{T}_{0,body}$ is known, $\underline{\mathbf{r}}_{P/leg}$ is computed with Eq. (20). The leg kinematics links up the latter and the researched joint references by :

$$\{\underline{\mathbf{r}}_{P/leg}\}_{leg} = \underline{\mathbf{f}}(\underline{\mathbf{q}}_{ref,leg}) \qquad (21)$$

A Newton-Raphson algorithm is applied to Eq. (21) to determine the leg joint references.

B. Gait algorithm

The gait algorithm could be seen as the upper level of the IKA. It manages the swing and support phases of the six legs. Some definitions are useful for the following :

- τ defines the tranfer phase or swing phase, i.e. the time during which the leg is in the air : the terminal position of the swing phase (for an observer linked to the robot body) is called Anterior Extreme Position (AEP);
- s defines the support phase : the terminal position of the support phase (for an observer linked to the robot body) is called Posterior Extreme Position (PEP);
- a complete step is performed in a time $T_{cycle} = \tau + s$;
- β_i is the fraction cycle during which the leg i is in support;
- ϕ_i is the cycle time fraction between the beginning of the leg i cycle (beginning of support phase) and the one of the reference leg;
- ϕ is the normalized time. If t is the current time, it is given by :

$$\phi = \frac{t - n_{step} \cdot T_{cycle}}{T_{cycle}} \qquad (22)$$

where n_{step} is the number of steps already done.

In this section, we only envisage forward wave gait, because *the longitudinal wave gait stability margin of a 2n-legged robot is maximized by wave gaits* ([8]). Figure 7 shows the well–known tripod and forward wave gaits.

The gait diagram can be decomposed into n_{div} divisions, each of them corresponding to a set of leg states. For example, in the tripod gait, there are two different sets of leg states ($n_{div} = 2$). We define the *state matrix* $\mathbf{S}$ ($n_{leg} \times n_{div}$), fulfilled with 1 if leg is in support phase, and 0 otherwise. At each time slice, the state of the gait can be found by computing the normalized time ϕ. For legs on the ground,

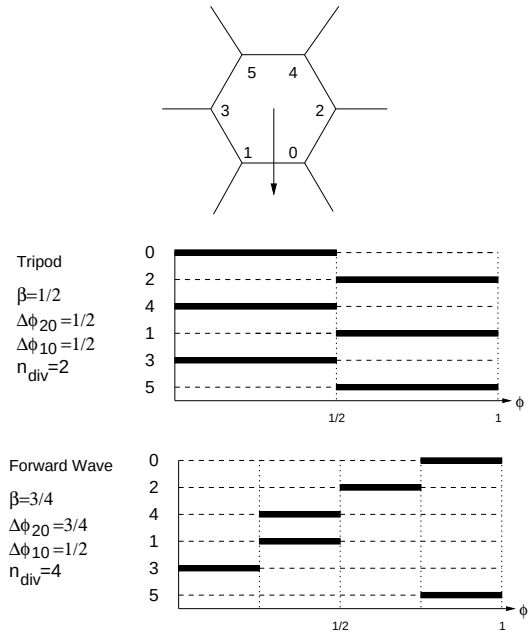

Fig. 7. Gait diagram

IKA is performed from a *fictive support body* which moves according to the desired main body references. For legs in swing phase, a *fictive swing body* is defined and moves following :

- a reverse motion of the desired travel of the main body;
- a triangular profile, which is reported to the feet, allowing them to leave the ground for the step execution.

Velocities of the fictive swing body are not exactly the same as those of the fictive support body : considering a forward wave gait, legs in swing phase have to move three times faster than legs on the ground. For example, if V_x is the X main body velocity reference, we compute at time k $q^k_{ref,0}$ and $q^k_{refswing,0}$, which are the support and the swing bodies references :

$$q^k_{ref,0} = q^{k-1}_{ref,0} + V_x \Delta t \qquad (23)$$

$$q^k_{refswing,0} = q^{k-1}_{refswing,0} - \frac{\beta}{1-\beta} V_x \Delta t \qquad (24)$$

In section IV, we show that this gait algorithm can not lead to a proper gait. The real motion has shocks and a lag with respect to the support body reference because legs triplet have an antagonist motion during the state change from swing to support giving rise to high friction forces on the ground.

C. Enhancement of the gait

To overcome antagonist motion of the legs during the state change, the leg profile has to be modified to have a smoother transition. In figure 8, blue profile is the enhanced profile. The swing phase is decomposed into five parts :

- **PEP Overlap** ① : motion of the foot goes on as if leg was pushing the robot;
- **Takeoff** ② : same as ① but foot leaves the ground;
- **Swing phase** ③
- **Landing** ④ : motion of the leg goes on as if leg was pulling the robot, but leg is still in the air;
- **AEP overlap** ⑤ : same as ④ but leg lands on the ground and begins its support phase.

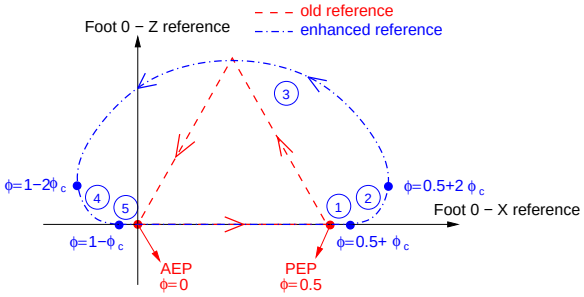

Fig. 8. Enhancement of the swing

Pratically, in the gait algorithm, the support and the swing bodies motions become the same during a period called *overlap* time. This overlap allows a smooth transition when changing the legs state, and avoids useless friction forces with the ground. It will be shown in section IV that the real motion of the robot is better, and body reference tracking is enhanced.

IV. Simulation results

In this section, we define for the main body (with $i = 0 \dots 5$) :

- q_i : the real motion of the DOF i, obtained by the dynamic simulation;
- $q_{ref,i}$: the desired motion of the DOF i, given as an input of the gait algorithm. It is used to compute the joint references of the legs in support phase;
- $q_{refswing,i}$: the reverse motion of the DOF i, given as an input of the gait algorithm. It is used to compute the joint references of the legs in swing phase.

At each timestep, the joint references of the legs ($\underline{\mathbf{q}}_{ref,i}$ with $i = 6 \dots 23$) are computed by the gait algorithm and delivered to the controllers. The commands are given as input to the motors, which supply the torques used in the multibody model of the robot.

A. IKA results

IKA is applied to the six legs, which are in contact with the ground. Inputs of the IKA are the main body desired references $(q_{ref,0} \dots q_{ref,5})$ presented in figure 9 and 10. The IKA ouputs are the eigthy joint references of the legs. We only present those of leg 0 $(q_{ref,6},\ q_{ref,7},\ q_{ref,8})$ in figure 11. The multibody model gives the resulting joint motions (q_6, q_7, q_8), and the real body motion $(q_0 \dots q_5)$. Note that at 0 s, the robot is "falling down" : this is needed to establish correctly the ground contact forces. The motion only begins after 0.3 s. The accurate tracking of the body references shows that our inverse kinematic algorithm works correctly.

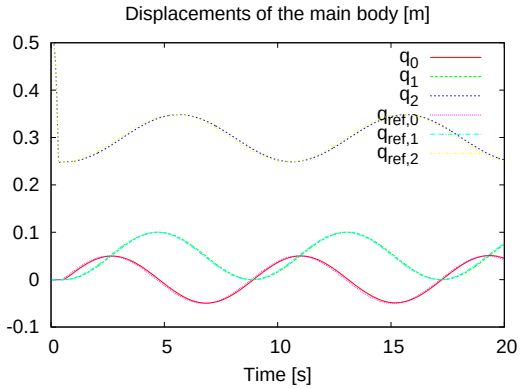

Fig. 9. Displacements of the main body [m]

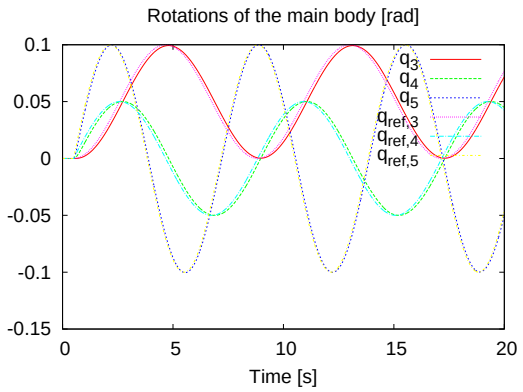

Fig. 10. Rotations of the main body [rad]

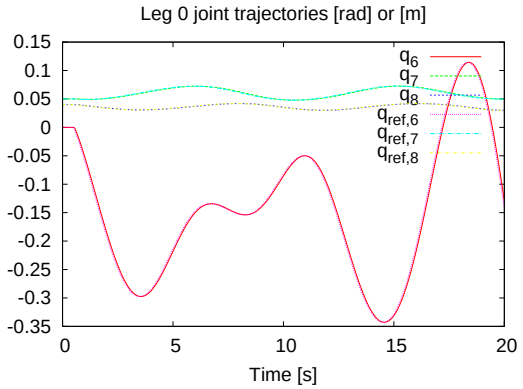

Fig. 11. Leg 0 joint trajectories [rad] or [m]

B. Gait algorithm results

Simulation has been done for a straight motion of the robot along X-axis, with a velocity of 0.3 m/s. In figure 12, we define :

- q_0 : the real motion of the main body along W-axis, obtained by dynamic simulation;
- $q_{ref,0}$: the desired motion of the main body, followed by a *fictive support body* : as before, it is the input of the gait algorithm, used to compute the joint references of the legs in support phase;
- $q_{refswing,0}$: the reverse motion of the fictive support body, called *fictive swing body* : it is the input of the gait algorithm, used to compute the joint references of the legs in swing phase;

At time 3 s, the robot begins to move. A complete step cycle lasts 5 s. From 3 s to 5.5 s, the legs in support phase have their reference from the IKA executed with q^0_{ref}. For legs in swing phase, IKA is executed with $q^0_{ref,swing}$. At time 5.5 s, the six legs are on the ground, and position of the fictive swing and support bodies are adjusted to the same value.

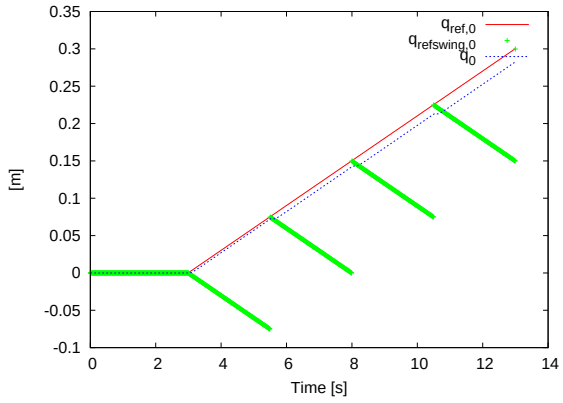

Fig. 12. Reference, fictive reference and motion along X-axis

During the state change in figure 12, friction forces with the ground are really important. Consequently, a drift between q_0 and $q_{ref,0}$ appears. The latter disappears in figure 13, where simulation for enhanced gait allows a smoother transition and gives higher tracking performance.

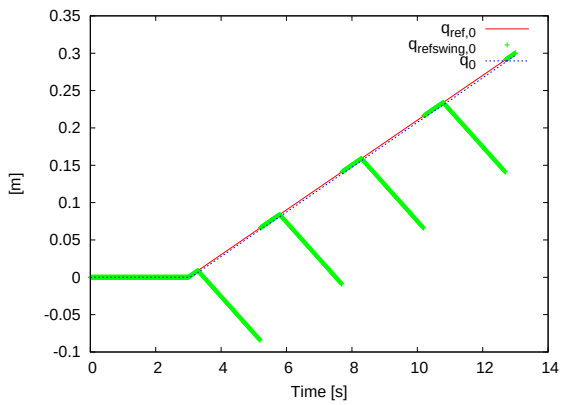

Fig. 13. Illustration of the overlap period for a motion along X-axis

V. Hardware and experimental results

Each leg owns a slave board (PIC18F6627 based microcontroller), and all of them communicate with a master board (PC INTEL DUAL CORE 3GHz, with 1.5Go RAM) through UDP/IP ethernet protocol. It defines packets of data, which are dispatched on the local network by means of sockets as depicted in figure 14 . The master

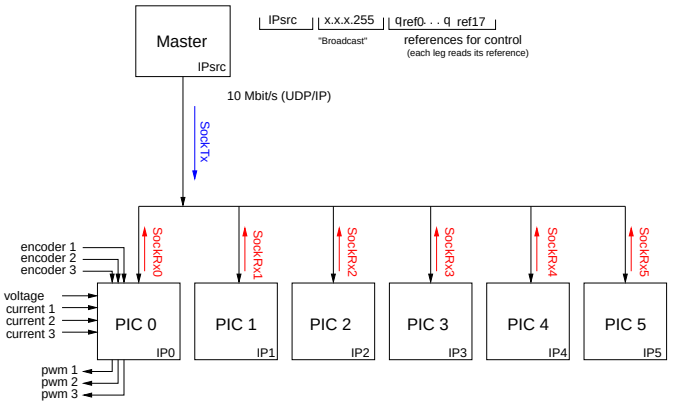

Fig. 14. Global communiation scheme

board handles the gait algorithm, i..e the leg coordination and the inverse kinematics. The control loop is rated at 10 ms with a precise timer. When top arises, joint references computed during the previous time slice are sent to the six slaves through a *broadcast* packet. Gait algorithm is then executed to find the further joint references. Finally, reception of informations coming from the slave occurs. Because UDP/IP is not a connexion-oriented protocol, some informations could be lost. Consequently, a selection routine is used : it consists in a polling action, amongst a set of file descriptors, each of them representing one connection with a slave. As soon as a socket is received, it is treated by the master, which saves joint positions, current and voltage in the motors. This selection is accompanied by a timeout, allowing the master to go on the task control even if a packet never reaches it. Moreover, tests have been performed and reveal that if communication with a leg is broken, the master board is able to detect it, and thus could adapt its gait algorithm to move the five-legged robot.

As far as slave boards are concerned, figure 15 shows a time diagram representing the local tasks. Immediatly they receive the new joint references, they compute the discretized PI controller to have new command values for the motors. Thereafter they save current and voltage in the motors, then new command is applied. Protection against broken communication with the master is given by stopping the motor commands if they do not receive any new joint references after 12 ms. Even if the master can receive data in a non-ordered way, each slave sends out in turn : this is represented by the waiting time h) in figure 15. It is interesting to note that 3 ms are sufficient for the control

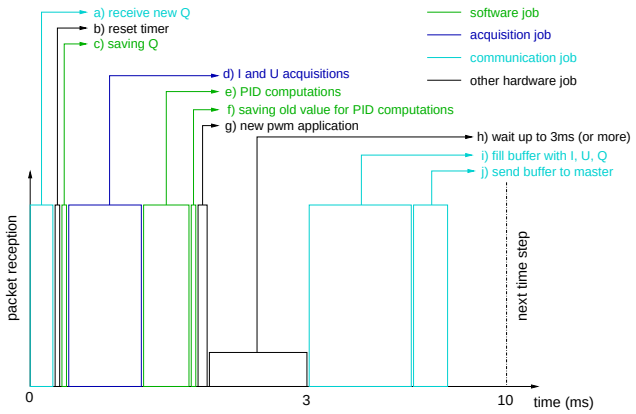

Fig. 15. Time diagram of the slave board

itself : then the approximation of an instantaneous control (no delay between the computations and the application of the new command) is correct.

AMRU 5 is able to move according to any fixed forward wave gait on a flat ground, with velocities from 0.3 m/s to 0.5 m/s. Main body can move in the XY plane, go up and down and can have roll, pitch and yaw references. Results of the references tracked by the controllers are quite similar to those described in section III. Main differences with the multibody model are the following :

1. friction : because friction is not yet identified, parameters of the controllers are not the same between simulation and experience;
2. flexibility in the legs : flexibility in the pantograph slows down the velocity of the gait with respect to the simulation. Indeed, even if the vertical degrees of freedom are responding instantaneously to the command, the feet do not leave the ground immediately. A proper gait requires an extension of the cycle time, consequently limiting the velocity of the main body.

VI. Conclusions and outlooks

A dynamic multibody model of the six-legged robot has been developed, including actuators, controllers and ground contact forces. Joint references are computed by a fixed gait pattern algorithm, and sent as input to the dynamic model of the robot. This gait algorithm has been successfully implemented on the decentralized control architecture of the hexapod machine.

The usefulness of a dynamic model has been emphasized through the overlap phase necessity : the consequences of an antagonist motion of the legs are not easy to guess, and direct implementation on the robot could lead to joint damages because of useless friction between the feet and the ground.

To reach an higher reactivity with the environment, which is the goal of walking robots, fixed gaits have to be replaced by free gaits. The algorithm proposed by Porta and Celaya in [2] is made of simple priority rules, which allows the leg to execute a step. It presents the advantage of simplicity, and converges towards tripod gait on a flat ground. Combined with the gait, a posture control minimizes a criterion based on the quadratic error between the actual posture and a reference posture : this gives to the main body a stable position.

However, the rules are not only based on position informations, but also on interaction with the environment.

Two main tasks are attributed to the sensing : detect contact with the ground, and avoid obstacles. In our approach we envisage to use current sensors in the motor to deal with the environment. Friction parameters for LuGre model must be identified, and implemented in the multibody model, which will allow to determine if current sensing in the motor is sufficient as sensing information or not. Indeed, because of joint friction, current in the motors will always be different from zero if there is a motion : consequently, it is important to have a precise friction model to separate friction and interaction effects. This approach presents two advantages : the integration of a current sensor is much easier and cheaper than a force sensor and the sensing is not only located at the extremity of the leg : therefore an obstacle collision could be detected wherever this collision occurs on the leg.

Acknowledgments

The authors would like to acknowledge Prof. Y. Baudoin, from the Royal Military Academy, for the AMRU 5 lending.

References

[1] F. Delcomyn, “Insect walking and robotics,” *Annu. Rev. Entomol.*, vol. 49, pp. 51–70, 2004.

[2] J.M. Porta and E. Celaya, “Reactive free-gait generation to follow arbitrary trajectories with a hexapod robot,” *Elsevier - Robotics and Autonomous Systems*, vol. 47, pp. 187–201, 2004.

[3] Gary B. Parker and Gregory J. E. Rawlins, “Cyclic genetic algorithms for the locomotion of hexapod robots,” in *Proceedings of the World Automation Congress, Robotic and Manufacturing Systems*. WAC ’96, May 1996.

[4] H. Kimura, K. Tscuchiya, A. Ishiguro, and H. Witte, Eds., *Adaptative Motion of Animals and Machines*, Springer Tokyo, 2006.

[5] O. Verlinden and G. Kouroussis, *EasyDyn 1.2.4 — C++ library for the easy simulation of dynamic problems*, Faculté Polytechnique de Mons, April 2007.

[6] C. Canudas de Wit, H. Olsson, K. Astrom, and P. Lischinsky, “A new model for control systems with friction,” *IEEE Trans. on Automatic Control*, vol. 40, pp. 419–425, 1995.

[7] P. Alexandre, *Le Contrôle Hiérarchisé d’un Robot Marcheur Hexapode*, Ph.D. thesis, Université Libre de Bruxelles, 1997.

[8] S.M. Song and K.J Waldron, “Machines that walk : The adaptative suspension vehicle,” *The MIT Press*, 1989.

[9] O. Verlinden, J.C. Habumuremyi, and G. Kouroussis, “Open source model of the amru 5 hexapod robot,” in *In International Symposium on Measurement and Control in Robotics*, Brussels, 2005.

Proceedings of the 8th National Congress on Theoretical and Applied Mechanics, May 28-29, Brussels, Belgium.

The Huggable Robot Probo, a Multi-disciplinary Research Platform

Kristof Goris[1], Jelle Saldien[1], Dirk Lefeber[1]
[1]Vrije Universiteit Brussel, Department of Mechanical Engineering
Pleinlaan 2-1050 Brussel
email: kristof.goris@vub.ac.be, jelle.saldien@vub.ac.be, dirk.lefeber@vub.ac.be

Abstract— **The concept of the huggable robot Probo is a result of the desire to improve the living conditions of children in hospital environment. These children need distraction and lots of information. In this paper we present the concept of this new robot. The robot will be employed in hospitals, as a tele-interface for entertainment, communication and medical assistance. To communicate according to social rules, the robot needs the ability to show facial expressions. Using a well defined set of Action Units (AU) it's possible to express some basic emotions. The emotions, represented as a vector in an 2D emotion space, are mapped to the DOF used in the robot. A prototype of the robot's head, capable of showing these basic emotions is presented. Besides the prototype of the real robot, a virtual model has been developed. With user friendly software these models can be used as an interface between an operator and a child. That way, Probo becomes a platform for experiments concerning human robot interaction with great opportunities in different disciplines.**

Keywords— **emotional interface, human-robot interaction, huggable robot, multidisciplinary research platform**

I. Introduction

During hospitalization, children are confronted with difficult situations. This can lead to serious mental health and other health consequences. Moreover, in hospital, a child's experiences are more limited due to the closed and protective environment. Several projects already exist that aim to use Information and Communication Technologies (ICT) like internet and webcams to allow hospitalized children to stay in contact with their parents, to virtually attend lectures at school and to provide information [1]. However, these ICT applications are usually computer animations displayed on PC, television screens or laptops. In fact, people are used to interact with embodied creatures and have evolved communication skills, which both need a body for expression [2], [3].

In this scope, the development of a social robot, called Probo, has started. The main objective is to offer solutions to some specific needs of hospitalized children by making use of a user friendly robot platform. The huggable robot Probo will assist in providing information and moral support to hospitalized children.

II. Probo, a Friendly User Interface

A. Concept

Probo has to be seen as an imaginary animal based on the ancient mammoths. Its name is derived from the word Proboscidea, the order of animals with a proboscis or trunk. By choosing a imaginary animal there are no exact similarities with well known creatures, so there are no or less expectations compared with a real animal. Safe interaction will be the first focus of Probo. Therefore the dimensions of this social pet robot are limited and comparable to the figure of a five years old child. Moreover, all moveable parts are actuated with soft actuators [3]. Probo's huggable and soft appearance, intriguing trunk and interactive touch screen in its belly, are striking (Figure 1). To communicate with the children, the robot is equipped with a fully actuated head. In [4] the importance of facial expressions in human face-to-face communication is described. For the display of emotions most of the DOF in its face are based on the Action Units (AU) defined by the Facial Action Coding System (FACS) developed by Ekman and Friesen [5]. AU express a motion of mimic muscles as 44 kinds of basic operation, with 14 AU to express the emotions of anger, disgust, fear, joy, sorrow, and surprise. These emotions are often supported as being the 6 basic emotions from evolutionary, developmental, and

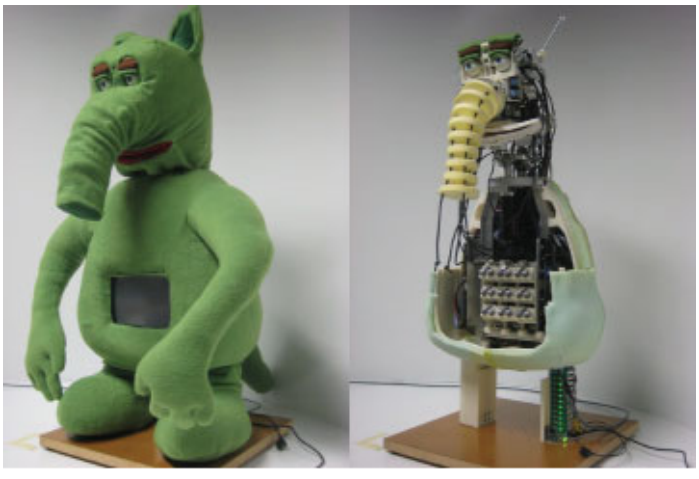

Fig. 1: The huggable social robot Probo, with and without removable fur jacket.

TABLE I: DOF and ranges of the actuated joints of Probo's head in comparison with other non-humanoid robot heads.

Kismet	iCat	**Probo**		
DOF [#]			**Range [°]**	
Eyes (3)	Eyes (3)	**Eyes (3)**	**Pan** **Tilt**	**100** **80**
Eyelids (2)	Eyelids (2)	**Eyelids (2)**		**150**
Brows (4)	Brows (2)	**Brows (4)**		**45**
Ears (4)		**Ears (2)**		**90**
Yaw (1)		**Mouth (3)**	**Yaw**	**45**
Lips (4)	Lips (4)		**Lipcorners**	**60**
Neck (3)	Neck (2)	**Neck (3)**	**Rotate** **Nod** **Bend**	**120** **70** **70**
		Trunk (3)		**360**

cross-cultural studies [6]. Table I shows the different degrees of freedom (DOF) of Probo's robot head in comparison with MIT's social robot Kismet [2] and Philips' iCat [7].

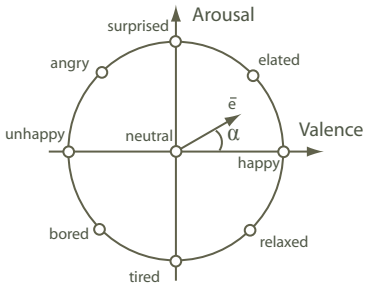

(a) Emotional space based on Russells circomplex model of affect.

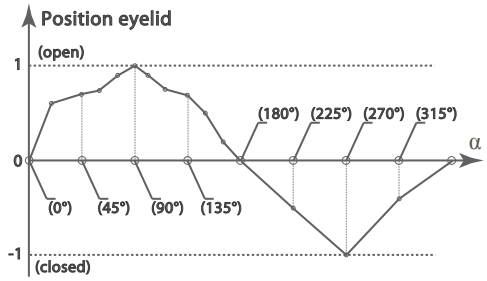

(b) Adjustable interface for defining the values of the DOF, in this case an eyelid, for each emotion.

Fig. 3: Display of emotions.

B. Emotional Interface

To realize a translation from emotions into facial expressions, emotions need to be parameterized. In [2], Kismet's facial expressions are generated using an interpolation based technique over a three-dimensional, componential *affect space* (arousal, valence, and stance). Cf. [2] our model has two dimensions; valence and arousal to construct an emotion space, based on the circumplex model of affect defined by Russell [8].

Figure 3a shows the emotion space of Probo. The x-coordinate represents the valence and the y-coordinate the arousal, consequently each emotion $e(v,a)$ corresponds to a point in the valence-arousal-plane (Figure 3a). In this way we can specify basic emotions on a unit circle, placing the neutral emotion $e(0,0)$ in the origin of the coordinate system. Now each emotion can also be represented as a vector with the origin of the coordinate system as initial point and the corresponding arousal-valence values as the terminal point. The direction α of each vector defines the specific emotion whereas the magnitude defines the intensity of the emotion. The intensity i can vary from 0 to 1, interpolating the existing emotion $i = 1$ with the neutral emotion $i = 0$. Each DOF that influences the facial expression is related to the current angle α of the emotion vector. An adjustable interface is developed to define the desired value for each angle $(0^\circ - 360^\circ)$ of the different DOF. By selecting one degree of freedom, we set a value for each basic emotion on the unit circle and use linear interpolation to obtain a contiguous relation. By adding more (optional) points or values the curve can be tuned to achieve smooth, natural transitions between different emotions. An example for the degree of freedom controlling the eyelid is shown in Figure 3b.

C. Real and Virtual Model

To interact and communicate with children a new 3D embodied social robot has been designed. During the development phase, a virtual model has been derived from the real CAD model. The virtual model, based on the real mechanics, was used as a tool to control the design criteria. For instance, by actuating the virtual model, the necessary DOF and ranges of the actuated joints could be checked, so that the robot head would be able to express some basic emotions. Additionally, with the virtual model it was possible to develop control software, without the need of the real model. That way, fast progress in software and hardware developments could be made simultaneously. The left figure in Figure 2 shows some movements of the robot during an experiment where the real model was linked with the virtual one.

D. Friendly User Interface

The huggable and friendly Probo will function as a robotic user interface between an operator and a child. The friendliness refers not only to the funny and attractive behavior of the robot pet, but it refers also to the easy and convenient way to control the robot. An operator, for in-

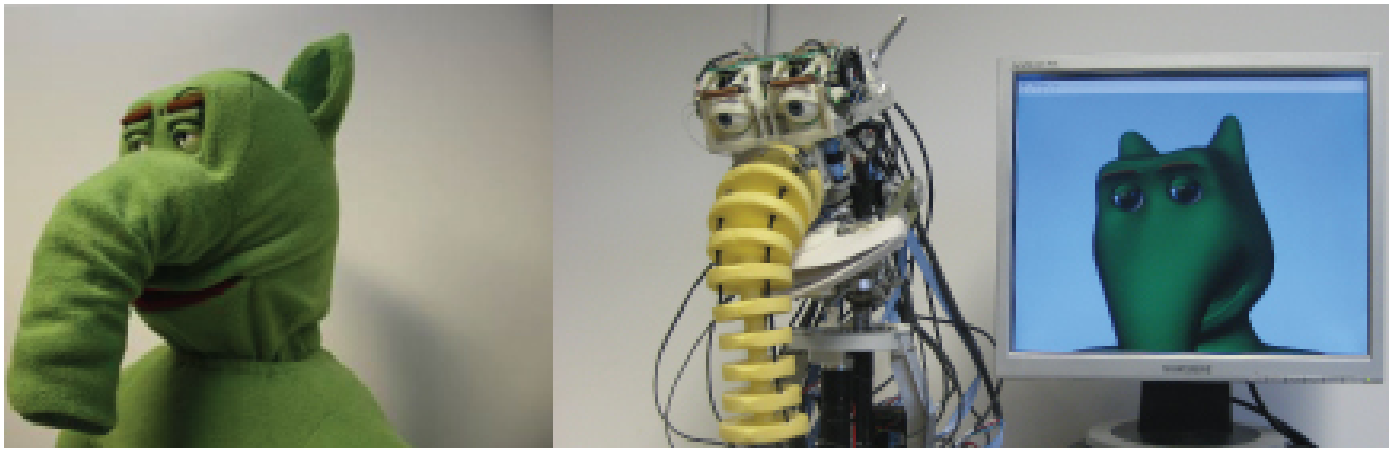

Fig. 2: Left: Real robot head with fur. Right: Mechanical head linked with virtual model.

stance a doctor, a nurse, a parent, a classmate or a teacher can manipulate the robot's actions, by either make use of a *Xbox* game controller, or an easy graphical user interface (GUI) made for a *Microsoft* operated system (PC, or smartphone). With this GUI, one can control the robot and make some sequences in movements, like animations. This can be done, intuitively, by dragging and dropping some icons on the screen.

III. Conclusions

To inform and comfort hospitalized children in an interactive and playful way, a new social pet robot, called Probo is being developed. Probo's main goal is to communicate with the children. Therefor a fully actuated robot head, capable of showing facial expressions, has been designed and build. Compared with other non-humanoid robot heads Probo has an intriguing trunk. By use of soft and flexible materials together with compliant actuators, the design is safe and as a consequence safe human/child robot interaction is assured. In addition to this, user friendly control software, and a virtual model based on the real robot are developed. With this real or virtual multidisciplinary testbed, new opportunities like robot assisted therapy will be explored in collaboration with pediatricians, sociologists and psychologists.

IV. Acknowledgments

This work was supported by the Brussels-Capital Region.

References

[1] Deborah Fels, Bradley Shrimpton, and Margaret Roberston, "Kids in hospital, kids in school," in *Proceedings of World Conference on Educational Multimedia, Hypermedia and Telecommunications 2003*, David Lassner and Carmel McNaught, Eds., Honolulu, Hawaii, USA, 2003, pp. 2358–2363, AACE.

[2] C.L. Breazeal, *Designing Sociable Robots*, Mit Press, 2002.

[3] K. Goris, J. Saldien, I. Vanderniepen, and D. Lefeber, "The Huggable Robot Probo, a Multi-disciplinary Research Platform," *Proceedings of the EUROBOT Conference 2008, Heidelberg, Germany, 22-24 May, 2008*, pp. 63–68, 2008.

[4] A. Mehrabian, "Communication without words," *Psychology Today*, vol. 2, no. 4, pp. 53–56, 1968.

[5] P. Ekman and W.V. Friesen, *Facial Action Coding System*, Consulting Psychologists Press, 1978.

[6] P. Ekman, "Are there basic emotions?," *Psychological review*, vol. 99, no. 3, pp. 550–553, 1992.

[7] AJN van Breemen, "iCat: Experimenting with Animabotics," *Proceedings, AISB 2005 Creative Robotics Symposium*, 2005.

[8] J. Posner, J.A. Russell, and B.S. Peterson, "The circumplex model of affect: An integrative approach to affective neuroscience, cognitive development, and psychopathology," *Development and Psychopathology*, vol. 17, no. 03, pp. 715–734, 2005.

Proceedings of the 8th National Congress on Theoretical and Applied Mechanics, May 28-29, Brussels, Belgium.

The interest of CPG's for locomotion control of self-reconfigurable robots

Chariot Christophe[1], Filippi Enrico[2], Verlinden Olivier[3]
[1,2]Department of Mechanical Engineering, Faculté Polytechnique de Mons
Rue du Joncquois, 53, 7000 MONS - Belgium
[3]Department of Theoretical Mechanics and Dynamics and Vibrations, Faculté Polytechnique de Mons
Boulevard Dolez 31, 7000 MONS - Belgium
email: christophe.chariot@umons.ac.be, enrico.filippi@umons.ac.be,olivier.verlinden@umons.ac.be

Abstract— **This paper first introduces the concept of collective robotics and then focuses on the self-reconfigurable robots subclass in section II.**
After that, the locomotion control is tackled in section III where CPG's are described. The presented structure is based on the well-known Matsuoka oscillator detailed in section IV-B and is illustrated in section V where a CPG-based control of a double pendulum is studied.

Keywords— **CPG, locomotion, control, self-reconfigurable, matsuoka**

I. Introduction

NOWADAYS , we find more and more technology concentrates in which many functionalities are embedded within single devices. This commercial niche particularly succeeds thanks to its natural convenience (all-in-one package) but also for its cost-effectiveness.
This principle can also be applied in robotics even if so far, the multi-task ability has always been limited. That's how, for a few years, the technical progresses have led to a new generation of robots able to fulfill a large number of different functions. The idea relies on the design of a generic structure that can adapt itself to its environment and according to the desired purpose rather than one with some specific and predetermined abilities. Such things are possible thanks to the developpment of collective robotics which thus particularly fits to exploration missions or to a rescue scenario in disaster area.
However, this technology brings new challenges and opens many research issues despite its attractive potential. More particularly, in the locomotion control point of view, suited bio-inspired control structures are thus considered and has already provided conclusive results.

In this paper, an introduction of collective robotics is given in section II with more details about self-reconfigurable robots in section II-C.
We then focus on the locomotion issue by describing CPG's and their interest in section III whose principles are detailed in section IV.
Finally, an example of a CPG-based control applied to a double pendulum is presented in section V.

II. Collective Robotics

A. General Principle

Collective robotics is based on the use and interaction of several robotic entities to achieve a common goal. Its principle relies on the adage "Unity is Strength" : the fulfillment of a given task is made possible thanks to the mutual assistance of several robots instead of a single one. Indeed, the abilities of each entity taken apart remain basic and limit its field of applications. Their collaboration considerably increases the number of possibilities which become greater than the sum of individualities.

In this way, many simple robots can accomplish complex missions and benefit from a substantial increase of the reliabiliy and of the flexibility by comparison with conventional robots.
Sections II-B and II-C describe two distinct categories included in collective robotics.

B. Robots Swarms

Robots swarms (see example in Fig. 1) can be compared to an ants colony : they are composed of many simple and autonomous entities which benefit from a collective intelligence. In both cases, an isolated individual can't do much but once gathered with others, complex behaviours emerge from the group. So, robots swarms are characterized by individuals able to move on their own and to communicate with their fellow beings on a more or less evolved way. They are thus autonomous in terms of displacement but the decision making results from a collective process which belongs to the community.
Robot swarms are particularly suited for reconnaissance missions, covering wide area in no time or combining efforts on a common goal (like moving an heavy load).

C. Self-reconfigurable Robots

A self-reconfigurable robot (SR robot) is a set of elementary robots that link and organise themselves in order to form an overall structure like lego bricks (see Fig.2). According to the combination of these robotic cells (also called modules) the resulting configuration suits to fulfill a

Fig. 1. The Swarm-Bots project [1]

given function. This means that SR robots can potentially present some multifunctions abilities.
To achieve this interesting characteristic, the design of the modules have to allow motion generation (through mobile parts and actuators) and self-reconfiguration (need of an interconnection mechanism).

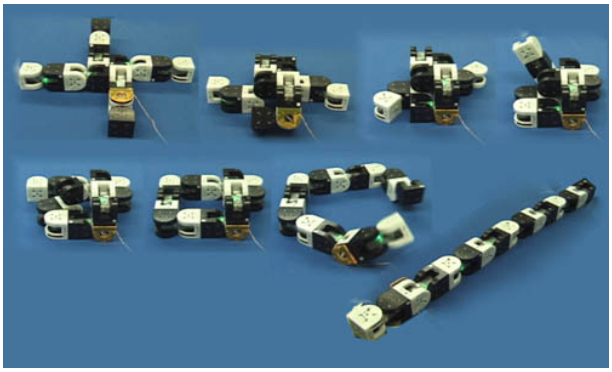

Fig. 2. The M-TRAN project [2]

C.1 Classification

Two main properties are often used to classify SR robot projects.

The first one is the geometric distribution of the modules in space : we destinguish lattice, chain and hybrid configurations (see Fig. 3).

- Lattice structures are organised according to a regular and periodic pattern showing similarities with molecular networks of crystals. The management and the movement of the modules within the structure is made easy thanks to the natural symmetry but they also suffer from a lack of mobility and flexibility. These systems would then rather be used in changing shape object applications than in dexterous motions generation.
- In chain-type structures, modules are assembled in serial-like link so that the resulting effect in obtained by addition of the modules dof's. These connections allow complex and dexterous motions as compensation of symmetry which makes the control of this flexible structure more tricky (combination of many dof's). They thus particularly fit to application requiring mobility like object manipulations or even locomotion.
- Finally, hybrid structures combine both lattice and chain principles so that they allow dexterous motion generation while keeping properties of a lattice organisation. This is a very interesting compromise between lattice-type and chain-type architectures in terms of mobility and modules organisation.

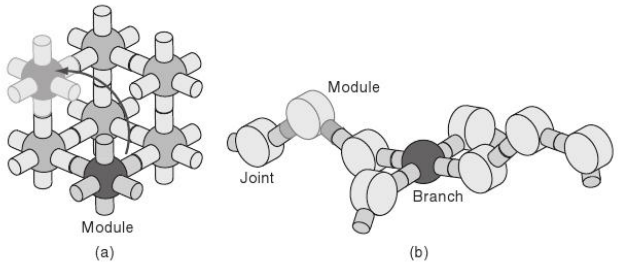

Fig. 3. Structures of SR robots : lattice-type (a) vs chain-type (b) - extracted from [3]

On the other side, SR robots projects can be classified according to the modules population.

- Homogeneous systems are composed of many strictly identical modules which means that every module has to embed every function (motion generation, interconnection device, power source,...). The design of such modules is thus particularly important and difficult but having a generic module lowers the production costs and is beneficial in terms of flexibility and robustness.
- Conversely, an heterogeneous system deals with a variety of specialised modules. The latter are thus designed to provide a specific contribution within the population and is thus very effective with regard to this function. However, the modules organisation has to manage different types of elements which is more complex and reduces the global flexibility.

III. Locomotion Control Using CPG's

In the following sections our interest is taken in homogeneous self-reconfigurable robots and the associated locomotion issue. Indeed, this technology has many advantages including multifunctionality, self-reconfiguration and high reliability but the control of such architecture is difficult to achieve with conventional techniques. Centralized control could be envisaged but presents bad robust-

ness, bad adaptiveness and is dependent on communication performances. This is also true for distributed architectures sharing global information between the modules. In this section we thus consider a special control structure able to deal with the huge number of dof's, to provide a coordinated and coherent motion of the whole and to work in a distributed way. This is a solution that has already been successfully applied to SR robots and which also seems to be, at present time, the most popular one due to the very promissing results it has provided as in [4] and [5].

A. Origin

Men have always tried, more or less successfully, to imitate biological principles based on his observations in order to extend his own abilities. With this in mind, advances in neurobiology and robotics have naturally led to new bio-inspired control structures.
Particularly, this work is about the locomotion issues related to rhythmic patterns generation. Indeed, oscillations are natural patterns that can be found in almost every living beings. Their implication in respiration or even heart beat is obvious but it's also a key point in the locomotion generation which is a periodic activity on its own.
The following sections detail how to take advantage of this and apply it in modular robotics.

B. CPG's

Strictly speaking, "Central pattern generators (CPG's) are neural networks that can endogeneously (i.e without rhythmic sensory or central input) produce rhythmic patterned outputs" [6]. Actually, this is the device that generates the fore-mentioned rhythmic activities.
This definition implies that a CPG is able to produce a periodic signal even with continuous steady-state input and without any feedback which also fits to the generation of locomotion underlying signals. Moreover, experiments on cats that had undergone a complete transection of their spinal cord have shown that they were able to produce a normal walk gait [7]. By extension, we can thus say that the rhythms generation of the locomotion mechanisms is separated from the cognitive part[1] and is thus produced locally.

C. Interest

Beyond the principle of biomimetism, the use of CPG's benefits from several properties especially interesting in our case.

[1]Even if the brain plays a major role in the whole locomotion process.

C.1 Distributed Architecture

As its oscillation is self-sustained, a CPG can deal with only simple input signals. This relieves the higher center of control of providing rich and complex signals which is significant, especially for complex systems having many dof's. Therefore, the input signal can be reduced to small dimension and high level data shared by every dof, like a value representing the required motion speed.
Moreover, several CPG's can be coupled together so that they oscillate in or out of phase according to a global pattern. The coupling can only involve the neighbouring entities so that the information is broadcast gradually.
That is to say that CPG's particularly fit to work in a distributed way.

C.2 Adaptiveness

As explained previously, the rhythms generation doesn't require any feedback contribution. However, the latter plays a major role to shape the periodic output and provide adaptiveness [8].
First of all, one can observe global entrainment, that is to say that the oscillation tends to align itself with the natural frequency of the entrained body. This property allows the control part to take the mechanical phenomena into account which leads to a good interaction between them.
Moreover, the sensory feedback is usefull for disturbance rejection which brings adaptiveness with regard to direct environment. The cycle is thus self-adapted to changes like ground geometry or friction conditions.
A consequence of CPG adapiveness is its ability to show complex behaviour like natural gait transitions. According to environment changes, the modular robot can switch from a gait to an other like Ijspeert's salamander robot which naturally and gradually switches from swimming to crawling when it reaches the bank [9]. Gait transitions can also happen due to input variations which only give global information. So, a legged robot naturally adapts its gait (walk,trot or gallop) depending on the required motion speed thanks to the cycle modulation of CPG's.
These properties are very attractive and interesting but the inner mechanisms that rule them are not fully masterized yet.

IV. Model of a CPG-based control architecture

A. Control Structure

A multibody system controlled by a structure using CPG, inspired from [4], is represented in Fig. 4. Each degree of freedom is driven by a CPG, we thus have a distributed control architecture. According to the complexity of the structure, the model can present different contribu-

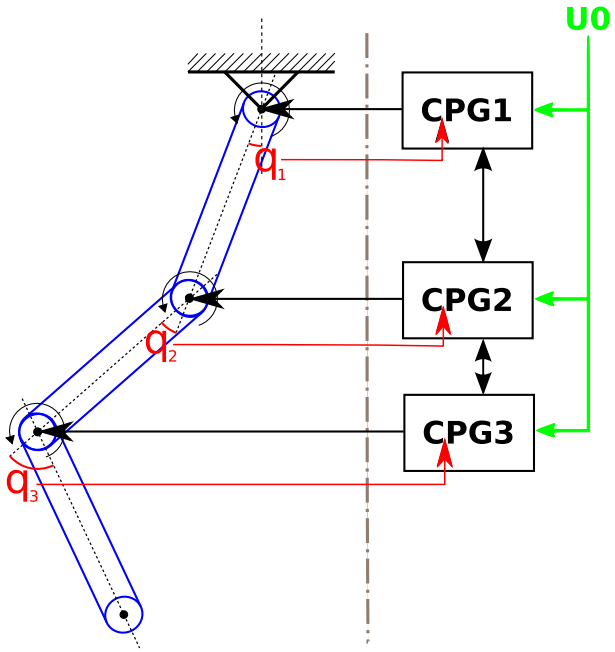

Fig. 4. A CPG-based control structure

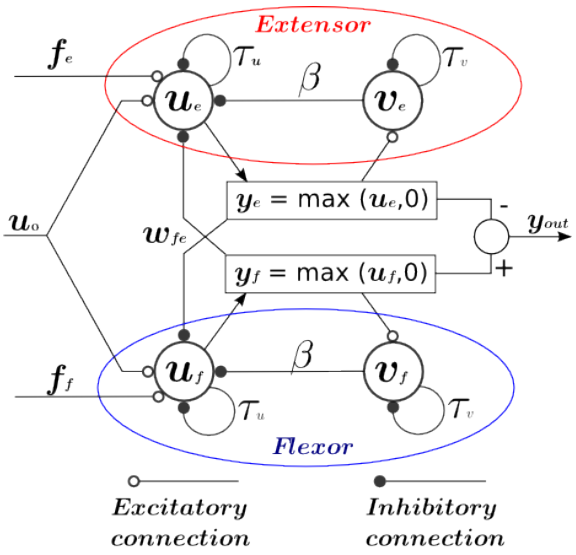

Fig. 5. Representation of The Matsuoka Oscillator inspired from [4]

tion of sensory feedback and coupling between the CPG's. As an example, the model of Fig. 4 considers direct feedback of the controlled dof and a simplified coupling. Indeed, the latter only involves neighbouring CPG by opposition with a complete coupling where each one depends on the others. Such structures are easily scalable to big systems as confirmed by biological experiments that have showed a lot of coupled rhythmic generators distributed in the lamprey spinal cords [8].

B. Non-Linear Oscillators

By definition a CPG-based control structure requires the use of non-linear oscillators :

1. Due to its periodic output, a CPG is defined as an oscillator ;
2. The self-sustained oscillations must be produced endogeneously which means that the use of linear systems has to be banished.

B.1 The Matsuoka Neural Oscillator

The Matsuoka oscillator described below is largely used in CPG-based controls and has many variants depending on the kind of contribution of coupling and feedback. It benefits from an easy and stable numerical integration compared to other models like the Van Der Pol oscillator [10]. It is modelled by two coupled neurons : an extensor motoneuron (subscript e) and a flexor motorneuron (subscript f), each of them having two state variables as depicted in Fig. 5 and described by the following equations.

$$\tau_u \dot{u}_e = u_0 + f_e - u_e + w_{fe} y_f - \beta v_e \quad (1)$$

$$\tau_v \dot{v}_e = y_e - v_e \quad (2)$$

$$\tau_u \dot{u}_f = u_0 + f_f - u_f + w_{fe} y_e - \beta v_f \quad (3)$$

$$\tau_v \dot{v}_f = y_f - v_f \quad (4)$$

$$y_e = \max(u_e, 0) \quad (5)$$

$$y_f = \max(u_f, 0) \quad (6)$$

$$y_{\text{out}} = y_f - y_e \quad (7)$$

u is called the firing rate and increases with the input u_0 and the feedback contribution while the fatigue v (scaled by β) tends to decrease the value of u. As the positive fire rate y of each neuron inhibits (through w_{fe}) the other, they constantly oscillate out of phase, τ_u and τ_v beeing the time constants related to the firing rate and the fatigue respectively. The output is generated by the difference of the positive fire rates (y_e and y_f). Each parameter of the oscillator affects the frequency of the ouput except u_0 that only changes its amplitude (even if modified structures of this oscillator allow more evoluted contribution of the input). Fig. 6 represents a simulation of the presented oscillator with simulink and illustrates its working. This simulation has been led for a constant input u_0 in open loop (no feedback contribution) and for the parameters given in Table I. It is of interest to mention that the periodic output is only guaranteed for a certain range of parameters values [11]. When the CPG is used on an actual system, the parameters of the oscillator are generaly tuned with a learning or optimization algorithm as in [12] where different solutions are compared. In most cases, the opimisation is based on a high-level performances criteria like the motion speed or energy consumption.

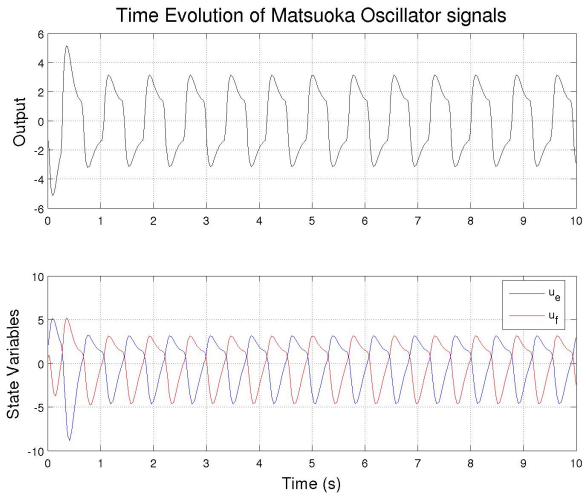

Fig. 6. Simulation of The Matsuoka Oscillator

Parameter	Value
τ_u	0.05
τ_v	0.6
β	5
w_{fe}	2.5
u_0	8.0

TABLE I
SIMULATION VALUES OF FIG. 6

V. EXAMPLE ON A DOUBLE PENDULUM

A. System Description

To illustrate the use of the Matsuoka oscillator as CPG, we have chosen a simple and common dynamical system: a double pendulum. The system is the one depicted in Fig.7 and is inspired from [13]. The rotational joint that links the first bar (parameter q_1) to the frame is kept free while the joint linking the two bars together (parameter q_2) is controlled, the pendulum is thus underactuated. The CPG output sets the angular value q_2 and has a feedback contribution of the pendulum through q_1 and is commanded by its input u_0.
In the following, no friction has been added, the system and the rotational joints are thus considered as ideal.

B. Simulation

The first step is the observation of the system response when controlled by a CPG in open loop. The oscillator model is the same as the one described in section IV-B. Fig. 8 thus shows the time responses of q_1 and q_2 without any sensory feedback. One can observe that q_2 actually corresponds to the output of the CPG which has no adaptiveness since its cycle remains unchanged and q_1 keeps a

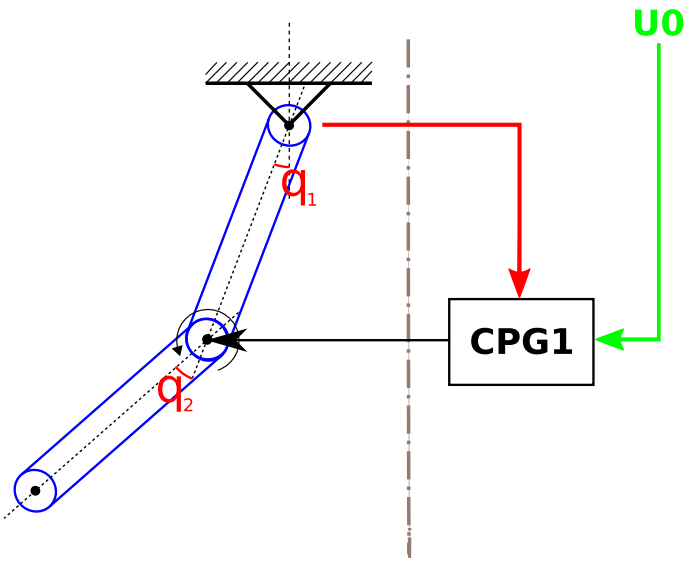

Fig. 7. Simulation of double pendulum

chaotic response.

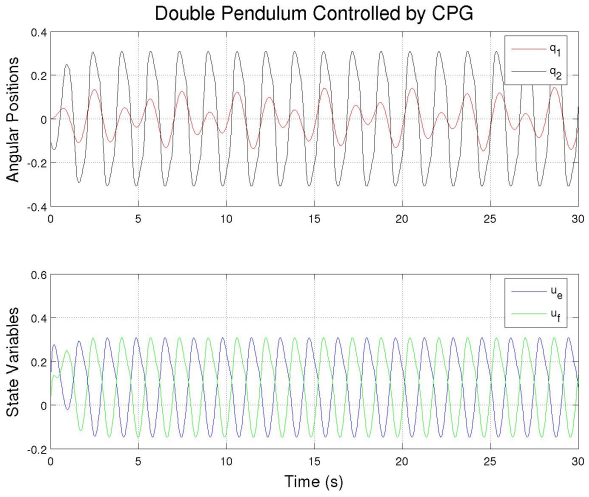

Fig. 8. Simulation of double pendulum without feedback

In order to observe global entrainment, sensory feedback has been added: f_e and f_f are then connected to the rotational value q_1 through a common weight factor f_c that sets the amplitude of the feedback contribution. The results in Fig. 9 are obtained for the values given in Table II : as the excitation increases the value of q_1, the feedback contribution becomes dominant and the excitation cycle tends to copy the natural frequency of the pendulum. After a while, the CPG output doesn't generate any excitation anymore since the pendulum has reached a steady swing state and has no friction to compensate.

This has been simulated again with several values of the

Parameter	Value
τ_u	0.4
τ_v	0.5
β	5
w_{fe}	2.5
u_0	1.0
f_c	8.0

TABLE II
SIMULATION VALUES OF FIG. 9

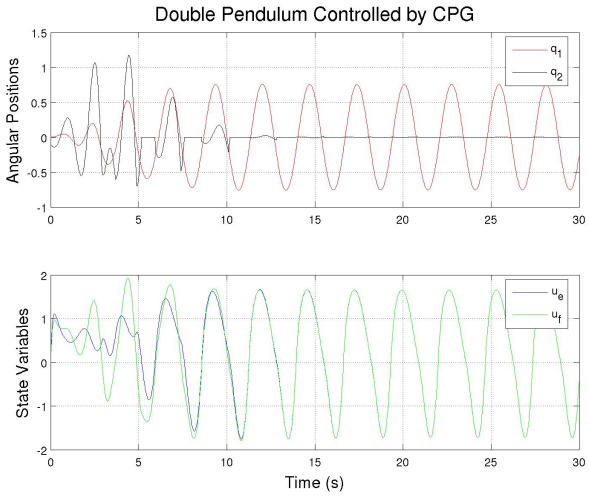

Fig. 9. Simulation of double pendulum : normal swing mode

CPG input u_0 and the same behaviour is observed. However, the amplitude of the pendulum swing globally increases with the value of u_0 until it reaches a giant swing mode : the pendulum describes a full rotation arround the first joint at constant angular speed. The latter has been observed in simulation (see results Fig. 10).

C. Parameters Tuning

The tuning of the parameters, that has led to the results presented in section V-B, has been obtained by trial and error. However, this has been done by observing the different contributions of some parameters on the global system. For example, the parameter f_c sets the importance of the feedback contribution in the cycle (that must be balanced with the order of magnitude of u_0) while τ_1 and τ_2 influence the CPG natural frequency. From our observations, the latter should be kept relatively close to the mechanical one to achieve adaptiveness.
Some tests have been led to observe natural mode transition (between normal swing and giant swing modes) but the system doesn't respond much to variations of u_0 online. We think that better results could be obtained with

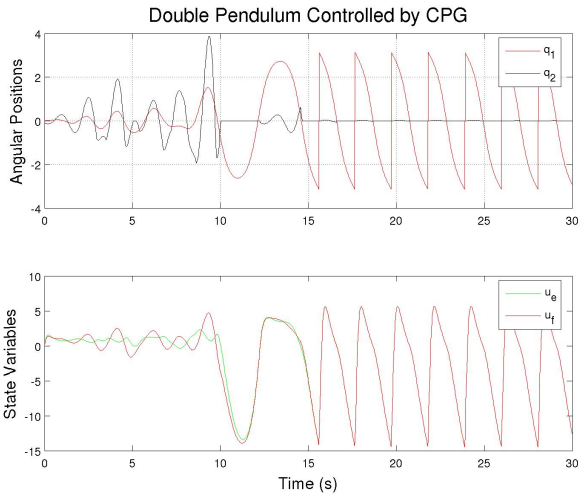

Fig. 10. Simulation of double pendulum : giant swing mode

perturbation on the system (in the form of friction for example) and with a more evolved contribution of the input. Some values would certainly be more effective but the main purpose of this first simulation is to exhibit the global entrainment of a CPG-controlled mechanical system.

VI. CONCLUSION & FURTHER WORK

In this paper, we have introduced the concept of self-reconfigurable robots in order to focus on their locomotion issue. Therefore a bio-inspired control architecture that particularly fits to distributed systems have been presented. The latter has then been illustrated with the simulation of an underactuated double pendulum controlled with the Matsuoka oscillator. By analysing the effects of its parameters variations we have got a step closer in the understanding of its inner mechanism and have succeeded in showing its global entrainment property. However, a more quantitative approach has to be led which implies a complete parametric analysis and the use of optimisation algorithms. Moreover, as the purpose is the application in real condition, it also would be apropriate to use a more complete model which includes friction and external disturbances.

This comes within the scope of the establishment of a complete methodology to design CPG's applied to self-reconfigurable robots locomotion.

REFERENCES

[1] "The swarm-bots project," http://www.swarm-bots.org/.
[2] "The m-tran project," http://unit.aist.go.jp/is/dsysd/mtran3/.
[3] Satoshi Murata and Haruhisa Kurokawa, "Self-reconfigurable robots," *IEEE Robotics & Automation Magazine*, pp. 71–78, March 2007.

[4] A. Kaminura H. Kurokawa E. Yoshida S. Murata K. Tomita S. Kokaji, "Automatic locomotion design and experiments for a modular robotic system," *IEEE/ASME Transactions on Mechatronics*, vol. 10, no. 3, 2005.

[5] Campbell Hoburg Mowry Pillai Goldstein Kirby, Aksak, "Distributed adaptive locomotion by a modular robotic system, m-tran ii," in *Proceedings of 2004 IEEE/RSJ International Conference on Intelligent Robots and Systems*, 2007.

[6] Scott L Hooper, "Central pattern generators," *Embryonic ELS*, 1999.

[7] Serge Rossignol, "Locomotion and its recovery after spinal injury," *Current Opinion in Neurobiology*, vol. 10, pp. 708–716, 2000.

[8] Auke Jan Ijspeert, "Central pattern generators for locomotion control in animals and robots : a review," *Neural Networks*, vol. 21, pp. 642–653, 2008.

[9] Sunny Bains, "Modular robots learn art of self-reinvention.," *eeTimes europe*, p. 1&12, 2007.

[10] Sean Ashley Bailey, *Biomometic Control WithFeedback Coupled Nonlinear oscillator - insect experiments, design tools and hexapedal robot adaptation results*, Ph.D. thesis, Stanford University, 2004.

[11] Kiyotoshi Matsuoka, "Sustained oscillations generated by mutually inhibiting neurons with adaptation," *Biological Cybernetics*, vol. 52, pp. 367–376, 1985.

[12] Yvan Bourquin, "Self-organization of locomotion in modular robots," M.S. thesis, Swiss Federal Institute of Technology, 2004.

[13] K. Matsuoka N. Ohyama A. Watanabe M. Ooshima, "A giant swing robot using a neural oscillator," *International Congress Series 1291*, pp. 153–156, 2006.

[14] Brian Kirby Jason Campbell Michael Philaetus Weller, Mustafa Emre Karagozler and Seth Copen Goldstein, "Movement primitives for an orthogonal prismatic closed-lattice-constrained self-reconfiguring module," in *Workshop on Self-Reconfiguring Modular Robotics at the IEEE International Conference on Intelligent Robots and Systems (IROS '07)*.

Proceedings of the 8th National Congress on Theoretical and Applied Mechanics, May 28-29, Brussels, Belgium.

Design and assessment of an autonomous ducted rotor UAV

Frank Buysschaert[1], Fryderyk Pomirski [2], Jérôme Sans[1], Mathieu Seiler[2], Moaad Yacoubi[1]
[1]Université Libre de Bruxelles, Department of Applied Sciences, Aero-Thermo-Mechanics Laboratory
50, F.D. Rooselvelt Avenue, 1050 Brussels, Belgium
[2]Ecole des Mines d'Alès
Avenue de Clavières, 30319 Alès, France
email: frank.buysschaert@ulb.ac.be

Abstract— **This article overviews the major disciplines involved in the design and construction of an autonomous ducted rotor UAV, developed in the Onera mini-drones competition framework. The concept as well as its prime components will be explained, issues exposed and possible solutions addressed. First flight tests without stability system have shown the feasibility of the concept. Flight tests with an operational inertial reference unit is part of future work.**

Keywords— **RUAV, MAV, UAS, duct, rotor, autonomous, IRU**

I. Introduction

FOLLOWING a succesfull "mini-drones" competition organized by Onera (the French Office National d'Etudes et de Recherches Aéronautiques) in 2007, the organization decided to continue on its élan by launching a second inter-university competition for the design and the development of small airborne observation platforms or MAVs in cooperation with the French Ministry of Defense DGA (Délégation Générale de l'Armement), which commenced in 2007 and is due to end in 2009. The goal of the competition comprises in short : find platforms useful for military purposes, directly or indirectly, by developing new and diverse technologies and by taking best of worlds. The platform must pass several milestones showing e.g. autonomous takeoff and landing, sufficient stability in perturbed atmospheres (gusts, steady wind), etc. Thanks to a successful collaboration in a similar framework in the past, Université Libre de Bruxelles (ULB) was contacted by Ecole des Mines d'Alès (France) to join the competition. It was then decided to use a Rotor Wing UAV (RUAV) configuration, based on a former design (Ema'tador, [1]) but smaller in size with only one rotor placed in a duct and with movable blades for control (Fig.1). The disciplines discussed in the subsequent sections are : *rotor and propulsion, aerodynamic design, structure and mass & balance, flight control system* and finally *data transmission and camera*. Each discipline will be described briefly. It is obvious that the operational ability of the RUAV not only depends on the successes made in several disciplines, but also by their capability to work as a whole system.

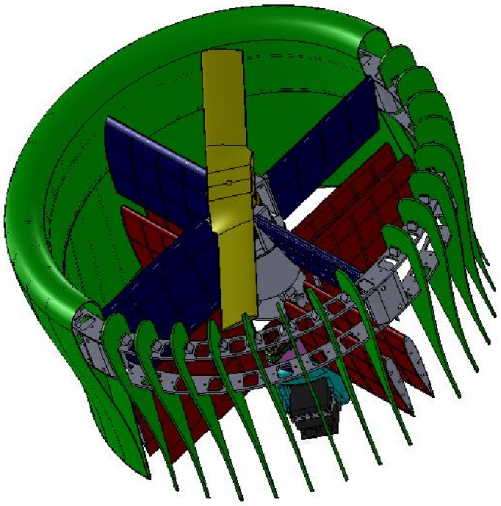

Fig. 1. The Dulbema RUAV with bare duct.

II. Rotor and propulsion system

RUAV design is larded with trade-offs between several parameters. First, the mission must be specified imposing directly minimum payload specifications, in this case a well performing camera, which has to navigate itself autonomously to targets of interest. Also, maximum dimensions (transportability) and minimum performance characteristics must be set. All these parameters affect the mass of the RUAV and its power consumption, thus also define the rotor geometry and the propulsion system in general (i.e. motor, gearbox, batteries). Since an internal combustion engine makes lots of noise and heat, produces greasy and camera obscuring smoke and introduces sufficient vibrations to the structure, all of which harming the operational effectiveness, an electrical brushless motor was selected, powered by high performance Lithium-Polymer batteries. The difficulty here is finding an energy efficient synergy between rotor, motor and batteries, all having their own optimum efficiencies while making a gearbox obsolete, which leads to a lower Empty Weight. From the experience gained with the Ema'tador project, one learnt that designing a rotor is a time consuming and complex business. As the prove of flight of the concept was a key requirement, the decision was made to reduce

Fig. 2. The selected propulsion system components.

the platform's complexity using an off-the-shelf model aircraft propeller. The selection was eased using a software program *Motocalc*. The program allows studying a combination of several engine and propeller configurations. The result of the study is a two bladed Menz 16/8 aircraft propeller driven by a Scorpion S4020-12 brushless motor. The energy comes from 4 ThunderPower LiPo batteries of 3850 mAh each. Plate 2 gives an overview. During flight, the batteries are discharged. This causes a drop of the battery voltage (Fig.3). The maximum performance of the RUAV depends strongly on the maximum thrust of the rotor. The maximum thrust of the rotor is in turn a function of the maximum rotor speed, which is proportional to the maximum voltage applied to the engine. Since this voltage decreases with time while the battery is discharged, the performance envelope of the RUAV gets narrower, a problem becoming critical when appealing on the last 10% of the battery capacity. Therefore each flight should be preceded by a meticulous evaluation of the mission in order to maximize the chances of recovering the platform. Table I gives a summary of some technical figures concerning the propulsion system. Future research will address the development of a new optimized rotor with the aid of CFD (*Fine/Turbo*^{TM} *of Numeca Int.*) with special attention given to the interaction between duct and rotor.

III. Aerodynamic Design

A real challenge with this type of RUAV is dimensioning all components such that they perform well aerodynamically within the constraints set by, inter alia, the propulsion system[1] and mass & balance limits[2]. The RUAV must operate in hover and in translational flight with angles of attack ranging from 0° to 180° (i.e. descent), and this at various speeds and atmospheric conditions [2]. A duct can improve the thrust-to-power-ratio of the rotor [3], but a bad rotor integration causes just the opposite [4]. Considering a flawless integration of the ro-

[1]By omitting for example the gearbox, the rotor must work at relatively high and variable angular velocities.

[2]E.g. it will be explained in Section IV that the center of gravity must be positioned as high as possible with respect to the control blades.

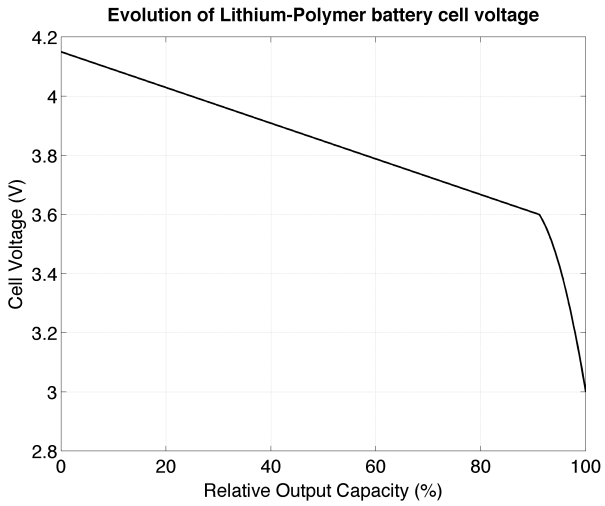

Fig. 3. LiPo battery cell voltage variation with output capacity (source ThunderPower Batteries Inc.).

TABLE I
Propulsion System Component Parameters

Brushless motor Scorpion S4020-12	
$P_{max,\ Cont.}$ (W)	1500
K_v (RPM/V)	542
I_{max} (A)	85
R_m (Ω)	0.020
mass (kg)	0.304

Lithium polymer batteries Thunder Power TP3850-3SXV	
Capacity/unit (mAh)	3850
Cells/unit (-)	3
Unit voltage (V)	11.1
Mass/unit (kg)	0.384
Units installed aboard	4 (2x2)

Propeller Menz 16/8	
Diameter (m)	0.4064
Pitch (m/rev)	0.2032
Installed thrust (N)	43

tor with disk area A_R in the duct with exit area A_e, then one would observe for a given lift an induced ducted-to-unducted rotor power ratio given by [3] :

$$\frac{P_{i,ducted}}{P_{i,unducted}} = \frac{1}{\sqrt{2a_d}} \tag{1}$$

where,

$$a_d = \frac{A_e}{A_R} \tag{2}$$

Equation 1 clearly shows that a value for a_d larger than unity reduces the rotor induced power. [5] explains that a ducted rotor becomes particularly interesting when used for stationary flight, an important phase in the mission specifications typical for RUAVs. Though beneficial, the models neglect interference losses (rotor-duct and rotor-fuselage[3]), the effects of the duct lip radius, the duct chord length, the duct profile thickness, and the air flow conditions. Therefore, wind tunnels tests are necessary which are above all required to improve and validate the, in most cases, less costly CFD calculations. Thanks to this approach, an appropriate profile with corresponding dimensions and angle settings can be found for the duct, rotor and control blades (example in Fig.4). Full scale wind tunnel tests will also serve as an aid to determine critical values for the flight control model. Some general aerodynamic characteristics are given in Table II.

The use of a ducted rotor with flight controllability obtained by blades put below the rotor requires a detailed aerodynamic study. On Figure 5, one can distinguish two rows of blades. The upper blade row serves as anti-torque mechanism, used to compensate the torque put by the electric motor on the structure, but also vouches for sufficient yaw control. The blades have flaps on the trailing edge (Fig.6), which is mandatory to gain acceptable levels of controllability. The lower row of symmetrical blades enables pitch and roll control. Since the exerted forces on the lower part of the airframe are less important, it was possible to give these blades a variable angle of incidence. Several blade profiles were examined with *Xfoil*. The blade chord dimensions for both blade rows depend strongly on the required rotor power and aerodynamic characteristics of the duct, but they are also particularly sensitive to the position of the centre of gravity. Remark that for the lower row, a biplane configuration has been selected.

IV. Structure and Mass & Balance

Needless to say that the use of high quality composite materials is mandatory when pursueing a stiff and lightweight structure. High stiffness allows the distance

[3]The outside torus wherein the rotor is installed is called *duct*, while the center part in which the rotor and motor are integrated is called *fuselage*.

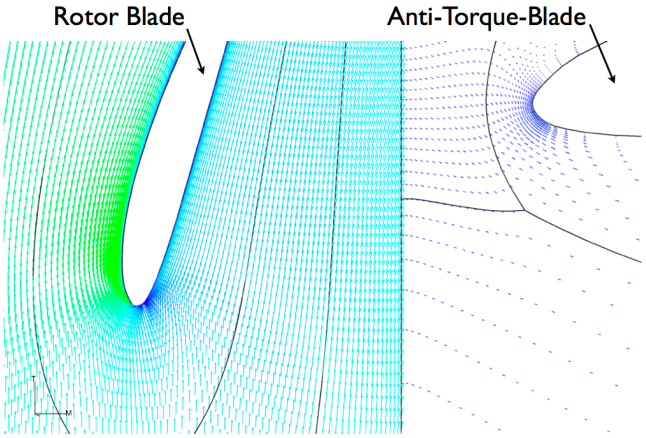

Fig. 4. Relative speed orientation of the airflow near the rotor and the anti-torque-blades (2D).

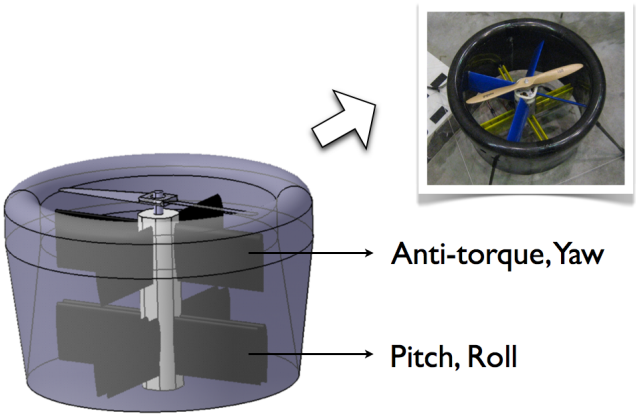

Fig. 5. Two blade rows must produce sufficient anti-torque, pitch, roll and yaw control.

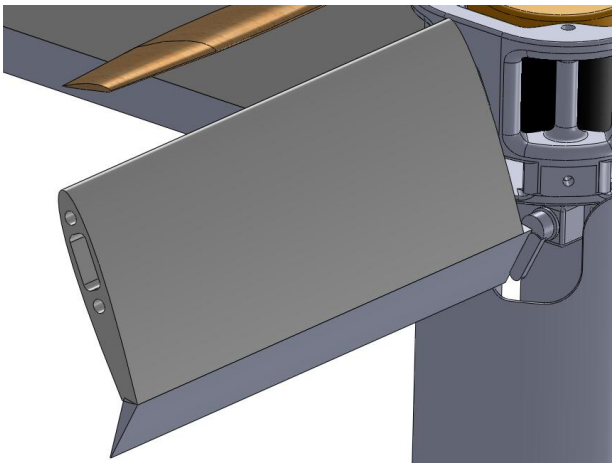

Fig. 6. The anti-torque blades are equipped with a trailing edge flap.

TABLE II
GENERAL AERODYNAMIC CHARACTERISTICS

Ratio of duct LE radius to rotor diameter (-)	0.11
Duct chord (m)	0.30
Duct profile thickness-to-chord ratio (-)	0.15
a_d	1.1

between the rotor and duct to be minimized. This minimization is somewhat tricky since on the one hand it increases the possibility of an impact of the rotor with the duct wherein the batteries are installed, but on the other it is necessary to avoid detrimental aerodynamic interference losses [4] [6]. Lowering the structural weight normally results in a lower power consumption - unless one opts for a larger payload capability or more performance -, which in turn makes the installation of a less powerful propulsion system possible. The associated benefit is that the engine and its peripherals such as the batteries will be lighter, which again reduces the weight of the structure. Another important parameter is the position of the center of gravity relative to the rotor and the duct suspension planes since it influences the inertial forces exerted on the platform, the required aerodynamic forces to gain controlled flight and thus the necessary structural strength and associated weight [7]. The higher the center of gravity is positioned, the more control authority will be obtained, but one should avoid doing so by lengthening the duct and fuselage since this increases the weight of the platform, which is an unwanted effect for reasons explained before (Fig.7). The best way to comply with this condition is by installing the heaviest parts such as the batteries in the upper part of the platform.

Thorough FEM calculations in *Solidworks* allow optimizing the structure (Fig.8), while modal analysis will allow the rotor to work at frequencies sufficiently remote from the critical frequencies. Besides the use of carbon composites for the duct and fuselage skin, balsa wood was selected for the ribs of the control surfaces and the duct (Fig.9), while glass fiber reinforced plastics assure adequate strength for the installed landing gear.

V. FLIGHT CONTROL SYSTEM

Key elements of the flight control system are the inertial reference unit (IRU) and the control-electronics. These components must determine the position of the RUAV with respect to the earth coordinate system, steer the RUAV towards the selected waypoints and targets and keep a balanced flight at all times (including takeoff and landing). This is done with the aid of a GPS receiver, accelerometers, an electronic compass and gyroscopes, all integreted in the IRU, installed in the fuselage of the RUAV. The IRU-signals enter an in-house made controller wherein consequently software determines the propeller angular velocity and the required angle settings of the control blades, brought in position via servos installed in the fuselage, and eventually used to control the position of the aircraft (Fig.10). Table III summarizes technical information of the IRU unit. The IRU unit should normally be installed in the center of gravity, which requires a detailed CAD analysis. In order to electrically uncouple the flight control system as from the propulsion system, a separate battery pack is foreseen in the fuselage.

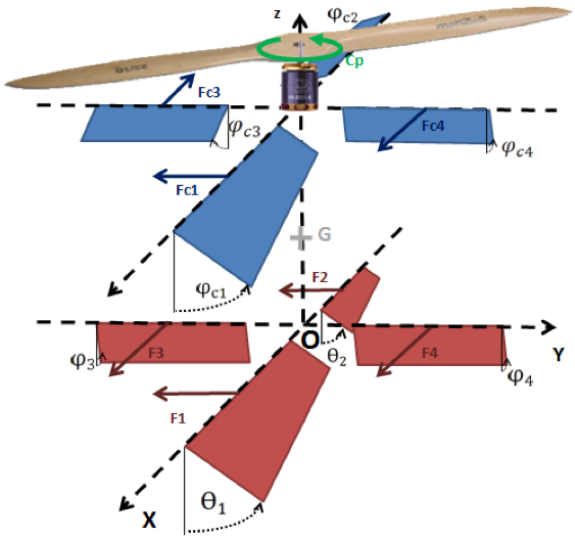

Fig. 7. Sufficient distance between the center of gravity (G) and the application points of the control blade forces must be strived for.

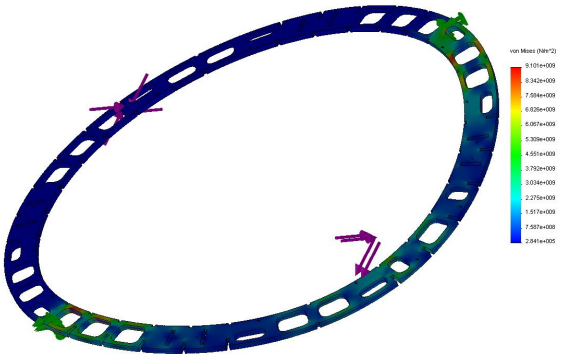

Fig. 8. The balsa ribs are fixed on PMMA rings (test configuration). Each ring is a critical part : it keeps the rather heavy batteries in place and guarantees the circular shape of the duct.

TABLE III
MTi-G Inertial Reference Unit

GPS	
Receiver type	16 channels, L1 frequency, C/A code
GPS Update Rate (Position / Velocity)	4Hz / 120Hz
Accuracy Position SPS	2.50 m
Maximum altitude	18 km
Maximum velocity	515 m/s

Interfacing	
Digital	RS-232
Operating voltage	4.5-30 V
Power consumption	540 mW

General data	
Dimensions (WxDxH)	58x58x33 mm
Mass	68 g
Ambient temperature operating range	-20 . . . 55°C

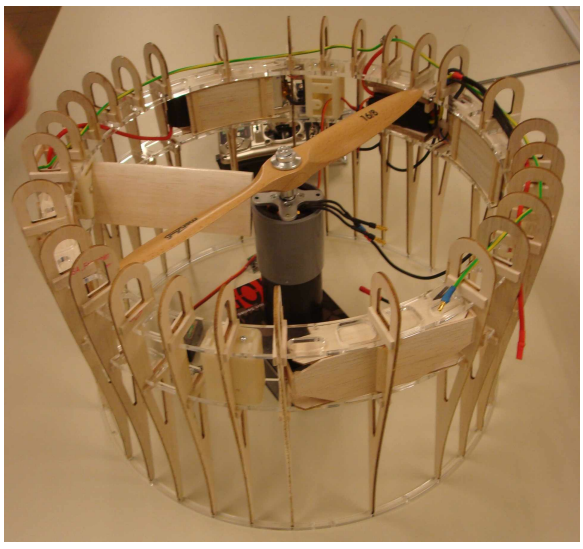

Fig. 9. Extensive use of balsa wood helps to reduce the weight significantly.

Fig. 10. MTi-G IRU (orange box) and circular print plates upon which CPUs will be soldered. The circular shape of the print plates increases the useful area available for the electronic components and facilitates the installation and fixation when placed in the cylindrical fuselage.

VI. Data transmission and camera

Besides the requirement that the RUAV must be able to fly its mission autonomously at all times, a live video stream must be guaranteed to enable the operator to inspect the (pre)determined targets, while a flight command data link must assure the ability to instantly modify or cancel parts of the flight plan. The live video stream undergoes special filtering to stabilize the image, even when a high optical zoom is selected. This capability allows the operator to recognize targets more easily, which increases the efficiency of the platform and probably its operational range (more flying time, less detecting time). The camera will be installed in the belly of the fuselage and is fed by the flight control system battery pack. A sophisticated mechanical system allows the camera to pitch horizontally and vertically (Fig.11). Table IV gives an overview of typical characteristics of the camera.

TABLE IV
CAMERA SPECIFICATIONS

SONY FCB-IX11AP Camera	
Image sensor	1/4 type Exview HAD CCD
Effective pixels	440 000
Lens optical zoom	10x
Lens digital zoom	4 x
Minimum illumination	1.5 lux
Video output	PAL
Operating temperature	0 . . . 50°C
Power consumption	1.6 . . . 2.1 W
Supply voltage range	6 . . . DC 12V
Mass	95 g
Dimensions (WxHxD)	39.3x44.8x65 mm

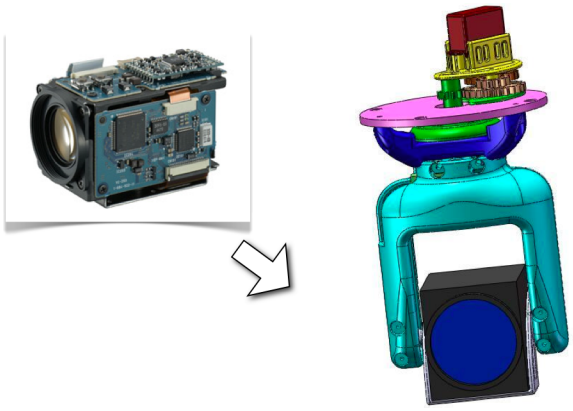

Fig. 11. A powerful lightweight camera installed on a flexible platform makes a perfect combination.

VII. CONCLUSIONS AND PERSPECTIVES

Until now, only flight tests at slow horizontal speeds and hover were performed but without the flight control system incorporating the IRU (Fig.12). Piloting the helicopter manually remains a demanding job for the pilot because of the severe coupling between the pitch, roll and yaw axes. This clearly proves that a sophisticated flight control system will be indispensable. Wind tunnel tests evaluating a broad flight envelope are due anytime soon, which will allow to examine and expand the flight envelope of the RUAV considerably and in a safe way, directly or indirectly via CFD. As a consequence of the chosen RUAV concept, better hover performance can be achieved thanks to the installation of a duct, however it was shown that then the aerodynamic and structural design are heavily interrelated. Also, special attention was given to the fact that the position of the center of gravity significantly affects the aerodynamic and structural design parameters and should therefore be closely monitored with the aid of a CAD program. Although not yet apt to fly autonomously, the Dulbema is on the verge of exploring its potential.

Fig. 12. Hover flight without the installation of the complex and expensive IRU-equipped flight control system.

REFERENCES

[1] Hendrick, P., Depouhon, A., *Optimal control strategies for a ducted RUAV*, RTO AVT, Firenze, Italy, 2007.

[2] Parlett, L.P., *Aerodynamic characteristics of a small-scale shrouded propeller at angles of attack from 0° to 90°*, NACA TN 3547, Langley Aeronautical Laboratory, Langley Field, VA, USA, 1955.

[3] Leishman, J.G., *Principles of helicopter aerodynamics*, Cambridge University Press, Cambridge, UK, 2002.

[4] Pereira, J. and Chopra, I., *Effect of shroud design variables on hover performance of a shrouded-rotor for micro air vehicle applications*, American Helicopter Society Paper AHS 2005, Alfred Gessow Rotorcraft Center, Department of Aerospace Engineering, University of Maryland, College Park, MD, 2005.

[5] Newman, S., *The foundations of helicopter flight*, Butterworth Heineman, Oxford, UK, 1994.

[6] Ahn, J., *Parametric design of a ducted fan system in forward flight and static conditions*, American Helicopter Society Paper AHS 2005, Dept. of Aerospace Engineering, Sejong University, Seoul, Korea, 2005.

[7] Josephs, H. and Huston, R., *Dynamics of mechanical systems*, CRC Press, Florida, USA, 2002.

Proceedings of the 8th National Congress on Theoretical and Applied Mechanics, May 28-29, Brussels, Belgium.

Multibody modelling of a travelling wave linear piezomotor

Jean-François Collard[1], Christophe Vloebergh[1], Bruno Dehez[1], Paul Fisette[1]
[1]Université catholique de Louvain, Center for Research in Mechatronics
Place du Levant 2 – 1348 Louvain-la-Neuve
emails: jf.collard@uclouvain.be, christophe.vloebergh@uclouvain.be,
bruno.dehez@uclouvain.be, paul.fisette@uclouvain.be

Abstract— **To predict the performance of a travelling wave linear piezoelectric actuator, the deformations of the beam through which the wave propagates is modelled via a rigid-multibody approach: the beam is considered as a succession of rigid segments linked by revolute joints with a given stiffness. Contrary to a finite-element modelling of the beam, this finite-segment model enables faster simulations and moreover an easier implementation of the contact model between the beam and a slider moving on it. In this work, it has been proposed to interpolate in a smooth manner between the positions and velocities of the rigid segments in order to smooth the contact model and therefore avoid numerical discontinuity problems. The simulation results are very promising and an accurate identification of the model parameters with the experimental results of a prototype will allow us to optimize the performance of the actuator.**

Keywords— **piezoelectric actuator, linear piezomotor, finite-segment modelling, multiphysic modelling.**

I. Introduction

TRAVELLING wave linear piezoelectric actuators use the limited deformations of piezoelectric ceramics to produce linear displacements of large amplitude. The working principle of these actuators is the following: when a travelling wave propagates through a beam, each material point on the beam surface describes an elliptic motion. Therefore, when a rigid slider is placed in contact with the beam, these material points successively enter into contact with the slider and transfer to it, by friction, a motion in a direction opposite to that of the travelling wave.

Obviously, the effective generation of a travelling wave is the key point for the efficiency of the driving system. There exist two main ways of generating such a travelling wave in a finite-length elastic beam.

The first one consists in locating two piezoelectric actuators at both ends of the beam. One is used to generate a wave while the other is used to absorb it in order to prevent the appearance of standing waves due to the reflection. However, in practice, it is difficult to find the right impedance of the absorbing actuator because it varies with the load, the temperature and the frequency (see [5]).

Another way of generating a travelling wave consists in using two piezoelectric actuators located at a specific distance from the tips of the beam. These distances are chosen in order to preferentially excite two similar standing waves space-shifted and time-shifted of a quarter period, their superposition producing a travelling wave [3]. The main advantage of this method is its easiness. For instance, the motion direction can be reversed by simply changing the phase shift from 90° to -90°. Nevertheless, it does not work at a resonant frequency of the beam, the amplitude of oscillations being therefore severely limited. In this work, this second method is implemented.

One of the main issues of this linear actuator system is how to model the friction contact between the flexible beam and the slider. The behaviour of the flexible beam can be simulated using analytical or finite-element models but these approaches cannot easily deal with the contact model when simulating the displacement of the slider on the beam [1]. This is why a model for a travelling wave linear piezomotor has been developed using a finite-segment multibody approach (see [2]) combined with an interpolation smoothing technique to solve the geometrical contact problem. The kinematic and dynamical equations of this model have been automatically generated using the *Robotran*© software, which provides the equations in a symbolic form using recursive algorithms [4]. The generated code is thus compact and efficient for simulations of large systems such as the finite-segment formulation used here.

In the following, the multibody model of the flexible beam and its interaction with the slider are first described. Then, the simulation results of the slider displacement on the beam are presented. Finally, some prospects will given in conclusion.

II. Multibody Model

The finite-segment model itself is described first before giving the details of the contact model between the beam and the slider.

A. Finite-Segment Model of the Flexible Beam

As proposed in [2], the basic idea of this multibody model is to consider the beam as a succession of small rigid segments. To model the bending motion of the beam, these segments are linked by revolute joints with stiffness parameter k_{ij} between two segments i and j (see Fig. (1)). It is also possible to consider structural damping effects

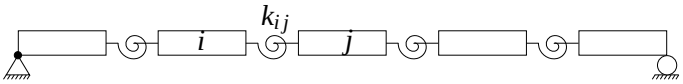

Fig. 1. Finite-segment model

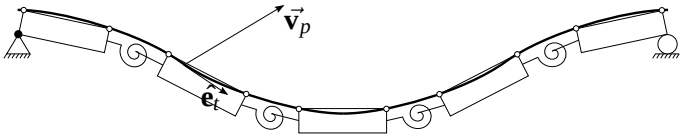

Fig. 2. Spline interpolation of the contact surface of the beam

via lumped dashpots. The stiffness parameter k_{ij} is given by:

$$k_{ij} = \frac{2E_iE_jI_iI_j}{E_iI_jl_j + E_jI_il_i}, \tag{1}$$

where E_i and E_j are the Young's moduli, I_i and I_j are the geometrical moments of inertia of the cross-sections, l_i and l_j are the lengths of the respective segments. In this case of identical segments, Eq. (1) reduces to:

$$k_{ij} = \frac{E\,I}{l}, \tag{2}$$

where $E = E_i = E_j$, $I = I_i = I_j$ and $l = l_i = l_j$.

The formalism chosen to model the multibody system uses relative generalized coordinates q to describe the relative joint variables between each body. To simulate the multibody system, the equations of motion are integrated after the reduction of the differential-algebraic equations using the *Coordinate Partitioning method* [6]. This partitioning between independent and dependent coordinates must be carefully performed since it may greatly affect the behaviour of the integrator in the case of closed-loop systems with long kinematic chains. The finite-segment approach provides excellent results for such a system with small deformations: the results of modal analysis are very close to the analytical solutions even for higher normal modes, providing that the number of segments is sufficient. For example, it has been shown in [1] that 49 segments are needed to obtained the right frequency of the 22^{nd} mode (4467 Hz) with a good accuracy (relative error less than 1%).

B. Friction Contact Model

The main advantage of the multibody formulation of this system is to be able to consider pretty easily the friction contact between the beam and a slider moving over it. Computing the contact force at a given instant requires:

- finding the contact point or contact surface;
- determining the constitutive law applying the contact force to each body.

In this preliminary model, it is assumed that the slider is a point with mass m_s and the chosen constitutive law of the tangential dry friction force F has the following form:

$$F = -\mu\, m_s\, g\, \tanh\left(K\left(\dot{q}_t^{slider} - \dot{q}_t^{beam}\right)\right), \tag{3}$$

where μ is the coefficient of kinetic friction, g is gravity, $\dot{q}_t^{slider}$ and $\dot{q}_t^{beam}$ are, respectively, the velocity of the slider and the velocity of the beam, along the tangential direction with respect to the beam, and K is the slope of the hyperbolic tangent at origin. Coefficients μ and K will be identified experimentally.

Since the beam is modeled as a succession of rigid segments, the contact line is thus piecewise linear with a discontinuous tangential velocity and may lead to numerical difficulties, like in the case of cam-follower contact modelling [7]. Therefore, it is proposed here to make the shape and the slope of the beam continuous when determining the contact point and the tangential direction. A possibility is to use a spline interpolation between the upper-corner point positions of each segment as shown in Fig. (2). Assuming that the slider always remains on the beam, the contact point is therefore taken at the longitudinal coordinate of the slider on the correct spline section. The tangential velocity of the beam $\dot{q}_t^{beam} = \vec{\mathbf{v}}_p \cdot \hat{\mathbf{e}}_t$ (see Fig. (2) is also computed thanks to a spline interpolation on the joint point velocities projected along the tangential direction.

III. Simulation

In order to produce a travelling wave, the piezoelectric actuators must vibrate at a given frequency f and must be located at a given distance d from both ends of the beam as explained in [1]. In this example, since the beam is made of aluminum and is 500 mm long, 20 mm large and 1 mm thick, the corresponding values of f and d are: $f = 4276$ Hz and $d = 11.6$ mm. For this frequency, 49 segments are sufficient to obtain a reasonable accuracy on the closest normal frequencies as explained in [1].

As a first result (see Fig. (III) and Fig. (III)), the displacement of the slider was simulated from 0 to 1 millisecond, considering only the tangential contact force acting on the slider by a segment of the beam. The slider is assumed to stick to the spline-interpolated beam. Figure (III) shows that the slider moves from the center of the beam (longitudinal position = 0 m) towards the left (negative position). Its mean longitudinal velocity is 1.5 cm/s. In Fig. (III), it is observed that the tangential contact force varies abruptly between its saturation values of $\pm 2 \cdot 10^{-3}$ N, according to Eq. (3). However its mean value is negative as is the mean tangential velocity of a beam surface contact point.

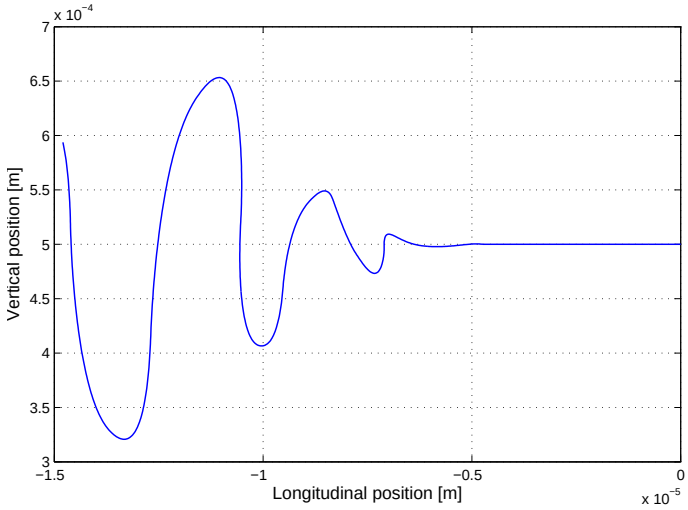

Fig. 3. Simulation results of slider trajectory from 0 to 1 ms when the beam is excited at 4276 Hz

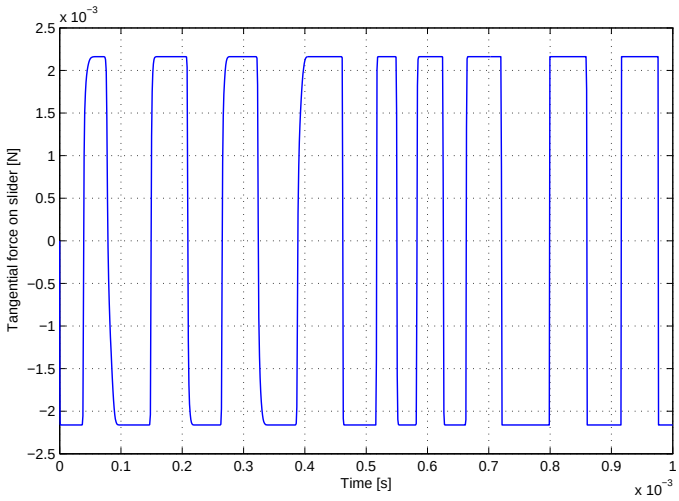

Fig. 4. Simulation results of the tangential contact force on slider when the beam is excited at 4276 Hz

IV. Conclusion and Prospects

This paper presents a rigid-multibody modelling approach to simulate the behaviour of a linear piezoelectric actuator made of a flexible beam. With respect to a finite-element modelling approach, this method is less time-consuming and enables a pretty easy implementation of a contact model between the beam and a slider body moving on it. This contact model has been implemented with a smoothing interpolation of the contact line to satisfy the real physical system geometry and to avoid numerical difficulties. The simulation of this model has shown very promising results to predict the displacement of the slider. A particular attention has been paid to time-integration accuracy and efficiency.

To refine the model, multiple contact points between the beam and the slider will be considered, as should be the case. The design of a prototype will also be made to identify the model parameters with the experimental results. Another improvement will be the implementation of an electromechanical model of the piezoelectric actuators themselves, called Mason's model [8]. This will lead to a full integrated multiphysics model of the system, including the multibody model of the beam, the electromechanical model of the piezoelectric actuators and a controller model. Thanks to simulations of this multiphysic model after identification with the experimental prototype, the slider motion could be predicted and the actuator performance could be optimized.

Acknowledgements

This research has been sponsored by the Région Wallonne (Division de la Recherche et de la Coopération scientifique). The scientific responsibility is assumed by its authors.

References

[1] C. Vloebergh, J.F. Collard, B. Dehez, F. Labrique. Study of a Travelling Wave Linear Piezomotor Using Analytical, Finite-Element and Lumped Parameter Models. *Proceedings of the Electrimacs 2008 Conference*, Montral, Canada, June 9–11, 2008.

[2] R.L. Huston, Y. Wang, Flexibility Effects in Multibody Systems In: M.F.O.S. Pereira, J.A.C. Ambrosio, *Computer-Aided Analysis of Rigid and Flexible Mechanical Systems*, NATO ASI Series E: Applied Sciences, **268**, Dordrecht, 351–376, 1993.

[3] B.G. Loh, P.I. Ro, An Object Transport System Using Flexural Ultrasonic Progressive Waves Generated by Two-Mode Excitation. *IEEE transactions on ultrasonics, ferroelectrics, and frequency control*, **47**, 994–999, 2000.

[4] J.C. Samin, P. Fisette, *Symbolic Modeling of Multibody Systems*, Kluwer Academic Publishers, Dordrecht, 2003.

[5] H. Sodano, D. Inman, G. Park, A review of power harvesting from vibration using piezoelectric materials. *The Shock and Vibration Digest*, **36**, 197–205, 2004.

[6] R.-A. Wehage, E.-J. Haug, Generalized coordinate partitioning for dimension reduction in analysis of constrained dynamic systems. *Journal of Mechanical Design*, **134**, 174–190, 1982.

[7] P. Fisette, J.M. Pterkenne, B. Vaneghem, J.C. Samin, Generalized coordinate partitioning for dimension reduction in analysis of constrained dynamic systems. *Nonlinear Dynamics*, **22**, 335–359, 2000.

[8] W.P. Mason, A Phenomenological Derivation of the First- and Second-Order Magnetostriction and Morphic Effects for a Nickel Crystal. Phys. Rev. **82**, 715, 1951.

Proceedings of the 8th National Congress on Theoretical and Applied Mechanics, May 28-29, Brussels, Belgium.

Hamiltonization and geometric integration of nonholonomic mechanical systems

T. Mestdag[1], A.M. Bloch[2] and O.E. Fernandez[2]
[1]Department of Mathematical Physics and Astronomy, Ghent University
Krijgslaan 281, S9, 9000 Gent, Belgium
[2]Department of Mathematics, University of Michigan
530 Church Street, Ann Arbor, MI-48109, USA
email: tom.mestdag@ugent.be, abloch@umich.edu, oscarum@umich.edu

Abstract— **In this paper we study a Hamiltonization procedure for mechanical systems with velocity-depending (nonholonomic) constraints. We first rewrite the nonholonomic equations of motion as Euler-Lagrange equations, with a Lagrangian that follows from rephrasing the issue in terms of the inverse problem of Lagrangian mechanics. Second, the Legendre transformation transforms the Lagrangian in the sought-for Hamiltonian. As an application, we compare some variational integrators for the new Lagrangians with some known nonholonomic integrators.**

Keywords— **nonholonomic systems, Lagrangian and Hamiltonian formalism, inverse problem, geometric integration.**

I. Introduction

MANY interesting mechanical systems are subject to additional velocity-dependent (i.e. nonholonomic) constraints. Typical engineering problems that involve such constraints arise for example in robotics, where the wheels of a mobile robot are often required to roll without slipping, or where one is interested in guiding the motion of a cutting tool.

The direct motivation for our paper [2] was to be found in interesting results that appeared in [3], where the authors propose a way to quantize some of the well-known classical examples of nonholonomic systems. On the way to quantization, the authors propose an alternative Hamiltonian representation for those nonholonomic systems. However, the "Hamiltonization" method introduced in [3] can only be applied to systems for which the solutions are already known explicitly.

Nonholonomic systems have a more natural description in the Lagrangian framework. In [2], we explained how one can associate to the nonholonomic equations of motion a family of systems of second-order ordinary differential equations and we applied the conditions of the inverse problem of the calculus of variations on those associated systems to search for the existence of a regular Lagrangian. (The inverse problem of the calculus of variations deals with the question of whether or not a given system of second-order differential equations is equivalent with the Euler-Lagrange equations of a yet to be determined regular Lagrangian, see e.g. [12]). If such an unconstrained regular Lagrangian exists for one of the associated systems, we can always find an associated Hamiltonian by means of the Legendre transformation. Since our method only made use of the equations of motion of the system it did not depend on the knowledge of its explicit solutions.

A system for which no exact solutions are known can only be integrated by means of numerical methods. In addition to the above mentioned application to quantization, our Hamiltonization method may also be useful from this point of view. Numerical integrators that preserve the underlying geometric structure of a system are called geometric integrators. A geometric integrator of a Lagrangian system uses a discrete Lagrangian that resembles as much as possible the continuous Lagrangian (see e.g. [11]). On the other hand, the succes of a so-called nonholomic integrator (see e.g. [4], [7]) relies not only on the choice of a discrete Lagrangian but also on the choice of a discrete version of the constraint manifold. It seems therefore reasonable that if a free Lagrangian for the nonholonomic system exists, the Lagrangian integrator may perform better than a nonholonomic integrator with badly chosen discrete constraints.

In the next section we recall the set-up and the main results of our paper [2]. In section III we compare some nonholonomic and variational geometric integrators for a few of the classical nonholonomic systems. In section IV, we indicate some ideas on how we wish to extend the results of this paper.

II. A class of nonholonomic systems

We will consider only a certain class of nonholonomic systems on $\mathbb{R}^n$: We will assume that the configuration space of the system is a space with coördinates (r_1, r_2, s_α), that the Lagrangian of the system is given by the function

$$L = \frac{1}{2}(I_1\dot{r}_1^2 + I_2\dot{r}_2^2 + \sum_\alpha I_\alpha \dot{s}_\alpha^2) \tag{1}$$

and that the nonholonomic constraints are all of the form

$$\dot{s}_\alpha = -A_\alpha(r_1)\dot{r}_2. \tag{2}$$

The nonholonomic equations of motion follow from d'Alembert's priciple (see e.g. [1]). For systems in our class they are given by the equations

$$\begin{cases} \dfrac{d}{dt}\Big(\dfrac{\partial L}{\partial \dot{r}_1}\Big) - \dfrac{\partial L}{\partial r_1} = 0, \\ \dfrac{d}{dt}\Big(\dfrac{\partial L}{\partial \dot{r}_2}\Big) - \dfrac{\partial L}{\partial r_2} = \lambda_\alpha A_\alpha, \\ \dfrac{d}{dt}\Big(\dfrac{\partial L}{\partial \dot{s}_\alpha}\Big) - \dfrac{\partial L}{\partial s_\alpha} = \lambda_\alpha, \end{cases}$$

together with the constraint equations (2). After eliminating the Lagrange multipliers by means of the constraints, one gets

$$\begin{cases} \ddot{r}_1 = 0, \\ \ddot{r}_2 = -N^2 K \dot{r}_1 \dot{r}_2, \\ \dot{s}_\alpha = -A_\alpha \dot{r}_2, \end{cases} \tag{3}$$

where $N(r_1) = (I_2 + \sum_\alpha I_\alpha A_\alpha^2)^{-\frac{1}{2}}$ is related to the invariant measure of the system and $K = \sum_\beta I_\beta A_\beta A'_\beta$. with $A'_\beta = \partial_{r_1} A_\beta$.

Some basic examples of nonholonomic systems that lie in this class are the following ones. The classic example of a nonholonomically constrained free particle has a Lagrangian and constraint given by

$$L = \frac{1}{2}\left(\dot{x}^2 + \dot{y}^2 + \dot{z}^2\right) \quad \text{and} \quad \dot{z} + x\dot{y} = 0.$$

A knife edge on a horizontal plane corresponds physically to a blade with mass m moving in the xy plane at an angle ϕ to the x-axis. Its Lagrangian and constraint are given by

$$L = \frac{1}{2}m(\dot{x}^2+\dot{y}^2)+\frac{1}{2}J\dot{\phi}^2 \quad \text{and} \quad \dot{x}\sin(\phi)-\dot{y}\cos(\phi)=0.$$

Also the vertically rolling disk is an example in our class. The assumption that the disk rolls without slipping over the plane gives rise to nonholonomic constraints. Let R be the radius of the disk. If the triple $(x,y,z=R)$ stands for the coördinates of its centre of mass, φ for its angle with the (x,z)-plane and θ for the angle of a fixed line on the disk and a vertical line, then the nonholomic constraints are of the form

$$\dot{x} = R\cos\varphi\dot{\theta} \quad \text{and} \quad \dot{y} = R\sin\varphi\dot{\theta}.$$

The Lagrangian of the disk is

$$L = \frac{1}{2}M(\dot{x}^2+\dot{y}^2)+\frac{1}{2}I\dot{\theta}^2+\frac{1}{2}J\dot{\varphi}^2,$$

where $I=\frac{1}{2}MR^2$ and $J=\frac{1}{4}MR^2$ are the moments of inertia and M is the total mass of the disk. For the vertically rolling disk N is a constant and $K=0$.

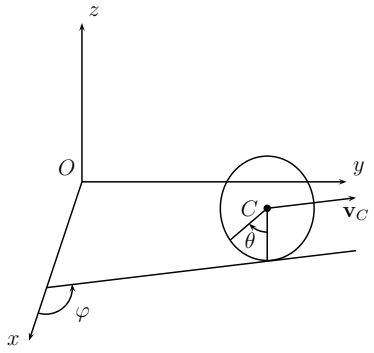

Fig. 1. The vertically rolling disk

Finally, also the examples of the mobile robot with fixed orientation and the two-wheeled carriage (see e.g. [8]) lie within our class.

The equations of motion (3) are a mixed set of first- and second-order differential equations. On the other hand, the Euler-Lagrange equations

$$\frac{d}{dt}\left(\frac{\partial\tilde{L}}{\partial\dot{q}^i}\right)-\frac{\partial\tilde{L}}{\partial q^i}=0$$

of a regular Lagrangian $\tilde{L}$ are second-order differential equations (only) [The tilde in $\tilde{L}$ will always denote that the Lagrangian is free, and that it should not be confused with the original Lagrangian L of the nonholonomic system.]. We therefore need a way to associate a second-order system to our nonholonomic system. One possible choice of doing so is the system

$$\begin{cases} \ddot{r}_1 = 0, \\ \ddot{r}_2 = -N^2K\dot{r}_1\dot{r}_2, \\ \ddot{s}_\alpha = -\left(A'_\alpha - N^2KA_\alpha\right)\dot{r}_1\dot{r}_2. \end{cases} \tag{4}$$

The above second-order system has the property that its solution set contains, among other, also the solutions of the nonholonomic dynamics (3) when restricted to the constraints. Another choice for an 'associated system' with the same property is e.g.

$$\begin{cases} \ddot{r}_1 = 0, \\ \ddot{r}_2 = -N^2K\dot{r}_1\dot{r}_2, \\ \ddot{s}_\alpha = (A'_\alpha - N^2KA_\alpha)\dot{r}_1\left(\dfrac{\dot{s}_\alpha}{A_\alpha}\right) \end{cases} \tag{5}$$

(no sum over α). It is clear, that there are in fact an infinite number of such associated second-order systems, but we will concentrate in this paper on the above two. For some other possible choices, see [2].

Proposition 1: 1. There does not exist a regular Lagrangian whose Euler-Lagrange equations are equivalent with the second-order system (4) (for the classical examples cited above).
2. The Euler-Lagrange equations of the Lagrangian

$$\tilde{L} = \frac{1}{2}I_1\dot{r}_1^2+\frac{1}{2N}\left(C_2\frac{\dot{r}_2^2}{\dot{r}_1}+\sum_\beta C_\beta\frac{\dot{s}_\beta^2}{A_\beta\dot{r}_1}\right) \quad (C_\alpha\neq 0) \tag{6}$$

are equivalent with the second-order system (5). If the invariant measure density N is a constant, then also

$$\tilde{L} = \frac{1}{2}I_1\dot{r}_1^2+\frac{1}{2}I_2\dot{r}_2^2+\frac{1}{2N}\sum_\beta a_\beta\frac{\dot{s}_\beta^2}{A_\beta\dot{r}_1} \quad (C_\alpha\neq 0) \tag{7}$$

is a regular Lagrangian for the system (5).

Proof: We give here only an outline of the method we've used to prove the statements. For full details, see [2]. Assume we are given a system of second-order ordinary differential equations

$$\ddot{q}^i = f^i(q,\dot{q}).$$

The search for a regular Lagrangian is known in the literature as 'the inverse problem of the calculus of variations', and has a long history (for a recent survey on this history, see e.g. [10] and the long list of references therein). In order for a regular Lagrangian $\tilde{L}(q,\dot{q})$ to exist we must be able to find functions $g_{ij}(q,\dot{q})$, so-called multipliers, such that

$$g_{ij}(\ddot{q}^j-f^j) = \frac{d}{dt}\left(\frac{\partial\tilde{L}}{\partial\dot{q}^i}\right)-\frac{\partial\tilde{L}}{\partial q^i}.$$

It can be shown [6], [12] that the multipliers must satisfy

$$\begin{aligned} &\det(g_{ij})\neq 0, \qquad g_{ji}=g_{ij}, \qquad \frac{\partial g_{ij}}{\partial\dot{q}^k}=\frac{\partial g_{ik}}{\partial\dot{q}^j}; \\ &\Gamma(g_{ij})-\nabla_j^k g_{ik}-\nabla_i^k g_{kj}=0, \\ &g_{ik}\Phi_j^k = g_{jk}\Phi_i^k; \end{aligned}$$

where

$$\nabla_j^i = -\frac{1}{2}\partial_{\dot{q}^j}f^i$$

and

$$\Phi_j^k = \Gamma\left(\partial_{\dot{q}^j}f^k\right)-2\partial_{q^j}f^k-\frac{1}{2}\partial_{\dot{q}^j}f^l\partial_{\dot{q}^l}f^k.$$

The symbol Γ stands for the vector field $\dot{q}^i\partial_{q^i} + f^i\partial_{\dot{q}^i}$ that can naturally be associated to the system $\ddot{q}^i = f^i(q,\dot{q})$. Conversely, if one can find functions g_{ij} satisfying these conditions then the equations $\ddot{q}^i = f^i$ are derivable from a regular Lagrangian. Moreover, if a regular Lagrangian $\tilde{L}$ can be found, then its Hessian $\dfrac{\partial^2\tilde{L}}{\partial\dot{q}^i\partial\dot{q}^j}$ is a multiplier.

The above conditions are generally referred to as the Helmholtz conditions. They are a mixed set of coupled algebraic and PDE conditions in (g_{ij}). We will refer to the penultimate condition as the '∇- condition,' and to the last one as the 'Φ-condition.' The algebraic Φ-conditions are of course the most interesting to start from. In fact, we can easily derive more algebraic conditions (see e.g. [5]). For example, by taking a Γ-derivative of the Φ-condition, and by replacing $\Gamma(g_{ij})$ everywhere by means of the ∇-condition, we arrive at a new algebraic condition of the form

$$g_{ik}(\nabla\Phi)^k_j = g_{jk}(\nabla\Phi)^k_i,$$

where

$$(\nabla\Phi)^i_j = \Gamma(\Phi^i_j) - \nabla^i_m\Phi^m_j - \nabla^m_j\Phi^i_m.$$

This $(\nabla\Phi)$-condition will, of course, only give new information as long as it is independent from the Φ-condition (this will not be the case, for example, if the commutator of matrices $[\Phi,\nabla\Phi]$ vanishes). One can repeat the above process on the $(\nabla\Phi)$-condition, and so on to obtain possibly independent $(\nabla\ldots\nabla\Phi)$-conditions. A second route to additional algebraic conditions arises from the derivatives of the Φ-equation in $\dot{q}$-directions. One can sum up those derived relations in such a way that the terms in $\partial_{\dot{q}_k}g_{ij}$ disappear on account of the symmetry in all their indices. The new algebraic relation in g_{ij} is then of the form

$$g_{ij}R^j_{kl} + g_{lj}R^j_{ik} + g_{kj}R^j_{li} = 0,$$

where

$$R^j_{kl} = \partial_{\dot{q}^j}(\Phi^k_i) - \partial_{\dot{q}^i}(\Phi^k_j).$$

As before, this process can be continued to obtain more algebraic conditions. Also, any mixture of the above mentioned two processes leads to possibly new and independent algebraic conditions. Once we have used up all the information that we can obtain from this infinite series of algebraic conditions, we can start looking at the partial differential equations in the ∇-conditions.

Let us now come back to the second-order systems (4) and (5) at hand. The proof of the proposition relies on the fact that for the first systems (4), the only matrices (g_{ij}) that satisfy the first few algebraic conditions must be non-singular. On the other hand, the two Lagrangians for the system (5) follow from an analysis of the Helmholtz conditions with carefully chosen anszatzes. For more details, see [2]. ∎

Remark that the Lagrangians are not defined for $\dot{r}_1 = 0$, and we will in general exclude the solutions with that property from the further considerations in this paper. Any regular Lagrangian system with Lagrangian $\tilde{L}$ can be transformed into a Hamiltonian one, by making use of the Legendre transformation

$$(q^i,\dot{q}^i) \mapsto (q^i, p_i = \frac{\partial\tilde{L}}{\partial\dot{q}^i}).$$

The corresponding Hamiltonian is then

$$\tilde{H} = p_i\dot{q}^i - \tilde{L}.$$

Similarly, the Legendre transformation maps the constraints, viewed as a submanifold of the tangent manifold, onto a submanifold in the cotangent manifold.

Proposition 2: Using the Legendre transformation, the Hamiltonian that corresponds to the Lagrangian (6) is given by

$$\tilde{H} = \frac{1}{2I_1}\left(p_1 + \frac{1}{2}N\left(\frac{p_2^2}{C_2} + \sum_\beta A_\beta\frac{p_\beta^2}{C_\beta}\right)\right)^2.$$

The corresponding constraints are

$$C_2p_\alpha = -C_\alpha p_2.$$

If N is constant, the Hamiltonian that corresponds to the Lagrangian (7) is

$$\tilde{H} = \frac{1}{2I_2}p_2^2 + \frac{1}{2I_1}\left(p_1 + \frac{1}{2}N\left(\sum_\beta\frac{A_\beta}{a_\beta}p_\beta^2\right)\right)^2,$$

and the constraints transform into

$$I_2N\dot{r}_1p_\alpha + a_\alpha p_2 = 0,$$

where $\dot{r}_1 = (p_1 + \frac{1}{2}N\sum_\alpha A_\alpha p_\alpha^2/a_\alpha)/I_1$.

In [2], [9] we explain how the above Hamiltonians can be directly derived from Pontryagin's Maximum principle.

III. Geometric integrators

A. Set-up

As we explained in the introduction, there are now two ways to compute a numeric approximation of a solution of a system in our class: we can use either a nonholonomic integrator for the original Lagrangian (1) and constraints (2) , or we can use a variational integrator for one of the Lagrangians (6) and (7) we have found in Proposition 1. Let us come to some details.

Geometric integrators are integrators that preserve the underlying structure of the system. In particular, variational integrators are integrators that are derived from a discrete version of Hamilton's principle. From this discrete variational principle one obtains the so-called discrete Euler-Lagrange equations as follows. For a mechanical system with Lagrangian L, one needs to choose a discrete Lagrangian $L_d(q_1,q_2)$ (a function on $Q\times Q$ which resembles as close as possible the continuous Lagrangian). A solution $q(t)$ is then discretised by an array q_k which are the solutions of the so-called discrete Euler-Lagrange equations

$$D_1L_d(q_k,q_{k+1}) + D_2L_d(q_{k-1},q_k) = 0. \tag{8}$$

These integrators preserve the symplectic and conservative nature of the algorithms. It is important to realize that a different choice for the discrete Lagrangian may lead to a different geometric integrator. The presence of additional holonomic constraints (i.e. 'integrable' nonholonomic constraints) can be included by introducing Lagrange's multipliers.

On the other hand, for a nonholonomic integrator of a nonholonomic system with Lagrangian L and constraints $\omega^a(q)\dot{q}^a =$

0, we need to choose both a discrete Lagrangian L_d and discrete constraint functions ω_d^a on $Q \times Q$. The nonholonomic discrete equations are then

$$\begin{cases} D_1 L_d(q_k, q_{k+1}) + D_2 L_d(q_{k-1}, q_k) = (\lambda_k)_a \omega^a(q_k), \\ \omega_d^a(q_k, q_{k+1}) = 0. \end{cases} \tag{9}$$

Usually, if Q is a vector space, one takes the discretization in one of the following ways (for certain α and certain h):

$$L_d(q_1, q_2) = L\left(q = (1-\alpha)q_1 + \alpha q_2, \dot{q} = \frac{q_2 - q_1}{h}\right), \tag{10}$$

$$\omega_d^a(q_1, q_2) = \omega_i^a\left(q = (1-\alpha)q_1 + \alpha q_2\right) \frac{q_2^i - q_1^i}{h}. \tag{11}$$

For the rest of the paper, we will concentrate on this discretization procedure. There are, however, many more possibilities to obtain a discrete Lagrangian and discrete constraints. For example, one could take a symmetrized version of the above procedure and use discrete Lagrangians and discrete constraints of the form

$$\begin{aligned} L_d(q_1, q_2) &= \frac{1}{2} L\left(q = (1-\alpha)q_1 + \alpha q_2, \dot{q} = \frac{q_2 - q_1}{h}\right) \\ &\quad + \frac{1}{2} L\left(q = \alpha q_1 + (1-\alpha)q_2, \dot{q} = \frac{q_2 - q_1}{h}\right), \\ \omega_d^a(q_1, q_2) &= \frac{1}{2} \omega_i^a\left(q = (1-\alpha)q_1 + \alpha q_2\right) \frac{q_2^i - q_1^i}{h} \\ &\quad + \frac{1}{2} \omega_i^a\left(q = \alpha q_1 + (1-\alpha)q_2\right) \frac{q_2^i - q_1^i}{h}. \end{aligned}$$

Also, if the system is invariant under a symmetry group, it is advantageous to construct the integrator in such a way that the discrete system inherits as many as possible of those symmetry properties, see e.g. [4].

The bottom line of the next sections is the following one. If a free Lagrangian for the nonholonomic system exists, it seems reasonable that the Lagrangian integrator may perform better than a nonholonomic integrator with badly chosen discrete constraints. In the next sections, we will test this conjecture on a few of the classical examples in our class: the vertically rolling disk, the knife edge and the nonholonomic particle. It will be convenient that for those systems an exact solution of the nonholonomic equations (3) is readily available.

B. The vertically rolling disk

For the vertically rolling disk, we have $(r_1, r_2, s_\alpha) = (\varphi, \theta, x, y)$. It is well-known that the solutions of the nonholonomic equations with initial conditions $u_\varphi = \dot{\varphi}(0) \neq 0$ and $u_\theta = \dot{\theta}(0)$ are all circles with radius $R(u_\theta/u_\phi)$:

$$\begin{aligned} \theta(t) &= u_\theta t + \theta_0, \qquad \varphi(t) = u_\varphi t + \varphi_0, \\ x(t) &= \left(\frac{u_\theta}{u_\varphi}\right) R \sin(\varphi(t)) + x_0, \\ y(t) &= -\left(\frac{u_\theta}{u_\varphi}\right) R \cos(\varphi(t)) + y_0. \end{aligned} \tag{12}$$

Let us put for convenience $M = 1$ and $R = 1$ and therefore $I = \frac{1}{2}$ and $J = \frac{1}{4}$. With that the (nonholonomic) Lagrangian and constraints are simply

$$L = \frac{1}{2}(\dot{x}^2 + \dot{y}^2) + \frac{1}{4}\dot{\theta}^2 + \frac{1}{8}\dot{\varphi}^2, \quad \dot{x} = \cos\varphi\dot{\theta}, \quad \dot{y} = \sin\varphi\dot{\theta}.$$

We will first compute the solution of the discrete nonholonomic equations (9) with the discrete Lagrangian (10) and the discrete constraints (11). Second, since the vertically rolling disk is one of those examples with a constant invariant measure density N, we can choose a Lagrangian from the second type (7). The simplest choice is probably

$$\tilde{L} = 1/2\left(\dot{\varphi}^2 + \dot{\theta}^2 + \frac{\dot{x}^2}{\cos(\varphi)\dot{\varphi}} + \frac{\dot{y}^2}{\sin(\varphi)\dot{\varphi}}\right). \tag{13}$$

We now investigate the variational integrator of this Lagrangian, where the discrete Lagrangian is given by (10). We will fix h (changing it did not have a significant effect) and only concentrate on what happens if we keep α variable. In figure 2 we have

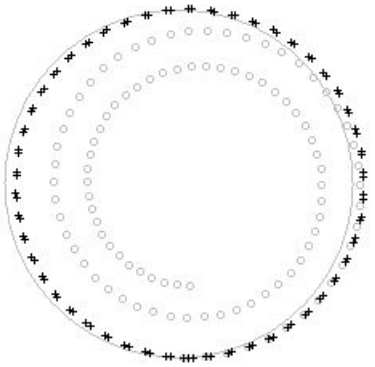

Fig. 2. Vertically rolling disk with $\alpha = 0$.

plotted the situation for $\alpha = 0$. For a given set of initial positions $(x_0, y_0, \theta_0, \varphi_0, \theta_1, \varphi_1)$ the other initial conditions were chosen in such a way that the solution lies initially on the discrete constraint manifold, i.e. in such a way that

$$x_1 = x_0 + \cos\varphi_0(\theta_1 - \theta_0), \quad y_1 = y_0 + \sin\varphi_0(\theta_1 - \theta_0).$$

Unlike the nonholonomic integrator (in grey with circle symbols) the variational integrator (in black with cross symbols) does not show a strong spiral-type solution but a circular path. It is true, however, that the variational solution deviates from the circle predicted by the initial conditions of the solution (12) (in grey in figure 2). However, since any circle is determined by 3 of its points, we can find a better match for the circle the variational discrete solution follows by considering the outcome (x_{k_i}, y_{k_i}) at three different times and by solving the three equations

$$(x_{k_i} - A)^2 + (x_{k_i} - B)^2 = C^2$$

for (A, B, C). If we do so, we obtain the matching circle (in dots) in figure 3.

It is well-known that the energy

$$E = \frac{1}{2}(\dot{x}^2 + \dot{y}^2) + \frac{1}{4}\dot{\theta}^2 + \frac{1}{8}\dot{\varphi}^2,$$

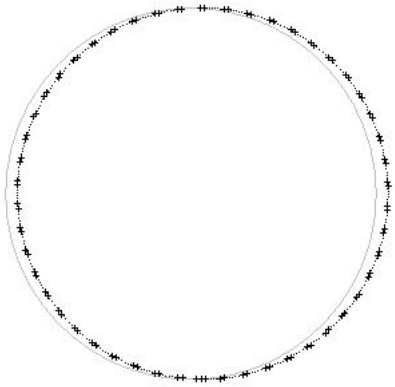

Fig. 3. Vertically rolling disk: circular path.

is conserved along the solutions (12) of the nonholonomic equations of motion. In figure 4 we investigate the performance of the two integrators on the energy function. The discrete version of the energy is the function we get by substituting, as usual, $1/h(q_k - q_{k-1})$ for $\dot{q}$ in the function E above. The straight line in figure 4 is the energy level predicted by the initial conditions. It is clear that the variational integrator (with crosses) does a better job than the nonholonomic one (with circles).

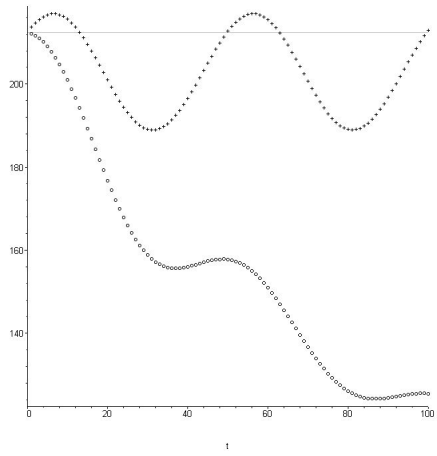

Fig. 4. Vertically rolling disk: the energy.

By construction the nonholonomic integrator conserves the constraints and the variational integrator does not. Indeed, in figure 6 we have plotted the constraint $\dot{x} - R\cos(\varphi)\dot{\theta} = 0$. Positive is that, although the variational integrator does not conserve this constraint, it reasonably oscillates around the zero level. Moreover, there is a method to fix this problem. We can introduce a 'modified' variational integrator which does conserve the constraints. This integrator considers the constraints as a constant along the (nonholonomic) motion. That is, it will use the variational discrete Lagrange equations (8) for the variables θ and φ (for the free Lagrangian $\tilde{L}$ given in (13)), but not the corresponding equations for x and y. To get a full system of equations, we supplemented this with the discrete constraints $\omega_d^a(q_k, q_{k+1}) = 0$ which can be written in terms of x_{k+1} and y_{k+1}. Figure 5 shows the modified integrator for $\alpha = 0$ (with box symbols). The circle in that figure is the one we had before, i.e. the one that matches the variational integrator. It shows that the modified integrator has the same circular behaviour as the variational integrator, and on top, it keeps the constraints conserved, see the box symbols on the zero level in figure 6.

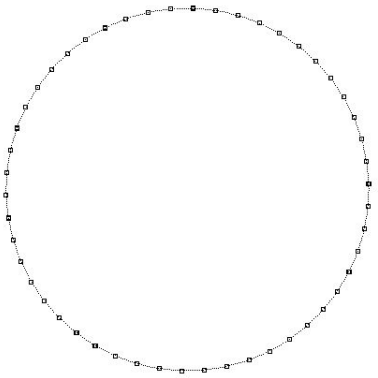

Fig. 5. Vertically rolling disk: the modified integrator.

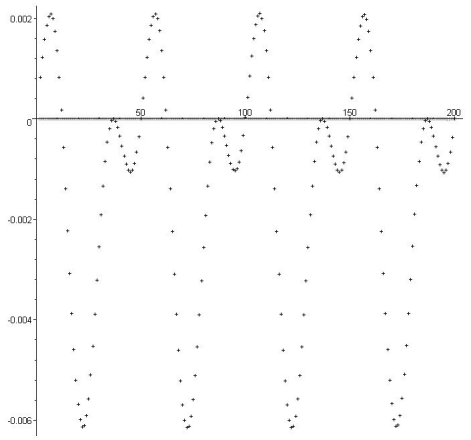

Fig. 6. Vertically rolling disk: the constraints.

Finally, figure 7 shows the effect of changing the parameter α. The results for the variational integrator (in black with cross symbols) remain accurate and more or less unchanged. For the nonholonomic integrator (in grey with circle symbols) the effect of changing α is that the inward spiral becomes an outward spiral. At some point (here $\alpha = 1/2$) the variational and nonholonomic integrator have the same accuracy.

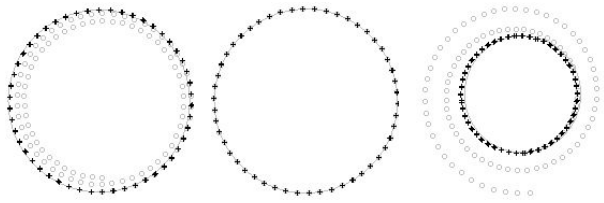

Fig. 7. Vertically rolling disk with $\alpha = 1/3, 1/2, 1$, repectively.

C. The knife edge

As was the case with the vertically rolling disk, also the solutions of the knife edge form a circular path in the (x, y)-plane.

Continuing the analogue with the previous example, the nonholonomic integration (in grey with circle symbols) results in a spiral, while the variational integration (in black with crosses) follows more closely the circular path, see figure 8.

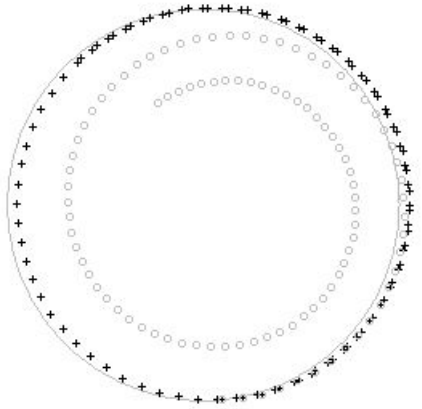

Fig. 8. The knife edge with $\alpha = 0$

D. The nonholonomic particle

The function

$$\tilde{L} = \frac{1}{2}\dot{x}^2 + \frac{\sqrt{1+x^2}}{2}\left(\frac{\dot{y}^2}{\dot{x}} + \frac{\dot{z}^2}{x\dot{x}}\right)$$

is a free Lagrangian for the nonholonomic particle. In each of the figures 9 and 10 the dashed black curve represents the exact solution, the thick black the variational solution and the thick grey the nonholonomic solution. The figures show that both the variational method and the nonholonomic one do not give very accurate solutions. However, changing the parameter α does not seem to affect the variational solution as much as it does the nonholonomic one. Indeed, the variational solution remains more or less of the same accuracy for the different α-values. On the other hand, the nonholonomic solution can be made more or less accurate by changing α. It seems that the best accuracy is reached somewhere in the neighbourhood of $\alpha = 1/3$, but how could one have guessed this beforehand? Remark also that this value is not same as the the best choice we had found for the nonholonomic integrator of the vertically rolling disk (where $\alpha = 1/2$ gave the best accuracy).

E. Preliminary conclusion

In each of the discussed examples the variational integrator (with one of the Lagrangians (6) and (7) of proposition 1) seemed to give better results than the known nonholonomic integrators. Unlike the outcome for the nonholonomic integrator, the results for the variational integrator seemed to be independent of or, at least, stable under changing the parameter α. Needless to say, the results above are, of course, very partial and are they are only intended to motivate further investigation on this topic. For example, we need to check if more involved discretization procedures, such as the ones mentioned at the end of section IIIA demonstrate the same behaviour as the one we have encountered so far.

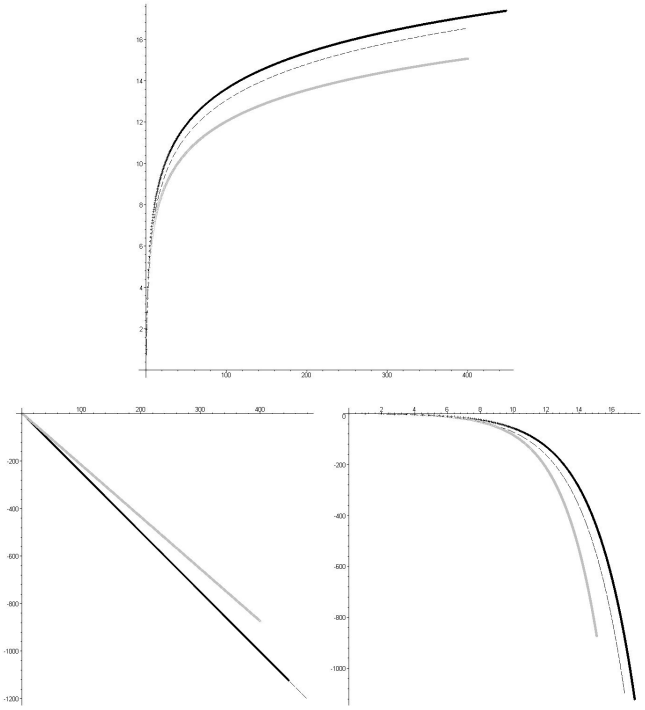

Fig. 9. The nonholonomic particle: *xy*-, *xz*- and *yz*-solution with $\alpha = 0$.

IV. Further systems

The class of nonholonomic systems treated above is very restricted. The reason is, of course, that the search for a solution of the inverse problem of the calculus of variations (in the proof of proposition 1) is too hard and too technical to be treated in the full generality of a nonholonomic systems with an arbitrary given Lagrangian and arbitrary given constraints. Also, since there are infinitely many possible choices for the associated systems, it is not clear from the outset which one of them will be variational, if any.

For these reasons, future extensions of the obtained results will strongly depend on well-chosen particular new examples. For example, we could try to find a free Lagrangian for a nonholonomic system with a potential of the form $V(r_2)$. Typical examples of such systems are the mobile robot with a fixed orientation

$$L = \tfrac{1}{2}m(\dot{x}^2 + \dot{y}^2) + \tfrac{1}{2}I\dot{\theta}^2 + \tfrac{3}{2}J\dot{\psi}^2 - 10\sin\psi,$$
$$\dot{x} = R\cos\theta\dot{\psi}, \quad \dot{y} = R\sin\theta\dot{\psi},$$

(an example that also appears in the paper [4]) or the knife edge on an inclined plane, where

$$L = \frac{1}{2}m(\dot{x}^2 + \dot{y}^2) + \frac{1}{2}J\dot{\phi}^2 + mgx\sin\alpha, \quad \dot{x}\sin\phi = \dot{y}\cos\phi.$$

In more general terms, such systems have a Lagrangian of the form

$$L = \frac{1}{2}(I_1\dot{r}_1^2 + I_2\dot{r}_2^2 + I_3\dot{s}^2) - V(r_2)$$

and a constraint of the form

$$\dot{s} = -A(r_1)\dot{r}_2,$$

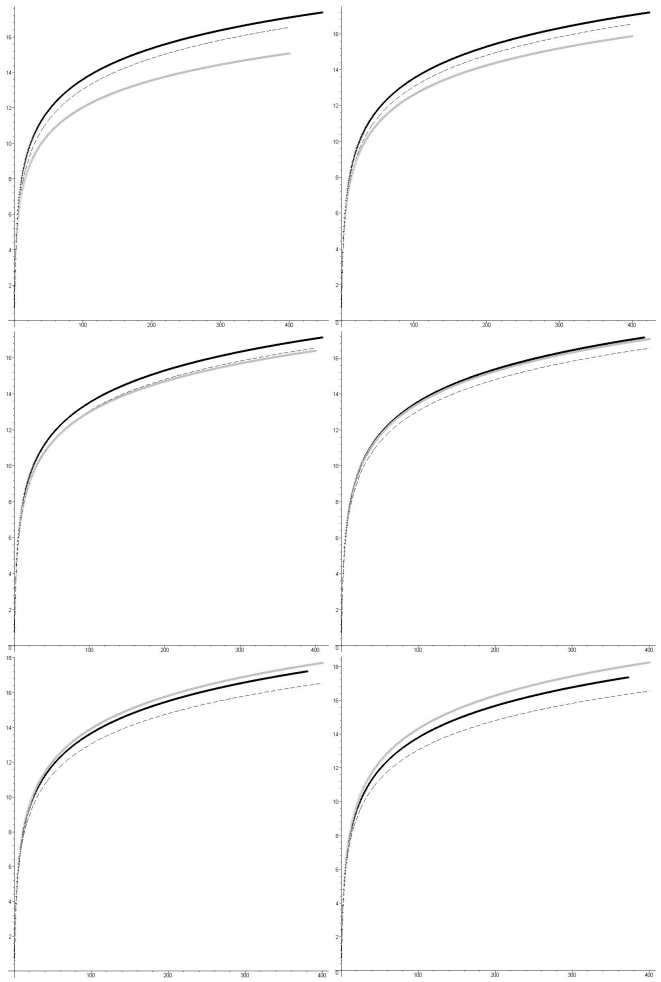

Fig. 10. The nonholonomic particle: xy-solution with $\alpha = 0, 1/5, 1/3, 1/2, 2/3, 4/5$, respectively.

and we can we can consider associated second-order equations, in a way that is analogous to the way we arrived at the second system (5) before: They are now of the form

$$\begin{cases} \ddot{r}_1 = 0, \\ \ddot{r}_2 = \Gamma_2(r_1)\dot{r}_1\dot{r}_2 + t_2(r_1, r_2), \\ \ddot{s} = \Gamma_3(r_1)\dot{r}_1\dot{s} + t_3(r_1, r_2). \end{cases} \tag{14}$$

Remark that compared to the equations (5), the presence of the extra potential brings the terms $t_i(r_1, r_2)$ into the picture. A first result is the following.

Proposition 3: There does not exists a regular Lagrangian for the second order systems (14).

Proof: As before, the proof follows from a careful analysis of the algebraic conditions which can be derived from the Helmholtz conditions. ■

For systems with more than one constraint, the result is still open. Remark that the proposition does not exclude the existence of an other variational 'associated' system.

ACKNOWLEDGMENTS

TM acknowledges a Marie Curie Fellowship within the 6th European Community Framework Programme and a postdoctoral fellowship of the Research Foundation - Flanders. The research of AMB and OEF was supported in part by the Rackham Graduate School of the University of Michigan, through the Rackham Science award, and through NSF grants DMS-0604307 and CMS-0408542.

REFERENCES

[1] A.M. Bloch, *Nonholonomic Mechanics and Control*, Springer (2003).
[2] A.M. Bloch, O.E. Fernandez and T. Mestdag, Hamiltonization of nonholonomic systems and the inverse problem of the calculus of variations, to appear in *Rep. Math. Phys.*, arXiv:0812.0437.
[3] M. Abud Filho, L.C. Gomes, F.R.A. Simao and F.A.B. Coutinho, The Quantization of Classical Non-holonomic Systems, *Revista Brasileira de Fisica* **13** (1983) 384-406.
[4] J. Cortes and S. Martinez, Nonholonomic integrators, *Nonlinearity* **14** (2001), 1365-1392.
[5] M. Crampin, W. Sarlet, G.B. Byrnes and G.E. Prince, Towards a geometrical understanding of Douglas's solution of the inverse problem of the calculus of variations, *Inverse Problems* **10** (1994) 245-260.
[6] J. Douglas, Solution of the inverse problem of the calculus of variations, *Trans. Amer. Math. Soc.* **50** (1941) 71–128.
[7] Y.N. Fedorov and D.V. Zenkov, Discrete Nonholonomic LL systems on Lie Groups, *Nonlinearity* **18** (2005), 2211-2241.
[8] O.E. Fernandez and A.M. Bloch, Equivalence of the Dynamics of Nonholonomic and Variational Nonholonomic Systems for certain Initial Data, *J. Phys. A: Math. Theor.* **41** 344005 (20pp).
[9] O. Fernandez, A.M. Bloch and T. Mestdag, The Pontryagin maximum principle applied to nonholonomic mechanics, Proc. 47th IEEE Conference on Decision and Control, Cancun (Mexico), Dec. 9-11, 2008, 4306–4311.
[10] O. Krupková and G.E. Prince, Second-order ordinary differential equations in jet bundles and the inverse problem of the calculus of variations, Chapter 16 of D. Krupka and D. J. Saunders (eds.), *Handbook of Global Analysis*, Elsevier (2007), 837-904.
[11] J.E. Marsden and M. West, Discrete mechanics and variational integrators, *Acta Num.* **10** (2001), 357–514.
[12] R.M. Santilli, *Foundations of Theoretical Mechanics I*, Spinger (1978).

Proceedings of the 8th National Congress on Theoretical and Applied Mechanics, May 28-29, Brussels, Belgium.

A system-level modal description of flexible multibody dynamics

Gert H.K. Heirman[1], Olivier Brüls[2], Wim Desmet[1]
[1]Katholieke Universiteit Leuven, Department of Mechanical Engineering
Celestijnenlaan 300B, B-3001 Heverlee (Leuven), Belgium
[2]Université de Liège, Department of Aerospace and Mechanical Engineering (LTAS)
Chemin des Chevreuils 1, 4000 Liège, Belgium
email: gert.heirman@mech.kuleuven.be, o.bruls@ulg.ac.be, wim.desmet@mech.kuleuven.be

Abstract— **Current modelling techniques only allow real-time simulation of strongly simplified models of flexible mechanisms. Both the number of degrees of freedom needed to accurately describe flexibility as the DAE-character of the system equations limit the computational efficiency. Body-level model reduction such modal synthesis is typically used to decrease the computational load of a simulation, but this cannot fully meet the demands for real-time simulation of flexible mechanisms. In this research, Global Modal Parametrization, a model reduction technique initially proposed for controller design for flexible mechanisms, is further developed to speed up simulation of multibody systems. The reduction is achieved by a system-level modal description, as opposed to the classic body-level modal description. As the dynamics is configuration-dependent, the system-level modal description is chosen configuration-dependent in such a way that the system dynamics is optimally described with a minimal number of degrees of freedom. Another novelty is GMP-based simulation. In a numerical experiment, simulation results for the original model equations are compared with simulation results for the model equations obtained after model reduction, showing a good match. The approximation errors resulting from the model reduction techniques are investigated by comparing results for different mode sets. The mode set affects the approximation error similarly as it does in linear modal synthesis.**

Keywords— **Non-linear Model Reduction, Flexible Multibody Dynamics, Global Modal Parametrization, Real-Time Simulation**

I. Introduction

BODY-LEVEL model reduction, e.g. linear modal synthesis, is used extensively in flexible multibody dynamics to efficiently represent the flexibility of a mechanism component. However, the resulting set of equations is still a rather large set of differential-algebraic equations (DAE). Both the DAE-character of the model equations, and the number of degrees of freedom needed to accurately represent flexibility, prohibit fast simulation of these systems. There is however an increasing demand for real-time and faster-than-real-time simulation of flexible multibody systems, such as in Hardware/Human/Software-in-the-Loop and Model Predictive Control applications. Formulations based on relative generalized coordinates may lead to efficient simulation tools [1] but the undesired DAE-character remains for systems with kinematic loops.

Few techniques exist for system-level model reduction of flexible multibody models. Most system-level model reduction techniques for non-linear models build reduced models based on data obtained from user-defined numerical experiments of the original unreduced model, e.g. techniques based on neural networks [2] and techniques based on projection on a fixed vector space [3]. The resulting reduced models only offer an accurate approximation in scenarios similar to the numerical experiments on which they are based. For these techniques, a good approximation for all possible states of the system requires many numerical experiments and limits the computational efficiency of the reduced model equations.

In this research, Global Modal Parametrization (GMP), a model reduction technique for flexible multibody systems proposed by Brüls for controller design of flexible mechatronic systems [4], is developed further for the purpose of speeding up simulation of flexible multibody systems. The reduction of the model is achieved by projection on a curvilinear subspace [5] instead of the classically used fixed vector space. Using a fixed vector space for highly non-linear systems requires the inclusion of many vectors in the vector space to ensure the state-dependent dominant dynamics of the system, i.e. the system's dominant eigenmodes and relevant static deformation patterns, are spanned by the vector space for each state of the system. The curvilinear subspace, however, is defined by imposing the tangent space spans, exactly and only, the state-dependent dominant eigenmodes, the rigid body modes and low-frequency elastic eigenmodes, and the relevant static deformation patterns. In this way, the dominant dynamics of a highly non-linear system can be represented by a minimal number of coordinates.

The use of GMP for simulation purpose is validated in a numerical experiment. Simulation results for the original model equations are compared with simulation results for the model equations obtained after the proposed model reduction methodology. The latter require much less degrees of freedom to represent the studied dynamical phenomena as compared to unreduced and body-level reduced models. The approximation errors resulting from the model reduc-

tion techniques are investigated by comparing results for different mode sets.

II. Model reduction by projection on curvilinear coordinate system

Flexible mechanisms can be represented by means of several modelling techniques, an overview can be found in [6]. Each technique offers its distinct trade-off between computational load and degree of approximation of several (non-linear) effects. Irrespective of the type of generalized coordinates used to represent a flexible mechanism, the equations of motion of a (flexible) multibody system can be written as a (non-linear) second-order DAE in terms of its generalized coordinates q:

$$M^{qq}(q)\,\ddot{q} + h^q(q,\dot{q}) + V_{,q} + \Phi_{,q}^T \lambda = g^q \quad (1)$$

$$\Phi(q) = 0 \quad (2)$$

In these equations:
- q is a vector of the n generalized coordinates, the value of q defines the *configuration* of the system.
- $M^{qq}(q)$ is the configuration-dependent mass matrix.
- $V_{,q}$ is the gradient of the potential energy with respect to q. Only potential energy due to structural deformation is considered in this term. The generalized forces due to other potential energy sources (e.g. gravity) will be taken into account through the source term g^q.
- g^q denotes the generalized forces due to external loads on a mechanical component.
- $\Phi(q) = 0$ expresses m kinematic holonomic constraints[1]. Its gradient $\Phi_{,q}^T$ is assumed to be of full rank for all configurations q.
- λ is a vector of m Lagrange multipliers associated with the constraints.
- $\Phi_{,q}$ is the matrix of constraint gradients, $\Phi_{,q}^T \lambda$ represents the reaction forces and moments enforcing the constraints.
- h^q gathers the centrifugal and Coriolis inertia forces which are quadratic in $\dot{q}$. Using the index summation convention, we have

$$(h^q)_i = (\Gamma^{qqq})_{ijk} \dot{q}_j \dot{q}_k \quad (3)$$

where $(\Gamma^{qqq})_{ijk}$ is:

$$(\Gamma^{qqq})_{ijk} = \frac{1}{2}\left(\frac{\partial (M^{qq})_{ij}}{\partial q_k} + \frac{\partial (M^{qq})_{ik}}{\partial q_j} - \frac{\partial (M^{qq})_{jk}}{\partial q_i}\right) \quad (4)$$

The overal motion is decomposed into a large amplitude rigid body motion q^r and a small amplitude elastic displacement q^f.

$$q = q^r + q^f \quad (5)$$

[1]Non-holonomic constraints are not considered in this work.

Both q and q^r satisfy the constraint equations Eqn. (2). q^r represents a non-deformed configuration. q^r will be further referred to as the *rigid body motion*. The term $V_{,q}$ in Eqn. (1) represents generalized forces due to elastic deformation. As only the elastic displacement q^f results in a change of the potential energy and as the small elastic deformation allow a linearization around the undeformed configuration q^r, this term can be rewritten as:

$$V_{,q} = K^{qq}(q^r)\, q^f + O({q^f}^2) \quad (6)$$

The number of rigid body degrees of freedom of the multibody system is referred to as s. The rigid body motion can be represented by θ, which is a selection of s coordinates out of the set of coordinates q. This representation of the system inevitably leads to singularities in the dead points corresponding to the coordinates θ. If the system has dead points corresponding to the coordinates θ, the analysis of the system should be limited to an area in which this representation is valid, i.e. away from the system's dead points. It will further be assumed that this is the case. The invertible, sufficiently continuous coordinate transformation ρ, which maps θ to the rigid body configuration q^r, can be defined:

$$q^r = \rho(\theta) \quad (7)$$

Its Jacobian $\rho_{,\theta}(\theta)$ can be interpreted as the matrix of rigid-body modes $\Psi^{q\theta}(\theta)$. Note that, for all values of θ and away from the system dead points, this matrix has maximal rank, its columns (the rigid-body modes) have finite length and are continuous for varying θ. A vector is continuous if all of its elements are continuous.

$$\rho_{,\theta}(\theta) = \Psi^{q\theta}(\theta) \quad (8)$$

The rigid body modes $\Psi^{q\theta}(\theta)$ respect the constraint equations by definition:

$$\Phi_{,q}\, \Psi^{q\theta} \equiv 0 \quad (9)$$

The degrees of freedom (DOF) q can be partitioned in:
- s rigid body DOFs θ
- n^g constrained DOFs q^g: the DOFs that don't belong to θ and on which an external loading will be applied during the intended simulation
- the internal DOFs q^i: the remainder of the DOFs

The elastic deformation q^f is considered as a deviation from the undeformed configuration q^r, which can be represented by $(n-m)-s$ independent coordinates $\hat{\delta}$ through an invertible, sufficiently continuous coordinate transformation σ.

$$q^f = \sigma(\theta, \hat{\delta}) \qquad \sigma(\theta, 0) \equiv 0 \quad (10)$$

q has to satisfy the constraint equations:

$$\Phi(\rho(\theta)+\sigma(\theta,\hat{\delta}))=0 \tag{11}$$

Linearizing around an undeformed configuration $(\theta,\hat{\delta})=(\theta,0)$ and ignoring second order terms, results in:

$$\Phi_{,q}\,\sigma_{,\hat{\delta}}(\theta,0)=0 \tag{12}$$

Under the small deformation assumption, $\sigma(\theta,\hat{\delta})$ can be approximated linearly:

$$q^f=\sigma_{,q}(\theta,\hat{\delta})\,\hat{\delta}=\Psi^{q\hat{\delta}}(\theta)\,\hat{\delta} \tag{13}$$

Note that, for all values of θ and away from the dead points, this matrix has maximal rank, its columns (the flexible modes) have finite length and are continuous for varying θ.

Furthermore, q^f can be approximated by projecting it on a (configuration-dependent) vector space $\Psi^{q\delta}(\theta)$. $\Psi^{q\delta}(\theta)$ is constructed as a subspace of $\Psi^{q\hat{\delta}}(\theta)$ for each configuration. In addition, for all values of θ and away from the dead points, this matrix has to be of full rank, its columns (the flexible modes) need to have finite length and need to be continuous for varying θ. In order to give a good approximation of the dynamics of the system, $\Psi^{q\delta}(\theta)$ should span the (configuration-dependent) dominant, system-level, flexible eigenmodes and static deformation patterns of the system for all values of θ. Several possibilities for sets of modes are described by Craig [7] and satisfy the demands on the mode set $\Psi^{q\delta}$ stated above [5]. Brüls [4] selected the Hurty mode set. In this work, a slightly different mode set will be used:

$\Psi^{q\delta}(\theta)$ consists of:

- $\Psi^{q\gamma}(\theta)$: n^g contraint modes $\Psi^{q\gamma}$ which are the static deformation patterns for a unit displacement at the constrained DOFs q^g while the rigid body DOFs θ are kept fixed.
- $\Psi^{qi}(\theta)$: all normal eigenmodes with an eigenfrequency below a certain threshold with as boundary conditions: rigid body DOFs θ kept fixed and constrained DOFs q^g kept free. The frequency threshold should be sufficiently higher than the maximal frequency in the spectrum of the excitation. In linear dynamics problems, this threshold is usually defined as 1.5 to 2 times the highest frequency in the spectrum of the excitation. Note that due to the variable dynamics, the eigenfrequencies are configuration-dependent. To consider inclusion of a certain eigenmode in the mode set, one should look at the lowest value of the eigenvalue for the range of configurations encountered in the intended simulation.

Both deformation patterns are evaluated for an undeformed system at rest.

This results in the total mode set:

$$\Psi^{q\delta}(\theta)=\begin{bmatrix}\Psi^{q\gamma} & \Psi^{qi}\end{bmatrix} \tag{14}$$

q^f is thus approximated by:

$$q^f=\Psi^{q\delta}(\theta)\,\delta \tag{15}$$

Using Eq. (5), Eq. (7) and Eq. (15) the parametrization can be written as:

$$q=\rho(\theta)+\Psi^{q\delta}(\theta)\delta \tag{16}$$

For the sake of overview, the modal degrees of freedom are bundled in a vector of length n_η:

$$\eta=\begin{bmatrix}\theta\\ \delta\end{bmatrix} \tag{17}$$

The differentiation of the parametrization leads to

$$q_{,\eta}(\theta,\delta)=\begin{bmatrix}\Psi^{q\theta}(\theta)+\dfrac{\partial\Psi^{q\delta}(\theta)}{\partial\theta}\delta & \Psi^{q\delta}(\theta)\end{bmatrix} \tag{18}$$

Introducing the parametrization in the model equations Eq. (1-4) and bearing Eq. (12) in mind result in [4]:

$$M^{\eta\eta}(\eta)\,\ddot{\eta}+h^{\eta}(\eta,\dot{\eta})+K^{\eta\eta}(\eta)\eta \;=\; g^{\eta} \tag{19}$$

with

$$M^{\eta\eta} \;=\; q_{,\eta}^T M^{qq} q_{,\eta} \tag{20}$$

$$K^{\eta\eta} \;=\; q_{,\eta}^T K^{qq}\begin{bmatrix}0 & \Psi^{q\delta}\end{bmatrix} \tag{21}$$

$$g^{\eta} \;=\; q_{,\eta}^T g^q \tag{22}$$

$$(h^{\eta})_i \;=\; (\Gamma^{\eta\eta\eta})_{ijk}\dot{\eta}_j\dot{\eta}_k \tag{23}$$

The components of $(\Gamma^{\eta\eta\eta})$ are easily obtained from Eq. (4) and Eq. (20):

$$(\Gamma^{\eta\eta\eta})_{ijk}=\frac{\partial q_u}{\partial\eta_i}\frac{\partial q_v}{\partial\eta_j}\frac{\partial q_w}{\partial\eta_k}(\Gamma^{qqq})_{uvw}+\frac{\partial q_u}{\partial\eta_i}\frac{\partial^2 q_v}{\partial\eta_j\partial\eta_k}(M^{qq})_{uv} \tag{24}$$

In conclusion, one could say the essence of the model reduction technique is twofold:

1. The rigid body dynamics are represented by a minimal number of coordinates θ.
2. The flexibility of the system is approximated by only considering the dominant (configuration-dependent) elastic eigenmodes and static deformation patterns.

This model reduction technique for flexible multibody dynamics, Global Modal Parametrization (GMP), was proposed by Brüls for non-linear controller design [4] and is further developed in this research for speeding up simulation.

III. USE OF GMP FOR SIMULATION

As both the parametrization of the rigid body position and the superimposed flexible deviation respect the constraint equations by definition (Eq. (9) and (12)), the model equations become a set of ordinary differential equations instead of the original set of differential-algebraic equations.

Furthermore, as the elastic deformation is approximated by a limited set of configuration-dependent modes, the number of degrees of freedom η is much smaller than the number of initial coordinates q and Lagrange multipliers λ. Adding an additional vector to the configuration-dependent vector set $\Psi^{q\delta}(\theta)$, and thus an additional DOF to δ, 1) increases the cost for computing the vector set $\Psi^{q\delta}(\theta)$ and the assembly of the reduced model equations Eq. (19) and (24), 2) increases the accuracy of the reduced model equations as an approximation of the original model equations and 3) increases the computational load for simulation of the reduced model equations. A trade-off has to be defined by the user.

The reduced dimension of the problem, as well as the switch from DAE to ODE, make the projected system equations much cheaper to solve. However, assembling the reduced system equations requires a considerable effort and can generally only be done numerically. The cost of this assembly can outweigh the advantage of the small resulting set of equations. However, as all elements of the projected model equations are defined by smooth functions using inputs that vary smoothly with θ, the elements of the projected model equations are continuous themselves. If these elements are calculated for a discrete set of configurations $\theta^{(k)}$ in a preparation phase, they can be calculated by interpolation for any value of θ encountered during simulation. Increasing the number of discrete configurations composing the database for interpolation 1) increases the computational load during the preparation phase, 2) increases memory requirements to store the database and 3) decreases the interpolation error on the projected model equation elements and the backtransformation. Again, a trade-off has to be defined by the user. Linear interpolation was used in this work for the sake of simplicity, though other more advanced interpolation methods are likely to give more accurate results. In real-time applications, at the end of each time step the coordinates η need to be transformed back to the coordinates q. This phase will further be referred to as the *back-transformation*.

The splitting up of the process in a preparation and simulation phase is described in [5]. In the applications envisioned in this research, such as real-time simulation, gain in simulation speed during actual simulation justifies an expensive preparation phase.

IV. NUMERICAL VALIDATION

The model reduction technique is applied to a system consisting of a flexible beam undergoing an imposed motion through a fixed slider joint (see Fig. 1). As the flexible beam moves through the slider joint, the slider joint constraint is imposed on a changing location on the beam: the connectivity and the dynamic properties of the system change. The system properties of this 2-dimensional problem are summarized in table I. The slider joint is imposed by enforcing zero displacement and rotation at the slider location.

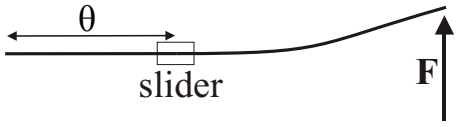

Fig. 1. System used for numerical experiment

Length (m)	0.53
Cross-section (m^2)	4.53E-4
Second moment of area (m^4)	1.427E-8
Density (kg/m^3)	7800
E (GPa)	210

TABLE I
SYSTEM PROPERTIES.

The beam has uniform properties and is modeled with 30 identical 2-noded beam elements, using cubic shape functions to represent lateral displacement due to bending. The rigid body coordinate θ is defined as the position of the beam relative to the non-moving sliding joint (see Fig. 1). The imposed motion is a harmonic function, shown in Fig. 2. The flexible beam is loaded at its end by a lateral force (see Fig. 1). The loading is a smoothed step function, shown in Fig. 3. The loading increases harmonically up to 0.2 s, and then levels out at its maximal amplitude. Both imposed motion and loading were selected such that high-frequency components in the input are limited. At $t = 0$ the system is undeformed. Simulation results are calculated for the original set of DAE's Eq. (1-2) and for the set of ODE's obtained after projection Eq. (19), both describing the configuration-dependent lateral dynamics.

The algebraic equations Eq. (2) of the initial DAE

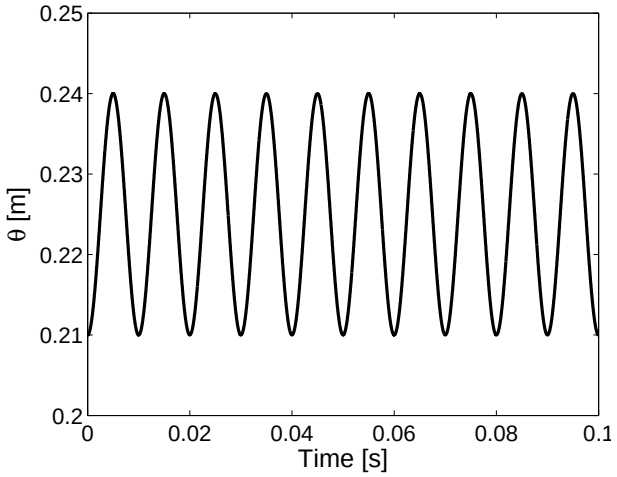

Fig. 2. Imposed motion through the slider

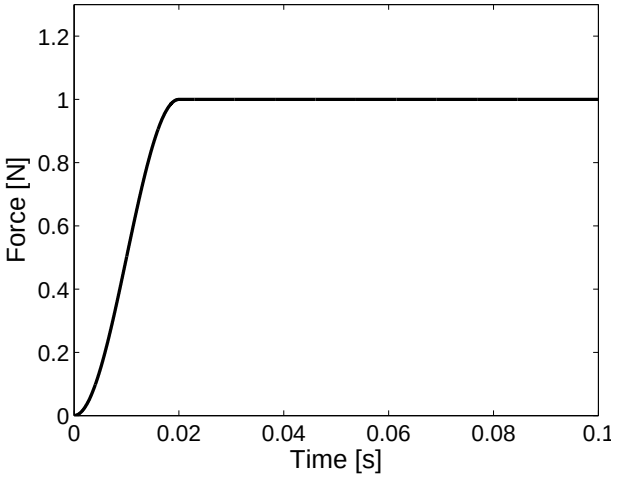

Fig. 3. Loading at the tip of the beam

Eq. (1-2) impose the use of an implicit solver which iterates within each time step until all equations are satisfied up to a user-defined tolerance. Although the ODE-character of the projected model equations also allows explicit solvers, the same implicit solver was used for simulation of both model equations: the generalized-α method [8]. The solver parameters were chosen as $\rho_\infty = 0.95$ (a small amount of numerical damping at high frequencies), timestep $h =$ 2e-5 s.

The convergence criteria for the original model equations were defined as:

$$abs\left(M^{qq}(q)\,\ddot{q} + h^q(q,\dot{q}) + V_{,q} + \Phi^T_{,q}\lambda - g^q\right) \quad < \quad \varepsilon^q \tag{25}$$

$$abs\left(\Phi(q)\right) \quad < \quad \varepsilon^\Phi \tag{26}$$

All elements of ε^q were set to 1e-8 N (resp. Nm), whereas those of ε^Φ were set to 1e-10 m (resp. rad). For a meaningful comparison of the simulation results of the original DAE and the projected model equations, the tolerance vector ε^q should be premultiplied analogously as the the original DAE is, resulting in the following convergence criterion:

$$abs\left(M^{\eta\eta}(\eta)\,\ddot{\eta} + h^\eta(\eta,\dot{\eta}) + K^{\eta\eta}(\eta)\eta - g^\eta\right) \quad < \quad abs\left(q^T_{,\eta}\varepsilon^q\right) \tag{27}$$

With these settings the convergence criterion on the original dynamic equations Eq. (25) proved to be the more critical one of both Eq. (25-26). One should conclude that the simulation results of the projected model equations offer the same precision as the simulation results of the original DAE for those modal degrees of freedom which the reduced model can represent. Note that the satisfaction of the constraint equation of simulation results of the projected model equations, after back-transformation, depends in the general case on the precision of 1) the back-transformation calculated for a discrete set of configurations in the preparation phase, 2) the interpolation technique used in the back-transformation, and 3) the calculated and interpolated modes satisfying the constraint equations Eq. (12). In this case study, only the latter will result in an error because the back-transformation is trivial.

Different configuration-dependent mode sets were investigated. In a first case, the mode set $\Psi^{q\delta}(\theta)$ consisted of only the first eigenmode: the first bending mode in which the loaded part of the beam participates. This very limited mode set was selected to clarify the approximation errors of the method. Fig. 4 shows the time history of the lateral displacement of the loaded end for both simulations: 1) the unreduced model, i.e. the original set of DAE's Eq. (1-2) and 2) the GMP-reduced model, i.e. the set of ODE's obtained after projection on the configuration-dependent mode set Eq. (19). The approximation error of the reduced model simulation results is shown in Fig. 5. Two effects can be observed:

- The approximation error clearly shows a low-frequency component indicating an overestimation of the static stiffness. This is to be expected because the mode set is not statically complete [7]. The modal description lacks a static deformation pattern for the loaded DOFs, for this case the loaded tip. A static input cannot be fully represented by this modal description $\Psi^{q\delta}(\theta)$.
- The approximation error also has a high-frequency component. The combination of input and non-linear effects clearly dynamically excites eigenmodes of higher eigenfrequency, which are not included in the modal description $\Psi^{q\delta}(\theta)$.

Adding a static deformation pattern to $\Psi^{q\delta}(\theta)$ for the loaded DOF gives a better approximation (see Fig. 6 and 7). The mode set $\Psi^{q\delta}(\theta)$ becomes statically complete; The

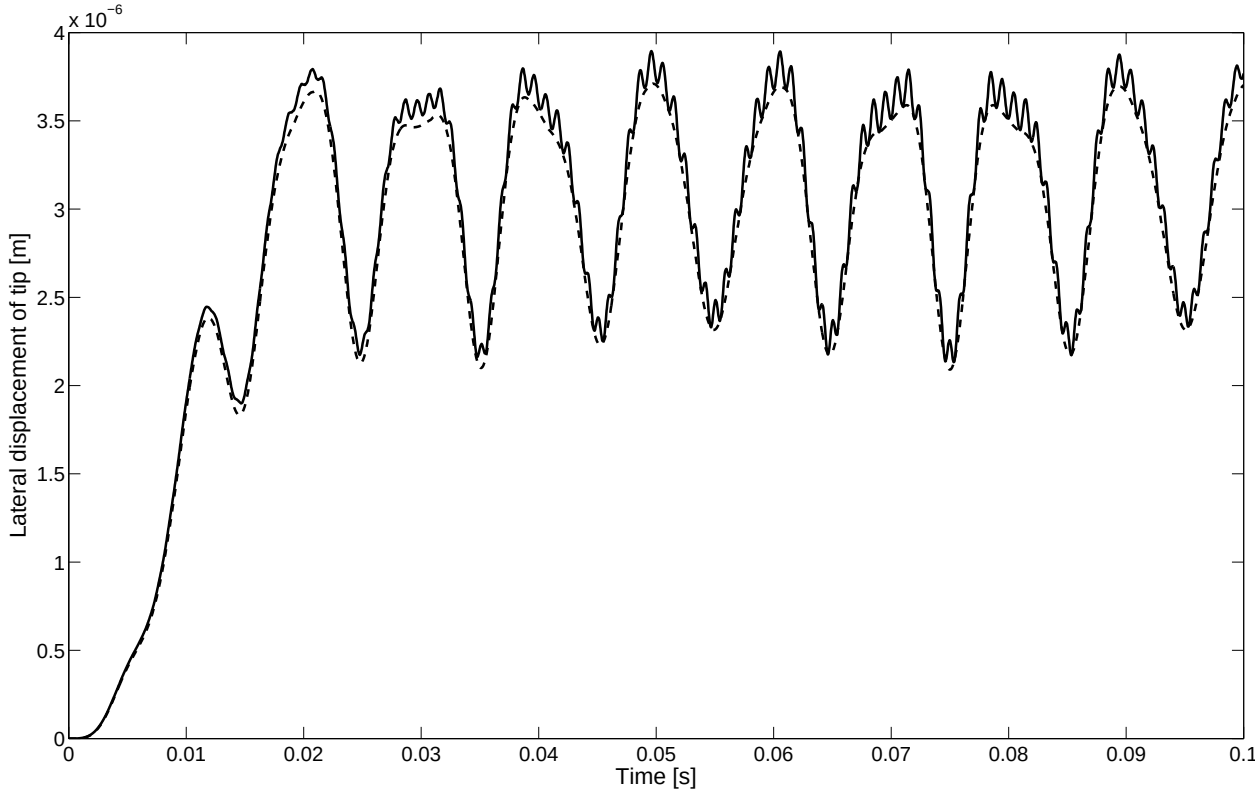

Fig. 4. Simulation results for the lateral displacement of the loaded end
full: original high-dimensional DAE, dashed: low-dimensional ODE obtained after GMP-reduction (1 eigenmode)

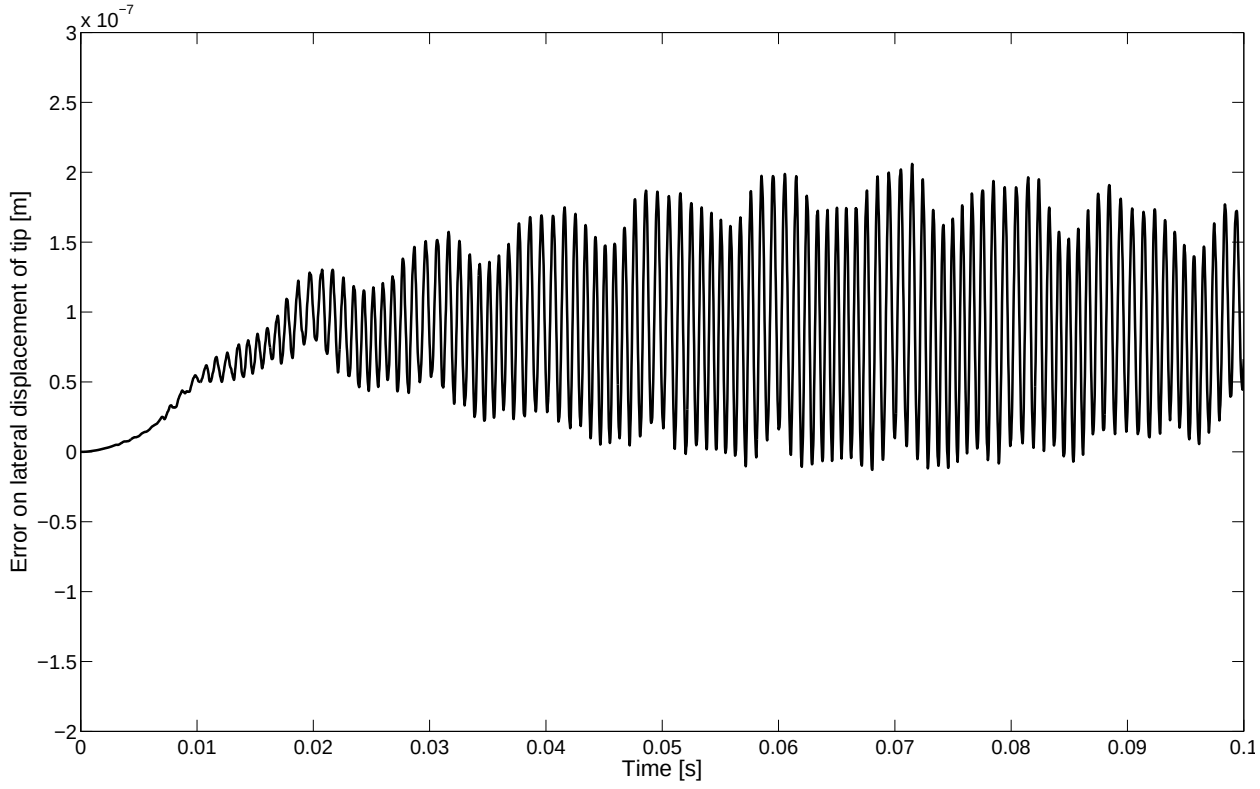

Fig. 5. Approximation error for the lateral displacement of the loaded end (1 eigenmode)

low-frequency content of the approximation error is reduced dramatically. The high-frequency component how-

ever remains similar both in frequency content and magnitude; higher-frequency dynamics are still not 'captured'.

In a last case, the configuration-dependent mode set $\Psi^{q\delta}(\theta)$ consists of the first 2 eigenmodes in which the loaded part of the beam participates. These are actually eigenmodes 1 and 3 for the configurations encountered during the specified imposed rigid body motion. The second eigenmode is a bending mode in which the unloaded part of the beam participates. This mode does not contribute significantly to the total system response. The simulation results for this case can be seen in Fig. 8 and 9. The effect of an additional eigenmode is 1) a decrease of the low-frequency component of the error, and 2) a better representation of the higher-frequency dynamics. Adding more modes to the modal set increases the precision, but also results in a higher computational load. A trade-off has to be specified by the user. One can conclude that the GMP-description gives a good precision, while only requiring a very limited number of degrees of freedom.

V. Conclusions

A methodology has been proposed to use Global Modal Parametrization, an existing model reduction technique, for simulation purposes. This system-level model reduction methodology significantly reduces the number of degrees of freedom needed to accurately describe and simulate flexible multibody systems. The original degrees of freedom are projected on a submanifold. The proposed model reduction methodology is a system-level model reduction technique, as opposed to the classic body-level model reduction. The resulting projected set of equations is a low-dimensional set of ODE's, which is considerably cheaper to solve than the original high-dimensional set of DAE's. The assembly of the projected model equations is done in an off-line preparation phase for a discrete number of configurations of the system. During the actual simulation, the elements of the projected model equations are then obtained by cheap interpolation. The combined interpolation and solving of the projected model equations is significantly cheaper than simulation of the original model equations. In the applications envisioned in this research, such as real-time simulation, gain in simulation speed justifies an expensive preparation.

The methodology is applied on a system with configuration-dependent dynamics resulting from variable boundary conditions: a flexible beam being clamped by a sliding joint at a continuously changing location. This numerical experiment shows the validity and the applicability of the methodology to systems with configuration-dependent dynamics, such as flexible multibody systems: the proposed description gives a good precision, while only requiring a very limited number of degrees of freedom. Different system-level mode sets are investigated. The effect of the mode set on the approximation error is explained and is similar to the effects of the mode set on the approximation error in linear modal synthesis.

In future research, this model reduction methodology will be applied to systems in which the configuration-dependency of the dynamics results from large relative rotations of bodies. The methodology will be implemented in a compiled programming language to allow comparison with existing computer packages. Both in the proposed model reduction procedure, as in the time integration solver, trade-offs between computational speed and accuracy have to be defined by the user. These trade-offs were not fully investigated in this research and will be addressed in the future.

Acknowledgments

The research of Gert Heirman is funded by a Ph.D. grant of the Institute for the Promotion of Innovation through Science and Technology in Flanders (IWT-Vlaanderen).

References

[1] U.L. Armesto, *Real-time Methods in Flexible Multibody Dynamics*, PhD thesis, University of La Coruña, Ferrol, September 2008.

[2] C.L. Bottasso, C-S. Chang, A. Croce, D. Leonello, L. Riviello, *Adaptive planning and tracking of trajectories for the simulation of maneuvers with multibody models*, Computer Methods in Applied Mechanics and Engineering, Vol. 195, No. 50-51, pp. 7052–7072, 2006.

[3] W. Schilders, H. van der Vorst, and J. Rommes Model order reduction: theory, applications, and research aspects Springer, Heidelberg, 2008.

[4] O. Brüls, P. Duysinx, J-C. Golinval, *The global modal parametrization for non-linear model-order reduction in flexible multibody dynamics*, International Journal for Numerical Methods in Engineering, Vol. 69, No. 5, pp. 947–77, 2007.

[5] G. Heirman, O. Brüls, P. Sas, W. Desmet, *Coordinate transformation techniques for efficient model reduction in flexible multibody dynamics*, Proceedings of the ISMA2008 International Conference on Noise and Vibration Engineering, Leuven, Belgium, September 15–17, 2008.

[6] T. M. Wasfy, A. K. Noor, *Computational strategies for flexible multibody systems*, Applied Mechanics Reviews, Vol. 56, No. 6, pp. 553–613, November 2003.

[7] R.R. Craig, *A review of time-domain and frequency-domain component mode synthesis methods*, Journal of Modal Analysis, Vol. 2, No. 2, pp. 59–72, 1987.

[8] J. Chung, G. Hulbert, *A time integration algorithm for structural dynamics with improved numerical dissipation: The generalized-alpha method*, ASME Journal of Applied Mechanics, Vol. 60, pp. 371–375, 1993

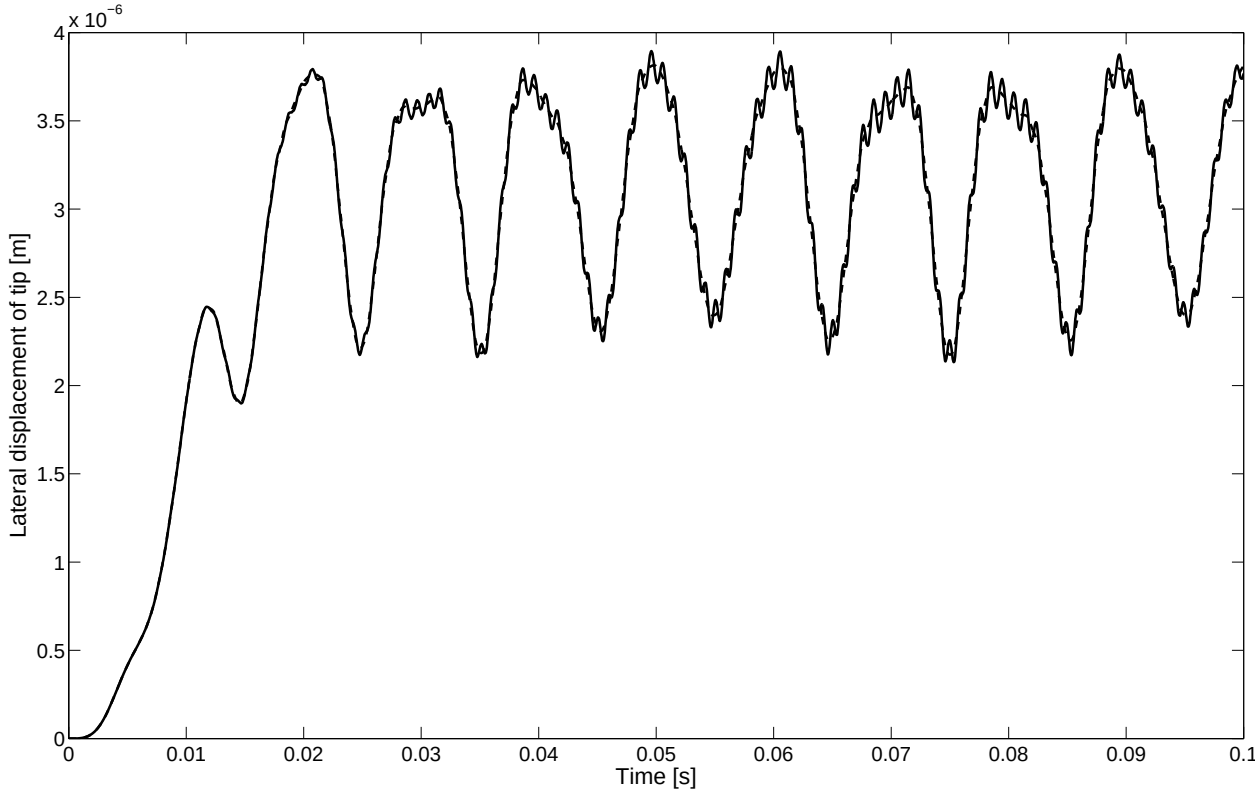

Fig. 6. Simulation results for the lateral displacement of the loaded end
full: original high-dimensional DAE, dashed: low-dimensional ODE obtained after GMP-reduction (1 eigenmode + 1 static mode)

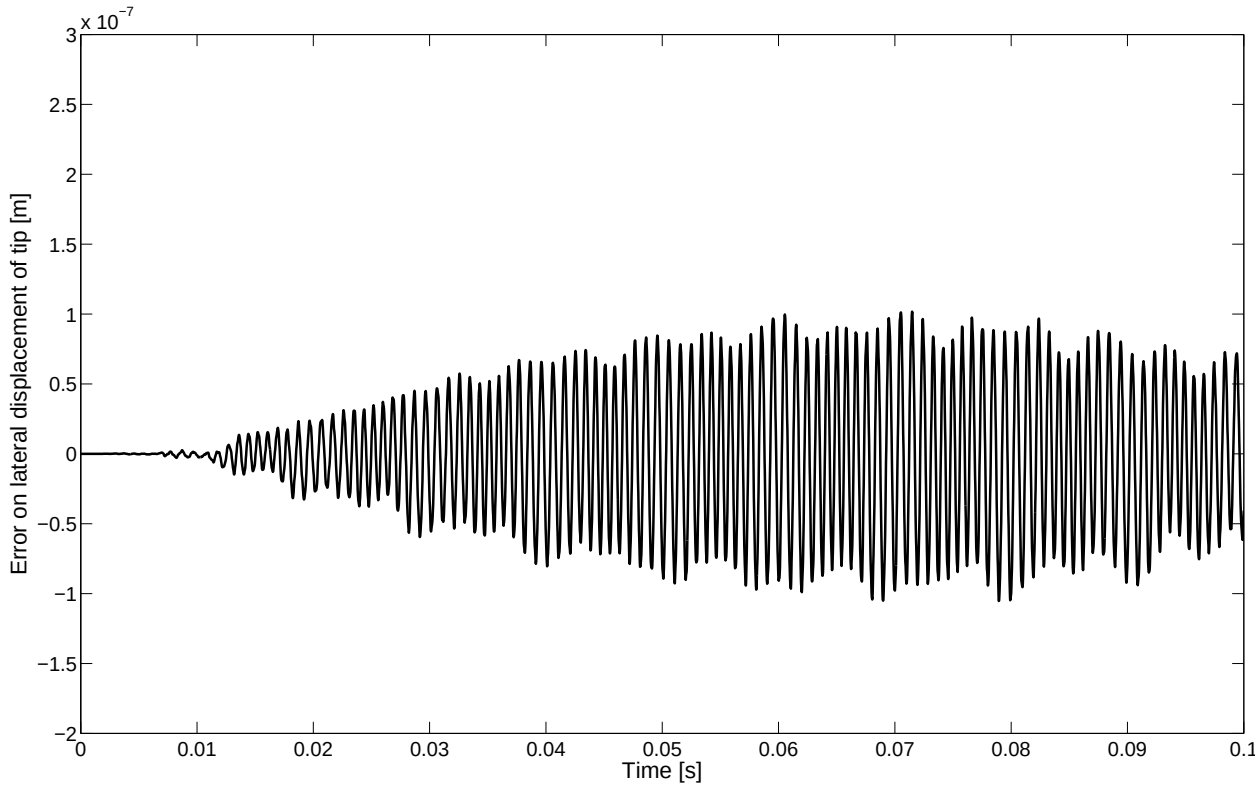

Fig. 7. Approximation error for the lateral displacement of the loaded end (1 eigenmode + 1 static mode)

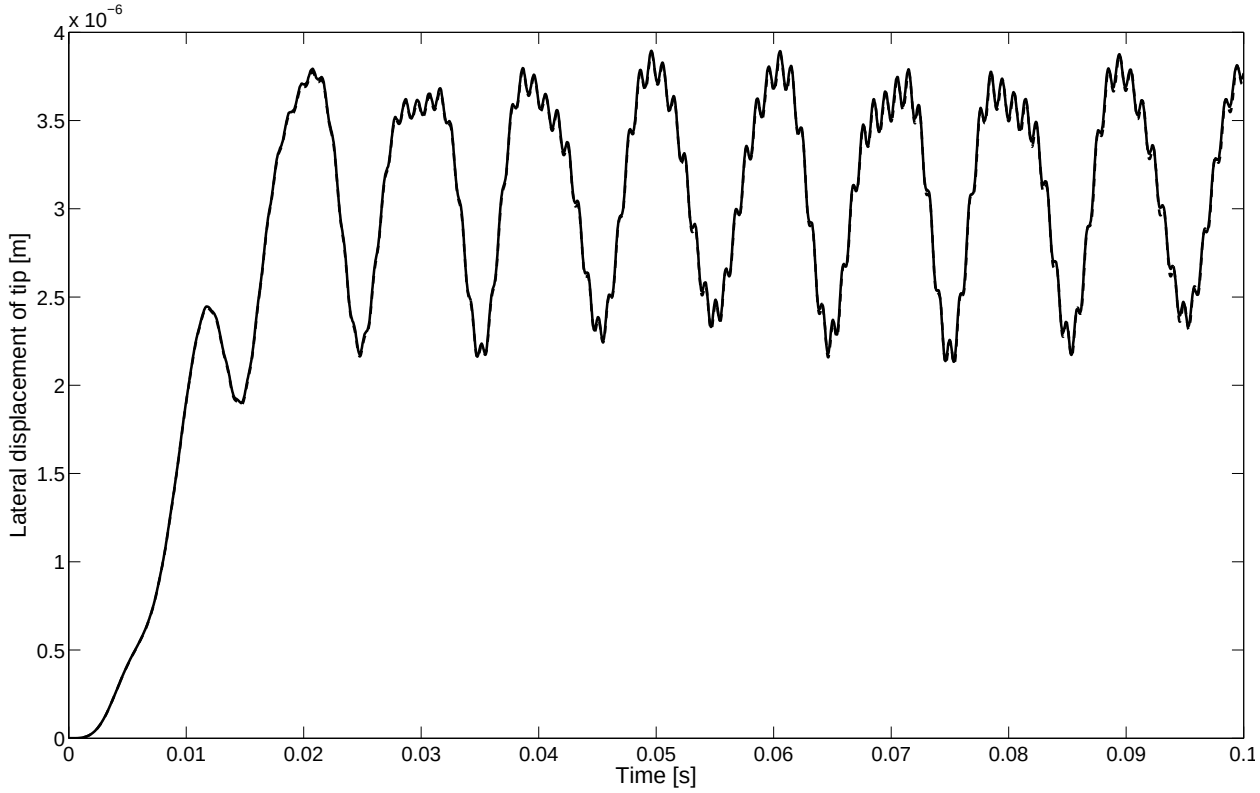

Fig. 8. Simulation results for the lateral displacement of the loaded end
full: original high-dimensional DAE, dashed: low-dimensional ODE obtained after GMP-reduction (2 eigenmodes)

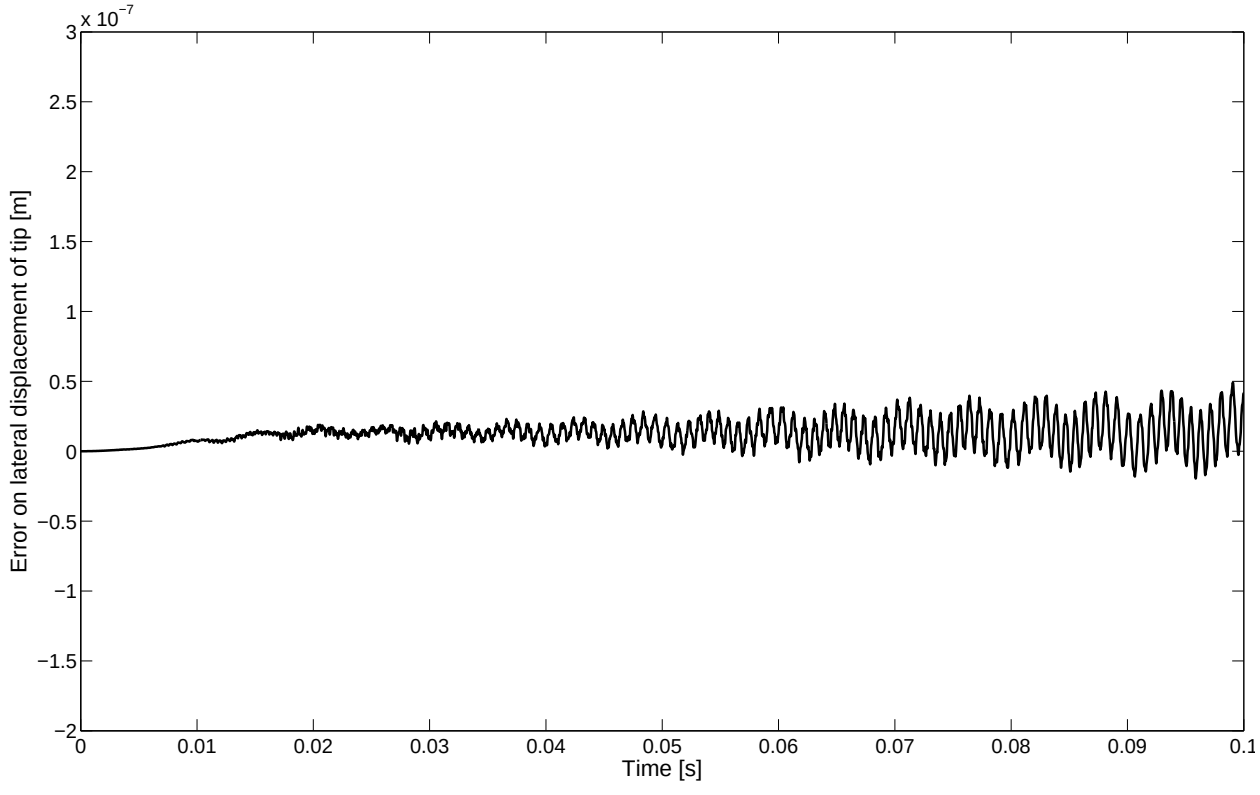

Fig. 9. Approximation error for the lateral displacement of the loaded end (2 eigenmodes)

Proceedings of the 8th National Congress on Theoretical and Applied Mechanics, May 28-29, Brussels, Belgium.

Contribution of symbolic generation to the sensitivity analysis of automotive suspension parameters

Poncelet Antoine[1], Collard Jean-Franois[1], Fisette Paul[1]
[1]Universit catholique de Louvain, Center for Research in Mechatronics
Place du Levant 2 – 1348 Louvain-la-Neuve
emails: antoine.poncelet@uclouvain.be, jf.collard@uclouvain.be, paul.fisette@uclouvain.be

Abstract— **The purpose of the present research relates to the sensitivity analysis of road vehicle comfort and handling performances with respect to suspension technological parameters. The envisaged suspension being of semi-active nature, this implies first to consider an hybrid modeling approach consisting of a 3D multibody model of the full car – an Audi A6 in our case – coupled with the electro-hydraulic model of the suspension dampers. Concerning parameter sensitivitie, the goal is to capture them for themselves – and not necessarily for optimization purpose – because their knowledge is of a great interest for the damper manufacturer.**

An important issue of the research is to consider objective functions which are based on complete time integrations along a given trajectory, the goal being – for instance – to quantify the sensitivity of the carbody rms acceleration (comfort) or of the vehicle overturning character (handling) with respect to suspension parameters. On one hand, the accuracy of the various partial derivatives computation can be greatly enhanced thanks to the symbolic capabilities of our ROBOTRAN multibody program. On the other hand, the computational efficiency of the process also takes advantage of the recursive formulation of the multibody equations of motion which must be time integrated with respect to both the generalized coordinates and their partial derivatives in case of the so-called direct method underlying sensitivity analysis.

Keywords— **multibody systems, sensitivity analysis, symbolic generation, vehicle dynamics**

I. Introduction

A. Research context

WITHIN the framework of our collaboration with the Tenneco Automotive Company which develops car suspension systems (Monroe™ dampers), it recently appeared that the role or – more specifically – the precise impact of suspension parameters on comfort and handling performances needed to be better quantified. For instance, in the course of a recent multibody modeling project with Tenneco, it was shown by simulation that, among the 21 (!) suspension parameters they have to deal with, some of them have – finally – no (or very little) influence on specific dynamic performances of the car (an Audi A6 in this case): this non-sensitive nature was, surprisingly for us, a very fruitful result for them. As another more recent example which relates to human subjective evaluation of car performances, it is obviously an accepted fact that the increase of the carbody roll motion has a negative effect, while a decrease does not necessarily have a positive one! This "unilateral" observation – which results only from human perceptions – allows us to illustrate the context and the purpose of the present research: the development of a precise, robust and efficient method to quantify suspension parameter sensitivity for given parameter ranges and specific car trajectories and excitations.

B. Problem formulation

The applications to be dealt with consist of modern cars with multi-link suspensions equipped with various possible morphologies of passive or semi-active hydraulic dampers. Considering the complexity of such systems and the fact that model validation is mandatory in such a collaborative research (see Fig. 1 for example), the model must be sufficiently refined and accurate. It consists of a 3D multibody model of the car, which includes multi-link suspension kinematics, wheel/ground force models issuing from [5], and a dynamic model of the suspension's hydraulic system [6] taking oil compressibility into account (see Fig. 2). Such a model and its experimental validation have previously been presented [8], the emphasis having been placed on the way to obtain an hybrid multibody-hydraulic model coupled at the equational level, without resorting to co-simulation techniques.

For the present project, the relevant sensitivity anal-

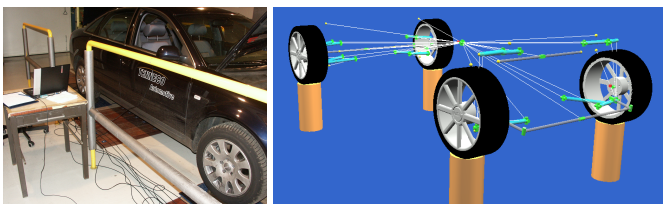

Fig. 1. Model validation - Up: Audi A6 on the shaker, Bottom: the MBS simulation (wireframe snapshot)

yses are already well defined in terms of parameters p and objective functions f to be considered: typically the former (p) denote suspension design parameters (orifice section, pipe length, electro-valve current etc.); the lat-

ter ($\psi(p,t)$) mainly concern rms – possibly filtered – accelerations, mean dissipated power, carbody yaw or roll rates etc., thus requiring a time integration from $t^0 \rightarrow t$ along prescribed trajectories (combining straight/curved, smooth/uneven stretches of road, etc.).
Further to our previous experience in vehicle dynamics, particular attention will be paid to the non-linear character of the multibody-hydraulic equations, with respect to both the generalized coordinates q and the envisaged parameters p, and to the computational cost of the objective function sensitivity $\frac{\partial \psi(p,t)}{\partial p}$. Indeed, the latter depends on full trajectories (from t^0 to t) and must be computed, not only around a nominal parameter value p_k, but for a range $p_{inf} < p_k < p_{sup}$, that is: $\frac{\partial \psi(p,t)}{\partial p}|_{p=p_k}, k = 1...n$.
Rather than investigating new sensitivity methods, the emphasis will primarily be placed here on the *problem formulation*, by tackling numerical/symbolic differentiation, time integrator accuracy and computer efficiency, within the framework of the so-called *direct* method [4].

II. Sensitivity Analysis: Formulation

In our case, we formulate the multibody dynamic equations in terms of relative joint coordinates q for which possible constraints must be satisfied at any time, as for instance to ensure body loop closure (ex.: car multi-link suspension mechanisms). The general formulation of the equations of motion can be written as:

$$M(q,\delta)\,\ddot{q} + c(q,\dot{q},f,\delta) = J^t \lambda \tag{1}$$

$$h(q) = 0 \tag{2}$$

$$\dot{h}(q,\dot{q}) = J(q)\dot{q} = 0 \tag{3}$$

$$\ddot{h}(q,\dot{q},\ddot{q}) = J(q)\ddot{q} + \dot{J}\dot{q}(q,\dot{q}) = 0 \tag{4}$$

where:
- M is the generalized mass matrix of the unconstrained system;
- δ gathers the system parameters (dimensions, mass, inertia, etc.) together;
- $f(q,\dot{q},\delta)$ represents all the – internal and external – contributive forces and torques acting on the system;
- $J \triangleq \frac{\partial h}{\partial q^i}$ denotes the constraint Jacobian matrix;
- $\dot{J}\dot{q}(q,\dot{q})$ is the quadratic term (expression in $\dot{q}^i\dot{q}^j$) of the constraints at acceleration level;
- λ represents the Lagrange multipliers associated with the constraints.

As far as we are concerned, we have definitively opted for the Coordinate Partitioning technique [1] in which the joint coordinates q – as well as the constraint Jacobian matrix J – are partitioned as follows:

$$q = \begin{pmatrix} u \\ v \end{pmatrix} \; ; \; J = \begin{pmatrix} J_u \\ J_v \end{pmatrix} \tag{5}$$

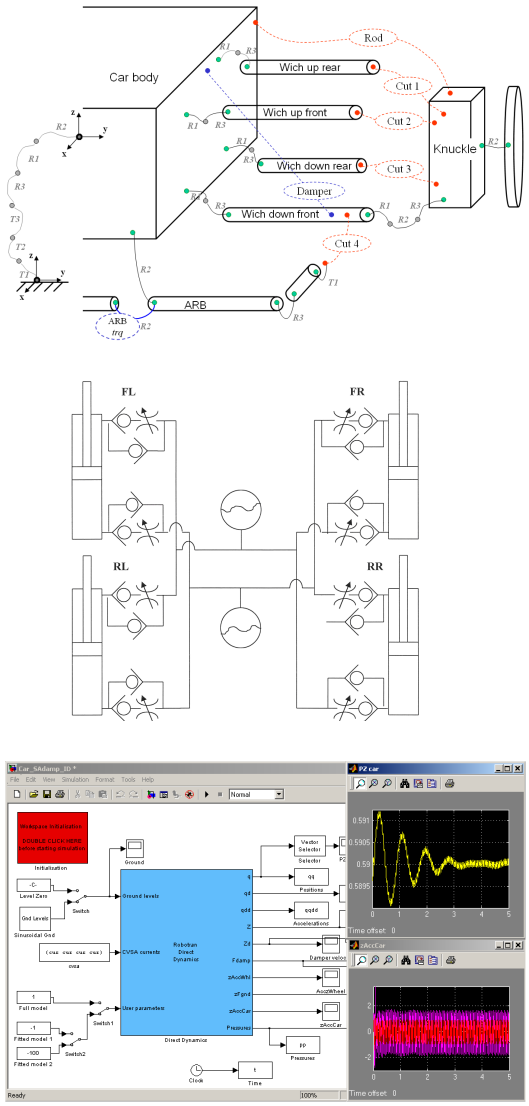

Fig. 2. Audi A6: ROBOTRAN multibody-hydraulic model and time simulation

where u denotes the subset of *independent* coordinates and v the subset of *dependent* coordinates. Based on this partitioning, it is possible to solve the constraints at position[1], velocity and acceleration levels,

$$v = v(u) \; ; \; \dot{v} = -J_v^{-1} J_u \dot{u} \; ; \; \ddot{v} = -J_v^{-1} \left(J_u \ddot{u} + \dot{J}\dot{q} \right) \tag{6}$$

and to reduce the DAE system (1 – 4) into a pure ODE system [7] witch can be synthetically written:

$$M_r(u,\delta)\ddot{u} + F_r(u,\dot{u},f,\delta) = 0 \tag{7}$$

This ODE system constitutes the equations of motion of the constrained multibody system described in terms of the independent generalized coordinates u. Finally, by solving this linear system (using for instance a Cholesky decomposition of the reduced mass matrix M_r), the independent

[1] using an iterative Newton-Raphson algorithm: $v^{k+1} = v^k + ...$

accelerations $\ddot{u}$ can be explicitly computed:

$$\ddot{u} = \phi(u, \dot{u}, f, \delta) \tag{8}$$

At this point, it is worth mentioning that for any MBS containing nonlinear constraints (ex. resulting from closed-loops), ROBOTRAN is able to generate the explicit reduced form (8) in a *fully symbolic* way, including the loop closure and the reduction process [2].
Thus for the explicit form (8), a *unique* function (in C, Matlab, ect.), generated by ROBOTRAN, computes the accelerations $\ddot{u}$ (and possible "sub-products" such as the Lagrange multipliers λ and the dependent coordinates v, $\dot{v}$, $\ddot{v}$) according to Fig. 3. The input of such functions are:
- u, $\dot{u}$: the generalized position and velocities (from the previous time step for instance);
- δ, the system parameters;
- p, any parameter (or set of parameters) with respect to which a sensitivity analysis is envisaged.

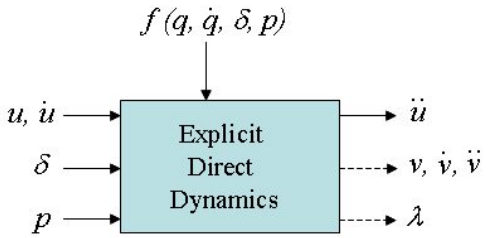

Fig. 3. Symbolic computation of the direct dynamics for constrained MBS

Let us emphasize that from a pure computational point of view, the availability of the explicit direct dynamics in symbolic form (based on recursive formalisms) allows us to simulate *better than real time* full car models with wheel/ground interactions and multi-link suspensions, in the SIMULINK environment. This efficiency, mainly due to the simplification capabilities of the ROBOTRAN symbolic generator, obviously represents an interesting "starting point" for the proposed sensitivity process, particularly costly computationally speaking.
In the multibody dynamic context, a typical objective function $\psi(p)$ for sensitivity analysis – or optimization – purpose (see [4], [3]) can be written as:

$$\psi(p) = G^1(t^1, u^1, \dot{u}^1, p) + \int_{t^0}^{t^1} F(t, u, \dot{u}, \ddot{u}, p)\, dt \tag{9}$$

in which:
- t^0 and t^1 are the initial and final simulation time;
- G^1 refers to the final state (ex. the configuration at t^1 of a given body of the system);
- F depends on the dynamic behavior of the system in the time interval $[t^0, t^1]$, such as the rms vertical acceleration of the car driver, the mean power dissipated at the wheel/ground contact, etc.

For the general objective function (9), sensitivity analysis consists in computing $\frac{d\psi}{dp}$, that is:

$$\begin{aligned}\frac{d\psi}{dp} &= \frac{\partial G^1}{\partial u^1}\cdot\frac{du}{dp}\bigg|_{t^1} + \frac{\partial G^1}{\partial \dot{u}^1}\cdot\frac{d\dot{u}}{dp}\bigg|_{t^1} + \frac{\partial G^1}{\partial p} \\ &\quad + \int_{t^0}^{t^1}\left(\frac{\partial F}{\partial u}\cdot\frac{du}{dp} + \frac{\partial F}{\partial \dot{u}}\cdot\frac{d\dot{u}}{dp} + \frac{\partial F}{\partial \ddot{u}}\cdot\frac{d\ddot{u}}{dp} + \frac{\partial F}{\partial p}\right) dt\end{aligned} \tag{10}$$

Let us first point out that in our case the only state variables are the *independent* coordinates u (and $\dot{u}$). Indeed, the remaining variables v (and $\dot{v}$) have been eliminated from the model during the reduction process (from the DAE (1 – 4) to the ODE (7) or 8)), v and $\dot{v}$ being expressed in terms of u and $\dot{u}$ according to the constraints solution.
Within expression (10), the unknown sensitivity matrices $\frac{du}{dp}(t)$, $\frac{d\dot{u}}{dp}(t)$ and $\frac{d\ddot{u}}{dp}(t)$ can be computed via the so-called *direct method* [4] which consists in solving the differential equations for sensitivity matrices *simultaneously* with the equations of motion as explained here below.
Considering the semi-explicit form of the dynamic equations (7), any δp yields a small change in the system response δu, $\delta\dot{u}$ and $\delta\ddot{u}$ and thus sensitivity matrices can be calculated via the following equations in which, for sake of simplicity, we have defined $\Gamma(u, \dot{u}, \ddot{u}, \delta) \triangleq M_r(u, \delta)\ddot{u} + F_r(u, \dot{u}, f, p)$:

$$M_r\cdot\frac{d\ddot{u}}{dp} + \frac{\partial\Gamma}{\partial\dot{u}}\cdot\frac{d\dot{u}}{dp} + \frac{\partial\Gamma}{\partial u}\cdot\frac{du}{dp} + \frac{\partial\Gamma}{\partial p} = 0 \tag{11}$$

This equation can be time integrated simultaneously with the equations of motion (7). When using first order time integration schemes, second order derivatives $\ddot{u}$ and $\frac{d\ddot{u}}{dp}$ can be gathered together to define a new auxiliary variable y:

$$y = \begin{pmatrix} y^1 \\ y^2 \end{pmatrix} \triangleq \begin{pmatrix} u \\ \dot{u} \end{pmatrix};\ \dot{y} = \begin{pmatrix} \dot{y}^1 \\ \dot{y}^2 \end{pmatrix} \triangleq \begin{pmatrix} \dot{u} \\ \ddot{u} \end{pmatrix};$$

and similarly for the sensitivities u_p:

$$y_p = \begin{pmatrix} y_p^1 \\ y_p^2 \end{pmatrix} \triangleq \begin{pmatrix} \frac{du}{dp} \\ \frac{d\dot{u}}{dp} \end{pmatrix};\ \dot{y}_p = \begin{pmatrix} \dot{y}_p^1 \\ \dot{y}_p^2 \end{pmatrix} \triangleq \begin{pmatrix} \frac{d\dot{u}}{dp} \\ \frac{d\ddot{u}}{dp} \end{pmatrix}$$

The global system reads:

$$\begin{aligned}\dot{y}^1 &= y^2 \\ \dot{y}^2 &= -M_r^{-1}(y^1, p)\left(F_r(y^1, y^2, f, p)\right) \\ \dot{y}_p^1 &= y_p^2 \\ \dot{y}_p^2 &= -M_r^{-1}(y^1, p)\left(\frac{\partial\Gamma}{\partial\dot{u}}\cdot\frac{dy_p^2}{dp} + \frac{\partial\Gamma}{\partial u}\cdot\frac{dy_p^1}{dp} + \frac{\partial\Gamma}{\partial p}\right)\end{aligned} \tag{12}$$

which has the following suitable form for first order integrators

$$\dot{z} = \phi(z,t) \text{ where } z \stackrel{\Delta}{=} \begin{pmatrix} y \\ y_p \end{pmatrix}$$

As previously mentioned, the reduced mass matrix inversion in (12_b, 12_d) will be advantageously replaced by a Cholesky decomposition process.
The computational cost of the equations of motion (12_b) can be noticeably reduced by means of the symbolic generation underlying the ROBOTRAN program (factor 8 to 10) and, additionally, by using the explicit formulation (8) (fully symbolic generation) instead of the semi-explicit one (7) (factor 2 to 4).

The main reason of the "symbolic versus numerical" benefit comes more from the *recursive* nature of the dynamic equations which is at the root of the recursive symbolic elimination of useless equations in ROBOTRAN (see Section III-B), than from the symbolic simplification of expressions, obviously also performed by the program.

III. Sensitivity Analysis: Symbolic Computation

A. Introduction

Considering now the sensitivity equations $(12)_d$, our goal is to generate them also symbolically. First of all, it is worth noting that the complexity of these equations mainly comes from the computation of the partial derivatives $\frac{\partial \Gamma}{\partial \ddot{u}}$ and $\frac{\partial \Gamma}{\partial u}$ for large multibody systems like those we have to deal with (full car with 3D suspensions, full railway vehicles, etc.) and for which the direct dynamics $(12)_b$ is far from being trivial for symbolic programs. Moreover, in the context of the Coordinate Partitoning process, the computation of equations $(12)_d$ is also not trivial and the associated complexity strongly depends on the availability of the various elements; in particular, if the constraints $h(q)$ are solved at position, velocity levels in distinct processes or "subroutines" according to equations (6), the partial derivatives of the dependent coordinates $\frac{dv}{dp}$ and $\frac{d\dot{v}}{dp}$ will be needed *explicitly*, as well as those related to the constraints and the Jacobian themselves, for the computation of $\frac{\partial \Gamma}{\partial \ddot{u}}$ and $\frac{\partial \Gamma}{\partial u}$.
At position level for instance, we have to compute

$$\frac{dv}{dp} = -J_v^{-1} \frac{\partial h}{\partial p}$$

which requires the explicit computation of the constraints sensitivity $\frac{\partial h}{\partial p}$. The same conclusion holds for constraints derivatives.
For these reasons, the *explicit* fully symbolic formulation (8) of the direct dynamics (see Fig. 3), is perfectly suited to a recursive symbolic differentiation process directly applied to the output $\ddot{u}$, to produce $\frac{d\ddot{u}}{\partial p}$ straightforwardly. This is the purpose of the two next Subsections.

B. Recursive Symbolic Generation in ROBOTRAN

To clarify the following explanations, we name a *recursive scheme* denotes any formalism (kinematic, dynamic, direct, inverse, ...) written as one or more algorithmic loops covering the kinematic chains of bodies. Typically, the well-known Newton/Euler recursive formalism, which underlies the ROBOTRAN symbolic generation of system (1) for unconstrained systems, represents a recursive scheme consisting of two algorithmic loops: one for the forward kinematics, the second for the backward dynamics [7].
To illusttrate the recursive nature of these formalisms, let us consider, in the forward kinematics, the relation which expresses the absolut angular velocity of a given body 3 with respect to body 2, its parent body in the chain:

$$\boldsymbol{\omega}^3 = \boldsymbol{\omega}^2 + \boldsymbol{\phi}^3 \dot{q}^3 \tag{13}$$

in which joint 3 is revolute along unit vector $\boldsymbol{\phi}^3$. The matrix form of this equation symbolically reads in the body 3 attached-frame $\{\hat{\mathbf{X}}^{\mathbf{3}}\}$:

$$\begin{array}{lcl} \text{OM13} & = & \text{qd(3)+ OM12} \\ \text{OM23} & = & \text{OM22*C3+OM32*S3} \\ \text{OM33} & = & \text{-OM22*S3+OM32*C3} \end{array} \tag{14}$$

where OMij denotes the i^{th} component of the j^{th} body angular velocity in frame $\{\hat{\mathbf{X}}^{\mathbf{j}}\}$, qd(j) denotes $\dot{q}^j$ and Cj, Sj represent $\cos(q^j), \sin(q^j)$ respectively.

In ROBOTRAN , each recursive equation of type (15), once symbolically evaluated, is stored in a dynamic list linked by C-pointers as indicated in Fig. 4. By "symbolically evaluated", we mean that the right hand side (RHS) of each equation is a symbolic expression – previously simplified – stored in the computer memory and located via C-pointers. The process can be summarized in two tips:
1. A recursive equation LHS=RHS (ex.: OM33= −OM22*S3+OM32*C3) is symbolically evaluated. The LHS (OM33) becomes a new *auxiliary* variable, i.e. an elementary expression, which is generated as soon as the RHS is evaluated.
2. The list is dynamically increased by one unit in which:
- pointer *ptr_previous* links the unit to the previous one in the recursive algorithm
(*ptr_previous* = NULL for the first element),
- pointer *ptr_next* will link the unit to the next one (*ptr_next* = NULL for the last element),
- pointer *ptr_left* points to the LHS leaf expression,

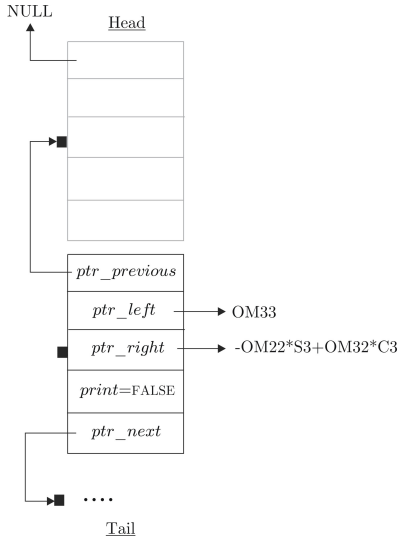

Fig. 4. C linked-list of recursive equations

- pointer *ptr_right* points to the RHS expression,
- The boolean flag *print* is a priori set to FALSE because the corresponding expression do not a priori contribute to the expected results.

Elimination process

The linked list is complete as soon as all the final results have been symbolically evaluated (ex.: M, c in equation (1) or $\ddot{u}$ in equation (8)).
Each result (ex. for the mass matrix: $M_{(i,j)}, i = 1:n, j = i:n$) having the same structure as the previous recursive equations (i.e. LHS = RHS) is also stored in the list, but of course with a *print* flag set to TRUE. Once they have been evaluated, the selection process can start by scanning the list from tail to head, and can be summarized as follows:
1. Start from the tail element of the list (i.e. the last symbolically evaluated equation (ex.: the first mass matrix element $M_{(1,1)}$),
2. Analyze the contents of the equation:
- if the corresponding *print* flag is TRUE, then for each auxiliary variable encountered in the RHS of the equation, find and mark, by setting *print* to TRUE, the recursive equation in the list which symbolically evaluates this variable,
- else, go directly to step 3, because the corresponding equation is superfluous,
3. Go to the previous element of the list whose address is given by the pointer *ptr_previous*:
- if the address is the NULL pointer, the head has been reached and the process is finished: go to step 4,
- else, return to step 2,
4. Print in the output file, by covering the list from head to tail, the equations whose *print* flag has been set TRUE.

Fig. 5 summarizes this process using an academic example. Thanks to this recursive simplification process, we

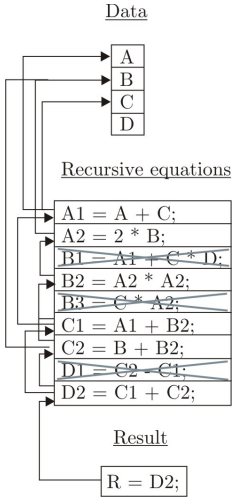

Fig. 5. Recusive elimination of superfluous equations

note that more than 30% of the equations are superfluous (for direct dynamics) which is far from being negligible.
In terms of symbolic computation performances, the multiple scanning of the list (required by step 2 in the process) can be quite time consuming for large systems because string comparison is performed thousands of times to find and mark interdependencies. The use of supplementary flags in the list elements, not detailed here, allows us to find and mark the useful equations in an immediate manner. This allows us to reduce the elimination process to a few seconds, even for more than 200 d.o.f. multibody systems.

C. Recursive symbolic differentiation

As mentioned in the Section II, sensitivity analysis of large constrained MBS led us to develop a specific procedure to symbollically differentiate a given recursive scheme with respect to a given (set of) parameter(s) p. In the context of differentiation, the equations produced by recursive multibody formalisms can be advantageously considered as interwoven functions ($f(g(h(...(x))))$). However, if the corresponding differentiation rules are applied blindly to a recursive scheme, we have observed that they produce a very large non-optimized symbolic output (ex. $\frac{d\ddot{u}}{\partial p}$) even for medium-sized multibody models: the interest of the recursive computation (see eqs. (13) and Fig. 4) is thus *completely* lost.
Therefore, we take advantage of the elimination procedure described in the previous Section to solve this problem. When evaluating a given recursive scheme, we assume –apriori– that each equation depends, explicitly or not, on the set of system parameters or variables (ex.: $p_1, p_2, ...p_k$) with respect to which the differentiation must be performed. For instance in the following equation:

$$\text{AUXJ} = \text{AUXI} + 2 * \text{P} \tag{15}$$

AUXJ explicitly depends on the variable P via the second term. A priori, it may also depend implicitly on P via the first term AUXI.
We thus systematically create and evaluate a new *recursive* variable, for instance AUXJ_P, for the partial derivative of the current equation with respect to P

$$\text{AUXJ\_P} = \text{AUXI\_P} + 2 \tag{16}$$

even if, in the end, it appears that this new auxiliary variable is 0 or simply useless. If it is useless, the elimination process described previously will detect it and remove the corresponding equation from the list, before printing. Such a technique gives rise to a *compact recursive computation* of the required derivatives. To illustrate this, let us consider in (17) and (18), the symbolic evaluation of one element ($J_{(3,1)}$) of the Jacobian matrix $\frac{dx}{dq}$ of a position vector $x(q)$ associated with a kinematic chain composed of nine joints.
In (17), the classical differentiation rule applied to $x(q)$, i.e. the resulting equation ($J_{(3,1)}$ = ...)**,** is far more consuming in terms of operators (220 $\{*,+,-\}$) than when obtained via the proposed recursive differentiation as (62 $\{*,+,-\}$).

```
J(3,1)  =  q8*(C1*C7*(-C3*S4*C5+S3*S5)
           -S1*(S2*(S3*S4*(-C5*C7+S5*C6*S7)
           +S7*(-C3*C5*C6+S3*C4*S6))+C7*(C2*C4*C5-S2*C3*S5))
           +S7*(C1*(C3*C4*S6+C6*(C3*S4*S5+S3*C5))
           -S1*C2*(-C4*S5*C6+S4*S6)))+D13*S1*S2
           +D14*(C1*S3+S1*S2*C3)+D15*(C1*S3+S1*S2*C3)
           +D16*(C1*(C3*S4*S5+S3*C5)+S1*(C2*C4*S5
           -S1*C2*(-C4*S5*C6+ S4*S6)));
           -S2*(-C3*C5+S3*S4*S5)))+D17*(C1*C6*(C3*S4*S5+S3*C5)
           +S1*(-S2*S3*(C4*S6+S4*S5*C6)+C6*(C2*C4*S5
           +S2*C3*C5))+S6*(C1*C3*C4-S1*C2*S4))
           +D18*(C1*S7*(C3*S4*C5-S3*S5)-S1*(S2*(S3*S4*(C5*S7
           +S5*C6*C7)+C7*(-C3*C5*C6+S3*C4*S6))+S7*(-C2*C4*C5
           +S2*C3*S5))+C7*(C1*(C3*C4*S6+C6*(C3*S4*S5+S3*C5))
           -S1*C2*(-C4*S5*C6+S4*S6)))+D19*(C1*S7*(C3*S4*C5
           -S3*S5)-S1*(S2*(S3*S4*(C5*S7+S5*C6*C7)
           +C7*(-C3*C5*C6+S3*C4*S6))+S7*(-C2*C4*C5+S2*C3*S5))
           +C7*(C1*(C3*C4*S6+C6*(C3*S4*S5+S3*C5))
           -S1*C2*(-C4*S5*C6+ S4*S6)));                    (17)
```

```
RO22  =  S1*S2;                 RO32  =  -C1*S2;
RO82  =  -S1*C2;                RO92  =  C1*C2;
RO23  =  RO22*C3+C1*S3;         RO33  =  RO32*C3+S1*S3;
RO53  =  -RO22*S3+C1*C3;        RO63  =  -RO32*S3+S1*C3;
RO54  =  RO53*C4+RO82*S4;       RO64  =  RO63*C4+RO92*S4;
RO84  =  -RO53*S4+RO82*C4;      RO94  =  -RO63*S4+RO92*C4;
RO25  =  RO23*C5-RO84*S5;       RO35  =  RO33*C5-RO94*S5;
RO85  =  RO23*S5+RO84*C5;       RO26  =  RO25*C6+RO54*S6;
RO36  =  RO35*C6+RO64*S6;       RO27  =  RO26*C7-RO85*S7;
RO87  =  RO26*S7+RO85*C7;       RL23  =  RO22*D13;
RL24  =  RO23*D14;              JT34_1  =  RL23+RL24;
RL25  =  RO23*D15;              JT35_1  =  JT34_1+RL25;
RL26  =  RO25*D16;              JT36_1  =  JT35_1+RL26;
RL27  =  RO26*D17;              RL28  =  RO27*D18+RO87*q(8);
JT37_1  =  JT36_1+RL27;         JT38_1  =  JT37_1+RL28;
RL29  =  RO27*D19;              J(3,1)  =  JT38_1+RL29;
```
(18)

For larger models and in particular for the explicit direct dynamics (8) of constrained multibody systems, the advantage of the recursive differentiation is really significant. In fact, the *explosive* increase in the size of the classical differentiation technique is quite understandable since it amounts to destroying the recursivity of the original scheme, leading to an *in extenso* formulation like in example 17. Although the proposed recursive differentiation process is very consuming in terms of both memory storage and symbolic CPU time – because thousands of "potential" partial derivatives are computed –, these drawbacks are negligible in ROBOTRAN since the storage requirement is drastically controlled during the symbolic process [7].

IV. Sensitivity Analysis: Illustrative Results

A typical sensitivity analysis we propose to carry out is briefly illustrated here below. The multibody model is based on the one previously shown in Fig. (2), but involving semi-active suspensions. The force-velocity damper relationship is function of an electro-valve current *i*: the valve section, when reduced or enlarged, induces a higher or a lower damping coefficient of the suspension.
Two sensitivity computations are proposed here:
1. The first one concerns passenger comfort and relates to the sensitivity of the rms vertical acceleration with respect to the electro-valve current for a given road excitation;
2. The second one deals with car handling and aims at showing the influence of the front anti-roll bar torsion stiffness (thus $p = K_{arb}$) on the under/oversteering character of the car, for a given pilot steering input.

A. Comfort-oriented sensitivity

According to Fig. 2, the car is shaked on the 4-poster test bench (left/right out-of-phase noisy sinusoidal input (1 Hz,

Amplitude : $\pm 10mm$). The acceleration of the carbody center of mass[2] is given in Fig. 6_{up} for illustrative purpose only. The rms value of the vertical acceleration can be

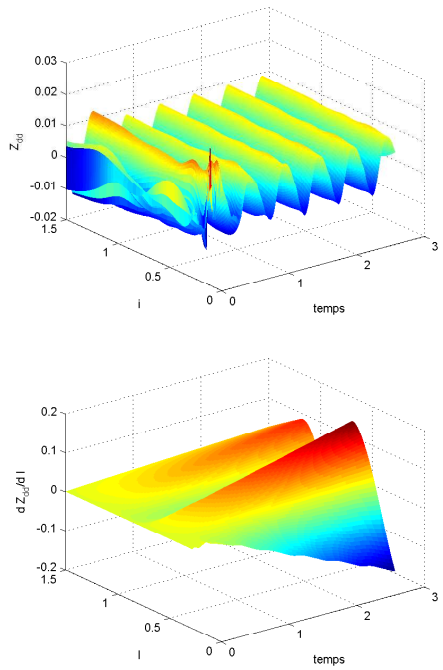

Fig. 6. Audi A6 on poster - Up: carbody acceleration, Bottom: carbody acceleration sensitivity

computed straightforwardly:

$$\ddot{z}^{rms} \triangleq \sqrt{\frac{1}{t_f - t_i}\int_{t_i}^{t_f} [\ddot{z}(t)]^2\, dt} = xxx\,\frac{m}{s^2} \text{ for the present simulation case.}$$

The sensitivity time history of the vertical acceleration $\ddot{z}_i$ for distinct damper electro-valve currents i (thus $p = i$) is shown in Fig. 6_{bottom}. While being more "cosmetic than pragmatic", this 3D plot contains relevant information for the manufacturers.

First of all, with respect to time t, the envisaged future trajectories will be composed of successive sections of different natures: smooth or uneven surfaces, sections with potholes or transverse discontinuities, etc. which will define successive time intervals for which dedicated objective function could be evaluated (like rms values or mean dissipated power, etc...).

With respect to the parameter p itself, it is useful to observe the evolution of the sensitivity with respect to some parameter range in order to make sure of the "robustness" of the dynamic behavior with respect to some parameter inaccuracy. Fig. 7_{up} shows, for instance the way the sensitivity of the rms acceleration $\ddot{z}_i^{rms}$ changes with respect to

[2]Other sensor points could easily be used, in particular considering the real passenger location.

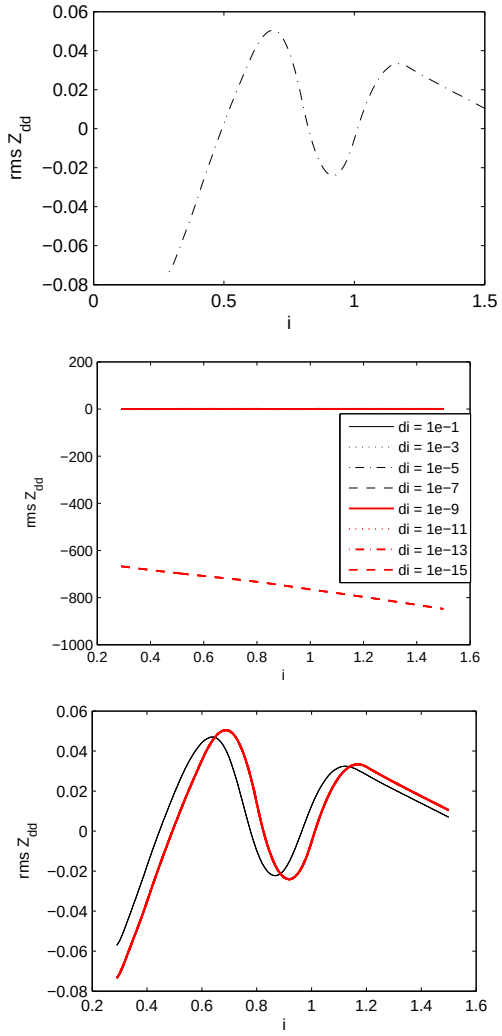

Fig. 7. Carbody rms acceleration - Up: influence of the electro-valve current, Center: repercussion of the numerical differentiation accuracy, Bottom: zoom of the center figure

the current i (range: 0.3 A to 1.5 A). Since it is rather difficult to "feel" the meaning of the absolute value of $\ddot{z}_i^{rms}$, the latter will be advantageously translated in some pragmatical "metric", as for instance the percentage of output variation for a given relative (ex. 1 %) or absolute (ex. 0.1A) variation of the considered parameter.

The purpose of Fig. $7_{center\,and\,bottom}$ is completely different: it simply illustrates the interest in using symbolical (i.e. analytical) differentiation technique, instead of numerical differentiation whose accuracy unavoidably depends on the parameter increment Δp. Moreover, with respect to symbolic differentiation, numerical approximation of gradients is unavoidably more time consuming since it requires at least two function evaluations: this additional cost is not negligible regarding the envisaged applications.

B. Handling-Oriented Sensitivity

In terms of car handling, lots of investigations can be carried out in terms of sensitivity with respect to suspension design. Within the frame of this paper, let us focus on the under/over-steering character of the car when negotiating a curve. In the literature, one can find various way to quantify this phenomenon, by comparing the so-called wheel slip angles of front and rear wheels, by considering or not the instantaneous centripetal acceleration of the car, etc. A simplest way – sufficient to illustrate our approach – consists in using for the objective function a more global parameter: the carbody slip angle β illustrated in Fig. 8_{up}. β is the angle between the car longitudinal orientation $\overrightarrow{\mathbf{X}}$ and the car instantaneous center of mass velocity $\overrightarrow{\mathbf{V}}$. the case illustrated refers to an oversteering situation since the car turns "too much" with respect to the normal trajectory T. Fig. 8_{bottom} represents the pilot steering input time history which is introduced via the steering rack displacement in the model.

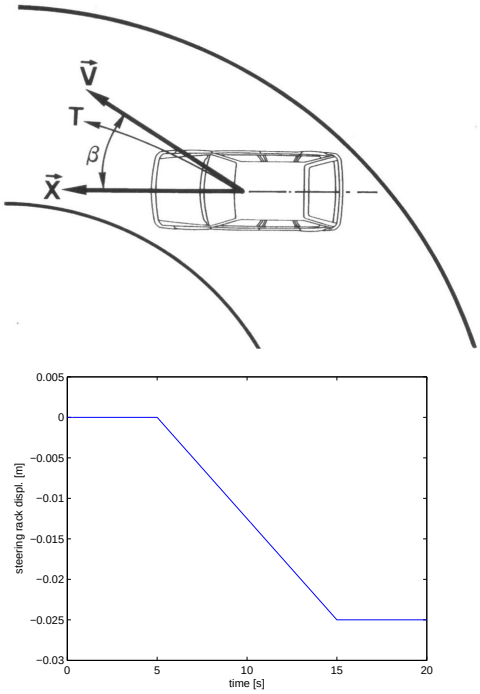

Fig. 8. Cornering situation - Up: car slip angle β, Bottom: steering rack displacement (imposed)

As regards the over/understeering behavior of a vehicle negotiating a curve, a well-established observation is the following: increasing the roll stiffness K of the front [resp. rear] suspension, via an anti-roll bar for instance, increases [resp. decreases] the car understeering behavior. It is for instance possible to transform an understeering car (as we are daily using) into an oversteering one, simply by adding an anti-roll bar to the rear suspension. Without entering into details, the reason of this phenomenon comes from the nonlinear relationship between the lateral cornering force and the normal force: the global lateral – or centripetal – force on a given suspension (featuring left + right wheels) decreases when the vertical load transfer increases, which is the case when a stiffer anti-roll bar is used for that suspension.

For the proposed steering excitation, Fig. 9_{up} shows the Audi A6 trajectory for different values of the front suspension anti-roll bar torsions stiffness K. Fig. 9_{middle} and 9_{bottom} relates to the vehicle configuration in steady state curving (line 's-s' in Figs. 8_{bottom} and 9_{up}). At this point, the vehicle – if stable – reaches a given slip angle β corresponding to a given amount of under/oversteer as shown in Fig. 9_{middle}. Its sensitivity β_K with respect to the front anti-roll bar stiffness K is plotted in Fig. 9_{bottom}. On can observe a rather smooth evolution, which will be

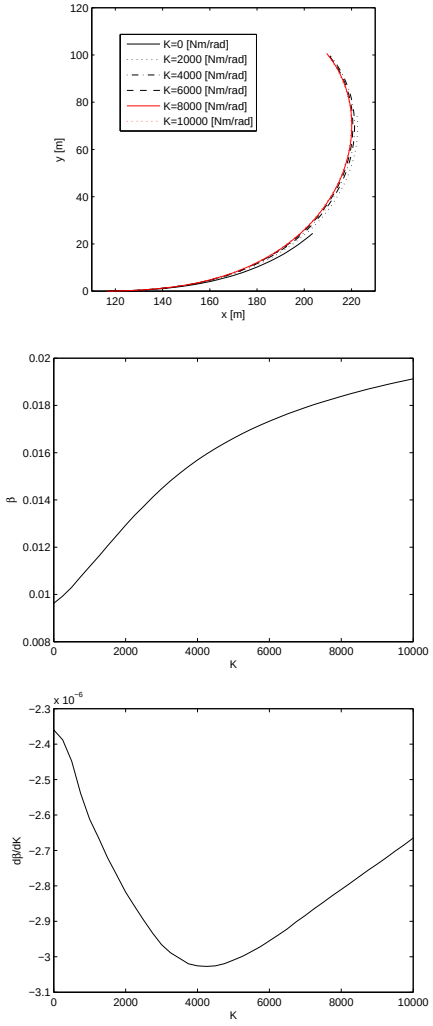

Fig. 9. Vehicle cornering behavior - Up: car trajectory, Center: car slip angle β versus K, Bottom: car slip angle sensitivity β_K versus K

not necessarily the case for situations in which the lateral forces are for instance closer to their saturation point.

V. Conclusions

The present work deals with the sensitivity analysis of constrained multibody models, the main applications being road vehicles equipped with modern suspensions. Considering the size of those systems and the necessity to use a rather refined multibody model to properly capture the required dynamic behaviors, the symbolic approach underlying the ROBOTRAN program is appealing for two reasons: the explicit and recursive computation of the generalized accelerations (direct dynamics) which are necessary for computing objective functions based on time integrations of the system (ex: car following a trajectory, ...) and the explicit – and also recursive – generation of the partial derivatives of the direct dynamics, with respect to a given (set of) parameter(s). All the process is based on the Coordinate Partitioning approach whose well-known computational cost is strongly reduced thanks to the symbolic simplification capabilities of the ROBOTRANprogram.
Direct method is used to compute and time integrate the multibody equations of motion simultaneously with the sensitivity differential equations, the main drawback with respect to other approaches (ex. the adjoint method) being the numerical cost. Once again, the symbolic generation allows us to minimize this problem.
Additional applications – in the field of vehicle dynamics – will be carried out in the next future to compare and quantify the process performances with respect to the adjoint approach.
In terms of results interpretation, both the objective functions and the parameters can be of different nature (acceleration, force, power, etc.. for the former; dimension, current, stiffness, etc. for the latter). Thus, it is proposed to establish some *sensitivity metric* with the damper manufacturer, to decide what is "acceptable or not" for a given vehicle dynamic situation.

VI. Acknowledgements

This research work was carried out in collaboration with the Belgian Company Tenneco Automotive (Sint-Truiden, Belgium): their assistance is gratefully acknowledged.

References

[1] R.A. Wehage and E.J. Haug. *Generalized coordinate partitioning for dimension reduction in analysis of constrained dynamic systems.* Journal of Mechanical Design 104, pp. 247-255, 1982.

[2] P. Fisette, T. Postiau, L. Sass and J.C. Samin. *Fully Symbolic Generation of Complex Multibody Models*, Mechanics Based Design of Structures and Machines, Marcel Dekker Inc., New York, 30/1, pp. 1-32, 2002.

[3] J.Y. Ding, Z.K. Pan and L.Q. Chen. *Second order adjoint sensitivity analysis of multibody systems described by differential-algebraic equations.* Multibody System Dynamics 18, pp. 599-617, 2007.

[4] P. Eberhard. *Analysis and Optimization of Complex Multibody Systems using Advanced Sensitivity Analysis Methods.* ZAMM, 76/3, pp. 40-43, 1996.

[5] H. B. Pacejka. *Tyre and Vehicle Dynamics (Second Edition).* Butterworth-Heinemann (Elsevier), Amsterdam, 2006.

[6] S. Duym. *Simulation, Modeling and Identification, for an Automotive Shock Absorber in the Context of Vehicle Dynamics.* Vehicle System Dynamics 33, 261-185, 2000.

[7] J.C. Samin and P. Fisette. *Symbolic Modeling of Multibody System*. Kluwer Academic Publishers, Dordrecht, the Nederlands, 2003.

[8] M. Delannoy, P. Boon, B. Vandersmissen and P. Fisette. *Modeling hybrid multibody systems: application to vehicle hydraulic semi-active suspensions.* Eccomas - Multibody Dynamics 2005, Madrid, Spain, 21-24, June 2005.

[9] W.F. Milliken and D.L. Milliken. *Race Car Vehicle Dynamics.* Society of Automotive Engineers, Inc., Warrendale, USA, 1995.

Proceedings of the 8th National Congress on Theoretical and Applied Mechanics, May 28-29, Brussels, Belgium.

On the use of Transmissibility in the field of: Operational Modal Analysis and Structural Health Monitoring.

Christof Devriendt, Gunther Steenackers, Patrick Guillaume
Department of Mechanical Engineering, Vrije Universiteit Brussel
Acoustics and Vibration Research Group
Pleinlaan 2, 1050 Brussels - Belgium
email: cdevrien@vub.ac.be

Abstract— **It is a well-known fact that linear dynamic behavior of structures can be studied by modeling the relation between force(s) [input(s)], acting on a structure, and their resulting structural vibration response(s) [output(s)]. In many applications it often becomes hard (or impossible) to experimentally measure the excitation. In these cases the available techniques have serious limitations, only in limited cases being possible to predict the behavior of a structure, quite often from more or less crude load estimation. In order to reduce this limitation, it is the aim of this research to increase the knowledge of the relations among the responses -the transmissibility- in structures, with multiple degrees of freedom and multiple excitations. This paper tends to give a short overview on its implications and the practical use that can be made of this knowledge in the fields of operational modal analysis and structural health monitoring. It will be shown how transmissibility measurements can directly be used to obtain modal parameters and it will be discussed how changes in the transmissibility properties of a structure can be a useful tool for damage detection. The results from this research shall provide solutions for some important requests of the industry, introducing new tools for the modal analysis of structures, detecting and assessing the structural damage, and better understanding the dynamic properties of a structure. The above objectives are of importance to the industry mainly for their contribution to a better safety of the structures and of the person dealing with them. The approach here proposed, based on techniques of transmissibility gives a more precise and efficient way of dealing with the above problems than the classical approach.**

Keywords— **Transmissibility, Operational Modal Analysis, Structural Health Monitoring**

I. Transmissibility functions

Transmissibility functions are defined as frequency response functions between like variables (motion response/motion input) as opposed to admittance functions which are frequency responses between conjugate variables (motions response/force input). While the last type of functions are widely used in the field of experimental modal analysis, transmissibility functions only recently made their appearance in the field of operational modal analysis [2]. It has been shown that under changing force distributions transmissibility measurements can be used to obtain modal parameters. Transmissibility functions can be measured without the knowledge of the excitation forces. It is estimated in the same way as the admittance functions, but the response is "normalized" by a reference response signal instead of an excitation signal. The transmissibility function $T_{ij}(s)$ between the output i and the reference-output j is defined as the ratio between the 2 responses $X_i(s)$ and $X_j(s)$, with s the complex parameter of the Laplace domain.

$$T_{ij}(s) = \frac{X_i(s)}{X_j(s)} \tag{1}$$

The properties of transmissibility functions differ considerably from those of the admittance functions. In general, the poles from the transmissibility functions do not correspond with the poles of the admittance functions whose poles are the system poles [2]. So, in general in transmissibility measurements each resonance is represented by a flat spot in the data instead of a peak.

One of the most interesting properties of transmissibility functions, recently shown in [2], is that the limit value of the transmissibility function (1) for the Laplace variable s going to the system's poles, λ_m, converges to

$$\lim_{s \to \lambda_m} T_{ij}(s) = \frac{\phi_{im}}{\phi_{jm}} \tag{2}$$

and becomes independent of the (unknown) forces. Therefore if we consider two transmissibility functions relating the same responses, but measured during two experiments with different loading conditions, they cross each other exactly at the resonances. This last property will allow us to obtain the modal parameters from the structure and will play a vital role in the proposed techniques for structural health monitoring using transmissibility functions.

II. Operational Modal Analysis

The goal of this section is to estimate the modal parameters directly from the set of transmissibility measurements. Classic frequency response driven modal parameter estimation methods identify first a rational polynomial transfer function model [6]. This model can be related to the physical parameters of the modal model in a second step.

The common-denominator model, or scalar matrix fraction description, is such a model and is discussed in the next paragraph [7].

The common-denominator model considers the relation between output o and input i as a rational fraction of two polynomials $B_{oi}(s)$ and $A(s)$, of which the denominator polynomial $A(s)$ is common for all input-output relations. In general the common-denominator model can be expressed as

$$\mathbf{H}(s) = \frac{\begin{bmatrix} B_{11}(s) & \dots & B_{1N_i}(s) \\ \vdots & \ddots & \vdots \\ B_{N_o1}(s) & \dots & B_{N_oN_i}(s) \end{bmatrix}}{A(s)} \tag{3}$$

with N_o and N_i respectively the number of considered outputs and inputs. The relation between the modal model and the common-denominator model is obtained by considering the frequency response function between the conjugate variables, namely the output-response o and the input-force i

$$\begin{aligned} H_{oi}(s) &= \frac{B_{oi}(s)}{A(s)} \\ &= \sum_{m=1}^{N_m} \left(\frac{\phi_{om} L_{im}}{s - \lambda_m} + \frac{\phi_{om}^* L_{im}^*}{s - \lambda_m^*} \right) \end{aligned} \tag{4}$$

with N_m the number of modes. The modal parameters λ_m, $\phi_{[:,m]}$ and $L_{[:,m]}$ are respectively the pole, mode shape and modal participation factor of mode m. The mathematical operator complex conjugate is denoted as $[.]^*$. The poles $\lambda_m = \sigma_m + \jmath\omega_m$ contain the damped natural frequencies $f_m = \omega_m/(2\pi)$ and the damping ratios $\zeta_m = -\sigma_m/(\sigma_m^2 + \omega_m^2)$. The complex operator is denoted as $\jmath$.

From this equality (4) it is clear that the structure poles are given by the roots of the denominator $A(s)$, while the mode shapes and participation factors are obtained from a singular value decomposition of the residue matrix $\mathbf{R}_m$ of mode m.

$$\mathbf{R}_m = \phi_{\mathbf{m}} \mathbf{L}_{\mathbf{m}}^{\mathbf{T}} \tag{5}$$

with the elements of the residue matrix $\mathbf{R}_m$ given by

$$\begin{aligned} r_{oi,m} &= \lim_{s \to \lambda_m} (s - \lambda_m) \frac{B_{oi}(s)}{A(s)} \\ &= \phi_{om} L_{im} \end{aligned} \tag{6}$$

and $\phi_m = [\phi_{1m} \phi_{2m} \dots \phi_{N_om}]^T$, $L_m = [L_{1m} L_{2m} \dots L_{N_om}]^T$.

In case of transmissibility measurements one considers the relation between output-response o and a reference-input-response ref. In order to be able to use a similar approach as the FRF-driven estimators and use the existing algorithms, the first step is to create a common-denominator model. All the structure poles must be the roots of this denominator.

By considering equation (2) it can easily be verified that the limit value of the subtraction of the summation of all measured transmissibility functions under an arbitrary loading condition 2, $T_{o2}(s)$ for $o = 1...N_o$ with N_o the number of outputs, and the summation of all measured transmissibility functions under a reference loading condition 1, $T_{o1}(s)$, for the Laplace variable s going to the system's poles, λ_m, satisfies

$$\lim_{s \to \lambda_m} \left(\sum_{o=1}^{N_o} T_{o2}(s) - \sum_{o=1}^{N_o} T_{o1}(s) \right) = 0 \tag{7}$$

This means that the system's poles, λ_m, are zeroes of the rational function

$$\Delta T(s) = \sum_{o=1}^{N_o} T_{o2}(s) - \sum_{o=1}^{N_o} T_{o1}(s) \tag{8}$$

From the above one can conclude that it is possible to construct a rational function with zeros equal to the system's poles, by combining two sets of transmissibility functions obtained under two different loading conditions. Therefore this function, $\Delta T(s)$, can be considered as a possible candidate for being a denominator that is common for all input-output relations with roots equal to the structure poles. Once the poles of the system are known, the damped natural frequencies f_m and the damping ratios ζ_m are subsequently obtained as

$$f_m = \frac{Im(\lambda_m)}{2\pi} \quad \text{and} \quad \zeta_m = -\frac{Re(\lambda_m)}{|(\lambda_m)|} \tag{9}$$

As has been shown in equation (2) the transmissibilities functions themselves are directly related with the mode shapes in the system poles, therefore in case of transmissibility measurements a possible common-denominator model of the transfer function matrix in case of two loading conditions and N_o output-responses could be expressed as

$$\mathbf{H}(s) = \frac{\begin{bmatrix} T_{11}(s) & T_{12}(s) \\ \vdots & \vdots \\ T_{N_o1}(s) & T_{N_o2}(s) \end{bmatrix}}{\Delta T(s)} \tag{10}$$

From this equality (10) it is again clear that the structure poles are given by the roots of the denominator $\Delta T(s)$,

while the unscaled mode shapes and operational participation factors are obtained from a singular value decomposition of the residue matrix $\mathbf{R}_m$ of mode m.

$$\mathbf{R}_m = \phi_{\mathbf{m}} \mathbf{K}_{\mathbf{m}}^{\mathbf{T}} \tag{11}$$

with the elements of the residue matrix $\mathbf{R}_m$ given by

$$\begin{aligned} r_{oi,m} &= \lim_{s \to \lambda_m} (s - \lambda_m) \frac{T_{oi}(s)}{\Delta T(s)} \\ &= \phi_{om} K_{im} \end{aligned} \tag{12}$$

and $\phi_m = [\phi_{1m} \phi_{2m} \ \dots \ \phi_{N_o m}]^T$, $K_m = [K_{1m} K_{2m} \ \dots \ K_{N_o m}]^T$,
with $K_{im} = \frac{\alpha_m}{\phi_{refm}}$ and α_m an arbitrary constant.

In general in the functions $\frac{T_{oi}(s)}{\Delta T(s)}$ each resonance of the structure is again corresponding with a peak .

From the above one can conclude that each element, $\frac{T_{oi}(s)}{\Delta T(s)}$, of the transfer matrix $\mathbf{H}(s)$ can be decomposed in a similar way as in equation (4)

$$\begin{aligned} H_{oi}(s) &= \frac{T_{oi}(s)}{\Delta T(s)} \\ &= \sum_{m=1}^{N} \left(\frac{\phi_{om} K_{im}}{s - \lambda_m} + \frac{\phi_{om}^* K_{im}^*}{s - \lambda_m^*} \right) \end{aligned} \tag{13}$$

with N (counting both the physical modes and the mathematical modes). As such, transmissibility driven stochastic identification algorithms can be considered as a stochastic counterpart of the FRF-driven deterministic algorithms. In both cases, spectral functions are used as primary data. By identifying the proposed common denominator model in a similar way as for the deterministic FRFs, by performing e.g. a parametric estimation in the frequency domain [8] [9], the damped resonant frequencies, the damping ratios and the unscaled mode shapes of each mode in the frequency range of interest can be obtained by one single identification algorithm.

In above theory will be illustrated by means of a simple numerical experiment on a steel free-free beam given in Figure 1 with dimensions: $0.7m \times 0.068m \times 0.025m$.

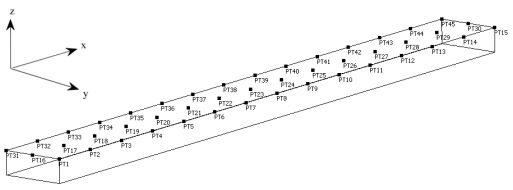

Fig. 1. Free-free beam.

A finite element model is created, using the commercially available software Comsol. In Comsol, a default meshing is applied resulting in 160 elements and the response functions are calculated, using a direct solver. The model allows us to apply in 45 points a force and to measure the responses in these points. The 45 points are equally distributed over the full length of the beam. Two experiments with two different loading conditions are performed. Loading condition 1 is an experiment with a unit harmonic point force applied in the vertical direction in location 1. During loading condition 2 the unit harmonic point force is applied in location 31. Both experiments are performed in the frequency range of 1Hz to 1600Hz.

By identifying the proposed common denominator model (10) in a similar way as for the deterministic FRFs, by performing e.g. a parametric estimation in the frequency domain [8] [9], the damped resonant frequencies, the damping ratios (Table 1) and the unscaled mode shapes, Figure 2 to Figure 5, of each mode in the frequency range of interest can be obtained by one single identification algorithm.

TABLE I
THE ESTIMATED DAMPED RESONANT FREQUENCIES AND DAMPING RATIOS

f_d [Hz]	ζ [%]
264.3	0.22
727.7	0.22
1400.5	0.22
1425.0	0.22

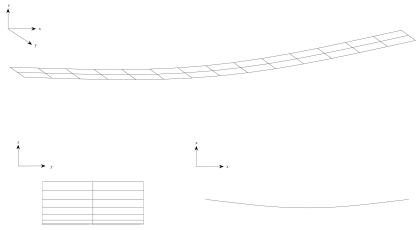

Fig. 2. First unscaled mode shape

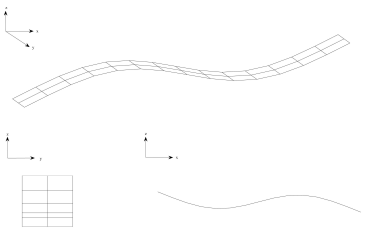

Fig. 3. Second unscaled mode shape

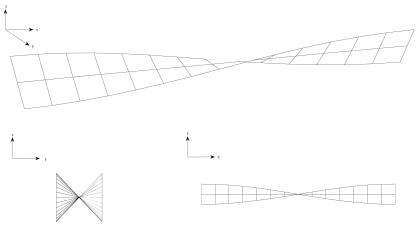

Fig. 4. Third unscaled mode shape

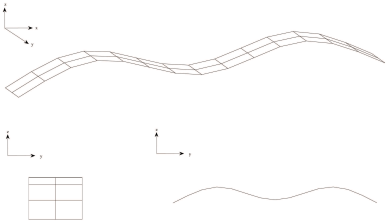

Fig. 5. Fourth unscaled mode shape

The above results show that a set of complex transmissibility measurements can be used directly to obtain the mode shapes of the tested structure. This is especially of high interest in the many cases where operating structures are excited by non-stationery (time varying) forces that cannot be measured. The central idea behind the technique is that the set of transmissibility functions become independent of the applied force in the system poles and that their value in the system poles is related with the scalar mode shape values. This property was already shown in [3] and is valid both in the case of a single point force or multiple distributed forces. This last situation is often the case when measuring in real operating conditions. The technique needs changing loading conditions, these can easily be obtained by a change in location of the force in the case of a single point force or a change in locations or amplitudes in the case of multiple distributed forces. Most of these changes can be automatically obtained by non-stationery (time varying) operating conditions.

III. Structural Health Monitoring

Another interesting case is the usage of the transmissibility concept in Structural Health Monitoring (SMH). There is only few work related with this topic and for shore a comprehensive work is represented by the the thesis of Johnson [12]. According to the author, the goal of structural health monitoring is to detect damage at or near its onset, before it becomes critical to a structure's function and integrity. One of the major challenges in detecting and locating small-scale structural damage is that this type of damage is local phenomena, and therefore a viable structural damage detection technique should be local in nature. Past research [15] has shown that the zeros, or antiresonances, of a system's transfer functions are much more sensitive to changes in the local structural properties than its poles, or resonances. Transmissibility functions in linear systems are local in nature because they are functions only input-output transfer functions zeros (antiresonances) and are completely independent of the poles (resonances).

In recent articles [11] [13] numerical and experimental examples were presented and the possibilities to use the transmissibility concept for damage detection seemed quite promising. In the work discussed so far, it was assumed that the operational conditions were constant. Operational conditions however imply that the amplitudes or locations of the working forces on the structure are not known and moreover that they might change between two successive measurements. In many situations the transmissibility functions, defined as a simple ratio between two measured responses, do depend on the amplitudes or locations of those forces. Therefore it is reasonable to expect that a change in loading conditions would imply a noticeable change in the transmissibility functions so it is not unthinkable that false damage detection might occur in such situations. A suitable operational damage detection method should however possess a high sensitivity in order to be able to detect damage in a very early stage even in the case of changing operational conditions. In this paper the effect of the frequency range will be discussed and it will be shown, although still on an exploratory basis, how the existing methods, in certain frequency ranges, can be used in a more robust way in order to avoid false damage detections that might occur if the transmissibility functions vary strongly because of the operational conditions.

The theory will be illustrated by means of a simple numerical experiment on a steel cantilever beam beam given in Figure 6 with dimensions: 1 m x 0.01 m x 0.01 m

Fig. 6. Cantilever beam

A finite element model is created, using the commercially available software Comsol. In Comsol, a default mesh is applied and the response functions are calculated, using a direct solver. The model allows us to apply a force in 10 points and to measure the responses in these points. The 10 points are equally distributed over the full length of the beam. Damage is applied by creating a cut of width 0.004 m and depth 0.0034 m between point 7 and point 8

Figure 7 shows the frequency response functions mea-

sured in point 7 for the undamaged and damaged structure. One can clearly notice a small shift between both functions. In the frequency range of interest the first resonance frequency of the beam is present. The first resonance frequency of the undamaged structure is at 8.15Hz and for the damaged structure it is at 8.00Hz

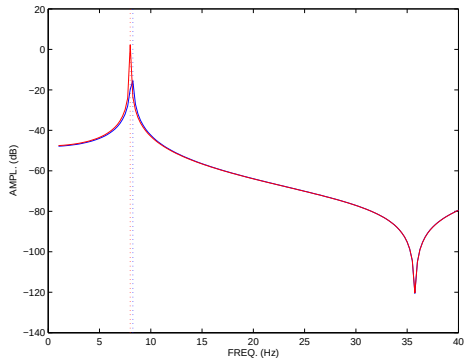

Fig. 7. Frequency response functions in point 7 for undamaged (blue) and damaged (red) case

Transmissibilities, as used in this paragraph, are still obtained by taking the ratio of two response spectra. By assuming a single force that is located in, say, the input degree of freedom (DOF) k, the transmissibility is defined as

$$T_{ij(k)}(s) = \frac{X_{ik}(s)}{X_{jk}(s)} \tag{14}$$

In the same way the transmissibility of the damaged structure can be defined

$$T^D_{ij(k)}(s) = \frac{X^D_{ik}(s)}{X^D_{jk}(s)} \tag{15}$$

A. *Constant location of applied force before and after damage*

Since the dynamic properties of a structure change in the case damage occurs it is natural to expect that the dynamic responses will change as well. Therefore one can expect that the transmissibility between two measured responses will change if damage occurs between them Figure 9 and will not change if there is no damage between them Figure 8.

The first step in order to detect and locate damage with transmissibility functions is the selection of a damage indicator. Maia et al [11] have already posed the following indicator based on transmissibility functions:

$$DI_{ij(k)} = \sum_{\omega} \left(T^D_{ij(k)}(\omega) - T_{ij(k)}(\omega) \right) \tag{16}$$

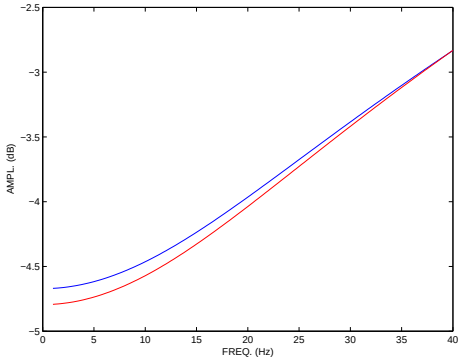

Fig. 8. Transmissibility functions between point 7 and point 8 (right figure) for undamaged (blue) and damaged (red) case

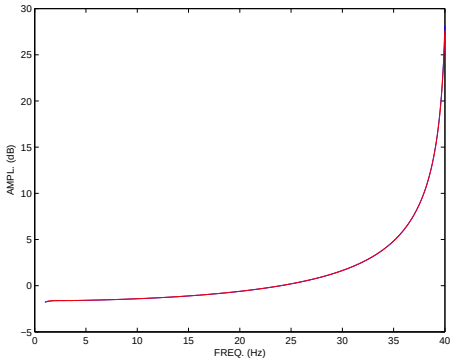

Fig. 9. Transmissibility functions between point 2 and point 3 for undamaged (blue) and damaged (red) case

By computing the transmissibility between two consecutive locations defined on the damaged structure, for the same force, and subtract the same tranmissbility of the undamaged structure, the damage location should be reveiled by the biggest value of the indicator. Johnson and Adams [13] have also posed a similar indicator:

$$DI_{ij(k)} = \sum_{\omega} \left(1 - \frac{T^D_{ij(k)}(\omega)}{T_{ij(k)}(\omega)} \right) \tag{17}$$

Note, neither indicator is independent of the order of the respons ratios [3].

$$DI_{ij(k)} \neq DI_{ji(k)} \tag{18}$$

Therefore Johnson [12] proposed to use a damage indicator that is independent of the ratio sequence by using the logarithm of the transmissibility, the damage feature:

$$DI_{ij(k)} = \sum_{\omega} \left(\frac{TP^D_{ij(k)}(\omega) - TP_{ij(k)}(\omega)}{TP_{ij(k)}(\omega)} \right) \tag{19}$$

with TP the transmissibility power defined as the absolute value of the common logartihm of the transmissibility

$$TP_{ij(k)}(\omega) = |log(T_{ij(k)}(\omega)| \tag{20}$$

It is clear that the transmissibility power and as such the damage power is independent of the sequence of the response ratio. Structural damage can be defined as a significant change in the damage feature. The damage indicator for a healthy strucutre should have values close to zero and values not equal to zero indicate the possible damage. It was shown by Johnson [12] that the proposed damage indicator 19 is able to correctly diagnose linear and non linear types of damage and able to provide good and consistent results in terms of detection, location, and quantification of the damage So far all presented damage indicators use a uniform weighted linear sum of all spectral lines of an arbitrary chosen frequency range. However it has been shown [14] that when e.g. using the damage indicator defined in equation 16 the results degenerate when we go along the frequency range and add more and more information. Maia et al [11] already addressed this sensitivity of the selected frequency range for a similar damage indicator based on frequency response functions and came to the same conclusion that this method fails in the case of higher frequencies. The reason for this is that the differences between the transmissibility functions of the damaged and undamaged structure at these higher frequencies become very high and the simple summation of such a result at the different frequencies may completely mask the true location. To overcome this problem Maia et al proposed in [14] a method based on occurrences. They suggested counting an occurrence at each frequency at that location where the difference between transmissibility function of the damaged and undamaged structure is a maximum. So they suggest summing the occurrences and not the difference themselves.

In the Figure 10 and Figure 11 one can respectively see the damage indicator without and with occurrences for the frequency range 0-40Hz. The X-as of the figure indicates the location of the possible damage. Location i indicates the location on the beam between the measured points i and i+1. In our case the damage is located between point 7 and point 8, therefore we expect to identify the damage at location 7. It clearly shows that using occurrences improves the detection of the damage, and therefore it was chosen in the rest of this paper to use the damage indicator defined in equation 19 combined with the occurrences approach.

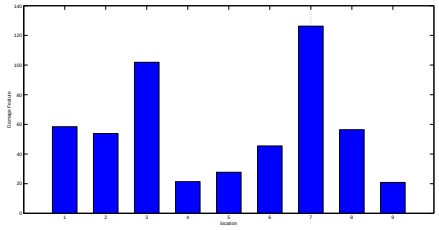

Fig. 10. Damage indicator without occurrences

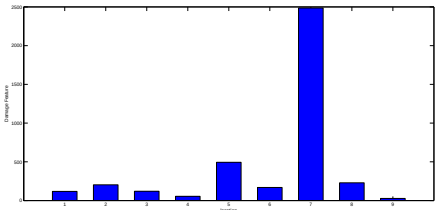

Fig. 11. Damage feature with occurrences

B. Different location of applied force before and after damage

As mentioned in the introduction the problem rises when the location of the applied force changes during operation. Transmissibility functions as defined in equation 9 and equation 15 depend on the location of the applied force.

$$T_{ij(k)} \neq T_{ji(l)} \tag{21}$$

Figure 12 shows the transmissibility function between point 7 and point 8 measured on the undamaged structure for loading case 1 (blue) and loading case 2 (red).

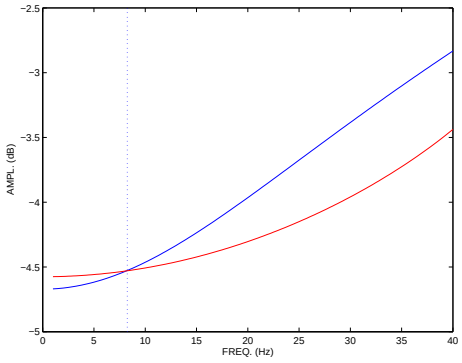

Fig. 12. Transmissibility function between point 7 and point 8 for undamaged structure for loading case 1 (blue) and loading case 2 (red)

These changes in the transmissibilty functions have significant implications because operating inputs may change in location during the use of a structure and inadvertently

cause the mentioned techniques to fail. In this case the damage indicator, calculated by combining transmissbility functions of the healthy structure but under different loads, can be different from zero Figure 13 . It can easily be understood that an undamaged structure will be falsely diagnosed with damage if the transmissibility functions are taken under varying loading conditions.

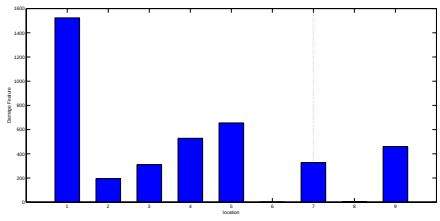

Fig. 13. Damage feature with occurrences for undamaged structure and changing loading conditions

Even when the structure is damaged it becomes impossible to determine the correct location of the damage. Often it may occur that the changes in the transmissibility functions due to the changing loading condition are higher then the changes due to the damage. Therefore the high values of the damage indicator at other locations may mask the true damage location Figure 14.

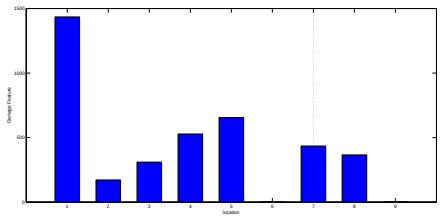

Fig. 14. Damage feature with occurrences for damaged structure and changing loading conditions

As we know from above, if we consider two transmissibility functions relating the same responses, but measured during two experiments with different loading conditions, they cross each other exactly at the resonances. This could already be seen in Figure 12, where we had a look to the transmissibility function between point 8 and point 7 during the two different loading conditions.

This knowledge can already be used as a simple indicator to eliminate false damage notifications. One could easily measure transmissibility functions of the structure over a successive time under varying loading conditions. Only when the intersection points of the transmissibility functions under varying loading conditions start to shift damage is occurring due to the shift of the natural frequencies of the structure 15.

In order to locate the damage, using the existing damage indicators, in the case the location of the applied force

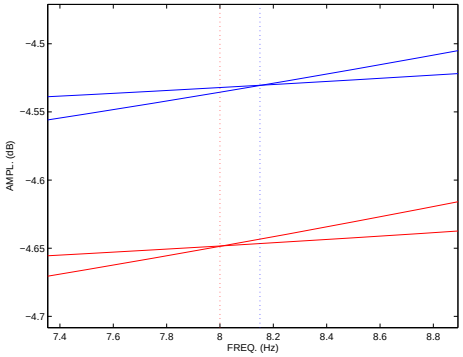

Fig. 15. Transmissibility function between point 7 and point 8 for 2 different loading conditions for the undamaged case (blue) and damaged case (red)

of the healthy structure is different of the location of the applied force of the damaged structure, a careful choice of the selected frequency band is proposed. Taking into account that the transmissibility functions at the natural frequency do not depend on the loading conditions, as was shown in equation 1, a proper choice would be to select only a small frequency band around this intersection point in order to calculate the damage feature with occurrences.

The next figures demonstrate this approach. The first natural frequency of the undamaged beam is 8.15Hz. Three different frequency intervals have been taken around the first natural frequency. It is obvious from the figures 16 to 17 that the damage indicator is only reliable in detecting damage in case of a sufficient small band around this natural frequency. Only in the frequency band 7-9 Hz successful damage localization is possible.

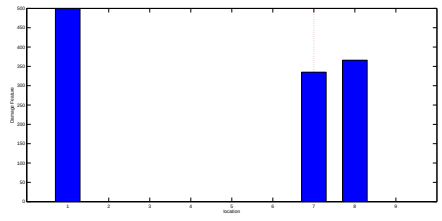

Fig. 16. Damage feature with occurrences for damaged structure under changing loading conditions, frequency range 2-14Hz

Taking in mind that the transmissibility functions in the system poles become independent of the loading conditions, above conclusions can easily be understood. Therefore the damage indicators based on transmissibility functions are only reliable in a small frequency band around the first intersection point of the transmissibility functions under changing loading conditions. In this band the change in the transmissibility functions is more influenced by the

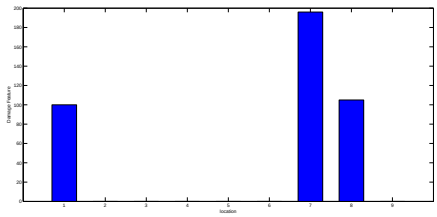

Fig. 17. Damage feature with occurrences for damaged structure under changing loading conditions, frequency range 6-10Hz

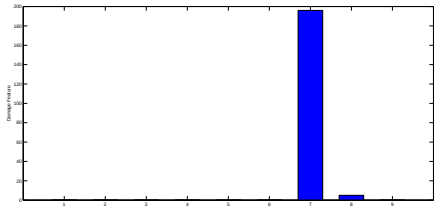

Fig. 18. Damage feature with occurrences for damaged structure under changing loading conditions, frequency range 7-9Hz

change of the dynamic parameters due to damage then by the change in loading conditions. In a broader band or in bands away from the intersection point the influence of the varying loading conditions will be more important then the damage and will again make reliable damage location impossible.

IV. Conclusions

It was the aim of this paper is to give a brief introduction to operational modal analysis and structural health monitoring using the ratios between responses -the transmissibility functions- in structures, with multiple degrees of freedom and multiple changing excitations.

It has been shown that a set of transmissibility measurements can directly be used to identify all operational modal parameters, eigenfrequencies, damping ratios and unscaled mode shapes using well known frequency domain identification techniques.

In the field of Structural Health Monitoring it has been shown that changing loading conditions do not automatically exclude the use of existing damage indicators based on transmissibility measurements. Caution has to be taken in the selection of the used frequency band in order to eliminate false damage notifications. It has been shown that, when taking a small frequency band around the first intersection point of the transmissibility functions under varying loading conditions, accurate results on damage location can be found.

Acknowledgments

The Institute for the Promotion of Innovation by Science and Technology in Flanders (IWT) and the Research Council (OZR) of Vrije Universiteit Brussel (VUB) are gratefully acknowledged.

References

[1] Operating deflection shapes from time versus frequency domain measurements, Patrick L. McHargue and Mark Richardson, proceedings 11 th IMAC Cinference, Kissimmee, Florida, February 1993.

[2] The use of transmissibility measurements in output-only modal analysis, Christof Devriendt and Patrick Guillaume,Mechanical Systems and Signal Processing Volume 21, Issue 7, October 2007, Pages 2689-2696.

[3] Identification of modal parameters from transmissibility measurements, Devriendt, Christof; Guillaume, Patrick, Journal of Sound and Vibration, Volume 314, Issue 1-2, p. 343-356. July 2008.

[4] D.j. Ewins, Modal Testing, Theory, Practice, and Application, John Wiley and Sons (ISBN 0 86380 218 4)

[5] Introduction to operating deflection shapes, Schwarz and Mark Richardson, CSI Reliability Week, Orlando, Florida, October 1999.

[6] R. Pintelon and J. Schoukens, System Identification: A Frequency Domain Approach, IEEE Press and John Wiley and Sons (ISBN 0-7803-6000-1).

[7] B. Cauberghe, Applied frequency-domain system identification in the field of experimental and operational modal analysis. PhD thesis, Department of Mechanical Engineering, Vrije Universiteit Brussel, Belgium, phd.avrg.be, 2004.

[8] R. Pintelon, P. Guillaume, Y. Rolain, J. Schoukens and H. Van Hamme, Parametric identification of transfer functions in the frequency domain: a survey. IEEE Transactions on Automatic Control, 39(11): 2245-2260, 1994.

[9] B. Peeters, H. Van der Auweraer, P. Guilaume, and J. Leuridan, The PolyMAX frequency-domain method: a new standard for modal parameter estimation? Shock and Vibration, 11, 395-409, 2004.

[10] Doebling, S.W., Farrar, C.R., Prime, M.B., Shevitz, D.W., Damage Identification and Health Monitoring of Structural and Mechanical Systems from Changes in Their Vibration Characteristics: A Literature Review., Los Alamos National Laboratory Report, LA-13070-MS, 1996.

[11] Maia, N.M.M., Sampaio, R.P.C., Ribeiro, A.M.R., Silva, J.M.M., (2001), Transmissibility Techniques for Damage Detection, Proc. of IMAC XIX, Kissimmee, Florida, USA

[12] Johnson, T.J., Analysis of Dynamic Transmissibility as a Future for Structural Damage Detection, MSc. Thesis, Purdue University, 2002

[13] Timothy J. Johnson, Douglas E. Adams, Transmissibility as a Differential Indicator of Structural Damage J. Vib. Acoust. – October 2002 – Volume 124, Issue 4, 634 (8 pages)

[14] Maia, N. M. M.; Silva, J. M. M.; Almas, E. A. M.; Sampaio, R. P. C., Damage Detection in Structures: from Mode Shape to Frequency Response Function Methods, Mechanical Systems and Signal Processing, Volume 17, Issue 3, p. 489-498.

[15] J.E. Mottershead., On the Zeros of Structural Frequnecy Response Functions and Their Sensitivities 1998b, Mechanical Systems and Signal Processing 12 (5), 591-597

Proceedings of the 8th National Congress on Theoretical and Applied Mechanics, May 28-29, Brussels, Belgium.

Free field vibrations due to traffic and construction activities on a concrete road

Mohammad Amin LAK, Geert LOMBAERT, Geert DEGRANDE
Department of Civil Engineering, K.U.Leuven
Kasteelpark Arenberg 40, B-3001 Leuven, Belgium
email: amin.lak@bwk.kuleuven.be

Abstract— **This paper presents the results of three vibration measurement campaigns: (1) vibrations by traffic on a (jointed) concrete pavement, (2) vibrations by traffic after road renovation by asphalt overlaying, and (3) vibrations during the construction works. During the first and second measurement campaign, the free field vibrations as well as the dynamic response of the body and the axles of a truck (Volvo FL180) have been measured. Parameters of a 4DOF model of the vehicle had been already obtained in the frame of another project [1] and [2], these parameters are adjusted by means of the measured response of the truck. In the third measurement, vibrations in the free field due to the operation of a multi-head breaker (MHB) have been measured. During the operation of the multi-head breaker, 4 cylinders with a weight of about** 700 kg **are dropped consecutively on the concrete slabs from a height of** 1.30 m **or** 1.80 m**. The results will be used to validate a numerical model for the prediction of vibrations due to traffic and due to the breaking/cracking of concrete roads.**

Keywords— **vibration measurements; traffic induced vibration; vehicle response; cracking and seating; multi-head breaker**

I. Introduction

A MAJOR part of the national roads in Belgium are jointed plain concrete pavement (JPCP). This kind of roads generally tends to crack into discrete sections. In order to improve the ride quality of these roads, and also to reduce traffic induced vibrations and noises in their vicinity, the roads are renovated. One of the renovation methods is 'cracking and seating'. In this method, the underlying concrete pavement is broken into relatively small pieces (less than $1\,\mathrm{m}^2$) by repeatedly dropping large weights. The pieces are then seated by 2 to 3 passes of a roller and overlayed with an asphalt layer.

The passage of traffic on the road as well as the operation of the multi-head breaker during the construction works generates vibrations in nearby buildings. In order to predict these vibrations, a numerical model is currently under development. Free field vibration measurements were necessary to validate the model. The renovation of a 500 m section of the N9 in Lovendegem (Belgium) provided a unique opportunity to perform these measurements.

Within the frame of this paper the experimental results of three vibration measurement campaigns are presented: (1) vibrations by traffic on a deteriorated concrete road, (2) vibrations by traffic after road renovation by asphalt overlaying, and (3) vibrations due to the operation of the MHB. In the first and second measurement campaign, simultaneous measurements in the vehicle and in the free field were performed.

These results are interesting from several aspects. The results of the first two measurement campaigns show how high the level of vibrations is in the vicinity of roads composed of JPCP. Also, they show how the renovation reduces the environmental vibrations in the vicinity of the road and improves the ride comfort. In addition, comparing the frequency content of the truck response and the vibrations in the free field, shows how the different eigenmodes of the truck contribute in the vibrations at different distances in the free field. The results of the third measurement campaign show how high the level of vibrations is at small distances from the road; and how the vibration level decreases with increasing distance from the road. However these works generate relatively high vibrations, experimental data are scarce in literature.

In the following sections, the characteristics of the vehicle and the road and the dynamic soil characteristics are presented first. Next, the MHB for the cracking/breaking of the concrete slabs is described. The experimental setups in the vehicle and in the free field are explained and an overview of the measurements is given. Finally, the results of the measurements for the vehicle and for the free field during the passage of the vehicle and during the operation of the MHB are presented. More comprehensive results can be found in [3], [4] and [5].

II. Characteristics of the Vehicle, Road, Soil and MHB

A. The Characteristics of the Vehicle

A Volvo FL180 truck is used to perform the experiments. This truck has two axles, a wheel base of 4.00 m and a mass of 6420 kg in empty condition. The mass carried by the front axle and the rear axle is 3465 kg and 2955 kg, respectively.

B. The Characteristics of the Road

The measurements are performed along the N9 (Grote Baan between Ghent and Eeklo) between kilometer points

60.700 to 61.175 in Lovendegem, Belgium. The measurement site in the free field is located at kilometer point 61.952. The N9 has three lanes for cars and one cycling lane on each side. Prior to the road renovation each car lane consists of concrete slabs with a width of 2.87 m and different lengths from 4 m up to 12 m. In between the concrete slabs, expansion joints are present. Furthermore, the concrete slabs show a lot of longitudinal and transversal cracks.

The height of joints and cracks is measured by means of a leveling instrument. The amplitude of the relative vertical displacement of the concrete plates during the passage of a truck at a very low speed is measured by means of a faultimeter [6]. Figure 1 presents the height as well as the maximum relative displacement of the joints and cracks that are located in the lane in the direction of Ghent. Crack number 68 is located at kilometer point 60.952 in front of the measurement line. For most of the joints, the relative motion of the plate ends during the passage of a truck at low speed is small compared to the height of the joints.

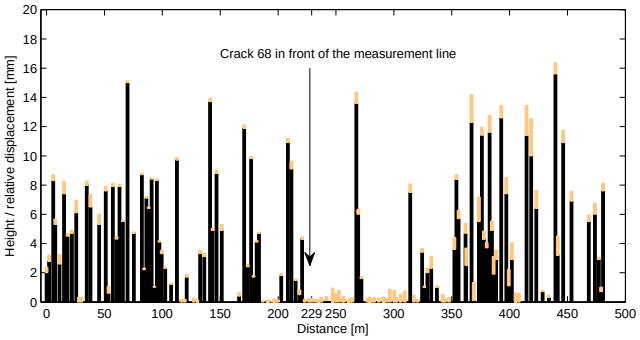

Fig. 1. The height (black) and the relative displacement (copper) of the cracks and joints of the concrete slabs.

Furthermore, before and after the renovation of the road, the road profile has been measured by means of the APL (Fr: Analyseur de Profil en Long). Figure 2 shows the resulting power spectral density (PSD) of the road unevenness before and after the road renovation. The APL was towed at two speeds of 21.6 km/h and 54 km/h. It records without distortion and attenuation road unevenness in the wavelength range between 0.3 and 15 m at a speed of 21.6 km/h and between 0.6 and 30 m at 54 km/h. The PSDs of both speeds are presented in figure 2. The thick line shows the curve that has been fitted to the PSDs of both speeds. The dotted part represents the extrapolation of the fitted line to the wavelengths longer than 30 m or shorter than 0.3 m. Comparing figures 2a and 2b shows how the renovation has improved the road quality.

C. The Dynamic Soil Characteristics

The soil at the measurement site mainly composes of fine gray blue sand. A spectral analysis of surface waves

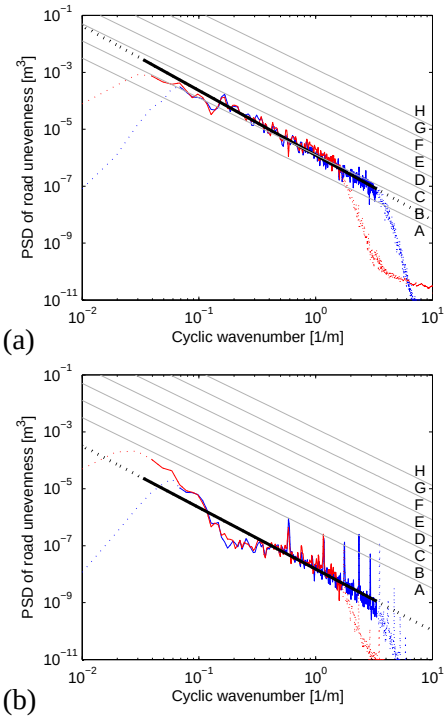

Fig. 2. PSD of the road unevenness (a) before and (b) after the road renovation for the APL speeds of 21.6 km/h (blue) and 54 km/h (red). Thick solid line shows the fitted curve.

(SASW) test was performed to identify the dynamic soil characteristics at the site [3]. In addition, a seismic cone penetration test (SCPT) was performed to get more information about the dynamic soil characteristics at a larger depth [7]. Figure 3 compares the shear wave velocity in the soil as a function of depth obtained by means of the SASW test and the SCPT. A satisfactory agreement between the results of both methods is observed. Table I summarizes the shear wave velocity profile (C_s) identified from the SASW test and the dilatational wave velocity (C_p) identified from the SCPT.

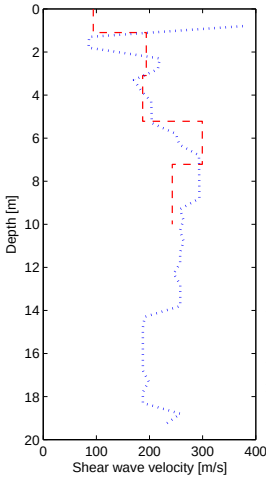

Fig. 3. Shear wave velocity as a function of depth obtained from the SASW test (dashed line) and the SCPT (dotted line).

TABLE I
SHEAR AND DILATATIONAL WAVE VELOCITY OF THE SOIL LAYERS.

Soil layers	Thickness [m]	C_s [m/s]	C_p [m/s]
Layer 1	1.1	94	170
Layer 2	2.0	194	250
Layer 3	2.1	187	350
Layer 4	2.0	299	500
Halfspace	∞	243	700-1100

D. The Characteristics of the MHB

There are several types of breakers and drop hammers for the cracking/breaking of concrete slabs. In this project a so-called 'multi-head breaker' (MHB) is used (figure 4). The MHB consists of 4 cylinders with a weight of about 700 kg. During its operation, the cylinders are dropped consecutively on the concrete slabs. The MHB has two levels of cracking intensity: level *AA* and level *BB*. In level *AA*, the cylinders are dropped about 130 times per minute from a height of 1.30 m, while in level *BB*, the height is 1.80 m and the cylinders hit the slabs about 75 times per minute. The MHB is pulled with a tractor with a speed of about 1 km/h. The cracking procedure is also referred to as 'breaking', 'fracturing', or 'fractionation' in the literature.

Fig. 4. Multi-head breaker (MHB) equipment.

III. MEASUREMENT SETUP

A. Measurement Setup in the Vehicle

The vehicle response is measured by a total of 12 accelerometers mounted on both the axles and the body of the truck. On each axle, 4 accelerometers are installed: two on the right side and two on the left side. Four accelerometers are installed on the chassis, one on the front right side, one on the front left side, one on the rear right side, and one on the rear left side (figure 5).

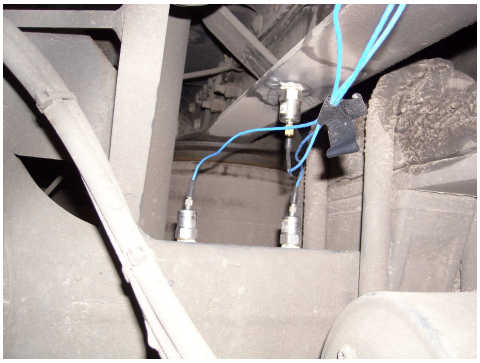

Fig. 5. Accelerometers installed on the left side of the rear axle and on the rear left side of the chassis.

The truck speed is measured by means of a GPS-based VBOX mini speed measurement, which is based on a 10Hz GPS engine. It is connected to the data acquisition system, and measures the truck speed with a precision of ± 0.1 km/h. On each side of the truck, one photoelectric sensor is installed in order to synchronize the truck and the free field measurement during the passages of the truck in both directions. When the truck passes in front of the measurement line, one of the photoelectric sensors of the truck detects the reflector in the free field in front of the measurement line and a pulse appears in the signal of the photoelectric sensor.

The A/D conversion is performed using a `NI PXI-1050` data acquisition system at a sampling rate of $f_s = 1000$ Hz. The recorded accelerations are subsequently filtered with a high-pass frequency of $f_h = 0.5$ Hz and a low-pass frequency of $f_l = 100$ Hz.

B. Measurement Setup in the Free Field

The free field response is measured by means of 15 accelerometers mounted on aluminium stakes with a cruciform cross section and a length $l = 0.3$ m.

For all measurement campaigns, the same setup is used (figure 6). The accelerometers are located at the ground surface $z = 0$ m, at different distances from 4 up to 64 m from the road. Four of the accelerometers measure the horizontal vibrations, two of them perpendicular to the road (x-direction) and two of them parallel with the road (y-direction) at 16 and 32 m from the road. During the passages, a photoelectric sensor is used to synchronize the measurements of the free field response and the truck response.

The A/D conversion is performed using a `LMS SCADAS III` data acquisition system at a sampling rate of $f_s = 2048$ Hz. In the measurement campaign after the road renovation a lower sampling frequency of $f_s = 1024$ Hz is

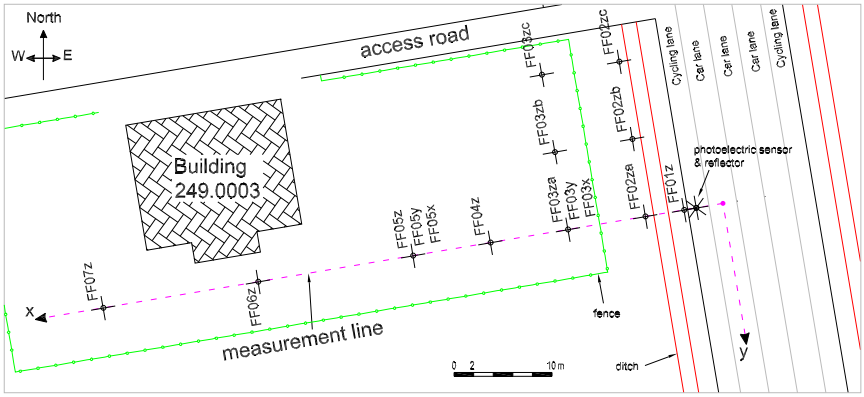

Fig. 6. Location of the measurement points in the free field.

used. In order to remove the direct current (DC) component, the accelerations are filtered with a high-pass filter with a cut-off frequency $f_h = 2\,\text{Hz}$. The accelerations $a(t)$ are integrated by means of the trapezium rule to obtain the velocity time histories $v(t)$. Before and after the integration, a window followed by a filter is applied in order to avoid drifting of the integrated signal.

IV. Overview of the Measurements

A. Measurements During the Traffic Passage

In the measurement campaign prior to the road renovation, 34 passages of the truck in both directions have been measured. In all passages, the truck passes on the lane in the direction of Ghent, next to the free field. The truck speed has been varied from 30 km/h up to 70 km/h with steps of 10 km/h.

In the measurement campaign after the road renovation, a total of 21 passages has been recorded within a vehicle speed range from 30 km/h to 80 km/h with steps of 10 km/h.

In the following section, the vehicle and the free field response are discussed in detail for one vehicle speed $v = 50\,\text{km/h}$. Results for the other speeds can be found in [4].

B. Measurements During the Cracking

Additionally, the free field response during the cracking of 40 m of the lane in the direction of Ghent is presented. This section of 40 m is centered around the measurement line. The speed of the MHB is about 1.0 km/h, so that it takes 145 s for the MHB to complete this section of 40 m.

V. Results

A. Vehicle Response

Figure 7 shows the time history of the acceleration of the rear axle and the rear side of the body for the vehicle speed $v = 50\,\text{km/h}$ before and after the renovation of the road.

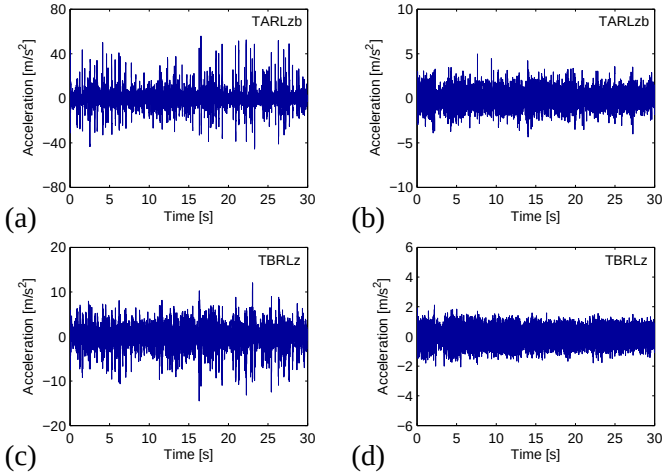

Fig. 7. Time history of the acceleration of the rear axle (a) before, and (b) after the renovation of the road, and of the rear side of the body (c) before, and (d) after the renovation of the road, for the vehicle speed $v = 50\,\text{km/h}$.

The passage of an axle on a crack generates a spike in the time history of the acceleration (figure 7a). As there is no distinct pulse in the vibration of the axle after the road renovation(figure 7b), it can be concluded that the road surface after renovation is quite smooth. Before the road renovation, the acceleration of the axle (figure 7a) is about 4 to 5 times larger than the acceleration of the body (figure 7c). This difference decreases to about 2 after the road renovation (figures 7b and 7d). The renovation of the road strongly reduces the truck response. This reduction is about 10 times for the rear axle, and about 6 times for the rear part of the body.

Figure 8 shows the frequency content of the acceleration of the rear axle and the rear side of the body for the vehicle speed $v = 50\,\text{km/h}$ before and after the renovation of the road.

The main part of the frequency content of the axle is situated between 0 and 40 Hz (figure 8a and 8b). The peak of the frequency content is observed at about 15 Hz, which

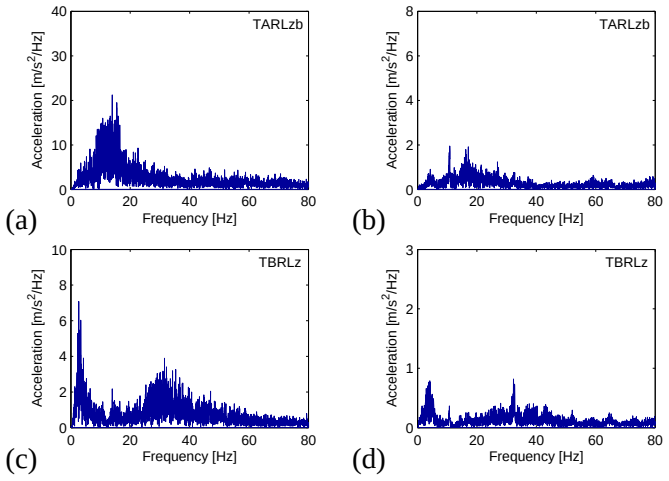

Fig. 8. Frequency content of the acceleration of the rear axle (a) before, and (b) after the renovation of the road, and of the rear side of the body (c) before, and (d) after the renovation of the road, for the vehicle speed $v = 50\,\text{km/h}$.

corresponds to the eigenfrequency of the axle hop mode. The frequency content of the acceleration of the body is spread over a wider range of frequencies from 0 up to more than 50 Hz (figure 8c and 8d). A distinct peak at low frequencies (about 4 Hz) is observable. This peak corresponds to the pitch and bounce mode of the vehicle.

Figure 9 shows the peak acceleration (PA) of the rear axle and the rear side of the body before and after the renovation of the road as a function of the vehicle speed.

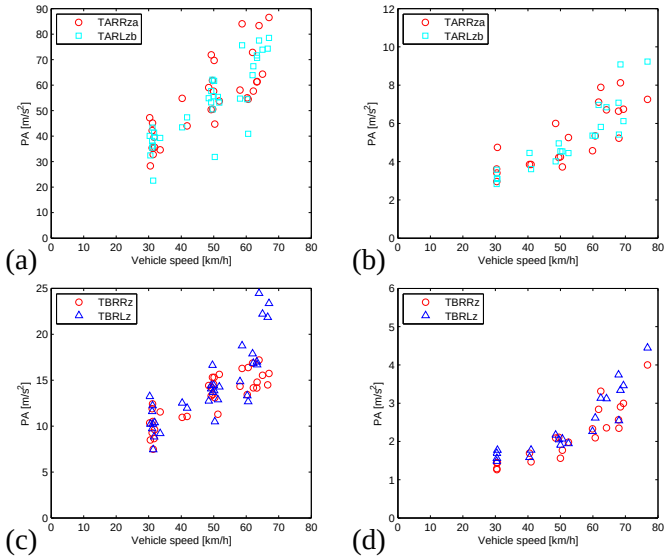

Fig. 9. Peak acceleration as a function of the vehicle speed for the rear axle (a) before, and (b) after the renovation of the road, and for the rear side of the body (c) before, and (d) after the renovation of the road.

The vehicle speed has a crucial influence on the PA of the body and the axle. The peak acceleration increases with an increasing truck speed. For higher vehicle speeds, the reduction of the PA due to the road renovation is slightly lower than for the lower vehicle speeds.

B. *Free Field Vibrations Due to Traffic*

Figure 10 shows the time history and the running RMS value of the velocities at three points in the free field, for the vehicle speed $v = 50\,\text{km/h}$ before and after the renovation of the road. These points are at 8 m, 16 m, and 48 m from the road. A 1 second time window is used to compute the running RMS value.

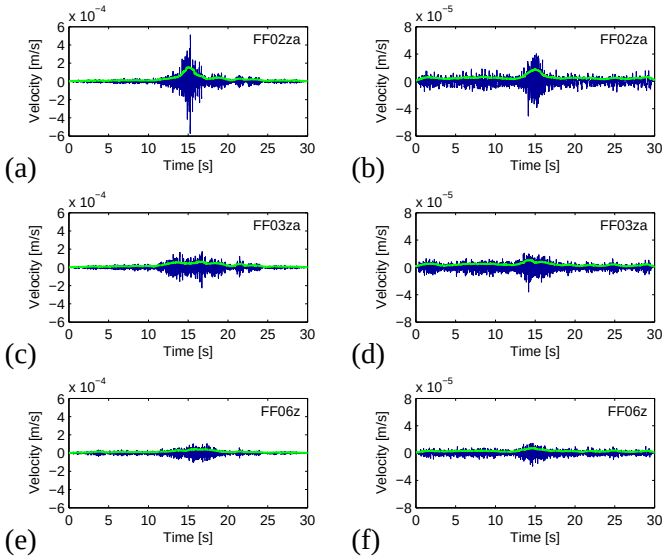

Fig. 10. Time history and the running RMS value of the velocities, before the renovation of the road at (a) 8 m, (c) 16 m, and (e) 48 m from the road, and after the renovation of the road at (b) 8 m, (d) 16 m, and (f) 48 m from the road.

The vibration velocity is shown as this quantity is used in most vibration norms and guidelines to evaluate the discomfort to people. This is due to the fact that the human body is equally sensitive to the vibrations in a frequency range between 1 Hz and 80 Hz [8].

The vibration duration increases with an increasing distance from the road (e.g. figures 10a and 10e), while the peak particle velocity (PPV) decreases due to the wave propagation in the soil. Comparing figures 10b, 10d, and 10f with the time history of the free field vibrations prior to the road renovation (figures 10a, 10c, and 10e) shows that the PPV has decreased by a factor of about 6. The running RMS value of the vibration velocity shows a very smooth variation with a maximum value at the time the truck passes in front of the measurement line. After the road renovation, the vibrations at the farthest point are very small and only slightly larger than the level of the background noise.

Figure 11 shows the frequency content of the velocities at the same three points in the free field for the same events.

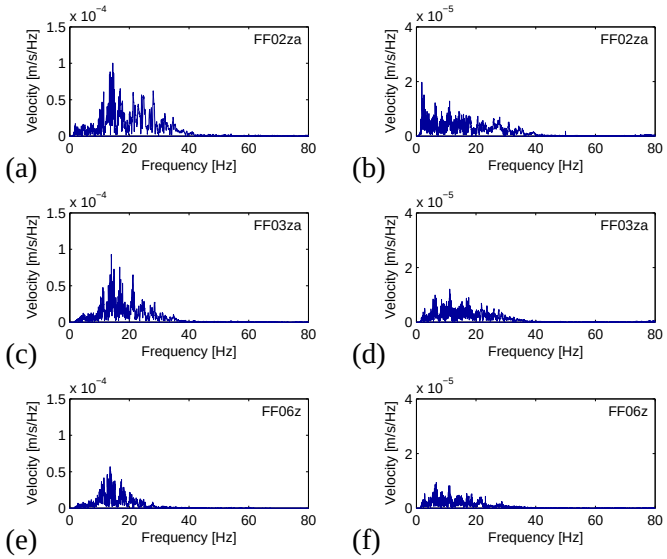

Fig. 11. Frequency content of the velocities, before the renovation of the road at (a) 8 m, (c) 16 m, and (e) 48 m from the road, and after the renovation of the road at (b) 8 m, (d) 16 m, and (f) 48 m from the road.

The frequency content of the velocity in the free field is mainly situated below 40 Hz. It decreases to lower frequencies at larger distances from the road because the higher frequency components are attenuated more severely than the lower frequency components due to the effect of material damping in the soil (e.g. figures 11e and 11a).

The frequency content shows the largest values near 15 Hz, which corresponds to the dominant frequencies of the accelerations of the axles. Before the road renovation, an additional small peak at low frequencies (about 2 or 3 Hz) can be observed (figure 11a), which corresponds to the dominant frequencies of the vehicle body motion. This peak at low frequencies is much more pronounced after the renovation of the road (figure 11b). At larger distances, the frequency content is dominated by contributions from the axle hop frequencies.

Figure 12 shows the peak particle velocity as a function of the vehicle speed for the free field response. The PPV clearly reduces with increasing distance from the road. The PPV increases slightly with the vehicle speed, except for the closest point (point `FF01z` at 4 m from the road), where the increase with the vehicle speed is stronger. This contradicts previous numerical predictions [9] for a linear vehicle model, where the vehicle speed has no influence on the vibrations generated by the passage on a joint in the road surface.

The perception threshold for vibrations is at about 0.14 mm/s [8]. It can be observed that before the renovation of the road, the vibrations are perceivable up to a distance of about 16 m from the road (figure 12c). However, after the renovation of the road, the PPV is below the perception threshold, even in the immediate vicinity of the

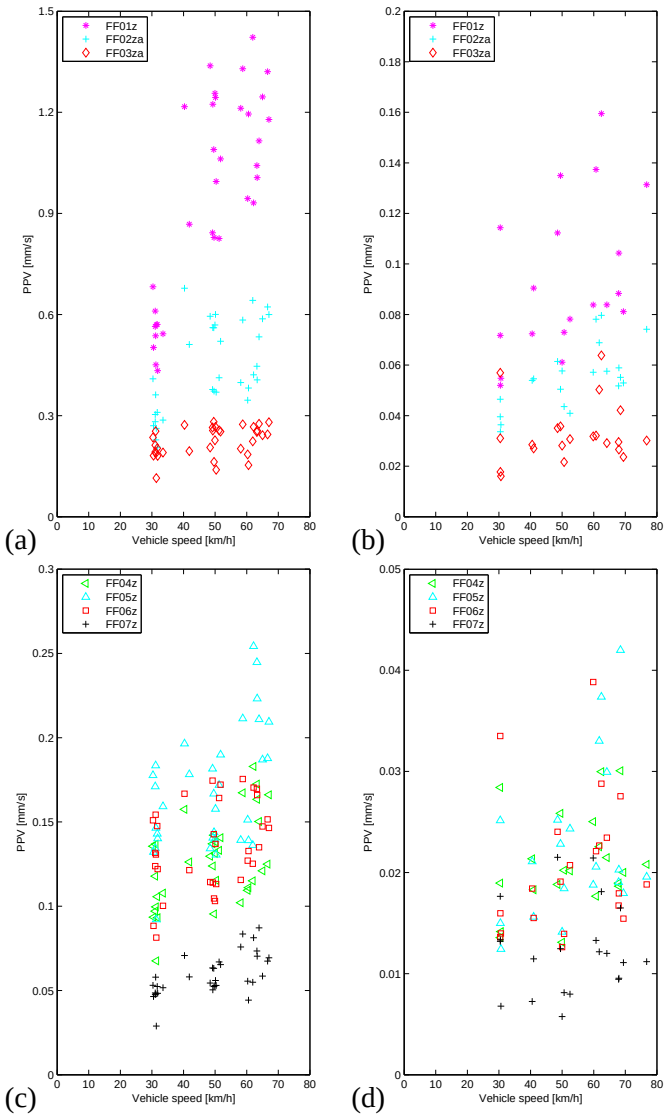

Fig. 12. Peak particle velocity of the free field response in the z-direction as a function of the vehicle speed, before the renovation of the road for receivers (a) up to 16 m, and (c) from 24 m up to 64 m from the road, and after the renovation of the road for receivers (b) up to 16 m, and (d) from 24 m up to 64 m from the road.

road (`FF01z`, figure 12b).

Since the truck speed has only a moderate effect on the PPV in the free field at distances larger than 8 m from the road, a reduction of the vehicle speed is not an effective measure to reduce the vibrations in the adjacent buildings.

Figure 13 shows the dominant frequency of the velocity in the free field as a function of the vehicle speed. The dominant frequencies are independent of the truck speed, except for the first point `FF01z`. Before the renovation of the road, the dominant frequencies are mainly situated in the frequency range between 10 Hz and 20 Hz. This frequency range corresponds to the dominant frequencies of the acceleration of the axles and, therefore, to the eigenfrequencies of the axles. After the road renovation, the

dominant frequencies are mainly situated at about 2 Hz and 15 Hz corresponding to both the eigenfrequencies of the pitch and bounce modes and the axle hop modes. Other sources of vibrations probably have affected the results and cause the scatter in the results after the road renovation.

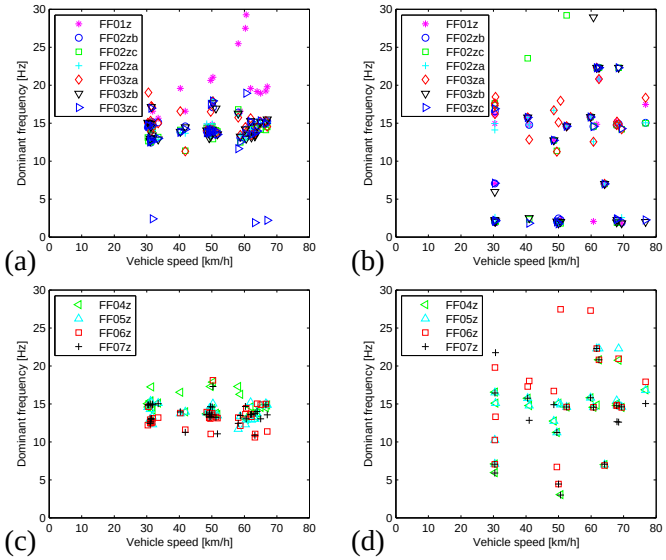

Fig. 13. Dominant frequencies of the free field response in the z-direction as a function of the vehicle speed, before the renovation of the road for receivers (a) up to 16 m, and (c) from 24 m up to 64 m, and after the renovation of the road for receivers (b) up to 16 m, and (d) from 24 m up to 64 m.

Figure 14 shows the vertical PPV as a function of the distance from the road for the vehicle speed $v = 50$ km/h before and after the renovation of the road. The PPV generally decreases with an increasing distance from the road.

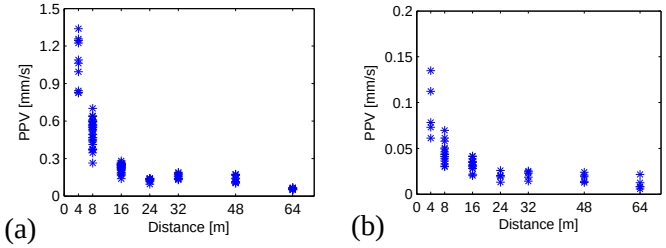

Fig. 14. Peak particle velocity as a function of the distance from the road for $v = 50$ km/h, (a) before and (b) after the renovation of the road.

C. Free Field Vibrations Due to Cracking

Figure 15 shows the time history of the velocities at three points in the free field during the cracking of 40 m of the lane in the direction of Ghent. These points are at 8 m, 16 m, and 48 m from the road. This section of 40 m is centered around the measurement line.

Each of the impacts of the MHB can be recognized in the time history of the vibration velocity. The vibration

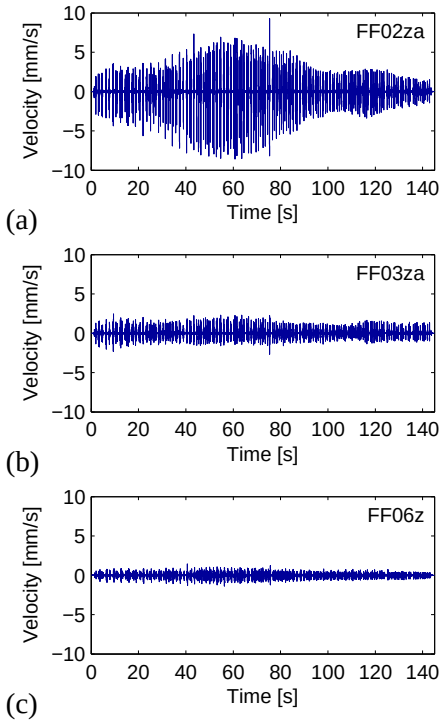

Fig. 15. Time history of the vertical vibration velocity in the free field at (a) 8 m, (b) 16 m, and (c) 48 m from the road.

level increases as the MHB approaches the measurement line, and decreases after it passes the measurement line.

Figure 15c shows an almost constant level of vibration during the entire time period. This is due to the fact that the distance between this point and the road is large, so that a change of 20 m in the position of the MHB does not significantly affect the total distance between the source and the receiver.

Figure 16 shows the frequency content of the velocities for the same points during the same event. The frequency content of the velocity in the free field is mainly situated between 10 Hz and 40 Hz.

Figure 17 shows the vertical peak particle velocity as a function of the distance from the road for the cracking of the three lanes. For clarity, a logarithmic scale has been chosen for the vertical axis with the PPV.

A very high level of vibrations with a PPV of 50 mm/s is observed at the point FF01z when the MHB operates on the adjacent lane in front of the measurement line.

The difference between the results for the three car lanes is more pronounced close to the road, where the distance between the source and the receiver is the smallest.

The PPV generally decreases with an increasing distance from the road. The PPV at point FF04z is less than the PPV at points FF05z and FF06z, that are located farther from the road. This has also been observed in the measurements of the free field vibrations during the passage of traffic, and might be due to the soil stratification at

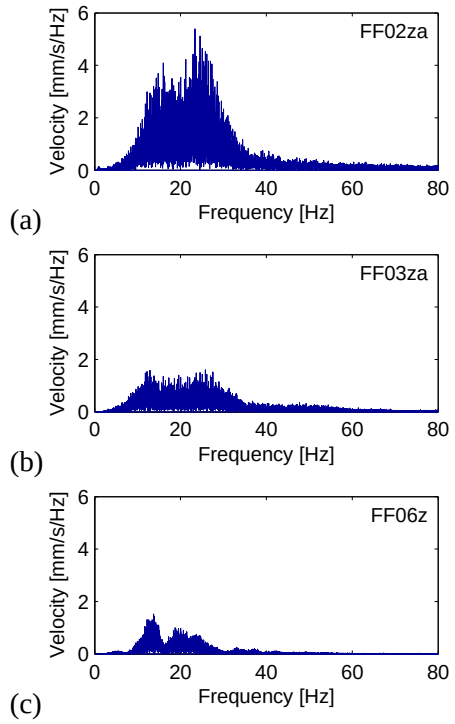

Fig. 16. Frequency content of the vertical vibration velocity in the free field at (a) 8 m, (b) 16 m, and (c) 48 m from the road.

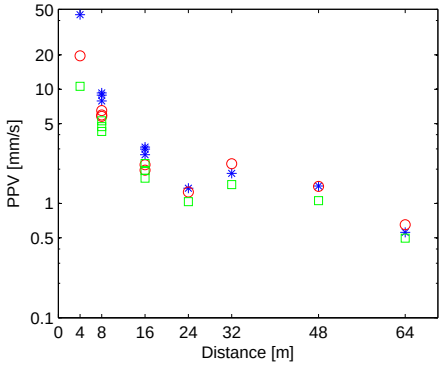

Fig. 17. Peak particle velocity as a function of the distance from the road for the cracking of the lane in the direction of Ghent (blue stars), the middle lane (red circles), and the lane in the direction of Eeklo (green squares).

the site or local soil conditions.

VI. Conclusions

At the measurement site along the N9 in Lovendegem, Belgium, simultaneous measurements of the vehicle and the free field response have been made before and after the renovation of the concrete road. These measurements provide a clear insight in the influence of the road renovation on both the vehicle response and the free field response. Furthermore, the results allow for a detailed investigation of the influence of the vehicle speed on the truck and the free field vibrations.

The renovation of the road reduces the vibrations significantly. The PA of the axles decreases by a factor of 10 to 15, while the PA of the body decreases by a factor of 3 to 7. The PPV in the free field is more than 5 times lower.

In addition, the vibrations in the free field have been measured during the breaking/cracking of the concrete road by means of a multi-head breaker (MHB). The free field vibrations have been measured at 15 points along a measurement line perpendicular to the road from 4 m up to 64 m from the road. The measurements have been performed during the cracking of the three car lanes of the N9 on a section of over 400 m.

The peak particle velocity at the closest point in the free field reaches a value of 50 mm/s. The PPV decreases substantially with increasing distance from the road and is about 0.5 mm/s at 64 m from the road.

Acknowledgments

The results presented in this paper have been obtained within the frame of the IWT-project VIS-CO 060884, 'Vibration controlled stabilization of concrete slabs for durable asphalt overlaying with crack prevention membrane', funded by IWT Vlaanderen (Institute for the Promotion of Innovation by Science and Technology in Flanders). The financial support of IWT Vlaanderen is gratefully acknowledged.

References

[1] F. Covemaeker and A.-C. Kiekens, "Trillingen ten gevolge van verkeer op een wegdek met kasseien," M.S. thesis, 2007.

[2] G. Lombaert, M. Schevenels, G. Degrande, F. Covemaekers, and A.-C. Kiekens, "Invloed van de langsvlakheid van de weg op de dynamische voertuigrespons en de trillingen in de omgeving," *OCW Mededelingen*, , no. 73, pp. 18–20, 2007.

[3] M.A. Lak, G. Lombaert, S.A. Badsar, M. Schevenels, and G. Degrande, "Determination of the dynamic soil characteristics with the SASW method at a site in Lovendegem," Report BWM-2008-11, September 2008, IWT-Project VIS-CO 060884.

[4] M.A. Lak, G. Lombaert, S.A. Badsar, E. Reynders, and G. Degrande, "Simultaneous vehicle and free field response measurement, during the passage of a truck before and after road renovation," Report BWM-2008-15, October 2008, IWT-Project VIS-CO 060884.

[5] M.A. Lak, E. Reynders, G. Lombaert, and G. Degrande, "Vibration measurement during the cracking of concrete slabs by means of a multi-head breaker," Report BWM-2008-16, October 2008, IWT-Project VIS-CO 060884.

[6] Belgian Road Research Center, "Joints et fissures vue en plan, N9 Lovendegem, 31/03/2008," .

[7] L. Areias, "Seismic cone test SCPT1. 249/003 Grote Baan (N9), Lovendegem," Tech. Rep., iGeotechnics, 2008, Report no. iG0608.

[8] International Organization for Standardization, *ISO 2631-1:1985: Evaluation of human body exposure to whole-body vibration - Part 1: General requirements*, 1985.

[9] G. Lombaert, G. Degrande, and D. Clouteau, "Numerical modelling of free field traffic induced vibrations," vol. 19, no. 7, pp. 473–488, 2000.

Proceedings of the 8th National Congress on Theoretical and Applied Mechanics, May 28-29, Brussels, Belgium.

Frequency domain modal parameter estimation in the OMAX framework

T. De Troyer[1], K. Deckers[2], P. Guillaume[2] and M. Runacres[1]
[1]Department of Industrial Sciences & Technology, Erasmushogeschool Brussel
Nijverheidskaai 170, 1070 Brussels - Belgium
[2]Department of Mechanical Engineering, Vrije Universiteit Brussel
Pleinlaan 2, 1050 Brussels - Belgium
email: tim.de.troyer@docent.ehb.be, kristel.deckers@vub.ac.be,
patrick.guillaume@vub.ac.be, mark.runacres@docent.ehb.be,

Keywords— **modal analysis, OMAX, parameter estimation**

Abstract— **Classical Experimental Modal Analysis (EMA) and Operational Modal Analysis (OMA) were recently combined into the so-called OMAX framework: Operational Modal Analysis with eXogeneous inputs. In this framework both the artificial forces and the ambient excitations are considered. The goal of this paper is to present a suitable OMAX procedure in case of structure-exciter interaction. This interaction introduces a correlation between the exciter input force and the unknown ambient excitation. The approach first estimates the frequency response function (FRF), then the (positive) power spectra (XP+) are compensated for the interaction. The parametric estimation of the modal parameters is then identical to the case without interaction.**

I. Introduction

THE COMBINED experimental-operational estimation of vibration data emerged from typical engineering applications like the testing of bridges and aeroplanes. In the flight flutter testing [1] of aeroplanes e.g., the wings are excited both by an applied force and by the atmospheric turbulence. Another example is the modal analysis of bridges: the structure is excited by ambient forces (wind, trafic) and by applied forces [2]. In classical Experimental Modal Analysis [3, 4], the ambient excitation is considered as disturbing noise that one should get rid off. In Operational Modal Analysishowever [5, 6], one only uses the response of the system caused by the unknown ambient forces. Modal parameter estimators in the OMAX framework consider both the deterministic contribution caused by the applied forces and the stochastic contribution caused by the unmeasurable forces [7, 8]. Both contributions contain useful information of the system.

As in classical frequency-domain EMA and OMA, the input data can be Averaged Based Spectral (ABS) functions (i.e. FRF and XP) or the input and output (I/O) fourier coefficients. The approach described in this paper focuses on ABS functions as input data. The FRF and XP models considered are frequency-domain rational fraction polynomial models. Both the single-reference common-denominator model and the polyreference matrix-fraction description can be used. The use of the frequency domain allows easy pre-filtering of the data and fast yet accurate algorithms to estimate the modal parameters. The FRF and XP are constructed from the measured input and output signals using fast FFT and correlation techniques.

If the artificial excitation is harmonic, the deterministic component can be calculated without leakage by averageing over an integer number of periods. If the excitation is random, or if only short data sequences are measured, other techniques are necessary to obtain the FRF and the XP. The main drawback of these techniques is the possibility of leakage errors. The advantage is that it is is quite easy to determine the stochastic part of the XP, as will be discussed in Section II-B.

An alternative approach is to feed the fourier transform of the measured input and output signals directly into the modal parameter estimator. The main drawback of this method is that it results in a non-linear optimization. This requires an iterative procedure, this algortihm is slower than the one-step FRF based estimators. Another major drawback is that it is not possible to compensate for the correlation between the applied and unmeasured inputs if the exciter interacts with the structure. It is not yet clear if the parametric estimator can be adapted to account for this correlation.

OMAX is really advantageous when some modes are not (well) excited by the applied force. This can be because it is difficult to inject sufficient energy at specific frequencies (e.g. bridges). It can also be that the force is applied in the node of a mode. In this case, an operational (broadband) input can reveal these modes. Figure 1 shows the FRFs obtained from shaker measurements compared with the analytical FRF for low noise. The shaker is applied in the node of the second, third and fourth mode. The FRFs of two different response locations are plotted. Figure 2 shows the same FRFs for a higher noise level. The angles (not shown) follow a similar behaviour. It is clear that the second, third and fourth mode are not (always) present in the FRF. The XP clearly shows five peaks.

In Section II the required pre-processing steps are

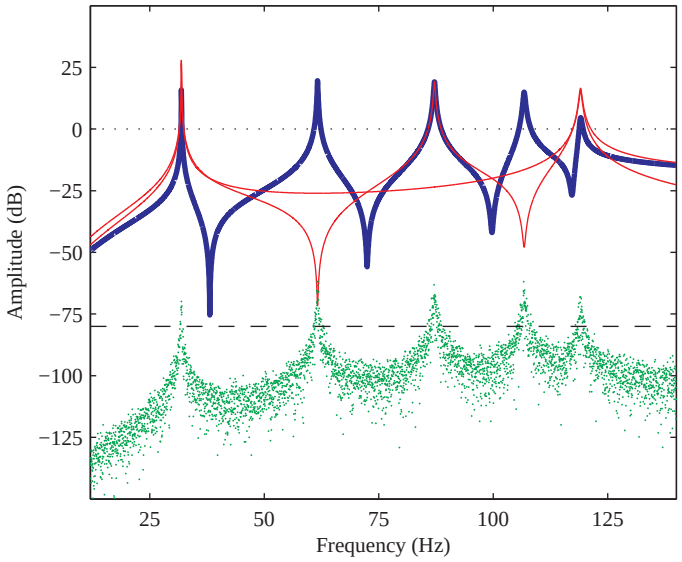

Fig. 1. Low noise level analytical (thick blue line) and estimated FRFs (thin red line), crosspower spectrum (green dots), applied force spectrum (black dotted line) and noise standard deviation (black dashed line)

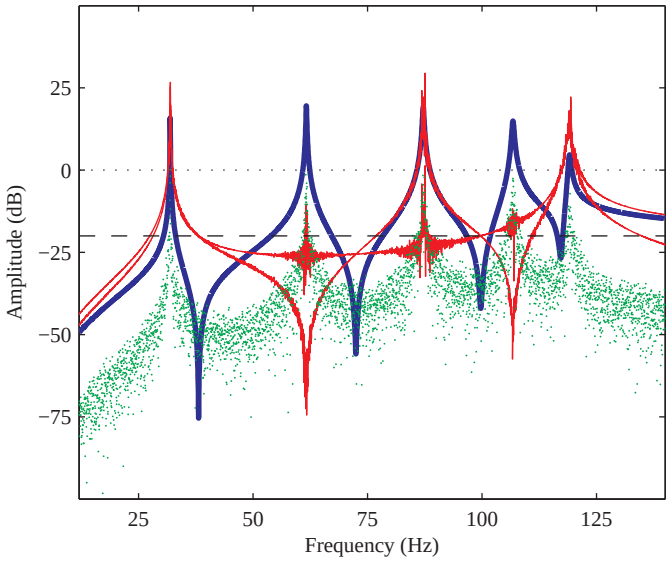

Fig. 2. High noise level analytical (thick blue line) and estimated FRFs (thin red line), crosspower spectrum (green dots), applied force spectrum (black dotted line) and noise standard deviation (black dashed line)

adapted for the OMAX approach with exciter-structure interaction. The comparison of the different frequency-domain estimators is done on a theoretical basis in Section III. Finally some conclusions are drawn.

II. Non-parametric identification

The FRF and XP are calculated from the fourier coefficients of the measured input and output signals. The system is assumed linear.

A. Deterministic part

Several classical approaches are used everyday to determine FRFs. Which one is best suited depends on the nature of the applied force. Starting from the fourier transform of the measured outputs $X(\omega_k) = \frac{1}{\sqrt{N}}\sum_n^{N-1} x(n)\exp(-\mathrm{j}2\pi\mathrm{kn/N})$ and forces $F(\omega_k) = \frac{1}{\sqrt{N}}\sum_n^{N-1} f(n)\exp(-\mathrm{j}2\pi\mathrm{kn/N})$, the crosspower spectra are obtained as

$$\begin{aligned} S_{XF}(\omega_k) &= \frac{1}{N_b}\sum_{b=1}^{N_b} X_b(\omega_k)F_b^H(\omega_k) \\ S_{FF}(\omega_k) &= \frac{1}{N_b}\sum_{b=1}^{N_b} F_b(\omega_k)F_b^H(\omega_k) \\ S_{FX}(\omega_k) &= \frac{1}{N_b}\sum_{b=1}^{N_b} F_b(\omega_k)X_b^H(\omega_k) \\ S_{XX}(\omega_k) &= \frac{1}{N_b}\sum_{b=1}^{N_b} X_b(\omega_k)X_b^H(\omega_k) \end{aligned} \tag{1}$$

with N_b the number of (possibly overlapping) blocks. The time samples can also be weighted with a suitable window (Hanning, Hamming, ...) before fourier transforming. This approach is also known as Welch procedure [9]. The H_1 and H_2 estimates are then found as

$$\begin{aligned} H_1(\omega_k) &= S_{XF}(\omega_k)S_{FF}(\omega_k)^{-1} \\ H_2(\omega_k) &= S_{XX}(\omega_k)S_{FX}(\omega_k)^{-1} \end{aligned} \tag{2}$$

If the force is periodic (e.g. a multisine), the use of the errors-in-variables estimator is proposed H_{ev} [10]. This is a special version of the instrumental variables estimator that yields consistent estimates of the FRFs without requiring any a priori noise information or the need for additional instrumental variables.

$$H_{ev}(\omega_k) = \left(\frac{1}{Np}\sum_{p=1}^{N_p} X_p(\omega_k)\right)\left(\frac{1}{Np}\sum_{p=1}^{N_p} F_p(\omega_k)\right)^{-1} \tag{3}$$

with N_p the number of periods.

B. Stochastic part

The responses contain both the deterministic part and the stochastic part.

$$X(\omega_k) = H(\omega_k)F(\omega_k) + G(\omega_k)E(\omega_k) \tag{4}$$

with X and F the measured responses and forces respectively. H is the FRF of the system (to be estimated), G is the filter of the (unknown) operational excitation E. This excitation is assumed zero mean normally distributed

(white noise) with unkown variance. In order to apply the classical OMA preprocessing algorithms (Welch periodogram and the correlogram method [11]), the deterministic component $H(\omega_k)F(\omega_k)$ must be removed from the responses.

If the force–and thus the response–is periodic, the mean value could be calculated over the period as for the H_{ev} estimator. The mean of the response could then be subtracted from the response to obtain only the stochastic part.

$$X_{s,p}(\omega_k) = X_p(\omega_k) - \left(\frac{1}{Np} \sum_{p=1}^{N_p} X_p(\omega_k) \right), \quad p = 1 \ldots N_p \quad (5)$$

This approach is wrong in the case of structure-exciter interaction. The responses are then corrupted due to the mass-loading effect of the shaker. In order to remove the deterministic part, an estimate is needed of the FRF of the decoupled system. The responses can then be compensated for the deterministic part; only the response due to the operational forces on the decoupled system remains .

$$X_{s,p}(\omega_k) = X_p(\omega_k) - H(\omega_k)F_p(\omega_k), \quad p = 1 \ldots N_p \quad (6)$$

The mathematical derivation is shown in Appendix.

If the responses are not corrected, or if only the mean is subtracted, the mass-loading effect is disregared. The obtained spectra are characteristic of the whole system-shaker combination. The resonance frequencies of this whole system obviously differ from the frequencies of the decoupled system, so an OMAX combination of uncorrected or wrongly corrected spectra would decrease rather than increase the accuracy of the estimates. Figure 3 illustrates this.

An important conclusion is that the correlogram method is not suited as the obtained spectra would be those of the system-shaker combination. The elimination of the deterministic part directly in the time-domain signal would require deconvoluting the response with the impusle response function.

C. Positive power spectra

The auto- and cross-power spectra have a four quadrant symmetry: they contain both the stable and unstable poles. It is better to calculate the so-called *positive* power spectra (XP+); these have the same structure as an FRF and they can be directly fed into the classical modal parameter estimators. The positive power spectra are obtained by inverse fourier transforming the power spectra, and then fourier transforming only the positive lags of the correlation function [8]. To avoid leakage the correlation function can be weighted by a rectangular or an exponential window.

The proposed pre-processing procedure can be summarized as follows:

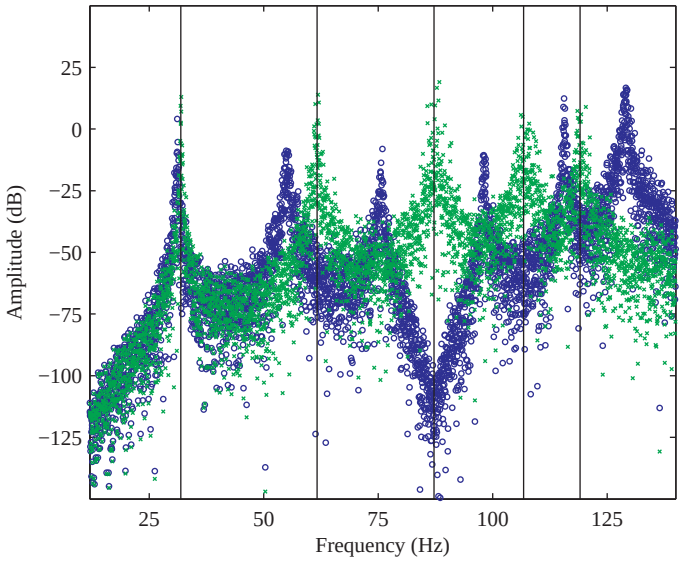

Fig. 3. Crosspower spectrum, corrected with a non-parametric estimate of the FRF (green crosses) and corrected with the mean of the responses (blue circles); the black vertical lines illustrate the location of the resonance frequencies of the uncoupled system

1. Measure N_p periods of the force $f_p(n)$ and response $x_p(n)$ of the signal (N points per period)
2. Fourier tranform the data: $F_p(\omega_k)$ and $X_p(\omega_k)$
3. Calculate the $H_{ev}(\omega_k)$ estimate through cyclic averageing for periodic signals (or $H_1(\omega_k)$ or $H_2(\omega_k)$ for other signals)
4. Determine the stochastic part of the response $X_{s,p}(\omega_k)$ by Eq. (6)
5. Calculate the power spectra and positive power spectra $S^+_{X_sX_s}(\omega_k)$ from the stochastic part of the response
6. Feed $[H_{ev}(\omega_k), S^+_{X_sX_s}(\omega_k)]$ into the parametric estimator

D. Pitfalls

The approach described in the previous section is sensitive to signal processing problems.

One pitfall is that the FRF is determined by averageing (H_1, H_2, H_{ev}). The estimated FRF will thus differ from the true FRF. This implies that, while correcting the responses for the deterministic contribution, some periodicity is introduced in stochastic part of response signal. The autocorrelation function will suffer from this periodicity. Moreover, for lightly damped systems, the fourier transform of the positive time lags of the autocorrelation function will show severe leakage problems. An exponential window function can be used, but this imposes a bias on the parametric estimates. The estimates must then be corrected for this bias afterwards.

Another point of attention is the number of positive time lags that are fourier transformed. This directly fixes the

number of spectral lines of the XP+. Due to the implicit circular convolution in the calculation of the XP, the number of spectral lines of the XP+ will be half of that of the FRF. In order to use existing parametric estimators, the number of spectral lines of the XP+ should be equal to those of the FRF. This can be obtained by zero-padding the time-domain signals [12]. However, this zero-padding can result in oscillation problems.

III. Parametric identification

A polynomial FRF or state-space (SS) model can be fitted through the measured data. Several frequency-domain modal parameter estimators exist that accept both FRF and XP as input. As the XP+ have the same modal structure as the FRF, they can be estimated without having to reformulate the estimator [8]. This is true for the state space, common-denominator and matrix fraction models that use the FRF as primary input data.

A. FRF and XP+ driven

The general OMAX parametric frequency-domain model can be written as

$$\begin{aligned} X(\omega_k) &= \hat{H}(\omega_k)F(\omega_k) + \hat{G}(\omega_k)E(\omega_k) \\ X(\omega_k) &= \frac{n(\omega_k)}{d(\omega_k)}F(\omega_k) + \frac{c(\omega_k)}{d(\omega_k)}E(\omega_k) \end{aligned} \tag{7}$$

with $n(\omega_k)$ the FRF model numerator, $d(\omega_k)$ the FRF model denominator and $c(\omega_k)$ the noise filter numerator. The denominator of the noise filter must be equal to the denominator of the FRF. This is the core of the OMAX approach: as both the deterministic (FRF: H) as stochastic (XP+: G) models share the same denominator, they have the same poles (resonance frequencies and damping ratios). Thus, by including the XP+, the accuracy of the estimated poles will increase because more data is used to estimate them. Different FRF models exist that lead to different estimation algorithms.

A.1 Common-denominator model

A scalar matrix-fraction description, better known as a common-denominator model, models the FRF between output $o(1,\cdots,N_o)$ and input $i(1,\cdots,N_i)$ as

$$\hat{H}_{oi}(\Omega_k,\theta) = \frac{N_{oi}(\Omega_k,\theta)}{d(\Omega_k,\theta)} \tag{8}$$

at frequency line k. $N_{oi}(\Omega_k,\theta)$ is the numerator polynomial and $d(\Omega_k,\theta)$ the common-denominator polynomial, defined by

$$\begin{aligned} N_{oi}(\Omega_k,\theta) &= \sum_{j=0}^{n} N_{oi,j}\,\Omega_k^j \\ d(\Omega_k,\theta) &= \sum_{j=0}^{n} d_j\,\Omega_k^j \end{aligned} \tag{9}$$

The coefficients $N_{oi,j}$ and d_j are the parameters to be estimated. These coefficients are grouped together in one parameter vector θ.

The linearized (weighted) equation error $E_{oi}(\omega_k)$ is obtained by replacing in Eq. (8) the model $\hat{H}_{oi}(\Omega_k,\theta)$ by the measured FRF $H_{oi}(\omega_k)$ and multiplying with the denominator polynomial $d(\Omega_k,\theta)$

$$E_{oi}(\omega_k) = W_{oi}(\omega_k)\big(N_{oi}(\Omega_k) - H_{oi}(\omega_k)\,d(\Omega_k)\big) \tag{10}$$

$W_{oi}(\omega_k)$ is a frequency-dependent weighting which can be used to improve the estimator. The estimates of the coefficients are then found by minimizing the least-squares cost function

$$l = \sum_{o,i}\sum_{k} |E_{oi}(\omega_k)|^2 \tag{11}$$

The main advantages of the common-denominator model is that it is flexible and that it allows a fast estimator: the least-squares complex frequency-domain estimator (LSCF) [13]. This estimator also yields very clear stabilization charts. The main drawback of this estimator is that it does not implicitely enforce a rank one constraint on the residues. A singular value decomposition (SVD) is then required to calculate the mode shapes and modal participation factors. This SVD reduces the accuracy of the FRF fit.

A.2 Right matrix-fraction description model

The PolyMAX estimator [14, 15] is the polyreference counterpart of the LSCF estimator. This estimator uses a right-matrix fraction description (RMFD) model. The relationship between N_o outputs and N_i inputs can be modeled in the frequency domain, at frequency line Ω_k

$$H(\Omega_k) = N(\Omega_k)D^{-1}(\Omega_k) \tag{12}$$

with $N(\Omega_k)$ the $N_o \times N_i$ numerator matrix polynomial and $D(\Omega_k)$ the $N_i \times N_i$ denominator matrix polynomial, defined by

$$\begin{aligned} N(\Omega_k) &= \sum_{j=0}^{n} N_j\,\Omega_k^j \\ D(\Omega_k) &= \sum_{j=0}^{n} D_j\,\Omega_k^j \end{aligned} \tag{13}$$

The matrix coefficients N_j and D_j are the parameters to be estimated. These coefficients are grouped together in one parameter matrix θ.

The least-squares cost function becomes

$$l = \sum_o \sum_k trace\left(E_o(\omega_k)^H E_o(\omega_k)\right) \tag{14}$$

with the $1 \times N_i$ row vector $E_o(\omega_k)$

$$E_o(\omega_k) = W_o(\omega_k)\big(N_o(\Omega_k) - H_o(\omega_k) D(\Omega_k)\big) \tag{15}$$

The PolyMAX estimator is fast and yields very clear stabilization charts, just as the LSCF. Moreover, a rank one constraint is implicitely imposed on the residues. The major drawback of the PolyMAX is that it is not consistent.

An important limitation for applications in the OMAX framework is that the number of reference responses must be equal to the number of inputs N_i of the FRF. This is due to the fact that the XP+ must have the same dimensions as the FRF to fit into the estimator.

A.3 Left matrix-fraction description model

The left matrix-fraction description (LMFD) considers all responses simultaneously. The FRF model is now

$$H(\Omega_k) = D^{-1}(\Omega_k) N(\Omega_k) \tag{16}$$

with $N(\Omega_k)$ the $N_o \times N_o$ numerator matrix polynomial and $D(\Omega_k)$ the $N_o \times N_i$ denominator matrix polynomial.

The least-squares cost function is now

$$l = \sum_i \sum_k trace\left(E_i(\omega_k)^H E_i(\omega_k)\right) \tag{17}$$

with the $1 \times N_o$ row vector $E_i(\omega_k)$

$$E_i(\omega_k) = W_i(\omega_k)\big(N_i(\Omega_k) - D(\Omega_k) H_i(\omega_k)\big) \tag{18}$$

The main drawback is that the size of the matrices is now proportional to the number of outputs N_o. Also the number of reference responses to fit in the OMAX framework must be equal to N_o. In typical modal analytical applications, the number of outputs is much higher than the number of inputs, so a RMFD is often more suited.

A.4 Subspace based identification

An excellent overview of the frequency-domain combined deterministic-stochastic subspace estimator can be found in [8]. The subspace methods are beyond the scope of this paper. One comparison is however appropriate. The FRF models discussed above estimate extra coefficients (the numerator coefficients of $\hat{G}(\omega_k)$). These coefficients are disregarded as they do not have a physical meaning. They only increase the uncertainty on the estimates, but it is the price one has to pay to use the classical estimators in the OMAX framework. The state-space model, however, is inherently suited to handle data in an OMAX framework.

B. Input-output driven

The frequency-domain estimators described in Section III-A can be reformulated to use directly the input and output fourier coefficients. The least-squares cost function is now

$$l = \sum_o \sum_b \sum_k |E_{o,b}(\omega_k)|^2 \tag{19}$$

and the error equation is reformulated as

$$E_{o,b}(\omega_k) = \frac{D(\Omega_k) X_{o,b}(\omega_k) - N_{oi}(\Omega_k) F_{i,b}(\omega_k)}{C_o(\Omega_k)} \tag{20}$$

with $C_o(\Omega_k)$ the numerator coefficients of the noise transfer function $G(\Omega_k)$, N_b is the number of blocks. This is a non-linear optimization problem that must be solved iteratively. The I/O approach will thus be slower than the one-step FRF based estimators. As the (non-parametric) FRF must be estimated first to eliminate the deterministic part from the responses, one is better to continue with the FRF and to calculate the XP+ than to return to the original spectra and minimize the non-linear cost function.

IV. Conclusions

In this paper, a description is given of an OMAX procedure suitable if exciter-structure interaction is present in the data. It is shown that the responses must be corrected for the deterministic part due to the applied force. This compensation is composed of a (non-parametric) estimate of the frequency response function of the *uncoupled* system. It is shown that response corrected with the mean of this response, results in the spectra of the coupled system. The resonance frequencies of this spectra obviously differ from those of the FRF, undermining an OMAX approach.

In a second step the *positive* power spectra are calculated. These spectra have the same structure as the frequency response function, so the classical frequency-domain parametric estimators can handle both without having to reformulate the algorithm.

Acknowledgements

The first author is research assistant of the department of Industrial Sciences & Technology of the Erasmushogeschool Brussel. This research was partially conducted in the context of the EUREKA project 3341, FLITE2. The financial support of the Fund for Scientific Research (FWO Vlaanderen); the Institute for the Promotion of Innovation of Science and Technology in

Flanders (IWT); The Concerted Research Action 'OPTI-Mech' of the Flemish Community; the Research Council (OZR) of the Vrije Universiteit Brussel (VUB) and the department of Industrial Sciences & Technology of the Erasmushogeschool Brussel (EhB) are gratefully acknowledged.

APPENDIX

I. CALCULATION OF THE STOCHASTIC PART

Mathematical derivation for a 2-DOF system with operational forces F_1 and F_2 and a shaker on the second mass. The stiffness of the stinger is k_{st} and the (electrical) force on the shaker is F_e

$$\begin{bmatrix} Z_{11} & Z_{12} & 0 \\ Z_{21} & Z_{22}+k_{st} & -k_{st} \\ 0 & -k_{st} & Z_e+k_{st} \end{bmatrix} \begin{Bmatrix} X_1 \\ X_2 \\ X_e \end{Bmatrix} = \begin{Bmatrix} F_1 \\ F_2 \\ F_e \end{Bmatrix} \tag{21}$$

The equations can be decoupled via the force that the stinger injects in the system

$$F_{st} = -k_{st}(X_2 - X_e) \tag{22}$$

This gives

$$\begin{bmatrix} Z_{11} & Z_{12} & 0 \\ Z_{21} & Z_{22} & 0 \\ 0 & 0 & Z_e \end{bmatrix} \begin{Bmatrix} X_1 \\ X_2 \\ X_e \end{Bmatrix} = \begin{Bmatrix} F_1 \\ F_2+F_{st} \\ F_e-F_{st} \end{Bmatrix} \tag{23}$$

or

$$\begin{Bmatrix} X_1 \\ X_2 \end{Bmatrix} = \begin{bmatrix} H_{11} & H_{12} \\ H_{21} & H_{22} \end{bmatrix} \left(\begin{Bmatrix} F_1 \\ F_2 \end{Bmatrix} + \begin{Bmatrix} 0 \\ F_{st} \end{Bmatrix} \right) \tag{24}$$

If first the FRF is estimated using a load cell to measure the F_{st}, then the output spectra of the decoupled system due to the operational forces only is obtained by

$$\left(\begin{Bmatrix} X_1 \\ X_2 \end{Bmatrix} - \begin{bmatrix} H_{11} & H_{12} \\ H_{21} & H_{22} \end{bmatrix} \begin{Bmatrix} 0 \\ F_{st} \end{Bmatrix} \right) = \begin{bmatrix} H_{11} & H_{12} \\ H_{21} & H_{22} \end{bmatrix} \begin{Bmatrix} F_1 \\ F_2 \end{Bmatrix} \tag{25}$$

REFERENCES

[1] M. W. Kehoe, "A historical overview of flight flutter testing," Nasa technical memorandum 4720, NASA, Dryden Flight Research Center, Edwards, October 1995.

[2] K. Deckers, T. De Troyer, E. Reynders, P. Guillaume, D. Lefeber, and G. De Roeck, "Applicability of low-weight pneumatic artificial muscle actuators in an omax framework," in *Proceedings of the International Conference on Noise and Vibration Engineering ISMA*, Leuven, Belgium, September 2008, pp. 2445–2456.

[3] W. Heylen, S. Lammens, and P. Sas, *Modal Analysis Theory and Testing*, Katholieke Universiteit Leuven, Department Werktuigkunde, Heverlee, 1997.

[4] N. Maia and J. Silva, *Theoretical and Experimental Modal Analysis*, Research Studies Press, Hertfordshire, 1997.

[5] E. Parloo, *Application of frequency-domain system identification techniques in the field of operational modal analysis*, Ph.d., Vrije Universiteit Brussel, department MECH, Pleinlaan 2, 1050 Brussel, Belgium, 2003.

[6] B. Peeters and G. de Roeck, "Reference-based stochastic subspace identification for output-only modal analysis," *Mechanical Systems and Signal Processing*, vol. 13, no. 6, pp. 855–878, nov 1999.

[7] P. Guillaume, P. Verboven, B. Cauberghe, and S. Vanlanduit, "Frequency-domain system identification techniques for experimental and operational modal analysis," in *Proceedings of 13th Symposium on System Identification SYSID*, Rotterdam, August 2003.

[8] B. Cauberghe, *Applied frequency-domain system identification in the field of experimental and operational modal analysis*, Ph.d, Vrije Universiteit Brussel, department MECH, Pleinlaan 2, 1050 Brussel, Belgium, 2004.

[9] P. D. Welch, "The use of fast fourier transform for the estimation of power spectra: A method based on time averaging over short modified periodograms," *IEEE Transactions on Audio and Electroacoustics*, vol. 15, no. 2, pp. 70–73, June 1967.

[10] P. Verboven, *Frequency-domain system identification for modal analysis*, Ph.d, Vrije Universiteit Brussel, department MECH, Pleinlaan 2, 1050 Brussel, Belgium, 2002.

[11] R. B. Blackman and J. W. Tukey, *The measurement of power spectra from the point of view of communication engineering*, Dover Publications, 1958.

[12] J. S. Bendat and A. G. Piersol, *Random Data: Analysis and Measurement Procedures*, John Wiley & Sons, New York, 1971.

[13] P. Guillaume, P. Verboven, and S. Vanlanduit, "Frequency-domain maximum likelihood identification of modal parameters with confidence intervals," in *International Conference on Noise and Vibration Engineering ISMA23*, Leuven, 1998, pp. 359–366.

[14] B. Peeters, G. Lowet, H. Van Der Auweraer, and J. Leuridan, "A new procedure for modal parameter estimation," *Sound and Vibration*, vol. 38, no. 1, pp. 24–29, 2004.

[15] B. Peeters, H. Van Der Auweraer, P. Guillaume, and J. Leuridan, "The polymax frequency-domain method: A new standard for modal parameter estimation?," *Shock and Vibration*, vol. 11, no. 3–4, pp. 395–409, 2004.

Proceedings of the 8th National Congress on Theoretical and Applied Mechanics, May 28-29, Brussels, Belgium.

Vibration cancellation of a pneumatically actuated cryocooler

B. de Marneffe, A. preumont
Active Structures Laboratory, Université Libre de Bruxelles, Belgium
bdemarne@ulb.ac.be, andre.preumont@ulb.ac.be

Abstract— **In this work we try to cancel the low-frequency part of the vibrations of a cryocooler. These vibrations are caused by the periodic impacts of internal mechanical parts inside the cooler. Three different control laws are compared on a small-scale demonstrator, namely the Filtered-x LMS (implemented in the time and in the frequency domain) and Repetitive Control. It is found that they share similar performances in terms of disturbance attenuation.**

Keywords— **periodic vibration, impact shock, cryocooler, repetitive control, filtered-x LMS, harmonic control**

I. Introduction

Cryocoolers are small cryogenic refrigerators that can reach very low temperatures (down to 3-4 Kelvin) but can extract only a very limited amount of heat from the structure to which they are connected, typically a few watts [1]. They are used in a wide range of applications, including Magnetic Resonance Imaging, cryopumping for the creation of high vacuum, and infrared or gamma-ray astronomical observations. The one investigated here is shown in Figure 1: it is used at the Very Large Telescope Interferometer (VLTI) of the European Southern Observatory (ESO) in Paranal (Chile).

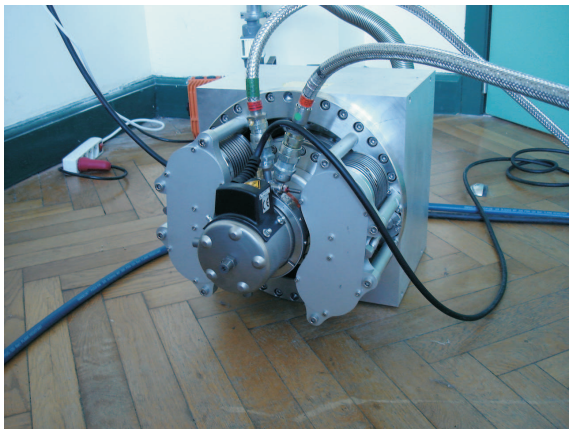

Fig. 1. The cryocooler considered in this work.

The "classical" thermodynamic processes undergo a drastic efficiency change when miniaturized, and for that reason the cryocoolers are usually based on other cycles, such as the Stirling cycle or the Gifford-McMahon (GM) cycle [1], [2]. These two cycles, unfortunately, require the presence of a cylinder (called "displacer") that moves back and forth within the machine, therefore creating unwanted vibrations. In some cases, the displacer is pneumatically actuated, which makes the situation even worse as the vibrations are no longer harmonic but instead caused by impact shocks. (The shocks occur when the displacer hits the limits of the cold head's inner space).

The consequences of these shocks can be dramatic: in our case, in particular, the VLTI cannot be used in its "interferometric" mode, therefore limiting the range of observations that can be done. Several passive solutions were tried, including the introduction of a classical isolation stage between the cooler and the instrument, but it was observed that the vibrations, although attenuated, were still one order of magnitude larger than the maximum tolerable level.

In this work we try to develop an active vibration cancellation system that reduces the impacts of the cooler's vibrations. The cancellation system is based on a proof-mass (inertial) actuator equipped with a voice coil transducer and an acceleration sensor. It is explained below that the classical feedback controllers have very limited effects in our case, which is why we use specific controllers based on the repetitiveness of the disturbance. Many such controllers exist in the literature, see e.g. [3], but not all of them can handle the many harmonics that result from the repetitive impacts. In this work we compare three controllers that seem to meet our requirements, namely the *filtered-x LMS* [4], the *harmonic control* [5, chap.3], or the *Repetitive Control* based on the Internal Model Principle (e.g. [6] and the references therein).

Section II describes the crycoller and the way that it is modelled. Section III describes the control hardware as well as the classical feedback controller that is used as a first control layer. Section IV recalls the principles of the periodic control algorithms, and finally section V presents a preliminary experimental validation on a small-scale laboratory demonstrator.

II. Modelling

The cryocooler is schematized in Figure 2a, along with its displacer that moves back and forth with a period time of 1s. The cooler is placed on a soft suspension so as to attenuate the effects of the impact shocks, and the connection between the cooler and the instrument is very soft, so that we can neglect it in this analysis.

If the cooler is considered to be rigid, it can be re-

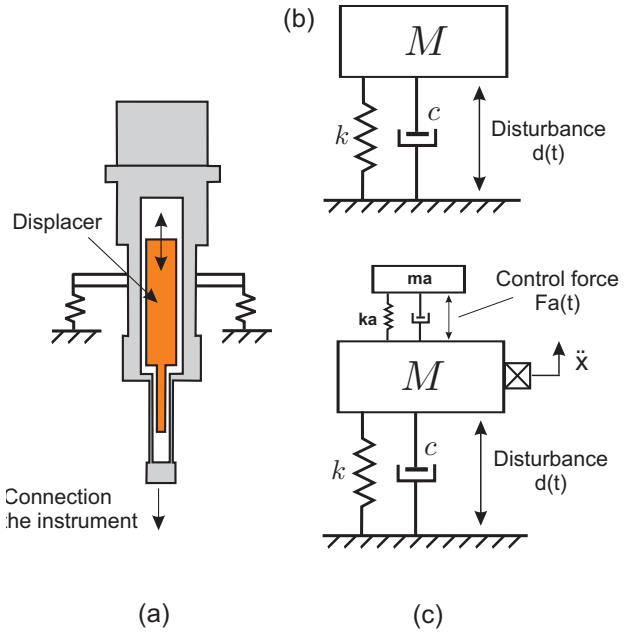

Fig. 2. (a) Representation of the cooler with its displacer and soft suspension. (b) Single-d.o.f. model of the cooler. (c) Control system.

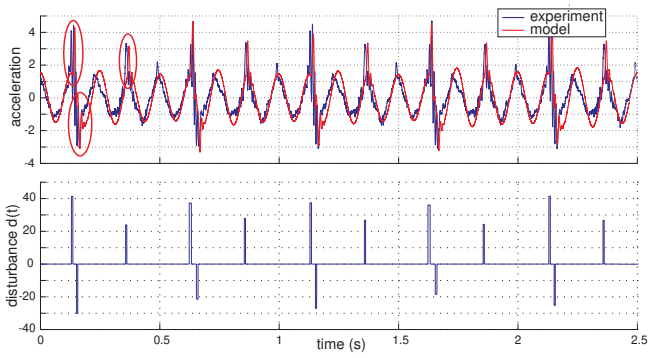

Fig. 3. Top: experimental and numerical acceleration of the cryocooler (filtered at 100 Hz). Bottom: periodic part of the disturbance $d(t)$.

duced to the single-d.o.f. system shown in Fig. 2b, where $M = 12.5$ kg is the mass of the cooler, $k \simeq 27.5$ kN/m is the stiffness of the suspension, and the disturbance $d(t)$ represents the reaction forces exerted on the cooler by the displacer during each impact. (This analysis is not totally true, though, because there are parts of the cycle where the displacer is fixed with respect to the cooler, thus adding its mass to M, but our controllers are sufficiently robust to handle this). The corner frequency of the suspension was measured to be about 7.5 Hz. No damper is actually introduced in it, so that it is very lightly damped ($\xi \simeq 0.2\%$).

In order to design the control system we have to find a signal $d(t)$ which is sufficiently representative (in terms of frequency decomposition, peak amplitude, and repetitiveness) of the "real" force exerted by the displacer, because

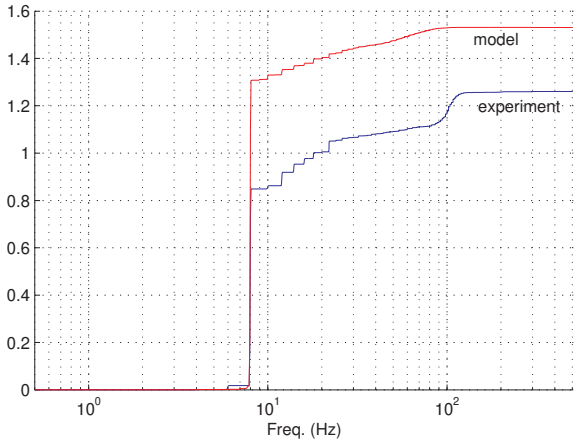

Fig. 4. Experimental and numerical cumulative Mean-Square acceleration of the cryocooler (in $(m/s^2)^2$).

we do not have access to the inside of the cooler and are thus obliged to guess what is happening in it. The simple approach taken here is based on the observation that the acceleration signal is made of 3 sharp peaks followed by free oscillations of the spring-mass system, see Fig. 3 (top). Accordingly, we tried to model $d(t)$ as a series of periodic pulses, with each pulse placed at the position of one peak as shown in Fig. 3 (bottom); physically, the pulses correspond to the impacts of the displacer against the cold head. The position, amplitude and duration of each pulse were chosen in such a way that the resulting vibration of the cold head is as close as possible to that observed experimentally, both in the time domain and in the frequency domain.

The results in time domain are shown in Fig. 3 (top): the correlation with the experiments is very good. The results are somewhat less good in the frequency domain, as shown in Fig. 4 which plots the experimental and numerical cumulative Mean-Square acceleration, defined by the frequency-dependent value

$$MS(\omega) = \int_0^{\omega} \Phi_{xx}(\omega^\star) d\omega^\star \qquad (1)$$

where $\Phi_{xx}(\omega)$ is the one-sided Power Spectral Density of the acceleration signal. The model overestimates the amplitude of the harmonic at 8 Hz and underestimates the amplitude of those at other frequencies; this conflict is due to the simplicity of the model, which has too few parameters to allow us to fix the amplitude of each harmonic independently. In spite of this, the model correctly predicts the order of magnitude of each harmonics as well as the frequency region where the disturbance is present, which is what we are really looking for for the design of the control system (in terms of bandwidth, power, stroke, etc.). Moreover, it was observed that the frequency behavior of the cooler can change from one day to the other, so there is no

point in trying to model it very precisely.

Note, finally, that d also has a random part caused by shocks, friction etc inside the cold head. That random part however is several orders of magnitude smaller than the periodic part, so that we can neglect it.

III. Control system

A. Actuator and sensor

The control system is schematized in Fig. 2c: a reaction mass m_a ($\simeq$2 kg) is placed, through a soft suspension (k_a, c_a) on top of the cooler, and a pair of opposite force $F_a(t)$ is exerted on M and on m_a by means of an electromagnetic transducer. The absolute acceleration $\ddot{x}(t)$ of the cooler is measured with a piezoelectric accelerometer.

The resonance frequency $\omega_a = \sqrt{k_a/m_a}$ of the inertial actuator should be lower than 1 Hz (the frequency of the disturbance) so that it behaves as an ideal point force transducer at all the frequencies that we wish to control (e.g. [7, chap.3]). Such a low frequency is however very difficult to achieve, if only because a very soft stiffness k_a leads to a very large static deflection of the transducer, so we were forced to take it ten times higher (i.e. approximately equal to the suspension frequency of the cryocooler). This brings acceptable values of the static deflection, but the price to pay is a larger control effort $F_a(t)$ and a larger deflection at all frequencies below ω_a, and more difficulties when designing the feedback controller. Note, on the other hand, that as the frequencies of the actuator and that of the structure are similar, the actuator behaves like a Tuned-Mass Damper and introduces some passive damping in the structure, which is favorable.

B. First control layer

The easiest way to control the vibrations of the cold head consists in implementing a classical feedback controller $H(s)$ linking the measured acceleration $\ddot{x}(t)$ to the force input $F_a(t)$. After some trial and errors a suitable controller was found, and the corresponding open-loop transfer function $H(s)G(s)$ is shown in Fig. 5 ($G(s)$ is defined to be the system's response $\frac{s^2X}{Fa}$). A pair of complex zeros is placed near the resonance to compensate for the second pair of poles introduced by the actuator. Note that, as the system parameters are very imprecise and might possibly change with time, no attempt was made to optimize $H(s)$: we only tried to attain reasonable disturbance rejection and a good robustness of the feedback loop. It is seen that the control is effective in a very limited frequency range ([4-12 Hz]) and that the maximum vibration reduction occurs at the resonance, where the disturbance is divided by 10. It is unfortunately not possible to further increase the gain or decrease the low-frequency limit

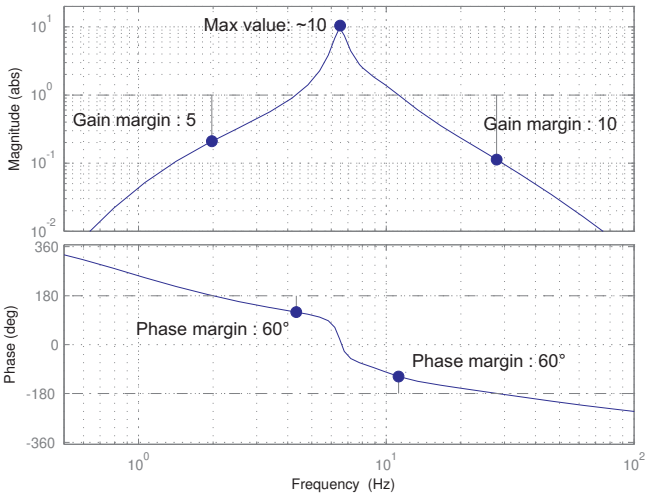

Fig. 5. Open-loop transfer function $H(s)G(s)$

below 4 Hz because it would induce unacceptably large displacements of the actuator.

Although the classical feedback controller somewhat improves the situation, it is clearly not enough, which is why we decided to add a second control layer, using this time algorithms specifically developed for periodic disturbances. In the following, it must be understood that the feedback controller is already included in the system, that is, the system's transfer function has changed from $G(s)$ to $G'(s) = G(s)/(1+G(s)H(s))$.

IV. Second control layer

In this section we briefly recall the principles of the various algorithms that we have implemented.

A. Filtered-x LMS

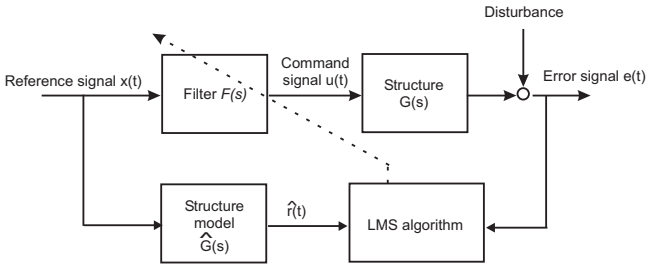

Fig. 6. Principles of the Filtered-x LMS.

The so-called filtered-x LMS algorithm is widely known (e.g. [4]), and its adaptation for the case of periodic disturbances is presented in [8]. As compared to [8] we add a leakage term which enhances the algorithm's robustness and we consider the case where G has a long impulse response.

The principles of the Fx-LMS are shown in Fig. 6. A reference signal x is sent to a FIR filter F whose output is

the command signal u of the actuator. F is adapted at each time step until the measured error e reaches a minimum. The adaptation law reads [5]:

$$f_i[n+1] = (1-\alpha\beta) f_i[n] - \alpha e[n] \hat{r}[n-i] \qquad (2)$$

where n is the present time step, f_i ($i = 0,..,N-1$) are the coefficients of the filter F, α is a positive parameter that controls the convergence rate, $\hat{r}$ is the signal obtained by filtering x through a model of the system $\hat{G}$, and finally β is a positive parameter that balances the importance given to the control effort with that given to the cancellation of e. Although this term decreases the performances of the algorithm, in many cases a small value of β significantly decreases the control effort and increases the system's robustness without too much impacting the results.

If the disturbance is periodic the implementation of the algorithm can be greatly simplified, decreasing by much its computational time. Indeed, we know that $d[n]$ is periodic, but nothing else: the reference signal $x[n]$ is thus an impulse train,

$$x[n] = \sum_{k=-\infty}^{\infty} \delta[nT_s - kT] \qquad (3)$$

with δ being Dirac's impulse function, $T_s = 10^{-3}$s is the sampling time and T=1s is the period of the disturbance. Thanks to (3), u and $\hat{r}$ are given by, respectively:

$$u[n] = f_{n-k^*N} \quad \text{and} \quad \hat{r}[n] = \sum_{\gamma=0}^{n_g} \hat{g}[n-(k^*-\gamma)N] \qquad (4)$$

where $N = T/T_s$ is the number of samples in a period, k^* is the largest integer not greater than n/N, $\hat{g}$ is the discrete-time impulse response of the system model $\hat{G}$, and n_g is the largest integer smaller than l_g/N where l_g is the length of $\hat{g}$. In other words, u and $\hat{r}$ can be obtained directly from F and $\hat{g}$, and no convolution is needed any more. The formulae are even easier if we define a N-point vector $\hat{g}_2$:

$$\hat{g}_2(j) \triangleq \sum_{\gamma=0}^{n_g} \hat{g}[j+\gamma N] \qquad (j = 0,..,N-1) \qquad (5)$$

Eq. 2 then becomes, with (4) and (5):

$$f_i[n+1] = (1-\alpha\beta) f_i[n] - \alpha e[n] \hat{g}_2[n-i-k^{**}N] \qquad (6)$$

where k^{**} is this time the largest integer not greater than $(n-i)/N$. The filtered-x LMS with periodic disturbance thus requires two memory vectors of length N (the f_i and $\hat{g}_2$) and a number of operations proportional to N at each time step (for updating the f_i). Note that if the system is well damped $\hat{g}$ is shorter than N, so that $n_g = 0$ and $\hat{g}_2 = \hat{g}$.

A.1 Performance

It is possible to summarize the algorithm by a single formula that directly gives the evolution of $u[n]$ (instead of using the intermediary filter F). Using (4a) and (6), one finds indeed:

$$u[n] = (1-\alpha\beta)^N u[n-N] - \alpha \sum_{j=0}^{N-1} e[n-N+j]\, \hat{g}_2[j] \qquad (7)$$

which points out that the periodic Fx-LMS algorithm really acts like a periodic signal generator whose output signal $u[0,..,N-1]$ is slightly modified after each period. Going into the frequency domain, and assuming zero initial conditions, (7) becomes:

$$U(z) = (1-\alpha\beta)^N z^{-N} U(z) - \alpha z^{-N} E(z) \hat{G}_2(z^{-1}) \qquad (8)$$

or:

$$U(z) = -\alpha \frac{z^{-N} \hat{G}_2(z^{-1})}{1-(1-\alpha\beta)^N z^{-N}}\, E(z) \qquad (9)$$

where $\hat{G}_2(z)$ is the z-transform of $\hat{g}_2$. It appears thus that the Fx-LMS algorithm, when adapted for periodic vibrations, turns into a feedback controller whose output signal u is obtained by filtering the error signal e trough the controller $\alpha \frac{z^{-N}\hat{G}_2(z^{-1})}{1-(1-\alpha\beta)^N z^{-N}}$. All the analysis tools developed for the feedback control, e.g. the Bode and Nyquist plots, can thus be used to assess its stability margins and performances. In particular, the system response to the disturbance d reads:

$$\frac{E}{D}(z) = \frac{1-(1-\alpha\beta)^N z^{-N}}{1-(1-\alpha\beta)^N z^{-N} + \alpha z^{-N} G(z) \hat{G}_2(z^{-1})} \qquad (10)$$

which is, at the k^{th} harmonic of $1/T$:

$$\frac{E}{D}(e^{j2\pi k \frac{T_s}{T}}) = \frac{1-(1-\alpha\beta)^N}{1-(1-\alpha\beta)^N + \alpha z^{-N} G(.) \hat{G}_2(.^{-1})} \qquad (11)$$

Noting that, at these frequencies, one has $\hat{G}_2 = \hat{G}$ and supposing that the model is accurate ($\hat{G} \simeq G$), Eq. (11) can be approximated by:

$$\frac{E}{D}(e^{j2\pi k \frac{T_s}{T}}) \simeq \frac{N\beta}{N\beta + |G(.)|^2} \qquad (12)$$

(where we have also used $(1-\alpha\beta)^N \simeq (1-N\alpha\beta)$). The periodic disturbance is thus well attenuated if $|G(.)|^2 >> N\beta$, and in that case the system response is proportional to $N\beta/|G(.)|^2$. (Note that the algorithm might well increase the system's response at frequencies other than the harmonics, but we do not care in this work because we know that the non-periodic disturbance is negligible).

A.2 Stability

Without going into much details, it can be shown that a sufficient condition for the stability of the feedback law (9) reads:

$$|(1-\alpha\beta)^N - \alpha\hat{G}_2(e^{-j\omega T_s})G(e^{j\omega T_s})| < 1 \qquad \forall\omega \qquad (13)$$

Consider first the case where $\hat{g}$ is short, i.e. $\hat{G}_2 = \hat{G}$. If $\beta = 0$, (13) implies $R_e(\hat{G}(e^{-j\omega T_s})G(e^{j\omega T_s})) > 0\ \forall\omega$, or in other words that the phase of $\hat{G}$ and G do not differ by more than $\pm 90°$, which is consistent with the Fx-LMS theory. That condition, however, is extremely difficult to enforce at all frequencies: there are always unmodelled modes, and $G \to 0$ at large frequencies for any physical process, indicating marginal stability. If $\beta > 0$, on the other hand, assuming $(1-\alpha\beta)^N \simeq (1-N\alpha\beta)$, it can be seen that (13) is automatically fulfilled at frequencies where $N\beta > |\hat{G}(.)G(.)|$, and uncertainties in the response of G do not impact the stability provided that $|G\hat{G}|$ is small enough at these frequencies.

To summarize the results (and assuming a good model and a short impulse response $\hat{g}$, that is $\hat{G}_2 \simeq \hat{G} \simeq G$), the value of $N\beta$ separates the frequency region where $N\beta > |G|^2$, in which the stability is not an issue (Eq. 13), from the regions where $N\beta << |G|^2$, in which the disturbance is effectively attenuated (Eq. 12).

If, on the other hand, the system is lightly damped and $\hat{g}$ is long, $\hat{G}_2$ might differ largely from $\hat{G}$ and it is difficult to draw general conclusions; the stability in that case must be checked directly from (13) or even from (9). Note, however, that the "most dangerous" frequencies for stability are the harmonics of $1/T$ (because the controller (9) has a very large response at these frequencies), and that at these frequencies $\hat{G}_2 = \hat{G}$ which indicates that the stability properties could be similar. Note, too, that the theory of the Fx-LMS (not necessarily periodic) guarantees the convergence if the model is precise enough and α small.

B. Harmonic control

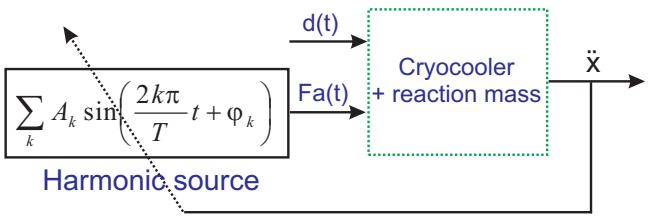

Fig. 7. Principles of the harmonic control.

The classical Fx-LMS described in section IV-A is effective, but it lacks any frequency selectivity because it has only two tuning parameters (α and β). Instead we would like to have a frequency-tunable convergence rate, increasing it in some important frequency regions (or where the system is well-known and the stability is not an issue) and decreasing it or even suppressing it in other regions.

If the disturbance is periodic this can be done with the so-called harmonic control shown in Fig. 7. A signal generator sends a sum of sine signals to the control input of the cryocooler $F_a(t)$; the amplitude and phase of each sine is progressively adapted, based on the measured error $e(t) = x(t)$, until $e(t)$ has no component at the selected frequencies. The theory of the harmonic control, which is summarized here, is taken from [5, chap.3]. Note that, unlike the Fx-LMS and RC algorithms, the harmonic control does not increase the disturbance between the harmonics (because the control input is made of pure tones).

B.1 Single-tone disturbance

Let us begin with the case of a sine disturbance, $d(t) = Asin(\omega_0 t + \phi)$. If one goes into the frequency domain, the Fx-LMS adaptation law becomes:

$$U(n+1) = U(n) - \alpha\hat{G}^*(e^{j\omega_0 T_s})E(n) \qquad (14)$$

(we do not use any leakage term here) where n now denotes the iteration index, U and E are the complex z-transform of the control input u and of the measured error e, respectively , and $\hat{G}^*(.)$ is the complex conjugate of the discrete system model $\hat{G}(.)$: the adaptation algorithm thus requires the modelling of G at the frequency ω_0 only.

It can be shown that the optimal value for α is given by:

$$\alpha_{opt} = \frac{1}{|G(e^{j\omega_0 T_s})|^2} \qquad (15)$$

(where we have assumed perfect modelling), which stresses that the optimal value of α is actually frequency-dependent, and it can also be shown that the algorithm is stable on condition that

$$0 \le \alpha \le \frac{2\cos\phi}{M|G(e^{j\omega_0 T_s})|^2} \qquad (16)$$

where ϕ and M are, respectively, the phase and amplitude mismatch between the plant and the model at the frequency ω_0. Note that the system cannot be stable, whatever the value of α, if the phase mismatch exceeds $\pm 90°$. These stability conditions are very similar to those of the Fx-LMS algorithm (13), but in this case they must be met at the single frequency ω_0 only, while (13) must be met for all ω.

B.2 Multi-tone disturbance

If the system is linear the harmonics do not interact and the controller can be decomposed into a set of independent control loops. The technique is illustrated in Fig. 8:

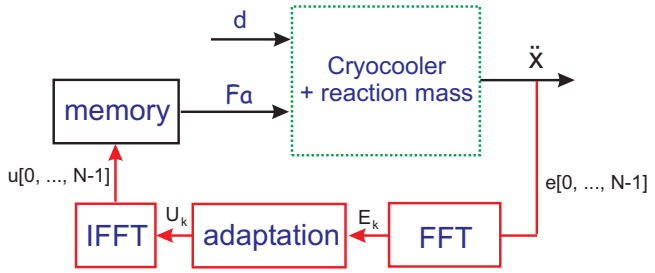

Fig. 8. Harmonic control for multi-frequency disturbances. The sequence "FFT→adaptation→IFFT" is executed at the end of each cycle.

1. The (discrete-time) error signal is recorded during one cycle: $e[0,..,N-1]$
2. An FFT is executed on $e[0,..,N-1]$, decomposing it into its complex harmonic E_k ($k = 0,..,N-1$).
3. The adaptation law (14) is executed (once per harmonic), producing the complex amplitudes of the control force U_k.
4. An inverse FFT is then performed on the U_k, so as to transform them into a time sequence $u[0,..,N-1]$ which is recorded in memory and executed during the next cycle.

As compared with the time-domain Fx-LMS, besides allowing a frequency-dependent convergence coefficient α_k, the technique also reduces the computing time (particularly for large values of N), because the FFT and IFFT operations can be executed off-line, and only the reading of the memory $u[.]$ and the recording of the error $e[.]$ are to be done in real-time.

C. Repetitive Control (RC)

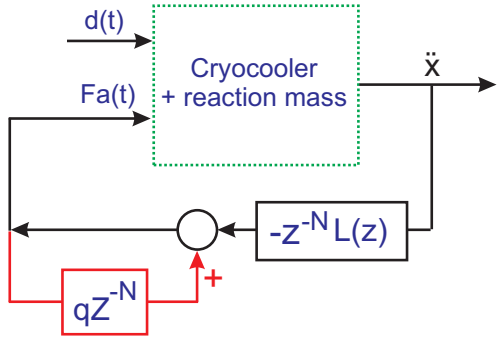

Fig. 9. Repetitive Control.

The theory of the RC is taken from [6], and the comparison with the Fx-LMS is also studied in [8].

Repetitive Control is a feedback technique based on the Internal Model Principle, which states (loosely speaking) that any stable feedback system will ultimately suppress any disturbance on condition that a "model" of that disturbance is included in the feedback path. In our case the "model" of the disturbance consists of a periodic signal generator obtained by inserting a time delay z^{-N} inside a positive feedback loop, as shown in Fig. 9. According to that Figure, the error signal is first filtered through $L(z)$, next delayed by $N = T/T_s$ sample times, and finally sent to the periodic signal generator. The FRF of the feedback path is:

$$U(z) = -\frac{z^{-N}L(z)}{(1-qz^{-N})}E(z) \tag{17}$$

its amplitude is proportional to $(1-q)^{-1}$ at each frequency multiple of $1/T$, indicating a good disturbance rejection if $q \simeq 1$.

It is readily seen that the FRF (17) is similar to (9), with q playing the role of $(1-\alpha\beta)^N$ and $\alpha\hat{G}_2(z^{-1})$ being replaced by the filter $L(z)$. In that sense Repetitive Control can be seen as a generalization of the periodic Fx-LMS, in which the design freedom in $L(z)$ can be used to reshape the system's frequency response and obtain the desired convergence properties.

C.1 Performances

The performance analysis is identical to that made in Section IV-A. The FRF between e and d reads, at the frequencies multiple of $1/T$:

$$\frac{E}{D}\left(e^{j2\pi\frac{T_s}{T}}\right) = \frac{1-q}{1-q+G(.)L(.)} \tag{18}$$

which means that there is a good attenuation as long as $GL >> (1-q)$, and that in that case the response is proportional to $(1-q)/GL$.

C.2 Stability and convergence

For both stability and convergence, $L(z)$ should approach $G^{-1}(z)$; actually, if $q = 1$ and $G(z)L(z) = 1$, the controller can be shown to converge in a single step. $G^{-1}(z)$ is however impossible to implement, if only because G, being a physical process, is proper, and thus G^{-1} has more zeros than poles.

Some kind of filtering is thus required, but one must take care that the phase lag introduced by the filter does not destabilize the system: indeed, the condition for stability reads

$$|q - GL| < 1 \tag{19}$$

which requires that $R_e(GL) > (q-1)$, i.e. the phase difference between G and L does not exceed $\pm 90°$ at frequencies where $|GL| \geq (1-q)$ (as before, (19) is automatically fulfilled at frequencies where $|GL| < (1-q)$).

The difficulty can be solved by the use of a so-called zero-phase filter $P(z)P(z^{-1})$. In short, $P(z^{-1})$ has the same amplitude as $P(z)$ but opposite phase, and it has the same impulse response but reversed in time, i.e. $p_1[n] = p_2[-n]$

where $p_1[.]$ is the response of $P(z^{-1})$ and $p_2[.]$ is the response of $P(z)$: $P(z^{-1})$ is thus non-causal, and only $z^{-N}P(z^{-1})$ can be implemented in real-time. In other words, the causal filter $z^{-N}P(z^{-1})P(z) = z^{-N}|P(z)|^2$ does not introduce any phase distortion, at the expense of a N-sample time delay.

Looking at Fig. 9, it appears that the delay z^{-N} is already present in the loop. A sensible choice for $L(z)$ consists thus in:

$$z^{-N}L(z) = z^{-N}\hat{G}^{-1}(z)P(z^{-1})P(z) = z^{-N}\hat{G}^{-1}(z)|P(z)|^2 \tag{20}$$

where P is any filter which amplifies the frequencies where we want the control to be effective, and attenuates the other frequencies.

It was shown that the Fx-LMS is but a particular case of Repetitive Control: in that case (and assuming $\hat{G}_2 \simeq \hat{G}$), one has $L = \alpha\hat{G}(z^{-1})$, that is, the phase of $LG = \alpha\hat{G}(z^{-1})G(z) \simeq \alpha|G(z)|^2$ remains close to 0 (which is good for the stability) but no attempt is made to reshape its amplitude (which is less good for the performances).

V. Experimental verification

A. Experimental setup

The concept has been experimentally demonstrated on the small-scale laboratory demonstrator shown in Fig. 10 and Fig. 11. It is build according to the model of Fig. 2c, that is, a small reaction mass m_a is connected, through a soft suspension, to a larger mass M representing the cooler. The suspension connecting the cooler to the ground is introduced by means of two flexible bearings, which are also used to guide M and ensure an axial movement. An electromagnetic actuator ("magnet 1" and "coil 1") is used to introduce the disturbance $d(t)$. A soft spring connects m_a and M, and coaxial displacement is ensured by the use of a ball bearing: the option "spring and ball bearing" was preferred to the use of flexible bearings because the relative displacement between the two masses might be quite large ($\pm$6mm). A second moving coil transducer is used to introduce the control force $F_a(t)$, and an accelerometer measures the movements of M. The reaction mass m_a is well damped thanks to the eddy currents that appear in the metallic support of coil 2.

The setup is designed to be as representative as possible of the real cryocooler, i.e. we kept the same mass ratio m_a/M, the natural frequencies and amplitude of the displacements are similar, and the disturbance $d(t)$ is a scaled version of the one taking place in the cooler, as identified in Section II. Any conclusion from this experiment therefore also applies to the control of the cryocooler. Note, too, that the behavior of the setup is far from linear, as the ball bearing introduces a large stick-slip phenomenon, and

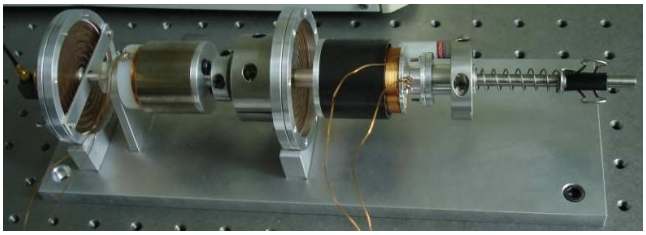

Fig. 10. Small-scale laboratory demonstrator.

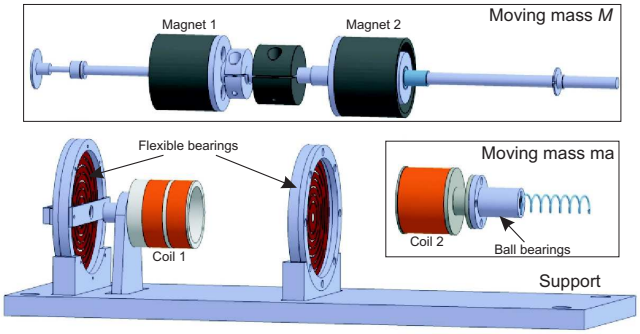

Fig. 11. Scattered view of the setup.

the constant of the moving coil transducer changes with the displacements (which are quite large). In spite of this, the experiment was successful, which increases the confidence that the control strategy will also be effective when applied on the real cryocooler.

B. Implementation of the algorithms

The control system is implemented with a DSpace DS1103 control board. The classical feedback described in section III-B is introduced with a sampling frequency of 10kHz: it calls no particular comment. The Fx-LMS and RC controllers are implemented with a S-function (at 1 kHz), and the harmonic control with the built-in FFT and IFFT functions of Matlab (at 8192 Hz such that $N = T_s/T$ is a power of 2).

In this work we try to cancel the displacement of the cryocooler, and not its acceleration, which is much easier as the displacement signal has a limited frequency range ($\simeq 0 \rightarrow 100$ Hz) while the acceleration has components up to tens of kHz (because of the shocks). The output of the accelerometer is thus integrated twice in the charge amplifier, such that all subsequent signal treatments deal with displacements instead of accelerations.

Remark: Although the theory is developed assuming a constant period T, in practice the period of the cooler varies slowly with time of about $\pm 0.15\%$. This variation can be measured (it is that of the frequency of the electrical network) and is taken into account by simply adjusting the beginning of each cycle of $F_a(t)$ by the appropriate amount of sample time. We experimentally compared the two sit-

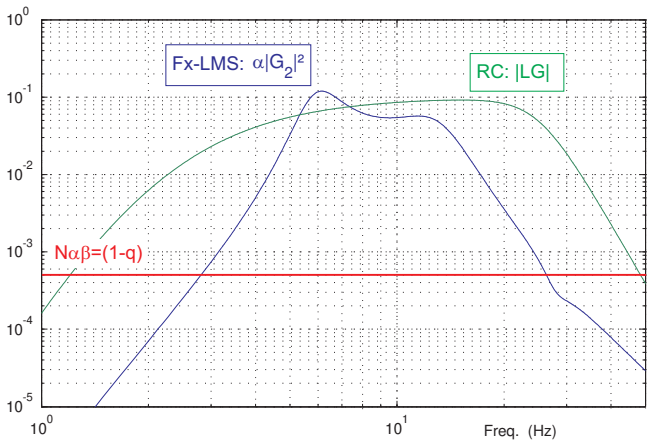

Fig. 12. FRF $\alpha|G|^2$ of the filtered-x LMS and $|LG|$ of the Repetitive Control. The forgetting factor $N\alpha\beta = (1-q)$ is also shown.

uations (T =cste or T varies and the algorithm is adapted) and concluded that the results are identical in both cases.

B.1 Fx-LMS

Thanks to the feedback controller, the system is well damped and its impulse response is shorter than T: we thus have $\hat{G}_2 = \hat{G}$. The FRF $\alpha|G(j\omega)|^2$ is plotted in Fig. 12, along with the chosen value of $N\alpha\beta$. Recalling the discussion of sections IV-A.1 and IV-A.2 (Eq. 12 and 13), it is seen that the algorithm should attenuate all the harmonics between 3 Hz and 25 Hz, and that the model $\hat{G}$ needs to be precise in that small frequency region only. We chose α such that $\max_{\omega} \alpha|G(j\omega)|^2 \simeq 0.1$ in order to have good robustness properties (the maximum value is about 1, see Eq. 13).

B.2 Repetitive Control

We took advantage of the design freedom of the RC to enlarge the frequency region where the algorithm is effective without changing the robustness. The result is shown in Fig. 12: with the same stability margin ($\max|LG| \simeq \max \alpha|G|^2$) and with the same forgetting factor ($(1-q) = N\alpha\beta$) as the Fx-LMS, the RC algorithm is effective in the region $[2-45]$ Hz. We deliberately chose 45 Hz as an upper limit, because the disturbance has little components above, and did not want to include the 1 Hz harmonic in the bandwidth because the attenuation of low-frequency harmonics requires a lot of control power.

B.3 Harmonic Control

Stability of the harmonic control doe not require the use of a forgetting factor, which is good for the performances of the algorithm. We applied the controller on all harmonics between 3 Hz and 30 Hz (for the same reasons as those

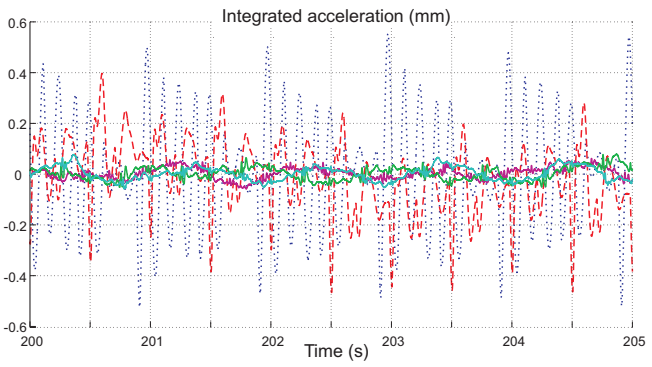

Fig. 13. Experimental displacement of M. Dotted: control OFF; dashed: classical feedback only; plain: classical feedback + specific controller (Fx-LMS, RC, harmonic control).

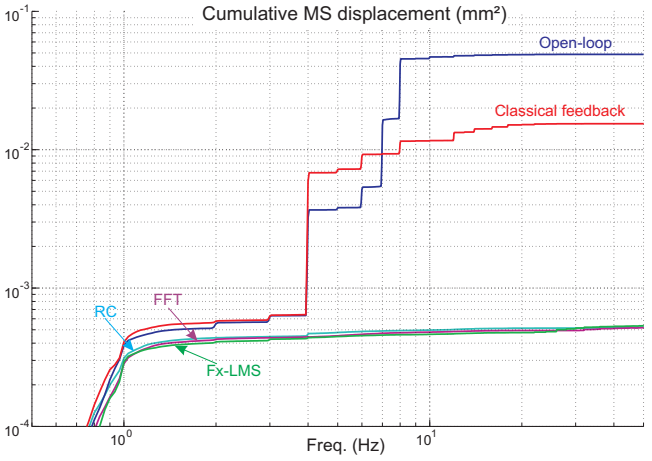

Fig. 14. Experimental cumulative Mean-Square displacement for various controllers.

explained for the RC), and some robustness is ensured by choosing the convergence coefficients α_k to be $\alpha_{k,opt}/10$, with the optimum coefficient $\alpha_{k,opt}$ given, for each frequency, by (15).

C. Results

Experimental displacement signals are shown in Fig. 13, and Fig. 14 plots the cumulative Mean-Square displacement defined by Eq. 1. It is found that the three "periodic" algorithms have the same performances and very efficiently attenuate the repetitive disturbance: for each controller the displacement signal after convergence is mainly composed of the harmonic at 1 Hz, which we do not want to control because it requires unacceptably large control input. In particular, the Mean-Square displacement is divided by 30 with respect to the case "classical feedback only" and by 90 with respect to the case "control off". (Note that, because the actuator introduces some damping, the response without control is itself lower than that

without actuator).

The fact that the three controllers have the same performances is easily explained by the observation that the main contribution to the cooler's displacement is in the range [6-18] Hz, i.e. well within the bandwidth of each controller. The extension of the bandwidth introduced in the RC has thus little effect on the result.

VI. Conclusions

It was found that the three algorithms that we investigated (namely the Filtered-x LMS, the harmonic control and the Repetitive Control) very efficiently attenuate the periodic part of the disturbance in a selected frequency region, and that all of them are sufficiently robust to modelling errors.

- The Fx-LMS is by far the easiest of the three (for the design AND the programming). It requires only a rough model of the system response, and it can be very efficiently implemented by Eq. 4a and Eq. 6. Its main drawback is its lack of frequency selectivity.
- The harmonic control, which is but a frequency implementation of the Fx-LMS, is the most "frequency selective" of the three algorithms, as it allows the tuning of the convergence rate "frequency per frequency". Besides, it does not increase the non-periodic part of the disturbance and does not require the use of a forgetting factor. Finding the appropriate coefficients is very easy, too (Eq. 15), and the computation time is not an issue as the FFT is performed off-line. It can, however, be more difficult to program as it requires the use of an FFT and of an IFFT.
- RC control was shown to be a generalization of the periodic Fx-LMS: its implementation is thus very similar (and thus very easy, too). It gives more design freedom than the Fx-LMS in choosing its frequency-shape, at the expense of some efforts in finding the appropriate filter $L(z)$.

Although the harmonic control and RC algorithms theoretically improve the results, it is found that, with the system at hand, the improvement is not significant.

Acknowledgement

This study is supported by the European Southern Observatory. The authors warmly thank G. Pinte from the Flanders' Mechatronics Technology Centre (FMTC) for his time and useful explanations when developing the Repetitive Control system.

References

[1] L. Duband and A. Raves, *Small cryocoolers*, in J.G. Weisend II (editor), The handbook of cryogenic engineering, Taylor & Francis, 1998.

[2] H.O. McMahon and W.E. Gifford, *Fluid expansion refrigeration method and apparatus*, US patent n2,906,101 (1959).

[3] C. Kempf, W. Messner, M. Tomizuka, and R. Horowitz *Comparison of Four Discrete-Time Repetitive Control Algorithms*, IEEE Control Systems Magazine, Dec. 1993, pp.48-54.

[4] C.R. Fuller, S.J. Elliott, P.A. Nelson *Active Control of Vibration*, Academic Press, 1996.

[5] S. Elliott, *Signal Processing for Active Control*, Academic Press, 2001.

[6] G. Pinte, *Active Control of Repetitive Impact Noise*, PhD Thesis, KULeuven, 2007.

[7] A. Preumont. *Vibration Control of Active Structures: and Introduction*. Kluwer, 2002. 2nd edition.

[8] B. Stallaert, G. Pinte, S. Devos, W. Symens, J. Swevers, P. Sas *Filtered-X LMS vs repetitive control for active structural acoustic control of periodic disturbances*. Proc. ISMA 2009, Leuven.

Proceedings of the 8th National Congress on Theoretical and Applied Mechanics, May 28-29, Brussels, Belgium.

Applications of a 2.5D coupled FE-BE methodology for the dynamic interaction between longitudinally invariant structures and the soil

S. François[1], M. Schevenels[1], P. Galvín[2], G. Lombaert[1] and G. Degrande[1]
[1]Department of Civil Engineering, Katholieke Universiteit Leuven,
Kasteelpark Arenberg 40, B-3001 Leuven, Belgium
[2]Escuela Técnica Superior de Ingenieros, Universidad de Sevilla,
Camino de los Descubrimientos, E-41092 Sevilla, Spain
email: stijn.francois@bwk.kuleuven.be

Abstract— **This paper presents a general 2.5D coupled finite element – boundary element methodology for the computation of the dynamic interaction between a layered soil and longitudinally invariant structures, such as railway tracks, roads, tunnels, dams, vibration isolation screens in the soil, and pipelines. The classical 2.5D finite element method is combined with a novel 2.5D boundary element method. The 2.5D Green's functions of a layered halfspace, computed with the direct stiffness method, are used in a boundary element method formulation. This avoids meshing of the free surface and the layer interfaces with boundary elements and effectively reduces the computational efforts and storage requirements. The proposed technique is applied to four examples: a road on the surface of a halfspace, a tunnel embedded in a layered halfspace, a dike on a halfspace and a vibration isolating screen in the soil.**

Keywords— **Boundary element method, elastodynamics, dynamic soil-structure interaction, 2.5D modelling**

I. Introduction

The calculation of three-dimensional dynamic soil-structure interaction problems is computationally demanding, since the radiation of waves towards infinity has to be taken into account [4], [24]. A number of assumptions is often made in an attempt to reduce the computational efforts. In many cases, the structure can be assumed to be periodic or to have an invariant cross section, which is a valid assumption for roads, railway tracks, tunnels, dams, vibration isolation screens in the soil, pipelines, and alluvial valleys.

For periodic structures, a Floquet transform can be used for the computation of the structural response and the radiated wave field [7], [13]. In the case of longitudinally invariant structures, a computationally efficient two-and-a-half-dimensional (2.5D) approach can be applied [3], [14], [31], where the Fourier transform of the longitudinal coordinate allows to represent the three-dimensional (3D) response of the structure and the radiated wave field on a two-dimensional mesh. 2.5D boundary elements are often used for the soil [27], [29], [30] while 2.5D finite elements are used for the structure [11], [12]. A number of examples of this approach have been presented by Sheng et al. [27] for the computation of tunnels and railway tracks. Andersen and Nielsen apply the methodology to study the effect of vibration isolating screens along a railway track [1], [2]. A similar approach is followed by Lombaert and Degrande [21] and Lombaert et al. [22] to predict vibrations induced by road [21] and railway traffic [22]. The latter model has been validated by means of field measurements [22] and used to assess the vibration isolation efficiency of a floating slab track [23].

The classical 2.5D boundary element method applied to embedded structures requires Cauchy principal value integrals of the singular fundamental tractions. For the evaluation of these Cauchy principal value integrals, a fully or locally enclosing elements technique [8] or an analytical integration [28] can be used.

In the present paper, a regularized boundary integral equation is used as an alternative to the evaluation of singular integrals. This global regularization of the boundary integral equation is based on the fact that the singularity of the static and dynamic fundamental solutions correspond at the source point [5], [6], [25]. This requires a generalization of the global regularization technique to the 2.5D boundary integral equation, allowing for regular integration.

In most cases, the boundary element method is based on the 2.5D fundamental solution of a homogeneous full space, for which a closed form analytical expression is available [29], [30]. The use of the homogeneous full space solution has the disadvantage that the free surface and the layer interfaces of the halfspace have to be discretized with boundary elements. Meshing of the infinite free surface and the interfaces of the halfspace requires mesh truncation, at which spurious reflections may occur. These spurious reflec-

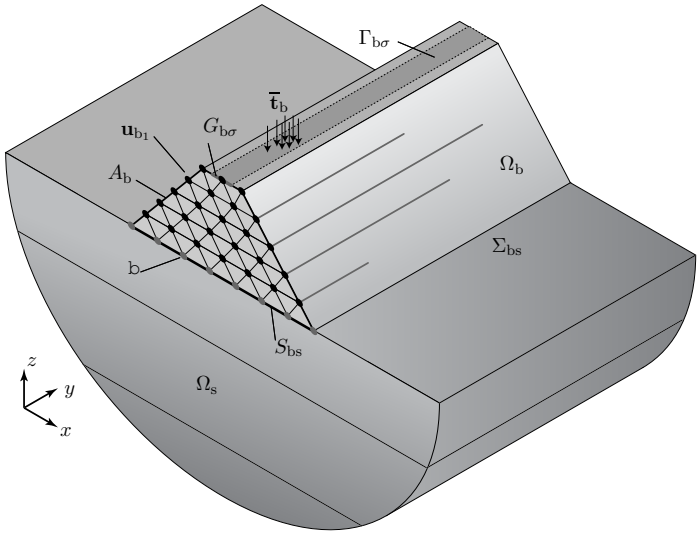

Fig. 1. The geometry of the coupled soil-structure system.

tions can be partially mitigated through the use of a special truncation element [27].

In the present paper, fundamental solutions of a layered halfspace are used in a 2.5D boundary element formulation as an alternative to the homogeneous full space solution. The layer interfaces and the surface of the halfspace no longer have to be meshed, avoiding spurious reflections at mesh truncations. The boundary element mesh can be limited to the interface between the structure and the soil, significantly reducing the size of the boundary element mesh.

II. 2.5D coupled finite element - boundary element methodology

A. Problem outline and domain decomposition

The dynamic soil-structure interaction problem is decomposed into two subdomains: the structure Ω_b and the semi-infinite layered soil Ω_s (figure 1). The dynamic soil-structure interaction problem is solved by enforcing continuity of displacements and equilibrium of stresses on the interface Σ_{bs} between both subdomains. The section A_b of the structure is invariant with respect to the longitudinal coordinate y. The dynamic soil-structure interaction problem is assumed to be linear and all equations are elaborated in the frequency domain. The dynamic equilibrium equation of the structure is discretized by means of 2.5D finite elements. The structure is considered as a 3D continuum, and can be modelled with 2.5D volume elements.

The structure is only discretized in the (x, z)-plane, where the displacements are dicretized as:

$$\mathbf{u}_b(\mathbf{x}, \omega) \simeq \mathbf{N}_b(x, z)\underline{\mathbf{u}}_b(y, \omega) \tag{1}$$

The equilibrium of the structure is solved by a Fourier transform of the longitudinal coordinate y to the horizontal wavenumber k_y, where the Fourier transform is defined as $\mathcal{F}[f(y), k_y] = \int_{-\infty}^{\infty} \exp(+ik_y y) f(y) dy$. The finite element degrees of freedom $\underline{\mathbf{u}}_b$ are divided into internal degrees of freedom $\underline{\mathbf{u}}_{b_1}$ and degrees of freedom $\underline{\mathbf{u}}_{b_2}$ on the soil-structure interface (figure 1). The resulting discretized equilibrium equation in the wavenumber domain reads as:

$$\begin{aligned}
\Bigg(-\omega^2 \begin{bmatrix} \mathbf{M}_{b_1b_1} & \mathbf{M}_{b_1b_2} \\ \mathbf{M}_{b_2b_1} & \mathbf{M}_{b_2b_2} \end{bmatrix} + \begin{bmatrix} \mathbf{K}^0_{b_1b_1} & \mathbf{K}^0_{b_1b_2} \\ \mathbf{K}^0_{b_2b_1} & \mathbf{K}^0_{b_2b_2} \end{bmatrix} \\
-ik_y \begin{bmatrix} \mathbf{K}^1_{b_1b_1} & \mathbf{K}^1_{b_1b_2} \\ \mathbf{K}^1_{b_2b_1} & \mathbf{K}^1_{b_2b_2} \end{bmatrix} \\
-k_y^2 \begin{bmatrix} \mathbf{K}^2_{b_1b_1} & \mathbf{K}^2_{b_1b_2} \\ \mathbf{K}^2_{b_2b_1} & \mathbf{K}^2_{b_2b_2} \end{bmatrix} - ik_y^3 \begin{bmatrix} \mathbf{K}^3_{b_1b_1} & \mathbf{K}^3_{b_1b_2} \\ \mathbf{K}^3_{b_2b_1} & \mathbf{K}^3_{b_2b_2} \end{bmatrix} \\
+k_y^4 \begin{bmatrix} \mathbf{K}^4_{b_1b_1} & \mathbf{K}^4_{b_1b_2} \\ \mathbf{K}^4_{b_2b_1} & \mathbf{K}^4_{b_2b_2} \end{bmatrix} + \begin{bmatrix} 0 & 0 \\ 0 & \mathbf{K}^s_{b_2b_2}(k_y, \omega) \end{bmatrix}\Bigg) \\
\times \begin{bmatrix} \tilde{\underline{\mathbf{u}}}_{b_1}(k_y, \omega) \\ \tilde{\underline{\mathbf{u}}}_{b_2}(k_y, \omega) \end{bmatrix} = \begin{bmatrix} 0 \\ \tilde{\underline{\mathbf{f}}}_{b_2}(k_y, \omega) \end{bmatrix}
\end{aligned} \tag{2}$$

where the matrices $\mathbf{M}_{b_ib_j}$ and $\mathbf{K}^0_{b_ib_j}$ correspond to the classical two-dimensional finite element mass and stiffness matrix. The matrices $\mathbf{K}^1_{b_ib_j}$ to $\mathbf{K}^4_{b_ib_j}$ account for the dependency of the solution on the wavenumber k_y. Finally, the wavenumber-frequency dependent soil stiffness matrix $\mathbf{K}^s_{b_2b_2}(k_y, \omega)$ is computed with the 2.5D boundary element method.

More details about the theoretical derivation and numerical details of the 2.5D finite element and boundary element methods are omitted in the present paper for brevity; more details can be found in an accompanying journal paper [10].

III. Applications

A. Road on a halfspace

As a first example, a road on a halfspace is considered (figure 2). The halfspace has a shear wave velocity $C_s = 150\,\mathrm{m/s}$, a dilatational wave velocity $C_p = 300\,\mathrm{m/s}$, a density $\rho = 1800\,\mathrm{kg/m^3}$ and a material damping ratio $\beta_s = \beta_p = 0.05$ in both deviatoric and volumetric deformation. The road consists of several layers which characteristics are summarized in table I. The road has a width of 4 m and the load is applied at the center of the road. The road is modelled with 40 2.5D shell elements of equal size. The soil is modelled with 2.5D boundary elements which matches the finite element mesh.

Layer	Type	d [m]	E [MPa]	ν [-]	ρ [kg/m^3]
1	Asphalt	0.15	9150	1/3	2100
2	Crushed stone	0.20	500	1/2	2000
3	Crushed concrete	0.25	200	1/2	1800

TABLE I
THE CHARACTERISTICS OF THE ROAD.

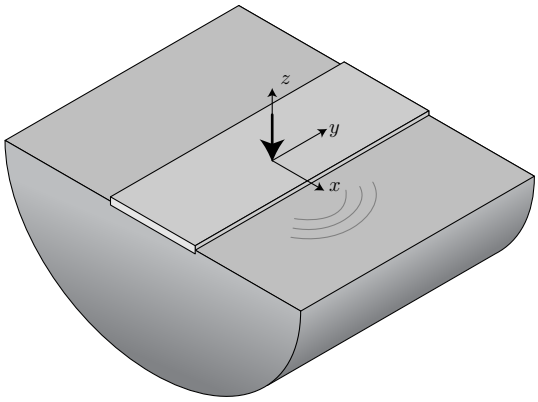

Fig. 2. Road on a halfspace.

The solution of the coupled FE-BE equation (2) results in the displacements of the road in the wavenumber-frequency domain. The wavenumber-frequency domain solution is subsequently transformed to the spatial domain by means of an inverse Fast Fourier Transform (FFT) of the wavenumber k_y to the coordinate y. The wavenumber sampling is specified in terms of the dimensionless wavenumber $\bar{k}_y = k_y C_\mathrm{s}/\omega$. As both the response of the road and the layered halfspace strongly decay for dimensionless wavenumbers larger than $\bar{k}_y = 1$ [19], [20], a maximum dimensionless wavenumber $\bar{k}_y = 3$ is sufficient to accurately compute the displacements in the spatial domain.

Nyquist's theorem states that the wavenumber step Δk_y should be smaller than $2\pi/y_\mathrm{max}$ where y_max is a distance where the solution is sufficiently attenuated. Specifying the distance y_max in terms of a number n of shear wavelengths λ_s, allows to determine the dimensionless wavenumber step as $\Delta\bar{k}_y = 1/n$. In the present analysis, $n = 100$ wavelengths are considered, resulting in 300 samples from $\bar{k}_y = 0$ to $\bar{k}_y = 3$.

Figure 3a shows the real part of the vertical displacements on the road and on the surface of the halfspace at 10 Hz. The wavelength of the Rayleigh waves in the soil is much larger than the width of the road. As a result, the wave field is characterized by nearly cylindrical wave fronts. The results are compared with the results obtained with a model previously proposed by Lombaert [19] and Lombaert and Degrande [20] (figure 3b). In this model, the road is modelled as a beam with a rigid cross section where only vertical tractions on the interface between the road and the halfspace are considered, referred to as relaxed boundary conditions. In the frequency range up to 50 Hz considered for road traffic, the results between the road modelled with shell elements and the road with a rigid cross-section compare well.

Figure 4 compares the real and imaginary part of the vertical displacement in the point $\{10\,\mathrm{m}, 0, 0\}^\mathrm{T}$ on the surface of the halfspace. The results obtained with both models agrees well, certainly for low frequencies.

In the case of a model of a railway track, for which higher frequency components are importatn, or in the case of a road with a large width, the assumption of a rigid cross-section deformation of the soil-structure interface may no longer be valid. The present methodology allows to investigate the validity of these assumptions made in existing models for railway traffic [22].

B. Tunnel in a layered halfspace

In this section, the wave field radiated by a concrete tunnel embedded in a layered halfspace due to a harmonic point load at the tunnel invert is considered. The displacements are computed with the proposed methodology and compared with the results obtained with the analytical Pipe-in-Pipe (PiP) model [15].

The center of the tunnel is situated at a depth of 14 m below the free surface. The tunnel has an internal radius $r_\mathrm{i} = 2.75\,\mathrm{m}$ and a wall thickness $t = 0.25\,\mathrm{m}$ (Figure 5). The concrete has a Young's modulus $E = 50000\,\mathrm{MPa}$, a Poisson's ratio $\nu = 0.30$, a density $\rho = 2500\,\mathrm{kg/m^3}$ and a hysteretic material damping ratio $\beta = 0.03$.

The soil consists of layer with a thickness of 6 m on top of a homogeneous halfspace. The surface layer has a shear wave velocity $C_\mathrm{s} = 275\,\mathrm{m/s}$, a dilatational wave velocity $C_\mathrm{p} = 1964\,\mathrm{m/s}$, a density $\rho = 1980\,\mathrm{m/s}$ and a material damping ratio $\beta_\mathrm{s} = \beta_\mathrm{p} = 0.04$ in both

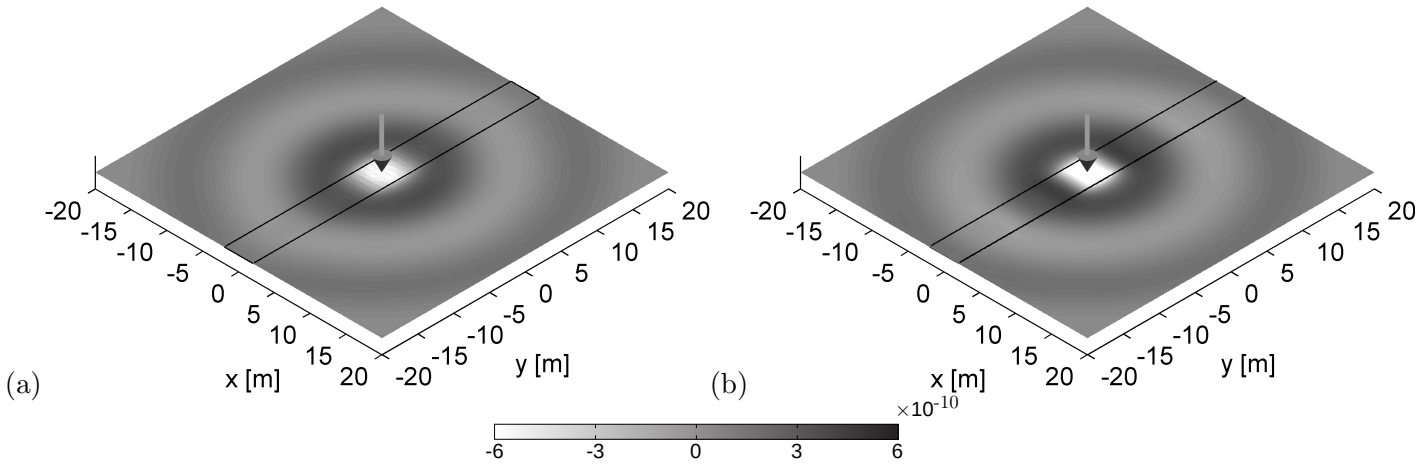

Fig. 3. Real part of the vertical displacements on the road and on the surface of the halfspace for a vertical point load applied on the road with a width of 4 m at a frequency of 10 Hz The results are shown for (a) a model using 40 2.5D shell elements and (b) the model of Lombaert and Lombaert and Degrande, modelling the road as a beam with rigid cross section.

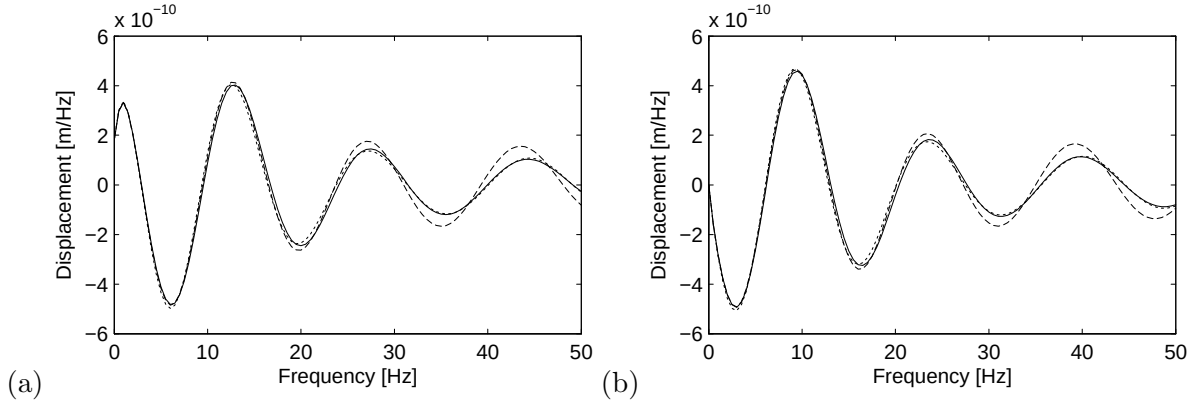

Fig. 4. (a) Real and (b) imaginary part of the vertical displacement in the point $\{10\,\mathrm{m}, 0, 0\}^{\mathrm{T}}$ on the surface of the halfspace for a point load applied at the center the road. The results are shown for (a) the model using 40 2.5D shell elements and (b) the model of Lombaert and Lombaert and Degrande, modelling the road as a beam with rigid cross section.

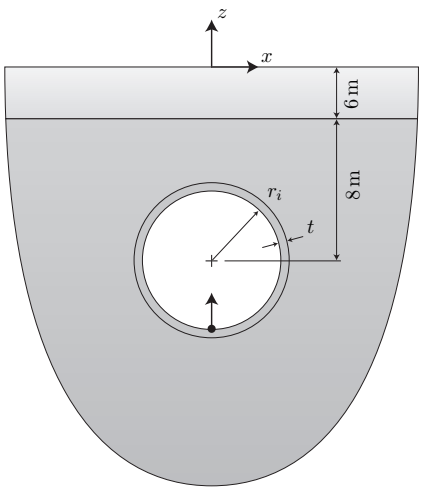

Fig. 5. Cross section of the tunnel.

deviatoric and volumetric deformation. The halfspace has a shear wave velocity $C_{\mathrm{s}} = 220\,\mathrm{m/s}$, a dilatational wave velocity $C_{\mathrm{p}} = 1571\,\mathrm{m/s}$, a density $\rho = 1980\,\mathrm{m/s}$ and a material damping ratio $\beta_{\mathrm{s}} = \beta_{\mathrm{p}} = 0.04$ in both deviatoric and volumetric deformation.

The response of the tunnel and the halfspace is computed using the 2.5D coupled FE-BE methodology. The tunnel is modelled with 36 equal-sized 2.5D shell elements around the circumference of the tunnel. The boundary element mesh matches the finite element mesh, which allows to compute the tunnel response by means of equation (2).

Figure 6 shows the vertical displacement at the surface of the layered halfspace due to a vertical point load at the tunnel invert at a frequency of 20 Hz. Waves generated at the tunnel invert propagate through the soil and result in Rayleigh waves

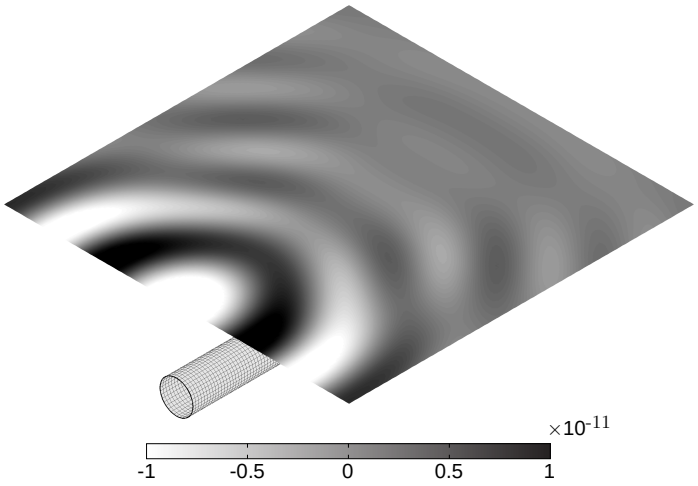

Fig. 6. Real part of the vertical displacement at the surface of the layered halfspace due to a vertical point load at the tunnel invert at a frequency of 20 Hz.

at the surface of the layered halfspace. The wavefronts on the surface of the halfspace are not cylindrical, which is a result of the dynamic interaction between the soil and the tunnel.

Figures 7a and 7b show the vertical free-field displacement at the point with coordinates $\{10\,\mathrm{m}, 10\,\mathrm{m}, -6\,\mathrm{m}\}^{\mathrm{T}}$ on the layer interface and at the point with coordinates $\{10\,\mathrm{m}, 10\,\mathrm{m}, 0\,\mathrm{m}\}^{\mathrm{T}}$ on the surface of the layered halfspace.

The results obtained with the presented 2.5D coupled FE-BE methodology are compared to the results obtained with the semi-analytical PiP model. In the PiP model, the tunnel-soil interaction is solved analytically, where the tunnel is assumed to be embedded in a homogeneous full space. The tunnel response is subsequently used to compute the displacements in the layered halfspace using the direct stiffness method, where the tunnel is replaced by a number of equivalent point sources in the layered halfspace [15]. A good agreement between both models is observed. The discrepancy between both models at higher frequencies is attributed to the limited wavenumber sampling in the PiP model for the computation of the free field response.

C. Wave propagation along a dike

In this section, the wave propagation along an earth dam is studied. This analysis has been performed in the framework of seismic tomography on earth dams [16], where the wave propagation along the dike is used to verify the structural integrity of the dike body.

A soft earth dam with a steep slope on top of a homogeneous halfspace is considered. The dam has a height $h = 5\,\mathrm{m}$, a base width $w_{\mathrm{b}} = 20\,\mathrm{m}$ and a top width $w_{\mathrm{t}} = 2\,\mathrm{m}$. The dam consists of a soft soil with a shear wave velocity $C_{\mathrm{s}} = 150\,\mathrm{m/s}$, a dilatational wave velocity $C_{\mathrm{p}} = 300\,\mathrm{m/s}$, a density $\rho = 2000\,\mathrm{kg/m^3}$, and a material damping ratio $\beta_{\mathrm{s}} = \beta_{\mathrm{p}} = 0.02$ in both deviatoric and volumetric deformation. The dam is founded on a homogeneous halfspace with a shear wave velocity $C_s = 300\,\mathrm{m/s}$, a dilatational wave velocity $C_{\mathrm{p}} = 600\,\mathrm{m/s}$, a density $\rho = 2000\,\mathrm{kg/m^3}$ and a material damping ratio $\beta_{\mathrm{s}} = \beta_{\mathrm{p}} = 0.02$ in both deviatoric and volumetric deformation.

The 2.5D coupled FE-BE methodology is used to compute the response of the dike and the surrounding soil due to a vertical point load on top of the dike. The dike is modelled using 2.5D volume elements (figure 8) and the subgrade is modelled using 2.5D boundary element mesh that matches the finite element mesh on the dike-soil interace.

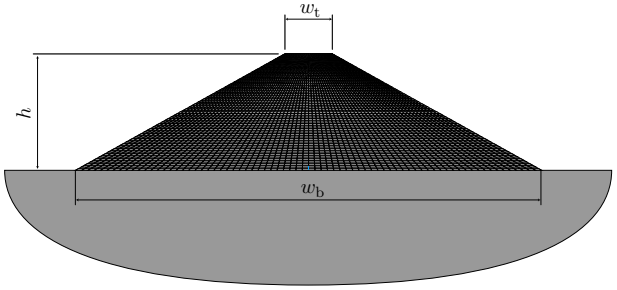

Fig. 8. Mesh of the dike using 2.5D volume elements.

Figure 9 shows the real part of the vertical displacement of the dike and the surface of the halfspace at frequencies of 5 Hz and 20 Hz. At 5 Hz, the wavelength $\lambda_{\mathrm{s}} = C_{\mathrm{s}}/f = 30\,\mathrm{m}$ of shear waves in the dike is much larger than the height of the dike. As a result, the Rayleigh waves penetrate into the underlying halfspace and the displacement amplitudes on the surface of the halfspace are comparable to the displacement

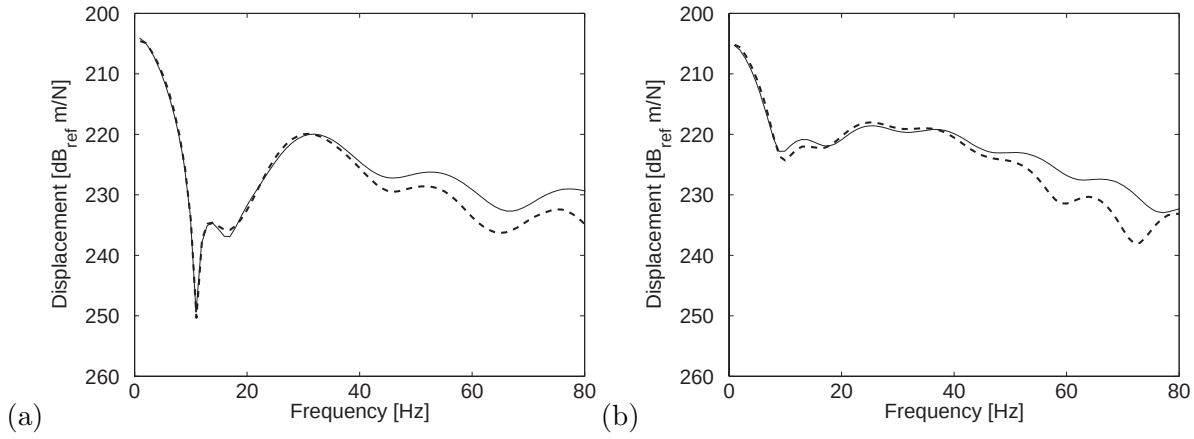

Fig. 7. Modulus of the vertical displacement in (a) the point with coordinates $\{10\,\mathrm{m}, 10\,\mathrm{m}, -6\,\mathrm{m}\}^{\mathrm{T}}$ and (b) at the point with coordinates $\{10\,\mathrm{m}, 10\,\mathrm{m}, 0\,\mathrm{m}\}^{\mathrm{T}}$. The results obtained with the presented methodology (dashed line) is compared with results obtained with the PiP model (solid line).

amplitudes on the dike.

At a frequency of 20 Hz, the wavelength equals $\lambda_{\mathrm{s}} = C_{\mathrm{s}}/f = 7.5\,\mathrm{m}$ of shear waves in the dike is of the same order of magnitude as the dike height. The Rayleigh waves are now concentrated in the dike body. As a result, the dike acts as a one-dimensional wave guide. As the Rayleigh waves are trapped within the one-dimensional wave guide, the waves are only attenuated by material damping and not by geometrical damping.

The present 2.5D model was used in a feasibility study for the application of Seismic Analysis of Surface Waves as a non-destructive technique to determine the dynamic soil characteristics of a layered soil medium from the dispersion of seismic surface waves [9].

The first step involves an in situ experiment where vibrations are generated at the soil's surface using a falling weight, an instrumented impact hammer or a hydraulic shaker and measured with geophones or accelerometers up to a distance from the source of typically 50 m. In the second step, an experimental dispersion curve is determined using the phase of the transfer functions between pairs of receivers. It is assumed that the response at sufficiently large distance from the source is dominated by dispersive surface waves. The experimental dispersion curve corresponds to the effective (dominant) wave velocity. An inverse problem is formulated as an optimization problem where the objective function is defined as the squared difference between the experimental and a computed theoretical dispersion curve.

The MASW method is commonly applied to sites with a flat free surface and the solution of the inverse problem is based on the assumption that the subgrade can be modelled as a layered elastic halfspace. When the MASW method is employed to determine the dynamic soil characteristics of dikes, the pertinent question is under what conditions the inverse problem can still be formulated based on the dispersion curve of a layered halfspace with a flat free surface where the elevated topography is not included.

D. Vibration isolating screen

In this example, the 2.5D coupled FE-BE methodology is applied to study the efficiency of a vibration isolating screen in the soil. A vibration isolating screen is a soft or stiff wave barrier. Due to the impedance contrast between the isolating screen and the soil, waves are reflected, effectively reducing vibration levels behind the screen.

Figure 10 shows a vibration isolating screen embedded in a homogeneous halfspace with a shear wave velocity $C_{\mathrm{s}} = 150\,\mathrm{m/s}$, a dilatational wave velocity $C_{\mathrm{p}} = 300\,\mathrm{m/s}$, a density $\rho = 1800\,\mathrm{kg/m^3}$ and a material damping ratio $\beta_{\mathrm{s}} = \beta_{\mathrm{p}} = 0.05$ in both deviatoric and volumetric deformation. The incident wave field is generated by a vertical point load acting on the surface of the halfspace at a distance of 5 m from the vibration isolating screen.

First, the reference case of a point load on the surface of a homogeneous halfspace is considered. This case corresponds to the 3D Green's displacements of a layered halfspace and is evaluated by means of the direct stiffness method [17], [18], [26]. Figure 11 shows the real part of the vertical displacement due to a vertical point source on the surface of the halfspace at 20 Hz and 40 Hz. The origin of the Cartesian frame of reference corresponds to the source location.

The displacement in the soil is dominated by

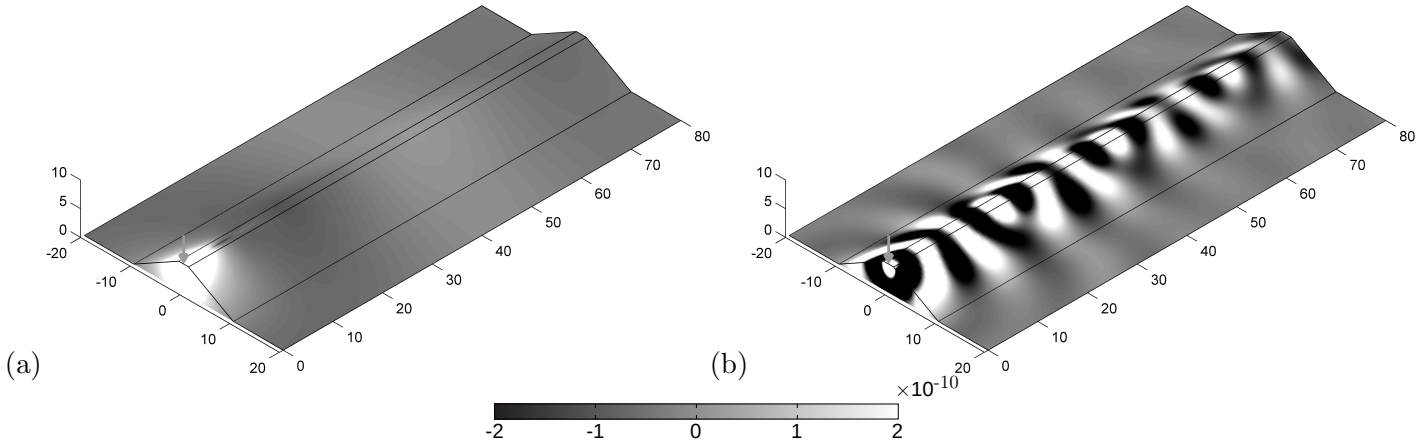

Fig. 9. Real part of the vertical displacement for a vertical point load on top of the dike at a frequency of (a) 5 Hz and (b) 20 Hz.

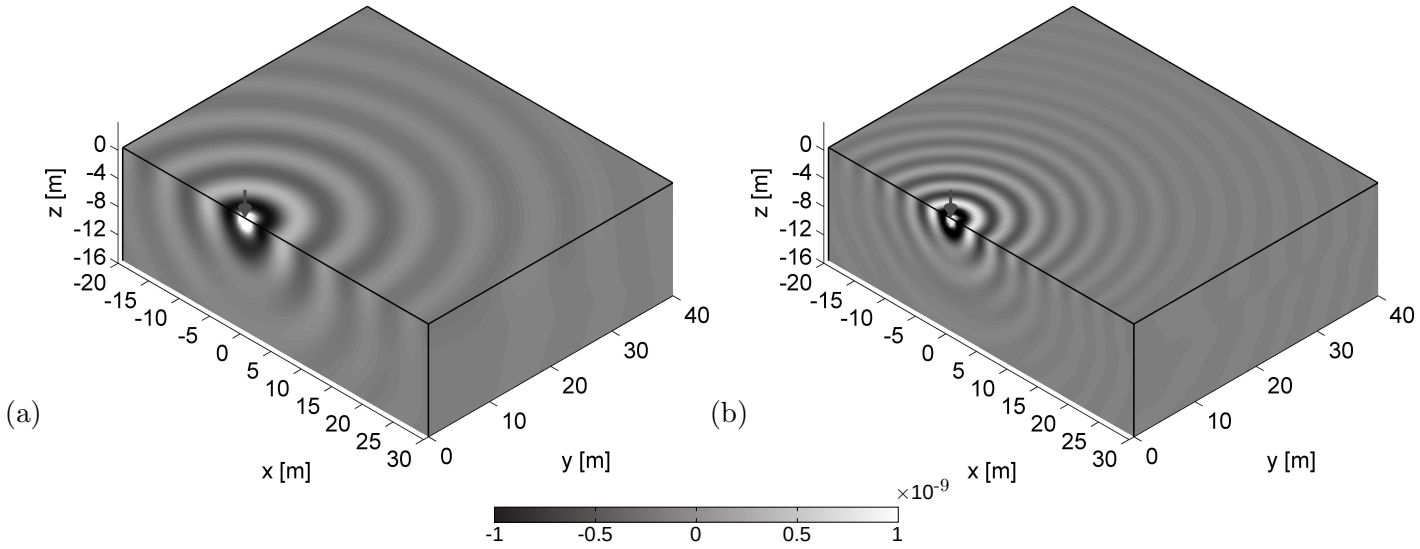

Fig. 11. Real part of the vertical displacement for a vertical point load at the surface of a homogeneous halfspace at a frequency of (a) 20 Hz and (b) 40 Hz.

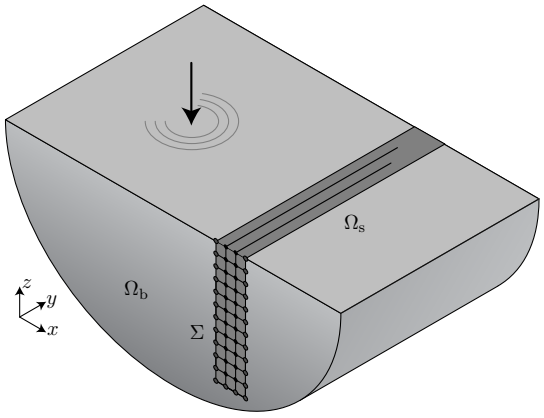

Fig. 10. 2.5D methodology for the computation of the vibration isolating screen.

Rayleigh waves with cylindrical wave fronts. The Rayleigh waves have a velocity $C_\mathrm{R} = 139.8\,\mathrm{m/s}$ which corresponds to a wavelength $\lambda_\mathrm{R} = C_\mathrm{R}/f = 6.95\,\mathrm{m}$ at the frequency $f = 20\,\mathrm{Hz}$ and $\lambda_\mathrm{R} = 3.48\,\mathrm{m}$ at a frequency $f = 40\,\mathrm{Hz}$. The penetration depth of the Rayleigh waves is proportional to the wavelength: most of the wave energy is located above a depth of one wavelength. The design of the vibration isolating screen should be based on this penetration depth at the lowest frequency of interest. A concrete isolating screen with a depth of 8 m is therefore expected to isolate vibrations above a frequency of 20 Hz. A concrete vibration isolating screen with a depth of 8 m and a width of 0.6 m is considered. The concrete has a Young's modulus $E_\mathrm{c} = 30\,\mathrm{GPa}$, a Poisson's ratio $\nu_\mathrm{c} = 0.2$ and a density $\rho_\mathrm{c} = 2600\,\mathrm{kg/m^3}$. The screen is modelled with 4-node rectangular 2.5D finite volume elements. The finite element mesh consists of 16 elements over the height of the trench and 4 ele-

ments over the width of the trench. The boundary element mesh matches the finite element mesh over the screen-soil interface, allowing for the computation of the response of the screen and the soil by means of equation (2).

A vertical point source is considered at the surface of the halfspace at a distance of 5 m from the centerline of the trench. Figure 12 shows the real part of the vertical displacement in the free field at frequencies of 20 Hz and 40 Hz. The incident waves are reflected on the vibration isolating screen, reducing vibration levels behind the screen. As the concrete is much stiffer than the soil, it acts as a rigid wave barrier and a small displacement amplitude is observed along the soil-screen interface.

The efficiency of the vibration isolating screen can also be quantified by the insertion loss $\mathrm{IL_z}$ of the vertical displacement, defined as the ratio of the vertical displacement amplitudes $|u_z^{\mathrm{iso}}(\omega)|$ and $|u_z^{\mathrm{uniso}}(\omega)|$ in the case with and without vibration isolating screen. The vertical insertion loss is expressed in dB:

$$\mathrm{IL_z} = 20\log_{10}\left(\frac{|\mathrm{u_z^{uniso}}(\omega)|}{|\mathrm{u_z^{iso}}(\omega)|}\right) \qquad (3)$$

Figure 13 shows the vertical insertion loss at 20 Hz and 40 Hz. This indicates that the vibration isolating screen effectively reduces the vibration levels behind the trench. The screening efficiency is larger at 40 Hz than at 20 Hz. At 40 Hz, two lines of destructive interference between a direct and reflected Rayleigh waves are observed.

IV. Conclusion

In the present paper, a general 2.5D coupled FE-BE methodology for the computation of the interaction between longitudinally invariant structures and a layered halfspace has been presented. For the boundary element model, a novel regularized 2.5D boundary integral equation has been used. The boundary element method is based on the fundamental solutions of a layered halfspace which are computed by means of the direct stiffness method. As a result, only the interface between the structure and the soil has to be discretized, reducing storage requirements with respect to the classical use of full space solutions.

The method has been demonstrated with four examples: a road on the surface of a halfspace, a tunnel embedded in a layered halfspace, a dike on a halfspace and a vibration isolating screen in the soil. All examples focus on the computation of the transfer function between a vertical point source and the displacements of the structure and in the soil. These transfer functions can subsequently be used to compute the response due to a moving load [21]. The examples demonstrate the practical use of the 2.5D method for the evaluation of the 3D radiated wave field in practical dynamic soil-structure interaction problems.

Acknowledgements

The results presented in this paper have been obtained within the frame of the SBO project IWT 03175 "Structural damage due to dynamic excitation: a multi- disciplinary approach". This project is funded by IWT Vlaanderen, the Institute of the Promotion of Innovation by Science and Technology in Flanders. The second and fourth author are postdoctoral research fellows of the "Fonds voor Wetenschappelijk Onderzoek Vlaanderen (FWO)" or the Research Foundation Flanders. The authors gratefully acknowledge financial support from these institutes. P. Galvín is pleased to acknowledge support from the Ministerio de Ciencia e Innovación of Spain under the grant JC2008-00136.

References

[1] L. Andersen and C.J.C. Jones. Coupled boundary and finite element analysis of vibration from railway tunnelsa comparison of two- and three-dimensional models. *Journal of Sound and Vibration*, 293:611–625, 2006.

[2] L. Andersen and S.R.K. Nielsen. Reduction of ground vibration by means of barriers or soil improvement along a railway track. *Soil Dynamics and Earthquake Engineering*, 25:701–716, 2005.

[3] D. Aubry, D. Clouteau, and G. Bonnet. Modelling of wave propagation due to fixed or mobile dynamic sources. In N. Chouw and G. Schmid, editors, *Workshop Wave '94, Wave propagation and Reduction of Vibrations*, pages 109–121, Ruhr Universität Bochum, Germany, December 1994.

[4] D.E. Beskos, T. Krauthammer, and I. Vardoulakis, editors. *Dynamic soil-structure interaction*. A.A. Balkema, 1984.

[5] M. Bonnet. *Boundary integral equation methods for solids and fluids*. John Wiley and Sons, Chichester, United Kingdom, 1995.

[6] H.D. Bui, B. Loret, and M. Bonnet. Régularisation des équations intégrales de l'élastodynamique et de l'élastostatique. *Comptes Rendus de l' Académie des Sciences: série II*, t.300(14):633–636, 1985.

[7] H. Chebli, R. Othman, D. Clouteau, M. Arnst, and G. Degrande. 3D periodic BE-FE model for various transportation structures interacting with soil. *Computers and Geotechnics*, 35:22–32, 2008.

[8] J. Domínguez. *Boundary elements in dynamics*. Computational Mechanics Publications and Elsevier Applied Science, Southampton, United Kingdom, 1993.

[9] S. François, M. Schevenels, and G. Degrande. Applicability of the MASW method on dykes. Report BWM-2007-06, Department of Civil Engineering, K.U.Leuven, March 2007. Report to Geotomographie Gmbh.

[10] S. François, M. Schevenels, G. Lombaert, P. Galvín, and G. Degrande. A 2.5D coupled FE-BE methodology for the dynamic interaction between longitudinally invariant

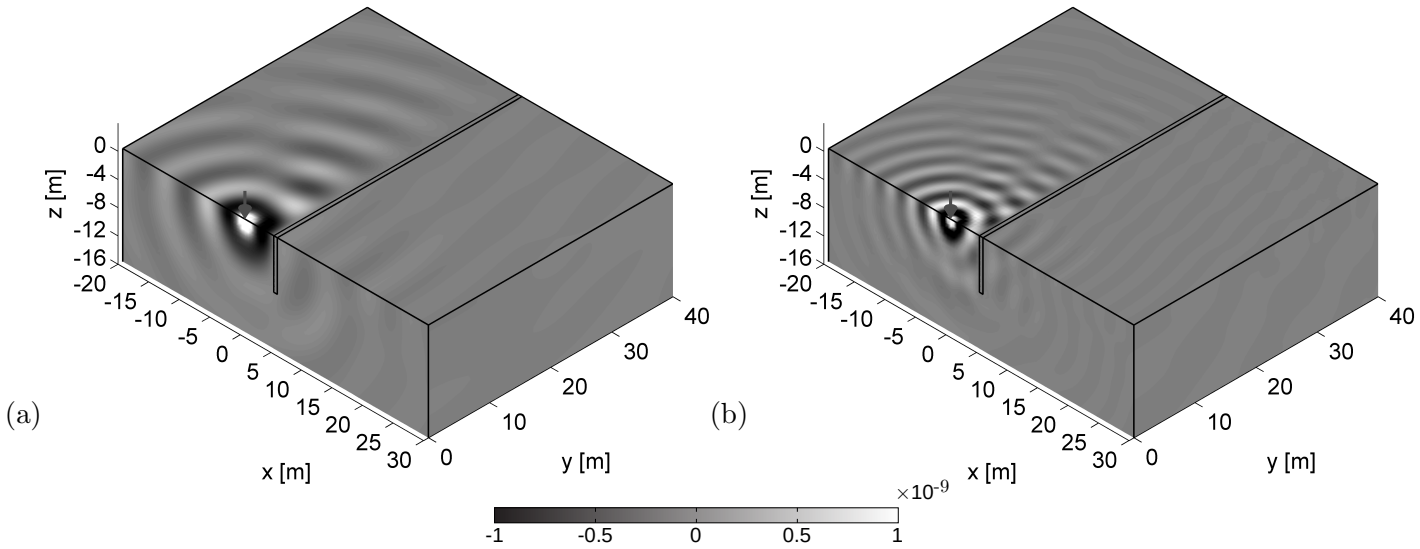

Fig. 12. Real part of the vertical displacement for a harmonic point load at a distance of 5 m from the center of the concrete vibration isolating screen at a frequency of (a) 20 Hz and (b) 40 Hz.

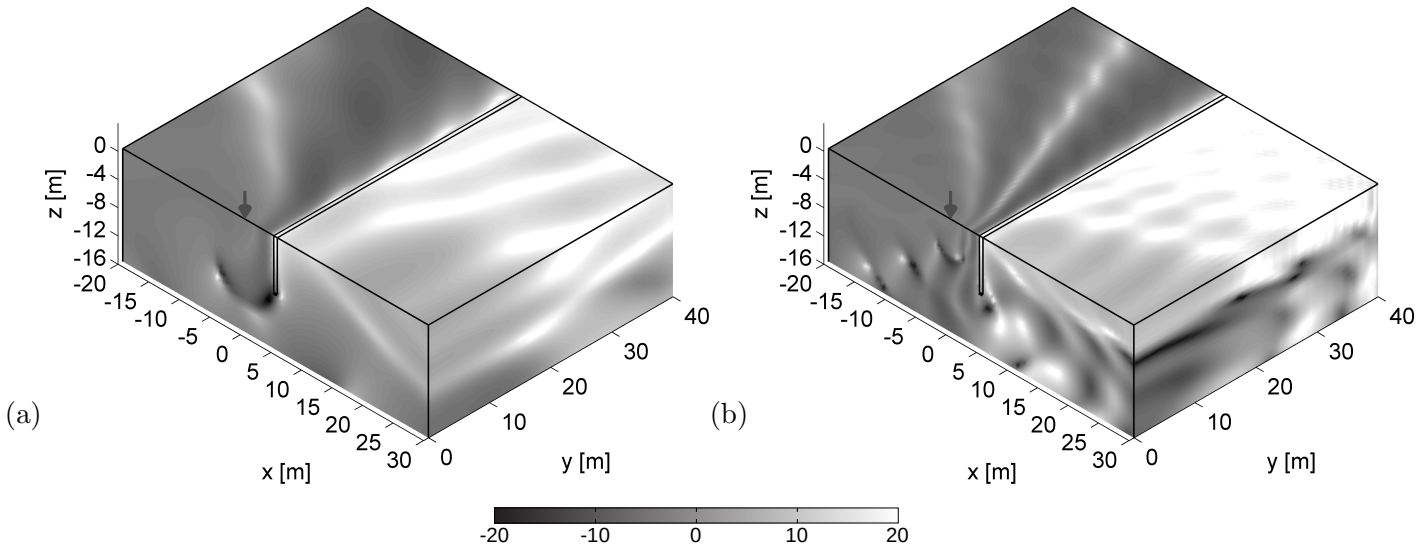

Fig. 13. Vertical insertion loss IL_z for a harmonic point load at a distance $d = 5$ m from the vibration isolating screen at a frequency of (a) 20 Hz and (b) 40 Hz for a concrete vibration isolating screen.

structures and a layered halfspace. *Computer Methods in Applied Mechanics and Engineering*, 2010. Submitted for publication.

[11] L. Gavrić. Finite element computation of dispersion properties of thin-walled structures. *Journal of Sound and Vibration*, 173(1):113–124, 1994.

[12] L. Gavrić. Computation of propagative waves in free rail using finite element technique. *Journal of Sound and Vibration*, 183(3):531–543, 1995.

[13] S. Gupta, M.F.M. Hussein, G. Degrande, H.E.M. Hunt, and D. Clouteau. A comparison of two numerical models for the prediction of vibrations from underground railway traffic. *Soil Dynamics and Earthquake Engineering*, 27(7):608–624, 2007.

[14] M.F.M. Hussein, S. Gupta, H.E.M. Hunt, G. Degrande, and J.P. Talbot. A computationally efficient model for calculating vibration from a railway tunnel buried in a halfspace. *International Journal for Numerical Methods in Engineering*, 2010. Submitted for publication.

[15] M.F.M. Hussein, L. Rikse, S. Gupta, H.E.M. Hunt, G. Degrande, J.P. Talbot, S. François, and M. Schevenels. Using the PiP model for fast calculation of vibration from a railway tunnel in a multi-layered half-space. In *9th International Workshop on Railway Noise*, Munich, Germany, September 2007.

[16] L. Karl, Fechner T., G. Degrande, and S. François. Application of surface waves for the geotechnical characterisation of dykes. In *Near Surface 2008, 14th European meeting of environmental and Engineering Geophysics*, Kraków, Poland, Sepember 2008.

[17] E. Kausel. *Fundamental solutions in elastodynamics: a compendium*. Cambridge University Press, New York, 2006.

[18] E. Kausel and J.M. Roësset. Stiffness matrices for layered soils. *Bulletin of the Seismological Society of America*, 71(6):1743–1761, 1981.

[19] G. Lombaert. *Development and experimental validation of a numerical model for the free field vibrations induced by road traffic*. PhD thesis, Department of Civil Engineering, K.U.Leuven, 2001.

[20] G. Lombaert and G. Degrande. Experimental validation of a numerical prediction model for free field traffic induced vibrations by in situ experiments. *Soil Dynamics and Earthquake Engineering*, 21(6):485–497, 2001.

[21] G. Lombaert, G. Degrande, and D. Clouteau. Numerical modelling of free field traffic induced vibrations. *Soil Dynamics and Earthquake Engineering*, 19(7):473–488, 2000.

[22] G. Lombaert, G. Degrande, J. Kogut, and S. François. The experimental validation of a numerical model for the prediction of railway induced vibrations. *Journal of Sound and Vibration*, 297(3-5):512–535, 2006.

[23] G. Lombaert, G. Degrande, B. Vanhauwere, B. Vandeborght, and S. François. The control of ground borne vibrations from railway traffic by means of continuous floating slabs. *Journal of Sound and Vibration*, 297(3-5):946–961, 2006.

[24] J.E. Luco and H.L. Wong. Seismic response of foundations embedded in a layered half-space. *Earthquake Engineering and Structural Dynamics*, 15:233–247, 1987.

[25] F.J. Rizzo, D.J. Shippy, and M. Rezayat. A boundary integral equation method for radiation and scattering. *International Journal for Numerical Methods in Engineering*, 21:115–129, 1985.

[26] M. Schevenels, S. François, and G. Degrande. EDT: An ElastoDynamics Toolbox for MATLAB. *Computers and Geosciences*, 2009. Accepted for publication.

[27] X. Sheng, C.J.C. Jones, and M. Petyt. Ground vibration generated by a harmonic load acting on a railway track. *Journal of Sound and Vibration*, 225(1):3–28, 1999.

[28] X. Sheng, C.J.C. Jones, and D.J. Thompson. Modelling ground vibrations from railways using wavenumber finite- and boundary-element methods. *Proceedings of the Royal Society*, 461:2043–2070, 2005.

[29] A.A. Stamos and D.E. Beskos. 3-D seismic response analysis of long lined tunnels in half-space. *Soil Dynamics and Earthquake Engineering*, 15:111–118, 1996.

[30] A.J.B. Tadeu, J.M.P. Antonio, and E. Kausel. 3D scattering of waves by a cylindrical irregular cavity of infinite length in a homogeneous elastic medium. *Computer Methods in Applied Mechanics and Engineering*, 191:3015–3033, 2002.

[31] A.J.B. Tadeu and E. Kausel. Green's functions for two-and-a-half-dimensional elastodynamic problems. *ASCE Journal of Engineering Mechanics*, 126(10):1093–1096, 2000.

Proceedings of the 8th National Congress on Theoretical and Applied Mechanics, May 28-29, Brussels, Belgium.

The determination of stiffness and damping parameters of soils with the SASW method

Mattias Schevenels, Sayed Ali Badsar, Geert Degrande
Department of Civil Engineering, K.U.Leuven
Kasteelpark Arenberg 40, 3001 Leuven, Belgium
email: mattias.schevenels@bwk.kuleuven.be

Abstract— **This paper focuses on the Spectral Analysis of Surface Waves (SASW) method for the determination of stiffness and damping parameters of shallow soil layers. The paper consists of three parts, addressing (1) the in situ SASW test, (2) the determination of the dispersion and attenuation curves from the measurement data, and (3) the inverse problem where the soil profile is identified. The existing practice is critically reviewed, and a number of improvements to the SASW method are presented. These include a technique to improve the efficiency of the in situ test, and a new method to determine the experimental attenuation curve. The efficiency of the test is improved by monitoring the signal-to-noise ratio during the experiment. The experimental attenuation curve is determined by means of a frequency-wavenumber analysis, using the half-power bandwidth method.**

Keywords— **Spectral Analysis of Surface Waves, Dynamic Soil Properties, Stiffness, Damping**

I. Introduction

THE Spectral Analysis of Surface Waves (SASW) test is a method to determine the dynamic shear modulus and the material damping ratio of shallow soil layers [6]. It is based on an in situ experiment where Rayleigh waves are generated by means of an impact hammer, a falling weight, or a hydraulic shaker. The resulting wave field is recorded by a number of sensors at the soil's surface and used to determine the dispersion and attenuation curves of the soil. An inverse problem is solved to identify the corresponding soil profile: the (theoretical) dispersion and attenuation curves are calculated for a given soil profile and compared to the (experimental) dispersion and attenuation curves derived from the SASW test. The soil profile is subsequently adjusted in order to minimize the distance between the experimental and the theoretical curves.

This paper consists of three parts, focusing on (1) the in situ SASW test, (2) the determination of the dispersion and attenuation curves from the measurement data, and (3) the inverse problem where the soil profile is identified. The existing practice is critically reviewed, and a number of improvements to the SASW method are presented. These include a technique to improve the efficiency of the in situ test, and a new method to determine the experimental attenuation curve.

The method is applied to a site in Lincent (Belgium), next to the high speed railway track L2 between Brussels and Köln. The soil at this site consists of a silt top layer with a thickness of 1.2 m, followed by a fine sand layer reaching to a depth of 3.2 m and a sequence of very stiff layers of arenite and clay.

II. The in situ test

The SASW experiment is usually performed using a relatively small number of receivers (about 10), located at exponentially increasing distances from the source. However, there is a trend to use a larger number of receivers (about 50-100) to capture the spatial variation of the wave field in a more accurate way. This is important for the determination of the attenuation curve. The attenuation curve is determined from the spatial decay of the wave field, which is more accurately measured in the case with a large number of receivers.

In the experiment performed in Lincent, surface waves are generated by means of a hammer impact on a small aluminium foundation. The response has been measured at 104 equidistant locations from 1 m to 104 m from the source.

The wave field recorded in the SASW test is contaminated by noise. To mitigate the influence of the noise, the test is repeated a number of times (i.e. multiple hammer impacts are recorded) and the average transfer function $\hat{H}(r,\omega)$ from the hammer force (channel i) to the free field response at a distance r (channel j) is computed. To this end, the H_1 estimator [2] is used:

$$\hat{H}(r,\omega) = \frac{\hat{S}_{ji}(\omega)}{\hat{S}_{ii}(\omega)} \tag{1}$$

The cross power spectral density $\hat{S}_{ij}(\omega)$ of channels i and j is computed as:

$$\hat{S}_{ij}(\omega) = \frac{1}{N}\sum_{k=1}^{N} \hat{x}_i^k(\omega)\hat{x}_j^{k*}(\omega) \tag{2}$$

where $\hat{x}_i^k(\omega)$ is the frequency content of the signal recorded in channel i for impact k, and $\hat{x}_j^{k*}(\omega)$ is the complex conjugate of $\hat{x}_j^k(\omega)$.

Figure 1a shows the modulus of the transfer function $\hat{H}(r,\omega)$ for the SASW test performed in Lincent. These results have been obtained using $N = 100$ hammer impacts.

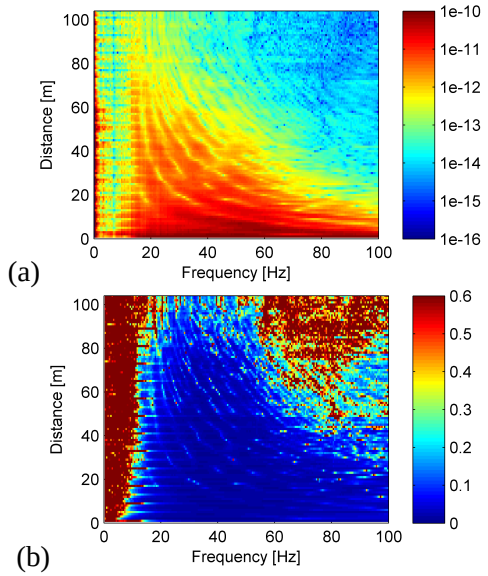

Fig. 1. (a) Modulus of the transfer function $\hat{H}(r,\omega)$ and (b) the coefficient of variation $\hat{\sigma}_H(r,\omega)/|\hat{H}(r,\omega)|$ for site in Lincent.

Due to the presence of noise, the transfer function $\hat{H}(r,\omega)$ obtained with the H_1 estimator is a random variable, in the sense that each experiment gives rise to a different estimation. Assuming that the noise is stationary, the variance $\hat{\sigma}^2_H(r,\omega)$ of the estimated transfer function $\hat{H}(r,\omega)$ can be computed as:

$$\hat{\sigma}^2_H(r,\omega) = \frac{1-\hat{\gamma}^2_{ij}(\omega)}{N\hat{\gamma}^2_{ij}(\omega)}|\hat{H}(r,\omega)|^2 \qquad (3)$$

The coherence $\hat{\gamma}_{ij}(\omega)$ of channels i and j is obtained as:

$$\hat{\gamma}^2_{ij}(\omega) = \frac{\hat{S}_{ij}(\omega)\hat{S}^*_{ij}(\omega)}{\hat{S}_{ii}(\omega)\hat{S}^*_{jj}(\omega)} \qquad (4)$$

The coefficient of variation of the transfer function $\hat{H}(r,\omega)$ is obtained as the ratio $\hat{\sigma}_H(r,\omega)/|\hat{H}(r,\omega)|$. A low value of the coefficient of variation corresponds to an accurate estimation of the transfer function. Equation (3) shows that the variance $\hat{\sigma}^2_H(r,\omega)$ is inversely proportional to the number of impacts N. As a result, the accuracy of the estimation increases proportionally to $\sqrt{N}$.

Figure 1b shows the coefficient of variation of the transfer function $\hat{H}(r,\omega)$ for the SASW test performed in Lincent. This coefficient is low in a frequency range with a lower bound of about 15 Hz and an upper bound that decreases with the distance from the source. Outside this frequency range, the coefficient of variation increases, indicating a lower signal-to-noise ratio.

The efficiency of the SASW test can be improved by online monitoring of the coefficient of variation of the transfer functions between the force and the free field response. If the coefficient of variation is computed after each impact, the number of impacts can be kept to a minimum by terminating the experiment as soon as the coefficient of variation is below a certain threshold.

III. The dispersion and attenuation curves

In the past two decades, much attention has been paid to the determination of the dispersion curve from the data recorded in the SASW test, resulting in several well established methods. The determination of the attenuation curve has been tackled only recently [5], [7].

In the existing methods to determine the attenuation curve, the measured response is expressed as a product of three factors:

$$\hat{h}(r,\omega) = \zeta(r,\omega)\exp\left(-i\frac{\omega}{C^{\mathrm{E}}_{\mathrm{R}}(\omega)}r\right)\exp\left(-\alpha^{\mathrm{E}}_{\mathrm{R}}(\omega)r\right) \qquad (5)$$

The first factor $\zeta(r,\omega)$ is the geometric spreading factor and accounts for the wave decay due to the geometric spreading of the wave fronts over an increasing area. This factor is equal to the wave decay in a soil without material damping and depends on the stratification of the soil. The second factor $\exp(-i\omega r/C^{\mathrm{E}}_{\mathrm{R}}(\omega))$ is a harmonic function that depends on the phase velocity $C^{\mathrm{E}}_{\mathrm{R}}(\omega)$ of the surface wave. The third factor $\exp(-\alpha^{\mathrm{E}}_{\mathrm{R}}(\omega)r)$ is an exponentially decaying function that accounts for the wave decay due to material damping. This function depends on the attenuation coefficient $\alpha^{\mathrm{E}}_{\mathrm{R}}(\omega)$. For each frequency, the attenuation coefficient $\alpha^{\mathrm{E}}_{\mathrm{R}}(\omega)$ is determined by fitting the modulus of the function $\hat{h}(r,\omega)$ to the modulus of the experimental transfer function $\hat{H}(r,\omega)$.

The existing methods have been applied to several synthetic examples and appear to have two disadvantages. First, the response of the soil in the SASW test is assumed to be due to a single surface wave. If multiple surface waves contribute to the response (e.g. due to the inclusion of a softer layer), this assumption does not hold and the resulting dispersion and attenuation curves are incorrect. Second, the estimation of the attenuation curve is based on an estimate of the geometric spreading factor $\zeta(r,\omega)$. The latter is computed using the shear wave velocity of the soil, which is determined by inversion of the experimental dispersion curve $C^{\mathrm{E}}_{\mathrm{R}}(\omega)$. Errors in the experimental dispersion curve and errors in the inversion procedure (e.g. due to the non-uniqueness of the inverse problem) lead to an incorrect estimate of the geometric spreading factor $\zeta(r,\omega)$ and, consequently, the experimental attenuation curve $\alpha^{\mathrm{E}}_{\mathrm{R}}(\omega)$.

An alternative method to determine the experimental attenuation curve has therefore been developed. First, the frequency-wavenumber content $\tilde{H}(k_r,\omega)$ of the transfer function $\hat{H}(r,\omega)$ is computed by means of a discrete approximation to the Hankel transformation [3]. Figure 2 shows the f–k spectrum $\tilde{H}(k_r,\omega)$ for the site in Lincent. This spectrum has been normalized for each in-

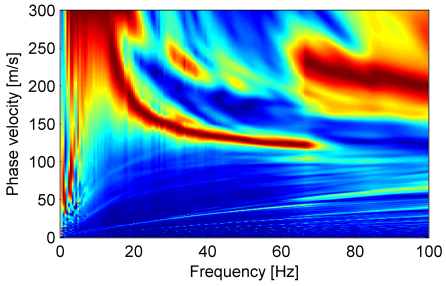

Fig. 2. Experimental f–k spectrum $\tilde{H}(k_r, \omega)$ for the site in Lincent. .

dividual frequency. It exhibits peaks corresponding to the Rayleigh modes. The peak corresponding to the fundamental Rayleigh wave is identified and the dispersion curve $C_R^E(\omega)$ is derived from the peak's position. This corresponds to the classical approach. The resulting dispersion curve is shown in figure 3a. The curve has been identified in the frequency range between 15 Hz and 68 Hz. Below 15 Hz, the position of the peak in the f–k spectrum becomes unclear due to the low signal-to-noise ratio. The highest frequency where the dispersion curve $C_R^E(\omega)$ can be identified is determined by the distance between two adjacent receivers. This distance is 1 m; the smallest wavelength that can be measured is therefore 2 m. In the high frequency range, the wavelength of the Rayleigh wave is smaller than 2 m. This gives rise to spatial aliasing, resulting in unreliable data that can not be used to determine the dispersion curve $C_R^E(\omega)$.

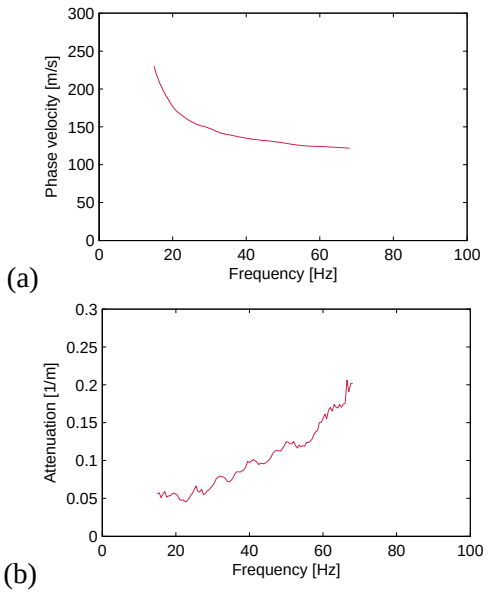

Fig. 3. Experimental (a) dispersion curve $C_R^E(\omega)$ and (b) attenuation curve $\alpha_R^E(\omega)$ for the site in Lincent.

Next, the attenuation curve $\alpha_R^E(\omega)$ is derived from the peak's width, using the half power bandwidth method. The half power bandwidth method has originally been developed in the field of structural dynamics to determine the modal damping ratio of a structure from the width of the peaks in the structure's frequency response function. It is demonstrated numerically that the half power bandwidth method is also applicable to the wavenumber content of the soil's response, resulting in the attenuation coefficient of the surface waves. The attenuation curve $\alpha_R^E(\omega)$ for the site in Lincent is shown in figure 3b.

In this alternative approach, the occurrence of multiple Rayleigh modes does not affect the attenuation curve of either the fundamental or the dominant Rayleigh wave, as all modes occur as separate, non-interfering peaks in the frequency-wavenumber spectrum. Moreover, the experimental attenuation curve is derived directly from the experimental data, avoiding the use of a (possibly incorrect) estimate of the soil's shear wave velocity.

IV. The inverse problem

The soil profile is finally determined from the experimental dispersion and attenuation curves through the solution of an inverse problem. The direct stiffness method [4] or an equivalent formulation is used to calculate the theoretical dispersion and attenuation curves of a soil with a given stiffness and damping profile. The profile is iteratively adjusted in order to minimize a misfit function that measures the distance between the theoretical and the experimental dispersion and attenuation curves. The minimization problem is usually solved with a gradient based local optimization method. As an alternative, a global optimization scheme can be used, such as the method of coupled local minimizers [1].

However, the dispersion and attenuation curves are insensitive to variations of the soil properties on a small spatial scale or at a large depth. The information on the soil properties provided by these curves is therefore limited. As a result, the solution of the inverse problem is non-unique: the soil profile obtained from the inversion procedure is only one of the profiles that fit the experimental data. The non-uniqueness of the solution of the inverse problem in the SASW method has been investigated in reference [8].

In the frame of the present paper, a classical deterministic inversion scheme based on a local optimization algorithm has been used. The resulting soil profile consists of a layer with a thickness of 2.65 m, a shear wave velocity of 138 m/s, and a material damping ratio of 0.048, on a half-space with a shear wave velocity of 266 m/s and a material damping ratio of 0.036. These results have been obtained assuming a density of 1800 kg/m^3 and a Poisson's ratio of 1/3.

V. Conclusion

The SASW test is an in situ test to determine the dynamic shear modulus and the material damping ratio of shallow soil layers. The test consists of three parts. First,

an in situ experiment is conducted. Next, the experimental results are used to determine the dispersion and attenuation curves of the soil. Finally, an inverse problem is solved where the corresponding soil profile is identified. This paper focuses on all three parts, critically reviewing the existing practice. A number of improvements are also presented, including a technique to improve the efficiency of the in situ test, and a new method to determine the experimental attenuation curve.

ACKNOWLEDGEMENTS

The first author of this paper is a postdoctoral fellow of the Research Foundation - Flanders. The results presented here have been obtained in the frame of the FWO project G.0595.06 “In situ determination of material damping in the soil at small deformation ratios”, funded by the Research Foundation - Flanders. The financial support is gratefully acknowledged.

REFERENCES

[1] G. Degrande, S.A. Badsar, M. Schevenels, G. Lombaert, and A. Teughels. Application of the Coupled Local Minimizers method to the optimization problem in the Spectral Analysis of Surface Waves method. *Journal of Geotechnical and Geoenvironmental Engineering, Proceedings of the ASCE*, 134(10):1541–1553, 2008.

[2] D.J. Ewins. *Modal testing: theory and practice*. Research Studies Press Ltd., Letchworth, UK, 1984.

[3] T. Forbriger. Inversion of shallow-seismic wavefields: I. Wavefield transformation. *Geophysical Journal International*, 153(3):719–734, 2003.

[4] E. Kausel and J.M. Roësset. Stiffness matrices for layered soils. *Bulletin of the Seismological Society of America*, 71(6):1743–1761, 1981.

[5] C.G. Lai. *Simultaneous inversion of Rayleigh phase velocity and attenuation for near-surface site characterization*. PhD thesis, Georgia Institute of Technology, 1998.

[6] S. Nazarian and M.R. Desai. Automated surface wave method: field testing. *Journal of Geotechnical Engineering, Proceedings of the ASCE*, 119(7):1094–1111, 1993.

[7] G.J. Rix, C.G. Lai, and A.W. Spang Jr. In situ measurement of damping ratio using surface waves. *Journal of Geotechnical and Geoenvironmental Engineering, Proceedings of the ASCE*, 126(5):472–480, 2000.

[8] M. Schevenels, G. Lombaert, G. Degrande, and S. François. A probabilistic assessment of resolution in the SASW test and its impact on the prediction of ground vibrations. *Geophysical Journal International*, 172(1):262–275, 2008.

Proceedings of the 8th National Congress on Theoretical and Applied Mechanics, May 28-29, Brussels, Belgium.

Simulation of blast-induced soil wave propagation

Bram Desmet [1,2], John Vantomme[1], Geert Degrande[2]
[1] Civil and Materials Engineering Department, Royal Military Academy
Renaissancelaan 30, B–1000 Brussels, Belgium
[2] Department of Civil Engineering, K.U.Leuven
Kasteelpark Arenberg 40, B–3001 Leuven, Belgium
e-mail: Bram.Desmet@rma.ac.be, John.Vantomme@rma.ac.be, Geert.Degrande@bwk.kuleuven.be

Abstract: **Surface or subsurface explosions cause soil vibrations that can have detrimental effects on structures at large distances. Controlling these effects necessitates an accurate prediction of the soil surface vibrations. The shock non-linearity, high velocities and high pressure levels associated with blast loading considerably complicate all possible prediction strategies. Confronted with the limitations of empirical and analytical modeling, a numerical simulation offers the needed alternative. In this paper a methodology for a coupled numerical model is proposed: a hydrocode is used for the non linear part of the model close to the explosion and is coupled to a linear elastic model for the wave propagation at larger distances. An optimal configuration of the Autodyn hydrocode tool is derived for blast-induced soil wave propagation simulations. The possibilities and limitations of the different solvers and modeling tools are examined in the perspective of their use for the simulation of an underground explosion. A composed model is proposed, dealing with the principal issues of the problem: the quality of the transmitting boundary conditions, the deformation of the grid, the solver and material interaction and the prevention of numerical material diffusion are taken in to account.**

Keywords: **Blast, Soil shock, Vibration prediction, Hydrocode, Autodyn**

I. Introduction

Soil vibrations caused by surface or subsurface explosions can have damaging effects on a structure at distances where the effects of an air shock by the same quantity of explosives can be neglected. To be able to calculate and control the resulting soil-structure interaction and the final structural vibrations the accurate prediction of the soil vibrations near the surface is necessary, taking in to account the nature, size and location of the explosive, the mechanical properties and behavior of the soil and the geometry of the site.

Empirical and analytical models are too limited or simplified to be useful for actual full vibrational analysis of a soil blast event. Empirical predictions focus on characteristic values, as the peak particle velocity, based on the generalization of large databases, using the theory of model similarity. They are uncomplicated and easy to use but the few parameters defining the soil, geometry and explosive load result in rough approximations of the vibration data. Typical examples are proposed by the TM 5-1300 [1], Dowding [2], Smith and Hetherington [3], Bulson [4] and Henrych [5].

Analytical models [5][6][7][8] go more deeply into the actual, albeit simplified, linear and non-linear soil behavior and into the wave propagation properties. While such methods provide more complete vibrational results, their use is limited to very specific, ideal configurations, ignoring the free surface, the geometry of the site and the actual explosion behavior.

Due to the different restrictions in both types of models, it is necessary to turn to numerical modeling to obtain the detailed results needed for a full vibrational analysis. A hydrocode enables the simulation of the highly non-linear (hydrodynamic and elastoplastic) events in the immediate surroundings of an explosion. It combines explicit time integration and adapted solver methodologies and material models to calculate the shock wave propagation and the extremely high material deformations [9].

Autodyn [10][11] is a publicly available hydrocode tool: though not specifically designed to perform blast induced soil vibration calculations, it can be configured to allow such a simulation. Autodyn has already been used for short simulations of the nearby soil blast effects, for example anti-personnel mine explosions [12][13] or cratering [14]. Other authors develop adapted material models for use in Autodyn simulations, while a limited number of larger scale simulations are available [15][16][17][18].

It is advisable to limit the use of hydrocode models to the non-linear domain, due to their important calculation cost and the fact that the material models and calculation methodologies are not optimized for linear elastic calculations.

Other methods have been developed specifically for this purpose, as used in the analysis of vibrations induced by traffic and industrial or construction activities. A combination of a hydrocode and a linear elastic seismic tool can allow a calculation from the explosive source to the structure. To ensure a prediction which is both accurate and time-efficient, an optimal balance between these tools is needed.

This paper focuses on the global methodology of the simulation of blast induced soil vibrations due to a subsurface explosion. The advantages and disadvantages of the different Autodyn functionalities are presented and an improved configuration for the non-linear part of the simulation is proposed.

II. Global Methodology

When observing the soil behavior at different distances from the explosion, three important zones can be distinguished [5], each calling for a different simulation approach. Immediately around the blast, the soil behaves hydrodynamically. The soil strength is exceeded and important deformations are obtained. The attenuation of the wave at a larger distance from the source causes the pressure to drop, but still causes plastic deformations. With further

attenuation of the pressure wave, the yield strength of the soil is no longer exceeded and a linear-elastic behavior can be observed. The non-linearity of the shock is a supplementary factor to take into account, calling for adapted simulation tools. As the shock wave advances, it degrades and a shock approach is no longer needed.

The first two zones can be simulated using Autodyn, while the third zone allows the use of linear elastic modeling tools. By the time the soil deformations have attenuated to a linear elastic level, the shock wave has degraded as well, so the shock wave only needs to be handled inside the Autodyn model. The entire problem can thus be covered using only two models.

Figure 1 shows the practical realization of this methodology on a quarterspace with the symmetry axis through the center of the explosive load, indicated by the star. Figure 1a indicates the extent of the three soil deformation zones around the explosion: hydrodynamic, elasto-plastic and linear elastic. Figure 1b shows the extent of the hydrocode simulation domain: it reaches into the linear elastic deformation zone and is limited by an absorbing boundary condition. Figure 1c shows the linear elastic simulation domain. The output of the hydrocode model is generated on a curve in between the boundary and the edge of the non-linear domain and is applied as an equivalent elastic source on its inner edge, as shown by Sharpe [8].

Throughout the entire hydrocode calculation, the stresses and displacements are registered on the elements on the output generation curve. These results are used as the input for a Boundary Element model of the linear elastic wave propagation zone. The radiated wave field in the far field can thus be obtained. This part of the model is yet to be implemented.

III. Non-Linear zone methodology

The non-linear part of the model is simulated using Autodyn, which is capable to model very high deformations and captures the formation and propagation of discontinuities, such as shock waves. Autodyn uses explicit time integration and combines a number of different solvers, mostly based on Finite Difference or Finite Volume methods, with adapted material models [10][11].

The different solvers, their interaction and the boundary conditioning in Autodyn are presented briefly. Their advantages and drawbacks are illustrated in the perspective of the global methodology of the blast-induced soil vibration simulation.

A. Application of the Euler solver

All of the Euler solvers in Autodyn use a fixed grid, through which the material can flow freely. In the described models, a higher order Godunov multi-material solver is used, as described by Van Leer [19][20]. The higher order precision is lost because of an averaging procedure over the volume of each cell.

The main advantage of the Euler solver is that it allows very large deformations, while avoiding heavily distorted grids or tangled cells. While computationally more demanding, it offers a good solution for the simulation of the explosive and the soil in the immediate surroundings of the explosion, where hydrodynamic soil behavior can occur.

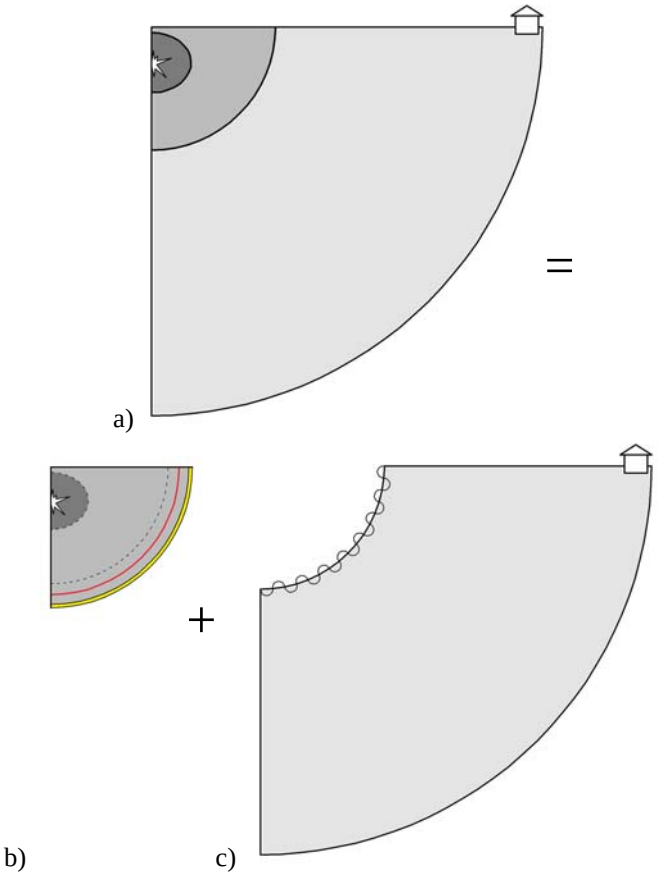

Fig. 1. Quarterspaces showing a) the target structure, the underground explosion, the hydrodynamic (dark grey), elasto-plastic (medium grey) and linear elastic (light grey) soil deformation zone, for calculation purposes subdivided in b) the hydrocode calculation domain, showing the edges of the soil deformation zones (dotted), the output generation line (red) and the absorbing boundary condition (yellow) and c) the linear elastic calculation domain with the target structure and the equivalent elastic load, applied on its inner edge.

The combination of the multi-material functionality and the averaging of the data over each cell causes numerical material diffusion. Due to this diffusion, the Euler solver has difficulties tracking material interfaces and free surfaces, as illustrated on figure 2, showing the material distribution in an Euler model of a 5 kg TNT eq. explosion at a depth of 4 m. The diffusion at the free surface and on the boundary between the TNT and the soil is clearly visible. A calculation of several seconds of such a model, as needed for the soil vibration simulation, leads inevitably to the disintegration of the soil part and not to the expected formation of an explosion cavity. The diffusion can be avoided by limiting the extent of the Euler model. A Lagrange part along the entire soil surface avoids having an Euler based free surface and consequently rules out the soil/air diffusion at this interface. Limiting the use of the Euler solver to the TNT alone also avoids the TNT/soil interface diffusion.

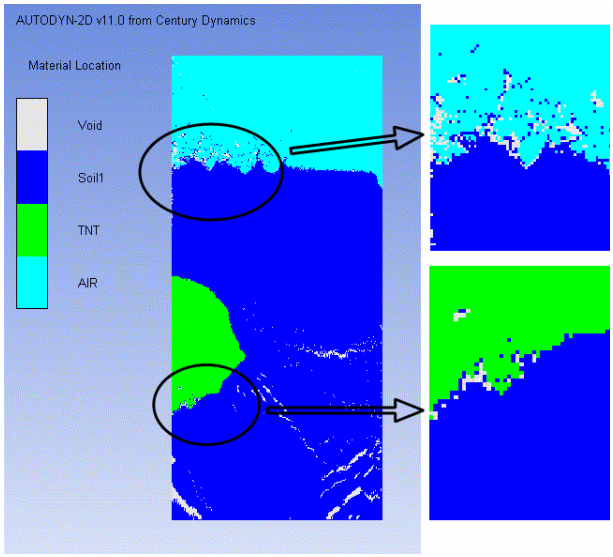

Fig. 2. Material distribution at 275 ms in the Euler model of a 5 kg TNT eq. explosion at a depth of 4 m, showing material diffusion and generation of void elements on the material boundaries and the free surface.

The possible formation of void areas in the multi-material Euler part causes another problem, as illustrated in figure 2. The explosive gases flow into the void cells at enormous spurious speeds, causing the time step to drop and inducing large energy errors. Limiting the use of the Euler solver to the TNT helps avoiding this problem, by preventing the diffusion of soil particles in the explosive gas.

B. Application of the Lagrange solver

The Lagrangian solver used in Autodyn is based on a Finite Difference scheme, developed by Wilkins [21][22]. It uses a structured grid of quadrilaterals with cell-centered and averaged state material quantities and a combination of pseudo-viscous damping forces, in order to capture the shock wave in an efficient and correct manner.

Mass conservation is obtained in each cell, and since the Lagrange cells can only contain one material, material diffusion can not occur, maintaining distinct material interfaces and free surfaces. Due to the absence of a remapping phase, the computational cost is considerably lower compared to the Euler or ALE solvers.

Since no material transport is allowed, total deformations are accumulated at the cell level, which can result in high grid distortions or tangled cells, leading to inaccuracies and small time steps.

C. Application of the Arbitrary Lagrangian Eulerian solver

The Arbitrary Lagrangian Eulerian (ALE) follows an identical computational cycle as the Lagrange solver, but introduces an optional rezoning procedure after the calculation of all cell-centered variables, as introduced in the SALE code by Amsden [23]. The rezoning inevitably comes with a supplementary computational cost. All nodes on material interfaces, as well as on the borders of the model do not take part in this rezoning procedure: they need to remain Lagrangian to conserve free surfaces and to avoid material diffusion. The number and extent of rezoning operations should be limited, since they induce minor calculation errors.

The rezoning of each node is governed by a motion constraint. Two examples are presented: the Equal-X constraint changes the X-coordinate of each node to the average of its four neighbors. The Equal-I constraint averages the distances between all the nodes on the same structural I grid line.

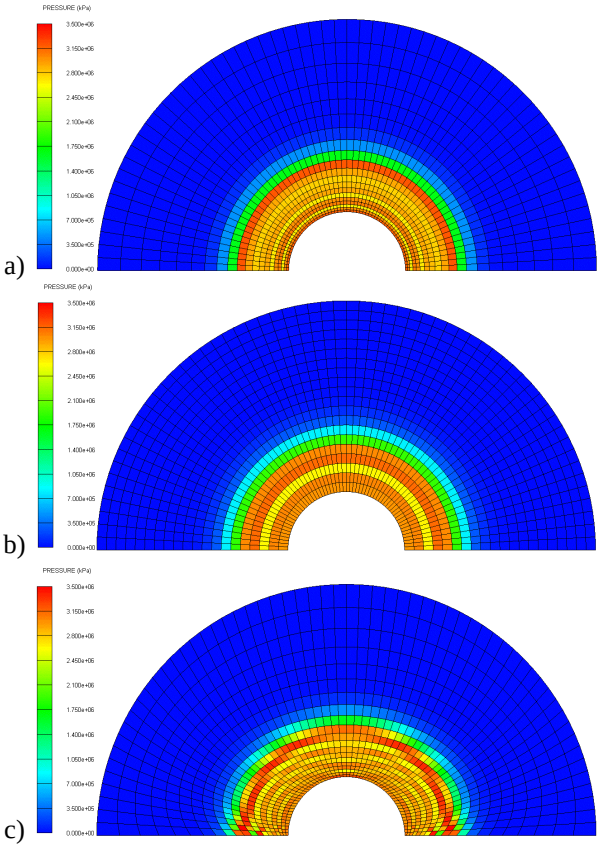

Fig. 3. Pressure distribution in a 2D axisymmetric spherical soil model with an internal cavity, expanding at a constant radial velocity for a) the Lagrange, b) Equal-I and c) Equal-X motion constraint.

The choice of a good rezoning strategy is crucial for the quality of the results. Figure 3 shows a 2D axisymmetric spherical soil model with an internal cavity expanding at a fixed radial velocity. The use of a Lagrange solver results in an undisturbed radial expansion and semi-circular pressure wave. Figures 3a, 3b and 3c show the grid and pressure distribution in the model at the end of a short calculation for the Lagrangian, Equal-I and Equal-X motion constraints. Near the edge of the cavity, the element size in the Lagrangian model is reduced significantly, which will eventually lead to tangled cells. The Equal-I motion constraint has managed to obtain equally radially distant nodes, and offers the most economical alternative. The Equal-X constraint situates somewhere in between, but will of course keep on adapting the grid throughout the calculation. Apart from the different final element sizes and shapes, a distinct deformation of the semi-spherical wave front is visible for the Equal-X motion constraint. Based on this approach, the Equal-I motion stands

out, since it conserves the spherical symmetry of the wave, as the reference Lagrange model.

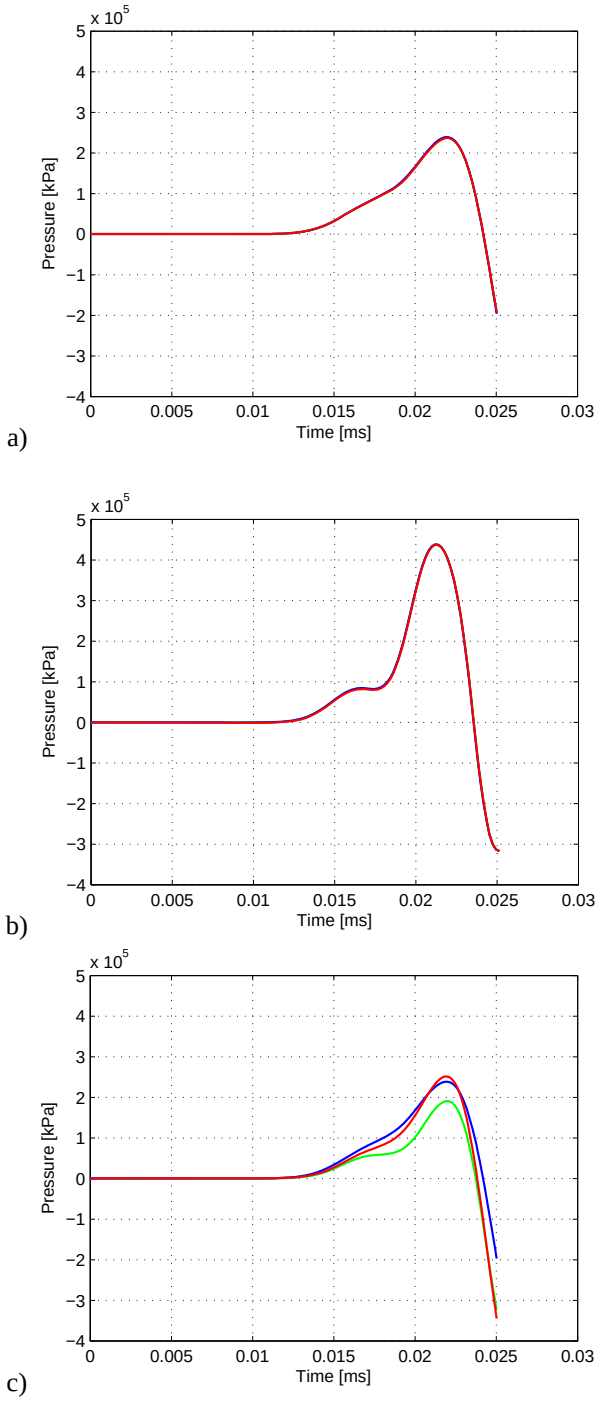

Fig. 4: Time history of the pressure at three points (red at 10°, green at 45° and blue at 90° from the symmetry axis) near the boundary of a 2D axisymmetric spherical soil model with an internal cavity expanding at a fixed radial velocity and a) Lagrange, b) Equal-I and c) Equal-X motion constraints.

Figure 4 shows the time history of the pressure at three points in each model, at the same distance from the center of the cavity. While the Lagrange and the Equal-I simulation show equal results in each of the three cells, indicating a conservation of the circular symmetric wave front, the pressure in the cells of the Equal-I model significantly diverges from the original, Lagrangian result. The deformation of the wave front is clearly visible by the diverging pressures for the Equal-X motion constraint. The absolute pressure levels are better conserved compared to the equivalent cells in the Lagrangian simulation.

D. Coupled solver models

The Euler-Lagrange coupling is designed to simulate fluid-structure interaction: Euler cells that are intersected by a Lagrange or ALE cell generate stresses on the Lagrange boundary face, while this boundary face provides a geometrical constraint for the flow in the Euler cells. Since there is no tensile or shear bond between the material on either side of the interface. Material continuity is thus not guaranteed. Only the interface between the explosive gases and the soil cavity can effectively be modeled by such an interaction. An Euler/Lagrange or Euler/ALE interface within the same material will cause pressure wave reflections and should thus be avoided. Figure 5 shows an example of such a reflection.

The Lagrange-Lagrange, ALE-ALE, ALE-Lagrange and Euler-Euler interactions are all based on nodal contact. For an Euler-Euler interaction, node to node contacts define the cell's interacting faces, through which the material can flow. For all other coupling, joined nodes simply behave as one.

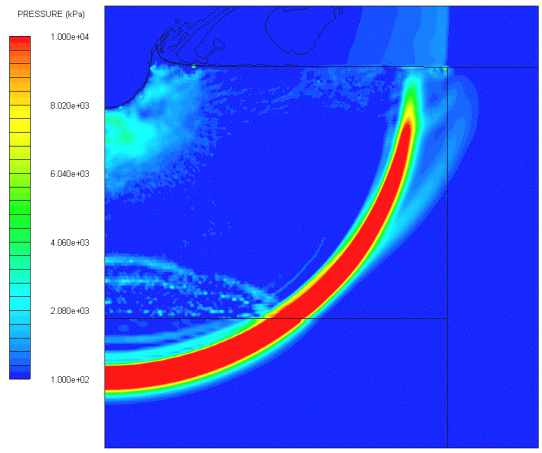

Fig. 5: Pressure wave reflections at the Euler/Lagrange boundary, 0.62 ms after the blast of a 50 kg TNT eq. surface explosion.

E. External boundaries

The standard boundary of a Lagrange or ALE model behaves as a free surface: a correct free surface behavior is obtained if no part of the free surface is modeled using Euler elements. All other model edges should be equipped with an absorbing boundary, allowing radiation of outward traveling waves without reflection.

In Autodyn, the absorbing boundary condition is based on the pressure jump conditions on the rearward facing characteristic of the normal component of the incoming wave. This guarantees an exact solution for the component of an elastic wave perpendicular to the boundary. It is approximate for shock waves and reflects the component of the particle velocity parallel to the boundary. Figure 6 illustrates the

reflections due to the use of a rectangular absorbing boundary.

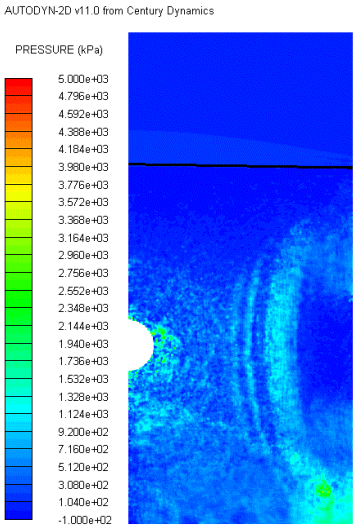

Fig. 6: Pressure distribution due to reflections on the rectangular transmitting boundary for a 5 kg TNT eq. explosion at a depth of 4 m, 2.5 ms after the explosion. The black line indicates the position of the free surface; the explosion cavity is plotted in white.

The reflections on this boundary can be minimized by positioning it far enough from the explosive, as to avoid non-elastic waves interacting with it. It also means assuring as much as possible the normal impact of all waves traveling towards the boundary. Practically, this is achieved by adopting a semi circular boundary in 2D axial symmetry, centered on the explosive load. Waves traveling in non radial directions, being reflected by the free surface or by a soil layer interface will be more affected by the boundary. To be able to apply this semi-circular boundary, the model needs to be semi-circular, which determines to a large extent the entire geometry and meshing strategy.

The limited capabilities of the absorbing boundary condition in Autodyn remain an important source of errors, even when following the aforementioned guidelines. A fully functioning alternative, leading to an improved performance, needs to be developed and implemented.

F. Improved Autodyn model composition

Figures 7a and b show a global view and a close-up near the explosion cavity of the material distribution and the grid of an improved model. The setup and geometry of the solvers, interactions and boundary have been chosen as to minimize possible errors.

The detonation is calculated on a 1D Euler wedge. The results of this model are remapped radially on the 2D model. The spherical symmetry is applied to all the elements of the 2D model. The Euler part of the model consists of two zones: a semi-circular inner zone, joined to a hollow circular disc shaped, radially meshed outer part, which extends underneath the ALE zone. The extent of this overlap can be estimated by empirical predictions on the blast cavity radius, taking the type of soil and the size of the load into account. The grid is designed so that the edge of the explosive gas material, resulting from the wedge calculation, corresponds to the face of one ring of Euler cells, avoiding initially partially filled cells. The string of joined nodes is indicated in white.

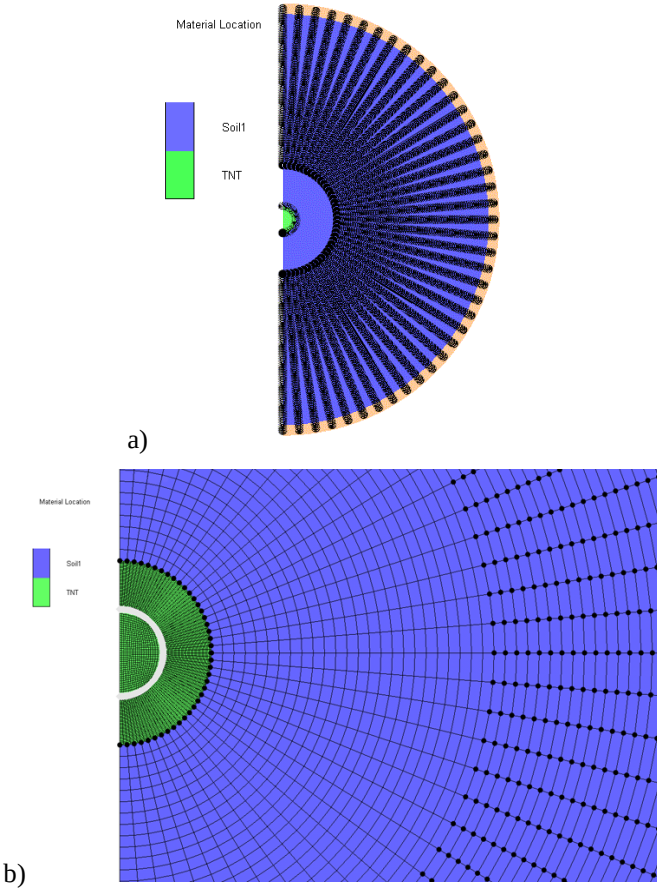

Fig. 7: Material distribution, joined nodes (white) and Lagrangian nodes (black dots) for a) the global composed Autodyn model and b) a close-up near the explosion cavity.

The inner radius of the ALE zone corresponds to the edge of the soil material resulting from the wedge calculation. The ALE nodes on the explosive cavity edge are necessarily Lagrangian. An Equal-X motion constraint is applied to the inner nodes, while the nodes at larger radii are Lagrangian, shown as black dots. The choice of the extent of the ALE motion constraint depends on the specific case and is subject to optimization after a number of trial runs: the ALE rezoning is only necessary where the cell deformations risk causing tangled or small cells. The outer radius of the ALE zone is provided with a standard Autodyn absorbing boundary condition, shown as a yellow ring in figure 7a. The ALE part and the outer Euler part are interacting along the inner ALE cavity edge.

This model can only be applied up to a discontinuity, the presence of a free surface or soil layers with different material properties. It can be adapted, or coupled to a hydrocode model part that deals with these discontinuities.

The above model is used in a simulation of a 5 kg TNT eq. explosion at a depth of 4 m. The radius of the model is 6m, with an Euler element size of 10 mm and an ALE element size ranging from 40 mm close to the explosive to 400 mm near the absorbing boundary. The soil is modeled using a shock

Hugoniot EOS [24] for a silty clay soil, combined with a piecewise linear Drucker-Prager strength model, as proposed and validated by Luccioni [25]. The result of an initial 1D Euler simulation, with 1 mm elements, is remapped on the 2D model, 2.2 ms after the detonation. The 2D simulation is run for 3 s, without instabilities or material diffusion. Since the free surface is not modeled, no surface wave is generated and all the results relate to the P- and S-wave.

Figure 8a shows the time history of the particle velocity, at a distance of 1 m at the same depth as the explosive. At 1.5 ms, a distortion of the wave can be observed: this is a part of the time history modeled in the 1D Euler model, where the influence of void fractions on the material velocity disturbs the velocity curve. This effect disappears after the remapping on the ALE grid.

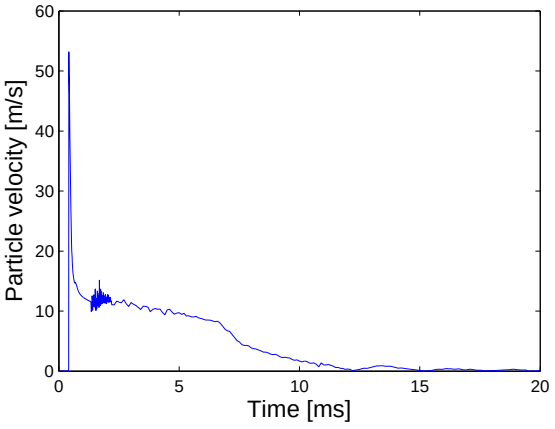

Fig. 8: Time history of the particle velocity at the explosion depth for a) an element near the explosion cavity and b) at positions at 3.2 m (blue), 3.7 m (green), 4.2 m (red) and 4.6 m (black) from the explosion.

Figure 8b shows the time history of the particle velocity for four different locations at the same depth but at larger distances from the explosion. The gradual decline of the shock wave can be observed: the peak particle velocity drops and the peak is widened. The first two curves show the particle velocity at two locations within the area initially modeled by the 1D Euler model: the fine mesh results in a good resolution. The time history of the particle velocity at the third and fourth point is situated in the ALE part of the simulation: the shocks are smeared out over the larger sized elements, resulting in disproportionally low and wide peaks. A smaller ALE element size is necessary in future models.

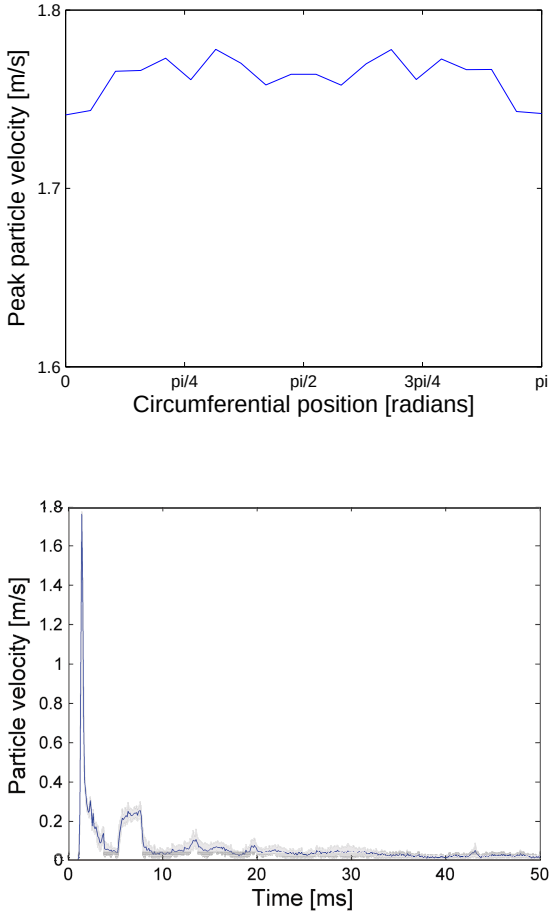

Fig. 9: a) Peak particle velocity in function of the circumferential position and b) time history of the mean particle velocity, with the standard deviation interval, for all locations at a 5.8 m radius around the explosive.

A certain asymmetry is obtained in the results, due to remapping imperfections near the symmetry axis, combined with calculation errors due to the ALE rezoning and the imperfection of the absorbing boundary layer. Figure 9a shows the variation of the PPV at a radius of 5.8 m along the model boundary, which is symmetric around the horizontal axis through the explosive cavity center. The mean PPV is 1.76 m/s with a maximal divergence of +/- 1%. Figure 9b shows the time history of the mean particle velocity at a 5.8 m radius and the corresponding standard deviation. The absolute value of the standard deviation is around 13 mm/s throughout the entire simulation, but attains a relative value of 50 % from 15 ms on, in the low velocity range of the simulation.

IV. CONCLUSIONS

The non-linear aspects related to explosions in the soil call for an adapted approach of the problem, and, where empirical or analytical models do not provide sufficiently detailed results, numerical simulations are a necessary tool for the full vibrational analysis of blast induced soil vibration effects.

A hydrocode is not developed to simulate the linear elastic behavior of a material and its replacement in this domain by a

more fitting numerical tool can reduce the calculation cost significantly. A combination of explicit hydrocode models and a linear elastic simulation model, a Boundary Element model for example, can offer an economic solution in a large domain, providing the extent of both calculation domains is equilibrated and adapted to the minimal range of the elastic soil behavior.

Autodyn offers a wide array of tools and solvers that allow the development of a basic solution strategy for the non-linear domain. The limitations of these utilities are diverse and a well-considered modeling strategy is needed to obtain a working model. Facing the restrictions of the standard transmitting boundary, the solver capabilities of Autodyn and the desired behavior of the material interface, a general circular symmetry of the model is essential. Measures need to be taken to avoid material diffusion and the rezoning motion constraints of ALE parts of the model need to be adapted to the situation. For the latter, the Autodyn Equal-X motion seems to be the better choice. The ALE rezoning calculation errors, together with the initial remapping error and the aforementioned imperfections lead to a deformation of the expected circular symmetric result.

ACKNOWLEDGMENTS

This research is a part of the SBO project IWT 03175 "Structural damage due to dynamic excitation: a multi-disciplinary approach", funded by the Institute for the Promotion of Innovation through Science and Technology in Flanders (IWT).

REFERENCES

[1] TM 5-1300, *Structures to resist the effects of accidental explosions*, Technical Manual, U.S. Army, 1990.

[2] H.C. Dowding, *Construction Vibrations*, Prentice Hall, 1996.

[3] P.D. Smith, J.G. Hetherington, *Blast and ballistic loading of structures*, Butterworth and Heinemann, 1994.

[4] P.S. Bulson, *Explosive loading of engineering structures*, E & FN Spon, 1997.

[5] J. Henrych, *The dynamics of explosion and its use*, North-Holland Publishing Co, 1976.

[6] G.M. Lyakhov, V.N Okhitin, Spherical detonation waves in media with volumetric viscosity, *Journal of Applied Mechanics and Technical Physics*, **6**, 126-137, 1977.

[7] B. Donaev, N. Mamadeliev, A.I. Yusupov, Propagation of a spherical wave in nonlinearly compressible and elastoplastic materials, *Journal of Applied Mechanics and Technical Physics*, **4**, 95-100, 1986.

[8] J.A. Sharpe, The production of elastic waves by explosion pressures. I. Theory and empirical field observations, *Geophysics*, **7**, 144-154, 1942.

[9] J.A. Zukas, *Introduction to hydrocodes*, Elsevier, 2004

[10] Autodyn, *Explicit Software for Non-Linear Dynamics, Theory manual*, Revision 4.3, Ansys Inc., 2005.

[11] Autodyn, *Explicit Software for Non-Linear Dynamics, User manual*, Revision 6.1, Ansys Inc., 2007.

[12] M. Grujicic, B. Pandurangan, R. Qiao, B.A. Cheeseman, W.N. Roy, R.R. Skaggs, R. Gupta, Parametrization of the porous-material model for sand with different levels of water saturation, *Soil Dynamics and Earthquake Engineering*, **28**, 20-35, 2008.

[13] D. Fiserova, A. Hameed, T.A. Rose, J.G. Hetherington, S. Prochazka, Evaluating numerical approaches in explosion modeling of surface laid mines, *Journal of Battlefield Technology*, **7**, 1-6, 2004.

[14] B.M. Luccioni, R.D. Ambrosini, R. Danesi, Influence of the soil properties on craters produced by explosions on the soil surface, *Mecanica Computacional*, **23**, 571-590, 2004.

[15] Z. Wang, H. Hao, Y. Lu, A three-phase soil model for simulating stress wave propagation due tot blast loading, *International Journal for Numerical and Analytical Methods in Geomechanics*, **28**, 33-56, 2004.

[16] G.W. Ma, H. Hao, Y.X., Zhou, Modeling of wave propagation induced by underground explosion, *Computers and Geotechnics*, **22**, Nr. 3/4, 283-303, 1998.

[17] C. Wu, Y. Lu, H. Hao, W.K. Lim, Y. Zhou, C.C. Seah, Characterisation of underground blast-induced ground motions from large-scale field tests, *Shock Waves*, **13**, 237-252, 2003.

[18] Z. Wang, Y. Lu, H. Hao, Numerical effects of water saturation on blast wave propagation in soil mass, *Journal of Engineering Mechanics*, **130**, No. 5, 551-561, 2004.

[19] B. Van Leer, Towards the ultimate conservative difference scheme V. A second-order sequel to Godunov's method, *Journal of Computational Physics*, **135**, 229-248, 1997.

[20] B. Van Leer, Towards the ultimate conservative difference scheme IV. A new approach to numerical convection, *Journal of Computational Physics*, **23**, 276-299, 1977.

[21] M.L. Wilkins, Use of artificial viscosity in multi-dimensional fluid dynamic calculations, *Journal of Computational Physics*, **36**, 281-303, 1980.

[22] M.L Wilkins, Calculation of elastic-plastic flow, *Methods of Computational Physics*, **3**, 211-263, 1964.

[23] A.A. Amsden, H.M. Ruppel, C.W. Hirt, SALE: A simplified ALE computer program for fluid flow at all speeds, *Los Alamos report LA-8095*, UC-32, 1980.

[24] D.S. Drumheller, *Introduction to wave propagation in nonlinear fluids and solids*, Cambridge University Press, 1998.

[25] B.M. Luccioni, R.D. Ambrosini, Craters produced by underground explosions, *Mecanica Computacional*, **25**, 1603-1614, 2006.

Proceedings of the 8th National Congress on Theoretical and Applied Mechanics, May 28-29, Brussels, Belgium.

Evaluation of structural power flow using an optimized regressive discrete Fourier series

C. Vuye[1,2], P. Guillaume[2], S. Vanlanduit[2], F. Presezniak[2] and G. Steenackers[2]
[1]Artesis Hogeschool Antwerpen, Dept. Of Applied Science & Technology
Paardenmarkt 92, B-2000 Antwerp, Belgium
[2]Vrije Universiteit Brussel, Dept. Of Mechanical Engineering, Acoustics and Vibration Research Group
Pleinlaan 2, B-1050 Brussels, Belgium
email: cedric.vuye@artesis.be, steve.vanlanduit@vub.ac.be

Abstract— **Evaluation of structural power flow (or structural intensity SI) in engineering structures is a field of increasing interest in connection with vibration analysis and noise control. In contrast to classical techniques such as modal analysis, SI indicates the magnitude and direction of the vibratory energy traveling in the structures, which yields information about the positions of the sources/sinks, as well as the energy transmission path. In this paper we propose a method to model operational deflection shapes, simulated or measured with a scanning laser Doppler vibrometer (SLDV). The model is a two-dimensional Fourier domain model that is estimated using a weighted non-linear least-squares method. From the wavenumber-frequency domain data thus obtained, the spatial derivatives that are necessary to determine the structural power flow are easily computed. It will be shown that the proposed method is less sensitive to measurement noise than traditional power flow estimation techniques. A numerical model of a simply supported plate excited by two shakers, phased to act as an energy source and sink, is used as a test case.**

Keywords— **power flow, Regressive Discrete Fourier Series, stabilization chart**

I. Introduction

PREDICTING and measuring elastic waves propagating through a structure can be of foremost importance in vibro-acoustic problems. The prediction and the measurement of the propagating elastic waves within a structure is usually referred to as structural power flow, vibration intensity, or structural intensity, the latter denominations coming from the analogy with acoustic intensity.

Power is defined as the time-averaged product of the generalized forces with the in-phase component of the generalized velocities. The power in a structure can be represented as a vector with both magnitude and direction since the directions of the generalized forces and velocities from which the power is computed are known [1]. When plotting power vectors, a flow type pattern develops and hence the term power flow. Power flow plots can be used to indicate the locations of the energy sources and sinks, as well as the paths of energy transmission between them, as shown in [2], [3]. Once the power flow has been determined, the structure can then be designed or controlled to channel and dissipate the energy as required. Many analytical and experimental power flow methods have been developed since 1970 when the first paper concerning power flow was published [4]. Traditional techniques involve the use of a number of accelerometers and a finite difference approximation to compute the power flow. More recent techniques often involve the use of a scanning laser Doppler vibrometer (SLDV) [5], [6], [7], [8], and some algorithm to model the Operational Deflection Shape (ODS). These algorithms are based on either spatial Fourier transforms [9], wavenumber processing techniques [10] or (two-dimensional) Fourier series in the spatial domain [11], [12].

In this paper we propose a new spatial modeling technique originally based on Regressive Discrete Fourier Series (RDFS). This method, introduced in [11], was later improved in [13], [14] which formed the further basis of our research.

The paper is outlined as follows. Section II will deal shortly with the theory behind power flow. In Section III the new algorithm named Two-Step Regressive Discrete Fourier Series (TSRDFS) is explained. Numerical results on a simulated ODS and on power flow will show the effectiveness of this algorithm in Section IV. Merits and limitations of the proposed method will finalize this paper.

II. Power flow

In this section the basic theory of power flow in thin homogeneous flat plates is reviewed, so that a coherent set of equations becomes available. This review contains only the most important formulae. For a complete review on the theory of power flow we recommend [2].

In classical plate theory the bending wave equation can be written as:

$$D\nabla^2\nabla^2 w(x,y,t) + \rho h \frac{\partial^2 w(x,y,t)}{\partial t^2} = F(t)\delta(x_0,y_0), \quad (1)$$

with $D = Eh^3/(12(1-\nu^2))$ the bending stiffness, E the Young's modulus, h the plate thickness, ν the Poisson's ra-

tio, $\nabla^2 = \partial^2/\partial x^2 + \partial^2/\partial y^2$ (two-dimensional Laplace operator), $w(x,y,t)$ the transverse displacement, ρ the mass density and $F(t)\delta(x_0,y_0)$ a point external force.

As shown in [3], [4] the power flow along the plate in each orthogonal direction, q_x and q_y, has three components:

$$\begin{aligned} q_x &= \Re[Q_x \dot{w}^* + M_x \dot{\theta_y}^* + M_{xy} \dot{\theta_x}^*], \\ q_y &= \Re[Q_y \dot{w}^* + M_y \dot{\theta_x}^* + M_{yx} \dot{\theta_y}^*], \end{aligned} \tag{2}$$

with shear forces Q_x and Q_y, bending moments M_x and M_y, twisting moments M_{xy} and M_{yx}, the transverse velocity $\dot{w}$ and angular velocities $\dot{\theta}_x$ and $\dot{\theta}_y$. The asterix represents the complex conjugate and $\Re$ means taking the real part of the above equation.

Using the equilibrium equations for a flat plate element, assuming harmonic vibration and no interaction between superposed waves, it can be shown from Eq. (2) that [2]:

$$\begin{aligned} q_x(x,y) = \frac{D}{2\omega}\Im\Bigg\{ & \frac{\partial}{\partial x}(\nabla^2\dot{W})\dot{W}^* - \nabla^2\dot{W}\frac{\partial \dot{W}^*}{\partial x} \\ & -(1-\nu)\left(\frac{\partial^2\dot{W}}{\partial x \partial y}\frac{\partial \dot{W}^*}{\partial y} - \frac{\partial^2 \dot{W}}{\partial y^2}\frac{\partial \dot{W}^*}{\partial x}\right)\Bigg\}, \\ q_y(x,y) = \frac{D}{2\omega}\Im\Bigg\{ & \frac{\partial}{\partial y}(\nabla^2\dot{W})\dot{W}^* - \nabla^2\dot{W}\frac{\partial \dot{W}^*}{\partial y} \\ & -(1-\nu)\left(\frac{\partial^2\dot{W}}{\partial x \partial y}\frac{\partial \dot{W}^*}{\partial x} - \frac{\partial^2 \dot{W}}{\partial x^2}\frac{\partial \dot{W}^*}{\partial y}\right)\Bigg\}, \end{aligned} \tag{3}$$

with ω the forcing frequency, W the Fourier transposed of w and $\Im$ the imaginary component.

Using the hypotheses of propagating, non-interactive waves Eq. (3) can be simplified to:

$$\begin{aligned} q_x(x,y) &= \sqrt{D\rho h}\,\Im\left\{\dot{W}\frac{\partial \dot{W}^*}{\partial x}\right\}, \\ q_y(x,y) &= \sqrt{D\rho h}\,\Im\left\{\dot{W}\frac{\partial \dot{W}^*}{\partial y}\right\}. \end{aligned} \tag{4}$$

It is clear from Eq. (4) that we not only need the transverse velocity $\dot{W}$ but also its partial derivatives $\partial\dot{W}/\partial x$ and $\partial\dot{W}/\partial y$.

When measurement noise and other forms of experimental error are present in the experimental (or simulated) data, the calculation of these partial derivatives can cause major problems. One method to obtain the necessary derivatives with less noise contamination is the use of two-dimensional spatial fitting techniques (e.g. RDFS), as explained in the next section.

III. Theoretical background

First of all the pole/residue modeling of an ODS will be explained, followed by our proposed method.

A. Pole/residue modeling

To understand how the pole/residue modeling works one can consider the following complex-valued multiharmonic function:

$$s(x) = \sum_{l=0}^{L} a_l e^{-\sigma_l x + i\omega_l x} \tag{5}$$

Evaluating this function at discrete locations $x = n\Delta x$, Δx denoting a constant spatial resolution and $n = 0 \ldots N-1$, results in the following sequence:

$$s[n] = s(n\Delta x) = \sum_{l=0}^{L} a_l \lambda_l^n \tag{6}$$

with $\lambda_l = e^{-\sigma_l x + i\omega_l \Delta x}$ and ω_l, σ_l denoting respectively the spatial frequency and damping of component l in the ODS.

The technique of pole/residue estimating from an ODS [13], boils down to the following steps. By taking a discrete Fourier transform (DFT) of the acquired signal a transfer function model is derived. From this model the poles and residues (or amplitudes) are extracted. The frequency ω_l and damping σ_l can be found in the estimated poles. The method will first be explained for the one-dimensional case and then be expanded to show the two- dimensional equations. Starting from the sequence in Eq. (7) using only one spatial component and taking the discrete Fourier transform:

$$s[n] = a\lambda^n \tag{7}$$

$$S[k] = \sum_{n=0}^{N-1} s[n] e^{-i2\pi\frac{kn}{N}} = \sum_{n=0}^{N-1} a\lambda_n z_k^{-n} \tag{8}$$

where $z_k = e^{\frac{i2\pi k}{N}}$. The expression in Eq. (8) can be written as follows by expanding the sum:

$$S[k] = a\frac{1-\lambda^N}{1-\lambda z_k^{-1}} \tag{9}$$

Applying the result from Eq. (9) to the sequence in Eq. (5), which is the general form for an ODS reveals:

$$S[k] = \sum_{l=1}^{L} \frac{\bar{a}_l}{1 - \lambda_l z_k^{-1}} \tag{10}$$

with $\bar{a}_l = a_l(1 - \lambda_l^N)$

This result can also be applied to the particular case where the ODS is real (Eq. (11)):

$$s(x) = \sum_{l=0}^{L} a_l e^{-\sigma_l x + i\omega_l x} + \sum_{l=0}^{L} a_l^* e^{-\sigma_l x - i\omega_l x} \tag{11}$$

Applying the result from Eq. (10) to this sequence reveals:

$$S[k] = \sum_{l=1}^{L} \frac{\bar{a}_l}{1 - \lambda_l z_k^{-1}} + \sum_{l=1}^{L} \frac{\bar{a}_l^*}{1 - \lambda_l^* z_k^{-1}} \tag{12}$$

where * indicates a complex conjugate.

Eqs. (10) and (12) are nothing else than pole/residue representations of the discrete Fourier transform $S[k]$. This clearly proves that it is possible to model sinusoids using a transfer function model in the frequency domain. Therefore it is possible by means of a simple least squares approach (or for more reliable results a Maximum Likelihood (ML) approach [15]) to retrieve values for the poles λ_l and the residues $\bar{a}_l$. The sinusoid frequencies can then be obtained from the poles and similarly the sinusoid amplitudes can be calculated from the residues with following formula: $a_l = \bar{a}_l/(1 - \lambda^N)$. This result also illustrates the fact that it is possible to compensate the residue estimates $\bar{a}_l$ for the leakage error. Indeed from the estimated poles λ_l and residues $\bar{a}_l$ an estimate of a_l has been derived.

To expand the technique to two dimensions one can start with Eq. (11), which can be written in a pole residue model the same way as in the 1D case:

$$S[k] = \sum_{l=1}^{L} \frac{\bar{a}_l}{(1 - \lambda_{x,l} z_x^{-1})(1 - \lambda_{y,l} z_y^{-1})} \tag{13}$$

where $\bar{a}_l = a_l(1 - \lambda_{x,l}^N)(1 - \lambda_{y,l}^N)$, $z_x = e^{\frac{i2\pi k_x}{N}}$ and $z_y = e^{\frac{i2\pi k_y}{N}}$. This result is clearly very similar to the result obtained in the 1D case and can be solved in a similar fashion using a least squares (or a maximum likelihood approach) to retrieve estimates for the residues $\bar{a}_l$ and for the poles $\lambda_{x,l}$ and $\lambda_{y,l}$.

B. Two-Step Regressive Discrete Fourier Series

Since starting from a 2D FFT (for a 2D ODS) and using the above mentioned technique in Section III-A proved to be difficult and time consuming, a new algorithm using only 1D FFT was developed as shown in Fig. 1. The problem of estimating the poles (including damping) and residues from a 2D FFT was by-passed by applying two separate 1D FFT, hence the name *Two-Step*. The different steps shown in the flow chart will be illustrated by means of the following example.

A simply supported steel plate with dimensions 380 mm $\times$ 300 mm $\times$ 1.6 mm is used. The plate has a Young's modulus of elasticity of 2.04E11 Pa, Poisson's ration of 0.29 and no structural damping was assumed. The mode shapes z_{mn} at resonance frequencies ω_{res} were determined using Eqs. (14) and (15) [16]:

$$z_{mn} = \sin\frac{m\pi x}{a} \sin\frac{n\pi y}{b}, \tag{14}$$

with m, n integers and a, b the length and width of the plate respectively.

$$\omega_{res} = \sqrt{\frac{D}{\rho h}} \left[\left(\frac{m\pi}{a}\right)^2 \left(\frac{n\pi}{b}\right)^2 \right]. \tag{15}$$

The first mode shape at 69 Hz with and without 10 % added Gaussian noise can be found in Fig. 2. These mode shapes with and without added noise will function as the input ODS for our algorithm. The next step is performing an FFT on the columns (and rows) of the 2D ODS. This FFT is then used to estimate the poles using a Maximum Likelihood Estimator (MLE) as can be seen on Fig. 3(a), where the full line shows the MLE estimation of the FFT results ('+'). This MLE is executed in a loop and every time the loop is executed more poles are estimated. With the help of the so-called stabilization chart in Fig. 3(b) it is possible to visualize which poles are 'stable' and are most likely to be the correct solutions [17], [18]. For clarity the figures on the MLE and stabilization chart were taken without added noise.

In this case it is easy to determine which poles are correct, since only two poles seem to be stable. The location of these poles can also be determined analytically for all mode shapes using $\pm m\pi/a$, with m the corresponding mode number. In this case, we obtain $\pm 8,25i$ for the poles which corresponds with $\pm 1,31$ as the spatial frequency. Two complex conjugate poles are needed of course to model a sine, since we use exponential functions in our estimator (with $\sin(x) = (e^{ix} + e^{-ix})/2i$).

After manually choosing the poles in both the x and y direction (circles in Fig. 3(b)), λ_x and λ_y respectively, a combination matrix C is formed as shown in Eq. (16):

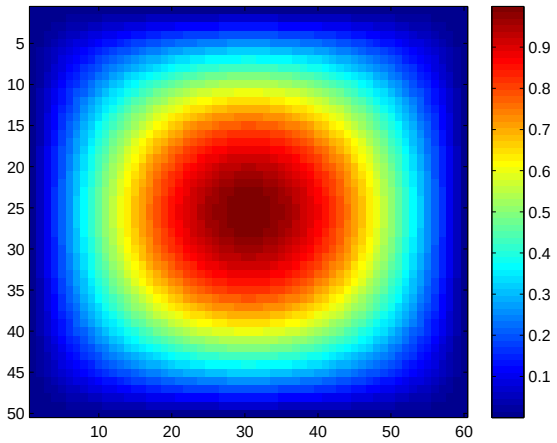

(a)

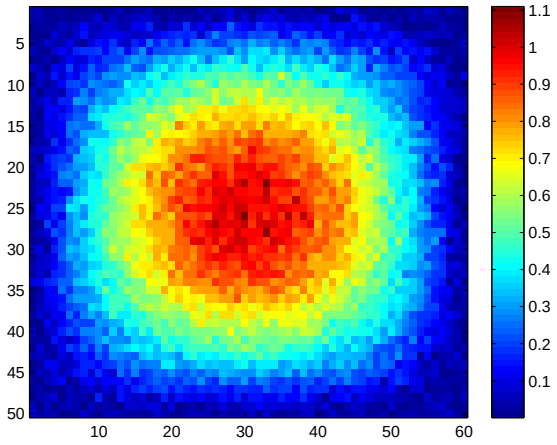

(b)

Fig. 2. Absolute value of the simulated mode shape at 69 Hz - (a) noiseless and (b) with 10 % noise added

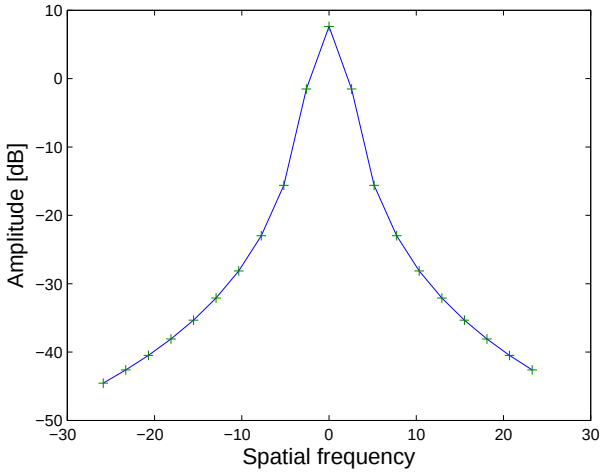

(a)

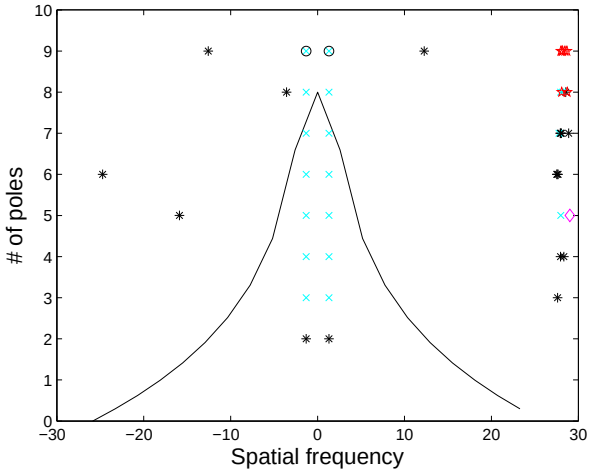

(b)

Fig. 3. (a) Maximum Likelihood estimated FFT results and (b) Stabilization chart for the x direction

$$C_{(x,y)} = \sum_{m=1}^{M} \sum_{n=1}^{N} e^{\lambda_{x,m}x} \times e^{\lambda_{y,n}y}, \tag{16}$$

with M,N the number of previously selected poles in x and y respectively. This matrix contains, in other words, the sum of all possible combinations of e^{λ_x} and e^{λ_y} for all points $p(x,y)$.

The following step consists of determining the residues by executing a left matrix divide as shown in Eq. (17):

$$RES_{(x,y)} = C_{(x,y)} \backslash z_{(x,y)}. \tag{17}$$

It is shown here that in our proposed method it is no longer necessary to compensate the residue estimates for the leakage error, as mentioned in Section III-A, since the residues are determined directly in the spatial domain.

In the final step the smoothed mode shape $z^{(s)}_{(x,y)}$ is calculated as shown in Eq. (18):

$$z^{(s)}_{(x,y)} = C_{(x,y)} \times RES_{(x,y)}. \tag{18}$$

During this algorithm the spatial derivatives $\partial z/\partial x$, $\partial z/\partial y$, $\partial^2 z/\partial x^2$, $\partial^2 z/\partial y^2$ and $\partial^2 z/\partial x \partial y$ are also determined. The corresponding errors between the original noiseless ODS and the smoothed ODS and their respective first order spatial derivatives were calculated using Eq. (19) and are shown in Table I.

$$err = \sqrt{\frac{\sum_{n=0}^{N_k-1} |(z^s(n) - z(n))|^2}{|z(n)|^2}}, \tag{19}$$

with N_k the total number of data points.

The proposed method is compared with the ORDFS method [14] and the Discrete Cosine Transform (DCT) which is used in e.g. the popular jpeg-compression standard. It will also be compared to the classical Discrete Fourier Transform (DFT) and the standard Regressive Discrete Fourier Series (RDFS) with $\alpha = 1.4$, which was prone to be an optimal value [11].

As can be seen the TSRDFS provides much better results for this simple case. Especially the errors on the spatial derivatives are much lower due to the fact that these are calculated analytically. The spatial derivatives of the other algorithms are determined using the Matlab function 'gradient'. Furthermore in this example the TSRDFS only needs 2 poles in each direction to reconstruct the original image, compared to 3×3 modes for the ORDFS and RDFS, which corresponds with 49 components for the DCT and DFT.

IV. Numerical simulations

To demonstrate the effectiveness of the proposed TSRDFS method and to validate the results a numerical simulation based on experimental results from [3] was used.

A. Simulated ODS

In this section the TSRDFS will be used to recreate a simulated ODS with and without added noise. The vibration pattern that will be used is the ODS of the simply supported plate as mentioned in Section III-B. The steel plate is now harmonically excited at f: 79 Hz by two point forces at locations $p_1(0.29, 0.09)$ and $p_2(0.09, 0.21)$. The forces have an amplitude and phase of (100 N, 0°) and (89 N, 174.6°) respectively. These amplitude and phase differences create a clear power flow from p_1, which acts as a source, to p_2, which acts as a sink.

Starting from the formulation of the analytical deflection shapes Eq. (14) the theoretical Frequency Response Function (FRF) was computed by modal superposition, using the first 10 modes, for the above mentioned frequencies. This synthesized FRF was then used to create the corresponding ODS.

The resulting ODS with and without 5% added Gaussian noise, are shown in Fig. 4. In this figure the resulting ODS is somewhat different from the one depicted in [3]. This is due to the slightly different boundary conditions and the mass loading effect of the electromagnetic shakers in their experimental setup, and the fact that we assume no damping.

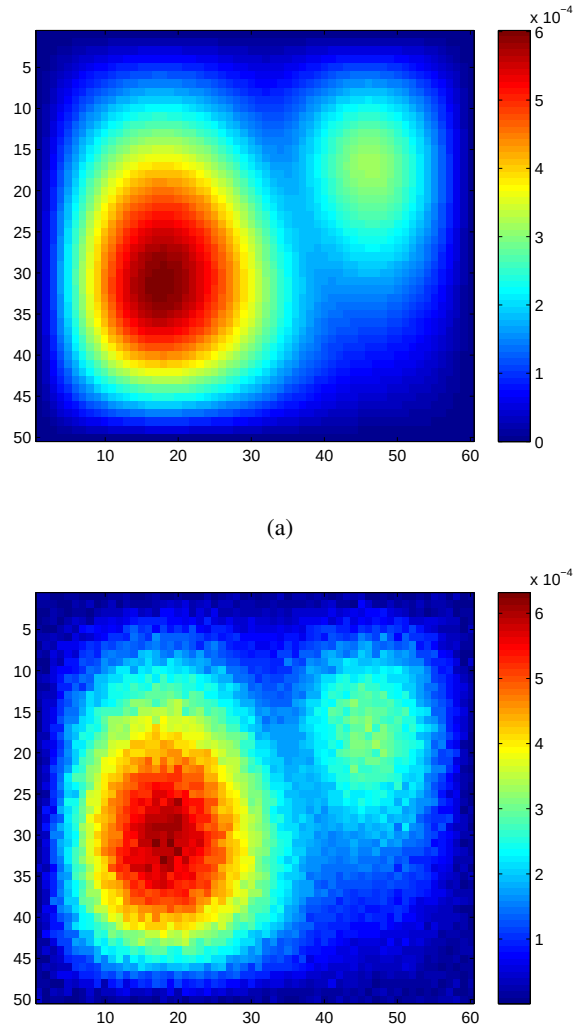

(a)

(b)

Fig. 4. Absolute value of the simulated ODS at 79 Hz - (a) noiseless and (b) with 5 % noise added

The results of the calculated errors are presented in Table II. Due to the added noise the best results in the case with 5 % added noise were found with only 4×4 modes for ORDFS and RDFS. Adding more modes has a negative effect on the results. Therefore the same number of modes was used in the noiseless case.

As can be seen our proposed method is able to deal with the added noise as good as the existing ORDFS and RDFS techniques. In this simple case, however, it is logic that all existing methods will give a good estimate of the ODS as there is no problem with leakage. As mentioned in Section II the spatial derivatives are needed to obtain the power flow. Even in this simple case DCT and DFT fail to estimate these derivatives when noise is present.

A downside for the proposed method can be seen in

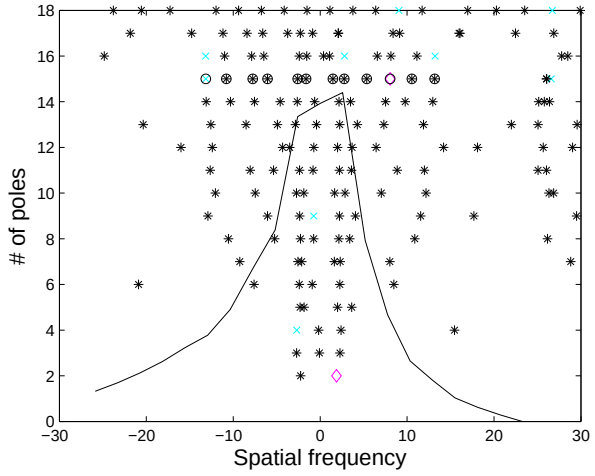

(a)

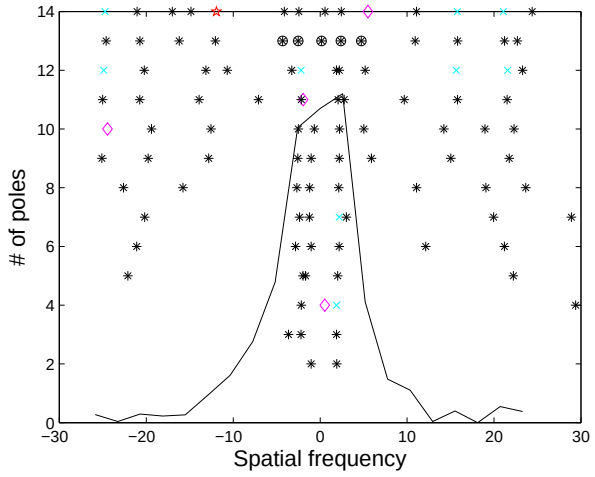

(b)

Fig. 5. Stabilization chart - (a) noiseless and (b) with 5 % noise added

Fig. 5. Here you see the stabilization charts for both the noiseless ODS and the ODS with 5 % added noise. Since the ODS is a sum of multiple mode shapes, more poles need to be estimated. They all are located in the spatial frequency band of $[-15, 15]$ which can prove to be difficult. In the noiseless case 6 complex conjugate pole pairs were selected for each direction to obtain an accurate model of the ODS. Because it is not as clear as in the previous example in Section III-B which poles are stable, this means that sometimes a trial-and-error approach is needed. In the case with 5 % added noise only 5 poles were selected in each direction. More poles could not be identified due to the added noise.
Estimating and selecting a larger number of poles though takes more computing time since the MLE loop has to be run multiple times and a much larger combination matrix is formulated.

B. Power flow simulations

In this section the results for the power flow will be discussed. In Fig. 6 it is shown that the power flow can be determined from the ODS even with 5 % added noise. The power flow is very clear from the source on the bottom right to the sink at the top left (marked by a dot). The arrows indicate the direction of the structural power flow and its relative magnitude. The resulting power flow corresponds very well with the experimental results in [3]. To visualize the location of the sink and source though, it was necessary to plot the divergence of the calculated power flow as shown in Figs. 7-8. These divergence plots were used previously to determine the location of sources and sinks in [2].

Fig. 7 shows the divergence plots of the power flow computed from (a) the noiseless ODS and (b) the ODS with added noise. It is clear that when no noise is added, no spatial smoothing techniques are necessary to visualize either the power flow or the location of sources and sinks. With actual measurements though noise will always be present, so that techniques such as the TSRDFS will be necessary or no sources or sinks can be localized as seen in Fig. 7(b).

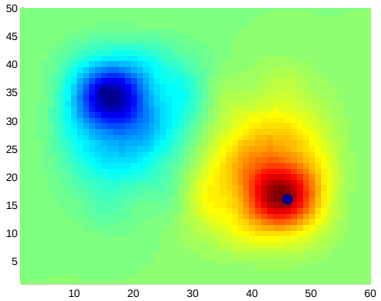

(a)

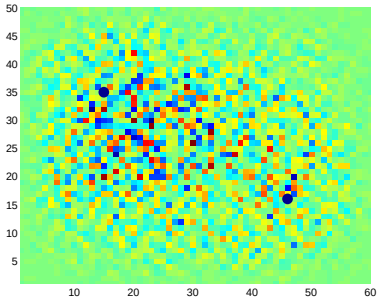

(b)

Fig. 7. Divergence of the power flow at 79 Hz - (a) noiseless and (b) with 5 % noise added

As can be seen in Fig. 8 it is possible to locate the source and sink quite accurately using the TSRDFS, while the localization with the RDFS is not as accurate (similar results were found for the ORDFS). Using DCT or DFT it was impossible to locate the source and sink.

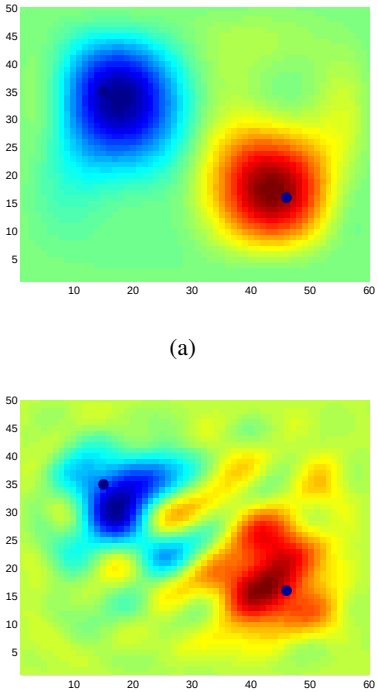

(a)

(b)

Fig. 8. Divergence of the power flow with 5 % added noise - (a) TSRDFS and (b) RDFS

V. Merits and limitations

In this paper a new algorithm based on regressive discrete Fourier series is proposed. It is shown that this algorithm works better than existing techniques on simple mode shapes, provides similar results on operational deflection shapes and provides more accurate results when calculating the structural power flow and localizing the energy sources and sinks. Furthermore we are positive that our proposed method will outperform the classical techniques in certain more difficult scenarios. This will be investigated in the following months.

The two major limitations for the moment are the used computer time (approx. 5 minutes for the complete simulations of Section IV) and the difficulty in localizing the correctly estimated poles. More work is necessary to avoid these obstacles.

Acknowledgments

This research has been sponsored by the Flemish Institute for the Improvement of Technological Research in Industry (IWT) and the Fund for Scientific Research (FWO). The authors also acknowledge the research council of both the Artesis Hogeschool Antwerpen and the Vrije Universiteit Brussel. The third author holds a grant as Postdoctoral Researcher from the FWO Flanders.

References

[1] G. Pavic, "Measurement of structurne borne wave intensity - part I - formulation of the methods," *Journal of Sound and Vibration*, vol. 49(2), pp. 221–230, 1976.

[2] J. R. F. Arruda and P. Mas, "Localizing energy sources and sinks in plates using power flow maps computed from laser vibrometer measurements," *Shock and Vibration*, vol. 5, pp. 235–253, 1998.

[3] J. D. Blotter, R. L. West, and S. D. Sommerfeldt, "Spatially continuous power flow using a scanning laser Doppler vibrometer," *Journal of Vibration and Acoustics*, vol. 124, pp. 476–482, 2002.

[4] D. U. Noiseux, "Measurement of power flow in uniform beams and plates," *Journal of the Acoustical Society of America*, vol. 47(1), pp. 238–247, 1970.

[5] Y. Zhang and J. A. Mann, "Measuring the structural intensity and force distribution in plates," *Journal of the Acoustical Society of America*, vol. 99(1), pp. 345–353, 1996.

[6] Y. Zhang and J. A. Mann, "Examples of using structural intensity and the force distribution to study vibrating plates," *Journal of the Acoustical Society of America*, vol. 99(1), pp. 354–361, 1996.

[7] J. C. Pascal, X. Carniel, and J. F. Li, "Characterisation of a dissipative assembly using structural intensity measurements and energy conservation equation," *Mechanical Systems and Signal Processing*, vol. 20, pp. 1300–1311, 2006.

[8] S. Z. Peng, "Laser Doppler vibrometer for mode shape and power flow analysis in coupled structures," *International Journal of Vehicle Noise and Vibration*, vol. 3(1), pp. 70–87, 2007.

[9] J. C. Pascal, T. Loyau, and X. Carniel, "Complete determination of structural intensity in plates using laser vibrometers," *Journal of Sound and Vibration*, vol. 161(3), pp. 527–531, 1993.

[10] J. C. Pascal, J. F. Li, and X. Carniel, "Wavenumber processing techniques to determine structural intensity and its divergence from optical measurements without leakage effects," *Shock and Vibration*, vol. 9, pp. 57–66, 2002.

[11] J. R. F. Arruda, "Surface smoothing and partial spatial derivates computation using a regressive discrete Fourier series," *Mechanical Systems and Signal Processing*, vol. 6(1), pp. 41–50, 1992.

[12] J. R. F. Arruda, S. A. V. do Rio, and L. A. S. B. Santos, "A space-frequency data compression method for spatially dense laser Doppler vibrometer measurements," *Shock and Vibration*, vol. 3(2), pp. 127–133, 1996.

[13] J. Vanherzeele, P. Guillaume, S. Vanlanduit, and P. Verboven, "Data reduction using a generalized regressive discrete Fourier series," *Journal of Sound and Vibration*, vol. 298, pp. 1–11, 2006.

[14] J. Vanherzeele, S. Vanlanduit, and P. Guillaume, "Reducing spatial data using an optimized regressive discrete Fourier series," *Journal of Sound and Vibration*, vol. 309, pp. 858–867, 2008.

[15] P. Guillaume, P. Verboven, and S. Vanlanduit, "Frequency-domain maximum likelihood identification of modal parameters with confidence intervals," *Noise and Vibration Engineering*, vol. 1, pp. 359–376, 1998.

[16] A. W. Leissa, *Vibration of plates*, National Aeronautics and Space Administration, 1969.

[17] P. Verboven, E. Parloo, P. Guillaume, and M. Van Overmeire, "Autonomous structural health monitoring - part I Modal parameter estimation and tracking," *Mechanical Systems and Signal Processing*, vol. 16(4), pp. 637–657, 2002.

[18] S. Vanlanduit, P. Verboven, P. Guillaume, and J. Schoukens, "An automatic frequency domain modal parameter estimation algorithm," *Journal of Sound and Vibration*, vol. 265, pp. 647–661, 2003.

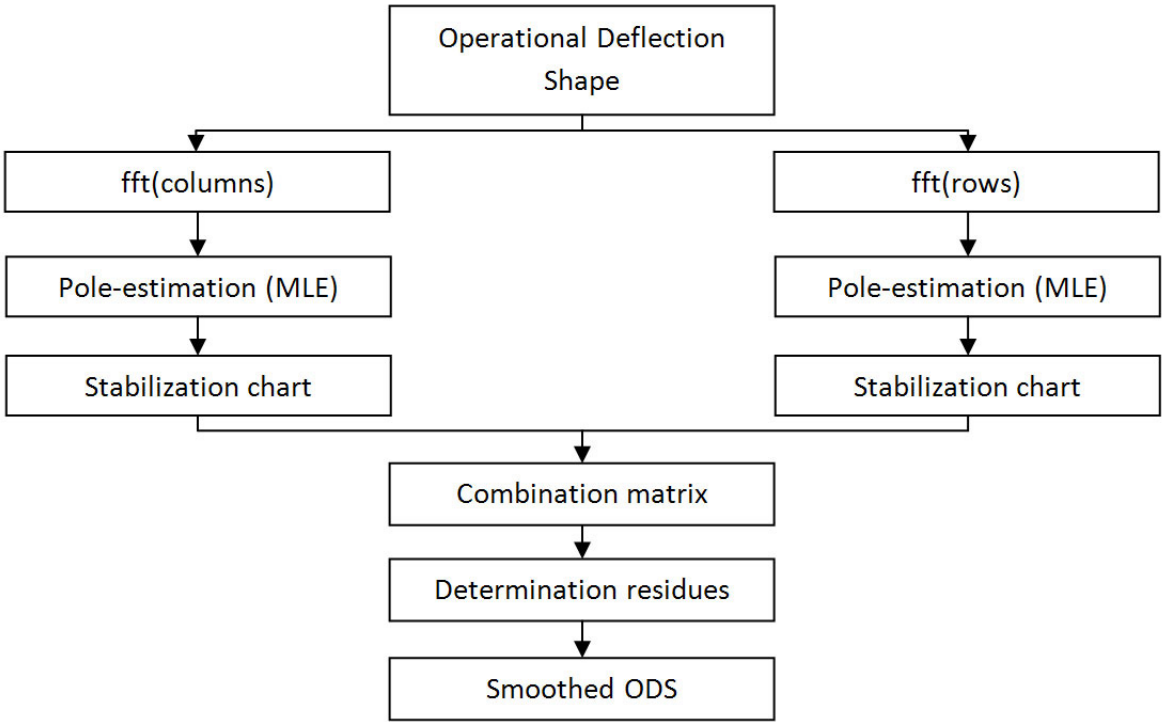

Fig. 1. Flow chart of the TSRDFS

TABLE I
ERRORS FOR THE MODE SHAPE AT 69 HZ.

	Errors without noise [%]			Errors with 10 % noise [%]		
Method	z	$\partial z/\partial x$	$\partial z/\partial y$	z	$\partial z/\partial x$	$\partial z/\partial y$
Two-Step RDFS	9e-5	2e-4	1e-4	0,91	2,28	2,32
Optimized RDFS	4e-3	0,06	0,08	1,14	5,26	5,26
RDFS	0,18	1,61	1,53	1,12	4,82	4,95
DCT	0,58	9,29	7,18	2,46	33,95	27,05
DFT	2,23	22,28	22,02	2,52	23,16	23,95

TABLE II
ERRORS ON THE ODS AND SPATIAL DERIVATIVES AT 79 HZ.

	Errors without noise [%]			Errors with 5 % noise [%]		
Method	z	$\partial z/\partial x$	$\partial z/\partial y$	z	$\partial z/\partial x$	$\partial z/\partial y$
Two-Step RDFS	0,06	0,48	0,67	2,77	6,73	8,33
Optimized RDFS	0,70	5,36	3,19	1,56	6,64	9,58
RDFS	0,70	5,36	3,19	1,56	6,64	9,58
DCT	1,66	13,72	17,00	2,77	23,26	27,44
DFT	1,42	10,87	14,76	2,96	22,15	25,41

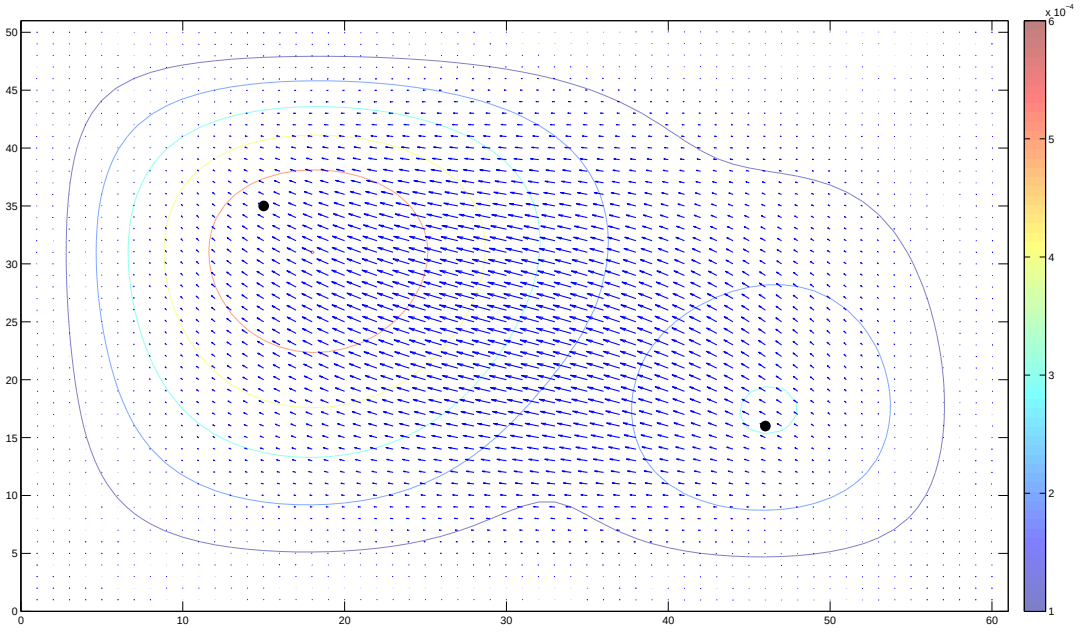

Fig. 6. Power flow of the ODS with 5 % added noise at 79 Hz using the TSRDFS

Proceedings of the 8th National Congress on Theoretical and Applied Mechanics, May 28-29, Brussels, Belgium.

On the use of a multi-level wave based modelling approach for the steady-state dynamic analysis of two-dimensional perforated solids

Karel Vergote, Bert Van Genechten, Dirk Vandepitte, Wim Desmet
Katholieke Universiteit Leuven, Department of Mechanical Engineering
Celestijnenlaan 300B - Box 2420, 3001 Heverlee (Leuven)
email: Karel.Vergote@mech.kuleuven.be

Abstract— **The Wave Based Method (WBM) is a novel Trefftz-based deterministic prediction technique which aims at relaxing the existing frequency limitations of the commonly applied Finite Element Method (FEM). Instead of dividing the problem domain into small elements, the domain is divided in a small number of large, convex subdomains. In each of those subdomains, the field variables are expressed in terms of global wave functions, which exactly satisfy the governing dynamic equations. The smaller system of equations and the absence of pollution errors make the WBM very suitable for the treatment of problems in the mid-frequency range, where element-based methods are no longer feasible due to the associated computational costs. A sufficient condition for convergence of the applied wave function expansion is the convexity of the considered problem domains. As a result, only problems of moderate geometrical complexity can be considered and some commonly applied geometrical features cannot be handled at all. A typical example of this is the study of the dynamic behaviour of a two-dimensional solid which contains one or more circular holes. Recently, an extension of the WBM for two-dimensional unbounded and bounded steady-state acoustic problems has been developed which allows the method to overcome these geometrical limitations in a very efficient way. This paper presents a numerical strategy for the study of two-dimensional elastodynamic problems with one or more circular holes, which is based on that modelling framework. The feasibility of the approach and the efficiency with respect to the FEM is illustrated by means of the dynamic analysis of a perforated membrane.**

Keywords—**Elastodynamics, Navier, Mid-frequency, Trefftz method, Wave Based Method**

I. Introduction

THE numerical simulation techniques for the study of elastodynamic problems can be divided into two groups: deterministic techniques and probabilistic techniques. The nowadays most commonly applied methods are the deterministic Finite Element Method (FEM) [1] and the probabilistic Statistical Energy Analysis (SEA) [2].

The element-based simulation techniques discretise the considered problem into a finite number of elements. Within these elements, the dynamic response variables are described by an expansion of simple (polynomial) shape functions, which do not satisfy governing differential equations intrinsically. As a result, as frequency increases, the prediction accuracy of the element based models decreases, mainly due to two types of errors: interpolation and pollution errors [3]. Keeping these errors within acceptable bounds requires the use of extremely dense problem discretisations, especially at higher frequencies. This results in prohibitively large numerical models for real-life structural problems. As a result, the applicability of the element based techniques is limited to problems in the low-frequency range.

The SEA divides the entire system into a limited number of components. The mathematical expression of the power balance between the various subsystems provides the space- and frequency-averaged dynamic behaviour of each of the structural system components. This method is however based on certain approximative assumptions, e.g. the fact that all of the subsystems have a high modal overlap in the frequency range of interest, which limit their use to high-frequency modelling.

In between the low-frequency application range of the deterministic element based techniques and the high-frequency application range of the statistical methods, there exists a wide frequency-gap, the so-called mid-frequency range, for which currently no adequate and mature prediction methods are available. One of the many modelling techniques which are currently being investigated in order to resolve this issue, is the deterministic Wave Based Method (WBM) [4]. This technique belongs to the family of so-called Trefftz methods [5] in that it applies globally defined wave functions, which are exact solutions of the governing differential equations, in contrast to the element based techniques which use approximating shape functions to describe the dynamic response variables. As a result, the use of very fine domain discretisations at higher frequencies is no longer re-

quired. The size of the numerical models and the associated computational requirements are substantially lower as compared to element based methods. Because of the enhanced convergence properties, the WBM has proven to be applicable for low- as well as mid-frequency steady-state structural problems [6], [7], [8]. For convergence purposes, the method requires the entire problem domain to be partitioned into convex subdomains. As a result, the computational efficiency of the WBM is most pronounced for problems with a moderate geometrical complexity.

In reality many systems can be approximated by a combination of simply shaped subdomains, but the majority of them however include structural details that have a non-negligible influence on the dynamic behaviour of the structure and complicate the required division in convex subdomains. Such an increase in subdomains is disadvantageous for the convergence rate of the method. Moreover, some very common geometrical features cannot be dealt with at all. A typical example of this is the study of the dynamic behaviour of a two-dimensional solid which contains one or more circular holes. Since the region between two holes or between a hole and the edge of the problem domain needs to be partitioned into convex subdomains, only an approximate, linearised representation of the circular edge can be used to construct a convergent WBM model. The resulting model is only a crude geometrical approximation of the actual problem and has the additional disadvantage of being inefficient since a reasonable representation accuracy of the circle requires many convex subdomains surrounding it. Recently, an extension of the WBM for two-dimensional unbounded [9] and bounded [10] steady-state acoustic problems has been developed which allows the method not only to overcome these geometrical limitations, but to do so in a very efficient way. This paper presents a numerical strategy for the study of two-dimensional elastodynamic problems with one or more circular holes, which is based on this modelling framework.

The first section of the paper describes the mathematical formulation of a general two-dimensional elastodynamic problem and gives an overview of the theoretical background of the WBM for these types of analyses. Next, the recently developed multi-level modelling concept for steady-state acoustic problems and its extension to the study of perforated membranes are presented. Finally, the feasibility of the approach and the efficiency with respect to the FEM is illustrated by means of the dynamic analysis of a perforated membrane.

II. WBM for membrane problems

This section describes briefly the membrane problem and the application of the WBM for that problem. As mentioned in the introduction, the WBM belongs to the category of indirect Trefftz methods. The WBM divides the domain in a small number of subdomains. Given the convexity of the considered subdomains, the convergence of the method is assured [4]. According to the Trefftz principle, the field variables within each subdomain are approximated by an expansion of basis functions, which exactly satisfy the governing dynamic equations. In this way the method only introduces an approximation error with respect to the the boundary conditions and the conformity between the subdomains. These errors are forced to zero in an integral sense through the application of a Galerkin weighted residual formulation.

A. Problem description

The coupled dynamic Navier equations describe the dynamic displacements [11] in two dimensional solids and the in-plane behaviour of a plate membranes,

$$\begin{aligned}\frac{\partial^2 w_x}{\partial x^2}+\frac{1-\nu}{2}\frac{\partial^2 w_x}{\partial y^2}+\frac{1+\nu}{2}\frac{\partial^2 w_y}{\partial x\partial y}+\frac{\rho(1-\nu^2)\omega^2}{E(1+j\eta)}w_x=0,\\ \frac{\partial^2 w_y}{\partial y^2}+\frac{1-\nu}{2}\frac{\partial^2 w_y}{\partial x^2}+\frac{1+\nu}{2}\frac{\partial^2 w_x}{\partial x\partial y}+\frac{\rho(1-\nu^2)\omega^2}{E(1+j\eta)}w_y=0,\end{aligned} \tag{1}$$

with E the Youngs modulus, ν the Poisson-coefficient, ρ the density, η the damping ratio and ω the radial frequency. Most modern FEM algorithms directly discretise this system of partial differential equations to derive the model matrices. The WBM, on the other hand, applies an expansion in terms of exact analytical solutions of the governing equations as basisfunctions. In order to enable the derivation of such a set of solutions for the coupled equations Vanmaele [6] proposes to decompose the total structural-dynamic strain field into a dilatational and a rotational component. This decomposition converts the coupled system of Navier equations into two uncoupled Helmholtz-type equations,

$$\nabla^2 e + k_l^2 e = 0, \tag{2}$$

$$\nabla^2 \Omega + k_t^2 \Omega = 0, \tag{3}$$

with ∇ the gradient operator, e the dilatational strain and Ω the rotational strain and the in-plane longitudinal and shear wavenumbers defined as,

$$k_l = \omega\sqrt{\frac{\rho(1-\nu^2)}{E(1+j\eta)}} \quad \text{and} \quad k_t = \omega\sqrt{\frac{2\rho(1+\nu)}{E(1+j\eta)}}. \tag{4}$$

In this way, the mutual coupling between the two strain fields is entirely contained within the boundary and continuity conditions which are specified along the subdomain boundaries. Since the plate membrane equations consists of two second-order partial differential equations, two boundary conditions must be specified at each point of the plate boundary Γ. The reader is referred to VANMAELE [6] for the definition of various commonly applied types of boundary conditions and their mathematical expression.

B. Field variable expansion

The steady state in-plane displacements w_x and w_y are approximated by the following field variable expansion,

$$\begin{Bmatrix} w_x \\ w_y \end{Bmatrix} \approx \begin{bmatrix} \mathcal{L}_{w_x} \\ \mathcal{L}_{w_y} \end{bmatrix} \begin{Bmatrix} \sum_{l=1}^{n_l} w_l \Psi_l \\ \sum_{t=1}^{n_t} w_t \Psi_t \end{Bmatrix}, \tag{5}$$

with dilatational and rotational wave functions Ψ_l and Ψ_t, the corresponding contribution factors w_l and w_t and $\mathcal{L}_{w_n}$ and $\mathcal{L}_{w_s}$ the differential operators to reconstruct the normal and shear displacements based on given strain fields:

$$\mathcal{L}_{w_n} = \begin{bmatrix} -\frac{1}{k_l^2}\frac{\partial}{\partial n} & \frac{1}{k_t^2}\frac{\partial}{\partial s} \end{bmatrix}, \tag{6}$$

$$\mathcal{L}_{w_s} = \begin{bmatrix} -\frac{1}{k_l^2}\frac{\partial}{\partial s} & -\frac{1}{k_t^2}\frac{\partial}{\partial n} \end{bmatrix}. \tag{7}$$

The wave functions Ψ_l and Ψ_t satisfy respectively the homogeneous plate membrane equations (2) and (3) irrespective of the contribution factors w_l and w_t.

VANMAELE [6] proposes to use the wave functions listed in Table I. These wave functions are divided into two sets. For the first set of dilatational and rotational wave functions, the functions associated with the first wavenumber are sine and cosine functions, respectively. For the second set, the functions associated with the first wavenumber are cosine and sine functions, respectively. It has been proven by DESMET [4] that the first set of wave functions is theoretically sufficient for the convergence of the WBM, provided that the domain is convex. However, when only the first set of wave functions is included, several boundary variables are described by a series of only sine functions such that convergence becomes slow if the imposed distributions are different from zero in the end points. Therefore a few functions of the second set can be added, which results in better convergence properties [6].

The corresponding wavenumbers are defined based on the dimensions ($L_x \times L_y$) of the preferably smallest rectangular box circumscribing the domain. Demanding that an integer number of half wavelengths equals the dimension of the rectangular box in the corresponding direction leads to the first wavenumbers,

$$k_{l_1,x} = \frac{l_1 \pi}{L_x} \quad \text{and} \quad k_{l_2,y} = \frac{l_2 \pi}{L_y}, \tag{8}$$

$$k_{t_1,x} = \frac{t_1 \pi}{L_x} \quad \text{and} \quad k_{t_2,y} = \frac{t_2 \pi}{L_y}, \tag{9}$$

The other components of the in-plane wavenumbers are calculated from the structural in-plane wavenumbers k_l and k_t:

$$k_{\{l,t\}_1,y} = \pm\sqrt{k_{\{l,t\}}^2 - k_{\{l,t\}_1,x}^2}, \tag{10}$$

$$k_{\{l,t\}_2,x} = \pm\sqrt{k_{\{l,t\}}^2 - k_{\{l,t\}_2,y}^2}. \tag{11}$$

The number of dilatational and rotational wave functions n_l and n_t that are included in the field variable expansion (5), is related to the frequency and the dimensions of the enclosing bounding box such that the largest wave number included in the model is a user defined truncation parameter T times the structural wavenumber at this frequency. As a result, the number of wave functions increases approximately linearly with the excitation frequency.

C. Evaluation of boundary conditions

The proposed field variable expansion (5) guarantees compliance with the governing differential equations (2) and (3). As a result, only the error on the boundaries has to be minimised. The error functions are orthogonalised with respect to a weighting function $\tilde{w}_{\{n,s\}}$ or its derivative. The weighted residual formulation, here applied to imposed force residuals, is expressed as:

$$\int_{\Gamma_T} \tilde{w}_n R_{T_n} \mathrm{d}\Gamma + \int_{\Gamma_T} \tilde{w}_s R_{T_s} \mathrm{d}\Gamma = 0. \tag{12}$$

The reader is referred to [6] for the definition of the boundary residuals R_{T_n} and R_{T_s}.

Like in the Galerkin weighting procedure, used in the FEM, the weighting functions $\tilde{w}_n$ and $\tilde{w}_s$ are expanded in terms of the same set of wave functions used in the wave function expansion (5). Equation (12) should be true for any $\tilde{w}_n$ and $\tilde{w}_s$ and thus for any combination of contribution factors of the basis

TABLE I
SETS OF WAVE FUNCTIONS FOR MEMBRANE PROBLEMS.

	Dilatational wave functions	Rotational wave functions
set 1	$\Psi_{l_1}(\mathbf{x}) = \sin(\mathrm{k_{l_1,x}x})\exp(-\mathrm{jk_{l_1,y}y})$ with $l_1 = 0, 1, \cdots, n_{l_1}$	$\Psi_{t_1}(\mathbf{x}) = \cos(\mathrm{k_{t_1,x}x})\exp(-\mathrm{jk_{t_1,y}y})$ with $t_1 = 0, 1, \cdots, n_{t_1}$
	$\Psi_{l_2}(\mathbf{x}) = \exp(-\mathrm{jk_{l_2,x}x})\sin(\mathrm{k_{l_2,y}y})$ with $l_2 = 0, 1, \cdots, n_{l_2}$	$\Psi_{t_2}(\mathbf{x}) = \exp(-\mathrm{jk_{t_2,x}x})\cos(\mathrm{k_{t_2,y}y})$ with $t_2 = 0, 1, \cdots, n_{t_2}$
set 2	$\Psi_{l_1}(\mathbf{x}) = \cos(\mathrm{k_{l_1,x}x})\exp(-\mathrm{jk_{l_1,y}y})$ with $l_1 = 1, \cdots, n'_{l_1}$	$\Psi_{t_1}(\mathbf{x}) = \sin(\mathrm{k_{t_1,x}x})\exp(-\mathrm{jk_{t_1,y}y})$ with $t_1 = 1, \cdots, n'_{t_1}$
	$\Psi_{l_2}(\mathbf{x}) = \exp(-\mathrm{jk_{l_2,x}x})\cos(\mathrm{k_{l_2,y}y})$ with $l_2 = 1, \cdots, n'_{l_2}$	$\Psi_{t_2}(\mathbf{x}) = \exp(-\mathrm{jk_{t_2,x}x})\sin(\mathrm{k_{t_2,y}y})$ with $t_2 = 1, \cdots, n'_{t_2}$

functions in the weighting expansions. Introducing the weighting expansion in the weighted residual formulation (12) leads to a small, but dense, complex and non-symmetric system of equations. Solving that system leads to the unknown wave contribution factors w_l and w_t. Backsubstitution of those contribution factors in the field variable expansion (5) leads to an analytical approximation of the sought displacement field.

III. A multi-level modelling concept in Wave Based modelling

The WBM has shown to be a very efficient modelling technique for the analysis of 2D elastodynamic problems [6]. However, when the problem geometry becomes more complicated, the efficiency of the method tends to deteriorate. This is due to the fact that the entire problem domain, which is modelled using the set of wave function expansions for bounded subdomains given in table I, needs to be partitioned in convex subdomains. As a result, since all the interior details are included within a single partitioning, a complex partitioning of the interior is often needed in order to be able to guarantee the convergence of the method.

A. A multi-level WBM modelling framework for 2D interior and exterior acoustic problems

Recently, the authors have developed a general modelling framework to remedy similar problems which arise when the WBM is applied to the study of 2D exterior acoustic problems [9]. In the case of an unbounded problem, the WBM methodology applies a truncation of the entire domain into a bounded and a (homogeneous) unbounded part through the introduction of a (usually circular shaped) truncation surface Γ_t (see figure 1). The region outside of Γ_t is considered to be a single additional subdomain, within which the field variables are approximated by a special set of unbounded wave functions $\Psi_i^{(ub)}$. These functions do not only satisfy the governing partial differential equation, but also prohibit waves from being scattered back into the computational domain, such that the propagation direction of the resulting approximation field is always outward. For the case of 2D Helmholtz problems with a circular truncation geometry, HERRERA [12] proposes a complete set of expansion functions for the acoustic pressure field exterior to an infinitely long cylinder on which Neumann boundary conditions are applied:

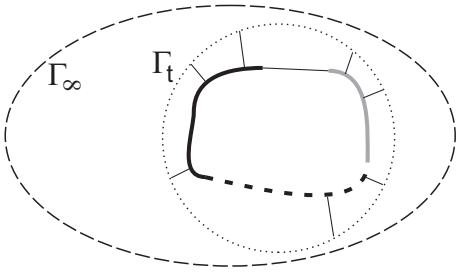

Fig. 1. General WBM modelling strategy for unbounded problems.

$$\Psi_i^{ub}(r,\theta) = \begin{cases} \Psi_{i_c}^{ub}(r,\theta) = H_n^{(2)}(kr)\cos(n\theta) \\ \Psi_{i_s}^{ub}(r,\theta) = H_n^{(2)}(kr)\sin(n\theta) \end{cases} \tag{13}$$

with $n = 0, 1, 2, \ldots$, r and θ the polar coordinates defined by the cylinder and $H_n^{(2)}(\bullet)$ the n-th order Hankel function of the second kind.

The modelling problems arising from this strategy are twofold. On one hand, when multiple acoustic scatterers are present in the problem, the circular truncation line Γ_t needs to enclose all the scatterers at once. As a result many unbounded wave functions need to be included in the model in order to accurately couple the expansions in the bounded and unbounded subdomains with similar spatial resolution. On the other hand, the fact that all the scatterers are included within a single circle results in a complex partitioning of the interior, which is exactly the same problem as described above for the 2D elastodynamic case.

The main idea of the multi-level WBM approach is to consider the multiple objects in the problem as being part of multiple 'levels' of the problem. In every level, the dynamic behaviour of one single object is studied. The incident field for this problem is composed of not only the truly imposed external excitations but also the scattered field from the other objects. Mathematically, this influence is described by adding the unbounded expansions associated to all involved levels as perturbation to the boundary fields on the truncation circles of each level, and by including these terms in the weighted residual formulation. When this is done for all the levels, the mutual interactions between all the submodels are restored and a system of algebraic equations is obtained for the coupled problem composed of all the levels. This system can then be solved to obtain all the unknown weighting factors in the field variable expansions. Using these factors, the scattering field can be calculated in each level. The total resulting field in the regions where the exterior subdomains geometrically overlap is then composed from the superposition of the fields of all levels. This procedure is illustrated graphically in figure 2. Since the incident field on a level is the result of a scattering calculation in the other levels, all the calculations have to be carried out simultaneously.

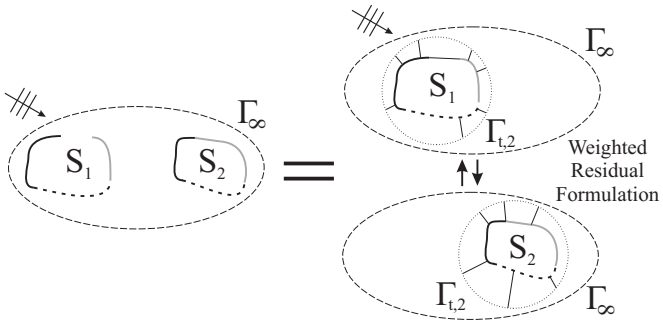

Fig. 2. Graphic representation of the multi-level modelling conceptunbounded

Van Genechten [10] recently successfully explored the possibility to extend the multi-level scattering concept to deal with circular inclusions and other inclusion configurations inside 2D bounded acoustic domains. In order to realise this, an intermediate multi-level model is created which can be used to calculate the scattering of the entire inclusion configuration inside the cavity. This model is constructed by assigning a separate unbounded level to each of the inclusions and by defining a corresponding set of basisfunctions as described above. The finiteness of the actual problem needs to be imposed in order to restrict the solution expansion to the true problem domain and in order to be able to impose the actual boundary conditions on the outer edge of the cavity. This can be done by modelling its interior acoustic behaviour using a standard WBM model of the cavity without the inclusions and then defining this model as a supplementary level in the multi-level WBM model. The field variable expansion of that bounded domain together with the unbounded field variable expansions of the other levels inside the bounded domain, describe the behaviour in the common domain. This procedure is illustrated for a general interior problem containing a single inclusion in figure 3.

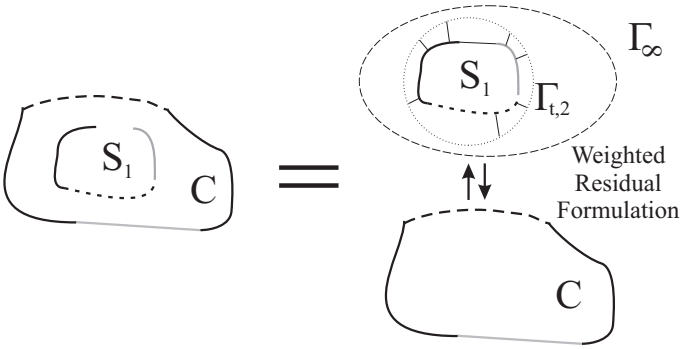

Fig. 3. Graphic representation of the multi-level modelling concept for bounded problems

B. Extension of the multi-level framework to 2D elastodynamic analysis of perforated membranes

As indicated in section II, the Navier system of two coupled partial differential equations can be decoupled by applying a decomposition of the membrane strain field into a dilatational and a rotational component. This results in a system of two uncoupled Helmholtz-equations (2) and (3) with associated wave

numbers k_l and k_t. These two equations can be solved by two independent approximation expansions who interact through the imposed boundary and continuity conditions along the subdomain edges. As a result, the modelling procedure described above for acoustic problems can be readily applied to each of the uncoupled Helmholtz equations governing the two strain components. When one or multiple holes are present in the problem domain, an unbounded level truncation circle is assigned to each of them and the strain field exterior to this circle is modelled using two unbounded wave function sets of type (13). The total set of wave functions in the region between the truncations and the exterior edge of the problem domain is now a superposition of the three types of functions given in table II. For each of the n_L levels L_i inside a bounded subdomain, a set of type UB is added. The total resulting displacement fields can be obtained by applying the displacement differential operators to the new composite set of wave functions:

$$\begin{Bmatrix} w_x \\ w_y \end{Bmatrix} \approx \begin{bmatrix} \mathcal{L}_{w_x} \\ \mathcal{L}_{w_y} \end{bmatrix} \begin{Bmatrix} \sum_{l=1}^{n_l} w_l \Psi_l + \sum_{i=1}^{n_L} \sum_{l=1}^{n_l^i} w_l^{(ub_i)} \Psi_l^{(ub_i)} \\ \sum_{t=1}^{n_t} w_t \Psi_t + \sum_{i=1}^{n_L} \sum_{t=1}^{n_t^i} w_t^{(ub_i)} \Psi_t^{(ub_i)} \end{Bmatrix}. \tag{14}$$

Introducing the field variable expansion (14) in the imposed boundary conditions along the circumscribing edge of the problem and the edges of the holes and applying a Galerkin weighted residual formulation results in a system of algebraic equations governing the weighting factors of all the expansion functions for the full elastodynamic problem.

IV. Numerical example

The potential of the WBM extended with the multi-level concept is demonstrated by means of a numerical validation example. Consider the square plate with 5 circular holes shown in figure 4. The plate is loaded by a unit line load at the top and bottom of the plate and has a thickness of $0.001m$. The material is an aluminium alloy ($E = 70 \cdot 10^9 N/m^2$, $\nu = 0.3$, $\rho = 2,790 kg/m^3$).

The symmetry of the problem makes it possible to model only a quarter of the problem. The resulting problem is a square plate with a circular hole in the middle and a quarter of a circle removed from one corner, see figure 5. It has symmetry boundary conditions at the bottom and left edge and a unit load

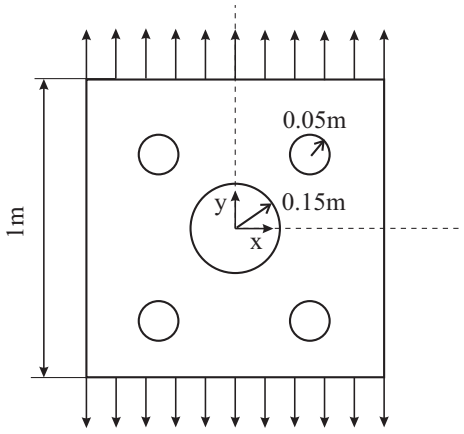

Fig. 4. Square plate with 5 circular holes.

at the top edge. The following response points are considered: $w_1(0.394m, 0.106m)$, $w_2(0.394m, 0.394m)$ and $w_3(0.106m, 0.394m)$. With the traditional WBM

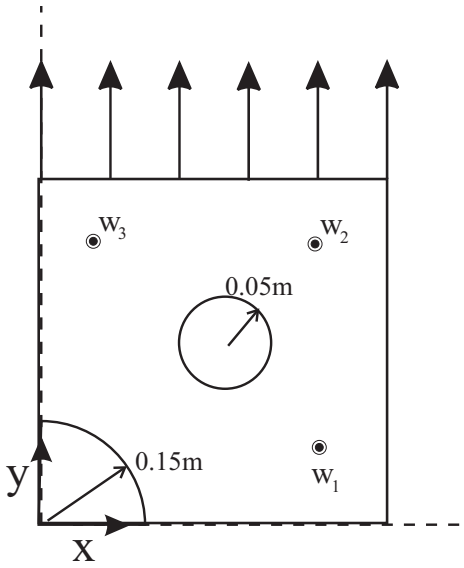

Fig. 5. Quarter segment of the problem.

it would not be possible to model this plate accurately, since it is impossible to divide the problem into convex subdomains. The circular hole and the quarter circle can be approximated by a large number of straight edges, but that would lead to a rough approximation and a large number of subdomains, which compromises the computational efficiency of the WBM. With the multi-level approach, it is possible to use only one bounded and two unbounded domains, which are coupled at the boundaries. One unbounded level is used for the circle and one for the quarter circle. The truncation circle of the unbounded level corresponding to the quarter circle lies partly out of the problem domain. Only the part inside the bounded domain is considered in the weighted residual formulation. It will be shown in this example that that is sufficient

TABLE II
SETS OF WAVE FUNCTIONS FOR MULTI-LEVEL MEMBRANE PROBLEMS.

	Dilatational wave functions	Rotational wave functions
set 1	$\Psi_{l_1}(\mathbf{x}) = \sin(\mathrm{k_{l_1,x}x})\exp(-\mathrm{jk_{l_1,y}y})$ with $l_1 = 0, 1, \cdots, n_{l_1}$ $\Psi_{l_2}(\mathbf{x}) = \exp(-\mathrm{jk_{l_2,x}x})\sin(\mathrm{k_{l_2,y}y})$ with $l_2 = 0, 1, \cdots, n_{l_2}$	$\Psi_{t_1}(\mathbf{x}) = \cos(\mathrm{k_{t_1,x}x})\exp(-\mathrm{jk_{t_1,y}y})$ with $t_1 = 0, 1, \cdots, n_{t_1}$ $\Psi_{t_2}(\mathbf{x}) = \exp(-\mathrm{jk_{t_2,x}x})\cos(\mathrm{k_{t_2,y}y})$ with $t_2 = 0, 1, \cdots, n_{t_2}$
set 2	$\Psi_{l_1}(\mathbf{x}) = \cos(\mathrm{k_{l_1,x}x})\exp(-\mathrm{jk_{l_1,y}y})$ with $l_1 = 1, \cdots, n'_{l_1}$ $\Psi_{l_2}(\mathbf{x}) = \exp(-\mathrm{jk_{l_2,x}x})\cos(\mathrm{k_{l_2,y}y})$ with $l_2 = 1, \cdots, n'_{l_2}$	$\Psi_{t_1}(\mathbf{x}) = \sin(\mathrm{k_{t_1,x}x})\exp(-\mathrm{jk_{t_1,y}y})$ with $t_1 = 1, \cdots, n'_{t_1}$ $\Psi_{t_2}(\mathbf{x}) = \exp(-\mathrm{jk_{t_2,x}x})\sin(\mathrm{k_{t_2,y}y})$ with $t_2 = 1, \cdots, n'_{t_2}$
set UB	$\Psi_{l_1}^{(ub_i)}(\mathbf{r}) = \mathrm{H_n^{(2)}}(\mathrm{k_l r})\cos(\mathrm{n}\theta)$ with $l_1 = 1, \cdots, n_{l_1}^{L_i}$ $\Psi_{l_2}^{(ub_i)}(\mathbf{r}) = \mathrm{H_n^{(2)}}(\mathrm{k_l r})\sin(\mathrm{n}\theta)$ with $l_2 = 1, \cdots, n_{l_2}^{L_i}$	$\Psi_{t_1}^{(ub_i)}(\mathbf{r}) = \mathrm{H_n^{(2)}}(\mathrm{k_t r})\cos(\mathrm{n}\theta)$ with $t_1 = 1, \cdots, n_{t_1}^{L_i}$ $\Psi_{t_2}^{(ub_i)}(\mathbf{r}) = \mathrm{H_n^{(2)}}(\mathrm{k_t r})\sin(\mathrm{n}\theta)$ with $t_2 = 1, \cdots, n_{t_2}^{L_i}$

and that it does not disturb the convergence of the method.

A. Steady-state elastodynamic models

The validation example in figure 5 is modelled using both linear and quadratic FE models and a number of multi-level WB models.

A.1 WB models

The WB models do not require a rediscretisation in order to refine the model. The perforated membrane in figure 5 can, as mentioned before, be modelled by constructing a multi-level WB model which combines a single square bounded subdomain and 2 unbounded levels. A variation of the truncation parameter T can be used to create several WB models with different numbers of structural WB degrees of freedom (dofs) for the bounded subdomain. The number of unbounded functions in the unbounded levels is chosen such that the spatial resolution of the bounded and unbounded wave functions are approximately the same.

A.2 FE models

In order to study the convergence behaviour of the FEM the perforated membrane is modelled using both linear and quadratic FEM models. The linear models use 4-noded quadrilateral elements to discretise the problem domain, while the quadratic FE models are built using 8-noded quadrilateral membrane elements. A baseline model with an average discretisation dimension $h \approx 0.025m$ is continuously refined in order to generate all the models, the details of which are given in table III. The most detailed quadratic FE model (model number 7) serves as a reference solution when comparing the computational accuracy of the different models at a single frequency. In table III h_{max} is the length of the longest side of a finite element in the discretisation, and t_{solve} is the frequency-independent CPU time needed to solve the different models for a single frequency. The commercial FEM software MD.Nastran r3b is used to carry out the FEM analyses and all calculations are performed on a 2.66GHz Intel Xeon based Linux-system with 32 gigabytes of RAM.

B. Numerical results and comparison with FEM

To illustrate that the multi-level extension of the Wave Based Method describes the elastodynamic membrane behaviour accurately, figure 6 shows a contour of the structural forced displacement amplitude at $18.4kHz$ obtained using both quadratic FE model

TABLE III
PROPERTIES OF THE VARIOUS FE MODELS

		Linear FE models		Quadratic FE models	
Model number	h_{max} $[m]$	$dofs$ $(= 2 \times \#nodes)$	t_{solve} $[s]$	$dofs$ $(= 2 \times \#nodes)$	t_{solve} $[s]$
FE 1	0.02500	4.484	0.03	13.282	0.17
FE 2	0.01000	13.560	0.13	40.382	0.67
FE 3	0.00750	24.114	0.24	71.942	1.37
FE 4	0.00500	54.322	0.69	162.366	4.07
FE 5	0.00250	216.086	4.09	647.054	26.0
FE 6	0.00100	1.346.018	49.2	4.035.038	395.0
FE 7	0.00050	5.371.238	389.2	16.107.678	3572.7

6 (4.035.038 dofs) and a multi-level WBM model containing only 406 basisfunctions in the displacement expansion (188 bounded and 40 unbounded dilatational dofs and 116 bounded and 62 unbounded rotational wave functions). The results show that the multi-level WBM is capable of accurately describing the spatial distribution of the dynamic displacement field within the perforated membrane.

In order to compare the computational efficiency of the multi-level WBM and the FEM in both the low- and mid-frequency range, a convergence analysis is performed. For all the models described in section IV-A, the forced structural displacements at $1kHz$, $8.75kHz$ and $25.75kHz$ are calculated in the three response points indicated in figure 5. The first frequency is in the low-frequency range, the second one is in the region where the low- and mid-frequency range overlap and the third one is far within the mid-frequency range. Based on the calculated displacement values, the average relative prediction error ϵ for the forced response amplitude is defined as:

$$\epsilon = \frac{1}{3}\sum_{j=1}^{3}\epsilon_j = \frac{1}{3}\sum_{j=1}^{3}\left|\frac{W_{model}(\mathbf{r_j}) - W_{ref}(\mathbf{r_j})}{W_{ref}(\mathbf{r_j})}\right|, \quad (15)$$

with $W_{model}(\mathbf{r_j})$ the calculated displacement amplitude and $W_{ref}(\mathbf{r_j})$ the reference displacement amplitude at each of the response locations $\mathbf{r_j}$ and the displacement amplitude defined as $W_\bullet = \sqrt{w_{\bullet,x}^2 + w_{\bullet,y}^2}$. These results are plotted against the CPU times needed to solve the different models. Only frequency dependent operations are taken into account in the calculation time. That means that for the FEM only the time needed to solve the system of equations is given, and for the WBM the time needed to build the WB system matrix as well as the time needed to solve the system of equations are given. The time to build the FE matrices is not taken into account for

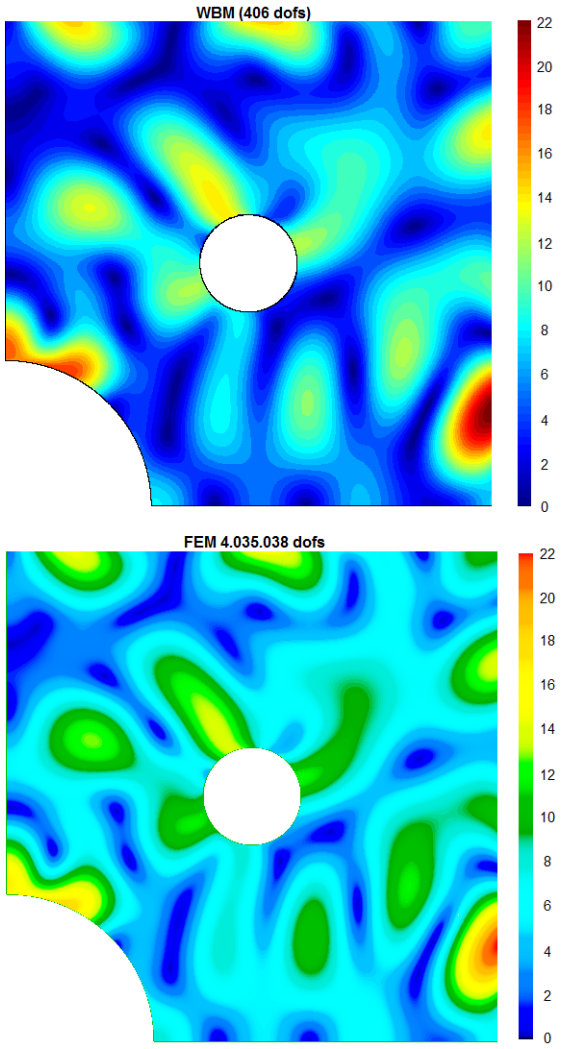

Fig. 6. Forced displacement amplitude $[10^{-9}m]$ at $18.4kHz$ predicted by the WBM (top) and FEM (bottom)

the FEM, since this effort is frequency independent and negligible when a large number of frequencies are considered.

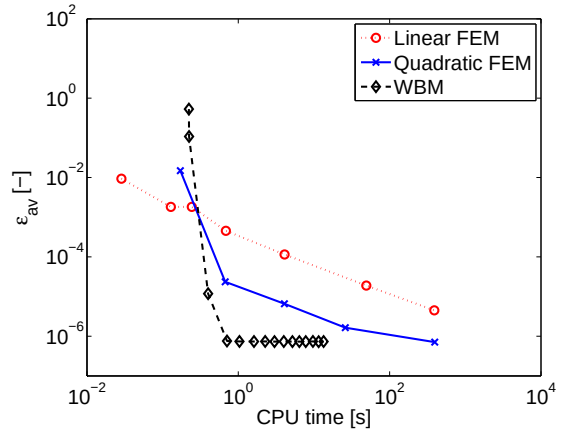

(a)$1kHz$

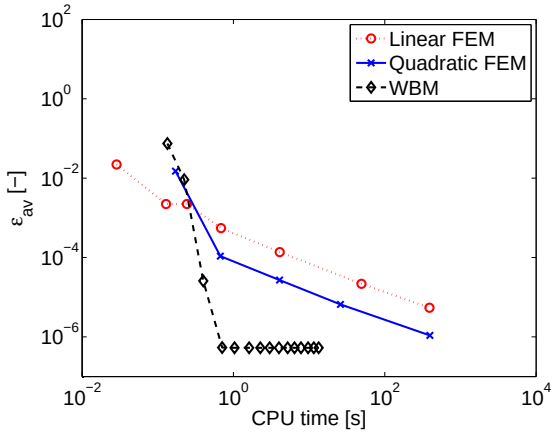

(b)$8.75kHz$

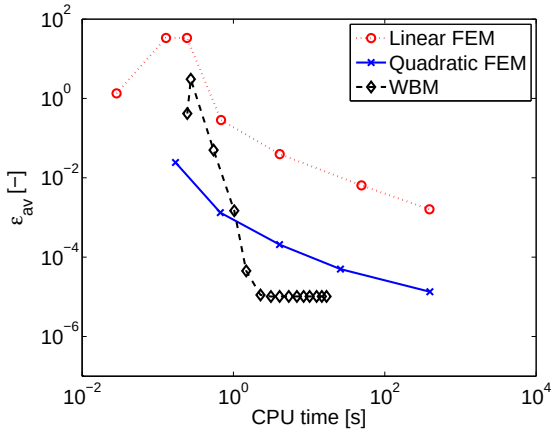

(c)$25.75kHz$

Fig. 7. Convergence curves for the linear and quadratic FEM and WBM with FE quadratic model 7 as reference.

Figures 7(a)-7(c) compare the convergence rate of the different WB models with that of the FE models in the low- and mid-frequency range. Each subfigure plots the global convergence curve for the quadratic FEM ($\times$ marker), the linear FEM ($\circ$ marker) and the WBM ($\diamond$ marker). The global curves for the FEM are obtained by incrementally refining the structural elements in the model. The convergence curves for the WB models are calculated by using an increasing number of wave functions (ranging from 36 till 1508 dofs) to model the structural displacement field field.

For the three frequencies shown here, the WB models converge faster to a certain prediction accuracy as compared to both the linear and quadratic FE models. Both the linear and quadratic models show an (almost) monotonic convergence behaviour. The WB convergence curves show a very steep decline, but stabilise at a fixed prediction accuracy of 10^{-5} to 10^{-6} depending on the frequency of interest. This type of convergence behaviour is typically seen when the model which is used as a reference solution has not yet converged to a better accuracy than the model with which it is compared. To prove that this is the case, figure 8 shows the convergence curves for the FEM and multi-level WBM methods at $8.75kHz$ which are obtained when the finest WBM prediction result is used as reference solution. The FEM convergence curves remain unchanged while the WBM curve no longer saturates but reaches a prediction accuracy of 10^{-11} in approximately 3 cpu seconds. These results show that the multi-level WB performs better clearly better than the quadratic and the linear FEM in both the low- and mid-frequency range.

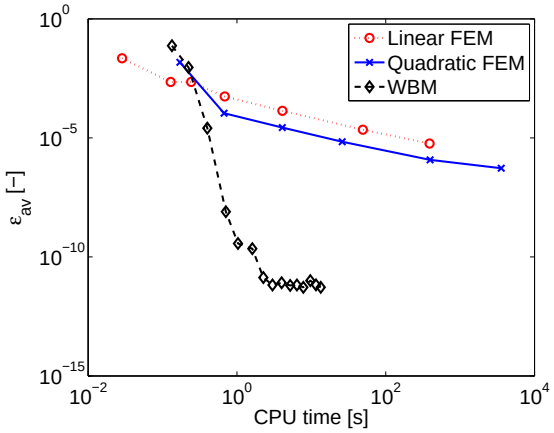

Fig. 8. Convergence curves for the linear and quadratic FEM and WBM at $8.75kHz$ with a WB model as reference.

V. Conclusions

This paper discusses a new multi-level modelling framework, aimed to alleviate or remove some of the geometrical constraints faced when applying the

WBM for the study of the dynamic behaviour of perforated membranes. The main idea of the approach is to consider the multiple objects in a problem as different 'levels' of the problem. Each level considers the reflection and scattering on the boundaries of one particular object, using existing WBM techniques for bounded and unbounded problems. A special compound wave function set and an adapted weighted residual formulation link the different levels together, yielding a single multi-level system, describing the entire problem.

The new method is validated based on the study of a quarter segment of a symmetric square plate with 5 holes, indicating both the excellent accuracy and the superior numerical performance as compared to classical element-based numerical modelling techniques. This reduction in computational load makes the WBM particulary suited for the treatment of membranes with multiple perforations in an extended frequency range, as compared to the element based methods.

In the future, this methodology will be applied to more complex membrane problems such as multi-material aggregates in an elastic material and wave propagation problems in unbounded solid media. Also, the general modelling framework will be extended to cope with the influence of perforations on the out of plane bending behaviour of (networks of) flat plates.

Acknowledgements

Karel Vergote and Bert Van Genechten are Doctoral Fellows of the Fund for Scientific Research - Flanders (F.W.O.), Belgium.

References

[1] O.C. Zienkiewicz and R.L. Taylor. *The finite element method - The three volume set (6th ed.)*. Butterworth-Heinemann, 2005.

[2] R.H. Lyon and R.G. DeJong. *Theory and application of statistical energy analysis (2nd ed.)*. Butterworth-Heinemann, 1995.

[3] P. Bouillard and F. Ihlenburg. Error estimation and adaptivity for the finite element method in acoustics: 2d and 3d applications. *Computer Methods in Applied Mechanics and Engineering*, 176:147–163, 1999.

[4] W. Desmet. *A wave based prediction technique for coupled vibro-acoustic analysis*. PhD thesis 98D12, K.U.Leuven, dept. of Mechanical Engineering, Leuven, 1998.

[5] E. Trefftz. Ein gegenstück zum ritzschen verfahren. In *Second International Congress on Applied Mechanics*, pages 131–137, Zürich, Switserland, 1926.

[6] C. Vanmaele. *Development of a wave based prediction technique for the efficient analysis of low- and mid-frequency structural vibrations*. PhD thesis 2007D11, K.U.Leuven, dept. of Mechanical Engineering, Leuven, 2007.

[7] C. Vanmaele, D. Vandepitte and W. Desmet. An efficient wave based prediction technique for plate bending vibrations *Computer Methods in Applied Mechanics and Engineering*, 196:3178–3189, 2007.

[8] K. Vergote, C. Vanmaele, D. Vandepitte and W. Desmet. On the use of an efficient wave based method for steady-state structural dynamic analysis. In *Proceedings of the 5th International Workshop on Trefftz Methods (Trefftz.08)*, Leuven, Belgium, pages 433–459,2008.

[9] B. Van Genechten, B. Bergen, B. Pluymers, D. Vandepitte, and W. Desmet. A novel modelling approach for sound propagation analysis in a multiple scatterer environment. *Journal of the Acoustical Society of America (JASA)*, 132:3757, 2008.

[10] B. Van Genechten, B. Bergen, D. Vandepitte, and W. Desmet. A novel wave based modelling approach for the mid-frequency analysis of helmholtz problems with multiple inclusions. In *Proceedings of Noise and Vibration: Emerging Methods (NOVEM2009)*, Oxford, UK, 2009.

[11] J. Dominguez. *Boundary Elements in Dynamics*. Computational Mechanics Publications, 1993.

[12] I. Herrera. *Boundary Methods: an Algebraic Theory*. Pitman Adv. Publ. Program, London, 1984.

Proceedings of the 8th National Congress on Theoretical and Applied Mechanics, May 28-29, Brussels, Belgium.

Conceptual design of a PEM fuel cell powered unmanned aerial vehicle

D. Verstraete, J. Steimes, O. Watteeuw and P. Hendrick
Université Libre de Bruxelles, Aero-Thermo-Mechanics Laboratory
Avenue F.D. Roosevelt 50 (CP 165/41)-1050 Brussel
email: Dries.Verstraete@ulb.ac.be, Johan.Steimes@ulb.ac.be,Olivier.Watteeuw@ulb.ac.be,
Patrick.Hendrick@ulb.ac.be

Abstract— **Fuel cells offer several advantages for the propulsion of small aircraft. For unmanned aerial vehicles their main benefits result from the reduced thermal signature and the possibility to increase range or endurance with only a relatively small mass penalty. However, due to the need for a completely electrical propulsion system, several challenges arise from the adoption of fuel cells as well.**

This paper describes the first design steps of a (relatively) small unmanned technology demonstrator aircraft with fuel cell propulsion. In a first section of the paper the specifications adopted for the design mission are laid down. Then, the determination of the drag and mass of the aircraft are reported. After this, the modeling of the propulsive chain is detailed. Finally, the design point for the wing of the unmanned aircraft is selected in a parametric study and its characteristics are described.

Keywords— **fuel cells, unmanned aerial vehicle, conceptual design**

I. Introduction

DUE to their potentially high specific energy, high efficiency and rapid refuelability Proton Exchange Membrane (PEM) Fuel Cells (FC) are increasingly considered for the propulsion of small manned and unmanned aircraft (see [1], [2], [5] and [7]). PEM fuel cells additionally offer a reduced thermal signature, less noise and a reduced environmental impact. The use of PEM fuel cells as the main power source for aircraft however also entails several challenges, mainly related to the relatively low power density, even for state-of-the art fuel cells. The resulting high weight of the fuel cell constraints the design space of the aircraft and might limit its performance. The adoption of a fuel cell as the main power source furthermore involves a completely new electrical power train for the aircraft and thereby changes the design of the aircraft significantly.

To gain insight in the consequences and challenges of adopting fuel cells as an aviation power source, the Aero Thermo Mechanics Laboratory of the Université Libre de Bruxelles has started the design of a demonstrator fuel cell powered UAV. The main research objectives of the current work are the development of accurate and validated models and tools for the design of fuel cell powered aircraft as well as the construction, flight testing and demonstration of a FC powered UAV. The UAV platform has been chosen for this work because of the large number of potential applications and its suitability in scale and cost for an academic research program. The UAV will be built around a 300 W PEM FC from Horizon Fuel Cells (see Fig. 1).

Fig. 1. The 300 W PEM FC from Horizon Fuel Cells

As it forms the cornerstone of any aircraft design, the first section of this paper details the specifications and the mission for which the UAV is designed. A second section of the paper then describes the determination of the mass and drag of the UAV components as well as the adaptations made to correlate with data on existing UAVs. Then, the modeling of the electrical components of the propulsive chain is addressed. Before concluding the selection of the design point of the wing of the aircraft is detailed and the characteristics of the UAV are reported.

II. Design specifications

REDUCING the required power is critical for a FC UAV as the design has to be centered around the available fuel cell. As stated previously, the Horizon Fuel Cells 300 W PEM FC is chosen as the powerplant for this specific UAV. The FC was selected for its relatively high power density, its autonomous air system and its fairly low price. As the air supply system is autonomous, no compressor is needed for low altitude flight which greatly simplifies the FC balance of plant and significantly reduces the weight of the complete power system. For the hydrogen system, high pressure storage is the preferred option for this type of application to reduce the volume of the tank. A pressure regulator is therefor mandatory. As the fuel cell needs to be purged on a regular basis, it does not supply its nominal power continuously. A backup battery

is thus foreseen which also serves as power booster to reduce the runway length at takeoff and to accelerate climb to the cruising altitude. The weight and dimensions of several of the main components are specified in Table I. As shown in [10], the fuselage is designed to provide sufficient space to fit the components and to minimize drag, leading to a fuselage length around 1.2 to 1.5 m (for one respectively 2 FC) and a thickness to length of about 23%.

TABLE I
COMPONENT SPECIFICATIONS.

Component	Dimensions [mm]	Mass [g]
Payload	$50 \times 50 \times 50$	200
Receiver	$46 \times 33 \times 32$	20
Fuel Cell	$220 \times 110 \times 70$	1700
Pressure Regulator	$50 \times 50 \times 50$	200
Batteries	$50 \times 45 \times 60$	310
Hydrogen Tank	$200 \times 50 \times 50$	870
Controller	$50 \times 50 \times 20$	25
Motor	$73 \times 65 \times 65$	400

Seen the limited available power, relatively modest requirements are imposed for the aircraft performance. A cruise altitude of 300 m is selected to avoid the need for an air compressor. The cruise speed is on the other hand fixed to 50 km/hr whereas the loiter and climb phase speed are set to 45 km/hr to limit the required power. The UAV is designed to climb to its cruising altitude in 5 minutes and stay aloft for about one hour.

III. DRAG AND MASS CALCULATION

IN the conceptual design of a FC UAV, the selection of correlations that are adapted to this specific class of aircraft is critical. As most correlations for both mass as well as drag estimation in the conceptual / preliminary design phase are statistically derived, they can only be applied to the specific class of aircraft for which they have been determined. However, as far as construction methods are concerned, the UAV class resembles general aviation aircraft quite closely. According to [3] the methods for general aviation aircraft can thus readily be applied to UAVs with a relatively high level of confidence, on condition that proper 'tuning' is performed based on available data on similar UAVs. This data was obtained from the FC UAV designed by Georgia Tech [2], and the methods have been correlated to this design as a validation. Below some specifics of the adopted correlation procedure for both drag and mass are given. More information can be found in [9] and [10].

For drag calculations conventional component drag correlations are used:

$$C_{D,0} = C_f \cdot F \cdot Q \cdot \frac{S_{wet}}{S_{ref}} \tag{1}$$

where $C_{D,0}$ is the component zero-lift drag coefficient, C_f is the flat plate skin friction coefficient, F is a form factor to account for the shape of the specific component and Q is an interference factor. S_{wet} and S_{ref} denote the wetted area of the component and the reference area which is taken here as the wing planform area. Form factors F can be found in several references (amongst others [4], [6] and [8]). Here, the correlations from [4] are adopted.

The main uncertainty in adopting this method lies in the determination of the skin friction coefficient C_f as its value depends on the level of laminar flow on the component. Calculations on the Georgia Tech UAV however showed that laminar flow can be assumed for the complete wing whereas for the fuselage, turbulent flow has been assumed in order to be (slightly) conservative. To ensure that the assumption of laminar flow over the wing remains valid for the complete design space under investigation, an upper limit on the wing chord is nevertheless imposed.

The component mass calculation is one of the most critical aspects in the conceptual UAV design, especially for this particular UAV seen the high mass of the FC and the large wing area that is required as a consequence of this high mass. Special attention was therefore paid to the adaptation of the component mass calculations. As suggested in [3], the correlations for general aviation aircraft are adapted to this particular class of UAV. To do so it is assumed that the correlation correctly represents the trend of the component mass to its main characteristics. A fudge factor is consequently used to adapt the correlation to the available data. This is shown below for the wing mass where the following correlation is adopted [6]:

$$W_w = U_w \cdot S_{w,\,exp} \cdot \left(\frac{t}{c}\right)_r^{-0.4} \cdot AR_w^{0.5} \tag{2}$$

where W_w is the wing mass, $S_{w,\,exp}$ is the exposed wing area, $(t/c)_r$ is the thickness-to-chord ratio at the wing root and AR_w is the wing aspect ratio. U_w is the wing mass fudge factor which is determined based on the wing mass of the Georgia Tech FC UAV [2]. For the other aircraft components a similar practice is adopted, as detailed in [10].

IV. PROPULSIVE CHAIN

ELECTRICAL propulsion for aircraft requires a redesign of the complete propulsive chain. An extensive study to model each of the main components of this chain is therefore performed in the early phases of the study. All in all, each of the selected components must

be compatible with the chosen fuel cell. A proper selection furthermore allows to avoid the need for a reduction gearbox as its use leads to a significant reduction in efficiency of the overall propulsive chain. The main elements of the chain are indicated on Figure 2.

Fig. 2. The elements of the propulsive chain

For each of these elements, except the hydrogen tank, a representative electrical model was set up to allow the analysis of the behavior of the complete propulsion system and the selection of the most suited components. This lead to the schematic given on Figure 3.

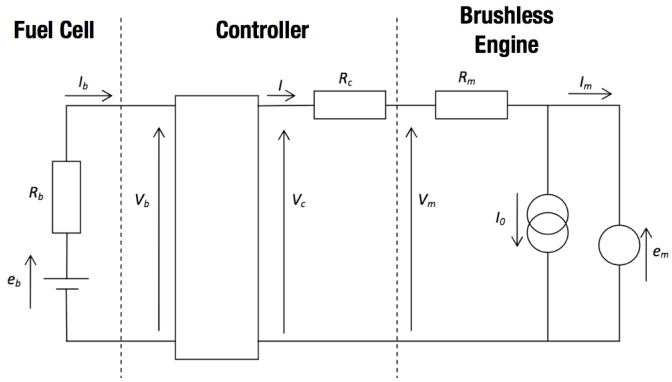

Fig. 3. Schematics of the main propulsive elements

Based on this electrical schematic, the following expression has been derived for the efficiency of the complete propulsive chain η_{tot}:

$$\eta_{tot} = \frac{C_{PWM} \cdot V_b - \frac{C_m + C_R}{K} \cdot (R_C + R_m) \cdot \frac{C_m}{K}}{e_b \cdot \frac{C_m + C_R}{K} \cdot C_{PWM}} \qquad (3)$$

where C_{PWM} is the pulse width modulation signal of the engine (controller), which sets the engine rating. C_m and C_R denote the engine and resisting (propeller) torque. R_C and R_M are the controller and engine internal resistance, and K is the equivalent of the engine K_v value (RPM/V) which determines the engine rotational speed for a given input voltage. K is used in the expression rather than K_v to indicate that the units have been adapted to rad/s/V. The other parameters of equation (3) are indicated on Figure 3.

For this particular application, seen the high input voltage of the FC, an engine with a low K_v was selected. As such a gearbox between the engine and the propeller is avoided, as this is a component with a fairly low efficiency. The Cyclon 110 engine is for this reason selected as it has a K_v of only 195 RPM/V. The engine is shown on Figure 4.

The Cyclon 110 has a nominal power of 1400 W, a mass of 400 g and an efficiency (according to the specs) of 91%.

Fig. 4. The Cyclon F3A and the Cyclon 110 engine

With the developed model and the pulse width modulation signal a set of propellers was tested analytically to determine the range of diameters and pitches that was appropriate for the UAV. In a first step, a 24 × 22 propeller (diameter × pitch) was analyzed. After all, the propeller adopted by Georgia Tech for their FC UAV had those dimensions [2]. However, the investigations showed, that for a systems with 2 FC in parallel and 1 engine and propeller, propellers around 15 × 13 were more appropriate. This is indicated on Figure 5. The red lines on the figure indicated the engine power for different PWM signals (position of the throttle at 20, 40, 60, 80 and 100%). The green line indicates the power available from the 2 FCs in parallel whereas the blue lines represent two different propellers with the same diameter but with a different pitch.

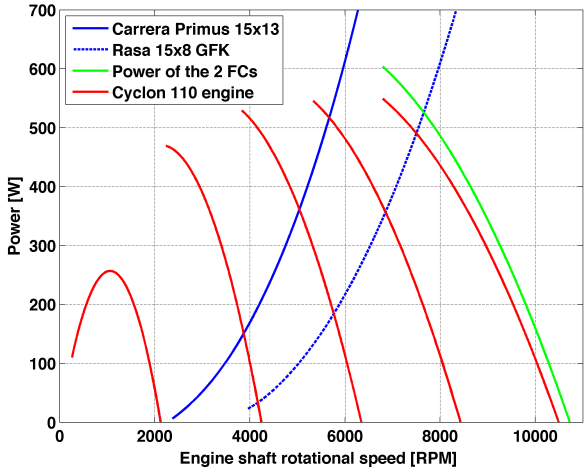

Fig. 5. Matching of the propellers with FC and engine

Based on this theoretical model, 3 different propellers were purchased and consequently tested in a wind tunnel. Even though a test bench for the Horizon 300 W FC is available, the engine propeller combinations were initially tested in combination with 10 LiPo batteries as this allowed an easier first integration. Tests were performed at different air speeds to derive the influence of the flight

speed. Figure 6 shows the results for an airspeed of 15 m/s for 3 different propellers of similar size.

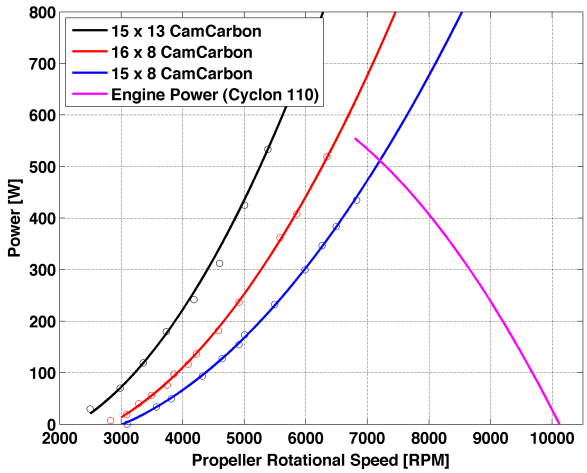

Fig. 6. Propeller - engine tests at an airspeed of 15 m/s

As the measurements of the propeller performance were made fairly rapidly with a low accuracy measurement system, more detailed measurements are in progress at the moment.

V. Selection of the final design point

SINCE the efficiency of the propulsive chain has been determined in the previous section, the final design point of the UAV can be selected now by an iteration on the design process. In a first step, the dimensions of the fuselage are re-determined. After all the fuselage needs to accommodate all the components specified in Table I as tightly as possible while yielding an external shape that leads to a fairly low drag. The positioning of the components is additionally restricted for reasons of control of the center of gravity of the aircraft as well as the logical order of the elements in the propulsive chain. All these considerations lead to the internal positioning of the components as shown on Figure 7 and a fuselage total length is around 1.5 m as indicated previously.

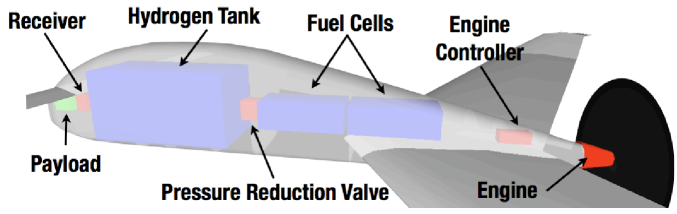

Fig. 7. Positioning of the components in the fuselage

Based on these fuselage dimensions, the design characteristics of the aircraft are determined through an iterative process as indicated on Figure 8. Starting from the data input (fuselage dimensions and shape, position of the components, design speeds, ...), a wing parametric study is executed to determine the optimum aspect ratio and area of the wing. After all the selection of a proper wing area is especially crucial for this design seen the high mass of the fuel cells which leads to a high overall aircraft mass. For each imposed combination of wing size and aspect ratio, the remaining UAV characteristics are determined. As shown on Figure 8, an iteration is made on the longitudinal wing position to obtain a proper longitudinal static margin. More information on the design process and the validation based on the characteristics of the Georgia Tech UAV can be found in [10].

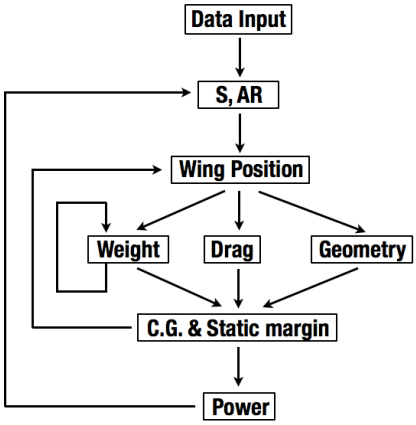

Fig. 8. Positioning of the components in the fuselage

This wing parametric study was executed for a conventional and a canard aircraft configuration. The results for the canard aircraft can be found on Figure 9. For the results of the conventional configuration the reader is referred to [10]. The red lines on Figure 9 indicate the span of the UAV. The green lines on the other hand show its mass, whereas the magenta lines represent the power margin in climb, which is defined as ratio of the power available at the propeller to the power required for climb. A similar power ratio is defined for cruise (full black lines) and for loiter (dashed black lines).

The shaded areas on Figure 9 represent limits imposed on the design. Besides a Reynolds number limit of 275000 to prevent a too high wing drag, the main limits are applied to the previously defined power ratios to ensure sufficient performance and power throughout the flight. For cruise and climb a power margin of 4 is imposed in order to have a sufficiently large range of flight speeds around the design speed. For climb, the power margin is reduced in order not to overly restrict the design space. A minimum margin of 2.5 is therefore adopted. Finally, the lift coefficient of the main wing is limited to 1. This fairly low limit is taken

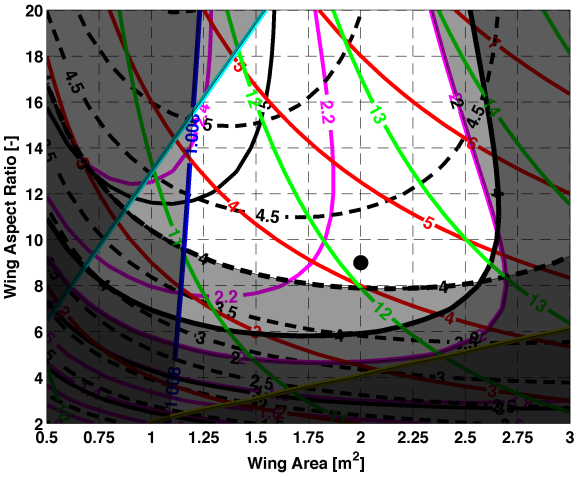

Fig. 9. Wing parametric study

to ensure that the canard will stall before the wing as this leads to a stable (nose down) stall behavior.

Taking all aforementioned constraints into consideration, the final design point of the wing of the canard configuration is selected at

$$S_w = 2 \qquad AR_w = 9$$

with the corresponding characteristics given in Table II.

TABLE II
CHARACTERISTICS OF THE FC UAV.

Characteristic	Value
Wing Area [m^2]	2
Wing Aspect Ratio [–]	9
Wing Span [m]	4.24
Wing Chord [m]	0.47
UAV Mass [kg]	12.14
Horizontal Tail Area [m^2]	0.14
Vertical Tail Area [m^2]	0.72
Cruise Power [W]	125

Figure 10 shows the layout of the canard FC UAV. As can be seen from the Figure the wing is swept back 25° to increase the tail arm for the vertical tail thereby reducing the size of the tails. The sweep angle is selected as a compromise between vertical tail size and weight and wing weight (which increases with increasing sweep). The vertical tail surfaces are furthermore located on the wing tips as this leads to several synergies. Not only will the tails function as winglets, reducing the strength of the wing tip vortices and hence the induced drag, the rudder surface area will also be reduced as the control surfaces will have the highest possible moment arm. Finally, the main landing gear will be integrated in the vertical tails to reduce its drag. After all, the landing gear struts contribute significantly to the drag of small size aircraft.

VI. CONCLUSIONS

This paper presents the first steps in the design of an unmanned aerial vehicle using fuel cells for its propulsion. The paper describes the design mission, the modeling of the UAV drag and weight as well as the electrical components of the propulsive chain. Based on the outcome of this modeling, a wing parametric study for a canard configuration is presented and the characteristics of the final design point are detailed.

As the paper only presents the very first steps in the design process, several more detailed studies are ongoing at the moment or will be undertaken in the near future. A full blown CFD study will be undertaken to finalize details of the wing and wing-body transition. Once these details are fixed a scale model will be constructed and tested in a wind tunnel. An in-depth stability assessment will be made to ensure adequate longitudinal and lateral stability of the UAV both statically as well as dynamically. Finally, measurements of the propeller characteristics to refine the model of the propulsive chain will also be made and the complete integrated propulsion system will be tested. Based on the outcome of these analyses the design process will be reiterated and the final configuration of the UAV will be constructed and flight tested.

REFERENCES

[1] S. Atreya, M. Mata and R. Jones, Power System Comparisons for a High Altitude Long Endurance (HALE) Remotely Operated Aircraft (ROA), *AIAA 5th Aviation, Technology, Integration and Operations Conference (ATIO)*, Arlington, Virginia, USA, September 2005.

[2] T. Bradley, B. Moffitt, R. Thomas and D.E. Parekh, Test Results for a Fuel Cell-Powered Demonstration Aircraft, *Society of Automotive Engineers Power System Conference*, New Orleans, Louisiana, USA, November 2006.

[3] A.J. Chaput, *Conceptual Design of UAV Systems*, Aerospace Short Course, University of Kansas, Continuing Education, Washington D.C., USA, August 2007.

[4] D. Corke, *Design of Aircraft*, Prentice Hall, 2002.

[5] M. Friend and D. Daggett, Fuel Cell demonstrator Airplane, *AIAA/ICAS International Air and Space Symposium and Exposition: The Next 100 years*, Dayton, Ohio, USA, July 2003.

[6] D. Raymer, *Aircraft Design: A Conceptual Approach*, Third Edition, AIAA Education Series, 1989.

[7] G. Romeo, I. Moraglio and C. Novarese, ENFICA-FC: Preliminary Survey & Design of 2-Seat Aircraft Powered by Fuel Cemms electric Propulsion *7th AIAA Aviation Technology, Integration and Operations Conference (ATIO)*, Belfast, Northern Ireland, September 2007.

[8] J. Roskam, *Airplane Design Part I: Preliminary Sizing of Airplanes*, DARCorporation, 1997.

[9] J. Steimes, *Développement d'un drone démonstrateur avec propulsion par pile à combustible: conception du drone*, M.Sc. Thesis, Université Libre de Bruxelles, Brussels, Belgium, June 2008.

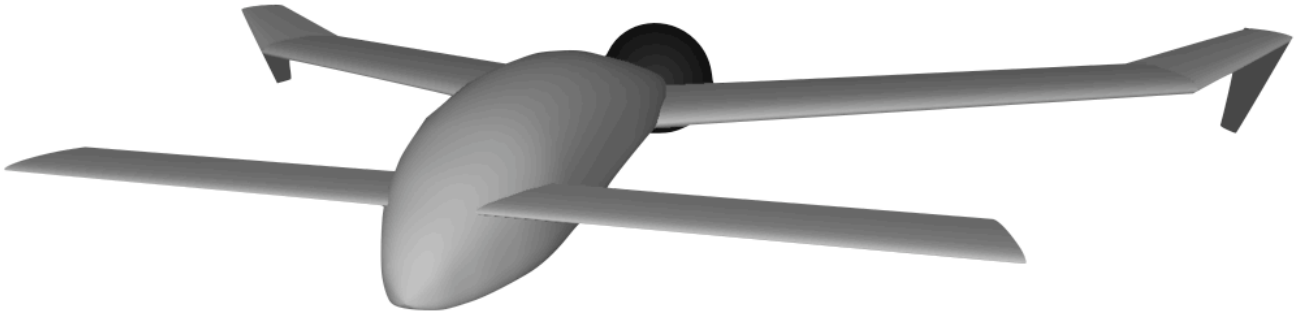

Fig. 10. Layout of the final UAV

[10] J. Steimes, P. Hendrick and D. Verstraete, Conceptual design of a demonstrator Fuel Cell UAV, *International Symposium on Light Weight Aerial Vehicle Systems and Subsystems*, Oostende, Belgium, March 2009.

[11] O. Watteeuw, *Développement d'un drone démonstrateur avec propulsion par pile à combustible: conception du système électrique*, M.Sc. Thesis, Université Libre de Bruxelles, Brussels, Belgium, June 2008.

Proceedings of the 8th National Congress on Theoretical and Applied Mechanics, May 28-29, Brussels, Belgium.

Chip Formation in Micro-milling

F. Ducobu, E. Filippi, E. Rivière-Lorphèvre
Service de Génie Mécanique, Faculté Polytechnique de Mons
Rue du Joncquois 53, B-7000 Mons - Belgium
Email: Francois.Ducobu@umons.ac.be, Enrico.Filippi@umons.ac.be, Edouard.Riviere@umons.ac.be

Abstract— **In the current context of miniaturisation, micro-machining processes are in full expansion. One of them is micro-milling, able to produce parts with features ranging from several** mm **to several** µm**.**
Despite the down-sizing of the macro-milling process, micro-cutting is not a simple scaling-down of macro-cutting. The new way of forming chips involves the so-called 'minimum chip thickness' phenomenon, below which no chip is formed. Estimating the minimum chip thickness value is one of the main challenges in micro-milling. A review of the current state-of-the-art in chip formation and minimum chip thickness in micro-milling is reported in this paper from an experimental and numerical point of view.
In order to model the chip formation process, 2D numerical simulations are performed using the finite element method and a commercial software programme, ABAQUS/Explicit v6.7. The Lagrangian formulation has been adopted and a chip separation criterion is used to make chip formation possible. Results of the finite element simulations are presented and compared to results found in the literature.

Keywords—**Micro-milling, chip formation, minimum chip thickness, orthogonal cutting**

I. Introduction

FOR a few years, the tendency towards miniaturisation has been gaining in importance and affects many fields, involving an increasing demand for micro-components. A growing development of micro-manufacturing techniques is consequently observed. Micro-milling is one of them. It consists in a micro-machining process using a cutting tool (called a 'micro-mill', typical diameter between 100 µm and 500 µm) rotating at a high speed to remove material from the workpiece and making it possible to produce parts and features between some mm and some µm [1], [2] and [3]. Up to now micro-milling seemed to be the most flexible and fastest way to produce complex tridimensional micro-forms, including sharp edges, with a good surface quality in many materials: metal alloys, composites, polymers and ceramics [4]. Its applications are quite varied, to cite a few: micro-injection moulds, watch components, optical devices, components for the aerospace, biomedical and electronic industries.

In order to present the main differences in chip formation due to the scaling-down from macro- to micro-milling, a short review of the current state of the art in chip formation and minimum chip thickness in micro-milling is carried out. Then the finite element model developed is presented, before commenting and comparing our results to those found in the literature.

II. Chip formation specificities in micro-milling

A. Minimum Chip Thickness

IN micro-milling the depth of cut and the feed per tooth are very small (of the same order of magnitude as the tool edge radius) and no chip is formed below a value called 'minimum chip thickness'. Chae et al. [1] define it as the critical depth of cut (between 5% and 38% of the tool edge radius, depending on the machined material [5]) below which no chip can be formed. Three different cases happen in micro-chip formation, as shown on Figure 1 (R: edge radius, h: depth of cut, h_m: minimum chip thickness).

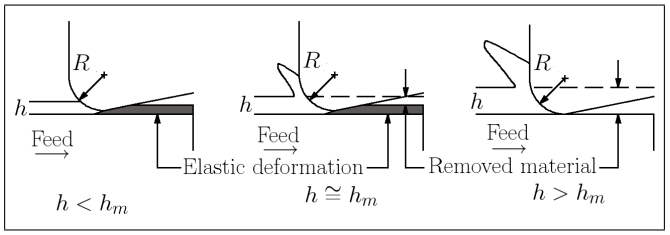

Fig. 1. Schematic representation of the minimum chip thickness in orthogonal cutting, inspired from [1]

Increase of cutting forces, burr formation and surface roughness are the consequences of the rise of slipping forces and the ploughing of the machined surface (highlighted by Bissacco et al. [6]) due to the minimum chip thickness phenomenon. Hence minimum chip thickness values must be determined and taken into account to choose adequate cutting parameters. Machined material and tool geometry greatly affect the minimum chip thickness value, complicating its estimation [7].

B. Negative Rake Angle

The macro-cutting assumption stating that the tool is sharp, completely cuts the surface and generates chips is not valid in micro-cutting. This is due to the highly negative rake angle caused by the small depth of cut being of the same order of magnitude as the tool edge radius (Fig-

ure 2). A highly negative rake angle leads to ploughing of the machined surface and elastic spring back of the workpiece. The spring back fraction occurring under the flank face leads to friction, raising the specific cutting energy.

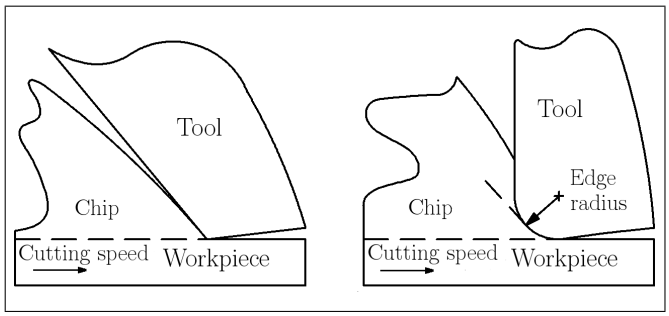

Fig. 2. Schematic representation of the negative rake angle in orthogonal cutting, inspired from [2]

C. Size Effect

At a small depth of cut, Filiz et al. [8] observed the so-called 'size effect': a decrease in the depth of cut leads to a non-linear increase in the specific cutting energy. Minimum chip thickness and specific cutting energy are thus closely related. The specific cutting energy could be an indicator making it possible to detect changes (from slipping to shearing) in the cutting mechanism and to monitor the process.

D. Influence of the Machined Material

In micro-milling, as the dimensions of the depth of cut, the tool or feature to produce are often smaller than the grain size of the machined material, its nature and micro-granular structure have to be taken into account [1] and [2]. Therefore it can no longer be considered as homogeneous and isotropic, contrary to the assumption made in macro-machining. The microstructure of the machined material takes on great importance in micro-milling.

Chae et al. [1] and Dornfeld et al. [2] report variations in cutting forces and vibrations during micro-machining due to the lack of homogeneity of the workpiece granular structure. This leads to variations in cutting condition (hardness in particular). Modifying the cutting conditions or the machine design is not a solution to eliminate them, as they are due to the nature of the machined material. Finally, averaged cutting coefficients from macro-cutting cannot be used any more.

E. Numerical Works

Up to now, very few numerical works about minimum chip thickness can be found in the literature.

A 2D ALE orthogonal cutting finite element model was developed by Woon et al. [9] in order to study the influence of the tool edge radius on chip formation. This model considers the workpiece material (AISI 4340 steel) as homogeneous and the tool is modelled as a perfectly rigid solid with and without edge radius. The results of their research show that the chip is formed by extrusion along the tool edge radius when the depth of cut is lower than a breaking value and confirm that the tool cannot be considered sharp in micro-milling.

In order to study the influence of the granular structure of the machined material on chip formation, Simoneau et al. [10] developed a 2D Lagrangian orthogonal cutting heterogeneous (AISI 1045 steel) finite element model with a sharp tool. They observed a new chip formation mechanism (Figure 3): the softest material (ferrite) is extruded between the hardest grains (pearlite). They called it a 'quasi-shear extrusion chip'. This shows that it is crucial to model the workpiece material as heterogeneous in micro-cutting.

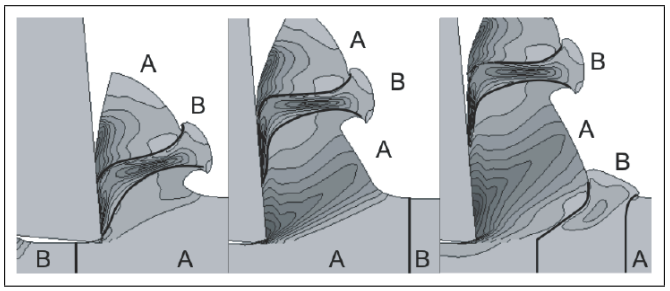

Fig. 3. AISI 1045 steel numerical chip formation (A: pearlite, B: ferrite) [10]

III. Numerical Model

THE chip formation is studied with a 2D plane strain orthogonal cutting model developed with the commercial software programme ABAQUS/Explicit v6.7. It only takes into account the area close to the cutting edge of the tool.

An explicit Lagrangian formulation is adopted as our interest is focused on the transient phase of the chip formation and the cutting refuse. Moreover the model must be able to produce saw-tooth chips, which cannot be achieved with an Arbitrary Lagrangian Eulerian (A.L.E.) formulation, contrary to Lagrangian formulation [11].

For a determined material, the minimum chip thickness depends on the depth of cut (h) and the cutting edge radius of the tool (r). Various h/r ratios have been considered in order to study the influence of the depth of cut on the chip formation process. Ten different cases have been simulated from $h/r = 5$ ($h = 100$ µm) to $h/r = 0.05$ ($h = 1$ µm): $h/r = 5$, 3, 1, 0.5, 0.375, 0.25, 0.2, 0.15, 0.1 and 0.05.

A. Overview

The workpiece is modelled as a rectangular block, while the tool is modelled with a 20 µm cutting edge radius, a 0° rake angle and a 5° clearance angle. The cutting speed is set to 300 m/min. The workpiece and the tool are meshed with three- and four-node linear elements. Figure 4 presents the initial geometry and mesh of the model when $h/r = 5$ (H: horizontal degree of freedom constrained, V: vertical degree of freedom constrained).

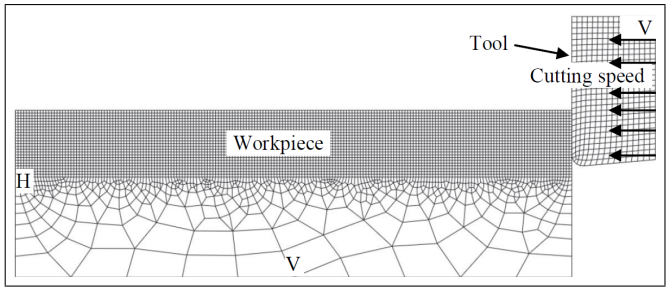

Fig. 4. Boundary conditions and initial mesh when $h/r = 5$

The workpiece material is a titanium alloy, Ti6Al4V, assumed to be homogeneous. Its behaviour is described by the Johnson-Cook plasticity model [12]. The tool material, tungsten carbide, is also homogeneous and its behaviour is described by a linear elastic law.

Friction at the chip - tool interface is implemented using a limiting shear friction model with a limiting shear stress and a friction coefficient [13]. All of the friction energy is converted into heat and 25% of this friction heat flows into the workpiece [14].

The two parts initial temperature is set to 20°C. Only conduction is considered and all the workpiece faces are adiabatic [15]. The efficiency of the deformation to heat transformation is assumed to be 90% [9], [13] and [14].

B. Chip Separation Criterion

Due to the Lagrangian formulation, a chip separation criterion based on an 'eroding element' method is introduced in the model to make chip formation possible. This separation criterion is based on crack propagation depending on the stress and strain state of the machined material. This chip formation approach, by ductile failure phenomenon, is composed of two steps.

In the first step, a damage initiation criterion must be fulfilled. The damage initiation criterion adopted is the Johnson-Cook shear failure model [12].

The second step concerns damage propagation, based on the fracture energy approach. This criterion uses the fracture energy, G_f, which is the energy required to open a unitary area crack. After damage initiation, the material behaviour is represented by a stress-displacement relation rather than a stress-strain relation [15]. As soon as the specified value of G_f is reached in a finite element, it is deleted and all of its stress components are put to zero. The suppression of a finite element introduces a crack in the workpiece, making it possible for the chip to come off.

IV. Results

A. Chip Formation and Morphology

Figures 5 to 10 show chip formation and machined material deformation for various h/r ratios values. A chip is undoubtedly formed when $h/r = 5$ to 0.375, which is not true for $h/r = 0.25$ to 0.05. Therefore it could be interesting to establish a criterion making it possible to give a ruling on the existence of a chip. An interesting point is the presence of a saw-tooth chip when $h/r = 5$ and 3, as observed experimentally in macro-cutting. This kind of chip is not found any more for smaller simulated h/r values. This can be due to the h/r ratio value or even to the short simulation time (some microseconds).

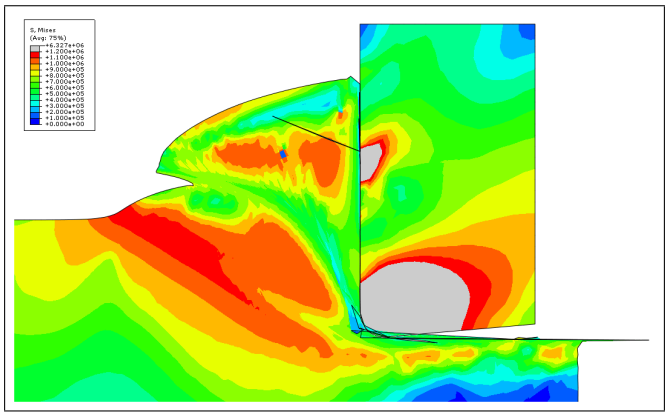

Fig. 5. Von Mises stress contours (10^3 Pa) during chip formation when $h/r = 5$

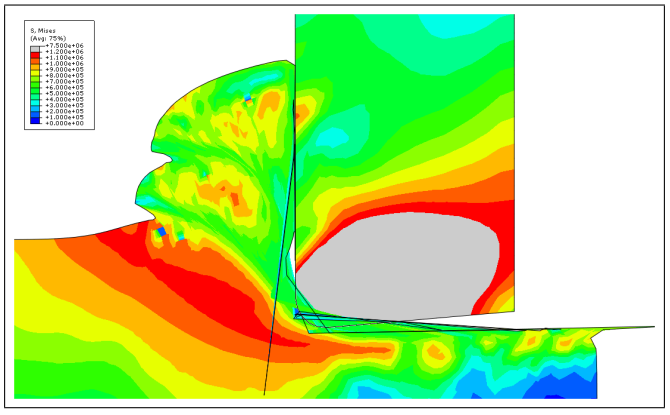

Fig. 6. Von Mises stress contours (10^3 Pa) during chip formation when $h/r = 3$

A primary shear zone is clearly visible on Von Mises stress contours when $h/r = 5$ and 3, as in macro-cutting

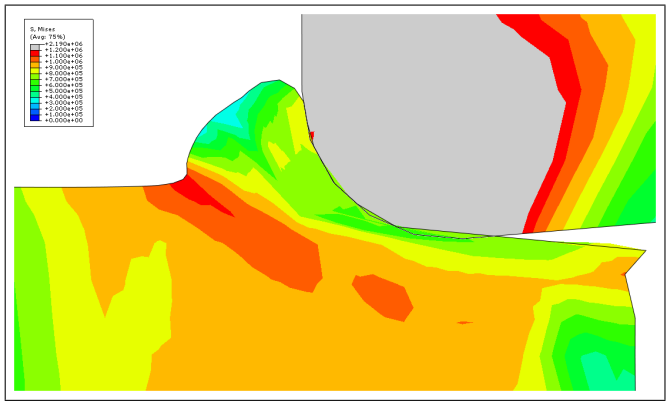

Fig. 7. Von Mises stress contours (10^3 Pa) during chip formation when $h/r = 0.375$

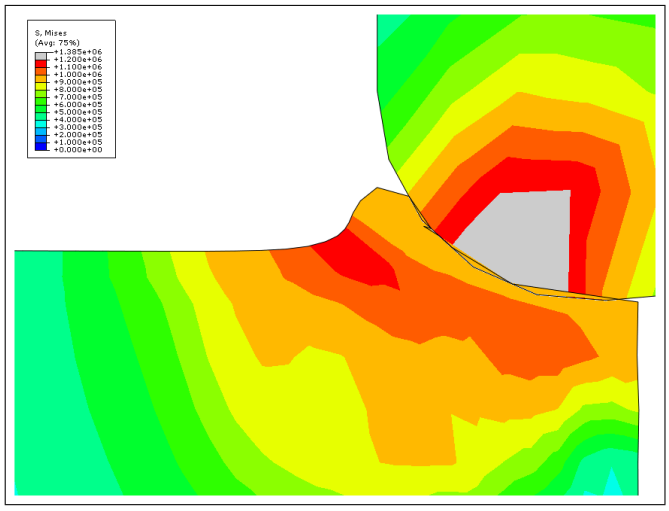

Fig. 8. Von Mises stress contours (10^3 Pa) during chip formation when $h/r = 0.25$

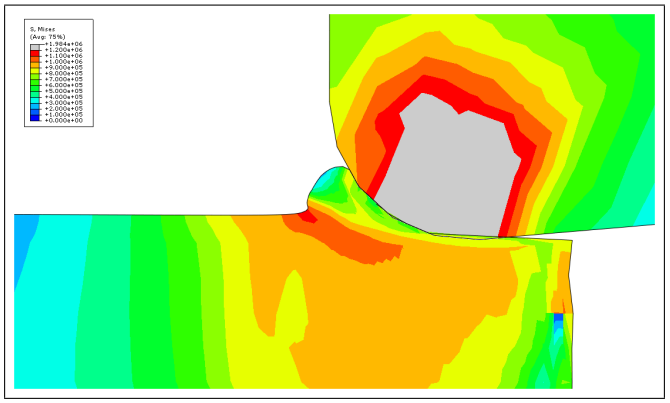

Fig. 9. Von Mises stress contours (10^3 Pa) during chip formation when $h/r = 0.2$

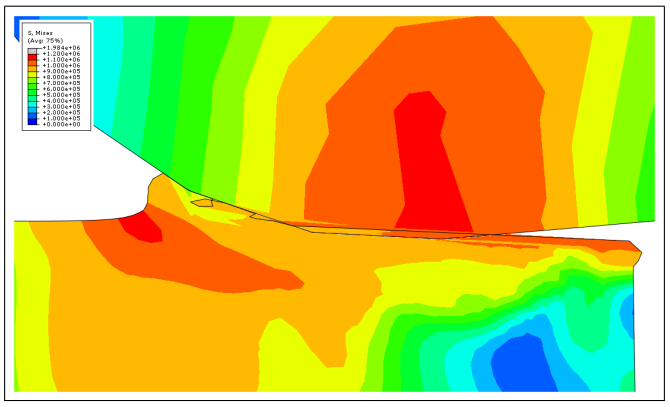

Fig. 10. Von Mises stress contours (10^3 Pa) during chip formation when $h/r = 0.05$

with a sharp tool. The more the h/r ratio decreases, the more the primary shear zone fades and it cannot be distinguished any longer from the $h/r = 0.25$ value. It is interesting to highlight that the $h/r = 0.375$ value could be a key value. Indeed a primary shear zone can still be seen but the stress value seems to be smaller.

These results are globally similar to those presented by Woon et al. [9] in the case of an A.L.E. model. Actually the cutting tool can no longer be considered as sharp and the h/r value has a great influence on the chip formation in micro-cutting. Changes in the chip formation mechanism are observed when the h/r ratio decreases, evolving away from macro-cutting.

B. Cutting Forces

Figure 11 shows the cutting and the feed forces for a 100 µm depth of cut. A cyclic evolution can be observed, as expected due to the saw-toothed chip. Indeed when the formation of a slipping plane occurs (corresponding to a tooth formation), a drop in the forces is observed. It also must be highlighted that the cutting force is greater than the feed force, which is also observed in macro-cutting.

Figure 12 represents the evolutions of the ratio between feed and cutting forces for the ten h/r simulated ratios. The $h/r = \infty$ value stands for the theoretical forces ratio value when the tool is infinitely sharp. The more the h/r ratio decreases, the more the forces ratio increases. When the h/r ratio becomes smaller than the unit, the feed force becomes greater than the cutting force. A change in the cutting mechanism is thus observed: an inversion between cutting and feed forces has occurred. These observations are similar to those made experimentally by Liu et al. [3].

Three different situations can be seen on Figure 12. When the h/r ratio value evolves between 5 and 1 the feed to cutting forces ratio is less than 1, as in macro-cutting. On the contrary from h/r values for 0.05 to 0.2, the forces ratio tends to 2. The three remaining h/r ratio are found between the forces ratio values 1 and 2. With a feed to cutting forces ratio criterion value of 2, the minimum chip thickness value would be between 4 µm and 7.5 µm.

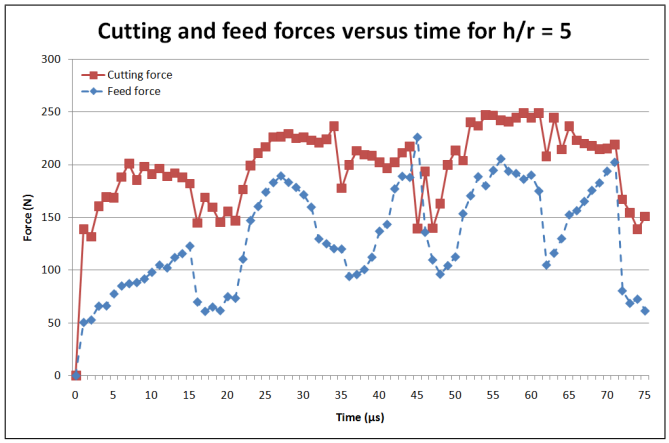

Fig. 11. Force evolutions during cutting when $h/r = 5$

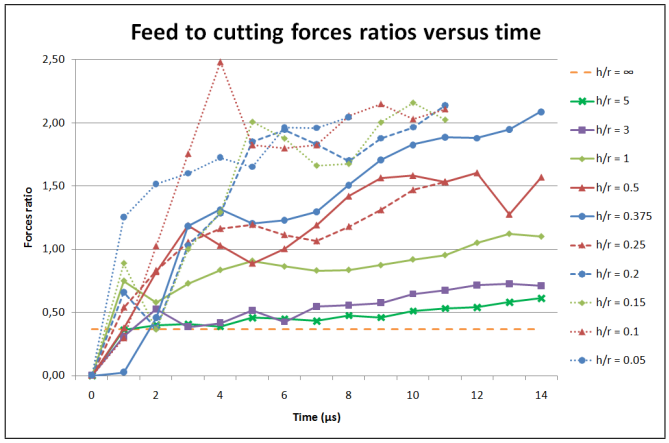

Fig. 12. Force ratio evolutions during cutting for various h/r ratios

C. Specific Cutting Energy

The evolutions of the ratio between the specific cutting energy and the theoretical specific cutting energy when the tool is infinitely sharp can be seen on Figure 13 for the ten simulated h/r ratios. For $h/r = 5$ and 3, the average value of the specific cutting energy value is close to the theoretical one. A non-linear rise in the specific cutting energy is noticed when the depth of cut decreases, in accordance with the previously presented size effect phenomenon.

Again, different cases are observed depending on the h/r value. The two h/r ratio values at both ends of the simulated range lead to specific cutting energy ratios that are clearly different. With a specific cutting energy ratio criterion value of 2, the minimum chip thickness would lie between 2 µm and 7.5 µm.

D. Vertical Displacement

The evolutions of the vertical displacement of a particular node is studied in this section for each simulated h/r ratio. For $h/r = 5$ and 3 (first situation on Figure 14), the

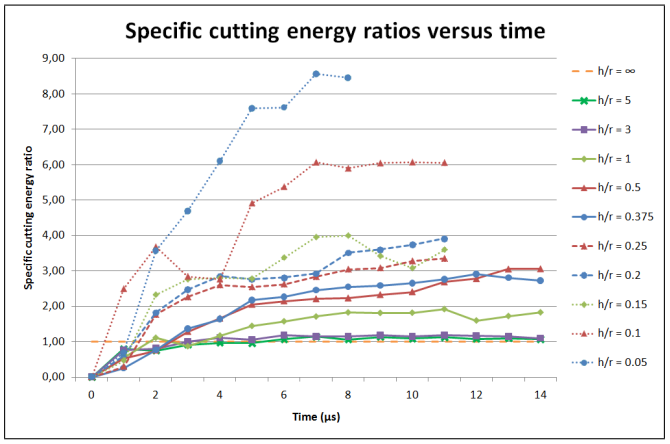

Fig. 13. Specific cutting energy ratio evolutions during cutting for various h/r ratios

node considered is the one situated at the same level as the upper node of the cutting edge radius of the tool. For h/r equal to or smaller than the unit (second situation in Figure 14), the node considered is the one at the upper right corner of the workpiece.

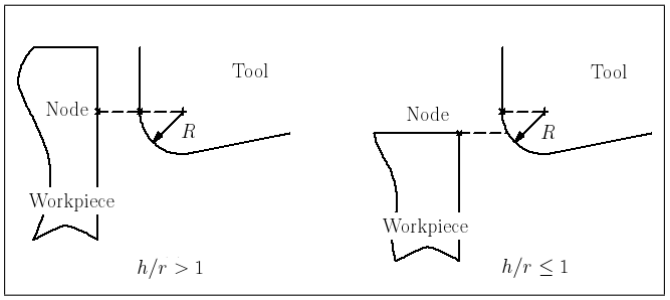

Fig. 14. Schematic localisation of the considered node

The vertical displacement of this particular node is interesting because a negative vertical displacement value means that no chip is formed and that the workpiece material is deformed and flows under the cutting edge of the tool (as in the first case of Figure 1). On the other hand a positive vertical displacement value means that a chip is formed.

Figure 15 shows that when h/r is smaller than 0.15 the vertical displacement is negative. For h/r values greater than 0.375, the vertical displacement is positive (the vertical displacement when $h/r = 1$ seems strangely large). The vertical displacement in the two remaining cases is not strictly positive or negative. The minimum chip thickness value in accordance with the node's vertical displacement would be between 3 µm and 5 µm.

E. Minimum chip thickness prediction

Each method results in a different range of probable minimum chip thickness values (Figure 16). The resultant

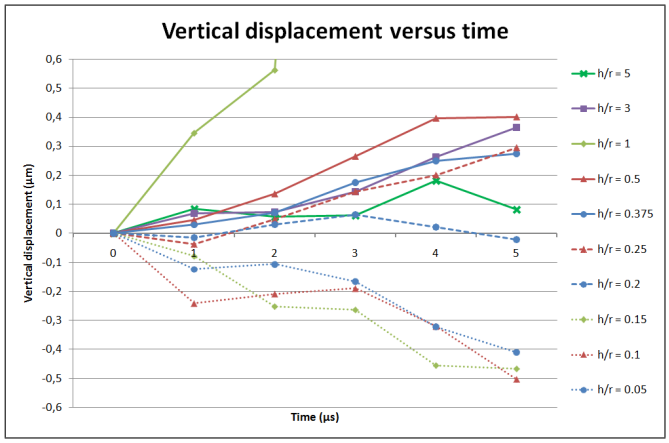

Fig. 15. Vertical displacement evolutions during cutting for various h/r ratios

of these three ranges is 4-5 µm (or 20-25% of the cutting edge radius of the tool). This can be considered as a first approximation of the minimum chip thickness value for Ti6Al4V with the geometry and the cutting condition of the model.

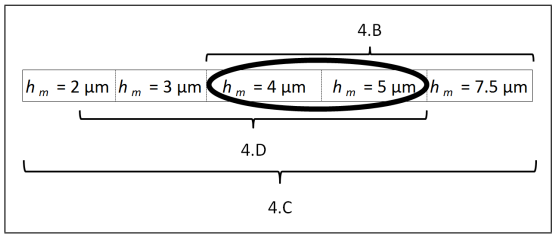

Fig. 16. Minimum chip thickness value ranges and resultant

Lastly, highly deformed finite elements can be observed during simulations. Those are not removed, contrary to what was expected. Some of them can be seen in the previous figures: they are the black lines interfering with the workpiece and the chip near the edge radius of the tool. This problem has to be solved.

V. Conclusions

CHANGES in the cutting phenomenon are induced by the transition from macro- to micro-milling. One of these changes is the chip formation involving the minimum chip thickness phenomenon, which has been reported in this paper.

The influence of the depth of cut on chip formation has been studied with the developed numerical model. A decrease in the depth of cut leads to changes in the cutting process mechanism and the cutting tool can no longer be considered sharp, contrary to the assumption with macro-cutting.

An evolution in the cutting to feed forces ratio has been highlighted when the depth of cut decreases. Beyond a critical value of the depth of cut (10 µm in this paper) the feed force becomes greater than the cutting force. This inversion could be used to determine the minimum chip thickness value.

It has also been observed that the depth of cut value greatly affects the specific cutting energy. Indeed it rises when the depth of cut decreases, which is known as the size effect. The minimum chip thickness value could be determined thanks to the evolution of the specific cutting energy.

Finally the vertical displacement of a particular node has been studied in order to determine if the machined material flows under the cutting edge of the tool instead of forming a chip. A small depth of cut (less than 4 µm in this paper) leads to a negative vertical displacement of the node. The transition from a positive to a negative vertical displacement could help in determining the minimum chip thickness value.

Each of the three methods ends in a different range of probable minimum chip thickness values, the intersection of them being 4-5 µm. The value of the minimum chip thickness for Ti6Al4V with the geometry and the cutting condition of the model is estimated at 4-5 µm, i.e. 20-25% of the cutting edge radius of the tool.

References

[1] Chae J., Park S., and Freiheit T., *Investigation of micro-cutting operations*, IJMTM, 45, 313–332, 2006.

[2] Dornfeld D., Min S., and Takeuchi Y., *Recent advances in mechanical micromachining*, Annals of the CIRP, 55, 745–768, 2006.

[3] Liu X., DeVor R., Kapoor S., and Ehman K., *The mechanics of machining at the micro scale: assessment of the current state of the science*, JMSE, 126, 666–678, 2004.

[4] Weule H., Hüntrup V., and Trischler H., *Micro-cutting of steel to meet new requirements in miniaturization*, Annals of the CIRP, 50:61–64, 2001.

[5] Ohbuchi Y. and Obikawa T., *Finite element modeling of chip formation in the domain of negative rake angle cutting*, ASME, 125, 324–332, 2003.

[6] Bissacco G., Hansen H.N., and De Chiffre L., *Size effect on surface generation in micromilling of hardened tool steel*, Annals of the CIRP, 55:593–596, 2006.

[7] Liu X., DeVor R., and Kapoor S., *An analytical model for the prediction of minimum chip thickness in micromachining*, ASME, 128, 474–481, 2006.

[8] Filiz S., Conley C., Wasserman M., and Ozdoganlar O., *An experimental investigation of micro-machinability of copper 101 using tungsten carbide micro-endmills*, IJMTM, 47, 1088–1100, 2007.

[9] Woon K., Rahman M., Fang F., Neo K., and Liu K., *Investigations of tool edge radius effect in micromachining: a FEM simulation approach*, JMPT, 167, 316–337, 2007.

[10] Simoneau A., Ng E., and Elbestawi M.A., *The effect of microstructure on chip formation and surface defects in micro-scale, mesoscale, and macroscale cutting of steel*, Annals of the CIRP, 55:97–102, 2006.

[11] Ducobu F., *Thèse de Doctorat – Etude du phénomène de coupe en micro-fraisage par enlèvement de copeaux: Rapport de réunion*

du 04/02/2009, Technical report, Faculté Polytechnique de Mons, 2009.

[12] Johnson G. and Cook W., *Fracture characteristics of three metals subjected to various strains, strain rates, temperature and pressures*, EFM, 21, 31–48, 1985.

[13] Özel T. and Zeren E., *Numerical modelling of meso-scale finish machining with finite edge radius tools*, IJMMM, 2, 451–768, 2007.

[14] Nasr M., Ng E.-G., and Elbestawi M., *Effects of workpiece thermal properties on machining-induced residual stresses - thermal softening and conductivity*, Proc. IMechE, Part B: JEM, 221, 1387–1400, 2007.

[15] Mabrouki T., Girardin F., Asad M., and Rigal J.-F., *Numerical and experimental study of dry cutting for an aeronautic aluminium alloy (A2024-T351)*, IJMTM, 48, 1187–1197, 2008.

Proceedings of the 8th National Congress on Theoretical and Applied Mechanics, May 28-29, Brussels, Belgium.

Textile Reinforced Inorganic Phosphate Cement composite moulds

J. Blom[1], P. Van Itterbeeck[1], J. Van Ackeren[1], J. Wastiels[1]
[1]Faculty of Engineering Sciences, Mechanics of Materials and Constructions (MeMc),
Vrije Universiteit Brussel,
Pleinlaan 2, 1050 Brussels – Belgium
email: johan.blom@vub.ac.be, petra.van.itterbeeck@vub.ac.be, johan.van.ackeren@vub.ac.be,jan.wastiels@vub.ac.be

I. ABSTRACT:

In this experimental study a production process is presented for a textile reinforced inorganic phosphate cement (TRC) composite mould. Driven by the need to produce faster, cheaper, without releasing toxic gases and in a less complex way, this moulding technique is an alternative for conventional metallic and thermoset moulds. The aim of this work is to replace a thermoset mould by a TRC equivalent and using it for small scale production.

Keywords: **Manufacturing, Textile reinforced cement, moulds**

II. INTRODUCTION

In a market dominated by thermoset composites, new processing techniques need to be developed, in order to meet the new demands of the industry (ref.:1&2). Driven by the need to produce faster, thermoplastic composites seem to be the future. Theoretically this is an interesting alternative, but processing a material that requires 200°C or even higher with conventional thermoset moulds seems impossible.

The presented technique to produce a mould uses textile reinforced cement (TRC). The production method of the TRC mould is based on the well known composite hand lay up method, but without releasing toxic gases and the possibility of cleaning the production tools with water. In this case the mould is developed to produce only a few prototype parts, using a hand lay up technique in an open mould at room temperature. This study is performed to assess the possibilities of TRC moulds, and to set up a structure for the future work, in order to use them at high temperatures.

The proposed technique will be used to produce a thin shell mould type. The photo below shows the thermoharder mould on the left (figure 1a) and the textile reinforced concrete (TRC) version on the right (figure 1b).

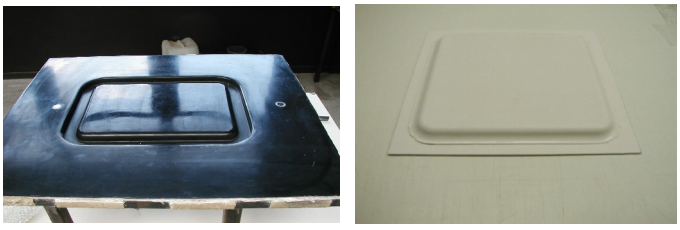

Figure 1: case study (a) the thermo harder mould and (b) the TRC version

III. TEXTILE REINFORCED INORGANIC PHOSPHATE CEMENT COMPOSITES

The TRC used in this study is a combination of inorganic phosphate cement (IPC) with a chopped strand mat of glass fibres. IPC has been developed at the "Vrije Universiteit Brussel" and is commercially available under the name Vubonite®. This material is an inorganic, non-alkaline resin, prepared by mixing a powder and a liquid component. The cementitious material is processed in the same way as a polymer resin. Processing time is adjustable and varies from a few minutes to about an hour. Hardening occurs spontaneously at room temperature and results in a cement with a neutral pH after hardening. Therefore, the glass fibres are not chemically attacked by the cementitious matrix. By using a fibre volume fraction which exceeds the critical fibre volume fraction, the fibres can ensure strength and stiffness at applied loads far exceeding the range at which matrix multiple cracking occurs. (ref.:4) Textile reinforced cementitious composites with glass fibres as reinforcement exhibit relatively high strength and ductility and thus provide an interesting new material for thin shells. Typical data for the pure resin, as well as for composites with unidirectional (UD) or random glass fibre reinforcement can be found in Table I.

TABLE I: properties of the IPC matrix; after VUBONITE® technical data sheet, (ref.: 3)

		pure	UD 300 g/m²	mat 300 g/m²
specific gravity (wet)	kg/dm³	1.9	2.0	2.0
specific gravity (dry)	kg/dm³	1.6	1.75	1.75
thickness laminate	mm/layer		0.9	0.9
compressive strength	MPa	60	60	60
tensile strength	MPa	10	100	30
stiffness (E-modulus)	GPa	18	7 - 25	3 - 20
coeff. thermal expansion	/K	8 E-6		
coeff. heat conduction	W/mK	+/- 1		
specific heat	J/gK	0.8		
fire safety		absolutely incombustible European class A1		

Another interesting property is that it can resist to high temperatures, without producing toxic gases. This material is also incombustible, according to the European standard EN13501-1. All these advantages make TRC an ideal material to develop a mould which can be used to produce fast, at high temperatures and without complex production tools.

IV. EXPERIMENTAL WORK

Materials used for Mould production

A. *Matrix*

The matrix used in this study is a mixture of a calcium silicate powder and a phosphate acid based solution of metal oxides. The weight ratio liquid to powder is 1/0,8. To improve the workability and the specific needs, fumed silica (Aerosil A200) was added as filler to the mixture in various amounts. The components are mixed using a "Heidolph RZR 2102" overhead mixer. The mixing is performed in two stages: first the liquid and the powder are mixed at 250 rpm until the powder is mixed into the fluid, after which the speed is increased to 2000 rpm. The fresh IPC mixture being acidic it attacks most types of metal. To avoid corrosion, the spindle of the mixer is made of stainless steel, while other production tools are in PVC. A series of tests was performed to determine the optimal quantity of filler. The results of the tests are listed in the table below (table II).

TABLE II: overview of the workability of the matrix

liquid	powder	Filler	mixing	spreading
100	80	0	++	--
100	80	2	++	--
100	80	4	+	-
100	80	6	+/-	+/-
100	80	8	+/-	++
100	80	10	-	+ +
100	80	12	--	+

The workability is defined as the ease of mixing and spreading of the matrix. Without filler, the matrix presents a low viscosity of around 2000 mPas. Mixing of the component is very easy (++) as shown in the photo below (fig.: 2)

Figure 2: workability of matrix without filler

The matrix is however not covering uniformly the surface of the substrate, and flows from a surface which is not perfectly horizontal (--). By adding more than 2 % of filler compared to the weight of liquid component, the primary mixing becomes more difficult, as shown in the picture below for 6% (fig.:3 left).

Figure 3: workability of matrix with 6% filler

After a few minutes of mixing, the mixture will however become uniform, but presents a higher plastic viscosity. The increased yield stress of the mixture makes it possible to apply it on inclined surfaces with a uniform covering (fig.: 3 right). Adding a high amount of filler results in a very sticky paste, which is only applicable using a brush instead of a roller: the primary mixing becomes almost impossible when adding 12 % or more of the filler.

The addition of 8 % of filler is considered to give the best balance between ease of mixing, and spreading characteristics, and will be used in this study. The pictures below (fig.: 4) illustrate the difference in aspect between the matrix with an addition of 0% and 8 % of filler.

Figure 4: workability of matrix with 0% and 8 % filler

B. *fibres*

The E-glass fibre reinforcements used in the composite moulds are chopped glass fibre mats with a fibre density of 300g/m² (Vetrotex M 5 (300), (fig.:5).

Figure 5: chopped glass fibre mats Vetrotex M 5 300 g/m²

C. *Surfacing veil*

A surfacing veil is used as first layer to get a better surface quality and preventing the glass fibre penetrating through the matrix top surface. Two types of surfacing veils are tested. One of the tested veils is water dissolvable (Owens Corning S20-FA16, 19 g/m²), resulting in a better workability. The water dissolvable veil is used in the corners of the mould (fig.:6)

Figure 6: water dissolvable surfacing veil

The density of the surfacing veil used in the centre of the mould (Owens Corning M524-ECR30A) is 30 g/m².

V. MOULD MAKING

A. *Making a master mould*

The master model is the first requirement to make a mould. This is the original part that is to be copied (fig.: 7).

Figure 7: original part

The orginal model is placed in a frame, making it possible to laminate the desired fibre reinforced cement mould. The complete asembly of the master mould setup is shown below (fig.:8).

Figure 8: mould setup

The master mould must be waxed with several coats of mould release wax “Moldwax 60-x3 Jost Chemicals” and polished in between coats, before the mould can be produced (fig.:9)

Figure 9: waxing of the master mould

B. *Production of the textile reinforced mould*

The mould is produced using a hand lay up technique. For each matrix layer an average consumption of 900 g/m² is used. The matrix is spread out on the master mould and equally distributed using a roller (fig.: 10).

Figure 10: spread out of the first layer

A surface veil is put on top by using a deaerating roller to press out the trapped air. The veil is used to prevent the penetration of the chopped glass fibre in the top surface of the mould (fig.:11).

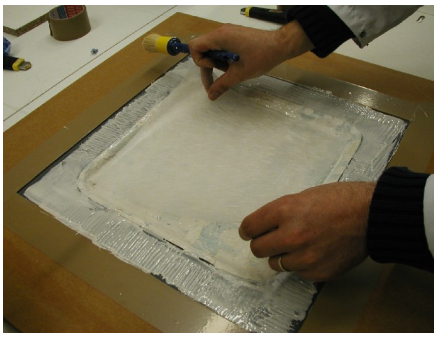

Figure 11: placing the surface veil

A new layer of matrix is spread out equally over the surface. The next step in the process is applying the chopped random fibre glass mat. It is important that the bonded surface of the fibre mat is facing up (fig.: 12 left).

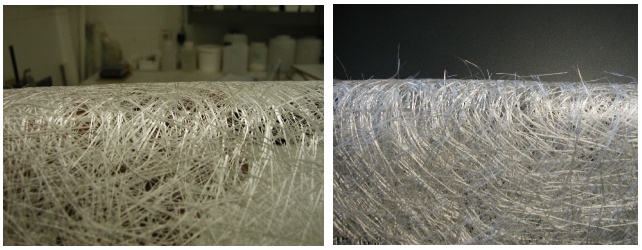

Figure 12: difference when bending a chopped random fibre mat

The fibre mat is firmly pressed into the matrix using a roller, to prevent trapped air bubbles and insure a good impregnation of the fibre mat (fig.: 13).

Figure 13: applying the matrix

In total four layers of glass fibres are applied. Finally the mould is packed in a plastic foil, thus preventing evaporation of water. Like most cementitious mixtures, the strength of IPC increases with time (curing). At first the mould is placed in ambient conditions for 24 hours. The curing effect can however be accelerated by heating the mould at 60°C during at least 24 hours. During the curing, both sides of the laminate are covered with plastic to prevent early evaporation of water.

VI. MAKING A GLASS FIBRE REINFORCED POLYESTER PART

The making of a part is the reverse of making a mould. The mould is waxed and polished (fig.:14).

Figure 14: waxing the mould

The mould will be covered first with a surface veil (Owens Corning M524-ECR30A) and the polyester matrix which is a two component polyester (Mida Composites, Eco Polyester, Finpol H 856-w + Mekp-Me) (fig.:15).

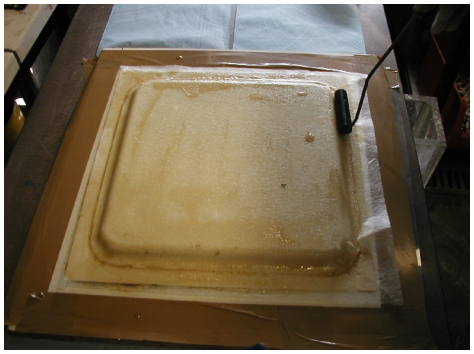

Figure 15: applying the matrix and the surface veil

In the next step layers of chopped fibre glass and resin will be put on top of the mould until the desired thickness is reached. In this test case a random chopped fibre glass mat is used (Vetrotex M 5 (300) (fig.:16).

Figure 16: applying the matrix and the random chopped fibre glass mat

Once completed, wedges are used to separate the part from the mould (fig.: 17).

Figure 17: separation of part from mould

VII. Conclusion

The presented technique to produce a mould using textile reinforced cement was successful in this case. After adapting the composition of the matrix, making a mould using a hand lay up method was easy to perform even in the corners. The glass fibre reinforced polyester part produced on the mould has a good quality (fig. 18). Prototyping and small series production are caning interest, especially when time to process is short.

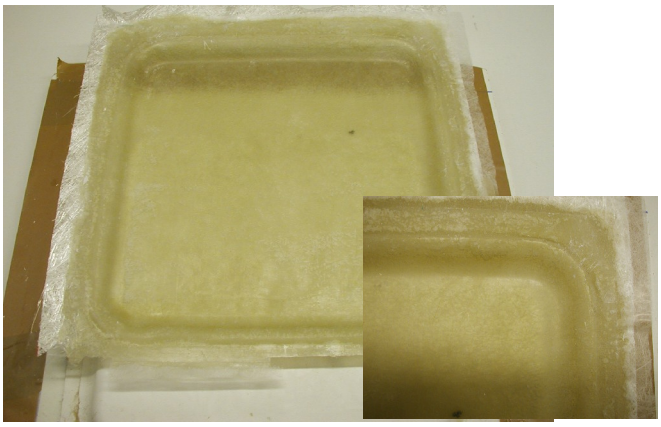

Figure 18: glass fibre reinforced polyester part

VIII. Future work

The future work involves the optimisation of the composite. A material research of inorganic phosphate cement in combination with fillers and fibres will be performed. The aim is to tune the composite so it would have a good workability in combination with strength and high temperature resistance. The optimized textile reinforced cement composite will be used to develop a mould which can be produced faster with less material and is useable at high temperatures (220 – 400°C). An experimental mould will be build in order to produce thermoplastic composite parts.

Finally the proposed moulding technique could be used in a large project, in order to produce large thermoplastic composite parts, for example ships or windmill blades.

References

[1] Global Composites Market 2005-2010: Opportunities, Markets and Technologies Lucintel January 1, 2005- Pub ID: EC1469876

[2] Ginger Gardiner, Wind Blade Manufacturing, Part II: Are thermoplastic composites the future? High Performance Composites, 10/21/2008

[3] Vubonite®, technical dat sheet, www.vubonite.com

[4] Lars Weigel, The stuff dreams are made of, New Energy magazine, March 2007

[5] J. Blom , H. Cuypers P,. Van Itterbeeck, J. Wastiels, Modelling the behaviour of Textile Reinforced Cementitious composites under bending, Prague, Fibre Concrete 4th International Conference, p.205-210, 2007

[6] S. Faignet, P. Bauweraerts, J. Wastiels and X. Wu , Mineral Polymer tooling system for making prototype fibre reinforced composite parts, Journal of Materials Processing Technology 48 (1995) 757-764

Experimental study of multilayer stent effects on haemodynamics in abdominal aortic aneurysm

C. Wailliez[1], G. Coussement[1]
[1]Fluids-Machines Department, Faculté Polytechnique de Mons
rue de Houdain 9, 7000 Mons - Belgium
email: Cecile.Wailliez@fpms.ac.be

I. Introduction

CARDIOVASCULAR diseases are a frequent cause of mortality in industrialised countries. One of these pathologies, called aneurysm, is a local dilatation of a blood vessel. In the present paper, the Abdominal Aortic Aneurysm (AAA) is studied. The traditional treatment is surgery (replacement of the diseased aorta by a prosthesis) but a recent less invasive treatment, the endovascular repair, exists, consisting in the placement of a stent (wired mesh tube)(figure 1) into the diseased artery without open surgery. Usually, these stents are covered and exclude the blood flow from the aneurysm. A new type of uncovered stents, called multilayer stents, is developed by Cardiatis. They have the particularity to allow the blood to flow into the aneurysm and it is expected that they behave differently from a covered stent and therefore influence differently the evolution of the aneurysm.

II. Objectives

The aim of this experimental study is to estimate haemodynamics changes induced by the presence of such uncovered multilayer stents and to show the advantages and disadvantages on the aneurysm growth. It is also performed to validate the numerical results obtained by a previous CFD study [1].

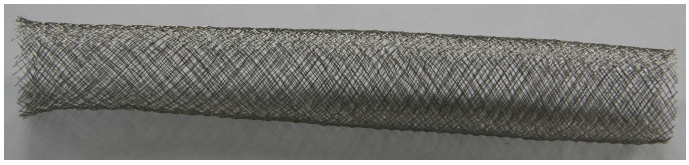

Fig. 1. Uncovered multilayer stent (Cardiatis)

III. Method

The flow in an abdominal aortic aneurysm model is visualized by using Particle Image Velocimetry (PIV). The model, made of plexiglas, is realised at real scale based on human dimensions. As the objective is to show the haemodynamic effects of the multilayer stent, the model of AAA is simplified compared to the anatomical geometry. It represents a fusiform aneurysm on a straight aorta without the iliac bifurcation (figure 2). One collateral artery is added at the level of the aneurysm to study its supply by blood. The aneurysm model is rigid by reason of easier and better measurements and to allow the comparison of the results with the CFD results.

IV. Results

Particle Image Velocimetry allows to study flow patterns, velocity field and wall shear stress in cutting planes of the AAA model. Different inclinations of the models have been studied. The results in the aneurysm sac in presence of a multilayer stent can be compared to the results without stent (because of the stent material opacity, the central flow can only be represented in the cases without stent). With multilayer stent, different patterns of the flow can be observed (figure 3) compared to the case without stent. The blood velocities in the aneurysm sac are reduced and the level of wall shear stress is lower.

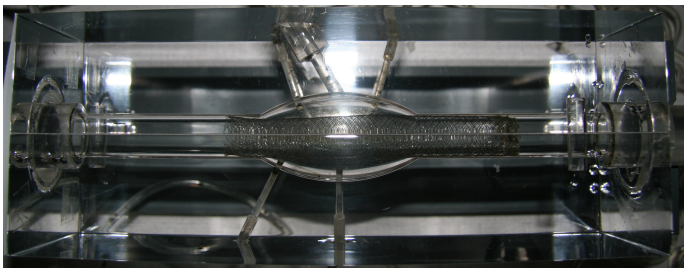

Fig. 2. Plexiglas model with stent

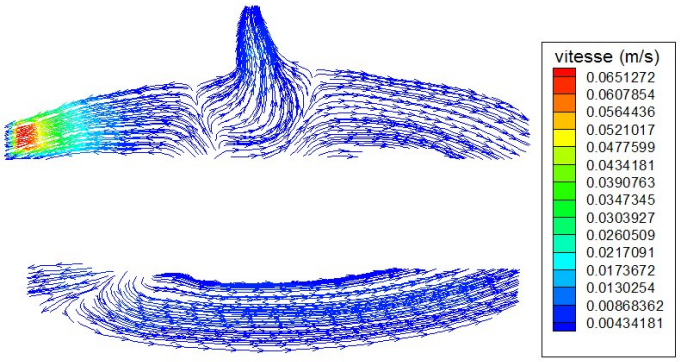

Fig. 3. Flow pattern in abdominal aortic aneurysm with multilayer stent (collateral plane)

V. Conclusions

This experimental study shows that the use of uncovered multilayer stent changes the flow patterns in the aneurysm by redirecting the blood flow, reduces the velocities and the wall shear stresses and allows to supply the collateral arteries.

References

[1] C. Wailliez, G. Coussement, *CFD study of multilayer stent effects on haemodynamics in abdominal aortic aneurysms*, European Journal of Mechanical and Environmental Engineering, accepted June 2008.

Proceedings of the 8th National Congress on Theoretical and Applied Mechanics, May 28-29, Brussels, Belgium.

Effect of root form on stress patterns in the periodontal ligament: An analytical study

A. Van Schepdael[1], J. Vander Sloten[1]
[1]Katholieke Universiteit Leuven, Division of Biomechanics and Engineering Design
Celestijnenlaan 300C, bus 2419-3001 Heverlee
email: an.vanschepdael@mech.kuleuven.be

Abstract— **To determine the movement of a single tooth, the stresses and strains inside the periodontal ligament have to be calculated. In this article, two geometrical approximations of a tooth root are used to estimate these stresses and the results are compared. The first approximation is an axisymmetrical paraboloid, the second one is an elliptic paraboloid. Results show that the forces necessary to accomplish a constant displacement of $u_x = 2.10^{-4}$ mm change by 10% when comparing a paraboloid root to an elliptic paraboloid root with an eccentricity of $e = 0.6$. An increase of the hydrostatic pressure and the appearance of several periodical components in the stress distribution can also be seen when eccentricity increases.**

Keywords— **orthodontics, tooth movement, periodontal ligament**

I. Introduction

THE primary aim of orthodontics is the prevention and correction of malocclusion. Currently the choice of the treatment program is based on the experience of the orthodontist and on a trial-and-error procedure. This can lengthen the duration, and thus the cost, of the treatment. In future it would be interesting to have a software environment that allows simulation of orthodontic and orthognatic treatments for each individual patient. A first step in the development of this software is the modeling of the orthodontic movement of a single tooth.

The aim of this project is to develop a model that can predict the movement of a tooth in response to a fixed appliance. Hereto the strains and stresses inside the periodontal ligament must be calculated. In order to limit the computational time, complete finite element analysis is not an option, although it can be used for validation purposes. Analytical formulas are thus preferred.

Two geometrical approximations of the tooth root are compared. The differences in the stress and strain patterns inside the periodontal ligament and in the forces necessary to achieve a given displacement are studied.

II. Methods

The type of tooth movement that occurs in response to an applied force is determined by the location of the centre of rotation relative to the centre of resistance. Although the periodontal ligament (PDL) is a non-linear and anisotropic material with a time-dependent hysteresis behavior, the location of the centre of resistance and the centre of rotation can be approximated within the margins of clinical results by assuming the periodontal ligament is a linear, isotropic material [1].

The approach used to calculate the displacement of the tooth due to the deformation of the periodontal ligament is based on an article written by C. Provatidis [2]. He uses a paraboloid to represent the tooth root of single-rooted teeth, since that geometric form resembles the form of the root of a maxillary central incisor (Fig. 1).

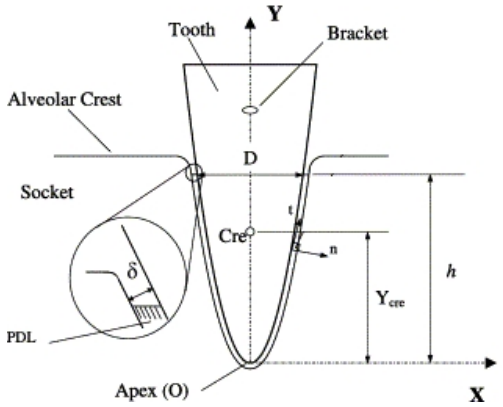

Fig. 1. The geometry of the tooth root.

The shape of the root, particularly in the case of a canine, can however be approximated better by using an elliptic paraboloid. A normal paraboloid is constructed by revolving a two-dimensional parabola around an axis. The cross-sections in a plane perpendicular to the revolution axis are circles, while in an elliptic paraboloid these cross-sections are ellipses.

The periodontal ligament is assumed to have a thickness $\delta = 0.229$ mm, measured perpendicular to the surface of the root. The young's modulus used for the PDL is $E = 0.68$ MPa and the Poisson coefficient is $\nu = 0.49$.

The equation of a two-dimensional ellipse with its centre at $(0,0)$ in polar coordinates (r,ϕ) is

$$r^2 = \frac{b^2}{1 - e^2 \cos^2 \phi} \tag{1}$$

where b is the short axis of the ellipse, and e is its eccentricity. In the case of an elliptic paraboloid, the short axis varies with the height:

$$b^2 = \frac{R^2}{h} y \tag{2}$$

where R is the length of the short axis at $y = h$.

The idea is to apply a translation, u_x, u_y or u_z, or a rotation, θ_x, θ_y or θ_z, to the tooth. Since an equilibrium in the periodontal ligament is reached in 2-10 minutes and forces applied in orthodontic treatment are small ($< 2N$), it is possible to assume that the tooth and the alveolar bone are rigid. In that case, the displacement of the tooth root deforms the periodontal ligament, resulting in strains ε_{ij}.

For the calculation of the strains, a local coordinate system (n,t,ϑ) is defined in each point (r,ϕ,y) on the surface of the elliptic paraboloid (1). The axis n is the normal on the surface, the axis t is perpendicular to n and tangent to the surface and the axis ϑ is defined so that (n,t,ϑ) forms a right-handed, orthogonal coordinate system. The relationship between the displacements u_x, u_y and u_z in the global coordinate system and u_n, u_t and u_ϑ in the local coordinate system are as follows.

$$\begin{aligned} u_n &= F\sin\alpha \cdot u_x + G\sin\alpha \cdot u_z - \cos\alpha \cdot u_y \\ u_t &= F\cos\alpha \cdot u_x + G\cos\alpha \cdot u_z + \sin\alpha \cdot u_y \\ u_\vartheta &= -G \cdot u_x + F \cdot u_z \end{aligned} \tag{3}$$

where F and G are coefficients that depend on x, z and the eccentricity e.

In the local coordinate system, the length of the PDL is equal to δ in the $n-$direction and 'very large', or infinity in the other directions. The strains are then described by the following expressions:

$$\begin{array}{lll} \varepsilon_{nn} = -\frac{u_n}{\delta} & \varepsilon_{n\vartheta} = -\frac{u_\vartheta}{2\delta} & \varepsilon_{nt} = -\frac{u_t}{2\delta} \\ \varepsilon_{tt} = 0 & \varepsilon_{t\vartheta} = 0 & \varepsilon_{\vartheta\vartheta} = 0 \end{array} \tag{4}$$

Considering a rigid displacement or rotation of the tooth, it is possible to determine u_x, u_y and u_z in every point of the surface, and define the strains in the local coordinate system. These strains then have to be transformed to the global coordinate system, as described in equations 5-6.

$$\begin{pmatrix} \varepsilon_{xx} & \varepsilon_{yx} & \varepsilon_{zx} \\ \varepsilon_{xy} & \varepsilon_{yy} & \varepsilon_{yz} \\ \varepsilon_{xz} & \varepsilon_{yz} & \varepsilon_{zz} \end{pmatrix} = T_2 \cdot T_1 \cdot \begin{pmatrix} \varepsilon_{nn} & \varepsilon_{tn} & \varepsilon_{\vartheta n} \\ \varepsilon_{nt} & 0 & 0 \\ \varepsilon_{n\vartheta} & 0 & 0 \end{pmatrix} \cdot T_1^T \cdot T_2^T \tag{5}$$

$$T_1 = \begin{pmatrix} \sin\alpha & \cos\alpha & 0 \\ -\cos\alpha & \sin\alpha & 0 \\ 0 & 0 & 1 \end{pmatrix}, T_2 = \begin{pmatrix} F & 0 & -G \\ 0 & 1 & 0 \\ G & 0 & F \end{pmatrix} \tag{6}$$

Since the PDL is approximated as a linear material, the stresses can be easily calculated, using the constitutive equations of a linear, isotropic material.

$$\sigma_{ij} = C_{ijkl}\varepsilon_{kl} \tag{7}$$

Tractions along the tooth surface are calculated as follows:

$$t_i = \sigma_{ij} n_j \qquad i = x,y,z \tag{8}$$

where $\overrightarrow{n} = (F\sin\alpha, -\cos\alpha, G\sin\alpha)$ is the normal on the surface. Forces and moments can be determined by integration of these tractions.

$$\begin{aligned} \overrightarrow{F} &= -\int_A \overrightarrow{t}\, dA \\ \overrightarrow{M} &= -\int_A \overrightarrow{r} \times \overrightarrow{t}\, dA \end{aligned} \tag{9}$$

The forces and moments are thus linearly related to the displacement of the tooth. This makes it possible to define a stiffness matrix K for the three-dimensional movement of the root.

$$\overrightarrow{F}_{tot} = \begin{bmatrix} \overrightarrow{F} \\ \overrightarrow{M} \end{bmatrix} = K\overrightarrow{u}_{tot} = K \begin{bmatrix} \overrightarrow{u} \\ \overrightarrow{\theta} \end{bmatrix} \tag{10}$$

III. Results

Elliptic paraboloids with an eccentricity between 0 and 0.6 are compared. By choosing an appropriate value for the short axis b, the surface area can be kept constant. This way, any side effects resulting from an increasing surface area are eliminated. The major differences between a normal and an elliptic paraboloid are discussed below. The applied displacements and rotations are $u_x = u_y = u_z = 2.10^{-4} mm$ and $\theta_x = \theta_y = \theta_z = 2.10^{-5} rad$. The displacements and force systems are described in the origin of the global coordinate system.

Table I shows the effect of the eccentricity on the forces necessary to move the root over the given distance. For every displacement, the corresponding force is displayed in the table.

TABLE I
FORCES NECESSARY FOR THE DISPLACEMENT

E	0	0.1	0.2	0.3	0.4	0.5	0.6
$u_x - F_x(N)$	1.08	1.08	1.06	1.04	1.00	0.96	0.90
$u_y - F_y(N)$	0.17	0.17	0.17	0.17	0.17	0.17	0.17
$u_z - F_z(N)$	1.08	1.08	1.09	1.11	1.14	1.18	1.25
$\theta_x - M_x(Nmm)$	8.92	8.97	9.00	9.15	9.37	9.68	10.14
$\theta_x - M_x(Nmm)$	0.040	0.040	0.040	0.041	0.047	0.059	0.088
$\theta_x - M_x(Nmm)$	8.94	8.94	8.80	8.67	8.44	8.14	7.76

The results show that the force F_x decreases by approximately 10%, while the force F_y remains constant and F_z increases. This implies a relationship between the cross-sectional area of the root in a plane perpendicular to the

main direction of motion and the force. The larger this area, the larger the force. The same is true for the moments and rotations.

Table 2 shows a significant increase in maximum hydrostatic pressure when rotating the tooth around the y-axis. In a normal paraboloid, the stresses inside the periodontal ligament are purely shear stresses, in an elliptic paraboloid, stresses have a hydrostatic component.

TABLE II
MAXIMAL HYDROSTATIC PRESSURE FOR ROTATION AROUND Y-AXIS

E	0	0.1	0.2	0.3	0.4	0.5	0.6
$P_{max}(10^{-2}MPa)$	0	1.9	7.7	18.0	33.2	54.9	85.5

The stress patterns in the periodontal ligament of the elliptic paraboloid also show periodical components in ϕ that are not present in the stress patterns of the normal paraboloid.

IV. CONCLUSIONS

Results have shown that the stress and strain patterns inside the periodontal ligament vary with the geometrical form of the root. Forces necessary to displace the tooth are different in an elliptic paraboloid compared to a normal paraboloid, although the total surface area of the root remains constant. Another implication is that, when using an elliptic paraboloid, behavior in the x- and the z-directions is different.

The impact of these results on the permanent displacement of the tooth depends on the link between initial displacement and bone remodeling.

ACKNOWLEDGMENTS

This research was funded by IWT-Vlaanderen and Materialise Dental NV (Belgium). An Van Schepdael is a research assistant of the Research Foundation Flanders (FWO-Vlaanderen).

REFERENCES

[1] C.G. Provatidis, *A comparative FEM-study of tooth mobility using isotropic and anisotropic models of the periodontal ligament*, Med Eng & Physics, 2000, Vol 22, 359.

[2] C.G. Provatidis, *An analytical model for stress analysis of a tooth in translation*, Int J Eng Science, 2001, Vol 39, 1361.

Proceedings of the 8th National Congress on Theoretical and Applied Mechanics, May 28-29, Brussels, Belgium.

On the Assessment of Antagonistic Muscle Forces During Forearm Flexion/Extension

Raison Maxime[1], Detrembleur Christine[2], Fisette Paul[1] and Samin Jean-Claude[1]
Université catholique de Louvain
[1]Center for Research in Mechatronics (CEREM)
Levant 2, 1348 Louvain-la-Neuve, Belgium
[2]Rehabilitation and Physical Medicine Unit (READ)
Tour Pasteur, Avenue Mounier 53, 1200 Bruxelles, Belgium
maxime.raison@uclouvain.be, christine.detrembleur@uclouvain.be, paul.fisette@uclouvain.be,
jc.samin@uclouvain.be

Abstract— **Today, the accurate assessment of muscle forces performed by the human body in motion is still expected for many clinical applications and studies. However, as most of the joints are overactuated by several muscles, any non-invasive muscle force quantification needs to solve a redundancy problem. Consequently, the aim of this study is to propose a non-invasive method to assess muscle forces in the human body during motion, using a multibody model-based optimization process that attempts to solve the agonistic and antagonistic muscle overactuation. The main originality of the proposed method is the cautious using of Electromyographic (EMG) data information, known by all to be noisy-corrupted, via a protocol divided into two main steps:**

1. **Muscle force static calibration,**
2. **Muscle force dynamical quantification.**

In this paper, the process is applied to a benchmark case : the force quantification of the elbow flexor and extensor muscle sets of subjects engaged in weightlifting and performing cycles of forearm flexion/extension. A statistical validation of this method shows a good inter-test reproducibility and a very good correlation between a. the net joint torques resulting from the obtained muscle forces and b. the net joint torques given by inverse dynamics.
Consequently, since the method is able to consider measured information on the actual muscle activation, it becomes a promising alternative to methods based on preset strategies, usually presented in literature, such as the strategy that maximizes endurance defined by Crowninshield et al.

Keywords— **Multibody, Biomechanics, Muscle force, Overactuation, Optimization, Inverse dynamics.**

I. Introduction

TODAY , the accurate assessment of internal efforts, and particularly the muscle forces performed by the human body in motion, is still expected for applications in many fields, like :

- Rehabilitation : for the evaluation and follow-up of patients with musculo-skeletal pathologies, e.g. using gait analysis for hemiparetic [1] or scoliotic [2] patients ;
- Ergonomics : for comfort analysis of vehicle drivers [3] or during vehicle accessibility motion [4] ;
- Prevention : in order to avoid the risks of wounds and the appearance of pathologies associated with motions, e.g. during maximal pushing efforts [5] ;
- Sports : in order to analyse and improve athletic performances, e.g. during pedaling [6] or somersault on trampoline [7].

However, as most of the joints are overactuated by several muscles (2.6 muscles in average per *degree of freedom* (DOF) in the human body [8]), any non-invasive muscle force quantification needs to solve a redundancy problem.

A. Redundancy problem formulation

Let us consider for instance the flexion/extension of the human elbow. As represented in Figure 1, this system is composed of three body members, the arm, the forearm and the hand, which are articulated around joints, the shoulder, the elbow and the wrist, respectively.

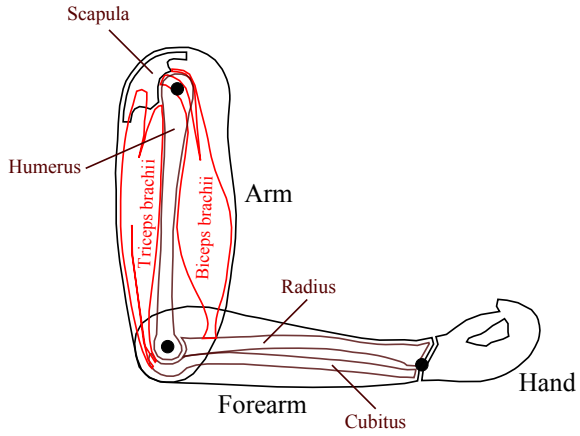

Fig. 1. Illustration of the human elbow, including a representation of the flexor muscle sets (biceps brachii) and extensor muscle sets (triceps brachii) that overactuate the elbow joint.

Particularly, the elbow joint flexion/extension is actuated by :

- The *flexor* (or *agonistic*) muscle set, mainly composed of the longus and brevis biceps brachii ;
- The *extensor* (or *antagonistic*) muscle set, mainly composed of the longus and lateral triceps brachii.

Consequently in this example, we can state that on the one hand, pure flexion/extension corresponds to one rotational DOF of the joint elbow, and that on the other hand, there is one flexor muscle set and one extensor muscle set, which together overactuate the elbow joint.

The link between the individual muscle forces produced about the joint and the corresponding equivalent torque at the elbow can be obtained via the *Principle of Potential Power*, as follows :

$$\mathbf{T}_E \cdot \Delta\omega_E = \sum_{i=1}^{N} \mathbf{F}_{m,i} \cdot \Delta\mathbf{v}_i \qquad (1)$$

where :

- $\mathbf{T}_E$ is the equivalent torque vector at the elbow joint ;
- $\mathbf{F}_{m,i}$ is the force vector performed by the i^{th} muscle set, for $i = 1, \ldots, N$ muscle sets; here this corresponds to the flexor set ($i = 1$) and extensor set ($i = 2$) ;
- $\Delta\omega_E$ is the potential variation of the angular velocity vector at the elbow during flexion/extension;
- $\Delta\mathbf{v}_i$ is the potential variation of the translation velocity vector of the i^{th} muscle set insertion points, for $i = 1, \ldots, N$ muscle sets; here this corresponds to the flexor set ($i = 1$) and extensor set ($i = 2$) ; both $\Delta\omega_E$ and $\Delta\mathbf{v}_i$ must be chosen compatible [9] with the kinematic description of the motion.

Practically, as vectors $\Delta\omega_E$ and $\Delta\mathbf{v}_i$ can be determined using kinematic measurements and anatomical information, and as the joint equivalent torque $\mathbf{T}_E$ can be determined using inverse dynamics, the only unknown variables in Equation (1) are the muscle forces, $\mathbf{F}_{m,i}$. As the motion of forearm pure flexion/extension is here considered as having one DOF, Equation (1) is a mathematically redundant system that has an infinite number of possible solutions for the muscle force repartition between $\mathbf{F}_{m,1}$ and $\mathbf{F}_{m,2}$.

B. Objective of this study

In this context, the aim of the present study is the development of a non-invasive method to quantify the muscle efforts of the human body in motion, on the basis of a model-based optimization that attempts to solve the muscle redundancy problem, including a cautious use of EMG data. The process is applied to a benchmark case : the force quantification of the elbow flexor and extensor muscle sets of subjects engaged in weightlifting and performing cycles of forearm flexion/extension.

II. Material and Methods

A. Principle

The principle of our method, schematically outlined by Figure 2, is divided into two main steps: the muscle force calibration in statics and the muscle force quantification in dynamics.

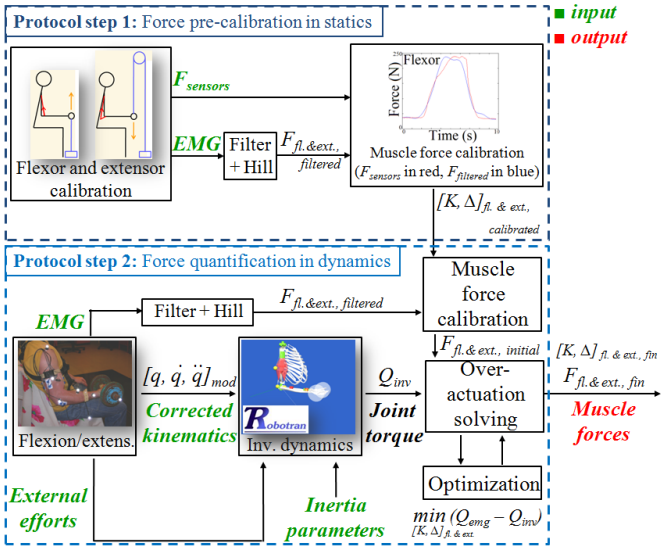

Fig. 2. General principle of the muscle force quantification, featuring both protocol steps.

A.1 Protocol step 1: force calibration

While EMG is reasonably proportional to the muscle force in *static* conditions [16], we must be aware that EMG is not sufficiently reproducible if the data recording does not exactly follow the same protocol. Consequently, we decided to calibrate the forces of the flexor and extensor muscle sets in isometric conditions, using proper EMG filtering and the Hill model [17]: here (Figure 2, step 1), the elbow angle is 90° in the sagittal plane; the subject pulls on a rope fixed to a strain gauge on the floor (flexors activated), then the subject pulls on a rope fixed to this strain gauge via a pulley on the ceiling (flexors and extensors activated). This calibration gives the scale (factor K) and offset (factor Δ) that will be used to calibrate muscle forces during the flexion/extension, which will only be used as "not too bad" initial values of forces as input for the muscle overactuation solving (Figure 2, step 2).

A.2 Protocol step 2: force quantification

As soon as the calibration is completed, the subjects, still equipped with exactly the same optokinetic and EMG sensors, are engaged in weightlifting and perform several cycles of forearm flexion/extension (Figure 2, step 2). For each of these trials, the model-based process comprises three consecutive steps, detailed in Section II-D:

1. **Kinematics identification:** an optimization process that estimates the joint configurations, q_{mod}, of the multibody model that best fits the experimental joint configurations, q_{exp}, measured by optokinetic sensors. The corresponding velocities, $\dot{q}$, and accelerations, $\ddot{q}$, are determined using numerical derivatives.

2. **Inverse dynamics:** an inverse dynamical model that provides the elbow contributive net torque Q_{inv} via recursive Newton-Euler equations of motion of the multibody model, available in symbolical form.

3. **Muscle overactuation solving:** an optimization process that computes the forces of the flexor and extensor muscle sets during forearm flexion/extension. Starting from the K and Δ factors given by step 1 of the protocol and the filtered flexor/extensor forces during flexion/extension, this optimization adapts K and Δ so that the elbow net torque Q_{emg}, computed from the muscle forces, given their insertion points, best fits the elbow net torque Q_{inv} given by the inverse dynamics.

B. Experimental set-up

The measurement set-up (Figure 3) is composed of seven optokinetic sensors (*Elite-BTS* acquisition system) fixed at the subject's joint landmarks, and also ElectroMyoGraphic (or EMG) data (*Elite-BTS*), which allow us to calculate the activation of the considered muscles during the motion.

The optokinetic data are sampled at 100 Hz and filtered by a 15 Hz adaptive low-pass numerical filter. The EMG data are first sampled at 1000 Hz, then synchronized with the data at 100 Hz, after being rectified and filtered by a 5^{th} order Butterworth low-pass filter (Ref. [17]) as will be developed in Section 3.3.1.

The experiments were performed by healthy subjects related to our laboratory, who gave their informed consent to perform the experiments.

C. Model and hypotheses

First of all, the system is modeled as a constrained multibody system, using kinematic loops. As we are using the coordinate partitioning method, independent and

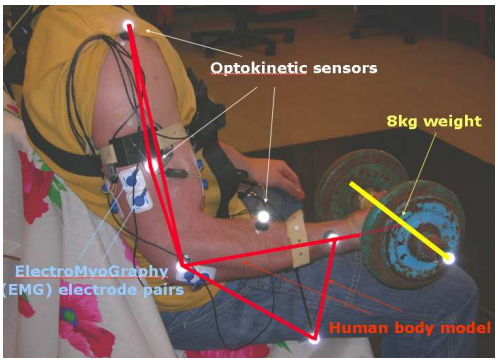

Fig. 3. Illustration of the subject carrying an 8 kg weight and performing several cycles of forearm flexion and extension, featuring the optokinetic sensors (white spheres) and the EMG electrodes (blue double grips). Superimposition of the multibody model (red segments) on the basis of the weight configuration (yellow line) and the optokinetic sensors.

dependent variables are systematically used to model this closed-loop system. In detail, the multibody system is composed of two rigid bodies (the arm and the forearm) articulated around spherical joints (the shoulder and the elbow), giving a total of six independent variables. The third body, the wrist, is attached to the forearm via a blocked rotational joint. The shoulder joint is considered as the reference point of the model, given that the subject is supposed to keep the shoulder joint fixed during the tests. Both flexor/extensor muscle sets I-A are modeled using kinematic loops in order to consider them as real bodies with mass and inertia parameters, using for each muscle set motion three dependent rotational variables and one independent translational variable.

A few characteristics and assumptions must be formulated about the different sets of inputs:

- The shoulder joint being considered as the reference point of the model, the forces $\mathbf{F}_{ext}$ and torques $\mathbf{M}_{ext}$ between the body and its environment, i.e. the "upper-shoulder", do not need to be measured by a dynamometric device, and these can be derived using the action-reaction principle.

- The body inertia parameters, i.e. the masses m_j, moments of inertia I_j and centre of mass positions $\overrightarrow{OM}_j$ of the j^{th} body member are taken from the inertia tables of De Leva [18]. The inertia parameter identification is not part of this research: indeed, previous investigations [19] showed that non-invasive in-vivo dynamical identifications of body parameters are presently inappropriate with the human body dynamics, because the resulting body parameters have significant inaccuracies due to experimental errors in the input data, such as the body configuration, or the external force and torque measurements.

• The system configuration, i.e. the experimental absolute coordinates x_{exp} of the reference points, are measured by the six optokinetic sensors. The corresponding joint coordinates q of the multibody model are numerically determined by a kinematic identification process and the corresponding velocities $\dot{q}$ and accelerations $\ddot{q}$ are presently estimated from the q by numerical differentiation techniques. Considering the joint kinematics, we are aware that more adequate elbow and shoulder joint models could be used: in particular, previous studies [20] have developed more complex three-dimensional joints for the shoulder. The present model has been implemented with spherical joints, which is sufficiently accurate [21] at present to develop our muscle overactuation solving method, but the model will be extended in the future to include more involved joints. Finally, let us note that the elbow flexion/extension is physiologically defined using only one DOF. However, in order to take into account the actual experimental kinematics, we decided to implement three DOFs at the elbow and we will further project the elbow torque Q onto the instantaneous angular velocity vector ω_E, in order to obtain elbow joint net torque Q_{inv} that contributes to the motion of flexion/extension, as follows :

$$Q_{inv} = \mathbf{Q} \cdot \frac{\omega_E}{||\omega_E||} \tag{2}$$

D. Process of muscle force quantification

As introduced in Section 2, the protocol and the underlying calculation process are divided into two main steps: the muscle force calibration in statics (detailed in Section II-D.1) and the muscle force quantification (Section II-D.2).

D.1 Muscle force calibration

While the EMG is reasonably proportional to the muscle force in *isometric* conditions [16], we must be aware that the EMG is not sufficiently reproducible if the data recording does not exactly follow the same protocol. Consequently, we decided to calibrate the forces of the flexor and extensor muscle sets in isometric conditions, using proper EMG filtering and the Hill model [17]: here (Figure 2, step 1), the elbow angle is 90° in the sagittal plane; the subject pulls on a rope fixed to a strain gauge on the floor (flexors activated), then the subject pulls on a rope fixed to this strain gauge via a pulley on the ceiling (flexors and extensors activated).

The muscle force calibration can be divided into five sequential steps to transform the raw EMG data of a muscle to its calibrated force, as described in the following subsections.

D.1.a EMG rectification. First of all, the raw EMG signal must be rectified, i.e. the absolute values of each signal sample are taken, in order to take into account the fact that the EMG electrodes record a signal of muscle fiber polarization-depolarization [17].

D.1.b EMG filtering. High-frequency noise, such as electrical interference or artifacts due to the motion, must be removed from the signal by applying a low-pass filter that has zero-phase delay properties, so filtering does not shift the signal in time; in practice, we have chosen the commonly recommended forward and reverse low-pass 5^{th} order Butterworth filter, with a cut-off frequency of 15 Hz in order to be sure to take the muscular contraction frequencies into account (knowing that the highest known muscular contraction frequencies are 12 Hz for a stressed muscle). Finally, this signal must be normalized with respect to its maximal value, in order to obtain a number between 0 and 1, representing the muscle fiber recruitment rate. Once this process is completed, the transformed EMG signal becomes the *filtered* signal labeled $e(t)$.

D.1.c Neural activation. The muscle does not contract exactly at the time instant at which the motor unit is triggered [17] : indeed, there is a time delay τ_{ne} during which the muscle is preparing to produce force, and once the muscle begins contracting, the tension ramps up to a peak that does not coincide with the EMG peak. One simple way to model this delay is using a first order differential equation [17] between the rectified and filtered EMG, $e(t)$, and the *muscle excitation* signal usually labeled $u(t)$, as follows :

$$\dot{e} = (u - e)/\tau_{ne} \tag{3}$$

where τ_{ne} is the *excitation time constant*. Let us note that $e(t)$ is still a number between 0 and 1, also representing the muscle fiber recruitment rate.

D.1.d Activation dynamics. The muscle excitation $u(t)$ can be related to the corresponding *muscle activation* $a(t)$ by a non-linear first order differential equation [22]:

$$\dot{a} = (u - a)/\tau_a(a,u) \tag{4}$$

where $\tau_a(a,u)$ is a time constant that varies with activation level and whether the muscle activation level is increasing or decreasing [22, 23]:

$$\tau_a(a,u) = \quad \tau_{act}(0.5 + 1.5a) \quad if\ u \geq a \tag{5}$$

$$\tau_{deact}/(0.5 + 1.5a) \quad if\ u < a \tag{6}$$

where τ_{act} is the *activation time constant* and τ_{deact} is the *deactivation time constant*. This relationship predicts that

the activation slows as activation level increases due to less efficient calcium release and diffusion [22, 24]. Similarly, deactivation slows when muscle activation level decreases because there is less calcium ions available for uptake by the sarcoplasmic reticulum [22, 24]. Let us note that, usually, τ_{act} = 15 ms and τ_{deact} = 50 ms according to Ref. [22, 24]. However, for older adults, τ_{deact} increases to 60 ms according to Ref. [23].

Finally, the muscle activity is normalized with respect to the maximum voluntary contraction activity [22, 24], so that $a(t)$ is a number between 0 and 1, representing the muscle fiber recruitment rate.

D.1.e Contraction dynamics. The transformation from raw EMG data to muscle force is partially based on the well-known *Hill model* (Ref. [22, 17]) and is widely spread (e.g. Ref. [25, 26, 23, 24]), for which the musculo-tendon complex is composed of the tendon and the muscle :

- the tendon is a passive wire that does not generate movement;
- the muscle consists in a parallel *Passive Element* (generally noted PE) with an active *Contractile Element* (generally noted CE) that generates contraction of the muscle controlled by neural excitation and then its lengthening or its shortening. Contractions of the muscle are assumed to be iso-volume [17].

Further, the muscle force F_m^{EMG} is computed using the *contraction dynamics* equation :

$$F_m^{EMG} = F_{max} \quad [\underbrace{a(t)\widetilde{F}_l^{CE}(\widetilde{l}_m)\widetilde{F}_v^{CE}(\widetilde{v}_m)}_{active} \quad \underbrace{+\widetilde{F}_l^{PE}(\widetilde{l}_m)+b_m\widetilde{v}_m}_{passive\ \ damping}] \quad (7)$$

where

- F_{max} is the maximal isometric force that a muscle can perform; F_{max} is evaluated here by statistical tables (Ref. [27]).
- $a(t)$ is the *muscle activation* (Ref. [22]), a number between 0 and 1 representing the muscle fiber recruitment rate; $a(t)$ is computed from the EMG data using the three consecutive steps of *EMG rectification and filtering* (Ref. [17]), *neural activation* (Ref. [17]) and *activation dynamics* (Ref. [22]) that will be developed in the following subsections;
- $\widetilde{F}_l^{CE}(\widetilde{l}_m)$, $\widetilde{F}_v^{CE}(\widetilde{v}_m)$ and $\widetilde{F}_l^{PE}(\widetilde{l}_m)$ represent the *active force-length*, *active force-velocity* and *passive force-length* relations (Ref. [17, 23]), respectively, which are defined by the Hill model; let us note that the $\sim$ sign above the variables means that these are normalized, i.e. the force components $\widetilde{F}_l^{CE}$, $\widetilde{F}_v^{CE}$, $\widetilde{F}_l^{PE}$ are normalized with respect to F_{max}, the muscle length $\widetilde{l}_m$ is normalized with respect to the muscle optimal fiber length l_m^{opt} (given by Ref. [27]) and the muscle velocity $\widetilde{v}_m$ is normalized with respect to the muscle maximal contraction velocity v_{max} (given by Ref. [27]).
- b_m is the damping factor, experimentally set to 0.1 by Ref. [28].

Despite the fact that this transformation process is widely spread, it is not trivial because it is based on a model, on factors given by statistical tables, and on raw EMG data that do not directly measure the muscle activation but the external electro-magnetic field generated by this activation.

As the last step of the process, F_m^{EMG} is computed using the *contraction dynamics* given by Equation (7). In this Equation, we can observe that $a(t)$ is given by the activation dynamics, that $\widetilde{l}_m$ and $\widetilde{v}_m$ can be computed from the muscle kinematic measurements, and that b_m is set equal to 0.1 by Ref. [28]. Consequently, we will essentially describe in this Section the formulations of the last elements of Equation (7), i.e. the force components $\widetilde{F}_l^{CE}$, $\widetilde{F}_v^{CE}$ and $\widetilde{F}_l^{PE}$, on the basis of different current References, as these formulations are continually improved :

1. The active force-length relationship $\widetilde{F}_l^{CE}$ of the muscle is represented by a Gaussian function [23]:

$$\widetilde{F}_l^{CE} = e^{-(\widetilde{l}_m-1)^2/\gamma} \quad (8)$$

where $\widetilde{l}_m$ is the normalized muscle fiber length, and γ is a shape factor that approximates the force-length relationship of individual sarcomeres, set to 0.45 [23].

2. The active force-velocity relationship $\widetilde{F}_v^{CE}$ of the muscle is represented by the following function [23]:

$$\widetilde{F}_v^{CE} = -A_f\left(1+\frac{0.25+0.75a}{\widetilde{v}_m}\right) \quad if\ \ \widetilde{F}_v^{CE} \leq a\widetilde{F}_l^{CE} \quad (9)$$

$$\frac{\frac{\widetilde{v}_m(2+2/A_f)\widetilde{F}_m^{len}}{(0.25+0.75a)(\widetilde{F}_m^{len}-1)}+1}{\frac{\widetilde{v}_m(2+2/A_f)}{(0.25+0.75a)(\widetilde{F}_m^{len}-1)}+1} \quad if\ \ \widetilde{F}_v^{CE} > a\widetilde{F}_l^{CE} \quad (10)$$

where

- a is the previously computed muscle activation;
- $\widetilde{v}_m$ is the normalized muscle contraction velocity;
- $\widetilde{F}_m^{len}$ is the maximum normalized muscle force achievable when the fiber is lengthening, set to 1.4 for young adults [23];
- A_f is a force-velocity shape factor, which was set to 0.25 [22].

Let us note that, using this formulation, the alternative choice of $\widetilde{F}_v^{CE}$ calculus is made by evaluating a posteriori the inequality between $\widetilde{F}_v^{CE}$ and $a\widetilde{F}_l^{CE}$.

3. The passive force-length relationship $\widetilde{F}_l^{PE}$ of the muscle is represented by an exponential function [23]:

$$\widetilde{F}_l^{PE} = \frac{e^{k^{PE}}(l^m - 1)/\varepsilon_m^0 - 1}{e^{k^{PE}} - 1} \tag{11}$$

where

- k^{PE} is a shape factor, set to 5 [23];
- ε_m^0 is the passive muscle strain due to maximum isometric force, set to 0.6 for young adults [23].

D.2 Muscle force quantification

The method will be developed considering the consecutive steps introduced in Section II-A.2, i.e. the kinematics identification that defines the model motion, the inverse dynamics that computes the elbow joint torque, and the proposed method to solve the muscle redundancy problem.

D.2.a Kinematics identification. Let us note from the start that inverse dynamics is a familiar tool to obtain results of joints efforts, but it is not obvious to obtain accurate results that could be usefully exploited, e.g. for the joint analysis of pathologic cases or the design of intelligent prostheses. The main reason is that the estimate of the internal forces is particularly sensitive to accelerations, and those ones are classically calculated by numerical derivatives starting from the measured positions, which dramatically amplifies the errors of measurement which are associated for them. Presently, the only way to obtain accurate results of joint efforts using inverse dynamics is a kinematic identification process, also known as solidification method [29]. The results of elbow joint torques, obtained via inverse dynamics using kinematic data corrected by a kinematic identification process.

This process estimates the joint coordinates of the multibody model that best fit the experimental joint positions $X_{exp,s}$. This kinematic optimization problem can be formulated as a nonlinear least-square problem applied for each body configuration, at each time instant t_k, $k = 1,\ldots,T$, where T is the last time sample of each test. Consequently, the cost function $f_{cost}(t_k)$ can be written at each time instant t_k as follows:

$$f_{cost}(t_k) = \sum_{s=1}^{n_{sens}} |X_{mod,s}(q(t_k)) - X_{exp,s}(t_k)|^2 \tag{12}$$

where

- the index $s = 1,\ldots,n_{sens}$ indicates the optokinetic sensor (n_{sens} = 7 as described in Figure 3b);
- $q(t_k)$ is the multibody joint coordinate vector at the time instant t_k, and is the variable of the optimization process;
- $X_{mod,s}(q(t_k))$ is the cartesian coordinate of the s^{th} optokinetic sensor at the time instant t_k, obtained from the $q(t_k)$, using the forward kinematic model of the multibody system;
- $X_{exp,s}(t_k)$ is the cartesian coordinate of the s^{th} optokinetic sensor at the time instant t_k, provided by the experimental set-up.

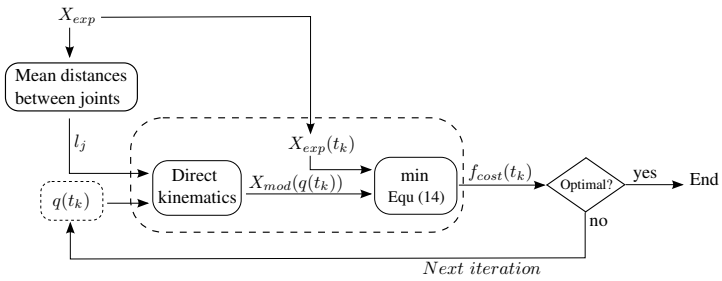

Fig. 4. Optimization process for a body configuration, at a time instant t_k

Figure 4 schematically outlines the optimization process, which involves two consecutive steps:

1. A pre-process calculates the mean distances l_j between the joints for each of the j^{th} body member, using the experimental joint cartesian coordinates $X_{exp,s}(t_k)$. The reason is that the approach is based on a multibody model, composed of rigid bodies, for which a variable size of the bodies would be irrelevant.

2. The model joint cartesian coordinates $X_{mod,s}$ are given by a forward kinematic model using the l_j distances and an initial value (set to zero) of the joint coordinates $q(t_k)$ that we want to determine. The cost function, presented by Equation (12) of this least-square optimization is defined as the sum of the square components of the absolute error vector between $X_{exp,s}(t_k)$ and $X_{mod,s}(q(t_k))$ of the n optokinetic sensors at the time instant t_k. In order to improve the numerical convergence, the optimal value of $X_{mod,s}(q(t_k))$ is obviously chosen as the initial condition of the next iteration at the time instant t_{k+1}.

Finally, now that the configurations q are properly corrected, the corresponding velocities, $\dot{q}$, and accelerations, $\ddot{q}$, can be obtained via numerical differentiations.

D.2.b Inverse dynamics. The multibody dynamical equations are obtained from a Newton-Euler formalism [30]: this algorithm provides the vector Q_{inv} of internal interaction torques and forces at the joints for any configuration of the multibody system, in the form of an inverse dynamical model (Equation (13)), or a semi-direct dynamical model

(Equation (14)) :

$$Q_{inv} = \phi(q,\dot{q},\ddot{q},F_{ext},M_{ext},g) \quad (13)$$
$$= M(q)\ddot{q} + c(q,\dot{q},F_{ext},M_{ext},g) \quad (14)$$

where

- q (7×1) is the vector of the human body relative generalized coordinates, i.e. successively 3 arm rotations + 3 forearm rotations + 1 hand rotation[1] = 7 components;
- $\dot{q}$ and $\ddot{q}$ (7×1) are the joint velocities and accelerations, respectively;
- $M(q)$ (7×7) is the generalized mass matrix;
- $c(q,\dot{q},F_{ext},M_{ext},g)$ (7×1) is the dynamical vector containing the gyroscopic, centripetal, Coriolis terms as well as the external forces F_{ext} (7×3) and torques M_{ext} (7×3) and gravity g (1×3) applied to the system.

D.2.c Muscle redundancy solving. As introduced in Section II-A.2, the key point of our muscle overactuation solving is based on an optimization process that computes the forces of the flexor and extensor muscle sets during forearm flexion/extension. Starting from the K and Δ factors given by step 1 of the protocol and the filtered flexor/extensor forces during flexion/extension, this optimization adapts the K and Δ factors of the flexors and extensors so that the corresponding elbow net torque Q_{emg} best fits the elbow net torque Q_{inv} given by the inverse dynamics, on the whole trajectory. Practically, this problem is formulated using the non-linear least squares method 'lsqnonlin' provide by Matlab.

III. Results

A. Muscle forces

A.1 Muscle force assessment

First, Figure 5a presents the time evolution (in red) of the elbow joint net torque Q_{inv} obtained from inverse dynamics, compared to the equivalent joint net torque (in blue) obtained from the calibrated Forces $F_{fl.\&ext.,initial}$ (output of protocol step 1) via Equation (1), and also compared to the equivalent joint net torque (in black) obtained from the optimized Forces $F_{fl.\&ext.,final}$ (output of protocol step 2) via Equation (1).

Secondly, Figure 5b compares several solutions of the Biceps brachii and Triceps brachii set contributions at one time instant t of the flexion/extension:

[1]momentarily blocked

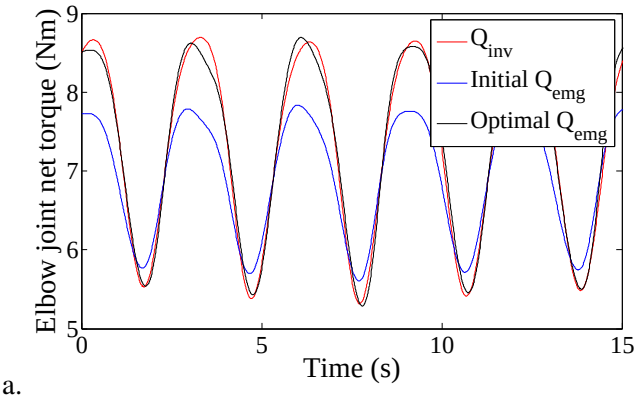

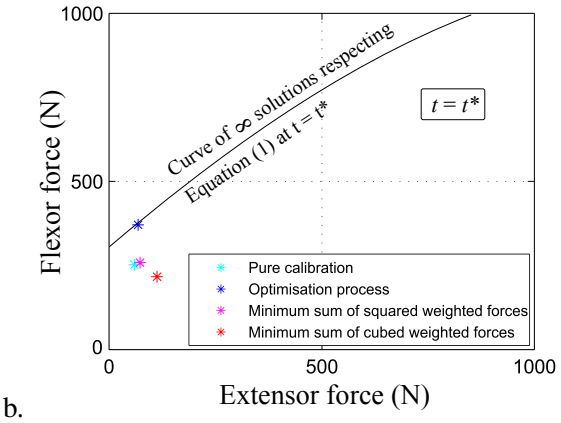

Fig. 5. a. Comparison between the elbow joint net torque Q_{inv} obtained from inverse dynamics, the equivalent joint net torque obtained from the calibrated Forces $F_{fl.\&ext.,initial}$ (output of protocol step 1) via Equation (1), and the equivalent joint net torque obtained from the optimized Forces $F_{fl.\&ext.,final}$ (output of protocol step 2) via Equation (1) b. Comparison of the solutions of the Biceps brachii and Triceps brachii set contributions at one time instant $t = t^*$: the solution of $F_{fl.\&ext.,initial}$ given by the pure calibration (cyan), the solution of $F_{fl.\&ext.,final}$ given by our proposed optimization process (blue), and the solutions of strategies that maximize endurance, i.e. that minimize the sum of the weighted forces at square (magenta) or at cube (red).

1. the solution of $F_{fl.\&ext.,initial}$ (in light blue) given by the pure calibration (output of protocol step 1, and input of protocol step 2);
2. the solution of $F_{fl.\&ext.,final}$ (in dark blue) given by our proposed optimization process (output of protocol step 2), corresponding to the re-scaled and re-shifted calibrated value of $F_{fl.\&ext.,initial}$;
3. the solution of a strategy that maximizes endurance [15], by minimizing the sum of the weighted forces at square (in magenta) or at cube (in red).

A.2 Statistical validation

For one subject, Figure 6 presents the results of muscle forces during forearm flexion/extension, using the final values of the K and Δ factors during the muscle overactu-

ation solving process.

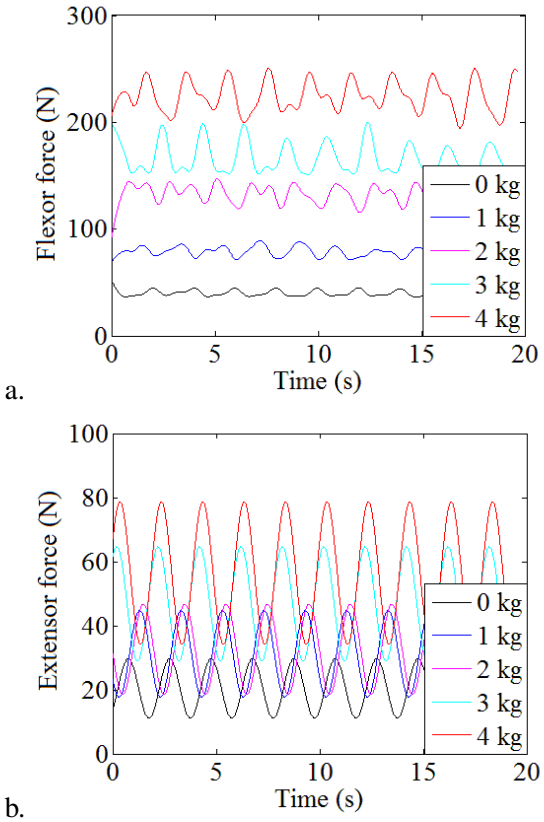

Fig. 6. Results of the summed flexor (biceps set) forces *(a)* and extensor (triceps set) forces *(b)* for one subject carrying weights from 0 to 4 kg and performing cycles of forearm flexion/extension at 1/2Hz.

First of all, Figs. 6 *(a)* and 6 *(b)* clearly – and fortunately – show a gradation of the forces according to the weights carried. More fundamentally, a statistical validation of this muscle effort quantification method was performed with six male and six female subjects carrying five different weights (from 0 to 4 kg) with several flexion/extension frequencies ($\frac{1}{2}$, $\frac{1}{3}$ and $\frac{1}{4}$ Hz). This validation shows a good inter-test reproducibility (also showing a fatigue effect) and a very good correlation (correlation factor $r = 0.99$) between Q_{inv} and Q_{emg} at the end of the identification process.

IV. Discussion

A. Joint kinematics and dynamics

The present inverse dynamical model of the human body (Figure 1), necessarily preceded by a kinematic identification of the model configurations, is proposed as a satisfying method to estimate the joint efforts in dynamical context [21]. This problem being deterministic, Q_{inv} becomes a sufficiently accurate result that can be exploited as a reference for the optimization process that attempts to solve the muscle force redundancy (protocol step 2).

Nevertheless, let us point out that three main limitations of the present inverse dynamical model must be discussed in order to improve the process in the future :

1. *A geometrical limitation, due to the use of spherical joints :* The results of the kinematic analysis for this experiment show that the spherical joints considered here sufficiently fit the envisaged motion, with a mean absolute error on the Cartesian coordinates that is inferior to 3 *mm* in each direction at each joint (shoulder + elbow). However, using previous investigation results, the present model will be extended to include more involved joints in the future, particularly to model shoulder [20] that is far from being a spherical joint.

2. *A kinematic limitation, due to the rigid multibody system assumption :* The proposed model is composed of rigid segments. However, in reality, the body is not composed of a set of rigid bodies. Rather, each body member consists of a rigid part (bone), and a non-rigid part (skin, muscle, ligament, tendon, connective tissue, and other soft tissue structures) [31]: during any motion, the skeletal structure of the body experience accelerations, whereas the soft tissue motion is delayed, due to damped vibrations of the member. Consequently, the errors in the optimized joint coordinates q may introduce kinematical errors in the velocities $\dot{q}$ and accelerations $\ddot{q}$, and thus introduce errors in the estimation of the internal efforts [21].

3. *A dynamical limitation, due to the approximation of the body inertia parameters :* The body inertia parameters, i.e. the masses, moments of inertia and centre of mass positions of the body members (the arm and the forearm) are approximated, using inertia tables [18]. Consequently, the errors in the estimated net joint efforts Q_{inv} increase if the corresponding body member accelerations increase. This is the reason why the present model is only proposed for rather low dynamics, such as our tests of forearm flexion/extension with a cycle frequency from $\frac{1}{4}$ to $\frac{1}{2}$ Hz, or other tests such as getting up from a seat [21], gait experiments [2] or other motions without significant dynamics or impact.

B. Muscle force quantification

If we make the assumption that the optimized kinematics and the net joint efforts Q_{inv} resulting from inverse dynamics are sufficiently accurate to attempt to solve the muscle overactuation problem (as discussed in IV-A), we still have to deal with two main problems [32] in order to estimate the muscle efforts:

1. the noisy-corrupted raw EMG signals; consequently,

we will discuss in Section IV-B.1 the role of the EMG processing, including the Hill model and its numerous parameters, and the choice of parameters that we decided to vary in the optimization process (Section II-D.2).

2. the undetermined number of solutions of muscular efforts; consequently in Section IV-B.2, we will compare our proposed solution with the main solutions of 'maximum endurance' strategy and 'EMG calibration' presented in the literature.

B.1 EMG processing and parameter choice

The raw EMG signals are noisy-corrupted and do not provide accurate quantitative values of the actual muscle excitation $u(t)$ and consequently of the actual muscle force F_m. However, we think that this information, combined with a matured EMG processing (Section II-D.1) and a muscle force calibration process can provide a first estimation of the muscle force that will constitute a reasonable initial value of the optimization process (Section II-D.2), which will compute the predicted muscle forces during the motion.

Further, if we attempt to solve the muscle overactuation problem using an optimization process, *"too many parameters is not good"* (Buchanan et al [26]): on the one hand, increasing the number of parameters to vary for a specific test shall certainly help to better fit the estimated joint torque Q_{emg} to the joint torque Q_{inv} obtained from inverse dynamics; but on the other hand, increasing the number of parameters may increase the sensitivity of the optimization process, and thus decrease the repeatability of the muscle force results from one test to another.

In consequence, we decided to use the EMG processing (Section II-D.1), and more specifically the Hill model, as a black-box based on parameter tables, so that we will not have to deal with too many parameters in the optimization process, and we prefer to deal with the scaling K and the shifting Δ factors of the muscle forces $F^{fl.\&ext.,initial}$ resulting from the Hill model.

B.2 Comparison to existing methods

If we use an anatomical model of the musculoskeletal system, an infinite undetermined number of solutions of muscular efforts can correspond to the joint efforts Q_{inv}, because the joints are overactuated. In order to find the best physiologically admissible solution, we decided to estimate the muscle forces from the kinematics, from the corresponding Q_{inv} that becomes our "reference value", and from the information contained by the EMG signal.

The comparison between all considered solutions (Figure 5b) shows that :

1. the solution of $F_{fl.\&ext.,initial}$ given by the pure calibration does not minimize $Q_{inv} - Q_{emg}$ but their role as initial values of our optimization process is clearly justified ;

2. the solution of $F_{fl.\&ext.,final}$ given by our proposed optimization process minimizes $Q_{inv} - Q_{emg}$ with a small difference between Q_{inv} and Q_{emg} (Figure 5a) and this can be proposed as an admissible solution of muscle force repartition ;

3. the solutions of strategies that maximize endurance [15] by minimizing the sum of the weighted forces at square or at cube do not minimize $Q_{inv} - Q_{emg}$; these are just approximation of the human motion strategies ; further, we can notice that the solution of $F_{fl.\&ext.,final}$ given by our proposed optimization is generally superior to the forces given by these strategies, which tends to confirm that the actual force repartition during motion does not always maximize endurance, and more generally varies from a strategy to another, as noticed Crowninshield et al [15] who developed and discussed these strategy models.

To end, the statistical validation shows a good inter-test reproducibility (also showing a fatigue effect) and a very good correlation (correlation factor $r = 0.99$) between Q_{inv} and Q_{emg} at the end of the identification process. This confirms that this method of muscle force calibration plus optimization, based on muscle activity measurements, is a promising alternative to methods based on strategies usually used in the literature.

In summary, today, we can say that there are as many solutions of muscular efforts as methods that attempt to predict these. Nevertheless, the solution of $F_{fl.\&ext.,final}$ given by our proposed protocol is coherent with the joint kinematics and system dynamics, also taking with precaution the experimental information on the muscle activation into account.

C. Prospects

The main prospects of this research is to quantify with a satisfying accuracy the main muscle set efforts of subjects in different dynamical contexts, and to apply the model to develop :

- complementary diagnostic and follow-up tools for several pathologies such as lumbalgy, hemiplegy, scoliosis and pathologies that can hardly be diagnosed, such as fibromyalgy ;
- dimensioning tools for the design and choice of adapted prostheses by physicians and clinicians ;

• studies of effort hardness and ergonomic adaptation, e.g. when people with disabilities go into/out of vehicles.

REFERENCES

[1] De Groote, F., Pipeleers, G., Jonkers, I., Demeulenaere, B., Swevers, J., and De Schutter. J. Physiology based inverse dynamic analysis of normal and hemiparetic gait, *Gait & Posture*, **26**(S17), 2007.

[2] Raison, M., Aubin, C.É., Detrembleur, C., Fisette, P., and Samin, J.C. Quantification of intervertebral efforts during walking : comparison between a healthy and a scoliotic subject. *Studies in Health Technology and Informatics*, 140, Research into Spinal Deformities **6**, 61-64, 2008.

[3] Silva, M., Ambrósio, J., and Pereira, M. A multibody approach to the vehicle and occupant integrated simulation. *International Journal of Crashworthiness*, **2**(1), 73-90, 1997.

[4] Debril, J.F., Pudlo, P., El Menceur, M., Gorce, P., and Lepoutre, F.X. Human Articulation Efforts Estimation in the Automobile Vehicle Accessibility Movement - A Pilot Study. In *Computer Science. Proceedings of the First International Conference on Digital Human Modeling*, Beijing, China, 23-32, 2007.

[5] Raison, M., Gaudez, C., Le Bozec, S., and Willems, P.Y. Determination of joint efforts in the human body during maximum ramp pushing efforts. *Journal of Biomechanics*, **40**(3), 627-33, 2007.

[6] Gergersen, C.S., and Hull, M.L. Non-driving intersegmental knee moments in cycling computed using a model that includes three-dimensional kinematics of the shank/foot and the effect of simplifying assumptions. *Journal of Biomechanics* **36**, 803-813, 2003.

[7] Blajer, W., and Czaplicki, A. Modeling and inverse simulation of somersaults on the trampoline. *Journal of Biomechanics*, **34**(12), 1619-1629, 2001.

[8] Amarantini. Estimation des Efforts Musculaires À Partir des Données Périphériques: Application à l'Analyse de la Coordination Pluri-Articulaire. *Thesis of the Université Joseph Fourier*, Grenoble 1, France, 2003.

[9] Willems, P.Y. *Introduction à la mécanique*. Ed. Masson, 208 pp, 1979.

[10] Weber, W., and Weber, E. *Mechanik der Menschlichen Gehwerkzauge*, Gottingen: Gottinger, 1836.

[11] Seireg, A., Arvikar, R.J. A mathematical model for evaluation of force in lower extremities of the musculo-skeletal system. *Journal of Biomechanics* **6**, 313-326, 1973.

[12] Penrod, D.D., Davy, D.T., and Singh, D.P. An optimization approach to tendon force analysis. *Journal of Biomechanics* **7**, 123-129, 1974.

[13] Dul, J., Johnson, G.E., Shiavi, R., and Townsend M.A. Muscular synergism II. A minimum-fatigue criterion for load sharing between synergistic muscles. *Journal of Biomechanics*, **17**(9), 675-84, 1984.

[14] Epstein, M., Herzog, W. *Theoretical Models of Skeletal Muscle*, John Wiley & Sons, Chichester, 1998.

[15] Crowninshield, R.D., and Brand, R.A. A physiologically based criterion of muscle force prediction in locomotion. *J. Biomech.*, **14**(11), 793-801, 1981.

[16] Bouisset, S. *Biomécanique et physiologie du mouvement*. Abrégés, Editions Masson, 304 pp, 2002.

[17] Zajac, F.E. Muscle and tendon: properties, models, scaling and application to biomechanics and motor control. *Crit. Rev. Biomed. Eng.*, **17**(4), 359-411, 1989.

[18] De Leva P. Adjustments to zatsiorsky-seluyanov's segment inertia parameters. *Journal of Biomechanics*, **29**(9), 1223-1230, 1996.

[19] Chenut, X., Fisette, P., and Samin, J.C. Recursive Formalism with a Minimal Dynamic Parametrization for the Identification and Simulation of Multibody Systems. Application to the Human Body. *Multibody System Dynamics* **8**, 117-140, 2002.

[20] Bao, H., and Willems, P.Y. On the kinematic modelling and the parameter estimation of the human shoulder, *Journal of Biomechanics*, **32**: 943-950, 1999.

[21] Raison, M., Detrembleur, C., Fisette, P., Samin, J.C., and Willems, P.Y. Determination of joint kinematics and dynamics in the human body : application to a subject getting up from a seat. *Proceedings of Eccomas Thematic Conf. on Adv. in Comput. Multibody Dyn.*, Madrid, 17 pp, 2005.

[22] Winters, J.M. An improved muscle-reflex actuator for use in large-scale neuromusculoskeletal models. *Ann. Biomed. Eng.* **23**, pp. 359-374, 1995.

[23] Thelen, D.G. Adjustment of Muscle Mechanics Model Parameters to Simulate Dynamic Contractions in Older Adults. *Transactions of the ASME*, **125**, 70-77, 2003.

[24] Venture, G., Yamane, K., and Nakamura, Y. Identifying musculotendon parameters of human body based on the musculo-skeletal dynamics computation and Hill-Stroeve muscle model. *Proceedings of 5th IEEE-RAS International Conference on Humanoid Robots*, 351-356, 2005.

[25] Anderson, F.C., and Pandy, M.G. Dynamic optimization of human walking. *J. Biomech. Eng.*, **123**(5), 381-390, 2001.

[26] Buchanan, T.S., Lloyd, D.G., and Besier, T.F. Neuromusculoskeletal Modeling: Estimation of Muscle Forces Moments and Movements Measurements of Neural Command. *Journal of Applied Biomechanics*, Human Kinetics Publishers, **20**, 367-395, 2004.

[27] Holzbaur, K.R.S., Murray, W.M., and Delp, S.L. A model of the upper extremity for simulating musculoskeletal surgery and analyzing neuromuscular control. *Annals of Biomedical Engineering*, **33**(6), 829-840, 2005.

[28] Lloyd, D.G., and Bessier, T.F. An emg-driven musculoskeletal model to estimate muscle forces and knee joint moment in vivo. *Journal of Biomechanics*, **36**, 765-776, 2003.

[29] Chèze, L., Fregly, B.J., Dimnet, J. A solidification procedure to facilitate kinematic analyses based on video system data. *Journal of biomechanics*, Vol. 28, p. 879-884, 1995.

[30] Fisette, P., Postiau, T., Sass, L., and Samin, J.C. Fully symbolic generation of complex multibody models. *Mechanics of Structures and Machines*, **30**(1), 31-82, 2002.

[31] Nigg, B.M., and Herzog, W. *Biomechanics of the musculoskeletal system*. Eds. Nigg BM and W Herzog, Second edition, Chichester and New York, 644 pp, 1999.

[32] Raison, M., Detrembleur, C., Fisette, P., Samin, J.C., and Willems P.Y. Estimation of human muscular efforts using a model based optimization method. *Proceedings CD of the 6th National Congress on Theoretical and Applied Mechanics*, 8 pp, 2006.

Proceedings of the 8th National Congress on Theoretical and Applied Mechanics, May 28-29, Brussels, Belgium.

Anisotropic continuum damage model coupled to viscoplasticity for a pressure dependent alveolar bone remodeling law

M. Mengoni, JP. Ponthot
Department of Aerospace and Mechanics, Université de Liège
Chemin des chevreuils 1, 4000 Liège - Belgium
email: mmengoni@ulg.ac.be, jp.ponthot@ulg.ac.be

Abstract— **This work proposes a phenomenological bone tissue constitutive law accounting for bone remodeling of the alveolar bone for orthodontic movements of the teeth. The proposed biomechanical constitutive law, inspired from [1], is based on a elasto-visco-plastic material coupled with Continuum anisotropic Damage Mechanics ([1] considered only the case of a linear elastic material coupled with anisotropic damage). It is here formulated as to be used explicitly for alveolar bone, whose remodeling cells, opposite to most bones, seem macroscopically to be triggered by the pressure state applied to the bone matrix. An application of the mechanical model is proposed on a 2D tooth and its surrounding parodontal tissues submitted to a tipping movement. It shows the use of a pressure dependent, anisotropic, remodeling law is necessary to obtain a global movement of the tooth if no other non linearities are considered in the problem.**

Keywords— **orthodontics, bone remodeling, biomechanics**

I. Introduction

ONE of the guiding principles in orthodontics is to gradually impose progressive and irreversible bone deformations. By optimizing load positions and intensities, orthodontic treatments can be reduced both in time and cost. This optimization requires a mechanical model of the biochemical phenomena involved and of the activated dental movement. The goal of this work is to provide a constitutive model able to simulate those coupled phenomena.

Dental movement is achieved through a biochemical process of skeletal adaptation to mechanical stimuli called bone remodeling. Therapeutic forces applied through orthodontic appliances change the physiological equilibrium. Loading of the skeletal system is thus altered and bone remodeling cells are triggered to modify the bone shape and density in order to achieve a new equilibrium and adjust the stress level. This state will be maintained until new mechanical external conditions trigger new remodeling events.

For most types of bones, remodeling processes take place in order to adjust the amount of tissue and its topology according to long term loading conditions, following what is called "Wolff's law" of bone adaptation [2], [3]. Bone resorption occurs when disuse is observed. This resorption tends to decrease the amount of bone tissue where it is of no mechanical relevance. Bone apposition occurs in overloaded conditions, in order to reinforce bone where it is necessary. Bone tissue therefore adapts its density in such a way to achieve an homeostatic state of stress. It also adapts its topology in order for the trabeculae to align along the principal stress directions. Bone remodeling therefore depends not only on the stresses intensities but also on their directions.

Contrary to the majority of bones, alveolar bone remodeling seems on a macroscopic scale to depend mainly on the pressure state [4], [5]. One can observe apposition on the tension side of a tooth when loaded with an abnormal mechanical environment, such as the one obtained with orthodontics appliances, as well as resorption on the compression side. When no non-linearities are considered in the periodontal ligament, this difference can be modeled if a pressure dependent remodeling law is used for the alveolar bone. The present work concentrates on the bone behavior during remodeling and assumes the pressure state of the bone matrix as the key stimulus to differentiate apposition and resorption in overloaded conditions.

II. Methods

On experimental basis [6], one can show that remodeling occurs to modify the density proportionately to the bone matrix density (ρ_0, density for a bone with null porosity) and as function of a remodeling rate $\dot{r}$ $[mm/s]$

$$\dot{\rho} = kS_v\rho_0\,\dot{r} \tag{1}$$

The terms kS_v accounts for the available bone specific surface area (S_v, internal surface area per unit volume, related to the density, $[mm^2/mm^3]$) as defined in [7].

This remodeling rate ($\dot{\rho}$) is shown to be a function of the deviation of a given mechanical stimulus (Ψ, function of the strain energy) from an homeostatic value ($\Psi^\star$). The remodeling process tends to reduce this deviation. In the case of alveolar bone, it is here considered as a function of the pressure.

$$\dot{r} \approx \pm c(p)(\Psi - \Psi^\star) \tag{2}$$

In order to reproduce the density change both for overload ($\Psi > \Psi^\star$) and underload ($\Psi < \Psi^\star$) of the alveolar bone, the

parameter c has to be positive in underuse and a function of the pressure state in overuse (positive in compression and negative in traction).

The change in density can be translated into a change in mechanical properties (Young's modulus E and Poisson's ratio ν) through a commonly accepted law :

$$\begin{aligned} E &= B(\rho)\rho^{\beta(\rho)} \\ \nu &= \nu(\rho) \end{aligned} \tag{3}$$

A. Model

As proposed in [8], the change in elastic properties due to remodeling can be integrated in an adaptative elasticity framework. However, this supposes the bone matrix as an elastic solid and is therefore limited to low strain levels. Doblaré and co-workers [1] proposed to formulate the previous set of equations within the Continuum Damage Mechanics framework, using an energy equivalence approach of damage. In the case of bone remodeling, damage can be understood as a measure of the void volume fraction inside the bone tissue. The measure of damage used is therefore virtual and actually reflects the bone density that can evolve (Equ.1). There is no actual damage in the tissue. The undamaged material is the ideal situation of bone with null porosity and perfect isotropy. The process of bone resorption corresponds to the classical damage evolution concept, since it increases the void fraction (porosity) and therefore damage (decreases the density). However, bone apposition can reduce damage and lead to bone repair, which has to be adequately considered in this extended damage theory. Damage repair can be considered here because the total energy dissipation includes biological dissipation due to metabolism on top of the mechanical dissipation which is negative for damage repair.

Equ.(1) can therefore be formulated as a damage variation function. This formulation allows Doblaré and co-workers in [1] to extend the density variation to an anisotropic formulation, using an anisotropic damage variable. Directionality therefore follows the idea suggested by Cowin [9] and links the anisotropic damage tensor to the fabric tensor. The use of the continuum damage theory allows to define independently the internal variables such as density and mechanical properties. It therefore is an improvement of the anisotropic extension of [6] which was proposed in [10]. Indeed, in [10], Jacobs and co-workers used a global optimization function to define the remodeling stimulus and therefore the internal variables were not independent. Even though the continuum damage formulation solves this difficulty, Doblaré and co-workers limited their approach in [1] to an elastic bone matrix as was done in [8]. In its isotropic formulation Doblaré's model therefore uses the following set of equations :

$$\text{effective strain} : \tilde{\varepsilon} = (1-d)\varepsilon \tag{4}$$

$$\text{effective stress} : \tilde{\sigma} = \frac{\sigma}{(1-d)} \tag{5}$$

$$\text{constitutive law} : \tilde{\sigma} = \mathbb{C}_0 : \tilde{\varepsilon} \tag{6}$$

$$\text{damage variation} : \dot{d} = f(d, \sigma, \dot{r}, \rho_0) \tag{7}$$

with d an isotropic damage variable, $\mathbb{C}_0$ Hooke's tensor for the undamaged material.

We propose to extend the model stated in [1] to a more generalized mechanical behavior of the bone matrix, considering it as an elasto-visco-plastic material. This model is also adapted to account for an explicit pressure dependence of the remodeling rate in the alveolar bone.

In order to couple continuum damage and plasticity, the use of a strain equivalence approach, relating the stress level in the damaged material with the stress in the undamaged material that leads to the same strain, is chosen. This approach keeps the physical definition of damage as related to the surface density of defects, opposite to the energy equivalence approachused in [1] because of its difference between strain and effective strain. The plasticity is therefore simply coupled to damage by expressing the plastic criterion in term of effective stresses instead of stresses. In its isotropic formulation the proposed model therefore uses the following set of equations :

$$\text{effective stress} : \tilde{\sigma} = \frac{\sigma}{(1-d)} \tag{8}$$

$$\text{constitutive law} : \overset{\triangledown}{\tilde{\sigma}} = \mathbb{M}_0 : E \tag{9}$$

$$\text{damage variation} : \dot{d} = f(d, \sigma, \dot{r}, \rho_0) \tag{10}$$

with d an isotropic damage variable, $\mathbb{M}_0$ an elasto-plastic material tensor for the undamaged material, E the strain rate (energy conjugated to the stress tensor, in a large deformation framework) and where the $\triangledown$ sign accounts for an objective time derivative.

When extending the strain equivalence approach (Equ.8-10) to anisotropic damage, according to Lemaitre and Desmorat [11], [12], one of the only effective stress ($\tilde{\sigma}$) definition that fulfills the conditions of being symmetric, compatible with the thermodynamics (existence of a stress potential) and that can express different effects on the hydrostatic and deviatoric behavior (by means of an hydrostatic sensitivity parameter, η) is represented by

$$\tilde{\sigma} = \mathtt{dev}(HsH) + \frac{p}{1 - \frac{\eta}{3}D_{kk}}I = \tilde{s} + \tilde{p}I \tag{11}$$

where s and p are respectively the stress deviator and the pressure and where $H = (I-D)^{-1/2}$ is a second order

symmetric tensor (called in this work the remodeling tensor), D being symmetric (as an extension of the isotropic damage variable, d).

The damage evolution is thermodynamically associated to the elastic strain energy Φ^{el} which can be written, considering an isotropic matrix (the elasticity parameters are of the number of two, the bulk modulus, K, and the shear modulus, G) as :

$$2\Phi^{el} = \frac{1}{2G}\mathtt{tr}(Hs^{el}Hs^{el}) + \frac{p^{el\,2}}{K(1-\frac{\eta}{3}D_{kk})} \tag{12}$$

An external mechanical stimulus, Y, is identified with the variable thermodynamically associated with the remodeling tensor H, choosing to use the stress as the external driving force, giving :

$$Y = \frac{\partial \Phi^{el}(\sigma, H)}{\partial H} \tag{13}$$

It is obtained in terms of the external independent variable (stress) and the internal variable (remodeling tensor or damage tensor) as

$$Y = -2\left[\frac{1}{K}\frac{\eta p^2}{3-\eta\mathtt{tr}(D)}H^{-3} + \frac{1}{2G}sHs\right] \tag{14}$$

If the remodeling criteria are chosen as in [1], one can show after a few calculation that

-for bone formation :

$$\overset{\triangledown}{H} = -\frac{3\beta k S_v \dot{r}}{2\mathtt{tr}(H^{-2}(J\mathbb{W})H)}\frac{\rho_0}{\rho}J\mathbb{W} \tag{15}$$

-for bone resorption :

$$\overset{\triangledown}{H} = -\frac{3\beta k S_v \dot{r}}{2\mathtt{tr}(H^{-2}(J^{-3}\mathbb{W})H)}\frac{\rho_0}{\rho}J^{-3}\mathbb{W} \tag{16}$$

with $\mathbb{W}$ a fourth order unit anisotropic tensor,
$J = \frac{1}{3}(1-2w)\mathtt{tr}(Y)I + wY$ and $w \in [0,3]$ can be related to $\eta \in [1,\infty[$ as a measure of the hydrostatic sensitivity.

The remodeling rate $\dot{r}$ is expressed, in its pressure dependent formulation, as :

$$\dot{r} = \begin{cases} c_f g_o & \text{if } g_o \geq 0,\ g_u < 0 \quad \text{and} \quad p > 0 \\ -c_r g_o & \text{if } g_o \geq 0,\ g_u < 0 \quad \text{and} \quad p < 0 \\ 0 & \text{if } g_o < 0,\ g_u < 0 \\ -c_r g_u & \text{if } g_u \geq 0,\ g_o < 0 \end{cases}$$

where c_r and c_f are two remodeling constants respectively for bone formation and bone resorption, p is the pressure (positive in tension) and g_o and g_u are the remodeling criteria (same units as the one of stresses) respectively for bone overload and bone underload used in [1] and expressed for a strain equivalence approach in continuum damage mechanics. These criteria express the deviation of the mechanical stimulus Ψ from its homeostatic value.

- overload criterion : $g_o \propto \Psi - (1+\Omega)\Psi^\star < 0$
- underload criterion : $g_u \propto 1/\Psi - 1/((1-\Omega)\Psi^\star) < 0$

The parameter Ω introduced in these definition accounts for a lazy zone. This is an interval around the homeostatic level for which no remodeling process takes place. The mechanical stimulus used is a function of the strain energy (through the external mechanical stimulus Y) at tissue level and the number of loading cycles considered in the time integration. It is expressed at the tissue level supposing stress in the tissue can be related to continuum stress through a proportionality coefficient experimentally shown to be the square of the reduced density [10] : continuum stress = $(\rho/\rho_0)^2 \times$tissue level stress.

Coupling with plasticity can be done assuming an additive decomposition of the strain rate :

$$E = E^{el} + E^{pl} \tag{17}$$

where E^{el} follows Hooke's law :

$$\overset{\triangledown}{\tilde{\sigma}} = \mathbb{C}_0 E^{el} \tag{18}$$

and E^{pl} can be calculated through the normality rule on the plastic criterion (associated plasticity) expressed in term of effective stresses.

When Von-Mises criterion is chosen (although it is clear that the relevant inelastic processes are different from that of classical plasticity), it results for isotropic hardening in :

$$E^{pl} = \frac{3}{2}\frac{\dot{\lambda}}{\tilde{\sigma}_{eq}}\mathtt{dev}(H\tilde{s}H) \tag{19}$$

where $\tilde{\sigma}_{eq}$ is the equivalent stress used for the Von-Mises criterion

$$\tilde{\sigma}_{eq} = \sqrt{\frac{3}{2}\tilde{s} : \tilde{s}} \tag{20}$$

and λ a flow parameter. This choice of criterion assumes that only shear stresses are responsible for plastic strains. As both remodeling triggering and damage variation are function of the pressure value, this assumption may be too restrictive.

This formulation is integrated in a finite element code (home made code Metafor [13]) using the following time-step integration : starting from a known stress state (s, p) and remodeling tensor (H), plasticity is computed using effective stresses ($\tilde{s}$, $\tilde{p}$) with a constant remodeling tensor, giving plastic deformations and final stresses. Damage evolution is then computed and a new remodeling tensor is determined. Stresses and plastic deformations are then re-evaluated, up to convergence of the updated remodeling

tensor (see [14] for details on the method). A consistent tangent operator has also been developed for this theory when integrated in an iterative process as the one exposed.

B. Application

We consider the potential of the pressure dependent model to predict the density evolution of alveolar bone tissue. As an example, we present a 2D model (plane strain state) of the parodontal tissue of a rigid tooth. The aim is to predict the bone density and its evolution from initial ideal situations (for both the geometry and the mechanical behavior) with given displacements that characterize the orthodontic appliances.

The root is parabolic and surrounded by a constant thickness ($0.2mm$) periodontal ligament (PdL) as well as trabecular and cortical bone [15]-[18]. It is of $12.6mm$ in height and $6mm$ in width at the collar. The ligament is surrounded by a trabecular bone of arbitrary variable thickness and a cortical layer of around $0.5mm$ in width (see Fig. 1).

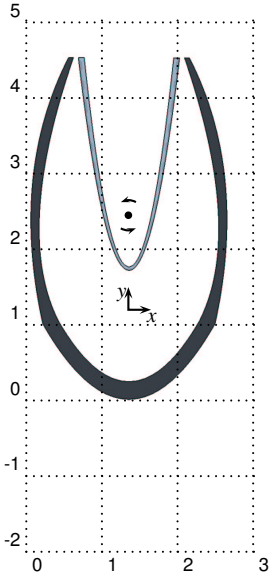

Fig. 1. Geometry - light gray : periodontal ligament, dark-gray : cortical layer, in between : alveolar bone. The dot represents the center of rotation

The PdL and cortical layer mechanical behaviors [15]-[18] are chosen elastic ($E_{\text{pdl}} = 0.6MPa$, $\nu_{\text{pdl}} = 0.45$, $E_{\text{cor}} = 16GPa$, $\nu_{\text{cor}} = 0.3$). The trabecular bone mechanical behavior is elasto-plastic with the proposed continuum damage model. The damage evolution follows the remodeling law proposed in this work.

Neither this problem nor the starting situations are "real" problems, therefore, the homeostatic values are not relevant (as well as the other parameters of the model, especially for a qualitative evaluation). A quasi-static loading is performed, the time-unit of the simulation is therefore also of no relevance.

In order to test the anisotropic behavior, we present four simulations.

The first two tests consider initial damage in only one direction (either along the vestibulo-lingual direction, x or along the root axis, y), both other initial damage values being set to zero. The non null initial damage is set to .9. It therefore corresponds to a mean initial damage of .3, getting a density of $1.9g/cc$, a porosity of 10% and a stiffness of $13GPa$ (calculated from the strain equivalence damage definition in case of isotropy : $d = 1 - \frac{E}{E_0}$ with E_0 the stiffness obtained for a bone of null porosity, $E_0 = 18.5GPa$). These values for density and stiffness are much higher than what they should be in a realistic test, for which the mean damage value would be around .8. However, this set of tests is proposed for the sake of comparison to analyze the anisotropic behavior of the model. The two other tests present the same initial mean damage chosen to be .3 : the third one considers an initial bone as isotropic with a uniform density distribution ; the last test considers initial damage in the geometry plane (x,y). We therefore get an initial damage in the two plane directions of .45 while it is zero on the third direction.

Remark 1 An initial damage considered only along the y axis corresponds to trabeculae of the alveolar bone aligned along the the tooth main axis and perpendicular to the main direction of movement. However initial damage only along the x axis corresponds to a bone whose trabeculae are aligned perpendicularly to the root axis along the direction of movement. Damage evolution for both these cases would therefore be dissimilar, allowing a greater damage variation for damage along the y axis than along the x axis as the trabeculae because the movement is perpendicular to the fibers main direction. **[end of remark]**

A tipping movement is applied to the tooth root with a center of rotation situated at $3mm$ from the root apex, i.e. below one third of the root length (see Fig. 1) as proposed in [19] among others. Tipping is kept to obtain an angle of two degrees with the vertical axis, the basal bone being fixed. As the root and surrounding tissues are symmetric, the rotation direction is of no relevance. Getting from an angle of zero to the final angle is done is 10 time units and this angle is kept for a remaining 90 time units. Damage variation is observed during this constant displacement period.

III. Results

A. Model

The discussion on the model characteristics that follows is done on the isotropic formulation of the model in order to decouple the effects due to the remodeling rate function and to the orientation of the structure.

As no more dependence on the orientation has to be represented, one can write $H = hI$, $w = 0$ and $\eta = 1$, both criteria g_o and g_u take a simple formulation given by :

$$g_o = U - (1+\Omega)U^\star < 0 \quad (21)$$
$$g_u = 1/U - 1/((1-\Omega)U^\star) < 0 \quad (22)$$

where U is expressed in Equ.(23) and $U^\star$ is a reference homeostatic value of U.

$$U(d,\tilde{\sigma}) \propto (1-d)^{3/4}\sqrt{2\bar{u}(\tilde{\sigma})} \quad (23)$$

where $d = 1-h^{-2}$ as in the strain equivalence approach and $\bar{u}$ is the effective elastic energy density (as also defined in [11], establishing the basis of the CDM theory, and accounting for the stress triaxiality) :

$$\bar{u}(\tilde{\sigma}) = \int \tilde{\sigma} : d\tilde{\varepsilon}^{el} = \frac{\tilde{J}_2^2}{2E}\left[\frac{2}{3}(1+\nu)+3(1-2\nu)\frac{\tilde{p}^2}{\tilde{J}_2^2}\right] \quad (24)$$

with $\tilde{J}_2 = \sqrt{\frac{3}{2}\tilde{s}_{ij}\tilde{s}_{ij}} = \frac{1}{1-d}\sqrt{\frac{3}{2}s_{ij}s_{ij}}$, s being the deviatoric stress tensor.

Finally, Equ.(15) and (16) both lead to the same damage variation (see Fig. 2), with $\dot{r}$ as defined by Equ.(17):

$$\dot{d} = -\beta k S_v \dot{r}\frac{\rho_0}{\rho}(1-d) \quad (25)$$

This damage variation is nothing but the expression of Equ (1) in term of the damage variable. As damage variation is positive for resorption and negative for formation, we can detect on Fig 2 different remodeling zones as well as the lazy zone as a function of damage. As expected through the introduction of the specific surface S_v, damage variation for values of damage close to 1.0 tend to high (negative) values but is reduced to zero for full damage (not on the figure). In resorption, although the remodeling rate increases (in absolute value) for a damage decay, damage variation does not reach high values due to the tendency of the specific surface to decrease faster than the remodeling rate increases. The discontinuity of damage variation for a damage value of about 0.83 is due to the slight slope discontinuity introduced by the particularization of Equ.(3) in the definition of bone Young's modulus (as in [20]).

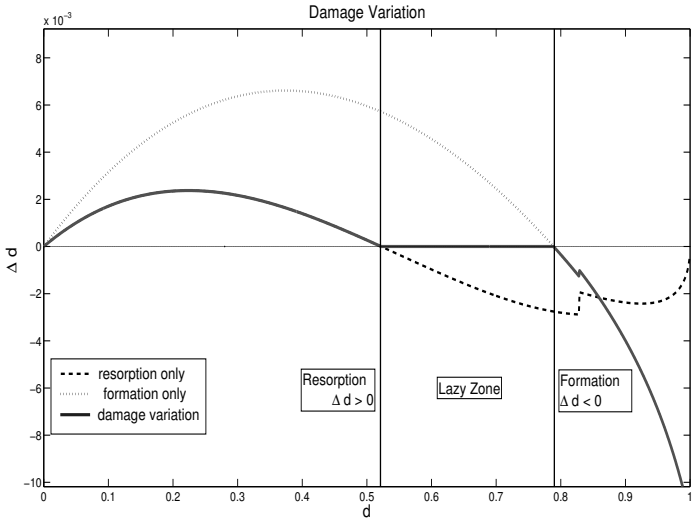

Fig. 2. Damage variation as a function of damage for a positive pressure

Once the remodeling model has been formulated, we need to check its ability to achieve qualitative results close to the ones obtained in experimental tests of actual alveolar bone. This is accomplished in the next section in which the model is applied to the study of the remodeling behavior in the alveolar bone submitted to orthodontic treatments with the four simulations presented earlier.

B. Application

Tipping movement of a tooth is obtained with displacement controlled simulations, the angle of rotation being increased from zero to two degrees in ten time-steps.

If the whole movement was rigid around the center of rotation, one would expect a displacement, due to the rigid rotation, at the collar of $-.33mm$ horizontally and $\pm.11mm$ vertically. However, as the bone is fixed at its base and as the rotation leads to deformation of the periodontal ligament as well as the bone, the movement actually observed leads to smaller displacements at the collar (see 4).

The mean damage evolution is shown in Fig.3 for each simulation on three sets of points (two at the apex, two at the collar and two at mid-height of the root - above the center of rotation) situated symmetrically around the root axis and adjacent to the periodontal ligament.

Observation 1 The mean damage variation observed is abrupt during loading of the tooth and tends to stabilize towards an equilibrium mean damage value when the angle of rotation is kept constant. For most cases, the variation during the constant displacement is in the same direction as the initial variation as the pressure state stays the same during the whole simulation. However, for the root mid-height this changes when damage is initially on the x direction only (see **observation 3** for explanation). **[end of observation]**

Observation 2 Damage variation at the collar is much less than at the apex or along the root for all four simulations and on both sides of the root main axis. Indeed the tipping movement leads to smaller shear and hydrostatic stresses at the collar than along the root ($J_2^{\text{collar}} \approx 1MPa$, $J_2^{\text{root}} \approx 3MPa$, $p^{\text{collar}} \approx .2MPa$, $p^{\text{root}} \approx 1-3MPa$). It also

gives a ratio hydrostatic stress to shear stress (used in the definition of $\bar{u}$, Equ.24) of .2 at the collar while it is of around 1 to 3 along the root. Therefore, the value of the external mechanical stimulus Y is smaller at the collar than along the root. The remodeling rate is also smaller because even tough reducing Y reduces Ψ, its value stays above its homeostatic value $\Psi^\star$ and overloaded conditions are still observed at the collar, $\dot{r}$ is therefore reduced and so is damage variation. **[end of observation]**

Observation 3 For each set of points, while overloaded conditions are kept for all simulations, one can see apposition on one side (reduction of mean damage) and resorption on the other (increase of mean damage). All points are therefore subjected, for the same vertical location, to traction on one side of the tooth and compression on the other. Nevertheless, one point can be submitted either to traction or to compression according to the initial anisotropy of damage.

For the root mid-height, the labial side is in compression (increase of damage) except for the simulation with initial damage on the x direction only for which the labial side is in traction. This can be explained as follows. As the tipping movement is a rotation along a center of rotation situated at one third of the root length (starting from the apex), there is a pressure gradient on each side of the root axis. On the labial side, the bone is in compression at the apex and in traction at the collar. On the lingual side, it is in traction at the apex and in compression at the collar. However, the change of pressure sign is not observed at the same vertical location for all four simulations. One will get most of the bone surrounding the root in traction on the lingual side when the initial damage is considered as fully isotropic or as non-zero on both plane directions while around two thirds are in traction for initial damage on the y direction and only one half is in traction for initial damage on the x direction. Therefore the pressure state at mid-height is in traction on the lingual side for the first three simulations while it is in compression for the last one.

The collar shows almost no damage variation for initial damage considered isotropic or on the two plane directions. Even tough mean initial damage is equal for all simulations, local values of damage are smaller for these two simulations than for the others and, as exposed earlier, stress intensities are smaller as well. Therefore, the remodeling rate is quite small and so is the mean damage variation.

The change in damage variation behavior at the collar between the two mono-directional damage simulations is explained in the same way as the change of behavior at the root mid-height.

However, at the apex, for all simulations, the points are either in traction or in compression on each side of the

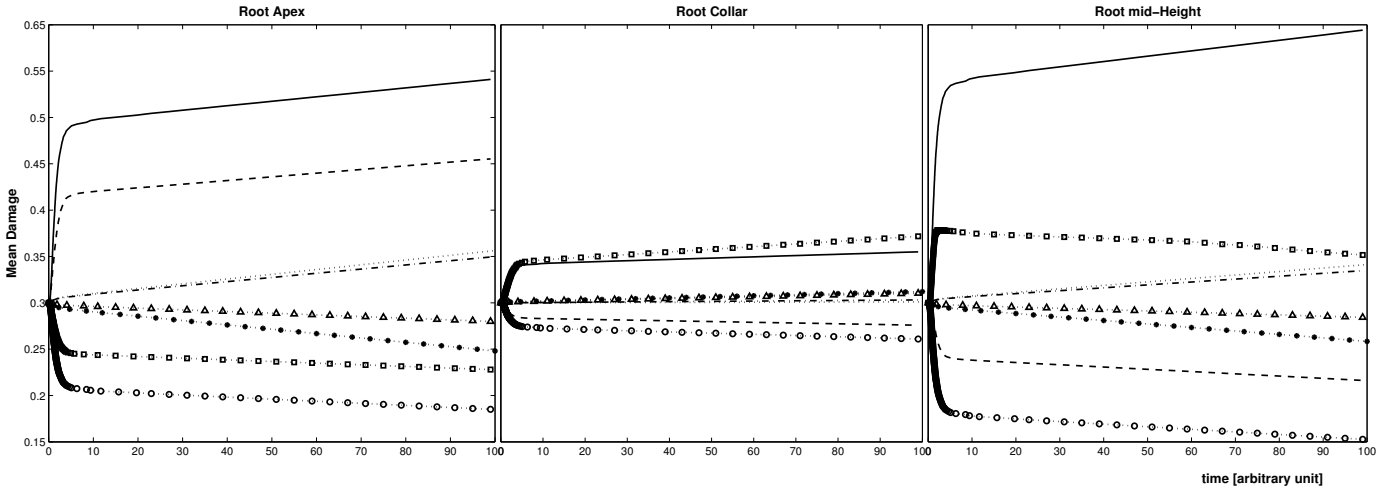

Fig. 3. MEAN DAMAGE COMPARISON ON THREE SETS OF POINTS : On all graphs, test with initial damage on x is in dashed line (labial side) and squares (lingual side), test with initial damage on y in plain line (labial side) and circles (lingual side), test with initial damage on the x,y plane is in dashed-dotted line (labial side) and triangle (lingual side) and test with initial isotropic damage is in dotted line (labial side) and plain circles (lingual side). The left graph is for two points situated at the apex, the labial side in compression and lingual side in traction, the middle graph for points at the collar, the labial side in traction and lingual side in compression, and the right graph at the root mid-height, the labial side in compression and lingual side in traction. On three cases, the points are situated symmetrically around the root axis, adjacent to the periodontal ligament. An angle of 2 degrees is obtained within the first ten time-steps and kept up to a hundred time-steps.

tooth. Damage variation is therefore qualitatively the same for all simulations. **[end of observation]**

Observation 4 As expected in Remark 1, both for the root mi-height and the root apex, mean damage variation for simulation with damage only on the x direction or only on the y direction, do not present the same order of values. Ratio between mean damage variation for the x initial damage simulation and the y one is about 1.5 at the root apex while it is about 5 at the mid-height. This is due to the alignment of the tissue fibers with the loading for the x initial damage simulation while fibers are perpendicular to loading on the other case. This difference in damage variation is not present at the collar because the bone width at that location is much smaller and loading lines more oblique to the fibers than lower on the root. **[end of observation]**

This set of observations shows that using an anisotropic model is quite necessary to describe bone remodeling as it allows, for a given mean damage value, to obtain different damage variation, both in intensity and repair/damaging behavior.

If a non pressure dependency was used for the remodeling rate coefficient in overload conditions, there would be no difference observed between the labial and lingual side of the tooth for each set of points. Therefore, each location would undergo apposition on both sides of the tooth (damage repair) and only bone growth would be observed. This would lead without any doubt to jaw problems maybe up to extrusion of a tooth. Therefore, a model not accounting for a non linear periodontal ligament mechanical law has to include a pressure dependency for the remodeling coefficient such as the one proposed. This pressure dependency could be avoided if the periodontal ligament mechanical law would lead to mechanical stimuli (proportional to the strain energy density) of the bone that would be smaller or larger than its homeostatic value according to pressure sign. The pressure dependency of the model would therefore be at the ligament level and not at the bone remodeling one.

IV. Conclusions

The present study introduces a numerical model for the simulation of orthodontic tooth movement based on the assumption that bone remodeling processes during tooth movement are controlled by elastic energy density as well as pressure state of the alveolar bone. In spite of the necessary idealizations, the proposed phenomenological description of bone remodeling specified for alveolar bone allows to qualitatively represent density variation of the bone surrounding a tooth when submitted to loading representing orthodontic appliances. The need to use a pressure dependent remodeling rate is shown to be useful to represent tooth movement as long as the periodontal ligament is supposed not to be dependent on the pressure state. This hypotheses may be too restrictive but has yet to be shown not valid as the use of an appliance would most of the time increase the strain energy on all sides of the tooth root.

We present in details an analysis of the importance to use an anisotropic damage as well as on the importance of the initial anisotropy considered. As damage represent density of the bone, anisotropy of damage represent trabeculae orientation. The initial anisotropy of damage depends on the trabeculae organization of the alveolar bone due to physiological equilibrium. It therefore is patient dependent and the need of an evaluation of the bone state previous to treatment is necessary if any optimization of treatment was to be considered. This evaluation should give the possibility to assess the fabric tensor of the bone tissue of the jaw. This fabric tensor is directly linked to the anisotropy and as proposed in [1] can be linked to the remodeling tensor.

Further work should consider an application of this remodeling law to a patient specific model, not only for the initial damage considered but mainly for the geometry of the problem as well as for various types of appliances and loading.

Acknowledgments

The authors would like to acknowledge Dr. PP Jeunechamps for his enlightenment on damage mechanics and the formulation of its coupling to plasticity Prof. M. Limme of the Orthodontics Department, for his suggestions as well as Prof. R. Charlier.

References

[1] M. Doblaré and J. M. García, "Anisotropic bone remodelling model based on a continuum damage-repair theory," *J. Biomech.*, vol. 35, no. 1, pp. 1–17, Jan 2002.

[2] S. C. Cowin, "Tissue growth and remodeling," *Annu Rev Biomed Eng*, vol. 6, pp. 77–107, 2004.

[3] W. E. Roberts, "Bone physiology of tooth movement, ankylosis, and osseointegration," Seminars in Orthodontics, 2000, Volume 6, Issue 3, September 2000, Pages 173-182.

[4] C. Bourauel, D. Freudenreich, D. Vollmer, D. Kobe, D. Drescher, and A. Jäger, "Simulation of orthodontic tooth movements. a comparison of numerical models," *J. Orofac. Orthop.*, vol. 60, no. 2, pp. 136–151, 1999.

[5] B. Melsen, "Tissue reaction to orthodontic tooth movement–a new paradigm," *Eur. J. Orthod.*, vol. 23, no. 6, pp. 671–681, Dec 2001.

[6] G. S. Beaupré, T. E. Orr, and D. R. Carter, "An approach for time-dependent bone modeling and remodeling–theoretical development," *J. Orthop. Res.*, vol. 8, no. 5, pp. 651–661, Sep 1990.

[7] R.B. Martin, "Porosity and specific surface of bone," *Crit. Rev. Biomed. Eng.*, vol. 10, no. 3, pp. 179–222, 1984.

[8] S. C. Cowin and D. H. Hegedus, "Bone remodeling i: theory

of adaptive elasticity," *Journal of Elasticity*, vol. V6, no. 3, pp. 313–326, July 1976.

[9] S. C. Cowin, R. T. Hart, J. R. Balser, and D. H. Kohn, "Functional adaptation in long bones: establishing in vivo values for surface remodeling rate coefficients," *J. Biomech.*, vol. 18, no. 9, pp. 665–684, 1985.

[10] C. R. Jacobs, J. C. Simo, G. S. Beaupre, and D. R. Carter, "Adaptive bone remodeling incorporating simultaneous density and anisotropy considerations," *J. Biomech.*, vol. 30, no. 6, pp. 603–613, June 1997.

[11] J. Lemaitre and R. Desmorat, *Engineering Damage Mechanics: Ductile, Creep, Fatigue and Brittle Failures*, Springer, 2005.

[12] R. Desmorat and S. Otin, "Cross-identification isotropic/anisotropic damage and application to anisothermal structural failure," *Engineering Fracture Mechanics*, vol. 75, pp. 3446–3463, 2008.

[13] Metafor, *A large strain finite element code*, LTAS - MN2L / University of Liège, http://metafor.ltas.ulg.ac.be/ , 2009.

[14] P.P. Jeunechamps, *Simulation numérique, à l'aide d'algorithmes thermomécaniques implicites, de matériaux endommageables pouvant subir de grandes vitesses de déformation. Application aux structures aéronautiques soumises à impact*, Phd thesis, University of Liège (Belgium), School of Engineering, Aerospace and Mechanics Department, 2008.

[15] C. Bourauel, D. Vollmer, and A. Jäger, "Application of bone remodeling theories in the simulation of orthodontic tooth movements," *J. Orofac. Orthop.*, vol. 61, no. 4, pp. 266–279, 2000.

[16] P. D. Jeon, P. K. Turley, and K. Ting, "Three-dimensional finite element analysis of stress in the periodontal ligament of the maxillary first molar with simulated bone loss," *Am. J. Orthod. Dentofacial Orthop.*, vol. 119, no. 5, pp. 498–504, May 2001.

[17] H. Qian, J. Chen, and T. R. Katona, "The influence of pdl principal fibers in a 3-dimensional analysis of orthodontic tooth movement," *Am. J. Orthod. Dentofacial Orthop.*, vol. 120, no. 3, pp. 272–279, Sep 2001.

[18] J. Schneider, M. Geiger, and F.-G. Sander, "Numerical experiments on long-time orthodontic tooth movement," *Am. J. Orthod. Dentofacial Orthop.*, vol. 121, no. 3, pp. 257–265, Mar 2002.

[19] D. Vollmer, C. Bourauel, K. Maier, and A. Jäger, "Determination of the centre of resistance in an upper human canine and idealized tooth model," *Eur. J. Orthod.*, vol. 21, no. 6, pp. 633–648, Dec 1999.

[20] C. R. Jacobs, *Numerical simulation of bone adaptation to mechanical loading*, Ph.D. thesis, Department of Mechanical Engineering.Stanford University, 1994.

Proceedings of the 8th National Congress on Theoretical and Applied Mechanics, May 28-29, Brussels, Belgium.

High Order Residual Distribution Schemes on Isoparametric Curved Elements

Martin Vymazal[1], Nadège Villedieu[1], Tiago Quintino[1], Herman Deconinck[1]
[1]Aeronautics and Aerospace Department, Von Karman Institute for Fluid Dynamics
Waterloosesteenweg 72, B-1640 Sint-Genesius-Rode, Belgium
email: martin.vymazal@vki.ac.be, villedie@vki.ac.be, quintino@vki.a.be, deconinck@vki.ac.be

Abstract— **Residual distribution schemes are discussed in the context of higher order spatial discretization for hyperbolic conservation laws. The discrete solution is globally continuous, defined by a Finite Element space based on triangular Lagrangian P_k elements. A natural subtriangulation of these elements allows the reuse of simple distribution formula previously developed for linear P_1 triangles. The paper introduces curved elements with piecewise quadratic and cubic approximation of the boundaries of the domain, using standard sub- or isoparametric transformation.**

Keywords— **residual distribution, high order, multidimensional upwind, isoparametric mapping**

I. Introduction

THE quest for ever more demanding numerical simulations both in terms of robustness and accuracy has resulted in a renewed interest in higher order discretizations over recent years. Indeed, the potential gain is enormous if the obstacles of lack of robustness, high computational cost and high memory consumption can be sufficiently alleviated.

Methods developed in the past have focused on shock capturing Finite Volume methods, extending them to higher order using higher–order polynomial reconstruction. The Piecewise parabolic Method of Woodward and Colella[1] is one of the first successful attempts in this direction, developed on structured grids. The seminal work of Osher, Harten and Shu[2], [4], [5] has led to the class of ENO schemes both on structured and unstructured grids, see also the unifying work on k-exact Finite Volume reconstructions on unstructured grids by T. J. Barth[6], [7], [8] .

Over the most recent years the emphasis has shifted towards higher order methods based on Finite Element approximation spaces. Today, it seems that Discontinuous Galerkin (DG) Finite Element methods [9], [10], [2] present a promising framework to generalize Finite Volume methods, preserving the use of Riemann solvers to resolve the inter-element discontinuities, and a massive research effort is underway to develop this approach. Another way to increase the order of Finite Volume methods is based on so called spectral Finite Volume[11], [12] and spectral Finite Difference methods[13].

The present paper follows a Residual Distribution approach[14], [3], [15], which is closer to continuous Finite Element methods, however allowing the use of a maximum principle to construct nonlinear monotonicity preserving and truely multidimensional stabilizations. In previous papers[16] we have exploited the close relation with continuous Finite Element discretizations to present a class of higher order residual distribution methods defined on P_k Lagrangian triangular Finite Elements. Here we focus on the use of curved elements to allow for a higher order representation of the boundaries of the domain, using sub- or isoparametric transformation from physical space to a Cartesian parent element. A detailed numerical study confirms that higher order boundary representation is a crucial ingredient for effective high order convergence of the method.

II. Notations and generalities

TO introduce the general setting we consider first the steady state solution of a scalar conservation law on a twodimensional spatial domain Ω:

$$\frac{\partial u}{\partial t} + \nabla \mathcal{F} = 0 \quad \forall (x,y) \in \Omega, \quad \forall t \geq 0 \tag{1}$$

We denote by $\tau_{h,k}$ a triangulation of the domain Ω, whereby each triangular element T of the triangulation $\tau_{h,k}$ consists of a Lagrangian P_k Finite Element equipped with $K = \frac{(k+1)(k+2)}{2}$ degrees of freedom as shown on figure 1 for P_1, P_2 and P_3 elements.

A. Approximation of the solution

For any given function $u(x,y,t)$, we define the spatial Finite Element approximation on $\tau_{h,k}$

$$u^{h,k}(x,y,t) = \sum_{i \in \tau_{h,k}} \psi_i^{h,k}(x,y)\, u_i(t) \,, \tag{2}$$

where $u_i(t)$ is the value of u at node i, i.e. $u_i(t) = u(x_i, y_i, t)$, while $\psi_i^{h,k}(x,y)$ denotes the $k-$th order Lagrangian basis function of node i.

Next, for higher order triangulations (i.e. $k > 1$), we introduce the P_1 conformal triangulation $\tau_{h,1}$ obtained by subdividing each P_k element in $N = k^2$ linear sub-elements. We denote by $\{T_s\}_{s=1,N}$ the P_1 sub-elements of T, as on figure 1. Hence, the triangulations $\tau_{h,k}$ and $\tau_{h,1}$ share the same unknowns (or degrees of freedom) $u_i(t)$ located at the same positions (x_i, y_i).

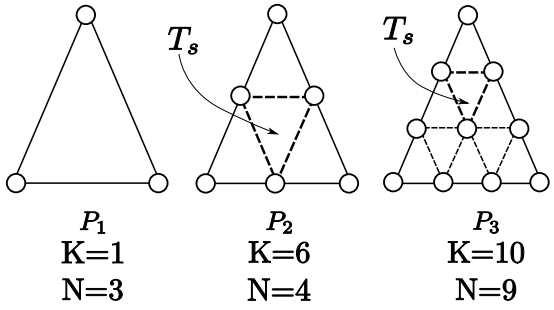

Fig. 1. P_1, P_2 and P_3 Lagrangian elements with P_1 subtriangulation

We define the local spacing h of the triangulation $\tau_{h,k}$ as the radius of the circle with surface equal to the surface of the local P_1 subtriangle. If the triangulation is globally uniform (but only then), we can compute h assuming that there are twice as many nodes as subtriangles, giving

$$h = \sqrt{\frac{|\Omega|}{2\pi DOF}} \quad \text{or} \quad h \propto \frac{1}{\sqrt{DOF}} \tag{3}$$

where $|\Omega|$ is the surface of the domain, and DOF the number of nodes (degrees of freedom) of the mesh.

B. Approximation of the geometry

In the simplest case the geometry of the P_k triangle is considered to be linear, defined by its three corner nodes. Hence, the intermediate nodes on the boundary of the element are all located on the straight edges and therefore the boundary of the domain Ω is approximated by a polygone. Such a discretization will be denoted as a P_1P_k discretization (P_1 for geometry and P_k for the solution). An example of a P_1P_2 element is given in figure 2(a).

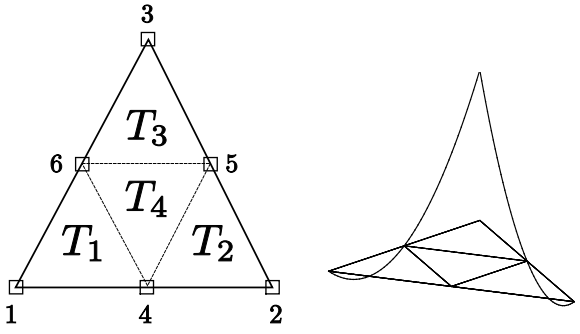

(a) P_2 element (b) Quadratic shape function

Fig. 2. P_1P_2 triangle - first order in terms of geometry, second order in terms of solution

However, one of the strong benefits of higher order elements is that they also allow for a higher order approximation of the geometry. In this work we will consider a piecewise quadratic and cubic approximation of the boundaries of the domain. This is obtained by assuming that the geometry of the P_k triangle is defined by the coordinates of 6 nodes (3 corner nodes and 3 mid-edge nodes), whatever the order of the solution might be, as shown on the right of figure 3. Such elements will be denoted as P_2P_k elements (P_2 for geometry and P_k for the solution). P_2P_2 elements are called isoparametric, while P_2P_k with $k > 2$ are called subparametric elements. The geometry of the curvilinear P_2 element is defined by the following (sub- or isoparametric) transformation to a parent element in ξ–η space (figure 3 left):

$$\begin{aligned} x(\xi,\eta) &= \sum_{i=1}^{6} \psi_i^{h,2}(\xi,\eta)\cdot x_i \\ y(\xi,\eta) &= \sum_{i=1}^{6} \psi_i^{h,2}(\xi,\eta)\cdot y_i \end{aligned} \tag{4}$$

where x_i and y_i are the known coordinates of the 6 nodes defined in physical space.

One can easily construct a mapping that transforms a face of reference triangle in ξ–η space to a face of a curvilinear triangle in x–y space: Since each shape func-

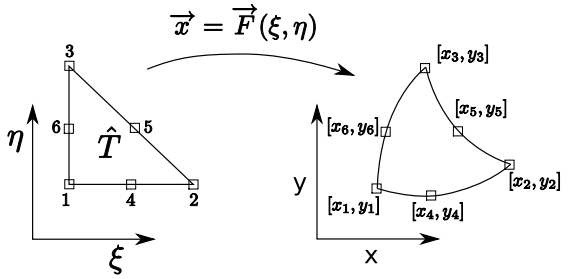

Fig. 3. Transformation of triangle geometry from reference to physical space using quadratic Lagrange shape functions

tion vanishes on a complete edge in ξ–η space, the boundaries of the triangle (defined by $\xi = 0$, $\eta = 0$ and $\xi + \eta = 1$ respectively) are quadratic functions of the parameter.

III. Residual Distribution method

FOR any triangulation $\tau^{h,k}$ the cell residual for a given triangle is defined as the integral over the triangle of the spatial operator:

$$\begin{aligned} \phi^T &= \oint_{\partial T} \mathcal{F}(u^{h,k})\cdot \hat{n}\, dl = \int_T \nabla \mathcal{F}(u^{h,k})\, d\Omega \\ &= \int_{T_s} \vec{a}(u^{h,k})\cdot \nabla u^{h,k}\, dx\, dy \end{aligned} \tag{5}$$

where we have used the expression for the Jacobian of the flux $\mathcal{F}(u)$ in (1),

$$\vec{a}(u) = \frac{\partial \mathcal{F}(u)}{\partial u} = \left(\frac{\partial f(u)}{\partial u}, \frac{\partial g(u)}{\partial u}\right) \tag{6}$$

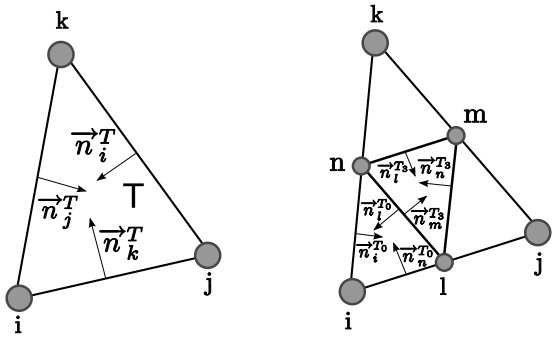

Fig. 4. Definition of the normal vectors $\vec{n}_i$ in P_1 and P_2 elements

We can also construct the residual over each P_1 subelement of $\tau^{h,k}$

$$\begin{aligned}\phi^{T_s} &= \oint_{\partial T_s} \mathcal{F}(u^{h,k})\cdot\hat{n}\,dl = \int_{T_s} \vec{a}(u^{h,k})\cdot\nabla u^{h,k}\,dx\,dy \\ &= \vec{a}^*\cdot\int_{T_s}\nabla u^{h,k}\,dx\,dy \end{aligned} \quad (7)$$

with $\vec{a}^*$ a properly defined local average of $\vec{a}(u)$ over the subtriangle such that conservation is preserved (so called Roe-average).

For a given P_1 triangle we consider the set of normal vectors $\{\vec{n}_j\}_{j\in T}$, defined by the inward normals to the edges of T facing each node $j \in T$ (see figure 4 left). The norm of $\vec{n}_i$ is equal to the length of the edge. In the general P_k case, with $k > 1$, we will assume that the $\vec{n}_j$'s are defined on the local P_1 sub-elements $T_s \in T$, as shown on figure 4 (right) for $k = 2$. For future use we define the upwind parameter

$$k_j = \frac{1}{2}\vec{a}^*\cdot\vec{n}_j \quad \text{implying} \quad \sum_{i\in T_s} k_i = 0 \quad (8)$$

Note that if we consider a P_1P_k element (P_k element for the solution but only P_1 triangles for the geometry, defined by the 3 corner nodes), the inward normals of the subelements can be deduced easily from the ones of the parent element by a simple rescaling (see figure 4).

A. Residual Distribution schemes on P_1 elements

We first recall briefly the Residual Distribution method on P_1 triangles. In the case of P_1 elements it is easy to verify that the cell residual can be expressed using the upwind parameters k_i if a conservative linearization has been used:

$$\phi^T = \oint_{\partial T}\mathcal{F}(u^{h,1})\cdot\hat{n}\,dl = \int_T \nabla\mathcal{F}(u^{h,1})\,d\Omega = \sum_{i\in T} k_i u_i \quad (9)$$

The basic idea then consists of distributing fractions of this cell residual to the three nodes of the element T. The fraction sent to node $i \in T$ is denoted ϕ_i and we require

$$\sum_{i\in T}\phi_i = \phi^T \quad (10)$$

This requirement can be written in terms of *distribution coefficients* β_i which for consistency sum to unity

$$\sum_{i\in T}\beta_i = 1, \qquad \beta_i = \frac{\phi_i}{\phi^T} \quad (11)$$

After assembling all contributions in the nodes, the nodal equation for node i reads, with $\mathcal{D}_i$ the set of all triangles that share node i.

$$\sum_{T\in\mathcal{D}_i}\phi_i = 0 \quad (12)$$

Since the distribution is restricted to the nodes of the triangle itself, the stencil of the scheme remains compact. This equation can be solved by embedding in a pseudo–time interation, i.e. by finding a steady state solution of

$$|S_i|\frac{du_i}{dt} + \sum_{T\in\mathcal{D}_i}\phi_i^T = 0, \quad (13)$$

where $|S_i|$ is the area of median dual cell.

A.1 Numerical distribution schemes

Many distribution schemes (defining the splitted residuals ϕ_i) have been developed in the past[3], [18], [15] . A particular class satisfies a multidimensional upwinding property ($\mathcal{MU}$). Such distributions satisfy the requirement that a node in a triangle does not receive a contribution if its opposed phase is an outflow phase. The condition is easily imposed by requiring $\phi_i = 0$ whenever $k_i < 0$. Denoting by k_i^+ and k_i^- the positive and negative part of the upwind parameter, $k^\pm = \frac{k\pm|k|}{2}$, two wellknown upwind schemes are given by

The N Scheme: The N scheme is a monotone first order scheme designed for the solution of the advection equation. The residuals sent to the nodes are defined by

$$\phi_i^N = k_i^+(u_i - u_{in}) \quad (14)$$

where

$$u_{in} = \frac{\sum_{i\in T} k_i^- u_i}{\sum_{i\in T} k_i^-} \quad (15)$$

is the inflow state of the element. This definition of the inflow state leads to a conservative discretization *only* if the state used to compute k_i results from a conservative linearization. A generalization which allows for an arbitrarily defined averaged state is given by:

$$u_{in} = \frac{\phi^T - \sum_{i\in T} k_i^+ u_i}{\sum_{i\in T} k_i^-} \quad (16)$$

Clearly equation (16) and (15) are identical if $\phi^T = \sum k_i u_i$. However, summing up equation (14) over the 3 nodes using (16) produces the conservative residual whenever ϕ^T has been computed using contour integration, independent of the linearization used for k_i.

LDA scheme: The Low Diffusion A scheme is a linearity preserving scheme with distribution coefficients defined as

$$\beta_i^{LDA} = \frac{k_i^+}{\sum_{m=1}^3 k_m^+} \tag{17}$$

Nonlinear blended (BX) scheme: Given a higher order linear scheme (*e.g.* the LDA-scheme) and a low order non-oscillatory scheme (*e.g.* the N-scheme), the simplest idea that can be used to construct a nonlinear scheme combining higher order and monotonicity is to blend the two linear schemes by means of some *nonlinear* smoothness monitor, leading to the split residuals

$$\phi_i^{\mathrm{B}} = (1-\theta)\phi_i^{\mathrm{LDA}} + \theta\phi_i^{\mathrm{N}} \tag{18}$$

where the nonlinear solution monitor θ should be as close as possible to 1 in correspondence of discontinuities, while ensuring that accuracy is kept by having 0 value on smooth parts of the solution. Different choices are possible as discussed in [17] .

B. Residual distribution schemes on P_k elements

Consider now the extension of multidimensional upwind ($\mathcal{MU}$) schemes to high order P_k elements. First, we compute the residual on each sub-element :

$$\phi^{T_s} = \int_{T_s} \nabla\mathcal{F}(u^{h,k})\,d\Omega = \oint_{\partial T_s} \mathcal{F}(u^{h,k})\cdot\hat{n}\,dl \tag{19}$$

Then, this residual is distributed to the 3 nodes of the sub-element, using any of the distribution schemes developed for P_1 triangles, e.g. the N-scheme (14)

$$\phi_i^{T_s,N} = k_i^+(u_i - u_{in}) \quad \text{with} \quad u_{in} = \frac{\phi^{T_s} - \sum_{i\in T} k_i^+ u_i}{\sum_{i\in T} k_i^-} \tag{20}$$

or the LDA scheme (17):

$$\phi_i^{T_s,LDA} = \beta_i \phi^{T_s} \tag{21}$$

The linearization used to compute the parameters k_i can be based on any linearized state over the subtriangle, without affecting accuracy nor conservation. After assembling all contributions for a given node, we end up with the following system of nodal equations to solve:

$$\sum_{T_s,\, i\in T_s} \phi_i^{T_s} = 0 \tag{22}$$

This system of equations can be solved using explicit or implicit pseudo-time iterations as discussed before.

C. Order of accuracy of Residual Distribution schemes

It has been shown that Residual Distribution schemes can reach order h^{k+1} for steady state solution under two conditions:

1. The cell residual ϕ^T should be approximated with order sufficently high order, namely

$$\phi^T = O(h^{k+2}) \tag{23}$$

This condition is automatically satisfied when the residual is approximated using a P_k finite element.

2. The distributed residual should be of the same order

$$\phi_i^T = O(h^{k+2}) \tag{24}$$

This condition is satisfied if condition 1. is satisfied, and if in addition the distribution coefficients β_i are uniformly bounded.

Clearly, both conditions are satisfied for the LDA-scheme on P_k triangles. However, it is wellknown that the N-scheme does not satisfy the second condition and reduces to first order on P_1 as well as on P_k, $k>1$ elements.

IV. Steady–state Euler equations

We consider briefly the extension to the 2D hyperbolic system of Euler equations

$$\nabla\cdot\mathcal{F} = 0, \tag{25}$$

in a domain Ω, where $\mathcal{F} = (\mathbf{F_1}, \mathbf{F_2})$ and $\mathbf{F}_i(u)$, $i = 1,2$ are vector valued functions $\mathbf{F}_i(u) : \mathbb{R}^2 \to \mathbb{R}^m$ for $u = u(x,y)$. Setting $m = 1$, equation (25) reduces to a steady scalar advection equation. For the Euler equations in 2D, $m = 4$ and

$$u = \begin{pmatrix} \rho \\ \rho v_1 \\ \rho v_2 \\ e \end{pmatrix}, \mathbf{F}_i(u) = \begin{pmatrix} \rho v_i \\ \rho v_1 v_i + p\delta_{1i} \\ \rho v_2 v_i + p\delta_{2i} \\ (e+p)v_i \end{pmatrix}, i = 1,2$$

The system is closed by the equation of state for ideal gas

$$p = (\kappa - 1)\left[e - \frac{1}{2}\rho(v_1^2 + v_2^2)\right], \quad \kappa = 1.4$$

We consider the same triangulation $\tau^{h,k}$ as before and the numerical solution $u^{h,k}$ is componentwise defined by equation (2). The residual distribution procedure to evolve $u^{h,k}$ in pseudo–time involves the same steps as for the scalar conservation law. First, the residual is computed over the subtriangles, giving

$$\phi^{h,k} = \int_{T_s} \nabla\cdot\mathcal{F}(u^{h,k})\,\mathrm{d}\Omega = \int_{\partial T_s} \mathcal{F}(u^{h,k})\cdot n\,\mathrm{d}l \tag{26}$$

Then, the distribution over the 3 nodes of the subtriangle is made using the schemes developed for P_1 triangles which have been generalized to systems[19], [17] .

V. Results

A. Sinus Bump

The first test case presented is a subsonic flow in a sine–bump channel with width equal to 1 and length equal to 4. The inlet Mach number $M_{in} = 0.5$. Solutions on three meshes are compared: the first mesh consists of P1 triangles and has 161 DOF as well as the second mesh, which contains P2 triangles only. The last mesh is a P3 subtriangulation of the computational domain with 175 DOF. Figure 5 shows Mach number isolines plotted in the range $\langle 0, 1.0 \rangle$ with step 0.025.

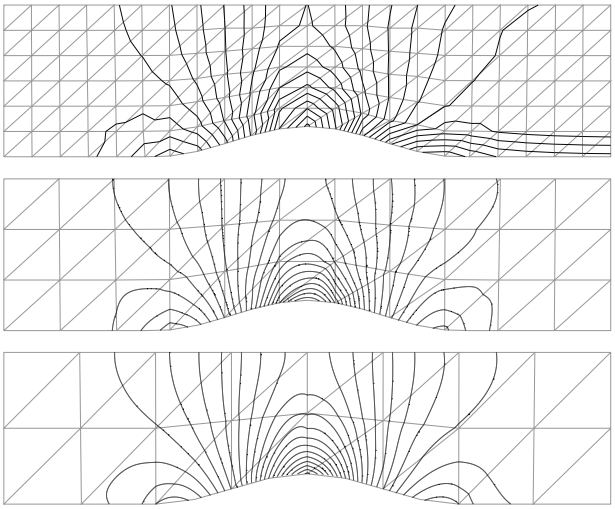

Fig. 5. Solution with LDA scheme on P_1, P_2 and P_3 elements in sinus bump channel (top to bottom)

The inlet entropy deviation $\Sigma - \Sigma_{in}$ is computed for every degree of freedom which lies on the bottom wall of the channel. Figure 6 shows that the entropy error is greatly reduced when the curvature of the boundary is taken into account.

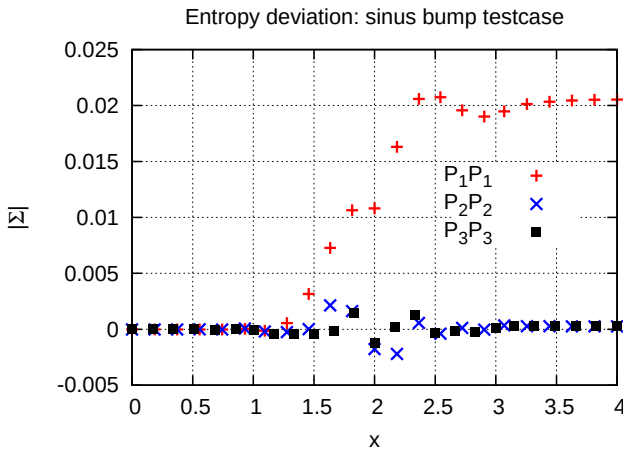

Fig. 6. Entropy deviation on bottom wall of the channel

B. Subsonic Cylinder

Next we present results for a more challenging testcase with stagnation point, namely the flow around a circular cylinder at $M_\infty = 0.38$. The diameter of the cylinder is 1 and the circular farfield boundary is located at 20 diameters from the center.

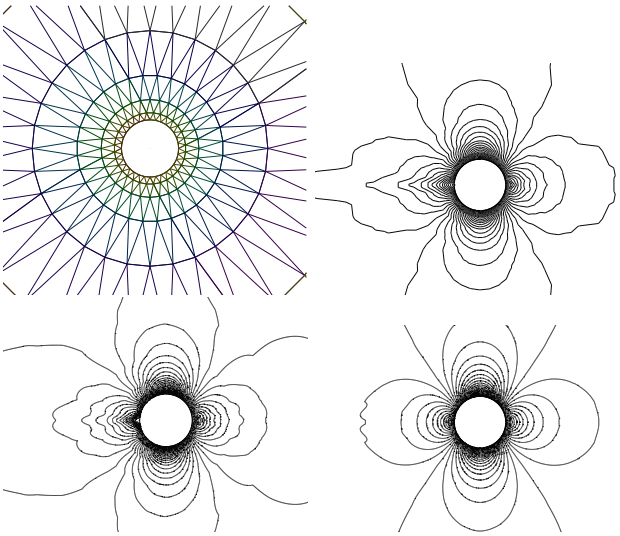

Fig. 7. Meshes for subsonic cylinder testcase and results with LDA scheme on P1 elements (top right), P2 elements (bottom left) and P3 elements.

The test was run on a relatively coarse O–grid having 32×8 points. The first number denotes the number of points in the circular direction and the second number refers to the number of concentric circles in the mesh (figure 7).

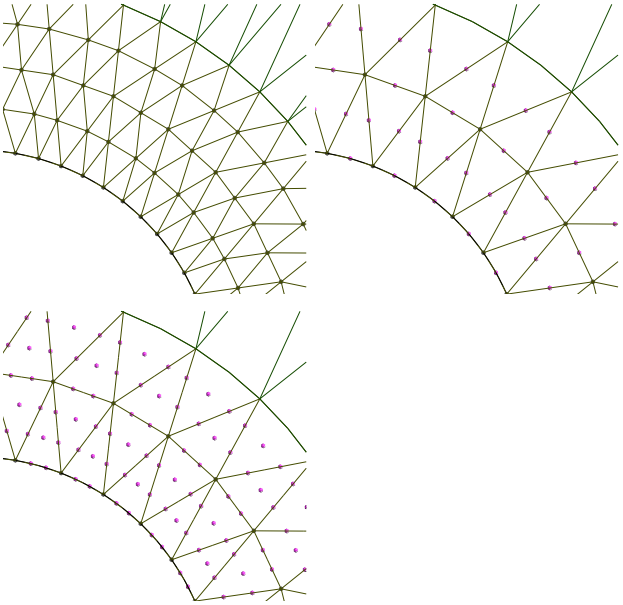

Fig. 8. Grid comparison: P1P1, P2P2 and P3P3 elements (left to right, top to bottom)

The P1 mesh was obtained by refining the P2 mesh in order to retain the number of DOF (1088 in this case). The P3 mesh contains 2400 degrees of freedom. Comparison of all three topologies close to the cylinder wall is detailed in figure 8.

Scheme with low–order representation of geometry tends to generate entropy layer on the wall of the cylinder as shown in the case of LDA on P1P2 elements (figure 9), which is formally third–order accurate, but introduces additonal error to the solution due to poor geometry resolution.

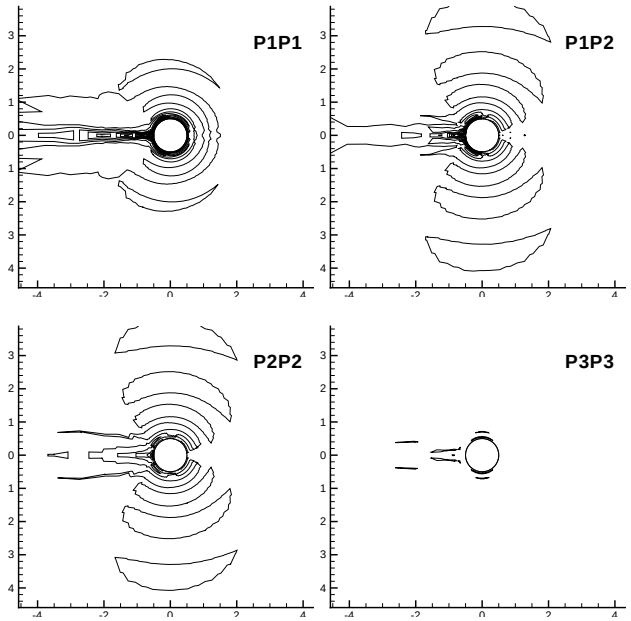

Fig. 9. Entropy isolines plotted in the interval $\langle 11.232, 11.259\rangle$ with $\Delta\Sigma = 0.001$.

C. Subsonic flow around NACA0012

The last test case was solved with p = 2 and p = 3 on two unstructured grids consisting of 2703 elements and having 5507 and 12315 degrees of freedom, respectively. The free stream Mach number is $M_\infty = 0.5$ and the angle of attack $\alpha = 2^\circ$.

VI. Conclusion

THIS contribution has focused on curved boundary representation for higher order Residual Schemes based on a curved boundary representation using subparametric or isoparametric transformation of the curved element to a Cartesian parent element. It has been demonstrated by numerical experiments that the curved boundary representation is needed to preserve high order accuracy for $P_{k,k>1}$ representation of the solution.

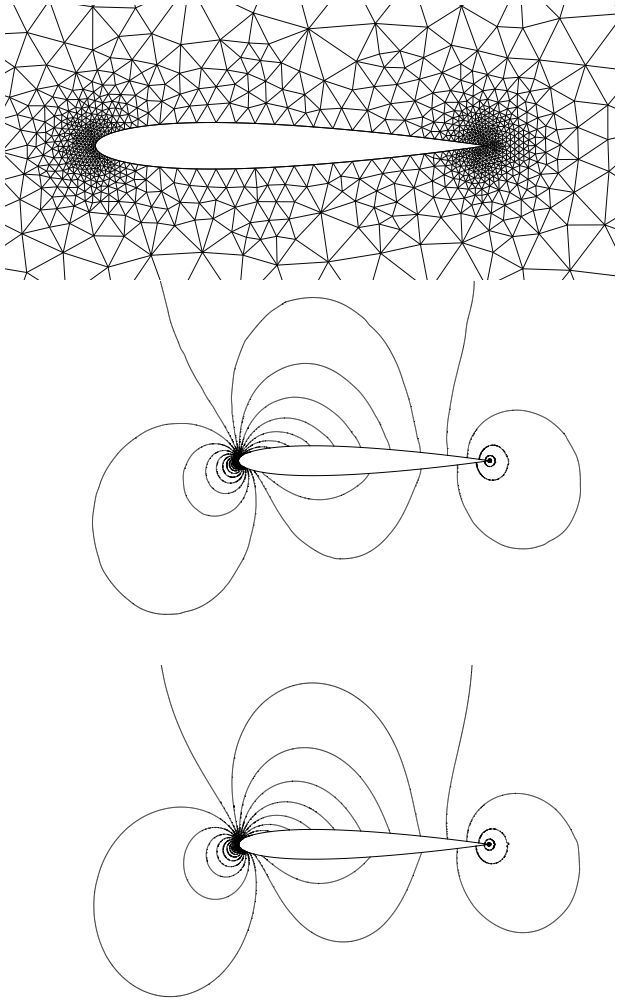

Fig. 10. Mesh and Mach number isolines (P2 top, P3 bottom), NACA0012, $M_\infty = 0.5$, $\alpha = 2^\circ$, $\Delta M = 0.025$.

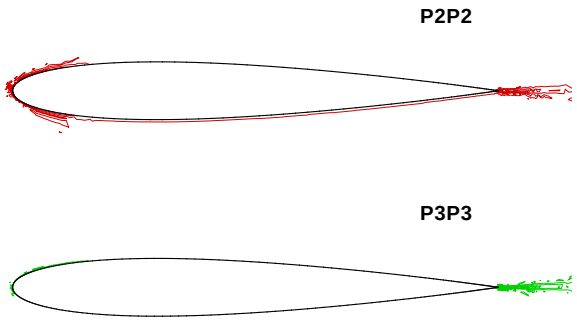

Fig. 11. Entropy isolines for subsonic NACA0012 test case. $\Sigma \in \langle 11.240, 11.244\rangle$, $\Delta\Sigma = 0.0001$.

REFERENCES

[1] Woodward, P. and Colella, P., "The numerical simulation of two–dimensional flows with strong shocks," *J. Comput. Phys.*, 1984, pp. 115–173.

[2] Xing, Y. and Shu, C.-W., "High–order well–balanced finite volume WENO schemes and discontinuous Galerkin methods for a class of hyperbolic systems with source terms," Submitted to *J. Sci. Computing*. Report SC-2004-08, Division of applied mathematics, Brown University: `http://www.dam.brown.edu/scicomp/publications/Reports/Y2005/BrownSC-2005-08.pdf`

[3] Ricchiuto, M., *Construction and analysis of compact residual discretizations for conservation laws on unstructured meshes*, Ph.D. thesis, Von Karman Institute for Fluid Dynamics and Université Libre de Bruxelles, Faculté des Sciences Appliquées, 2005.

[4] Hu, C. and Shu, C.-W., "Weighted essentially non-oscillatory schemes on triangular meshes", *J. Comput. Phys.*, Vol. 150, 1999, pp 97–127.

[5] Shu, C. W, "High-Order Methods for Computational Physics,", *High–Order ENO and WENO schemes for computational fluid dynamics*, edited by T. Barth and H. Deconinck, Vol. 9 of *Lecture Notes in Computational Science and Engineering*, Springer–Verlag, Heidelberg, 1999, pp. 439–582.

[6] Barth, T., "Numerical Methods for Conservation Laws on Structured and Unstructured Meshes," *VKI LS 2003-05, 33rd Computational Fluid dynamics Course, VKI, 2003.*

[7] Barth, T. and Ohlberger M., "Finite volume methods: foundation and analysis", *Encyclopedia of Computational Mechanics*, edited by E. Stein, R. de Borst and T. Hughes, John Wiley & Sons, Ltd., 2004.

[8] Barth, T. and Frederickson, P., "High–order solution of the Euler equations on unstructured grids using quadratic reconstruction," AIAA paper 90-0013, January 1990, 28th AIAA Aerospace Sciences Meeting, Reno, Nevada (USA).

[9] "Discontinuous Galerkin Methods for Convection–Dominated Problems," *High–Order ENO and WENO schemes for computational fluid dynamics*, edited by T. Barth and H. Deconinck, Vol. 9 of *Lecture Notes in Computational Science and Engineering*, Springer–Verlag, Heidelberg, 1999, pp. 69–224.

[10] Bassi, F. and Rebay, S., "High–order accurate discontinuous finite element solution of the 2D Euler equations," *Journal of Computational Physics*, Vol. 85, 1997, pp. 138–251.

[11] Wang, Z. J. and Liu, Y., "Extension of the spectral volume method to high–order boundary representation," *Journal of Computational Physics*, Vol. 211 (2006), 2005, pp. 154–178.

[12] Wang, Z., "Spectral (Finite) Volume method for conservation laws on unstructured grids: basic formulation," *J. Comput. Phys.*, Vol. 178, 2002, pp. 210–251.

[13] Van den Abeele, K., Lacor, C., and Wang, Z. J., "On the connection between the spectral volume and the spectral difference method," *J. Comput. Phys.*, Vol. 227, No. 2, 2007, pp. 877–885.

[14] Deconinck H. and Abgrall, R., "Introduction to Residual Distribution Methods," *VKI Lecture Series 2006-01, Comput. Fluid Dynam.*, 2005.

[15] van der Weide, E., *Compressible Flow Simulation on Unstructured Grids Using Multi–dimensional Upwind Schemes*, Ph.D. thesis, Von Karman Institute for Fluid Dynamics and TU Delft, 1998.

[16] Ricchiuto, M., Villedieu, N., Abgrall, R. and Deconinck, H., "High–order residual distribution schemes: discontinuity capturing crosswind and extension to advection–diffusion," *VKI Lecture Series 2006-01, Comput. Fluid Dynam., 2005.*

[17] Dobeš, J. and Deconinck, H., "Second order blended multidimensional upwind residual distribution schemes for steady and unsteady computations," *Journal of Computational Physics*, Vol. 195, 2006, pp. 474–507.

[18] Paillere, H., *Multidimensional upwind residual distribution schemes for the Euler and Navier–Stokes Equations on Unstructured Grids*, Ph.D. thesis, Von Karman Institute for Fluid Dynamics and Université Libre de Bruxelles, Faculté des Sciences Appliquées, 1995.

[19] van der Weide, E. and Deconinck, H., "Positive matrix distribution schemes for hyperbolic systems," *Computational Fluid Dynamics*, Wiley, New York, 1996, pp. 747–753.

Proceedings of the 8th National Congress on Theoretical and Applied Mechanics, May 28-29, Brussels, Belgium.

Highly Transient Mixed Flows with Air/Water Interactions: Homogeneous Equilibrium Model and Friction Correlations

F. Kerger[1,2], P. Archambeau[1], S. Erpicum[1], B.J. Dewals[1,2] and M. Pirotton[1]
[1]Research Unit of Hydrology, Applied Hydrodynamics and Hydraulic Constructions (HACH), Department ArGEnCo, University of Liege, Belgium,
[2]Belgian Fund for Scientific Research F.R.S-FNRS
email: fkerger@ulg.ac.be

Abstract: **An original 1D unified numerical model dealing with aerated mixed flow is derived and applied to the case of a gallery. The mathematical model is based on a new area-integration of the Homogeneous Equilibrium Model (HE-Model) over the cross-section of a free-surface flow and consists in a simple set of equations analogous to the Saint-Venant equations for single-phase flow. The frictional pressure drop is computed by means of three types of correlations, namely the homogeneous friction, the Lockhart-Martinelli correlation and the Müller-Steinhagen and Heck correlation. Performances of each method are compared. Finally, both free-surface and pressurized flows are mathematically modeled by means of the free-surface set of equations (Preissmann slot model). The original concept of the negative Preissmann slot is proposed to simulate sub-atmospheric pressure. This model is shown to be particularly well suited for the simulation of bubbly and intermittent flows**

Keywords: **Numerical Simulation, Mixed Flow, Two-phase Flow, Preissmann Slot, Two-phase Frictional Pressure Drop**

I. INTRODUCTION

Mixed flows, characterized by the simultaneous occurrence of free-surface and pressurized flows, are frequently encountered in rivers networks, sewer systems, storm-water storage pipes, flushing galleries, bottom outlets,… As a matter of fact, some hydraulic structures are designed to combine free-surface and pressurized sections (e.g. water intakes). In addition, dynamic pipe filling bores may occur in hydraulic structures designed only for conveying free-surface flow under an extreme water inflow or upon starting a pump. During such a transition, highly transient phenomena appear and may cause structural damages to the system [1], generate geysers through vertical shafts [2], engender flooding,… What is more, air/water interactions may arise, particularly at the transition bore [3], and alter thoroughly the flow regime and its characteristics. On account of the range of applications affected by mixed flows, a good prediction of mixed flow features is an industrial necessity. Numerical simulation of mixed flow remains however challenging for two main reasons. Dissimilarity in the pressure term arises between the classical sets of equations describing free-surface and pressurized flows. Air/water interaction has to be taken into account through a two-phase flow model.

Different mathematical approaches to describe mixed flows have been developed to date. First, the so-called *shock-tracking approach* consists in solving separately free-surface and pressurized flows through different sets of equations [4, 5]. However, such an algorithm is very complicated and case-specific so that it cannot be applied for practical applications. Second, the *Rigid Water Column Approach* [6] treats each phase (air/water) separately on the basis of a specific set of equations. The latter approach succeeds in simulating complex configurations of the transition but fails in its attempt to describe all flow regimes. What is more, using the method for practical application is not possible because of the complexity and specificity of the algorithm. Third, the so-called *shock-capturing* approach is a family of method which computes pressurized and free-surface flows by using a single set of equations [7-10]. In this paper, a shock-capturing approach is used, based on the model of the Preissmann slot [7]. Free-surface flow and pressurized flow are this way equally solved through a free surface set of equations. An original concept developed by the authors, the *negative Preissmann slot*, extends the Preissmann slot model to simulate sub-atmospheric pressurized flows.

Computing air-water interaction requires using a two-phase flow model. On the one hand, to authors' knowledge, no mixed flow model takes into account the effect of entrained air in the water flow. Only the air phase pressurization is usually modeled, as in the Rigid Water Column [6] and in the shock-capturing model of Vasconcelos [8]. On the other hand, usual multiphase flow investigations focus mainly on fully pressurized flow in small diameter pipes for chemical and mechanical engineering applications. There have been only a few attempts, often based on a transport equation [11], to simulate air entrainment in large hydraulic structures. Consequently, the current research aims at applying classical model for multiphase flow to civil engineering applications. In this paper, a Homogeneous Equilibrium Model (HE-Model) coupled with the Preissmann slot model is derived. For this purpose, the local instant formulation [12], which characterized each phase individually and the interfacial transfers, is time-averaged; By introducing macroscopic variables in terms of mixture properties and assuming equilibrium between each phases, the 3D HE-Model is established. Then, a new area-integration of the Homogeneous Equilibrium Model (HE-Model) over the cross-section of a free-surface flow gives a simple mathematical model analogous to the Saint-Venant equations for single-phase flow. Finally, the 1D HE-model derived is closed by specification of constitutive equations. The pressure constitutive equation is derived by using a non-dimensional analysis of the neglected momentum equations and the Phase change source term is derived from experimental measures. The frictional pressure drop is computed by means of three types of correlations, namely the homogeneous friction, the Lockhart-Martinelli correlation and the Müller-Steinhagen

and Heck correlation. Performances of each method are compared.

These developments have been implemented in the one-dimensional module of the software package WOLF. WOLF is finite volume flow simulation modelling system developed within the Laboratory of Hydrology, Applied Hydrodynamics and Hydraulic Constructions (HACH) of the University of Liege.

Application to this new model to the case of flows in a gallery is presented in this paper. Experimental results from a physical model build in the Laboratory of Structures Hydraulics of the University of Liege are used for comparison with numerical results.

II. Homogeneous Equilibrium Model

A. 3D Time-averaged Governing Equations

If we assume that each sub-region bounded by interfaces in an air-water flow may be considered as a continuum, the standard single-phase Navier-Stokes equations holds for each subregion with appropriate jump and boundary conditions. This is the Local Instant Formulation (LIF) [12] which is summarized in Fig. 1.

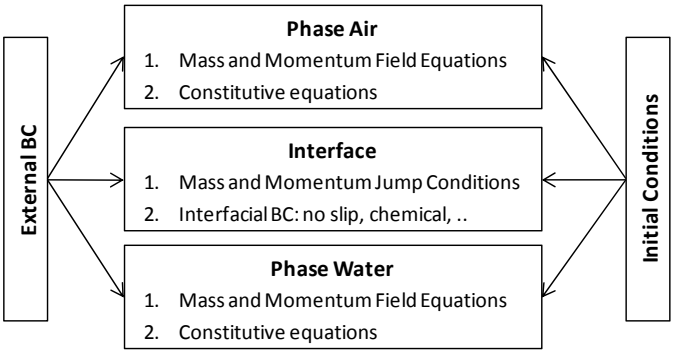

Fig. 1 : Local Instant Formulation according [12]

In principle, a two-phase flow model should solve the local instant formulation. Obtaining a solution this way is however mathematically difficult and beyond the present computational capability for many engineering applications. On account of this, practical model have been developed. Majority of them is notably derived by application of averaging procedure on the LIF. Many averaging methods have been developed to date and used to study two-phase flow systems: the Eulerian Averaging, the Lagrangian Averaging and the Boltzmann statistical averaging [13]. In the present work, the Eulerian time averaging procedure is chosen because it is proven to be particularly useful for turbulent two-phase flow. As pointed in Fig. 2, it results into different models according the choice of the macroscopic variables.

The first type of model is called two-fluid model. Each phase is treated as a separate fluid with its own set of governing equations [14]. Difficulties stem from the derivation of interfacial conditions [12]. In the second type of method, it is assumed that the multiphase flow may be described as a single phase flow of mixture variables which refers to the motion of the centre of mass. The motion of the dispersed phase is then treated in terms of diffusion through the mixture. This model is usually called drift-flux model [15]. Since the momentum equation for this phase is neglected, a constitutive equation for the relative velocity is required. In particular, if all phases are assumed to move at the same velocity (the relative velocity is negligible), it results in the Homogeneous Equilibrium Model (HE-Model).

Homogenous flow theory provides the simplest technique for analyzing multiphase flows. Using suitable averaged properties, the fluid is treated as a pseudo-fluid that obeys the usual equations of a single-component flow. This assumption is particularly suited for dispersed bubbly flow. The model is commonly used for the simulation of heat exchangers [16, 17], two-phase flow in ducts [18],…In the current section, the layout of the 3D HE-Model is presented and then the 1D free-surface HE-Model resulting from an original area-integration is introduced.

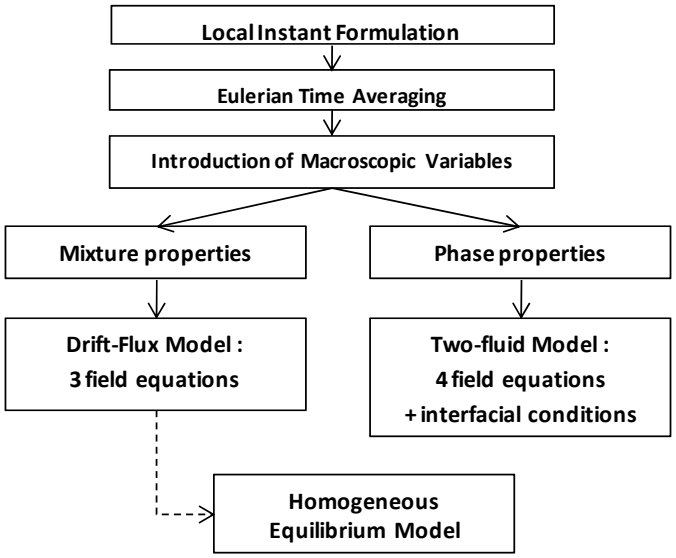

Fig. 2 : Modelling approaches

3D HE-model is derived through the time averaging of the Local Instant Formulation for multiphase flow, the introduction of suitable mixture variables and the assumption of equilibrium between phases. For further details, we refer the interested reader to the classical book of Ishii and Hibiki [12]. The resulting field equations are written as:

- The continuity equation:

$$\frac{\partial \rho_m}{\partial t} + \nabla\left(\rho_m \mathbf{v}_m\right) = 0 \tag{1}$$

- The diffusion equation:

$$\frac{\partial \alpha_g}{\partial t} + \nabla\left(\alpha_g \mathbf{v}_m\right) = \Gamma_g \tag{2}$$

- The momentum equation:

$$\frac{\partial \rho_m \mathbf{v}_m}{\partial t} + \nabla\left(\rho_m \mathbf{v}_m \mathbf{v}_m\right) = -\nabla p_m + \nabla\left(\tau_m + \tau^T\right) + \rho_m \mathbf{g} + \mathbf{M}_m \tag{3}$$

where ρ_m[kg/m³] is the mixture density, $\mathbf{v}_m$[ms^{-1}] is the mixture velocity vector (under the assumption of velocity equilibrium, $\mathbf{v}_m = \mathbf{v}_{water} = \mathbf{v}_{air}$), α_g[-] is the air void fraction, Γ_g[s^{-1}] is the phase change volume generation, p_m[Nm^{-2}] is the mixture pressure, τ_m[Nm^{-2}] and τ^T[Nm^{-2}] are the viscous and turbulent stress tensors, g[ms^{-2}] is the gravity and $\mathbf{M}_m$[kgs^{-2}m^{-}

^{2}] is the interfacial momentum source. It is worthwhile noting that the simplicity of equations (1) to (3) results from the wise choice of the mixture macroscopic properties.

Closure of the HE-model requires the definition of the mixture variables and a constitutive equation. Air and water are supposed to be incompressible Newtonian fluid, and the mixture properties are written as follows:

$$\begin{aligned}\rho_m &= \alpha_g\rho_g + \left(1-\alpha_g\right)\rho_w \cong \left(1-\alpha_g\right)\rho_w \\ \tau_m &= \left[\alpha_g\mu_g + \left(1-\alpha_g\right)\mu_w\right]\left(\nabla.\mathbf{v} + \left(\nabla.\mathbf{v}\right)^T\right)\end{aligned} \tag{4}$$

At this point, no assumption is needed for the constitutive equations of the turbulent stress τ^T, the phase change volume generation Γ_g, the pressure distribution p_m and the mixture momentum source $\mathbf{M}_m$. These terms will be taken into account by means of macroscopic laws specifically derived for the 1D model.

B. 1D Area-integrated HE-Model

In many cases, the computational domain is essentially one-dimensional (both the flow depth and width are way smaller than the flow length) and the computation effort can be greatly reduced by simplifying two-equations of momentum and area-integrating the remaining equations [19]. The originality of the present paper is to consider a free-surface flow in the integration process. It is indeed shown in section III.D how the free-surface set of equations can be used to simulate pressurized flow as well. It results in the 1D free-surface HE-Model.

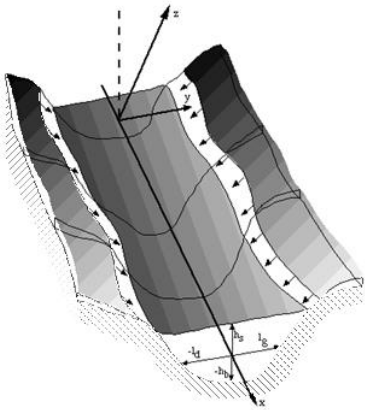

Fig. 3 : Domain of integration

For this purpose, a Cartesian coordinate system oxyz is set in such a way that x-axis is parallel to the predominating flow direction of the computational domain (Fig. 3). The whole process of integration is beyond the scope of this paper. The derivation is performed by analogy to the integration of the Saint-Venant equations for pure water flow as exposed in [19] but the basis equations are in this case a two-phase flow model. Briefly, momentum equations (3) along both the y-axis and the z-axis are simplified by means of a non-dimensional analysis and reduce to a pressure distribution over the flow section:

$$\begin{cases}\dfrac{\partial p}{\partial z} = -\rho_m g\sin\theta_z \\ \dfrac{\partial p}{\partial y} = 0\end{cases} \tag{5}$$

Successive integration over the flow width (y-abscissa) and the flow depth (z-abscissa) are performed on the basis of the Leibniz integral rule [19] and adapted boundary conditions at the bottom, free-surface and banks of the cross-section. The success of the method relies on choosing wisely the definition of the area-average . As a consequence, the area-average of a general function f is defined as:

$$\langle f\rangle(x,t) \triangleq \frac{1}{\Omega}\int_\Omega f(x,y,z,t)\,dA \tag{6}$$

where Ω[m²] is the flow cross-section area. Likewise, the 1D mixture velocity is chosen as the mixture density weighted area-average of the 3D mixture velocity:

$$\tilde{u}_m \triangleq \frac{\langle\rho_m u_m\rangle}{\langle\rho_m\rangle} \tag{7}$$

The resulting field equations are written as:

- The area-integrated continuity equation:

$$\frac{\partial\left(1-\langle\alpha_g\rangle\right)\Omega}{\partial t} + \frac{\partial\left(1-\langle\alpha_g\rangle\right)\tilde{u}_m\Omega}{\partial x} = 0 \tag{8}$$

- The area-integrated diffusion equation:

$$\frac{\partial\langle\alpha_g\rangle\Omega}{\partial t} + \frac{\partial\langle\alpha_g\rangle\tilde{u}_m\Omega}{\partial x} = \left\langle\frac{\Gamma_g}{\rho_g}\right\rangle\Omega \tag{9}$$

- The area-integrated momentum equation:

$$\begin{aligned}&\frac{\partial\left(1-\langle\alpha_g\rangle\right)\tilde{u}_m\Omega}{\partial t} + \frac{\partial\left(1-\langle\alpha_g\rangle\right)\tilde{u}_m\tilde{u}_m\Omega}{\partial x} \\ &= \\ &g\left(1-\langle\alpha_g\rangle\right)\Omega\left(\frac{\partial Z}{\partial x} - S_F\right) - gp_w\frac{\partial\langle\alpha_g\rangle}{\partial x} \\ &-\frac{1}{\rho_w}\frac{\partial}{\partial x}\left(\sum_k COV\left(\alpha_k\rho_k u_k u_k\right)\Omega\right)\end{aligned} \tag{10}$$

Where

$$p_w = \int_{-h_b}^{h_s}\left(h_s - z\right)l(z)\,dz \tag{11}$$

and Z[m] is the free surface elevation, S_F[-] is the friction slope (resulting from the integration of the viscous, turbulent shear stress and the interfacial momentum source). In equation (10), the covariance term has been introduced as the difference between the average of a product and the product of the average of two-variables [20]. Since the profile of velocity is assumed to be flat in the present paper, the covariance term reduces to zero.

C. Constitutive Equation for the Phase Change

To close the partial differential system, we still need to give an expression for the phase change volume generation Γ_g. Literature is abundant for empirical relations. To keep the generality of the model, a very fundamental relation given in [11] for air entrainment in free-surface flow is used:

$$\left\langle\frac{\Gamma_g}{\rho_g}\right\rangle\Omega = -m\Gamma\left(\alpha-\alpha_{eq}\right) \tag{12}$$

where Γ and α_g are constants calibrated with experimental results. The onset of air entrainment is controlled by the parameter m=1 or m=0.

D. Numerical Scheme

Discretization of equations (4)-(7) is performed by means of a finite volume scheme with an original flux vector splitting [21]. The scheme has been proven to be 1st order accurate and very robust. The time discretization is achieved with a classical 3-step Runge-Kutta algorithm [22]. The efficiency of such an explicit method is well known because of its low computation-cost. Moreover the coefficients have been tuned to emphasize the dissipation and the stability properties of the scheme.

III. Constitutive Equation for the Friction

Head loss in pressurized and free-surface single phase flow can be readily calculated by means of the Darcy-Weisbach equation [19] coupled with the Moody-Stanton diagram, the Blasius equation or the Colebrook implicit relation.

However, additional head-loss has to be accounted for in two-phase flow. Due to the importance of a correct evaluation of the frictional pressure drop, pressure drop and void fraction data have been collected for horizontal, vertical and inclined gas-liquid systems and many attempts have been made to develop general procedures for predicting these quantities. Thus, the literature contains a plethora of engineering correlations for pipe friction, channel friction and some data for other interesting components such as pumps. In this paper, a comparative study of the three most widespread correlations is proposed. In particular, the various formulations are applied on a practical application in civil engineering.

A. Homogeneous Friction

When the mixture is thoroughly mixed both air and water can be assumed to move at the same velocity and the frictional pressure drop can be approximated by the friction coefficient for a single phase flow calculated on the basis of suitable "mixture parameters". This model is called homogeneous model [17, 23] or no-slip model [24]. The most thorough discussion of the model is given by Wallis [17]. The frictional pressure gradient is then calculated by means of the Darcy-Weisbach equation:

$$-\left(\frac{dp}{dx}\right)_F = \langle \rho_m \rangle g \Omega S_F = \langle \rho_m \rangle f \frac{\tilde{u}_m^2}{2D_h} \Omega \tag{13}$$

where f is the friction factor and D_h is the hydraulic diameter which is defined as:

$$D_h = 4R_h = 4\frac{\Omega}{\partial\Omega} \tag{14}$$

R_h is the hydraulic radius which is given by the cross-sectional area Ω divided by the wetted perimeter $\partial\Omega$.

In chemical and process engineering, the friction factor f is usually computed with an explicit Blasius-like correlation as follows:

$$f = \begin{cases} 64\,Re_f^{-1} & \text{ik} \quad Re_f \le 2500 \\ 0.3164\,Re_f^{-0.25} & \text{ik} \quad Re_f > 2500 \end{cases} \tag{15}$$

In civil engineering, the implicit Colebrook-White correlation for the friction factor is preferred as it takes into account the pipe roughness as well:

$$f = \begin{cases} 64\,Re_f^{-1} & \text{ik} \quad Re_f \le 2500 \\ \sqrt{\frac{1}{f}} = -2\log\left(\frac{k_D}{3.7D_h} + \frac{2.51}{Re_f\sqrt{f}}\right) & \text{ik} \quad Re_f > 2500 \end{cases} \tag{16}$$

where k_D[m] is the roughness height.

In both equations (15) and (16), the Reynolds number Re is the mixture Reynolds defined as:

$$Re_{f,m} \triangleq \frac{\langle \rho_m \rangle \tilde{u}_m D_h}{\langle \mu_m \rangle} \tag{17}$$

The mixture viscosity μ_m is approximated with rheological models that take into account the void fraction. Many correlations are available but the authors found that the McAdams formulation [25] gives the most reliable results:

$$\frac{1}{\langle \mu_m \rangle} = \frac{\langle x_g \rangle}{\mu_g} + \frac{1 - \langle x_g \rangle}{\mu_w} \tag{18}$$

where the quality x_g is defined as:

$$\langle x_g \rangle = \frac{\langle \alpha_g \rangle \rho_{air}}{\langle \rho_m \rangle} \tag{19}$$

B. Lockhart-Martinelli Correlation (LM)

Two-phase friction pressure drop are still nowadays often modeled on the basis of the classical theory established by Lockhart and Martinelli [26]. Two-phase flow is considered to be divided into liquid and gas streams. Correlations are constructed with the results for the frictional pressure gradient in single-phase pipe flows of each of the two fluids. They are calculated on the basis of the Darcy-Weisbach equation applied to each single-phase stream:

- For the water flow:

$$-\left(\frac{dp}{dx}\right)_{F,w} = \rho_w f_{f,w} \frac{\left(\tilde{u}_m\left(1 - \langle \alpha_g \rangle\right)\right)^2}{2D_h} \Omega \tag{20}$$

- For the gas flow:

$$-\left(\frac{dp}{dx}\right)_{F,g} = \rho_g f_{f,g} \frac{\left(\tilde{u}_m \langle \alpha_g \rangle\right)^2}{2D_h} \Omega \tag{21}$$

The friction factors are calculated by means of the Blasius-like equation (15). In the original paper of Lockhart and Martinelli [26] they found that the strict determination of X^2 using the exact Blasius equation does not fit adequately when compared with experimental data. They achieve agreement when setting $f = 0.184\,Re_f^{-0.2}$ for turbulent flow. These values are normally used nowadays in chemical engineering and have been validated for civil engineering applications in [27].

The pressure drops computed this way are then correlated with the Lockhart-Martinelli parameter defined as:

$$X^2 \triangleq \left(\frac{dp}{dx}\right)_{F,w} \Big/ \left(\frac{dp}{dx}\right)_{F,g} \tag{22}$$

X^2 gives a measure of the degree to which the two-phase mixture behaves as the water rather than as the gas.

In addition, the two-phase frictional pressure drop is expressed in terms of two-phase multipliers defined as:

$$\Phi_{f,w}^2 \triangleq \frac{\left(\frac{dp}{dx}\right)_F}{\left(\frac{dp}{dx}\right)_{F,w}} \quad \text{and} \quad \Phi_{f,g}^2 \triangleq \frac{\left(\frac{dp}{dx}\right)_F}{\left(\frac{dp}{dx}\right)_{F,g}} \tag{23}$$

In the initial paper of Martinelli and Lockhart [26], the relations of $\Phi_{f,w}^2$ and $\Phi_{f,g}^2$ as a function of X^2 was presented in graphical forms for the 4 flow regimes: turbulent-turbulent, viscous-turbulent, turbulent-viscous and viscous-viscous. For sake of easier numerical application, Chisholm [28] develop simplified equations:

$$\Phi_{f,w}^2 = 1 + \frac{N}{X} + \frac{1}{X^2} \tag{24}$$

$$\Phi_{f,g}^2 = 1 + N.X + X^2 \tag{25}$$

The coefficient N can thereby be set according to the flow regime defined previously according to table 1.

Tableau 1 : Coefficient N according to[28]

Liquid	Gas	N
Turbulent	Turbulent	20
Viscous	Turbulent	12
Turbulent	Laminar	10
Viscous	Laminar	5

C. Approach of Muller-Steinhagen and Heck (MSM)

Müller-Steinhagen and Heck [29] suggested a new correlation for the prediction of the frictional pressure gradient in two-phase flow in pipes. The effort was explicitly aimed at developing an approach which is simpler in application but still reliable in terms of accuracy. According to them, the pressure drops of the respective single-phase flows are calculated as follows:

$$\left(\frac{dp}{dx}\right)_{F,w0} = f_{f,w0}\frac{\left(\langle\rho_m\rangle\tilde{u}_m\right)^2}{2\rho_w D_h} = A_{MSH} \tag{26}$$

And

$$\left(\frac{dp}{dx}\right)_{F,g0} = f_{f,g0}\frac{\left(\langle\rho_m\rangle\tilde{u}_m\right)^2}{2\rho_g D_h} = B_{MSH} \tag{27}$$

And the friction factors are computed with Blasius-like correlation (15) where the Reynolds numbers used are given by the two following relations:

$$Re_{f,g0} = \frac{\langle\rho_m\rangle\tilde{u}_m D_h}{\mu_g} \quad \text{and} \quad Re_{f,w0} = \frac{\langle\rho_m\rangle\tilde{u}_m D_h}{\mu_w} \tag{28}$$

The equation developed for the roughly linear increase of the pressure drop with increasing quality for x<0.7 can be written:

$$G_{MSH} = A_{MSH} + 2\left(B_{MSH} - A_{MSH}\right)\langle x_g\rangle \tag{29}$$

To cover the full range of flow quality $0 \le \langle x_g \rangle \le 1$, a superimposition of equations (27) and (29) is used:

$$\left(\frac{dp}{dx}\right)_F = G_{MSH}\left(1 - \langle x_g\rangle\right)^{1/C} + B_{MSH}\langle x_g\rangle^C \tag{30}$$

A value of C=3 was found by curve fitting measured data.

To determine the reliability of the method, Müller-Steinhagen and Heck [29] assessed their correlation against a data bank containing 9313 measurements of pressure gradient for different fluids, different pipe diameter and different flow conditions. They reported accuracy similar to the more complicated methods. However, for engineering applications, Keller [27] shows this method does not reach the same degree of accuracy than the Lockhart-Martinelli correlation when compared to measurement on scale model.

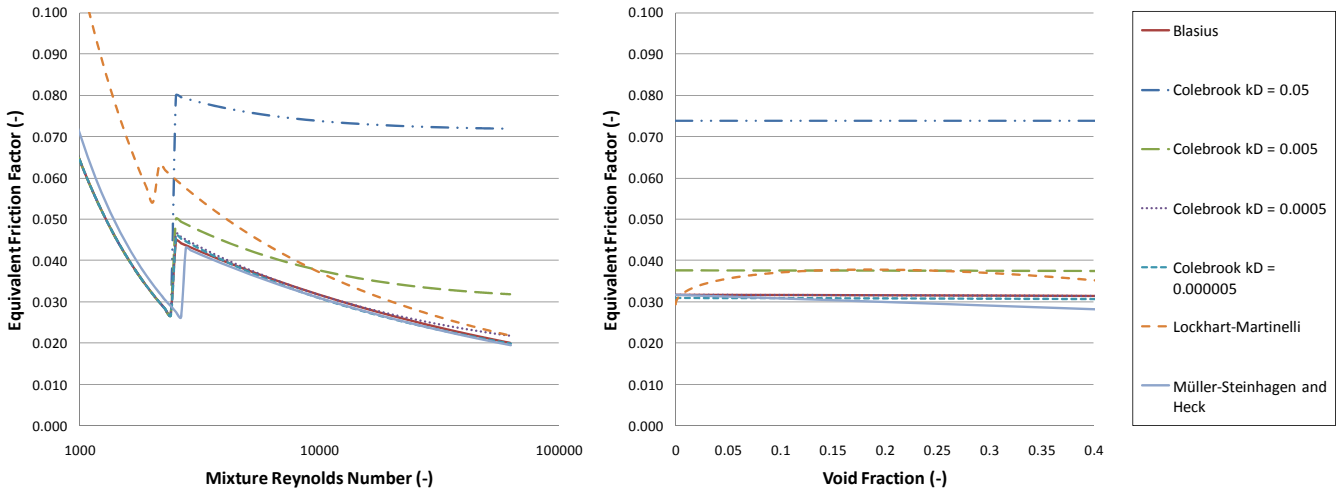

Fig. 4 : Comparison between various friction correlations

D.Comparison of the Methods

In view of the previous description of the various friction correlations, it is clear that not only the friction factor but also the kinetic term is affected by the presence of air. As a result, correlations cannot be compared in all generally by means of a Moody-like diagram. A particular case is hence specified for sake of comparison. We consider a pressurized flow in a circular pipe of 0.5m of diameter. Fig. 4 gives then the equivalent friction factor (defined as the pressure drop divided by the mixture kinetic energy) plotted against the mixture Reynolds number (for a local void fraction of 10%) and the local void fraction (for a discharge of 5m³/s). Similar analyses have been made with various cross-section shapes, with various hydraulic diameter as well as with free-surface flow. The following conclusions stay consistent. We conclude

from Fig. 4 that homogeneous theory and MSM theory gives analogous results for smooth pipes and LM method gives slightly bigger friction factor, especially for laminar flow. However, if the pipe roughness becomes important, all the method based on Blasius-like formulation underestimate the friction factor.

Under the assumption that a small void fraction (α_g<5%) does not affect drastically the onset of a boundary layer at the pipe walls, homogeneous Colebrook-White correlation is consequently preferred since it takes into account the pipe roughness, which is a determinant parameter in civil engineering.

IV. Preissmann Slot Model

Pressurized flows are commonly described through the Water Hammer equations [30] derived from the equations of continuity and motion in closed pipe. According to the Preissmann slot model [7], pressurized flow can be equally calculated through the free-surface equations by adding a conceptual slot at the top of a closed pipe (Fig. 5b). When the water elevation is above the pipe crown, it provides a conceptual free-surface flow, of which the gravity wavespeed is given by $c=\sqrt{g\Omega/T_s}$ (T_s is the slot width). Strictly speaking, the pressure wave celerity of a flow in a full pipe, referred by a[m/s], depends on the properties of the fluid, the pipe, and its means of support. In first approximation, its value is not dependant of the pressure value and may be computed on the basis of solid mechanics relations [30]. It is then easy to choose a slot width T_s which equalizes the gravity wavespeed c to the water hammer wavespeed a:

$$T_s \triangleq \frac{g\Omega}{a^2} \qquad \text{with} \qquad a^2 \triangleq \Omega\frac{dp}{d(\rho\Omega)} \tag{31}$$

From a hydraulic point of view, all the relevant information is summarized in the relation linking the water height and the flow area (H-A). A specific relation corresponds to each geometry of the cross section (Fig. 5a). Adding the Preissmann slot leads to linearly extend the relation beyond the pipe crown head. In order to simulate pressurized flows with a piezometric head below the pipe crown, the authors propose a new concept, called *negative Preissmann slot*. It consists in extending the Preissmann straight line for water height below the pipe crown (Fig. 5c). To each water level below the pipe crown corresponds two values of the flow area: one for the free surface flow and one for the pressurized flow. The choice between the two relations is done according to the local aeration conditions (closed pipe or presence of an air vent). For further details, we refer the interested reader to the following paper [31] totally dedicated to this mathematical model.

For steady flow applications, the choice of the slot width may be arbitrary. On the one hand, the wave celerity does not affect the steady state of a flow. On the other hand, explicit numerical schemes are characterized by a time step Δt that is limited by a CFL condition of the form:

$$NbC \le 1 \qquad \text{with} \qquad NbC \triangleq \max\left(|u_m|+c\right)*\frac{\Delta x}{\Delta t} \tag{32}$$

It seems then reasonable to impose a wider slot than the width calculated with equation (31) in order to decrease the number of computation steps.

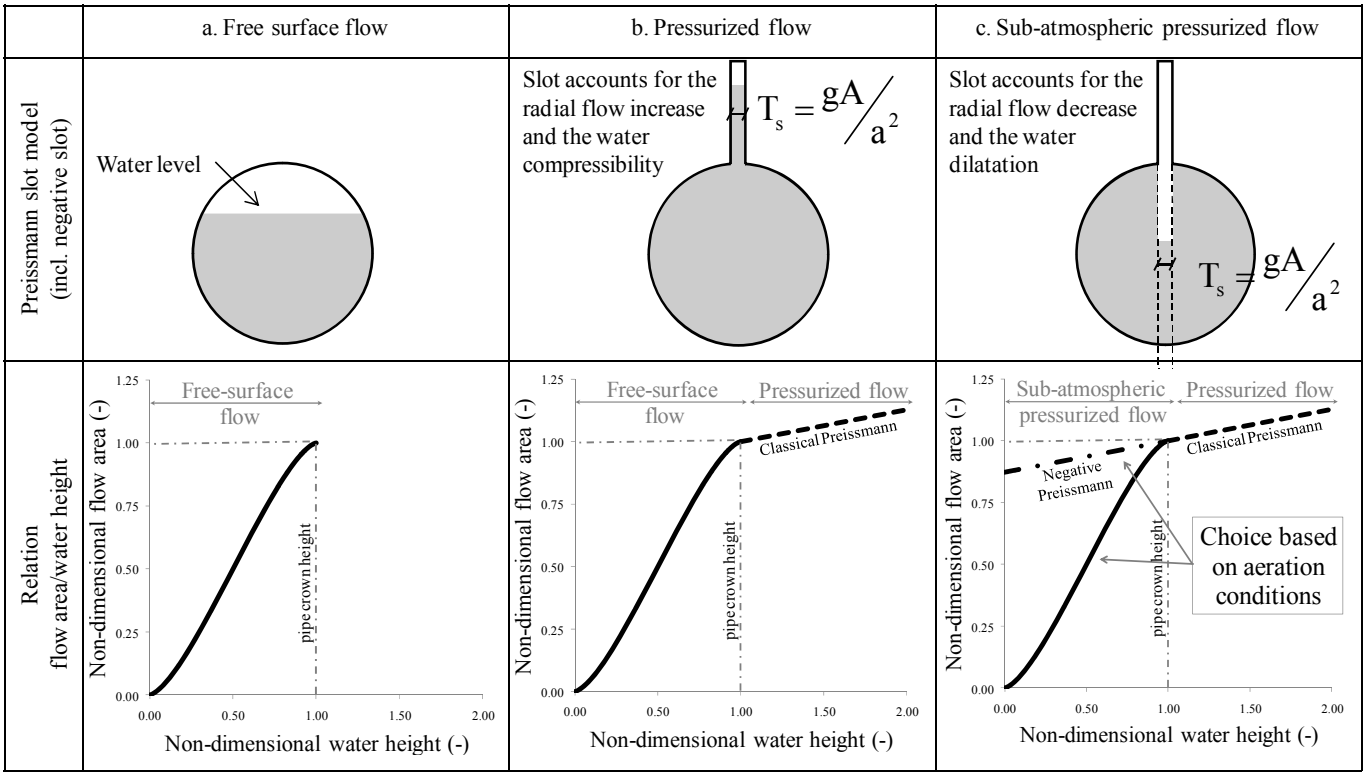

Fig. 5 : The Preissmann slot method under different flow conditions

V. Steady Flow Application

This section outlines the application of the 1D HE-Model for simulating stationary mixed flows taking place in a gallery. Numerical results are compared with experimental results provided by experimental investigations carried out in the Laboratory of Structures Hydraulics (HACH) of the University of Liege. The model (Fig. 6) includes a plexiglas circular pipe linking two tanks. Topography of the upstream and downstream tanks has been built regarding realistic in-situ natural conditions. The gallery inlet and outlet structures are also represented. Experimental apparatus, measurement systems and results are described in details in [32].

A. Experimental Investigations

Investigations focus mainly on stationary flows and aims at determining the flow discharge through the gallery as a function of the upstream pressure head. Strong air/water interactions may alter the flow behaviour. In particular, the flow discharge through the gallery is strongly influenced by air/water interaction, and consequently depends of the aeration rate as well.

Various two-phase flow patterns are observed according to the flow discharge through the gallery. Fig. 7 shows the experimental relation between the flow discharge and the upstream pressure head (zero level is set at the upstream reservoir bottom level). The curve defines 5 areas corresponding to the 5 flow patterns (Fig. 7) traditionally mentioned in the literature [17]:

1. A *smooth stratified flow.*
2. A *wavy stratified flow.*
3. An *intermittent flow* that includes *slug flow* as well as *plug flow.*
4. A *bubbly flow.*
5. A pure water *pressurized flow.*

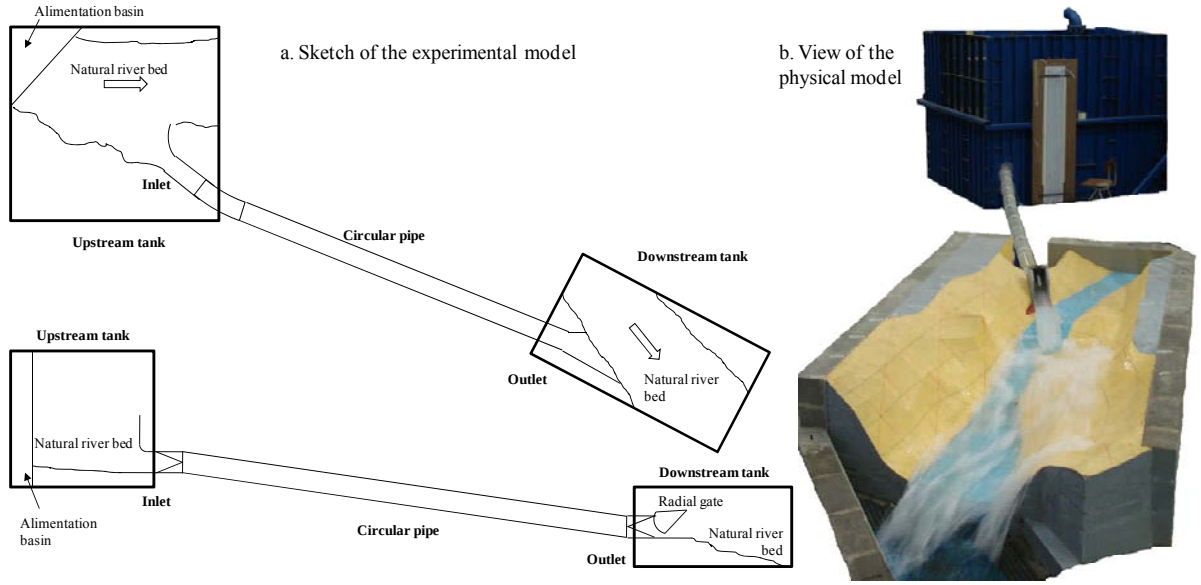

Fig. 6 : Experimental setup

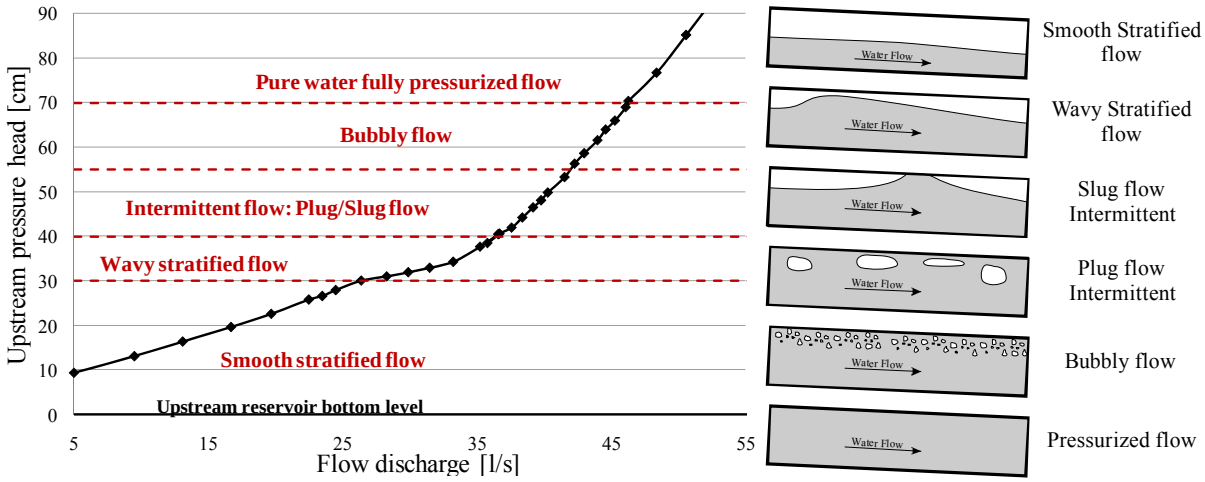

Fig. 7 : Experimental discharge curve (upstream pressure head-flow discharge) and observed flow patterns

B.Pure Water Simulation

In this section, simulations are performed under the assumption of a pure water flow (void fraction is equal to zero), with a spatial discretization step Δx=3.33cm and a CFL number limited to 0.5. As exposed in section III, the Homogenous Colebrook-White correlation is used with the McAdam formulation for the mixture viscosity and a roughness height $k_D = 2.10^{-5}$m. Comparison of results computed with other two-phase friction correlations is provided in section V.D. The flow discharge varies between 5l/s and 55l/s. A first head/discharge relation (dotted line in Fig. 10) is computed with the HE-Model and assuming a free surface appears in each mesh if the water height is below the pipe crown (air phase above the free surface is at atmospheric pressure). The second head/discharge relation (continuous line) is computed by activating the negative Preissmann slot (sub-atmospheric pressurized flow).

Numerical results are in good accordance with experimental data for smooth stratified flows and fully pressurized flows. Bubbly and intermittent flows show a similar behavior to the sub-atmospheric pressurized flows. A periodic instability between two unstable steady flow regimes occurs in the area of wavy stratified flows. The instability induces large period (10s to 60s) oscillations of the water level in the upstream reservoir. For further details over this regime, we refer the interested reader to the paper of Erpicum and al. [32].

Experimental and numerical data for the distribution of the total head and the pressure head (water level for free surface flow) along the gallery length are given in Fig. 8 for a smooth stratified flow (discharge of 9.5l/s) and a fully pressurized flow (discharge of 48.4l/s). In the latter case, results are in full agreement. In the former case, a slight discrepancy is observed in the total head curve. It results from the effect of the air phase flowing above the free surface that is not taken into account in the computation.

A comparison of the results given by the computation for an intermittent flow of 38.4l/s discharge is shown in Fig. 9. Pressure distribution along the gallery is computed in Fig. 9b under the assumption of a free surface flow. Large discrepancies of the results are observed. In Fig. 9a, activation of the negative Preissmann slot gives the curve corresponding to a pressurized flow. We consequently identify a large area of sub-atmospheric pressure in the upstream part of the pipe. Results are now in better accordance and it has been concluded that the aeration rate of the pipe is not sufficient to induce the apparition of a free surface flow. However, some differences still remain due to the air-water interactions.

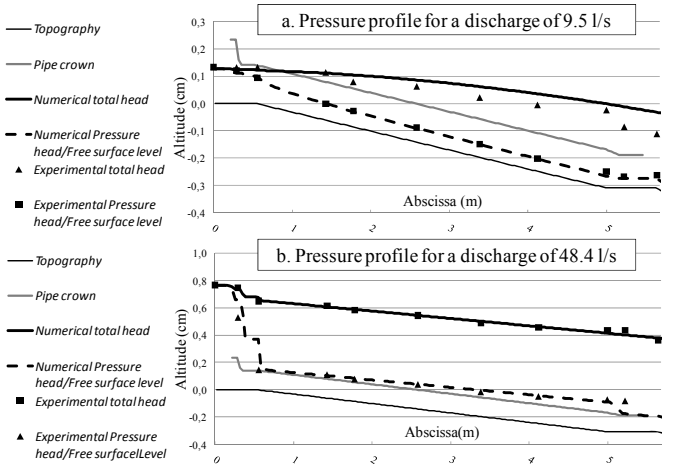

Fig. 8 : Computed total head and pressure head distribution for a smooth stratified flow and a pressurized flow

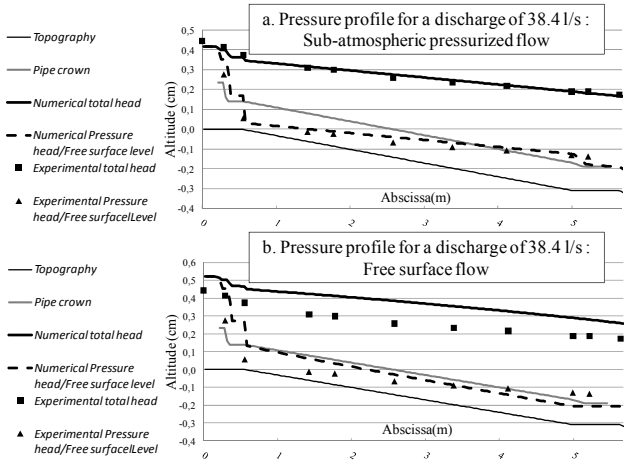

Fig. 9 : Computed total head and pressure head distribution for an intermittent flow sub-atmospheric pressurized flow and free-surface flow computation

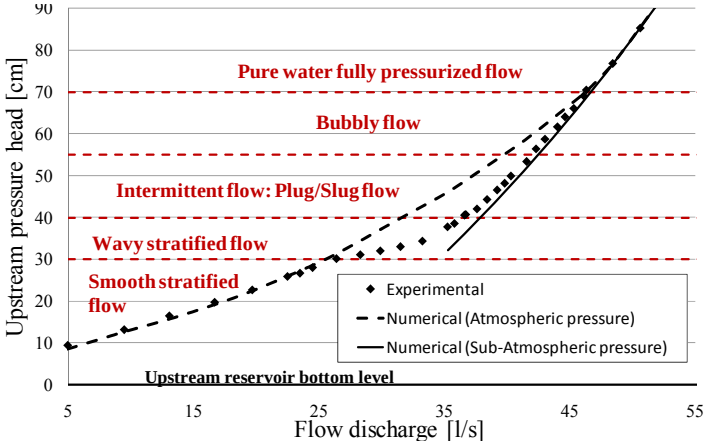

Fig. 10 : Computed flow discharge relation for pure water simulations

C. Air-water Mixture Simulation

Application of the HE-Model enables to overcome the results discrepancy observed in section V.B for bubbly and intermittent flows (Fig. 9). The effect of the entrained air on the water flow is accurately computed by using the equation (12) for the phase change volume generation Γ_g. The parameter Γ is set at 25 and α_g is calibrated according to the flow pattern observed. For bubbly flows, as bubbles arise from the air dissolved in water, equilibrium void fraction is chosen between 0.5% and 2%. For intermittent flows, an additional air supply is provided through a vertical vortex appearing at the water intake. Equilibrium void fraction is then chosen between 2% and 4.5%.

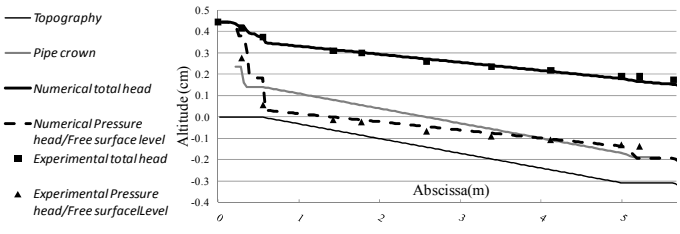

Fig. 11 : Computed total head and pressure head distribution for a bubbly (flow discharge of 38.4 l/s and void fraction of 4.5%)

Fig. 12a shows a comparison between experimental and numerical data for the discharge curve. Taking into account air/water interactions in the computation obviously gives more accurate results for bubbly and intermittent flows. The void fraction relation corresponding to this new relation is given in Fig. 12b.

A comparison between experimental data and numerical results computed with the HE-Model is drawn on Fig. 11. Computation is performed with a flow discharge of 38.4l/s and a void fraction of 4.5%. Results are shown in full agreement.

D. Influence of the Friction Law

In this section, computation is performed for a bubbly flow of 36.5 l/s and a void fraction of 4.5%. The 4 friction correlations introduced above are considered: Homogeneous Colebrook-White ($k_D = 2.10^{-5}$m), Homogeneous Blasius, Lockhart-Martinelli and Müller-Steinhagen and Heck. Results in terms of the upstream total head, which is the parameter the most affected by the friction, are given in Tab. 1. Obviously, accuracy of the results is only slightly affected by the choice of the friction correlation. It is worthwhile noting the Homogeneous Colebrook-White gives the most conservative results (it gives the biggest head-loss). Again, it results from the fact that the Homogeneous Colebrook-White correlation is the only one that considers the pipe roughness in the calculation. As a result, this method seems the most reliable for civil engineering application for which pipe roughness is clearly a major parameter.

Tab. 1 : Comparison of friction correlations

	Upstream Total Head [cm]	Error [%]
Experimental	40.53	2.5%
Homogeneous Colebrook	39.5036	2.5%
Homogeneous Blasius	39.5027	2.5%
Lockhart-Martinelli	39.5004	2.5%
Müller-Steinhagen and Heck	39.5018	2.5%

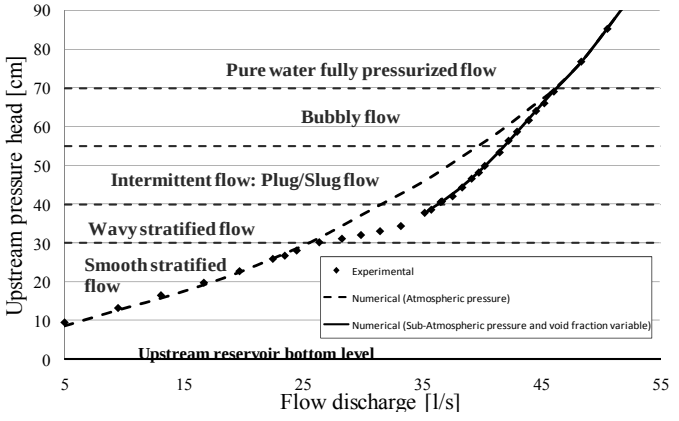

a. Head/Discharge relation computed with variable void fraction

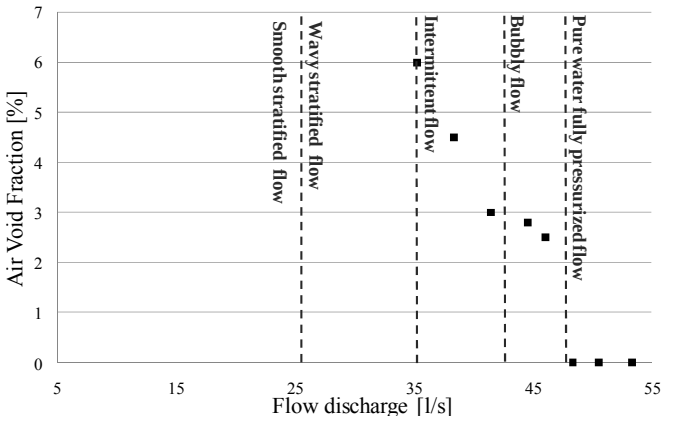

b. Void fraction distribution in bubbly and intermittent flows

Fig. 12 : Results of air-water mixture simulation

CONCLUSIONS

The original mathematical model derived in this paper is a first step towards a completely unified model for the simulation of highly transient mixed flow in multi-scale hydraulic structures. Thanks to the Preissmann slot method, both free-surface and pressurized flow are calculated through the free-surface set of equation by adding a narrow slot at the top of the pressurized sections. In addition, an original negative Preissmann slot has been added to simulate sub-atmospheric pressure. Area-integration of the Homogeneous Equilibrium Model over the cross section give a simple set of equations, analogous to the Saint-Venant equations, for analyzing air-water flows. This assumption has been shown to be particularly well-suited for the simulation of bubbly and intermittent flows.

The fundamental concepts introduced in the previous pages pave the way for further research. Experimental research is required to develop appropriate source terms as phase change volume generation and friction correlation. Development of a stratified air/water model would give us insight into wavy stratified flows. All results should be then easily extended to multidimensional problems.

REFERENCES

[1] Zhou F., Hicks F.E., and Steffler P.M., *Transient Flow in a Rapidly Filling Horizontal Pipe Containing Trapped Air.* Journal of Hydraulic Engineering, 2002. **128**(6): p. 625-634.

[2] Guo Q. and Song C., *Dropshaft Hydrodynamics under Transient Conditions.* Journal of Hydraulic Engineering, 1991. **117**(8): p. 1042-1055.

[3] Vasconcelos J. and Wright S., *Experimental Investigation of Surges in a Stormwater Storage Tunnel.* Journal of Hydraulic Engineering, 2005. **131**(10): p. 853-861.

[4] Cardle J. and Song C., *Mathematical Modeling of Unsteady Flow in Storm Sewers.* International Journal of Engineering Fluid Mechanics, 1988. **1**(4): p. 495-518.

[5] Politano M., Odgaard A.J., and Klecan W., *Numerical Evaluation of Hydraulic Transients in a Combined Sewer Overflow Tunnel System.* Journal of Hydraulic Research, 2007. **133**(10): p. 1103-1110.

[6] Li J. and McCorquodale A., *Modeling Mixed Flow in Storm Sewers.* Journal of Hydraulic Engineering, 1999. **125**(11): p. 1170-1180.

[7] Preismann A. *Propagation des intumescences dans les canaux et rivieres*. in *First Congress of the French Association for Computation*. 1961. Grenoble, France.

[8] Vasconcelos J., Wright S., and Roe P.L., *Improved Simulation of Flow Regime Transition in Sewers : The Two-Component Pressure Approach.* Journal of Hydraulic Engineering, 2006. **132**(6): p. 553-562.

[9] Bourdarias C. and Gerbi S., *A Finite Volume Scheme for a Model Coupling Free Surface and Pressurized Flows in Pipes.* Journal of Computational and Applied Mathematics, 2007. **209**: p. 109-131.

[10] Bourdarias C., Gerbi S., and Gisclon M., *A kinetic formulation for a model coupling free surface and pressurized flows in closed pipes.* Journal of Computational and Applied Mathematics, 2008. **218**(2): p. 522.

[11] Dewals B.J., Andre S., Pirotton M., and Schleiss A. *Quasi 2D-numerical model of aerated flow over stepped chutes*. in *30th IAHR Congress*. 2003. Greece.

[12] Ishii M. and Hibiki T., *Thermo-fluid dynamics of two-phase flow*. First ed, ed. U. Springer Science. 2006: Springer Science, USA. 430.

[13] Manninen M., Taivassalo V., and Kallio S., *On the mixture model for multiphase flow*, V.t.u. (VTT), Editor. 1996, Technical Research Center of Finland: Espoo. p. 67.

[14] Bonizzi M. and Issa R.I., *A model for simulating gas bubble entrainment in two-phase horizontal slug flow.* International Journal of Multiphase Flow, 2003. **29**(11): p. 1685-1717.

[15] Hibiki T. and Ishii M., *One-dimensional drift-flux model for two-phase flow in a large diameter pipe.* International Journal of Heat and Mass Transfer, 2003. **46**(10): p. 1773-1790.

[16] Clerc S., *Numerical Simulation of the Homogeneous Equilibrium Model for Two-phase Flows.* Journal of Computational Physics, 2000. **161**: p. 354-375.

[17] Wallis G.B., *One-dimensional Two-phase Flow*, ed. M.-H.B. Company. 1969. 410.

[18] Guinot V., *Godunov-type Schemes: An introduction for engineers*, ed. E. Science. 2003, Amsterdam. 480.

[19] Cunge J.A., Holly F.M., and Verwey A., *Practical Aspects of Computational River Hydraulics*. Monographs and surveys in water resources engineering. 1980, Boston: Pitman Advanced Pub. Program.

[20] Ishii M., *One-dimensional drift-flux model and constitutive equations for relative motion between phases in various two-phase flow regimes*. 1977. p. Medium: X; Size: Pages: 62.

[21] Dewals B.J., Erpicum S., Archambeau P., Detrembleur S., and Pirotton M., *Depth-Integrated Flow Modelling Taking into Account Bottom Curvature.* Journal of Hydraulic Research, 2006. **44**(6): p. 787-795.

[22] Leveque R.J., *Finite Volume Methods for Hyperbolic Problems*. First Edition ed. Cambridge texts in Applied Mathematics, ed. Cambridge University Press. 2002, Cambridge: Cambridge University Press,. 540.

[23] Brennen C.E., *Fundamentals of Multiphase Flows*. 2005: Cambridge University Press.

[24] Awad M.M. and Muzychka Y.S. *Bounds on Two-Phase Flow - Part 1 - Frictional Pressure Gradient in Circular Pipes*. in *ASME International Mechanical Engineering Congress and Exposition*. 2005. Orlando, Florida.

[25] McAdams W.H., Woods W.K., and Heroman L.C., *ASME Int. Develop. Heat Transf. Part II* Transactions of the ASME, 1942. **64**(3): p. 193-200.

[26] Lockhart R.W. and Martinelli R.C., *Proposed correlation of data for isothermal two-phase, two-component flow in pipes.* Chemical Engineering Progress, 1949. **45**: p. 39-48.

[27] Keller U., *Intermittent flow in hydraulic conduits*, in *Versuchanstalt für Wasserbau, Hydrologie und Glaziologie der Eidgenössichen*. 2006, ETH Zürich: Zürich. p. 250.

[28] Chisholm D., *influence of pipe surface roughness on friction pressure gradient during two-phase flow.* Journal of Mechanical Engineering Science, 1978. **20**(6): p. 353-354.

[29] Müller-Steinhagen H. and Heck K., *A simple friction pressure drop correlation for two-phase flow in pipes.* Chemical Engineering and Processing, 1986. **20**(6): p. 297-308.

[30] Wylie E.B. and Streeter V.L., *Fluid transients*. Première ed, ed. M.-H. Inc. 1978. 385.

[31] Kerger F., Archambeau P., Erpicum S., Dewals B.J., and Pirotton M., *Simulation numérique des écoulements mixtes hautement transitoire dans les conduites d'évacuation des eaux.* La Houille Blanche, 2009. **accepted**.

[32] Erpicum S., Kerger F., Archambeau P., Dewals B.J., and Pirotton M. *Experimental and numerical investigation of mixed flow in the flushing gallery of a dam*. in *Multiphase Flow* 2008. New Forest.

Proceedings of the 8th National Congress on Theoretical and Applied Mechanics, May 28-29, Brussels, Belgium.

FlexMG: A new library of multigrid preconditioners for large-scale CFD calculations

M. Rasquin[12], G. Degrez[12], H. Deconinck[2]
[1]Université Libre de Bruxelles, Department of Aero-Thermo-Mechanics
CP 165/41, 50 Avenue F. D. Roosevelt, 1050 Brussels
[2]von Karman Institute for Fluid Dynamics, Aeronautics and Aerospace Department
72 Chaussée de Waterloo/Waterloosesteenweg, 1640 Rhode-St-Genèse/Sint-Genesius-Rode
email: michel.rasquin@ulb.ac.be, gerard.degrez@ulb.ac.be, deconinck@vki.ac.be

Abstract— **A new library called FlexMG has been developed for large-scale CFD calculations. This library allows to use various types of iterative solvers preconditioned by algebraic multigrid methods. Two families of multigrid preconditioners have been implemented, of smooth aggregation-type and finite-element-type. These two families of multigrid preconditioners can be used as a stand-alone solver or coupled to a GMRES method. After analyzing the accuracy of our solvers on a typical test case, their performance in terms of convergence rate, average number of iterations per time step, computational speed and memory consumption are compared with the performance of a direct sparse LU solver as a reference.**

Keywords— **algebraic multigrid, smooth aggregation, finite-element, GMRES, CFD**

I. Introduction

COMPUTATION of turbulent flows requires the unsteady Navier-Stokes equations to be solved on highly refined meshes over a considerable number of small time steps. For applications of practical interest, requirements in terms of computation time and memory consumption remain one of the key aspects for such simulations, which can be accomplished only by using state-of-the-art numerical methods and supercomputing facilities. Indeed, one of the main challenges of contemporary CFD is to solve ever larger problems in a scalable manner (i.e. both memory and computation time requirements scale linearly with problem size). Direct solvers such as exact LU factorizations work well for small problems only. For larger problem sizes, poor scalability is observed, especially in terms of memory [1]. Traditional fixed-point iterative methods (Jacobi, Gauss-Seidel, ILUT for instance) scale well in terms of memory consumption, but not at all in terms of computation time. The reason for this is that such methods are only effective for damping out high wave number errors; as soon as these have been removed, convergence stagnates on the remaining low wave number error components. Krylov accelerators [2], [3] represent a significant improvement over fixed-point methods. Indeed, unlike fixed-point methods, they look for an optimized solution that minimizes the residual at each iteration. Nevertheless, unless scalable preconditioners are used, even these algorithms fail to provide adequate scaling. The missing ingredient is multigrid, a technique which relies on a series of increasingly coarser approximations of the original 'fine' problem. The underlying concept is always the same: low wave number errors on fine grids become high wave number errors on coarser levels. Hence, they may be effectively removed by recursively applying fixed-point methods on coarser levels [4]. In this context, a new library of iterative solvers preconditioned by algebraic multigrid has been developed for CFD applications and is presented in this paper.

II. Background

In this study, our library FlexMG is tested within the combined spectral/finite-element code SFELES [5], [6]. This unsteady and incompressible Navier-Stokes solver is based upon a combination of finite element in-plane discretization and a spectral discretization in the transverse direction (or azimuthal if working in axisymmetric coordinates). Together with a pseudo-spectral treatment of the nonlinear terms, this approach allows to transform 3D problems into a series of N 2D linear problems in Fourier space that are decoupled within each time step. At each time step, N sparse linear systems (corresponding to N Fourier modes) need to be solved with eight unknowns per node (i.e. real and imaginary components of u, v, w and p). For each system $A_m x = b_m$ (associated to a Fourier mode m), only the linear terms of the Navier-Stokes equations (time derivative, pressure, diffusion) are contained in the stiffness matrix A_m while all non-linear terms (convection and stabilization terms) are contained in the right hand side b_m. Moreover, the size of each system A_m is equal to eight times the number of nodes, except for modes 0

and $\frac{N}{2}$ which are purely real. However, in what follows, the two systems associated to these real modes are grouped together so that the size of each system is always identical.

The considered linear systems are in general very large, nearly symmetric, constant in time and can be very stiff due to highly anisotropic stretched meshes needed to resolve viscous boundary layers. Exact LU factorization is quite efficient for this code, provided that the number of nodes per finite-element plane is not too large. Indeed, since the stiffness matrix is constant in time, the factorization is performed only once at the first time step and stored for the whole computation. Nevertheless, the number of unknowns per finite-element plane is limited by the memory consumption of this method. The possibility of solving these systems using various types of algebraic multigrid methods is therefore currently explored.

III. Multigrid Preconditioners

Let

$$Ax = b \tag{1}$$

be the problem to solve. Multigrid is an iterative procedure which relies on a series of increasingly coarser approximations of the original 'fine' problem. The underlying concept is the following: low wave number errors on fine grids become high wave number errors on coarser levels which can be effectively removed by applying fixed-point (also called relaxation) methods on coarser levels [4]. A typical multilevel correction scheme with two grid levels is described in Fig. 1.

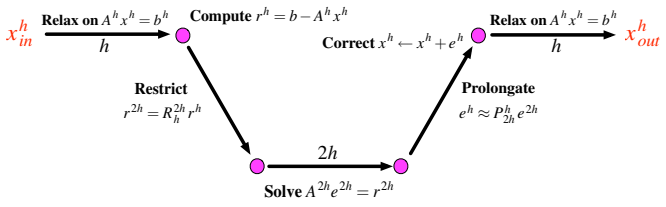

Fig. 1. Multilevel correction scheme.

A typical V multigrid cycle starts at the finest level with an arbitrary initial guess as a solution. Some relaxation iterations are performed on the fine grid to remove the high wave number errors. The residual on the finest level is then computed and transferred from the fine level to the next coarser level. The remaining low wave number errors on the fine grid appears now as high wave number errors on the coarse grid and can thus be eliminated efficiently with some additional relaxation iterations at the coarse level. The transfer from a fine level to the next coarser one is called 'restriction'. After some relaxation cycles on the coarse level, the solution of the coarse problem is then restricted again to next coarser level and so forth until the coarsest level is reached.

At the coarsest level, the system is usually solved exactly with a direct solver since the size of the problem at that level has decreased significantly. The solution obtained at the coarsest level is than interpolated back to the finer level. The transfer from a coarse level to the next finer one is called 'prolongation'. The solution of the fine grid problem is then corrected and interpolated to the next finer level after some relaxation iterations, called post multigrid sweeps. The solution is finally prolongated till the finest level is reached. In conclusion, each grid is responsible for eliminating a particular wave number of the bandwidth of errors.

The main difficulty of these multilevel correction scheme lies in the construction of the coarse grid stiffness matrices and the grid transfer operators to interpolate the solution from a coarse level to a fine level (prolongators) and vice versa (restrictors). FlexMG provides two main procedures of building the prolongators which are described in the next section. The inverse operation is ensured by the restrictors which are simply taken as the transpose of the prolongators in all cases. At each level (except the finest), the stiffness matrices are built according to a Galerkin formulation [7], [8]:

$$A_{coarse} = R_{fine \to coarse}\ A_{fine}\ P_{coarse \to fine} \tag{2}$$

The multilevel correction scheme described in this section can be used alone or coupled to a well-known GMRES method (Generalized Minimum RESidual [2], [9]). When used as a stand-alone solver, the whole process illustrated in Fig. 1 is repeated until satisfactory convergence is reached. One of the main drawbacks of such a method is its lack of robustness. Indeed, nothing guarantees that this method will converge in all cases. To obviate this problem, the multilevel correction scheme can also be used as a preconditioner of a GMRES method.

Considering a right preconditioning of the system described in Eq. (1)

$$(A\,M^{-1})\,u = b \quad \text{and} \quad x = M^{-1}\,u \tag{3}$$

and letting

$$K_k = \text{span}\{\ r^0,\ A\,M^{-1}\,r^0,\ \ldots,\ (A\,M^{-1})^{k-1}\,r^0\ \} \tag{4}$$

be its Krylov subspace of dimension k, with r^0 the initial residual and M^{-1} a cheap approximation of A^{-1}, the basic idea of GMRES is to look for a solution

x^k (at iteration k) that belongs to the subspace K_k and minimizes the residual r^k.
The solution for this method can then be written as

$$u^k = u^0 + V_k\, y_k \quad (5)$$
$$x^k = M^{-1}\, u^k \quad (6)$$

where V_k is an orthonormal basis for the Krylov subspace of dimension k already defined in Eq. (4). At each iteration of the GMRES procedure, a new search vector for the solution is determined by computing an optimal linear combination of all the previous search vectors. Optimal here means which minimizes the residual, as mentioned above [2], [9].
After deriving the whole multilevel correction scheme for k iterations (k V cycles) and provided that the initial guess $x^0 = 0$, the solution of the problem $A\,x = b$ can be written as $x^k = P_k^{-1}\, b$ with P_k^{-1} an explicit approximation of A^{-1} which depends on k. If k is fixed (usually one when coupled to GMRES), the multigrid preconditioner P_k^{-1} remains constant and can be used as well as a preconditioner for the traditional GMRES method when computing a new search vector in the Krylov subspace (take $M^{-1} = P_k^{-1}$). This is in practice what is done in FlexMG.

IV. Construction of the Prolongators

As it was mentioned in the previous section, all multigrid methods require the definition of a succession of coarse grids based on the original fine grid in order to construct the prolongation and restriction operators. Two distinct families of multigrid preconditioners have been implemented in FlexMG for that purpose and are presented in the next two subsections.

A. Aggregation-Type Multigrid (MG - Agg)

The prolongators of this first family are based on a clustering procedure of nodes into aggregates or 'super-nodes' [10]. These aggregates correspond to a combination of several nodes from the original grid and will constitute new degrees of freedom on the coarser grid levels. The coarse grids are therefore generated automatically and only the initial fine mesh is required. This method is illustrated in Fig. 2, with the usual circular cylinder test case in $2D$.
From the construction of these aggregates, it is possible to build piecewise constant prolongation operators for which the solution of each aggregate at a coarse level is prolongated to each of its fine nodes (or fine aggregates) without any other operation. Every row of these piecewise constant prolongators has therefore one and only one non zero entry equal to one. These

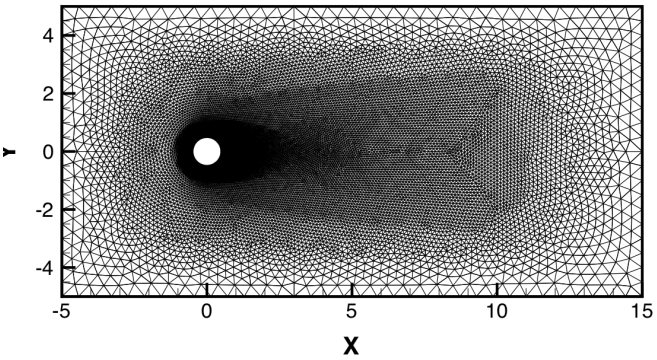

(a) Level 0 - Initial fine mesh (20 Knodes)

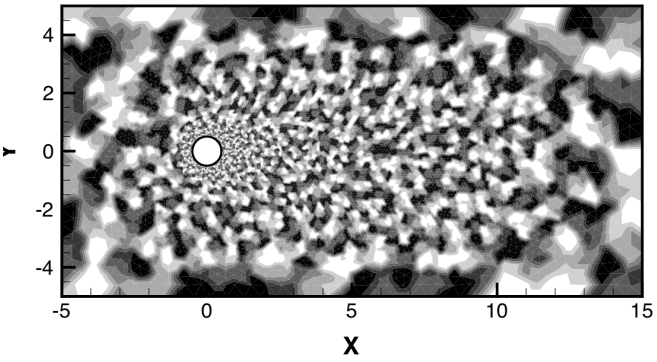

(b) Level 1 - High number of aggregates.

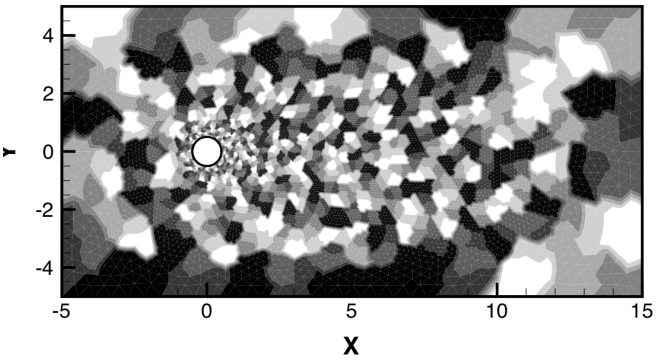

(c) Level 2 - Moderate number of aggregates.

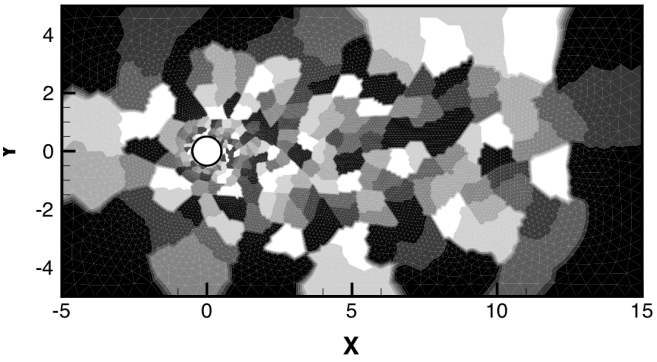

(d) Level 3 - Low number of aggregates.

Fig. 2. Aggregation process for the construction of the prolongators in MG - Agg. Each color zone represents an aggregate of nodes (or aggregate of aggregates).

prolongators are however not optimal because they introduce substantial high wave number error components by themselves. To improve these piecewise constant prolongation operators, two different smoothers have been implemented in FlexMG and are applied after every transfer of the solution from one coarse grid to a fine grid. In practice, the piecewise constant prolongation and smoothing operators are grouped together to form smooth prolongation operators.

A.1 Smooth Aggregation-Type Multigrid based on a Constant Least Square Fitting Technique (MG - AggSmthCLSF)

For the first smoothing strategy, each node (or aggregate) on a certain level is assigned the value of a constant least square fitting function based on the value of the solution of its direct neighboring nodes (or aggregates). It turns out that this constant least square fitting technique is equivalent to a local average based on the solution of its direct neighboring nodes (or aggregates). For each node (or aggregate), the value of this local fitting function can be written as $Sol = cst$, with cst equal to the local average value mentioned above. This smoother is illustrated in Fig. 3(a) with a $1D$ example and in Fig. 4(b) with a $2D$ example.

A.2 Smooth Aggregation-Type Multigrid based on a Linear Least Square Fitting Technique (MG - AggSmthLLSF)

For the second smoother, each node (or aggregate) on a certain level is assigned the value of a local plane whose coefficients are computed from a least square method based on the value of the solution *and* the position of its direct neighboring nodes (or aggregates). The position of an aggregate is simply taken as the center of gravity computed from the position of all its nodes. One speaks here about linear least square fitting technique since the local fitting function for each node (or aggregate) can be written as $Sol = ax+by+c$ with (x, y) the position of the considered node (or aggregate) and (a, b, c) the coefficients of the plane obtained with a least square method. This smoother is illustrated in Fig. 3(b) with a $1D$ example and in Fig. 4(c) with a $2D$ example.

One can observe in Fig. 3 that there is no difference between the solution smoothed with the constant and the linear least square fit, simply because the points are equidistant in this $1D$ example. In Fig. 4, the difference is small and hard to notice. In practice, it will be shown in the next section that the prolongators smoothed with a constant or linear least square method dramatically improve the convergence rate and computation time, compare to the initial non smooth piecewise constant prolongators. Concerning the smooth prolongators, the linear least square fit will lead to slightly better but comparable results on unstructured grids, as shown in the next section as well. Finally, it is worth mentioning that, in $2D$, the rows of both the prolongators smoothed with the constant or linear least square fit have in average 3.8 non zero entries per line whose sum is equal to one.

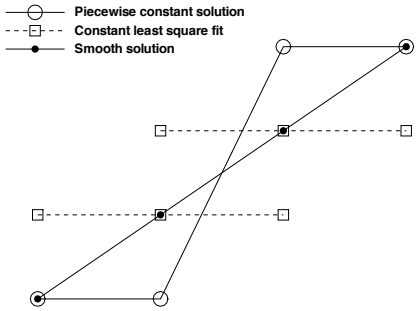

(a) Solution smoothed at the two middle nodes with a constant ($Sol = cst$) least square fit (AggSmthCLSF).

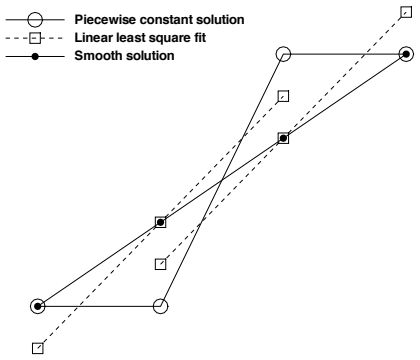

(b) Solution smoothed at the two middle nodes with a linear ($Sol = ax+b$) least square fit (AggSmthLLSF).

Fig. 3. Aggregation-type multigrid - Comparison of two smoothing strategies based on a least square fitting technique and applied after the transfer of the solution from a coarse grid with two aggregates to a fine grid with four nodes ($1D$ example).

B. Finite-Element-Type Multigrid (MG - FE)

The prolongators of the second family of preconditioners implemented in FlexMG are based on a finite-element interpolation between the nodes of the coarse grid and the fine grid, as illustrated in Fig. 5. Contrary to aggregation-type multigrid, the subgrids are not built automatically and the meshes of the sub-

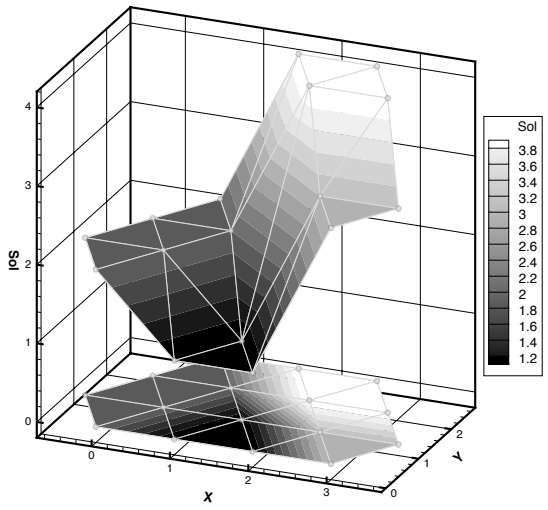

(a) Non smooth piecewise constant solution (Agg).

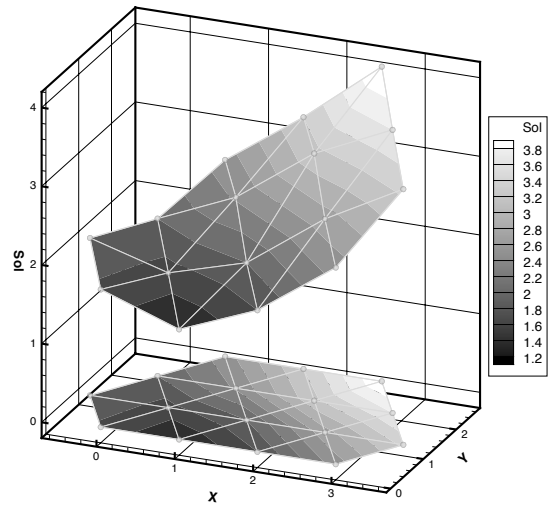

(b) Solution smoothed at each node with a constant ($Sol = cst$) least square fit (AggSmthCLSF).

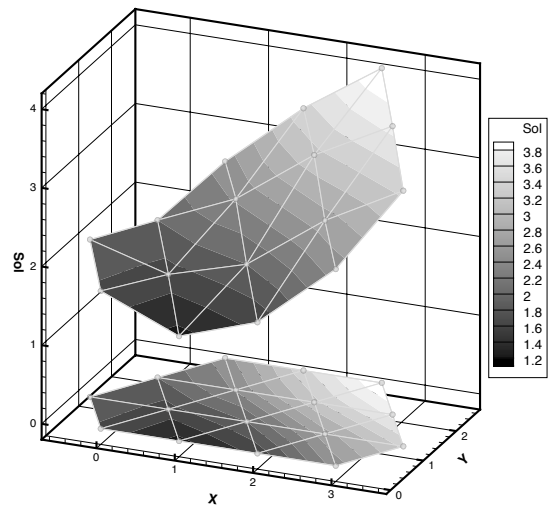

(c) Solution smoothed at each node with a linear ($Sol = ax+by+c$) least square fit (AggSmthLLSF).

Fig. 4. Aggregation-type multigrid - Comparison of two smoothing strategies based on a least square fitting technique and applied after the transfer of the solution from a coarse grid with four aggregates to a fine grid with 16 nodes ($2D$ example).

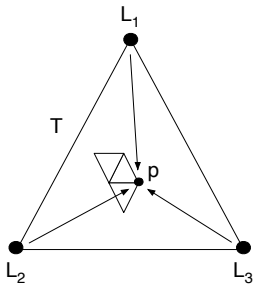

Fig. 5. Finite-element interpolation for the construction of the prolongators in MG - FE.

levels must be provided by the user. The prolongated solution in any fine node p is obtained from a linear combination of the solution at the three coarse nodes L_i forming the finite element T enclosing the fine node p [8]. for $2D$ test cases, the rows of the prolongators have therefore three non zero entries whose sum is equal to one, except for the boundary nodes. Moreover, the prolongators of this method do not require any additional smoothing operation since they are already sufficiently smooth by construction.

V. Settings and Results

The multigrid preconditioners presented in the previous sections have been tested either as a stand-alone multigrid solver or coupled to a GMRES method. Four multigrid preconditioners are considered here: aggregation-type multigrid without smoothing (MG - Agg), smooth aggregation-type multigrid based on a constant and linear least square fit (MG - AggSmthCLSF and MG - AggSmthLLSF) and finite-element-type multigrid (MG - FE), which makes eight different solvers.

At each level of the multilevel correction scheme, one single pre and post relaxation iteration is applied, using a fixed-point method preconditioned by ILUT. For every configuration of the solver requiring an ILUT matrix, a LFIL equal to 10 is set (LFIL in this study follows the definition of the SPARSKIT package [11], i.e. the number of non-zero elements per line in both the incomplete L and U factorizations from ILUT; the average number of non-zero entries per line in the initial stiffness matrix A is about 18). Three sublevels are used in the multilevel correction scheme, dividing each time the number of unknowns by a factor ≈ 4. Finally, an absolute convergence threshold of $\| r^k \| \leq 10^{-12}$ is imposed (computations in double precision).

As mentioned in Section II, FlexMG has been linked to a combined finite-element/spectral code called

SFELES. This code is able to perform DNS and LES of $3D$ incompressible turbulent flows on unstructured meshes. In this work, the classical test case of the unsteady flow over a circular cylinder at low Re number is considered on a series of increasingly fine anisotropic meshes. First, the accuracy of FLEXMG is checked. Then, the performance of our solvers in terms of convergence rate, average number of iterations per time step, computation time and memory consumption is compared with the performance of a direct sparse LU solver called SUPERLU [12] as a yardstick.

A. Problem Description

A computation of the unsteady laminar $2D$ flow past a circular cylinder at $Re = 100$ is considered in this work [1]. However, the explicit treatment of the nonlinear terms of the Navier-Stokes equations (convection, stabilization and eventually LES turbulence model) in the right-hand side of the linear system in Eq. 1 preserves the convergence properties of our multigrid preconditioners even for higher Reynolds number flows [13].
Following the description of our code SFELES in Section II, only mode 0 is required for this $2D$ computation. However, for some implementation reasons, mode $\frac{N}{2}$ is also solved within the same linear system and then discarded. The size of the system associated to this $2D$ problem is thus equal to eight times the number of nodes (real components of u, v, w and p for modes 0 and $\frac{N}{2}$).
A Dirichlet velocity inlet condition is applied upstream of the cylinder while a Neumann outlet condition is applied far downstream. Slip-wall conditions are applied on the sides of the domain (top/bottom). Computations are performed on three meshes (20, 80 and 320 Knodes) to analyze the performance of our solvers. All runs to determine linear solver accuracy and performance were restarted using an already established solution illustrated in Fig. 6.

B. Accuracy

First, the solution obtained with the SUPERLU package is compared with the eight iterative solvers preconditioned by multigrid presented in Section V. The code ran for 55890 time steps with $\Delta t\, U_\infty / D = 0.0005$, which corresponds to 10 complete periodic vortex sheddings. Figure 7(a) shows that all solvers produce the same temporal evolution of the U velocity at a point downstream of the cylinder. In addition to the time-accurate monitoring of a single point, the complete time-averaged flow field is also compared to the direct LU solution. The results

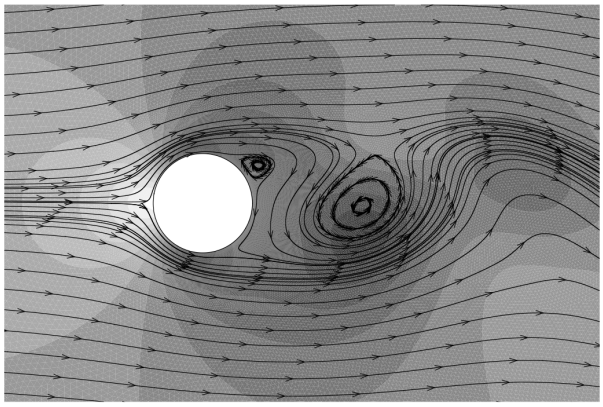

Fig. 6. Pressure field and streamlines around a cylinder at $Re = 100$ - 80 Knodes mesh - von Karman vortices.

both in terms of zeroth-order (mean velocities, not shown here) and first order (see Fig. 7(b)) statistics are found to be identical.

C. Performance

It has been observed that the performance of the eight iterative solvers tested in this work are sensitive to the time step and therefore to the CFL number used in the simulations. Indeed, decreasing this CFL number leads to a better preconditioning (although more iterations are required to simulate the same physical phenomenon). Below a certain value, no more influence of the CFL number on the multigrid preconditioning is however noticed. Therefore, a time step equal to $\Delta t\, U_\infty / D = 0.0001$ has been chosen in order to keep the CFL number around 0.15 for the three considered meshes (20, 80 and 320 Knodes). The final objective is to study the efficiency of the multigrid preconditioners and not the influence of the CFL number on the stability of the temporal discretization used in SFELES. In the next four paragraphs, the convergence rate is analyzed for one typical time step while the average number of iterations per time step and the computation time is computed over 1000 time steps.

C.1 Convergence rate

In addition to the eight iterative solvers preconditioned by multigrid, the convergence rate of a traditional fixed-point method and GMRES method, both preconditioned by ILUT is shown in Fig. 8 (FP - ILUT and GMRES - ILUT). FP - ILUT (our favorite relaxation procedure in the multilevel correction scheme) converges rapidly at the beginning but then stagnates since it fails to remove efficiently the

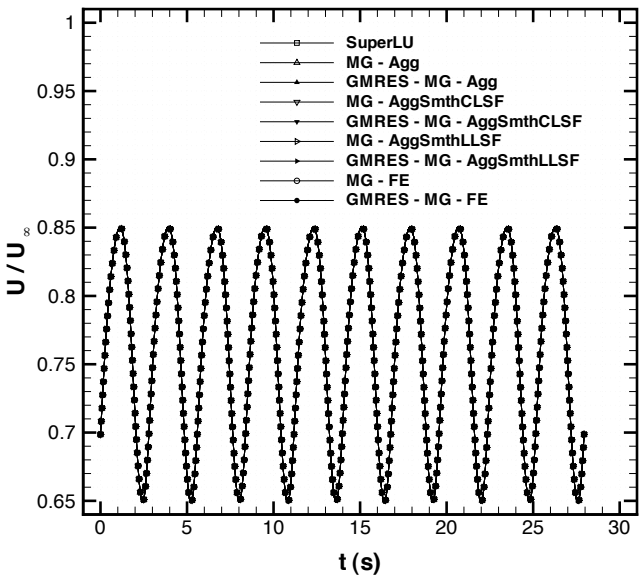

(a) Evolution of U/U_∞ nondimensional velocity at a control point located 5 diameters downstream of the center of the cylinder.

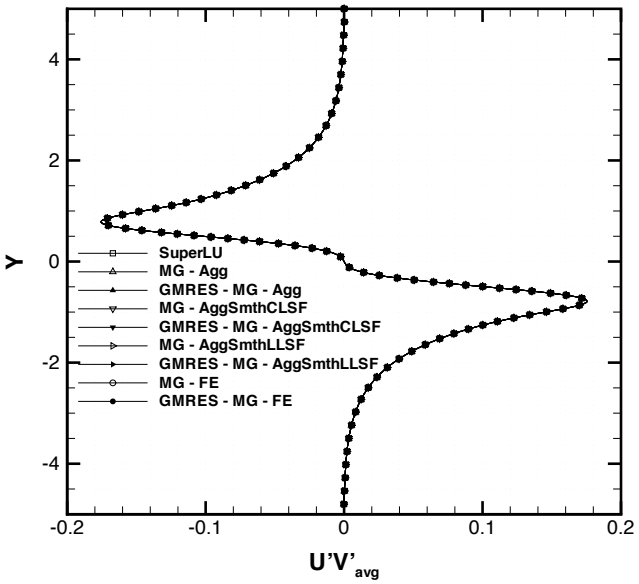

(b) Time-averaged $U'V'$ Reynolds stress along a vertical line located 1.75 diameters downstream of the center of the cylinder.

Fig. 7. Validation of the linear solver accuracy on the 20 Knodes mesh - $Re = 100$.

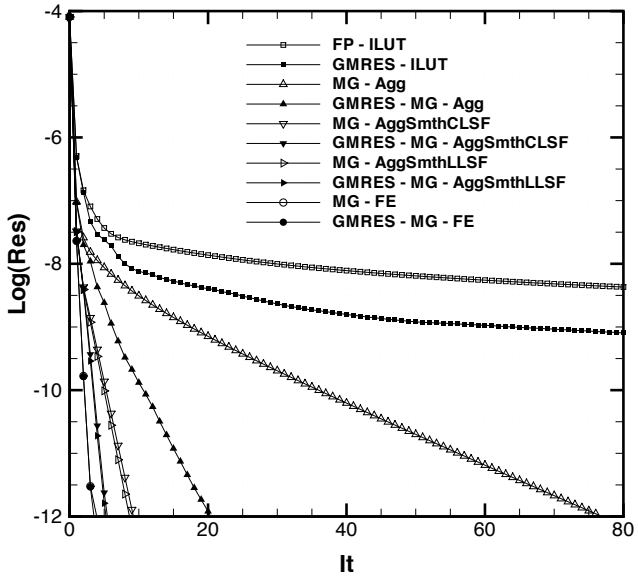

Fig. 8. Typical convergence curves of different iterative procedures preconditioned by ILUT and Multigrid (Fixed-Point method, stand-alone multigrid cycle and GMRES) - 80 Knodes mesh.

remaining high wave number errors. GMRES - ILUT is already a big improvement over FP - ILUT but still requires too many iterations for this case before reaching the convergence threshold of 10^{-12}. One can also observe that GMRES - ILUT is characterized by accelerations of convergence whenever an eigenvalue of the stiffness matrix is correctly approximated by an eigenvalue of the Hessenberg matrix constructed during the GMRES procedure [2], [9], [8]. Despite its lack of robustness, MG - Agg is already better than GMRES - ILUT but the lack of smoothness of its prolongators is clearly underlined when compared to the other smooth stand-alone multigrid cycles. GMRES - MG - Agg is able to compensate strongly this drawback and illustrates the efficiency of GMRES methods in general. But the smoothing of the prolongators for the stand-alone MG - Agg cycle even leads to a greater improvement (see MG - AggSmthCLSF and MG - AggSmthLLSF). A slight improvement can still be noticed when MG - AggSmthCLSF and MG - AggSmthLLSF are used as a preconditioner of GMRES. As mentioned in Subsection IV-A, few differences can be noted between AggSmthCLSF and AggSmthLLSF in terms of convergence rate, although AggSmthLLSF seems to be slightly better for both our stand-alone multigrid cycle and GMRES method. Finally, the best convergence rate is observed for MG - FE and GMRES - FE. No improvement is brought this time by GMRES, showing the efficiency of the MG - FE preconditioner. It should however be reminded that one of the main shortcomings of stand-alone multigrid cycles is their lack of robustness, which is not underlined in this study when considering the circular cylinder test case.

C.2 Average Number of Iterations per Time Step

The convergence rates shown in Fig. 8 already give an idea of the average number of iterations per time step for the 80 Knodes mesh. Ideally, convergence should be achieved in a more or less fixed number of iterations for all three meshes, as on the coarsest mesh an exact LU factorization is used. However, only MG - FE and GMRES - MG - FE in Fig. 9 exhibit this property for the three considered meshes after 1000 time steps. For the other solvers with smooth prolongators, this property is seen on the two biggest meshes only. However, it has been observed for the 80 Knodes mesh that both stand-alone multigrid cycles and GMRES methods preconditioned by AggSmthCLSF and AggSmthLLSF tend to solve the problem with only five iterations for a larger number of time steps. This trend is however not observed for MG - Agg, even though the number of iterations per time step decreases approximately by half compared to Fig. 9 when the number of time steps increases (25 iterations instead of 49 for the 20 Knodes mesh and 38 instead of 77 for the 80 Knodes mesh - see Fig. 9). This outlines again the importance of using smooth prolongators in a multilevel correction scheme.

C.3 Computation Time

For both SuperLU and FlexMG, only the CPU time needed to solve linear systems is shown in Fig. 10. Set-up times (LU factorization, construction of coarse grid levels, prolongators and Galerkin matrices, ...) have not been included as these tasks need to be done at the first iteration of the solver only. All results are normalized w.r.t. the time required by SuperLU on the 20 Knodes mesh. SuperLU is the fastest solver in double precision but its memory consumption prevents to compute the 320 Knodes case on an 8 GB machine. MG - FE is the fastest iterative solver and could even be faster than SuperLU if computations were made in single precision with a convergence threshold of 10^{-5} [13]. GMRES - MG - FE is slower than MG - FE because the construction of the Krylov subspace takes some additional time and is not counterbalanced in this case by a lower number of iterations per time step (see Fig. 9). GMRES preconditioned by either MG - AggSmthCLSF or MG - AggSmthLLSF is faster than their stand-alone multigrid cycle because GMRES improves here the convergence rate (Fig. 8) and solves the problem in less iterations (Fig. 9). As mentioned in the previous paragraph, this trend should appear to go in the reverse direction for a larger number of time steps because of the same reason as for GMRES - FE. As expected, the slowest solver is the stand-alone MG - Agg cycle but nevertheless, it should be pointed out the impressive improvement brought by GMRES for this multigrid preconditioner without smooth prolongators.

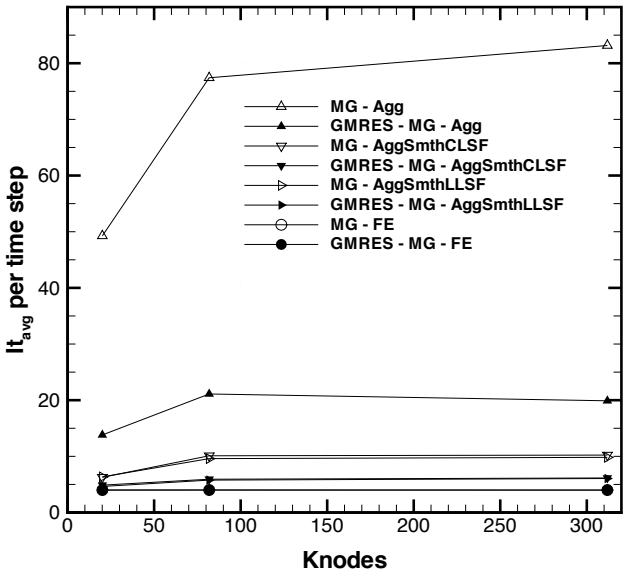

(a) Average number of iterations per time step

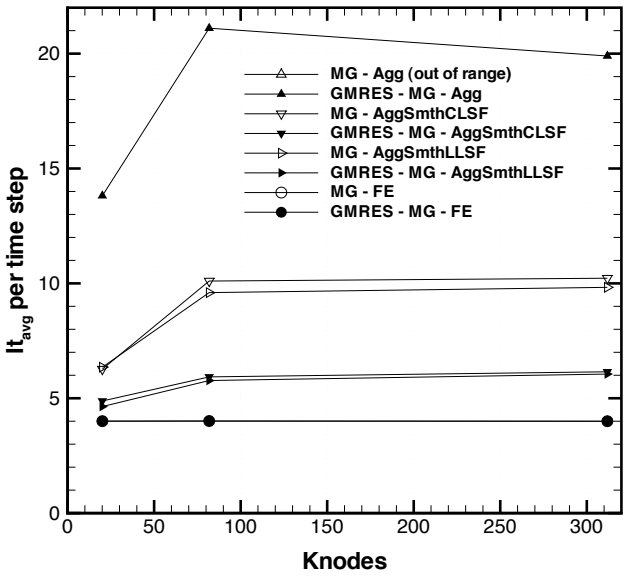

(b) Average number of iterations per time step - Zoom.

Fig. 9. Average number of iterations per time step - $Re = 100$.

C.4 Memory Consumption

Memory required by FlexMG and SuperLU is presented in Fig. 11. All results are normalized w.r.t. the memory required by SuperLU on the 20 Knodes mesh. One can observe the very high memory consumption of the SuperLU solver, which prevents to compute the 320 Knodes test case on a computer

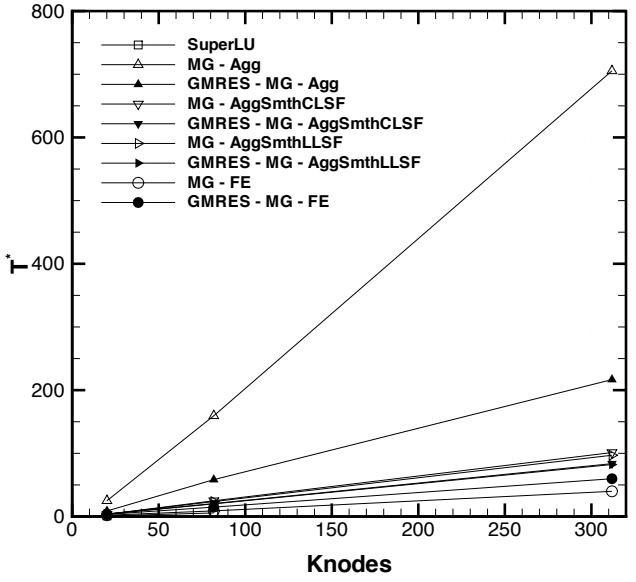

(a) Linear system solution time (normalization factor = 0.22 s).

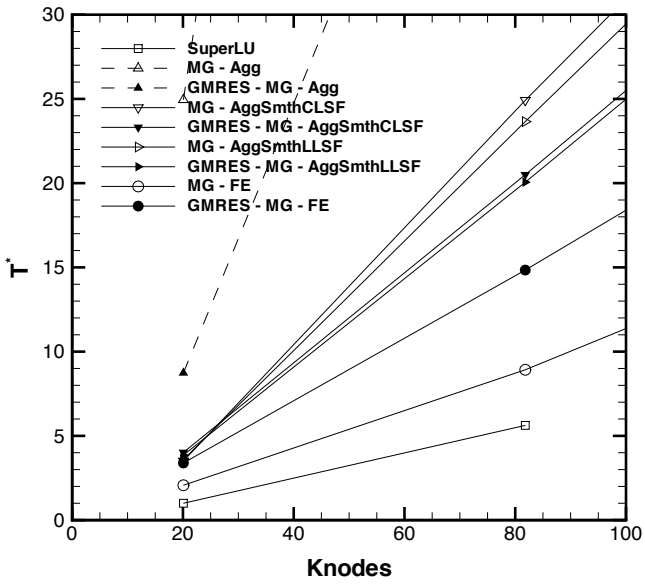

(b) Linear system solution time - Zoom (normalization factor = 0.22 s).

Fig. 10. Linear system solution time normalized with the solution time of the direct sparse LU solver on the 20 Knodes mesh - $Re = 100$.

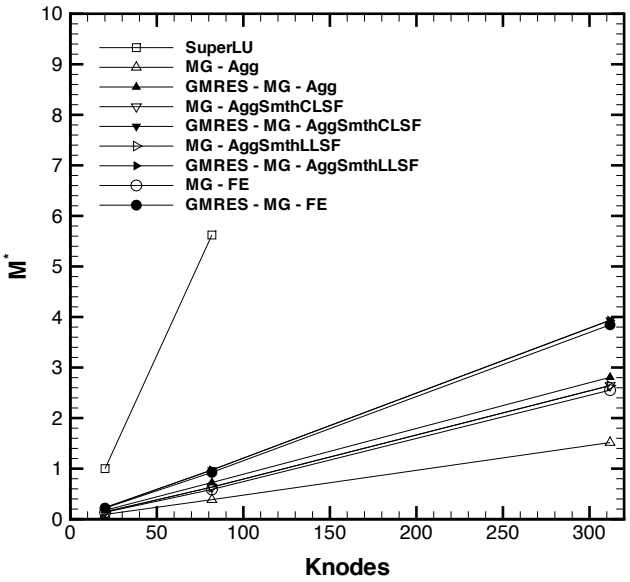

(a) Memory usage (normalization factor = 766.5 MB).

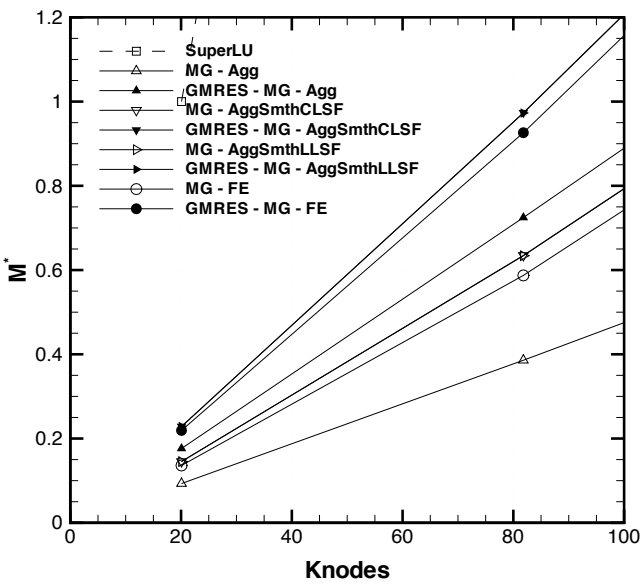

(b) Memory usage - Zoom (normalization factor = 766.5 MB).

Fig. 11. Memory usage normalized with the memory of the direct sparse LU solver on the 20 Knodes mesh - $Re = 100$.

with 8 GB of RAM. On the other hand, stand-alone multigrid and GMRES solvers exhibit much lower, linear memory requirements. More memory is however required for the GMRES methods compared to the stand-alone multigrid cycles since their Krylov subspace needs to be stored (a maximum of 50 Krylov vectors is set in this study). The MG - Agg preconditioner is also less memory consuming than the three other multigrid preconditioners since its non smooth prolongators and restrictors are sparser. Finally, MG - AggSmthCLSF and MG - AggSmthLLSF both require exactly the same amount of memory but a little bit more than MG - FE because the number of non zero entries per line in their prolongators and restrictors is slightly larger.

VI. Conclusions

In this contribution, a new smooth aggregation/finite-element-type algebraic multigrid solver for large-scale CFD calculations has been implemented. Already, its performance in terms of memory consumption and

computation time are promising. Computations that were out of reach because of lack of memory when using an exact LU factorization, are now allowed in a reasonable computation time. For the circular cylinder test case at $Re = 100$, an absolute convergence threshold of 10^{-12} can be reached in 4-5 iterations when considering a stand-alone multigrid cycle or GMRES method preconditioned by finite-element-type or smooth aggregation-type multigrid.

Despite the shortcomings of algebraic multigrid preconditioners for convection-dominated problems, theses ones are particularly well adapted for our CFD code since convection is not treated implicitly. Consequently, only elliptic and parabolic terms contribute to the linear systems.

As far as the aggregation-type multigrid is concerned, the importance of smoothing the prolongators has been assessed in order to compete with the finite-element-type multigrid. The latter is still faster and a little bit less memory consuming than smooth aggregation-type multigrid. However, subgrids for finite-element-type multigrid still need to be provided by the user while sublevels are automatically built for aggregation-type multigrid.

Finally, multigrid and GMRES methods are thought to cure their respective deficiencies, i.e. lack of robustness for the former and lack of scalability for the latter. This lack of robustness for multigrid methods was not underlined in this study when considering the circular cylinder test case but this should become more obvious with other more complicated test cases. Finally, this contribution is a first step in the development of a scalable parallel linear solver and sets the framework for continued study and improvement of multigrid preconditioners for CFD applications.

Acknowledgements

The first author is supported by a FRIA fellowship from the French Community of Belgium. Developments in SFELES were supported by the Higher Education and Scientific Research Division of the French Community Government at ULB (ARC project 02/07-283). Computations are performed amongst other on the Linux cluster ANIC4, funded by several contracts (http://anic4.ulb.ac.be). The first author is also thankful to Fabien Delalondre (Rensselaer Polytechnic Institute) for the brainstorming sessions about some possible smoothing strategies for the prolongators in the aggregation-type multigrid.

References

[1] G. Larson, D. Snyder, D.V. Abeele, and T. Clees, "Application of single-level, pointwise algebraic, and smoothed aggregation multigrid methods to direct numerical simulations of incompressible turbulent flows," *Computing and Visualization in Science*, vol. 11, no. 1, pp. 27–40, 2008.

[2] Y. Saad and M.H. Schultz, "GMRES: A generalized minimal residual algorithm for solving nonsymmetric linear systems.," *SIAM Journal of Scientific and Statistical Computing*, vol. 7, no. 3, pp. 856–869, 1986.

[3] Gerard L. G. Sleijpen and Henk A. van der Vorst, "An overview of approaches for the stable computation of hybrid BiCG methods," *Appl. Numer. Math.*, vol. 19, no. 3, pp. 235–254, 1995, Special issue on iterative methods for linear equations (Atlanta, GA, 1994).

[4] William L. Briggs, Van Emden Henson, and Steve F. McCormick, *A multigrid tutorial: second edition*, Society for Industrial and Applied Mathematics, Philadelphia, PA, USA, 2000.

[5] Deryl O. Snyder, *A Parallel Finite-Element/Spectral LES Algorithm for Complex Two-Dimensional Geometries*, Ph.D. thesis, von Karman Institute for Fluid Dynamics and Utah State University, 2002.

[6] Yves. Detandt, *Numerical Simulation of Aerodynamic Noise in Low Mach Number Flows*, Ph.D. thesis, von Karman Institute for Fluid Dynamics and Université Libre de Bruxelles, 2007.

[7] Tanja Clees, *AMG strategies for PDE systems with AMG strategies for PDE systems with applications in industrial semiconductor simulations*, Ph.D. thesis, University of Cologne, Germany, 2005.

[8] Emanuel Issman, *Implicit solution strategies for compressible flow equations on unstructurd meshes*, Ph.D. thesis, von Karman Institute for Fluid Dynamics and Université Libre de Bruxelles, 1997.

[9] Yousef Saad, *Iterative Methods for Sparse Linear Systems*, Society for Industrial and Applied Mathematics, Philadelphia, PA, USA, 2003.

[10] Petr Vaněk, Jan Mandel, and Marian Brezina, "Algebraic multigrid by smoothed aggregation for second and fourth order elliptic problems," *Computing*, vol. 56, pp. 179–196, 1996.

[11] Y. Saad, "Sparskit: A basic tool-kit for sparse matrix computations," 2000.

[12] J.W. Demmel, S.C. Eisenstat, J.R. Gilbert, X.S. Li, and J.W.H. Liu, "A Supernodal Approach to Sparse Partial Pivoting," *SIAM Journal on Matrix Analysis and Applications*, vol. 20, pp. 720–755, 1999.

[13] M. Rasquin, T. White, G. Degrez, H. Deconinck, and D. Vanden Abeele, "Development of an aggregation/geometric multigrid solver for large-scale cfd calculations," in *proceedings of the 15th Annual Conference of the CFD Society of Canada*, 2007.

Proceedings of the 8th National Congress on Theoretical and Applied Mechanics, May 28-29, Brussels, Belgium.

Modeling of mass transfer in (electro)chemical reactors using a hybrid spectral/finite-elements method

M. Krivilyov[1,3], M. Rasquin[2], R. Laguerre [2], G. Degrez[2], J. Fransaer[1]
[1] K.U.Leuven – Department of Metallurgy and Materials Engineering
Kasteelpark Arenberg 44 – 3001 Leuven – Belgium
[2] Université Libre de Bruxelles – Department of Aero-Thermo-Mechanics
CP 165/41, 50 Avenue F. D. Roosevelt – 1050 Brussels – Belgium
[3] Udmurt State University – Department of Physics
Universitetskaya str. 1 – 426034 Izhevsk – Russia
email: mk@udsu.ru, mrasquin@ulb.ac.be, rlaguerr@ulb.ac.be,
gerard.degrez@ulb.ac.be, jan.fransaer@mtm.kuleuven.be

Abstract: **A numerical tool for the analysis of the mass transfer in the purely turbulent regime in (electro)chemical reactors of the Taylor-Couette type is suggested. Comparison of the preliminary results of modeling with the empirical formula of Eisenberg shows a good agreement.**

Keywords: **combined FEM/spectral methods, electrochemistry**

I. Introduction

Turbulent flow is a phenomenon which is encountered in many chemical and electrochemical processes that usually include conjugate transfer of heat, mass and electric charge. For example, forced flow is used to enhance the deposition rate during electrolytic deposition on surfaces. However, as the fluid flow influences the concentration of ions and hence the local current density on the electrode the quality of a deposited layer strongly depends on the proper control of the flow conditions. Therefore, study of flow in electrochemical reactors is of practical importance and numerical simulation is one of the promising tools. Experimental studies of transport phenomena in electrochemical processes were performed by different authors [1,2,3] but only a few studies are devoted to 3D numerical modeling. A comprehensive study was performed in [4] where LES modeling was used for the description of the fluid flow in a reactor with a planar geometry. Experiments using the Taylor-Couette reactor (Fig.1) with a rotating cylindrical electrode (RCE) are also common in electrochemistry and this geometry is used in our research.

Due to curvature and centrifugal acceleration, instabilities develop, producing annular vortices called Taylor vortices, which eventually lead to fully turbulent flow with increasing of the Reynolds number. Based on the three dimensionless parameters identified by Chandrasekhar [5], multiple flow structures have been reported for this geometry. The first parameter is the ratio of the inner to outer cylinder diameters denoted by $\eta = r_i / r_o$. The second one corresponds to the Reynolds number based on the gap between the two cylinders: $\mathrm{Re} = \omega r_i (r_o - r_i)/\nu$, where ν is the kinematic viscosity. The reactor's height $h/(r_o-r_i)$ scaled by the gap width $s=r_o-r_i$ corresponds to the last parameter. In the present analysis, the inner cylinder rotates while the outer one is at rest. Our objective was to develop a numerical tool for the analysis of the mass transfer in the purely turbulent regime in reasonable computational time. Such a tool can assist or even replace experimental studies where data on mass transfer are difficult to extract with classical electrochemical methods. This work is an extension of our previous work [6] where only the fluid flow was studied.

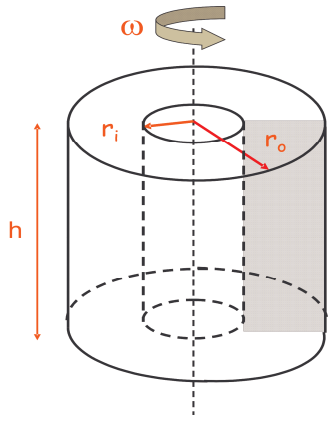

Fig. 1. Sketch of the reactor with Taylor-Couette geometry.

II. Model

Mass transfer in an electrochemical reactor with Taylor-Couette geometry is modeled using a hybrid spectral/finite-element method [7-10]. This method assumes periodicity in one direction so the spectral approach is used for discretization of governing equations in the azimuthal direction. In the transverse direction discretization is performed by means of finite elements allowing complex axisymmetric geometries. No subgrid model was applied so the modeling was a pure DNS type. The governing equations are (i) incompressible Navier-Stokes for the velocity and pressure fields and, (ii) convection-diffusion equations for the concentration fields. We advance the governing equations in time in a 2nd order accurate manner, by setting the following continuity, momentum and scalar variable residuals R_C^{n+1}, $\mathbf{R}_{\mathrm{M}}^{\mathrm{n+1}}$ and $R_{\phi_i}^{n+1}$ correspondingly to zero at each new time step $n+1$:

$$R_{\mathrm{C}}^{n+1} = \nabla \cdot (\mathbf{u}^{n+1}) = 0, \tag{1}$$

$$\begin{aligned}\mathbf{R}_{\mathrm{M}}^{n+1} &= \frac{\left(\mathbf{u}^{n+1} - \mathbf{u}^{n}\right)}{\Delta t} + \nabla p^{n+1/2} - \frac{1}{2\,\mathrm{Re}}\nabla^2\left(\mathbf{u}^{n+1} + \mathbf{u}^{n}\right) \\ &+ \left(\frac{3}{2}\right)\left(\frac{1}{2}\right)\left\{\left(\mathbf{u}^{n}\cdot\nabla\right)\mathbf{u}^{n} + \nabla\cdot\left(\mathbf{u}^{n}\otimes\mathbf{u}^{n}\right)\right\} \\ &- \left(\frac{1}{2}\right)\left(\frac{1}{2}\right)\left\{\left(\mathbf{u}^{n-1}\cdot\nabla\right)\mathbf{u}^{n-1} + \nabla\cdot\left(\mathbf{u}^{n-1}\otimes\mathbf{u}^{n-1}\right)\right\} = 0,\end{aligned} \tag{2}$$

$$\begin{aligned}R_{\phi_i}^{n+1} &= \left(\phi_i^{n+1} - \phi_i^{n}\right)/\Delta t - \frac{1}{2\mathrm{Pe}}\nabla^2\left(\phi_i^{n+1} + \phi_i^{n}\right) \\ &+ \left(\frac{3}{2}\right)\nabla\cdot\left(\mathbf{u}^{n}\phi_i^{n}\right) - \left(\frac{1}{2}\right)\nabla\cdot\left(\mathbf{u}^{n-1}\phi_i^{n-1}\right) = 0.\end{aligned} \tag{3}$$

where **u** is the flow velocity, p is the pressure, Δt is the time interval of iteration and Pe is the Péclet number $\mathrm{Pe} = \omega r_i (r_o - r_i)/D_i$, ϕ_i and D_i are the concentration and the diffusion coefficient of the i-th chemical component. Herein, the pressure, viscous and diffusion terms are treated in an implicit manner using the Crank-Nicolson scheme, whereas the convective terms are treated explicitly using the Adams-Bashforth method. The convective terms in Eq. (2) and (3) are written in the sqew-symmetric and divergence forms correspondingly [10].

The azimuthal direction is periodic for the considered geometry. It is natural then to represent any flow unknown q (where q represents either the pressure p, or any component of the velocity vector **u**, or the scalar variable φ_i) by means of a truncated Fourier series in this direction. In cross planes formed by the two remaining directions, we introduce a finite element representation on a structured triangular mesh (i.e. P1 elements). This mesh was generated from quadrilateral finite elements oriented along the radial, tangential and vertical isolines by splitting each quadrilateral element in two triangular one. Since we have a natural period of 2π in the azimuthal direction, such hybrid spectral/FE approach approximates variables using the following discretization method written in the cylindrical coordinate system (r, θ, z):

$$q^n(r,\theta,z) = \frac{1}{N_\theta}\sum_{k=-N_\theta/2+1}^{N_\theta/2}\sum_{j=1}^{N_{nod}} Q_{k,j}^{n} N_j(r,z)\, e^{ik\theta}, \tag{4}$$

where $i = \sqrt{-1}$, N_θ is the number of modes in the expansion, $Q_{k,j}^{n}$ are the Fourier coefficients associated with the j-th element at the n-th time step. Herein, to ensure the real-valuedness of the solution, the Fourier coefficients must obey the symmetry relation $Q_k = Q_{-k}^{*}$.

III. Numerical Implementation

It can be shown that the above approach allows decoupling the 3D non-linear problem (see Eqs. (1)-(3)) into a series of decoupled 2D non-linear problems, one for each Fourier mode. Coupling still occurs through the (nonlinear) convective terms, which are however treated explicitly and therefore do not complicate the (costly) linear solution phase. For the complete detail of the discretization procedure, the reader is referred to [8-10]. The discretized equations can be easily computed directly in terms of the Fourier components, except for the convective terms, which couple each Fourier mode to all others. The convective terms are therefore computed in physical space and then transformed to Fourier space using the Fast Fourier Transform (FFT) algorithm. The basic idea behind this pseudo-spectral solution procedure is as follows:

1. evaluate the convective terms in physical space, using the previously calculated $\mathbf{u}^{n}$ and $\mathbf{u}^{n-1}$;
2. transform these terms to Fourier space using the FFT algorithm;
3. set up the linear problems corresponding to each Fourier mode;
4. apply appropriate boundary conditions for each Fourier mode;
5. solve the linear systems to obtain the updated solution unknowns $Q_{k,j}^{n+1}$ in Fourier space;
6. apply the inverse Fourier transform to obtain the updated unknowns q^{n+1} in physical space.

This algorithm has been implemented for use on distributed memory parallel computers. The finite element mesh is divided into a number of partitions, which are stored on different processors. Before each linear solve, data belonging to each Fourier mode is gathered on a separate processor, such that all 2D linear solves can be performed simultaneously, but in a sequential manner (one linear solve per processor).

In our study, the concentration field is treated as a passive scalar and described by a convection-diffusion equation Eq. (3) which first requires computation of the velocity field from the hydrodynamic part given by Eqs. (1)-(2). It assumes that the concentration fields depend on the flow field but the flow field is not influenced by the concentration fields. Both convection-diffusion and hydrodynamic equations are solved at different instances of the code and they are coupled via dynamic data exchange at every time step using the MPI technique. This structure of the code yields an optimal distribution of load according to available computational resources. In other words, Navier-Stokes and passive scalar equations can be solved on the same or different processors.

IV. Results

The model Eqs. (1)-(3) have been used for the simulation of fluid flow and mass transfer at different regimes. First, a hypothetical electrochemical solution with an unphysical diffusion coefficient of $D=10^{-3}$ m^2/s was simulated at a Reynolds number of Re=80 and a Schmidt number of $\mathrm{Sc}=\nu/D=0.001$ (ν is the kinematic viscosity), Fig. 2. Since the Schmidt number is small, this test corresponds to problems where mass transfer is controlled by diffusion, i.e. Pe<<1 (Pe=Re Sc). As can be seen from Fig. 2, the numerical solution coincides with the analytical solution [3]:

$$C = \frac{C_{r_i}\ln(r_o/r) + C_{r_o}\ln(r/r_i)}{\ln(r_o/r_i)}. \tag{5}$$

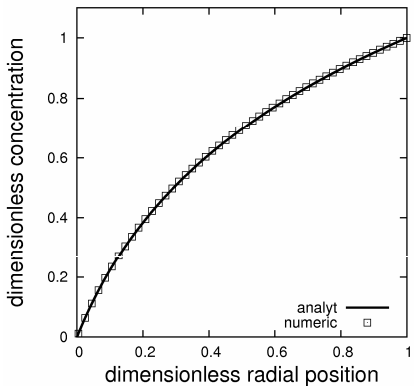

Fig. 2. Comparison between the analytical Eq. (5) and numerical solutions at Re=80 and Sc=0.001 given by the dimensionless concentration C/C_0 as a function of dimensionless radial position $(r–r_i)/s$, where C_0 is the nominal concentration.

The main study was performed for the ferri-ferrocyanide solution containing the supporting electrolyte 100 mM NaOH with a pH of approximately of 13. The properties of this solution are: the diffusion coefficient is D=5.6×10^{-10} m^2/s, a valency number n=1, a nominal concentration C_0=10 mM, a kinematic viscosity ν=10^{-6} m^2/s (yielding a large Schmidt number Sc=1785). The following electrochemical reaction is considered at RCE which is the inner (rotating) cylinder:

$$Fe(CN)_6^{3-} + e^- \rightarrow Fe(CN)_6^{4-}. \qquad (6)$$

The estimated thickness δ_C of the concentration boundary layer is given as a function of the Reynolds number in Table 1. This parameter varies between 166 and 20 μm as the rotation rate goes from 50 to 1000 rpm so a fine mesh is needed for adequate resolution of the concentration layer near the electrode. The adaptive mesh was used to resolve this issue with the stretch factor of 1.05 in the direction perpendicular to the electrode surface. As a result, the radial length of the finite element near the electrode was 2 μm which provides sufficient accuracy in all calculations, Fig. 3. The concentration boundary layer is located completely inside the hydrodynamic boundary layer and the mesh captures variations of both the hydrodynamic and concentration variables.

An analytical solution for the diffusion-convection problem at Re>1 does not exist. Our simulations yield good agreement with the empirical relationship of Eisenberg [11] which gives the limiting current density j as a function of the rotation speed:

$$j = 0.0791\, n\, \mathrm{F}\, C_0\, U_{rot} \left(\frac{2 r_i U_{rot}}{\nu} \right)^{-0.3} \left(\frac{\nu}{D} \right)^{-0.644}, \qquad (7)$$

where F is Faraday's constant, U_{rot} is the tangential velocity at the rotating electrode. Equation (7) is valid in a wide interval of Reynolds numbers.

TABLE I
Estimated thickness δ_C of the diffusion layer near the rotating electrode as a function of the rotation speed ω and the Reynolds number Re. The radial length δ_r of the smallest FE element is given for comparison. The calculations are performed for a 10 mM ferri-ferrocyanide solution containing 100 mM of NaOH.

ω, rpm	Re	δ_C, μm	δ_r, μm
50	910	166	2
100	1820	102	
200	3640	63	
500	9100	33	
1000	18200	20	

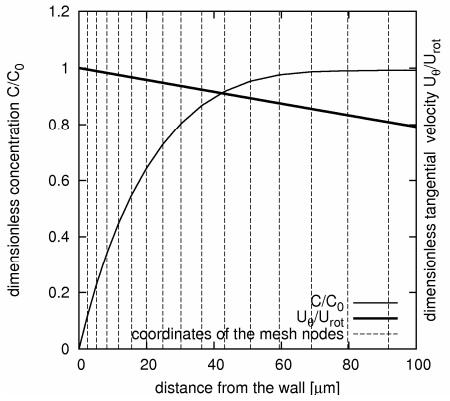

Fig. 3. The dimensionless concentration C/C_0 and dimensionless tangential velocity U_θ/U_{rot} (U_{rot} is the tangential velocity at the rotating electrode) as a function of distance from the rotating electrode. Data are extracted from the solution averaged in time at Re=9100. The radial positions of the mesh nodes are depicted as vertical lines.

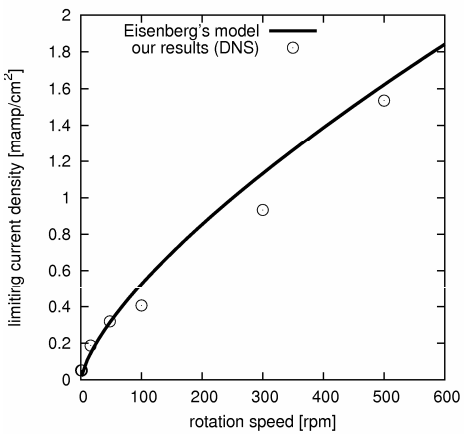

Fig. 4. Comparison of the numerical data with the empirical Eisenberg's relation Eq. (7) at the Reynolds numbers Re<10000. The dimensions of the reactor are: r_i=6 mm, r_o=35 mm, h=50 mm. The properties of the solution are: 10 mM ferri-ferrocyanide solution containing 100 mM NaOH as supporting electrolyte, D=5.6×10^{-10} m^2/s, n=1, ν=10^{-6} m^2/s.

In our simulations the limiting current density was calculated as

$$j = -n\,\mathrm{F} D \nabla C\,, \qquad (8)$$

where ∇C is the gradient of concentration averaged in time near the surface of the electrode. The numerical solution has a better agreement with Eisenberg et al. at small rotation speeds, Fig. 4. At high rotation speeds, the difference between solutions is about 10%. These simulations have been performed in the axisymmetrical mode. Further calculations in full 3D should evidence if the disagreement comes from inaccuracy of the mathematical model or discretization scheme. The discretization scheme contains a specific relaxation parameter which allows increasing the time step at the expense of accuracy. Since characteristic time and space scales of the mass transfer by diffusion are few order of magnitude smaller than the scales of convection at Sc>>1, we used a high value of the relaxation parameter to study mass transfer at a long time. Decreasing of this parameter and the time step may be a possible solution to improve agreement with the relation of Eisenberg.

V. Conclusions

1. The presented results are the first step towards the full-scale simulations of turbulent mass transfer in a rotating cylinder geometry. The method is capable of modeling turbulent mass transfer in the bulk of the reactor what affects the local concentration and current distributions in the vicinity of the electrode.
2. DNS results showed a good agreement with both analytical [3] and experimental results [11,12]. The presented technique is especially useful for modeling of systems for which the Schmidt number Sc~1 where analytical and empirical models are not available.

Acknowledgements

M.K. and J.F. acknowledge the financial support from the Institute for the Promotion of Innovation by Science and Technology in Flanders through the MuTEch project (IWT, contract nr. SBO 040092). M.R. was supported by a fellowship from FRIA (Fonds pour la formation à la Recherche dans l'Industrie et dans l'Agriculture).

References

[1] V.G. Levich, *Physicochemical Hydrodynamics*, Prentice-Hall, 1962.
[2] D.R. Gabe and D.J. Robinson, *Mass transfer in a rotating cylinder cell - Part II. Turbulent flow*, Electroch. Acta, **17**, 1129–1137, 1972.
[3] J. Newman and K.E. Thomas-Alyea, *Electrochemical Systems*, Wiley: John & Sons, 2004.
[4] F. Gurniki, *Turbulent convective mass transfer in electrochemical systems*, PhD, Royal Institute of Technology, Sweden, 2002.
[5] S. Chandrasekhar, *Hydrodynamic and hydromagnetic stability*, Oxford University Press, 1961.
[6] M. Krivilyov, Y. Detandt, D. Vanden Abeele, G. Degrez and J. Fransaer, *Direct numerical simulations of Taylor-Couette flow using a hybrid spectral/finite-element approach*, Proceedings of NCTAM-VII, Mons, Belgium, CD-ROM, 2006.
[7] M. Manna and A. Vacca, *An efficient method for the solution of the incompressible Navier-Stokes equations in cylindrical geometries*, J. Comp. Phys., **151**, 563–584, 1999.
[8] D. Vanden Abeele, G. Degrez and D. Snyder, *A combined spectral/finite elements method for the direct and large eddy simulation of turbulent flows in complex, two dimensional geometries*, Proceedings of CMFF 03, 783–790, 2003.
[9] D. Snyder, *Development of a finite-element/spectral incompressible Navier-stokes solver for application to LES*, PhD, von Karman Institute, Belgium, 2002.
[10] Y. Detandt, *Numerical computation of aerodynamic noise in subsonic regime*, Université Libre de Bruxelles, Belgium (2008).
[11] M. Eisenberg, C.W. Tobias and C.R. Wilke, *Ionic Mass Transfer and Concentration Polarization at Rotating Electrodes*, J. Electrochem. Soc., **101,** 306–319, 1954.
[12] L. Stappers and J. Fransaer, *The effect of turbulence on the electrodeposition of composite coatings*, J. Electrochem. Soc., **152**, 392–398, 2005.

Proceedings of the 8th National Congress on Theoretical and Applied Mechanics, May 28-29, Brussels, Belgium.

Hydrogen micromix combustion – Introductory study – Cold flow

E. RECKER, W. BOSSCHAERTS
Department of Mechanical Engineering, Royal Military Academy
Avenue de la Renaissance 30, 1000 Brussels – Belgium
email: elrecker@rma.ac.be, walter.bosschaerts@rma.ac.be

Abstract: **With the final objective of optimizing the "Micromixing" combustion principle with means of the commercial CFD code FLUENT, Reynolds averaged Navier-Stokes Simulation (RANS) is used to get a preliminary estimation of the flow field. The vortical structures, mean velocity field and scalar concentration are in good agreement with the former experimental and numerical investigations. Furthermore, the numerical simulation validation is investigated. Validating the scalar field against a literature test case appears to be the best option. The velocity field and vortical structures are best assessed by a comparison to in house Particle Image Velocimetry (PIV) measurements on an upscaled geometry. More generally, this preliminary study permits to decide on the future approach in "Micromixing" research.**

I. INTRODUCTION

Control of pollutant emission has become a major factor in the design of modern combustion systems. The "Liquid Hydrogen Fuelled Aircraft – System Analysis" FPS project funded in 2000 by the European Commission can be seen as such an initiative [1]. In the frame of this project, the Aachen University of Applied Sciences (ACUAS) developed experimentally the "Micromix" hydrogen combustion principle and implemented it successfully on the Honeywell APU GTCP 36-300 gas turbine engine.

II. MICROMIX HYDROGEN COMBUSTION PRINCIPLE

Lowering the reaction temperature, eliminating hot spots from the reaction zone and keeping the time available for the formation of NO_x to a minimum are the prime drivers in NO_x reduction. The "Micromix" hydrogen combustion principle meets those requirements by minimizing the flame temperature working at small equivalence ratios, improving the mixing by means of Jets In Cross-Flow (JICF) and reducing the residence time in adopting a combustor geometry providing a very large number of very small diffusion flames uniformly distributed across the burner main cross section (Fig. 1.) [2].

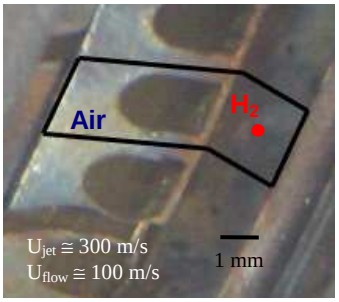

Fig. 1. Individual injection zone.
(courtesy ACUAS)

Compared to the unconverted APU, the NOx emission are reduced by a ratio 10, confirming the promising innovative "Micromix" combustion principle (Fig. 2.)

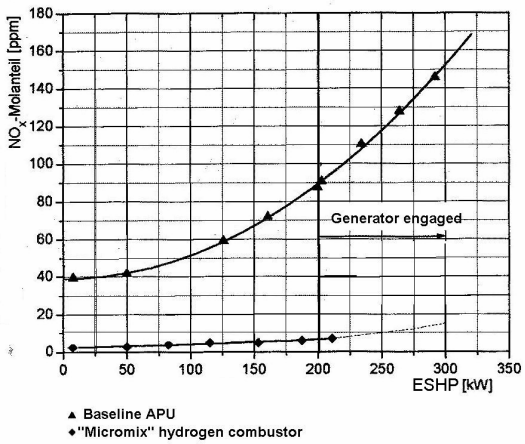

Fig. 2. "Micromix" hydrogen combustor emission level.
(courtesy ACUAS)

III. JETS IN CROSS-FLOW

Jets In Cross-Flow are defined as the flow field where a jet of fluid enters and interacts with a cross-flowing fluid.

A jet issuing in the +y-direction, into a cross-flow in the +x-direction will bend in the stream-wise direction. As the jet bends, fluid is entrained, and vorticity in both the issuing jet and the free stream stretches and aligns to form four dominant flow structures (Fig. 3.) [3].

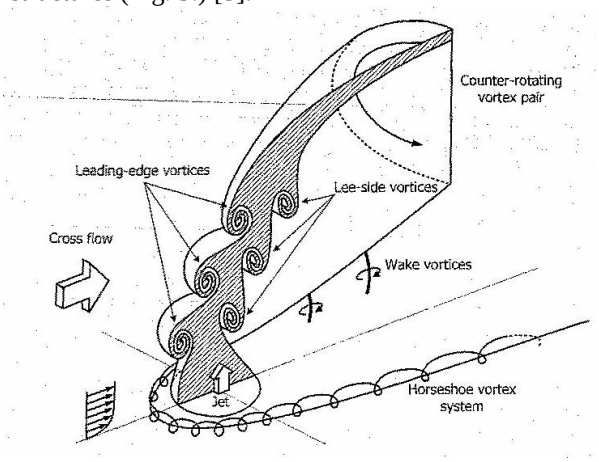

Fig. 3. Schematic drawing of the vortical structures in JICF

The dominant flow structure in JICF is the Counter-Rotating Vortex Pair (CRVP). These vortices are created in the near field and occupy the entire cross-section, becoming

synonymous with the jet in the far field. The length scales of these vortices are significantly greater than those of the eddies containing the turbulent energy and are therefore considered to be associated with the mean flow rather than the turbulence.

A horseshoe vortex is formed upstream of the jet at the cross-flow wall. The adverse pressure gradient at the cross-flow wall forces the wall boundary layer to separate and to form a vortex. It is then convected and stretched by the flow and wraps around the jet nozzle like a neck lace. The horseshoe vortex is weak and either incorporates into the wake vortex structure or merges with the CRVP.

The jet shear layer vortices (leading-edge / lee-side vortices) are produced directly at the jet orifice. The jet stream and cross-flow form a mixing layer with a Kelvin-Helmholtz instability, which causes a roll-up near the edges of the jet. In contrast to the free jet, where the vortex sheet rolls up "axisymmetrically", in the case of JICF, the vortex sheet can roll up freely only at the upstream and the lee-side of the jet column.

Wake vortices are vertical structures observed downstream of the jet that join the CRVP and the wall boundary fluid.

The most dominant quantity to characterise a JICF is the momentum ratio defined as:

$$r_m = \sqrt{\frac{\rho_j \cdot U_j^2}{\rho_g \cdot U_g^2}} \qquad (1)$$

The "Micromixing" JICF operates at a $r_m \approx 1$, which is low for combustor type mixing. The Reynolds numbers Re_{jet} and $Re_{jet/freestream}$, based on the jet diameter and jet velocity and on the jet diameter and free-stream velocity, are respectively 930 and 650.

Experimental investigations of the flow physics of the jet in cross-flow have been quite plentiful. The bibliographic study is limited to look at relevant previous investigations.

For JICF with $r_m < 1$, Andreopoulos and Rodi [4] observed jet pipe blockage. The cross-stream fluid acts like a partial cover over the exit, causing the fluid to bend around and to accelerate. The jet bending was seen to start already inside the pipe with some pipe fluid that was observed to be entrained into the horseshoe vortex. To take this blockage into account, the jet pipe has to be included into the computational domain.

They separated the development of turbulent kinetic energy k into three regions, the first one being over the exit. Downstream of the exit, k is produced in the shear layer above the wake region. Further downstream, less turbulent kinetic energy is produced and that having been produced further upstream is convected downstream and diffused by the turbulent motion towards the wall.

Kelso, Lim & Perry [5] investigated the structure of JICF for r_m ranging from 2 to 6 and $Re_{jet/freestream}$ in the range of 440 to 6200. Downstream of the jet, there appeared to be a node which resides a short distance downstream of the edge of the nozzle. Regardless of r_m, there was only little variation in the location of the node (between x/D = 1 and 2, y/D = 0.4 and 1) (Fig. 4.).

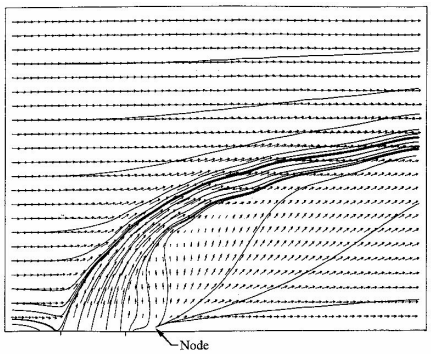

Fig. 4. Time-averaged vector field and streamlines in the vertical centre-plane. $r_m = 2.2$

Peterson and Plesniak [6] (r_m = 0.5 - 1 ; Re_{jet} = 6000 - 12000) noticed a reversed flow region extending from the trailing edge of the hole to approximately x/D = 1.65. In addition, immediately downstream of the jet, two vortices roll-up (Fig. 5.).

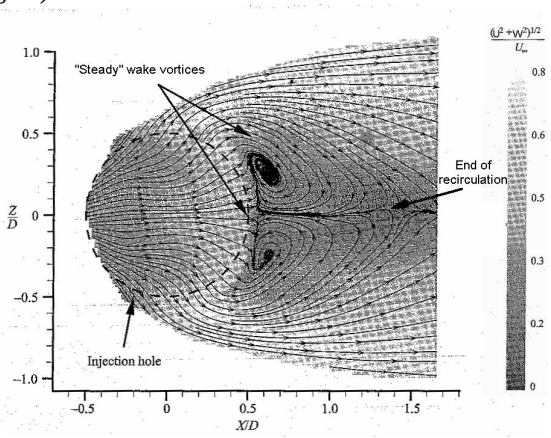

Fig. 5. (X, Z)-plane velocity fields, $r_m = 0.5$, y/D = 0.1

Smith & Mungal [7] studied the mixing of JICF for a range of r_m from 5 to 25 and Re_{jet} ranging from 16600 to 41500. They observed that the entrainment is significantly higher on the downstream side of the jet as compared to the upstream side. This observation shows the need for a high spatial discretization at the downstream region of the nozzle. The average is characterised by a smooth shape, which is Gaussian, while the instantaneous profiles are marked by sharp rises in concentration resulting in small plateau's of high concentration fluid (Fig. 6.).

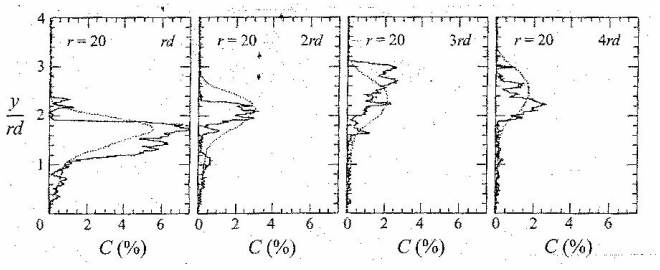

Fig. 6. Instantaneous jet concentration field side view, z = 0, $r_m = 20$

This strong unsteady behaviour leads to the conclusion, that a local Large Eddy Simulation (LES) approach is highly indicated for reproducing and predicting JICF mixing.

Su & Mungal [8] measured the planar scalar mixing in a JICF with r_m = 5.7 and Re_{jet} = 5000. They observed that the deepest penetration on the outer boundary occurs in the centre-plane, with progressively a shallower penetration for increasing off-centre positions z. Meanwhile, on the wake side of the flow, with increasing y, the boundaries for the off-centre-planes all lie further from the centre-line trajectory than does the boundary in the centre-plane. This corresponds to a kidney-like shape of the flow cross-section. In addition they noticed that the jet cross-section takes on a bimodal profile in which the scalar maxima lie off the centre-plane.

IV. Simulation

A. Rational

Despite the known shortcomings of the first order two-equation RANS models, the "Micromix" JICF is studied using a first-order two equation model to get a preliminary estimation of the flow field. The Shear Stress Transport (SST) model appears to best fit with the need of accurately predicting adverse pressure gradient flows.

An individual air-hydrogen injector is simulated. The computational domain is composed of three blocks (A, B and C) (Fig. 7.). Block B comprises the air and hydrogen injection areas. Block C extends beyond block B in order to not constrain the jet and minimise the effects of confinement by the boundary. A 2 mm length pipe is included. The cross-flow inflow plane is located 4.76 mm upstream of the air injection holes to reproduce diffuser inflow conditions (Block A). The air/hydrogen longitudinal spacing is intentionally left blank.

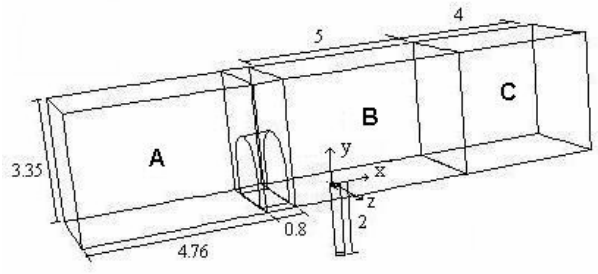

Fig. 7. Computational domain

The grid is unstructured and composed of 600000 tetrahedra. Departing from the jet/cross-flow centre-line, the mesh increases radially outward. The mesh has been refined at the edge of the jet nozzle and in the downstream region. As limitations in computational cost imposed to control the number of cells, in blocks A and C, the mesh size grows more rapidly. Meshing allows to resolve the viscous boundary sub-layer. Fig. 8. shows an end view of the mesh centred on an hydrogen injection hole and a top view of the hydrogen injection tube.

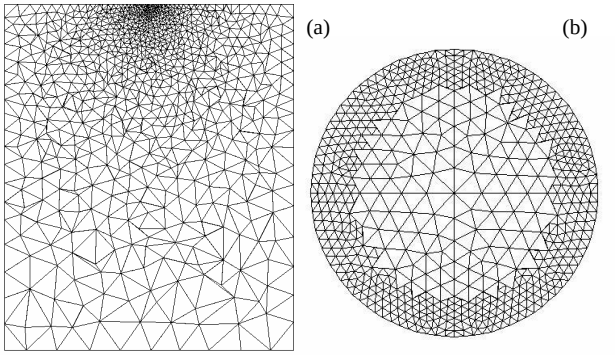

Fig. 8. (a) End view, mesh, x = 0; (b) Top view, mesh hydrogen injection tube

The boundary conditions are specified as follows. At the cross-flow and jet inflow plane, the mass flow and temperature are specified. At the outflow plane, the pressure is imposed. On the lateral and top surfaces, free-slip boundary conditions are prescribed, while on the bottom, a no-slip boundary condition is enforced.

The FLUENT flow solver is used. FLUENT uses a finite volume based technique. In this work, the segregated solution method, the second-order upwind scheme and the Semi-Implicit Method for Pressure-Linked Equations (SIMPLE) pressure-velocity coupling algorithm have been adopted. The SST model is applied.

B. Results

The vortical structures, mean velocity field and scalar concentration are in good agreement with the former experimental and numerical investigations.

U & V mean velocity contours, vectors and profiles are shown in Fig. 9. and 10. Fig. 9. illustrates the strong interaction of jet and cross-flow in the exit region which can be considered as equivalent to placing a partial cover over the jet exit. Also illustrated in this figure is the lifting of the cross-stream over the bent-over jet.

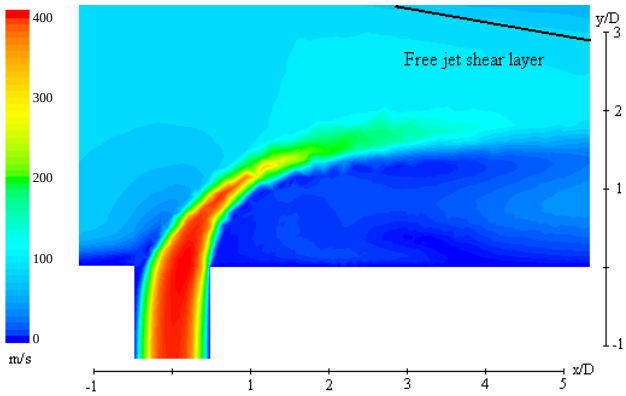

Fig. 9. Side view, U-V velocity contours, z = 0

The jet bending can be seen to start already inside the pipe and is completed at x/D ≈ 4. The jet penetrates the cross-flow by 1.8D. Near the outer edge, the velocity overshoots the free-

stream value down to x/D ≈ 6. The jet stays well inside the cross-flow and no break-through is observed.

The separation of the oncoming boundary-layer (Fig. 10.) is shown by way of the vortex just upstream of the exit, which forms the origin of the horseshoe vortex. Some cross-flow fluid is entrained into the pipe.

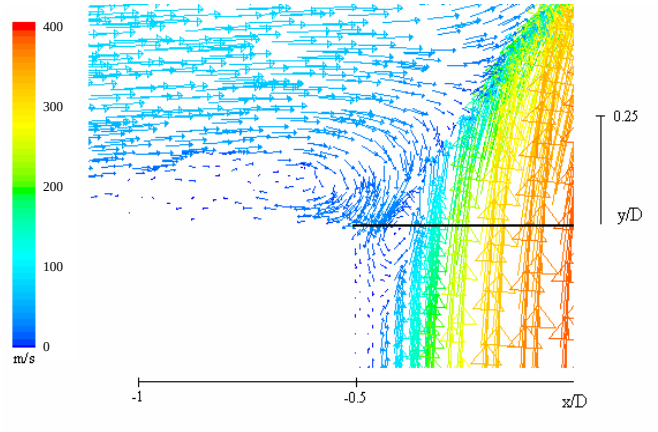

Fig. 10. Side view, U-V velocity vectors, z = 0

The jet cross-sectional velocity field and CRVP development are depicted in Fig. 11. and 12. For reasons of clarity, only one velocity vector out of three is represented.

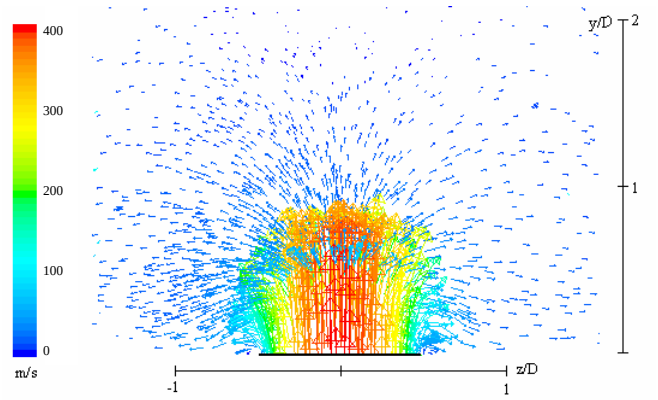

Fig. 11. Plane 1: End view, V-W velocity field, x = 0

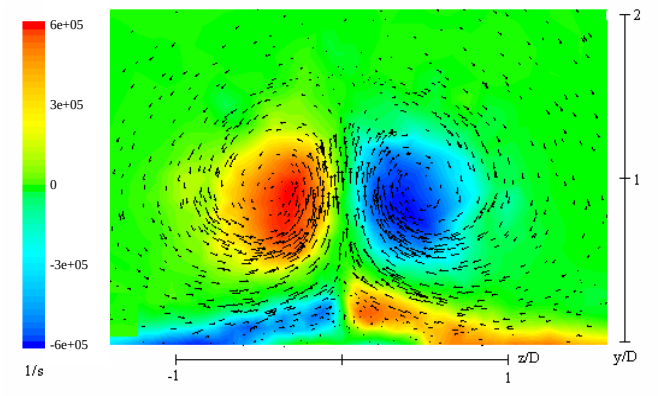

Fig. 12. Plane 3: End view, V-W velocity field & vorticity contour, x = 4D

The vertical velocity component of the jet begins to shear the boundary-layer fluid outboard of the jet (Fig. 11.), creating stream-wise vorticity consistent with that of the CRVP. Fig. 12. shows the continuing development of the primary CRVP, which grows larger in scale but smaller in vorticity magnitude. From those figures, it is evident that the CRVP dominates the far field. Furthermore the action of the CRVP draws the fluid away from the wall, creating a region of low velocity downstream of the jet along the x-axis.

Fig. 13. shows the top view velocity distribution of the jet efflux into the cross-flow at the y = 0.1D plane. One velocity vector out of 15 is sketched. By entrainment the fluid at the stream-wise centreline of the hole is drawn outwards to the jet boundary. Downstream of the injection hole, the jet/free-stream mixture accelerates and converges upon the spanwise centreline of the hole. A reversed flow region extending from the trailing edge of the hole to x/D ≈ 3 draws outboard fluid in behind the jet. The “steady” wake vortices observed by Peterson & Plesniak [6] are well resolved. Immediately downstream of the jet, the two “steady” wake vortices roll-up.

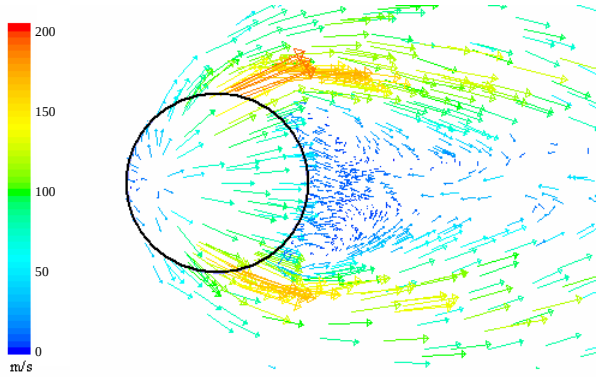

Fig. 13. Top view, U-Z velocity vectors, y = 0.1D

No wake vortices are observed in any of these planes, stressing their unsteady nature.

The length and velocity scales of the vortical and flow structures are approximated in Table I.

Table I
Vortical and flow structures length and velocity scales

	CRVP near field	CRVP far field	Steady wake	Recirculation
l_s (mm)	0.1	0.3	0.15	1
v (m/s)	10	30	15	75

Contours of time-averaged H_2 mass fraction on the symmetry plane are shown in Fig. 14. For clarity reasons, the H_2 mass fraction is only shown from 0.05 on. The figure shows that the H_2 mass fraction decreases with increasing distance from the jet exit, as expected. Also, the jet width is larger on the downstream side as compared to the upstream side of the centre streamline. Close to the jet exit , both the downstream and upstream sides of the jet contribute about the same to the entrainment. Moving further, the contribution of the downstream side increases significantly.

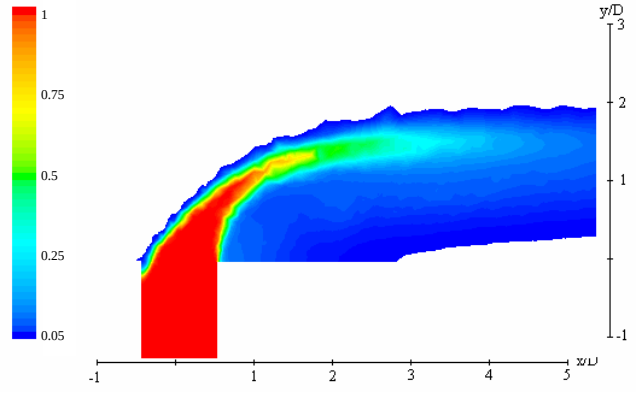

Fig. 14. Side view, H_2 mass fraction, z = 0

Fig. 15. shows the contours of mean pressure on the symmetry plane with U-V vectors in overlay. Pressure colour map is centred on P_a.

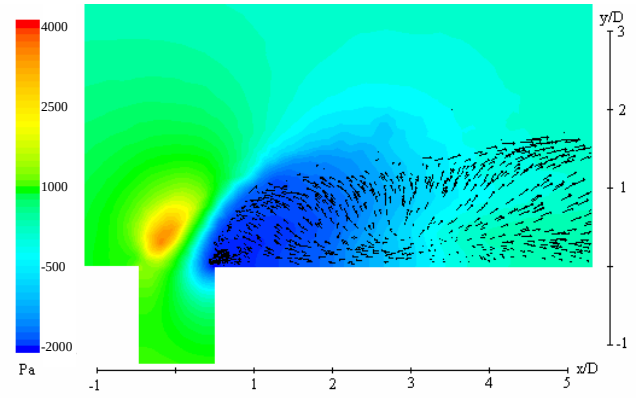

Fig. 15. Side view, contours of static pressure & U–V velocity vectors, z = 0

A node is observed in the vicinity of the co-ordinate x ≈ 3D and y ≈ 0.25D. The node is observed slightly more downstream and closer to the wall than in the measurements of New, Lim & Luo [3] (between x/D = 1 and 2, Y/D = 0.4 and 1). The cross-flow fluid passes around the jet and converges toward this node. The stream-wise location of the node corresponds to the end of the recirculation zone immediately downstream of the jet.

The highest pressure is observed near the upstream edge of the jet, beginning close to the jet exit and extending until the jet noticeably bends. The lowest pressure is observed at the downstream edge of the jet. Moving in the x-direction, the static pressure begins to increase. The velocity vectors downstream of the jet shows that the pressure gradient drives the cross-flow fluid toward the jet. This observation combined with the jet/free-stream mixture converging upon the spanwise centre-line, the lifting action of the CRVP and the reversed flow region contribute to the high entrainment in the downstream region.

Fig. 16. and 17. show a top view near the jet exit (y = 0.5D) and an end view (x = 4D) of the H_2 mass fraction respectively. The jet deforms from a roughly circular cross-section to a kidney-shaped cross section. The maximum H_2 mass fraction is situated in the side lobes and the mean H_2 mass fraction exhibits a Gaussian distribution.

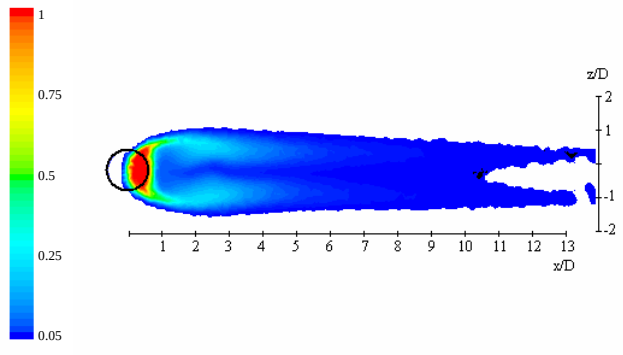

Fig. 16. Top view, H_2 mass fraction, y = 0.5D

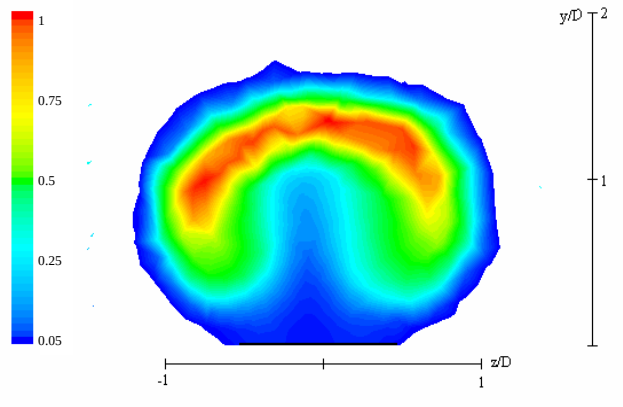

Fig. 17. End view, H_2 mass fraction, x = 4D

These mixing results are in agreement with the observations made by Smith & Mungal [7] and Su & Mungal [8].

The SST model allowed to identify the main JICF flow features. The vortical structures, mean velocity field and scalar concentration are in good agreement with the former experimental and numerical investigations. Nevertheless, it has to be stressed that the numerical results are of qualitative nature only.

Evidence is given in Fig. 18. The figure shows a contour side view of the turbulent kinetic energy with an upstream and downstream y-vorticity iso-line in overlay.

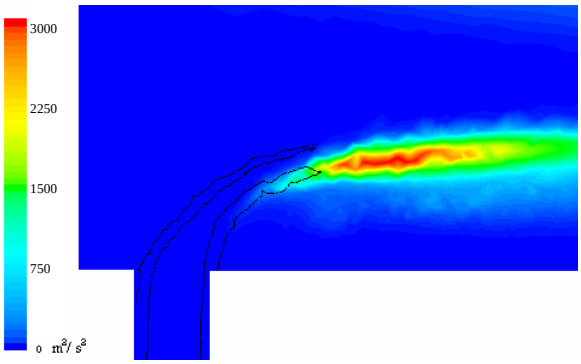

Fig. 18. Side view, k contours, y-vorticity iso-lines, z = 0

The turbulent kinetic energy region in the shear layer above the wake observed by Andreopulos & Rodi [4] is visible, but the region above the jet exit is not captured by the simulation.

The turbulent kinetic energy above the jet exit seems to be underestimated. This shortcoming can mainly be attributed to the underestimate of turbulence intensity in the shear-layers due to the incapability of the SST model to account for streamline curvature. LES, taking into account streamline curvature, should give more precise results and help to explain the features that are put into evidence during experiments.

V. Simulation Validation

The experimental investigation of the "Micromix" JICF is far beyond the current velocity/scalar measurement capabilities (both in dynamic range and spatial resolution).

The validity of the computations can be approached whether by validating the model against literature test cases, whether by scaling up an individual "Micromix" injection zone. As no "in house" concentration field measurement equipment is available, comparison with literature test cases is currently the only option.

In order to obtain meaningful statements concerning the validity of the RANS computations of the individual "Micromix" injection zone, test cases are needed which are close to the real problem with respect to the Reynolds number and r_m.

The experiments carried out by Andreopulos and Rodi [4] at $r_m = 1$ best fit with the flow field characteristics, despite the high $Re_{jet} = 41000$.

As the experimental investigations of mixing in JICF are relatively limited, the concentration measurements of Su & Mungal [8] are the best option ($r_m = 5.7$; $Re_{jet} = 5000$).

Scaling up as an option for simulation validation is assessed by analysing the modification of the flow field due to a scaled geometry and inflow conditions.

The "Micromix" individual injection zone geometry was scaled up by a factor 10. r_m and Re were defined as invariants. The air and hydrogen mass flow were adjusted accordingly.

As mixing is to be validated through literature test cases, the similarity analysis is limited to the jet trajectory, velocity field and vortical structure.

The 1:1 jet trajectory is compared to the 10:1 jet trajectory in Fig. 19. As one can see, both jet trajectories obey a r_mD scaling law.

The 10:1 CRVP velocity field and vortical structure are compared to the 1:1 results in Fig. 20. The 1:1 velocity field and the vortical structures are reproduced to facilitate the comparison. The "Micromix" individual injection zone geometry and the scaled up results are presented in line. The 1:1 flow characteristics are presented on top.

Those results suggest that the CRVP "Micromix" structural effects scale with D. Velocity scaling is not as conclusive, but a Reynolds dependence seems to be an acceptable approximation.

The boundary layer separation, horse-shoe vortex, "steady" wake vortices and reversed flow region show a similar trend [9].

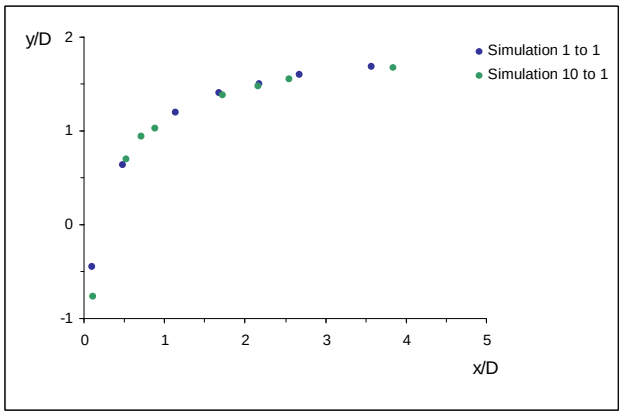

Fig. 19. Jet trajectory scaling

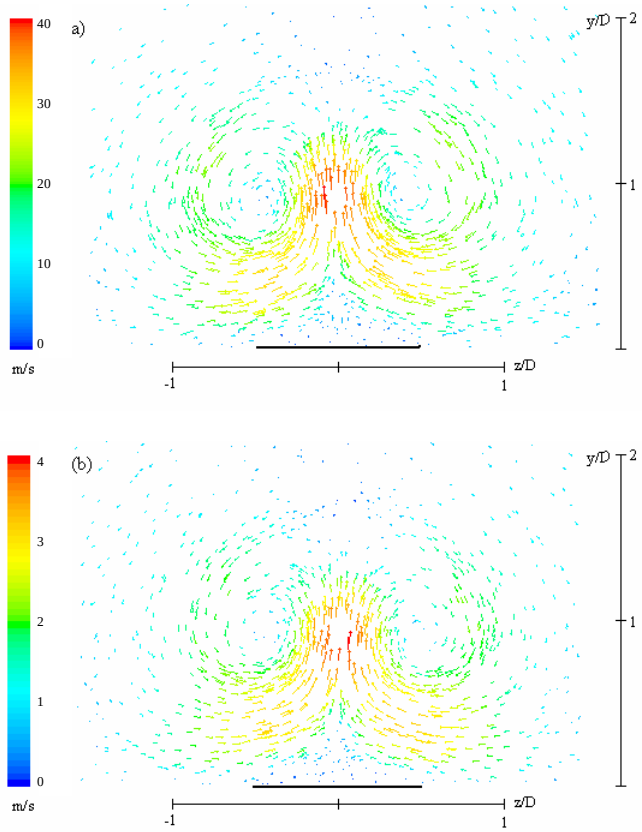

Fig. 20. End view, V-W velocity field, x = 4D
(a) 1:1 scale; (b) 10:1 upscale

Defining r_m and Re as invariants, the jet trajectory, velocity field and vortical structure are assumed to scale with r_mD and D respectively. However, it has to be emphasised, that the validity of this assumption remains to be investigated and hopefully confirmed. This similarity would allow to scale up the "Micromix" individual injection zone geometry and flow characteristics to fit with the experimental requirements, such as measurement equipment characteristics, experimental set-up constraints and easiness of validation prototype manufacturing.

VI. Conclusions

In this introductory work, the "Micromix" combustion principle is addressed using RANS. The aim of the study is to

get a preliminary estimation of the flow field and to outline the future research approach. Although the vortical structures, mean velocity field and scalar concentration are in good agreement with the former experimental and numerical investigations, the strong unsteady behaviour leads to the conclusion, that LES is required for reproducing and predicting JICF mixing. As the experimental investigation of the "Micromix" JICF is far beyond the current velocity/scalar measurement capabilities (both in dynamic range and spatial resolution), test cases close to the real problem are needed to assess the computations. The concentration measurements of Su & Mungal [8] and PIV measurements on an upscaled geometry are decided on.

REFERENCES

[1] A. Westernberger, Liquid Hydrogen Fuelled Aircraft – System Analysis, 5th Framework program of the European Communities, 2000

[2] M. Schelzig and G. Bleimund, Diplomarbeit FH Aachen, Inbetriebnahme und Optimierung einer Mikro-Misch-Brennkammer in der APU GTCP 36-300 sowie deren Reglerkreisoptimierung, 2000

[3] T.H. New, T.T. Lim, S.C. Luo, Effects of jet velocity profiles on a round jet in cross-flow, Experiments in Fluids, Vol. 40, pp. 859-875, 2006

[4] J. Andreopoulos, W. Rodi, Experimental investigation of jets in a cross-flow, J. Fluid Mechanics, Vol. 138, pp. 93-127, 1984

[5] R.M. Kelso, T.T. Lim, A.E. Perry, An experimental study of round jet in cross-flow, J. Fluid Mechanics, Vol. 306, pp. 111-144, 1995

[6] S.D. Peterson, M.W. Plesniak, Evolution of jets emanating from short holes into cross-flow, J. Fluid Mechanics, Vol. 503, pp. 57-91, 2004

[7] S.H. Smith, M.G. Mungal, Mixing, structure and scaling of the jet in cross-flow, J. Fluid Mechanics, Vol. 357, pp. 83-122, 1997

[8] L.K. Su, M.G. Mungal, Simultaneous measurements of scalar and velocity field evolution in turbulent cross-flowing jets, J. Fluid Mechanics, Vol. 513, pp. 1-45, 2004

[9] E. Recker, Hydrogen micro-mix combustion chamber, Introductory study – Cold flow, ULB DEA, 2007

Proceedings of the 8th National Congress on Theoretical and Applied Mechanics, May 28-29, Brussels, Belgium.

Lateral-torsional and lateral-distortional buckling of I-section members with web openings

Delphine Sonck, Jan Belis, Guy Lagae, Wesley Vanlaere, Rudy Van Impe
Laboratory for Research on Structural Models, Ghent University
Technologiepark-Zwijnaarde 904, B-9052 Zwijnaarde – Belgium
Email: Delphine.Sonck@UGent.be, Jan.Belis@UGent.be, Guy.Lagae@UGent.be, Wesley.Vanlaere@UGent.be, Rudy.VanImpe@UGent.be

Abstract: **The use of beams with large circular web openings has increased steadily during the last decade. However, not all aspects of the design of cellular beams have been studied extensively, such as lateral-torsional buckling, a general buckling mode of the beam. Currently, two approaches exist for calculating the critical lateral-torsional buckling moment of cellular beams, but these are not very accurate and there is a need for a new design rule. In order to demonstrate this need we have done numerical simulations in Abaqus for a number of geometries, of which this paper summarizes the most important results. The first approach for calculating the critical moment is accurate for some cases, but, due to web distortion, very unsafe for other cases. The second approach is overly conservative. To formulate a design rule in the future, more research will be needed.**

Keywords: **Lateral-torsional buckling, Web openings, Lateral-distorsional buckling, Finite element analysis, Abaqus**

I. INTRODUCTION

In steel constructions, the floor height can be decreased by providing large web opening in the beams, allowing for the passage of utility and service lines. If these web openings appear in a regular pattern, castellated or cellular beams, which can also be applied to optimise material use, arise.

The structural behaviour of steel beams with large web openings is still the subject of a large number of studies, since the presence of the openings affects the behaviour considerably [1] . For instance, new failure modes such as the Vierendeel mechanism can manifest themselves, but the openings also have a serious impact on known failure modes for beams loaded in bending about their strong axis, such as shear buckling and lateral-torsional buckling (LTB). In the latter failure mode, a beam in bending buckles in a general fashion. The lateral displacement of the compressed part of the beam is restrained by the part of the beam in tension, resulting in a combined torsional and lateral movement of the cross-section.

In the past, very limited research has been made about lateral-torsional buckling of beams with web openings. For castellated beams subjected to a constant bending moment, LTB was studied in [2]. The conclusion of this study was that the presence of the web holes has a negligible effect on the beams' lateral stability, and that the cross-sectional properties used for determining the LTB strength should be calculated at a cross-section at the middle of the castellation. This conclusion was generally adopted, and is repeated in ENV3, annex N [3] where the LTB resistance of cellular beams is calculated using cross-sectional properties at the middle of the openings. In the software program ARCELOR Cellular Beams, another approach is being used: the resistance of the beam depends on the lateral buckling resistance of the compressed tee section at the opening [4]. The stabilising effect of the tee section in tension is not considered. The latter approach is very conservative, while the former can be on the safe side for some cases and on the unsafe side for other cases. Consequently, there is a need for an extensive research regarding LTB of beams with web openings, in order to obtain a safe and economic design rule.

An important factor that certainly has to be examined when studying LTB, is the influence of web distortion. This distortion occurs due to an interaction between LTB and local buckling [5],[6]. Since these are the failure modes for respectively short and long members, web distortion occurs for intermediate length beams, and especially for those with slender webs. The S-shaped distortion (Fig. 1) causes a reduction of the effective torsional stiffness of the beam, resulting in a lower LTB critical moment. Lateral-distortional buckling (LDB) instead of LTB occurs. A for most cases overly conservative approximation of the LDB strength can be obtained by setting the torsion constant equal to zero in the expressions for the LTB moment [7].

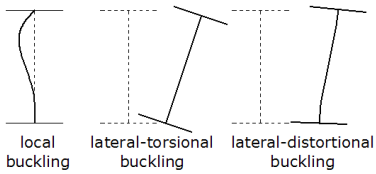

Fig. 1. Cross section for local buckling, LTB and LDB.

In our research of the LTB behaviour, we made numerical simulations with the finite element program Abaqus. The web distortion was quantified from the results of the simulations for each considered case. Simulations were made for beams with and without circular web openings, and the influence of the section geometry, the location of the opening and the size of the opening was examined. The present contribution gives the results of this research for two selected section geometries, and compares these results with the different calculation approaches for the LTB strength.

II. Investigated Sections

In this paper, the results for two different sections (Fig. 2) will be shown. These sections were gathered from a larger group because of the contrasting nature of their structural behaviour. The height h of the examined sections remains constant, while the width b and the ratio of the web thickness to the flange thickness t_w/t_f vary (TABLE 1). In section 1, the web is relatively more compact, while in section 2 the web is relatively more slender. The length of the members varied between 4 m and 30 m.

TABLE 1

GEOMETRICAL PROPERTIES OF THE SECTIONS

	Section 1	**Section2**
h (m)	0.36	0.36
b (m)	0.17	0.17
t_w (m)	0.008	0.008
t_f (m)	0.013	0.023
t_w/t_f	0.62	0.35

Two values were considered for the diameters of the web openings, while the spacing s between the possible locations of the openings was fixed at one value (TABLE 2). In this manner the possible locations of the centres of the openings remained constant for a given length of the steel beam. Both regularly spaced openings and groups of isolated openings were considered.

TABLE 2

OPENING DIAMETERS AND SPACING

	diameter (m)	**s (m)**
Opening 1	0.335	0.4
Opening 2	0.2	0.4

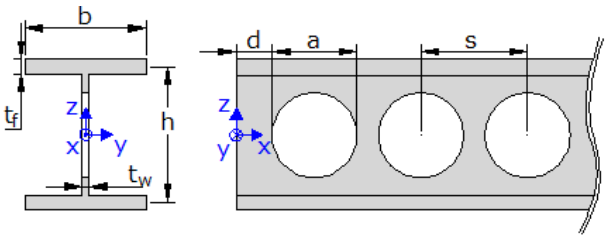

Fig. 2. Geometrical properties of the sections.

III. Current Design Rules

When LTB occurs, the beam buckles in a general fashion. The lateral displacement of the compressed part of the beam is restrained by the part of the beam in tension, resulting in a combined torsional and lateral movement of the cross-section. According to ENV3, annex F [8], the classical elastic critical moment M_{cr} for a doubly symmetric, plain webbed, I-section member loaded by a uniform moment about its strong axis, and supported by fork bearings at its ends is given by (1).

$$M_{cr} = \frac{\pi^2 EI_Z}{L^2}\sqrt{\frac{I_W}{I_Z} + \frac{L^2 GI_T}{\pi^2 EI_Z}} \qquad (1)$$

If the ENV approach is followed and $M_{cr,op}$ – the critical bending moment for a beam with web openings – is calculated using the cross-sectional properties at the centre of the opening, the length L of the beam, the warping constant I_W, the shear modulus G and the Young's modulus E remain unaltered in (1). The only factors that change are the torsion constant I_T and the second moment of area about the weak axis I_Z. The change of I_Z will only be small, but in some cases the change in I_T has a non-negligible influence on the value of $M_{cr,op}$ (Fig. 4 and Fig. 5). An easier way of taking into account the web openings, is by setting the value of the web thickness t_w equal to zero in the expressions for M_{cr}. This value, $M_{cr,tw=0}$ is always smaller than $M_{cr,op}$.

An estimate of the critical moment for I-section members when web distortion is taken into account, $M_{cr,dist}$, can be obtained by setting the value of the torsion constant I_T equal to zero in (1) [7]. For very slender webs this is an accurate approach, but for more compact webs this approach is overly conservative.

The LTB critical moment for sections with web openings can also be calculated by regarding the compressed "upper tee" of the section as a compression member that buckles laterally (based on [4]). The critical compressive normal force N_{cr} is calculated as the Euler buckling force. The critical moment $M_{cr,N}$ (2) is then obtained by multiplying this normal force with the distance d between the centers of gravity of the upper and lower tee section (Fig. 3).

$$M_{cr,N} = d.N_{cr} = d.\frac{\pi^2 EI_{Z,T}}{L^2} \qquad (2)$$

For very large openings, d will approach the height h of the section, and $M_{cr,N}$ will approach $M_{cr,dist}$ (in which I_T=0). This is quite logical, because I_T is the torsional stiffness of the beam, which vanishes completely for large web openings. The part of the beam in tension will no longer be able to restrain the lateral movement of the compressed part, and the compressed part will buckle laterally.

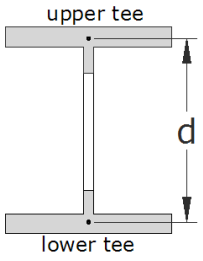

Fig. 3. Upper and lower tee.

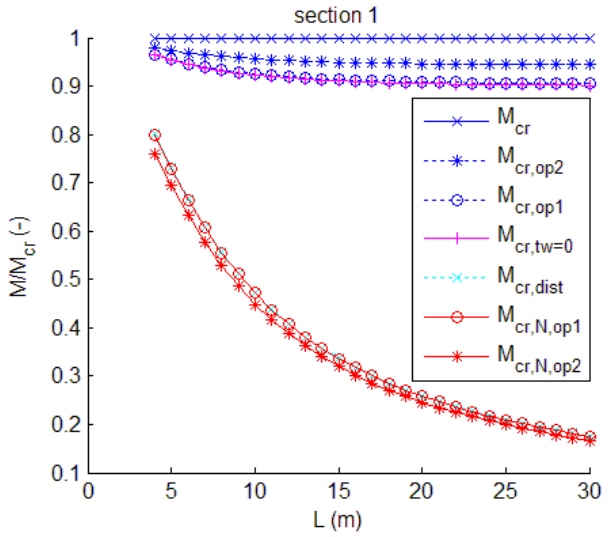

Fig. 4. Section 1. M/M_{cr} according to current design rules.

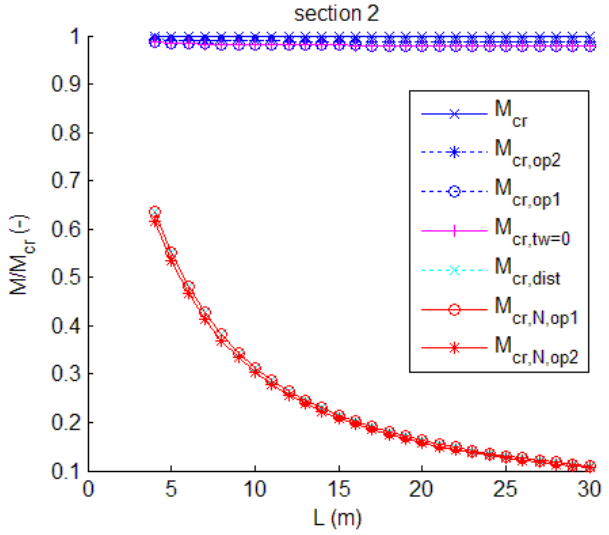

Fig. 5. Section 2. M/M_{cr} according to current design rules.

The values of the LTB critical moment according to the current design rules were calculated for section 1 and 2. The results are presented in Fig. 4 and Fig. 5, as well as in TABLE 3 and TABLE 4.

TABLE 3

SECTION 1. M/M_{CR} ACCORDING TO CURRENT DESIGN RULES

section 1	**L (m)**	**6**	**10**	**18**
plain web	**M_{cr} (kNm)**	166	84	43
	$M_{cr,dist}/M_{cr}$ (%)	67	47	29
web openings	**$M_{cr,op1}/M_{cr}$ (%)**	95	93	91
	$M_{cr,op2}/M_{cr}$ (%)	97	96	95
	$M_{cr,tw=0}/M_{cr}$ (%)	95	92	91
	$M_{cr,N,op1}/M_{cr}$ (%)	67	47	29
	$M_{cr,N,op2}/M_{cr}$ (%)	64	45	27

TABLE 4

SECTION 2. M/M_{CR} ACCORDING TO CURRENT DESIGN RULES

section 2	**L (m)**	**6**	**10**	**18**
plain web	**M_{cr} (kNm)**	405	224	120
	$M_{cr,dist}/M_{cr}$ (%)	48	31	18
web openings	**$M_{cr,op1}/M_{cr}$ (%)**	98	98	98
	$M_{cr,op2}/M_{cr}$ (%)	99	99	99
	$M_{cr,tw=0}/M_{cr}$ (%)	98	98	98
	$M_{cr,N,op1}/M_{cr}$ (%)	48	31	18
	$M_{cr,N,op2}/M_{cr}$ (%)	47	30	18

For sections with relatively slender webs, such as section 2, the contribution of the web to the torsion stiffness and the bending stiffness is small, even without the web opening. Hence, the influence of web openings on $M_{cr,op}$ is small. Even if we disregard the contribution of the web completely by calculating $M_{cr,tw=0}$, the reduction of M_{cr} is not more than 2% (TABLE 4). The values calculated by using the compressed tee approach are much lower, and here the web openings can cause a reduction of more than 80 percent. As mentioned in [7], for relatively slender webs such as in section 2, web distortion is to be feared. If we calculate the maximum effect of web distortion by setting I_T equal to zero, a reduction of more than 80% seems possible. However, this probably won't be the case for this section, as this is a very conservative approach. One can see that the values calculated for $M_{cr,N,op1}$ and $M_{cr,dist}$ are more or less the same, which was to be expected because of the large size of opening 1.

For sections with more compact webs such as section 1, the contribution of the web to the LTB strength will be higher, and the presence of the openings will affect $M_{cr,op}$ more. For large openings, the reduction can go as far as 9%, which is not longer negligible (TABLE 3). On the other hand, web distortion is less to be feared for this kind of section.

IV. NUMERICAL SIMULATIONS

A. Finite element model

The structural behaviour of beams with and without web openings was investigated by performing numerical simulations with the finite element package Abaqus. Shell elements of the type S8R5 were used for the web and the flanges. The material of the elements is purely elastic steel, with a Young's modulus E of 210 GPa, and a Poisson's ratio of 0.3.

At both ends of the beam, rigid bodies were attached to the web, in order not to allow web distortion at the supports (Fig. 6). Because the rigid bodies are not attached to the flanges, the warping of the latter is not prevented. The displacements in the lateral (y) and the vertical (z) direction together with the rotation about the x-axis of the reference point of the rigid bodies are restrained (Fig. 2). In one of the two reference points the movement in the x-direction is constrained as well.

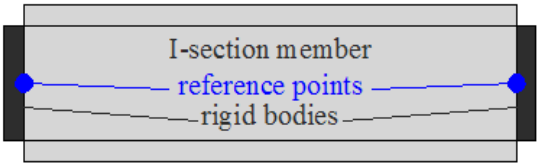

Fig. 6. Rigid bodies used in numerical simulations.

A moment about the y-axis was applied at both reference points, and a linear buckling analysis was performed. The lowest eigenvalue was determined, and the associated eigenmode was examined to determine the web distortion, as described in the next paragraph. The eigenmode given by Abaqus as the result of a linear buckling analysis is normalized so that the maximum displacement is equal to 1 (m).

B.Measurement of web distortion

Using the results of the numerical simulations in Abaqus, it is possible to calculate the web distortion by using the coordinates of the nodes in the deformed and undeformed states. The principle will be explained for a regular mesh with quadrilateral elements. For each node in the web, a non-distorted displaced location is calculated, based on the displaced locations of the upper and lower nodes of the web (Fig. 7). These non-distorted locations are then compared with the actual displaced locations of the nodes. For each node, the distance between these two locations is calculated. The beam is divided into parts lengthwise, where each cut corresponds with the locations of the upper and lower web nodes, and for each part the maximum distance is calculated. To obtain a measure for the whole beam, the mean of all these maxima is calculated.

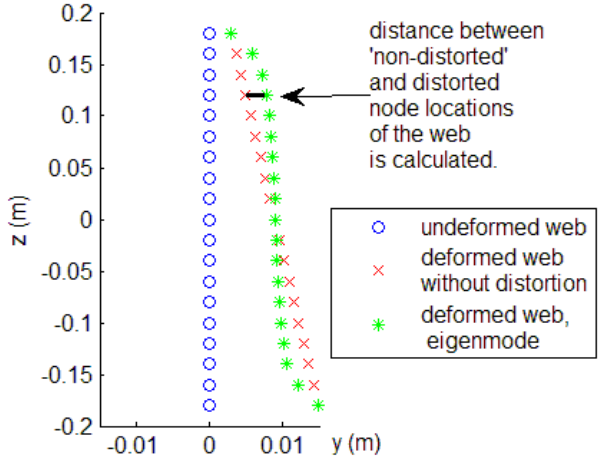

Fig. 7. Measurement of distance for calculation of web distortion.

C.Numerical simulations for plain-webbed beams

1) LTB critical moment

For members with section 2, the moment $M_{cr,ABQ}$ obtained from the linear buckling analyses in Abaqus is substantially lower than the calculated, classical moment M_{cr}. For members with section 1, $M_{cr,ABQ}$ approximates M_{cr} much better (Fig. 8). As we can see in Fig. 9, this is due to the web distortion. The web distortion for section 2-members is indeed higher than the distortion for section 1-members of the same length. This is logical, since the ratio t_w/t_f is smaller for section 2 than for section 1. For shorter beams, the web distortion and the reduction of M_{cr} are higher than for longer beams, which is also in agreement with what is reported in the literature.

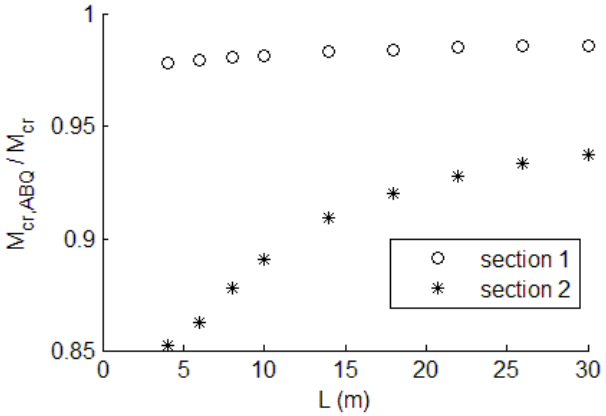

Fig. 8. Variation of $M_{cr,ABQ}$ in function of length.

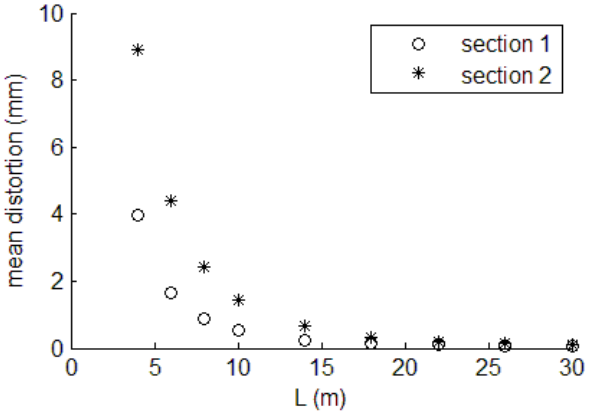

Fig. 9. Variation of mean distortion in function of length.

2) Distortion across beam length

If we now look at the distortion across the length of the beam, we can see that the web distortion reaches its maximum values near the edges and at the centre of the beam (Fig. 10-Fig. 12). As expected, the distortion for beams with a length of 6 m is the highest, and the distortion for beams with relatively slender webs such as the section 2-beams is also higher.

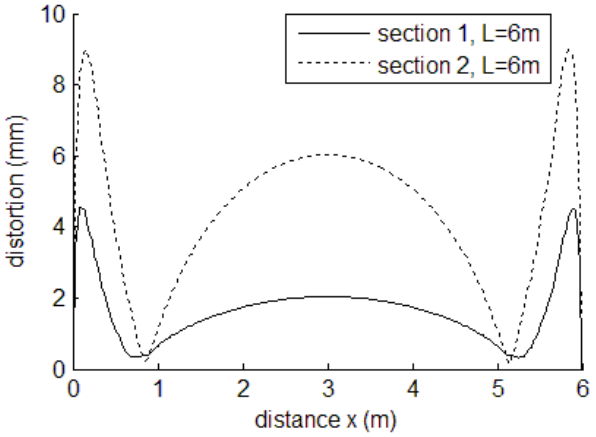

Fig. 10. Distortion over length of beam (L=6m).

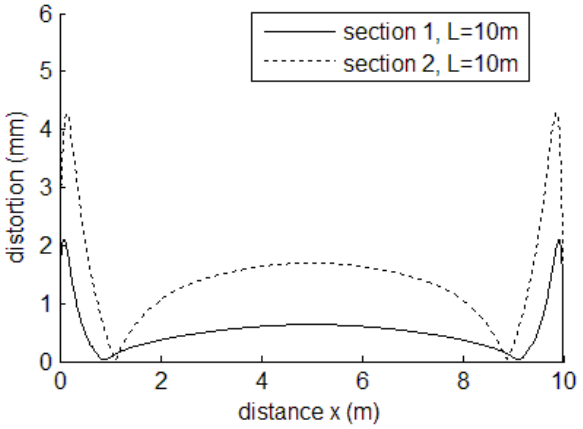

Fig. 11. Distortion of length of beam (L=10m).

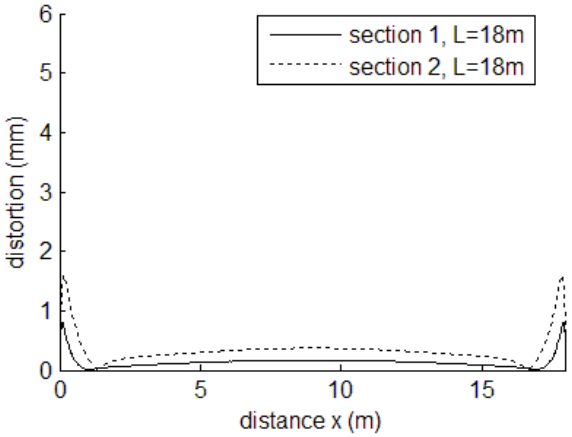

Fig. 12. Distortion over length of beam (L=18m).

D.Numerical simulations of beams with web openings

1) Influence of opening location

As described earlier, the possible opening locations are fixed, but the actual locations of the web openings can vary, as does the diameter of the opening. The influence of the opening location on the LTB moment was examined for members with a length L of 10 m. The total possible number of openings for this length is 24.

If two openings, at locations i and i+1 (Fig. 13), are introduced in the web, the influence is the greatest for opening location i=1, both for members with section 1 and section 2 (Fig. 14). The variation in LTB moment with the location of the opening however, is negligibly small for these cases.

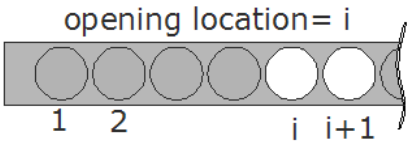

Fig. 13. Web openings for opening location=i.

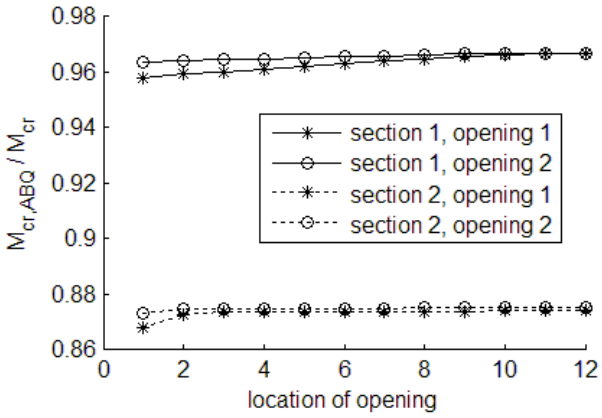

Fig. 14. Variation of $M_{cr,ABQ}/M_{cr}$ with opening location.

2) LTB critical moment for cellular beams

If the openings are applied at all possible locations, cellular beams arise. Numerical simulations were carried out for 3 lengths, 2 sections and 2 opening diameters.

For a plain-webbed beam with section 1, web distortion is small because of the relatively high web thickness. This higher value of t_w/t_f, however, causes a greater influence of the openings on the value of $M_{cr,op}$. For cellular beams with section 1, the values of $M_{cr,ABQ}$ (TABLE 5) and $M_{cr,op1}$ or $M_{cr,op2}$ (TABLE 3) correspond well. The openings increase the distortion of the beams with section 1, but the distortion is still smaller than that of a section 2 beam without openings. As previously said, this is due to the relatively high thickness of the web in section 1. The distortion is larger for shorter beams which complies with the foregoing part of this contribution. For the large web openings, the distortion of the web is logically larger.

For beams with section 2, the values of $M_{cr,ABQ}$ (TABLE 6) are considerably smaller than $M_{cr,op1}$ and $M_{cr,op2}$ (TABLE 4). Similarly as for plain-webbed beams, the distortion reduces the LTB critical moment to a considerable amount. In the results, $M_{cr,ABQ}$ and $M_{cr,op1}$ differ up to 18% of M_{cr} for opening 1. However, the values of $M_{cr,ABQ}$ are still substantially larger than $M_{cr,dist}$ (TABLE 4), so not all torsional stiffness is lost.

TABLE 5

SECTION 1. $M_{CR,ABQ}/M_{CR}$ AND DISTORTION.

section 1	L (m)	6	10	18
$M_{cr,ABQ}/M_{cr}$	no opening	0,98	0,98	0,98
	opening 1	0,92	0,91	0,91
	opening 2	0,95	0,95	0,95
distorsion (mm)	no opening	1,65	0,53	0,14
	opening 1	3,33	0,99	0,22
	opening 2	2,33	0,69	0,16

TABLE 6

SECTION 2. $M_{CR,ABQ}/M_{CR}$ AND DISTORTION.

section 2	L (m)	6	10	18
$M_{cr,ABQ}/M_{cr}$	no opening	0,86	0,89	0,92
	opening 1	0,80	0,84	0,88
	opening 2	0,83	0,87	0,90
distortion (mm)	no opening	4,40	1,46	0,34
	opening 1	8,15	2,92	0,69
	opening 2	6,49	2,18	0,50

V. CONCLUSION AND PERSPECTIVES

Two different methods for calculating the LTB critical moment of a beam with web openings exist. These methods were examined by numerical simulations in Abaqus for a limited number of geometries. The results for 2 sections are given: section 1, which has a relatively more compact web (high t_w/t_f), and section 2, with a more slender web (low t_w/t_f).

The first method, in which the cross-sectional properties at the centre of the opening are used to calculate the critical moment, gives results that agree fairly well with the ones obtained in the numerical simulations, $M_{cr,ABQ}$, for the section geometry with the more compact web. For the section with the slender web, the web doesn't remain straight in the buckled position, causing a reduction of the torsional stiffness. Consequently the values of $M_{cr,op1}$ and $M_{cr,op2}$ calculated following the first method are higher than the values $M_{cr,ABQ}$ obtained during the numerical simulations. Hence, due to web distortion, the first method gives unsafe results for the section with the slender web, which is hard to accept.

The second method considers only the lateral buckling resistance of the tee section in compression at the web opening to calculate the LTB resistance. This method is overly conservative for both sections and underestimates the critical moment to a large extent.

These results show that there is a need for a design rule that considers the effect of the web distortion on one hand, and is not uneconomic on the other hand. In order to obtain this result, more factors which can have an effect on the LTB strength must be taken into consideration. The section and web opening geometry must be varied to a greater extent, and the moment distribution, location of loading and boundary conditions at the beam edges must be taken into account. A vast number of non-linear simulations, in which plasticity, imperfections, and residual stresses are introduced, must be carried out in order to develop a safe and economic design rule.

ACKNOWLEDGEMENTS

The fourth author is a Postdoctoral Fellow of the Research Foundation – Flanders (FWO). Therefore, the authors would like to express their gratitude for the financial support of the FWO.

REFERENCES

[1] D. Kerdal, D. A. Nethercot, *Failure modes for castellated beams*, J. Constr. Steel Research 4 (295-315), 1984

[2] D. A. Nethercot, D. Kerdal, *Lateral-torsional buckling of castellated beams*, The Struct. Eng. 60B(3) (53-61), 1982

[3] CEN, European Committee for Standardisation, *Annex N: Openings in webs*, ENV 1993-1-1:1992, Eurocode 3: Design of steel Structures – Part 1-1: General rules and rules for buildings, 1992

[4] CTICM, *ARCELOR Cellular Beams-Detailed Technical Description*, Technical documentation for software ARCELOR Cellular Beams v2.32, 2006

[5] M. A. Bradford, *Lateral-distortional buckling of steel I-section members*, J. Constr. Steel Research 23 (97-116), 1992

[6] B.W. Schafer, S. Ádány, *Understanding and classifying local, distortional and global buckling in open thin-walled members*, Proceedings of the Structural Stability Research Council Annual Stability Conference, Montreal, 2005

[7] D. W. White, S.-K. Jung, *Effects of web distortion on the buckling strength of noncomposite discretely-braced steel I-section members*, Eng. Struct. 29 (1872-1888), 2007

[8] CEN, European Committee for Standardisation, *ENV 1993-1-1:1992, Eurocode 3: Design of steel Structures – Part 1-1: General rules and rules for buildings*, 1992

Proceedings of the 8th National Congress on Theoretical and Applied Mechanics, May 28-29, Brussels, Belgium.

An adapted dynamic programming algorithm for the identification of moving forces

Eliz-Mari Lourens, Geert Lombaert, Geert Degrande, Guido De Roeck
Department of Civil Engineering, K.U. Leuven
Kasteelpark Arenberg 40, 3001 Leuven - Belgium
email: elizmari.lourens@bwk.kuleuven.be, geert.lombaert@bwk.kuleuven.be, geert.degrande@bwk.kuleuven.be, guido.deroeck@bwk.kuleuven.be

I. Introduction

THE forces transmitted to a bridge by vehicles traversing the deck constitute the live load components in bridge design codes and thus form an integral part of bridge design. Although it's possible to measure static loads using weigh-in-motion (WIM) systems, the dynamic wheel loads may significantly increase road surface damage and obtaining information on them remains of interest. This is traditionally done in one of two ways, namely by measurement using an instrumented vehicle or by computation with a vehicle-bridge interaction model. Direct measurement is expensive and prone to bias whereas the results of a vehicle-bridge interaction analysis largely depend on the knowledge of input parameters and the accuracy of the model. In recent years considerable attention has been given to the reconstruction of these dynamic loads from measured vibration responses, an alternative which can be applied under real traffic conditions without the need for an instrumented vehicle or the interruption of traffic.

Developments include the time domain method [1], the frequency-time domain method [2] and the interpretive method [3], all having the disadvantage of being computationally expensive as well as difficult to apply to more complex structures. These drawbacks were to a large extent removed by applying the dynamic programming algorithm [4] to the moving force identification problem [5]. The classic formulation of the algorithm, however, placed a restriction on the type of measurements (displacements/velocities/accelerations/strains) that could be used in the inversion process. In this paper an adapted dynamic programming algorithm is developed which effectively removes this restriction.

II. Adapted dynamic programming

A. Classic formulation

By departing from a state-space model of the dynamic system the dynamic programming algorithm solves for the components of the unknown forces in the time domain, recursively. The recursion relies on the availability of recursion formulae, derived by assuming a certain relationship between the measured and reconstructed data, i.e. an observation equation. The observation equation used in the classic formulation can be written as follows for an arbitrary time step k

$$\mathbf{d}_\mathrm{k} \simeq \mathbf{Q}\mathbf{x}_\mathrm{k} \tag{1}$$

where $\mathbf{d}_\mathrm{k}$ signifies the measurement data at time step k. Since the state vector $\mathbf{x}$ contains only displacements and velocities the observation equation assumes that the data is either displacements, velocities or combinations thereof such as strains.

B. Adapted algorithm

Relying on the same theory used to obtain the original recursion formulae, new recursion formulae are derived for a more general observation equation

$$\mathbf{d}(\mathbf{t}) \simeq \mathbf{S}_\mathrm{a}\ddot{\mathbf{u}}(\mathbf{t}) + \mathbf{S}_\mathrm{v}\dot{\mathbf{u}}(\mathbf{t}) + \mathbf{S}_\mathrm{d}\mathbf{u}(\mathbf{t}) \tag{2}$$

where $\mathbf{S}_\mathrm{a}$, $\mathbf{S}_\mathrm{v}$ and $\mathbf{S}_\mathrm{d}$ are selection matrices for acceleration, velocity and displacement, respectively, in which the locations of the measurements and/or difference relations can be specified. A more versatile dynamic programming algorithm is thus developed, bringing with it advantages related to identifying the unknown forces using acceleration as opposed to strain or displacement data.

III. Numerical examples

The advantages of using acceleration measurements are illustrated by means of a numerical example. The bridge is modelled as a simply supported beam and the moving forces are generated using a 4-DOF model of a moving vehicle and an assumed vehicle speed and wavelength for the road unevenness. To represent measurement error white noise is added to the computed response of the system.

IV. Conclusions

The adapted dynamic programming algorithm is shown to be an effective alternative to the classic formulation, bringing with it the gains connected to performing the identification using acceleration as opposed to displacement or strain data.

Acknowledgments

The research presented in this article has been performed within the framework of the project OT-05-41 "A generic methodology for inverse modelling of dynamic problems in civil and environmental engineering". This project is funded by the Research Council of the K.U. Leuven. Their financial support is gratefully acknowledged.

References

[1] S.S. Law, T.H.T. Chan, *Moving force identification: a time domain method*, Journal of Sound and Vibration, Vol. 201, pp. 1-22, 1997.
[2] S.S. Law, T.H.T. Chan, Q.H. Zeng, *Moving force identification: a frequency and time domain analysis*, Journal of dynamic systems, measurement and control, Vol. 121, pp. 394-401, 1999.
[3] T.H.T. Chan, S.S. Law, T.H. Yung, *An interpretive method for moving force identification*, Journal of Sound and Vibration, Vol. 219, pp. 503-524, 1999.
[4] D.M. Trujillo, H.R. Busby, *Practical inverse analysis in engineering*, CRC Press LLC, 1997.
[5] S.S. Law, Y.L. Fang, *Moving force identification: optimal state estimation approach*, Journal of Sound and Vibration, Vol. 239, pp. 233-254, 2001.

Proceedings of the 8th National Congress on Theoretical and Applied Mechanics, May 28-29, Brussels, Belgium.

The buckling behaviour of steel cylinders with engaged columns

Wesley Vanlaere, Delphine Sonck, Dieter Callewaert, Rudy Van Impe, Guy Lagae
Laboratory for Research on Structural Models, Ghent University
Technologiepark-Zwijnaarde 904 – 9052 Zwijnaarde
email: Wesley.Vanlaere@UGent.be, Delphine.Sonck@UGent.be, Dieter.Callewaert@UGent.be, Rudy.VanImpe@UGent.be, Guy. Lagae@UGent.be

Abstract: **The structural behaviour of steel cylinders with engaged columns is studied in this contribution. If a cylinder is placed on local supports, elevated compressive stresses in the cylindrical wall near the supports can lead to local instability and the failure of the entire structure. In order to solve this problem, engaged support columns attached to the shell wall can lead to a smoother introduction of the load in the shell. The behaviour of these cylinders with engaged columns is studied by performing different types of numerical analyses. The effect of geometric nonlinearity, plasticity and geometric imperfections is studied. The results show that especially the imperfections lead to an important reduction of the failure load of the cylinder.**

Keywords: **Cylindrical shells, Buckling, Numerical simulations**

I. Introduction

Steel silo's often rest on a limited number of support columns, in order to facilitate emptying operations. The presence of these local supports leads to stress concentrations in the cylindrical wall just above the supports. Since we are dealing with thin-walled steel structures, the presence of these elevated compressive stresses can lead to the instability of the shell wall and therefore to the failure of the entire structure.

The past decades, a lot of attention has been given to this problem and multiple solutions have been proposed (Fig. 1). A first solution is to increase the wall thickness of the entire cylinder to reduce the compressive stresses (Fig. 1a). This was investigated by Guggenberger et al. [1]. However, this means that additional material is also used in parts of the cylinder where the stresses are not elevated. Since the high stresses only appear in the lower part of the cylinder, an improvement can be made by increasing only the wall thickness of a bottom course [2] (Fig. 1b). Nevertheless, also in this solution material is placed in areas where the stresses are low, i.e. in the part of the cylindrical wall between the supports.

A further reduction of the cost price can be achieved by adding the additional material as stiffeners (Fig. 1c). Above each support longitudinal stiffeners of limited length can be placed in combination with a ring stiffener at the bottom of the cylinder and a ring stiffener above the longitudinal stiffeners [3]. These stiffeners lead to a cost efficient design for larger silo's.

In practice however, for smaller silo structures the solution is often to support them on engaged columns attached to the side of the shell (Fig. 2). These engaged columns cause a gentler introduction of the load into the cylindrical shell and therefore the stress distribution above the column terminations is somewhat smoothened. Very few investigations of the structural behaviour or the strength of such an arrangement have ever been made [4].

In this paper, the structural behaviour of cylinders with engaged columns is investigated and results are presented.

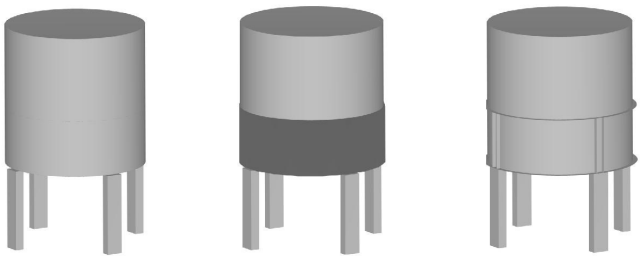

Fig. 1. Different solutions to the stability problem.

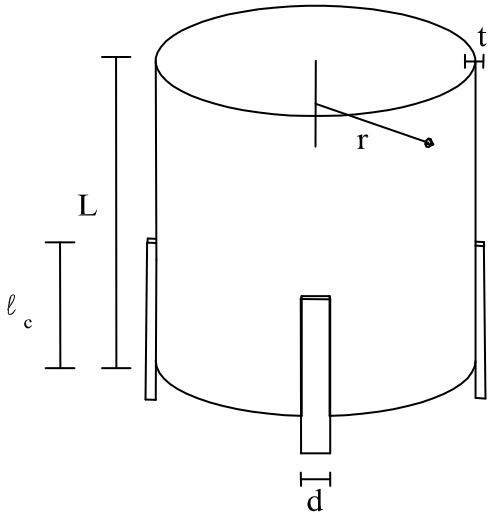

Fig. 2. A cylinder with engaged columns.

II. Numerical Simulations

A. The Numerical Model

The structural behaviour of steel cylinders with engaged columns is investigated by performing numerical simulations with the finite element package ABAQUS. In this paper, the results for only one geometry are given. The cylinder geometry is characterised by a radius to thickness ratio *r/t* equal to 500 and a length to radius ratio *L/r* of 2. The cylinder

rests on 4 columns. The column is attached to the cylinder wall over 1/4th of the cylinder length (L/ℓ_c = 4). The width of the support columns is equal to 0,1429 times the cylinder radius (d/r = 0,1429). The radius of the cylinder is taken equal to 350 mm as this is the size of the scale model that is tested in an experiment.

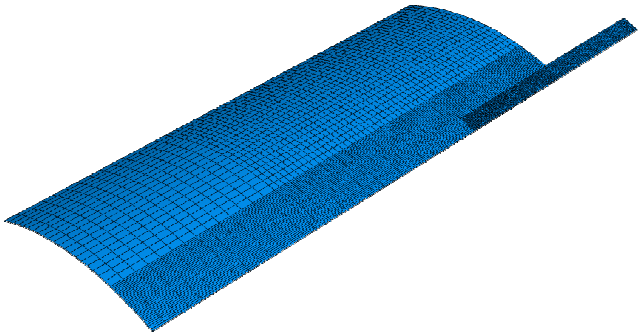

Fig. 3. The numerical model of the cylinder with engaged columns.

For this geometry, a numerical model is made. The cylinder and the engaged support columns are included in the model, but in order to reduce the computational time the symmetry of the geometry is taken into account and only a segment of 45° in circumferential direction is included in the model. This means that 1/8th of the cylinder and half of a support column are included. Symmetry boundary conditions are applied on the longitudinal edges of the model. For the top and bottom of the cylinder, the boundary condition restrain the radial displacements. Shell elements (S8R5) are used for the cylinder. The cylinder is compressed by means of a uniform line load at the top of the cylinder.

In order to be able to focus on the behaviour of the cylinder, the engaged columns are assumed to be flexurally and axially rigid. For that purpose, the columns are modelled with rigid elements (R3D4). The boundary conditions model a clamped column.

The numerical model is shown in Fig. 3. In this figure, the mesh of the model is also given. As can be seen, the mesh is denser in the region near the support, since the elevated stresses as well as the buckles are expected in this area of the model.

The material properties in the numerical model include a Young's modulus E of 200 GPa, a Poisson's ratio ν of 0,3 and for the analyses with nonlinear material behaviour a yield stress σ_y of 250 MPa. For this nonlinear material behaviour, a bilinear stress-strain relationship was assumed.

B.The Different Types of Analyses

In EN 1993-1-6 [5], different types of analyses are listed. The most relevant analyses for this paper are:

- Linear elastic bifurcation analysis (LBA). This is an eigenvalue analysis.
- Geometrically nonlinear analysis (GNA). This analysis uses a large displacement theory with elastic material behaviour.
- Materially nonlinear analysis (MNA). This analysis uses a small displacement theory with plastic material behaviour.
- Geometrically and materially nonlinear analysis (GMNA). This analysis uses a large displacement theory and plastic material behaviour.
- Geometrically and materially nonlinear analysis with imperfections (GMNIA). This analysis uses a large displacement theory, plastic material behaviour and geometric imperfections are explicitly included.

C.Results of the Analyses

With the different analysis types, an assessment can be made of the importance of different effects, like geometrical nonlinearity, plasticity and the presence of imperfections for this cylinder with engaged columns [6]. The results of the different analyses are summarised in Table 1.

The first numerical simulation is an eigenvalue analysis (LBA). The first eigenvalue found with this analysis leads to a prediction of the failure load of the entire cylinder equal to 150,2 kN. This theoretical failure is accompanied by the failure pattern shown in Fig. 4, i.e. the first eigenmode. As can be expected, this eigenmode is characterised by buckles in the cylinder above the column terminations. This is of course the region where the stresses are elevated.

TABLE I

RESULTS OF THE NUMERICAL SIMULATIONS

Analysis	Failure load [kN]
LBA	150,2
GNA	110,3
MNA	177,0
GMNA	105,2
GMNIA	
first eigenmode	73,0
weld depression	58,2

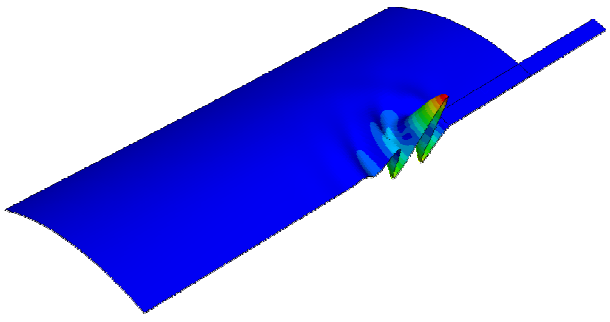

Fig. 4. The first eigenmode of the cylinder with engaged columns.

When a large displacement theory is used (GNA), the geometrical nonlinearity reduces the predicted failure load to 110,3 kN. This means a reduction of more than 25%. Also for this analysis, the location of the buckles is above the column terminations, but higher than for the LBA analysis (Fig. 5).

When a small displacement theory is used, but plasticity is taken into account (MNA), the numerical simulation predicts a

plastic collapse at a load of 177,0 kN. This load can be compared to the maximum theoretical plastic load:

$$F_{pl} = \sigma_y \cdot t \cdot 8 \cdot \left(\frac{2}{\sqrt{3}} \cdot \frac{d}{2} + \frac{1}{\sqrt{3}} \cdot \ell_c \right) = 181,9 kN \qquad (1)$$

This collapse load corresponds to a simple theoretical calculation of full plasticity around the engaged column. Apparently, the result of the numerical simulation corresponds well to the theoretical value. The failure pattern found in the simulation is shown in Fig. 6. Again, the largest deformations appear above the column termination.

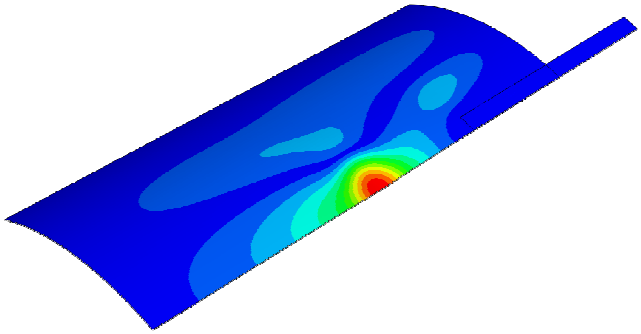

Fig. 5. The deformation pattern of the GNA.

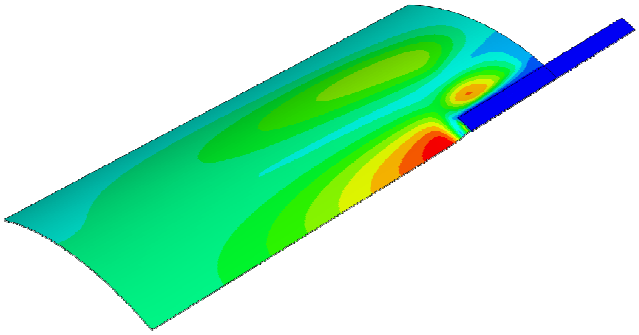

Fig. 6. The deformation pattern of the MNA.

For the next analysis that was performed, a large displacement theory was used in combination with nonlinear material behaviour (GMNA). In this analysis, a failure load equal to 105,2 kN was found. This is a lower value than the failure load corresponding to a GNA analysis. This means that the plasticity has a detrimental effect on the failure load. This is perhaps a bit unexpected since the result of the MNA is significantly higher than the GNA, suggesting that elastic instability occurs before plasticity can play a role. However, since we are dealing with stress concentrations above the column terminations, local yielding will appear before the full plastic capacity of the structure is utilised. The failure pattern for the GMNA is given in Fig. 7. The failure pattern is similar to the one for the GNA analysis although the buckle appears closer to the column termination.

The last performed analysis type is an analysis based on a large displacement theory, nonlinear material behaviour and taking into account geometric imperfections. The amplitude of the imperfections Δw_0 is taken equal to one wall thickness. Two types of imperfections were investigated: an imperfection with the shape of the first eigenmode (Fig. 4) and an axisymmetric weld depression, which is a realistic shape of the shell wall near a weld. More information on this shape is given in Section III and Fig. 8.

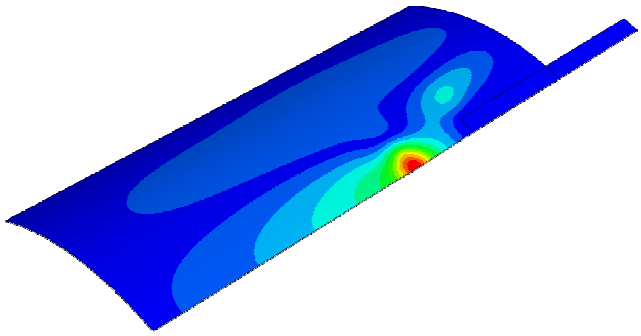

Fig. 7. The deformation pattern of the GMNA.

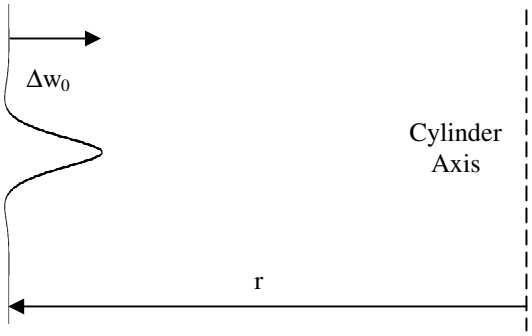

Fig. 8. The shape of a weld depression.

The results in Table 1 show that the presence of imperfections leads to a further important reduction of the carrying capacity of the structure. The presence of an imperfection with the shape of the first eigenmode leads to a further reduction of the failure load of 30%. The situation is even worse if the weld depression is included. This imperfection shape leads to an additional reduction of the failure load of almost 45%.

The corresponding failure patterns are given in Fig. 9 and Fig. 10. Both failure patterns are characterised by buckles above the column termination. If the weld depression is used as imperfection shape, the buckle is located somewhat higher, but this is caused by the location of the axisymmetric imperfection. More information is given in Section III.

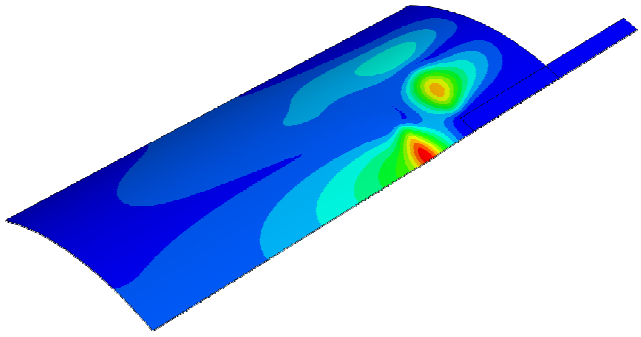

Fig. 9. The deformation pattern of the GMNIA with the first eigenmode as imperfection shape.

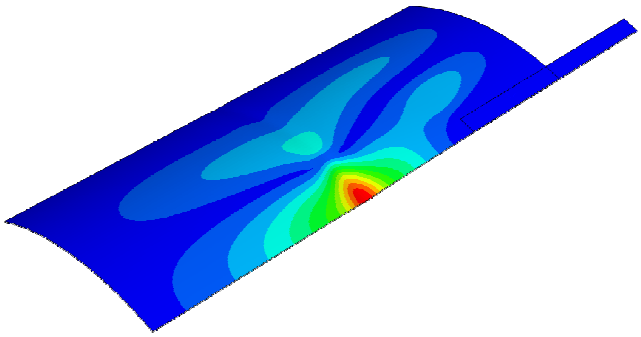

Fig. 10. The deformation pattern of the GMNIA with a weld depression as imperfection shape.

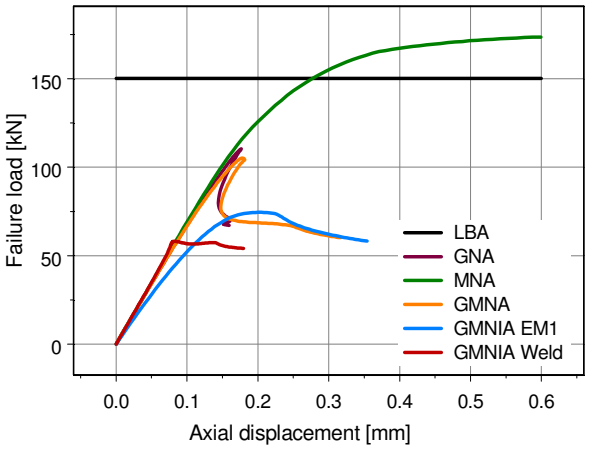

Fig. 11. Load-displacement curves for the different analyses.

For the different analyses types, the corresponding load-displacement curves are given in Fig. 11. The graph shows that for the analyses with geometric nonlinearity a sudden decrease in the load appears when the shell buckles if no geometric imperfections are included in the analyses. If the imperfections – eigenmode 1 (EM1) or a weld depression (Weld) – are included, the load-displacement curves still exhibit a maximum but the decrease is not so pronounced.

III. Weld Depression

For thin-walled shell structures, the presence of geometrical imperfections can lead to a dramatic reduction of the buckling strength. Therefore, when performing numerical simulations to investigate the structural behaviour of these structures, it is necessary to include these imperfections in the simulations. Furthermore, for the development of a design rule or for the design of a shell structure, it is important to study different shapes of imperfections and to choose the most appropriate shape to include in the simulations.

A possible approach is to include a realistic imperfection pattern in the finite element model. An example of such an imperfection is the deviation of the perfect shell that is caused by welding different strakes together. This weld depression (Fig. 8) was studied by Rotter and Teng and a Type A weld depression is defined by [7]:

$$\Delta w = \Delta w_0 \cdot e^{-(\pi x/\lambda)} \cdot \left(\cos \frac{\pi \cdot x}{\lambda} + \sin \frac{\pi \cdot x}{\lambda} \right) \qquad (2)$$

in which λ is the linear half-wavelength of meridional bending, x is the axial distance from the weld centre, Δw is the deviation from the nominal radius and Δw_0 is the amplitude of the imperfection. The linear bending half-wavelength is defined by:

$$\lambda = \frac{\pi}{\left[3 \cdot \left(1 - \nu^2\right)\right]^{1/4}} \cdot \sqrt{r \cdot t} \simeq 2,44 \cdot \sqrt{r \cdot t} \qquad (3)$$

The effect of such a weld depression was studied by performing different GMNIA simulations with an imperfection amplitude equal to one wall thickness. The location of the centre of the weld depression was varied between the column termination and the top of the cylinder. The results of these simulations are presented in Fig. 12. This graph shows that the most detrimental effect is obtained if the axial coordinate of the centre of the weld depression is equal to 2,1 ℓ_c . Clearly if the weld is too close to the column termination, the rigid column reduces the drop in failure load. If the weld is located too far from the column termination, it is located in an area with reduced stresses and has therefore not such a detrimental effect. The value of 2,1 ℓ_c can be explained with the deformation pattern of the GNA as in this deformation pattern (Fig. 5), the elastic buckle is located at 2,0 ℓ_c.

In Fig. 10, the deformation pattern for a GMNIA analysis with a weld depression at 2,1 ℓ_c is shown. The buckle appears at the location of the weld.

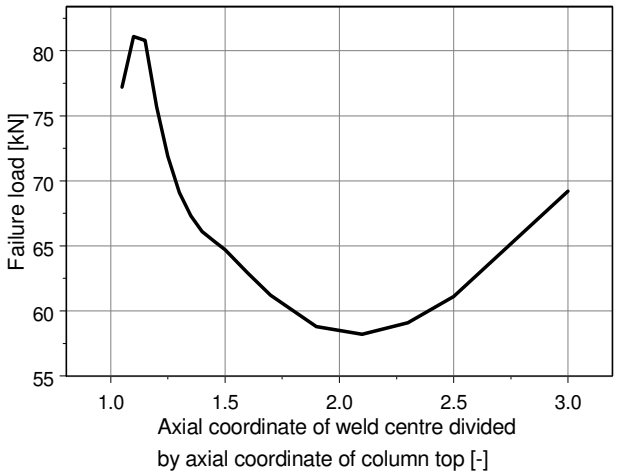

Fig. 12. The effect of the location of the weld depression on the failure load of the GMNIA analysis.

IV. Imperfection Sensitivity

A. General

In all the previous GMNIA analyses, the amplitude of the imperfection is taken equal to one wall thickness. In [5] values are given for the amplitude of equivalent geometric imperfections based on the dimensions of the shell and the appropriate quality class. These amplitudes can be larger or smaller than one wall thickness. Therefore, the effect of the amplitude of the imperfection is studied here for the cylinders on engaged columns with the two different imperfection shapes.

B.Eigenmode

The dimensionless amplitude of the imperfection with the shape of an eigenmode is varied between $\Delta w_0/t$ = -1,5 and $\Delta w_0/t$ = 1,5. A positive amplitude corresponds to the orientation of the dimples and buckles as given in Fig. 4. The results of the GMNIA analyses are given in Fig. 13. This graphs clearly shows that even with a small amplitude the imperfection leads to an important reduction of the failure load ($\Delta w_0/t$ = ±0,2 leads to a reduction of 25%). A further increase of the imperfection amplitude has a less detrimental effect: for the positive values of the amplitude the reduction of the failure load stays constant at 30%. For the negative amplitudes a further increase of the amplitude leads to a mild decrease of the failure load. All the performed GMNIA analyses led to a failure pattern similar to the one in Fig. 9.

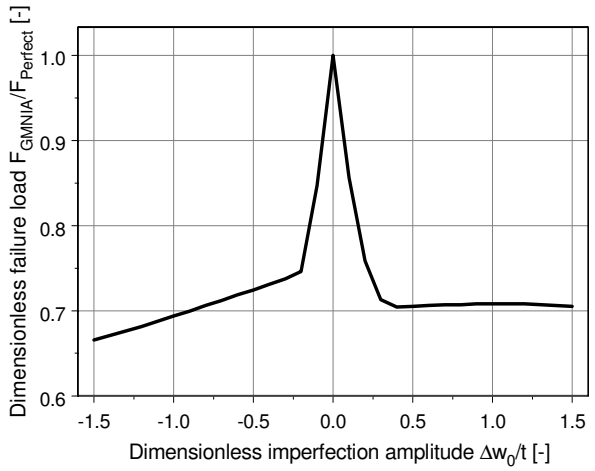

Fig. 13. Sensitivity of the failure load to the amplitude of the geometric imperfection with the shape of the first eigenmode.

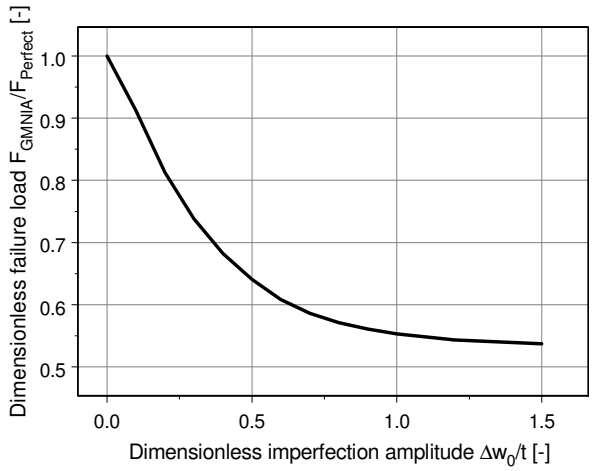

Fig. 14. Sensitivity of the failure load to the amplitude of the weld depression located at 2,1 ℓ_c.

C.Weld Depression

Also for the weld depression with the centre located at 2,1 ℓ_c, the dimensionless amplitude is varied. However, since welding only leads to a local reduction of the shell radius, the dimensionless amplitude is varied between $\Delta w_0/t$ = 0 and $\Delta w_0/t$ = 1,5. The results of the GMNIA analyses are summarised in Fig. 14. The smooth curve in Fig. 14 is steep for small imperfection amplitudes ($\Delta w_0/t$ = 0,2 leads to a reduction of 20%) and flattens out for larger amplitudes. However, for these larger amplitudes, the effect of a weld depression is more detrimental than the effect of an eigenmode as imperfection shape. Also for the weld depression, all the analyses had a deformation pattern similar to the one in Fig. 10, i.e. a pattern that is characterised by a dimple at the location of the weld depression.

V.CONCLUSIONS

In this contribution, the results of an initial study regarding the structural behaviour of cylindrical shells supported by engaged columns are investigated. The columns are assumed to be flexurally and axially rigid. The results of different types of analyses are given and the influence of different effects as geometric nonlinearity, plasticity and imperfections are studied. Clearly all these effects have to be included in the numerical simulation if the failure load of the structures is determined. Especially the imperfections have a detrimental effect on the stability of the cylinders. Different imperfection shapes and imperfection amplitudes have been investigated. It is the goal of our study to develop a design rule in accordance with the framework of the Eurocode [5]. Therefore, the next step in our investigations is to derive capacity curves for the cylinders with engaged columns based on numerical simulations of cylinders with different geometries.

ACKNOWLEDGEMENTS

The first author is a Postdoctoral Fellow of the Research Foundation – Flanders (FWO). Therefore, the authors would like to express their gratitude for the financial support of the FWO.

REFERENCES

[1] W. Guggenberger, R. Greiner, J.M. Rotter, *The behaviour of locally-supported cylindrical shells: unstiffened shells*, Journal of Constructional Steel Research, Vol. 56, 2000, 175-197.

[2] W. Guggenberger, R. Greiner, J.M. Rotter, *Cylindrical shells above local supports*, In: Buckling of Thin Metal Shells, London: Spon Press, 2004, 88-128.

[3] W. Vanlaere, *Plooigedrag van verstijfde cilinders op lokale steunpunten,* PhD thesis (in Dutch), Ghent University, Belgium, 2006.

[4] Y. Zhaoa, J. Yua, *Stability behavior of column-supported steel silos with engaged columns*, Proceedings of the Fourth International Conference on Advances in Steel Structures, Shanghai, 2005, 1521-1526.

[5] EN 1993-1-6, *Eurocode 3: Design of Steel Structures – Part 1-6: Strength and Stability of Shell Structures*, CEN, Brussels, 2007.

[6] ECCS TC8 TWG 8.4 Shells, *Buckling of Steel Shells – European Design Recommendations*, 5th Edition, 2008.

[7] J.M. Rotter, *Cylindrical shells under axial compression*, In: Buckling of Thin Metal Shells, London: Spon Press, 2004, 42-87.

[8] J.M. Rotter, *Shell Buckling and Collapse Analysis for Structural Design – The New Framework of the European Standard*, In: Festschrift for Professor Chris Calladine, Cambridge, 2002.

Proceedings of the 8th National Congress on Theoretical and Applied Mechanics, May 28-29, Brussels, Belgium.

Global size and shape optimization of trusses

Saartje Arnout, Geert Lombaert, Guido De Roeck
Department of Civil Engineering, K.U.Leuven,
Kasteelpark Arenberg 40, B-3001 Leuven, Belgium
email: saartje.arnout@bwk.kuleuven.be

Abstract— **In this paper, a double loop optimization procedure is presented for the combination of size and shape optimization of truss structures. In the outer loop, the shape design variables are optimized. Each step in this shape optimization contains a complete size optimization, so optimal bar sections are used for every proposed shape. The size optimization in the inner loop is performed with a local, gradient-based optimization method. The shape optimization problem is shown to have multiple local minima. Two global optimization methods are compared and their effectiveness is evaluated. A simple truss configuration is used to demonstrate the procedure. It is investigated how the shape parametrization affects the optimization efficiency.**

Keywords— **truss optimization, global optimization, coupled local minimizers, genetic algorithms**

I. Introduction

IN modern architecture, there is a tendency towards complex structures. These structures are frequently constructed with discrete members such as trusses or Vierendeel girders. Within the frame of the current research, the structural optimization of trusses is considered in this paper.

The truss optimization problem can be stated in many ways. In general, the volume is used as a measure of the cost of the truss structure. Since this objective function neglects all construction related costs, Kripakaran [1] proposes a realistic objective function, including a term depending on the number of different products in the structure. A wide variety of constraints can be imposed to ensure a usable result. Examples are a minimal serviceability [2] or aesthetical constraints about the shape of the truss [3]. In this paper, both displacements and stresses are constrained for one load case. Buckling of bars in compression is avoided by reducing the maximal stress for these members, as done by Pedersen [2].

To minimize the cost, structural optimization is used to change the size, shape and topology of the truss structure. In size optimization, the sections of the bars are optimized. In shape optimization, the location of the joints is changed. Topology optimization decides wether a bar should be included in the structure or not. However, these three types of changes are not independent. The optimal bar sections are, for example, strongly related to the shape and topology of a structure [4], [5], [6]. In this paper, the topology of the truss is assumed to be fixed. A double loop optimization procedure is proposed to combine shape and size optimization: for every proposed shape, the optimal bar sections are used. The size optimization is not based on fully stressed design as in [4], [6], it is a complete optimization until convergence.

In this paper, it is an aim to locate the global minimum of the structural optimization problem. However, the use of a local optimization algorithm is justified for the sizing optimization. When a local method is used for the shape optimization however, multiple local minima occur. The number of local minima is strongly dependent on the parametrization of the shape of the truss. Two global optimization methods are used to avoid suboptimal results. The first method is the method of the Coupled Local Minimizers (CLM) [7], [8]. In this method, the information of several local optimizers is combined to avoid local optima. The use of gradient information by the local optimizers enforces faster convergence. However, the calculation of gradients is expected to be rather cumbersome due to the optimization in each function evaluation. Therefore, genetic algorithms [9] are a valuable alternative for the outer optimization loop. The influence of the shape parametrization on the efficiency of both methods is considered.

II. Truss size and shape optimization

A. Problem statement

In general, the truss size optimization problem is stated as:

$$\min_{\mathbf{A}} V(\mathbf{A}) \qquad \text{s.t.} \qquad \begin{array}{rcl} \mathbf{A}_l & \leqslant \mathbf{A} \leqslant & \mathbf{A}_u \\ \mathbf{u}(\mathbf{A}) & \leqslant & \mathbf{u}_{\max} \\ \sigma(\mathbf{A}) & \leqslant & \sigma_{\max} \end{array} \tag{1}$$

with $\mathbf{A}$ a vector containing the bar sections to design. To reduce the number of design variables, the bars can be divided in groups with the same section. This grouping can be dynamic during optimization [1]. V is the volume of the structure, as the aim of the optimization is to minimize the material use. The vector $\mathbf{u}$ collects the displacements of the nodes of the truss. The displacements are constrained by $\mathbf{u}_{\max}$, typically L/300 for a span L. The vector σ contains the stresses in the bars of the truss. The stress is constrained by $\sigma_{\max}$, which is typically the yield stress of the

material divided by a safety factor. For bars in compression, the maximal stress is further reduced to avoid buckling. The displacements and stresses are computed with the finite element method.

The truss shape and size optimization problem is an extension of the size optimization problem:

$$\min_{\mathbf{A},\mathbf{x}} V(\mathbf{A},\mathbf{x}) \qquad \text{s.t.} \qquad \begin{array}{rcl} \mathbf{A}_l & \leqslant \mathbf{A} \leqslant & \mathbf{A}_u \\ \mathbf{x}_l & \leqslant \mathbf{x} \leqslant & \mathbf{x}_u \\ \mathbf{u}(\mathbf{A},\mathbf{x}) & \leqslant & \mathbf{u}_{\max} \\ \sigma(\mathbf{A},\mathbf{x}) & \leqslant & \sigma_{\max} \end{array} \tag{2}$$

The vector $\mathbf{x}$ defines the shape of the truss. This parametrization of the shape can be done in many ways. An obvious choice is to use the coordinates of each node as design variables. This choice maximizes the freedom of shape. Other choices can reduce the search space. To reduce the number of design variables, modelling techniques as described by Imam [10] can be used.

In literature, $\mathbf{A}$ and $\mathbf{x}$ are sometimes considered as independent design variables, e.g. by Pedersen [2]. However, optimal bar sizes exist for every shape, so $\mathbf{A}$ is defined implicitly by $\mathbf{x}$. In this view, the truss shape and size optimization problem can be reformulated as:

$$\min_{\mathbf{x}} V(\mathbf{A},\mathbf{x}) \quad \text{s.t.} \quad \begin{array}{rcl} \mathbf{A} & \text{from} & \text{eq. (1)} \\ \mathbf{x}_l & \leqslant \mathbf{x} \leqslant & \mathbf{x}_u \\ \mathbf{u}(\mathbf{A},\mathbf{x}) & \leqslant & \mathbf{u}_{\max} \\ \sigma(\mathbf{A},\mathbf{x}) & \leqslant & \sigma_{\max} \end{array} \tag{3}$$

In other words, to evaluate the objective and constraint functions for a current shape $\mathbf{x}$, it is necessary to perform a truss size optimization. This strategy results in the double loop procedure presented in figure 1. Each step in the shape optimization contains a complete size optimization. The outer loop is a shape optimization with respect to the shape design variables $\mathbf{x}$. The inner loop is the truss size optimization for each trial of $\mathbf{x}$, resulting in an optimal $\mathbf{A}$ for this trial.

B. Example

The problem under consideration is similar to the problems discussed by Gil [4]. A two dimensional truss with 17 nodes and 31 bars is considered, with a topology as presented in figure 2. Two hinges support the structure. In this example, there is only one load case: a unit load (1 kN) acting on node 10 to 16. However, this could easily be extended to a combination of multiple load cases as prescribed by Eurocode 1.

The truss is made of steel with a modulus of Young of 210 GPa and a Poisson coefficient of 0.3.

The objective function is the volume of the structure. A linear finite element analysis is performed to compute displacements and stresses. The maximal displacement is 32×10^{-3} m. This is guaranteed by limiting the largest displacement. The maximal stress is 235 MPa with a safety factor γ_M of 1.1. For bars in compression, the buckling length is computed and the maximal stress is reduced with a factor $\chi \leqslant 1$ according to Eurocode 3. The stress is constrained for each bar individually. In total, there are 32 constraints that have to be satisfied both in the inner and the outer optimization loop.

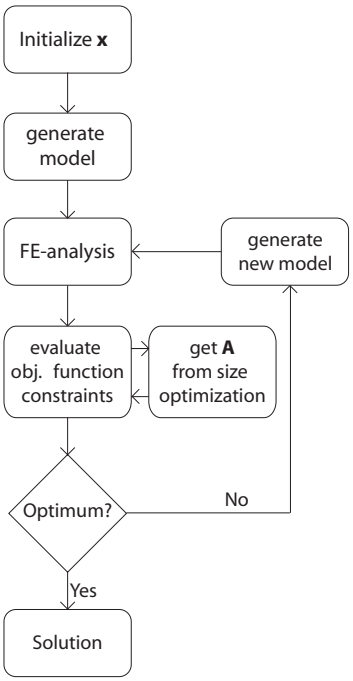

Fig. 1. Double loop to combine size and shape optimization.

III. Inner loop size optimization

A. Optimization method

The size optimization, as presented in Eq. (1), will be performed using a deterministic local optimization algorithm. An SQP method with BFGS-updates for the Hessian is chosen. An active-set strategy is used to account for the constraints. This is implemented in MATLAB's `fmincon`.

The use of a local optimization algorithm is assumed to be acceptable as it is expected that the local optimization will end at the global minimum or at least close to it. In fact, the objective function is linear in the design variables. If the optimization is started with the lower bound of the bar sections $\mathbf{A}_l$, there is a large chance that the nearest minimum will be the global minimum. This assumption is advantageous because this optimization will be carried out a lot of times, so the calculation time is very important. Moreover, it is important that the result is uniquely defined, so no stochastic operators can be used to find the

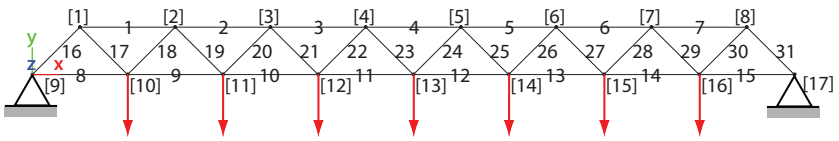

Fig. 2. Topology of the considered truss structure with [node] and element numbers.

global minimum.

B. Calculating sensitivity

The gradient of the objective function is easy to obtain, as the volume is linear in the design variables. In addition, the gradients of all constraints are used by the optimization method. The most general way to obtain this information is the *overall finite difference* method (OFD). This is a very simple method, based on the perturbation of the design variables. Unfortunately, OFD is time consuming if there are a lot of variables. Moreover, the perturbation must be carefully chosen to get accurate results [11]. To overcome these difficulties, the *adjoint variable method* is used, which is a specialized method for structural sensitivities [12]. This method is based on the differentiation of the discrete equations of equilibrium with respect to the design variables. As a result, the gradient calculations are reformulated as the computation of displacements due to additional load cases on the original structure. For the total gradient, one additional load case is needed for each constraint function. These load cases can be solved all at once, as they all act on the same structure. If the exact derivative of the stiffness matrix can be provided, the exact gradient is obtained, which is very advantageous, but requires access to the finite element code. This is generally considered as a disadvantage. In this paper, the MATLAB finite element toolbox StaBIL was used, which is developed at the Structural Mechanics division of the K.U.Leuven.

C. Example

The problem of the inner size optimization loop of the example can be written as (see Eq. (1)):

$$\min_{\mathbf{A}} V(\mathbf{A}) \quad \text{s.t.} \quad \begin{array}{rcl} 0.05\ 10^{-3}\ \text{m}^2 \leqslant \mathbf{A} & \leqslant & 500\ 10^{-3}\ \text{m}^2 \\ \sigma(\mathbf{A}) & \leqslant & \frac{235\chi}{\gamma_M}\ \text{MPa} \\ \mathbf{u}(\mathbf{A}) & \leqslant & 32\ 10^{-3}\ \text{m} \end{array} \tag{4}$$

To decrease the number of sizing variables, the bars are gathered in seven groups with the same bar section. These groups are based on the stress distribution in the geometry of figure 2. The groups are not modified during optimization.

The optimal bar sections for a certain shape can be computed with the local optimization algorithm. As mentioned, the lower bound of the bar sections is used as a starting point. The optimal bar sections and volume for three shapes are presented in table I.

IV. Outer loop shape optimization

In this section, the outer loop shape optimization is considered. The objective function, i.e. the volume, is no longer linear in the design variables. Changing the shape can transform the structural behaviour, e.g. from a truss working as a beam to a truss working as an arch. Thanks to this transformed structural behaviour, the constraints can be satisfied with smaller bar sections. Contrarily, if the same change makes the bars longer, this compensates for the decrease of the volume. As a consequence, the objective function is expected to be irregular. Moreover, due to the optimization in each function evaluation, continuity is not guaranteed. This implies that the calculation of gradients is rather cumbersome. Furthermore, the number of variables can be large, depending on the shape parametrization.

A. Example

The optimization problem can be stated according to Eq. (3):

$$\min_{\mathbf{x}} V(\mathbf{A},\mathbf{x}) \quad \text{s.t.} \quad \begin{array}{rcl} \mathbf{A} \quad \text{from} & & \text{eq. (4)} \\ \mathbf{x}_l & \leqslant \mathbf{x} \leqslant & \mathbf{x}_u \\ \sigma(\mathbf{A},\mathbf{x}) & \leqslant & \frac{235\chi}{\gamma_M}\ \text{MPa} \\ \mathbf{u}(\mathbf{A},\mathbf{x}) & \leqslant & 32\ 10^{-3}\ \text{m} \end{array} \tag{5}$$

For the current load case, an arch-like structure is expected to be optimal, similar to [4]. Bars in compression are discouraged by the buckling constraint. As a consequence, an arch in tension will be more efficient than a pressure arch.

As mentioned, the design variables $\mathbf{x}$ should be chosen carefully. Using the x- and y-coordinate of every node as a design variable is an obvious choice that ensures maximal freedom of shape. If symmetry is used, this strategy totals to 15 design variables for the example. However, this choice results in a high-dimensional design space that is difficult to explore. Furthermore, the design space includes a lot of irregular and unwanted structures. These structures can be excluded by another choice of design variables. The distances in the x-direction between adjacent nodes are used as design variables to preserve the sequence of the nodes. The same strategy can be used in the

TABLE I
THE OPTIMAL BAR SECTIONS AND OBJECTIVE FUNCTION VALUE FOR THREE GIVEN SHAPES.

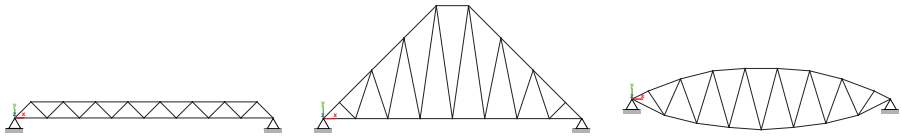

A(1) [10^{-3}m^2]	0.2283	0.2024	0.1708
A(2) [10^{-3}m^2]	0.2655	0.1705	0.1598
A(3) [10^{-3}m^2]	0.1928	0.0500	0.0500
A(4) [10^{-3}m^2]	0.0641	0.0529	0.0500
A(5) [10^{-3}m^2]	0.1033	0.1033	0.0910
A(6) [10^{-3}m^2]	0.0500	0.1624	0.0500
A(7) [10^{-3}m^2]	0.0500	0.0500	0.0500
Volume [10^{-3}m^3]	7.5730	10.9616	6.1050

y-direction to ensure the lower nodes remain located below the upper nodes. This strategy also sums up to 15 design variables. As the design space is smaller, optimization will be more efficient. Further on, this strategy will be called *distance modelling*.

A third option is to use global design variables that define the coordinates of the nodes instead of using these coordinates directly. In the current example, both the upper and lower array of nodes are assumed to be located on a curve. In this paper, two parabolic curves are used. The three points that define each parabola are the supports and a keypoint on the symmetry plane. Only the height of the keypoint is variable. An extra variable is added to define how the nodes are distributed over the parabola. Consequently, only three design variables are used. This strategy will be called *parabola modelling*. The number of design variables is reduced substantially. Moreover, the design variables have a more global influence on the shape. As a consequence, optimization will be faster and there will be less local minima. However, the freedom of shape is reduced considerably. Only parabolic shapes are generated during the optimization. For this example, it will turn out that the global minimum is not excluded. However, other choices (e.g. bilinear) result in suboptimal structures for this example. Nevertheless, the restricted freedom of shape can be intended to account for a designer's preference.

B. Local optimization

The local optimization algorithm can be applied immediately to the problem as stated in Eq. (5). The starting point is the second shape of table I. The algorithm takes very small steps and converges after 28 iterations with 551 function evaluations. The original shape and the result of the optimization are presented in the first row of table II. As can be seen, an arch strategy appears in the solution. However, this local optimum has a larger volume than the third structure of table I, so it is certainly not the global minimum. Other initial shapes and the respective result of local optimization are included in table II. It is clear that multiple local minima exist.

Additionally, some initial shapes and results with the parabola modelling are presented in table III. Some of the local minima in table II can not be reached with the parabola modeling. Due to the restriction of the search space, the number of local minima is decreased. As a consequence, the results of optimization are better than for the distance modelling. Optimization is also faster, as an optimum is found in 100 to 350 function evaluations, depending on the starting shape.

The optimality of a tension arch is confirmed by the computed local optima. By comparing the results of multiple initial shapes, additional assumptions can be made about the global minimum. The last two local optima of table II satisfy all constraints with all bars having the minimal section. The geometry with the shortest bars thus has the smallest volume. The best tension arch is the last optimum of table III. The height of the truss is degenerated. As there are no moments induced in the structure, a chain-like structure is indeed optimal for the given load case. The chain-like structures of table III are therefore considered to be the global optimum of this problem. This will be confirmed by the global optimization methods. A slightly different problem statement, e.g. with an extra asymmetrical load case, would have resulted in a different optimum.

C. Coupled local minimizers

The first global optimization method considered is the method of the Coupled Local Minimizers (CLM) [7], [8]. The theoretical formulation is derived for an objective function $f(\mathbf{x})$ with several minima [8]. Assume m constraints $g_j(\mathbf{x}) \leqslant 0$ should be satisfied. Consider a popula-

TABLE II

INITIAL GEOMETRIES (LEFT COLUMN) AND RESPECTIVE RESULT OF LOCAL OPTIMIZATION WITH DISTANCE MODELLING.

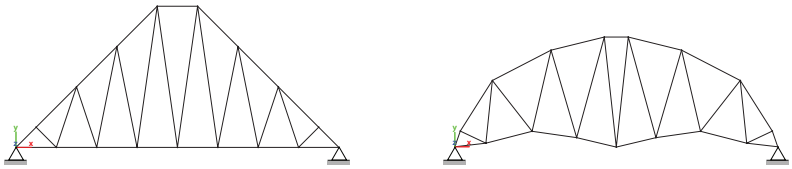

V=10.9616 10^{-3}m^3 → V=6.9259 10^{-3}m^3

V=6.1050 10^{-3}m^3 → V=4.7537 10^{-3}m^3

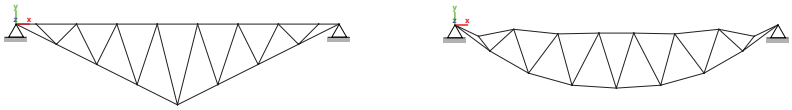

V=6.2970 10^{-3}m^3 → V=3.2617 10^{-3}m^3

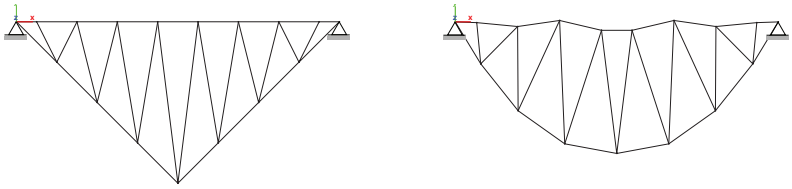

V=17.2692 10^{-3}m^3 → V=5.0855 10^{-3}m^3

TABLE III

INITIAL GEOMETRIES (LEFT COLUMN) AND RESPECTIVE RESULT OF LOCAL OPTIMIZATION WITH PARABOLA MODELLING.

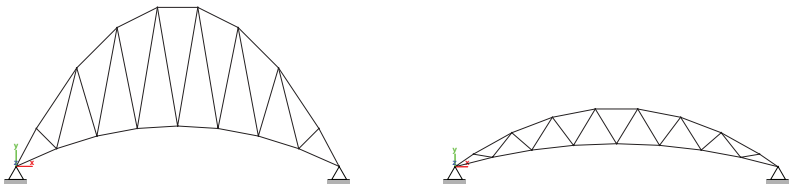

V=9.7021 10^{-3}m^3 → V=5.3835 10^{-3}m^3

V=3.4044 10^{-3}m^3 → V=2.3657 10^{-3}m^3

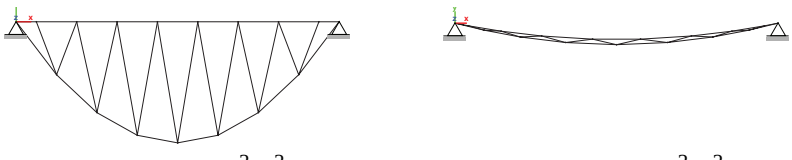

V=5.0718 10^{-3}m^3 → V=2.3633 10^{-3}m^3

tion of t search points. The searches of these points are coupled by using their average function value as the objective function:

$$\langle f \rangle = \frac{1}{t} \sum_{l=1}^{t} f(\mathbf{x}^{(l)}) \tag{6}$$

with $\mathbf{x}^{(l)}$ the l-th search point in the population. Moreover, synchronization constraints are imposed to the search points, to enforce them to end at the same point. This results in the following problem statement:

$$\min_{\mathcal{X}} \langle f \rangle \quad \text{with} \begin{cases} \mathbf{x}^{(l)} - \mathbf{x}^{(l+1)} = 0 & l = 1,2,\ldots,t \\ g_j(\mathbf{x}^{(l)}) \leqslant 0 & j = 1,\ldots,m \\ & l = 1,2,\ldots,t \end{cases} \tag{7}$$

with $\mathbf{x}^{(t+1)} = \mathbf{x}^{(1)}$. The vector $\mathcal{X} = [\mathbf{x}^{(1)} \ldots \mathbf{x}^{(t)}]^T$ gathers all the search points of the population.

The constrained optimization problem is transformed into an unconstrained problem using the augmented Lagrangian method. This method reformulates the objective function as:

$$\begin{aligned} \mathfrak{L}_A(\mathcal{X}, \Upsilon, \Lambda_{\text{ineq}}) &= \frac{\eta}{t} \sum_{l=1}^{t} f(\mathbf{x}^{(l)}) \\ &+ \sum_{l=1}^{t} [v^{(l)}]^T [\mathbf{x}^{(l)} - \mathbf{x}^{(l+1)}] + \frac{\gamma}{2} \sum_{l=1}^{t} \|\mathbf{x}^{(l)} - \mathbf{x}^{(l+1)}\|^2 \\ &+ \sum_{j=1}^{m} \sum_{l=1}^{t} \lambda_{\text{ineq},j}^{(l)} \alpha_j^{(l)} + \frac{\gamma_{\text{ineq}}}{2} \sum_{j=1}^{m} \sum_{l=1}^{t} (\alpha_j^{(l)})^2 \end{aligned} \tag{8}$$

In this expression, α_j is defined as:

$$\alpha_j^{(l)} = \max \left\{ g_j(\mathbf{x}^{(l)}), -\frac{\lambda_{ineq,j}^{(l)}}{\gamma} \right\} \tag{9}$$

The new objective function $\mathfrak{L}_A$ adds two terms per constraint to the average function value: a quadratic penalty term and a linear penalty term. The constants η, γ and γ_{ineq} are weighting factors of the objective function and the quadratic penalty terms. Their values have a large influence on the optimization process as they define the balance between exploration and exploitation. The weighting factors of the linear term are called Lagrange multipliers. The vector $\Upsilon = [v^{(1)} \ldots v^{(t)}]^T$ contains the Lagrange multipliers for the convergence constraints. The vector $\Lambda_{ineq} = [\lambda_{ineq,1}^{(1)}, \lambda_{ineq,2}^{(1)} \ldots \lambda_{ineq,m}^{(t)}]^T$ contains the Lagrange multipliers for the m inequality constraints. To evaluate this function, an evaluation of the original objective and constraint functions is needed for each search point. When calculating the gradient of this function, the gradient of the objective function and the constraints is computed for each search point with OFD. This implies an extra function evaluation for each design variable for each search point.

Augmented Lagrange methods are based on subsequent optimizations of $\mathfrak{L}_A$ with respect to $\mathcal{X}$ only. A trust region Newton method is used for such an optimization step. The Lagrange multipliers and the weighting factors are maintained constant during each optimization step. From one optimization step to the next, the Lagrange multipliers are updated. In this way, after k iterations, Υ_k will contain a reasonable estimate of the optimal Lagrange multipliers, and

$$\min_{\mathcal{X}} \mathfrak{L}_A(\mathcal{X}, \Upsilon_k, \Lambda_{\text{ineq},k}) \tag{10}$$

will result in the global minimum $\mathcal{X}^*$ of $\mathfrak{L}_A$.

If this method is applied to the example with the distance modelling, the optimization is laborious. Even with a small number search points, the calculation times are very high due to the large number of variables. The time needed to tune the parameters is proportionally high.

In contrary, using the parabola modelling, good results are found rather easily, thanks to the smaller search space. Three search points are used and $\eta = 500$, $\gamma = 0.1$ and $\gamma_{\text{ineq}} = 1$. During the first optimization of $\mathfrak{L}_A$ with respect to $\mathcal{X}$, the search points yet identify the best strategy, in this case a tension arch. As can be seen in figure 3, this strategy is adopted by each search point after the first optimization step. After this optimization step, the Lagrange multipliers are updated and a new optimization of $\mathfrak{L}_A$ is started. Within 18 such iterations of optimization and updating, using about 4000 function evaluations, the algorithm converges to three near-optimal structures, equivalent to the best local optimization result. Figure 3 presents the three search points after the first, second, third and last optimization step.

D. Genetic algorithm

To avoid gradient calculation, a genetic algorithm (GA) is used [9]. The MATLAB Genetic Algorithm and Direct Search toolbox [13] is used as a base to develop a suitable algorithm. Some operators are customized. The general flowchart is presented in figure 4. First, N individuals are initialized randomly. Each individual defines a truss structure, equivalent to a search point in CLM. The fitness function consists of the volume and a logarithmic penalty term for each violated constraint. Selection is based on the fitness value of each individual, where the fitness values are first scaled linearly to decrease the influence of very fit individuals. Bad outliers are given a zero probability for selection. These measures preserve diversity in the population. Some of the selected individuals are combined with classical single point crossover. The remaining selected individuals undergo Gaussian mutation. In all operators, upper and lower bounds of $\mathbf{x}$ remain respected. A new generation is created until the convergence crite-

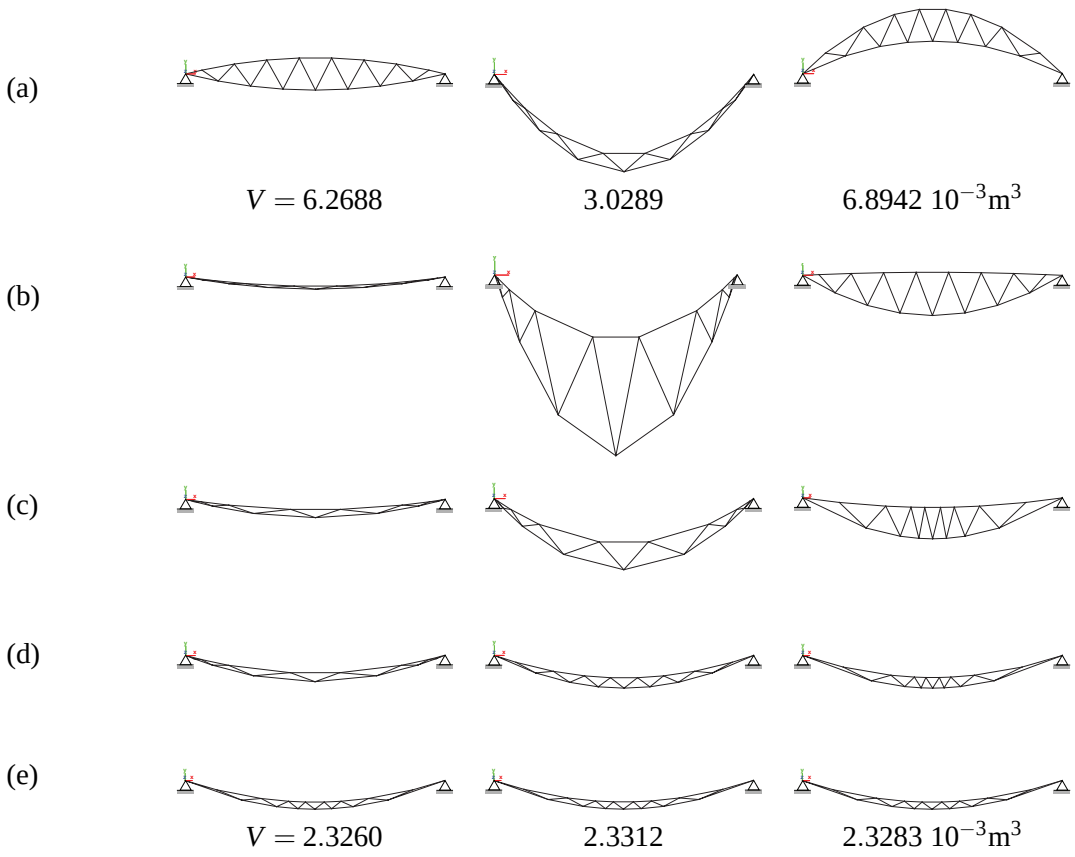

Fig. 3. Search points: (a) initial shapes and shapes after (b) the first, (c) second, (d) third and (e) last local optimization of $\mathfrak{L}_A$ with respect to x.

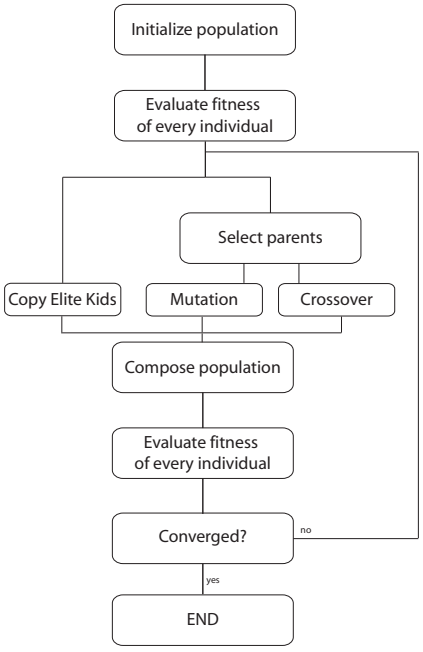

Fig. 4. Flowchart of the genetic algorithm.

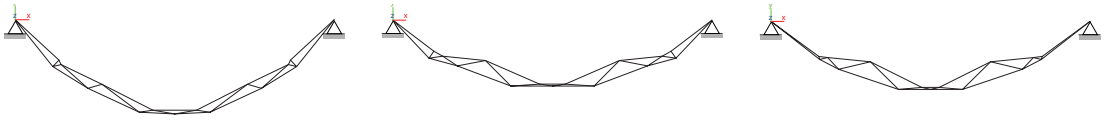

(a) $V = 2.674$ (b) 2.526 (c) 2.445 10^{-3}m^3

Fig. 5. Genetic algorithm: best individuals after (a) 300, (b) 600 and (c) 1000 generations with distance modelling.

(a) $V = 2.456$ (b) 2.355 (c) 2.338 10^{-3}m^3

Fig. 6. Genetic algorithm: best individuals after (a) 10, (b) 50 and (c) 300 generations with parabola modelling.

ria are met. This method is applied to the example with distance modelling. The population contains 40 individuals. The best individual after 300, 600 and 1000 generations is presented in Fig. 5. These individuals are all similar to the chain-like optimum of the local optimization, only obtained with parabola modelling before. The best individual after 1000 generations has only a slightly higher volume. For this example, an acceptable solution is thus found within 40000 function evaluations. Because the genetic algorithm explores the search space in a stochastic way, the parametric modelling of the shape is of even more importance. As the parameters of the parabola modelling have a global influence on the truss, the genetic operators are more meaningful. Moreover, the low number of design variables is a strong advantage. With the same population size as before, a very good individual is yet found in the tenth iteration. After 300 iterations, the best individual is equivalent to the best result of local optimization. The best individuals after 10, 50 and 300 generations are presented in figure 6. For this example, about 12000 function evaluations are used to find the optimum.

E. Evaluation

Local optimization showed that, as expected, the shape optimization outer loop can result in local minima. Therefore, global optimization methods are used: the method of the Coupled Local Minimizers (CLM) and a genetic algorithm (GA). In this paragraph, both global methods are compared to each other and to local optimization.

In contrast to CLM, no gradient information is accounted for in GA. However, the genetic algorithm is not consistently faster, as this information is not available to define a good search direction. In GA, the emphasis is on ranking the individuals. This is advantageous if an unwanted or impossible structure is proposed by the random search (e.g. two nodes on the same location). In that case, a large penalty term can be added which prevents the structure from being selected and an accurate evaluation of the objective function is avoided. In CLM, it is necessary to compute the gradient information exactly, even for irregular structures. Furthermore, intermediate results of GA are meaningful. Each generation can be considered as a group of interesting individuals. In CLM, intermediate results have less significance, because they are an intermediate trade off between exploration and exploitation terms. In addition, the number of parameters in a genetic algorithm is high, but none of them is crucial. However, the optimization can take long if the parameters are not tuned. In CLM, there are only three parameters but optimization can fail to locate the optimal region if they are not well chosen. It is concluded that CLM is faster but more demanding than GA.

It is observed that tuning a global optimization method is not trivial. CLM has three crucial parameters. In genetic algorithms, parameters are not as crucial but proper tuning can save a lot of time. In contrary, local optimization algorithms have no tuning parameters. In addition, it is observed that the number of function evaluations needed to find the global minimum is really high. In CLM, the number of search points must be high enough. At least 20000 function evaluations are needed. With a genetic algorithm, an acceptable solution was found after 40000 function evaluations. A local optimization algorithm uses for this example only about 550 function evaluations but with no guarantee of the global character of the optimum. However, the use of an alternative modelling increased the efficiency of the global optimization methods substantially. In that case, CLM uses 4000 function evaluations and the genetic algorithm finds a good solution in about 12000 function evaluations. The number of function evaluations in a local optimization are also reduced to 300. Additionally, the stochastic properties of GA must be considered. The results for one run are not necessarily representative for other runs. Nevertheless, for this rather simple example, a good assumption of the global minimum could be made by multi-start local optimization based on struc-

tural insight.

The observations encourage the development of a hybrid strategy: using a global method to locate good performing regions and subsequently using local algorithms to locate the exact minimum in these regions. In that strategy, a genetic algorithm could be preferred, as it is possible to find a diverse population of fit individuals. However, if the structural behaviour of the truss can be anticipated for, a manual exploration of the search space can be more efficient. Indeed, in the considered example, at least ten local optimizations can be done with the same resources as one global optimization.

V. Conclusions

In this paper, a double loop procedure is presented for size and shape optimization of truss structures where optimal bar sections are used for every proposed shape.

A local optimization is used for the size optimization in the inner loop. The use of the discrete method for gradient evaluations makes the optimization significantly faster. Therefore, a full optimization loop until convergence can be used.

When a local method is used for the outer loop, i.e. the shape optimization, however, multiple local minima are found. Global optimization methods are desirable to find the global optimum. The global methods considered locate the global minimum, but both tuning the solution parameters and solving the problem takes a lot of time. This encourages the use of a hybrid strategy. If the structural behaviour can be anticipated for, a multi-start local optimization might even be the most efficient.

A careful parametrization of the shape turns out to be very important. Modelling techniques can be used to reduce the number of design variables and to accelerate optimization. If the search space is significantly reduced, the global minimum can be excluded. In reality however, the limitation of the design space can correspond to the designer's preference and/or the feasibility of construction.

VI. Acknowledgements

The first author is a Ph.D. fellow of the Research Foundation - Flanders. The second author is a postdoctoral fellow of the Research Foundation - Flanders. The financial support is gratefully acknowledged.

References

[1] P. Kripakaran, A. Gupta, and J.W. Baugh Jr., "A novel optimization approach for minimum cost design," *Computers and Structures*, vol. 85, pp. 1782–1794, 2007.

[2] N.L. Pedersen and A.K. Nielsen, "Optimization of practical trusses with constraints on eigenfrequencies, displacements, stresses, and buckling," *Structural and Multidisciplinary Optimimization*, vol. 25, pp. 436–445, 2003.

[3] M. Ohsaki, N. Tsuneyoshi, and Y. Isshiki, "Shape-Size Optimization of Plane Trusses with Designer's Preference," *Journal of Structural Engineering, Proceedings of the ASCE*, vol. 124, no. 11, pp. 1323–1330, november 1998.

[4] L. Gil and A. Andreu, "Shape and cross-section optimisation of a truss structure," *Computers and Structures*, vol. 79, pp. 681–689, 2001.

[5] S. Rajeev and C.S. Krishnamoorthy, "Genetic algorithms-based methodologies for design optimization of trusses," *Journal of Structural Engineering, Proceedings of the ASCE*, vol. 123, no. 3, pp. 350–358, march 1997.

[6] D. Wang, W.H. Whang, and J.S. Jiang, "Combined shape and sizing optimization of truss structures," *Computational Mechanics*, vol. 29, pp. 307–312, 2002.

[7] J.A.K. Suykens, J. Vandewalle, and B. De Moor, "Intelligence and cooperative search by Coupled Local Minimizers," *International Journal of Bifurcation and Chaos*, vol. 11, no. 8, pp. 2133–2144, 2001.

[8] A. Teughels, G. De Roeck, and J.A.K. Suykens, "Global optimization by Coupled Local Minimizers and its application to FE model updating," *Computers and Structures*, vol. 81, no. 24-25, pp. 2337–2351, 2003.

[9] Z. Michalewicz, *Genetic Algorithms + Data Structures = Evolution Programs*, Springer, New York, USA, 1999.

[10] M.H. Imam, "Three-dimensional shape optimization," *International Journal for Numerical Methods in Engineering*, vol. 18, no. 5, pp. 661–673, 1982.

[11] J. Nocedal and S.J. Wright, *Numerical Optimization*, Springer, New York, USA, 1999.

[12] H. Eschenauer, N. Olhoff, and W. Schnell, *Applied structural mechanics: fundamentals of elasticity, load-bearing structures, structural optimization*, Springer, Berlin, 1997.

[13] The MathWorks, *MATLAB Genetic Algorithms and Direct Search Toolbox User's Guide*, 2008.

Proceedings of the 8th National Congress on Theoretical and Applied Mechanics, May 28-29, Brussels, Belgium.

Rate Dependent Moment-Curvature Relations for the Progressive Collapse Analysis of RC Structures

Berta Santafé[1], Thierry J. Massart[2], Philippe Bouillard[2], John Vantomme[1]
[1]Royal Military Academy - Civil and Materials Engineering Dept.
Renaissance Ave. 30, 1000 Brussels (Belgium)
[2]Université Libre de Bruxelles - Building, Architecture and Town Planning Dept. (BATir)
F.D. Roosevelt Ave. 50, CP 194/2, 1050 Brussels (Belgium)
email: bsantafe@rma.ac.be, thmassar@batir.ulb.ac.be, philippe.bouillard@ulb.ac.be, jvantomme@rma.ac.be

Abstract— **This contribution deals with the modeling of reinforced concrete structures in the context of progressive collapse simulations. Depending on the initial triggering event, the progressive collapse phenomenon may involve high strain rates in structural members. Since the behaviour of concrete is sensitive to the strain rate, a numerical representation of the strain rate effects on the material behaviour is needed. A Perzyna viscoplastic model is adopted to couple strain rate effects to the plastic response for both concrete and steel, leading to an increase in the flow properties with respect to the strain rate. The rate dependence in the elastic domain is also accounted for. The parameters of the constitutive laws for concrete and steel have been chosen in such a way that the dynamic increase factors (DIF) -i.e. the ratio of dynamic to static strength- obtained with the proposed constitutive models are in good agreement with the experimental results available in the literature. The introduction of these one-dimensional constitutive laws for concrete and steel in a perfectly-bonded layered beam model provides strain rate dependent relations between the bending moment and the curvature for given RC cross-sections. This multilevel approach is used to compare the structural response of a planar frame subjected to the loss of a vertical load bearing element using rate independent material laws with the one obtained through rate dependent ones.**

Keywords— **Progressive Collapse, RC structures, strain rate effects, viscoplastic model, layered beam**

I. Introduction

PROGRESSIVE Collapse is a situation in which a local failure in a structure leads through load redistribution to a widespread generalized damage to a disproportionate extent. For a wide range of triggering events, progressive collapse is a dynamic phenomenon involving high deformation rates. As a result, the overall response of the members or the entire structure is likely to entail dynamic effects, as well as nonlinear effects both geometrically and in the material response. Regarding this last type of effects, this contribution focuses on the need to take into account the rate dependence - i.e. viscous effects - in the material modeling.

Reinforced concrete structures subjected to high loading rates are expected to have a different response from the one observed when loaded statically. For instance, concrete shows a strongly rate dependent behaviour [1-4], with both compressive and tensile strengths increasing significantly with the strain rate. Experimental tests carried out by means of the Split Hopkinson Bar confirm this phenomenon [5,6]. Since progressive collapse strongly depends on stress redistribution, this material strain rate dependence may lead not only to a rate dependence in the local strength, but also to a different response of the complete structure. The aim of this contribution is to show that the strain rate dependence at the material level can have a significant effect in the structural behaviour, and particularly in the failure mode of reinforced concrete structures undergoing progressive collapse.

Different approaches dealing with the issue of progressive collapse simulation can be found in the literature. This paper aims at contributing to the one referred to as the "alternate load path" approach; one of the main design strategies which consists in considering stress redistribution in a structure after the loss of a vertical support element. The first contributions to this approach included simplified static approaches [7], often used in the context of a succession of elastic analyses. The United States Department of Defense (DoD) [8] and the General Services Administration (GSA) [9] suggest step-by-step procedures for linear static, non-linear static and non-linear dynamic analysis, although not all these procedures are described in detail. Later works [10-12] included static non-linear calculations accounting for dynamic inertial effects via load amplification factors. The DoD and GSA guidelines specify a dynamic amplification factor of 2 to be applied to the loads in order to account for dynamic effects in static computations, which has been proved to be highly conservative by some authors [12,13]. Some of these publications identified equivalent static pushover procedures, avoiding this safety margin considered to be excessively large.

As far as contributions in the framework of structural progressive collapse are concerned, viscous effects do not appear to be accounted for, except when numerical damping is introduced at the structural level. Here the viscous effects are directly deduced from the rate dependence at

the material level. With the aim of proving that material rate dependence plays an important role in a progressive collapse analysis, and thus cannot be neglected, this paper intends to give a tentative answer to the following questions: a) How can the strain rate effects be incorporated in a RC structure analysis?; b) Are these effects noticeable in the structural level?

To do so, numerical simulations on a reinforced concrete planar frame modeled with rate dependent beam elements will be carried out and discussed.

II. Rate Effects in the RC Constitutive Relations

A. Principles

It is by now well known that the mechanical properties of concrete strongly depend on the strain rate, especially in compression. Numerous experimental tests have been carried out [1-3] in order to quantify this phenomenon. The CEB (Comité Euro-International du Béton) provides analytical relations for the dynamic increase factors as a function of the strain rate [1]. The Young's modulus dependence on the strain rate is given as well. Later works from Malvar and Crawford [3] proposed a modified CEB formulation based on experimental data.

The most natural way to account for the rate effects in a material model is the introduction of viscous terms in the constitutive law. The viscoplastic model is often adopted in the context of concrete modeling under dynamic loads [14-17], mainly for the material modelling at the small scale. For instance, Pedersen et al. [14] developed a rate dependent macroscopic material model based on the microscopic and mesoscopic behaviour of concrete. As a complementary approach, straightforward one-dimensional constitutive laws for concrete and steel are used here, aiming at characterizing the rate dependence of reinforced concrete beam sections in a phenomenological way, in order to reflect these rate effects at the structural level.

The application of these constitutive models in the layers of a perfectly-bonded layered beam model allows to incorporate the rate dependence in the cross-sectional level. For instance, the integration of the rate dependent response of the layers along the cross section provides relations between the generalized strains (average axial strain $\bar{\varepsilon}$ and curvature χ) and generalized stresses (axial force N and bending moment M) as a function of the generalized strain rates ($\dot{\bar{\varepsilon}}$ and $\dot{\chi}$), in a Euler-Bernouilli beam formulation.

B. Material rate dependence for concrete and steel

A Perzyna type viscoplastic model [18,19] is adopted for the introduction of the strain rate effects in the plastic domain for both concrete and steel. This model uses a relationship between the overstress and the viscoplastic strain rate via the following expression:

$$\dot{\varepsilon}^{vp} = \frac{1}{\eta}\left(\frac{f}{|\bar{\sigma}_0|}\right)^N \frac{df}{d\sigma} \tag{1}$$

where η and N are viscosity parameters, with $N \geq 1$. Note that these parameters are here also dependent on the strain rate ($\dot{\varepsilon}$). $\bar{\sigma}_0$ is the initial yield stress -different in tension and compression in the case of concrete- and f is the yield function, which represents the overstress. Since concrete presents different yield strengths in tension and compression, a multi-surface plastic criterion has been used.

In the particular case of concrete modeling, an exponential yield stress evolution is applied in order to model the negative slope in the stress-strain curve, representing the softening due to concrete cracking. In the elastic domain, the rate dependence is introduced via a strain rate dependent Young's modulus, $E(\dot{\varepsilon})$, so that the strains at peak stress obtained are in good agreement with those proposed in [2]. The compressive stress-strain curves for concrete obtained with this model for several strain rates are depicted in Figure 1. The parameters of the constitutive law have been chosen in such a way that the dynamic increase factors (DIF) obtained with the proposed constitutive models are in good agreement with the ones determined by Malvar and Crawford [3], based on experimental results. The interest has been focused on the compressive behaviour of concrete, considered to be more sensitive to the strain rate than the tensile one [2,3]. The dynamic increase factors for the compressive strength of concrete versus the strain rate, obtained with the viscoplastic model for a C30 concrete grade, are also shown in Figure 1. For the steel reinforcements, the evolution of the yield stress has been modeled using a hardening power-law. The Young's modulus has been kept constant, since the elastic behaviour of steel is not considered to exhibit rate effects [4]. The static Young's modulus and the yield stress evolution laws are detailed in Table I, with κ a scalar parameter representing the viscoplastic strain history.

The set of residuals to be minimized in the return-mapping algorithm for the solution of the stress update in viscoplasticity are the following:

$$\sigma_{n+1} - \sigma_{n+1}^{trial} + E \cdot \Delta\varepsilon_{n+1}^{vp} = 0 \tag{2}$$

$$\Delta\varepsilon_{n+1}^{vp} \cdot \eta - \Delta t_{n+1}\left(\frac{f}{|\bar{\sigma}_0|}\right)_{n+1}^N \left.\frac{df}{d\sigma}\right|_{n+1} = 0 \tag{3}$$

with $\sigma_{n+1}^{trial} = \sigma_n + E \cdot \Delta\varepsilon_{n+1}$ the trial stress and f the yield function, defined as:

$$f = \begin{cases} \sigma - \bar{\sigma} & \text{for } \sigma \geq 0 \\ \bar{\sigma} - \sigma & \text{for } \sigma < 0 \end{cases} \tag{4}$$

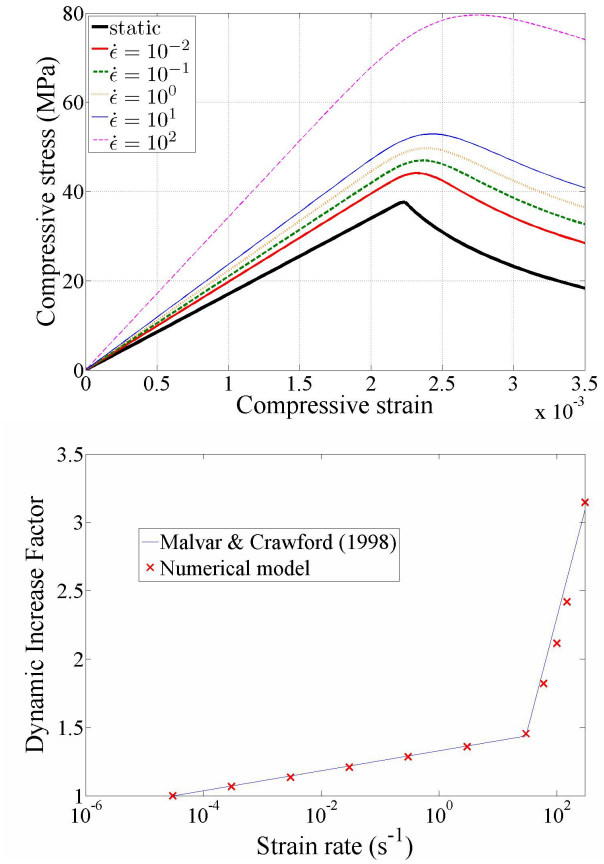

Fig. 1. Rate-dependent response of the model in compression: stress-strain curves (top) and DIFs (bottom)

TABLE I
STATIC MATERIAL PROPERTIES.

CONCRETE	E_{st} (GPa)	$\bar{\sigma}$ (MPa)
tension	32	$3.25e^{-7000\kappa}$
compression	17	$-37.5e^{-300\kappa}$
STEEL	E_{st} (GPa)	$\bar{\sigma}$ (MPa)
tension	200	$500(1+60\kappa)^{0.2}$
compression	200	$-500(1+60\kappa)^{0.2}$

C. Extraction of the rate dependent sectional behaviour with a layered beam approach

The introduction of these one-dimensional constitutive laws for concrete and steel in a layered beam model [20-22] provides strain rate dependent relations between the beam generalised stresses (normal force N and bending moment M, according to Bernouilli's hypothesis) and generalised strains (axial strain $\bar{\varepsilon}$ and curvature χ), to be applied at each integration point in a FE calculation. Note that such averaged relations can only be applied as such in classical structural computations provided they do not exhibit overall softening, in order to keep a well-posed description. This layered approach is summarised in Figure 2, showing that only the longitudinal reinforcements are taken into account. Note that the structural scale assumption (Bernouilli) remains consistent with this approach at the fine scale. A perfect bond is assumed between the layers (i.e. no delamination between them).

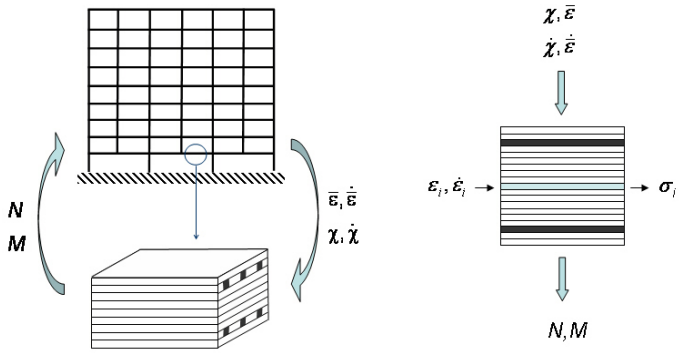

Fig. 2. Layered beam model: generalized strains evaluation

The element-wise stresses (N,M) in each integration point for the beam element are evaluated from the strains ($\bar{\varepsilon}$,χ) as follows: first, the axial strains in each layer (ε_i) are computed, as well as the corresponding strain rates ($\dot{\varepsilon}_i$):

$$\varepsilon_i = \bar{\varepsilon} - \bar{y}_i \cdot \chi \tag{5}$$

$$\dot{\varepsilon}_i = \dot{\bar{\varepsilon}} - \bar{y}_i \cdot \dot{\chi} \tag{6}$$

where $\bar{y}_i$ is the average vertical coordinate with respect to the section mid-height for layer i. Then the layer-wise stresses (i.e. the axial stresses σ_i) are obtained by applying the 1D constitutive laws (i.e. the return-mapping algorithm) on each layer. For the layers containing the steel reinforcements, the stresses in concrete and steel are computed separately, then the average stress is obtained depending on the steel volume fraction of the considered layer. The stress is computed at the mid-height of the layer, and assumed to be constant over its thickness. Finally the cross-section generalised stresses (N,M) are evaluated by integrating the layer-wise one-dimensional stresses through the cross-sectional area of the beam:

$$N = \sum \sigma_i \cdot \Omega_i \tag{7}$$

$$M = -\sum \sigma_i \cdot \bar{y}_i \cdot \Omega_i \tag{8}$$

with Ω_i the cross-sectional area of the layer. The cross-sectional consistent tangent operator is derived from the previous relations as:

$$\begin{Bmatrix} \partial N \\ \partial M \end{Bmatrix} = \begin{bmatrix} \sum H_i \cdot \Omega_i & -\sum H_i \cdot \bar{y}_i \cdot \Omega_i \\ -\sum H_i \cdot \bar{y}_i \cdot \Omega_i & \sum H_i \cdot \bar{y}_i^2 \cdot \Omega_i \end{bmatrix} \begin{Bmatrix} \partial \bar{\varepsilon} \\ \partial \chi \end{Bmatrix} \tag{9}$$

where H_i is the layer-wise consistent tangent operator. The rate dependent bending moment-curvature relations (obtained for different constant strain rates) for the RC section described in Figure 3 are shown in Figure 4. As expected, the section exhibits larger resistance for negative bending since the upper reinforcement ratio is larger than the lower one. The use of a rate dependent model for concrete and steel leads to an enhancement in the sectional behaviour. However, this enhancement is larger for positive bending. For instance, the maximal bending moment at a constant curvature rate of $\dot{\chi} = 100$ (rad/m)/s is 56% higher than in the static case (using a rate-independent model), whereas for negative bending at $\dot{\chi} = -100$ (rad/m)/s this value corresponds to 33%. This effect may lead to an increase in the cross-sectional strength of the beam during progressive collapse, if a bending reversal (from negative to positive values) occurs due to the loss of a bearing member.

III. Rate effects on a model problem

A. *Problem description for a RC planar frame subjected to the loss of a vertical support*

Figure 5 shows the structure to be studied, consisting of a three-storey six-bay planar frame. The floor span is 6m, whereas the floor height is 4m. The span of the floor in the perpendicular direction is 4m. The loads applied to the first and second floors are those corresponding to the slab and beam weight and the service loads. For the top floor, only the slab and beam self-weights are accounted for. Their numerical values are also shown in the figure.

The objective is to analyse the structural response when the central ground floor column is removed. In particular, the interest is focused on the effect of the removal rate on the structural resistance. As a model problem, the simplified substructure illustrated in Figure 6 was employed to model the portion of the planar frame adjacent to the failing member, in order to study the response in the vicinity of the initial failure. It consists of a doubly-clamped beam with a central support. This approximate configuration is considered to represent the boundary conditions of the studied beam due to the symmetry of the problem. The loads coming from the upper floors are also accounted for through a point vertical load applied in the middle of the beam, as can be seen in Figure 6.

Due to the symmetry of this simplified structure, only the half of it has been modeled. A preliminary static test (i.e. no viscous effects considered) has been performed applying the regular loads. This computation provides the reaction forces (R_x, R_y, M_z) exerted on the beam by the support which will vanish next in the progressive collapse simulation. For symmetry reasons, only the vertical reaction R_y is non-zero. Then, computations are carried out in the substructure where the support has been removed and

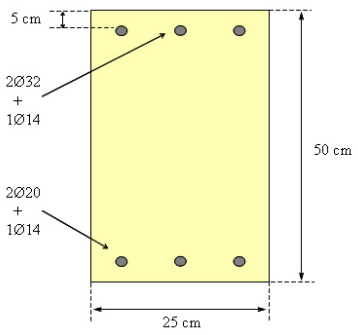

Fig. 3. Description of the RC section.

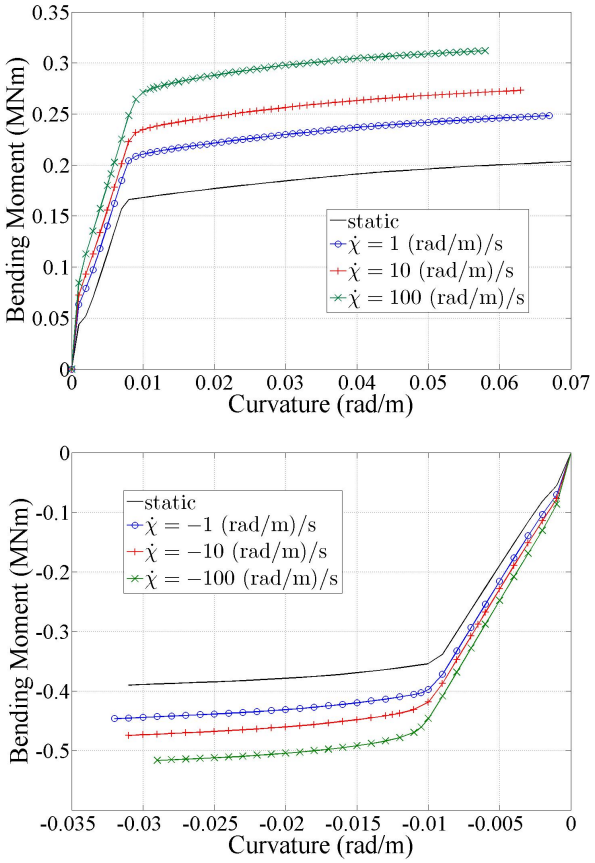

Fig. 4. Rate dependent moment-curvature relations: positive bending (top) and negative bending (bottom).

replaced by this vertical load (load R in Figure 7). This reaction force is then gradually decreased from its initial value to zero in a time t_r, while the regular loads are kept constant.

All computations have been performed using a geometrically linear description assumption. Inertial effects are not considered in this first approach, since the focus of interest here is the viscous effect. Different vanishing rates for the reaction force R have been applied (i.e. different removal times t_r), in order to assess the level of rate dependence in the response of the structure. The cross sectional description of the beam can be found in Figure 3. The reinforcement ratios (both upper and lower) have

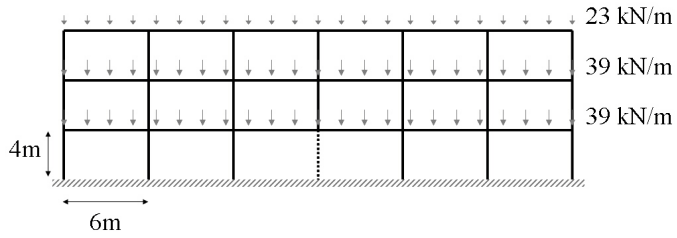

Fig. 5. Three-storey six-bay structure subjected to central ground floor column removal

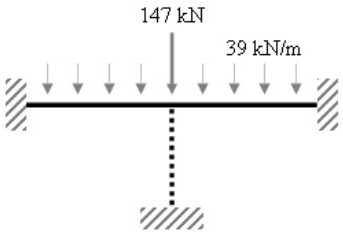

Fig. 6. Substructure used to model the vicinity of the initial failure

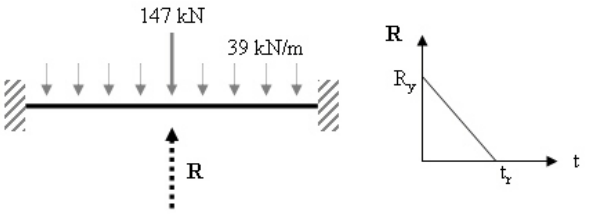

Fig. 7. Load pattern for the column removal simulation

been calculated for the structure under its regular loads. For the sake of simplicity, a continuous reinforcement is considered along the entire length of the beam. The response of the material models used for concrete and steel is depicted in Figure 8, which shows the quasi-static stress-strain curves for both materials. As can be seen, the softening in the compressive behaviour of concrete has been deactivated, in order to follow the simplified bilinear stress-strain relation for the design of RC cross-sections proposed in [23]. Note however that more complex laws with softening could be used as well.

Failure is expected to occur in the clamped sections, where the bending moment reaches the highest value. Note that failure is considered to arise in an element when the compressive strain in any of its layers reaches the value of 0.35%, following [23]. Using a rate dependent approach, the enhancement of the compressive response of concrete may lead to an increase of the cross-sectional behaviour. As a result, the clamped sections may be able to bear larger values of the bending moment before failure.

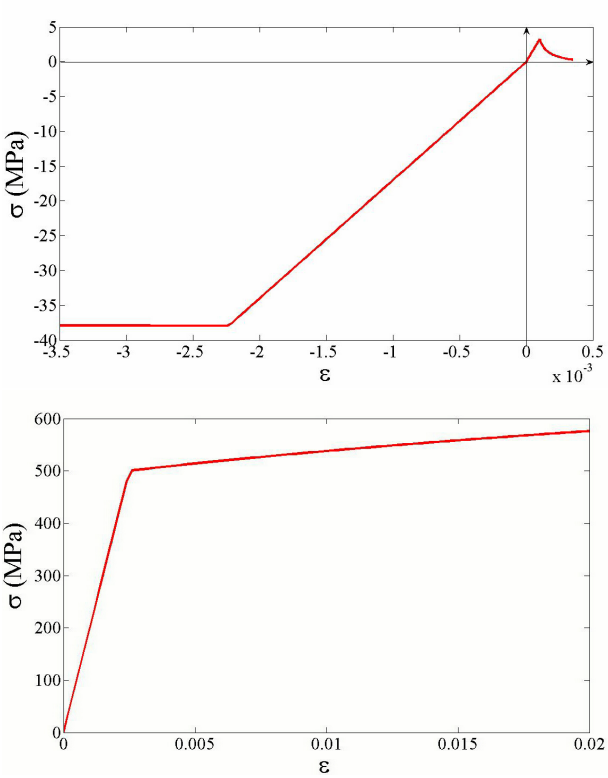

Fig. 8. Static stress-strain curves for concrete (left) and steel (right)

B. *Analysis of the structural rate dependence*

If the force exerted by the column is decreased in a quasi-static way (applying a removal time t_r large enough), the bending moment reached in the clamped sections when failure occurs is 664 kNm. When using smaller times, in other words higher loading rates, viscous effects show up. Table II reports the results for different removal rates. It also shows the fraction of the reaction force R still exerted when failure occurs in the clamped sections. Note that 100% represents that the reaction is fully applied (the support is still present), whereas 0% means that the support has been completely removed.

It can be observed that for higher rates (thus for shorter times t_r), the final bending moment can reach higher values as a result of the increase in the compressive strength of concrete, which involves an increase of the structural resistance. If the reaction force is removed in t_r=10^{-3}s, failure occurs at the end of the removal phase (%R≈0). In these conditions, in which the loading rate could realistically represent a blast loading scenario [24], the beam may experience an increase of almost 50% in the bending moment reached compared to the one obtained in a quasi-static computation. For shorter vanishing times, the beam does not even reach failure.

These results show how the strain rate effects have an influence in the structural resistance. These effects might

TABLE II
BENDING MOMENT AT THE CLAMPED SECTIONS AND VALUE OF THE REACTION FORCE R FOR WHICH FAILURE OCCURS, FOR DIFFERENT REMOVAL TIMES t_r.

t_r (s)	R	M_{max} (kNm)	DIF
10^{10}	30%	664	1.00
10^{5}	30%	665	1.00
10	20%	756	1.14
1	17.5%	800	1.20
10^{-1}	15%	810	1.22
10^{-2}	10%	857	1.29
10^{-3}	$\approx 0\%$	975	1.47
10^{-4}	no failure	1055	1.59

play an important role in the load redistribution following the sudden failure of a structural member. Since the structural elements can bear higher stresses before failure, load redistribution through the neighbouring elements may be strongly altered as a result of the rate effect.

C. Discussion

From the previous results it can be highlighted that the strain rate effects may induce a significant strength enhancement at the structural level. The particular conditions of the studied case (which is representative of a progressive collapse scenario) favoured this effect, although it may not be the case for different loading circumstances. Here, the increase in the compressive strength of concrete due to the rate effects results in an enhancement of the resistance in the clamped sections, since the loss of the column entails an increased compression in the formerly compressed part of the RC section. The sufficient amount of steel reinforcement in the tensioned part (i.e. the upper bars) allows for this compression growth.

The softening in the constitutive laws for concrete in compression has been deactivated. However, if an evolution law including softening were adopted, computations could be only carried out provided softening does not show up at the structural level. In that case, strain localization and mesh dependence issues would arise. A viscoplastic hinge approach would be then necessary to avoid mesh dependency.

As already mentioned, the rate effects at the structural level may lead to a different load redistribution in the structure following the sudden failure of a bearing member. In a viscoplastic hinge approach, the hinges appearance scheme may be strongly affected by this structural rate dependence. These results suggest that the rate independent computations may lead to excessively conservative safety margins.

Concerning the inertial effects, they should be taken into account in a full structural computation. Since this contribution is mainly focused on the viscous effects, inertia has not been considered.

IV. CONCLUSIONS

In the framework of Progressive Collapse calculations, the need to characterize the rate dependent behaviour of materials becomes evident: the high strain rate that this phenomenon involves will affect the material response. Hence the need to find a material model which takes into account this rate dependence, in order to be able to represent its effect on the response of structural elements.

In particular, a layered beam model has been developed, using a Perzyna type viscoplastic law for the characterization of the strain rate effect on concrete and steel.

A simplified (non-inertial) computation on a RC planar frame shows that the loading rate has a significant effect in the structural response of a structure. The result obtained gives an indication on the role that the rate effects might play in the load redistribution of a structure following a member failure, which may result in an increased resistance to progressive collapse. This in turn may imply that the quasi-static or rate independent computations could lead to excessive safety margins.

REFERENCES

[1] P.H. Bischoff and S.H. Perry, Compressive Behaviour of Concrete at High Strain Rates. *Materials and Structures*, **24**, 425–450, 1991.

[2] International Federation for Structural Concrete (*fib*), Constitutive modelling of high strength/high performance concrete, State-of-art report. *fib Bulletin* **42**, 2008.

[3] L.J. Malvar and J.E. Crawford, Dynamic increase factors for concrete. *28th DDESB seminar*, Orlando, FL, USA, 1998.

[4] J. Magnusson, *Structural Concrete Elements Subjected to Air Blast Loading*. Licentiate Thesis. TRITA-BKN. *Bulletin* **92**, SRN KTH/BKN/B–92–SE, 2007.

[5] D.L. Grote, S.W. Park and M. Zhou, Dynamic behavior of concrete at high strain rates and pressures: I. experimental characterization. *International Journal of Impact Engineering*, **25**, 869-886, 2001.

[6] Q.M. Li and H. Meng, About the dynamic strength enhancement of concrete-like materials in a split Hopkinson pressure bar test. *International Journal of Solids and Structures*, **40**, 343-360, 2003.

[7] B. Ellingwood and E. Leyendecker, Approaches for design against progressive collapse. *J. Struct. Div. ASCE*, **104** (ST3), 413-423, 1978.

[8] Department of Defense (DoD), *Unified Facilities Criteria (UFC): Design of structures to resist progressive collapse*, UFC 4-023-03. Washington D.C., 2005.

[9] United States General Services Administration (GSA), *Progressive collapse analysis and design guidelines for new federal office buildings and major modernization project*. Washington D.C., 2003.

[10] G. Kaewkulchai and E. Williamson, Beam element formulation and solution procedure for dynamic progressive collapse analysis. *Computers and Structures*, **82**, 639-651, 2004.

[11] B.A. Izzuddin, A.G. Vlassis, A.Y. Elghazouli and D.A. Nethercot, Progressive collapse of multi-storey buildings due to sudden

column loss – Part I: Simplified assessment framework. *Engineering Structures*, **30**, 1308-1318, 2008.

[12] K. Menchel, *Progressive collapse: comparison of main standards, formulation and validation of new computational procedures*. Ph.D. Thesis, Université Libre de Bruxelles, 2008.

[13] K. Menchel, T. J. Massart, Y. Rammer and Ph. Bouillard, Comparison and study of different progressive collapse simulation techniques for RC structures, *Journal of Structural Engineering (ASCE)*, In press, 2008.

[14] R.R. Pedersen, A. Simone and L.J. Sluys, An analysis of dynamic fracture in concrete with a continuum visco-elastic visco-plastic damage model. *Engineering Fracture Mechanics*, **75**, 3782-3805, 2008.

[15] J.F. Georgin and J.M. Reynouard, Modeling of structures subjected to impact: concrete behaviour under high strain rate. *Cement and Concrete Composites*, **25**, 131-143, 2003.

[16] Juan José López Cela, Analysis of reinforced concrete structures subjected to dynamic loads with a viscoplastic Drucker-Prager model. *Applied Mathematical Modelling*, **22**, 495–515, 1998.

[17] R. Lorefice, G. Etse and I. Carol, Viscoplastic approach for rate-dependent failure analysis of concrete joints and interfaces. *International Journal of Solids and Structures*, **45**, 2686-2705, 2008.

[18] R. de Borst, L.J. Sluys and M.G.D. Geers, Computational methods for material nonlinearities. *Graduate School on Engineering Mechanics*, Delft University of Technology, Delft, The Netherlands, 1998.

[19] O.M. Heeres, A.S.J. Suiker and R. de Borst, A comparison between the Perzyna viscoplastic model and the Consistency viscoplastic model. *European Journal of Mechanics A/Solids*, **21**, 1-12, 2002.

[20] A. Anthoine, J. Guedes and P. Pegon, Non-linear behaviour of reinforced concrete beams: from 3D continuum to 1D member modelling. *Computers and Structures*, **65**, No. 6, 949–963, 1997.

[21] L. Davenne, F. Ragueneau, J. Mazars and A. Ibrahimbegovic, Efficient approaches to finite element analysis in earthquake engineering. *Computers and Structures*, **81**, 1223-1239, 2003.

[22] R.S. Oliveira, M.A. Ramalho and M.R.S. Corrêa, A layered finite element for reinforced concrete beams with bond-slip effects. *Cement and Concrete Composites*, **30**, 245-252, 2008.

[23] *EN 1992-1-1, Eurocode 2: Design of concrete structures - Part 1-1: General rules and rules for buildings*, December 2004.

[24] P.D. Smith and J.G. Hetherington, *Blast and ballistic loading of structures*, Butterworth Heinemann, London, 1994.

Proceedings of the 8th National Congress on Theoretical and Applied Mechanics, May 28-29, Brussels, Belgium.

Nested inverse method for mechanical material parameter identification using DIC and FE computed deformation fields.

B. Belkassem[1], S. Bossuyt[1], H. Sol[1]
[1]Vrije Universiteit Brussel – Department of Mechanics of Materials and Constructions,
Pleinlaan 2, 1050 Brussels, Belgium.
email: bachir.belkassem@vub.ac.be, sven.bossuyt@vub.ac.be, hugo.sol@vub.ac.be

Abstract: **Inverse methods offer a powerful tool for the determination of material properties. Contrary to standard tests, these methods can deal with complex, heterogeneous stress and strain fields which have a larger information content and allow the simultaneous identification of several material parameters.**

For the identification of material parameters the presented inverse method compares an experimentally measured strain field with a strain field computed by a finite element (FE) model. The material parameters in the FE model are iteratively tuned in such a way that the numerically computed strain field matches the experimentally measured field as closely as possible. The experimental strain field is obtained by digital image correlation (DIC).

A difficulty to overcome is the coupling of full-field measurements to numerical results. It is found that the numerical simulation of the experiment can also contribute to a more efficient and precise measurement processing. Therefore the DIC is implemented within a FE framework which allows the integration between experimental part and numerical part to occur at a deeper level in the material parameter identification procedure.

Keywords: **inverse method, digital image correlation, finite elements, material parameters**

I. INTRODUCTION

Many companies optimize their designs, products, construction parts or forming operations by means of FE simulations, resulting in a reduction of the length and the cost of the "trial and error" –phase. The success of a FE simulation, however, largely depends on the accuracy of the input data, i.e. the geometry, the boundary conditions, the load distribution, the contact properties, the material data, etc. A good knowledge of the (mechanical) material properties is thus of utmost importance to assure a sufficiently accurate simulation.

A common way to evaluate the stress-strain relation of a material is by performing standard (tensile) tests [1]. The deformation fields which are generated during these tests are homogeneous and do not resemble the complex heterogeneous deformation fields which occur in real processes. The obtained material behavior with these tests is often insufficient to simulate reliably the complex material behavior occurring under complex loading conditions. This implies that the use of conventional tests, with carefully designed tests specimens, not always allow to correctly predict the actual material behavior in the construction part. Inverse methods allow taking into account complex specimen geometries and loading conditions and hence have an increasing interest in the engineering community. The obtained (constitutive) material parameters are more realistic, since the resulting heterogeneous deformation fields are much closer to deformation states occurring in construction parts. Moreover, inverse methods allow the simultaneous identification of several material parameters.

New important developments in the field of optical full-field measurements techniques, such as digital image correlation (DIC), make it possible to measure this complex deformation fields with relative ease [2-4]. By combining DIC measurements with FE simulations of material tests in an inverse method, it has now become possible to characterize the full deformation behavior under complex loading conditions with much higher accuracy than before [5-11]. Different implementations of inverse methods exist [12]. Often the (material) parameters are iteratively updated by minimizing a cost function. Cost functions have a scalar value which is function of the difference between the experimental and the computed response of the physical system under study, e.g. by comparing displacement fields [13,14], strain fields [9-11], resonant frequencies [15-16], etc. The current implementations of DIC based inverse methods are rather time-consuming, mainly because of the thorny problems that appear at the conversion of the measurement results to the coordinate system of the finite element model. Also, existing DIC methods exhibit some shortcomings, especially when used in an inverse method. Since traditional (subset-based) image correlation is used to obtain deformation parameters of a point one by one by mapping a subset with the point in the centre over a pair of digital images, and there is no requirement of inter-subset continuity during the correlation process, wrong data points can be observed. In addition, the discrete displacement field data that are obtained directly from existing DIC algorithms usually need to be improved through post processing by use of smoothing techniques, such as finite element smoothing and least-squares polynomial fitting, after which the strain can be computed in the same points as the considered integration points of the numerical model.

Thus, the coupling of full-field measurements to numerical results can be greatly improved. The simulation of the experiment can not only be adapted to the measurement results, but also contribute itself to more efficient and more precise measurement processing. Therefore the DIC is implemented within a FE framework which allows the integration between experimental part and numerical part to occur at a deeper level in the material parameter identification procedure.

The interested image area (or Area of Interest AOI) is discretized into finite elements, linked by nodes, which are all

involved in a common image correlation process. The element-based correlation method satisfies naturally to the inter-element continuity requirement and has the advantage that the underlying deformation field can be improved by implicitly adopting finite element smoothing [17].

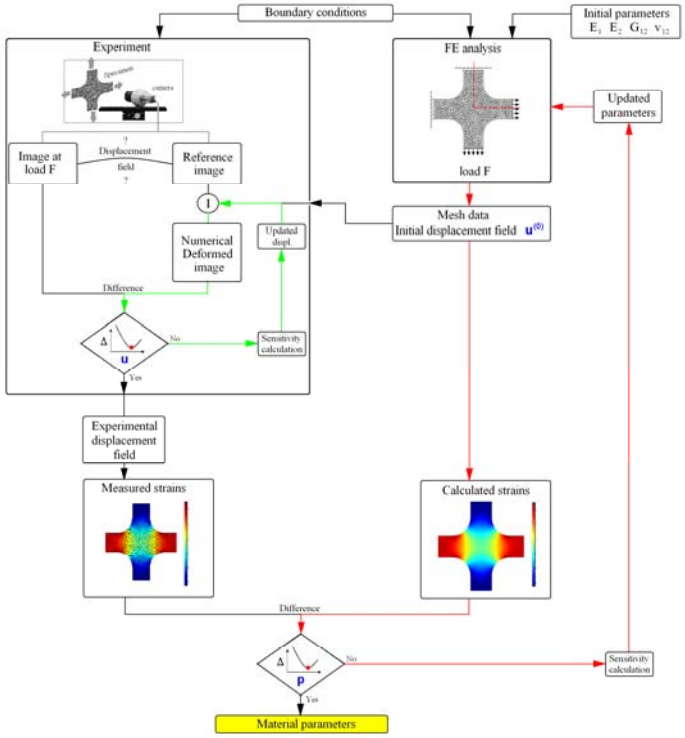

Figure 1: Flowchart of the nested inverse method

II.NESTED INVERSE METHOD FOR MATERIAL PARAMETER IDENTIFICATION

In contrast to a direct problem which is the classical problem where a given experiment is simulated in order to obtain the stresses and the strains, inverse problems are concerned with the determination of the unknown state of a mechanical system using information gathered from the response to stimuli on the system [18]. The inverse problem is a problem where certain input data of the direct problem are deduced from the comparison between the experimental results and the numerical FE-simulation of the considered experiment. Not only the boundary information is used, but relevant information coming from full-field surface measurements is also integrated in the evaluation of the material behavior. The inverse method presented in this paper aims to have an identical description for the deformation fields in the experimental part as well as in the numerical simulation. This is achieved by adopting a finite element framework for the DIC technique. This approach provides the material parameter identification procedure with a natural interface between experimental and numerical part.

Figure 1 illustrates the general methodology of the proposed nested inverse method. The procedure can be summarized as follows: an object is subjected experimentally to a certain loading condition; the resulting surface deformations are measured and from these deformations follow the unknown material parameters.

The method is called nested or hierarchical since it contains two inverse problems, but at a different level:

- An inverse method for the identification of mechanical material parameters based on the comparison of deformations (called parameter identification), and
- An inverse method for the measurement of surface deformations based on the comparison of digital images (called FEM based DIC).

A. Experimental Part

The experimental part consists of taking several pictures of the object of interest with a digital camera. Each picture corresponds to a certain loading step. The image corresponding to the initial state of the object is called the reference image, the other images are called deformed image with respect to the loading step they were taken at. By comparing the reference image and a deformed image it is possible to determine the displacement and deformation fields on the surface of a planar specimen. The following sections describe briefly the FEM based DIC technique that will determine directly the complete, two-dimensional displacement field during the image correlation process on digital images.

1) Principle of FEM based DIC

The entire AOI is discretized into finite elements, linked by nodes that are all involved in a common image correlation process by use of algorithms implemented in a MATLAB/COMSOL environment. Since this DIC procedure is meant to yield suitable experimental data for the parameter identification procedure, the discretization into finite elements is done by mapping the mesh, used in the numerical simulation of the experiment, onto the AOI of the reference image (Figure 1, 2). Therefore the mesh information, i.e. nodal coordinates, element connectivity, element type and element order, is extracted from the numerical model at the first iteration of the parameter identification loop.

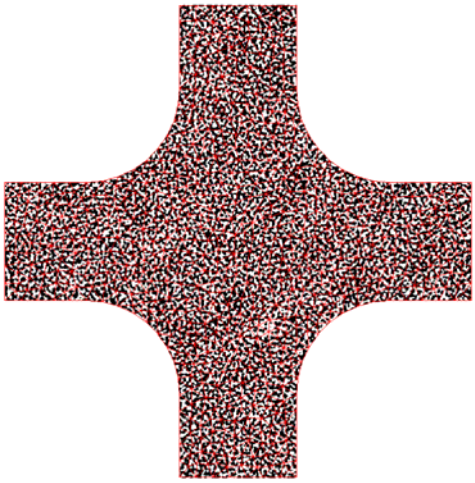

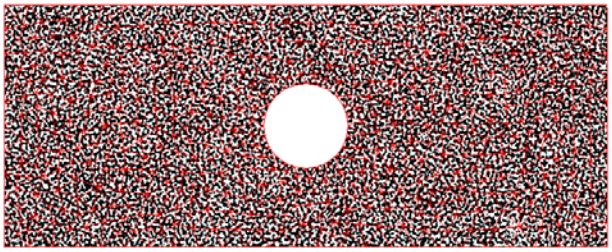

Figure 2: Mapping of the FEM mesh onto the AOI of the reference image

2) Optimization

According to the traditional DIC algorithms the unknown displacement field is found iteratively by minimizing a correlation coefficient. This correlation coefficient expresses the difference between the deformed image and the numerically deformed reference image. The latter is obtained by deforming the reference image along a given displacement field expressed as nodal displacements (using the shape functions of the elements it is possible to know the whole displacement field). From the difference an improved set of nodal displacements is generated and used to deform the reference image again. This is repeated till the correlation coefficient reaches a minimum. The set of nodal displacements that minimizes this correlation coefficient is considered to be the experimental displacement field. In this iterative determination of the experimental displacement field the choice of a good optimization algorithm is essential.

- *Selection of the starting values*

Before beginning the optimization procedure it is necessary to provide the algorithm with starting values for the unknown nodal displacements. In practice the convergence region of most optimization methods is limited; if the starting values are selected outside this region, the method will diverge. Even if there is convergence, the final result can depend upon the starting values if the cost function has local minima. Thus the choice of the starting values is important. The starting value $\mathbf{u}^{(0)}$ for the experimental displacement field is obtained from the converged simulation at the first iteration of the material parameter identification loop, i.e. the nodal displacements resulting from the converged simulation performed with the starting values for the material parameters and the force corresponding to the deformed image under study.

- *Generation of an improved set of nodal displacements*

The generation of the improved set of nodal displacements is the kernel of the optimization algorithm. Several techniques are possible. Here, the method of Levenberg-Marquardt is used. This is a combination of the Gauss-Newton method and the gradient method.

The unknown nodal displacements $\mathbf{u}$ are found iteratively by minimizing a correlation coefficient or cost function. This is the least squares norm of the discrepancy between the measured and the calculated intensities:

$$C(\mathbf{u}) = \sum_i \left[f(k) - g(i,\mathbf{u}) \right]^2 \tag{1}$$

with i a linear indexation of all pixels within the AOI, g and f respectively the discrete grey value distribution functions of the deformed reference image and the experimental deformed image.

In the Levenberg-Marquardt method new updates are generated using following formula

$$\boldsymbol{\delta}^{(k)} = \left(\mathbf{S}^{(k)^T} . \mathbf{S}^{(k)} + \lambda \mathbf{I} \right)^{-1} . \mathbf{S}^{(k)^T} \left(\mathbf{f} - \mathbf{g}(\mathbf{u}^{(k)}) \right) \tag{2}$$

with which the updated nodal displacements can be calculated using following formula

$$\mathbf{u}^{(k+1)} = \mathbf{u}^{(k)} + \boldsymbol{\delta}^{(k)} \tag{3}$$

where:

- $\mathbf{u}$ is the nodal displacement column; $\mathbf{u} = \left[u_x^1 \ \cdots \ u_x^n \ \ u_y^1 \ \cdots \ u_y^n \right]^T$ with n the number of vertices in the mesh,
- $\mathbf{I}$ is the identity matrix,
- λ is a scalar,
- $\mathbf{f}$ is the column containing the measured intensities,
- $\mathbf{g}(\mathbf{u}^{(k)})$ is the column containing the computed intensities, obtained by deforming the reference image along the set of nodal displacements $\mathbf{u}^{(k)}$,
- $\mathbf{S}^{(k)}$ is the sensitivity matrix and expresses the sensitivity of the pixel intensity with respect to the unknown nodal displacements. $S_{ij}^k = \dfrac{\partial g(i,u^{(k)})}{\partial u_j}$ with j = 1, …, 2n; and i a linear indexation of all pixels within the AOI. (4)

Sensitivity calculation

The computation of the sensitivity matrix requires the determination of the partial derivatives of the pixel intensities with respect to the unknown nodal displacements. Given the displacement functions and the intensity interpolation functions used to calculate $g(i,\mathbf{u})$, the first-order partial derivatives are readily derived:

$$S_{ij}^k = \frac{\partial g(i,u^{(k)})}{\partial u_j} = \frac{\partial g(i,u^{(k)})}{\partial x} . \frac{\partial x}{\partial u_j} + \frac{\partial g(i,u^{(k)})}{\partial y} . \frac{\partial y}{\partial u_j} \tag{5}$$

where:

$\frac{\partial g(i,u^{(k)})}{\partial x}$ and $\frac{\partial g(i,u^{(k)})}{\partial y}$	can be derived from the intensity interpolation function (Bilinear, Bicubic, Bicubic B-Spline, …),
$\frac{\partial x}{\partial u_j}$ and $\frac{\partial y}{\partial u_j}$	can be derived from the displacement functions

- *The stop criterion*

The iteration loop of the optimization method is stopped at the moment that the stop criterion is met. There are a number of ways of choosing this criterion. The stop criterion programmed in the present optimization algorithm is based on the evaluation of the nodal displacements. More specifically, the iteration loop is stopped when there is no longer a significant improvement of the nodal displacements, with further iteration.

3) Calculation of the deformation fields

The set of nodal displacements that fulfils the stop criterion of the above mentioned optimization loop is used to calculate the subsequent strain components at each integration point of the mesh. These values are stored in the vector $\boldsymbol{\varepsilon}^{exp}$.

B. Numerical Model

The numerical model is the finite element simulation of the experiment, containing all information about geometry, loading conditions, boundary conditions, material model, etc. The geometry is meshed once; this is in the first iteration of the parameter identification loop. Within each iteration step of the identification loop, this model is solved for an updated set of material parameters. After convergence the model returns the stress and strain components at each integration point of the mesh.

C. Optimization algorithm

Starting from an initial value, a better set of material parameters is generated, and this process is repeated until it is decided that the process has converged (Figure 1). So there are three important steps in the search routine: the selection of the starting values, the generation of an improved set of material parameters and the stop criterion. These steps will be discussed briefly hereafter.

1) Selection of the starting values

Before beginning the optimization procedure it is necessary to provide the algorithm with starting values for the unknown parameters. Values obtained with standard testing are an obvious choice for the starting values.

2) Generation of an improved set of parameters

The generation of the improved set of parameters is the kernel of the optimization algorithm. Here, the optimization of the constitutive parameters is performed by a Gauss-Newton method. The identification is performed in an iterative way by minimizing a cost function which expresses the discrepancy between the experimentally measured and the numerically computed strain fields. A possible expression is a least squares formulation:

$$C(\mathbf{p}) = \sqrt{\sum_{i=1}^{n}\left(\boldsymbol{\varepsilon}_i^{num}(\mathbf{p}) - \boldsymbol{\varepsilon}_i^{exp}\right)^2} \tag{6}$$

with $\mathbf{p}$ the parameter update column, n the number of integration points considered, $\boldsymbol{\varepsilon}_i^{exp}$ the experimentally measured strains and $\boldsymbol{\varepsilon}_i^{num}(\mathbf{p})$ the numerically computed strains as a function of the unknown material parameters. The minimization of the cost function can be formally expressed by requiring that the partial derivatives of the cost function with respect to the different material parameters are zero:

$$\frac{\partial C(\mathbf{p})}{\partial p_j} = \frac{1}{C(\mathbf{p})}\sum_{i=1}^{3n}\left(\varepsilon_i^{num}(\mathbf{p}) - \varepsilon_i^{exp}\right)\frac{\partial \varepsilon_i^{num}}{\partial p_j} = 0 \tag{7}$$

By developing a Taylor expansion of the numerical (FEM) strains around a given parameter set, an expression is obtained in which the difference between the present parameters and their new estimates is given by:

$$\begin{aligned}\varepsilon_i^{num}(\mathbf{p}) &\cong \varepsilon_i^{num}(\mathbf{p}^{(k)}) + \sum_{j=1}^{m}\frac{\partial \varepsilon_i^{num}(\mathbf{p}^{(k)})}{\partial p_j}\left(p_j - p_j^{(k)}\right)\\ &\cong \varepsilon_i^{num}(\mathbf{p}^{(k)}) + \sum_{j=1}^{m} S_{ij}^{(k)}\left(p_j - p_j^{(k)}\right)\end{aligned} \tag{8}$$

with $\mathbf{p}^{(k)}$ the unknown material parameter column at iteration step k, m the number of unknown material parameters and the $S_{ij}^{(k)}$ sensitivity matrix at iteration step k. This sensitivity matrix S_{ij} expresses the sensitivity of the three strain components (we only consider in-plane deformation) with respect to the unknown material parameters for all data points considered in the updating algorithm.

Substitution of Eq. (8) into Eq. (7) yields the updates of the unknown parameters:

$$\Delta\mathbf{p} = \left(\mathbf{S}^{(k)T}.\mathbf{S}^{(k)}\right)^{-1}.\mathbf{S}^{(k)T}\left(\boldsymbol{\varepsilon}^{exp} - \boldsymbol{\varepsilon}^{num}\left(\mathbf{p}^{(k)}\right)\right) \tag{9}$$

with $\Delta\mathbf{p}$ the parameter update column, $\boldsymbol{\varepsilon}^{exp}$ the experimentally measured strain column, $\boldsymbol{\varepsilon}^{num}\left(\mathbf{p}^{(k)}\right)$ the numerically computed strain column as a function of the unknown material parameters at iteration step k and $\mathbf{S}^{(k)}$ the sensitivity matrix at iteration step k.

Sensitivity calculation

$$\mathbf{S} = \begin{bmatrix} \frac{\partial \varepsilon_x^1}{\partial p_1} & \frac{\partial \varepsilon_y^1}{\partial p_1} & \frac{\partial \varepsilon_{xy}^1}{\partial p_1} & \cdots & \frac{\partial \varepsilon_x^n}{\partial p_1} & \frac{\partial \varepsilon_x^n}{\partial p_1} & \frac{\partial \varepsilon_x^n}{\partial p_1} \\ \frac{\partial \varepsilon_x^1}{\partial p_2} & \frac{\partial \varepsilon_y^1}{\partial p_2} & \frac{\partial \varepsilon_{xy}^1}{\partial p_2} & \cdots & \frac{\partial \varepsilon_y^n}{\partial p_2} & \frac{\partial \varepsilon_y^n}{\partial p_2} & \frac{\partial \varepsilon_y^n}{\partial p_2} \\ \vdots & \vdots & \vdots & \ddots & \vdots & \vdots & \vdots \\ \frac{\partial \varepsilon_x^1}{\partial p_m} & \frac{\partial \varepsilon_y^1}{\partial p_m} & \frac{\partial \varepsilon_{xy}^1}{\partial p_m} & \cdots & \frac{\partial \varepsilon_{xy}^n}{\partial p_m} & \frac{\partial \varepsilon_{xy}^n}{\partial p_m} & \frac{\partial \varepsilon_{xy}^n}{\partial p_m} \end{bmatrix}^T \quad (10)$$

The components of the sensitivity matrix $\mathbf{S}$ can be derived analytically from the constitutive relation between stress and strain, which is given by following expression in the case of a linear orthotropic plane stress problem:

$$\begin{Bmatrix} \varepsilon_x \\ \varepsilon_y \\ \varepsilon_{xy} \end{Bmatrix} = \begin{bmatrix} \frac{1}{E_1} & -\frac{\nu_{21}}{E_2} & 0 \\ -\frac{\nu_{12}}{E_1} & \frac{1}{E_2} & 0 \\ 0 & 0 & \frac{1}{2 \cdot G_{12}} \end{bmatrix} \begin{Bmatrix} \sigma_x \\ \sigma_y \\ \sigma_{xy} \end{Bmatrix} \quad (11)$$

Due to symmetry ν_{21} can be computed from the other engineering constants. There are hence only four independent engineering constants left to evaluate: E_1, E_2, G_{12} and ν_{12}.

The twelve elements of the sensitivity matrix belonging to one and the same integration point in the FEM mesh are expressed in table 1:

TABLE I
Derivatives of the strain components with respect to the different parameters

∂../∂..	E_1	E_2	G_{12}	ν_{21}
ε_x	$-\frac{\sigma_x}{E_1^2}+\frac{\nu_{12}\sigma_y}{E_1^2}$	0	0	$-\frac{\sigma_y}{E_1}$
ε_y	$\frac{\nu_{12}\sigma_x}{E_1^2}$	$-\frac{\sigma_y}{E_2^2}$	0	$-\frac{\sigma_x}{E_1}$
ε_{xy}	0	0	$-\frac{\sigma_{xy}}{2.G_{12}^2}$	0

The stresses that are used in the calculation of the derivatives are taken from the converged simulation in the actual iteration step. The values of the parameters are taken from the previous iteration step.

3) The stop criterion

The iteration loop of the optimization method is stopped at the moment that the stop criterion is met. The stop criterion programmed in the present optimization algorithm is based on the evaluation of the material parameters. More specifically, the iteration loop is stopped when there is no longer a significant improvement of the material parameters, with further iteration.

III. NUMERICAL TEST

Instead of performing an actual experiment, the nested identification procedure is first tested based on a virtual experiment. The considered experiment is a uni-axial tensile test on a rectangular test specimen of a fictitious orthotropic material. In order to generate a heterogeneous stress and strain distribution the specimen is rendered with a central hole. The values of the four engineering constants that characterize this material, as well as the selected set of starting values used to initialize the identification procedure are given in table 2.

Starting from a reference image (800 by 600 pixels, 8bit) of the test specimen the deformed image of the virtual experiment is obtained by deforming the reference image numerically along a deformation field. This field is the result of the converged FE-simulation of the experiment, using the initial values for the material parameters.

The FE-simulation is based on linear iso-parametric triangular elements of the Lagrange type. As the thickness of the specimen is assumed to be small compared to its length and width and as the applied tensile loads are parallel to the plane of the specimen it is legitimate to assume plane stress conditions. A 3D formulation of the problem is therefore not useful and would needlessly increase CPU-time. The specimen is 50 mm long and 20 mm wide. The central hole has a diameter of 7 mm. The boundary and load conditions are defined as follows along the loading axis: one edge is fixed for displacements along the axis and one edge is subjected to a distributed load of 250 N/mm.

TABLE II
The values of the independent engineering constants

	E_1 (GPa)	E_2 (GPa)	G_{12} (GPa)	ν_{12}
Initial values	25	20	10	0.3
Starting values	15	15	15	0.5

These two images, reference image and deformed image, are now considered to be "experimentally" obtained.

The objective is to identify the initial values of the engineering constants used for the virtual experiment. The criterions adopted to stop the iterative process are 0.001 pixels for FEM based DIC and 0.1% for the material parameter identification. These values represent the minimum significant improvement with further iteration. The mesh that is generated within the nested inverse method consists of 1002 elements, linked by 548 nodes.

The results of the presented method are shown in figures 3 and 4. The iterative procedures of the FEM based DIC and the identification process stopped after respectively 9 and 10 iterations and required respectively 62 and 12 seconds of CPU-time. The computations were done on a computer with a dual core, 2.13 GHz processor and 2 GB RAM. The obtained values for the four independent engineering constants match

to within 0.05% the initial values used to generate the virtual experiment.

Note that the mesh used during the identification procedure differs from the one used to generate the virtual experiment, although both meshes have approximately the same density. The purpose of the difference between both meshes is to avoid the inverse crime [19].

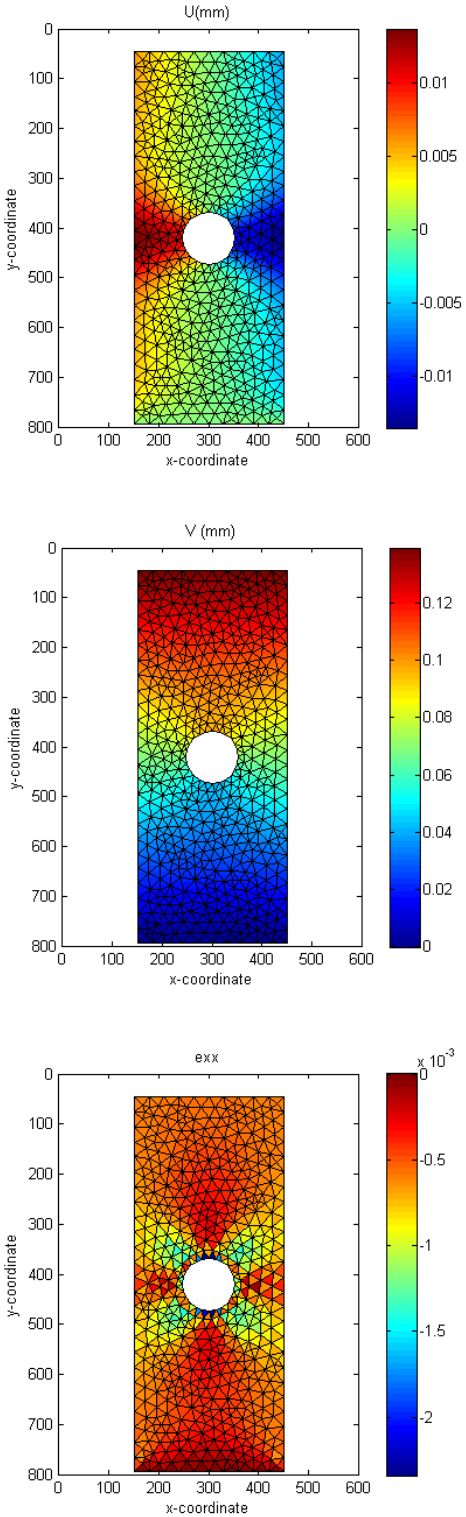

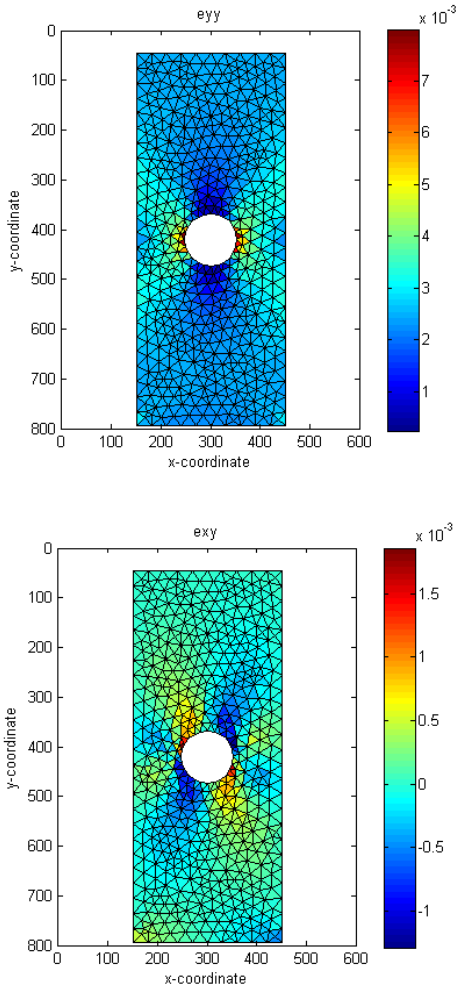

Figure 3: Displacement and deformation fields obtained with FEM based DIC

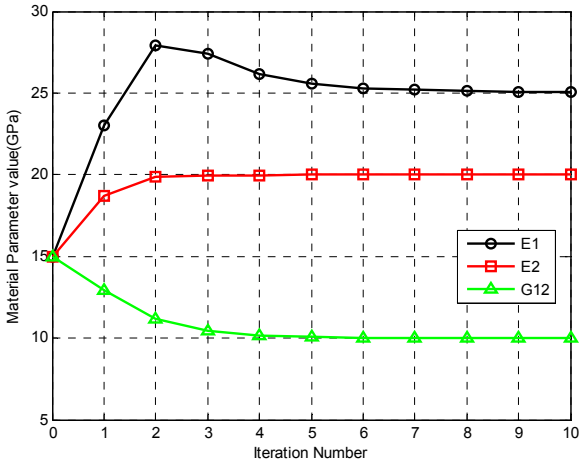

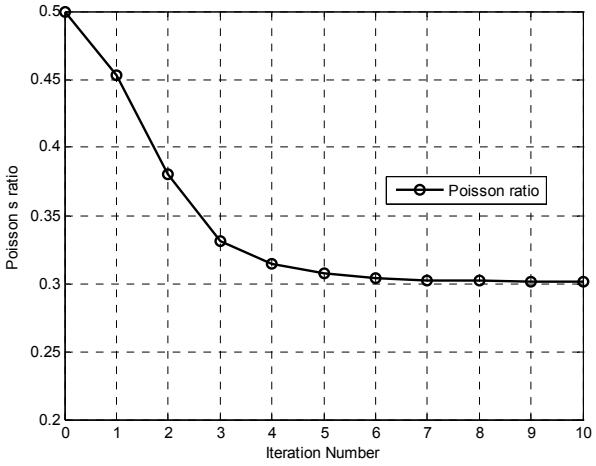

Figure 4: Convergence plots for the four independent engineering constants

IV. CONCLUSIONS

The presented nested inverse method foresees the material parameter identification of a natural interface, between the experimental and the numerical counterpart. This interface is achieved by adopting the same description for both parts, which allows them to interact at a deeper level of the identification procedure. The method simplifies also the procedure for the eventual user, as in this implementation the user only needs to provide the procedure with starting values for the unknown material parameters, the experimental images and their corresponding load step. In the current implementation the user must also project or map the FEM mesh on the AOI, but this is done with relative ease thanks to a graphical user interface.

The method can be used for any type of geometry using any type of element and element order.

ACKNOWLEDGEMENTS

This research is funded by a PhD grant of the Institute for the Promotion of Innovation through Science and Technology in Flanders (IWT-Vlaanderen).

REFERENCES

[1] ASTM Standard E8M-96, Standard test methods for tension testing of metallic materials [metric]. In Annual Book of ASTM Standards, vol. 03.01, pp. 76-96, 1996.

[2] Peters, W.H., Ranson, W.F., Digital imaging techniques in experimental stress analysis, Opt. Eng. 21, 427-432, 1982.

[3] Sutton, M.A., Wolters, W.J., Peters, W.H., Ranson, W.F., McNel, S.R., Determination of displacements using an improved digital correlation method, Image Vision Comput. 1**,** 133–139, 1983.

[4] Chu, T.C., Ranson, W.F., Sutton, M.A., Peters, W.H., Applications of digital image correlation techniques to experimental mechanics, Exp. Mech. 25**,** 232–244, 1985.

[5] Ghouati, O., Gelin, J.-C., Identification of material parameters directly from metal forming processes. Journal of Materials Processing Technology, 560–564, 1998.

[6] Ghouati, O., Gelin, J.-C., A finite element-based identification method for complex metallic material behavior. Computational Materials Science 21, 57–68, 2001.

[7] Meuwissen, M., Oomens, C., Baaijens, F., Petterson, R., Janssen, J., Determination of the elasto-plastic properties of aluminum using a mixed numerical-experimental procedure. Journal of Materials Processing Technology 75, 204–211, 1998.

[8] Kajberg, J., Lindkvist, G., Characterization of materials subjected to large strains by inverse modeling based on in-plane displacement fields. International Journal of Solids and Structures 42, 3439–3459, 2004.

[9] Lecompte, D., Smits, A., Sol, H., Vantomme, J., Van Hemelrijck, D., Elastic orthotropic parameter identification by inverse modeling of biaxial tests using digital image correlation. In Proceedings of the 8th European Mechanics of Materials Conference on Material and Structural Identification from full field Measurements. Pp53-61, Cachan France, 13-15 September 2005.

[10] Cooreman, S., Lecompte, D., Sol, H., Vantomme, J., Debruyne, D., Elasto-plastic material parameter identification by inverse methods: Calculation of the sensitivity matrix. / International Journal of Solids and Structures 44, 4329–4341, 2007.

[11] Ramault, C., Makris, A., Sol, H., Van Hemelrijck, D., Lecompte, D., Lamkanfi, E., Van Paepegem, W., Development of an Inverse Method for Material Characterization using a Biaxially Loaded Cruciform Composite Specimen, In Proceedings of SEM Annual conference, Albuquerque, New Mexico USA, 1-4 June 2009.

[12] Avril, S., Bonnet, M., Bretelle, A.-S., Grédiac, M., et al, Overview of Identification Methods of Mechanical Parameters Based on Full-Field Measurements, Experimental Mechanics 48:381-402, 2008.

[13] Flores, P., Development of Experimental Equipment and Identification Procedures for Sheet Metal Constitutive Laws. PhD thesis, Universite de Liège, 2006.

[14] Sol, H., De Visscher, J., Hua, H., Vantomme, J. De Wilde, W.P., La Procédure Résonalyser. La revue des Laboratoires d'essais, vol. 46, 1996.

[15] Sol, H., Hua, H., De Visscher, J., Vantomme, J., De Wilde, W.P., A mixed numerical/experimental technique for the non-destructive identification of the stiffness properties of fiber reinforced composite materials. Journal of NDT&E International 30 (2), 88–91, 1997.

[16] Shi, Y., Sol, H., Hua, H., Transverse shear modulus identification by an inverse method using measured flexural resonance frequencies from beams. Journal of Sound and Vibrations 285 (1–2), 425–442, 2005.

[17] Sun, Y., Pang, J.H.L., Wong, C.K., Su, F., Finite element formulation for a digital image correlation method. Journal of Applied Optics, Vol. 44, No 34, 2005.

[18] Bui, H.D., Inverse problems in the Mechanics of Materials: An Introduction, CRC Press, Inc., Florida, 1994.

[19] Calvetti, D., Somersalo, E., Introduction to Bayesian Scientific Computing. Ten lectures on subjective computing. Survey and Tutorials in the Applied Mathematical Science, Volume 2, Springer, 2007.

Proceedings of the 8th National Congress on Theoretical and Applied Mechanics, May 28-29, Brussels, Belgium.

Study on the influence of design parameter variation on the dynamic behaviour of honeycomb sandwich panels

Stijn Debruyne[2], Dirk Vandepitte[1], Eric Debrabandere[2], Marc Hongerloot[2]
[1]Department of Mechanical Engineering, Katholieke Universiteit Leuven
Celestijnenlaan 300b, 3001 Heverlee – Belgium
[2]Department of Industrial Science, Katholieke Hogeschool Brugge Oostende
Zeedijk 101, 8400 Ostend – Belgium
email: stijn.debruyne@khbo.be, dirk.vandepitte@mech.kuleuven.be, eric.debrabandere@khbo.be, marc.hongerloot@khbo.be

Abstract: **Sandwich panels are layered structures that consist of at least five layers : two thin face sheets that are bonded with bonding layers to the thick core. The core has a very low density whereas the face sheets are stiff and strong. The entire panel combines high mechanical properties with a very low areal mass. Most of the structural characteristics of the panel (material selection and thickness of each layer) can be selected independently of other parameters, and the overall characteristics of the panel depend on the particular selection of parameters. Because of the wide range of panel parameters, numerical modelling is useful to provide insight into the structural characteristics of a particular panel. This paper studies the effect of design parameter variations on the dynamic behaviour of honeycomb sandwich panels. The dynamic behaviour includes natural frequencies, mode shapes and damping of such panels with free boundary conditions. In the first section the structure of honeycomb sandwich panels is illustrated, in particular those with a ThermHex core. For a typical honeycomb panel the different design parameters are outlined.**
Natural frequencies and mode shapes can be predicted approximately using analytical models. Some of the methods are outlined in this article.
The second section of the paper presents the numerical modelling of a sandwich panel using commercial finite element codes. Different core modelling strategies are compared, e.g. geometrically correct or as a homogenised equivalent material. Advantages and drawbacks of the different methods are outlined. Different ways of modelling damping in the panels are also presented.
The third section discusses the experimental validation. To validate the finite element models, measurements are carried out on some test panels. Free-free boundary conditions are provided by elastically suspending the panels. To make measurements totally contactless, the test panels are excited acoustically and the vibration measurement is performed with a laser vibrometer. The way the data are captured and processed is also outlined.
Measured natural frequencies and mode shapes are compared with the calculated results from the different FE models and the analytical models. The techniques that are used for this comparison are briefly discussed.

The different FE models are updated using results from a sensitivity analysis. This analysis is performed theoretically for every design parameter and is discussed in detail. Results from the updated models are again compared with those obtained from measurements.
The uncertainty on different design parameters is studied and discussed. The influence of these various uncertainties on the natural frequencies and mode shapes is investigated using Monte Carlo simulations.

Keywords: **honeycomb sandwich panel, design parameter uncertainty, dynamic behaviour**

I. INTRODUCTION

Honeycomb sandwich panels consist of a thick honeycomb core that is bonded to thin face sheets. The structure of such a panel is shown in fig. 1. The coordinate system is used throughout this text, although the axes can also be indicated with numbers 1 to 3. The panels discussed in this article are built up with a ThermHex core. This type of honeycomb core is fabricated according to the folded honeycomb concept.
During this process a thermoplastic sheet is successively cut, folded and glued to form a completely closed honeycomb core. This process is shown in fig. 2.
The test panels that are discussed here have a core that is bonded to thin sheets of galvanised steel.
The elastic mechanical properties of a typical honeycomb core are described and analytically calculated by Gibson & Ashby [2]. They propose formulas for calculation of the in-plane and out-of-plane elastic moduli and Poisson ratios of the core.
As honeycomb sandwich panels become more and more important as structural parts in the automotive and aerospace industry, the need for accurate modelling of the dynamic behaviour of such panels increases. Accurate modelling requires knowledge of the different design parameters that determine the dynamic behaviour, which in this case are natural frequencies and mode shapes.
The main work on the dynamics of sandwich panels is related to conventional foam-core structures. Little work has been carried out on honeycomb panels. Nilsson & Nilsson [3] tried to analytically predict natural frequencies of a honeycomb sandwich plate with free boundary conditions using Blevins [4] formula in which areal mass and equivalent bending stiffness are frequency dependent.

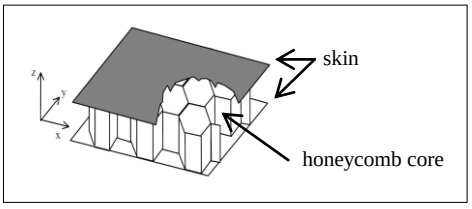

Fig. 1. Honeycomb sandwich panel

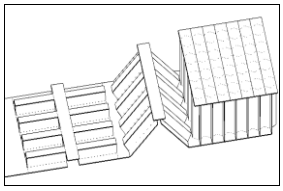

Fig. 2. The folded honeycomb process for completely closed honeycombs.

Another way to predict natural frequencies and mode shapes of a honeycomb panel is by means of the finite element method. In the past years, different new approaches have been developed which incorporate high order shear deformation of the core. Work in this area has been carried out by Topdar [5] and Qunli Liu [6][7]. The latter stated that the shear moduli of the core are important factors in the determination of the values of the natural frequencies and the sequence of mode shapes, especially at high frequencies. At low frequencies natural frequencies are mostly determined by the bending stiffness of the panel.

II. Considered design parameters

Honeycomb panels are complex structures with a high number of design parameters. It is therefore difficult to accurately predict their dynamic behaviour, certainly when some of the parameters are very difficult or even impossible to measure in a direct way. When the design parameters are studied one has to mention whether the honeycomb core of the model used is homogenized or not.
For the general honeycomb panel structure shown in fig. 1 table 1 gives an overview of the different design parameters studied in this article. They can be divided into two groups, geometric and material parameters. The abbreviations for the different parameters will be used throughout the article.

TABLE I

STUDIED DESIGN PARAMETERS FOR A PANEL WITH A NON HOMOGENIZED THERMHEX CORE AND ISOTROPIC SKINS.

	parameter description	symbol	unit
geometry	overall panel width	w	mm
	overall panel length	l	mm
	skin thickness	t_s	mm
	core thickness	t_c	mm
	cell wall thickness	t	mm
	cell size	D	mm
material	core material elastic modulus	E_c	MPa
	core material poisson ratio	μ_c	/
	core material density	ρ_c	kg/m³
	skin elastic modulus	E_c	MPa
	skin poisson ratio	μ_s	/

In table 1 the cell size D is the diameter of the circumscribing circle, minus the cell wall thickness, of a regular hexagonal cell. Note that, at this stage, no parameters concerning the bonding layer between core and skin are considered. In a first approach the glue is considered as a perfect rigid connection of core and skin.
It is obvious from fig. 1 and 2 that a honeycomb core has 3 planes of symmetry, hence it can be considered as an orthotropic material. In that case the elastic behaviour of the homogenised core is determined by 9 independent elastic constants. Note that the Thermhex core shown in fig. 2 is in fact a three layer material. The bonding layer between core and skins is now a uniform layer. In fact, a honeycomb sandwich panel that is built up with two isotropic skins and a Thermhex core can be seen as a 7 layer laminate. Table 2 gives an overview of the design parameters of such a laminate, studied in this article. As in table 1 the parameters can here be divided in the same two groups.

TABLE 2

STUDIED DESIGN PARAMETERS FOR A PANEL WITH A HOMOGENIZED THERMHEX CORE AND ISOTROPIC SKINS.

	parameter description	symbol	unit
geometry	overall panel width	w	mm
	overall panel length	l	mm
	skin thickness	t_s	mm
	core thickness	t_c	mm
	outer core layer thickness	t_{cl}	mm
	bonding layer thickness	t_b	mm
material	core elastic modulus 1	E_{c1}	MPa
	core poisson ratio 12	μ_{c12}	/
	core shear modulus 12	G_{c12}	MPa
	core elastic modulus 3	E_{c3}	MPa
	core poisson ratio 13	μ_{c13}	/
	core shear modulus 13	G_{c13}	MPa
	core elastic modulus 2	E_{c2}	MPa
	core poisson ratio 23	μ_{c23}	/
	core shear modulus 23	G_{c23}	MPa
	equivalent core density	ρ_{ec}	kg/m³
	glue elastic modulus	E_b	MPa
	glue poisson ratio	μ_b	
	glue density	ρ_b	kg/m³
	skin elastic modulus	E_s	MPa
	skin poisson ratio	μ_s	/
	skin density	ρ_s	kg/m³
	outer core layer elastic modulus	E_{cl}	MPa
	outer core layer density	ρ_{cl}	kg/m³
	outer core layer poisson ratio	μ_{cl}	/

III. Finite element models

A. Description of FE - methods used

A geometrically accurate and realistic FE model of a sandwich panel with a honeycomb core inevitably has large numbers of nodes and elements. This article presents two different approaches to build a simplified model. The finite element software used for all models is Siemens UGS NX6.
A first way of modelling a honeycomb sandwich panel (with ThermHex core) is to fully model the panel's core geometry. This is illustrated in figure 3. Each cell wall is meshed with 8 (2x4) rectangular 4 node shell elements. The skin faces are meshed with triangular 3 node shell elements. For visibility only one meshed skin face is shown. For a panel with length 300 mm and width 200 mm the finite element model has over 117000 elements. It is obvious that the major drawback of this FE – approach is the high computational effort due to the high number of elements.
Another problem is that the uniform bonding layer between core and skin, and the uniform layer of core material are not modelled. The contribution of mass and stiffness to structural

behaviour is not taken into account. The properties of these intermediate layers are not well known.

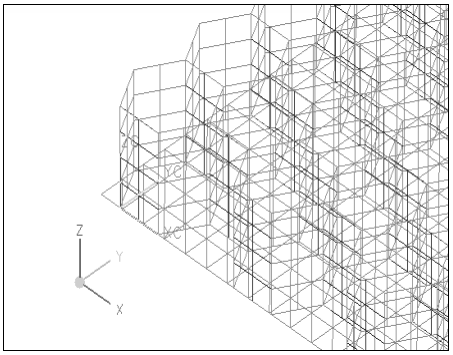

Fig. 3. Close-up of honeycomb panel model with fully modelled core.

A second way to model a honeycomb sandwich panel is by means of homogenisation of the core. As mentioned in the introduction a honeycomb core can be modelled as an orthotropic material. The 9 independent elastic constants are calculated by simulating tensile and shear tests on a sample of honeycomb core with 10 x 10 cells. The principle is shown in fig. 4.

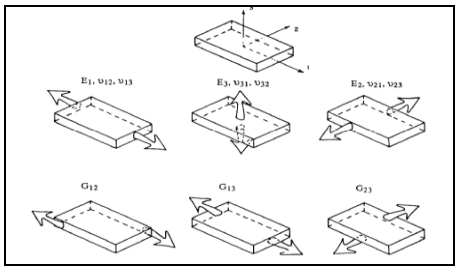

Fig. 4. Principle of determining the elastic constants of an orthotropic material.

The mass density of an equivalent homogenised regular honeycomb core is determined with equation (1) from Gibson & Ashby [2].

$$\frac{\rho^*}{\rho_s} = \frac{2 \cdot t}{\sqrt{3} \cdot l} \cdot \left(1 - \frac{t}{2 \cdot \sqrt{3} \cdot l}\right) \qquad (1)$$

In equation (1) ρ_s is the mass density of the honeycomb core material and ρ^* is the equivalent mass density of the homogenized core material. The cell wall thickness is expressed by t and l is the cell wall width. Due to the continuous folding process of the honeycomb core the cell walls parallel to the folding direction have a double thickness. For each hexagonal cell this counts for 2 walls.

Once these core parameters are determined the panel is modelled as a 7 layer laminate, thus including two uniform bonding layers. The elastic properties of the bonding layer are not known but they are estimated.

The whole panel is meshed with rectangular 8 node shell elements. For the same panel with dimensions 300 x 200 mm now only 121 elements are used.

From the FE models the first 10 natural frequencies and mode shapes are calculated for a panel with free-free boundary conditions. At this stage no damping is introduced in the models.

B. Comparison of the different FE - methods

The two FE models described in section IV.A are compared in this section. They are adopted for a honeycomb panel with dimensions and properties given in table 3. The face sheets are made from steel and the ThermHex core from polypropylene.

TABLE 3

DIMENSIONS AND PROPERTIES OF HONEYCOMB TEST PANEL.

parameter description	symbol	value
overall panel width	w	200 mm
overall panel height	l	300 mm
skin thickness	t_s	0,3 mm
core thickness	t_c	7,55 mm
cell wall thickness	t	0,18 mm
cell size	D	8 mm
bonding layer thickness	t_b	0,1 mm
core material elastic modulus	E_c	1500 MPa
core material poisson ratio	μ_c	0,39
core material density	ρ_c	1100 kg/m³
skin elastic modulus	E_c	210000 MPa
skin poisson ratio	μ_s	0,3
glue elastic modulus	E_b	10 MPa
glue density	ρ_g	1000 kg/m³
glue poisson ratio	μ_b	0,3

Figure 5 shows the corresponding modes and their frequencies, obtained by a geometrically realistic model of the core. both FE models. Figure 6 gives a comparison of the first 10 natural frequencies, calculated with both FE methods.

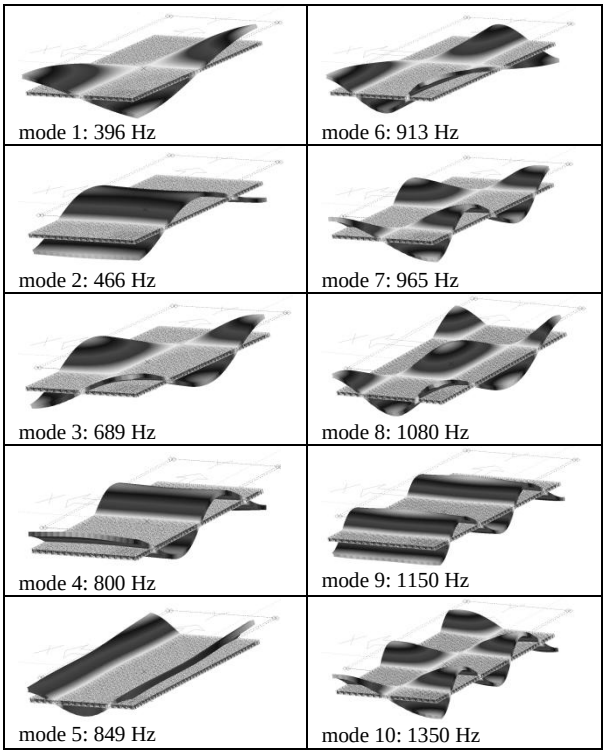

Fig. 5. First 10 calculated mode shapes, obtained by modelling the honeycomb core geometrically realistic.

The resemblance between the mode shapes of the two series, obtained by the different FE models, is checked visually. The mode sequence of both series is not identical. Only the natural frequencies of corresponding mode shapes are compared. This explains why in case of the 7 layered laminate, mode 5 has a lower natural frequency than mode 4. The relative deviations between both FE models varies between 2 and 17 %. The difference tends to increase as frequency increases.

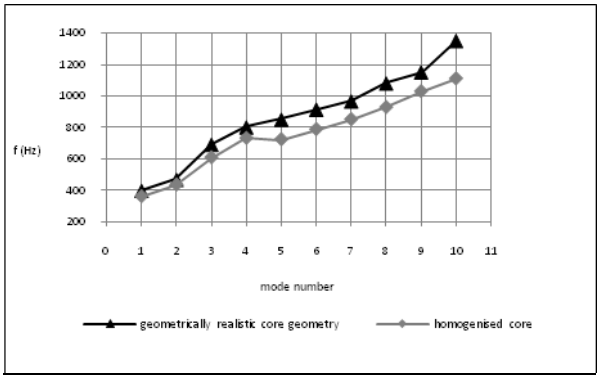

Fig. 6. Natural frequencies of the first 10 modes for FE models with geometrically realistic core geometry (black), and with homogenised core (grey).

The rather large differences between the two models have a number of reasons. In the model with the non-homogenised core the bonding layer is not modelled, thus making the panel stiffer than in the case where the bonding layer is considered. As the frequency increases, shear deformation of core an skins becomes more important. The fact that the bonding layer between core and skin is primarily shear loaded explains partly that the relative difference between the two methods increases with frequency. A second reason is that the cell walls parallel to the folding direction have a double thickness in the FE model. In reality these double cell walls are in fact 2 single walls, placed next to each other. This makes that the shear moduli of the modelled core are overestimated. As a result the modelled panel is stiffer as frequency increases.

C. *Modelling of damping*

With the proportional damping model, the damping matrix is calculated with the modal stiffness and modal mass matrices, using equation (2).

$$[C] = \alpha[K] + \beta[M] \qquad (2)$$

The mass and stiffness damping constants, α and β are determined by choosing the fractions of critical damping at two different frequencies and solving simultaneous equations for the constants. In this way, damping can be modelled as a linear function of frequency.

IV. EXPERIMENTAL VALIDATION

A. *Experimental set-up*

In the experimental modal analysis a contactless measurement method is used. The panel is suspended from elastic wires to attain free-free boundary conditions. Its properties are given in table 3. A regular grid of 11 x 11 measurement points is marked on the panel. The panel is excited acoustically by a loudspeaker. The excitation signal used is random noise with a bandwidth of 1,6 kHz. The response of the panel is measured with a laser vibrometer. Measurements are performed in an anechoic room. A Bruel & Kjaer 7536 data system is used for data acquisition. Experimental frequency response functions are identified from the measured data.

B. *Processing measured data*

Figure 7 shows the summed FRF for the test panel described in table 3.

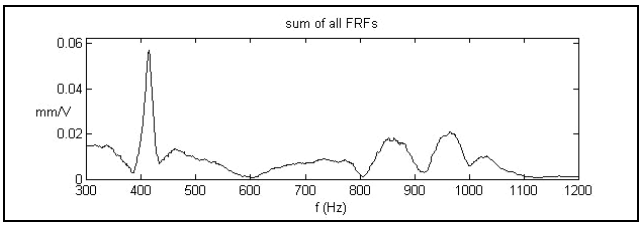

Fig. 7. Sum of all frequency response functions for the test panel described in table 3.

In figure 7 a number of peaks is visible in the chosen frequency band from 300 to 1200 Hz. Only the one at 414 Hz seems well isolated and thus the corresponding resonance frequency is easily readable. The other peaks are rather wide, making it difficult to visually detect a specific resonance frequency. This is the result of the coupling of two or more nearby modes, due to the high damping in the structure. The simple peak picking method should be used with caution.
Figure 8 shows the measured deflection shapes, corresponding to modes 2, 4, 5 and 8 from figure 5.

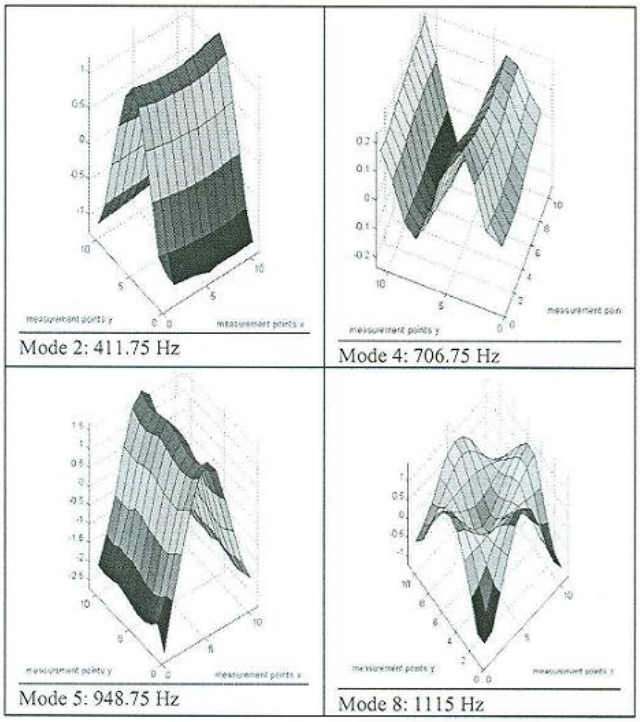

Fig. 8. Measured deflection shapes corresponding to modes 2, 4, 5 and 8 from figure 5.

To support the identification of modes an MNET [10] procedure (mixed numerical experimental technique) is used. The comparison of simulated modes and measured deflection shapes is done using the Modal Assurance Criterion [9], expressed in equation (4). This mathematical criterion compares two real vectors X and Y of the same size, producing a value between 0 and 1. If the MAC value equals 1, the vectors are identical. If zero, the vectors have nothing in common.

$$MAC_{XY} = \frac{(X^t Y)^2}{(Y^t Y)(X^t X)} \quad (4)$$

In equation (4), the superscript t denotes the transpose of the vector. Table 4 gives the resulting MAC values of the comparison of measured deflection shapes with the reference set of simulated mode shapes. Only the first 9 modes are considered.

TABLE 4

RESULT OF MODE SHAPE COMPARING ALGORITHM.

Simulated mode frequency (Hz)	Measured frequency (Hz)	MAC value	Deviation (%)
1	364.25	0.7469	-1.36
2	411.75	0.9818	5.4
3	619.25	0.6925	-1.98
4	706.75	0.7895	3.28
5	948.75	0.9698	-23.96
6	996.5	0.4931	-21.16
7	1079.25	0.4389	-21.32
8	1115	0.7506	-16.95
9	989.5	0.6743	3.79

Table 4 gives a good agreement for most modes. The well isolated peak with 411.75 Hz indeed has a deflection shape corresponding to mode 2, the first bending mode of the rectangular panel. This is confirmed by the good corresponding MAC value.
The measured mode at 948.75 Hz also correlates well. The other MAC values are lower, in particular those for modes 6 and 7. In general, a MAC value below 0.1 indicates that there is no similarity between the two considered vectors (or mode shapes); a MAC value below 0.4 indicates a low correlation of two modes. Obviously simulated mode 7 has no well corresponding measured deflection shape.
The other MAC values vary from 0.5 to 0.8. These values indicate a rather good correlation, although some of the measured deflection shapes are indeed coupled due to high damping, as mentioned earlier.

C. Discussion

A coupled mode of e.g. 2 mode shapes can mathematically be regarded as a linear combination of those 2 mode shapes. Therefore it is investigated whether a measured deflection shape is a linear combination of a few reference mode shapes. To illustrate this, the measured deflection shape with frequency 364.25 Hz is considered. Table 4 gives a MAC value of 0.7469 when the correspondence with simulated mode 1 is regarded. When the correspondence between the measured deflection shape and the first 5 reference modes is checked, table 5 is obtained.

TABLE 5

CORRESPONDENCE BETWEEN MEASURED DEFLECTION SHAPE AT 364.25 HZ AND FIRST 5 REFERENCE MODE SHAPES.

Mode	1	2	3	4	5
MAC	0.7469	0.0528	0.0023	0	0

Table 5 clearly shows that the measured deflection could be a combination of the first 3 simulated modes. There is obviously no relation between experimental mode 1 and simulated modes 3, 4 and 5.
Apart from the high damping, there is another reason why the MAC values from table 4 do not all exceed 0.9. As mentioned in section V.A the test panel is excited with random noise sound from a loudspeaker. The real sound pressure fields from the speaker are not yet taken into account.

V. MODEL UPDATING

Generally the aim of model updating is to minimise the differences between simulated and experimental results, which are in this case natural frequencies and mode shapes of a rectangular honeycomb sandwich panel with free-free boundary conditions.

A. Sensitivity analysis

The first step in performing a model updating procedure is studying the influence of every design parameter, discussed in section III, on the natural frequencies and mode shapes of the freely suspended panel. Such a study is called a sensitivity analysis. Suppose there are n_p design parameters p_j that govern a system response r_i. The change of that response due to a change of the design parameters can be expressed by equation (5).

$$\Delta r_i = \frac{\partial r_i}{\partial p_1}\Delta p_1 + \frac{\partial r_i}{\partial p_2}\Delta p_2 + \ldots + \frac{\partial r_i}{\partial p_{n_p}}\Delta p_{n_p} \qquad (5)$$

When all responses n_r are considered, equation (5) can be written in matrix form, giving equation (6).

$$[\Delta r] = [S]\,[\Delta p] \qquad (6)$$

The matrix S is referred to as the sensitivity matrix, its elements are called the sensitivity coefficients. To express the relative importance of each design parameter, the sensitivity coefficients are generally transformed to relative sensitivity coefficients and to avoid an ill conditioned sensitivity matrix all coefficients are normalised, according to equation (7).

$$s_{ij} = \frac{\partial r_i}{\partial p_j}\frac{p_j}{r_i} \qquad (7)$$

The sensitivity analysis as outlined above is carried out for the test panel with the design parameters given in table 2. For computational convenience the model with homogenised core is used here for the analysis. The analysis is performed, starting from the initial design parameter values, given in table 3. Each design parameter of the FE model is given a certain variation and the resulting change of the responses, in this case the first 10 natural frequencies, are determined. Every parameter is first varied in a wide range in order to investigate to which extent the system responses change linearly to a change of a certain parameter. For every parameter 6 variations are considered in the interval [-50%; 50%], spread symmetrically around the initial estimated parameter value. This step is necessary because the explained principle of a sensitivity analysis involves linearisation of the studied system behaviour. Only first order sensitivity is used in this study. Small parameter perturbation steps should be used in case the system behaviour is not linear.
Figure 7 shows the sensitivity matrix for the test panel, modelled as a 7 layer laminate with initial design parameters given in table 2.

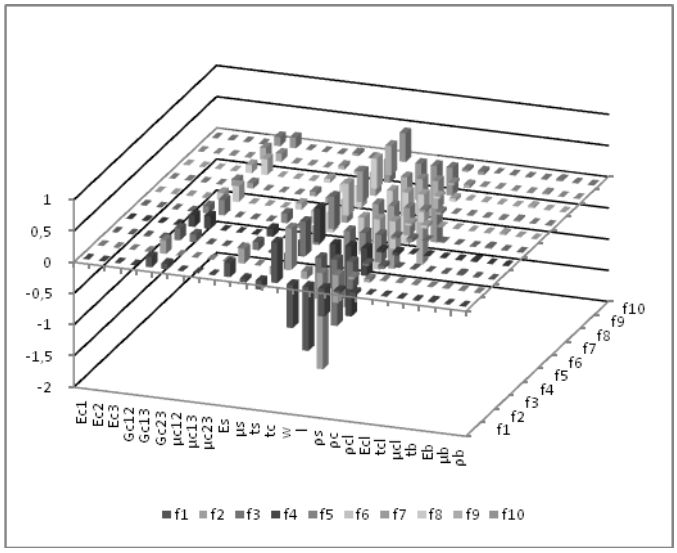

Fig. 7. Sensitivity matrix for the test panel with parameters as in table 2.

Figure 7 shows a strong variation among the different sensitivity coefficients. As mentioned earlier in the introduction, the parameters that determine the bending stiffness of the panel and the shear moduli of the homogenised core are the main parameters that govern the panel's dynamic response. For a honeycomb panel the bending stiffness per unit width increases with increasing skin thickness t_c As frequency increases, shear moduli G_{c13} and G_{c23} become more important in determining the panel's dynamic behaviour.
Along the frequency range studied, the influence of the mass densities of core and skin on the dynamic response does not change significantly.

B. Simulated versus experimentally determined natural frequencies

Table 4 shows a good correlation between simulated modes 2, 5 and 8 on the one hand, and their corresponding experimental modes on the other hand. The natural frequencies, simulated and experimentally determined, of these modes are given in table 6.

TABLE 6

COMPARISON OF THE FREQUENCIES OF 3 SIMULATED AND MEASURED MODE SHAPES.

Mode	$f_{simulation}$ (Hz)	$f_{measurement}$ (Hz)	Deviation (%)
2	434	411.75	5.40
5	729.9	706.75	3.28
8	926	1115	-16.95

Table 6 shows that the difference between simulated and measured natural frequencies increases with increasing frequency. Table 6 is used for further model updating as the 3 considered mode shapes cover the whole range of studied modes.

C. Design parameter uncertainty

The values of the different design parameters, given in table 3 are not exact. Some of them are given by the manufacturer's specification, others are estimated. The precise determination of a parameter value is sometimes impossible. In that case, a range should be specified for the parameter. When many samples of a population are available, a probability interval and a probability density function should be defined. In most cases a uniform or a normal distribution is used to consider the uncertainty of a specific parameter. However, the exact distribution of a parameter is seldom known. For convenience, a uniform distribution is considered here. For each studied design parameter, the probability interval is centred around its corresponding estimated value from table 3. For different kinds of parameters, relative interval widths vary as given by table 7.

TABLE 7

RELATIVE PROBABILITY INTERVAL WIDTHS.

Parameter description	Relative probability interval width (%)
Overall panel dimensions	1
Skin material properties	2
Core outer layer properties	10
Homogenized core material properties	20
Bonding layer material properties	50

The overall panel dimensions are easily be measured. The probability interval width of these parameters is therefore set equal to the measurement accuracy of 1%.

With this test panel the skin faces are made from steel. Its mass density and stiffness were experimentally determined and compared to manufacturer's specifications, leading to the proposed interval width of 2%. Mass density and stiffness were also experimentally determined for the core material. In this case, comparison with values from the panel manufacturer gave a tolerance of 10%.

The elastic properties of the homogenized honeycomb core were calculated from FE models. These were compared to analytically determined values, calculated with Gibson and Ashby's [2] formulas. This approach lead to an interval width of 20%.

For the properties of the bonding layer material just some estimated values were available. These parameter values were not determined experimentally so no comparison could be carried out. This leads to the large interval width of 50%.

The considered interval widths of core and bonding layer parameters are rather wide. It is perhaps questionable if the linearised parameter influence, resulting from the sensitivity analysis (see section VI A), approaches the real parameter influence in an acceptable way. As an example the relative sensitivity of mode 2 to the homogenised core shear modulus G_{c13} is shown in figure 8.

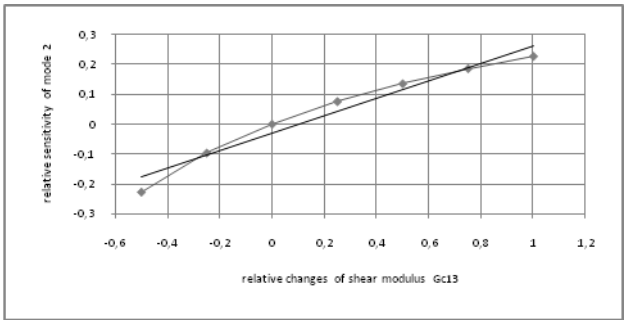

Fig. 8. Mode 2 relative sensitivities for relative changes of shear modulus G_{c13}. A Linear least squares approximation is added.

From the linear least squares approximation in figure 8 it is obvious that the influence of shear modulus G_{c13} on the frequency of mode 2 is not linear. In this case however, the horizontal axis covers a relative change of 100 % which is far more than the parameter variations considered in this study. If a symmetric interval of 20 % around the initial value of G_{c13} is considered, a linear approximation is very good in that interval (correlation 0,9997), as shown in figure 9.

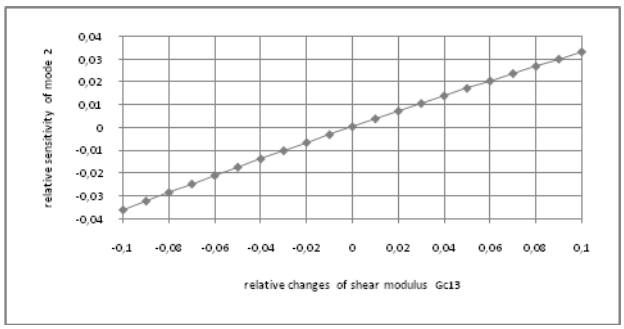

Fig. 9. Mode 2 relative sensitivities for changes of shear modulus G_{c13} in the interval [-0.1;0.1].

For the other design parameters similar conclusions can be drawn. If the probability intervals are kept small enough, the linearisation process of the sensitivity analysis will not create severe errors. In future research more precise sensitivity analysis will be carried out. For each design parameter a more correct interval width and probability function will be taken into account.

D. Model updating: results and discussion

For the test panel with design parameters given in table 2 and probability intervals in table 8 the results of the sensitivity analysis, as described in previous section C, are used to perform a model updating procedure. It is outlined in figure 10.

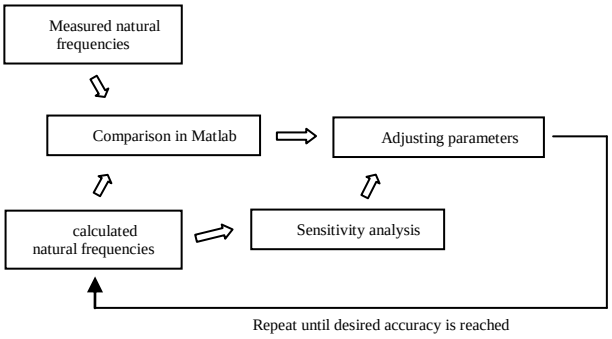

Fig. 10. Procedure for model updating.

When an infinitely large population of a certain parameter is considered, the mean value of the population is equal to the real expected parameter value. The smaller the size of the population, the more the population mean differs from the real expected value. To limit the error e between the calculated mean value and the real expected value, the population should have a minimum size n_{min}. According to Montgomery [16], equation (8) calculates the required population size in case of a Normal parameter distribution.

$$n_{min} = \left(\frac{3.\sigma_{ini}}{e}\right)^2 \quad (8)$$

In equation (8), σ_{ini} is the standard deviation of the initial maximum difference between calculated and measured frequency. In this study, e is the allowed absolute error on the calculated natural frequencies mean values. In this case 1 % of the initial maximum error is taken.

The principle of Monte Carlo simulations is that for a set of parameters random values are generated, taking into account the probability distribution for each parameter. In this case a uniform distribution is taken for every design parameter. For every set of random parameter values the output of the system, in this case natural frequencies of a honeycomb panel, is calculated. Monte Carlo simulations are a very useful tool in determining the probability distribution on the output of a process or the response of a system, considering input parameter uncertainty. In order to get good knowledge of the output distribution, the Monte Carlo simulations should be carried out a number of times. The higher the number of iterations, the more accurate the distribution prediction is.

In this study, each set of design parameters is used to calculate the values of the natural frequencies of modes 2,5 and 8. For this, the results of the sensitivity analysis are used.

The number of iterations used here is n_{min}, calculated with equation (8). As a result of these Monte Carlo simulations, the distributions of the 3 considered natural frequencies are calculated, taking into account design parameter uncertainty.

The goal of the updating procedure in this study is to minimize the difference between calculated and measured natural frequencies by tuning the different design parameters. Here the updating procedure is combined with Monte Carlo simulations. In this way, not only a set of optimised design parameter values and their corresponding natural frequencies are obtained, but also the probability distribution of the calculated natural frequencies is estimated.

As a result of the model updating procedure, improved values for the 3 natural frequencies of modes 2, 5 and 8 are calculated. These calculated values are in fact the mean values from a distribution, which is known from the Monte Carlo simulations. The set of design parameters, yielding these frequencies, represent the optimised design parameter mean values.

In this case the whole updating procedure is carried out 3 times. For simplicity every cycle the same relative probability interval width is taken for a specific parameter.

For every kind of distribution there are certain parameters that compare the shape of the distribution to the shape of a normal distribution. In this study the skewness γ and the kurtosis δ are used. They are calculated with equation (9).

$$\gamma = \frac{\tilde{\mu}_3}{\sqrt{\tilde{\mu}_2^3}} \quad \text{and} \quad \delta = \frac{\tilde{\mu}_4}{\tilde{\mu}_2^2} \quad (9)$$

In equation (9), $\tilde{\mu}_i$ is the i-th moment of the distribution. A positive skewness means that the distribution is asymmetric to the right. The skewness of a normal distribution is therefore equal to zero. The kurtosis of a normal distribution is 3. A kurtosis value greater than 3 means that the distribution is more pointed than a normal distribution.

For the calculated natural frequencies of the 3 studied modes, table 8 gives the mean value, standard deviation of a Normal distribution, skewness and kurtosis after the third iteration.

TABLE 8

DISTRIBUTION PARAMETERS FOR THE 3 CALCULATED NATURAL FREQUENCIES AFTER THE THIRD ITERATION

Mode	Mean frequency (Hz)	Standard deviation (Hz)	Skewness	Kurtosis
2	410.97	13.69	-0.0096	2.93
5	706.26	23.46	-0.0092	2.92
8	1011.08	33.73	-0.010	2.94

The skewness and kurtosis values indicate that the calculated frequency distributions are nearly Normal.

An overview of the obtained relative errors on the 3 natural frequencies is given in table 9 for each iteration.

TABLE 9

RELATIVE ERRORS ON THE 3 NATURAL FREQUENCIES DURING THE MODEL UPDATING PROCEDURE FOR THE FIRST 3 ITERATIONS

Mode	$Error_{initial}$ (%)	$Error_{iteration1}$ (%)	$Error_{iteration2}$ (%)	$Error_{iteration3}$ (%)
2	5.40	3.23	1.16	-0.19
5	3.28	2.11	0.87	-0.07
8	-16.95	-13.73	-10.41	-9.32

As is indicated in table 9, the first iteration yields the most significant error reduction. Iterations 2 and 3 still produce

some error reduction. It is clear however that in spite of a further increase in the number of iterations the error with mode 8 will stay around 10%. This indicates that, with the current set of design parameters and FE model, the errors cannot be substantially further reduced. There are a number of reasons for this.

In the updating procedure, the frequencies of the experimental modes are assumed to be correct. If there are any errors on the identified natural frequencies, the updated model may not converge to the measured model.

A second reason could be that some initial values of some design parameters were fully estimated, e.g. the stiffness and thickness of the bonding layer. Earlier it has been mentioned that, with increased frequency, the importance of shear deformation increases. As the bonding layer is mainly shear loaded, an underestimation of e.g. the glue stiffness leads to an underestimation of calculated natural frequencies. According to the results of the previously described sensitivity analysis an underestimation of the glue stiffness of 10% leads to an underestimation of 0.23 % of the natural frequency from mode 2. Hence it seems unlikely that a wrong estimation of the glue parameters could explain the large errors in the calculated frequencies for modes 2 and 4. Future research will be done in this area, using more and larger test panels. Also measurements will be carried out to determine honeycomb core elastic properties more accurately. Further work must also be done on the specific variability of every design parameter.

VI. CONCLUSIONS

In this article the composition of typical honeycomb sandwich panels is discussed, in particular panels with a thermoplastic ThermHex core. The different design parameters of such panels are outlined.

Two ways of building up finite element models in commercial software are outlined. Advantages and shortcomings of both methods are discussed.

The experimental determination of mode shapes and their natural frequency has been discussed thoroughly, emphasising on the fact that high structural damping may lead to complications in this area.

The different steps, leading to the updating of FE models, are discussed extensively. These include design parameter uncertainty, sensitivity analysis and the use of Monte Carlo routines. The results of the application on a test panel are discussed.

The real uncertainties on the different design parameters will be thoroughly studied, using an elaborate amount of test honeycomb panels. Special attention will be made to the true elastic properties of the bonding layer and to the frequency dependency of elastic material properties.

REFERENCES

[1] Dan Zenkert, *An introduction to Sandwich Construction*, Emas Publishing, 1996.

[2] L.J. Gibson & M.F. Ashby, *Cellular solids*, Pergamon Press, 1988.

[3] E. Nilsson & A.C. Nilsson, *Prediction and measurement of some dynamic properties of sandwich structures with honeycomb and foam cores*, Journal of sound and vibration, (2002) 251(3), 409-430.

[4] R.D. Blevins, *Formulas for natural frequency and mode shape*, Krieger Publishing Company 1984.

[5] P. Topdar, *Finite element analysis of composite and sandwich plates using a continuous inter-laminar shear stress model*, Journal of sandwich structures and materials, 2003, 5, 207.

[6] Qunli Liu, *Role of anisotropic core in vibration properties of honeycomb sandwich panels*, Journal of thermoplastic composite materials, 2002, 15;23.

[7] Qunli Liu, *Effect of soft honeycomb core on flexural vibration of sandwich panel using low order and high order shear deformation models*, Journal of sandwich structures and materials, 2007; 9; 95.

[8] Qunli Liu, *Prediction of natural frequencies of a sandwich panel using thick plate theory*, Journal of sandwich structures and materials, 2001;3;289.

[9] W. Heylen, S. Lammens, P. Sas, *Modal analysis Theory and testing*, KU Leuven, 2003.

[10] Tom Louwagie, *Vibration – based methods for the identification of the elastic properties of layered materials*, Doctoraatsproefschrift D/2005/7515/80, 2005.

[11] S. Adhikari en J.Woodhouse, *Identification of damping: part I, viscous damping*, Journal of sound and vibration (2001) 243(1) 43-61.

[12] Junhong Park, *Transfer function methods to measure dynamic mechanical properties of complex structures*, Journal of sound and vibration 288 (2005) 57-79.

[13] Fang-Lin Huang, *A new approach to identification of structural damping ratios*, Journal of sound and vibration 303 (2007-) 144-153.

[14] L. Valdevit, *Structurally optimized sandwich panels with prismatic cores*, International journal of solids and structures 41 (2004) 5105-5124.

[15] Meifen He, *A study on composite honeycomb sandwich panel structure*, Materials and design 29 (2008) 709-713.

[16] Montgomery Douglas, Design and analysis of experiments, Arizona State University, 1996

Proceedings of the 8th National Congress on Theoretical and Applied Mechanics, May 28-29, Brussels, Belgium.

Modelling of the dynamic behavior of electronic boards used for spatial applications

D. Wattiaux[1], O. Verlinden[1], Ch. De Fruytier[2]
[1]Service de Mcanique Rationnelle, Dynamique et Vibrations, Faculté Polytechnique de Mons
31 Boulevard Dolez B, 7000 Mons - Belgium
[2]Thales Alenia Space ETCA
101 Rue Chapelle Beaussart, 6032 Mont-sur-Marchienne - Belgium
email: david.wattiaux@fpms.ac.be, olivier.verlinden@fpms.ac.be, christophe.defruytier@thalesaleniaspace.com

Abstract— **For several years, Thales Alenia Space Etca designs and develops modular equipments intended to be embarked on board of spatial vehicles. During their operating life, these equipments are subjected to severe mechanical vibrations which can produce failures of the electronic and magnetic components, as for examples the contact losses of electromagnetic relays or the appearance of cracks in the ferrite cores. Thales and the Faculté Polytechnique de Mons (FPMs) develop numerical tools in order to simulate their dynamic behavior to vibrations. This paper presents a dynamic modelling of electronic units composed by a multilayer PCB and an aluminium frame used for stiffening and fixing the PCB inside the electronic box. The equivalent mechanical properties of the PCB depend on the number of the layers and the proportion of copper/polyimide in each layer. They have been experimentally estimated from the identification of its first natural modes. Different rules of mixtures have been envisaged for estimating the mechanical properties of the polyimide. The assembly frame/PCB has been experimentally validated at low frequency by the comparison between the experimental and numerical transmissibilities.**

Keywords— **Spatial electronic equipments, Multilayer PCB, Orthotropic material model, Modal Analysis, Finite Element Method**

I. Introduction

THALES Alenia Space Etca industry, located in Charleroi (Belgium), is the Belgian leader in electronics for space applications (satellite launchers and space vehicles). The company, which has 40 years of expertise in this field, is the number 1 in Europe for electrical supplies and distribution equipments on board of satellites and the number 2 in Europe for the supplies of satellite transmitter tubes. It is also the main supplier of control and command units for the Ariane 5 launcher. Thales Alenia Space ETCA is the biggest subsidiary of Thales Alenia Space France. For more than forty years, the company has been a major player in the field of electronic constructions for the space industry in Europe, an industry that represents over 70 % of its turnover. Almost 80 % of its turnover comes from exports, mainly to European countries, but also to India, China, Japan and Russia.

Since a few years, Thales Alenia Space Etca develops a concept of modular equipments. This concept allows to cover a wide range of spatial applications and to reduce the costs of development and manufacture. As illustrated in Figures 1 and 2, the modular equipements are made up of an assembly of electronic units composed of a PCB (Printed Circuit Board) and an aluminium frame on which the PCB is screwed. The frames are machined in Aluminium 6061 and are used for stiffening and fixing the PCB inside the electronic box.

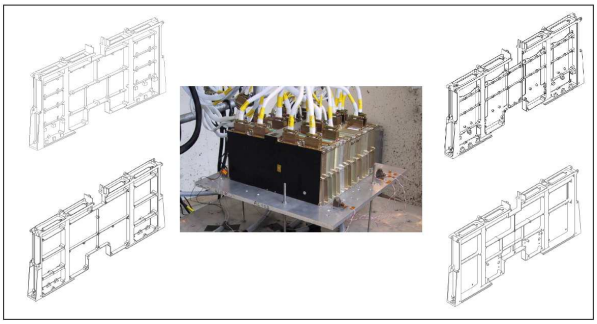

Fig. 1. Example of a modular equipment developped by Thales Alenia Space Etca

The PCBs are multilayer structures, each layer being composed by a non-conductive polyimide substrat coated by copper sheets. The polyimide is a laminate composite which is often used in the space industry to build PCBs because it presents excellent thermal and mechanical properties and a good chemical resistance. The conductive pathways are etched on the PCB by removing the unwanted copper by photographic techniques. The electronic and magnetic components are fastened to the PCB with thermal glue.

During the flight of the satellite, the electronic equipements which are embarked inside the launcher are submitted to severe vibrations. This is due to the numerous pyrotechnic devices, such as pyrotechnic valves or Mild Detonating Fuses, which are used to carry out various operations like separation of structural elements (booster sep-

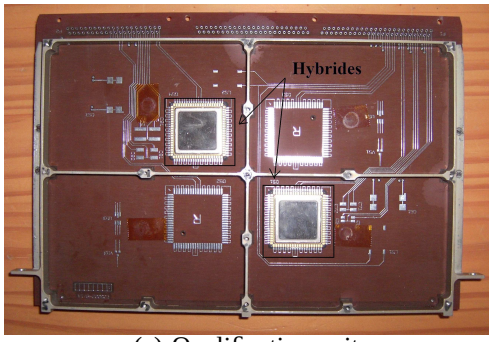

(a) Qualification unit

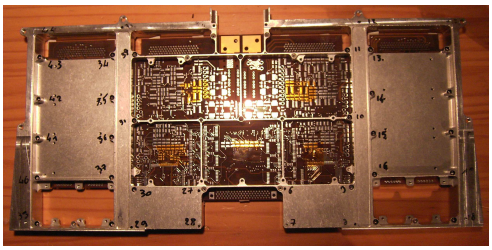

(b) DHP unit

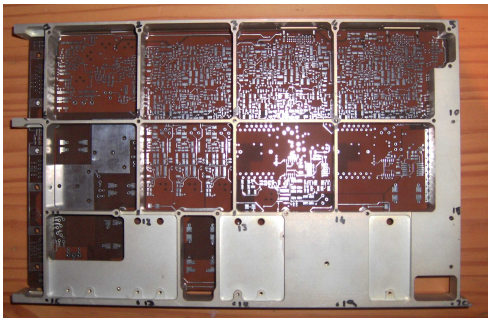

(c) Medium Power unit

Fig. 2. View of the different configurations of electronic units making up the modular equipments

aration,...), unlocking mechanisms (unfolding solar panels,...) or activation of on-board operating subsystems (Table I). The shock wave generated by the blast of these pyrotechnic devices produces severe vibrations inside the space shuttles which can cause failures in the electronic units. The most common damages are relay chatter, cracks of magnetic components or crystals and ceramic lift off.

The objective of this study consists in elaborating a Finite Element model of electronic units in order to optimize the location on the PCB of the electronic and magnetic components which are sensitive to vibrations. In this paper, we shall present the results for two configurations of the assembly frame/PCB:

- the *Qualification unit* which is used to check and quantify the vibration resistance of the electronic and magnetic components;
- the *DHP unit* which is an electronic unit of some satellites.

TABLE I
PYROTECHNIC APPLICATIONS IN ASTRONAUTICS [1]

Program	Number of installed pyrotechnic devices
Mercury	46
Gemini	139
Saturn	≈ 150
Apollo (CSM/SLA/LM)	314
Apollo (CSM/SLA) for Skylab	249

The Qualification PCB is composed of 8 layers whereas the one of the DHP is composed of 12 layers. The proportion polyimide/copper varies from a layer to the other.

II. COMPUTER MODELLING THE ALUMINIUM FRAMES

A. Finite Element model of the aluminium frame

The aluminium frames have been built under a classical FE software (`ANSYS 8.1`) and has been validated and updated from an experimental modal analysis. The geometry of the frames have been imported to `ANSYS` from a CAD software and has been meshed with 3D tetrahedral structural solid elements (`SOLID 187`). The element `SOLID 187` is defined by 10 nodes with 3 degrees of fredoom per node. The FE model of the qualification and DHP frames are shown in Figures 3 and 4 respectively. In total, 124471 elements have been used to describe the DHP frame and 27843 elements for the Qualification frame.

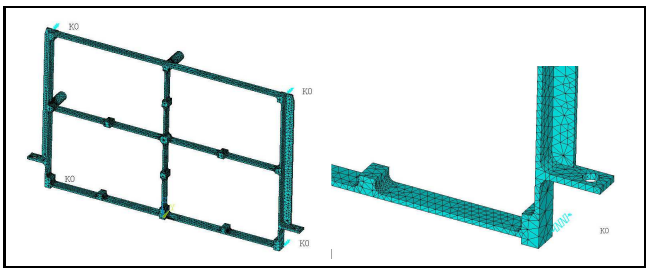

Fig. 3. Finite Element model of the Qualification frame

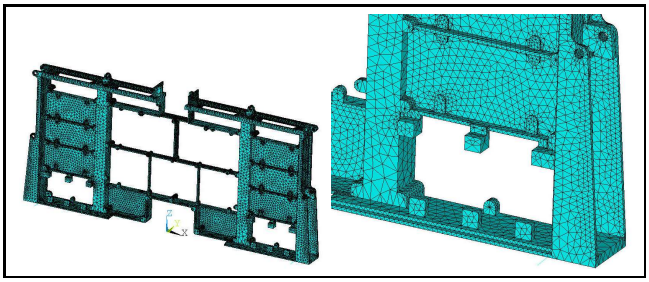

Fig. 4. Finite Element model of the DHP frame

During the experimental modal analysis, the frames

were supported by 4 moss blocks, as illustrated in Fig 5. These boundary conditions have been taken into account in our FE model by the introduction of spring-damper elements for which the stiffness and damping values have been estimated from the measurement of the rigid mode shapes. Besides, the sensors used to measure vibratory responses of the frames have been modeled with structural mass elements (MASS21).

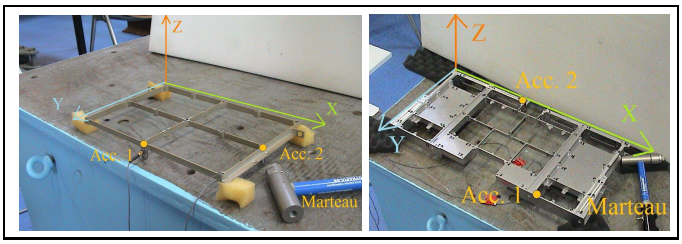

Fig. 5. Setup for the experimental modal analysis – Qualification frame (left) and DHP frame (right)

Given that the frames are machined in aluminium 6061, the material properties are perfectly known and are given in Table II.

TABLE II
MATERIAL PROPERTIES OF THE ALUMINIUM 6061

Young's modulus E	69 GPa
Poisson's ratio ν	0.33
Density ρ	2700 kg/m^3

B. Model validation

A model validation has been realized by comparing the modal properties of the test facility deduced from the model and the ones experimentally identified from measured frequency response functions. The Frequency Response Functions (FRF) $H_{ij}(\omega)$ have been measured in the frequency range [0 – 2048 Hz] with a frequency resolution of 0.5 Hz in the direction perpendicular to the frame. The measurements and the identification of the modal characteristics have been carried out with the LMS Tes.Lab software. The natural frequencies f_k, damping factors ξ_k and modal vectors $\{\vec{\psi}_k\}$ have been identified using the Least Square Complex Exponential (LSCE) method [2] and compared to the ones deduced from the FE model. Two comparison criteria have been used: the relative difference between natural frequencies and the Modal Assurance Criterion (MAC).

The relative difference between natural frequencies is calculated as follows [2]:

$$\Delta = \frac{\left| f^E - f^S \right|}{f^S} \tag{1}$$

where the superscripts ^{E} and ^{S} are used for experimental and model data respectively.

The experimental and numerical mode shapes are matched from the Modal Assurance Criterion (MAC) defined by [2];

$$\mathrm{MAC} = \frac{\left(\{\psi^E\}^T \{\psi^S\} \right)^2}{\left(\{\psi^E\}^T \{\psi^E\} \right) \left(\{\psi^S\}^T \{\psi^S\} \right)} \tag{2}$$

where $\{\psi^E\}$ and $\{\psi^S\}$ denote the experimental and simulated modal vectors respectively.

Tables III and IV summarize for the Qualification and DHP frames respectively the first experimental and analytical modes which are correlated with a MAC value greater than 0.6 and a relative frequency difference lower than 10 %. These results allow to validate the FE model of aluminium frames.

TABLE III
CORRESPONDENCE BETWEEN EXPERIMENTAL AND NUMERICAL MODAL CHARACTERISTICS – QUALIFICATION FRAME

f^E (Hz)	f^S (Hz)	Δ (%)	MAC
111	106.5	3.8	0.99
325.5	345	6	0.92
466.5	489	4.8	0.98
665.5	702.5	5.6	0.82
1234	1255	1.7	0.71

TABLE IV
CORRESPONDENCE BETWEEN EXPERIMENTAL AND NUMERICAL MODAL CHARACTERISTICS – DHP FRAME

f^E (Hz)	f^S (Hz)	Δ (%)	MAC
113	108	4.4	0.99
159	157	1.4	0.99
388	381	1.9	0.91
423	431	1.8	0.87
839.5	835	0.5	0.73
1293.5	1267	2.1	0.88

C. Shell vs solid elements

With some geometric simplifications, the dynamic behavior of the aluminium frames can be also modeled with

shell elements (SHELL63). The SHELL63 element is defined by 4 nodes and has six degrees of freedom at each node. The use of shell elements allows to reduce efficiently the calculation time. For example, in the case of the DHP, the modelling of the frame with shell elements allows to decrease approximatively the calculation time of a factor 45. Nevertheless, for complex geometries of the frame, the shell elements don't allow to describre with accuracy the dynamic behavior. The comparison between the predictions obtained with shell elements (SHELL63) and structural solid elements (SOLID187) is shown in Figures 6(a) and 6(b) for the Qualification and DHP frames respectively.

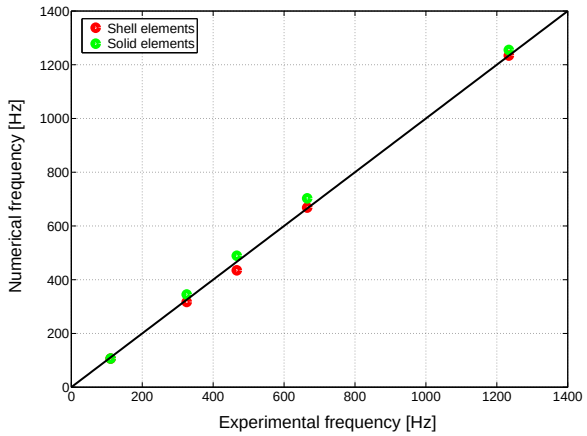

(a) Qualification frame

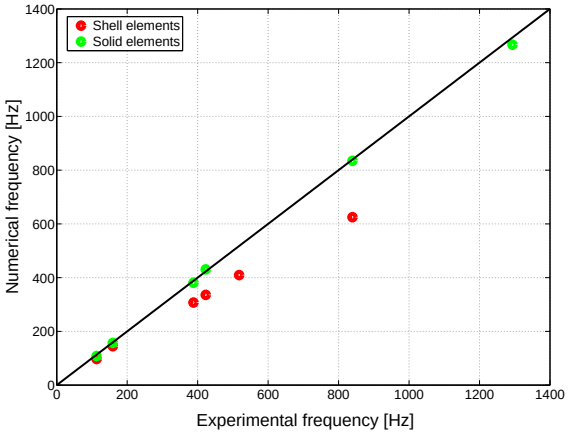

(b) DHP frame

Fig. 6. Comparison of the predictions obtained with shell elements (SHELL63) and structural solid elements (SOLID187)

III. Identification of the equivalent mechanical properties of the PCB

A. Introduction

The PCB is a multilayer structure where each layer is a mixture of copper and polyimide.

The mechanical properties of the PCB depend on the mechanical properties of the copper and the poliymid but also of the proportion of copper/polyimide in each layer. The equivalent mechanical properties of the PCB to introduce in the Finite Element model in order to simulate its dynamic behavior can be estimated from the identification of the first natural modes.

B. Theoretical background

For linear material, stress vector is related to the strains vector by the Hooke's law [3]:

$$\{\varepsilon\} = [D]^{-1}\{\sigma\} \tag{3}$$

where $\{\sigma\} = \{\sigma_x\ \sigma_y\ \sigma_z\ \sigma_{xy}\ \sigma_{yz}\ \sigma_{xz}\}^{\mathrm{T}}$ represents the stress vector and $\{\varepsilon\} = \{\varepsilon_x\ \varepsilon_y\ \varepsilon_z\ \varepsilon_{xy}\ \varepsilon_{yz}\ \varepsilon_{xz}\}^{\mathrm{T}}$ the strain vector. The flexibility matrix $[D]^{-1}$, called also the compliance matrix, is given by [4]:

$$[D]^{-1} = \begin{bmatrix} \frac{1}{E_x} & -\frac{\nu_{xy}}{E_x} & -\frac{\nu_{xz}}{E_x} & 0 & 0 & 0 \\ -\frac{\nu_{yx}}{E_y} & \frac{1}{E_y} & -\frac{\nu_{yz}}{E_y} & 0 & 0 & 0 \\ -\frac{\nu_{zx}}{E_z} & -\frac{\nu_{zy}}{E_z} & \frac{1}{E_z} & 0 & 0 & 0 \\ 0 & 0 & 0 & \frac{1}{G_{xy}} & 0 & 0 \\ 0 & 0 & 0 & 0 & \frac{1}{G_{yz}} & 0 \\ 0 & 0 & 0 & 0 & 0 & \frac{1}{G_{xz}} \end{bmatrix} \text{ where}$$

typical terms are:

- E_i: Young's modulus in the i direction
- G_{ij}: shear modulus in the ij plane
- ν_{ij}: major Poisson's ratio
- ν_{ji}: minor Poisson's ratio

In practice, only nine independent material parameters have to be specified because of the symmetry of the the flexibility matrix $[D]^{-1}$:

$$\frac{\nu_{yx}}{E_y} = \frac{\nu_{xy}}{E_x} \quad ; \quad \frac{\nu_{zx}}{E_z} = \frac{\nu_{xz}}{E_x} \quad ; \quad \frac{\nu_{zy}}{E_z} = \frac{\nu_{yz}}{E_y} \tag{4}$$

In the framework of Love-Kirchhoff hypotheses, the mechanical properties of a thin plate are completely defined by four independent elastic constants: E_x, E_y, G_{xy} and ν_{xy} [5].

For an isotropic material, the number of the elastic constants amounts to 2: Young's modulus E and the Poisson's ratio ν; the shear modulus G being given by:

$$G = \frac{E}{2(1+\nu)} \tag{5}$$

C. Updating process of the equivalent mechanical properties of the PCB

The shell elements (SHELL63) has been used to model the PCB. We have chosen an element size of about 5 mm

to mesh the PCB.

The 4 independent elastic constants E_x, E_y, G_{xy} and ν_{xy} are deduced by a least-squares optimization process that minimizes the difference between natural frequencies of the mode shapes which are coupled:

$$\varepsilon = \sum_{k=1}^{N} \left| f_k^{\text{Simulated}} - f_k^{\text{Measured}} \right|^2 \qquad (6)$$

where f_k^{Measured} et $f_k^{\text{Simulated}}$ represent the experimental and numerical natural frequencies respectively and N is the number of coupled mode shapes. For reminder, two mode shapes are considered coupled if their MAC value is larger than 0.60.

The equivalent mechanical properties of the PCB correspond to the quadruplet (E_x, E_y, G_{xy}, ν_{xy}) for which the function error ε is minimal.

We have assumed that the density ρ of the PCB is homogeneous and it is estimated from the ratio between the mass and the volume of the PCB.

D. Results for the Qualification PCB

D.1 Isotropic material model

The equivalent mechanical properties (E and ν) obtained with an isotropic model are shown in Table V.

TABLE V
EQUIVALENT MECHANICAL PROPERTIES OF THE QUALIFICATION PCB – ISOTROPIC MATERIAL MODEL

Young's modulus E	33.7 GPa
Shear modulus G	11.3 GPa
Poisson's ratio ν	0.49
Density ρ	2745 kg/m^3

Table VI summarizes the experimental and simulated modes which are correlated with a MAC value greater than 0.6. The MAC matrix is illustrated in Figure 7. The isotropic model provides results with a reasonable accuracy; the relative difference between experimental and simulated natural frequencies is smaller than 10%, except for the first torsional mode at 77 Hz. Moreover, it has some difficulties to reproduce correctly the mode shapes at 249 Hz and 256 Hz.

D.2 Orthotropic material model

The equivalent mechanical properties (E_x, E_y, G_{xy} and ν_{xy}) identified with an orthotropic material model are given in Table VII. The Young's moduli in the x and y directions

TABLE VI
CORRESPONDENCE BETWEEN EXPERIMENTAL AND NUMERICAL MODAL CHARACTERISTICS – QUALIFICATION PCB

f^E (Hz)	f^S (Hz)	Δ (%)	MAC
77	89	15.4	0.97
104	97	6.2	0.98
188	202	7.3	0.95
green249	234	5.7	0.63
green256	249	2.7	0.63
350	332	5.1	0.96
387	392	1.2	0.94
404	426	5.3	0.99
612	591	3.5	0.80

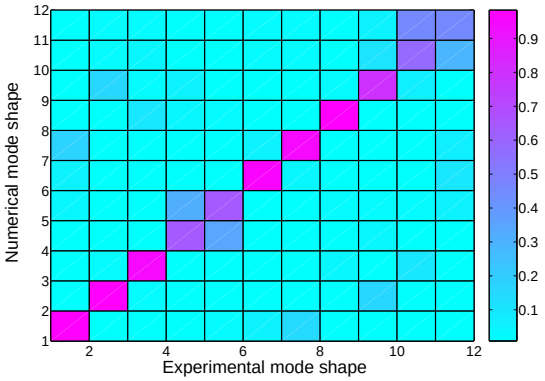

Fig. 7. MAC matrix – Isotropic material model

are identical and they are comparable with the Young's modulus which has been identified from an isotropic material model. Nevertheless the shear modulus G_{xy} is smaller than the one obtained with an isotropic model.

TABLE VII
EQUIVALENT MECHANICAL PROPERTIES OF THE QUALIFICATION PCB – ORTHOTROPIC MATERIAL MODEL

E_x	34.03 GPa
E_y	34.05 GPa
G_{xy}	7.57 GPa
ν_{xy}	0.51
ρ	2745 kg/m^3

Table VI summarizes the experimental and numerical modes which are correlated with a MAC value greater than 0.6. The MAC matrix is represented in Figure 7. The orthotropic model leads to better results than the isotropic model: the relative difference between experimental and simulated natural frequencies is smaller than 2%. Besides,

the mode shapes at 249 Hz and 256 Hz are reproduced with a greater accuracy.

TABLE VIII
CORRESPONDENCE BETWEEN EXPERIMENTAL AND NUMERICAL MODAL CHARACTERISTICS – QUALIFICATION PCB

f^E (Hz)	f^S (Hz)	Δ (%)	MAC
77	77	0	0.98
104	103	0.2	0.98
188	188	0	0.95
green249	249	0	0.89
green256	257	0.2	0.89
350	349	0.2	0.96
387	386	0.4	0.94
404	412	2	0.98
612	625	2	0.92

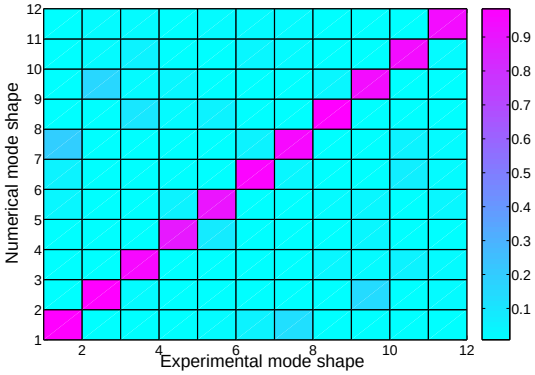

Fig. 8. MAC matrix – Orthotropic material model

E. Results for the DHP

The equivalent mechanical properties of the DHP have been identified using an orthotropic model and are given in Table IX. Given that the distribution of the copper in each layer is inhomogeneous, unlike the qualification PCB, the Young's moduli in the x and y directions are not similar.

TABLE IX
EQUIVALENT MECHANICAL PROPERTIES OF THE DHP – ORTHOTROPIC MATERIAL MODEL

E_x	18.20 GPa
E_y	31.18 GPa
G_{xy}	6.39 GPa
ν_{xy}	0.16
ρ	2446 kg/m^3

The first 8 experimental and simulated modes, correlated with a MAC value greater than 0.6 and a relative frequency difference lower than 5% are summarized in table X. Given that we have considered in our approach a homogeneous density, our model doesn't allow to compute with a high accuracy the mode shapes, in particular for the modes at higher frequencies.

TABLE X
CORRESPONDENCE BETWEEN EXPERIMENTAL AND NUMERICAL MODAL CHARACTERISTICS – DHP

f^E (Hz)	f^S (Hz)	Δ (%)	MAC
66	63	4.8	0.97
76	76	0	0.98
139	142	2.3	0.98
157	154	1.8	0.95
220	222	1.4	0.75
246	249	1.2	0.66
293	285	2.5	0.76
393	382	2.8	0.75

F. Identification of the mechanical properties of the polyimide

The mechanical properties of the polyimide can be estimated from the equivalent mechanical properties of the PCB in using the classical laminate theory.

For a laminate plate, the bending moment $\{M\} = \{M_x\, M_y\, M_{xy}\}^T$ is retated to the curvatures $\{\kappa\} = \{\kappa_x\, \kappa_y\, \kappa_{xy}\}^T$ by the following equation [4]:

$$\begin{bmatrix} M_x \\ M_y \\ M_{xy} \end{bmatrix} = \begin{bmatrix} D_{11} & D_{12} & 0 \\ D_{12} & D_{22} & 0 \\ 0 & 0 & D_{66} \end{bmatrix} \begin{bmatrix} \kappa_x \\ \kappa_y \\ \kappa_{xy} \end{bmatrix} \tag{7}$$

The components D_{ij} of the bending stiffness matrix D are given by [6]:

$$D_{ij} = \frac{1}{3}\sum_{k=1}^{N} Q_{ij}^k \left(h_k^3 - h_{k-1}^3\right) \tag{8}$$

where h_k represents the algebraic distance from the mid-surface of the plate to the upper surface of the k^{th} layer, N the number of layers, and Q_{ij}^k the components of the reduced stiffness matrix associated with layer k. The coefficients Q_{ij}^k are defined by:

$$Q^k = \begin{bmatrix} \frac{E_x^k}{1-\nu_{xy}^k\nu_{yx}^k} & \frac{\nu_{yx}^k E_x^k}{1-\nu_{xy}^k\nu_{yx}^k} & 0 \\ \frac{\nu_{xy}^k E_y^k}{1-\nu_{xy}^k\nu_{yx}^k} & \frac{E_y^k}{1-\nu_{xy}^k\nu_{yx}^k} & 0 \\ 0 & 0 & G_{xy}^k \end{bmatrix} \tag{9}$$

with,

- E_x^k : Young's modulus of layer k in the x direction
- E_y^k : Young's modulus of layer k in the y direction
- G_{xy}^k: shear modulus of layer k in the xy plane
- ν_{xy}^k: major Poisson's ratio of layer k
- ν_{yx}^k: minor Poisson's ratio of layer k

The mechanical properties of each layer k depend on the proportion of copper. In the hypothesis of a constant strain field, the mechanical properties of each layer k can be estimated from the following rule of mixture:

$$E_x^k = E_{x,c}.S_c^{*k} + E_{x,p}.S_p^{*k} \quad (10)$$

$$E_y^k = E_{y,c}.S_c^{*k} + E_{y,p}.S_p^{*k} \quad (11)$$

$$G_{xy}^k = G_{xy,c}.S_c^{*k} + G_{xy,p}.S_p^{*k} \quad (12)$$

$$\nu_{xy}^k = \nu_{xy,c}.S_c^{*k} + \nu_{xy,p}.S_p^{*k} \quad (13)$$

where suffixes $_c$ and $_p$ denote copper and polymide materials, respectively. The surface fractions S_c^{*k} and S_p^{*k} represent the porportion of copper and polyimide in each layer k. As illustrated in Figure 9, the strain field can be approximately considered as constant in the different layers of the PCB. These results have been obtained in applying a constant axial load on the PCB.

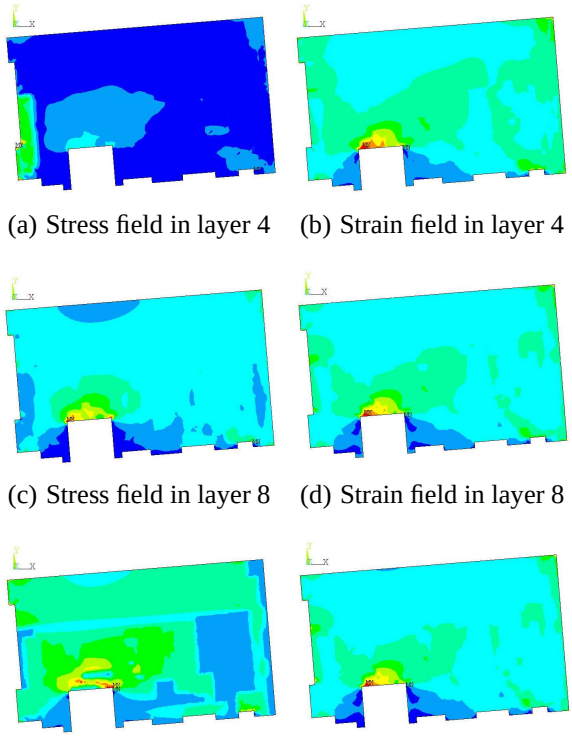

(a) Stress field in layer 4 (b) Strain field in layer 4

(c) Stress field in layer 8 (d) Strain field in layer 8

(e) Stress field in layer 10 (f) Strain field in layer 10

Fig. 9. Stress and strain fields simulated in differents layers of the DHP

The mechanical properties of the polyimide deduced from the global properties of the PCB with this rule of mixture are given in Table XI.

TABLE XI
ESTIMATED MECHANICAL PROPERTIES OF POLYIMIDE

	blueQualification PCB	blueDHP
E_x	16.16 GPa	12.11 GPa
E_y	16.18 GPa	12.36 GPa
greenG_{xy}	0,07 GPa	1,38 GPa
ν_{xy}	0.66	0.62
ρ	1704 kg/m^3	1732 kg/m^3

For a given PCB, the Young's moduli identified for the polyimide in the x and y directions are identical. Nevertheless, the results slightly vary from one PCB to another one, which can be explained by different manufacturing processes for the two PCBs.

On the other hand, the shear moduli obtained with this rule of mixture are incoherent; the shear modulus of the Qualification PCB is much smaller than the one of the DHP whereas its Young's moudlus is greater. More realistic results can be obtained for the shear modulus using an another rule of mixture:

$$\frac{1}{G_{xy}^k} = \frac{1}{G_{xy,c}}.S_c^{*k} + \frac{1}{G_{xy,p}}.S_p^{*k} \quad (14)$$

Although, this new rule of mixture is theoretically verified in the hypothesis of a constant stress field, its use leads to more coherent results (Table XII); the order of magnitude of shear moduli are similar.

TABLE XII
COMPARISON BETWEEN THE SHEAR MODULI IDENTIFIED FROM THE TWO RULES OF MIXTURE

black Shear modulus	blueOld rule	blueNew rule
redQualification	0.07 GPa	4.9 GPa
redDHP	1.38 GPa	3.84 GPa

IV. VALIDATION OF THE ASSEMBLY FRAME/PCB

In order to validate the modelling of the assembly frame/PCB, we have compared the numerical frequency response with the experimental one. The experimental setup that we have used for the experience is shown in Figure 10.

The acceleration of the equipement foundation has been measured with two piezoelectric sensors fixed by magnetization on the table of the shaker which has been used to generate the vibrations. Three piezoelectric sensors have

been glued on the PCB for measuring its vibratory response.

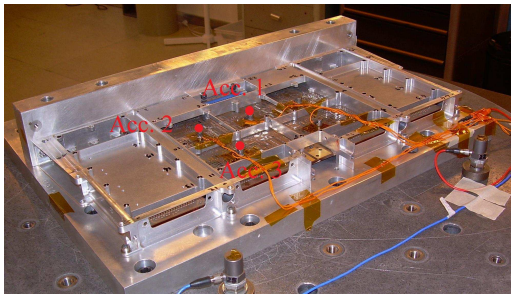

Fig. 10. View of the experimental setup

The Finite Element model of the assembly frame/PCB is illustrated in Figure 11. The screws operating the contact between the frame and the PCB are described by constraint equations which impose an identical displacement field to the set of nodes coinciding with the fixing screws. In Figure 11, the CP conditions are displayed by green symbols.

The equipement used to fix the assembly frame/PCB on the table of the shaker has been taken into account in the FE model blocking the nodes coinciding with the fixing screws (red symbols in Figure 11).

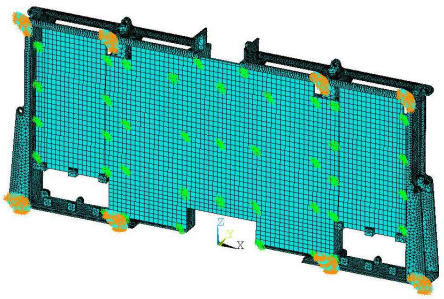

Fig. 11. Finite Element model of the assembly frame/PCB

The transmissibility between the acceleration of the foundation equipment and the acceleration of the PCB at the node 3 (`Acc.3`) has been measured in the frequency range [0 – 2 kHz]. The location of the accelerometers are shown in Fig. 10. The comparison between experimental and numerical transmissibilities is shown in Fig. 12. For the simulation, we have introduced in our FE model a constant damping ratio of 2% which corresponds to the mean value measured experimentally in the frequency range [0 – 2 kHz].

Our FE model allows to reproduce with a good accuracy the first natural mode; the relative difference between the numerical and experimental frequencies is of 2%. However, it doesn't allow to simulate accurately the other natural modes. Although our model presents some limitations, it can be exploited to estimate the maximum response and the stress field of the equipment when it is subjected to a random vibration. If the excitation is defined in terms of a Power Spectral Density $PSD_{input}(f)$, the Root Mean Square acceleration a_{rms} is given by the Miles' equation [7]:

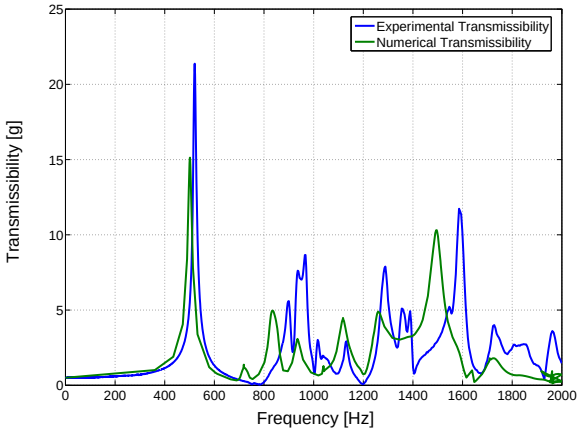

Fig. 12. Comparison between the experimental and numerical transmissibilities at node Acc.3

$$a_{rms} = 3\sqrt{\frac{\pi}{2} \cdot f_1 \cdot Q \cdot PSD_{input}(f_1)} \qquad (15)$$

where $f1$ represents the first natural frequency and Q corresponds to the dynamic amplification factor, equal to $= \frac{1}{2\xi}$ with ξ being the damping ratio.

V. Conclusions

This paper has presented a dynamic modelling of Printed Circuit Boards (PCB) used in the modular equipments developed by Thales Alenia Space Etca. The PCBs are multilayer structures where each layer is a mixture of copper and polyimide. An aluminium frame is used for stiffening and fixing the PCB inside the electronic box.

In this study, we have analyzed two configurations of the assembly frame/PCB. The Finite Element Method (FEM) has been used to describe the dynamic behavior of the aluminium frames and the PCB specimens. The FE models of the aluminium frame have been updated and validated up to 1200 Hz. For the PCBs, we have used an orthotropic material model. The equivalent mechanical properties to introduce in the FE model are experimentally identified from the measurement of the natural modes at low frequencies. The theory of the elastic multilayers plate and the use of appropriate rules of mixture have allowed to estimate the mechanical properties of the polyimide. The

assembly frame/PCB has been validated by the comparison at low frequencies between experimental and numerical transmissibilities measured in the frequency range [0 – 2 kHz].

The principal interest of our approach is that it can be easily adapted to wide range of PCBs. In particular, it allows to optimize the location on the PCB of the electronic components which are sensitive to vibrations in order to improve their reliability.

Our future works will consist in identifying the mechanical properties of the polyimide by modal analysis from a PCB without copper sheets in order to validate the results that we have obtained with the two PCBs studied in this paper.

REFERENCES

[1] D. Wattiaux, O. Verlinden, C. Conti, and Ch. De Fruytier. Prediction of the vibration levels generated by pyrotechnic shock using an approach by equivalent mechanical shock. *Vibration and Acoustic Journal*, 130(4):11 pages, 2008.

[2] N. Maia. *Theoretical and Experimental Modal Analysis*. Research Studies Press, England, 1997.

[3] M. Geradin and R. Rixen. *Thorie des Vibrations - Application la dynamique des structures*. Masson, Paris, 1992.

[4] S.W. Tsai and H.T. Hahn. *Introduction to composite materials*. Technomic, USA, 1980.

[5] M.E. McIntyre and J. Woodhouse. On measuring the elastic and damping constants of orthotropic sheet materials. *Acta Metallurgica*, 36(6):1397–1416, 1988.

[6] J.R. Vinson and R.L. Sierakowski. *The behavior of structures composed of composite materials*. Martinus Nijhoff, Netherlands, 1986.

[7] C. Lalanne. *Elaboration des spcifications*, volume 5 of *Vibrations et chocs mcaniques*. Hermes, Paris, 1999. `http://www.hermes-science.com`.

Proceedings of the 8th National Congress on Theoretical and Applied Mechanics, May 28-29, Brussels, Belgium.

Microphone positioning optimization for conditioning inverse tonal aeroacoustic problems

Flavio Presezniak[1], Gunther Steenackers[1], Patrick Guillaume[1]
[1]Vrije Universiteit Brussel, Department of Mechanical Engineering
Pleinlaan 2-1050 Brussel
email: fpresezn@vub.ac.be

Abstract— **The reconstruction of the forces responsible for the tonal noise on fans has been subject of several works on the past years. The inversion of the tonal noise problem is done making use of the transfer function derived from the blade force equation. The condition number of this transfer function matrix plays an important role on the inverse problem reducing the influence of the measurement noise on the final result. This parameter has a direct influence of the problem geometry, thus, an important participation of the measurement positions. With the objective to investigate the influence of the measurements positions and find an optimal measurement grid, several analysis and optimizations are performed. A tonal noise application with optimization of the microphone positions is performed. When comparing these new results with existing results from using classical measurement grids, like hemispherical or arc distributed microphones, a drastic reduction of the conditional number is achieved.**

Keywords— **Tonal noise,Aeroacoustic, Inverse problem, Global Optimization**

NOMENCLATURE LIST

a_1	inner rotor radius
a_2	outer rotor radius
B	number of blades
φ_s, r_s	source polar coordinates on rotor plane
φ, θ, r	spherical coordinates in radiation space
x,y,z	cartesian coordinates in the radiation space
f_z	axial pressure component acting on the rotor
f_z^0	time average value of the axial pressure
f_z^0	circunferential average value of f_z^0
g_{1z}	Green function
$[H]$	transfer function matrix
i	imaginary number
I	number of radial elements
J	number of points on the discretized radiation space
J_{sB+q}	Bessel function of order *(sB+q)*
k	wave number
p	acoustic pressure
q	source strength vector
q_{min}, q_{max}	minimum and maximum circunferential order q
Δr_1	distance between two radial elements
κ	condition number
Ω	angular velocity of the rotor
ω_1	blade passage angular frequency
$\|\cdot\|$	2-norm

Subscripts and indices

q, l	circumferential index
s, n	frequency index
i	radial element
j	radiation space discretization index
L	condensed source discretization index *(i,q)*
z	axial component

Superscripts

$+$	pseudo-inverse

I. INTRODUCTION

THE reconstruction of aeroacoustic sources strength for rotating blades has received special attention over the past years. In order to identify this strength, an inverse problem needs to be performed. The model for the blade tonal noise, commonly used for source strength reconstruction, is presented by Morse and Ingard [1].

Based on this model, several scientific references, like Gérard *et al.* [2] have performed the inverse problem. It was possible to verify that one of the most important parameters to solve this is the conditioning of the inverse problem. This parameter indicates the sensitivity if the solution to small errors, such as measurement noise.

With the objective to reduce the condition number of the transfer function matrix, a regularization can be performed. For the aeroacoustic problems the *Tikhonov* regularization is commonly used, which is presented in the work of Kim and Nelson [3] and Gérard, Berry and Masson [4].

With respect to the aeroacoustic problem of rotating blades, the conditioning issue also has a influence of the measurement location. This means that placing the microphones on determined positions makes it possible to reduce the condition number and reduce the necessity of reg-

ularization. Analyzing the presented model [1], it is possible to verify that the condition number does not only depend on the microphones positions, but also on the source position radius (r_s), seen on Figure 1.

For the static sources, a study concerning the condition number has been performed by Nelson and Yoon [5], to verify the influence on different relations between the source and microphones positions, like distance between sources and measurement positions but also eccentricity between sources and microphones have been analyzed. As a conclusion, it was possible to verify that *"the conditioning of the inverse problem was highly dependent on the geometry of sources and measurement position"*.

For the tonal noise of axial fans, the influence of different measurement position arrangements can be observed [4]. Two microphones position arrays are tested for the condition number: an arc distribution and a hemispheric distribution. The results show an important reduction of the condition number especially in the high frequency range.

This paper has the objective to better understand the influence of the variables on the condition number for the tonal noise transfer function matrix. Different parameter optimization problems are performed in order to find the optimal microphone distribution that minimizes the condition number over the considered frequency band. A parametric analysis is performed in order to identify the influence of all the possible microphone position variables, with the objective to improve the optimization procedure. The optimized microphone positions will be compared to the classical hemisphere and arc microphone distribution presented by Gérard *et al.* [4].

II. Direct Model for Tonal Noise for Axial Fans

The two important models for the sound pressure field generated by forces acting over the blade are the Ffowcs Williams-Hawking (FW-H) and the Morse and Ingard equation. While in the Morse-Ingard model the forces are posed on a spectral domain (circumferential Fourier series) and in the FW-H the force source terms are introduced on a spacial domain using a retarded time formulation.

Both equations are derived by following different strategies. In the FW-H equation, the derivation starts with the Lighthill acoustic analogy to introduce the effects of solid boundaries in contradiction to the Morse-Ingard formulation that introduces the forces as a dipolar source term on the Helmoltz equation to derive the sound pressure field. Despite those differences, both equations produce very similar results for the sound pressure field.

The general FW-H equation for aeroacoustics includes monopolar, dipolar and quadrupolar source terms. For a low speed fan, the dipolar source term is the most important term present. In the case of rotating surfaces, one also has the presence of quadrupole and monopole terms in the equation. The quadrupole term that represents a generation of sound due to the turbulent volume sources, is only significant when the mach number at the blade tip is higher than 0.85. The monopole source is due to the volume displacement effects of moving surfaces and is also called "thickness noise". The efficiency of this thickness noise is low at low fan speed rotation since the circumferential phase velocity of the fluid pressure fluctuations generated by the moving blades is way below the sonic velocity.

In this paper, the Morse-Ingard model [1] for the transfer function for tonal noise will be used. This model considers the cases of *uniform* and *nonuniform* flows. In uniform flow, the force acting over the blade will be independent of the blade angular position, resulting on a time-independent force distribution different from the nonuniform flow, where the force is a blade angular position dependent, making the problem much more complex.

The coordineate system for this case is presented on Figure 1 where it is possible to observe that the model uses a polar coordinate system to identify a source position over the fan and spherical coordinate system to identify a measurement point.

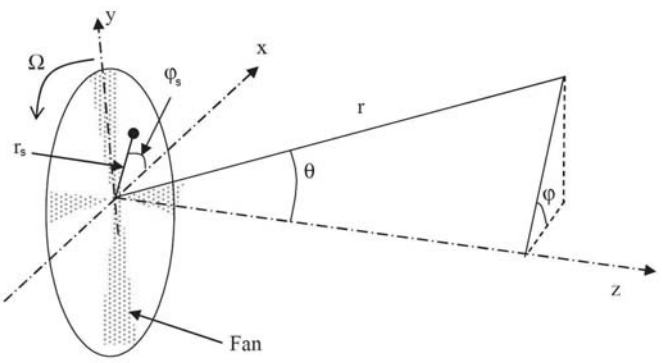

Fig. 1. Fan coordinate system

A. Uniform Flow

In the case of *uniform* flow, only the amplitude of the periodic force is not depended of φ_s but the phase is proportional to φ_s. Thus, acording to Morse and Ingard[1], the component z of the periodic force at $\varphi_s = 0$ is

$$f_z(t; r_s, 0) = \sum_{-\infty}^{+\infty} A_s(r_s)\, e^{-is\omega_1 t} \tag{1}$$

and for any other φ_s

$$f_z(t;r_s,\varphi_s)=\sum_{-\infty}^{+\infty}A_s(r_s)\,e^{-is\omega_1\left(t-\frac{\varphi_s}{\Omega}\right)}=f_z^0\sum\alpha_s e^{isB\varphi_s}e^{-is\omega_1 t} \tag{2}$$

with $\omega_1=B\Omega$ and $\alpha_s=A_s/f_z^0$.

The φ_s component of the force, that is considerably smaler than the z component for a well design fan, thus, this component will be negleted in this study.

Some expressions for α_s and for f_z^0 as function for the thrust force and torque repectively can be found on Morse and Ingard[1].

B. Non-uniform Flow

In the *nonuniform* flow, the response is considerably more complicated, since the force depends on r_s and φ_s. A simplification can be done as long as the flow is time-independent. The force distribuition will still periodic, with the fundamental frequency $\omega_1=B\Omega$, but now, the amplitude factors f_φ^0 and f_z^0 will be functions of φ_s. This dependence can be written in terms of Fourier series,

$$f_z^0(\varphi_s)=\bar{f_z^0}\sum_{-\infty}^{+\infty}\beta_q e^{iq\varphi_s} \tag{3}$$

with Eq. (3) on Eq. (2) it is possible to obtain the general expression

$$f_z(t;r_s,\varphi_s)=\bar{f_z^0}\sum_{sq}\alpha_s\beta_q e^{i(sB+q)\varphi_s-is\omega_1 t} \tag{4}$$

that consider the both types of flows.

C. The Radiated Sound

With the expression for the source force, it is possible to obtain the corresponding sound field, using the apropriate Green function. The acoustic source is distributed over a circle with the same radius of the propeler. Following Morse and Ingard[1] a point dipole source at the position r_s and φ_s in the propeler, produces the sound field

$$g_z=-ik\cos\theta\frac{e^{ikr}}{4\pi r}\sum_{m=-\infty}^{+\infty}i^m J_m(kr_1\sin\theta)\,e^{im(\varphi-\varphi_s)}e^{-i\omega t} \tag{5}$$

Applying this expression to obtain the sound produced by the sth harmonic of the proopeler-blade passage frequency $\omega_1/2\pi$, it is set in the g_z expression $\omega=s\omega_1$ and $k=s\omega_1/c=sk_1$. Thus, the sound field from the z component of the force is

$$p_z(r,\varphi,\theta)=\int\int f_z(r_s,\varphi_s)\,g_z(r_s,\varphi_s;r,\theta,\varphi)\,r_s dr_s d\varphi_s \tag{6}$$

where f_z and g_z is give by Eq. (4) and Eq. (5) repectively. The integral over φ_s is zero execept when $m=sB+q$, in which the integral is 2π. Then the sound pressure becomes [4]

$$p_z(r,\varphi,\theta)=-\tfrac{ik_1\cos\theta}{4\pi r}\sum_{s=-\infty}^{+\infty}\sum_{q=-\infty}^{+\infty}i^{sB+q}e^{isk_1 r}e^{i(sB+q)\varphi-is\omega_1 t}\times\int_{a_1}^{a_2}s\,\bar{f_z^0}(r_s)\,\alpha_s(r_s)\,\beta_q(r_s)\,J_{sB+q}(sk_1 r_s\sin\theta)\,2\pi r_s dr_s \tag{7}$$

Following Gérard *et al.*[4] the Eq. (7) can be written in terms of a time harmonic expansion

$$p(t;r,\varphi,\theta)=\sum_{s=-\infty}^{+\infty}p_s(s\omega_1;r,\varphi,\theta)\,e^{-is\omega_1 t} \tag{8}$$

with

$$p_s(s\omega_1;r,\varphi,\theta)=-\tfrac{ik_1\cos\theta}{4\pi r}\sum_{s=-\infty}^{+\infty}\sum_{q=-\infty}^{+\infty}i^{sB+q}e^{isk_1 r}e^{i(sB+q)\varphi}\times\int_{a_1}^{a_2}s\,\bar{f_z^0}(r_s)\,\alpha_s(r_s)\,\beta_q(r_s)\,J_{sB+q}(sk_1 r_s\sin\theta)\,2\pi r_s dr_s \tag{9}$$

The integral over r_s can be discretized in I equally separated points and the sum truncated over q circunferential harmonics. The radiation space is also discretized on J locations. Thus the Eq. (9) becomes

$$p_{sj}=p_s(s\omega_1;r_j,\varphi_j,\theta_j)=-\tfrac{ik_1\cos\theta_j}{4\pi r}\sum_{s=-\infty}^{+\infty}\sum_{q=-\infty}^{+\infty}i^{sB+q}e^{isk_1 r_j}e^{i(sB+q)\varphi_j}\times\sum_{i=1}^{I}s\,\bar{f_z^0}(r_{si})\,\alpha_s(r_{si})\,\beta_q(r_{si})\,J_{sB+q}(sk_1 r_{s1}\sin\theta)\,2\pi r_{si}\Delta r_{si} \tag{10}$$

where the subindices i and j represents respectively the source and radiation space discretization.

Writing this equation on a compact form

$$p_{sj}=\sum_L H_{sjL}\,f_{sL} \tag{11}$$

where the i and q indices have been condensed into a single index $L=(i,q)$, f_{sL} is a source vector that characterizes the dipole strength distribuition at radial location i, for the time harmonic s and circunferential harmonic q. Thus, the transfer function can be written as [4]

$$p_{sj}=\sum_L H_{sjL}\,f_{sL} \tag{12}$$

where the i and q indices have been condensed into a single index $L=(i,q)$, f_{sL} is a source vector that characterizes the dipole strength distribuition at radial location i, for the time harmonic s and circunferential harmonic q. Thus, the transfer function can be written as follows [4]

$$H_{sjL} = -\frac{isk_1 \cos\theta_j}{2r_j} i^{sB+q} e^{isk_1 r_j} e^{i(sB+q)\varphi_j} \Delta r_s J_{sB+q}\left(sk_1 r_{si} \sin\theta_j\right) r_{si} \tag{13}$$

III. Condition Number

The condition number of a matrix determine the sensitivity of the solution of an inverse problem to small errors, like noise, present on the measured pressure vector. The direct aeroacoustic problem is

$$p = Hq \tag{14}$$

and thus, the solution of the inverse problem passes to the invertion of the matrix H. The condition number of the H matrix, for a problem with M microphones and N sources points is defined as

$$\kappa(H) = \left\|[H]_{m\times n}\right\| \ \left\|[H]^{+}_{m\times n}\right\| \tag{15}$$

In terms of singular value decomposition, $\|H\| = \sigma_{\max}$ and $\|H^{+}\| = 1/\sigma_{\min}$. Therefore, the condition number is defined as

$$\kappa(H) = \sigma_{\max}/\sigma_{\min} \tag{16}$$

According to Nelson and Yoon[5], let's assume that small deviations on p produces small deviations δq in the solution, and then

$$H(q+\delta q) = (p+\delta p) \tag{17}$$

For two matrices A and B, a proprety of the 2-norm says that $\|AB\| \leq \|A\| \ \|B\|$. Aplying this property to the small deviations, $\delta q = H^{+}\delta p$, it is possible to verify that $\|\delta q\| \leq \|H^{+}\| \ \|\delta p\|$ and that $\|p\| \leq \|H\| \ \|q\|$. Therfore, it is possible to write

$$\|\delta q\| \ \|p\| \leq \|H\| \ \left\|H^{+}\right\| \ \|\delta p\| \ \|q\| \tag{18}$$

with the definition of the condition number

$$\frac{\delta q}{q} \leq \kappa(H)\,\frac{\|\delta p\|}{p} \tag{19}$$

The above equation showns the importance of the condition number to the solution. It is possible to verify that small perturbations in p, δp, will be amplifyed if the H matrix have a large condition number. In practical, extraneous noise introduced into the measurements of the acoustic pressure will have a large impact on the solution for the acoustic source strength if the matrix is badly conditined, with a large condition number κ.

IV. Optimization of the Microphone Positions

In order to achieve the smallest condition number, an optimization problem is defined and solved to find the optimal microphone positions in the available measurement space. Initially, the optimization problem is solved for 4 microphones but also a generalized solution for numerous microphones is given. The position of the microphones in the measurement space is described in polar coordinates, yielding the radius r and angles θ and ϕ as optimization parameters. The definition of the microphone optimization parameters is shown in Figure 1.

A. Optimization of 4 Microphone Positions

The condition number is a function of the frequency, as shown in Figure 7. Optimization over a frequency range is possible but it is also possible to optimize an objective function consisting of only one element when the optimized (eg. minimum) value is unattainable. It is decided to optimize the rms-value of the condition number (κ_{rms}) replacing the actual condition number (κ) as a function of frequency. The definition of κ_{rms} is given in Eq. (20) with $[\omega_{min}, \omega_{max}]$ the considered frequency range for the condition number.

$$\kappa_{rms} = \sqrt{\frac{1}{\omega_{max}-\omega_{min}} \int_{\omega_{min}}^{\omega_{max}} [\kappa(\omega)]^2 d\omega} \tag{20}$$

The optimization problem is stated in Eq. (21) as:

$$\begin{aligned} &\text{minimize } \ell_1(r_{1..4}, \theta_{1..4}, \phi_{1..4}) = \kappa_{rms} \\ &\text{subject to } 0 \leq \phi_{1..4} \leq 2\pi \\ &\qquad\qquad 0 \leq \theta_{1..4} < \pi/2 \\ &\qquad\qquad 0 \leq r_{1..4} \leq 3 \end{aligned} \tag{21}$$

where $\ell_1(r_{1..4}, \theta_{1..4}, \phi_{1..4})$ is the real valued scalar objective function, taking into account lower and upper bounds for the real variables $r_{1..4}$, $\theta_{1..4}$ and $\phi_{1..4}$.

The integration in Eq. (20) is performed numerically by using the trapezoidal rule over the range of frequencies specified for the calculation of the condition number (from 0 Hz to 2500 Hz).

The maximum allowable radius r of the microphones is limited to the physically available space for the microphone distribution. The limits of the angles $\theta_{1..4}$ and $\phi_{1..4}$ allow to position the microphones over a complete sphere.

Instead of optimizing the complete optimization problem for 12 parameters at once, first only the four θ-angles

are optimized in order to draw conclusions on the optimal microphone positions. Based on engineering judgement, one can assume that an even distribution over the complete circle for the $\phi_{1..4}$-angles may give an acceptable result for the microphone positions. The microphone radius values $r_{1..4}$ need to be chosen in the available measurement space. The remaining parameters are thus given a fixed value of $r_{1..4} = 1$ m and $\phi_{1..4} = [0, \pi/2, \pi, 3\pi/2]$.

Due to symmetry of the optimization problem, a number of different local minima are to be expected. The optimization problem is solved by using a modified version of the regressive optimization approach developed by Steenackers *et al*[6]. Solving the optimization problem for the $\theta_{1..4}$ parameters yields the results listed in Table I.

TABLE I
OPTIMIZATION RESULTS OF THE CONDITION NUMBER RMS-VALUE (κ_{rms}) FOR MICROPHONE ANGLES $\theta_{1..4}$.

κ_{rms}	θ_1 [rad]	θ_2 **[rad]**	θ_3 **[rad]**	θ_4 **[rad]**
98.95	1.5533	1.5533	1.5533	1.5533

From the results in Table I, one can conclude that all parameters have the same θ-value that converges to 90^o with a minimized value of $\kappa_{rms} = 98.95$. From the calculations in Table II one can also detect that κ_{rms} is decreasing when the θ-angle increases. This can also be seen in Figure 2 where κ_{rms} is calculated as a function of θ. For for small θ-values,κ_{rms}=2336.9 ($\theta = 1^o$) and from that point decreases to a minimum value of κ_{rms}=98.95 for $\theta = 89^o$. As there is a singularity in Eq. (13) for $\theta = 90^o$, one cannot calculate an accurate condition number for this value. For $\theta = 0^o$ all microphones are at the same position and thus this θ value is also discarted. When calculating κ_{rms} for other $\theta_{1..4}$-combinations yields a higher rms-value.

TABLE II
CALCULATION OF THE CONDITION NUMBER RMS-VALUE (κ_{rms}) FOR MICROPHONE ANGLES $\phi_{1..4}$.

κ_{rms}	θ **[rad]**	ϕ_1 **[rad]**	ϕ_2 **[rad]**	ϕ_3 **[rad]**	ϕ_4 **[rad]**
356.72	0.35	0	$\pi/2$	π	$3\pi/2$
239.58	0.70	0	$\pi/2$	π	$3\pi/2$
189.85	1.05	0	$\pi/2$	π	$3\pi/2$
159.68	1.40	0	$\pi/2$	π	$3\pi/2$

In the optimization problem stated in Eq. (21), the θ-values are limited within the range of the circle's first quarter. A combination of the θ-range together with the ϕ-range makes it possible to consider a complete sphere. From the optimal θ-values listed in Table I one can now also optimize the ϕ-angles in order to find the optimal microphone distribution. Note that the solution where one or more $\phi_{1..4}$-angles are equal must be discarded as this means that one or more microphones are coinciding. This solution is not allowed.

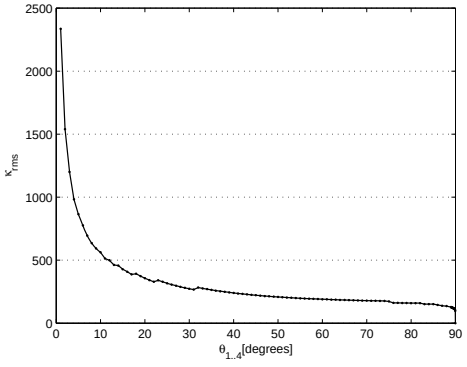

(a)

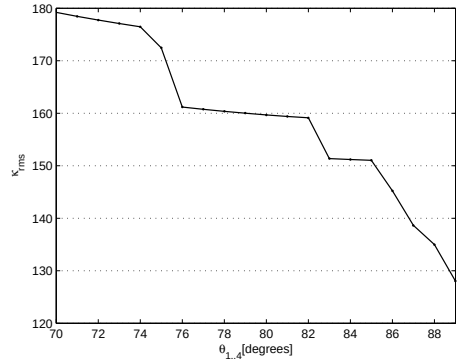

(b)

Fig. 2. Influence of the $\theta_{1..4}$ position on the condition number rms-value (a) between 0 and 90^o and (b) zoomed-in.

Starting from the θ-solution of Table I with κ_{rms}=98.95, 4 optimized ϕ-angles need to be optimized that do not coincide. Multiple (local) minima can occur due to symmetry of the optimization problem. In order to overcome this issue, the following optimization strategy will be applied: the number of parameters is reduced from 4 to 3 parameters by keeping the first microphone fixed at reference position $\phi = 0^\circ$. The position of the other 3 microphones will be optimized by constraining the ϕ-angles within a region of 120°, as shown on Figure 3. By solving the optimization problem this way, a unique solution will be found.

When solving the optimization problem with the $\theta_{1..4}$-values listed in Table I, one finds the optimized values for the $\phi_{1..4}$-parameters listed in the first row of Table III. For the optimized $\theta_{1..4}$-values, the same optimized values for the $\phi_{1..4}$-parameters are found as the ones previously assumed for the optimization of $\theta_{1..4}$. From these results, one can conclude that the optimal microphone distribution is indeed the one where the microphones are distributed

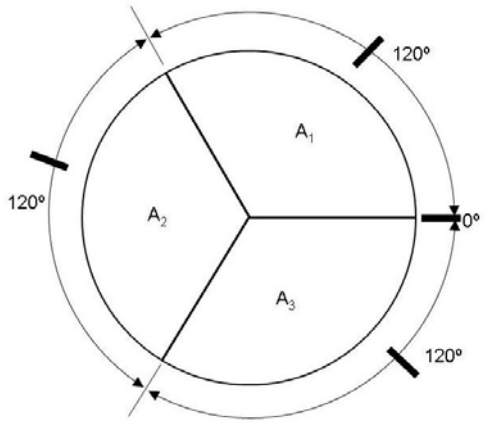

Fig. 3. Allowable ϕ-angles for optimization of the microphone positions.

evenly over the complete circle. In the case of 4 microphones, the microphones are positioned at a multiple of 90^o. In addition, when changing the optimal ϕ-angles with the same constant offset, the same minimized κ_{rms}-value is found. This indicates that the absolute values of the $\phi_{1..4}$ are not important, only the relative (uniform) distribution over the ϕ-circle. Changing the allowable $\phi_{1..4}$-range to $1/2$ or $1/4$ of a circle yields higher minimized κ_{rms}-values, as listed in the second row of Table III. One can thus conclude that distributing the microphones in a uniform manner over a complete circle will result in the smallest condition number.

TABLE III
OPTIMIZATION RESULTS OF THE CONDITION NUMBER RMS-VALUE (κ_{rms}) FOR MICROPHONE ANGLES $\phi_{1..4}$.

κ_{rms}	$\theta_{1..4}$ **[rad]**	ϕ_1 **[rad]**	ϕ_2 **[rad]**	ϕ_3 **[rad]**	ϕ_4 **[rad]**
98.95	1.5533	0	$\pi/4$	$\pi/2$	$3\pi/4$
524.89	1.5533	0	$\pi/3$	$2\pi/3$	π
753.21	1.5533	0	$\pi/8$	$3\pi/8$	$\pi/2$

When calculating κ_{rms} as a function of the radius r, one will notice that the radius parameter does not change the condition number when all radius values are identical. This means that for the radius, the optimal distribution for the microphones is the one where they are distributed over a circle with the same origin of the source rotation center.

When calculating the condition number for non-identical radius values yields a higher κ_{rms}-value. One can thus conclude that the microphones must be positioned and distributed on a circle with a chosen (fixed) radius. The actual value of the chosen radius does not have an influence on the κ_{rms}-value, as long as all $r_{1..4}$ are equal. This is also visible in Figure 4 where two different radii are considered for the 4 microphones. The first two microphones are assigned radius value r_1 while the other two microphones are positioned on radius value r_2. It is clear that on the response surface where $r_1 = r_2$, the condition number is the smallest with all $\kappa_{rms} = 399.02$. Optimization of the 4 microphone positions results in a minimized condition number as a function of frequency, visualized in Figure 5.

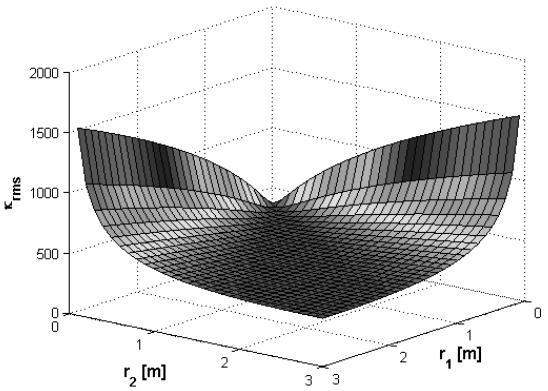

Fig. 4. Condition number rms-value (κ_{rms}) as a function of radius values r_1 and r_2.

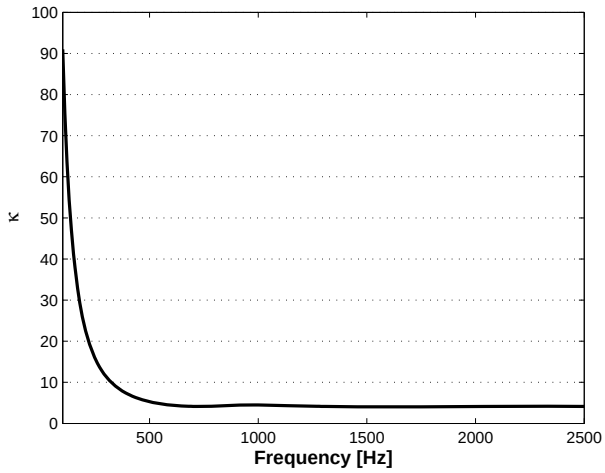

Fig. 5. Condition number (κ) as a function of frequency.

B. Optimization of 64 Microphone Positions

In order to make the simulation and optimization problem in accordance with the results obtained by Gérard *et al.*[4], the number of microphones is extended to 64. As the number of parameters is now equal to 192, the same optimization approach will now be applied to find the optimal parameter values that define the position of the 64 microphones and yield the smallest κ_{rms}-value for the condition number. First, only the 64 θ-angles are optimized in

order to draw conclusions on the optimal microphone positions. The remaining parameters are given a fixed value of $r_{1..64} = 1$ m and the $\phi_{1..64}$-angles are evenly distributed over a complete circle.

In accordance with the optimization results listed in Table I, minimization of the condition number results in the solution $\kappa_{rms} = 1.1263 \cdot 10^5$ with all 64 θ-angles the same value converging to 90^o(Table IV). When calculating κ_{rms} for other $\theta_{1..64}$-combinations yields a higher κ_{rms}-value. In order to optimize the $\phi_{1..64}$-angles, the same optimization strategy will be applied as described in Section IV-A, using the θ-value of Table IV and $r_{1..64} = 1$ m.

TABLE IV
OPTIMIZATION RESULTS OF THE CONDITION NUMBER RMS-VALUE (κ_{rms}) FOR MICROPHONE ANGLES $\phi_{1..64}$.

κ_{rms}	$\theta_{1..64}$ **[rad]**	$\phi_i (i = 1..64)$ **[rad]**
$1.1263 \cdot 10^5$	1.5533	$i \times \pi/32$

From the optimization results, one can again conclude that the optimal microphone distribution is the one where the microphones are distributed evenly over the complete circle. From Table V one can also detect that κ_{rms} is decreasing when the θ-angle increases. This can also be seen in Figure 6 where κ_{rms} is calculated as a function of θ for $\theta \in \left]0, \pi/2\right[$. The smallest κ_{rms}-value is found at identical angles $\theta_{1..64} = 90^o$ with $\kappa_{rms} = 1.1263 \cdot 10^5$.

TABLE V
OPTIMIZATION RESULTS OF THE CONDITION NUMBER RMS-VALUE ('κ_{rms}') FOR MICROPHONE ANGLES $\phi_{1..64}$.

κ_{rms}	$\theta_{1..64}$ **[rad]**	$\phi_i (i = 1..64)$ **[rad]**
$3.5852 \cdot 10^6$	0.35	$i \times \pi/32$
$1.0151 \cdot 10^6$	0.70	$i \times \pi/32$
$5.5922 \cdot 10^5$	1.05	$i \times \pi/32$
$4.3247 \cdot 10^5$	1.40	$i \times \pi/32$

When calculating κ_{rms} as a function of the radius r, one will notice that the radius parameter does not change the condition number when all radius values are identical. When calculating the condition number for non-identical radius values, one finds a higher κ_{rms}-value. One can thus conclude that the microphones must be positioned and distributed on a circle with a chosen (fixed) radius. The actual value of the chosen radius does not have an influence on the κ_{rms}-value, as long as all $r_{1..64}$ are equal.

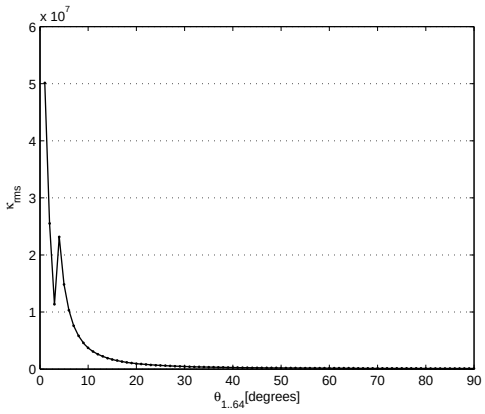

Fig. 6. Influence of angles $\theta_{1..64}$ on the condition number rms-value ('κ_{rms}').

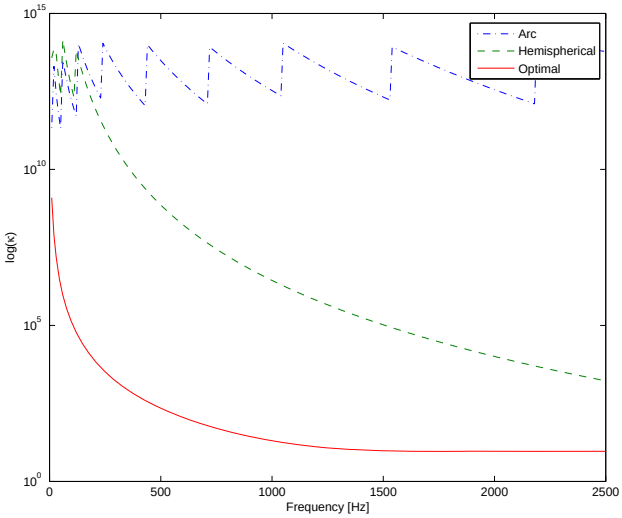

Fig. 7. Optimal solution

C. Generalized conclusions

Based on previous optimization results in Sections IV-A and IV-B, one draws the following generalized conclusions with respect to the optimized microphone positions:

- When optimizing $\theta_{1..n}$, all $\theta_{1..n}$ must be equal and the smallest κ_{rms}-value is achieved for $\theta_{1..n} = 90^o$.
- When optimizing $\phi_{1..n}$, a uniform microphone distribution over the allowable ϕ-range yields the smallest κ_{rms}-value. The smallest value is achieved when distributing the microphones evenly over a complete circle.
- When optimizing the microphone radius values $r_{1..n}$, all $r_{1..n}$ must be equal, concluding that the microphones must be positioned and distributed on a circle with a chosen (fixed) radius. The actual value of the chosen radius does not have an influence on the κ_{rms}-value, as long as all $r_{1..n}$ are equal.

In practice, this means that the problem with the optimal microphone distribution is much better conditioned, resulting in a lower noise influence on the inverse problem.

V. Conclusions

The reconstruction of the forces responsible for the tonal noise on fans has been subject of several works on the past years. The inversion of the tonal noise problem is done making use of the transfer function derived from the blade force equation. The condition number of this transfer function matrix plays an important role on the inverse problem reducing the influence of the measurement noise on the final result. This parameter has a direct influence of the problem geometry, thus, an important participation of the measurement positions. With the objective to investigate the influence of the measurements positions and find an optimal measurement grid for the tonal noise application. Several analysis and optimizations are performed. In this paper, the Morse-Ingard model [1] for the transfer function for tonal noise will be used.

This paper has the objective to better understand the influence of the variables on the condition number for the tonal noise transfer function matrix. Different parameter optimization problems are performed in order to find the optimal microphone distribution that minimizes the condition number over the considered frequency band. A parametric analysis is performed in order to identify the influence of all the possible microphone position variables, with the objective to improve the optimization procedure. The optimized microphone positions will be compared to the classical hemisphere and arc microphone distribution presented by Gérard *et al.* [4], a drastic reduction of the conditional number is achieved.

Based on the optimization results, one can conclude that all $\theta_{1..n}$ must be equal and as close as possible to 90^o, $\phi_{1..n}$ must be evenly distributed over the allowable range and all $r_{1..n}$ must be equal. The microphones must be positioned and distributed on a circle with a chosen (fixed) radius. As a result of the optimization, the κ_{rms}-value dropped from approximately $7.4 \cdot 10^7$ to $1.15 \cdot 10^5$ when compared to the hemispheric microphone distribution.

Acknowledgements

This research has been sponsored by the Flemish Institute for the Improvement of the Scientific and Technological Research in Industry (IWT), the Fund for Scientific Research - Flanders (FWO) Belgium. The authors also acknowledge the Flemish government (GOA-Optimech) and the research council of the Vrije Universiteit Brussel (OZR) for their funding.

References

[1] P. M. Morse and K. U. Ingard, *Theoretical Acoustics*, McGraw-Hill - New York, 1968.

[2] A. Gérard, A. Berry, and P. Manson, "Evaluation of tonal aeroacoustic sources in subsonic fans using inverse models," *American Institute of Aeronautics and Astronautics Journal*, vol. 45, pp. 98–109, 2007.

[3] Y. Kim and P. A. Nelson, "Optimal regularization for acoustic source reconstruction by inverse methods," *Journal of Sound and Vibration*, vol. 275, pp. 463–487, 2004.

[4] A. Gérard, A. Berry, and P. Manson, "Control of tonal noise from subsonic axial fan. part 1: Reconstruction of aeroacoustic sources from far-field sound pressures," *Journal of Sound and Vibration*, vol. 288, pp. 1049–1075, 2005.

[5] P. A. Nelson and S. H. Yoon, "Estimation of acoustic source strength by inverse methods: Part i, conditioning of the inverse problem," *Journal of Sound and Vibration*, vol. 233, pp. 643–688, 2000.

[6] G. Steenackers, P. Guillaume, and S. Vanlanduit, "Development of a regressive finite element model optimization technique making use of transmissibilities," *Structural and Multidisciplinary Optimization, Accepted 31 August 2008, DOI 10.1007/s00158-008-0313-9*, pp. 1–16, 2008.

Proceedings of the 8th National Congress on Theoretical and Applied Mechanics, May 28-29, Brussels, Belgium.

On the use of B-spline functions in a wave based prediction technique for solving bounded Helmholtz problems

Elke Deckers, Bert Drofmans, Bert Van Genechten, Bart Bergen, Dirk Vandepitte, Wim Desmet
Department of Mechanical Engineering, Division PMA, Katholieke Universiteit Leuven
Celestijnenlaan 300B, 3001 Leuven - Belgium
email: Elke.Deckers@mech.kuleuven.be

Abstract— **The application of numerical simulation techniques for the analysis and the optimization of the acoustic behavior of all kinds of products has become very important in almost every phase of a design process. Within this scope, the K.U.Leuven develops the Wave Based Method (WBM). This deterministic method is based on an indirect Trefftz approach. The WBM applies globally defined wave functions which satisfy the governing differential equation. The acoustic response of the system is then expressed as a summation of wave functions multiplied by contribution factors, which result from an integral formulation of the boundary conditions of the system.**
This paper discusses an extension of this method. Currently, curved surfaces within the WBM are considered as very fine segmentations in short, flat pieces. This paper describes the possibility to use B-splines for the description of curved edges. The introduction of B-splines within the WBM mainly requires an adaptation of the numerical integration procedure. The Gauss-Legendre integration procedure is used and the integration occurs over the parameter domain. A comparative study with the finite element method and the original WBM indicates that the application of B-splines and the adapted numerical integration procedures lead to accurate and computationally affordable wave models. The most important contribution of this research to the WBM is the possibility to inherently tackle curved edges as well as straight edges in the modeling phase. The influence of small geometric adaptations to the models is easily evaluated. The performance of the proposed procedure for uncoupled acoustic problems is illustrated by means of a number of numerical validation examples.

Keywords— **acoustics, wave based method, bounded domains, Trefftz, numerical modeling, mid-frequency**

I. Introduction

THE most commonly used deterministic prediction techniques for solving steady-state interior acoustic problems are currently based on the finite element method (FEM) [1] and the boundary element method (BEM) [2]. The use of element based techniques is practically restricted to low frequencies, however, because the size of the numerical models increases rapidly with increasing frequency, so that the computational cost becomes very large. At higher frequencies probabilistic methods, such as the statistical energy analysis (SEA) [3], are well-established. However, SEA runs into problems at lower frequencies, when the theory and assumptions behind SEA break down. As a result, a mid-frequency gap exists for which no mature prediction techniques are available.
A recently developed Wave Based Method (WBM) [4], has proven to be a computationally efficient alternative for the element based techniques in the mid-frequency range. The method is based on an indirect Trefftz-approach. The WBM is already well-established for uncoupled acoustic [5], uncoupled elastic [6] and fully coupled vibro-acoustic problems [7], [8].
Currently, the WBM is only capable to cope with straight edges. As a consequence, curved edges need to be approximated by many tiny straight edges. This article introduces B-splines [9] in the WBM to model curved edges more efficiently. This mainly requires an adaptation of boundary condition integration procedure. A numerical validation case indicates the advantages of the use of B-splines within the WBM.
Section II shortly describes the mathematical problem description. Section III summarizes the basic principles of the WBM. In section IV, we discuss the use of B-splines within the WBM. Section V evaluates the novel method and compares it with FE and WB models. Advantages are demonstrated. Some conclusions and plans for future work are included in section VI.

II. Mathematical problem description

Figure 1 shows a steady-state interior acoustic problem. The fluid has a density ρ and a speed of sound c. A closed boundary $\Omega = \Omega_z \bigcup \Omega_p \bigcup \Omega_v$ surrounds the fluid domain V. The domain is excited by an acoustic point source q at circular frequency ω. Under the assumption of an inviscid fluid, an adiabatic process and a linear system, the governing differential equation is the Helmholtz equation:

$$\nabla^2 p(\mathbf{r}) + k^2 p(\mathbf{r}) = -j\rho\omega\delta(\mathbf{r}, \mathbf{r_q})q. \qquad (1)$$

$\nabla^2 \bullet = \frac{\partial \bullet}{\partial x^2} + \frac{\partial \bullet}{\partial y^2} + \frac{\partial \bullet}{\partial z^2}$ is the Laplace operator, k is the acoustic wave number ω/c, δ is the Dirac-delta function. On every point of the boundary one acoustic variable or one relation between acoustic variables has to be defined for the problem to be well-posed.
The boundary $\delta V = \Omega$ of the acoustic problem domain V

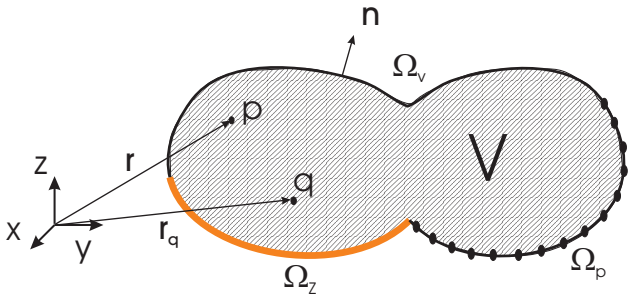

Fig. 1. Acoustic domain with different boundary conditions

consists of three parts to which one of the three following boundary conditions applies:

- $\mathbf{r} \in \Omega_v$: $\mathcal{L}_v(\mathrm{p}(\mathbf{r})) = \bar{v}_n(\mathbf{r})$, normal velocity boundary condition
- $\mathbf{r} \in \Omega_p$: $\mathrm{p}(\mathbf{r}) = \bar{p}(\mathbf{r})$, pressure boundary condition
- $\mathbf{r} \in \Omega_Z$: $\mathcal{L}_v(\mathrm{p}(\mathbf{r})) = p(r)/\bar{Z}_n(\mathbf{r})$, normal impedance boundary condition

$\bar{v}_n$, $\bar{p}$ and $\bar{Z}_n$ are, respectively, the predefined normal velocity, the predefined pressure and the predefined normal impedance. $\mathcal{L}_v$ is the velocity operator $\frac{j}{\rho_0 \omega}\frac{\partial \bullet}{\partial n}$ and $\frac{\partial \bullet}{\partial n} = \mathbf{n}^T \nabla \bullet$ is the derivative in the normal direction and $\mathbf{n}$ is the normal vector $[n_x\ n_y]^T$ on the boundary of the fluid domain.

The Helmholtz equation together with associated boundary conditions defines a unique pressure field $p(\mathbf{r})$. Once this pressure field is known, other acoustic quantities such as the acoustic velocity, the intensity and the acoustic power can be derived.

III. The Wave Based Method

The WBM is a deterministic method and is developed by the NVH group of the department of Mechanical Engineering of the K.U.Leuven. The dynamic response variables, in this case pressures, are described using wave functions, which are exact solutions of the underlying differential equation. As a result, no approximation error is made inside the domain, but only at the boundaries, since the wave functions may violate the problem boundary conditions. The resulting wave based models are small which leads to an enhanced computational efficiency. Five major steps are distinguished in the wave based modeling procedure [4], [10]:

1. *Partitioning of the considered problem domain into a number of* convex *subdomains*.

An important restriction is that the problem geometry need to convex. A non-convex problem domain needs to be partitioned in convex subdomains. Convexity of the subdomains is a sufficient condition for the WBM to converge towards the exact solution of the problem.

2. *Selection of a set of wave functions for each subdomain*.

The steady-state acoustic pressure field $\mathrm{p}^{(\alpha)}(\mathbf{r})$ in acoustic subdomain $\mathrm{V}^{(\alpha)}$ is approximated by a solution expansion $\hat{p}^{(\alpha)}(\mathbf{r})$:

$$p^{(\alpha)} \simeq \hat{p}^{(\alpha)}(\mathbf{r}) = \sum_{w=1}^{n_w^{(\alpha)}} p_w^{(\alpha)} \phi_w^{(\alpha)}(\mathbf{r}) + \hat{p}_q^{(\alpha)}(\mathbf{r}) = \Phi_w^{(\alpha)}(\mathbf{r})\mathbf{p}_w{}^{(\alpha)} + \hat{p}_q^{(\alpha)}(\mathbf{r}) \quad (2)$$

$\mathbf{p_w}^{(\alpha)}$ is the vector of the unknown weighting factors for each of the selected wave functions. The corresponding known wave functions are collected in the row vector $\Phi_w^{(\alpha)}(\mathbf{r})$. $\hat{p}_q^{(\alpha)}(\mathbf{r})$ represents the particular solution of the non-homogenous differential equation in case acoustic sources are present in the considered domain.

Each acoustic wave function $\phi_w^{(\alpha)}(\mathbf{r})$ exactly satisfies the Helmholtz equation (1). For the 2D case, these functions are:

$$\Phi_w^{(\alpha)}(\mathbf{r}(\mathbf{x},\mathbf{y})) = \begin{cases} \phi_{w_r}^{(\alpha)}(\mathbf{r}(x,y)) = \cos(k_{xw_r}^{(\alpha)} x) e^{-jk_{yw_r}^{(\alpha)} y} \\ \phi_{w_s}^{(\alpha)}(\mathbf{r}(x,y)) = e^{-jk_{xw_s}^{(\alpha)} x} \cos(k_{yw_s}^{(\alpha)} y) \end{cases} \quad (3)$$

with wave numbers

$$(k_{xw_r}^{(\alpha)}, k_{yw_r}^{(\alpha)}) = \left(\frac{w_1^{(\alpha)}\pi}{L_x^{(\alpha)}}, \pm\sqrt{k^2 - (k_{xw_r}^{(\alpha)})^2} \right) \quad (4)$$

$$(k_{xw_s}^{(\alpha)}, k_{yw_s}^{(\alpha)}) = \left(\pm\sqrt{k^2 - (k_{yw_s}^{(\alpha)})^2}, \frac{w_2^{(\alpha)}\pi}{L_y^{(\alpha)}} \right) \quad (5)$$

with w_1,w_2=0,1,2,... and $L_x^{(\alpha)}$ and $L_y^{(\alpha)}$ are the dimensions of the (smallest) bounding box circumscribing the considered subdomain. In order to apply the WB formulations into a numerical scheme, the infinite function series has to be truncated to a finite sized wave function basis set:

$$w_i = \lceil max((N_p \cdot k/\pi \cdot L_i + T_1), T_2) \rceil. \quad (6)$$

N_p, T_1 en T_2 are parameters to be chosen by user. $\lceil \bullet \rceil$ returns the integer just larger than the double precision argument.

3. *Construction of the WB system matrices via a weighted residual formulation of the boundary conditions and the continuity conditions at the common subdomain interfaces*.

Typically this requires the evaluation of integrals of the following form (in the case of the part of the boundary $\Omega_v^{(\alpha)}$ of subdomain $V^{(\alpha)}$ on which normal velocity boundary conditions are applied):

$$\mathbf{A}_{\mathrm{v}}^{(\alpha)} = \int_{\Omega_{\mathrm{v}}^{(\alpha)}} \frac{\mathrm{j}}{\rho_0 \omega} \Phi^{(\alpha)\mathrm{T}} \mathbf{n}^{(\alpha)\mathrm{T}} \mathbf{B}^{(\alpha)} \mathrm{d}\Omega \quad (7)$$

$\mathbf{B}^{(\alpha)} = \nabla\Phi^{(\alpha)}$ is the matrix which collects the gradient components of the acoustic wave functions. The WB matrix equation is denoted in a condensed form as:

$$\mathbf{A}\ \mathbf{p_w} = \mathbf{b} \quad (8)$$

4. *Solution of the wave model, yielding the wave function contribution factors p_w associated with each wave function.*
5. *Postprocessing to derive the acoustic pressure fields and other relevant acoustic quantities from the wave functions and their associated contribution factors.*

IV. B-SPLINES (2D)

At present, the boundaries in the WBM are all straight edges or circle segments. Very many small lines are needed to accurately approximate a curved boundary. The WBM imposes no constraints on the geometrical description of domain boundaries, only on the convexity of the applied subdomain partitioning. The aim of this study is to extend the WBM with a simple, geometrically more accurate description of curved boundaries.
B-splines offer the possibility to model curved edges easily, unambiguously and continuously. Furthermore many CAD packages apply B-splines for geometric modeling, enabling the straightforward construction of problem geometries and allowing easy access to the B-spline parametrizations of the domain boundaries.

A. Construction

A pth-degree B-spline curve is defined by [9]:

$$\mathbf{C}(u) = \sum_{i=0}^{n} N_{i,p}(u)\mathbf{P}_i \qquad voor\ a \leq u \leq b \tag{9}$$

where the $\{\mathbf{P}_i\}$ are the control points, and the $\{N_{i,p}\}$ are the pth-degree B-spline basis functions defined on the nonperiodic (and nonuniform) knot vector (m+1 knots)

$$\mathrm{U} = \{\underbrace{a,\ldots,a}_{\text{p+1}}, u_{p+1},\ldots,u_{m-p-1}, \underbrace{b,\ldots,b}_{\text{p+1}}\}$$

The ith B-spline basis function of p-degree (order $p+1$) is defined as

$$N_{i,0}(u) = \begin{cases} 1, & if\ u_i \leq u < u_{i+1} \\ 0, & elsewhere \end{cases} \tag{10}$$

$$N_{i,p}(u) = \frac{u-u_i}{u_{i+p}-u_i} N_{i,p-1}(u) + \frac{u_{i+p+1}-u}{u_{i+p+1}-u_{i+1}} N_{i+1,p-1}(u) \tag{11}$$

This equation can yield the quotient 0/0. This quotient is defined to be zero. In this study a and b are assumed to be 0 and 1. The B-splines coincide with the first and last control point. Important properties are:
- $N_{i,p}(u)$=0 if u is outside the interval $[u_i, u_{i+p+1})$ (local support property). A shift of control point P_i only affects $\mathbf{C}(u)$ in the interval $[u_i, u_{i+p+1})$.
- In case the control points form a convex polygon, this causes the B-spline curve to be convex too.

Example:
Figure 2 shows the second degree B-spline basis functions with knot vector U={0,0,0,0.2,0.5,0.8,1,1,1}. Figure 3 shows the B-spline acquired with these basis functions and with control points (1,1), (1,5), (5,6), (7,7), (5,2) en (2,3). These points are indicated by circles. The B-spline intersects the first and the last control point.

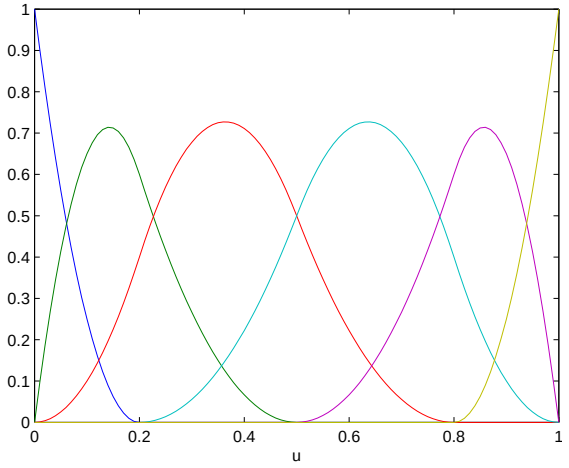

Fig. 2. B-spline basis functions

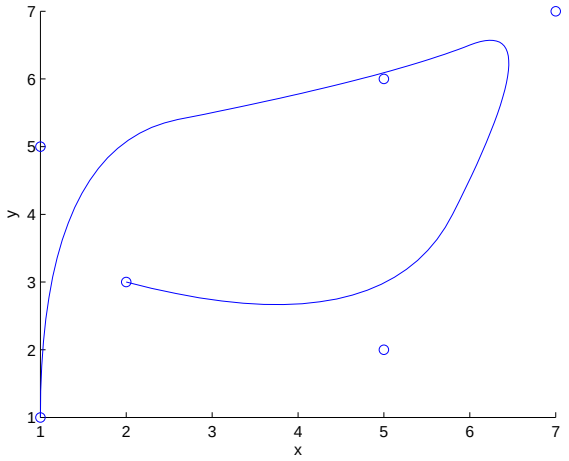

Fig. 3. B-spline curve and control points

B. Application to the WBM

As shown in equations (4)-(5) the dimensions of the bounding box are needed to evaluate the different wave numbers. In case of B-splines, the ultimate points on the curves need to be known. An expression for the normal velocity on the B-spline boundaries is necessary to compose the system matrices. And of course, the numerical integration scheme has to be adapted. These matters are considered in the next paragraphs.

B.1 Bounding box

For every subdomain the dimensions of the bounding box L_x and L_y need to be known. The extreme points of

the subdomains are usually unknown when B-splines are used to describe boundaries. There are 2 options:
1. The extreme coordinates of the control points of the B-spline can be used to estimate the bounding box dimensions. This generally leads to an overestimation. Consequently, more acoustic wave functions will be used in the solution expansion, which are possibly unnecessary. The advantage of this option is that the coordinates of the control points are directly available.
2. One can use the real geometry of the B-spline to determine the smallest bounding box. This can be done manually, e.g. by means of a CAD-program, which requests the intervention of the user. Another possibility is to determine these dimensions automatically via an optimization procedure, which takes more time. The advantage of these options is that the smallest number of degrees of freedom will be used in the WBM.
The second option is used here. The bounding box dimensions are manually determined.

B.2 Evaluation of pressure and normal velocity

Expressions for the acoustic pressure and velocity are needed on the boundaries of the problem domain to construct the system matrices. The acoustic pressure is determined by equation (2). The normal velocity can be calculated if the normal vector **n** is known in each point of the boundary Ω of the problem domain.
The kth derivative of the B-spline **C**(u) is defined as [9]

$$\mathbf{C}^k(u) = \sum_{i=0}^{n} N_{i,p}^k P_i \qquad voor\ a \leq u \leq b \tag{12}$$

The kth derivative of the basis function $N_{i,p}$ is recursively defined as

$$N_{i,p}^k(u) = \frac{p!}{(p-k)!} \sum_{j=0}^{k} a_{k,j} N_{i+j,p-k}(u) \tag{13}$$

$$N_{i,0}(u) = \begin{cases} 1, & if\ u_i \leq u < u_{i+1} \\ 0, & elsewhere \end{cases} \tag{14}$$

with:

$$\begin{cases} a_{0,0} = 1 \\ a_{k,0} = \frac{a_{k-1,0}}{u_{i+p-k+1} - u_i} \\ a_{k,j} = \frac{a_{k-1,j} - a_{k-1,j-1}}{u_{i+p+j-k+1} - u_{i+j}} \\ a_{k,k} = \frac{-a_{k-1,k-1}}{u_{i+p+1} - u_{i+k}} \end{cases} \tag{15}$$

This way, the tangent and as a consequence also the normal is know in each point.

B.3 Numerical integration

Integrals as shown in equation (7) have to be evaluated to compose the system matrices. This is done numerically by means of Gauss-Legendre quadrature. The length of the B-spline has to be known to determine how many integration points (Gaussian points) are needed to perform the integration accurately (minimum number of integration points per acoustic wave length). The total length of the B-spline can be obtained by calculating the length of a refined piecewise linear approximation of the curve:

$$l = \int_0^l 1 \cdot ds = \sum_{i=0}^{n-1} \sqrt{(x_{i+1} - x_i)^2 + (y_{i+1} - y_i)^2} \tag{16}$$

The numerical integration is performed over the parameter u which describes the B-spline and not over the physical length of the B-spline. As a result, the location of the Gaussian points are also divided between 0 and 1. For each Gaussian point, the value of the determinant of the Jacobian is required to perform the mapping from the parameter domain to the real curve. In contrast with straight edges for which the Jacobian is a constant, the Jacobian differs from point to point for a B-spline. In this case the determinant of the Jacobian is given by [11]:

$$|J| = \sqrt{\left(\frac{dx}{du}\right)^2 + \left(\frac{dy}{du}\right)^2}. \tag{17}$$

The values of dx/du and dy/du have already been obtained for the determination of the normal vector in each point.

V. Validation example

A validation example verifies the adapted WBM and shows the advantages with respect to the conventional WBM.

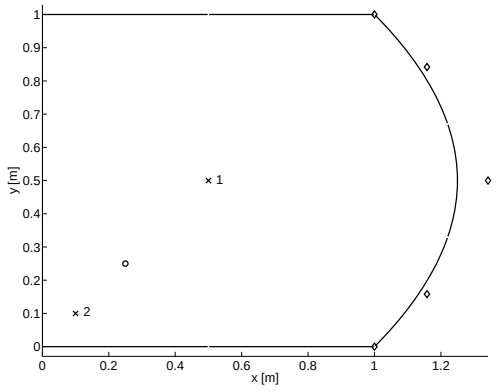

Fig. 4. Geometry of the acoustic cavity

Figure 4 shows the considered acoustic problem domain. The dimensions of the bounding box are L_x = 1.25 m and L_y = 1 m. The fluid is air, c = 339m/s^2 and ρ = 1.225 kg/m^3. The circle (0.25,0.25) indicates a harmonic point source with an amplitude of 1 m^2/s. The four edges are rigid and the right-hand side of the cavity is described by a 3th degree B-spline. The diamonds indicate the location of

the control points of the B-spline and table I contains their coordinates. The knot vector is $U = \{0,0,0,0.5,1,1,1\}$.

TABLE I
CONTROL POINTS OF THE B-SPLINE.

Control point	Coordinates
Point 1	(1 1)
Point 2	(1.158114 0.841886)
Point 3	(1.341886 0.5)
Point 4	(1.158114 0.158114)
Point 5	(1 0)

Two crosses in the domain indicate the location of post-processing points at which frequency response functions (FRFs) and convergence results are computed. Table II contains their coordinates.
A finite element reference model has been built to allow a comparison of the results. This model consists of 641601 nodes.

Figure 5 and 6 show contour plots of the amplitude of the acoustic pressure in the cavity at 800Hz calculated with the FEM and the WBM, respectively, where a good agreement can be observed.

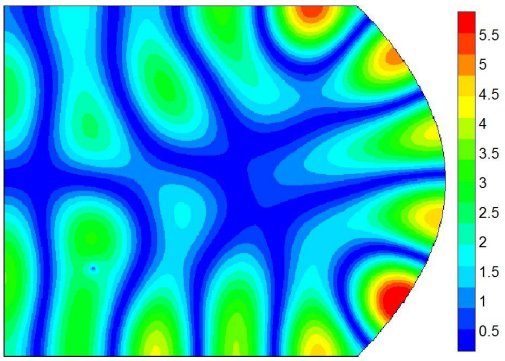

Fig. 5. Contour plots of the amplitude of the acoustic pressure at 800 Hz calculated with FEM

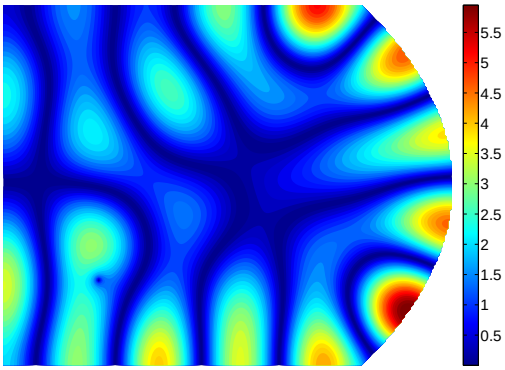

Fig. 6. Contour plots of the amplitude of the acoustic pressure at 800 Hz, calculated with WBM

TABLE II
COORDINATES OF THE POST-PROCESSING POINTS.

Point	Coordinates
Point 1	(0.487807 0.521033)
Point 2	(0.0816668 0.1)

Figure 7 shows FRFs calculated with the FEM and the adapted WBM at point 1. Also here, a good agreement can be observed.

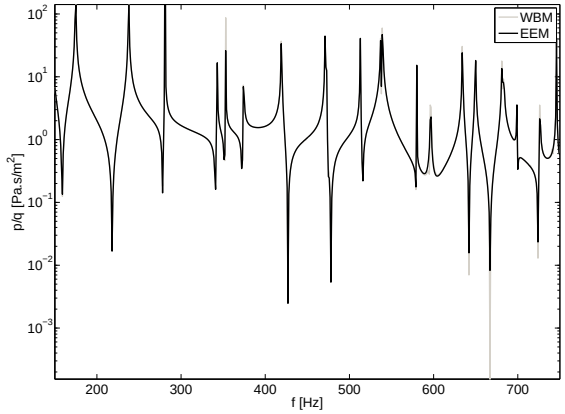

Fig. 7. FRF of the FE model and the WB model in point 1

Next, a comparison is made between the conventional WBM with straight edges and the WBM with B-splines. It is necessary to approximate the smooth B-spline with many straight lines to use the conventional WBM, otherwise there is a loss of accuracy, especially at higher frequencies. Compared with the FEM both methods converge towards the same relative error, because the FEM results are limited to an accuracy of 10^{-5} Pa. Therefore, a very fine WB model is used as a reference. The relative error is calculated in point 2 at 500Hz with the following formula:

$$\varepsilon = \frac{(p - p_{ref})}{p_{ref}} \tag{18}$$

Figure 8 shows the absolute value of the relative error on the pressure calculated with the conventional WBM and the adapted WBM. GLI-P indicates Gauss-Legendre integration over the parameter domain, GLI-D indicates that discrete segments are used to approximate the B-spline. The adapted WBM is clearly faster. The result obtained with the conventional WBM is more accurate when more segments are used to approximate the B-spline, but also the CPU-time increases. Figure 9 shows this trade-off between accuracy and CPU-time. The B-spline is approximated with 200, 400 and 800 segments respectively.
These figures show that the use of the adapted WBM is

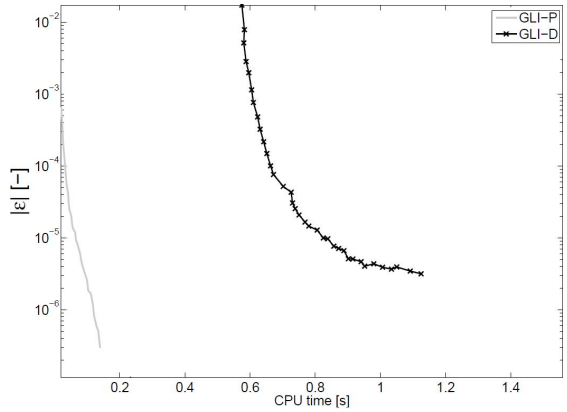

Fig. 8. Absolute value of the relative error on the pressure calculated with the conventional WBM and the adapted WBM with respect to the reference pressure calculated with the WBM in point 2 at 500Hz

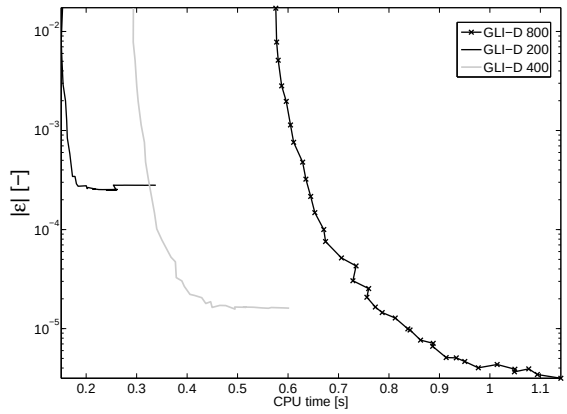

Fig. 9. Absolute value of the relative error on the pressure calculated with the conventional WBM with respect to the reference pressure calculated with the WBM and the GLI-L in point 2 at 500Hz. The B-spline is divided in respectivily 200, 400 and 800 straight lines

the proper way to take into account curved domain boundaries. The use of B-splines leads to a more efficient and accurate result for complex geometries.

A second advantage of the application of B-splines is that the influence of small geometric modifications can be verified in an easy way. The change of the location of one or more control points leads to a slightly different geometry. As in the case of the FEM or the conventional WBM it is not necessary to mesh the curve again in fine segments which is time consuming. Changes of the acoustic behavior can be easily verified by means of the FRF. Figure 10 shows the change in geometry when control point 3 of table I shifts a bit to the right or the left.

Figure 11 shows the FRF obtained in point 1 for the three different geometries.

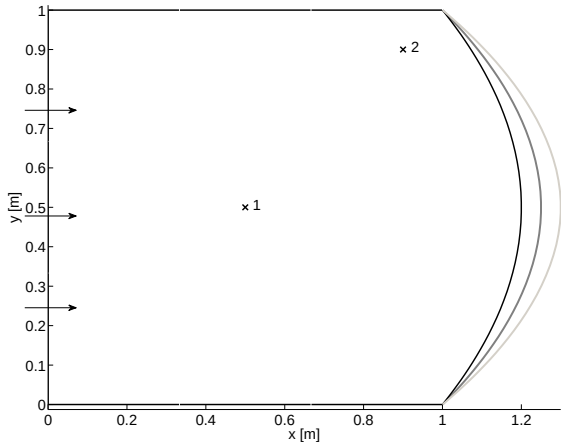

Fig. 10. Change of geometry by moving one control point of the B-spline

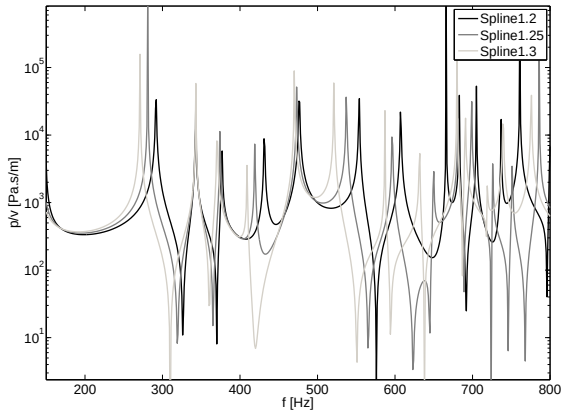

Fig. 11. FRF of the 3 models with a slightly different geometry in point 1

VI. Conclusions

This paper describes an adaptation of the WBM to model curved edges with B-splines. This provides a simple and accurate description of curved lines, which can be obtained using readily available geometrical modeling computer programs.

The application of B-splines within the WBM leads to computationally more efficient and accurate results with respect to the conventional method. The influence of small geometric modifications on the acoustic behavior can be easily evaluated.

An extension to 3D problems is also possible. A B-spline surface can be constructed with a bidirectional net of control points [9]. This can be used in the WBM, on condition that the numerical integration is adapted. Some first models were tested, but future research will evaluate and demonstrate possible benefits.

Acknowledgements

Elke Deckers and Bert Van Genechten are Doctoral Fellows of the Fund for Scientific Research - Flanders

(F.W.O.), Belgium. The Institute for the Promotion of Innovation by Science and Technology in Flanders (Belgium) (IWT) is gratefully acknowledged for their support of the doctoral research of Bart Bergen.

REFERENCES

[1] O. C. Zienkiewicz, R. L. Taylor, J. Z. Zhu and P. Nithiarasu, *The Finite Element Method - The three volume set (6th ed.)*, Butterworth-Heinemann, 2005.

[2] O. Von Estorff, *Boundary Elements in Acoustics: Advances and Applications*, WITpress, 2000.

[3] R.H. Lyon, R. G. DeJong, *Theory and application of statistical energy analysis (2nd ed.)*, Butterworth-Heinemann, Boston et al., 1995.

[4] W. Desmet, *A wave based prediction technique for coupled vibro-acoustic analysis*, KULeuven, division PMA, PhD. thesis 98D12, 1998.

[5] B. Van Hal, W. Desmet and D. Vandepitte *A coupled finite element-wave based approach for the steady state dynamic analysis of acoustic systems* Journal of Computational Acoustics, 11(2), p.285-303, 2003.

[6] C. Vanmaele, *Development of a wave based prediction technique for the efficient analysis of low- and mid-frequency structural vibrations*, KULeuven, division PMA, PhD thesis, 2007

[7] B. Pluymers, W. Desmet, D. Vandepitte and P. Sas, *Application of an efficient wave based prediction technique for the analysis of vibro-acoustic radiation problems*, Journal of Computational and Applied mathematics, 168, p.353-364, 2004.

[8] B. Pluymers, W. Desmet, D. Vandepitte and P. Sas, *On the Use of a Wave Based Prediction Technique for Steady-State Structural-Acoustic Radiation Analysis*, Journal of Computer Modeling in Engineering & Sciences, 7(2), p.173-184, 2005.

[9] L. Piegl , W. Tiller, *The NURBS Book, 2nd Edition*, Springer 1997.

[10] B. Pluymers, W. Desmet, D. Vandepitte and P. Sas, *Wave based modelling methods for steady-state interior acoustics: an overview*, Proceedings of the International Conference on Noise and Vibration Engineering ISMA2006, Leuven, Belgium, (2006) 2303-2358.

[11] C.A. Brebbia, J.C.F. Telles, L.C. Wrobel, *Boundary Element Techniques, Theory and Applications in Engineering*, Springer-Verlag, 1984.

Proceedings of the 8th National Congress on Theoretical and Applied Mechanics, May 28-29, Brussels, Belgium.

Finite-amplitude homogeneous waves in pre-strained incompressible materials

Elizabete Rodrigues Ferreira, Philippe Boulanger
Université Libre de Bruxelles, Département de Mathématique
Campus Plaine C.P.218/1, 1050 Brussels - Belgium
email: erodrigu@ulb.ac.be, phboul@ulb.ac.be

Abstract— **In this paper, general incompressible non linear elastic materials and generalized neo-Hookean materials are considered. We deal with the propagation of finite-amplitude linearly polarized transverse waves in such materials subjected to an arbitrary static homogeneous deformation. For general incompressible materials, it is shown that a linearly polarized transverse wave may propagate when the propagation direction n and the polarization direction a are both in the same principal plane of the static deformation. For generalized neo-Hookean materials, it is shown that a linearly polarized transverse wave may propagate for *any* propagation direction n. When n is not along a principal direction of the strain tensor B associated with the static deformation, the polarization direction a is uniquely determined. It is along the projection of Bn onto the plane orthogonal to n. In the special case when n is along a principal direction of B, the polarization direction a is arbitrary orthogonal to n. A property of the energy flux and energy density associated with these linearly polarized waves is exhibited.**

Keywords— **Non linear elasticity, exact wave solutions, general incompressible elastic materials, generalized neo-Hookean materials, energy density and energy flux.**

I. Introduction

In this paper we consider the propagation of finite-amplitude linearly polarized transverse homogeneous plane waves in incompressible materials which are maintained in a state of arbitrary static homogeneous deformation (pre-strain). Although the materials are assumed to be isotropic, the static deformation let them behave as anisotropic for wave propagation. This effect is called "strain-induced anisotropy". Many results are available in the literature for the propagation of waves of infinitesimal amplitude in materials subjected to a large deformation (see, for instance, [1] [2] [3]). In all such papers, the equations are linearized around the state of static deformation (theory of incremental elastic deformations, see also [4]). Here, however, we are interested in finite-amplitude waves, thus no assumption is made about the amplitude of the waves. In this case, exact and explicit results are much sparser.

For general incompressible homogeneous isotropic elastic materials Green [5] showed that linearly polarized finite-amplitude plane waves may propagate along a principal axis of the underlying homogeneous static strain. Later, Carroll [6] showed for Mooney-Rivlin materials that such waves may propagate in any direction in a principal plane of the basic static strain. Then, Currie and Hayes [7] showed that two linearly polarized finite-amplitude transverse waves, polarized in directions orthogonal to each other and to the propagation direction, may propagate along any direction in a deformed Mooney-Rivlin material. Later, Boulanger and Hayes [8] [9] made a detailed study of homogeneous plane waves propagating in deformed Mooney-Rivlin materials. In a recent book [10] by one of the authors (E. Rodrigues Ferreira), a large collection of new results for finite-amplitude waves (including plane waves and two-dimensional waves) in pre-strained elastic materials is presented. Here, we focus on a few of these results concerning general incompressible materials and a sub-class of these called "generalized neo-Hookean materials".

For general incompressible materials, which are characterized by two constitutive functions, we show that the equations of motion lead to an expression for the additional pressure due to the wave, a scalar non linear wave equation, and a "propagation condition". In general, the propagation condition cannot be satisfied together with the non linear wave equation. However, here, we show that the propagation condition is identically satisfied when the propagation direction **n** and the polarization direction **a** are both in the same principal plane of the static deformation. Thus, the propagation of such waves is possible and governed by a scalar non linear wave equation.

We also consider a sub-class of incompressible materials, characterized by one constitutive function, called "generalized neo-Hookean materials", because when this function reduces to a constant we retrieve the usual neo-Hookean model. We again obtain an expression for the additional pressure due to the wave, a scalar non linear wave equation, and a "propagation condition". Here, it is shown that the propagation condition may be satisfied for *any* propagation direction **n**, with a suitable choice of the polarization direction **a**. When **n** is not along a principal direction of the strain tensor **B** associated with the static deformation, the polarization direction **a** is uniquely determined. It is along the projection of **Bn** onto the plane orthogonal to **n**. In the special case when **n** is along a principal direction of **B**, the polarization direction **a** is arbitrary orthogonal to **n**.

Finally, we consider the energy density and the enrgy flux associated with these linearly polarized wave motions. Both for general incompressible materials and generalized neo-Hookean materials, we consider simple wave solutions of the scalar non linear wave equation. For these, a property relating the energy flux and energy density is obtained: the projection onto the propagation direction **n** of the energy flux vector is equal to an integral of the derivative of the energy density multiplied by the wave speed, these two being functions of the signal level. Remarkably, this is the same property as obtained in [11] for longitudinal simple waves in deformed Hadamard materials (a compressible counterpart to the incompressible Mooney-Rivlin model). However, here we deal with transverse simple waves in incompressible materials.

II. Basic equations

Isotropic elastic materials are characterized by a strain-energy density W, measured per unit volume in the undeformed state, which is a function of $\mathrm{I}_1, \mathrm{I}_2, \mathrm{I}_3$, the principal invariants of the left Cauchy-Green strain tensor $\mathbf{B}$:

$$\mathrm{I}_1 = \mathrm{tr}\,\mathbf{B}\ ,\ 2\mathrm{I}_2 = (\mathrm{tr}\,\mathbf{B})^2 - \mathrm{tr}\,(\mathbf{B}^2)\ ,\ \mathrm{I}_3 = \det\mathbf{B}\ . \tag{1}$$

The components of $\mathbf{B}$, in a rectangular Cartesian coordinate system, are

$$B_{ij} = \frac{\partial x_i}{\partial X_A}\frac{\partial x_j}{\partial X_A}\ , \tag{2}$$

where $x_i, (i = 1,2,3)$, are the coordinates at time t of the point whose coordinates are $X_A, (A = 1,2,3)$, in the undeformed reference configuration.

Here we consider isotropic incompressible nonlinear elastic materials. The incompressibility constraint requires that the third strain invariant $\mathrm{I}_3 = 1$. Thus, for general incompressible elastic materials, the strain energy density W is of the form $W = W(\mathrm{I}_1, \mathrm{I}_2)$. The Cauchy stress tensor $\mathbf{T}$ is given by

$$\mathbf{T} = -(p - D\mathrm{I}_2)\mathbf{1} + C\mathbf{B} - D\mathbf{B}^{-1}\ , \tag{3}$$

where p is an undetermined pressure. Here C and D are constitutive functions depending on the strain invariants I_1, I_2, and given as partial derivatives of strain energy by

$$C = C(\mathrm{I}_1, \mathrm{I}_2) = 2\frac{\partial \mathrm{W}}{\partial \mathrm{I}_1}\ , \tag{4}$$

$$D = D(\mathrm{I}_1, \mathrm{I}_2) = 2\frac{\partial \mathrm{W}}{\partial \mathrm{I}_2}\ . \tag{5}$$

We also consider special incompressible materials for which the strain energy depends only on the first strain invariant I_1: $W = W(\mathrm{I}_1)$, so that $D = 0$ and $C = C(\mathrm{I}_1)$. The corresponding Cauchy stress tensor is thus given by

$$\mathbf{T} = -p\mathbf{1} + C\mathbf{B}\ . \tag{6}$$

Such models generalize the classical neo-Hookean model for which C is a constant. We call these materials "generalized neo-Hookean material". One can find in the literature different models of incompressible materials of this form. For example, the Yeoh model [12], the Arruda-Boyce model [13], the Fung model [14], and the Knowles model [15] are generalized neo-Hookean materials.

III. Equations for waves in pre-strained materials

Suppose now that a general incompressible elastic material is first subjected to a large static homogeneous deformation (pre-strain) defined by

$$\mathbf{x} = \mathbf{F}\mathbf{X}\ ,\quad x_i = F_{iA}X_A\ , \tag{7}$$

where F_{iA} is a constant deformation gradient. The corresponding constant left Cauchy-Green strain tensor is $\mathbf{B} = \mathbf{F}\mathbf{F}^T$ and its principal invariants $\mathrm{I}_1, \mathrm{I}_2$ and $\mathrm{I}_3 = 1$ are constants. On this state of homogeneous static deformation, we superpose a time-dependent displacement field, representing a finite-amplitude homogeneous plane wave propagating in the direction of the unit vector **n**, and linearly polarized in the direction of the unit vector **a**. Thus, a particle being at **X** in the undeformed state is first brought to **x** in the state of static deformation, and then brought to $\overline{\mathbf{x}} = \overline{\mathbf{x}}(\mathbf{x}, t)$ in the superimposed motion. Here we seek solutions of the equations of motion in the form

$$\overline{\mathbf{x}} = \mathbf{x} + g(\eta, t)\,\mathbf{a}\ ,\quad \overline{x}_i = x_i + g(\eta, t)\,a_i\ , \tag{8}$$

$$\overline{p} = p + q(\eta, t)\ , \tag{9}$$

where x_i is given by (7), p is the constant pressure associated with the homogeneous static deformation, and

$$\eta = \mathbf{n}\cdot\mathbf{x}. \tag{10}$$

Note that the incompressibility constraint requires the orthogonality of the vectors **n** and **a**, thus $\mathbf{n}\cdot\mathbf{a} = 0$. Thus the waves are necessarily transverse. The deformation gradient tensor $\overline{\mathbf{F}} = \partial\overline{\mathbf{x}}/\partial\mathbf{X}$ associated with the motion (8) is given by

$$\overline{\mathbf{F}} = (\mathbf{1} + g_\eta\,\mathbf{a}\otimes\mathbf{n})\mathbf{F}\ , \tag{11}$$

where the subscript η denotes the partial derivative with respect to η. The corresponding left Cauchy-Green strain tensor $\overline{\mathbf{B}} = \overline{\mathbf{F}}\,\overline{\mathbf{F}}^T$ and its principal invariants are given by

$$\overline{\mathbf{B}} = (\mathbf{1} + g_\eta\,\mathbf{a}\otimes\mathbf{n})\mathbf{B}(\mathbf{1} + g_\eta\,\mathbf{n}\otimes\mathbf{a})\ , \tag{12}$$

$$\bar{\mathrm{I}}_1 = \mathrm{I}_1 + 2\mathrm{g}_\eta\,\mathbf{n}\cdot\mathbf{B}\mathbf{a} + \mathrm{g}_\eta^2\,\mathbf{n}\cdot\mathbf{B}\mathbf{n}\ , \tag{13}$$

$$\bar{\mathrm{I}}_2 = \mathrm{I}_2 - 2\mathrm{g}_\eta\,\mathbf{a}\cdot\mathbf{B}^{-1}\mathbf{n} + \mathrm{g}_\eta^2\,\mathbf{a}\cdot\mathbf{B}^{-1}\mathbf{a}\ , \tag{14}$$

$$\bar{\mathrm{I}}_3 = \mathrm{I}_3 = 1\ . \tag{15}$$

The inverse $\overline{\mathbf{B}}^{-1}$ of the left Cauchy-Green strain tensor is

$$\overline{\mathbf{B}}^{-1} = (\mathbf{1} - g_\eta\, \mathbf{n}\otimes\mathbf{a})\mathbf{B}^{-1}(\mathbf{1} - g_\eta\, \mathbf{a}\otimes\mathbf{n})\,. \qquad (16)$$

Let $\overline{W} = W(\bar{\mathrm{I}}_1, \bar{\mathrm{I}}_2)$ be the strain energy density associated with the motion (8). The corresponding Cauchy stress tensor $\overline{\mathbf{T}}$ is given by

$$\overline{\mathbf{T}} = -(\overline{p} - \overline{D}\,\bar{\mathrm{I}}_2)\mathbf{1} + \overline{C}\,\overline{\mathbf{B}} - \overline{D}\,\overline{\mathbf{B}}^{-1}\,, \qquad (17)$$

where

$$\overline{C} = C(\bar{\mathrm{I}}_1, \bar{\mathrm{I}}_2) = 2\frac{\partial \overline{W}}{\partial \bar{\mathrm{I}}_1}\,, \qquad (18)$$

$$\overline{D} = D(\bar{\mathrm{I}}_1, \bar{\mathrm{I}}_2) = 2\frac{\partial \overline{W}}{\partial \bar{\mathrm{I}}_2}\,. \qquad (19)$$

In the absence of body forces, the equations of motion for the motion (8)(9) are

$$\rho\,\ddot{\overline{\mathbf{x}}} = \mathrm{div}_{\overline{\mathbf{x}}}\overline{\mathbf{T}}\,, \quad \rho\frac{\partial^2 \overline{x}_i}{\partial t^2} = \frac{\partial \overline{T}_{ij}}{\partial \overline{x}_j}\,, \qquad (20)$$

where $\mathrm{div}_{\overline{\mathbf{x}}}$ denotes the divergence operator with respect to $\overline{\mathbf{x}}$ and where ρ is the constant mass density of the material.

The unit vectors $\mathbf{n}, \mathbf{a}$ being orthogonal, we complete with the unit vector $\mathbf{b} = \mathbf{n}\times\mathbf{a}$ an orthonormal triad $(\mathbf{n},\ \mathbf{a},\ \mathbf{b})$. Let (η, ξ, ζ) be the components of $\mathbf{x}$ in this triad

$$\eta = \mathbf{n}\cdot\mathbf{x}\,, \quad \xi = \mathbf{a}\cdot\mathbf{x}\,, \quad \zeta = \mathbf{b}\cdot\mathbf{x}\,, \qquad (21)$$

and let $(\overline{\eta}, \overline{\xi}, \overline{\zeta})$ be the components of $\overline{\mathbf{x}}$ in this triad

$$\overline{\eta} = \mathbf{n}\cdot\overline{\mathbf{x}}\,, \quad \overline{\xi} = \mathbf{a}\cdot\overline{\mathbf{x}}\,, \quad \overline{\zeta} = \mathbf{b}\cdot\overline{\mathbf{x}}\,. \qquad (22)$$

Thus, with respect to rectangular Cartesian axes along $(\mathbf{n},\ \mathbf{a},\ \mathbf{b})$, the motion (8) reads

$$\overline{\eta} = \eta\,, \quad \overline{\xi} = \xi + g(\eta, t)\,, \quad \overline{\zeta} = \zeta\,. \qquad (23)$$

The components of the stress tensor $\overline{\mathbf{T}}$ are functions of η and t, or equivalently $\overline{\eta}$ and t. Thus, using axes along $(\mathbf{n}, \mathbf{a}, \mathbf{b})$ the equations of motion (20) read

$$0 = \frac{\partial \overline{T}_{\eta\eta}}{\partial \overline{\eta}} = \frac{\partial \overline{T}_{\eta\eta}}{\partial \eta}\,, \qquad (24)$$

$$\rho\frac{\partial^2 g}{\partial t^2} = \frac{\partial \overline{T}_{\xi\eta}}{\partial \overline{\eta}} = \frac{\partial \overline{T}_{\xi\eta}}{\partial \eta}\,, \qquad (25)$$

$$0 = \frac{\partial \overline{T}_{\zeta\eta}}{\partial \overline{\eta}} = \frac{\partial \overline{T}_{\zeta\eta}}{\partial \eta}\,. \qquad (26)$$

IV. Linearly polarized transverse waves in general incompressible materials

We now compute, for general incompressible materials, the components of $\overline{\mathbf{T}}$ entering these equations. Using the expression (17) of $\overline{\mathbf{T}}$, we obtain

$$\overline{T}_{\eta\eta} = -p - q + \overline{D}\mathrm{I}_2 + \overline{C}\mathbf{n}\cdot\mathbf{B}\mathbf{n} - \overline{D}\mathbf{n}\cdot\mathbf{B}^{-1}\mathbf{n}\,, \qquad (27)$$

$$\overline{T}_{\xi\eta} = \overline{C}\mathbf{a}\cdot\mathbf{B}\mathbf{n} - \overline{D}\mathbf{a}\cdot\mathbf{B}^{-1}\mathbf{n} + g_\eta(\overline{C}\mathbf{n}\cdot\mathbf{B}\mathbf{n} + \overline{D}\mathbf{a}\cdot\mathbf{B}^{-1}\mathbf{a})\,, \qquad (28)$$

$$\overline{T}_{\zeta\eta} = \overline{C}\mathbf{b}\cdot\mathbf{B}\mathbf{n} - \overline{D}(\mathbf{b}\cdot\mathbf{B}^{-1}\mathbf{n} - g_\eta\mathbf{b}\cdot\mathbf{B}^{-1}\mathbf{a})\,. \qquad (29)$$

Introducing (27) into the equation of motion (24), we obtain

$$-q_\eta + \mathrm{I}_2\overline{\mathrm{D}}_\eta + \overline{\mathrm{C}}_\eta\mathbf{n}\cdot\mathbf{B}\mathbf{n} - \overline{\mathrm{D}}_\eta\mathbf{n}\cdot\mathbf{B}^{-1}\mathbf{n} = 0\,, \qquad (30)$$

where $\overline{C}_\eta$ and $\overline{D}_\eta$, the partial derivatives of $\overline{C}$ and $\overline{D}$ with respect to η, are

$$\overline{C}_\eta = \frac{\partial \overline{C}}{\partial \eta} = \frac{\partial \overline{C}}{\partial \bar{\mathrm{I}}_1}\frac{\partial \bar{\mathrm{I}}_1}{\partial \eta} + \frac{\partial \overline{C}}{\partial \bar{\mathrm{I}}_2}\frac{\partial \bar{\mathrm{I}}_2}{\partial \eta} = \overline{C}_1\frac{\partial \bar{\mathrm{I}}_1}{\partial \eta} + \overline{C}_2\frac{\partial \bar{\mathrm{I}}_2}{\partial \eta}, \qquad (31)$$

$$\overline{D}_\eta = \frac{\partial \overline{D}}{\partial \eta} = \frac{\partial \overline{D}}{\partial \bar{\mathrm{I}}_1}\frac{\partial \bar{\mathrm{I}}_1}{\partial \eta} + \frac{\partial \overline{D}}{\partial \bar{\mathrm{I}}_2}\frac{\partial \bar{\mathrm{I}}_2}{\partial \eta} = \overline{D}_1\frac{\partial \bar{\mathrm{I}}_1}{\partial \eta} + \overline{D}_2\frac{\partial \bar{\mathrm{I}}_2}{\partial \eta}, \qquad (32)$$

and are thus given by

$$\overline{C}_\eta = 2g_{\eta\eta}\,[\overline{C}_1(\mathbf{n}\cdot\mathbf{B}\mathbf{a} + g_\eta\,\mathbf{n}\cdot\mathbf{B}\mathbf{n}) - \overline{C}_2(\mathbf{n}\cdot\mathbf{B}^{-1}\mathbf{a} - g_\eta\,\mathbf{a}\cdot\mathbf{B}^{-1}\mathbf{a})]\,, \qquad (33)$$

$$\overline{D}_\eta = 2g_{\eta\eta}\,[\overline{D}_1(\mathbf{n}\cdot\mathbf{B}\mathbf{a} + g_\eta\,\mathbf{n}\cdot\mathbf{B}\mathbf{n}) - \overline{D}_2(\mathbf{n}\cdot\mathbf{B}^{-1}\mathbf{a} - g_\eta\,\mathbf{a}\cdot\mathbf{B}^{-1}\mathbf{a})]\,. \qquad (34)$$

Using (4)(5), we note that

$$\overline{C}_1 = 2\frac{\partial^2 \overline{W}}{\partial \bar{\mathrm{I}}_1^2} = 2\overline{W}_{11}\,,\ \overline{D}_2 = 2\frac{\partial^2 \overline{W}}{\partial \bar{\mathrm{I}}_2^2} = 2\overline{W}_{22}\,, \qquad (35)$$

$$\overline{C}_2 = \overline{D}_1 = 2\frac{\partial^2 \overline{W}}{\partial \bar{\mathrm{I}}_1 \partial \bar{\mathrm{I}}_2} = 2\overline{W}_{12}\,. \qquad (36)$$

The additional pressure $q(\eta, t)$ due to the wave is then given by

$$q(\eta, t) = \mathrm{I}_2\overline{\mathrm{D}} + \overline{\mathrm{C}}\mathbf{n}\cdot\mathbf{B}\mathbf{n} - \overline{\mathrm{D}}\mathbf{n}\cdot\mathbf{B}^{-1}\mathbf{n}\,, \qquad (37)$$

up to an arbitrary additive function of time alone.

Introducing (28) into the equation of motion (25), and using (33)(34), we obtain

$$g_{tt} - v^2(g_\eta)g_{\eta\eta} = 0\,, \qquad (38)$$

where

$$\begin{aligned}\rho v^2(g_\eta) = {} & 2\overline{C}_1(\mathbf{n}\cdot\mathbf{B}\mathbf{a} + g_\eta\,\mathbf{n}\cdot\mathbf{B}\mathbf{n})^2 \\ & + 2\overline{D}_2(\mathbf{n}\cdot\mathbf{B}^{-1}\mathbf{a} - g_\eta\,\mathbf{a}\cdot\mathbf{B}^{-1}\mathbf{a})^2 \\ & - 2(\overline{C}_2 + \overline{D}_1)(\mathbf{n}\cdot\mathbf{B}\mathbf{a} + g_\eta\,\mathbf{n}\cdot\mathbf{B}\mathbf{n}) \\ & \quad (\mathbf{n}\cdot\mathbf{B}^{-1}\mathbf{a} - g_\eta\,\mathbf{a}\cdot\mathbf{B}^{-1}\mathbf{a}) \\ & + \overline{C}\mathbf{n}\cdot\mathbf{B}\mathbf{n} + \overline{D}\mathbf{a}\cdot\mathbf{B}^{-1}\mathbf{a}\,.\end{aligned} \qquad (39)$$

This equation is a non linear wave equation for $g(\eta, t)$.

Introducing (29) into the equation of motion (26), we obtain

$$\overline{C}_\eta \mathbf{b}\cdot\mathbf{Bn} - \overline{D}_\eta(\mathbf{b}\cdot\mathbf{B}^{-1}\mathbf{n} - g_\eta\, \mathbf{b}\cdot\mathbf{B}^{-1}\mathbf{a}) + \overline{D} g_{\eta\eta}\, \mathbf{b}\cdot\mathbf{B}^{-1}\mathbf{a} = 0\,. \tag{40}$$

Using the expressions (31) and (32) of $\overline{C}_\eta$ and $\overline{D}_\eta$, and dividing by $2g_{\eta\eta}$ (assumed not to be zero), we obtain the following "propagation condition"

$$\begin{aligned} &\overline{C}_1(\mathbf{n}\cdot\mathbf{Ba} + g_\eta\, \mathbf{n}\cdot\mathbf{Bn})(\mathbf{b}\cdot\mathbf{Bn}) \\ &- \overline{C}_2(\mathbf{n}\cdot\mathbf{B}^{-1}\mathbf{a} - g_\eta\, \mathbf{a}\cdot\mathbf{B}^{-1}\mathbf{a})(\mathbf{b}\cdot\mathbf{Bn}) \\ &- \overline{D}_1(\mathbf{n}\cdot\mathbf{Ba} + g_\eta\, \mathbf{n}\cdot\mathbf{Bn})(\mathbf{b}\cdot\mathbf{B}^{-1}\mathbf{n} - g_\eta\, \mathbf{b}\cdot\mathbf{B}^{-1}\mathbf{a}) \\ &+ \overline{D}_2(\mathbf{n}\cdot\mathbf{B}^{-1}\mathbf{a} - g_\eta\, \mathbf{a}\cdot\mathbf{B}^{-1}\mathbf{a})(\mathbf{b}\cdot\mathbf{B}^{-1}\mathbf{n} - g_\eta\, \mathbf{b}\cdot\mathbf{B}^{-1}\mathbf{a}) \\ &+ \frac{\overline{D}}{2}\mathbf{b}\cdot\mathbf{B}^{-1}\mathbf{a} = 0\,. \end{aligned} \tag{41}$$

In general, the propagation condition is an equation for g_η so that it cannot be satisfied together with the non linear wave equation for $g(\eta,t)$. Hence, in general, linearly polarized transverse homogeneous plane waves may not propagate. However, it may happen that the propagation condition is identically satisfied for appropriate choices of the triad $(\mathbf{n},\mathbf{a},\mathbf{b})$. We are then left with a single equation for $g(\eta,t)$ and the propagation of such waves is possible.

Here, we present such an appropriate choice of the triad $(\mathbf{n},\mathbf{a},\mathbf{b})$. We consider waves propagating and polarized in a principal plane. Thus, we assume that the propagation direction $\mathbf{n}$ and the polarization direction $\mathbf{a}$ are both in the same principal plane of the static deformation, so that the vector $\mathbf{b}$ is along a principal direction. Thus,

$$\mathbf{n}\cdot\mathbf{Bb} = \mathbf{n}\cdot\mathbf{B}^{-1}\mathbf{b} = \mathbf{a}\cdot\mathbf{Bb} = \mathbf{a}\cdot\mathbf{B}^{-1}\mathbf{b} = 0\,. \tag{42}$$

Indeed, in this case, the propagation condition (41) is identically satisfied. A finite-amplitude homogeneous transverse plane wave propagating along $\mathbf{n}$ and linearly polarized along $\mathbf{a}$ may thus propagate in a general incompressible material of the form (3) provided g satisfies the non linear wave equation (38). The additional pressure due to the wave is given by (37).

Using (42), we have

$$\mathbf{a}\cdot\mathbf{B}^{-1}\mathbf{a} = (\mathbf{n}\cdot\mathbf{Bn})(\mathbf{b}\cdot\mathbf{Bb})\,, \tag{43}$$

$$\mathbf{n}\cdot\mathbf{B}^{-1}\mathbf{a} = -(\mathbf{a}\cdot\mathbf{Bn})(\mathbf{b}\cdot\mathbf{Bb})\,. \tag{44}$$

Introducing (43)(44) into (39), we obtain for the squared wave speed of the non linear wave equation (38),

$$\begin{aligned} \rho v^2(g_\eta) = {} & 2(\mathbf{n}\cdot\mathbf{Ba} + g_\eta\, \mathbf{n}\cdot\mathbf{Bn})^2[\overline{C}_1 + (\overline{C}_2 + \overline{D}_1)\mathbf{b}\cdot\mathbf{Bb} \\ & + \overline{D}_2(\mathbf{b}\cdot\mathbf{Bb})^2] + \mathbf{n}\cdot\mathbf{Bn}\,(\overline{C} + \overline{D}\mathbf{b}\cdot\mathbf{Bb})\,, \end{aligned} \tag{45}$$

or, alternatively, recalling (35)(36),

$$\begin{aligned} \rho v^2(g_\eta) = {} & 4(\mathbf{n}\cdot\mathbf{Ba} + g_\eta\mathbf{n}\cdot\mathbf{Bn})^2[\overline{W}_{11} + 2\overline{W}_{12}\mathbf{b}\cdot\mathbf{Bb} \\ & + \overline{W}_{22}(\mathbf{b}\cdot\mathbf{Bb})^2] + 2\mathbf{n}\cdot\mathbf{Bn}\,(\overline{W}_1 + \overline{W}_2\mathbf{b}\cdot\mathbf{Bb}). \end{aligned} \tag{46}$$

Special case: propagation along a principal direction.

If we take $\mathbf{n}$, $\mathbf{a}$, and $\mathbf{b}$ along principal directions, we have (42) and also

$$\mathbf{a}\cdot\mathbf{Bn} = \mathbf{a}\cdot\mathbf{B}^{-1}\mathbf{n} = 0\,. \tag{47}$$

Let $\mathbf{i},\mathbf{j},\mathbf{k}$ be the unit vectors along the principal axes of the static strain, and $\lambda_1^2,\lambda_2^2,\lambda_3^2$ and $\lambda_1^{-2},\lambda_2^{-2},\lambda_3^{-2}$ be the corresponding eigenvalues of $\mathbf{B}$ and $\mathbf{B}^{-1}$, respectively. Note that the incompressibility constraint requires that $\lambda_1\lambda_2\lambda_3 = 1$. Here, we choose $\mathbf{n} = \mathbf{i} = (1,0,0), \mathbf{a} = \mathbf{j} = (0,1,0), \mathbf{b} = \mathbf{k} = (0,0,1)$. Thus, we have

$$\mathbf{n}\cdot\mathbf{Bn} = \lambda_1^2 \quad , \quad \mathbf{a}\cdot\mathbf{Ba} = \lambda_2^2 \quad , \quad \mathbf{b}\cdot\mathbf{Bb} = \lambda_3^2\,. \tag{48}$$

The principal invariants (13) (14) are now given by

$$\bar{\mathrm{I}}_1 = \mathrm{I}_1 + \mathrm{g}_\eta^2\lambda_1^2 \quad , \quad \bar{\mathrm{I}}_2 = \mathrm{I}_2 + \mathrm{g}_\eta^2\lambda_2^{-2}\,. \tag{49}$$

Thus, a non linear wave, propagating along $\mathbf{n} = \mathbf{i} = (1,0,0)$ and linearly polarized along $\mathbf{a} = \mathbf{j} = (0,1,0)$ may propagate provided g satisfies the non linear wave equation (38) with

$$\begin{aligned} \rho v^2(g_\eta) = {} & 4g_\eta^2\left[\overline{W}_{11}\lambda_1^4 + 2\overline{W}_{12}\lambda_1^2\lambda_2^{-2} + \overline{W}_{22}\lambda_2^{-4}\right] \\ & + \overline{C}\lambda_1^2 + \overline{D}\lambda_2^{-2}\,. \end{aligned} \tag{50}$$

Of course, a wave propagating along $\mathbf{n} = \mathbf{i} = (1,0,0)$ and linearly polarized along $\mathbf{b} = \mathbf{k} = (0,0,1)$ may also propagate. In this case, the squared wave speed is given by

$$\begin{aligned} \rho v^2(g_\eta) = {} & 4g_\eta^2\left[\overline{W}_{11}\lambda_1^4 + 2\overline{W}_{12}\lambda_1^2\lambda_3^{-2} + \overline{W}_{22}\lambda_3^{-4}\right] \\ & + \overline{C}\lambda_1^2 + \overline{D}\lambda_3^{-2}\,, \end{aligned} \tag{51}$$

where the principal invariants (13) (14) are now given by

$$\bar{\mathrm{I}}_1 = \mathrm{I}_1 + \mathrm{g}_\eta^2\lambda_1^2 \quad , \quad \bar{\mathrm{I}}_2 = \mathrm{I}_2 + \mathrm{g}_\eta^2\lambda_3^{-2}\,. \tag{52}$$

Thus, two linearly polarized waves may propagate along the principal direction $\mathbf{n} = \mathbf{i} = (1,0,0)$, one is polarized along $\mathbf{a} = \mathbf{j} = (0,1,0)$ and the other is polarized along $\mathbf{a} = \mathbf{k} = (0,0,1)$. These waves are governed by a non linear wave equation of the form (38), and the squared wave speeds are respectively given by (50)(51).

Note that here, for propagation along a principal direction, we retrieve results obtained by Green [5].

V. Linearly polarized transverse waves in generalized neo-Hookean materials

Now, we consider "generalized neo-Hookean materials", so that $D = 0$ and $C = C(\mathrm{I}_1)$.

Taking $D = 0$ in (27) (28) (29), we obtain the following expressions for the appropriate components of the stress tensor $\overline{\mathbf{T}}$:

$$\overline{T}_{\eta\eta} = -p - q(\eta,t) + \overline{C}\mathbf{n}\cdot\mathbf{Bn} \,, \tag{53}$$
$$\overline{T}_{\xi\eta} = \overline{C}(\mathbf{a}\cdot\mathbf{Bn} + g_\eta\, \mathbf{n}\cdot\mathbf{Bn}) \,, \tag{54}$$
$$\overline{T}_{\zeta\eta} = \overline{C}\mathbf{b}\cdot\mathbf{Bn} \,. \tag{55}$$

Introducing (53) into the equation of motion (24), we obtain

$$-q_\eta + \overline{C}_\eta \mathbf{n}\cdot\mathbf{Bn} = 0 \,. \tag{56}$$

The additional pressure $q(\eta,t)$ due to the wave is then given by

$$q(\eta,t) = \overline{C}\mathbf{n}\cdot\mathbf{Bn} \,, \tag{57}$$

up to an arbitrary additive function of time alone. Using

$$\overline{C}_\eta = 2\overline{C}_1\, (\mathbf{n}\cdot\mathbf{Ba} + g_\eta\, \mathbf{n}\cdot\mathbf{Bn})\, g_{\eta\eta} \,, \tag{58}$$

and introducing (54) into the equation of motion (25), we obtain

$$g_{tt} - v^2(g_\eta) g_{\eta\eta} \ = 0 \,, \tag{59}$$

where

$$\rho v^2(g_\eta) = 2\overline{C}_1(\mathbf{n}\cdot\mathbf{Ba} + g_\eta\, \mathbf{n}\cdot\mathbf{Bn})^2 + \overline{C}\mathbf{n}\cdot\mathbf{Bn} \,. \tag{60}$$

This equation is a non linear wave equation for $g(\eta,t)$.

Introducing (55) into the equation of motion (26), we obtain the following propagation condition

$$\overline{C}_\eta \mathbf{b}\cdot\mathbf{Bn} = 0 \,, \tag{61}$$

i.e. a condition to be satisfied so that finite-amplitude waves may propagate along $\mathbf{n}$ with linear polarization along $\mathbf{a}$.

Assuming $\overline{C}_\eta \neq 0$, this propagation condition is

$$\mathbf{b}\cdot\mathbf{Bn} = 0 \,. \tag{62}$$

Note that if $\overline{C}_\eta = 0$, then $\overline{C}$ is constant and we retrieve the neo-Hookean model. The condition $\mathbf{b}\cdot\mathbf{Bn} = 0$ together with $\mathbf{b}\cdot\mathbf{n} = 0$ requires that $\mathbf{b}$ is along $\mathbf{n}\times\mathbf{Bn}$, except when $\mathbf{n}$ is along a principal direction of $\mathbf{B}$. Thus, for any given $\mathbf{n}$ (not along a principal direction), $\mathbf{b}$ is along $\mathbf{n}\times\mathbf{Bn}$ and hence $\mathbf{a} = \mathbf{b}\times\mathbf{n}$ is along $\mathbf{Bn} - \mathbf{n}(\mathbf{n}\cdot\mathbf{Bn})$. Hence, the polarization direction $\mathbf{a}$ is uniquely determined: it is along the projection of $\mathbf{Bn}$ onto the plane orthogonal to $\mathbf{n}$. Thus, for generalized neo-Hookean materials a linearly polarized transverse wave may propagate for *any* propagation direction $\mathbf{n}$. When $\mathbf{n}$ is not along a principal direction of $\mathbf{B}$, the polarization direction $\mathbf{a}$ must be along the projection of $\mathbf{Bn}$ onto the plane orthogonal to $\mathbf{n}$.

Special case: propagation along a principal direction.

If we take $\mathbf{n}$ along a principal direction, we have $\mathbf{Bn} = \lambda^2\mathbf{n}$. Thus, the propagation condition $\mathbf{b}\cdot\mathbf{Bn} = 0$ is automatically satisfied by any $\mathbf{b}$ orthogonal to $\mathbf{n}$, and hence $\mathbf{a}$ is arbitrary orthogonal to $\mathbf{n}$. In this case, the wave speed (60) reduces to

$$\rho v^2(g_\eta) = 2\overline{C}_1\lambda^4 g_\eta^2 + \overline{C}\lambda^2 \,. \tag{63}$$

Note that, here, $\bar{\mathrm{I}}_1$ is given by $\bar{\mathrm{I}}_1 = \mathrm{I}_1 + \lambda^2 \mathrm{g}_\eta^2$.

Thus, in the special case when $\mathbf{n}$ is along a principal direction of $\mathbf{B}$, the polarization direction $\mathbf{a}$ may be any direction orthogonal to $\mathbf{n}$.

VI. Energy density and energy flux

Here we consider the energy density and the energy flux associated with a motion of the type (8)(9) in incompressible materials subjected to the static homogeneous deformation (7). Let W and $\overline{W}$ be the strain energy densities corresponding, respectively, to the static deformation (7) and to the motion (8), both measured per unit volume of the undeformed state. Then, the energy density $\mathcal{E}$, measured per unit volume of the homogeneously deformed state (7), and the corresponding energy flux vector $\boldsymbol{\mathcal{R}}$ are [11]

$$\mathcal{E} = \tfrac{1}{2}\rho\dot{\overline{\mathbf{x}}}\cdot\dot{\overline{\mathbf{x}}} + \mathrm{I}_3^{-1/2}(\overline{\mathrm{W}} - \mathrm{W}) \,, \tag{64}$$
$$\mathcal{R}_k = -\dot{\overline{x}}_i \overline{P}_{ik} \,, \tag{65}$$

where $\overline{\mathbf{P}}$ is the Piola-Kirchhoff stress tensor with respect to the state of homogeneous static deformation, defined by

$$\overline{P}_{ik} = \left(\frac{\bar{\mathrm{I}}_3}{\mathrm{I}_3}\right)^{1/2} \overline{T}_{ij} \left(\frac{\partial x_k}{\partial \overline{x}_j}\right) \,. \tag{66}$$

Of course, here, because of the incompressibility constraint, $\bar{\mathrm{I}}_3 = \mathrm{I}_3 = 1$. The energy density and the energy flux satisfy the energy balance equation

$$\frac{\partial \mathcal{E}}{\partial t} + \frac{\partial \mathcal{R}_k}{\partial x_k} = 0 \,, \tag{67}$$

where x_k are the coordinates in the state of homogeneous static deformation, and the partial derivative with respect to time has to be taken at fixed $\mathbf{x}$.

Now, we consider the energy density and the energy flux vector associated with the finite-amplitude transverse plane wave that may propagate in a principal plane with linear polarization in the same plane in a general deformed incompressible material. Using (17) and (66), we obtain, for the Piola-Kirchhoff stress tensor,

$$\overline{\mathbf{P}} = -(\overline{p} - \overline{D}\,\bar{\mathrm{I}}_2)(\mathbf{1} - g_\eta\, \mathbf{n}\otimes\mathbf{a}) + \overline{C}(\overline{\mathbf{B}} - g_\eta\, \overline{\mathbf{Bn}}\otimes\mathbf{a}) - \overline{D}(\overline{\mathbf{B}}^{-1} - g_\eta\, \overline{\mathbf{B}}^{-1}\mathbf{n}\otimes\mathbf{a}) \,. \tag{68}$$

Introducing the expression (14) of $\bar{\mathrm{I}}_2$, (12) of $\overline{\mathbf{B}}$, and (16) of $\overline{\mathbf{B}}^{-1}$ into the expression (68) of the Piola-Kirchhoff stress tensor , using $\dot{\mathbf{x}} = g_t\ \mathbf{a}$ and recalling (42), we obtain, for the energy density (64) and the components of the energy flux (65) in the basis $(\mathbf{n},\mathbf{a},\mathbf{b})$,

$$\begin{aligned}
\mathcal{E} &= \tfrac{1}{2}\rho g_t^2 + \overline{W} - W\ , && (69)\\
-\boldsymbol{\mathcal{R}}\cdot\mathbf{n} &= g_t\ [\overline{C}(\mathbf{n}\cdot\mathbf{B}\mathbf{a} + g_\eta\ \mathbf{n}\cdot\mathbf{B}\mathbf{n})\\
&\quad - \overline{D}(\mathbf{n}\cdot\mathbf{B}^{-1}\mathbf{a} - g_\eta\ \mathbf{a}\cdot\mathbf{B}^{-1}\mathbf{a})]\ , && (70)\\
-\boldsymbol{\mathcal{R}}\cdot\mathbf{a} &= g_t\ [-p + \overline{C}(\mathbf{a}\cdot\mathbf{B}\mathbf{a} - \mathbf{n}\cdot\mathbf{B}\mathbf{n} + g_\eta\ \mathbf{a}\cdot\mathbf{B}\mathbf{n})\\
&\quad - \overline{D}(\mathbf{a}\cdot\mathbf{B}^{-1}\mathbf{a} - \mathbf{n}\cdot\mathbf{B}^{-1}\mathbf{n} + g_\eta\ \mathbf{a}\cdot\mathbf{B}^{-1}\mathbf{n})]\ , && (71)\\
-\boldsymbol{\mathcal{R}}\cdot\mathbf{b} &= 0\ . && (72)
\end{aligned}$$

Now, we consider the energy density and the energy flux associated with the finite-amplitude transverse plane wave that may propagate in generalized neo-Hookean materials for *any* propagation direction $\mathbf{n}$ (not along a principal direction), with polarization direction $\mathbf{a}$ along $\mathbf{B}\mathbf{n} - \mathbf{n}(\mathbf{n}\cdot\mathbf{B}\mathbf{n})$. In this case the Piola-Kirchhoff stress tensor reduces to

$$\overline{\mathbf{P}} = -\overline{p}(\mathbf{1} - g_\eta\ \mathbf{n}\otimes\mathbf{a}) + \overline{C}(\overline{\mathbf{B}} - g_\eta\ \overline{\mathbf{B}}\mathbf{n}\otimes\mathbf{a})\ . \qquad (73)$$

For the energy density and the components of the energy flux in the basis $(\mathbf{n},\mathbf{a},\mathbf{b})$ we now obtain

$$\begin{aligned}
\mathcal{E} &= \tfrac{1}{2}\rho g_t^2 + \overline{W} - W\ , && (74)\\
-\boldsymbol{\mathcal{R}}\cdot\mathbf{n} &= \overline{C} g_t\ (\mathbf{n}\cdot\mathbf{B}\mathbf{a} + g_\eta\ \mathbf{n}\cdot\mathbf{B}\mathbf{n})\ , && (75)\\
-\boldsymbol{\mathcal{R}}\cdot\mathbf{a} &= g_t[-p + \overline{C}(\mathbf{a}\cdot\mathbf{B}\mathbf{a} + \mathbf{n}\cdot\mathbf{B}\mathbf{n} + g_\eta\ \mathbf{a}\cdot\mathbf{B}\mathbf{n})], && (76)\\
-\boldsymbol{\mathcal{R}}\cdot\mathbf{b} &= \overline{C} g_t\ (\mathbf{b}\cdot\mathbf{B}\mathbf{a})\ . && (77)
\end{aligned}$$

We have shown that the linearly polarized transverse waves that may propagate in deformed general incompressible elastic materials and in deformed generalized neo-Hookean materials are both governed by a second order non linear wave equation of the same form (38) or (59). Now, we consider simple wave solutions of this non linear wave equation propagating with positive speed $v = v(g_\eta)$, given by (45) for the general incompressible materials, and given by (60) for the generalized neo-Hookean materials. For such waves, we have $g_t = -\varphi(g_\eta)$, where φ is the function defined by $\varphi'(g_\eta) = v(g_\eta)$ with $\varphi(0) = 0$ (see, for instance, [16]),

$$g_t = -\varphi(g_\eta) = -\int_0^{g_\eta} v(e)de\ . \qquad (78)$$

Using this in the expressions of the energy density $\mathcal{E}$ and the component $\boldsymbol{\mathcal{R}}\cdot\mathbf{n}$ of the energy flux, we note that $\mathcal{E}$ and $\boldsymbol{\mathcal{R}}\cdot\mathbf{n}$ are now both functions of g_η :

$$\mathcal{E} = E(g_\eta) \quad , \quad \boldsymbol{\mathcal{R}}\cdot\mathbf{n} = R(g_\eta)\ . \qquad (79)$$

Taking the derivatives of these functions with respect to g_η, and using the chain rule, we obtain

$$R'(g_\eta) = v(g_\eta)E'(g_\eta)\ , \qquad (80)$$

and hence

$$\boldsymbol{\mathcal{R}}\cdot\mathbf{n} = R(g_\eta) = \int_0^{g_\eta} v(e)\ E'(e)de\ . \qquad (81)$$

Thus, the projection onto the propagation direction $\mathbf{n}$ of the energy flux vector is equal to an integral of the derivative of the energy density multiplied by the wave speed, these two being functions of the signal level g_η. Remarkably, this is the same property as obtained in [11] for longitudinal simple waves in deformed Hadamard materials. However, here we deal with transverse simple waves in incompressible materials.

For waves of infinitesimal amplitude, (38) must be linearized so that $v(g_\eta)$ has to be replaced by $v(0)$. Then, (81) becomes $\boldsymbol{\mathcal{R}}\cdot\mathbf{n} = v(0)E$, in agreement with results proved by Hayes [17] for the mean energy flux and mean energy density in the context of linear conservative systems and time-harmonic plane waves. Thus, (81) generalises this property to non linear simple waves.

References

[1] Green, A.E., Rivlin, R.S. and Shield, R.T. General theory of small elastic deformations superposed on finite elastic deformations, *Proceedings of the Royal Society of London*, **A211**, 128–154, (1952).

[2] Toupin, R.A. and Bernstein, B. Sound waves in deformed perfectly elastic materials. Acousto-elastic effect, *J. Acoust. Soc. Amer.*, **33**, 216–225, (1961).

[3] Hayes, M. and Rivlin, R.S. Propagation of a Plane wave in an isotropic Elastic material subject to a Pure Homogeneous Deformation, *Arch. Rat. Mech. Anal.*, **8**, 15–22, (1961).

[4] Ogden, R.W. *Non-linear Elastic Deformations*, Dover, New York, (1997).

[5] Green, A.E. A note on wave propagation in initially deformed bodies, *Journal of the Mechanics and Physics of Solids*, **11**, 119–126, (1963).

[6] Carroll, M.M. Some results on finite-amplitude elastic waves, *Acta Mechanica*, **3**, 167–181, (1967).

[7] Currie, P. and Hayes, M. Longitudinal and transverse waves in finite elastic stain, Hadamard and Green materials, *J. Inst. Maths Applics*, **5**: 140–161, (1969).

[8] Boulanger, Ph. and Hayes, M. Finite-amplitude waves in deformed Mooney-Rivlin materials, *Q. J. Mech. appl. Math.*, **45**, 575–593, (1992).

[9] Boulanger, Ph. and Hayes, M. Further properties of finite-amplitude plane waves in deformed Mooney-Rivlin materials, *Q. J. Mech. appl. Math.*, **48**, 427–464, (1995).

[10] Rodrigues Ferreira, E. *Finite-amplitude waves in deformed elastic materials*, VDM-Verlag Dr Müller, (2009).

[11] Boulanger, Ph., Hayes, M. and Trimarco, C. Finite-amplitude plane waves in deformed Hadamard materials, *Geophys. J. Int.*, **118**, 447–458, (1994).

[12] Yeoh, O.H. Characterization of elastic properties of carbon-black-filled rubber vulcanizates, *Rubber Chemistry and Technology*, **63**, 792–805, (1990).

[13] Arruda, E.M. and Boyce, M.C. A three-dimensional constitutive model for the large stretch behavior of rubber elastic materials, *Journal of the Mechanics and Physics of Solids*, **41**, 389–412, (1993).

[14] Fung, T.C.B. Elasticity of soft tissues in simple elongation, *American Journal of Physiology*, **213**, 1532–1544, (1967).

[15] Knowles, J.K. The finite anti-plane shear field near the tip of a crack for a class of incompressible elastic solids, *International Journal of fracture*, **13**, 611–639, (1977).

[16] Whitham, G.B. *Linear and Nonlinear waves*, Wiley, J. and sons, New-York, (1974) .

[17] Hayes, M. Energy flux for trains of inhomogeneous plane waves, *Proc. R. Soc. Lond.*, **A 370**, 417–429 , (1980).

Proceedings of the 8th National Congress on Theoretical and Applied Mechanics, May 28-29, Brussels, Belgium.

Trailing Edge Noise of a Controlled-Diffusion Airfoil at Moderate and High Angle of Attack

J. Christophe[1], J. Anthoine[1], S. Moreau[2]
[1]Environmental and Applied Fluid Dynamics Department, von Karman Institute for Fluid Dynamics
Chaussée de Waterloo 72, 1640 Rhode-St-Genèse - Belgium
[2] GAUS, Département de génie mécanique, Université de Sherbrooke
Sherbrooke (Quebec), J1K 2R1 - Canada
email: christju@vki.ac.be, anthoine@vki.ac.be, stephane.moreau@USherbrooke.ca

Abstract— **This paper proposes to study the flow and corresponding noise around a segment of an automotive blade (CD-airfoil) at design conditions, namely a 8° angle of attack, and a higher angle of attack of 15° for which there is experimental evidence that the flow regime has significantly changed. This study encompasses two aspects, the flow resolution around the profile using the commercial solver Fluent 6.3 and the noise propagation using Amiet's theory based on the trailing edge wall-pressure spectrum or Curle's analogy using the pressure distribution along the blade. All along, computational results are compared to experiments taken in the large anechoic chamber from Ecole Centrale de Lyon (ECL). For the 8° case, two mesh refinements in the spanwise direction and two boundary conditions in spanwise direction, periodic and symmetric, and combination of both are studied. It reveals that both improvement of mesh and use of periodic spanwise boundary condition, have an influence on the trailing edge spectrum, decreasing the low frequency content to approach experimental results. Furthermore, these numerical parameters help to predict correctly the spanwise coherence measured experimentally. On the contrary, this numerical configuration is not improving the mean and rms velocity profiles in the wake of the airfoil and can even have a negative effect on the energy spectrum of the wake velocity. Acoustic results show satisfactory agreement using Curle's analogy especially in the low frequency range with experimentally measured noise, the sound radiated being under-predicted abobe 1 kHz. Amiet's theory is over-predicting the sound radiated compared to experiments due to the over-prediction of the wall-spectrum at trailing edge. The first attempt to compute the flow around the same airfoil at 15° angle of attack reveals that, again, the wall-pressure spectrum is over-predicted at low frequencies. Furthermore, it appears that the computational domain in the spanwise direction is too restrited to capture correctly the low frequency content of the flow. The computation is then largely over-predicting the spanwise coherence at low frequencies.**

Keywords— **Trailing edge noise, Aeroacoustic analogy, Large-Eddy-Simulation**

I. Introduction

TRAILING-EDGE noise or broadband self-noise, caused by the scattering of boundary-layer vortical disturbances into acoustic waves, occurs at the trailing edge of any lifting surface. It can even become the dominant source of noise generated by rotating machines such as fans, turboengines [1], [2], wind turbines [3], [4], and other high-lift devices [5], [6] in the absence of any other interaction noise source. These noise levels can be hopefully reduced by properly identifying the sources of self-noise, and subsequently modifying design parameters that affect these noise sources. The large computational costs associated with unsteady turbulent flow simulations have however limited most numerical studies to simplified geometries such as airfoils. The first LES of the flow over the Valeo Controlled-Diffusion (CD) airfoil was performed by Wang [7] at a moderate angle of attack (a.o.a) of 8°, which corresponds to the design condition or the maximum static efficiency of the associated fan. It used a large structured mesh with 5.1 million nodes to yield stable and accurate flow solutions. Subsequent attempts to reduce the computational costs included the use of non-boundary conforming methods such as the Lattice Boltzmann method and Immersed Boundary method [8], as well as hybrid solution methods such Detached Eddy Simulations [9]. These techniques yielded less accurate mean wall-pressure distributions (larger laminar recirculation bubble near the leading edge and possibly turbulent flow separaration near the trailing edge) and frequency spectra near the trailing edge than those obtained by Wang [7]. An alternative approach was then taken by Moreau *et al.* [10], involving the flow solver CDP and several LES on unstructured grid topologies. It showed that accurate results for all flow quantities could be obtained with the unstructured flow solver, provided the grid remained smooth and regular enough in all directions.

The present work proposes to study the influence of spanwise boundary conditions (symmetric or periodic) and spanwise mesh refinement on the LES flow and acoustic results for this moderate angle of attack ($\alpha_w = 8^\circ$). This will help to define the methodology to apply and possibly improvements required in such airfoil flow conditions to reach reliable results compared to experiments. This encompasses the correct resolution of the flow around the airfoil and the prediction of the trailing edge noise. Two different approaches have been explored to model the far field acoustic pressure: the extended Amiet's theory [11] based on the diffraction of pressure fluctuations near the trailing edge by a flat plate of finite chord, and Curle's analogy using the pressure distribution on the airfoil surface or in its simplified version, using the lift airfoil coefficient neglecting then the retarded time between dipole sources on the airfoil surface.

Furthermore, the present study aims at extending this large body of work at design condition, to a first attempt of computation at larger angles of attack ($\alpha_w = 15^\circ$), for which there is experimental evidence that the flow regime has significantly changed. This paper proposes then to investigate the possibility to use similar methods for the high angle of attack as for the moderate one. Same methods are then applied to the higher angle of attack; comments about applicability of those methods to high angles of attack and comparisons between results obtained for both angles of attack are proposed.

II. Experimental database

The experimental data were collected in the large anechoic wind tunnel of the Ecole Centrale de Lyon (ECL). The airfoil mock-up has a 13.4 cm constant chord length (c) and a 0.3 m span (L). It is held between two horizontal side plates fixed to the nozzle of the open-jet wind tunnel as shown in Fig. 1 (top). These plates are 25 cm ($\approx$1.85 c) apart and the width of the rectangular jet is 50 cm ($\approx$3.7 c). As shown by Moreau *et al.* [12], this aspect ratio insures that the 3-D effects at midspan are therefore minimized. All of the tests presented here were run with a speed U_∞ = 16 m/s, which corresponds to a Reynolds number

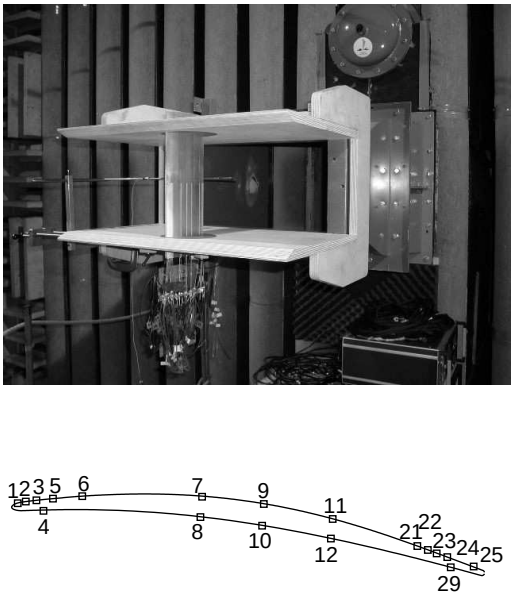

Fig. 1. ECL experiment : (top) Complete nozzle setup and (bottom) RMP locations on the CD airfoil.

based on the airfoil chord length Re_c=1.6$\times$10^5 and angles of attack with respect to the chord, α_w, of 8° or 15°.

The CD airfoil mock-up is equipped at midspan with 21 flush-mounted remote Electret microphone probes (RMP) (Pérennès & Roger [5]). The RMPs measure both the mean and fluctuating pressure within a frequency range of 20 Hz–25 kHz. Figure 1 (bottom) shows the layout of the streamwise RMPs at the midspan plane of the CD airfoil. Three additional RMPs in the spanwise direction near the trailing edge allow measuring spanwise coherence lengths. Details of the wall-pressure measurements in this configuration can be found in Moreau & Roger [13]. The far-field noise is measured simultaneously using a single B&K 1.27 cm (1/2') Type-4181 microphone in the midspan plane at a distance of 2 m from the airfoil trailing edge. Figures 16 and 20 in Moreau & Roger [13] show that at 15° both the noise sources given by the wall-pressure fluctuations and the consequent sound radiated in the far-field have a much larger low-frequency content than at the design condition.

III. Large-Eddy Simulation for CD-airfoil

A. Flow solver

The LES is based on the spatially filtered, incompressible Navier-Stokes equations with the dynamic subgrid-scale model (Germano *et al.* [14]; Lilly [15]). Equations are solved with the finite volume solver Fluent 6.3. using central difference scheme for spatial discretizations and the Non-Iterative-Time-Advancement (NITA) scheme for time advancement. Both schemes are therefore second-order accurate in space and time. Preliminary RANS computations are required to provide the LES boundary conditions for computations at both angles, as described in the next section. These are performed using the Shear-Stress-Transport (SST) $k-\omega$ turbulence model developed by Menter [16], with again second order accurate solution for all variables.

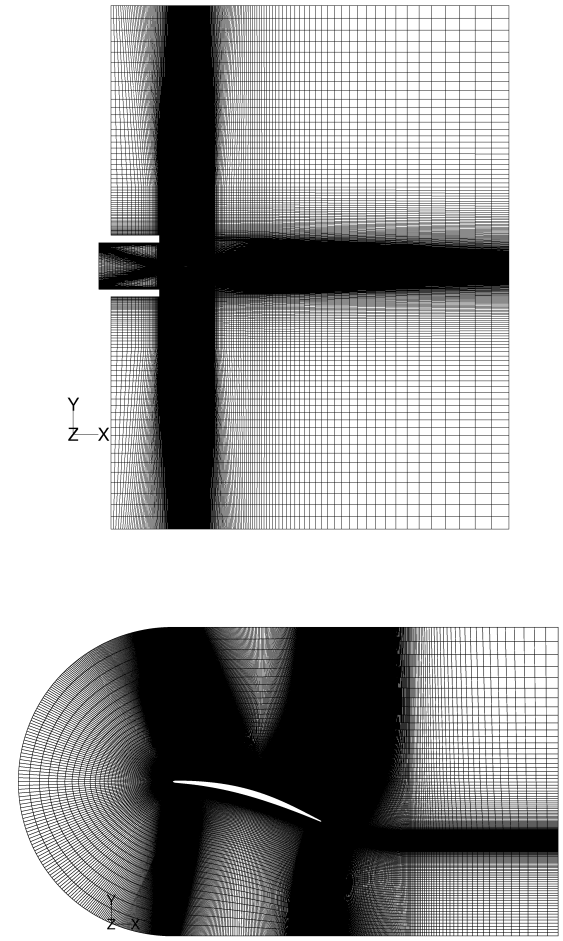

Fig. 2. Top: Grid topology of ECL large wind tunnel setup for initial RANS computation. Bottom: LES truncated domain, extracted from the full wind tunnel setup for the 15° computation.

B. Grid topologies and boundary conditions

It has been shown by Moreau *et al.* [12] that the flow around an airfoil in open-jet wind tunnel facility differs significantly from that around an isolated airfoil in a uniform stream. In the present case, for both angles of attack, the airfoil is immersed in a jet of finite width, which is deflected by the circulation created by the airfoil and has then an impact on the airfoil loading and the corresponding noise created. This can be seen by the large deflection evident in these bounding shear layers (Moreau *et al.* [17]). One possibility would be to include both the jet and the airfoil in the LES computations, but, would make the computation expensive, if not impossible. In order to match closely experiments with the LES computations, the following procedure is used. As shown by Moreau *et al.* [12], a 2-D Reynolds-Averaged Navier-Stokes (RANS) simulation of the complete open-jet wind tunnel configuration including the nozzle, the airfoil and part of the anechoic chamber is first required to capture the strong interaction between the jet and the CD airfoil and its impact on the airfoil load at any incidence. The full RANS simulation on the grid shown in Fig. 2 (top) provides

velocity boundary conditions for the smaller LES truncated domain which is embedded between the two boundary shear layers of the jet. To allow a reasonably large LES domain within the jet core, the largest nozzle available in the ECL facility was employed. The jet width at the nozzle exit 3.7 times the airfoil chord c. This method has proved its efficiency, the first LES of the CD airfoil at a small angle of attack of 8° performed by Wang [7] closely reproduced the experimental conditions found in the ECL large anechoic wind tunnel. A similar strategy has been used in the trailing-edge flow simulation of Wang [18].

Yet, the lower Reynolds number Re_c and the larger jet-width to chord ratio in the present experiment again allows a computational domain around the full airfoil for both angles of attack. In case of 8° a.o.a., the size of computational domain is : $4\ c$ in the streamwise (x) direction, $2.5\ c$ in the crosswise (y) direction and a width ($0.1\ c$) in the spanwise (z) direction. The resulting LES grid is a single block-structured C-mesh, shown in Fig. 2 (b), with 960 × 84 × N cells, where N can be 32 or 64, in the present computations. Smooth grid-distribution and orthogonality at the wall are again applied and the grid-stretching ratio is limited in the streamwise and crossflow directions to ensure numerical stability. The near-wall grid spacing, except near the leading edge, follows LES criteria found for instance in Baggett *et al.* [19], to reach maximum values of $x^+ = 34$, $y^+ = 1.1$ and $z^+ = 20$ on the airfoil surface.

Compared to the 8° case, the 15° computation used a straighter configuration to account for the different flow topology and to better capture the larger wake, as it will be illustrated later. The computational domain size is similar : $3.5\ c$ in the streamwise (x) direction, $2.5\ c$ in the crosswise (y) direction and a width ($0.1\ c$) in the spanwise (z) direction, the mesh being a little be shorter in the streamwise direction to save mesh cells. Again, the mesh results in a single block-structured C-mesh, shown in Fig. 2 (c), with 1685 × 105 × 32 cells. This mesh reaches maximum values of $x^+ = 40$, $y^+ = 3$ and $z^+ = 30$ on the airfoil surface, acceptable for LES computations.

For both angles of attack, the LES use a no-slip boundary condition on the airfoil surface, a convective outflow boundary condition at the exit plane, and the steady RANS velocity (U and V) along the upper and lower boundaries. For the 8° case, symmetric or periodic boundary conditions are applied in the spanwise direction, while the 15° case uses symmetry boundary conditions.

Computations were run for at least 5 flow-through times, based on the freestream velocity and airfoil chord length, before a statistically steady state was reached and mean values were collected. Airfoil surface pressure and wake velocity statistics were then acquired for a period of at least 4 flow-through with a sampling rate of 50 kHz for the 8° cases while the 15° computation was run for 10 flow-through, the convergence of the flow statistics being slower.

IV. Acoustic methods

A. Curle's analogy

Curle [20] provides the following integral solution of Lighthill's analogy [21], in the presence of solid surfaces in the source region:

$$\rho'(\mathbf{x},\mathbf{t}) = \frac{\partial^2}{\partial x_i \partial x_j} \iiint_V \left[\frac{T_{ij}}{4\pi c_0^2 |\mathbf{x}-\mathbf{y}|}\right] d^3\mathbf{y} - \frac{\partial}{\partial x_i} \iint_{\partial V} \left[\frac{p' n_i}{4\pi c_0^2 |\mathbf{x}-\mathbf{y}|}\right] d^2\mathbf{y}. \quad (1)$$

where $T_{ij} = \rho v_i v_j + (p' - c_0^2 \rho')\delta ij - \sigma_{ij}$ is Lighthill's tensor where p is the pressure, ρ is the density, v_i is the i-th velocity component and σ_{ij} is the viscous stress tensor, and where the free-field Green's function has been used. In the surface integral of (1), the viscous contribution of Tij has been neglected, the surface is assumed non-vibrating and with no-slip, and the bracketed terms are to be evaluated at the retarded time $t^* = t - |\mathbf{x}-\mathbf{y}|/\mathbf{c_0}$. Curle [20] demonstrated that for a compact distribution of sources at low Mach numbers, the contribution from the volume integral in (1) is of quadrupolar character and can be neglected. We proceed accordingly in this work by retaining the dipolar source only. The acoustic results presented below for Curle's analogy have been obtained using a boundary integral implementation of this analogy in the commercial Boundary Element solver Virtual.Lab Acoustics Rev 8B.

B. Amiet's theory

In Amiet's theory, the trailing-edge noise is derived by iteratively solving scattering problems at the airfoil edges. The system of partial differential equations that arise at each iteration in this multiple scattering problem is solved using Schwarzschild's solution. The main trailing-edge scattering obtained by Amiet [22], assuming the airfoil extends toward infinity in the upstream direction, has been corrected by a leading-edge back-scattering contribution which fully accounts for the finite chord length (Roger & Moreau [11]). The radiated sound field is calculated by integrating the induced surface sources on the actual chord length, c and the mock-up span, L, assuming convection of frozen turbulent boundary layer eddies past the trailing edge.

The predicted sound field in the midspan plane at a given observer location $\vec{x} = (x_1, x_2, 0) = (R, \theta, z = 0)$ and for a given radian frequency ω (or wavenumber k) then reads :

$$S_{pp}(\vec{x},\omega) = p_a(\vec{x},\omega)\, p_a^\star(\vec{x},\omega) = \left(\frac{\sin\theta}{2\,\pi\,R}\right)^2 (k\,c)^2\, \frac{L}{2}\, |I|^2\, \Phi_{pp}(\omega)\, l_y(\omega) \quad (2)$$

where Φ_{pp} is the wall-pressure power spectral density and l_y the spanwise correlation length near the trailing edge. The radiation integral I involving both the free stream velocity U_∞ and the convection speed as parameters can be found in Roger & Moreau [11].

V. CD-airfoil at 8° a.o.a. - Boundary condition and mesh refinement effects

A. Flow-field description

The flow topology in the 8° runs is first illustrated in Fig. 3 by the iso-contours of constant Q factor, which show the level of vorticity and the size of the turbulent structures in the flow at a given instant. It shows for all cases a laminar boundary layer

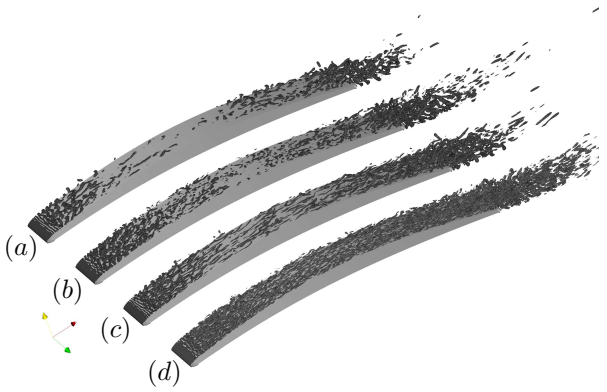

Fig. 3. Flow topology described by the Q factor ($Q = 1000s^{-2}$ iso-contours) for all 8° computations : (a) 32 spanwise cells and symmetric boundary conditions, (b) 32 spanwise cells and periodic boundary conditions, (c) 64 spanwise cells and symmetric boundary conditions, (d) 64 spanwise cells and periodic boundary conditions.

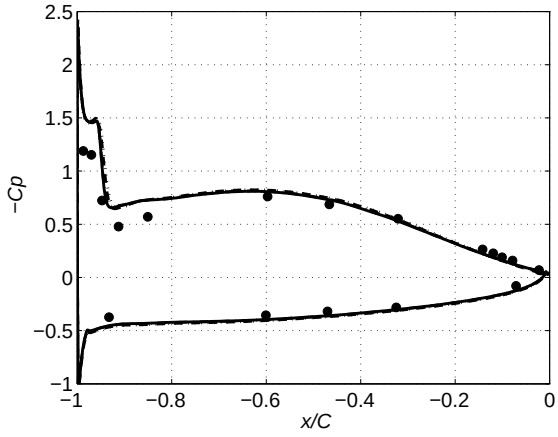

Fig. 4. Mean wall-pressure coefficient $-C_p$ along blade surface for all 8° computations : (dot) 32 spanwise cells and symmetric boundary conditions, (dash-dot) 32 spanwise cells and periodic boundary conditions, (dash) 64 spanwise cells and symmetric boundary conditions, (plain) 64 spanwise cells and periodic boundary conditions.

on the lower (pressure) side of the airfoil, and a transitional and turbulent boundary layer on the upper (suction) side. Transition on the suction side is trigerred by an unsteady laminar separation near the leading edge, where small vortices are born close to the reattachment point of the laminar recirculation bubble. The leading edge separation can be quantitatively identified as a region of negative skin friction coefficient. The streamwise extent of the recirculation bubble is then determined and found as 8.6%c in case of symmetric cases and 7.1%c in case of periodic cases, independently of the mesh refinement. These values are slightly over-predicting the reciculation bubble size observed in previous computations, 3.7%c for the structured LES of Wang [7] using identical mesh and 5%c for the CDP unstructured cases [10]. Yet, in a previous computations by Moreau *et al.* [9], using a different solver, a too large separation of 11.2%c was observed. Therefore both extent of the laminar separation region and consequent positive pressure gradient are more dependent on the LES code and mostly on its subgrid-scale model implementation than on the grid itself provided it is fine and sufficiently regular near the wall. Moreover, the detailed transition process, including the precise locations of separation and reattachment, are difficult to predict. It strongly depends on the incoming flow disturbances. No free-stream turbulence is provided in the computations, whereas in the experiments, the residual turbulence level of the incident flow is approximately 0.8% of the mean velocity. The variations from one experiment to another can also be large as illustrated by Wang [7].

The flow re-laminarizes towards mid-chord because of the favorable pressure gradient. When this gradient becomes adverse, the boundary layer thickens again and more and larger vortices are created towards the trailing edge. Like its laminar counterpart on the pressure side, the turbulent boundary layer remains attached as it passes the trailing edge despite of the strong adverse gradient.

Furthermore, the influence of the spanwise boundary conditions and the mesh refinement in the spanwise direction is clearly observed in Fig. 3. As expected, smaller structures are formed directly after the recirculation bubble with 64 cells in the spanwise direction instead of 32. These structures are then convected along the airfoil chord, resulting in a wake containing more structures with a finer grid. In the recirculation region, no speficic differences are observed with the mesh refinement. Similarly, the symmetric boundary conditions in the spanwise direction are forcing larger scale structures after the recirculation region than periodic boundary conditions, avoiding development of three-dimensional effects due to the strong condition imposed by the spanwise boundary conditions. Moreover, vortex shedding seems to appear from the pressure side at the trailing edge, that was not clearly identified in case of periodic boundary conditions, resulting in larger structures in the airfoil wake. Such a vortex shedding pattern is clearly seen in the experimental velocity spectra as shown below.

B. Mean-pressure coefficient ($-C_p$) and pressure spectra

The mean and fluctuating wall-pressure were analyzed for each of the LES runs and compared with the RMPs measurements by Moreau & Roger [13]. The mean pressure on the surface, characterized by the pressure coefficient $-C_p$, is shown in Fig. 4. These results show that the four LES computations at 8° a.o.a are in reasonable good agreement with experiments. This also illustrates that the approach, consisting in transfer of flow boundary conditions between the RANS and LES computations, provides high fidelity in terms of global flow conditions. It was also verified that the RANS simulations in both the full tunnel setup and the truncated LES domain yielded the same profile loading. Only small differences are observed between the four present computations in the leading edge recirculation region. This observation is coherent with the difference in the recirculation bubble size described in Sec. V-A.

The wall-pressure spectra near the trailing edge are compared with the measurements above RMP#25 in Fig. 5 (top) for all 8° computations. All LES results are very similar, particularly for $f > 2000$ Hz, where all the numerical pressure spectra agree

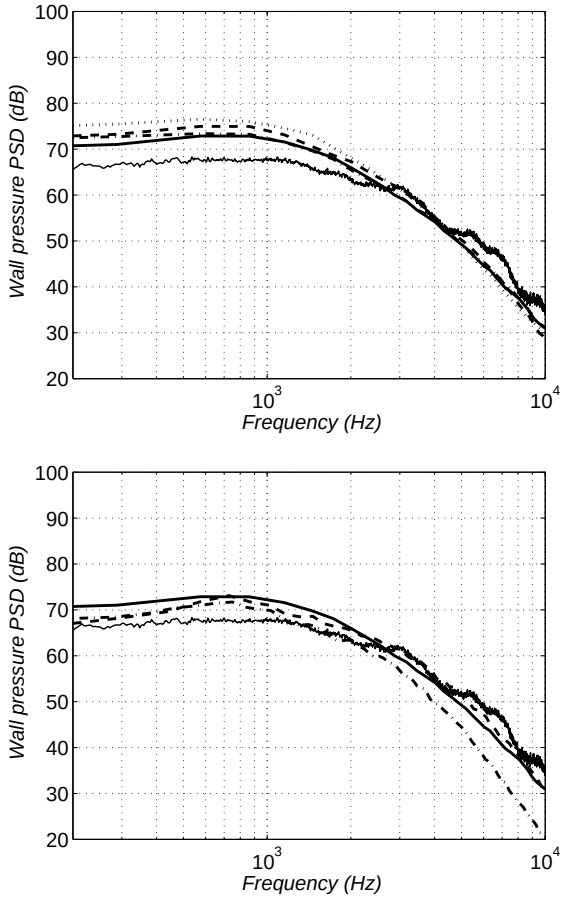

Fig. 5. Frequency spectra of pressure fluctuations on the suction side in the leading edge area ($x/c = 0.02$): (top) for all present 8° computations, (dot) 32 spanwise cells and symmetric boundary conditions, (dash-dot) 32 spanwise cells and periodic boundary conditions, (dash) 64 spanwise cells and symmetric boundary conditions, (plain) 64 spanwise cells and periodic boundary conditions. (bottom) Comparison with previous litterature data : (plain) present computation with 64 spanwise cells and periodic boundary conditions, (dash-dot) Wang's computation and (dash) CDP computation. (thin plain) Experiments.

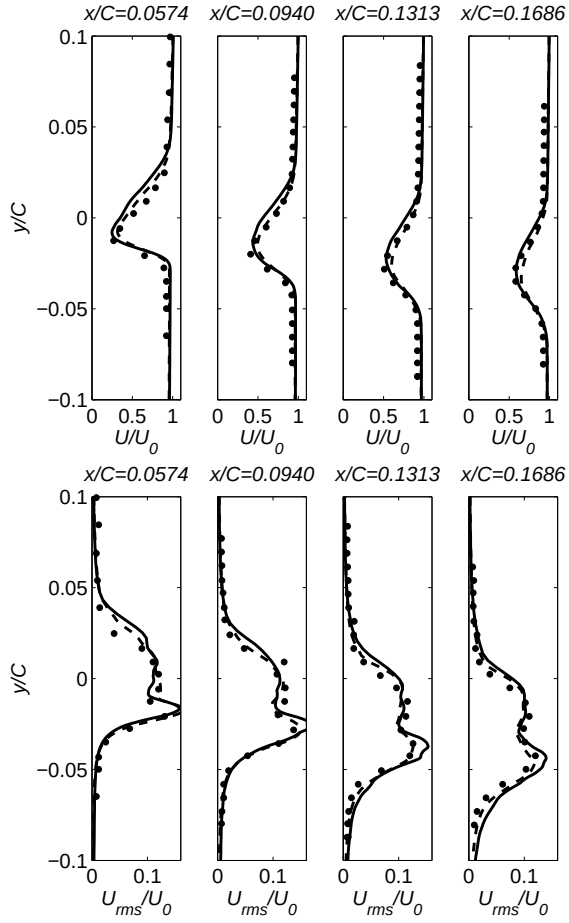

Fig. 6. Wake velocity data. (top) Normalized mean velocity $\bar{U}/U_0$ and (bottom) Normalized rms velocity fluctuations $\tilde{U}/U_0$ at four x/c locations. (dash) 64 spanwise cells and symmetric boundary conditions, (plain) 64 spanwise cells and periodic boundary conditions, (dots) Experiments.

with the experimental one. The main differences appear at low and mid frequencies where the effects of the boundary condition in the spanwise direction and the mesh refinement are observed. A first observation is that the behavior of the pressure spectrum at low frequencies is different depending on the mesh refinement, the 32 spanwise cells computations having almost a plateau at low frequencies while the 64 spanwise cells computations have a slight negative slope in the spectrum with decreasing frequencies. Each improvement in the mesh refinement or in the spanwise boundary conditions is reducing the gap between the numerical and experimental pressure spectra: the refinement of the mesh is mainly reducing the spectrum amplitude at low frequencies (below 500 Hz) while imposing periodic boundary conditions instead of symmetric ones is reducing the spectrum amplitude at low and mid frequencies (below 2 kHz). Note that the difference between the 32 cells symmetric computation and the 64 cells periodic computation is up to 5dB on the pressure spectrum at the trailing edge. Nevertheless, the latter is still overpredicting the pressure spectrum at low and mid frequencies compared to experiments (up to 5dB).

A comparison of the present 64 cells periodic computation with other computations in the same conditions on the identical grid, but using different codes, is presented in Fig. 5 (bottom). The wall-pressure spectra near the trailing edge are very similar for all computations, especially for frequencies below 2 kHz. The CDP and present results show better agreement with the experimental data at higher frequencies than those obtained by Wang [7], which tail off more quickly with frequencies, suggesting that boundary layers lacks very small scale structures. At low frequencies, the present computation predicts higher amplitude of the wall-pressure spectrum compared to other CFD results (around 2-3 dB).

The wall-pressure spectra in the spanwise direction for all LES show collapsing PSD and a statistically homogeneous turbulence is obtained at the trailing edge, which is one of the assumption of Amiet's acoustic model used below.

C. Velocity statistics in the wake

Velocity data were extracted for each computation, at locations that matched those of the hot-wire probes in the experi-

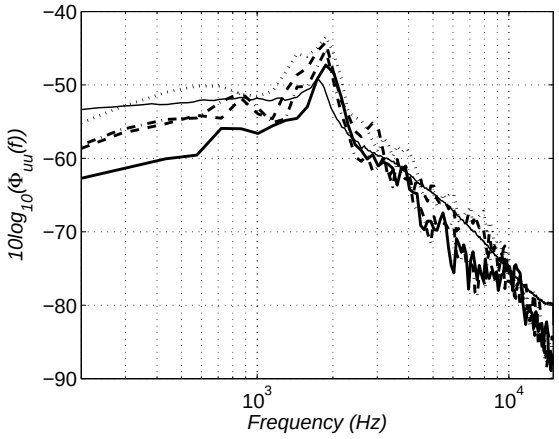

Fig. 7. Wake energy spectra of the streamwise velocity on the pressure side at $(x/c, y/c) = (0.057, -0.023)$. (dot) 32 spanwise cells and symmetric boundary conditions, (dash-dot) 32 spanwise cells and periodic boundary conditions, (dash) 64 spanwise cells and symmetric boundary conditions, (plain) 64 spanwise cells and periodic boundary conditions, (thin plain) Experiments.

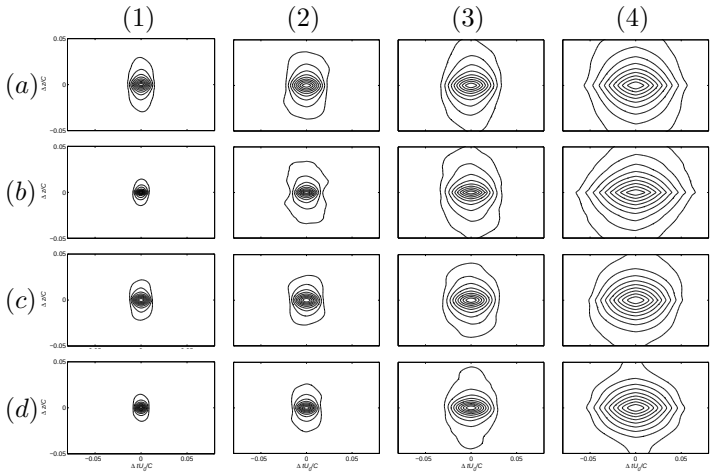

Fig. 8. Coutours of space-time correlations of the fluctuating pressure on the suction surface of the airfoil as a function of spanwise and temporal separations, at streamwise locations (1) $x/c = -0.60$, (2) $x/c = -0.23$, (3) $x/c = -0.02$, (4) $x/c = 0$ (trailing edge) for all present 8° computations, (a) 32 spanwise cells and symmetric boundary conditions, (b) 32 spanwise cells and periodic boundary conditions, (c) 64 spanwise cells and symmetric boundary conditions, (d) 64 spanwise cells and periodic boundary conditions. Contours values are from 0.1 to 0.9, with increment of 0.1.

ments of Moreau *et al.* [10]. Figure 6 shows the mean and rms of velocity fluctuations (for the component u) at four different measurement stations from $x/c = 0.0574$ to $x/c = 0.1686$. For clarity, only results obtained for a mesh refinement of 64 cells in the spanwise direction are presented, for symmetric and periodic spanwise boundary conditions. For all stations, and for both spanwise boundary conditions, computations present very similar shapes with a wake deficit very close to those of the experiments. It can be observed that the periodic boundary conditions closely match the experiments in the lower part of the wake (pressure side) up to the maximum mean velocity peak, compared to symmetric boundary conditions. On the contrary, in the upper part of the wake (suction side), symmetric boundary conditions show better agreement with experiments, the periodic boundary conditions largely overpredict the mean velocity amplitude. This effects are attenuated with the distance from the airfoil trailing edge.

Concerning the rms velocity fluctuations, both boundary conditions show qualitatively similar profiles than those observed in the experiments.Both computations reproduce correctly the position of the maximum peak of turbulence intensity (the location of the higher shear in the wake). The amplitude of this peak is better predicted by the symmetry boundary conditions for the all stations, particularly for the farthest downstream locations. At the first station ($x/c = 0.0574$), both computations are overpredicting the turbulence intensity in the upper part of the wake, around $y/c = 0.03$, about 5% for the streamwise component.

Velocity wake spectra in the wake region were measured experimentally for frequencies up to 15 kHz. Figure 7 plot the streamwise energy spectra for all 8° computations at $x/c = 0.057$ and the cross-flow locations $y/C = -0.023$. At this location in the wake, all computations present similar behavior at high frequencies, and a qualitative agreement compared to experiments. Around $f = 2000$ kHz, a shedding frequency is measured on the lower side of the wake. This feature is captured by all computations but the amplitude is overpredicted. At low frequencies, the use of mesh refinement and periodic boundary conditions is not correctly reproducing experimental observations, with a difference up to 10 dB. Finally, for $4 < f < 10$ kHz, periodic boundary conditions show different shape of the energy spectrum with differences compared to symmetric boundary conditions, up to 5dB.

In conclusion, different trends are observed between the wall-pressure spectra and the velocity spectra in the wake of the airfoil. Both the mesh refinement in the spanwise direction and the periodic boundary conditions are improving the comparison with experiments while opposite trends are seen in the energy spectra in the wake.

D. Correlation and coherence

The evolution of the spatial and temporal scales in the turbulent boundary layer along the chord is analysed through the space-time correlation of the fluctuating pressure of the airfoil surface, given by:

$$C(\mathbf{x}, t, \mathbf{r}, \tau) = < p(\mathbf{x}, t) p(\mathbf{x} + r, t + \tau) > \qquad (3)$$

Figure 8 shows these correlations in function of temporal and spanwise spatial separations at four streamwise locations ($x/c = -0.60$, -0.23, -0.02 and 0) for the four present computations. In all four computations, a significant growth of the spanwise and temporal scales is observed from the first station to the third, due to the growing of the boundary layer which is accelerated by the adverse pressure gradient. A similar growth of the streamwise scales can be deduced from the temporal scales through Taylor's assumption. At the station $x/c = -0.60$, before mid-chord and after the recirculation bubble, a much smaller scale size is observed for computations using spanwise

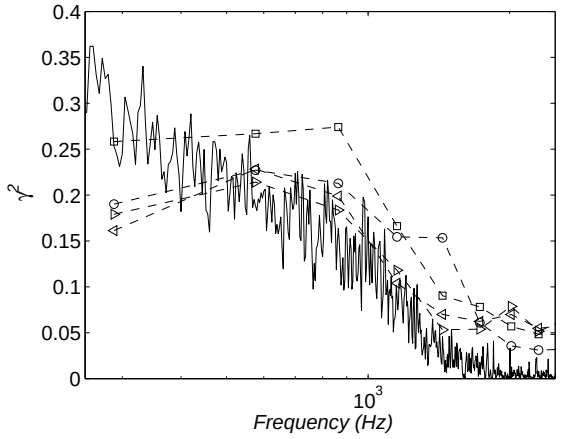

Fig. 9. Spanwise coherence of fluctuating pressure on the suction surface at $x/c = -0.02$ plotted against frequency for a spanwise separation of $\Delta z/c = 0.02$. (circle) 32 spanwise cells and symmetric boundary conditions, (square) 32 spanwise cells and periodic boundary conditions, (right triangle) 64 spanwise cells and symmetric boundary conditions, (left triangle) 64 spanwise cells and periodic boundary conditions, (plain) experiments.

periodic boundary conditions. At the same station, one can see the effect of the mesh refinement reducing in a less stronger way the spatial and time scales compared to the effect of periodicity. These observations are coherent with those of Sec. V-A. Along the airfoil chord, those scales are growing with shorter distance from the trailing edge. Again the mesh refinement has an effect near the trailing edge, scales being smaller in the case of the periodic boundary conditions. The influence on the mesh refinement is less evident than before mid-chord. Those observations are coherent with the near trailing-edge spectrum decribed in Sec. V-B. At the trailing-edge station, $x/c = 0$, there is more influence from the pressure side boundary layer than from the suction one. Therefore, spatial and temporal scales are much larger than those of its close neighbor, $x/c = -0.02$. Again, the effects of the periodic boundary conditions and the mesh refinement in the spanwise direction can be observed, leading to smaller scales in the case of the periodic boundary conditions and the finer mesh. For all computations, only half of the domain size in the spanwise direction is required to have a decay of the spanwise correlation coefficient to between 0.1 and 0.2. For this specific configuration and flow conditions, the domain size used in the spanwise direction is large enough as shown by the fast decay of the correlation[7].

From the previous results, the coherence length scale can be computed and is defined as :

$$\gamma^2(\mathbf{x}, \mathbf{r}, \omega) = \frac{|\Phi_{pp}(\mathbf{x}, \mathbf{r}, \omega)|^2}{|\Phi_{pp}(\mathbf{x}, 0, \omega)||\Phi_{pp}(\mathbf{x}+\mathbf{r}, 0, \omega)|} \tag{4}$$

corresponding to a two-point correlation in frequency domain. The cross spectrum function Φ_{pp} is the Fourier transform of the space-time cross-correlation function defined previously :

$$\Phi_{pp}(\mathbf{x}, \mathbf{r}, \omega) = \int_{-\infty}^{\infty} C(\mathbf{x}, t, \mathbf{r}, \tau) e^{-i\omega\tau} d\tau \tag{5}$$

The coherence length scale of the source field in the spanwise direction is a key parameter in the trailing edge noise predictions, for example using Amiet's theory, as it can be used to compute the spanwise correlation length, a direct input parameter of the model. It represents the size of the source region which radiates independently from neighboring sources, in a statistical sense.

In Fig. 9, a comparison is made between experimental and computed values, for the four computations, of the spanwise coherence of fluctuating pressure, at a position near the trailing edge $x/c = -0.02$ for a spanwise separation of $\Delta z/c = 0.02$. It shows that both periodic computations are able to predict correctly the experimental spanwise coherence measured while the coarse symmetric boundary conditions are overpredicting the measured value. Note that the coherence at low frequencies, specially for large separations as measured in experiments, are really sensitive to sample size and numerical errors. The accuracy at low frequency should be improved in further work.

E. Acoustic results

The acoustic methods, decribed above in Sec. IV, are using data on the airfoil surface, the whole wall-pressure distribution for Curle's analogy while Amiet's theory is using the wall-pressure spectrum and the spanwise correlation length near the trailing edge. All this information is directly available from the computations or the experiments.

This section is only considering the 64 spanwise cells and periodic boundary condition computation for Curle's analogy. The position of the receiver is in the midspan plane above the airfoil ($\theta = 90°$) at a distance $R = 2m$.

Results from Amiet's theory are presented in Fig. 10 (top) and compared to experimental data obtained in the ECL facility. All the acouctic computations with Amiet's theory are using averaged wall-pressure spectrum close to the trailing edge defined in Sec. V-B. Therefore, the over-prediction observed on the wall pressure spectra at the trailing edge compared to experiments is directly transferred to the acoustic predictions. In fact, all acoustic computations are over-predicting the sound radiated in the far field in the low and mid frequency range with a maximum deviation up to 10 dB for the worst prediction. Similarly to the wall-pressure predictions, improvements are observed when mesh refinement is applied in the spanwise direction or/and periodic boundary conditions in the spanwise direction are used.

All acoustical methods are compared with experiments in Fig. 10 (bottom). Firstly, Curle's analogy is considered through its BEM (Boundary Element Method) implementation in the commercial solver Virtual.Lab. For this acoustic computation, the sources have been sampled every 50 iterations (24 kHz) covering a period of 4 flow-through times. Additionnaly, the Curle's analogy using only lift force is used. This one is then considering the integration of the vertical force over the airfoil, neglecting then the retarded time due to airfoil geometry. This assumption is correct if the airfoil can be considered as geometrically compact. Figure 10 (bottom) shows that both Curle's methods are predicting reasonably the experimental measurements most of frequency range. Main discrepancies are appearing for $f \geq 1$ kHz, where both Curle's methods underpredict noise measurements, the Curle computation using pressure distribution tailing off more quickly at high frequencies than the com-

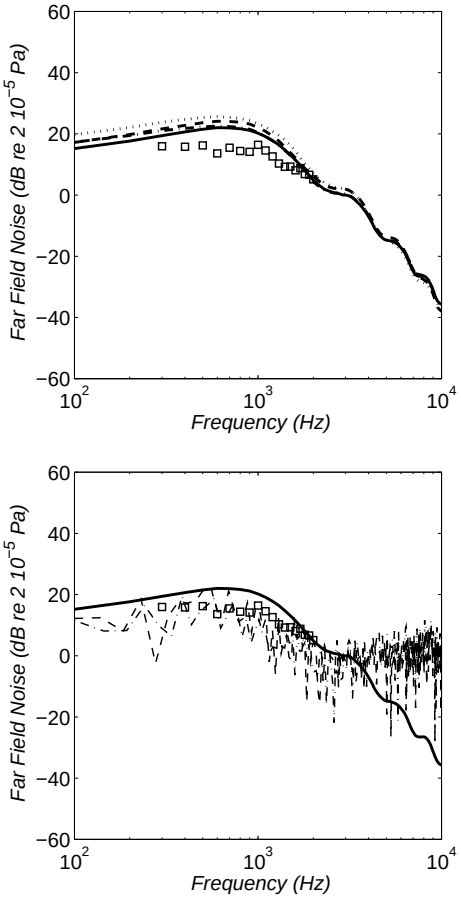

Fig. 10. Far field acoustic spectra in the mid span plan above the airfoil ($\theta = 90°$) at R=2m from the traling edge. (top) Amiet's computations for all present $8°$ computations, (dot) 32 spanwise cells and symmetric boundary conditions, (dash-dot) 32 spanwise cells and periodic boundary conditions, (dash) 64 spanwise cells and symmetric boundary conditions, (plain) 64 spanwise cells and periodic boundary conditions. (bottom) Comparison of acoustic methods on the 64 spanwise cells and periodic boundary condition case : (plain) Amiet's theory, (dash) Curle's analogy using compact dipole approximation and (dash-dot) Curle's analogy using pressure distribution on acoustic mesh. (square) Experiments

putation using only lift force. At low frequencies, both methods predict same noise levels. Note that the noise at high frequency has a complete different behavior between Curle's methods and Amiet's theory. The main difference between both methods is coming from the fact that Curle's analogy is using free field Green's function while Amiet's theory is considering diffraction at both trailing and leading edges. Curle's anology is then not adapted to the high frequency range where diffraction occurs.

VI. CD-airfoil at 15° a.o.a. - Comparisons with lower a.o.a

This section is related to the first attempt to compute the flow around the same CD-airfoil as in the previous section and the corresponding sound radiated, but with a higher angle of attack of $\alpha = 15°$. This computation is using symmetric boundary

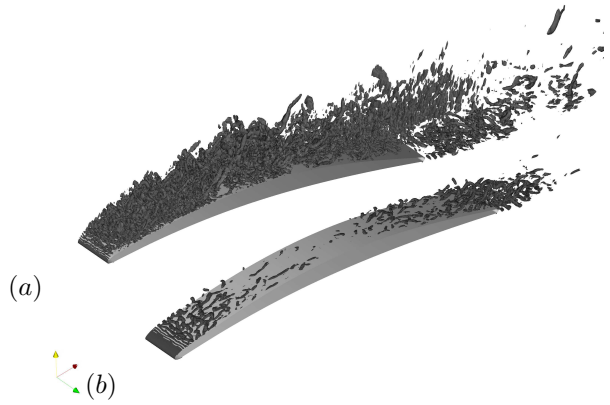

Fig. 11. Flow topology described by the Q factor ($Q = 1000s^{-2}$ iso-contours) (a) $8°$ and (b) $15°$.

conditions in the spanwise direction and 32 cells in the spanwise direction. To compare with results at $8°$ angle of attack, the only computation considered is then the one in the same conditions.

A. Flow-field description

The flow topology in the runs is illustrated in Fig. 11 by the contours of constant Q factor. As already explained in section V-A, the $8°$ case presents small vortices that are born close to the reattachment point of the laminar recirculation bubble. The flow re-laminarizes towards mid-chord because of the favorable pressure gradient. When this gradient becomes adverse, the boundary layer thickens again and more and larger vortices are created towards the trailing edge. The $15°$ case shows strong creation of vorticity right at the leading edge, with large vortices shed from the suction side of the airfoil. Yet there are still some smaller vortices that remain attached to the wall and roll over the airfoil suction side and graze at the trailing edge. A much thicker wake is therefore expected for the case investigating high angle of attack. Some weak vortex shedding can also be seen in the near-wake on the pressure side while the pressure side boundary layer stay attached along the airfoil chord.

B. Mean-pressure coefficient ($-C_p$) and pressure spectra

The mean and fluctuating wall-pressure were analyzed for each of the LES and RANS runs and compared with the RMPs measurements by Moreau & Roger [13]. As for the $8°$ cases, it has been verified for the $15°$ angle of attack case, that the loading on the profile is identical between both RANS computations in the full tunnel setup and the truncated domain. The mean pressure on the surface, characterized by the pressure coefficient $-C_p$, is shown in Fig. 12 (top). At both incidences the LES cases agree better with the experimental data than the RANS $k-\omega$ SST results. At $8°$ the LES captures the boundary-layer transition on the suction side, which is triggered by an unsteady laminar separation near the leading edge, whereas the RANS simulations produce too much turbulence to yield the proper recirculation bubble. At $15°$ the LES significantly improves the boundary-layer growth on the suction side and captures the pressure gradient much better along the chord than the RANS $k-\omega$ SST simulation.

The wall-pressure spectra near the trailing edge are compared

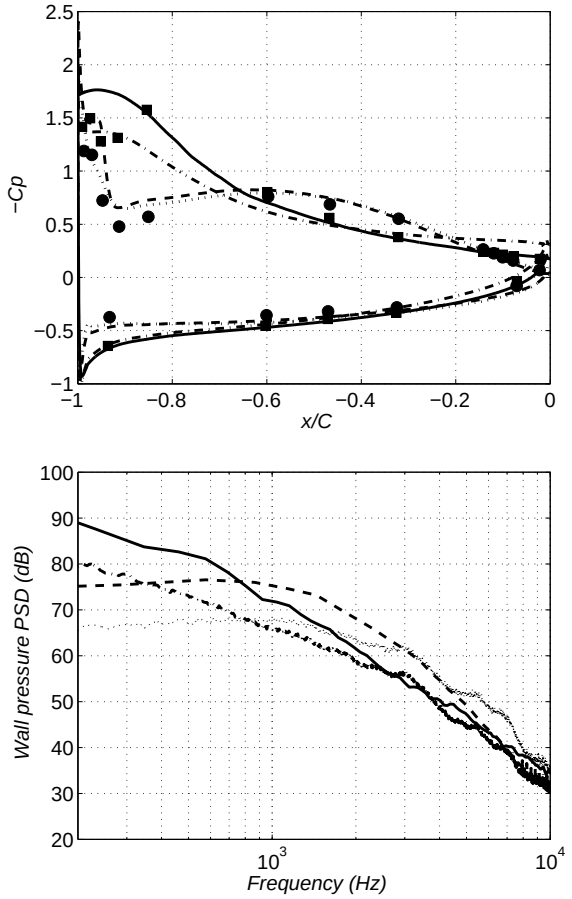

Fig. 12. (top) Mean wall-pressure coefficient $-C_p$ along all blade surface for 8° cases, RANS (dots) and LES (dash) computations and for the 15° cases, RANS (dash-dot) and LES (plain) computations. (bottom) Frequency spectra of pressure fluctuations on the suction side in the leading edge area ($x/c = 0.02$) for 8° cases, experiments (dots) and LES (dash) computation and for the 15° cases, experiments (dash-dot) and LES (plain) computation.

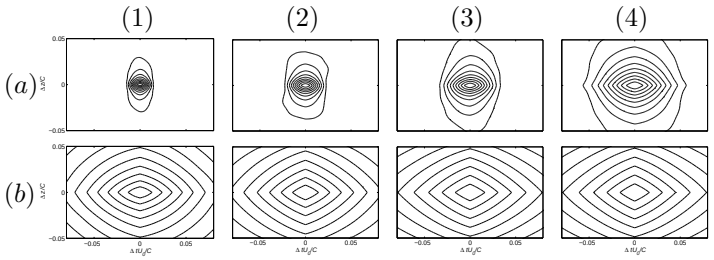

Fig. 13. Contours of space-time correlations of the fluctuating pressure on the suction surface of the airfoil as a function of spanwise and temporal separations, at streamwise locations (1) $x/c = -0.60$, (2) $x/c = -0.23$, (3) $x/c = -0.02$, (4) $x/c = 0$ (trailing edge) : (a) 8° computation and (b) 15° computation. Contours values are from 0.1 to 0.9, with increment of 0.1.

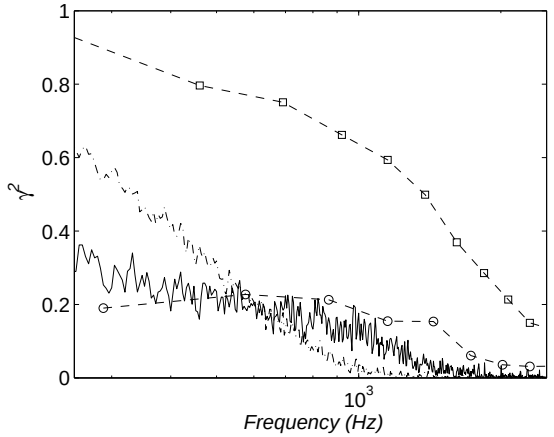

Fig. 14. Spanwise coherence of fluctuating pressure on the suction surface at $x/c = -0.02$ plotted against frequency for a spanwise separation of $\Delta z/c = 0.02$ and for the 8° computation, (plain) experiments and (circle) LES, and the 15° computation, (dash-dot) experiments and (square) LES.

with the measurements above RMP#25 in Fig. 12 (bottom), corresponding to $x/c = -0.02$, for both incidences. The LES show similar results for both angles of attack. As already observed previously, the 8° case overpredict the wall-pressure spectrum at low and mid frequencies by about 10 dB. The 15° computations present similar overprediction in low and mid frequencies, up to 10 dB also. In both cases, the spectrum predicted by computations is recovering experimental results around 2 kHz and has a qualitatively good agreement with experiments for frequencies above this limit. Note that the shape of the spectrum is completely different in both cases. For the 8° case, the wall-pressure frequency spectrum is more rounded with a plateau at low frequencies while the shape is linearly decreasing with frequencies for the 15° case. These behavior are correctly reproduced by the computations. Again for the 15° case, the wall-pressure spectra in the spanwise direction show collapsing PSD and a statistically homogeneous turbulence around the trailing edge, which is one of the assumption of Amiet's acoustic model.

C. Correlation and coherence

The evolution of the spatial and temporal scales in the turbulent boundary layer along the chord is again analysed through the space-time correlation of the fluctuating pressure of the airfoil surface, for both computations. Figure 13 shows these correlations in function of temporal and spanwise spatial separations at four streamwise locations ($x/c = -0.60$, -0.23, -0.02 and 0) for both angles of attack. As explained above for the 8° case, a significant growth of the spanwise and temporal scales is observed from the first station to the third, due to the growing of the boundary layer which is accelerated by the adverse pressure gradient. This behavior is not reproduced at all for the 15° computation that has almost the same size of scales for all stations. This could be explained by the fact that the decay of the spanwise correlation coefficient is slow with the spanwise separation compared to the 8° case. The domain size used in the spanwise direction for the 15° case is then too small with respect to the scales contained in the flow. A kind of blockage is then appearing, avoiding the growth of scales with the developing boundary layer from the leading edge in the case of the 15° angle of attack.

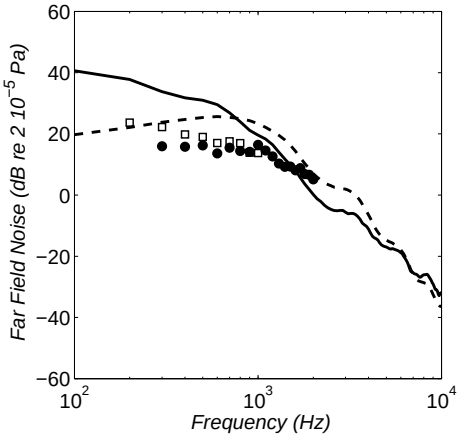

Fig. 15. Far field acoustic spectra in the mid span plan above the airfoil ($\theta = 90°$) at $R = 2$ m from the trailing edge. (dash) Amiet's prediction for the $8°$ computation and (dots) corresponding experiments and (plain) Amiet's prediction for the $15°$ computation and (square) corresponding experiments.

In Fig. 14, a comparison is made between experimental and computed values, for both angles of attack, of the spanwise coherence of fluctuating pressure, at a position near the trailing edge $x/c = -0.02$ for a spanwise separation of $\Delta z/c = 0.02$. It shows that in the $8°$ case, the computation was able to obtain a satifactory agreement compared to measured values. In the $15°$ case, the computation is completely over-predicting the coherence for the all frequency range.

D. Acoustic results

Figure 15 compares the LES acoustic predictions using Amiet's model, with the ECL measurements in the midspan plane above the airfoil ($\theta = 90°$) at a distance $R = 2$ m. Again the method used the computed wall-pressure spectra and the experimental correlation length, the current simulations being too short to correctly sample the low frequency content. Both LES yield similar discrepancies at low frequencies (up to 10 dB) and merge with experimental data beyond 1 kHz. This is consistent with the previous comparison of wall-pressure spectra (Fig. 12), and stress the importance and the difficulty of computing accurate noise sources. The experimental trend for both incidences is however well-reproduced by the LES simulations : at low incidence ($8°$) the numerical and experimental acoustic spectra go to a plateau or decrease whereas at high incidence ($15°$) they keep on increasing, continuously yielding a much larger low-frequency content. The crossing between the two flow conditions also occurs similarly at about 700 Hz.

VII. Conclusion

The investigation of the flow and the corresponding noise has been studied around a segment of an automotive blade (CD-airfoil) at design conditions, namely a $8°$ angle of attack, and a higher angle of attack for which there is experimental evidence that the flow regime has significantly changed. This study encompasses two aspects, the flow resolution around the profile using the commercial solver Fluent 6.3 and the noise propagation using Amiet's theory based on the trailing edge wall-pressure spectrum and Curle's analogy using the pressure distribution along the blade. All along, computational results are compared to experiments taken in the large anechoic chamber from ECL for a Reynolds number $Re_c = 1.6 \times 10^5$. For both angles of attack, a two steps method has been used to reproduce the experimental flow conditions. First a RANS computation has been run on the complete test section including the airfoil, nozzle and part of the anechoic chamber. Secondly, the resulting velocity profiles are then used as inlet boundary condition for a LES in a smaller domain, embedded between the two boundary shear layers of the jet. For both angles of attack, this method has shown its efficiency by capturing correctly the blade loading compared to experiments.

For the $8°$ case, two mesh refinements and two boundary conditions in the spanwise direction, periodic and symmetric, and combination of both are studied. In all cases, on the suction side, computations have shown a turbulent boundary layer triggered by a laminar reciculation bubble at the leading edge while a laminar attached boundary layer is observed on the pressure side, coherent with experiments. Smaller coherent structures were appearing when mesh refinement and periodic boundary conditions are used. It reveals that both improvement of mesh and use of periodic spanwise boundary condition, has an influence on the trailing edge spectrum, decreasing the low frequency content to approach experimental results. The scales refinement, using mesh refinement and periodic boundary conditions, has also been observed through space-time correlations of the fluctuating pressure at different stations along the pressure side. Furthermore, these numerical parameters help to predict correctly the spanwise coherence measured experimentally. On the contrary, this numerical configuration is not improving mean and rms velocity profiles in the wake of the airfoil and can even have a negative effect on the energy spectrum of the wake velocity. Acoustic results show satisfactory agreement using Curle's analogy especially in the low frequency range with experimentally measured noise, the sound radiated being under-predicted abobe 1 kHz. Amiet's theory is over-predicting the sound radiated compared to experiments due to the over-prediction of the wall-spectrum at trailing edge.

The first attempt to compute the flow around the same airfoil at $15°$ angle of attack has been conducted. This computation shows strong creation of vorticity right at the leading edge, with large vortices shed from the suction side of the airfoil. It reveals that, again the wall-pressure spectrum is over-predicted at low frequencies but the general shape of the corresponding experimental spectrum is correctly reproduced. Furthermore, through space-time correlations, it appears that the computational domain in the spanwise direction is too small to correctly capture the low frequency content of the flow. The computation is then largely over-predicting the spanwise coherence at low frequencies. Again acoustic results using Amiet's theory are over-predicting the sound radiated compared to experiments due to the over-prediction of the wall-spectrum at trailing edge.

Acknowledgments

The authors would like to thank RQCHP (Réseau québécois de calcul de haute performance) and Stanford University for providing the necessary computational resources. First author is supported by a fellowship from Fonds pour la formation à la

Recherche dans l'Industrie et dans l'Agriculture

REFERENCES

[1] I. J. Sharland, "Sources of noise in axial flow fans.," *J. Sound Vib.*, vol. 1(3), pp. 302–322, 1964.

[2] S. Caro and S. Moreau, "Aeroacoustic modeling of low pressure axial flow fans.," in *6^{th} AIAA/CEAS Aeroacoustics Conference. AIAA Paper 2000-2094*, Lahaina (Hawaii), 2000.

[3] H. H. Hubbard and K. P. Shepherd, "Aeroacoustics of large wind turbines.," *J. Acoust. Soc. Am.*, vol. 89, pp. 2495–2507, 1991.

[4] R. Parchen, R. Hoffmans, A. Gordner, and K. A. Braun, "Reduction of airfoil self-noise at low mach number with a serrated trailing edge.," in *6^{th} International Congress on Sound and Vibration, 3433–3440*, Copenhagen (Denmark), 1999.

[5] S. Pérennès and M. Roger, "Aerodynamic noise of a two-dimensional wing with high-lift devices.," in *4^{th} AIAA/CEAS Aeroacoustics Conference. AIAA Paper 98-2338*, Toulouse (France), 1998.

[6] B. A. Singer, D. P. Lockard, and K. S. Brentner, "Computational aeroacoustic analysis of slat trailing-edge flow.," *AIAA J.*, vol. 38(9), pp. 1558–1564, 2000.

[7] M. Wang, S. Moreau, G. Iaccarino, and M. Roger, "Les prediction of wall pressure spectra on a low speed airfoil.," in *Annual Research Briefs*, Center for Turbulence Research, Stanford Univ./NASA Ames., 2004.

[8] S. Moreau, G. Iaccarino, S. Kang, Y. Khalighi, and M. Wang, "Towards a large eddy simulation of a low speed fan blade.," in *Proceedings of the Summer Program*, Center for Turbulence Research, Stanford Univ./NASA Ames., 2004.

[9] S. Moreau, F. Mendonca, O. Qazi, R. Prosser, and D. Laurence, "Influence of turbulence modeling on airfoil unsteady simulations of broadband noise sources.," in *11^{th} AIAA/CEAS Aeroacoustics Conference. AIAA Paper 2005-2916*, Monterey (California), 2005.

[10] S. Moreau, D. Neal, Y. Khalighi, M. Wang, and G. Iaccarino, "Validation of unstructured-mesh les of the trailing-edge flow and noise of a controlled-diffusion airfoil.," in *Proceedings of the Summer Program*, Center for Turbulence Research, Stanford Univ./NASA Ames., 2006.

[11] M. Roger and S. Moreau, "Back-scattering correction and further extensions of amiet's trailing edge noise model. part 1: theory.," *J. Sound Vib.*, vol. 286 (3), pp. 477–506, 2005.

[12] S. Moreau, M. Henner, G. Iaccarino, M. Wang, and M. Roger, "Analysis of flow conditions in free-jet experiments for studying airfoil self-noise.," *AIAA J.*, vol. 41(10), pp. 1895–1905, 2003.

[13] S. Moreau and M. Roger, "Effect of airfoil aerodynamic loading on trailing edge noise.," *AIAA J.*, vol. 43(1), pp. 41–52, 2005.

[14] M. Germano, U. Piomelli, P. Moin, and W. H. Cabot, "A dynamic subgrid-scale eddy viscosity model.," *Phys. Fluids A*, vol. 3(7), pp. 1760–1765, 1991.

[15] D. K. Lilly, "A proposed modification of the germano subgrid-scale closure method.," *Phys. Fluids A*, vol. 4, pp. 633–635, 1992.

[16] F. R. Menter, "Two-equation eddy-viscosity turbulence models for engineering applications.," *AIAA J.*, vol. 32(8), pp. 1598–1605, 1994.

[17] S. Moreau, D. Neal, and J. Foss, "Hot-wire measurements around a controlled diffusion airfoil in an open-jet anechoic wind tunnel.," *J. Fluid Engineering*, vol. 28(4), pp. 699–706, 2006.

[18] M. Wang and P. Moin, "Computation of trailing-edge flow and noise using large-eddy simulation.," *AIAA J.*, vol. 38(12), pp. 2201–2209, 2000.

[19] J. S. Baggett, J. Jimenez, and A. G. Kravchenko, "Resolution requirements in large-eddy simulations of shear flows.," in *Proceedings of the Summer Program*, Center for Turbulence Research, Stanford Univ./NASA Ames., 1997.

[20] N. Curle, "The influence of solid boundaries upon aerodynamic sound," *Proc. R.Soc. London Ser. A*, vol. 231(1187), pp. 505–514, 1955.

[21] M.J. Lighthill, "On sound generated aerodynamically: I. general theory," *Proc. R.Soc. London Ser. A*, vol. 211(1107), pp. 564–587, 1952.

[22] R. K. Amiet, "Noise due to turbulent flow past a trailing edge.," *J. Sound Vib.*, vol. 47(3), pp. 387–393, 1976.

Proceedings of the 8th National Congress on Theoretical and Applied Mechanics, May 28-29, Brussels, Belgium.

Mechanical properties of friction stir spot welds of 6063-T6 aluminum alloy

Caroline Jonckheere, Aude Simar, Bruno de Meester
Unité de Production Mécanique et Machines, Université Catholique de Louvain
Place du Levant 2, B-1348 Louvain-la-Neuve
email: caroline.jonckheere@uclouvain.be

Abstract— **The development of materials with better performances calls for new joining methods. The friction stir welding process and its variant, friction stir spot welding, is one of them. The process being young, it needs further understanding. Hence, the influence of the welding parameters and of the tool dimensions on the tensile properties of the joints is investigated. Three type of fracture in tension are observed. They are shown to be dependent on the distribution of joint line remanents in the weld. It is shown that a too small tool must be avoided since it causes the fracture of the sample in traction through the weld itself. The other welding parameters have no clear and significant influence on the strength of the joint.**

Keywords— **Friction stir spot welding, 6063-T6 aluminum alloy, hooking effect**

I. Introduction

FRICTION Stir Welding or FSW, has been patented in 1991 by TWI (*The Welding Institute*) and has been increasingly used in areas such as rail, aerospace, automotive industry and many others [1]. This process has indeed many advantages in terms of the quality of the joints obtained, the means required for the implementation of the weld, the comfort of the welder and the environment [2].

Friction Stir Spot Welding (*FSSW*) is a derivative of classical FSW. The motion of the tool is limited to a vertical movement of plunging and retreating after a possible dwell time (Figure 1). The FSSW uses, like FSW, the heat generated by friction and stirring of the material due to the rotation and penetration of a tool in the plates to be welded. The heat results in softening and mixing of the material of the two parts to be welded. On cooling, the stirred matter consolidates and forms the joint.

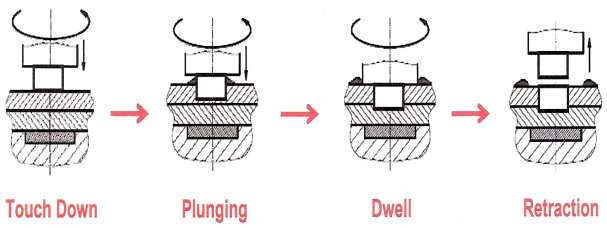

Fig. 1. FSSW main phases. Figure from [3]

The process is relatively young and is not yet fully understood. In this paper, the influence of the welding parameters and of the tool geometry on the tensile properties and the fracture of the welded joints is investigated.

Three types of fracture in tension have been observed. The tool size appears to be the most significant parameter controlling the type of fracture and the joint strength.

II. Experimental procedure

90 mm long workpieces cut from extruded 30 mm wide by 3 mm thick profiles of AA 6063-T6 alloy were welded on a CNC milling machine using a small anvil for clamping the parts to be welded. The spot welds were located at the center of a 30x30 mm square where the two workpieces to be welded overlap. They were cleaned prior to welding with acetone to avoid contamination of the joints from grease and other impurities on the surface of parts.

Based on literature [4], [5], [6] and past experience, the following geometries were chosen for the tool:

- Two basic cylindrical tools with a threaded cylindrical pin and a flat shoulder. The pin and the shoulder diameters are respectively equal to 4 and 10 mm for the first tool here named 'small tool', and 5 and 15 mm for the second tool here named 'large tool',
- Tool pin lengths ranging from 3.5 to 5.7 mm by 0.5 mm.

The operating parameters were the following:

- Identical penetrating and retreating speeds equal to 5 or 12 mm/min, named hereafter *Plunge Rate* or PR, and no dwell time,
- Tool rotating speeds equal to 1000, 1500 or 2000 rpm, always clockwise so that the material was pushed downwards by the thread on the tool pin,
- A plunge depth identical to the toolpin length, i.e. such as the shoulder just touches the plates, except for the 5.7 mm long pin for which the plunge depth was 5.5 mm.

The choice of the welding conditions was made in view of highlighting the influence of each individual parameter (see Table I).

Tensile tests were conducted on 150 mm long samples with a classical tensile machine with crosshead displacement equal to 5 mm/min. Given the geometry of test specimens, platelets of the same alloy were sticked on each side in order to maintain the alignment and to reduce the distorsion of the welded samples.

Some welded joints were also cut in two along their length and shortened to obtain a sample of approximately

40 mm long. Each sample was then molded in resin and polished to obtain a polished mirror state. After etching in a solution of NaOH to 20% for 20 minutes [7], the sample were observed through an optical microscope and a scanning electron microscope (*SEM*).

III. Results and discussion

In this section, the three observed type of fracture are first presented. The incidence of fracture type and the effect of tool size on the weld tensile strength is then discussed. Finally, the effects of the others welding parameters on the ultimate tensile force are examined and found to be less significant.

TABLE I
WELDING PARAMETERS CORRESPONDING TO THE TENSILE TESTED WELDS

Large tool, plunge rate equal to 5 mm/min.			
Toolpin length [mm]/ Rotating speed [rpm]	1000	1500	2000
3.5		X	
4.0	X	X	X
4.5		X	
5.0		X	
5.7		X	
Large tool, plunge rate equal to 12 mm/min.			
Toolpin length [mm]/ Rotating speed [rpm]	1000	1500	2000
3.5		X	
4.0	X	X	X
4.5		X	
5.0		X	
5.7		X	
Small tool, plunge rate equal to 5 mm/min.			
Toolpin length [mm]/ Rotating speed [rpm]	1000	1500	2000
3.5		X	
4.0	X	X	X
4.5		X	
5.0		X	
5.7		X	
Small tool, plunge rate equal to 12 mm/min.			
Toolpin length [mm]/ Rotating speed [rpm]	1000	1500	2000
3.5		X	
4.0	X	X	X
4.5		X	
5.0		X	
5.7		X	

A. *Types of fracture*

The macrography of Figure 2 shows the four zones typical of a friction stir spot welded joint: the nugget, the thermomechanically affected zone (*TMAZ*), the heat-affected zone (*HAZ*) and non-affected base material (*BM*).

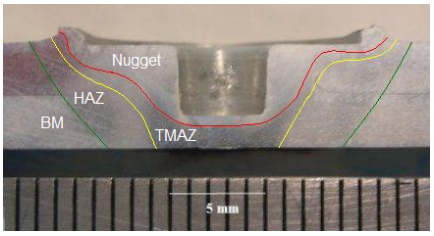

Fig. 2. The four zones of a friction stir spot weld.

The tip of the natural notch at the surfaces in contact between the welded plates is curled upwards (Figure 3). This phenomenon is due to the material flow during welding. The surfaces between the two plates diverts up or down as the tool runs clockwise or in the opposite direction respectively. This is called the *hooking effect* [7].

Some macrographies show darker marks suggesting an extension of the interface inside the welds as can be seen also on Figure 3. Those marks will be named hereafter *joint line remanents*.

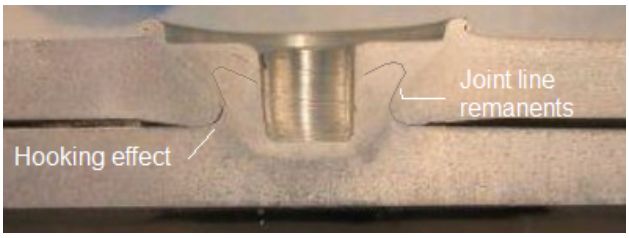

Fig. 3. Macrography of a weld. The hooking effect and the extension of the joint line remanents are highlighted. The joint line remanents have been redrawn for better visibility.

During the tensile test, cracking initiated in all cases from the tip of the hooking defect. After initiation at the interface of the plates to be welded, the direction of crack propagation follows generally the joint line remanents but the direction of that propagation varied greatly from one sample to another. Three directions were observed, each corresponding to one different type of fracture. Observation of the broken specimens allows to distinguish three distinct types of fracture here named 1, 2 and 3 respectively, whose corresponding fracture surfaces are schematically represented in Figure 4. These three types of fracture have also been reported in [4].

- In type 1, the piece breaks without being greatly distorted. The overall fracture occurs in the middle of the

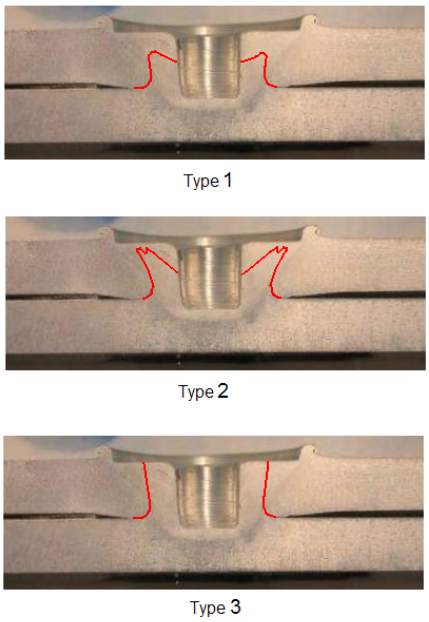

Fig. 4. Localization of the fracture surfaces of the tensile samples according to the three types of fracture.

Fig. 5. Samples broken according to the three fracture types. From top to bottom: Top plate viewed from the top at the trace left by the shoulder, upper plate viewed from the bottom, bottom plate viewed from top at the hole left by the pin. (a) failure by type 1. (b) failure by type 2. (c) failure by type 3.

weld, similarly to the failure of a rivet by shearing

- In type 3, the piece breaks after large distortions. The overall fracture occurs in the middle of the mark left by the shoulder, in a way similar to the pull of a button.
- Type 2 is a compromise between types 1 and 3. A tear begins first on the trace left by the shoulder, but the piece finally breaks at its mid-height, as in the case of type 1. Distorsion occurs, but less than in type 3.

Figure 5 presents samples that fractured according to these three types.

A.1 Fracture of type 1

In the case of a fracture according to the type 1, the crack initiates at the tip of the hooking defect and propagates along the TMAZ to the upper edge of the sample. Once at approximately mid-height of the hole left by the tool pin, it directs towards that hole, following the joint line remanents shown in Figure 6.

This fracture according to type 1 is similar to that of a hollow rivet by shear: the crack finally spreads by shear during the tensile test because the welded section is insufficient.

A.2 Fracture of type 3

In the case of type 3 failure, the crack initiates also at the hooking defect just along the TMAZ but propagates upwards until it reaches the upper surface of the sample, following the joint line remanents shown in Figure 7.

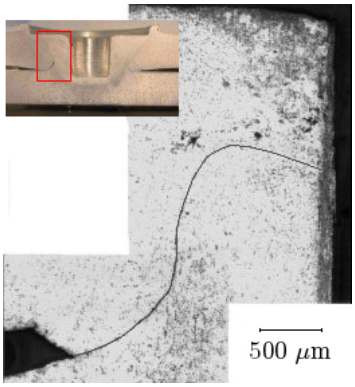

Fig. 6. Joint line remanents on a sample failed under type 1. The joint line remanents have been redrawn for better visibility. The inset shows the location of the micrography.

It is observed in that case that the pattern of the joint line remanents stops just some microns away from the top edge of the sample, shown in black on the top of Figure 8. This explains why the cracking path ends on the upper surface in the mark left by the tool shoulder.

Figure 8 shows that the joint line remanents appear as a succession of cavities closely approaching (at about 50 microns) the upper edge of the sample, shown in black on

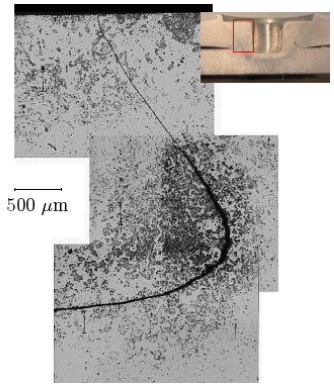

Fig. 7. Joint line remanents on a sample failed under type 3. The joint line remanents have been redrawn for better visibility. The inset shows the location of the micrography.

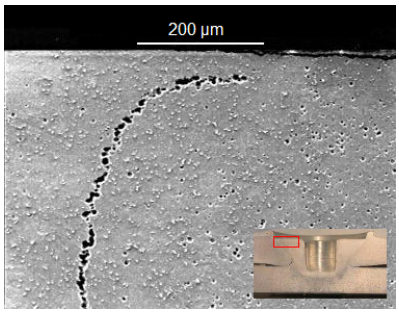

Fig. 8. Focus on the joint line remanents on a sample broken by type 3 and chemically attacked.

the top of the illustration. These are probably the glitter of oxides which, disbouded by the chemical attack, gave rise to observed cavities.

It seems therefore that the thin oxide layer present on the surfaces to be welded follows the material flow during welding and then orient the fracture path while the sample is being broken. A knowledge of the influence of welding parameters on the material flow within the joint during welding would therefore allow the understanding of why one type of fracture is favored in a given weld, and lead to the prediction of the fracture type.

A.3 Fracture of type 2

In the case of fracture of type 2, the crack first initiates also at the tip of the hooking defect but propagates in zig-zag before finally heading towards the hole left by the tool pin. The corresponding joint line remanents are shown in Figure 9. This may also be viewed as a sub-case of the fractures by type 1 since the sample finally breaks by shearing the weld.

In conclusion, all the observed samples show a joint line remanents along the TMAZ. Depending on the welding conditions, they are distributed along three directions: starting from the joint interface and following the hooking defect, they extend toward the hole left by the pin (Figure 6), towards the upper surface of the sample (Figure 7) or oscillate between these two directions (Figure 9). This gives rise to three possible failure types, designated by types 1, 3 and 2 respectively.

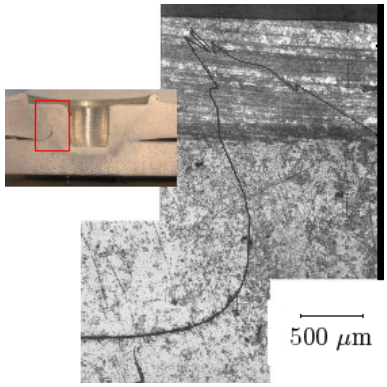

Fig. 9. Joint line remanents on a sample failed under type 2. The joint line remanents have been redrawn for better visibility. The inset shows the location of the micrography.

Welding parameters giving fracture according to type 3 should be chosen. Indeed, the corresponding welds break outside the weld, and not through the weld itself that should be considered in that case as a weak link.

B. Incidence of fracture type and effect of tool size on tensile strength

Figure 10 shows little influence of the fracture type on the ultimate tensile force.

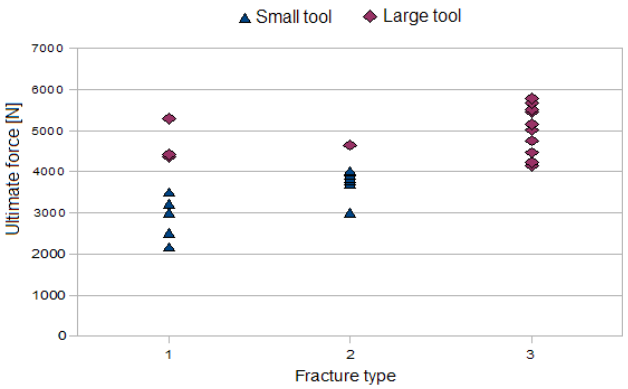

Fig. 10. Influence of the fracture type on the ultimate force.

This figure shows that the ultimate force is generally the highest in the case of type 3 fractures and likely to be the lowest in the case of type 1 fractures. Ultimate forces ob-

served in the case of fracture by type 1 may be high, but this is not always guaranteed. This figure rather shows that the ultimate forces corresponding to the large tool are systematically higher than those corresponding to the small tool. For that reason, the large tool should be preferred as will be discussed later, in section III-C. One can also see on this figure that all but four welds made with the large tool break according to type 3. Those welds were realized either with the longest pin or with a plunge rate of 12 mm/min. Those welding conditions should thus also be avoided.

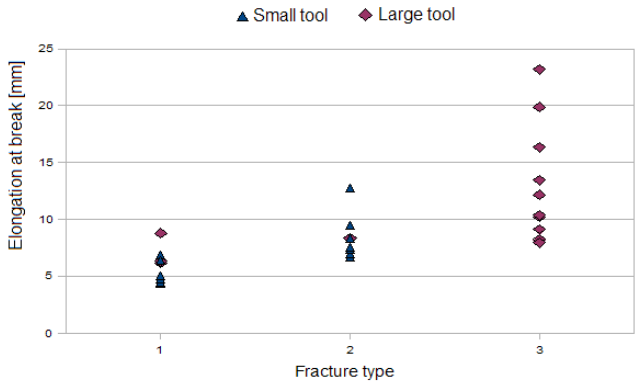

Fig. 11. Influence of fracture type on the elongation at fracture.

The elongation at break is influenced by the failure type as shown on figure 11. It seems to be higher in the case of type 3 fractures and lowest in the case of type 1 fractures. Small elongations at break may also be observed for type 3 fractures, but the corresponding tensile force will despite this be high.

Figure 12 shows that there is virtually no influence of failure type on the elongation under the ultimate load. Therefore, it is highly likely that the crack propagation occurs after reaching the maximal load and therefore has no influence on the ultimate tensile force.

These last two results suggest that the crack propagation only occurs after maximum loading: the sample is then distorted to enable the two pieces to separate. That distortion is higher in the case of type 3 fracture than in the case of type 1 fracture. This is why elongation at fracture is influenced by the fracture type. This justifies the observations already made in Figure 10 showing no direct link between the fracture type and the ultimate force. Indeed, the ultimate force is linked to hardening and deformation of the samples submitted to tension. It is also shown that the failure type is linked to the direction of crack propagation and its spreads till fracture of the sample. These two phenomena are fundamentally different.

In conclusion, the large tool should be preferred because

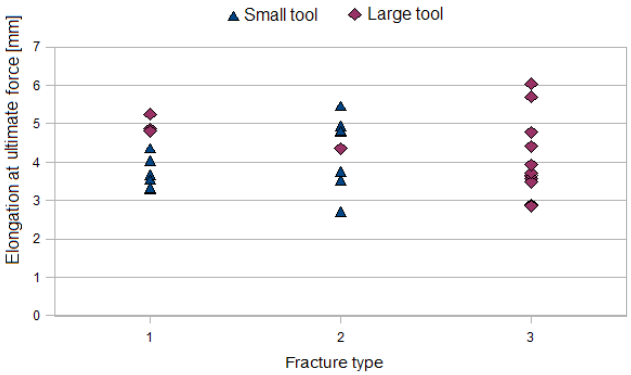

Fig. 12. Influence of failure type on the elongation at ultimate force.

it leads to a higher ultimate force and a type 3 fracture, outside the weld itself. A small elongation at fracture may be observed but this is not a problem, since the ultimate force will anyway be high.

C. *Effect of welding parameters on tensile strength*

The tensile tests have not revealed a clear influence of the welding parameters on the ultimate tensile force, except concerning the tool size as already apparent in Figure 10. This is again shown in Figure 13. The large tool leads to the highest ultimate forces. This is due to the larger welded area when using the large tool compared to the small tool.

In the following, only the large tool will be considered, since the small tool systematically leads to a fracture by type 1 or 2, which means a less favorable type of fracture in the weld itself.

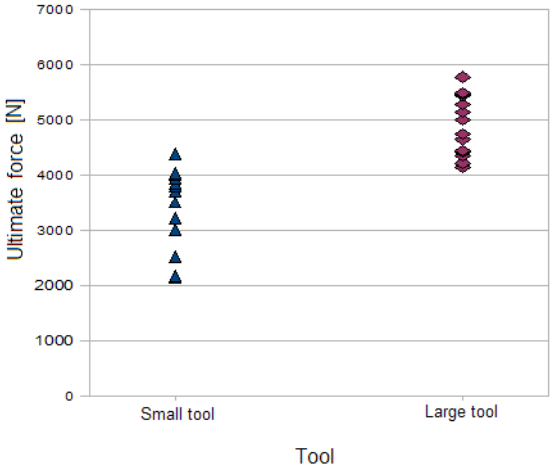

Fig. 13. Influence of the tool size on the ultimate tensile force for all sets of welding parameters

The effect of the length of the tool pin on the ultimate force is shown in Figure 14. A maximum of the ultimate force is observed for a plunge rate of 12 mm/min. In the case of the lowest plunge rate, the effect of the tool pin length is unclear and does not seem significant.

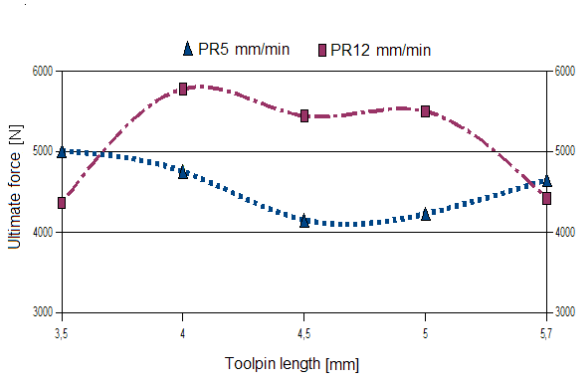

Fig. 14. Influence of the length of the tool pin on the ultimate tensile force for the large tool, at a rotation speed of 1500 rpm and both plunge rates

Considering both plunge rates, no real influence of the tool pin length between 3.5 and 5.7 mm may be observed. However, it is obvious that a too short or a too long pin must be avoided. If the pin is shorter than 3 mm, the material of the lowest plate will not be stirred. If the pin is longer than 6 mm, it will leave a hole right through the plates.

Figure 15 presents the influence the plunge rate on the ultimate tensile force. The study was done on samples welded with all pin lengths while the rotating speed was kept constant at 1500 rpm.

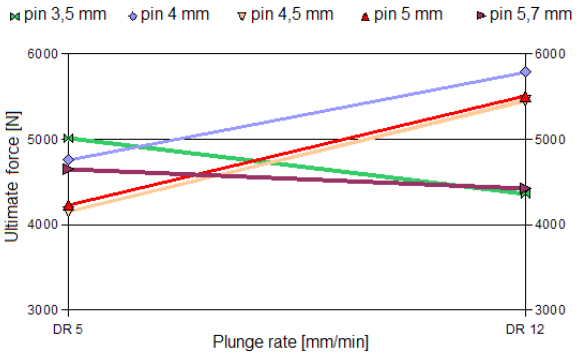

Fig. 15. Influence of the dwell rate on the ultimate tensile force for the large tool, a rotating speed of 1500 rpm and various pin lengths.

With two exceptions corresponding to the extreme pin lengths as already seen on Figure 14, the ultimate force increases with plunge rate. This may be attributed to the weld becoming colder. However, as already mentioned in section III-B, a plunge rate of 12 mm/min should be avoided because it may lead to fracture type other than the preferred type 3.

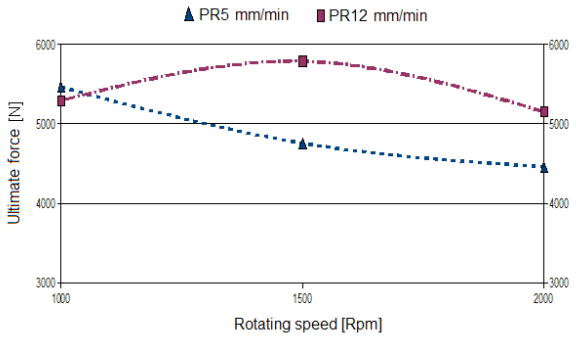

Fig. 16. Influence of the rotating speed of the tool on the ultimate tensile force, for a pin length of 4.0 mm and different dwell rates.

Figure 16 shows the effect of the rotating speed of the tool on ultimate force in the case of a tool pin length of 4.0 mm. An overall decrease in force when increasing the tool rotation speed is observed for the lower plunge rate while a maximum is observed at 1500 rpm with the higher one. It seems that, in the case of a low plunge rate, an increase in tool rotating speed and thus in heat input deteriorates the quality of the weld. Since this conclusion may not be transposed to the higher plunge rate, no real conclusion on the influence of the rotating speed may be drawn.

IV. Conclusions

Welds were performed using different sets of parameters selected in order to distinguish the influence of each parameter on ultimate force during a tensile test. During these tests, three distinct types of failure were observed.

Observations on non-broken samples allow to reveal the hooking effect at the tip of the natural notch existing in spot welds. Joint line remanents are distributed along the thermomechanically affected zone and in the weld. They influence the crack propagation. During tensile test, the crack first initiates at the tip of the natural notch between the plates to be welded. It follows then the heat affected zone and propagates finally along the joint line remanents in one of three possible directions: towards the upper edge of the sample, to the hole left by the tool pin or oscillating between these two directions. The direction of crack propagation corresponds to the three different failure types observed in tension.

The flow of material around the tool should control how these particles will spread within the joint, and thus the direction of crack propagation.

Type 3 fracture should be preferred since it occurs outside the weld itself. The ultimate force is generally the highest in that case and likely to be the lowest in the case of type 1 fractures but this is mainly due to the tool size.

The elongation at break is also influenced by the failure type and is generally higher in the case of type 3 fracture and the lower in the case of type 1 fracture. Small elongations at break may be observed despite a fracture by type 3. This is not a problem, since the ultimate force will anyway be higher with the large tool. For that reason, and because fracture by type 3 only occurs for welds made with the large tool, this tool is preferred.

All but four welds made with the large tool break according to type 3. Those welds were realized either with the longest tool pin or with a plunge rate of 12 mm/min. Those welding parameters should thus also be avoided. Apart from this, no clear influence of the welding parameters has been observed.

ACKNOWLEDGMENTS

- Laurence Ryelandt for her assistance in microscopic observations
- Aude Simar is a postdoctoral researcher of the FNRS-FRS

REFERENCES

[1] Institut de soudure, *FSW: Friction Stir Welding*, 2008 (February 2008) < http://www.isgroupe.com/soudage-fsw-friction-stir-welding.html >

[2] A.M. da Silva, J.F dos Santos and G. Amancio, *Editorial of* International seminar on Friction based spot welding processes, GKSS, Geesthacht, Germany, March 2006

[3] S. Khosa, T. Weinberger and N. Enzinger, *Material flow investigations during FSSW of AL 6082-T6 by FEA and experimental using different tool geometries*, UIIW University-Industry International Workshop, Nantes, France, June 2007

[4] D. Mitlin, V. Radmilovic, T. Pan, J. Chen, Z. Feng and M.L. Santalla, *Structure properties relations in spot friction welded 6111 aluminium*, Materials Science and Engineering, 2006, A441, pages 79 to 96

[5] D.A.Wang and S.C. Lee, *Microstructure and failure mechanisms of friction stir spot welds of aluminium 6061-T6 sheets*, Journal of Materials Processing Technology, 2007, nr 186, pages 291 to 297

[6] S. Lathabai, M.J. Painter, G.M.D Cantin and V.K. Tyagi, CSIRO Manufacturing and Infrastructure Technology, Woodville, Australia, *Friction spot joining on an extruded Al-Mg-Si Alloy*, Scripta Materialia, 2006, nr 55, pages 899 to 902

[7] G. Avereyn, *Etude des paramètres de soudage par friction-malaxage des joints à recouvrement en aluminium*, Mémoire présenté en vue de l'obtention du grande d'ingénieur civil mécanicien, année académique 2005-2006, Université catholique de Louvain

Proceedings of the 8th National Congress on Theoretical and Applied Mechanics, May 28-29, Brussels, Belgium.

Design and production of cruciform composite specimens for in-plane biaxial tests

Carla Ramault[1], Andreas Makris[1], Danny Van Hemelrijck[1], Ebrahim Lamkanfi[2], Wim Van Paepegem[2]
[1] Vrije Universiteit Brussel - Department of Mechanics of Materials and Construction
Pleinlaan 2 - 1050 Brussels
[2] Ghent University - Department of Mechanical Construction and Production
Sint-Pietersnieuwstraat 41 - 9000 Ghent
Email: cramault@vub.ac.be

Abstract: **This paper focuses on the design of a cruciform specimen for biaxial in-plane tensile testing. Using a Finite Element model and experimental data, a proper specimen geometry was developed. The specimen has an adapted fillet corner radius to increase the load transfer to the specimen centre and has a reduced thickness in the centre to ensure biaxial failure in this zone. The production of this specimen is until now accomplished by milling material away from the centre, which can cause damage of the specimen material. Other production techniques are analysed. Also, the effect of the lay-up in the reinforced arms on the strain distribution in the central gage section of the specimen is examined.**

Keywords: **In-plane Biaxial Testing, Specimen Design, Digital Image Correlation Technique, Polymer Matrix Composites**

I. Introduction

In general, composite laminates are developing multi-axial stress states [1]. To get an accurate representation of the behaviour of composite materials in a structure, tests under a uniaxial stress state do not satisfy. Therefore biaxial testing has to be considered. Despite the large demand for this experimental biaxial information there is little existing experimental capability to evaluate the multi-axial response of composite materials [2].

The commonly used method to apply biaxial loads to a composite specimen is the combined torsion and tension/compression or pressure and tension/compression of a thin-walled tubular specimen. In real constructions, components in fibre reinforced composite materials are often made in the form of flat or gently curved panels. Consequently the biaxial behaviour of the tubes is different from the real behaviour. The most appropriate method for biaxial testing consists of applying in-plane biaxial loads to cruciform specimens. Therefore, a plane biaxial test device and a suitable cruciform specimen geometry have been developed at the Vrije Universiteit Brussel [3].

The most difficult issue of biaxial testing is probably designing an appropriate specimen. The specimen that was developed has an adapted fillet corner radius and a reduced thickness in the centre to ensure biaxial failure in the gauge section. It fulfils the specific conditions necessary for a correct biaxial test. Nevertheless, there are still some strain concentrations present in the specimen [4]. In this paper it will be investigated if the specimen can be optimised, focussing on the specimen production method. The aim is to achieve a strain field which is as uniform as possible.

II. Biaxial Testing

A. Biaxial Test Device

Many techniques to produce biaxial stress states in a specimen can be distinguished [5]. They are divided into two categories : (i) tests using a single loading system and (ii) tests using two or more independent loading systems. In the first category the biaxial stress ratio depends on the specimen geometry -which is their main disadvantage-, whereas in the second category it is specified by the applied load magnitude. An example of a system belonging to the second category is the application of in-plane biaxial loads to a cruciform specimen belongs to the second category.

The plane biaxial test rig shown in Figure 1 was developed at the Vrije Universiteit Brussel. It consists of four independent servo-hydraulic actuators with a capacity of 100kN in each perpendicular direction. The use of hydraulic actuators represents a very versatile technique for the application of the loads. When only one actuator per loading direction is used [6], the centre of the specimen will move. This causes a side bending of the specimen, which results in undesirable non-symmetric strains. Systems -like the one used by the authors- with four actuators [7] and a close-loop servo control using the measured loads as feedback system, allow the centre of the specimen to stand still.

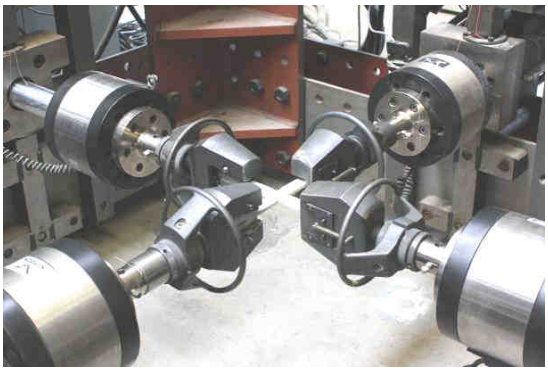

Fig. 1 Biaxial Test Bench.

As no cylinders with hydrostatic bearings were used, failure or slip in one arm of the specimen will result in sudden radial forces which could seriously damage the servo-hydraulic cylinders and load cells. To prevent this, hinges were used to connect the specimen to the load cells and the servo-hydraulic cylinders to the test frame. Using four hinges in each loading direction results in an unstable situation in compression and consequently only tension loads can be applied.

B.Purpose of Biaxial Testing

The biaxial tests, accomplished in the past and present at the author's institution, have as main intention the strength and stiffness characterization of fibre reinforced composite materials [8]. Both quasi-static and dynamic loading conditions are studied. The strength or failure characterization of the material is necessary to evaluate existing failure criteria. As the geometry of a biaxial specimen is complicated compared to a uniaxial beam specimen, we cannot use the same simple analytical formulas to retrieve the present stresses as in a uniaxial test. The calculation of the stresses is not straightforward and consequently the importance of strain determination increases.

The stiffness determination is very important if we consider biaxial fatigue tests. As the mechanical material parameters cannot be obtained as with classical uniaxial tests, other identification methods have to be considered. An inverse method, which can be formulated as an optimization problem where the function to be minimized is an error function that expresses the difference between a numerical and an experimental strain field, was developed at the Vrije Universiteit Brussel [9]. In a first stage, the inverse method was developed to obtain the orthotropic elastic material parameters of a cruciform composite specimen under quasi-static loading. In a second stage, the method will be used in fatigue tests. These tests require a tool to study the degradation development of the orthotropic elastic parameters.

III. Cruciform Specimen Design

A. Specimen Geometry

Designing an appropriate specimen is probably the most difficult issue of biaxial testing. In order to achieve a successful biaxial test, the cruciform specimen has to fulfil some conditions: (i) specimen failure in biaxially loaded test zone, (ii) minimization of strain concentrations outside this zone, (iii) maximization of the region of uniform biaxial strain, (iv) repeatable results [10]. Various specimen geometries have been compared by Smits et al [3] in order to obtain a proper cruciform specimen design. Finite element simulations of several well chosen geometries have been carried out and compared to experimental results. The considered material is glassfibre reinforced epoxy with a $[(\pm 45° \; 0°)_4 \; (\pm 45°)]$ lay-up, typical for wind turbine blades.

In Figure 2, 4 of the analysed geometries are shown. In geometry a, which is a flat specimen with rounded corners, failure will occur in the arms since the central gauge section has a larger load bearing area. To reduce the size of this area, material is milled away in the centre of the specimen in geometry b. This results in an increase of the principal strains in the gauge section. However, still too much load is transferred directly from one arm to the perpendicular arm instead of trough the centre. By increasing the rounding of the corner this problem can be solved. The principal strain field from geometry c shows that it is possible to have the largest strains in the central gauge section. In geometry d, the central reduction is increased, but this results in higher strain concentrations.

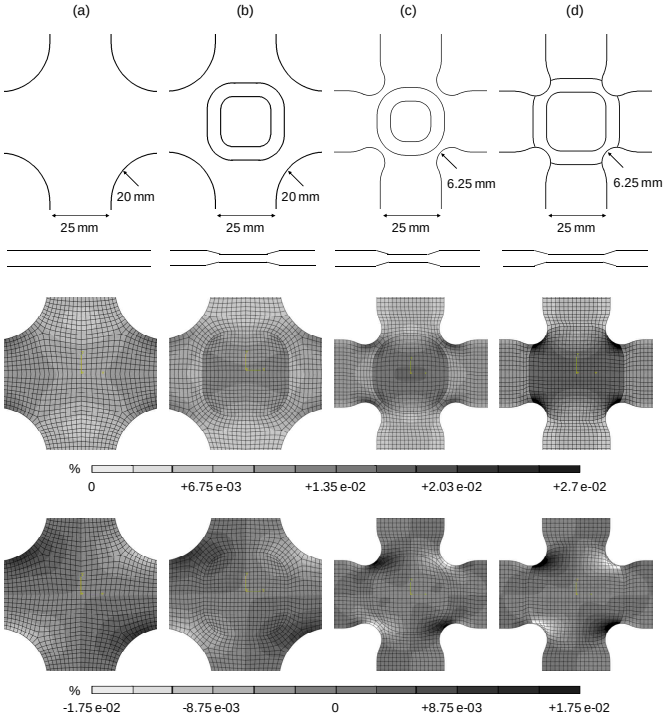

Fig. 2 Four tested and analysed specimen geometries and the corresponding first principle strain and shear strain fields from FE simulations.

Geometry c, with a total length of 250 mm, an arm-width of 25 mm, a corner fillet radius of 6.25 mm and a reduced central thickness, was validated as a proper specimen for biaxial failure testing (Fig. 3). The thickness of the arms and the central zone are respectively 6.57 mm and 3.59 mm.

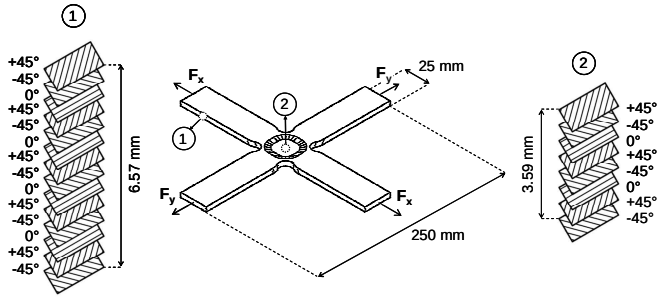

Fig. 3 Cruciform specimen design.

B. Results

1) Full field measuring techniques

The calculation of the stress field of the cruciform specimen is not straightforward due to the uncertainty of the load transmitting area size. Therefore, it is easier and more accurate to work with strains for the analysis of the experiment and the formulation of the failure envelopes. In order to get an idea of the surface strains of the entire specimen, full field measuring techniques instead of local techniques have to be used. In the author's work, the most frequently used technique is the Digital Image Correlation Technique (DICT), but also experiments using Electronic Speckle Pattern Interferometry (ESPI) were performed.

DICT offers the possibility to determine displacement and deformation fields at the surface of objects under any kind of loading, based on a comparison between images of the applied speckle pattern taken at different load steps. The software processes and visualizes the data gathered in order to obtain an impression of the distribution of displacements and strains in the measured object.

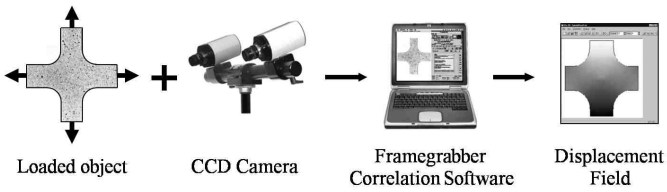

Fig. 4 Principle of the Digital Image Correlation Technique.

Each picture taken with a CCD camera corresponds to a different load step. The cameras of the current set-up use a small rectangular piece of silicon, which has been segmented into 1392 by 1040 pixels. Each pixel stores a certain grey scale value ranging from 0 to 4095 (12 bit), in accordance with the intensity of the light reflected. Two images of the specimen at different states of loading are compared by using a pixel grey value in the undeformed image and searching for the pixel in the deformed image, in order to maximize a given similarity function. A grey-value is not a unique signature of a pixel, so neighbouring pixels are also used. Such a collection of pixels is called a subset. The displacement result, expressed in the centre of the subset, is an average of the displacements of the pixels inside the subset. The step size defines the number of pixels over which the subset is shifted in x- and y-direction to calculate the next result. The image correlation routine allows locating every subset of the initial image in the deformed image. Subsequently, the software determines the displacement values of the centres of the subsets, which yields an entire displacement field. Figure 4 depicts the use of the DICT for a biaxial experiment.

2) Failure envelopes

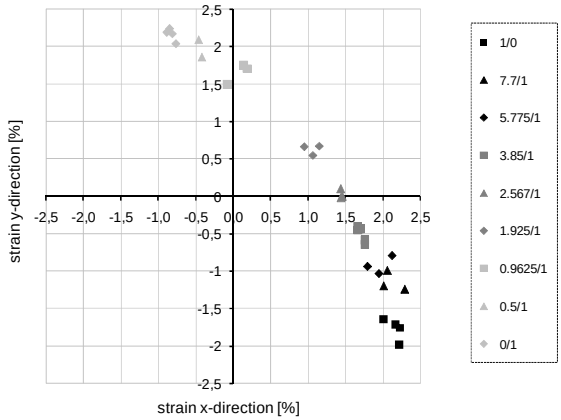

Fig. 5 Failure envelope for the considered material in strain space (ε_{xx} - ε_{yy}).

Many experiments were carried out on the cruciform geometry to determine the failure envelope for the considered material in tension-tension. Therefore, several quasi-static tests were carried out, using 9 different loading ratios. Failure was defined as total failure of the specimen, resulting in a sudden drop of the loading force. DIC allows us to determine the failure strains in the centre of each specimen. Plotting all the results gives us the failure envelope of the considered material in strain space (Fig. 5). The experimentally obtained failure envelopes can be compared with these obtained by existing failure criteria [11].

3) Experimental versus numerical strain fields

An extended analysis of the strain distribution in the biaxially loaded cruciform specimen was performed by comparing experimentally obtained strain fields with numerical strain fields [4]. For the experimental results, several strain measuring techniques, namely Digital Image Corellation (DIC), Electronic Speckle Pattern Interferometry (ESPI) and strain gages were evaluated. For the numerical results, a 3D model was composed using the Abaqus software.

Comparing the strain results shows there is a good agreement between all applied techniques (Fig. 6). The uniformity of the strains in the biaxially loaded zone can be confirmed. Nevertheless, there are strain concentrations present at the edges of the gauge section, near the tapered zone. These concentrations are a result of the surface discontinuity (due to the milling) and cause a delamination between the central gauge section and the upper layers of the arms. DICT and ESPI consider these cracks as large deformations and thus find large and inaccurate strain peaks near these cracks. For these zones, strain gages have to be used to retrieve the correct experimental strains.

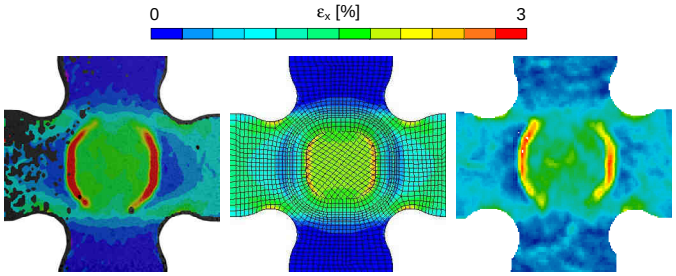

Fig. 6 ε_{11} field of a biaxially loaded specimen (glassfibre-epoxy) obtained with DIC, FEM and ESPI.

C. Discussion

At present, acceptable results are obtained by biaxially testing the designed cruciform geometry. Nevertheless, the specimen can still be optimized. As pointed out in this section, the first cracks will appear at the edges of the central gauge section and not in the centre itself. In the following sections of this paper, we will focus on optimisation through adaptations in the specimen production method. The aim is to reduce the strain concentrations and delay or exclude the delaminations near the tapered zone.

IV. Optimisation of Specimen Production Method

A. Milling or Tabbing

Currently, the cruciform specimens are produced by manufacturing a plate with a thickness equal to the thickness of the arms and milling material away in the centre (Fig. 7a). Using this technique, which we will call the milling-method, the gage section can get damaged if fibres are pulled out. A more secure production method can be the tabbing-method (Fig. 7b). On the composite plate with the thickness of the central gauge section, the extra layers of the arms are glued on both sides. Consequently, there is no risk in damaging the central gauge section. On the other hand, bad adhesion of one of the layers can cause delaminations and an improper failure mode of the specimen. Therefore, we will compare results obtained on specimens produced by the two methods.

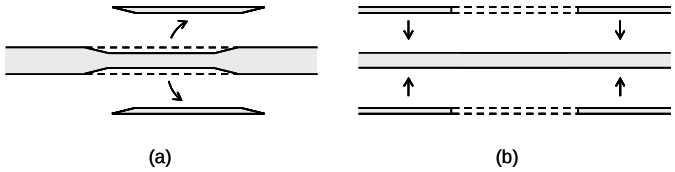

Fig. 7 Production of the specimens : (a) milling of the centre (b) use of reinforcing tabs.

B. Test set-up

For the specimens produced with the tabbing-method, cruciform plates without a hole and tabbing plates with a hole were manufactured. To verify the influence of the adhesive, two different epoxy-glues are used. For one specimen, Araldite AW 106 with hardener HV953U was used. We will refer to it as adhesive A. For the other specimen, Epicote 828 LVEL with hardener Lab 2053 H was used. We will refer to it as adhesive E. The second adhesive was used because it is more ductile as adhesive A. Also, it is frequently used for gluing tabs to uniaxial specimens and cures at room temperature. Before gluing the tabs, the plate surfaces were prepared properly.

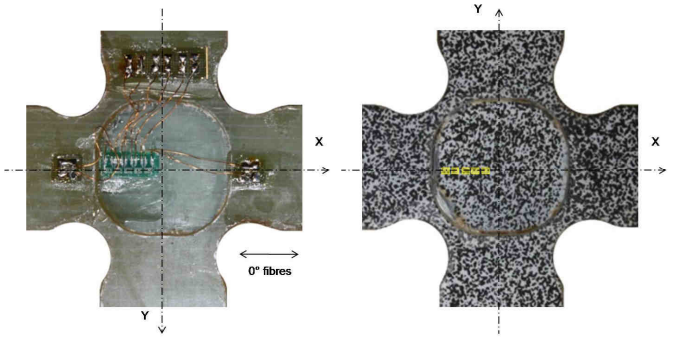

Fig. 8 5-element strain gage and corresponding DIC-zones on the other side of the specimen.

For this analysis the loading ratio 3.85/1 was applied, i.e. a 3.85 times higher load is applied in the x direction as in the y direction. The specimens are observed by DIC to obtain the strain fields in every loading step. On the other side of the specimen, a uniaxial 5-element strain gage with elements of 1mm was glued to measure ε_x from the edge to the centre of the biaxially loaded zone (Fig. 8). All these results are compared with earlier results of specimens produced by the milling-method.

C. Results

In table 1, the failure loads and average strains at failure in the gauge section are summarised. It can be observed that the specimen with adhesive A obtains a higher failure load and failure strains compared to the specimen with adhesive E. Nevertheless, the values for both tabbed specimen are significantly lower as these for the milled specimen.

Figure 9 presents the ε_x, $\varepsilon\xi_y$ and ε_y fields at a certain load (17.3 kN/4.5 kN) for the three specimens. Examining the ε_x field, one can notice that the strains in the gauge section for the tabbed specimens are a little bit higher compared to these of the milled specimen. Combined with the fact that in the arms in x-direction no or only low loads are present, it can be stated that the tabs are at this load already partly debonded. Most of the load is transferred through the middle layer in the cases (b) and (c) while in case (a) the total thickness of the arms is used to transfer the loads from the clamp to the central gauge section. The higher shear in the corners of the tabbed specimens can also be related to this problem of debonding.

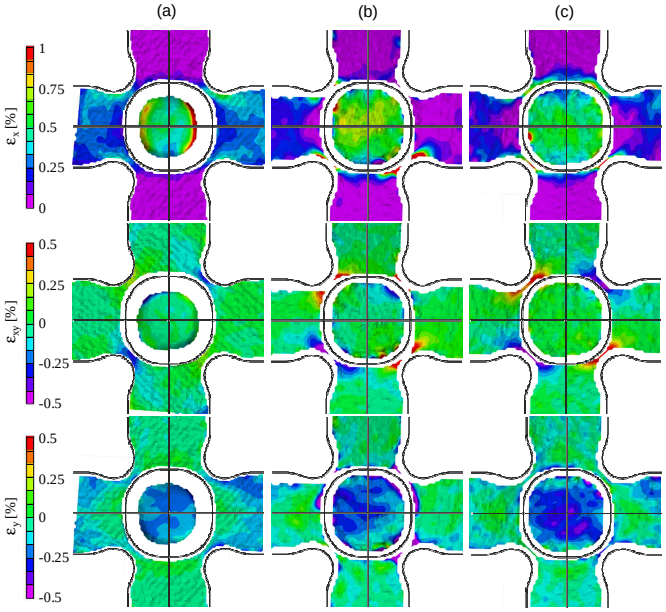

Fig. 9 ε_x, ε_y and ε_{xy} fields for (a) the milled specimen, (b) tabbed specimen with adhesive A and (c) tabbed specimen with adhesive E at a load of 17.3 kN/4.5 kN.

D. Discussion

Using the tabbing method to produce the specimen in stead of the milling method results in much lower failure loads and lower strains at failure in the central gauge section. This is the result of premature failure of the tabs. Already at an early stage in the loading process, cracking of the specimen due to debonding of the tabs can be heard. When we examine the

tabbed specimens after failure, we can notice that the tabs are totally separate from the central layer (Fig. 10). No fibres are pulled out of the laminates, only the glue failed.

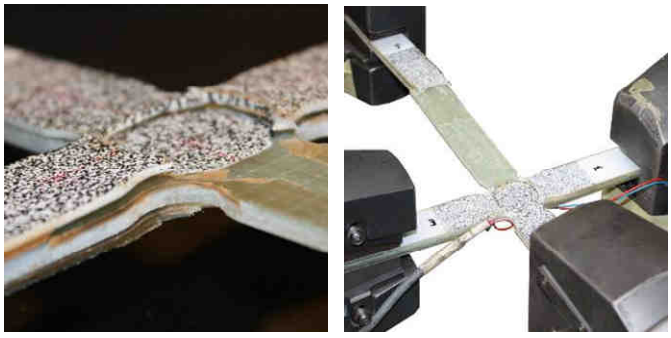

Fig. 10 Specimen failure : debonding of the tab.

V. Tab Layup Design

A. Modification of tab layup

In the previous section IV, the layup of the specimen remained in all cases [$(\pm 45° \ 0°)_4$ $(\pm 45°)$]. With this layup, there are strain concentrations near the edges of the gauge section [12]. Between the upper ±45° lamina of the central laminate and the lower 0° lamina of the tab interlaminar shear strains are present. These strains can cause delaminations of the lamina.

Reversing the tab layup, in order that the lower tab lamina has the same ±45° orientation as the upper central lamina, reduces the interlaminar shear strains significantly. This was verified with a 3D finite element model. In Fig. 11, one can notice that the strains in x-direction are reduced significantly by reversing the layup of the tabs. The efficiency of this intervention in practice will be examined in this section.

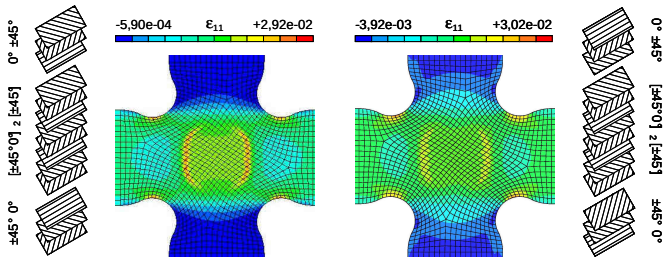

Fig. 11 FE results of the ε_x strain field (upper central lamina) with standard and reversed tab layup.

B. Test set-up

The influence of the tab layup on the strain field and on the failure loads of the specimen was investigated on specimens manufactured by the tabbing method. Two specimens with reversed tab layup (further referred to as tabbing R) were manufactured, both with a different adhesive as in section IV. The specimens were loaded till failure at a load ratio of 3.85/1. Strains are measured by strain gages and DIC. The results are compared with the previously obtained results for the standard layup, further referred to as tabbing N.

C. Results

TABLE I

Failure load and average failure strain (DICT and strain gages) for all specimens

	$F_{x,failure}$ [kN]	$Dict_{,avg}$ $\varepsilon_{x,failure}$ [%]	$Dict_{,avg}$ $\varepsilon_{y,failure}$ [%]	$SG_{,avg}$ $\varepsilon_{x,failure}$ [%]	$SG_{,avg}$ $\varepsilon_{y,failure}$ [%]
Milled Arms N	44	2.09	-0.68	-	-
Adhesive A Tabbing N	30.6	1.85	-0.66	1.82	-
Adhesive A Tabbing R	33.7	1.89	-0.58	1.87	-
Adhesive E Tabbing N	24.8	1.13	-0.47	-	-0.41
Adhesive E Tabbing R	25.6	1.32	-0.40	1.39	-

The failure loads of all specimen, shown in table 1, can be compared. For both adhesives, higher failure loads are obtained for specimens with tabbing R compared to specimens with tabbing N. Also for the failure strains in x direction, higher values are obtained with the reversed tabbing. Although the failure loads and the strains in the central gauge section of the specimen are closer to these obtained by the milled specimens, there is still a big difference between milled and tabbed specimens.

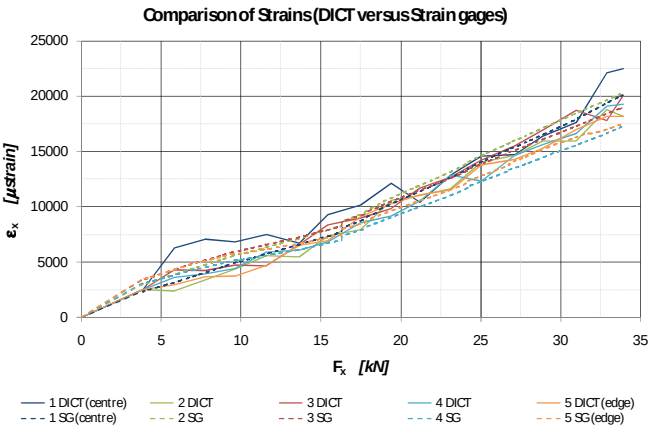

Fig. 12 Force in the x-direction versus strain in the x-direction. Specimen with tabbing R and adhesive A.

As an additional investigation, the strains obtained by strain gages can be compared with the strains obtained by DIC. In table 1, one can already notice the good agreement between the two measuring methods for the average strain measurements. When we compare the separate strain measurements at the 5 strain gage locations (Fig. 12), we can observe that the results correspond well. For the specimen with reversed tabbing, slightly higher strains are present in the centre as near the edge of the central gauge section. This is a

good result considering that biaxial failure has to occur in the centre. It also points out the efficiently of the reversed tab layup, since with tabbing N ε_x was higher near the edge as in the centre of the biaxial zone.

D. Discussion

Using a reversed tabbing layup proves his benefit in higher failure loads and higher strains at failure. The tabs debond in a later stage in the loading process compared to the standard tab layup. This can be validated by DIC measurements. Also, the cracking sounds of debonding tabs are noticed at higher loads.

VI. Conclusions

The design of a suitable specimen for in-plane biaxial testing is not straightforward. Some conditions, like failure in the biaxially loaded central zone of the specimen, have to be fulfilled. A proper specimen with reduced central thickness and an adapted corner fillet radius was developed at the Vrije Universiteit Brussel.

In order to optimise the specimen production method, results obtained on specimens produced by a milling method were compared with results obtained on specimens produced by using tabs. Problems occurred with the tabbing method in the form of debonding of the tabs. Consequently, lower failure loads were obtained and failure did not occur in the biaxially loaded central zone. Additional studies on the adhesion of the glue on the glassfibre epoxy laminate surface are necessary.

In order to reduce strain concentrations which are present at the edges of the central gauge area, the use of a reversed tabbing layup was investigated. Interlaminar shear strains between the upper lamina of the central area(±45°) and the lower lamina of the tab (0°) case ε_x strain concentrations. It was proved numerically and experimentally that these concentrations are reduced significantly by reversing the tab layup. Consequently, higher failure loads are obtained.

Acknowledgements

This research is partly funded by the European Commission under the 6th (EC) RTD Framework Program within the framework of the specific research and technological development program “Integrating and strengthening the European Research Area” (Upwind).

The authors would also like to thank Christoph Kensche and Jan Bossaerts from Hexion for the supply of epoxy adhesive.

References

[1] W.P. Lin, H.T. Hu, *Parametric study of failure stresses in fibre reinforced composite laminates subjected to biaxial tensile load,* Journal of Composite Materials, vol 36 (12), 1481-1504, 2002.

[2] P.D. Soden, M.J. Hinton, A.S. Kaddour, *Biaxial test results for strength and deformation of a range of E-glass and carbon fibre reinforced composite laminates : failure exercise benchmark data*, Composites Science and Technology, vol 62 (12), 1489-1514, 2002.

[3] A. Smits, D. Van Hemelrijck, T.P. Philippidis, A. Cardon, *Design of a cruciform specimen for biaxial testing of fibre reinforced composite laminates*, Composites Science and Technology, vol 66 (7-8), 964-975, 2006.

[4] C. Ramault, A. Makris, D. Van Hemelrijck, E. Lamkanfi, W. Van Paepegem, *Strain Distribution in a Biaxially Loaded Cruciform Composite Specimen*, Proceedings of the 13th European Conference on Composite Materials, Stockholm, Sweden, 2008.

[5] A. Makris, C. Ramault, A. Smits, D. Van Hemelrijck, A. Clarke, C. Williamson, M. Gower, R. Shaw, R. Mera, E. Lamkanfi, W. Van Paepegem, *A review of biaxial test methods for composites*, Proceedings of the 13th International Conference on Experimental Mechanics, Alexandropoulis, Greece, 2007.

[6] M. Chaudonneret, P. Gilles, R. Labourdette, H. Policella, *Machine d’essais de traction biaxiale pour essais statiques et dynamiques,* La Recherche Ae´rospatiale, 5, 299-305, 1977.

[7] A. Makinde, L. Thibodeau, K.W. Neale, *Development of an apparatus for biaxial testing using cruciform specimens*, Experimental Mechanics, vol 32 (2), 138-44, 1992.

[8] D. Van Hemelrijck, A. Makris, C. Ramault, E. Lamkanfi, W. Van Paepegem, D. Lecompte, *Biaxial testing of fibre reinforced composite laminates*, IMECHE Part L J. of Materials : Design and Applications, vol 222 (4), 231-239, 2008

[9] D. Lecompte, A. Smits, H. Sol, J. Vantomme, D. Van Hemelrijck, *Mixed Numerical-Experimental technique for orthotropic parameter identification using biaxial tensile tests on cruciform specimens*, International Journal of Solids and Structures, vol 44 (5), 1628-1642, 2007.

[10] J.P. Boehler, S. Demmerle, S. Koss, *A new direct biaxial testing machine for anisotropic materials*, Experimental Mechanics, vol 34 (1), 1-9, 1994.

[11] A. Makris, C. Ramault, D. Van Hemelrijck, E. Lamkanfi, W. Van Paepegem, T. Philippidis, *Biaxial Failure Envelopes for Glass Fibre Reinforced Composite Laminates*, Proceedings of the SEM annual conference and exposition, Albuquerque, USA, 2009.

[12] E. Lamkanfi, W. Van Paepegem, J. Degrieck, A. Makris, C. Ramault, D. Van Hemelrijck, *Geometrical influence on the strain distribution in biaxial composite specimens*, Proceedings of the 13th European Conference on Composite Materials, Stockholm, Sweden, 2008.

Proceedings of the 8th National Congress on Theoretical and Applied Mechanics, May 28-29, Brussels, Belgium.

Turning Point Based Control of Pneumatic Artificial Muscles for Fatigue Testing

K. Deckers, P. Guillaume, D. Lefeber
Vrije Universiteit Brussel, Department of Mechanical Engineering
Pleinlaan 2-1050 Brussel
email: kdeckers@vub.ac.be

Abstract— **This paper introduces the idea of using pneumatic actuators based on Pneumatic Artificial Muscles for applications such as fatigue testing. These muscles are most commonly used for robotic applications. Since they have some interesting advantages such as a high force-weight ratio and low operating pressures (about 6 bar), their application domain can be increased to the field of fatigue testing. The only disadvantage here is their nonlinear behavior.**
Time Waveform Replication (TWR) is commonly used as a control strategy to impose a given force (or displacement) target during fatigue testing. TWR belongs to the class of (linear) Iterative Learning Control strategies, which in general works well for systems with an approximately linear behavior. Larger errors occur when the nonlinear effects are more pronounced. To correctly perform a fatigue test, however, only the so called turning points of the signal need to be accurately controlled. Indeed, the controlled force signal should have the same turning points as the target signal; they do not have to be exactly equal to each other for all time samples. This relaxation of the problem formulation allows for an easy-to-implement control strategy based on the on-off control of the pneumatic muscles. This will be illustrated by means of experimental fatigue test results performed on an airplane component, using an actuator based on the Pneumatic Artificial Muscles. It will also be shown to be possible to reduce the testing time significantly by controlling the PAMs in this way.

Keywords— **Turning Points, Fatigue Testing, Pneumatic Artificial Muscles, ON/OFF control**

I. Introduction

A. Standard Fatigue Testing of Airplane components

THE structural dynamics and life time expectancy of airplane components are very important research subjects. In this paper we consider the case study of performing a fatigue test on a slat track of an Airbus A320 airplane using Pneumatic Artificial Muscles (or PAMs) as actuators. A slat track is the component of the airplane that, together with the slat, enables the pilots to increase/decrease the area of the wings during take-off/landing. Figure 1 shows the whole mechanism: the leading edge of the wing and the slat, connected through the slat track, which is operated with a rack and pinion combination and supported by 4 main rollers and side rollers in the fixed wing and connected to the slat through its linkage.

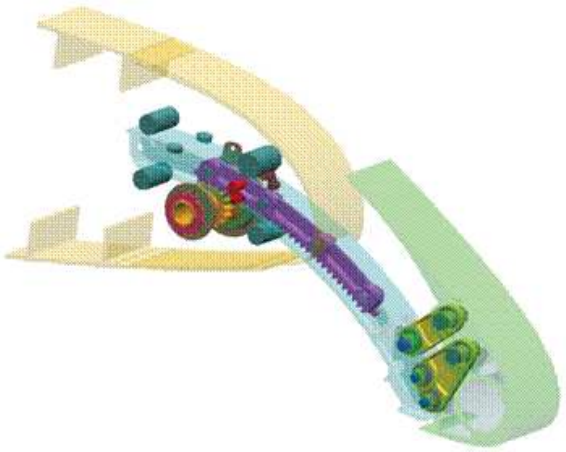

Fig. 1. The slat tracks of an A320

To quantify the fatigue life of slat tracks, extensive tests are performed on a test rig. Because the fatigue strength of slat tracks is very high, fatigue tests will typically take several weeks. To reduce the amount of testing time, adapted tools (for instance from the LMS TecWare software package) can be used [1]. In this paper, a procedure that is standard practice in fatigue testing is used to perform this task for the slat track fatigue test:

- A measurement of the operational load of the slat track is recorded in-flight.
- The data is transformed into so-called rainflow cycles (RFCs) [2].
- From the rainflow cycles, the cumulative damage is calculated (for instance using the Basquin relations [3]).
- Then, all rainflow cycles that do not contribute significantly to the total damage are eliminated.
- Finally, reduced time data are reconstructed from the filtered rainflow cycles. This can be done either with [4] or without [5] preservation of the time order of the original signal.

The procedure presented above is a standard practice in fatigue testing. The result is a set of so-called turning points (TPs), which has a much smaller size than the original load signal. Between two consecutive turning points an interpolation is implemented to convert the digital series of turning points into an analog input signal. This analog

signal will be considered the target or reference trajectory $y_r(t)$ and is shown in Figure 2.

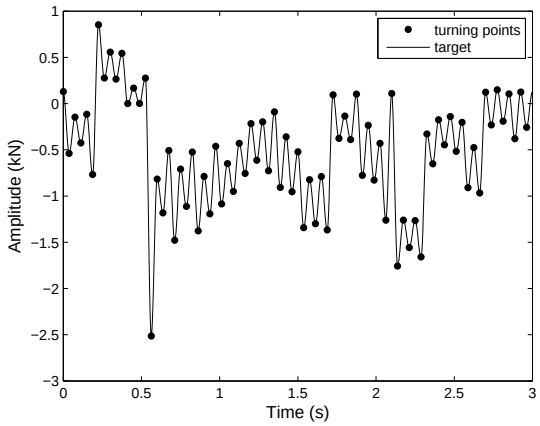

Fig. 2. Analog input signal extracted from the turning point series for the slat tracks of an A320

Essentially these turning points are characteristics of the measured signal that determine the damage done to the structure when applying this signal. It is commonly accepted that any applied force signal having these turning points as maxima (respectively minima), will result in the same damage to the structure as the original measured force. It is therefore very important that during testing the turning points are reached with as much precision as possible.
The standard fatigue test of an Airbus A320 slat track is performed on a hydraulic test rig, operating at a high pressure and temperature. In this paper we will consider a test setup based on Pneumatic Artificial Muscle actuators.

B. Concept of the Pneumatic Artificial Muscles

The Pneumatic Artificial Muscles, or PAMs, are generally applied in the field of robotics, to simulate human muscle behavior. These muscles are lightweight actuators that can apply several kN of pulling force, depending on their size. It is therefor very interesting to use them as actuators in applications other than robotics.

Fig. 3. Design of the Fluidic Muscle DMSP by Festo AG & Co.KG

Different types of PAMs exist, e.g. the second generation Pleated Pneumatic Artificial Muscle (or PPAM), which was developed at the department of Robotics and Multibody Dynamics at the Vrije Universiteit Brussel ([6]), and the Fluidic Muscle DMSP developed by Festo AG & Co.KG which is commercially available ([7]. The muscle considered in this implementation is the commercially available Festo DMSP (see Figure 3).
This actuator comes in different sizes and configurations. The basic concept lies in the combination of an impervious, flexible hose and a covering of woven fibres as tensile material in a rhomboidal mesh. This results in a three dimensional grid structure. The pressurized air flowing inwards changes the shape of the grid structure by expansion, thus generating a tensile force in the axial direction. The grid structure causes the muscle to shorten up as internal pressure is increased. This corresponds to a stroke of approximately 25 percent of the initial unloaded length.

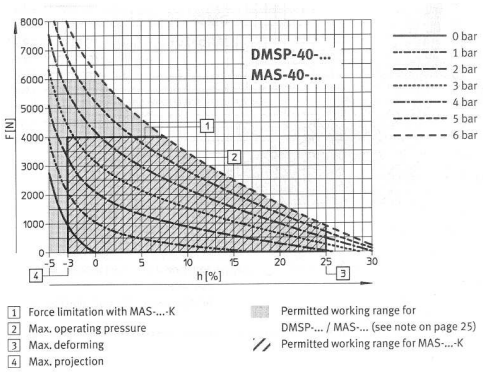

Fig. 4. Pulling force versus contraction of the DMSP40

Figure 4 shows the force-contraction relation of the PAM which was used during this research. At low contractions the allowed force is restricted to protect the pressed end fittings from damage. The force-contraction relation shown is that of a DMSP40 (this means that the contractible membrane's inner diameter is 40 mm) which has a total nominal length of 30 cm and weighs less than 0.800 kg. It can exert up to 1500N of pulling force at a pressure of only 6 bar.
The muscle can only exert pulling forces, due to its design principle explained above. This has to be taken into account when designing a test setup.

C. Controlling the fatigue test

Most often an algorithm called Time Waveform Replication (or TWR) is applied in fatigue testing. This algorithm, however, does not always result in the desired accuracy. Especially when the controlled actuator exhibits a nonlinear behavior such as e.g. the behavior of the PAM, it is possible that the algorithm converges before reaching the desired accuracy. This paper will therefore introduce

a new algorithm, based on an on/off control of the pneumatic muscle, that provides better results. In Section II the setup using a PAM as actuator will be described which is used to perform a fatigue test on a slat track of an Airbus A320 airplane. This setup will be used to compare the different control methods with respect to accuracy and application speed of the designed force signal. Section III gives a short introduction to TWR and presents our new method, . Section IV compares the experimental results of these algorithms performed on the setup described in Section II. All conclusions will be summarized in the last section.

II. Test setup

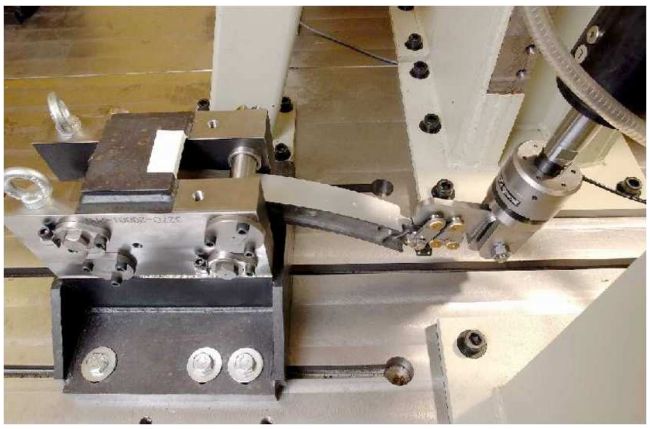

Fig. 5. Fatigue test setup for the slat tracks of an A320 using an hydraulic actuator

To perform fatigue tests on a slat track a hydraulic test rig is commonly used (see Figure 5). This setup is now adjusted slightly by replacing the hydraulic actuator by a PAM. The result is shown in Figure 6. To compare the introduced A2TWR algorithm to the classical TWR algorithm this altered setup is considered in both cases. The specimen under test is an A320 slat track which is clamped at an angle consistent with the slat setting during take-off/landing. The control signal is sent to the proportional valve which is actuated in an on/off fashion and connected to the pneumatic muscle which actuates the slat track at the end point. The resulting forces are measured and stored. For this setup the original rack and pinion, and the original side and main rollers are used to obtain a reliable result.

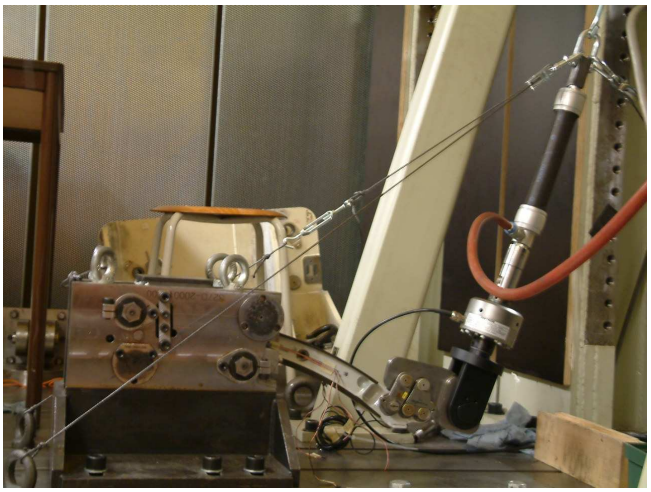

Fig. 6. Fatigue test setup for the slat tracks of an A320 using a PAM as actuator

III. The Control algorithm

A. The TWR updating rule

Iterative learning control (ILC) is based on the notion that the performance of a system that executes the same task multiple times can be improved by learning from previous executions (trials, iterations, passes).The objective of ILC is to improve performance by incorporating error information into the control for subsequent iterations. In doing so, high performance can be achieved with low transient tracking error despite large model uncertainty and repeating disturbances. Since fatigue testing applies the same reference trajectory (the analog signal resulting from the turning points of a single flight) for hundreds of thousands of times, a single trajectory can be considered to be one period of a periodic signal.
Several good surveys on ILC are available ([8], [9], and [10]).

Assuming a linear model $\widehat{P}$ is available for the unknown system P – this can be a nonparametric model (for example a measured FRF matrix) or a parametric model (for example an experimentally identified state space model) – a widely used ILC algorithm in the frequency domain is given by

$$U_{j+1}(k) = U_j(k) + \widehat{P}^{-1}(k)E_j(k) \tag{1}$$

where j is the iteration index,$U_j(k)$ is the control input and $Y_j(k)$ is the measured output. The error is defined as $E_j(k) = Y_r(k) - Y_j(k)$ and $U_0(k) = \widehat{P}^{-1}(k)(Y_r(k))$, with $Y_r(k)$ the reference trajectory. As mentioned al signals are considered in the frequency domain. To guarantee convergence a relaxation factor λ can be introduced, with a value $0 < \lambda \leq 1$.

$$U_{j+1}(k) = U_j(k) + \lambda\widehat{P}^{-1}(k)E_j(k) \tag{2}$$

This update law is called Time Waveform Replication. It is the solution for tracking a periodic signal currently applied in the industry. Figure 7 shows the flow chart of the TWR algorithm.

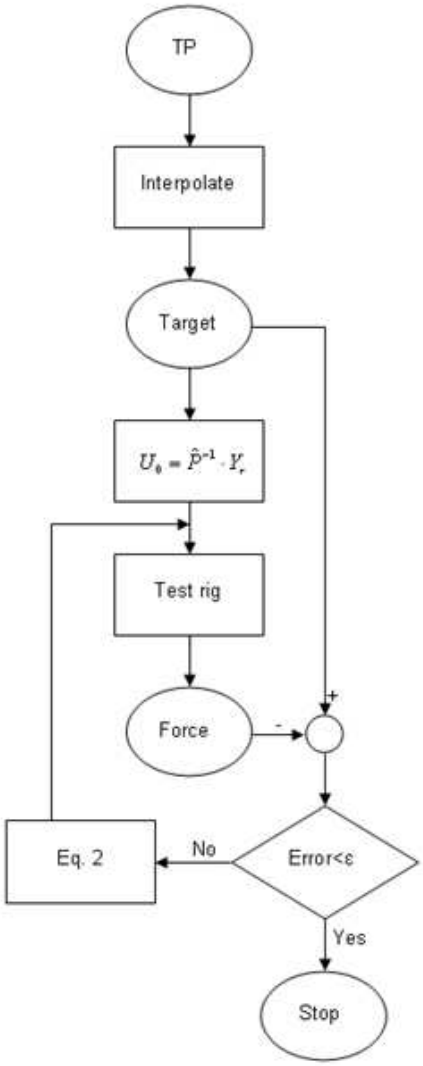

Fig. 7. Flow chart of the TWR algorithm

B. *The On/Off Control algorithm*

Since only the turning points are significant in determining the damage done to the structure, it is not necessary to control the entire analog target signal (as is the case with the TWR algorithm). It is therefore quite logical to control the setup in an on/off fashion. Two ways of on/off control are possible:

- The controlled input signal is a block wave with constant time intervals and varying amplitudes. This means that the time during which the valve is opened is a constant for each block and equal to the time the valve is closed. To control the magnitude of the output signal the amplitude of the blocks wave is adapted. Figure 8 illustrates this principle on a simple targetsignal. The limitations for this strategy are the fact that the input signal is a pressure signal, which means it should not exceed the maximum working pressure of the pneumatic muscles and it can never become negative.

- The controlled input signal is a block wave with constant amplitudes and varying time intervals. This means that we start with a block wave with maximum amplitude and adapt the opening and closing times of the valve to achieve the correct control. It is very important to start with a relatively small period of the input signal to avoid overshooting the turning points and thus overdamaging the specimen under test. Figure 9 illustrates this principle on our simple exemplary target signal.

It should be noted that the principle of on-off control is feasible because the pneumatic muscle have a first order dynamic behavior. If this was not the case, overshoots would be possible and therefore damage to the actuator or setup.

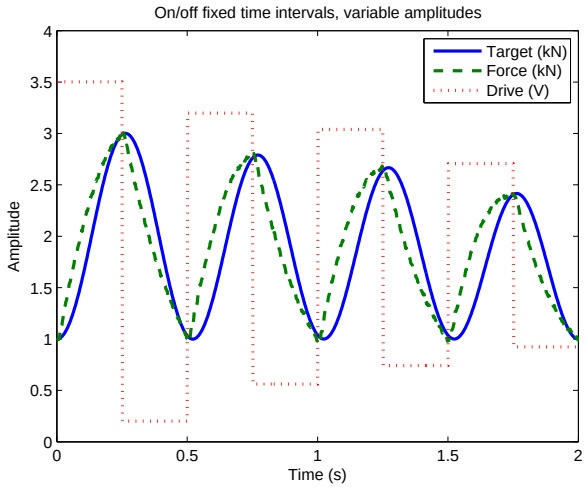

Fig. 8. Illustration of the variable amplitude approach on a simple example

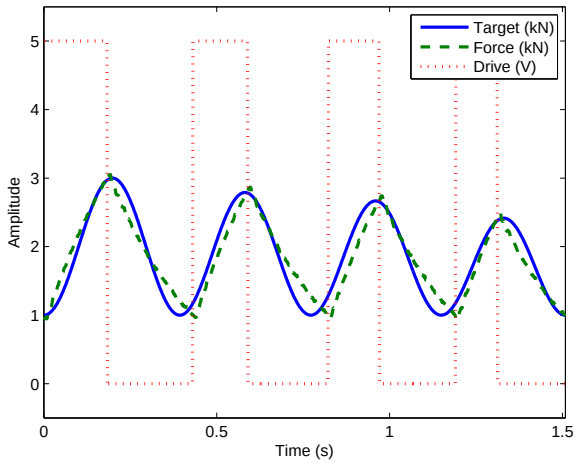

Fig. 9. Illustration of the variable time approach on a simple example

By comparing Figures 8 and 9 it can be seen that the second approach gives a similar result to the first one, but

with a smaller period. In other words, the seconds method allows us to perform the same fatigue test faster than the first method. For this reason we chose to implement this method and test it on the test setup of Section II.

IV. Experimental results

In this section both the classical TWR and the newly introduced on-off control will be applied to the setup of Section II. Taking into consideration that only the turning points need to be controlled to perform an accurate fatigue test, the accuracy of the proposed algorithms is checked by looking at the so-called "turning point" errors. The turning point errors are defined as the deviations of the turning points of the measured force signal with respect to the turning points of the desired signal. Two types of errors are considered: the rms value of the turning point errors (the 2-norm, $\|\|_2$) and the maximum turning point error occurring ($\|\|_\infty$).

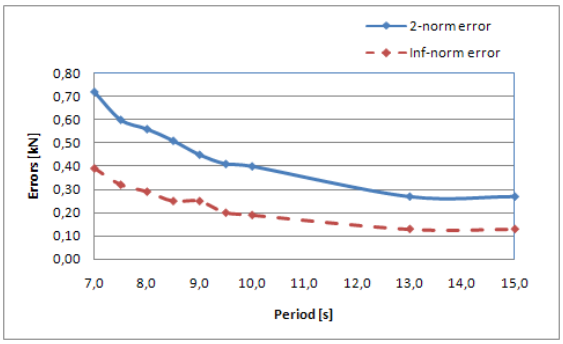

Fig. 10. Turning point errors for the classical TWR algorithm for different application speeds

Figure 10 gives the 2-norm and infinity norm turning point error of the classical TWR algorithm for different application speeds. With this control strategy it was impossible to apply the signal with a period of less than 7 seconds, due to convergence problems. When applying the on-off algorithm the resulting period is $T = 2.48s$ and the turning point errors are $\|\|_2 = 0.47kN$ and $\|\|_\infty = 0.18kN$. The magnitude of these errors are consistent with the errors for the classical TWR algorithm, but with a period of $9s$ for the 2-norm error and $10s$ for the infinity norm error. The new algorithm therefore enables us to reduce testing time with a factor four.

The resulting forces applied to the slat track are shown in Figure 11 together with the turning points to give an idea of the magnitude of these turning point errors.

V. Conclusions

In this paper we discussed the use of Pneumatic Artificial Muscles as actuators for performing a fatigue test on an A320 slat track. A pneumatically driven setup based on the commonly used hydraulic setup was presented as well as an on-off type of control as the control strategy for this setup. Experiments were performed comparing the turning point errors of both the classical TWR algorithm and this introduced on-off control. These experiments have shown that the classical TWR control method has a minimum period of $7s$ to perform a single fatigue test cycle. To achieve acceptable turning point errors this periods should even be $9s$. The on-off algorithm does however enable us to perform a fatigue test faster with the same accuracy as the classical TWR algorithm. In this case a period of only $2.47s$ is erequired.We can therefore conclude that the proposed control strategy delivers a very good speed up of the testing process.

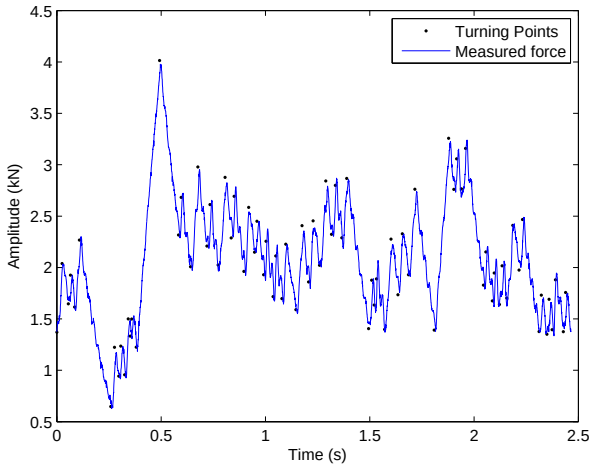

Fig. 11. Desired turning points and forces applied to the slat track using the on-off algorithm

Acknowledgments

Research funded by the Institute for the Promotion of Innovation through Science and Technology in Flanders (IWT-Vlaanderen). The authors also acknowledge the Flemish government (GOA-OPTIMech), the Fund for Scientific Research - Flanders (FWO), and the research council of the Vrije Universiteit Brussel (OZR) for their funding.

References

[1] P. Weal, C. Liefooghe, and K. Dreßler, "Product durability engineering -improving the process.," *Sound and Vibration*, vol. 31, no. 1, pp. 68–79, 1997.

[2] Y. Murakawi, *The rainflow method in fatigue.*, Oxford: Butterworth Heinemann, 1992.

[3] O.H. Basquin, "The exponential law of endurance tests.," in *Proceedings of the American Society for Testing and Materials*, 1910, vol. 10, pp. 625–639.

[4] K. Dreßler, M. Hack, and W. Krüger, "Stochastic reconstruction of loading histories from a rainflow matrix.," *Zeitschrift für Ange-*

wandte Mathematik und Mechanik, vol. 77, no. 3, pp. 217–226, 1997.

[5] B. Gründer, M. Speckert, and M. Pompetzki, "Design of durability sequences based on rainflow matrix optimization.," *SAE*, vol. 980690, pp. 63–70, 1998.

[6] B. Verrelst, *A dynamic walking biped actuated by pleated pneumatic artificial muscles: Basic concepts and control issues.*, Ph.D. thesis, Vrij Universiteit Brussel, January 2005, http://lucy.vub.ac.be/publications/PhD_Verrelst.pdf.

[7] *Festo Fluidic Muscle DMSP, Festo brochure Fluidic Muscle.*, www.festo.com.

[8] D.A. Bristow, M. Tharayil, and A.G. Alleyne, "A survey of iterative learning control, a learning-based method for high-performance tracking control.," *IEEE Control Systems Magazine*, pp. 96–114, June 2006.

[9] H.-S. Ahn, Y.Q. Chen, and K.L. Moore, "Iterative learning control: brief survey and categorization 1998 – 2004," Revised version submitted to IEEE Transaction on SMC Part-C Applications & Reviews, Aug. 2006., August 2006.

[10] H.-S. Ahn, Y.Q. Chen, and K.L. Moore, "Iterative learning control: Robustness and monotonic convergence for interval systems.," *Communications and Control Engineering Series*, ISSN 0178-5354.

[11] K. Smolders, *Tracking Control of Continuous-Time Nonlinear Systems: A modal-Based Iterative Learning Approach.*, Ph.D. thesis, Katholieke Universiteit Leuven, December 2007.

[12] S. Vanlanduit and P. Guillaume, "Multisine load cycle design for fatigue testing.," *International Journal of Fatigue*, vol. 26, pp. 95–102, 2004.

Proceedings of the 8th National Congress on Theoretical and Applied Mechanics, May 28-29, Brussels, Belgium.

Experimental material determination of viscoelastic glass/ionomer laminates

Dieter Callewaert, Didier Delincé, Jan Belis, Rudy Van Impe
Laboratory for Research on Structural Models, Ghent University
Technologiepark-Zwijnaarde 904, 9052 Zwijnaarde
email: Dieter.Callewaert@UGent.be, Didier.Delince@UGent.be,
Jan.Belis@UGent.be, Rudy.VanImpe@UGent.be

Abstract: **To use laminated glass as a structural building material, a better understanding of its mechanical properties is necessary. The Laboratory for Research on Structural Models is performing experimental tests and numerical simulations to gain a better insight into the influence of the viscoelastic interlayer (PVB and SG) on the mechanical behaviour of glass laminates. Among others, the study determines the resistance taking the time- and temperature dependent behaviour of the laminate into account.**

For this research, an optimised torsion test set-up has been built based on numerical simulations with different support types. Also three-point bending tests are being performed in a climatic chamber in which temperature and humidity are controlled. Further comparison of these test results at different temperatures should produce a complete image of the stiffness of laminated glass, which could be used as a basis for safe but economic design recommendations for laminated glass components.

Keywords: **Viscoelasticity, Laminated glass, Experimental**

INTRODUCTION

Since the early 90's of the previous century, the traditional building material glass has gradually been given an extra function. After serving for many centuries as a transparent infill panel for openings in buildings, it was discovered that this brittle material was strong enough to carry a significant load. By transferring important building loads through glass elements - to fulfil the increasing architectural wish for transparency - the concept of *Structural glass* was born.

LAMINATED GLASS

The most applied technique to increase the post-failure behaviour of the brittle glass is to laminate multiple glass sheets together with a soft interlayer material. This way, some plasticity is added to the component. In case of an impact on the element, the interlayer can partially absorb the impact energy, which will hopefully limit failure to only one glass sheet. Additionally, the glass fragments remain attached to the interlayer, so the probability that people get injured is drastically reduced.

The lamination technique is derived from the automotive sector, where the window shield needs to keep its integrity during a car crash. For this, generally glass/Polyvinyl Butyral (PVB) laminates are used. Because this PVB interlayer is relatively soft, it is not ideal for structural glass, because here usually, the laminate must be as stiff as possible to restrict the deflections. For this reason, DuPont de Nemours developed an improved ionomer interlayer material: SentryGlas®, or shortly SG (formerly known as SentryGlas® Plus, or briefly SGP).

EXPERIMENTAL PROGRAMME

This SG is a visco-elastic material, which means that the material properties vary in function of the loading duration and the temperature. Because these properties have a large influence on the strength and stiffness of the laminated product, it is important to have a good insight in this complex behaviour. Consequently, the Laboratory for Research on Structural Models executed an experimental programme.

In this, three point bending tests are complemented with torsion tests at different temperatures between 5°C and 65°C. The loading durations varied between two days and multiple weeks.

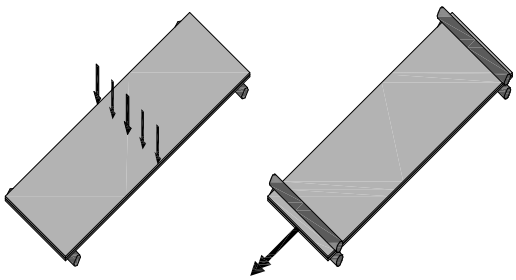

Fig. 1. Basic principle of the test programme.

To incorporate the influence of the lamination process - a cycle of high temperatures and high pressures – on the SG material properties, all tests are performed on glass/SG laminates. This way, the tested material has an identical history as in reality.

THREE-POINT BENDING TESTS

Three-point bending tests are relative simple tests to define the bending stiffness of a material. For the multi-layered glass/SP laminates, test series are executed about the weak axis (largest influence of interlayer properties). To avoid the influence of the self-weight of the test specimens, they are placed vertically on two supports while the force is introduced horizontally, as illustrated in Figure 2.

Fig. 2. Large three-point bending test setup.

Because the length of the span between the supports determines the test accuracy, tests are executed on both 1.1 m and 3 m long test specimens. The changing accuracy between these two similar test series is caused by a different proportional behaviour of the laminate to an identical change in the properties of the interlayer material. This is illustrated in Figure 3, representing the relative bending stiffness – the theoretical stiffness in proportion to the stiffness of a monolithic glass plate – in function of the material properties of the interlayer, independent of the type of interlayer material.

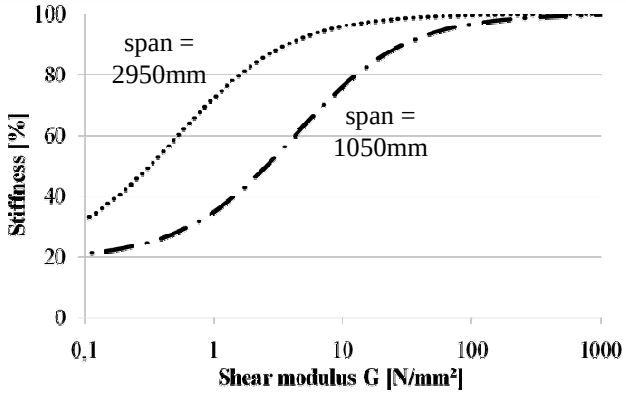

Fig. 3. Relative bending stiffness of the test specimens in function of the shear modulus of the interlayer.

TORSION TESTS

To check if the derived material properties are applicable for different loading conditions, also torsion tests are executed simultaneously. With this, it is possible to compare two different stress distributions and to verify the existing theories to calculate the bending and torsion stiffnesses.

The torsion test setup for this test programme (shown in Figure 4) is mainly based on the setup used by Kasper [1]. Hereby, the test specimen is clamped between a fixed support and a rotating support. The applied torsion moment is introduced as a concentrated force on a lever arm with a fixed length.

Fig. 4. Torsion test setup.

EXPERIMENTAL PROCEEDING

All tree test setups were built up in a closed chamber with controlled temperature and air-humidity. In this room, the air control always started at least 60 hours before the beginning of the first test. This ensured the right temperature of the interlayer for each test.

To investigate the influence of different kinds of stress progressions, both creep as relaxation tests were executed. For this, respectively a constant load (line load or torsion moment) or a constant deformation was applied to the test specimen.

DISCUSSION

A thorough comparison between the torsion and bending results, complemented with an extensive FEM analyse, should result in a safe and applicable material model for the SG interlayer. With this, also other loading conditions than pure torsion or three-point bending should be examined. This way, it can be verified if these two simplified loading conditions are appropriate for a full experimental analyses of new interlayer materials.

ACKNOWLEDGEMENTS

This work was supported by the Fund for Scientific Research-Flanders (FWO-Vlaanderen. grant nr. G.0184.07). Additionally, the authors wish to acknowledge the support of Lerobel. More information about this research can be found in other publications from the authors of this article, e.g. [2] and [3].

REFERENCES

[1] Ruth Kasper, *Tragverhalten von GlasTrägern*, Aachen, 2005.

[2] Dieter Callewaert, Didier Delincé, Jan Belis and Rudy Van Impe, *Temperature-dependent Behaviour of Glass/Ionomer Laminates: Preliminary Test Results*, Proceedings of Challenging Glass – Conference on Architectural and Structural Applications of Glass (pp. 431-437), Delft, 2008.

[3] Dieter Callewaert, Jonathan Depaepe, Kenneth De Vogel, Jan Belis, Didier Delincé and Rudy Van Impe, *Influence of Temperature and Load Duration on Glass/Ionomer Laminate: Torsion and Bending Stiffness*, Proceedings of ISAAG2008 (pp. 51-63), München, 2008.

Proceedings of the 8th National Congress on Theoretical and Applied Mechanics, May 28-29, Brussels, Belgium.

2D Permeability Tensor Identification of Fibrous Reinforcements for RTM

Morren Gerd[1, 2], Sol Hugo[1], Bossuyt Sven[1]
[1]Vrije Universiteit Brussel – Department of Mechanics of Materials and Constructions
Pleinlaan 2 – 1050 Brussel
[2]Erasmushogeschool Brussel – Department of Industrial Sciences and Technology
Nijverheidskaai 170 – 1070 Brussel
email: gerd.morren@vub.ac.be, hugos@vub.ac.be, sven.bossuyt@vub.ac.be

Abstract: **The simulation of a resin flow through a porous medium by FE-models has become a very important aspect for the design of a high-performance RTM produced composite part. The key parameters to perform RTM flow simulations are the permeability values of the fibre reinforcement. The measurement of this material parameter is still not standardized and many different set-ups have been proposed. This paper presents an inverse method, or a so-called mixed numerical/experimental technique, for the identification of the permeability values. In this iterative inverse technique an experimental observation on a highly automated central injection rig, called "PIERS set-up" (Permeability Identification using Electrical Resistance Sensors), is compared with a computed observation using a numerical model that simulates exactly the same experiment. In this model the permeability values will appear as parameters which will be iteratively tuned in such a way that the computed observation matches the experiment. The inverse method with the PIERS set-up allows a fast and accurate identification of the permeabilities. Moreover, this article presents a solid test specimen, produced with a stereolithography technique, which can be used as a reference sample for calibration and comparison of permeability measurement set-ups and for validation of numerical permeability computation software.**

Keywords: **permeability, Fabrics/textiles, Numerical analysis, Resin transfer moulding (RTM)**

I. INTRODUCTION

The science and technology of composite materials has generated a large number of processes by which components can be manufactured. Interest in the Resin Transfer Moulding (RTM) production technique has risen significantly over the past few years, due to increased demands with respect to finish quality, production volumes, cycle times and environmental impact.

In RTM, the fibre reinforcement is initially dry and is often assembled outside the mould, as a preform in the shape of the finished part. After the mould is closed with a dry fibre preform inside, a liquid resin is injected, which polymerizes to yield a rigid composite. The driving force for the flow of the resin is a pressure difference. One of the key issues in RTM process design for a good impregnation is accurate knowledge of the flow behaviour of the resin through the reinforcement. Although it is often feasible to find a reasonable injection strategy by trial and error, this method is risky and costly, especially if expensive moulds need to be manufactured, or when the material costs are very high.

Therefore flow simulation software has been developed, which assists the designer in the development of a new mould design [1, 2]. Through injection simulations performed on a computer, the problem areas in a mould can be identified and the mould layout, i.e. the positions of resin injection points and air vents, as well as the injection strategy, can be adapted accordingly [2, 3]. Moreover, the software can assist the designer in optimizing the injection process in order to obtain a robust production process with the shortest possible cycle time [4].

However, these simulation codes need reliable input data like mould geometry, fluid viscosity, reinforcement porosity and reinforcement permeability. The permeability of a porous medium is a material parameter, which may be described as "the ease with which a fluid flows through the reinforcement" [5] and is expressed by a symmetrical tensor [6, 7]. Measurement of the permeability is not yet standardized, and many different set-ups have been proposed. Moreover, the measurements are very sensitive to various factors and hence prone to error [4].

This article describes a new method for the identification of the in-plane permeability tensor. The proposed inverse method is a so-called mixed numerical/experimental technique (MNET) for material property identification. MNETs have been previously used at dept. MeMC, e.g., for determining anisotropic thin plate rigidities and in a non-destructive procedure for identification of stiffness [8] and damping properties [9] of orthotropic materials (Resonalyser). The principle of the MNET is to compare experimental observations from a test set-up with computed values from a numerical model which simulates the experiment. In this numerical model the permeability values will appear as parameters which will be iteratively tuned in such a way that the computed observation matches the experiment [10]. The relevant experimental data is obtained via the highly automated "PIERS" (Permeability Identification using Electrical Resistance Sensors) central injection rig and the numerical model is, in fact, a customized finite element model of the experiment.

This paper also presents a textile-like solid specimen that is produced with a stereolithography technique. It is designed as a reference for calibration and comparison of permeability measurement set-ups and for validation of numerical permeability computation software [11, 12].

Note that this paper actually only briefly discusses the MNET for permeability identification and the reference material. For more detailed information, the reader is referred to [10] and [11, 12] respectively, on which this paper is based.

II. The Mixed Numerical/Experimental Technique (MNET) for Permeability Identification

A summary of the mixed numerical/experimental technique is given by the following flow chart (Fig. 1):

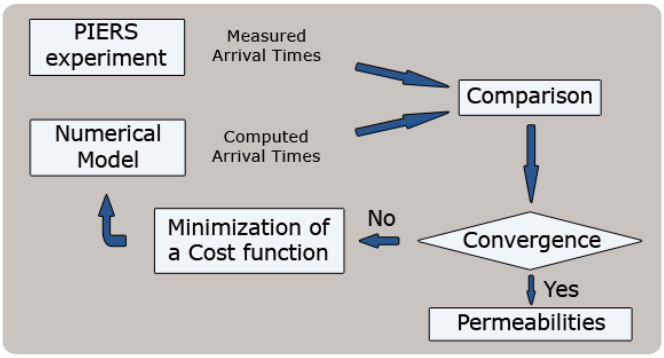

Fig.1. The inverse method.

In a two-dimensional central injection experiment the flow front arrival times at a number of precisely known positions are recorded. On the other hand, there is a numerical model that simulates exactly the same experiment. In this model the permeability values will appear as parameters and the results are compared with those of the actual experiment. In general there will be a discrepancy between the two results. The parameters of the numerical model are then updated and the simulation is run again. The results are compared with the measurements, and if the agreement is not yet sufficient, the model parameters are updated again and the simulation is repeated. This iterative solving process is continued until satisfying agreement between experiment and simulation is reached. The parameter values that were used in the last simulation are taken as the permeability values of the object under study.

A. Experimental Part (PIERS set-up)

The experimental part of the proposed MNET is represented by the PIERS set-up. This set-up (Fig. 2) was described in detail elsewhere [13, 14]. As shown in Fig. 2, the mould cavity in the set-up consists of two so-called sensor plates (300 mm x 300 mm). These steel plates each hold 60 electrical sensors which are positioned on radial lines, every 30°. Each radial line has five sensors, at 25, 55, 85, 115 and 145 mm from the centre of the plate (Fig. 3).

The sensor plates are built into a hydraulic press which lifts the lower sensor plate and spacers (Fig. 4) until the spacers contact the upper sensor plate. The four spacing rods are specifically developed to assure the correct cavity height between the two sensor plates for the placement of the reinforcement. After placing the reinforcement and closing the mould, the test fluid can be injected. This is done centrally in the reinforcement through a hole of Ø 6 mm in the middle of the lower sensor plate. As the flow front propagates through the reinforcement, the fluid will make contact with the electrical sensors. Since a somewhat electrically conductive fluid (corn syrup) is used, the wetting of these DC-resistance sensors will be observable as a sudden decrease of the sensor's resistance. This decrease is recorded by a PC equipped with a data acquisition system and stored as an arrival time for that sensor. Major advantages of the PIERS set-up are its high bending stiffness and high testing rate. Five to ten experiments per hour can easily be achieved, which is tenfold the testing rate of many traditional set-ups [14].

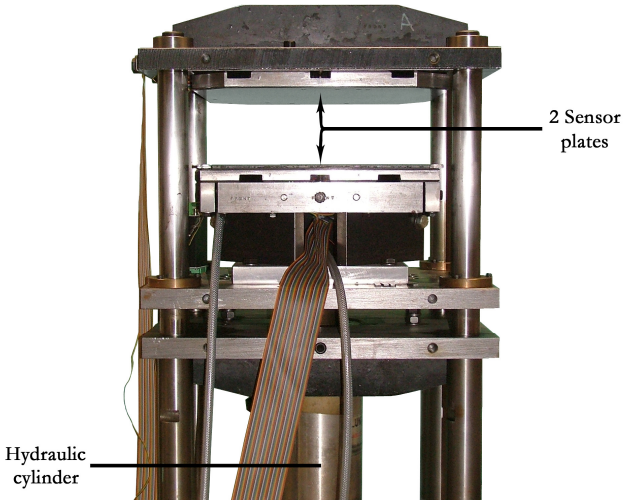

Fig. 2. The PIERS set-up.

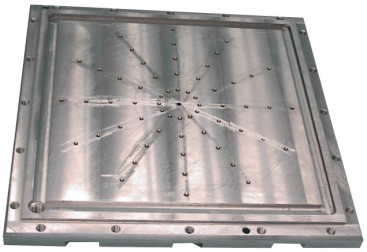

Fig. 3. Sensor plate.

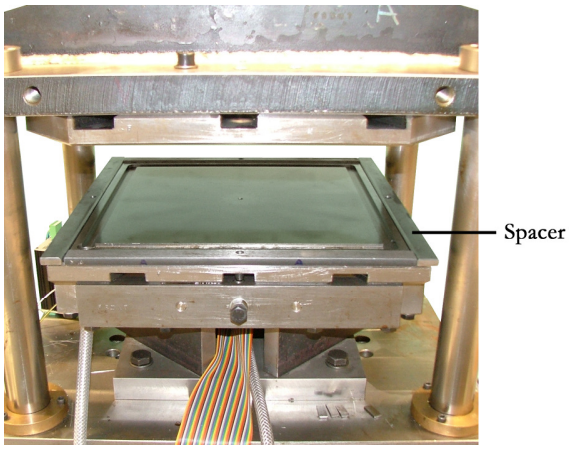

Fig. 4. The set-up with the spacers.

B. The numerical model

The impregnation of a fibrous reinforcement, as occurring during the experiment, is usually modelled as a flow through

porous media. It is governed by Darcy's law, i.e., the fluid velocity vector **u** is proportional to the pressure gradient

$$\mathbf{u} = -\frac{\mathbf{K}}{\mu}\nabla p \qquad (1)$$

where **K** is the permeability tensor (m^2), p the resin pressure (Pa), and μ the fluid viscosity (Pa s) assumed constant for a Newtonian resin. Combining Eq. (1) with the continuity equation for incompressible flow, $\nabla \cdot \mathbf{u} = 0$, gives an elliptical partial differential equation for the pressure field

$$\nabla \cdot \left(\frac{\mathbf{K}}{\mu} \nabla p \right) = 0 . \qquad (2)$$

In order to solve this equation, boundary conditions must be specified. In this case, Dirichlet boundary conditions are applicable: a given injection pressure on the circumference of the inlet orifice, which is stationary, and ambient pressure at the fluid front, which moves along with the fluid until it reaches the edge of the fabric.

It should be noted that Darcy's law was observed for the steady flow in a porous medium. Inside the saturated part of the mould and for relatively small time steps, it is reasonable to approximate the transient impregnation process by a succession of quasi-steady states satisfying Darcy's law. At each time step, Eq. (2) is solved to obtain the pressure field. From this, the flow rates across each segment of the boundary can be computed by Eq. (1). The flow velocity, multiplied by the time increment Δt, is used to update the position of the resin front, resulting in a new domain over which to calculate the pressure distribution for the next time step.

The numerical model has been entirely programmed in a MATLAB© environment. A finite element formulation using linear elements has been chosen [15] (Fig. 5).

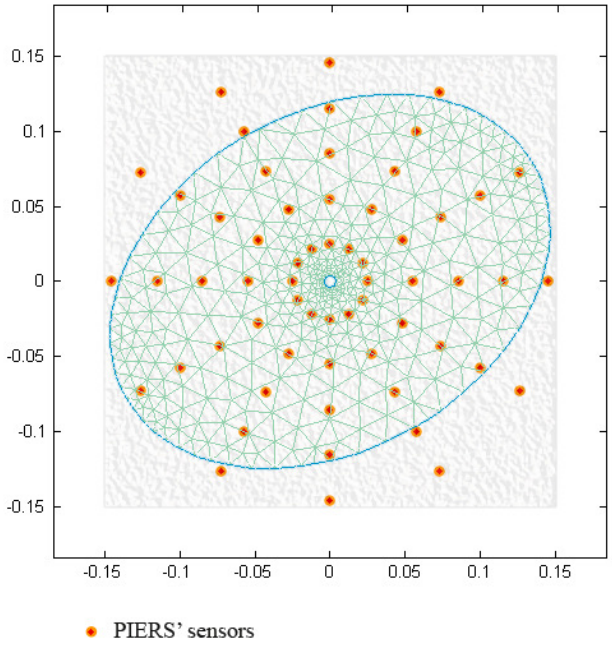

Fig. 5. The wetted part of the mould cavity is subdivided into a finite number of triangles.

The numerical model has been validated with an analytical solution for an injection into isotropic material. It was observed that the simulated arrival times converge to the analytical times if the mesh is refined. For the last sensors, the relative error decreases underneath 0,1% without significantly jeopardizing the inverse method's speed.

C.The optimization algorithm

In general for any optimization procedure, starting from some initial parameter value(s), a possibly improved set of parameters is generated, and this process is repeated until it is decided that the process has converged (Fig. 1). So there are three basic steps in the optimization algorithm:

1)Selection of the starting values

Before beginning the optimization procedure it is necessary to generate starting values. In practice the convergence region of most optimization methods is limited; if the starting values are selected outside this region, the method will not converge to the desired optimum. Even if there is convergence, the final result can depend upon the starting values if the cost function has local minima.

The starting permeabilities along the principal axes are calculated via an analytical approximation of the injection [16–18]. This approach was initially used in the previous software program for permeability identification, called "PMPI" (porous media permeability identification) [14]. Its main limitation is that only data from sensors which are reached before the flow front reaches an edge of the reinforcement can be used because the analytical approximation assumes an infinitely large reinforcement geometry. This forms a significant drawback when the anisotropy (ratio of the principal permeability values) of the reinforcement is high and will be further elaborated in Section D. Nonetheless, the analytical approximation provides a good estimation of the permeability values. The starting value for the rotation angle is provided by visual evaluation of the experiment.

2)Generation of an improved set of parameters

The generation of the improved set of parameters is the kernel of the optimization algorithm. Several different techniques are possible. Here, the method of Levenberg–Marquardt is used [19, 20]. This is a combination of the Gauss–Newton method and the gradient method. New parameter updates are generated using the formula

$$\boldsymbol{\delta}^{(j)} = \left(\mathbf{J}^{(j)T} \mathbf{J}^{(j)} + \lambda \mathbf{I} \right)^{-1} \mathbf{J}^{(j)T} \left(\mathbf{T}^{exp} - \mathbf{T}^{(j)} \right) \qquad (3)$$

with which the updated permeability vector can be calculated using the formula:

$$\mathbf{K}^{(j+1)} = \mathbf{K}^{(j)} + \boldsymbol{\delta}^{(j)} \qquad (4)$$

where:

K is the permeability column; $\mathbf{K} = \begin{bmatrix} \mathbf{K}_{xx} \\ \mathbf{K}_{xy} \\ \mathbf{K}_{yy} \end{bmatrix}$,

I is the identity matrix,

λ is a damping parameter,

$\mathbf{T}^{exp}$ is the column containing the flow front arrival times at

the sensors of the PIERS set-up,

$\mathbf{T}^{(j)}$ is the column containing the calculated flow front arrival times at the sensor locations,

$\mathbf{J}$ is the Jacobian matrix; $\mathbf{J} = \begin{bmatrix} \frac{\partial \mathbf{T}_1}{\partial \mathbf{K}_{xx}} & \frac{\partial \mathbf{T}_1}{\partial \mathbf{K}_{xy}} & \frac{\partial \mathbf{T}_1}{\partial \mathbf{K}_{yy}} \\ \vdots & \vdots & \vdots \\ \frac{\partial \mathbf{T}_n}{\partial \mathbf{K}_{xx}} & \frac{\partial \mathbf{T}_n}{\partial \mathbf{K}_{xy}} & \frac{\partial \mathbf{T}_n}{\partial \mathbf{K}_{yy}} \end{bmatrix}$,

and n denotes the number of activated sensors and $\mathbf{T}_i$ the arrival time of the sensor i (with: i=1, …, n).

The evaluation of this Jacobian matrix, is a delicate issue. The partial derivatives of the numerical model with respect to the permeabilities $\left(\partial \mathbf{T}/\partial \mathbf{K}_{xx}, \partial \mathbf{T}/\partial \mathbf{K}_{xy}, \partial \mathbf{T}/\partial \mathbf{K}_{yy}\right)$ can be approximated using backward, centred or forward differences. The forward and backward finite difference approaches require less additional FE-analyses than the centred differences approach because the response $\mathbf{T}_i(\mathbf{K})$ is anyhow known. Backward differences will be used in this procedure. So, the sensitivity coefficients, for a sensor i, are defined by:

$$\frac{\partial \mathbf{T}_i(\mathbf{K})}{\partial \mathbf{K}_j} \cong \frac{\mathbf{T}_i(\mathbf{K}) - \mathbf{T}_i(\mathbf{K}, \mathbf{K}_j - \Delta \mathbf{K}_j)}{\Delta \mathbf{K}_j} \tag{3}$$

where $\mathbf{T}_i(\mathbf{K})$ is the ith response of the FE-model for a given parameter set in which parameter $\mathbf{K}_j$ has a slightly modified value. $\Delta \mathbf{K}_j$ is the considered perturbation of the jth parameter and $\mathbf{K}$ is the entire set of permeabilities.

Note that the Jacobian matrix needs to be calculated in every iteration step of the MNET. These calculations are not prohibitively time consuming due to the speed of the numerical model and the limited number of parameters. Furthermore, it appeared to be advisable to systematically normalize the Jacobian matrix.

3)The halting criterion

The iteration loop of the optimization method is halted when the halting criterion is met. There are a number of ways of choosing this criterion. The halting criterion programmed in the presented optimization algorithm is based on the evaluation of a least-squares formulation of the difference between the experimental and the numerical flow front arrival times. More specifically, the iteration loop is halted when there is no longer a significant decrease of the least-squares cost function with further iteration.

D.Discussion

Before the discussed inverse method was developed, the PIERS measurement data was processed via a commonly used analytical approximation of the injection, as was proposed by Adams and Rebenfeld [16-18]. However, since it assumes the preform to be infinite in extent, the measurement has to be aborted once an edge of the reinforcement is reached (Figure 6a). Thus, sensors which are to be reached after the flow profile began to be affected by the edge of the reinforcement are rendered useless. The amount of unusable sensors, evidently, depends vastly on the degree of anisotropy of the fibre reinforcement.

Since the finite element model (of the presented inverse method) changes the boundary conditions appropriately when the fluid front reaches an edge of the reinforcement, the experiment can usefully continue until all sensors are reached (Figure 6b). Hence, the full array of 120 sensors can be used in every identification process allowing for a more accurate determination of the entire permeability tensor.

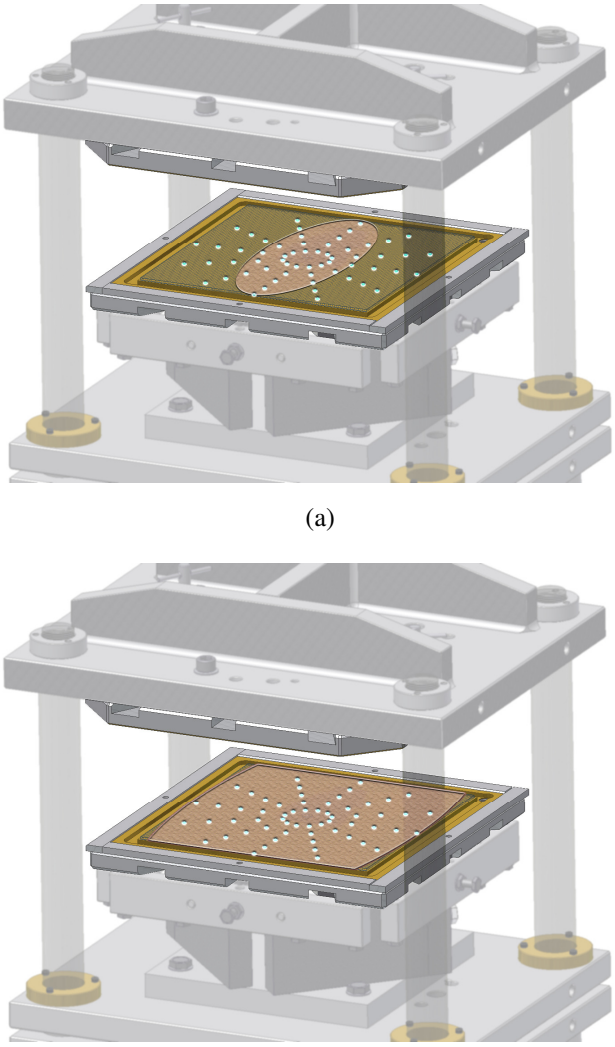

(a)

(b)

Fig. 6. The heart of the PIERS set-up with the fibre reinforcement and centrally injected fluid. The 60 sensors of the lower mould half are marked.

As a direct result of using a greater number of sensors, the data processing scheme is more robust: if one sensor registers a deviant measurement, this will have a smaller influence on the final outcome of the calculation. In this context, it is worth noting that not all sensors contribute equally to the determination of the permeability tensor: data is weighted by reliability, and sensors in the direction of a principal component of the tensor contribute mostly to that component. In the experiments, it is observed that arrival times at sensors near the inlet are less reliable. Sensors further from the inlet already measure an average over a greater amount of time and

material, so that the variability of those results is inherently lower. Thus the ability of the inverse method to use all of the available sensor data is especially significant in the direction of the smaller permeability, where fewer sensors are reached in time to be used in the analytical approach.

III. The Stereolithography (SL) Reference Material

Permeability values often cause problems because there are no standardized methods for permeability measurements. Moreover, the measurements are very sensitive to various factors and large scatter in the identified permeability values is usually observed [14]. Such scatter is not surprising, since the permeability is affected by details of the geometry of the porous medium, which are highly variable for typical reinforcements. As the test specimen usually consists of a stack of layers, and each individual layer and the interface between layers allow a mixture of micro (filament level) and macro (fibre bundle level) flows, the variability is possibly created by [12]:

- nesting of the layers;
- mixture of micro and macro flows;
- (non-uniform) shearing, stretching and compression of the textile layers;
- production variability and sampling procedure in the textile production;
- saturated and non-saturated fluid flow.

Testing of a series of textile specimens therefore yields a statistical distribution of permeability values instead of deterministic values. The test rig itself also contributes to a broader distribution of identified permeability values due to errors on the pressure measurement, fluid viscosity values, limited mould cavity stiffness, boundary race effects and fluid velocity measurement. In practice, these sources of scatter will act simultaneously, making it difficult to distinguish the possible contributions. The maximum permeability value can easily be fourfold the minimum value, and relative standard deviations of 30% are common. Measured values obtained in different labs can differ even more (by a factor of 10). These issues are a problem for the calibration of test rigs and for comparison of results from different test rigs. Moreover, it presents a difficulty when numerical flow simulation software, for the numerical prediction of the permeability, is to be experimentally validated.

Therefore, we developed a solid test specimen that can be used as a reference sample (Fig. 7) [11, 12]. This object was produced with a stereolithography (SL) production technique. The additive nature of the SL process allows the production of a structure with specific and complex internal features so that a kind of ‘‘artificial” reinforcement can be created in which the fluid flow path is curved much as it would be in conventional textiles. Moreover, this production technique enabled a design which, while it resembles typical reinforcements in important respects, avoids all of the aforementioned sources of variability, inherent to real textiles, and various modelling issues of the flow simulation software. Since the permeability properties of the specimen do not vary from test to test, an excellent repeatability of the experiments is expected; any discrepancy between different measurements will be attributed to the set-up and data processing.

As a result, this SL specimen can be used as a reference sample for calibration of test rigs and for comparison of results from different test rigs. Additionally, the SL sample has a simple unit cell (Fig. 8 & 9), with accurately known geometry, which allows a correct and complete specification of the geometry in numerical permeability prediction software, allowing greater confidence in the experimental validation of such simulation programs than could be obtained with the various textiles used in previous validation efforts [21–23].

A SL specimen was produced for the 2D central injection rig, called “PIERS set-up”. Such specimen could be used for 1D experiments as well and the structure can be easily adapted for through the thickness experiments and possible extra requirements of other test rigs to be used.

A tolerance of 0.1mm can be easily obtained on all the dimensions. The same tolerances were found on subsequently produced specimens, confirming that the stereolithography manufacturing process offers the repeatability and precise control of geometry required for a standard reference specimen.

The newly designed resin additionally allows a rigid structure, with a very good surface quality and a wear resistance, which can be cleaned with water.

In [12], the first permeability measurements of the textile-like solid reference samples are presented. The measurement data was processed using the presented inverse method and the analytical approach, which was used before. Given the reference specimens’ unique features, hitherto unproven differences in the effectiveness between both data processing schemes could be demonstrated. The variability of results from the inverse method, using the finite element model, is lower than with the analytical approach. This is primarily attributed to the fact that the finite element model continues to be valid after the fluid front reaches the edge of the specimen, so that all of the available sensor data can contribute to the comparison between calculation and experiment.

Also, the experimental results are shown to be in good agreement with the values predicted using numerical permeability computation software.

On a final note, a project is initiated to perform a round-robin study between different research institutes. SL specimens will be sent to the participating partners such that results of permeability measurements can be compared on an objective basis.

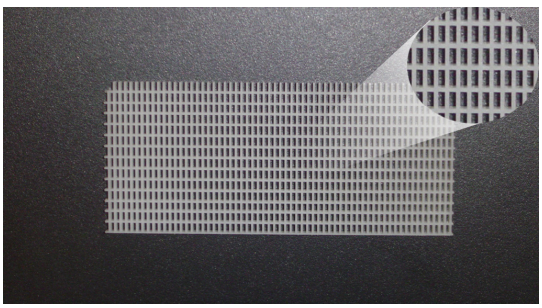

Fig. 7. A stereolithography test specimen.

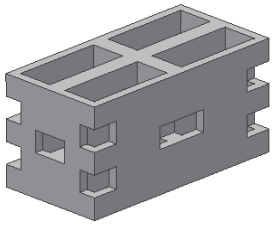

Fig. 8. Unit cell with outer dimensions 6 x 3 x 3 mm.

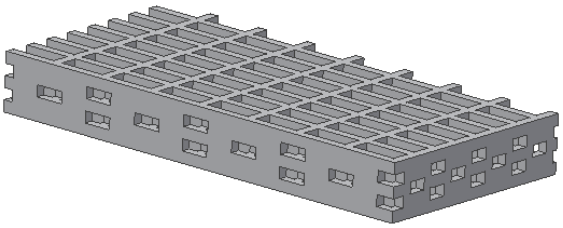

Fig. 9. CAD drawing of 16 joined unit cells.

IV. Conclusions

A mixed numerical/experimental technique for the identification of the full in-plane permeability tensor is proposed. The technique is based on an existing central injection rig and an inverse method, adjusting the parameters in a finite element model of the experiment to optimize the agreement between measured and calculated flow front arrival times. A least-squares formulation of the difference between the experimental and the numerical flow front arrival times is used, along with a Levenberg–Marquardt optimization algorithm. The full array of 120 sensors can be used in every identification process because the finite element model, in contrast to an analytical approximation, is more versatile and allows the advantages of the inverse approach to be used to the fullest.

This paper also presented a reference material that is produced with a stereolithography technique. On the one hand it resembles typical reinforcements in important respects. But, on the other hand, it avoids the sources of scatter, inherent to real textiles, in the experiments and various modelling issues of the flow simulation software. Consequently, the specimen allows isolating the variability arising from measurement techniques *per se* and an objective comparison of the techniques. Moreover, it allows greater confidence in the experimental validation of simulation programs than could be obtained with the various textiles used in previous validation efforts.

References

[1] Gauvin R et al. Permeability measurement and flow simulation through fiber reinforcement. Polym Compos 1996;17(1):34–42.

[2] Baichen L, Bickerton S, Advani SG. Modelling and simulation of resin transfer moulding (RTM) – gate control, venting and dry spot prediction. Composites Part A 1996;27A(2):135–41.

[3] Huber U, Maier M. Methodical application of liquid composite molding simulation. In: Proceedings of the international conference on high performance structures and composites. Sevilla, Spain; 2002. p. 545–56.

[4] Parnas RS. Liquid composite molding. Munchen: Carl Hanser Verlag; 2000.

[5] Steenkamer DA, McKnight SH, Wilkins DJ, Karbhari VM. Experimental characterization of permeability and fiber wetting for liquid moulding. J Mater Sci 1995;30(12):3207–15.

[6] Adler PM. Porous media: geometry and transports. Stoneham, MA, USA: Butterworth-Heinemann; 1992.

[7] Bear J. Fundamentals of transport phenomena in porous media. Dordrecht, Netherlands: Nijhoff; 1984.

[8] Sol H. Identification of anisotropic plate rigidities using free vibration data. Brussels: Vrije Universiteit Brussel; 1986.

[9] De Visscher J. Identification of the complex stiffness matrix of orthotropic materials by a mixed numerical experimental method. Brussels: Vrije Universiteit Brussel; 1995.

[10] Morren G, Bossuyt S, Sol H. 2D permeability tensor identification of fibrous reinforcements for RTM using an inverse method. Composites Part A 2008; 39A(9): 1530-1536.

[11] Morren G, Gu J, Sol H, Verleye B, Lomov S. Stereolithography specimen to calibrate permeability measurements for RTM flow simulations. Advanced Composites Letters 2006; 15(4): 119-125.

[12] Morren G, Bottiglieri M, Bossuyt S, Sol H, Lecompte D, Verleye B, Lomov S. A Reference Specimen for Permeability Measurements of Fibrous Reinforcements for RTM. Composites Part A 2009; 40(3): 244-250.

[13] Hoes K, Dinescu D, Sol H, Vanheule M, Parnas RS, Luo Y, et al. New set-up for measurement of permeability properties of fibrous reinforcements for RTM. Composites Part A 2002;33(7):959–69.

[14] Hoes K. Development of a new sensor-based set-up for experimental permeability identification of fibrous media. Brussels: Vrije Universiteit Brussel; 2003.

[15] Wang V, Hieber CA, Wang KK. Dynamic simulation of and graphics for the injection molding of three-dimensional thin parts. J Polym Eng 1986;7(1):21–45.

[16] Adams KL, Miller B, Rebenfeld L. Forced in-plane flow of an epoxy resin in fibrous networks. Polym Eng Sci 1986;26:1434.

[17] Adams KL, Rebenfeld L. In-plane flow of fluids in fabrics: structure/flow characterization. Text Res J 1987;57:647.

[18] Adams KL, Russel WB, Rebenfeld L. Radial penetration of aviscous liquid into a planar anisotropic porous medium. Int J Multiphase Flow 1988;14(2):203–15.

[19] Levenberg K. A method for the solution of certain problems in least squares. Quarter Appl Math 1944;2:164–8.

[20] Kleinermann J.-P. Identification paramétrique et optimation des procédés de mis à forme par problème inverse. Liège: Université de Liège; 2000.

[21] Verleye B. Computation of the permeability of multi-scale porous media with application to technical textiles. Leuven: Katholieke Universiteit Leuven; 2008.

[22] Verleye B, Croce R, Griebel M, Klitz M, Lomov S, Morren G, et al. Permeability of textile reinforcements: simulation, influence of shear and validation. Compos Sci Technol 2008;68(13):2804–10.

[23] Verleye B, Klitz M, Croce R, Roose D, Lomov S, Verpoest I. Computation of permeability of textile with experimental validation for monofilament and non crimp fabrics. Berlin: Springer; 2007. p. 93–109.

Proceedings of the 8th National Congress on Theoretical and Applied Mechanics, May 28-29, Brussels, Belgium.

Modelling coating quality in fluidised bed coating: Spray model

M. Vanderroost[1], F. Ronsse[1], F. Depypere[2], K. Dewettinck[2] , J.G. Pieters[1]
[1]Department of Biosystems Engineering, Ghent University, Coupure Links 653, 9000 Gent, Belgium
[2]Laboratory of Food Technology and Engineering, Ghent University, Coupure Links 653, 9000 Gent, Belgium
email: mike.vanderroost@ugent.be

Abstract: **Fluidised beds are widely used in industrial applications, for example the coating of particles. Most of the research done on this process concerns the modelling of the hydrodynamics and the mechanics of the three-phase system (solid, gas and liquid) in a fluidised bed reactor, but little research has been performed on developing a quality model of the coating process. A quality model should be able to predict the quality of the process in terms of coating thickness and uniformity and the occurrence of unwanted side-effects, including agglomeration, attrition and spray loss. Therefore, a new quality model was developed for the coating process in a top-spray fluidised bed. The first step in the development of the new model was the creation of an accurate spray model that describes the movement and the heat and mass transfer of the droplets in the coating process. As a first, qualitative, step in the identification of the spray model, a sensitivity analysis was carried out to verify to impact of different input variables on the output variables of the model.**

Keywords: **sensitivity analysis, droplet evaporation, three-phase system**

I.Introduction

Fluidised beds are widely used in industrial applications, with applications in the coating of particles. In the process of top spray coating, particles are fluidised by heated air that is coming from the bottom of the reactor. A nozzle placed above the fluidised bed sprays coating material towards the particles in the form of small droplets (Fig.1). While travelling through the bed, the particles and the droplets exchange heat and moisture with each other, with the air and with the reactor wall.

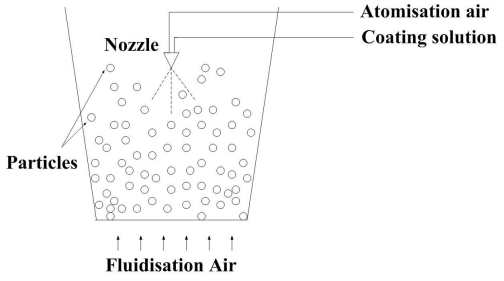

Fig. 1. Fluidised bed coating reactor.

Most of the research done on fluidised beds concerns the modelling of the hydrodynamics and the mechanics of the three-phase system (solid, gas and liquid) in a fluidised bed reactor, but little research has been performed on developing a quality model of the coating process. A quality model has to be able to predict the quality of the process in terms of coating thickness and uniformity and the occurrence of unwanted side-effects, including agglomeration, attrition and spray loss. The first step in the development of the new quality model is the creation of an accurate spray model that describes the movement and the heat and mass transfer of the droplets in a countercurrent airflow. The aim of this paper is to present a sensitivity analysis of the spray model to verify the impact of the different input variables on the output variables of the system.

II.Nomenclature

ACV	Number of axial control volumes
CV	Control volume
D_{dr}	Mean diameter droplets at nozzle (µm)
$GR_{N(P)}$	Translation factor for a negative (positive) perturbation with respect to the general reference value
M_{LN}	Mass flow liquid at the nozzle (l/min)
R	Radial Distance (relative to the central axis)
RCV	Number of radial control volumes
$SR_{N(P)}$	Translation factor for a negative (positive) perturbation with respect to the second reference value
T_{dr}	Temperature of the water droplets (K)
T_{in}	Temperature inlet air (K)
T_{LN}	Temperature liquid at the nozzle (K)
T_{out}	Temperature outlet air (K)
V_{IA}	Velocity inlet air at the bottom (m/s)
X_{in}	Absolute humidity inlet air (kg/kg)
X_{out}	Absolute humidity outlet air (kg/kg)
Z	Height (relative to the bottom of the reactor)
Z_N	Height of nozzle (relative to the bottom of the reactor)

III.Model Description

A.Reactor

The reactor, in which the droplets move, was modelled as a 2D axisymmetric volume which is divided in cylindrical shell control volumes. Thermodynamic behaviour (heat and mass transfer) of the gasphase, the walls and the droplets in the reactor was described by the equations given by Ronsse *et al.* [1]. A graphical representation of the division of the reactor in cylindrical shell control volumes can be found in Fig.2.

B.Droplets

The droplets are assumed to move freely in the reactor and are characterised by temperature, velocity and diameter. They

interact with the air or the wall. The droplets originate from the nozzle with a predefined statistical distribution (diameter, velocity and starting angle distribution). The spray model was largely based upon the work of Ronsse *et al*. [2], but several changes were added: instead of using an individual droplet sub model, the theory of population balances [3] was applied to model a large amount of droplets at the same time with different sizes, starting velocities and angles.

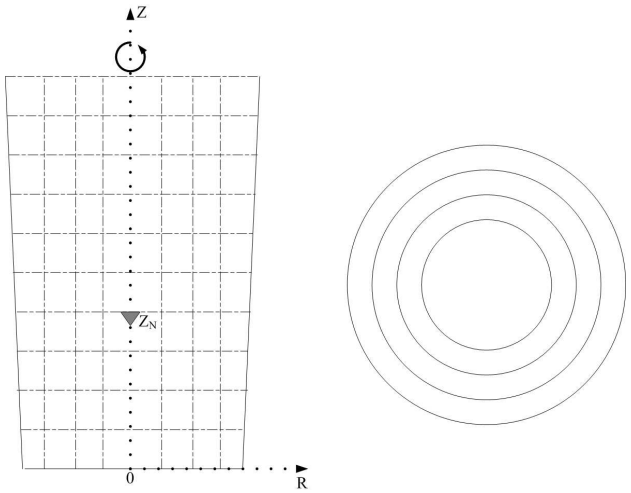

Fig. 2. Discretisation of the reactor into control volumes: (a) Side View, (b) Top View

C.Gasphase

The fluidisation airflow was modelled based on the fluid flow in circular pipes. Depending on the Reynolds number, this flow can be laminar (Re<2300), transitional (2300<Re<4000) or turbulent (Re>4000).

The atomisation airflow, which can be turned on or off in the spray model, was modelled as a jet flow. When the droplets at the nozzle are produced without an atomisation airflow, it is assumed that the motion of the droplets at the nozzle will develop an entrainment flow that is modelled as a jet flow with the same maximum velocity as the droplets at the nozzle and the same spreading characteristics as the nozzle. This means that the air inside the reactor will partly recirculate due to the entrainment airflow. The development of a jet flow is described by a Gaussian velocity profile with a linear increasing standard deviation as a function of the distance to the nozzle. Four important zones, related to the central velocity decay, can be distinguished [4] (Fig.3):

- Zone 1, the initial zone, close to the nozzle, where the central velocity equals the outlet velocity.
- Zone 2, the transition zone where the velocity decreases proportional to $(Z_N\text{-}Z)^{-0.5}$.
- Zone 3, the fully developed zone where the velocity decreases proportional to $(Z_N\text{-}Z)^{-1}$.
- Zone 4, the impingement zone at the bottom of the reactor or the termination zone where the velocity decreases to zero.

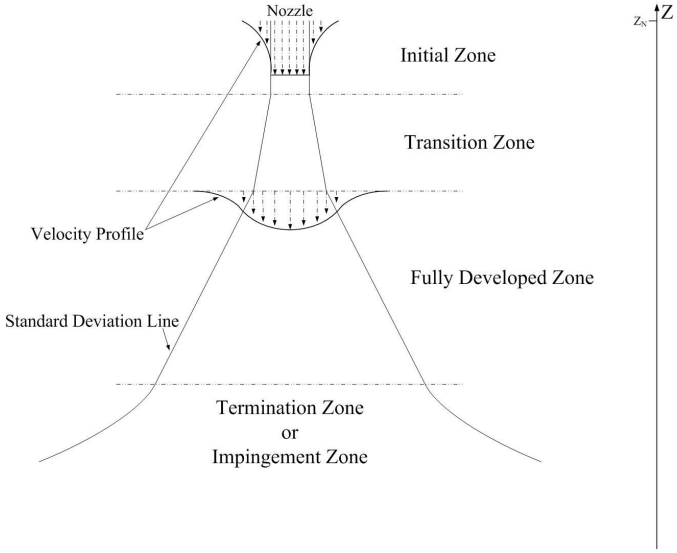

Fig. 3. Atomisation Airflow.

With both airflows a hypothetical airflow pattern was built based on conservation of mass flow in each control volume.

D.Model Implementation

The model was programmed in C++ (Microsoft Visual Studio).

IV.SENSITIVITY ANALYSIS

A.Introduction

To verify the impact of the different input variables on the output variables of the spray model, a sensitivity analysis was carried out. The input variables taken into consideration for the sensitivity analysis are listed in Table I:

TABLE I

INPUT VARIABLES AND THE CONSIDERED REFERENCE VALUES

Input Variables	**General Reference Value**	**Second Reference Value**	**Perturbation**	**Unit**
V_{IA}	0.6	1.4	± 0.1	m/s
M_{LN}	3.0	4.0	± 0.1	l/min
T_{LN}	313.15	333.15	± 1.00	K
D_{dr}	1000	500	± 50	µm
T_{in}	293.15	303.15	± 1.00	K
X_{in}	0.01099	0.00362	± 0.0005	kg/kg

T_{out}, X_{out} and T_{dr} are the considered output variables. T_{dr} is the temperature of the droplets at 0.1m above the bottom of the reactor at the central axis. The main characteristics and dimensions of the reactor, used for the simulations, are represented in Table II and describe the reactor that will be used to experimentally validate the spray model in the near future.

TABLE II

CHARACTERISTICS AND DIMENSIONS OF THE REACTOR

Dimensions	Value	Unit
height reactor	3.0	m
position nozzle	2.5	m
Ø bottom reactor	0.48	m
Ø top reactor	0.48	m
wall thickness	0.01	m
wall density	1390	kg/m³
ACV	30	/
RCV	5	/

B.Methods

To describe the sensitivity of the model, each input parameter was varied individually. The translation factor, describing the relative change of an output variable Ω as a result of a relative change of the input variable ω (= perturbation), was calculated using the one-sided difference approach:

$$\frac{1}{K_\omega} \approx \frac{\omega}{\Omega(\omega)} \cdot \frac{\Omega(\omega+\Delta\omega)-\Omega(\omega)}{\Delta\omega} \qquad (1)$$

For the sensitivity analysis, a general reference set (GR) of values of the input variables was defined. For each input parameter, a second reference (SR) value was defined to investigate how the sensitivity changes for a different reference value of that input parameter. For each reference value, the translation factor was calculated for a negative ($\Delta\omega<0$) and a positive perturbation ($\Delta\omega>0$) of the input parameter. The reference values of the input parameters and the absolute changes can be found in Table I.

C.Results

C.1. Reference Case

The atomisation flow was switched off for all simulations because in the first phase of the experimental validation of the spray model atomisation flow was not present. Each simulation was terminated after 18.0s, i.e. the time after which a steady state condition is certainly reached (Fig. 4).

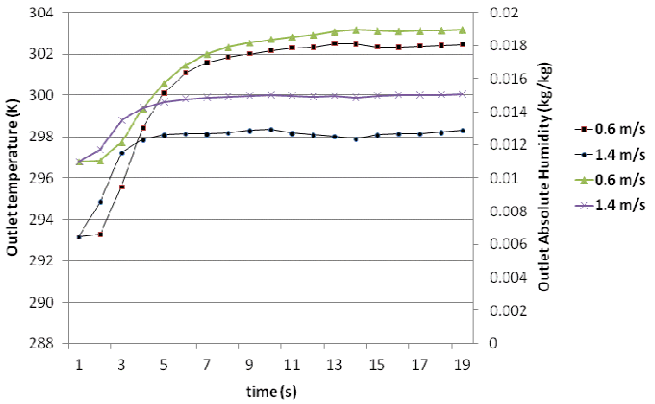

Fig. 4. Simulated evolution of the outlet air temperature and the outlet air absolute humidity for the two reference values of the velocity of the inlet air (V_{IA} = 0.6 and 1.4 m/s).

C.2. Sensitivity Analysis

The results of the translation factor calculations for each output variable have been represented graphically in Figures 5 to 7. The values of the output parameters that are used for the calculations are the values after 18.0s of simulation.

1) Outlet air temperature

For the input variable V_{IA}, the translation factors all have a small negative value, which means that there is an negative proportional relation between these input variables and the output variable T_{out}. This can be explained by the fact that for higher inlet air velocities, the hot vapour from the evaporating droplets will be carried away much faster with the airflow, resulting in a decreasing air temperature and humidity at the top of the reactor. From Fig. 5 it can also be seen that T_{LN} and T_{in} have a relatively large influence on T_{out} compared with the other input variables, which was expected. Although the evaporation rate of the droplets gets bigger for higher values of T_{LN}, the influence of this input parameter on T_{out} and X_{out} (Fig. 6) becomes smaller because the relative change of the evaporation rate of the droplets becomes smaller for higher values of T_{LN}. The absolute humidity of the inlet air has a negligible influence on T_{out}.

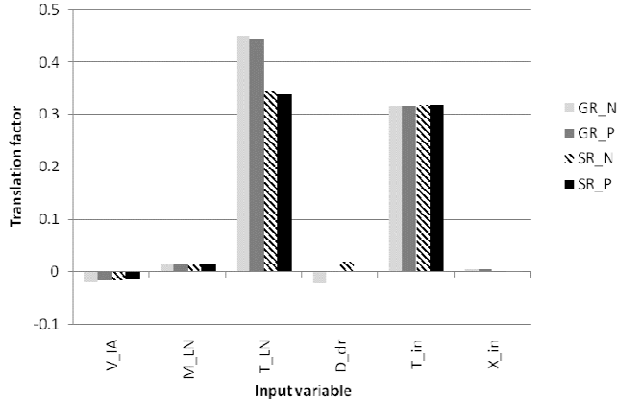

Fig. 5. Translation factors describing the predicted effects of variation on the outlet air temperature, T_{out}

2) Outlet air absolute humidity

Based on Fig. 6, it can immediately be seen that the influence of T_{LN} on the output variable X_{out} is of a magnitude higher than the rest of the input parameters. This means that small variations in the liquid inlet temperature result in very large variations in the evaporation rate of the droplet. The input variables, X_{in} and T_{in}, related to the inlet air, also have an expected important influence on X_{out}. For increasing values of D_{dr}, X_{out} will decrease. This can be explained by the fact that the ratio between the droplet surface area and the droplet volume becomes smaller, which leads to a decrease of the evaporation rate. The positive value of GR_P for the input parameter D_{dr} is a consequence of the small oscillations of the outlet temperature and absolute humidity at the steady state condition (Fig. 4).

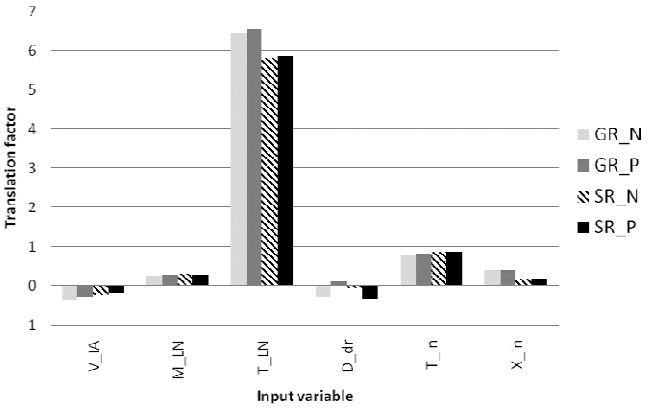

Fig. 6. Translation factors describing the predicted effects of variation on the outlet air absolute humidity, X_{out}

3) Droplet temperature

From Fig. 7 one can clearly see that the input variable T_{LN} which is directly related to the droplets, has an important influence on the temperature of the droplets at 0.1m above the bottom of the reactor at the central axis.

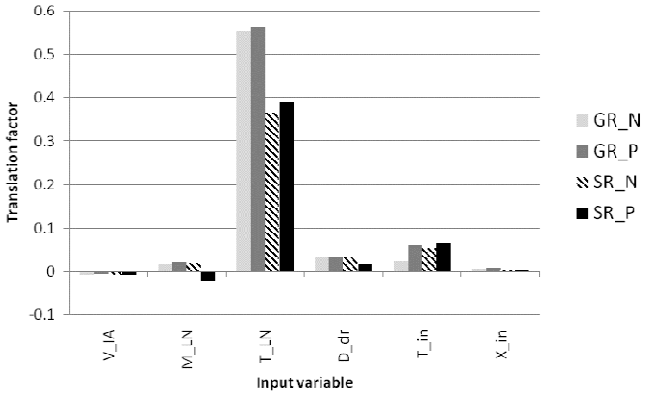

Fig. 7. Translation factors describing the predicted effects of variation on the temperature of the droplets, T_{dr}

V. Conclusions

For inclusion in a fluidised bed model, a spray model has been developed and a sensitivity analysis was carried out. Based on these results it can be concluded that the temperature of the liquid has the largest influence on all the considered output parameters. For the outlet air temperature as output parameter, the input air temperature has a comparable influence. The absolute humidity of the outlet air changes strongly for small changes in the temperature of the droplets at the nozzle. Except for the input parameter T_{LN}, the translation factors for the second reference values were approximately the same as the ones for the general reference values, which indicates a more or less linear correlation. The sensitivity analysis was a first, qualitative, step in the identification of the model. In the near future experiments will be carried out to quantitatively validate the spray model.

Acknowledgements

The authors would like to acknowledge the financial support of the Special Research Fund (BOF) of the Ghent University.

References

[1] F. Ronsse, J.G. Pieters, K. Dewettinck (2005). *Combined population balance and thermodynamic modelling of the batch top-spray fluidised bed coating process. Part I—Model development and validation.* Journal of Food Engineering 78 (2007) 296–307.

[2] F. Ronsse, J.G. Pieters, K. Dewettinck (2005). *Combined population balance and thermodynamic modelling of the batch top-spray fluidised bed coating process. Part II—Model and process analysis.* Journal of Food Engineering 78 (2007) 308–322.

[3] D. Ramkrishna, (2000). *Population Balances, Theory and Applications to Particulate Systems in Engineering*. Academia Press, ISBN 0-12-576970-9.

[4] Z. Yue, (1999). *Air jet velocity decay in ventilation applications.* Installationsteknik, Bulletin n°48, ISSN 0248-141X.

Proceedings of the 8th National Congress on Theoretical and Applied Mechanics, May 28-29, Brussels, Belgium.

Small scale biomass heating systems: standards, quality labelling and market driving factors

V. K. Verma[1], S. Bram[2] and J. De Ruyck[3]
[1,2,3]Vrije University Brussel-Department Mechanical Engineering
Pleinlaan 2, 1050 Brussel, Belgium
e-mail: vverma@vub.ac.be, sbram@vub.ac.be, jdruyck@vub.ac.be

Abstract: **In the present study a comparative evaluation of several existing quality labels and standards for small scale biomass heating systems (BHS) and the biomass fuels they use was performed. With the introduction of pellet fuels, biomass heating technology achieved enough maturity to successfully compete with oil/gas heating devices in terms of ease of use, utilization of energy and pollutant emissions.**

From indoor air quality and related health risks point of view, quality labelling of both BHS and fuel they use leads to stricter emissions, efficiency and safety requirements as compared to National and EU standards. Several measures supporting this green energy market in the active countries (Sweden, Nordic countries, Germany, France and Austria) were investigated. It was found that policies and financial incentives such as the Finance Law (2005-2009) in France and Market Incentives Programme (1999-2006) in Germany are the most successful. German regulations and quality label (Blue Angel) provide the stringent quality requirements for residential BHS.

In Belgium, Wallonia is the most active region for biomass energy utilization (83470 kW for residential heating in 2007). A quality label for small scale BHS however does not yet exist. An equivalent label (Optimaz) exists for oil fired residential boilers. Emphasis has been placed upon using Optimaz as a reference and to compare with other existing quality labels. As a result, an effort had been made to move ahead in the preliminary study for development of a quality label for Belgian.

Keywords: **Quality labelling; quality standards; pellets fuel; pellet boilers.**

I. ABBREVIATIONS

1.BImSchV- implementation of the first federal emission control ordinance, Germany.

AEN/CTN- the national technical standardisation committee on solid biofuels, Spain.
BHS - biomass heating systems.

Boverket- the national board of housing, building and planning, Sweden.

CEN/TC- European committee for standardization.

CO- carbon monoxide.

DIN-CERTO- certification institute of DIN-Deutsches institute für normung- German standardisation institute.

EN- European standard.

EU- European Union.

kW- kilo watt.

MLE- medium and large energy systems.
NOx- nitrogen oxides.

OGC- organic gaseous carbon.

RES- renewable energy system.
SIS- the Swedish standards institute.

SME- small and medium energy systems.
UZ 37- eco-label directive-37, Austria.

Wt- weight.

II. INTRODUCTION

The potential benefits of biofuels (i.e. solid biomass, biodiesel and bioalcohols, including bioethanol and biobutanol, also called biogasoline) have been recognised throughout the 20th century with their local availability, environmental friendly image, lower global warming potential as compared to the fossil fuels. With the turn of the century it became clear that the fossil fuel age is coming to an end [1], and fossil residential heating accounts for about 15% of the total energy consumption in several European countries. In the 1950s, oil fired residential heating became very popular in most of the European countries; however, oil heating enthusiasm decreased during the 1970s oil crises. Since then the interest in oil burning has continued to fall with increasing oil prices and environmental awareness, and biofuels like wood have become more popular being CO_2 neutral [2,3,4]. Traditional residential wood heating systems are inefficient and emit large quantities of pollutants, especially particulate matter. Continuous progress in technology in pellet heating technology however reduced these emissions remarkably [2]. Already in the 1970´s, wood pellets were manufactured in USA and Canada and pellet burners were developed. In 1980´s, for the first time wood pellets were introduced into North America and since then, wood pellet firing is increasingly used in private households. In Europe, wood pellets were utilized for heating systems for the first time in Sweden and Denmark, also in the 1980´s [2]. In Germany industrial wood pellet production started as recently as the late 1990's and the use of wood pellets as fuel is allowed since 1996 also for small firing plants with a nominal load below 15 kW. In Austria, (imported) wood pellets and pellet room heaters which were developed following the US-American models are on market since the 1990´s. Based on log wood and wood chips firings, the Austrian heating manufacturers

built additionally special pellet boilers in the last years [3]. The predictable raise in fuel prices and taxes, as well as high technical standards for BHS, their environmental friendly image and direct government incentives seem to be sufficient motivations to invest in this green energy technology, in several EU countries [1,2,3,4,5].

In the EU context, the majority of today's small-scale biomass heating systems (BHS) are installed in Sweden, France (traditional matter, simple technology and cheap), Austria, Switzerland and Germany (sophisticated and more expensive technology), with a still raising tendency [4]. The Italian market is dominated by pellet stoves [5]. With the introduction of pellet fuels and pellet burners, biomass heating technology acquires enough maturity to successfully compete with existing oil/gas heating devices in terms of easy of use, utilization of energy and pollutant emissions in countries like Germany, Sweden, Austria, Switzerland and Italy. After having overcome initial barriers like familiarity, education and quality control, market in these countries has fully developed [2,4,5,6,7,8,9].

Compared to the conventional heating systems, such as oil or gas boilers, biomass heating technology still has some disadvantages in terms of more space demand, efficiency, emission and maintenance [3,4,9,10,11]. Another barrier is the adoption of widespread biomass fuels for combustion, which makes it difficult to setup particular fuel standardization criteria as is the case with oil or gas fuel. However, intelligent design, sophisticated technology and use of high quality fuel (wood pellets) can minimize these disadvantages. Further, the small water content and the small granulometry of the wood pellets lead to an optimal combustion with low emissions [4,11].

However, extensive use of biomass fuels in the residential sector might lead to poor indoor air quality and related health risk if obsolete boilers are used or heating units are inappropriately used or poorly maintained. Emission regulations are necessary to protect inhabitants from hazardous gases, dust and to encourage the manufacturers to optimize their products for the lowest possible emissions [4,10,12]. Therefore, quality **labelling** of such devices, as well as of the fuel they use, is one of the upmost important concerns [7,10]. Some European countries are active in the respective national/regional regulations and/or equivalent quality labels. In most of the countries either these regulations are inexistent (e.g. Belgium) or the countries have decided to wait (e.g. Spain) for common EU regulations, standards and quality labels for BHS and/or for biomass fuels [2,5]. In addition to this unequal approach, high capital cost and risk perception may hamper the growth of this green energy market [4,7,13] and it is important to understand the local regulations, policies, incentives and quality labels in countries with established biomass heating market, in order to establish a balanced sustainable heat market **[**14**].**

Belgium is a federal state with three distinct regions and energy regulations, Flanders, Brussels and Wallonia. There are no national regulations for emissions from residential BHS, even in Wallonia is the most active region [13,15] for biomass energy utilization. Only a limited work has yet been done in order to provide the knowledge of existing regulations and quality standards concerning residential BHS in the EU countries. Therefore, the present work concentrated on comparative evaluation of the concerned matter. The Belgian 'Optimaz' label for oil heaters has been advanced as a reference to move ahead on the preliminary study for the development of a quality label for pellet boilers in Belgian situation. Furthermore, supporting factors for uplifting this green heating market were investigated.

III. METHODOLOGY

The research work presented here is based on the literature study from several National and International journals/conference proceedings. Informations on quality labels were collected from concerned quality label granting bodies and data are presented here with major emphasis on the pellet boilers only. Distinction has been made for the quality standards for pellet fuels and pellet fuel burning devices (i.e. pellet boilers). The term 'Pellet boiler' used in this article represents a 'Unit' consisting of a pellet burner with a standard boiler. In Belgium, an equivalent quality label (Optimaz) exists for liquid fossil fuel burning residential boilers, which is considered here as a reference. Data on the Belgian pellet heat market were collected from http://www.cra.wallonie.be.

IV. RESULTS AND DISCUSSION

A. Government Regulations For Residential BHS

Governmental regulations are necessary in order to ensure a safe, environmental friendly and healthy operation of boilers via forcing the manufacturers to optimize their product's performance. At the EU level, the European standard 'EN 303-5, 'Heating boilers for solid fuels, manually and automatically stocked, nominal heat output up to 300 kW- Terminology, requirements, testing and marketing' was published in 1999. However, countries like Germany, Austria, Great Britain, Switzerland and Sweden are active with their own national standards which are usually stricter in terms of emissions (CO, OHG, NO_x and particulate matters), efficiency and safety requirements as compared to EU regulations (Table 1).

The EU standard, EN-303-5 was published in Germany as DIN-EN-303-5 in 1999 and identified three quality classes of boilers, based on efficiency and emission requirements (Table 2). However, due to the emission limit values of **1.BimSchV**- Germany **(**Implementation of the first federal emission control ordinance-Germany**)**, only the class-2 and class-3 boilers of this table were authorized. In Table 1, only limit values for class-3 boilers were listed to make an easy comparison. German regulations are the stringent among other exiting European and/ or national regulations in term of permissible efficiency and emission values. In Germany these standards are given by 'German Ministry of Economic Affairs and Technology'. If a boiler or stove does not reach these standard requirements, no subsidy is given by German Government. For a small-scale pellet combustion units (3-50 kW) equipped with automatic pellet feeding, a subsidy of 55 Euro per kW was given by German authority [16].

In Sweden, use of pellet boilers and pellets fuel for house hold heating purposes is regulated by Swedish regulations

given by 'The National Board of Housing, Building and Planning' (Boverket) [17] and 'The Swedish Standards Institute' (SIS). Boverket recommends limit values for small scale biomass combustions only, whereas SIS requires their compliance with the values given by European Standards EN-303-5, which has since 1999 been applied as Swedish Standard (Table 1) [4].

TABLE I
OFFICIAL REGULATIONS FOR EMISSIONS FROM SMALL-SCALE WOOD COMBUSTION SYSTEMS.

Regulation	Mode	Nominal power (kW)	Limit value for emission (mg m^{-3} dry flue gas with 10 vol-% O_2, 0°C, 1013 mbar)		
			CO	OGC	Dust
EN 303-5	M	< 50	5000	150	150
	A	< 50	3000	100	
Swedish Boverket	M/A	< 50	2000	150[a]/ 250[b,c]	100
German – FME&L[c,d]	M/A	< 15	250[e]/ 500[f]	-	50
BimSchV[c,g]	M/A	15-50	4000	-	150

(Source: Fiedler F., 2004)

[a] For pellet boiler,
[b] For pellet heating stoves.
[c] Limit values are defined for 13 vol-% O_2 in the dry flue gas.
[d] Boiler efficiency has to be minimal 85%.
[e] Nominal load.
[f] Low load.
[g] No regulation for boiler/stoves smaller 15 kW.
M- Manual.
A- Automatic.
German –FME&L- Federal Ministry of Economics and Labour

In Austria, BimSch (Federal Low for Emission Protection- Austria) regulates the emissions from pellet burning appliances in addition to Ö-Norms-EN-303-5 as an equivalent EU regulation. Styria district Government applied **15a-B-VG** to the independent domestic wood burning appliances with aim to optimize the energy conservation and was recognized in July 1998 as the Austrian federal standard by the Austrian government. The requirements that an appliance had to meet were one of the most stringent in EU countries with extremely low emission rates of pollutants (CO, NO_x, hydrocarbons and dusts) and a compulsory minimum heat output efficiency of 78% [18].

EN 12809 (Residential independent boilers fired by solid fuel-Nominal heat output up to 50 kW- Requirements and test methods) was published in 2001 and specified the requirements related to the design, manufacture, construction, performance (efficiency and emission), safety and user instructions together with associated test methods and test fuels [19]. CEN/TC-57 (Pellet burners for small heating boilers- Definitions, requirements, testing and marking) is under preparation, which will cover pellet burners with a nominal thermal load of not more than 70 kW, intended to fit with appropriate boilers for hot water generation in compliance with EN-303-2 and EN 303-5, fired with high quality pellets as defined in prEN-14961-2 (CEN/TC 335/WG2 N143-Dated 12/2007). This standard will cover all the external equipments which influence the safety of systems; and will describe the requirements and test methods for safety, combustion quality, operating characteristics and maintenance. In addition, EN-14785 (Residential space heating appliances fired by wood pellets- Requirements and test methods) was approved by CEN in 2006. It also provides guidelines for a pellet burning appliance in order to fulfil domestic hot water and/or central heating hot water demands [20].

In Belgium, at present there is no National or Federal regulation for residential pellet boilers. However, "Royal Decree concerning output requirements for new boilers for warm water, fed with liquid fuels and with a nominal capacity which is equal to or higher than 4 kW and equal is to or lower than 400 kW" was published in 1997. It defined the output requirements for a liquid fossil fuelled fired boiler (4-400 kW). Similarly, the "Royal Decree governing NO_X and CO emission values of flue gases from central boilers and burners, with a nominal thermal capacity equal to or lower than 400 kW-(Belgian Bulletin of Acts, Orders and Decrees of 30 January 2004" was published in 2004, which defines NO_X and CO emission requirements for liquid fossil fuelled boilers and burners up to 400 kW [20,21].

TABLE II
QUALITY CLASSES OF BOILERS USING BIOGENOUS FUELS AS PER DIN-EN-303-5 (AUTOMATIC SYSTEM WITH A NOMINAL LOAD < 50 KW).

Parameter	Class 1	Class 2	Class 3
Boiler efficiency	47+ 6 log Q_N	57+6 log Q_N	67+6 log Q_N
CO[a] (mg m^{-3})	15000	5000	3000
OGC (mg m^{-3})	1750	200	100
Dust[b] (mg m^{-3})	200	180	150

[a] Limit values are given for both at nominal and low load.
[b] Values are given only at nominal load.
Q_N Nominal heat output.
OGC- organic gaseous carbon.
Note: Limit values are defined for 10 vol -% O_2 in the dry flue gas.

B. Government Regulations For Biomass Fuel (Wood Pellets) For Residential Heating

Use of biomass pellets for residential heating incorporates benefits such as reduced CO_2 emissions from combustion of fossil fuels [22], reduced SO_2 formation through a decrease in fuel bound sulphur and reduced NO_x formation through a reduction in fuel bound nitrogen [11,23,24]. Because of lower emission values, small-scale wood pellets burning appliances (up to 15 kW) were exempted from air quality regulations in Germany [16]. However, high quality of pellet fuel is desirable for high combustion characteristics of any appliance [3,56,12,25,26]. The higher is the water content, the lower will be the density and consequently the heating values [25]. Alkali metal contents of pellets affect ash properties and are responsible for slagging problems of boilers [27,28,29,30]**.** Physico-mechanical properties (diameter and mechanical durability) of pellets play an important role in pellet supply from hopper to burner. Higher fine contents of pellets may cause blockage of the pellet supply system, therefore, additives/ binding agents can be used to improve the pressing (mechanical durability) properties of raw materials used wood pellets production [31,32]**.** Such a binding agent could be natural substances, such as corn or maize starch, but also chemical glues, which should not be used but are tolerated by Swedish standard (SS 187120- Table 3). In order to ensure high combustion efficiency with the least gaseous and particulate emissions, high quality of pellet fuel is a prerequisite [4].

In most of the European countries, national quality standards for wood pellets are inexistent either because;

- There is no or only a small domestic pellet heat market established, the market is too young and amounts of domestic consumption is too unimportant.

Or

- Some countries with a vital pellet market have stopped or even not started national standardisation activities, as they decided to wait for the European standard.

Many European Countries, such as Estonia, Latvia, Lithuania, Greece, Cyprus, Poland, Portugal, Spain, Malta, Netherlands, Luxemburg, **Belgium**, Ireland, Hungary, Czech Republic, Slovakia, Slovenia or Bulgaria do not have any National standard as there is no well established pellet market. However, some countries such as Spain has started developing standards for solid biofuels via 'The National Technical Standardisation Committee on Solid Biofuels (AEN/CTN 164)' [2,4].

Finland and Denmark, the biggest pellets producers have decided to wait for the European pellets standard (CEN/TC 335). In Denmark, 'Biomass Regulation (BEK-638, 03/07/1997)' is the only legislation in this area, which directed that wood pellets must be produced from clean wood without any kind of contamination. A maximum of 1% (by wt) remains of glue (fibre board's) is allowed, however, there is no regulation for e.g. water or ash content which are important parameters for the combustion properties [2,4,10].

A document (prEN-14961-2) has been prepared by the Technical Committee CEN/TC 335/WG-2-N143 'Solid Biofuels- Fuel specifications and classes -Part 2: Wood pellets for domestic consumers' to put forward a common EU standard for pellet fuel for domestic applications [33]. Meanwhile technical standards prCEN/TS-14588: 2003(E)- Solid biofuels, terminology, definitions and description, as well as prCEN/ TS-14961: 2004(E)- Solid biofuels- Fuel Specifications and classes, which also include pellets, are available. National standards for pellet fuel so far exist in Switzerland, Sweden, Germany, Austria, U.K. and Italy with variations from prEN-14961 (Table 3). As the EU standard come into existence, member countries will discard their National standards [2].

The Italian standard, CTI-R-04/5, was published in March-2004 for solid biofuels and defined the quality requirements of bio-pellets for energetic purposes. This standard already relates to the technical specification defined by CEN-TC335.

The Swedish standard (SS-187120) differentiates wood pellets into three groups (Table 3) based on the dimensions and ash content [18,35]. It is thought that a diameter of 6mm is optimal for most of the transport systems in Austria and Germany. However, in Sweden a diameter of 8 mm is more common. An important quality parameter, the abrasion value which determines the mechanical stability of pellets, is tested in Austria, by so called lingo-test. Austrian regulations (Ö-Norms) provide the stringent quality requirements for pellet fuel [2,4]. In Belgium, DIN*plus* certification of wood pellets is the dominated one in absence of appropriate Belgian quality labels/standard. Pellets-mandi (www.pellets-mandi.be) was the first to get DIN*plus* certification [36].

C. Quality labelling of residential BHS: Optimaz Vs others

In addition to these governmental regulations, some customer made regulations exist in several EU countries in the form of ecolabel /quality label/marks which strengthen the biomass heating market. Globally, the earliest labelling for wood stoves seems to be the U.S. EPA-labelling, which is well described in EPA-600/R-98-174a. In Europe, Scandinavian countries (Swan), Sweden (P-mark), France (Flamme Verte), Germany (Blue Angel), Austria (UZ-37) and Ireland (SEI) are active with quality labelling of residential BHS. Most of the quality labels stricter requirements of efficiency, emissions (CO, OGC, NO_x and dust) and safety as compared to the respective National or EU regulations (Table 4). Therefore, a quality labelled boiler has a better reputation in any of these market. For the sake of convenience only quality requirements for boiler are presented in Table 5.

TABLE IV

QUALITY LABELS STRICTER THE EMISSIONS REQUIREMENT (mg m^{-3} DRY FLUE GAS WITH 10 VOL-% O_2) OF BIOMASS BOILERS AS COMPARED TO THE NATIONAL REGULATIONS.

Boiler	Sweden		Germany		Austria	
	Au	Swan label	Au	Blue Angel	Au	UZ-37 mg/MJ
Heat range	≤50 kW	≤100 kW	≤15 kW	≤15 kW	15-50 kW	≤400 kW
OGC	150	70	-	5[e]/5[f]	-	3[e]/3[f]
CO	-	1000[a]/ 2000[b]	250[e]/ 500[f]	100[e]/ 300[f]	4000	60[e]/ 135[f]
Dust	-	70	50	20[e]/ SV[f]	150	15[e]/SV[f]

[a] Automatically fed boiler.
[b] Manually fed boilers.
[e] Nominal load
[f] Low load.
SV-Value must be specified.
Au- authority.

Swan-mark is a common label for environmentally friendly products in Nordic countries (Sweden, Norway, Denmark, Iceland and Finland), which also specifies the requirements for pellet boiler, stoves and pellet fuel, but so far only one manufacturer had certified its pellet boilers (LIN-KA Maskinfabrik A/S, Denmark). A Swan labelled product has advantage to be sold in all member countries with an environmentally safe reputation. Swan, in addition to the requirements of safety, emission and efficiency (while burning Swan labelled wood pellets), restricted the use of halogenated plastic components and heavy metal pigments in manufacturing/ packaging of the boilers. Minimum size requirements for a hot water storage tank to be attached to a Swan labelled boilers is a plus (Table 6).

Sweden is active with P-marking of pellet burners (≤ 25 kW) and boilers (≤ 100 kW) which additionally require the minimum number of safety devices against blow back fire for pellet boilers with (at least two) or without (at least three) an integrated pellet hopper [37]. P-mark limits the maximum allowable auxiliary power consumption by a pellet boiler (≤ 1 % of thermal output) as by Blue Angel and UZ-37. This does not cover any requirement for external fuel transport systems (feed systems) between the fuel store and the burner.

Ireland is active with SEI (Sustainable Energy Ireland) with minimum allowable efficiency of 80 %, however, for

emissions, the boiler must fulfil the requirements of EN-303-5 in addition to compliance with the Low Voltage Directive (TH 42075; Directive 73/23/EEC) and the Machinery Directive (TH 42073; Directive 98/37/EC) of CE marking [38].

In 2003, requirements for certification of wood pellet heating systems with the label 'Blauer Engel' have been introduced by the 'German Federal Environmental Agency'. The first certified products were the pellets stoves of the company Wodtke. Blue Angel defines the most stringent emission and efficiency requirements and strictly recommends the use of DIN*plus* certified pellets as fuel [39]. Maximum 1 % auxiliary power consumption of the total heat output is allowed. UZ-37 is an equivalent quality label in Austria which allows ≤ 2.5% radiation heat losses from a pellet boiler (Table 5) while using O-NORM-M 7135 certified wood pellets (Table 3). In France, 'Flamme Verte' is the active label for residential BHS, however; emission requirements of this label are poor as compared to the other existing quality labels in European countries (Table 5).

In Belgium a quality label for pellet boilers does not yet exist. The Optimaz label (http://www.informazout.be/nl/home/optimaz_webdoc) represents an equivalent label for liquid fossil fuelled residential boilers (condensation and non condensation boiler, ≤ 70 kW) which could be taken as a reference point for the development of quality label for pellet boiler in Belgian situation. Inspirations to select Optimaz as a reference point came from its good reputation on Belgian market, involvement of the same testing laboratory (www.aardgas.be/ www.gaznaturel.be) for pellet boiler testing and maximum output range (70 kW) of Optimaz for residential boilers. Furthermore, a pellet boiler should be comparable for ease in use and performance (emissions and efficiency) to an existing oil boiler, where Optimaz provided an excellent example in Belgian context.

DIN*plus* certified and/or prEN-14961 equivalent wood pellets could be recommended as standard pellet fuel to be used for residential heating purposes in Belgian situation, as DIN*plus* certified pellets have advantages, being the stringent, dominated over Belgian pellet marker with its good reputation and quality characteristics close to prEN14961. The Belgian biomass heat market represents a potential LACK/ NEED of 'Belgian Quality Label' for pellet fuel as well as for pellet boilers by the fact that in absence of 'Belgian Quality label', DIN*plus* certified pellets dominated over Belgian pellet market (http://www.pellets-mandi.be/; http://www.badgerpellets.com/; http://www.granilux.eu; http://www.distripellet.be/) and pellet boiler manufactures apply for quality labelling of their boilers to nearby countries.

At EU level, a quality label named 'Eco-Label with a flower logo' had been developed based on criteria specified by the EU Eco-labelling Board (EUEB), however, limit values for emission and efficiency have not yet been finalized. The concerned work is ongoing under the supervision of bio-intelligence services [40,41].

D. BHS: market driving factors with special reference to Wallonia- Belgium market

In most of the EU countries pellet fuel is cheaper than fossil fuels, even though, there are a few crucial factors which hamper the biomass heating market in several EU countries even being potentially rich in biomass resources available for biomass heating purposes (e.g. Belgium). At national level, the two most important factors to accelerate or slow down pellet heating market are;

- Regulations/ policies and
- Financial incentives

Only a few European countries (Denmark, Sweden, Austria, and more recently, Germany and France) have national policies that encourage biomass for heat. Regulations such as 'Federal Building Code and Federal Land Utilization Ordinance' in Germany or 'Permit Procedure' in Sweden limited bioheat development whereas regulations like 'Wood Fuel Programme' in France or 'Energy Saving Ordinance' in Germany had a positive impact [42]. Increased sale of pellet heating devices in Ireland was directly related to the Irish Government aggressively subsidized, 'Bioheat Development Programme'. The scheme started with massive grants for wood fuel boilers which in some cases covered nearly the total cost. As a result, the sale of Irish boilers was increased more than 50 % [42]. Financial help for replacing old oil or wood boilers with modern pellets technology was made available within the framework of 'Swedish Local Investment Program (**LIP**)' for environmentally friendly technologies up to 2002. Meanwhile a new programme called 'The Local Climate Investment Program (**KLIPM**)' has been started containing similar incentives. In France 'Finance Law (2005-2009)' introduced a tax credit for sustainable development and rational use of energy via promoting high efficiency equipment and represents an excellent example of direct effect of financial support on pellet heat market (Fig. 1). BHS are eligible for a tax credit up to 50 %, however, a minimum efficiency of 65 % is a prerequisite and equipments have to meet a certain technical standard.

In Germany, the MAP (Market Incentives Programme, September, 1999) has supported automatically feed wood pellet heating systems in a range of 8-100 kW with a grant of 25 euro per kW and at least 1000 euro for systems that reached an efficiency of 90 %. In addition, the systems which met particularly challenging environmental requirements (i.e. secondary measures for emission reduction) got a double amount of this basic grant. However, stop of this subsidy affected the growth of pellet boiler market drastically (Fig. 2) in second half of 2006 [8,42].

The Government of Vorarlberg (one of the smallest and the westernmost of nine Austrian federal provinces) had been promoting various kinds of biomass energy technologies since early 1990s, mainly by means of non-refundable capital grants. In the Energy Concept Vorarlberg 2010 ("News from the Future"), the goal was stipulated to increase the use of biomass for energy between 1996 and 2010 by 30 % [7,43]. The Austrian government recently introduced a promotion programme, 'Förderaktion Holzheizungen-2008 (Promotion action for wood heating-2008)' from 1 April to 30 November 2008. The programme supported all central heating systems in private houses that were fuelled with pellets, wood chips or firewood. Grants were 800 euro for pellets systems and 400 euro for systems using wood chips or firewood. This grant could be combined with other subsidies from municipal or provincial bodies. In order to receive a grant, thermal output is

limited to 50 kW and emission limits must satisfy the Austrian Ecolabel-UZ 37 [44].

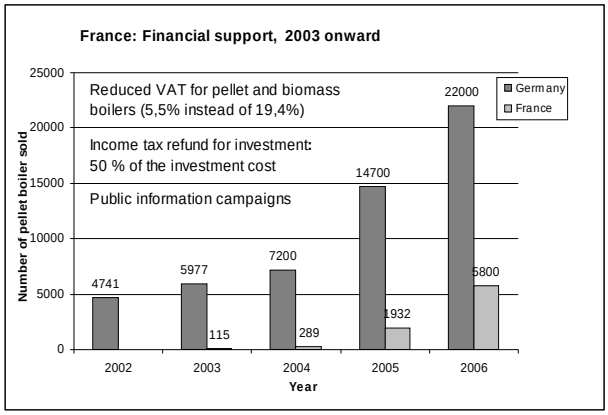

(Source: www.aebiom.org)

Fig. 1. Effect of financial support on pellet heating market in France.

(Source: www.aebiom.org)

Fig. 2. Effect of stop of financial support on pellet heating market in Germany.

In Belgium, financial incentives have been setup for investment on renewable energy systems (RES) at federal and regional levels such as the **ECHOP** programme (Wallonia region). Subsidies are granted to companies investing in renewable energy systems (20 percent for SME and 10 percent for MLE). In the Flemish region, a Research & Development programme and incentives for renewable electricity market [0.05 euro per kWh produced from wind and hydro energy and 0.025 euro per kWh produced from other resources (mainly biomass)] are available (www.erec-renewable.org). Similarly, the Wallonia region is supporting an NGO called **ERBE** whose objective is to promote wood biomass utilization for heat. ERBE, in addition to carrying out information campaigns, proposes audits and feasibility studies for biomass heat projects. Following supports are available in the Wallonia region for pellet heating devices by authorities [13,15,36,42,45].

Full automatic pellet boilers = 1750 euro
Full automatic pellet stove boilers = 1500 euro
Pellet stoves = 250 euro
Tax deduction at federal level

However, to receive these grants equipments have to comply with European Standards. New Wallonia subsidies for biomass devices requested these devices to respect quality criteria in terms of efficiency and CO emissions. The devices which respect these criteria are brought together in a list regularly updated and available on websites http://energie.wallonie.be or http://www.valbiom.be.

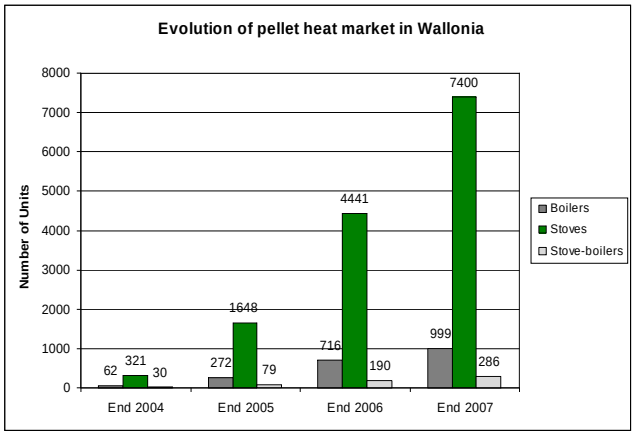

(Source: Marchal D., 2007)

Fig. 3. Pellet heat market growth in Wallonia-Belgium.

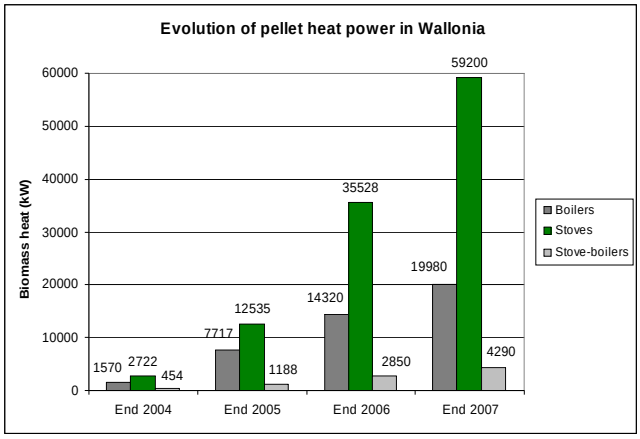

(Source: Marchal D., 2007)

Fig. 4. Biomass heat (kW) market growth in Wallonia- Belgium.

As a result of these promotions schemes, the Wallonia biomass heating market is exponentially growing (Fig. 3 and Fig. 4). At the end of 2007, the number of boilers and stoves sold in Wallonia market was 16 and 23 times higher than in 2004. The number of sold combi-stove-boilers multiplied 10 times over the same period of time. Residential heat generation from biomass was 18 times higher at the end of 2007 (83 470 kW) as compared to 2004 (4746 kW). Even after such a potentially growing biomass heat market, there are no National regulations or quality labelling scheme for BHS in Belgium. Therefore, the Belgian pellet heat market represents a potential lack of 'Belgian Quality Label' for pellet fuel as well as for pellet boilers by the fact that in absence of 'Belgian Quality label', DIN*plus* certified pellets dominates over Belgian pellet market (http://www.pellets-mandi.be/; http://www.badgerpellets.com/; http://www.granilux.eu; http://www.distripellet.be/)) and

boiler manufactures apply for quality labelling of their boilers to neighbouring countries. Quality labelling might be helpful to further uplift this green energy marker by winning the trust of local people/consumers without the boundaries of federal regulations and to promote this green energy in other federal states of Belgium in absence of National regulations. The other regions are poor in terms of information systems and financial incentives to promote pellet heating market.

V. CONCLUSIONS

Biomass heating systems from an energetic perspective can provide a very attractive and feasible option for 100 percent renewable domestic hot water and space heating demands. In several European countries existing technology is working reliably and most of the products are tested and certified. The technology, design of pellet stoves/boilers and quality of pellet fuels sold across Sweden, Austria, Switzerland, Italy, Germany and so on differs only marginally. Some regulations at EU level have already been published and some are on their way; which mainly concern efficiency, emissions, safety techniques and installation in homes. German standards as well as quality label (Blue Angel) provide the stringent permissible limits for emission and efficiency for the pellet boilers.

Financial incentives play a key role in development of pellet heating market. The pellet heat market is booming in several EU countries however, lack of sufficient information/ promotion systems for local public and governmental financial supports (incentives) are slowing down this growth, even after having great biomass resource potential e.g. Belgium. Furthermore, strong political regulations and financial incentives needed to financially support the consumers willing to use this green heating technology but high capital cost of the system slows down their enthusiasm.

The Belgian pellet heat market suffers from a potential lack of 'Belgian Quality Label' for pellet fuels as well as for pellet boilers. A Belgian Quality Label might help to uplift the pellet heat marker by winning the trust of consumers. In Belgian context, the "Optimaz label" could be taken as a reference point to move ahead for the development of a quality label for residential pellet boilers. Future research work will compare real life emissions from selected boilers with the laboratory measurements.

ACKNOWLEDGEMENTS

The present project is supported by the Belgian Government through the Belgian Science Policy, contract SD/EN/04A Q-Direct, coordinated by 3E. The collaboration of Prof. Dr. Ir. Y. Schenkel, Mr. M. Temmerman and Mr. D. Marchal from 'Walloon Agricultural Research Centre Gembloux', Belgium is also gratefully acknowledged.

REFERENCES

[1] R. Luque, L.H. Davila, J.M. Campelo, J.H. Clark, J.M. Hidalgo, D. Luna, J.M. Marinas, A.A. Romero, Biofuels: a technological perspective. Energy & Environmental Science,1, 5(2008) 542-564.

[2] B. Hahn, Existing guidelines and quality assurance for fuel pellets: Pellet for Europe, UMBERA. 2004.

[3] J. Vinterback, Pellet 2002: The first world conference on pellets, Biomass and Bioenergy. 27 (2004) 513-520.

[4] F. Fiedler, The state of the art of small-scale pellet-based heating systems and relevant regulations in Sweden, Austria and Germany. Renewable and Sustainable Energy Reviews, 8 (2004) 201-221.

[5] www.pelletcentre.info

[6] T. Klason, X.S. Bai, Computational study of the combustion process and NO formation in a small-scale wood pellet furnace, Fuel. 86(10-11)(2007) 1465-1474.

[7] R. Madlener, M. Koller, Economic and CO_2 mitigation impacts of promoting biomass heating systems: An input–output study for Vorarlberg, Austria, Energy Policy, 35 (12)(2007) 6021-6035.

[8] A.Verbruggen, Stalemate in energy markets: supply extension versus demand reduction, Energy Policy, 31(14)(2003) 1431-1440.

[9] J. Kjällstrand, M. Olsson, Chimney emissions from small-scale burning of pellets and fuelwood-examples referring to different combustion appliances, Biomass and Bioenergy. 27 (6)(2004) 557-561.

[10] I. Obernberger, G. Thek, Physical characterisation and chemical composition of densified biomass fuels with regard to their combustion behaviour, Biomass and Bioenergy. 27 (2004) 653-669.

[11] W. Heschel, L. Rweyemamu, T. Scheibner, B. Meyer, Abatement of emissions in small-scale combustors through utilisation of blended pellet fuels, Fuel Processing Technology. 61(3)(1999) 223-242.

[12] M. Olsson, J. Kjällstrand, Low emissions from wood burning in an ecolabelled residential boiler, Atmospheric Environment. 40 (6)(2006) 1148-1158.

[13] D. Marchal, Current development on Belgian pellets market. *In:* European pellet Conference, Wels (Austria), 1 March, 2007.

[14] A. Verbruggen, Stalemate in energy markets: supply extension versus demand reduction, Energy Policy. 31(14)(2003) 1431-1440.

[15] D. Marchal, R. Crehay, A. Stappen, G. Warnant, Y. Schenkel, Wood pellet use in Wallonia (Belgium): Evaluation and environmental impact. Pellets (2006) 225-227.

[16] Erste Verordnung zur Durchführung des Bundes-Imissionschutzgesetzes (Verordnung über kleine und mittlere Feuerungsanlagen, 1-BImSchV) BGBl. I S. 491, 1997.

[17] http://www.boverket.se

[18] Boverkets byggregler, BBR 7, BFS 1998:38, Boverket., 2002, http://www.boverket.se, 1998. Erste Verordnung zur Durchführung des Bundes-Imissionschutzgesetzes (Verordnung über kleine und mittlere Feuerungsanlagen, 1-BImSchV) BGBl. I S. 491, 1997.

[19] EN 12809, Residential independent boilers fired by solid fuel-Nominal heat output up to 50 kW- Requirements and test methods. (2001/A1).

[20] EN 14785, Residential space heating appliances fired by wood pellets- Requirements and test methods. (2006).

[21] http://www.ibn.be/NL/homenl.html

[22] S. Bram, J. De Ruyck, D. Lavric, Using biomass: A system perturbation analysis, Applied Energy. 86(2) (2009)194-201.
[23] A. Kristin, P. Rayme, A comparison of avoided greenhouse gas emissions when using different kinds of wood energy, Biomass and Bioenergy. 30(7)(2006) 605-617.
[24] E.E. Hughes, D.A. Tillman, Biomass cofiring: status and prospects 1996, Fuel Processing Technology. 54 (1-3)(1998) 127-142.
[25] M. Olsson, J. Kjällstrand, G. Petersson, Specific chimney emissions and biofuel characteristics of softwood pellets for residential heating in Sweden, Biomass and Bioenergy. 24(1)(2003) 51-57.
[26] C. Ryu, Y.B. Yang, A. Khor, N.E. Yates, V.N. Sharifi, J. Swithenbank, Effect of fuel properties on biomass combustion: Part I. Experiments-fuel type, equivalence ratio and particle size, Fuel. 85(7-8)(2006) 1039-1046.
[27] L. Tobiasen, R. Skytte, L.S. Pedersen, T.S. Pedersen, M.A. Lindberg, Deposit characteristic after injection of additives to a Danish straw-fired suspension boiler, Fuel Processing Technology. 88(11-12)(2007) 1108-1117.
[28] H. Wiinikka, R. Gebart, C. Boman, D. Boström, M. Öhman, Influence of fuel ash composition on high temperature aerosol formation in fixed bed combustion of woody biomass pellets, Fuel. 86(1-2)(2007)181-193.
[29] M. Öhman, C. Boman, H. Hedman, A. Nordin, D. Boström, Slagging tendencies of wood pellet ash during combustion in residential pellet burners, Biomass and Bioenergy. 27(6)(2004) 585-596.
[30] M. Öhman, A. Nordin, H. Hedman, R. Jirjis, Reasons for slagging during stemwood pellet combustion and some measures for prevention, Biomass and Bioenergy. 27(6)(2004), 597-605.
[31] H. Wiinikka, R. Gebart, Experimental investigations of the influence from different operating conditions on the particle emissions from a small-scale pellets combustor, Biomass and Bioenergy. 27(6)(2004) 645-652.
[32] A. Messerer, V. Schmatloch, U. Pöschl, R. Niessner, Combined particle emission reduction and heat recovery from combustion exhaust-A novel approach for small wood-fired appliances, Biomass and Bioenergy. 31(7)(2007) 512-521.
[33] E. Alakangas, J. Valtanee, J.E. Levlin, CEN Technical Specification for Solid biofuels-fuel specification and classes, Biomass and Bioenergy. 30(2006) 908-914.

[34] http://www.informazout.be/nl/home/optimaz_webdoc

[35] Svensk Standard SS-EN 303-5, Värmepannor - Del 5: Värmepannor för fasta bränslen, manuellt och automatiskt matade, Swedish Standards Institut, SIS, 1999.

[36] http://www.pellets-mandi.be/

[37] http://www.sp.se/en/Sidor/default.aspx

[38] http://www.sei.ie/

[39] http://www.blauer-engel.de/

[40] http://www.ecosolidfuel.org/documents_15.php
[41] http://www.biois.com/default.htm

[42] http://www.aebiom.org/

[43] AVLR, Neuigkeiten aus der Zukunft. Energiekonzept Vorarlberg 2010. Schlussbericht (News from the Future. Energy Concept Vorarlberg 2010. Final Report, in German). Amt der Vorarlberger Landesregierung, Bregenz, März. (2001).

[44] http://www.holzcluster-steiermark.at/en/desktopdefault.aspx/tabid-482/1121_read-10691

[45] ITEBE - European Technical Institute for Wood Energy. http://www.itebe.org/

TABLE III

QUALITY REQUIREMENTS OF PELLET FUEL AS PER THE RESPECTIVE REGULATION/QUALITY STANDARD/QUAL

Parameter	DIN*plus*	DIN51731	Ö-Norm M-7135	Swan Label		SS 187120		
				G_1	G_2	C_1	C_2	C
Diameter(mm)	4-10	4-10	4-10	≤ 6	≤ 8	≤ 25	≤ 25	≤ 2
Length (mm)	5×D[a]	≤ 50	5×D	5×D	5×D	4×D	5×D	6×D
Density (kg dm^{-3})	≥ 1.12	≥ 1-1.4	≥ 1.12	0.63 < x ≤ 0.7	0.7 < x ≤ 0.78	≥ 0.6[d]	≥ 0.5[d]	≥ 0.5
Humidity (% wt)	≤ 10	≤ 12	≤ 10	< 9.0	< 9.0	≤ 10	≤ 12	≤ 1
Ash (% wt)	≤ 0.5	≤ 1.5	≤ 0.5	≤ 0.5	≤ 0.5	≤ 0.7	≤ 1.5	≤ 1
Heating value (MJ kg^{-1})	≥ 18	15.5-19.5	≥ 18	≥ 16.9	≥ 16.9	≥ 16.9	≥ 16.9	≥ 15
Sulphur content (% wt)	≤ 0.04	≤ 0.08	≤ 0.04	≤ 0.04	≤ 0.04	≤ 0.08	≤ 0.08	-
Nitorgen content (% wt)	≤ 0.30	≤ 0.3	≤ 0.3	≤ 0.3	≤ 0.3	-	-	-
Chlorine content (% wt)	≤ 0.02	≤ 0.03	≤ 0.02	≤ 0.02	≤ 0.02	≤ 0.02	≤ 0.02	-
Abrasian/fine content (% wt)	≤ 2.3	-	≤ 2	≤ 2[b]	≤ 2[b]	≤ 0.8[b]	≤ 1.5[b]	≤ 1.5
Mechanical durability (% wt)	≥ 97.5	-	≥ 97.5	≥ 97.5	≥ 97.5	-	-	-
Binding agent/additives (% wt)	< 2	-	< 2	-	-	TS	TS	TS
Ash melting behaviour °C	-	-	-	IT ≥ 1300[c] HT ≥ 1400[c]	-	-	-	-

[a] No more that 20 % of the pellet may be longer that 7.5 x diameter.
[b] Particle in weight % < 3.15 mm.
[c] Initial temperature (IT) tested on ash produced at 550°C.
G_1 and G_2 represent the respective pellet group as per Swan mark.
C_1, C_2 and C_3 represent the respective pellet class as per Swedish regulations.
TS- type and amount should be specified.
In Belgium most of the suppliers get their certification by DIN*plus*.

TABLE V

QUALITY REQUIREMENTS OF PELLET BOILERS AS PER THE RELEVANT QUALITY LABELS.

Quality Label	Efficiency (%)	Power (kW)	Operation Mode	CO_2 ($\%_{min}$)	Limit value mg m^{-3}, 10 vol-% O_2 in th flue gas, 0°C at 1013 mbar			
					CO	OGC	NO_x	Dust
P-mark	≥ 80[a]/ ≥ 86[b]	≤ 25[c]/ 100[d]	automatic	ND	2000	75	-	-
Swan mark**	≥ 79	≤ 100	nominal	ND	2000	70	340	70
			low	ND	2000	70	-	-
Blue Angel[e]	≥ 90/	≤ 15	nominal	ND	100	5	150	20
	≥ 88		low	ND	300	5	150	SV
	≥ 90/	15-50	nominal	ND	100	5	150	30
	≥ 88		low	ND	250	5	150	SV
UZ-37-Austria[f]	≥ 90	≤ 400	nominal	ND	60	3	100	15
			low	ND	135	3	-	-/SV
Flamme Verte**	≥ 70	≤ 50	manual	ND	6500	225	-	165
			automatic	ND	4000	150	-	165
	≥ 70	50-70	manual	ND	3750	150	-	165
			automatic	ND	3500	115	-	165
SEI-Ireland**	≥ 80	≤ 10	automatic	ND	2500	80	-	150
Optimaz**	≥ 89	≤ 70	nominal	12.5	110	-	120	1Bacha
	≥ 89		low					
Optimaz-el**	≥ 91	≤ 70	nominal	12.5	110	-	120	1Bacha
	≥ 97		low					
EU-ecolabel	NYD	NYD	NYD	NYD	NYD	NYD	NYD	NYD

[a] When tested according to sections 5.2 and 5.3 of SP-METHOD 2502.
[b] when tested according to sections 5.2 and 5.3 of SP-METHOD 2503.
[c] Burners only.
[d] Boilers with or without hot water tank.
[e] Values measured in the dry exhaust gases (0°C, 1013 mbr) with oxygen content of 13 %.
[f] Values are given in mg MJ^{-1}.
SV-specify the values; NYD- Not yet defined; Optimaz and Optimaz el values in mg kWh^{-1} and fuelled with liquid fuels; ** Permissible efficiency base

TABLE VI

SPECIAL REQUIREMENTS/ FEATURE OF EACH QUALITY LABEL.

Parameter		Optimaz	P-mark	Swan	Blue Angel	UZ-37	SEI-Ireland
Heat output range (kW)		≤70	≤25[a]/ ≤100	≤100	≤ 15/ 15-50	≤100	≤ 10/ 10-200
Plastic component				√		√	
Surface treatments (not allowed)	Heavy metal pigment			√		√	
	Organic solvents			√		√	
Packaging (prohibition of Cl-plastic)				√		√	
Auxiliary PD (% Heat output)			≤1		≤1	≤1	
Maintenance use (% Heat output)		≤ 0.8					
Radiational losses (% Heat output)						≤2.5	
Surface temperature (°C_{max})			≤ 35 at 20 AT				
Blow back burn protection			√				√
Hot Water Tank				√[b]			
High emissions limit value							

[a] Burners only.
[b] 5× size of firebox.
AT- Ambiant temperature.
'√' sign is an indication of the presence of a defined/ special requirement by the respective quality label.

One-dimensional Numerical Investigation of an Enthalpy based model for the Pyrolysis of Wet Charring materials

Shivanand R. Wasan[1], Pieter Rauwoens[1], Jan Vierendeels[1], Bart Merci[1,2]
[1] Department of Flow, Heat and Combustion mechanics (IR03), Ghent University-UGent,
Sint-Pietersnieuwstraat-41, B-9000 Ghent, Belgium
[2] Postdoctoral Fellow of the Fund of Scientific Research – Flanders (Belgium) (FWO-Vlaanderen)
email: Shivanand.Wasan@UGent.be, Pieter.Rauwoens@UGent.be, Jan.Vierendeels@UGent.be, Bart.Merci@UGent.be

Abstract: **Solid phase modelling coupled to gas phase combustion of volatiles helps to investigate the flame spread over solids. The present work focuses on the solid phase. Numerical simulations of pyrolysis of wet charring materials are performed. When the solid is exposed to an external heat flux, the moisture is assumed to flow out first, leaving behind dry solid. This solid then further heats up and after a while generates a mass flow rate of combustible volatiles during the 'pyrolysis' process, i.e. the degradation of the solid material. Evaporation and pyrolysis, possibly occurring simultaneously, are assumed to take place in infinitely thin fronts. Pyrolysis is thus modelled as an infinitely fast, irreversible endothermic process at the 'pyrolysis temperature', ignoring all kinetics. The cases considered are one-dimensional. Enthalpy is the basic model variable. The temperature distribution inside the material, along with the evaporation and pyrolysis front positions, are reconstructed from the enthalpy distribution.**

Keywords: **pyrolysis, wet charring, flame spread**

I. INTRODUCTION

Flame spread is important during the development of a fire. In order to perform numerical simulations, it is important to keep the model for the degradation of the solid phase (‘pyrolysis’) simple. Calculations in the solid phase can then be combined with gas phase turbulent combustion simulations. In [1-4], such a simple pyrolysis model is developed and applied to some basic test cases. Here we very briefly repeat the most important features and apply the model to a wet charring material.

Depending upon the residue left after pyrolysis, there are two categories of materials, namely non-charring and charring. In non-charring solids, no residue (char) is left. The focus of our study is on charring materials, although the model is also applicable to non-charring materials [3,4]. We do not discuss this in-depth here.

II. MODEL DESCRIPTION

The physical process is as follows. The solid is heated, resulting in an increase in temperature. When the material contains unbound moisture and the temperature becomes sufficiently high, the liquid moisture starts to evaporate (assumed at 373K here). Dry ‘virgin’ material is left behind after the moisture left. The temperature increases further and the pyrolysis process starts. The dry virgin material degrades and volatile combustible gases are generated. These move towards the heated surface and can react in the gas phase as they mix with the oxygen.

The possible inward flux of water vapour and pyrolysis volatiles is ignored in our model.

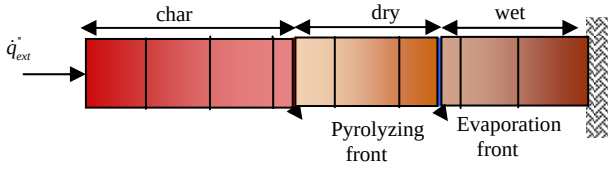

Fig. 1. One-dimensional configuration.

In our model, the solid material is divided into three zones (fig.1):

- Wet virgin material,
- Dry virgin material,
- Char material.

These different layers are separated by the mentioned fronts. The evaporation front is, during evaporation, constantly at evaporation temperature ‘T_{evap}’ (= 373k), while the pyrolysis front temperature ‘T_{pyr}’ is also kept constant during the pyrolysis process. During a cooling phase, the front temperatures can be lower than T_{evap} and T_{pyr}.

As mentioned, an enthalpy based model approach is followed in the simulation of the pyrolysis process. We do not consider finite rate kinetics. In [5] it is explained how Arrhenius type models can be ‘translated’ into the model type we use.

Our approach, based on a thermodynamic description of the phenomena, is an elaboration of the theory as described in [6] into an enthalpy-based pyrolysis model on a fixed computational mesh [2].

We consider five constituents:

- (dry) virgin solid material; *(v)*
- char; *(c)*
- combustible volatiles; *(g)*
- liquid water (‘moisture’); *(w,l)*
- water vapour. *(w,v)*

For each of the five constituents, the relation between enthalpy and temperature reads:

$$h_i(T) = h_i^o(T_{ref}) + \int_{T_{ref}}^{T} c_i(T)\,dT \qquad (1)$$

The total specific enthalpy (kJ/kg) is the sum of the formation enthalpy at a reference temperature T_{ref} and the thermal enthalpy. For gases and water vapour, the thermal capacity at constant pressure is used.

The specific enthalpy at position (x) can is a mass-weighted sum of the specific enthalpies of the constituents, present at (x):

$$h(x,t) = \sum_i \alpha_i(x,t) h_i\left(T_i(x,t)\right) \qquad (2)$$

with $\alpha_i(x,t) = \tilde{\rho}_i(x,t) / \tilde{\rho}(x,t)$ and $\tilde{\rho}(x,t) = \sum_i \tilde{\rho}_i(x,t)$. Here $\tilde{\rho}_i(x,t)$ denotes the local mass concentration of this constituent. We assume that the specific enthalpy of each constituent only depends on the temperature.

We use the concept of 'heat of pyrolysis': the isothermal process at $T = T_{pyr}$ consumes an amount of energy equal to $(m_v\text{-}m_c)\Delta Q_{pyr}$, producing $(m_v\text{-}m_c)$ pyrolysis gases from m_v virgin material and leaving behind m_c char, all at $T = T_{pyr}$. Evaporation is modeled similarly as an isothermal process at T = 373K. Evaporation of a unit mass of liquid water consumes L_v, the latent heat of evaporation.

The solid material is divided into '*n*' fixed control volumes '*V*'. The energy equation for a fixed volume reads:

$$\frac{\partial}{\partial t}\int_V \tilde{\rho} h\,dV = -\int_S \vec{\dot{q}}'' \cdot \vec{n}\,dS \qquad (3)$$

with '$\vec{\dot{q}}'' \cdot \vec{n}$' the sum of the conductive and convective heat fluxes out of the volume '*V*' through its boundary '*S*'. The convective fluxes concern transport by the water vapour and/or pyrolysis gases, generated at the evaporation and/or pyrolysis front. We assume that all gases leave the solid as soon as they are generated and that they are always in local thermal equilibrium with the solid. Conduction is modelled by Fourier's law.

III. Solution procedure

The entire solution procedure is described in [3]. Starting from the initial conditions, time steps Δt are taken. Stepping is performed in an iterative manner.

Here, we describe what must be done when there is an evaporation and/or pyrolysis front.

If the evaporation and/or pyrolysis process is ongoing, the evaporation and/or pyrolysis front temperature is constant, equal to 373K and/or T_{pyr}. Thus, the enthalpy update leads to a new temperature field and a motion of the evaporation and/or pyrolysis front to a new position. The front is allowed to move backwards during the iterative procedure in stepping from the previous physical time to the next physical time, but it must not move backwards, compared the most recent position in physical time, as evaporation and/or pyrolysis is an irreversible process. Note that evaporation is treated as an irreversible process because the water vapour leaves immediately.

It is possible that the evaporation and/or pyrolysis process stops due to insufficient incoming heat flux. Then the evaporation and/or pyrolysis front does not move and the new temperature field and evaporation and/or pyrolysis front temperatures are computed. In the case of heating, it is possible that the fronts are allowed to move again.

From the latest situation, the conduction and convection fluxes are computed for each computational cell. From the fluxes, the enthalpy update is computed from Eq. (3).

From the new enthalpy field, the temperature field, the positions of the evaporation and/or pyrolysis front and the evaporation and/or pyrolysis front temperatures are reconstructed.

As long as no evaporation is taking place, only the temperature field must be reconstructed.

IV. Results and discussion

In [1], we applied the model to a wide range of one-dimensional configurations of dry charring materials. We very briefly mention some of the results and then apply the model to wet charring material. Ambient temperature and initial temperature in the solid are set to 300K.

A. Influence of solid thickness

We illustrate that the model captures well the effect of the solid thickness. We use the numerical moving grid reference results of [7]. The solid material thickness varies from 2mm (thermally thin) to 50mm (thermally thick).

The front surface undergoes a constant externally imposed heat flux of 50kW/m^2. The back surface is perfectly insulated.

The physical time step size in the simulations is set to 0.1s. 40 cells are used. In [3] we illustrate that the sensitivity of the results to these choices is small.

The thermo-physical properties for particle board are used [7]:

ρ_v=600kg/m^3, ρ_c=60kg/m^3, $c_v = c_c$=2500J/(kg.K), k_v=0.36W/(m.K), k_c=0.23W/(m.K), c_g=0J/(kg.K), ΔQ_{pyr}=8.7 10^5 J/kg, T_{pyr}=648K, ε=1.0, h=15W/m^{2}K.

Figure 2 proves good agreement with the moving grid results over the entire range of thicknesses.

Pyrolysis starts earlier for the smaller thickness, due to more rapid heating of the material up to the pyrolysis temperature. For thicknesses larger than 10 mm, the onset of pyrolysis remains practically unchanged. The heating process is then as if the solid were of infinite thickness.

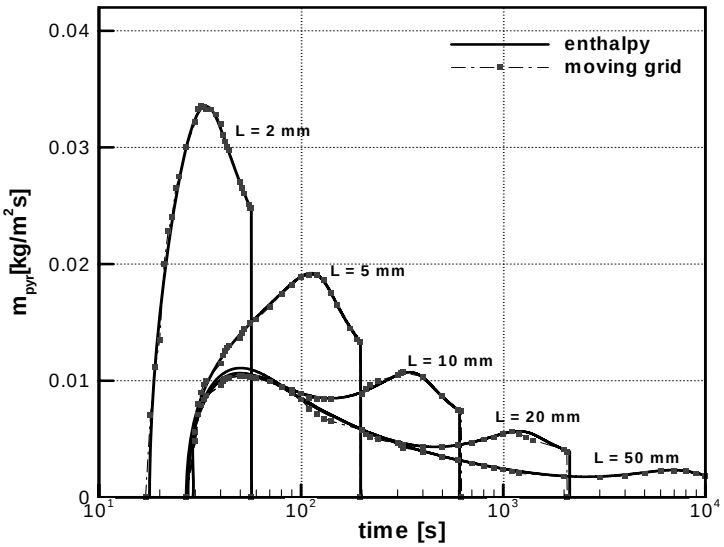

Fig. 2. Mass flow rate of pyrolysis gases (different material thicknesses).

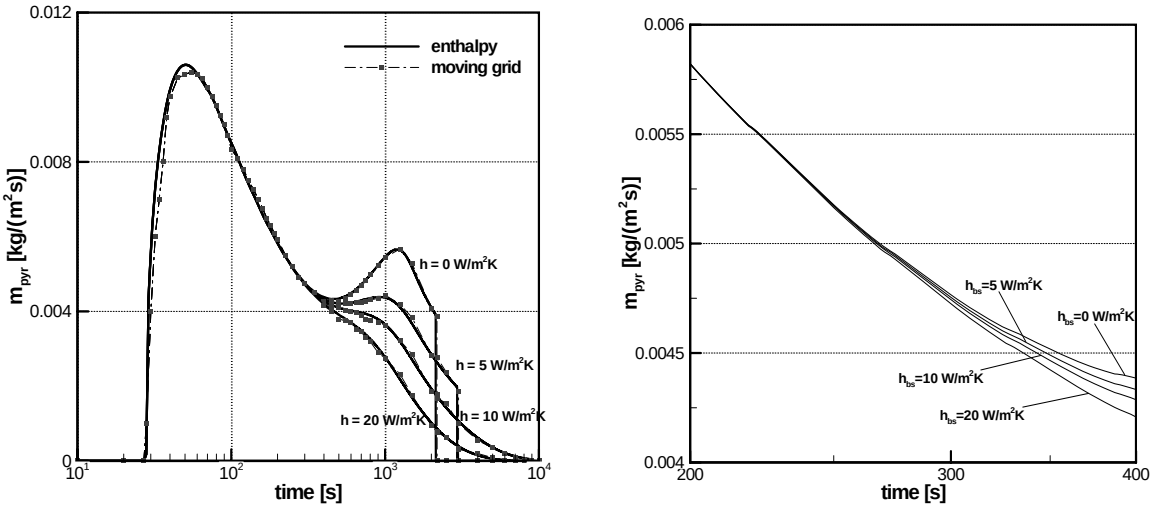

Fig. 3. Influence of back surface boundary condition (h_{bs}) and fixed front surface boundary condition (h_s = 10W/m^{2}K); mass flow rate of pyrolysis gases (left); zoom (t = 200s - 400 s, top right).

For the thermally thin materials (L<10 mm), the mass flow rate evolution in time contains a single peak. The peak is higher for the smaller thicknesses: the heating process is faster and, consequently, the pyrolysis front moves faster.

For the thermally thick materials, there are two peaks. The second peak is due to the so called 'back effect' [8].

B.Effect of boundary condition on the back side

As second illustration, we vary the back side boundary condition:

$$\dot{q}''_{bs} = h_{bs}(T_{bs} - T_{amb}) \qquad (5)$$

We use the same model parameters and material properties as in the previous section. Radiative emission at the back surface is ignored.

Figure 3 (left) confirms the agreement with the moving grid model results again. The back effect is only observed for sufficiently low values of the back boundary convective heat transfer coefficient.

In [9], it is reported that with the integral model the mass flow rate curves cross each other when 'h_{bs}' is varied. This unphysical feature is not observed with the present model, as illustrated in the zoom (figure 3, right).

C.Wet charring materials

We now discuss simulation results for wet charring materials, using the material properties from [10]. The solid is 30mm thick. The external heat flux is 40kW/m^2. We compare results for dry material and for a moisture content of 14%.

The thermo-physical properties of the material considered are:

$$\rho_v = 710\ {}^{kg}/_{m^3},\ \rho_c = 180\ {}^{kg}/_{m^3},\ L_v = 2.27\cdot 10^6\ {}^{J}/_{kg},$$
$$c_{vd} = 1460\ {}^{J}/_{(kgK)},\ c_c = 1100\ {}^{J}/_{(kgK)},\ k_{vw} = 0.31\ {}^{W}/_{(mK)},$$
$$k_{vd} = 0.24\ {}^{W}/_{(mK)},\ k_c = 0.10\ {}^{W}/_{(mK)},\ T_{pyr} = 550K,$$
$$\Delta Q_{pyr} = 4.18\cdot 10^5\ {}^{J}/_{kg},\ h = 10\ {}^{W}/_{(m^2K)},\ \varepsilon = 0.9,$$
$$c_g = 1900\ {}^{J}/_{(kgK)},\ c_{w,v} = 2000\ {}^{J}/_{(kgK)},\ c_{w,l} = 4184\ {}^{J}/_{(kgK)}$$

The indices *v,w* and *v,d* indicate wet virgin and dry virgin respectively. The time step size is 0.5s and 50 cells are used.

Figure 4 shows the mass loss rate evolution in time. The right figure is a zoom for the first 100s.

In the wet material, first the water evaporates when the surface temperature reaches 373K (after 2s). The moisture clearly leaves the solid much earlier than flammable volatiles, as pyrolysis does not start until the surface temperature reaches T_{pyr}. From that moment onwards, the two fronts move and the total mass flow rate (dash-dotted line) equals the sum of the two mass flow rates. In the dry material (solid line), pyrolysis starts earlier (after 11s) than in the wet material (after 32s). Indeed, the evaporation process consumes energy in the wet material. When the evaporation front reaches the back side of the solid, there is a drop in the total mass flow rate, but rapidly the pyrolysis mass flow rate increases, because from then on, all heat is used for the pyrolysis process. The pyrolysis front moves slower than the evaporation front. It is also slower for the case of wet material than for the dry material (lower peak in the wet material).

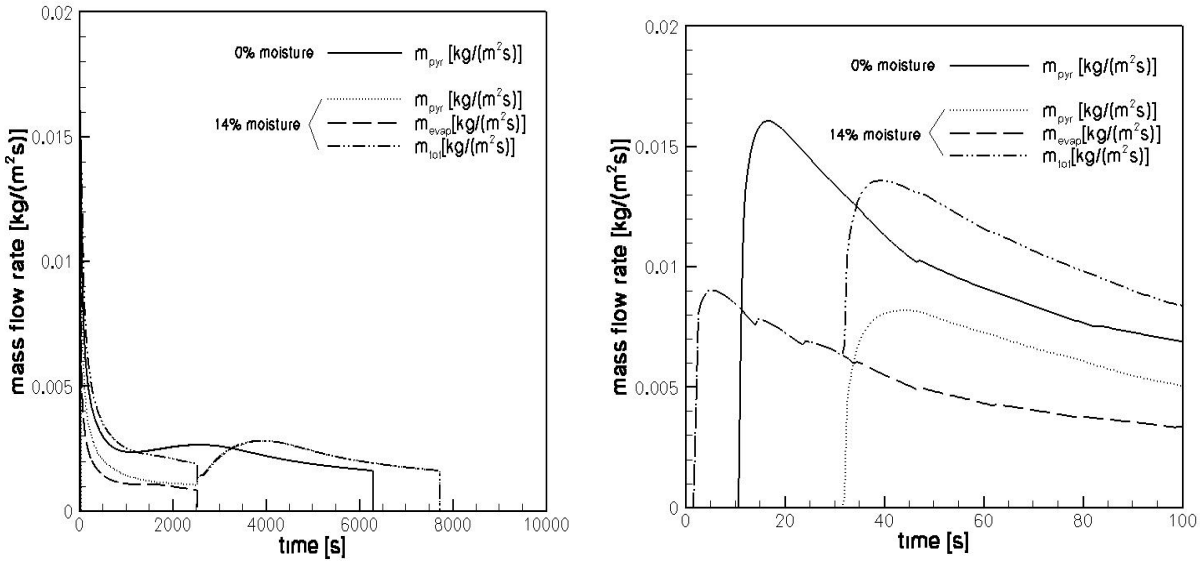

Fig.4. Mass flow rate in time: up to 10,000s (left); bottom row: up to 100s (right).

V. Conclusions

We applied an enthalpy based pyrolysis model. Numerical reference results, obtained with the more complex moving grid model, are well reproduced.
Effects of variable boundary conditions and presence of moisture are well reproduced.

VI. Acknowledgement

This project G.0130.06 is funded by Fund of Scientific Research - Flanders (Belgium) (FWO-Vlaanderen).

References

[1] Wasan, S. R., Rauwoens, P., Vierendeels, J., and Merci, B., Application of an Enthalpy Based pyrolysis model in the Numerical Simulations of Pyrolysis of charring materials, Fire and Materials (submitted).

[2] Wasan, S. R., Rauwoens, P., Vierendeels, J., and Merci, B., *An enthalpy-based pyrolysis model for charring and non-charring materials in case of fire. Part I: Model description*, Combustion and Flame (submitted).

[3] Wasan, S. R., Rauwoens, P., Vierendeels, J., and Merci, B., *An enthalpy-based pyrolysis model for charring and non-charring materials in case of fire- Part II: Application to basic test cases*, Combustion and Flame (submitted).

[4] Wasan, S., Rauwoens, P., Vierendeels, J. and Merci, B., Numerical *Simulations of Pyrolysis of Charring and Non-Charring Materials using an Enthalpy Based model* , Mediterranean Combustion Symposium (in press)

[5] Park, W. C., Atreya, A., and Baum, H. R., *Determination of pyrolysis temperature for charring materials*, Proceedings of the Combustion Institute, 32, pp. 2471-2479, 2009.

[6] Kung, H.C., *A Mathematical Model of Wood Pyrolysis*, Combustion and Flame, 1972, vol 18, 185-195.

[7] E. Theuns, J. Vierendeels, P. Vandevelde, *Validation of the integral model for the pyrolysis of charring materials with a moving grid*, J. of Computational and Applied Mathematics, vol. 168, pp. 471-479, 2003.

[8] M. J. Spearpoint and J. G. Quintiere, *Predicting the burning of wood using an integral model*, Combustion and Flame, vol. 123, pp. 308-325, 2000.

[9] E. Theuns, B. Merci, J. Vierendeels and P. Vandevelde, *Critical evaluation of an integral model for the pyrolysis of charring materials*, Fire Safety Journal, vol. 40, pp. 121-140, 2005.

[10] de Ris J. L., and Yan Z., Modeling ignition and pyrolysis of charring fuels. *Proceeding of the 5th International Conference on Fire and Materials '98*, 111-121, San Antonio, TX, USA, 1998.

Proceedings of the 8th National Congress on Theoretical and Applied Mechanics, May 28-29, Brussels, Belgium.

Detailed study of the impact of co-utilization of biomass in a natural gas combined cycle power plant through perturbation analysis

F. Delattin[1]*, J. De Ruyck[1], S. Bram[1]
[1]Vrije Universiteit Brussel – Department of Mechanical Engineering
Pleinlaan 2 – 1050 Brussel
*email: frank.delattin@vub.ac.be

Abstract: **Co-utilization of fossil fuels and biomass is a successful way to make efficient use of biomass for power production. When replacing only a limited amount of fossil fuel by biomass, measurements of net output power and input fuel rates will however not suffice to accurately determine the marginal efficiency of the newly introduced alternative fuel. The present paper therefore proposes a technique to determine the marginal biomass efficiency with more accuracy. The co-utilization of natural gas and a small perturbing fraction of biomass in an existing Combined Cycle Plant (500MW$_{th}$ Drogenbos, Belgium) is taken as case study. In this particular plant, biomass is introduced into the cycle as fuel for a primary steam reforming process of the input natural gas.**

This paper proposes a perturbation analysis that has been developed to allow for an accurate assessment of the marginal efficiency of biomass by using only accurately measurable variables. To achieve this, effects of co-utilization were studied in each component of the gas turbine down to its steam bottom cycle to identify the components most affected by the limited perturbing amount of biomass. The procedure is validated through process simulation, where accurate marginal efficiencies can be compared with the efficiency obtained from the perturbation analysis. A full off-design simulation is required to achieve this result, which was validated through experiments at part load and at variable air inlet temperatures. Through the use of process simulation, the accuracy of the mathematical model could be verified for each formula and each assumption. The model was found to accurately predict marginal efficiencies of the introduced biomass for biomass shares as low as 0.1%.

Keywords: **energy, co-utilization, biomass, perturbation analysis, steam reforming**

1.NOMENCLATURE

Abbreviations

bc		Bottom cycle
CC		Combined Cycle
C_p	kJ/kgK	Constant heat capacity
e		Excess
f		Function
h	kJ/kg	Specific enthalpy
HP	bar	High Pressure
K	/	Heat capacity ratio
W	kW	Power
$\dot{m}$	kg/s	Mass flow rate
LHV	kJ/kg	Lower Heating Value
LP	bar	Low Pressure
p	kPa	Static pressure
$\dot{Q}$	kW	Heat rate
SMR	/	Steam to Methane Ratio
T	K/ºC	Temperature
TIT	K	Turbine Inlet Temperature
TOT	K	Turbine Outlet Temperature
$\dot{W}$	kW	Power

Symbols

α		Slope of pressure in compressor map
ψ	%	Biomass input fraction
η	%	Efficiency
y	%	Molar fraction

Prefix

∂	Perturbation (adapted scenario – reference scenario)
Δ	Difference

Superscripts

o	Reference state
i	Specie i
mar	Marginal
mol	Molar
ref	Reference
th	Thermal

Subscripts

air	Air (relevant to the air feed)
aspen	As calculated by process simulation tool Aspen

bio	Biomass (relevant to the biomass feed)
biostack	Exhaust gas from the bioburner
BB	Redirected to the bioburner
cold	Cold side of a heat exchanger
comp,C	Compressor
hot	Hot side of a heat exchanger
in	Entering the specific component, inlet
net	Net
NG	Natural Gas (relevant to the natural gas feed)
out	Leaving the specific component, outlet
refo	Reformer
water	Water (relevant to the water feed)
stack	Stack (relevant to the exhaust gas feed)
steam	Steam (relevant to the steam feed)
turb	Turbine

2. INTRODUCTION

The co-utilization system simulated in the present paper combines the advantages of external combustion (no gas cleaning) with the advantages of internal combustion (higher efficiencies). The full process is treated in the details in references [1,2]. Co-utilization is realized by using the heat from the external combustion of biomass to achieve the partial endothermic primary reforming of natural gas into mainly hydrogen and carbon monoxide (see Figure 1). The obtained syngas is then routed to the gas turbine.

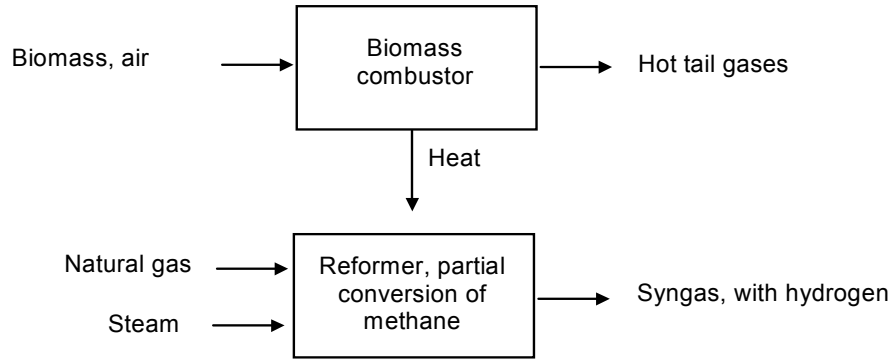

Fig 1: Concept of steam reforming based on external biomass combustion [1,2]

The main chemical reactions involved are ([1,2])

$$CH_4 + H_2O \leftrightarrow CO + 3H_2 \quad (206\ kJ.mol^{-1}) \tag{1}$$

$$CO + H_2O \leftrightarrow CO2 + H_2 \quad (-41\ kJ.mol^{-1}) \tag{2}$$

In this way, the biomass energy is transferred into syngas as chemical energy and the biomass exhaust gases are kept separate from the syngas and the internal parts of the gas turbine. The gas input, the obtained syngas and the biomass combustion tail gases all need further integration in a heat exchanger network for optimal energy recovery. The syngas must also be conditioned to meet the specifications given by the gas turbine supplier [1,2].

In order to determine the effects of the biomass combustion on gas turbine performance and efficiency, a marginal biomass efficiency must be defined. The reference lower heating value (LHV) efficiency η^{ref} is determined for the original and unperturbed gas turbine cycle in which all the energy input is natural gas. By means of η^{ref}, the remaining fossil fuel in the adapted cycle would provide a power output equal to $\dot{W}^{ref}$ and the surplus work can be attributed to the biomass combustion. A marginal LHV efficiency η^{mar} of the biomass can thus be defined as follows:

$$\eta^{mar} = \frac{\dot{W}_{net} - \eta^{ref} LHV^{ref} \dot{m}_{NG}}{\dot{m}_{bio} LHV_{bio}}$$

$$\eta^{ref} = \frac{\dot{W}^{ref}_{net}}{\dot{m}^{ref}_{NG} LHV^{ref}} \tag{3}$$

The biomass input fraction is defined as follows:

$$\Psi_{bio} = \frac{\dot{m}_{bio}}{\dot{m}_{NG} + \dot{m}_{bio}} \tag{4}$$

Through this proposed route, an absolute maximum of 20% of the energy input can be replaced by

biomass[1]. Practical shares are expected to be in the range of 5 to 10%. With these small fractions, the relative errors of the measured power and fuel result in an inaccurate calculation of η^{mar}. The problem arises in the numerator where two large numbers have to be subtracted. As the absolute errors of both terms need to be added, the relative error of the numerator can easily reach high values of 50% or more. The marginal efficiency will therefore have an intolerably large relative error and the obtained efficiencies are useless.

Mathematical modelling of gas turbines has been applied to a large extent in the past, mainly to predict and understand the off design behaviour of the different gas turbine components [3-10]. Under different circumstances, simplified linearized techno-economic models were developed to have a quick but fairly accurate tool to estimate performance and electricity cost [11-16]. Large efforts have been made in order to expand these simplified models to incorporate transient behaviour during start-up or brusque load changes [17-22].

An estimation of the transient gas turbine behaviour or the electricity cost, fall outside the scope of the perturbation model. It is mainly the focus to allow accurate determination of performance and efficiency using only accurately measurable parameters. Then, the components most affected by the introduction of biomass through the proposed route are to be identified and discussed.

3. THE REFERENCE AND ADAPTED POWER CYCLES

The reference Combined Cycle (CC, Drogenbos, Belgium) is shown in Figure 2. A series of heat exchangers in the Heat Recovery Steam Generator (HRSG) preheat, evaporate and superheat steam. Feed water (1) supplied from the condenser by the feed water pump is heated in the preheater and rerouted until the temperature of ~105°C, suitable for the deaerator drum, is reached (2). The water is split-up (3) into a low pressure (LP) and a high pressure (HP) circuit and preheated before entering the appropriate pressure drum. Saturated water in the LP drum is recirculated through the LP evaporator (4). Water is drawn from the deaerator drum and passed through the HP economizer (6) before entering the HP drum (7). Steam is produced in the HP drum and superheated through the HP superheater (8) before being expanded in the HP steam turbine for power generation (9). The LP steam is superheated (5) and added to the expanded HP steam to generate additional power in the LP steam turbine (10). The steam turbine exhaust is finally condensed before re-entering the bottom cycle (11).

This CC can next be adapted to partially replace a limited fraction of natural gas by biomass [1]. The introduction of biomass through primary steam reforming interacts with the existing combined cycle in a particular way. The concept of co-utilization of biomass through steam reforming, simplified on display in figure 3, is explained more in detail as follows:

Part of the input fuel is diverted and premixed with enough water to reach a steam-methane ratio (SMR) of 2 before entering the reforming reactor. The steam-methane ratio is kept as low as allowed by coking problems [23][2]. The pre-mixing is done in a saturation tower where steam is evaporated more gradually leading to better aligned composite curves [1]. The pressure in the reformer is adjusted to yield a slight overpressure to the combustion chamber of the CC. The endothermic reforming reactions are fed by the heat of combustion from the biomass burner. The combustion air is taken from the turbine exhaust gas. Its flow rate is adjusted to yield 6% of excess oxygen in the combustor. The heat in the combustion tail gas is to be used as a heat source within the heat exchanger network of the adapted cycle. The syngas is cooled to a temperature suited for the combustor. The gas turbine cooling is considered by routing 10% of the compressor mass flow directly to the turbine (which in fact does not affect the results of the present exercise).

The compressor was modelled in Aspen Plus using a generic compressor map, as displayed in Figure 4. At the design point, the relation between the compressor pressure and flow rate can be linearized (see Eq. 11).

4. PERTURBATION METHOD

The CC is adapted to partially run on biomass and it will therefore operate under off-design and non

[1] To determine the maximum biomass input fraction, all the available natural gas was rerouted to the reformer to react at 600°C and SMR of 2 into syngas. A higher biomass input fraction can be achieved by increasing the operating temperature in the reforming reactor, but this would decrease the biomass marginal efficiency as more redundant heat needs to be recycled in the heat exchanger network [2].

[2] Yamazaki experimentally lowered SMR to 1 without resulting in severe coking problems, but as the considered catalyst would require special treatment under these conditions, a more commercially applied surplus of 100% water was used in our Aspen simulations.

optimal conditions. A perturbation analysis is developed to accurately determine the marginal efficiency of the biomass using only accurately measurable variables, and taking into account all off-design conditions. To achieve this, effects of co-utilization are studied in each component of the gas turbine down to its steam bottom cycle to identify the components most affected by the perturbation.

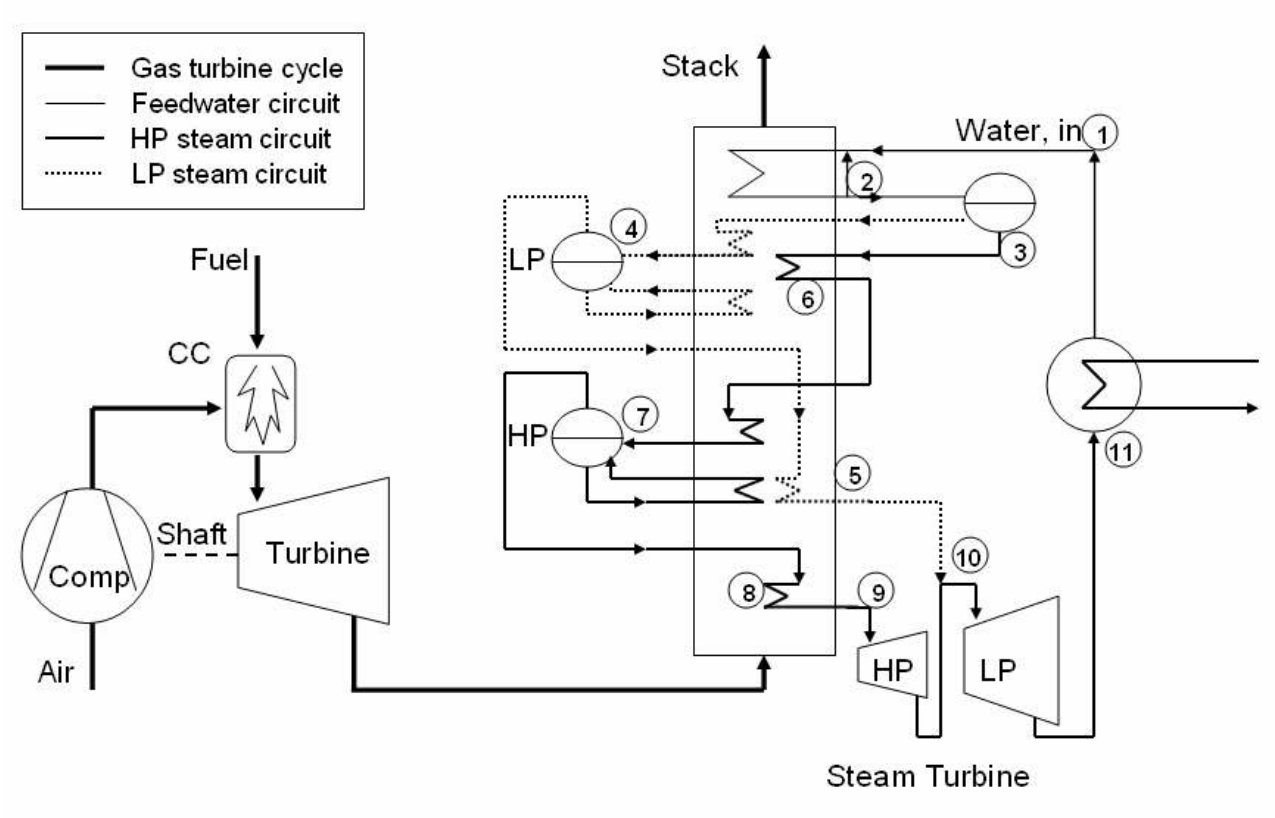

Fig. 2: Simplified schematic diagram of the simulated CC

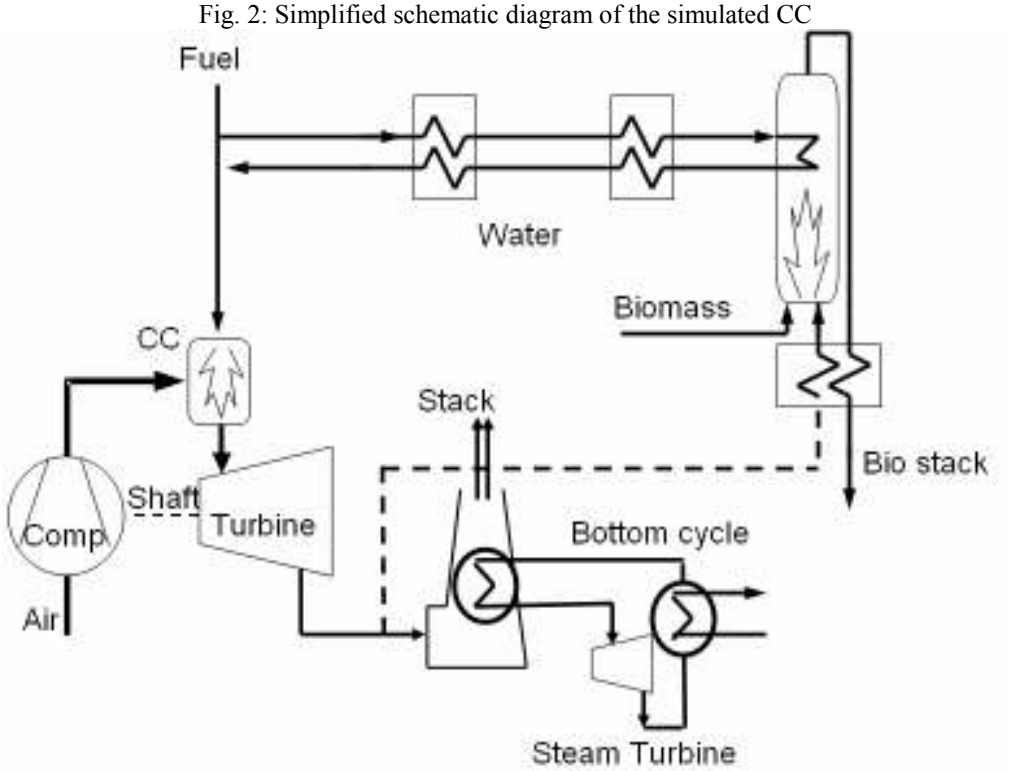

Fig. 3: Simplified schematic diagram of a co-utilising CC

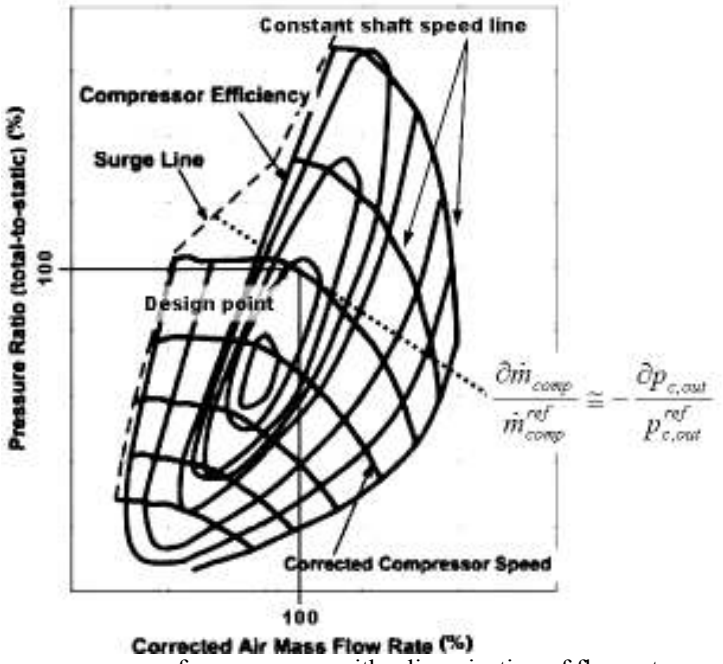

Fig. 4: Typical generic compressor performance map with a linearization of flow rate versus pressure ratio at the design point

When comparing a gas turbine cycle operated at its design and at off-design conditions, all the variables of the off design process can be expressed as follows:

$$X = X^{ref} + \partial X \qquad (5)$$

Where X^{ref} is the value of the variable in the reference cycle (design conditions) and X the value of the variable in the perturbed cycle (off-design conditions). The difference between both is the perturbation created by adapting the cycle or by running it at non optimal conditions. All the perturbations will hence be preceded by the letter '∂' in this paper.

The problem in Eq. (3) is the numerator where a difference between two large numbers needs to be calculated. The measurement errors on both will be larger than the difference itself, making it impossible to use the formula as such. As a solution it is proposed to apply a perturbation analysis, as follows:

$$\dot{W}_{net} = \dot{W}_{net}^{ref} + \partial \dot{W}_{net} \qquad (6)$$

$$\dot{m}_{NG} = \dot{m}_{NG}^{ref} + \partial \dot{m}_{NG} \qquad (7)$$

Eq. 3 can now be rewritten as follows:

$$\eta^{mar} = \frac{\dot{W}_{net}^{ref} + \partial \dot{W}_{net} - (\dot{m}_{NG}^{ref} + \partial \dot{m}_{NG})\eta^{ref} LHV_{NG}}{\dot{m}_{bio} LHV_{bio}} = \frac{\partial \dot{W}_{net} - \partial \dot{m}_{NG}\eta^{ref} LHV_{NG}}{\dot{m}_{bio} LHV_{bio}} \qquad (8)$$

The numerator now shows a subtraction of numbers that are much smaller. As can be seen in this equation, the marginal efficiency can be calculated using the perturbations of the natural gas mass flow rate and the perturbation of the net power generated in the entire cycle. It is therefore possible to reduce the relative error induced in the numerator significantly, leading to an accurate estimation of the marginal biomass efficiency.

The perturbation on $\partial \dot{W}$ consists of several contributions:

- $\partial \dot{W}_{comp}$, the perturbation of the power demand of the compressor,
- $\partial \dot{W}_{turb}$, the perturbation of the generated power of the gas turbine,
- $\partial \dot{W}_{steam}$, the perturbation of the generated power in the bottom cycle, and

- $\partial \dot{W}_{aux}$, the perturbation of the auxiliary power demanded in the gas turbine cycle

The first three are strongly dependant upon the perturbations on flow rates. The mass flow rate through the gasturbine is governed by the gas turbine choking condition:

$$\frac{\dot{m}_{turb}\sqrt{TIT}}{p_{turb,in}} = Cte \tag{9}$$

Or, after differentiation

$$\frac{\partial \dot{m}_{turb}}{\dot{m}_{turb}^{ref}} + 0.5\frac{\partial TIT}{TIT^{ref}} = \frac{\partial p_{turb,in}}{p_{turb,in}^{ref}} \tag{10}$$

For the time being, it will be assumed that $\partial TIT =$ 0 through appropriate adjustment of the TOT. $\partial \dot{m}_{turb}$ and $\partial p_{turb,in}$ are both non zero, and linked to the compressor characteristics. Since only small perturbations are considered, it can be assumed that:

$$\frac{\partial p_{c,out}}{p_{c,out}^{ref}} \cong -\alpha \frac{\partial \dot{m}_{comp}}{\dot{m}_{comp}^{ref}} \tag{11}$$

Where the constant α corresponds to the slope of the pressure characteristic in the compressor map (see Figure 4). The flow rates are linked through the mass balance

$$\dot{m}_{turb} = \dot{m}_{comp} + \dot{m}_{water,refo} + \dot{m}_{NG} \tag{12}$$

Or, after differentiation

$$\partial \dot{m}_{turb} = \partial \dot{m}_{comp} + \partial \dot{m}_{water,refo} + \partial \dot{m}_{NG} \tag{13}$$

In order to obey the first law of thermodynamics, the overall energy balance of the complete cycle must be respected. In this overall system, inputs are natural and biomass, and outputs are the net produced power and both the natural gas and biomass combustor stacks (see Figure 3). Therefore, Equation (14) displays the different energy flows in and out of the cycle:

$$\dot{m}_{NG}LHV_{NG} + \dot{m}_{bio}LHV_{bio} = \dot{W}_{net} + \dot{m}_{stack}C_{p,stack}\left(T_{stack} - T_0\right) + \dot{m}_{biostack}C_{p,biostack}\left(T_{biostack} - T_0\right) + \dot{m}_{steam}\left(-\Delta_v H_{water}^{312.5K}\right) \tag{14}$$

or, after differentiation

$$\partial \dot{m}_{NG}LHV_{NG} + \dot{m}_{bio}LHV_{bio} = \partial \dot{W}_{net} + \partial\left(\dot{m}_{stack}C_{p,stack}T_{stack}\right) + \partial\left(\dot{m}_{biostack}C_{p,biostack}T_{biostack}\right) + \partial \dot{m}_{steam}\left(-\Delta_v H_{water}^{312.5K}\right) \tag{15}$$

Where $\Delta_v H_{water}^{312.5K}$ is the enthalpy of vaporization of water at 0.055 atm and 312.5K and where:

$$\dot{W}_{net} = \dot{W}_{turb} + \dot{W}_{comp} + \dot{W}_{steam} \tag{16}$$

$$\dot{m}_{biostack} = \dot{m}_{air,BB} + \dot{m}_{bio} \tag{17}$$

The two stack temperatures in equations 14 and 15 can be assumed constant. Hence the only remaining unknown variables are $\partial \dot{W}_{net}$, $\partial \dot{m}_{stack}$ and $\partial \dot{m}_{steam}$ which will be computed in more detail in the sections below.

Compressor

$$\dot{W}_{comp} = \dot{m}_{comp}\left(h_{c,out} - h_{c,in}\right) \tag{18}$$

Where, assuming a perfect gas:

$$\Delta h \cong \widetilde{C}_{p,c}\left(T_{c,out} - T_{c,in}\right) \tag{19}$$

For the purpose of this paper, environmental conditions were frozen in order to attribute all perturbations solely to the influence of biomass and its by-product syngas. Consequently, $C_{P,C,in}$ and $T_{C,in}$ are constant.

Differentiation of equations 18 and 19 yield:

$$\frac{\partial \dot{W}_{comp}}{\dot{W}_{comp}^{ref}} \cong \frac{\partial \dot{m}_{comp}}{\dot{m}_{comp}^{ref}} + \frac{\partial \widetilde{C}_{p,c}}{\widetilde{C}_{p,c}^{ref}} + \frac{\partial T_{c,out}}{\left(T_{c,out} - T_{c,in}\right)} \tag{20}$$

The change in flow rate is dictated by the choking condition of the turbine downstream (Equation 10). The perturbation of the outlet temperature can be found from the Poisson equation in combination with the isentropic efficiency:

$$T_{c,out,is} = T_{c,in}\left(\frac{p_{c,out}}{p_{c,in}}\right)^{\frac{K-1}{K}} \tag{21}$$

$$\eta_{comp}^{is} = \frac{T_{c,out,is} - T_{c,in}}{T_{c,out} - T_{c,in}} \tag{22}$$

Or, after differentiation:

$$\frac{\partial T_{c,out,is}}{T_{c,out}} = \left(\frac{K-1}{K}\right)\frac{\partial p_{c,out}}{p_{c,out}} + \ln\left(\frac{p_{c,out}}{p_{c,in}}\right)\frac{1}{K}\frac{\partial K}{K} \tag{23}$$

$$\frac{\partial T_{c,out}}{T_{c,out} - T_{c,in}} = \frac{\partial T_{c,out,is}}{T_{c,out,is} - T_{c,in}} - \frac{\partial \eta}{\eta} \tag{24}$$

The change in efficiency should be obtained from the compressor map (Figure 4) in the same way as the pressure change in equation (11).

$$\frac{\partial \eta}{\eta} \cong \beta \frac{\partial \dot{m}_{comp}}{\dot{m}_{comp}^{ref}} \tag{25}$$

With outlet conditions estimated, $C_{P,C,out}$ can be calculated iteratively. The perturbation on the compressor work can now be computed from known variables.

Turbine

The perturbation on the turbine work output is more complex due to changes in the gas composition as well as differences in temperature and pressure.

$$\dot{W}_{turb} = \dot{m}_{turb}\left(h_{t,out} - h_{t,in}\right) \tag{26}$$

$$\frac{\partial \dot{W}_{turb}}{\dot{W}_{turb}^{ref}} \cong \frac{\partial \dot{m}_{turb}}{\dot{m}_{turb}^{ref}} + \frac{\partial h_{t,out} - \partial h_{t,in}}{h_{t,out}^{ref} - h_{t,in}^{ref}} \tag{27}$$

The change in flow can be rewritten using Eq. 13. The enthalpy changes must be further detailed through

$$h \equiv \Sigma y_i h_i^{mol} \Rightarrow \partial h = \Sigma(\partial y_i h_i^{mol} + y_i \partial h_i^{mol}) \tag{28}$$

where y_i are the molar fractions of the different species. The turbine outlet temperature (TOT) is measured and kept constant in the actual gas turbine cycle, and the change in composition will inflict a difference in turbine inlet temperature (TIT). It will however be assumed that the TOT control is modified to keep TIT constant for purposes of maintaining efficiency and turbine output power. Hence only the outlet ∂h_i will be affected by temperature change, which can be found in exactly the same way as for the compressor. The turbine inlet pressure is also perturbed, but the pressure loss in the combustion chamber is assumed to be unaffected:

$$TIT = Cte \tag{29}$$

$$\partial p_{turb,in} = 0.95\partial p_{c,out} \tag{30}$$

The perturbations on the molar fractions y_i can easily be determined from the species mass balances as follows:

$$y_i = \frac{\dot{m}_{i,turb}}{\dot{m}_{turb}} \tag{31}$$

Or, through differentiation:

$$\frac{\partial y_i}{y_i} = \frac{\partial \dot{m}_{i,turb}}{\dot{m}_{i,turb}} - \frac{\partial \dot{m}_{turb}}{\dot{m}_{turb}} \tag{32}$$

There are only four species in this flow, namely N_2, CO_2, H_2O and O_2. By mass balance, these flow perturbations can be written as:

$$\partial \dot{m}_{N_2} = y_{N_2,comp}.\partial \dot{m}_{comp} + y_{N_2,NG}.\partial \dot{m}_{NG} \tag{33}$$

$$\partial \dot{m}_{CO_2} = \frac{44}{12}.y_{C,NG}.\partial \dot{m}_{NG} \tag{34}$$

$$\partial \dot{m}_{H_2O} = \partial \dot{m}_{water,refo} + \frac{18}{1}.y_{H,NG}.\partial \dot{m}_{NG} \tag{35}$$

$$\partial \dot{m}_{O_2} = y_{O_2,comp}.\partial \dot{m}_{comp} - \frac{32}{44}\partial \dot{m}_{CO_2} - \frac{2}{18}\partial \dot{m}_{H_2O} \quad (36)$$

All variables in the equations are known values.

Bottom cycle

$$\dot{W}_{steam} = \dot{m}_{steam}\left(h_{steam,out} - h_{steam,in}\right) \quad (37)$$

$$T_{turb,in} \cong Cte \quad (38)$$

$$p_{turb,in} \cong Cte \quad (39)$$

$$\partial \dot{W}_{steam} \cong \frac{\partial \dot{m}_{steam}}{\dot{m}^{ref}_{steam}} \dot{W}^{ref}_{steam} \quad (40)$$

Knowledge of the variation of the steam turbine inlet temperature $T_{turb,in}$ requires modelling the heat exchanger network (HRSG) with information that is usually unavailable to the end-user. A mathematical model of the heat exchanger could increase accuracy of the perturbation calculation. As will appear from the results the induced error is small, which can be explained by the limited impact of the flow rates on Reynolds and Nusselt numbers in the heat exchange process.

The bottom cycle is designed in such a way that when more or less heat is offered in the stack gases, more or less steam is produced. Furthermore, the design of most bottom cycles is such that the exit stack temperature is held constant, where the TOT can be assumed constant as well. The same can be said for the steam cycle where on one hand the water is condensed at a constant temperature and the steam turbine inlet temperature kept nearly constant on the other hand. As the heat offered by the stack gases is equal to the heat demanded by the steam generation and superheating, one could model this relation in a simple way as:

$$\frac{\partial \dot{m}_{steam}}{\dot{m}^{ref}_{steam}} \cong \frac{\partial \dot{m}_{stack}}{\dot{m}^{ref}_{stack}} \quad (41)$$

$$Q_{hot} = \dot{m}_{stack} C_{p,stack}(T,p)\left(TOT - T_{stack,exit}\right) \equiv Q_{cold} = \dot{m}_{steam} C_{p,steam}(T,p)\left(T_{steamturbine,in} - T_{condens,out}\right) \quad (42)$$

$$\partial \dot{m}_{stack} = \partial \dot{m}_{comp} + \partial \dot{m}_{NG} + \dot{m}_{water,refo} - \dot{m}_{air,BB} = \partial \dot{m}_{turb} - \dot{m}_{air,BB} \quad (43)$$

In order to determine the perturbation of the stack flow rate, it has been found that the greatest perturbations are the added water in the syngas content and the combusted air, diverted and recycled to combust biomass in the bio-burner.

Full process simulation

As a reference basis, the CC was simulated in Aspen, based upon technical sheets, readouts and measurements done in the existing CC of Drogenbos, Brussels, Belgium. This CC with a net power generation of ~500MW is constructed using two gas turbines and a single, two pressure-level steam cycle of 75/6.5 bars and a maximum injection temperature of 525°C in the HP steam turbine.

Table 2 describes the reference data used to simulate the reference cycle and later on the adapted, co-utilizing cycle (only one of the two gas turbines was simulated). It shows the input and output data for the model on pure natural gas or in mixture with syngas.

The adiabatic turbine efficiency was set at 0.86 to produce the exhaust temperature close to 560°C (833 K), which is the value published for the existing CC [24]. The compressor is simulated to work under an adiabatic efficiency of 88.5% to match compressor outlet conditions to the values published by the gas turbine manufacturer.

Table 2: Comparison of simulation data (as predicted by Aspen)

	Pure NG	1% bio-input	3% bio-input	6% bio-input
Ambient pressure (atm)	1	1	1	1
Compressor pressure ratio	9.63	9.64	9.65	9.67
Turbine backpressure (atm)	1.02	1.02	1.02	1.02
TIT (°C)	1047	1047	1047	1047
TOT (°C)	560.0	560.0	559.8	559.8
Cooling air fraction (%)	10.00	10.00	10.00	10.00
HRSG outlet temp. (°C)	519.2	519.3	519.3	519.3
(Mixed) Fuel composition (%mol)				

CH4	100.0	86.26	64.49	44.51
CO	0.0	0.88	2.27	3.55
CO2	0.0	2.03	5.24	8.19
H2	0.0	10.75	27.79	43.41
N2	0.0	0.00	0.00	0.00
H2O	0.0	0.08	0.21	0.34
Stack temperature (°C)	97	97	97	97
Biostack temperature (°C)	/	97	97	97
Flow rate NG (kg/s)	10.29	10.20	9.99	9.70
Diverted NG (kg/s)	/	1.27	4.00	7.76
Flow rate air (kg/s)	547.8	547.5	546.9	546.1
Flow rate turbine (kg/s)	558.0	558.3	558.9	559.7
Flow rate syngas (kg/s)	/	1.92	6.02	11.69
Flow rate steam (bc) (kg/s)	83.24	82.58	81.30	79.28
Net power (MW)	255.7	255.3	254.9	254.2
Cycle efficiency (%)	49.56	49.50	49.40	49.20
Marginal efficiency (%)	/	43.44	43.44	43.45

5.RESULTS

This paragraph summarizes the results from the comparison of the reference CC and the CC co-utilizing natural gas and biomass in a variety of ψ values. The main goals of this comparison are first to identify the components most perturbed by the introduction of biomass through primary steam reforming, to determine the marginal biomass efficiency in an accurate manner and finally to validate the perturbation method. The errors propagating from simplified equations and formulae are indicated on the figures. The common rules of error analysis and propagation were used.

$$Y = f(X_1, X_2, ..., X_N) = f(X_1^0, ..., X_n^0) + \sum_{i=1}^{N} \left.\frac{\partial f}{\partial X_i}\right|_0 (X_i - X_i^0) \tag{44}$$

$$\Delta Y = \sum \left.\frac{\partial f}{\partial X_i}\right|_0 \Delta X_i \quad \text{([25])} \tag{45}$$

Matlab was used to solve the perturbed equations using only the three accurately measurable variables $\dot{m}_{bio}$, $\dot{m}_{water,refo}$ and $\dot{m}_{air,BB}$.

Figure 5 shows the comparison of the relative perturbations of all the computed flow rates. The solid lines represent the values predicted by the perturbation model whereas the dashed lines represent the values predicted by Aspen for the compressor, turbine, steam and natural gas flows. The errors induced by simplification are neglectable for the compressor and turbine flow rates, and their predicted solid and dashed lines coincide. The biggest error can be found for the steam flow rate, where the assumption of constant turbine inlet and stack outlet temperatures is oversimplified. For all the flow rate calculations, the perturbation model predicts closely to the values simulated by Aspen, with the largest relative error being 5.2% for $\partial\dot{m}_{steam}$. It is to be observed that some irregularities are visible on the ASPEN steam flow rates which are due to convergence uncertainties.

The compressor airflow lowers as more syngas is combusted. Because of the relatively low heating value of syngas, gas turbines fired on syngas have a significantly larger fuel gas mass (and hence, volume) flow rate compared to a pure natural gas case. The balance follows from the choked conditions at the inlet of the turbine (Equation 18).

The air diverted from the turbine exhaust gases, causes a decrease in the amount of heat offered to the bottom cycle. As a consequence $\dot{m}_{steam}$ is lowered significantly. The loss of power, generated by the steam turbine, is compensated in the turbine as is explained further down.

The fuel mass flow rate is controlled by the turbine inlet temperature, which needs to be fixed at 1047 °C at full load. As a result of the co-utilization of biomass, syngas fulfills part of the condition and a reduced amount of natural gas is demanded.

Figure 6 displays the comparison of power perturbations predicted by the perturbation model (solid lines) and simulated by Aspen (dashed lines) in

the different gas turbine components. The accuracy of the calculated power in the different components strongly follows the accuracy of the associated flow rates (as can be seen from the perturbed equations). Therefore, the predicted and simulated values for compressor and turbine nearly coincide, and the biggest induced inaccuracy is found in the steam turbine perturbation. Once more, the perturbation model seems to follow Aspens simulations closely. With a maximum relative error for $\partial \dot{W}_{net}$ of 3.5%, the model is assumed to be satisfactory in predicting power perturbations in the adapted gas turbine cycle.

As can be expected from equation 7, a reduced compressor flow rate requires less compressor power. As the airflow diminishes, the compressor will operate (according to its performance map in figure 4) at higher outlet pressures. At constant shaftspeed, a deviation from the operating point will cause a reduction in compressor efficiency, translated in an increased outlet temperature. As the airflow passing through decreases, the compressor power demand is lowered linearly. For 5% biomass input fraction, the net power output is lowered roughly 0.1%.

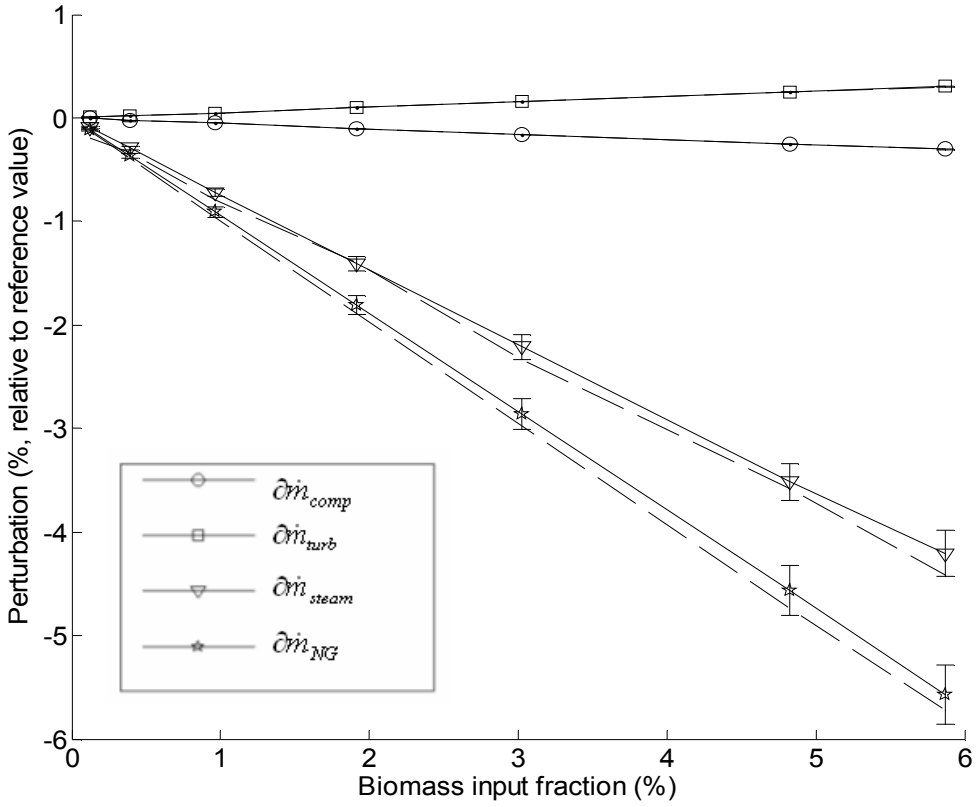

Fig. 5: Comparison of the flow rate perturbations (solid), relative to their reference flow values (dashed) versus biomass input fraction

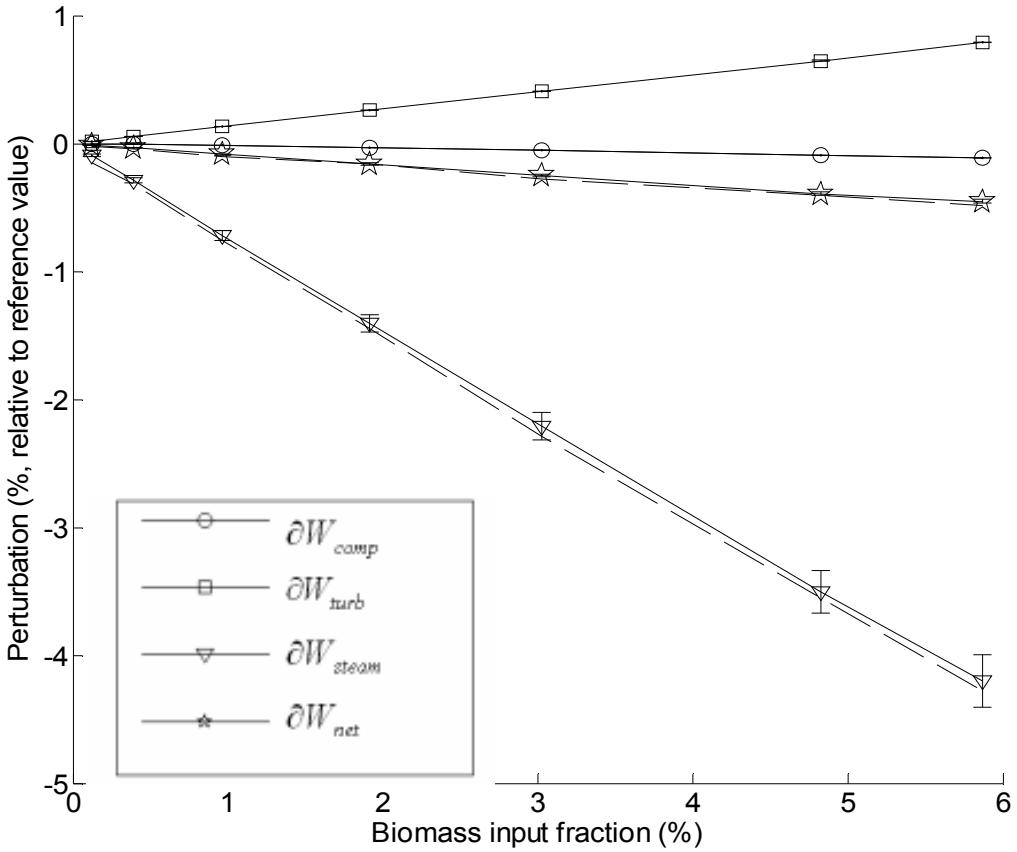

Fig. 6: Comparison of the gas turbine component power perturbations (solid), relative to their reference values (dashed) versus biomass input fraction

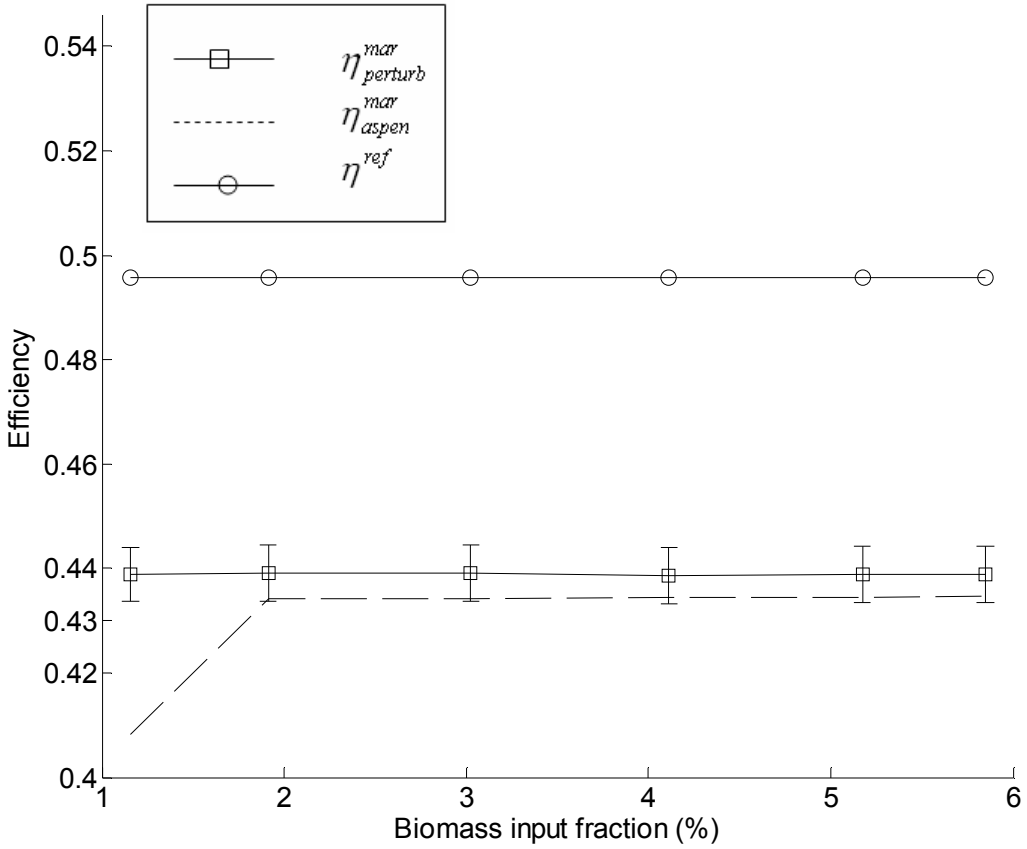

Figure 7: Comparison of the marginal biomass efficiency as calculated by Aspen (dashed line) and as predicted by the perturbation model (solid line).

The increased mass flow rate through the turbine and the decreased turbine outlet enthalpy result in a considerable power increase. When 5% of natural gas is replaced by biomass through the proposed route, the turbine will generate roughly 0.7% more power.

The strongest influence of the co-utilization can be found in the bottom cycle. The diversion of stack gases causes a significant reduction in the heat available for the HRSG. Consequently, as seen in Figure 5, the amount of superheated steam lowers considerably. As a result, the power generated in the bottom cycle reduces with the biomass input fraction: per percent biomass energy input, ~0.75% steam turbine power is lost. This reduction is compensated by the increased flow rate in the turbine and a reduction in compressor power, but the net outcome is still a small reduction in net output power.

During the simulations, it was noted that the perturbation $\partial \dot{W}_{aux}$ could be neglected without losing accuracy in the calculation of $\partial \dot{W}_{net}$. Consequently $\partial \dot{W}_{aux}$ was not included in the perturbation model.

Figure 7 displays the relevant gas turbine efficiencies. With a reference cycle efficiency of 49.5%, the marginal efficiency seems to lose roughly 5% according to both simulated and predicted values. This can be explained by:

- The fact that part of the fuel is diverted to a different route through the combustor and next to the stack, without being expanded in the turbine.
- The diversion of part of the water from the steam cycle.

The marginal biomass efficiency remains fairly constant throughout the entire simulated range of biomass input fraction.

The propagation of errors throughout the perturbation model ends up in a maximum relative error of ~1% in the marginal biomass efficiency. The model systematically overshoots the efficiencies given by Aspen, but it is satisfactory accurate, even in the lowest ψ values of 1% or smaller.

6. CONCLUSIONS

A perturbation model using only thermodynamic and chemical laws was setup to quantify the impact of biomass addition in a power cycle, starting from measurable quantities. Compared to the results predicted by process simulation, the model generally produces accurate estimates of the perturbed mass flow rates, power generation and marginal biomass efficiency. The maximum relative error on the marginal biomass for ψ = 0.5% was estimated at 1%, making it possible to quantify the effects of nearly any fraction of alternative energy on performance and efficiency of the adapted gas turbine cycle.

The effect of co-utilizing biomass on the different cycle components is most pronounced in the bottom cycle and turbine. The compressor is fairly untouched and will work close to its design point, even at a biomass input fraction of 5% or more. The changes in fuel composition result in enthalpy changes at the turbine inlet and outlet, as well as a significant change in TOT (assuming the TIT is constant). The effects of the perturbation on the turbine were estimated accurately with a maximum relative error of 0.2%. The route for biomass as proposed in this article requires recycling of a part of the turbine exhaust gases, thus diminishing the heat offered to the bottom cycle. As a result, the power generated by the steam turbine is lowered significantly. As the bottom cycle is operated in a complex way, characterized by the installation, simplifications had to be made, lowering the accuracy of the predicted power to a maximum relative error of 4.8%.

This study demonstrates the possibility to accurately deduct the marginal efficiency of biomass using only accurately measurable variables.

7. ACKNOWLEDGEMENTS

The present work is supported by the Belgian Power Utility Company ELECTRABEL.

8. REFERENCES

[1] De Ruyck J., F. Delattin, S. Bram Co-utilization of biomass and natural gas in combined cycles through primary steam reforming of the natural gas, *ECOS 2005*, Vol. 2, p. 835-845

[2] De Ruyck J., F. Delattin, S. Bram, V. Lavric, Co-utilization of biomass and natural gas in steam injected gas turbines through primary steam reforming of the natural gas, *Romanian Journal of Chemistry*, in press 2005

[3] J.Y. Shin, Y.J. Jeon, D.J. Maeng, J.S. Kim, S.T. Ro; Analysis of the dynamic characteristics of a combined cycle power plant; Energy 27, 2002, 1085-1098

[4] A. Andreini, B. Facchini; Gas Turbines Design and Off-design performance analysis with emissions evaluation; Engineering for Gas Turbines and Power 126, 2004, 83-91

[5] Ahluwalia KS, Domenichini R. Dynamic modeling of a combined cycle power plant. ASME J Eng Gas Turbines Power, 1990,112:164–7

[6] B.F. Möller, M. Genrup, M. Assadi, On the off-design of a natural gas-fired combined cycle with CO2 capture, Energy 32, 2007, 353-359

[7] Q.Z. Al-Hamdan, M.S.Y. Ebaid, Modeling and simulation of a gas turbine engine for power generation, Transactions of ASME 128, 2006, 302-317

[8] C. Kong, J. Ki, Components map generation of gas turbine engine using genetic algorithms and engine performance deck data, Transactions of ASME 129, 2007, 312-317

[9] Y.G. Li, P. Pilidis, M.A. Newby, An adaptation approach for gas turbine design-point performance simula-tion, Engineering for gas turbines and power 128, 2006, 789-795

[10] L.G. Alves, S.A. Nebra, Basic chemically recuperated gas turbines – power plant optimization

and thermodynamics second law analysis, Energy 29, 2004, 2385-2395

[11] Jolly S, Gurevich A, Pasha A. Combined cycle HRSGs: evaluation of start-up at bottled-up conditions. ASME paper 93-GT-408, 1993

[12] Dechamps PJ. Modeling the transient behavior of combined cycle plant. ASME paper 94-GT-238, 1994

[13] Akiyama T, Matsumoto H, Asakura K. Dynamic simulation and its applications to optimum operation support for advanced combined cycle plants. Energy Convers Mgmt 38, 15-17, 1997,1709–23

[14] Kim JH, Song TW, Kim TS, Ro ST. Model development and simulation of transient behavior of heavy duty gas turbines. ASME J Eng Gas Turbines Power 123, 2001, 589–94

[15] Kim JH, Kim TS, Ro ST. Analysis of the dynamic behavior of regenerative gas turbines. Proc Inst Mech Eng, Part A, J Power Energy 215, 2001, 339–46.

[16] Kim JH, Kim TS, Song TW, Ro ST. Dynamic simulation of full start-up procedure of heavy duty gas turbines. ASME paper 2001-GT-0017, 2001

[17] Kim TS, Lee DK, Ro ST. Dynamic behavior analysis of a heat recovery steam generator during start-up. Int J Energy Res 24, 2000, 137–49

[18] Y. Solantausta, A.T. Bridgwater, D. Beckman, Feasibility of power production with pyrolysis and gasification systems, Biomass and Bioenergy 9, 1995, 257-269

[19] M.J.A. Tijmensen, A.P.C. Faaij, C.N. Hamelinck, M.R.M. van Hardeveld, Exploration of the possibilities for production of Fischer Tropsch liquids and power via biomass gasification, Biomass and Bioenergy 23, 2002, 129-152

[20] M. Rodrigues, A.P.C. Faaij, A. Walter, Techno-economic analysis of co-fired biomass integrated gasification/combined cycle systems with inclusion of economies of scale, Energy 28, 2003, 1229-1258

[21] T.S. Kim, Comparative analysis on the part load performance of combined cycle plants considering design performance and power strategy, Energy 29, 2004, 71-85

[22] J.H. Kim, T.S. Kim, J.L. Sohn, S.T. Ro, Comparative analysis of off-design performance characteristics of single and two-shaft industrial gas turbines, Transactions of ASME 125, 2003, 954-960

[23] S. Adelman, M. Hoffman, J. Baughn, A Methane-Steam Reformer for a Basic Chemically recuperated Gas Turbine, ASME Journal of Engineering for Gas Turbines and Power 117, 1995, 16-23

[24] F.J. Brooks, GE gas turbine performance characteristics, GER-3567H, GE Power Systems, 2000, Schenectady, N.Y.

[25] H.Vanherzeele, Theorie der meetfouten, Uitgaven Vrije Universiteit Brussel, 1998

Proceedings of the 8th National Congress on Theoretical and Applied Mechanics, May 28-29, Brussels, Belgium.

Modified actuator disk with non-uniform loading and blade wake velocity deficit

B. Marinus[1], J. Pelletier[1], A. Cuny[2] and W. Bosschaerts[1]
[1]Department of Mechanics, Royal Military Academy
Avenue de la Renaissance 30, 1000 Brussels - Belgium
[2]Department of Mechanics, Academies of Saint-Cyr Coëtquidan
56381 Guer - France
email: benoit.marinus@rma.ac.be, walter.bosschaerts@rma.ac.be

Abstract— **The present work intended to develop an actuator disk to efficiently model running propellers in more complex systems in those cases where the flow in the propeller itself is not on focus. Modern actuator theory is used in conjunction with novel features such as finite disk thickness, radial load distribution and blade wake velocity deficit modelling. The model is then validated by comparison with numerical studies of an isolated propeller as these comparisons clearly show the ability of the present actuator to deliver reliable flow estimates together with specific periodic flow features.**

Keywords— **propeller, actuator disk**

Nomenclature

A	Disk area perpendicular to axis	
$a(.), b$	Correlation coefficient	
C_T	Thrust coefficient	$C_T \equiv T/(\rho_\infty n^2 D^4)$
$c(.)$	Correlation coefficient	
c	Local blade chord	
c_m	Blade mean chord	
D	Propeller diameter	$D = 2R_{tip}$
$e(.)$	Correlation coefficient	
$\mathcal{F}(.)$	Generic function	
$f(.)$	Correlation coefficient	
J	Advance ratio	$J = v_\infty/(nD)$
M_∞	Free-stream Mach number	
n	Rotational speed in RPS	
p	Pressure	
R	Blade radius	
ΔR	Blade radial span	$\Delta R = R_{tip} - R_{root}$
r	Local radius	
Δr	Local radial span	
T	Propeller net thrust	
t	Local net thrust	
v	Velocity	
β_{ref}	Blade angle at 75% radius	
ω	Angular velocity	$\omega = d\theta/dt = 2\pi n$
ρ	Specific mass	
θ	Angular coordinate in a ortho-axial plane	
$\Delta\theta$	Angular sector between two blades	
ξ	Reduced radial coordinate	$\xi = r/R_{tip}$

Sub- and superscript

$\cdot_d$	Quantity at downstream face of propeller disk
$\cdot_i$	Induced quantity
$\cdot_p$	Propeller related quantity
$\cdot_r$	Radial quantity
$\cdot_s$	Quantity infinitely far downstream of propeller disk
$\cdot_u$	Quantity at upstream face of propeller disk
$\cdot_x$	Axial quantity
$\cdot_{out}$	Quantity at blade root
$\cdot_{root}$	Quantity at blade root
$\cdot_{tip}$	Quantity at blade tip
$\cdot_\infty$	Free-stream quantity
$\cdot_\theta$	Angular quantity
$.'$	Iterative quantity
$.^*$	Corrected quantity

I. Introduction

THIS paper presents work conducted toward a modified actuator disk model to be used in a preliminary design process or in optimisation of more complex structures. Indeed, recent work by Malard et al[1], Moens and Gardarein[2], Goble and Hooker[3] or Zhang et al[4] stressed the need for a cheap but reliable model that should be used to simulate the flow from a running propeller onto other airplane surfaces in those situations where the flow in the propeller itself is of no or little importance.

Most efforts use some variant of the actuator disk that replaces the running propellers quite efficiently except for the unsteady flow features of propeller slipstream. The aim of the present study is to develop an accurate actuator disk modified to reproduce some of the non-uniform features as radial load distribution and blade wake velocity deficit. Doing so, some of the major shortcomings of the actuator disk, i.e. the uniformity both in radial and ortho-radial directions, are relieved while preserving its major advantage: numerical cheapness. This renders the tool very useful for preliminary studies or optimisation as both require cheap and almost 'interactive' models that allow for fast decision making based on reliable results.

II. Modified Actuator Disk

A. Actuator disk model

The starting point is the general momentum theory first proposed by Froude. This very classical actuator disk theory includes contraction of the streamtube and rotation in the slipstream ([5], [6]). It relies on two basic assumptions:
1. inviscid and incompressible flow,
2. and uniform axial and tangential velocity distributions in each axial section of the streamtube.
Additionally, the flow in the slipstream is supposed to be irrotational except along the axis so that the circulation is constant for different radial positions.

The introduction of rotation or swirl in the slipstream causes the common hypothesis concerning uniformity of the pressure field in axial sections to be relaxed but is the origin of high average static pressures in the slipstream.

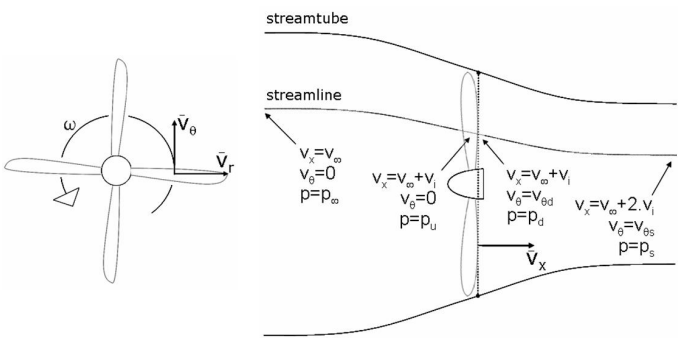

Fig. 1. Classical momentum theory model with rotation of the slipstream.

According to Schouten[7], this is relaxed when wake roll-up is introduced instead of a rigid wake. But the effects on propeller efficiency, henceforth on propeller thrust and torque are limited. So the authors shares the advice of Ribner[8] that neglect of wake roll-up only slightly affects the velocities induced over the propeller blades.

In the frame of the preceding hypotheses, and when wake roll-up is neglected, axial and tangential velocities are computed from propeller data such as thrust, RPM and area together with flight data as specific mass at flight altitude and flight velocity. Figure 1 sketches the model with the streamtube divided into a section extending from infinity to the upstream face of the propeller plane (which is infinitely thin) and a section extending from the downstream face to infinity.

The induced velocity v_i is computed from propeller thrust T, propeller angular velocity ω and propeller tip radius R_{tip} together with the free-stream velocity v_∞ and free-stream fluid density ρ:

$$v_i = \sqrt{\frac{v_\infty^2}{4} + \frac{\omega^2 R_{tip}^2}{4}\left(1 - \sqrt{1 - \frac{4T}{A_p \rho \omega^2 R_{tip}^2}}\right)} - \frac{v_\infty}{2} \quad (1)$$

where A_p is the propeller disk area and where the thrust T is obtained either from a preliminary study, or some experimental results or even an isolated propeller numerical study.

The induced velocity v_i is then used to compute the axial velocity at the actuator disk:

$$v_{xd} = v_{xu} = v_\infty + v_i \quad (2)$$

Note that in general momentum theory, there is no jump in axial velocity between the upstream and downstream face of the actuator disk as in the basic actuator theory known as axial momentum theory (developed by Rankine).

The angular velocity of the slipstream infinitely far downstream ω_s is computed through:

$$\omega_s = \frac{4(v_\infty + 2v_i)v_i}{\omega R_{tip}^2} \quad (3)$$

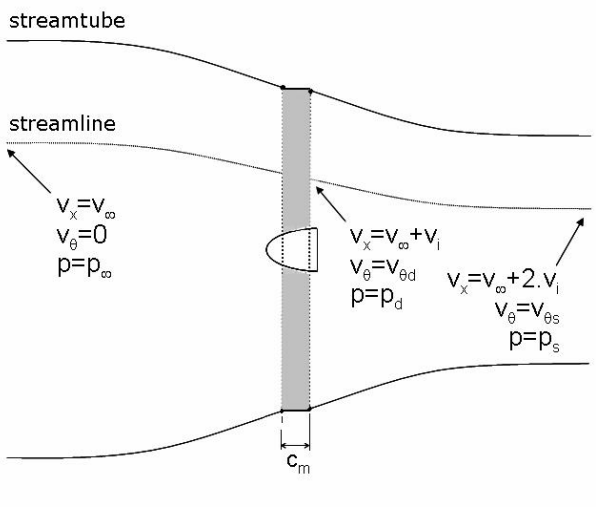

Fig. 2. Introduction of a finite thickness disk.

And finally, the tangential velocity downstream of the disk $v_{\theta d}$ is computed:

$$v_{\theta d} = \frac{v_\infty + v_i}{v_{xs}} r\omega_s \quad (4)$$

with

$$v_{xs} = v_\infty + 2.v_i$$

where v_{xs} is the axial velocity infinitely far downstream and r is the radius of the considered streamline. In contradiction to the axial velocity, there is a jump across the disk for the tangential velocity due to the angular momentum imparted to the fluid through the propeller disk, since $v_{\theta u} = 0$.

B. Modifications

B.1 Finite thickness

The first modification to the classical theory is the introduction of a finite thickness to the actuator disk so that the flow around the actuator should be as close as possible to the flow outside the envelope of the propeller.

The actuator disk is therefore replaced by an actuator cylinder (the shaded area on figure 2). A hole is pierced through the actuator cylinder so that it fits onto the spinner. The disk thickness c_m is the mean chord of the blades computed by:

$$c_m = \frac{1}{R_{tip}} \int_{R_{root}}^{R_{tip}} c.dr$$

where c is the local chord, but no account is taken for high blade sweep that would make the volume swept by the blades extend further downstream.

In order to ensure mass conservation through the disk, the axial velocity v_x in a section A of the cylinder located between A_u and A_d is adapted by a factor A_d/A derived from incompressible mass conservation theory such that the downstream face of the cylinder carries the classical induced velocities:

$$v_x = \frac{A_d}{A}(v_\infty + v_i) \quad (5)$$

$$\text{where } \frac{A_d}{A} = \mathcal{F}(x) \quad (6)$$

with $\mathcal{F}(x)$ depending on the spinner profile expressed in axial coordinate x.

B.2 Radial load distribution

The second modification concerns the introduction of a radially distributed propeller load. This way, the propeller induced axial and tangential velocities become dependant on the radius.

Unlike Zhang et al[4] who use a sixth order Bessel function to model radial load distribution, the present model uses a second order polynomial inspired by blade element theory ([6], [9], [10], [11], [12]) and found to match adequately both experimental and numerical data ([13], [14]). This load distribution is compared to the uniform case in figure 3. The radial load distribution is given by:

$$t(\xi) = a(\xi - 1)(\xi - \xi_2) + \frac{T.R_{tip}}{\Delta R} \quad (7)$$

where t is the local net thrust and $\xi = \frac{r}{R_{tip}}$ is the reduced radial coordinate and ΔR is the blade span. This equation must satisfy

$$\int_{\xi_{root}}^{1} t(\xi)d\xi = \int_{\xi_{root}}^{1} \left[a(\xi - 1)(\xi - \xi_2) + \frac{T.R_{tip}}{\Delta R} \right] d\xi = T \quad (8)$$

which yields

$$\int_{\xi_{root}}^{1} \left[a(\xi - 1)(\xi - \xi_2) \right] d\xi = 0$$

where a is chosen so that the thrust produced at the root is 25% of the maximum local thrust t_{max} and ξ_2 is chosen so that equation 8 is satisfied. Doing so the maximum local thrust occurs around 75% radius. Note that the last term of equation 7 is precisely the local thrust t_{mean} in the case of a uniform load distribution as in the classical actuator theory.

As any ring of the actuator cylinder outlet surface, with thickness Δr centred around r, is enclosed between two streamlines, the local thrust produced by this ring can be used to compute the induced velocity of the corresponding disk increment (see [11]):

$$v_i(r) = \sqrt{\frac{v_\infty^2}{4} + \frac{1}{4}\left(\omega_s^2 \frac{v_\infty + v_i'}{v_{xs}'} r^2 + \frac{t_{r-\Delta r/2}^{r+\Delta r/2}}{\pi \rho r \Delta r} \right)} - \frac{v_\infty}{2} \quad (9)$$

where v_i' is obtained from equation 1, $v_{xs}' = v_\infty + 2v_i'$ and $t_{r-\Delta r/2}^{r+\Delta r/2}$ is the thrust produced by this ring and is approximated by a step approach. The induced velocity v_i is now radially dependent and replaces equation 1. Of course, a similar development leads to the expression of the radially dependent angular velocity $\omega_s(r)$ that replaces equation 3:

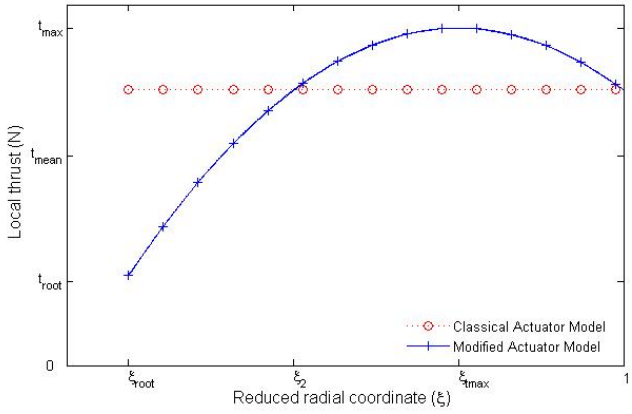

Fig. 3. Comparison of load distributions in the classical and modified actuator models.

$$\omega_s(r) = \frac{2(v_\infty + 2v_i)v_i}{\omega r \Delta r} \quad (10)$$

B.3 Wake velocity deficit

The last modification consists in implementing periodic blade wake velocity deficits. As boundary layer development on the suction and pressure faces of real propeller blades results downstream in a wake; 'fictive' blades are introduced in the modified actuator by implementing local deficit profiles at the considered positions of the blades. Nevertheless, no actual solid blade surface is implemented in the actuator disk, so there is no need for real boundary layer modelling. Although the velocity deficit profiles depend strongly on geometrical features of the blades such as their thickness at the considered radial section, these profiles have shown to be adequately approximated by Gaussian curves depending on purely flow related quantities. So even when the blade wake model is used in the actuator, no knowledge of the blade geometry is required.

Together with this axial velocity deficit, a tangential increment exists. It stems from the bounded vorticity around the blades. At first order, this increment can also be approximated by a Gaussian profile in the ortho-radial direction whose amplitude and width depend on the considered radial section.

This modification offers the advantage of delivering the main unsteady flow feature of propeller flow at extremely low cost, indeed the numerical cost of implementing actuator rotation is very low as no mesh modification nor moving meshes are required. It is sufficient to set the velocity conditions from the actuator theory at different mesh points according to time as dictated by both the number of blades and the propeller RPM.

All quantities necessary for the previous modifications are extracted from numerical studies of isolated propellers and are applicable over a wide range of operating conditions for a given propeller geometry.

The wake velocity deficit is implemented in the axial velocity by modifying equation 2 both by equation 9 and by

Nb	Type	M_∞	J	β_{ref}	C_T	$T(N)$
1	SR-1	0.6	3.08	60°	0.41	200
2	SR-1	0.7	3.04	59.5°	0.42	286
3	SR-1	0.7	2.86	59.5°	0.52	399
4	SR-1	0.8	3.08	58.5°	0.37	322
5	SR-3	0.6	3.00	60°	0.46	240
6	SR-3	0.7	3.06	59.5°	0.48	322
7	SR-3	0.7	3.26	59.5°	0.41	245
8	SR-3	0.8	3.08	58.5°	0.45	389
9	SR-6	0.75	4.36	66.4°	0.25	124

TABLE I
Test cases.

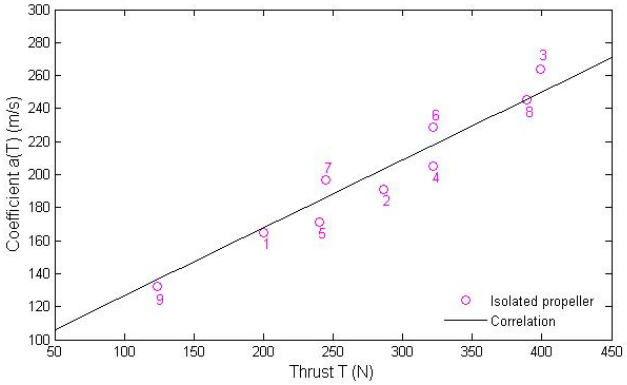

Fig. 4. Correlation for the $a(T)$ coefficient. Numbers indicate the corresponding case from table I.

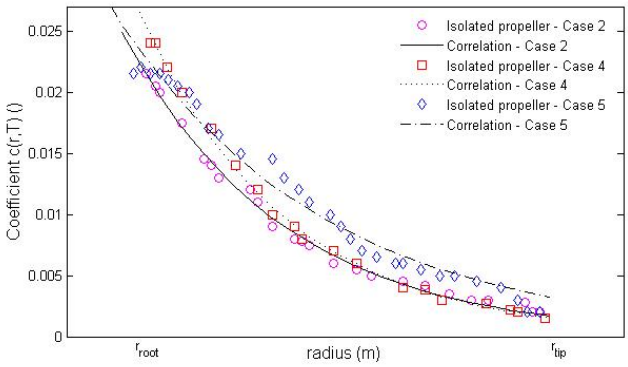

Fig. 5. Correlation for the $c(r,T)$ coefficient for three cases.

introducing a wake velocity deficit term so that the ortho-radial uniformity is broken:

$$v_{xd}(r,\theta) = v_{xu}(r,\theta) = v_\infty + v_i^*(r) - a(T)\exp -\frac{(\theta-b)^2}{c(r,T)^2} \tag{11}$$

where $v_i^*(r)$ is the induced velocity from equation 9 incremented to satisfy mass conservation through the disk with the deficits taken into account, $a(T)$ is a coefficient solely depending on the thrust and imposes the magnitude of the deficit, θ is the tangential coordinate, b is the periodic tangential location of the blade deficit considered (b would be $\pi/4$-periodic for an eight bladed propeller) and $c(r,T)$ is a coefficient depending on r and T that influences the deficit wideness.

The tangential velocity increment that develops past the trailing edge of the blade can be efficiently modelled in the same, although opposite, way. Nevertheless, this increment has not yet been implemented in the present results as further investigations with regard to the behaviour of the correlation coefficients is needed.

III. Study of the model parameters

Extensive studies have shown that the parameters $a(T)$, b and $c(r,T)$ have interesting behaviour for a given family of geometrically similar propellers. For example, the NASA $SR-1$, $SR-3$ and $SR-6$ propellers have different geometries though they present the same features: thin swept blades. In the present work, $0.622m$-diameter propellers have been studied.

Correlation work done on those three propellers operating at three different free-stream Mach numbers with different advance ratios and blade angle as shown in table I, conducted to formulate $a(T)$ as a linear expression of T independent of any other variable. This correlation is shown on figure 4.

As shown on figure 5, the $c(r,T)$ parameter exhibits an inverse exponential behaviour with respect to the radius r given by an equation of the type:

$$c(r) = e\exp(fr)$$

where e is a positive non-dimensional number and f is a negative non-dimensional number. Once again, correlation work has shown that e and f are nicely correlated to the thrust T by linear behaviour as can be deduced from figures 6 and 7. At present, no convincing explanation has been found for the poor correlation of case 7. So, in the end, $c(r,T)$ is written as:

$$c(r,T) = e(T)\exp(f(T)r) \tag{12}$$

The coefficient $a(T)$, together with equation 12 and linear expressions for $e(T)$ and $f(T)$ are implemented along with equation 11 in the actuator disk to compute the axial velocity. These equations have the advantage of depending exclusively on parameters already needed for actuator disk calculations, namely r and T as b depends solely on the number of blades, so that no additional data is necessary as long as a family of geometrically similar propellers is used.

IV. Verification

Figure 8 gives a side and front view of the mesh used. It shows the boundary layer mesh build around the spinner but also the traces of the supposed location of the blades due to the mesh refinement in the ortho-radial direction.

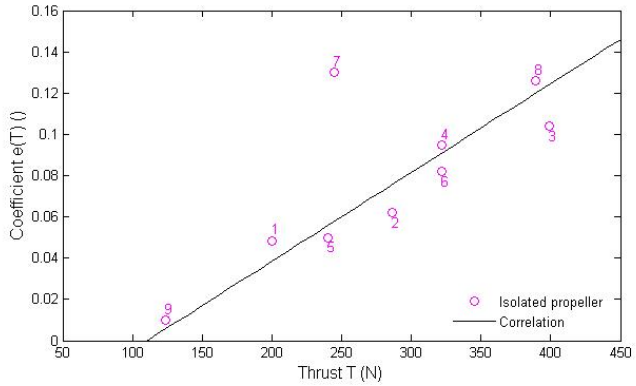

Fig. 6. Correlation for the $e(T)$-coefficient. Numbers indicate the corresponding case from table I.

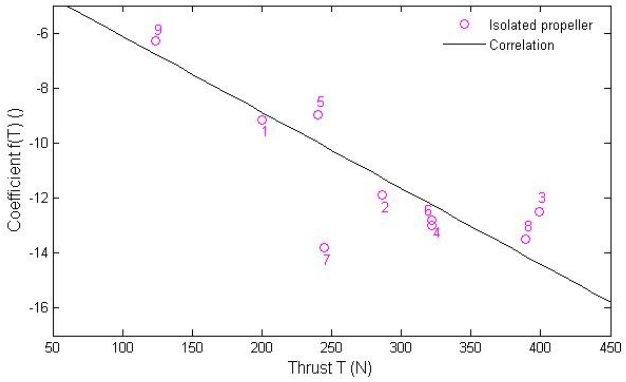

Fig. 7. Correlation for the $f(T)$-coefficient. Numbers indicate the corresponding case from table I.

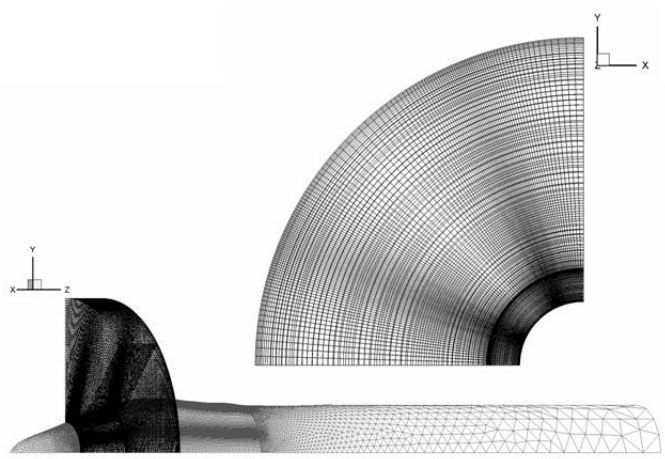

Fig. 8. Front (*top-right*) and side (*bottom*) view of the actuator mesh. Only one quadrant is presented.

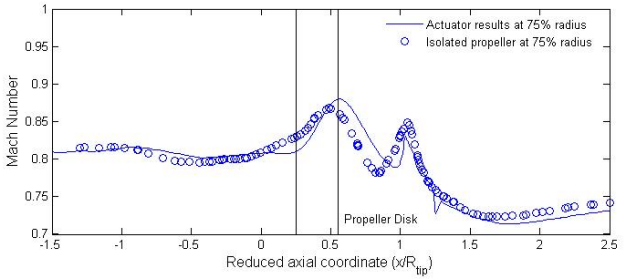

Fig. 9. Mach number comparison for a NASA SR-1 propeller at $M_\infty = 0.8$, $J = 3.08$ and $\beta_{ref} = 58.5°$ at 75% radius.

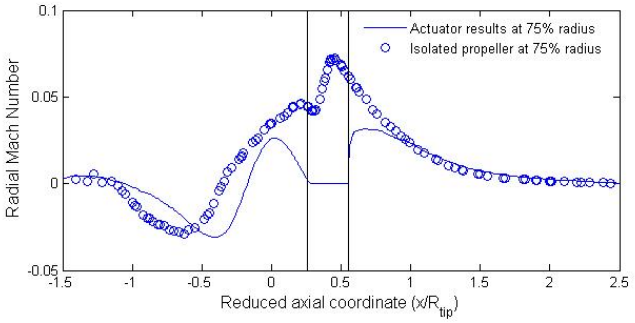

Fig. 10. Radial Mach number comparison for a NASA SR-1 propeller at $M_\infty = 0.8$, $J = 3.08$ and $\beta_{ref} = 58.5°$ at 75% radius.

The modified actuator disk results are compared to an extensive numerical study of various isolated propeller configurations. The results, shown on figures 9, 10 and 11, are in good agreement and confirm the ability of the model to retrieve good estimates for major flow features up- and downstream of the propeller disk despite the fact that the actuator volume itself is treated using incompressible assumptions and that no corrections are applied. Indeed, the (total) Mach number together with the tangential Mach number are nicely correlated with the isolated simulation. The radial Mach number results shown on figure 10 show good agreement up- and downstream of the propeller disk where the flow is treated as compressible. The zero radial velocity imposed in the current implementation in the actuator disk, in order to enforce non-contraction of the streamtube, is clearly the major source of discrepancy in the close vicinity of the disk as is strongly suggested from figure 10. This will be corrected in future versions of the code by computing the radial velocity from mass conservation in three dimensions whereas mass conservation is now purely realized through the axial and tangential velocities. Despite this shortcoming, the present model is already proficient in predicting reliable flow estimates.

Figures 12 and 13 show a comparison of the axial velocity deficit at four different radii. The agreement is convincing through all the blade span. The underprediction of the deficit magnitude at 39% radius, and the overprediction at 99% radius are believed to find their origin both in the shape of the actual blade and in the use of correlated val-

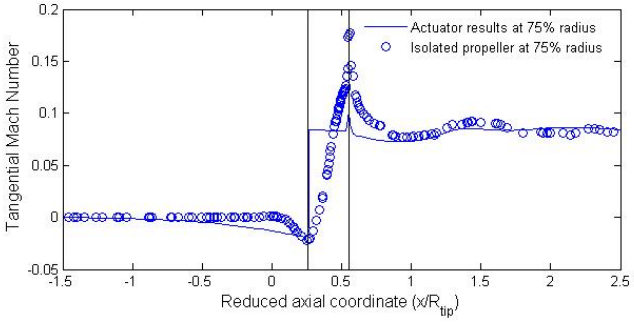

Fig. 11. Tangential Mach number comparison for a NASA SR-1 propeller at $M_\infty = 0.7$, $J = 3.04$ and $\beta_{ref} = 59.5°$ at 75% radius.

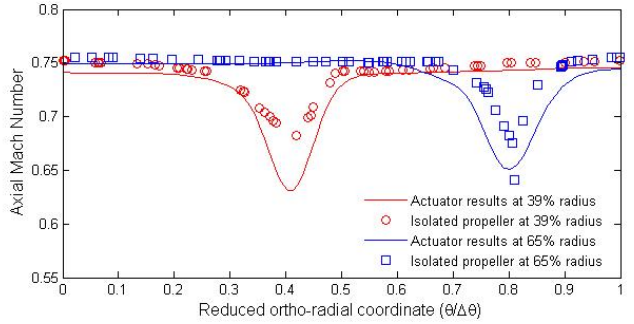

Fig. 12. Axial Mach number deficit comparison for one blade of a NASA SR-1 propeller at $M_\infty = 0.7$, $J = 3.04$ and $\beta_{ref} = 59.5°$ at two radii (39% and 65%).

ues for the coefficients of equations 11 and 12. The same agreement has been obtained for the other cases in table I, with both depth and width generally close to isolated propeller simulations. The agreement is considered satisfacting given the approximations made and the cheapness of the model.

Figures 14 and 15 show contours of Mach numbers at four different radii respectively when computed with the actuator disk and with the isolated propeller. These show clearly the main difference between both approaches as the local flow features in the blade passages are not included in the mathematical model of the actuator. Up- and downstream of the disk, the agreement is good given the low order model used. The agreement seems to get better along the blade span although the strong flow features occurring near blade tip seem to disturb the flow in a way that is not caught by the actuator implementation. Nevertheless,the actuator model delivers a correct averaged flow.

At low radius near blade root, the higher Mach number region found aft of the disk in the actuator case is believed to come from the fact that the boundary layer that develops around the spinner is modelled in this case while it is not accounted for in the isolated simulation. The displacement thickness associated to that boundary layer together with centrifugal forces causes greater flow blockage at lower radii, thereby increasing the Mach number at the radius of the cut in the actuator model.

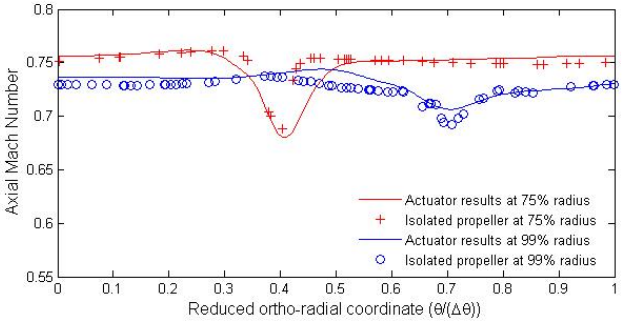

Fig. 13. Axial Mach number comparison for one blade of a NASA SR-1 propeller at $M_\infty = 0.7$, $J = 3.04$ and $\beta_{ref} = 59.5°$ at two radii (75% and 99%).

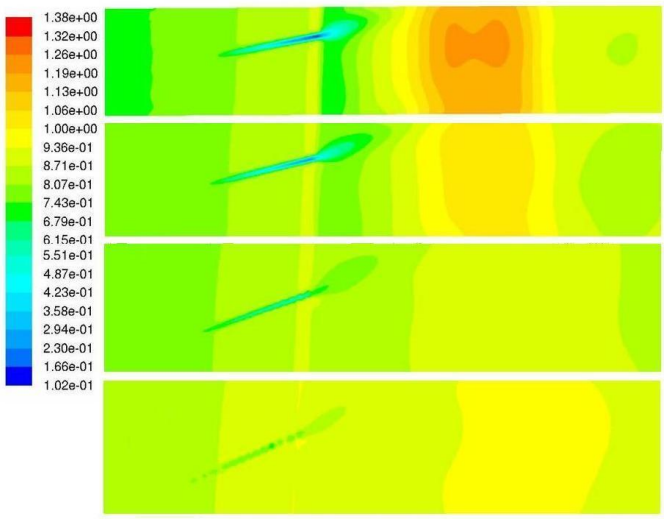

Fig. 14. Mach number contours with the **actuator disk** at four radii (39%, 50%, 75% and 99%) for the NASA SR-3 propfan at $M_\infty = 0.8$ with $J = 3.08$ and $\beta_{ref} = 58.5°$. Note that the constant radii sections have been shrunk to facilitate comparison between radii.

These figures show acceptable agreement with respect to velocity deficit. It appears to be nicely correlated both in depth and width within the framework set in the discussion of figures 12 and 13. As commonly accepted in actuator disk usage and shown in the isolated contours, the flow behind a blade is fully mixed at a distance of the order of one blade radius. This distance is nicely retrieved with the modified actuator except for the tip region. Implementing non-zero radial velocities would not only enhance the profile of figure 10, it could also retrieve more accurate flow features at the tip as the presence of strong blade tip vortices is the reason for the bigger mixing length.

Finally figure 16 shows Mach number contours at two radii (39% radius close to blade root and 75% radius). Good correspondance is obtained downstream of the propeller disk and the major discordance concerns the flow in the blade passage.

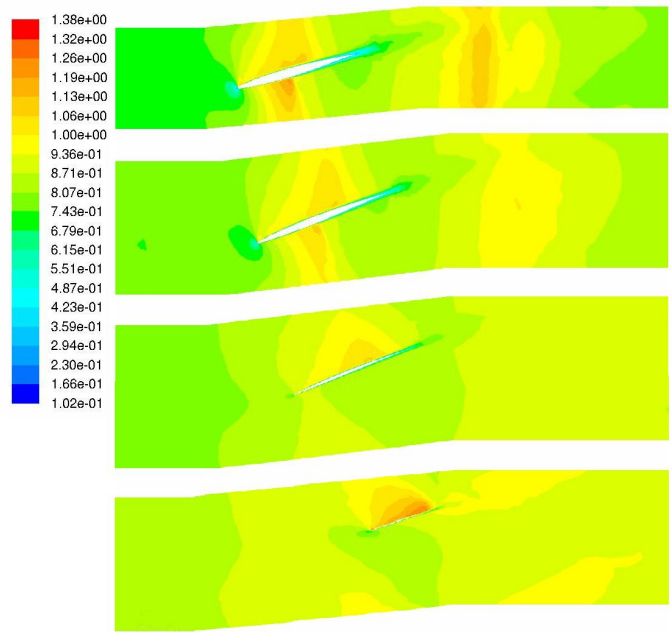

Fig. 15. Mach number contours with the **isolated blade** at four radii (39%, 50%, 75% and 99%) for the NASA SR-3 propfan at $M_\infty = 0.8$ with $J = 3.08$ and $\beta_{ref} = 58.5°$. Note that the constant radii sections have been shrunk to facilitate comparison between radii.

V. Conclusions

A modified actuator disk model has been developed. It accounts for rotation in the slipstream, radial load distribution, finite thickness of the propeller disk and blade wake axial velocity deficit. The model has been validated through extensive comparison with studies of isolated full propellers and offers the advantage to be extremely inexpensive for simulations of the effect of propellers on other airframe structures in early design stages. The model is extremely cheap and can therefore be used 'on-line'.

The modified actuator offers the advantage to raise the limitations inherent to classical actuators. Indeed, blade wake velocity deficit modelling offers the advantage to deliver major unsteady propeller flow features at low cost hence unsteady effects on items placed within one radius from the propeller plane can be assessed early in the design or optimization cycle.

Future improvements consist in implementing non-zero radial velocity in the actuator disk. Doing so, the flow patterns should be even more accurately retrieved at all radii, especially near blade tip.

Acknowledgments

The authors wish to acknowledge the Belgian Defence Scientific and Technologic Research initiative for its funding of the present study.

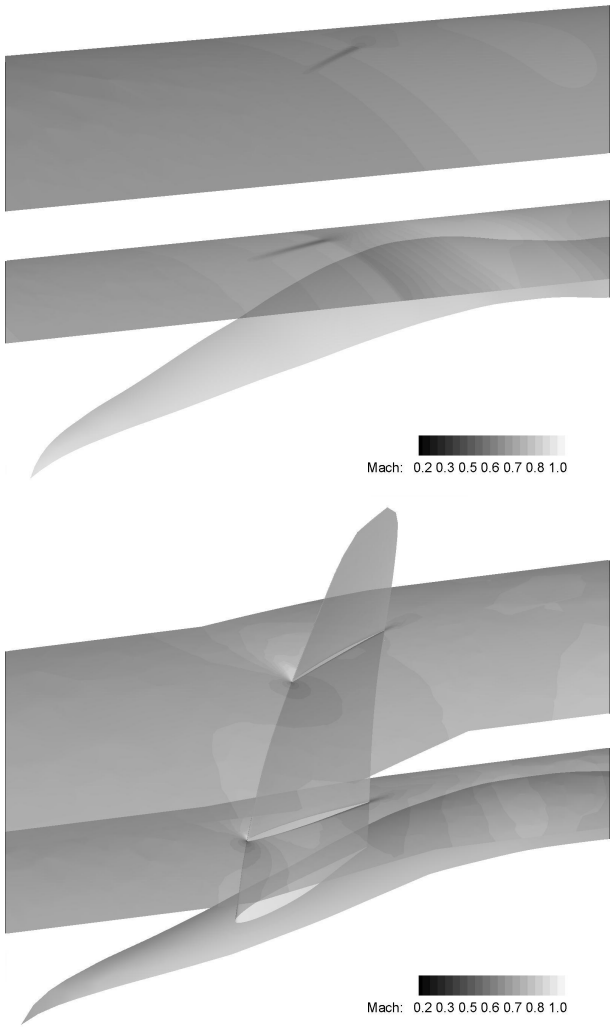

Fig. 16. Mach number contours at two radii for both models (*top*, modified actuator disk model - *bottom*, isolated propeller blade) in test case Nr 2.

References

[1] L. Malard, J.-M. Bousquet, O. Atinault, and Larcher J.-L., "High speed testing and cfd investigation for the new generation military transport aircraft development," in *35th AIAA Fluid Dynamics Conference and Exhibit*, Toronto (Canada), June 6-9 2005, AIAA, number AIAA 2005-4744.

[2] F. Moens and P. Gardarein, "Numerical simulation of the propeller/wing interaction for transport aircraft," in *19th AIAA Applied Aerodynamics Conference*, Anaheim (USA), June 11-14 2001, ONERA, number AIAA 2001-2404, AIAA.

[3] B.D. Goble and J.R. Hooker, "Validation of an unstructured grid euler/navier-stokes code on a full aircraft with propellers," in *39th AIAA Aerospace Sciences Meeting and Exhibit*, Reno (USA), January 8-11 2001, AIAA, number AIAA 2001-16797.

[4] F. Zhang, M. Khalid, J. Syms, and N. Ball, "Numerical investigation of propeller effects on the aurora aircraft," in *19th Applied Aerodynamics Conference*, Anaheim (USA), June 11-14 2001, AIAA, number AIAA 2001-31187.

[5] H. Glauert, *Aerodynamic theory Vol 4 Div L - Airplane propellers*, Durand, Berlin (Germany), 1935.

[6] W.F. Phillips, *Mechanics of flight*, John Wiley & sons, Hoboken (USA), 2004.

[7] G. Schouten, "Theodorsen's propeller performance with rollup and swirl in the slipstream," *Journal of Aircraft*, vol. 36, no. 5, pp. 892–895, 1999.

[8] H.S. Ribner, "Neglect of wake roll-up in theodorsen's theory

of propellers," *Journal of Aircraft*, vol. 34, no. 6, pp. 814–816, November-December 1997.

[9] H.V. Borst, "Summary of propeller design procedure and data. volume i: aerodynamic design and installation," Technical Report 73-34A, Army Air Mobility Research and Development Laboratory, Rosemont (USA), November 1973.

[10] A.J. Bocci and J.I. Morrison, "A review of ara research into propeller aerodynamic prediction methods," in *Aerodynamics and Acoustics of Propellers*, Toronto (Canada), October 1-4 1984, AGARD, number AGARD CP-366.

[11] J.T. Conway, "Analytical solutions for the actuator disk with variable radial distribution of load," *Journal of Fluid Mechanics*, vol. 297, pp. 327–355, 1995.

[12] J.T. Conway, "Exact actuator disk solutions for non-uniform heavy loading and slipstream contraction," *Journal of Fluid Mechanics*, vol. 365, pp. 235–267, 1998.

[13] R.M. Bass, B. Munniksma, and J. van Hengst, "Aerodynamic and structural aspects of propeller and drive for a 1/5 scale wind tunnel programme," in *Aerodynamics and Acoustics of Propellers*, Toronto (Canada), October 1-4 1984, AGARD, number AGARD CP-366.

[14] B. Marinus, "Multidisciplinary evaluation of known propeller configurations," Project Report 2007-15, von Karman Institute for Fluid Dynamics, Rhode-Saint-Genese (Belgium), June 2007.

Proceedings of the 8th National Congress on Theoretical and Applied Mechanics, May 28-29, Brussels, Belgium.

Numerical investigation of the self-similarity of a two-dimensional shear-layer

C. Carton de Wiart[1,2], F. Thirifay[1], G. Winckelmans[2], A.Roshko[3] C. Bailly
[1] Cenaero, 6041 Gosselies, Belgium
[2] Department of Mechanical Engineering, Université catholique de Louvain (UCL), 1348 Louvain-La-Neuve, Belgium
[3] Graduate Aeronautical Laboratories, California Institute of Technology, 91125 Pasadena, CA, USA
email: corentin.carton@cenaero.be

Abstract— **This paper presents the results of a two-dimensional spatially developing shear-layer simulation. A vortex method (VIC-FM), assuring no dispersion errors, is used to capture correctly the turbulent structures. Several outflow conditions are tested to measure their influence on the results in the turbulent self-similar region. Two sizes of the domain are used. The second domain, longer than the first one, was initially created to increase the range of the self-similar region independent of the boundary conditions and to validate the results obtained on the shorter domain. The different outflow conditions showed that there is no significant influence on the results in the turbulent self-similar region. The results on the extended domain have validated those on the shortest. They have also unveiled the possibility of multiple self-similar regions in such 2-D turbulence.**

Fluid mechanics, shear-layers, self-similarity

I. Introduction

THE present contribution reports the results of a two-dimensional numerical simulation of a shear-layer. One of the canonical shear flows, the shear-layer is a technically important and scientifically interesting turbulent flow and has received much attention because of the so-called "coherent structures". The canonical free turbulent flows, which include jets and wakes, are interesting not only because they are technically important but also because their specification requires a minimum of empirical coefficients and so makes them useful objects for modeling and theoretical exploration. A central task for turbulence theory is to predict the coefficients but what is important is to define their experimental values accurately. In this case, the two-dimensional shear-layer is defined as the meeting of two flows with different velocity (U_1 and U_2). The upstream flows are taken uniform and separated by a semi-infinite plate located in $y = 0$. At the origin ($x = 0$), the flows meet and create the so-called shear-layer.
The difficulties are connected with the initial boundary layers from the splitter plate and with outflow conditions. The canonical, self-similar flow should become independent of the initial boundary layers at some reasonable distance downstream. On the other hand, outflow conditions will have some upstream effects. In assessing the effects of this and other difficulties, it is usually assumed that, if the growth rate $d\delta/dx$ is found to be constant in some part of the mixing layer, then its value is candidate for definition of the self-similar flow. A stronger candidate for the definition of the self-similarity is the constancy of the maximum Reynolds stress $-\overline{u'v'}/(\Delta U)^2$. In the present work, different configurations of the outflow condition were used in order to evaluate their impact on the self-similarity area.
The simulations studied here are high-resolution simulations, over a large spatial extent to allow self-similar development to significantly high Reynolds number, and over a long time to provide statistical convergence of mean values. The compactness of the vorticity fields makes the use of the vortex method very attractive as it only requires computational elements where the vorticity is non-zero. Another advantage of this method is the Lagrangian operator, eliminating the need to explicitly treat the convection derivative : convection dominated flows are well treated by vortex methods. Recent significant developments have been made in the field or vortex methods. In this case, the Vortex-In-Cell method, combined to Fast-Multipole method developed by Cocle et al. [1] was used.

II. Mathematical formulation and numerical procedure

A. Equations for two-dimensional flows

The velocity-vorticity formulation of the Navier-Stokes equations for incompressible flows is used (1) with a VIC-FM [1] solver (Vortex-In-Cell, Fast-Multipole) here as developed by F. Thirifay [2]. The equations are

$$\frac{D\omega}{Dt} = \nu \bigtriangledown^2 \omega \,, \qquad \bigtriangledown^2 \psi = -\omega \tag{1}$$

where ω is the vorticity and ψ is the streamfunction (with $u = \frac{\partial \psi}{\partial y}$ and $v = -\frac{\partial \psi}{\partial x}$).
The VIC method, using vortex particles, is very efficient for convection dominated flows. Indeed, the Lagrangian treatment eliminates the need to explicity treat the convection derivative. Coupled with the VIC approach, the FM method provides the correct boundary conditions for the stream function in order to solve the Poisson equation (1) on the grid.
The particles are convected using

$$\frac{d}{dt}\mathbf{x_p} = \mathbf{U_p} + \mathbf{u_a} + \mathbf{u_{part}} \tag{2}$$

where $\mathbf{U_p} = \frac{U_1+U_2}{2}\mathbf{e_x}$ is the constant potential velocity, $\mathbf{u_a}$ is the velocity induced by the inflow and outflow conditions and $\mathbf{u_{part}}$ is that induced by the particles.
The diffusion of the vorticity are computed using a second order centered finite differences. The particles are projected on the grid to solve the Poisson equation (1).

B. Redistribution

The particles are redistributed every few time steps in order to maintain a good spatial uniformity. A third order redistribution

scheme, using the position and the strength of the particles, interpolates the values on the grid. This grid goes smoothly from uniform to polar to correspond to the growth rate of the shear-layer (see Fig. 1). This "trumpet" mapping is given by

$$\begin{aligned} x &= \frac{h_0}{C}\sinh(iC)\cos(jC)\,, \\ y &= \frac{h_0}{C}\cosh(iC)\sin(jC)\,, \end{aligned} \tag{3}$$

where h_0 is the size of the smallest cell (in the uniform region) and C is the growing rate parameter. The shape of each cell is roughly a square, thus maintaining a good aspect ratio.

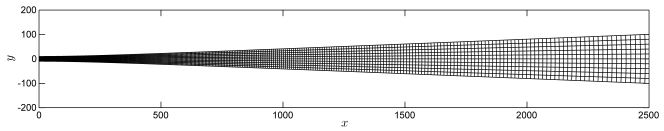

Fig. 1. Redistribution mapping. The simulation cells are four times smaller than shown.

C. Inflow and outflow conditions

The inflow and outflow conditions are defined by two vortex sheets. The stream function taking account of those sheets is given by

$$\begin{aligned} \psi_a &= \frac{\Delta U}{4\pi}\left(\int_{-\infty}^{0}\log((x-x')^2+y^2+\varepsilon^2)dx'\right. \\ &\left.+\int_{L}^{\infty}\log((x-x')^2+(y+y_s)^2+\varepsilon^2)dx'\right) \end{aligned} \tag{4}$$

with ε and E respectively the thickness parameter of the inflow and the outflow sheets. The outflow sheet position is shifted by $-y_s$. The vorticity profile at the inflow is represented at Fig. 2 Various ε and positions of the outflow vortex sheet have been tested to measure their influence on the results in the self-similar region of the flow.

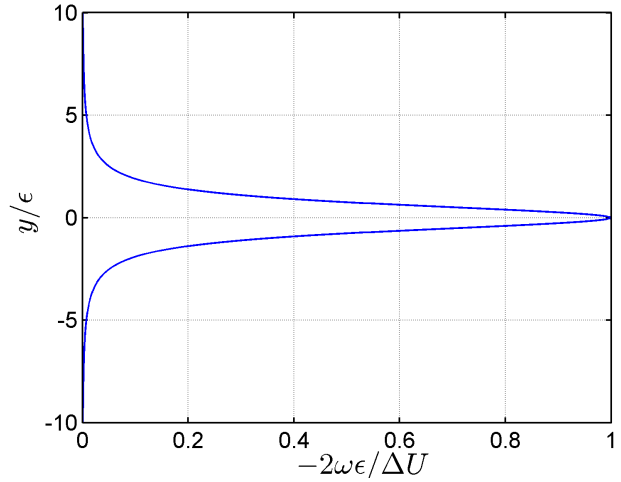

Fig. 2. Vorticity profile of the regularized vortex sheet

D. Computation parameters

The velocities at the inflow condition are taken as $U_1 = 1$ and $U_2 = 0.38$. The value $U_2/U_1 = 0.38$ is chosen to correspond to the case studied by Brown and Roshko [3]. The computational domain extends from $x = 0$ to $x = 2500$ and up to $x = 3500$ for the largest grid. The thickness parameter of the inflow sheet is $\varepsilon = 1$, which gives an initial momentum thickness equal to $\theta_0 = \pi/4$, with a Reynolds number $Re = \frac{\Delta U\theta_0}{\nu} \simeq 50$. The relation between the momentum thickness and the thickness parameter is usefull to set the thickness of the outflow sheet. The position and that thickness of the outflow sheet are chosen to correspond at the momentum thickness computed from previous simulations.

The timestep for the second order Runge-Kutta scheme is taken as $dt = 2h_0/U_2 \simeq 2.6$, which satisfy well the accuracy condition for vortex methods $\omega_{max}dt \simeq 0.6 < 1$.

Two parameters are used to define the vortex sheet at the outflow: the y-shift, y_s and the thickness E. To measure correctly their influence on the flow, the following computations are done:

- VIC1: the thickness parameter is the same as the inflow condition ($E = \varepsilon$). The outflow sheet is located on $y = 0$,
- VIC2: the thickness parameter is computed from the VIC1 simulation. The outflow sheet is still located on $y = 0$,
- VIC3: the position of the outflow vortex sheet is deduced from the VIC1 simulation. The tickness parameter is the same as that of the inflow sheet,
- VIC4: the thickness parameter and the position of the outflow sheet are both computed from simulation VIC1.
- VIC5: the parameters of the outflow condition are the same as those of the VIC4 computation but the domain is extended up to $x = 3500$.

III. Mean flow data

The profiles of the mean velocity are obtained from long time averaging: 140 t_c are necessary to converge the statistics, where t_c is defined as the time required to travel once the computational domain at the global convection velocity $\mathbf{U_p}$. From each converged mean velocity profile, $U(y)$, the momentum thickness θ, the vorticity thickness δ_w and the position of the dividing streamline $y^\bullet$ have been computed:

$$\theta = \int_{-\infty}^{\infty}\frac{(U_1-U)(U-U_2)}{\Delta U^2}\,dy\,, \tag{5}$$

$$\delta_w = \frac{\Delta U}{(\partial U/\partial y)_{\max}}\,. \tag{6}$$

The position of the dividing streamline is defined as the streamline along which a self-similar shear layer develops, and is determined from

$$\begin{aligned} &\int_{-\infty}^{y^\bullet}U(U-U_2)\,dy+\int_{-\infty}^{y^\bullet}(\overline{u'^2}-\overline{v'^2})\,dy\;= \\ &\int_{y^\bullet}^{\infty}U(U_1-U)\,dy+\int_{y^\bullet}^{\infty}(\overline{u'^2}-\overline{v'^2})\,dy\,. \end{aligned} \tag{7}$$

A snapshot of the statistically converged vorticity field on the extended domain is shown in Fig. 3. The flow goes from laminar to turbulent (yet, of course, 2-D). After the laminar part,

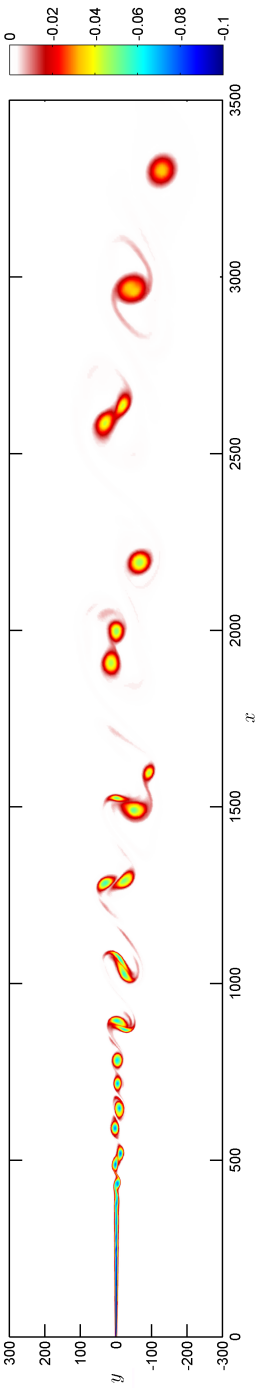

Fig. 3. Snapshot of the vorticity field

we observe a transition region where the Kelvin-Helmholtz instability starts developing. The waves are seen to grow and develop discrete vortex structures. Further downstream, beyond $x \simeq 700$, we observe a different state of the shear layer which can be interpreted as a "fully turbulent" self-similar state. This interpretation is supported by the scaling which one obtains in this region. The similarity variable is defined as

$$\eta = \frac{y}{x - x_0},$$

where x_0 is the virtual origin of the self-similar turbulent shear layer.
First of all, it is essential to define correctly this origin in order to compute the growing rates with accuracy. For this, the y location of the points having the same velocity at different positions x are reported on a xy graph. The intersection of the linear fits of those values gives the virtual origin of the turbulent shear layer (fig. 4).

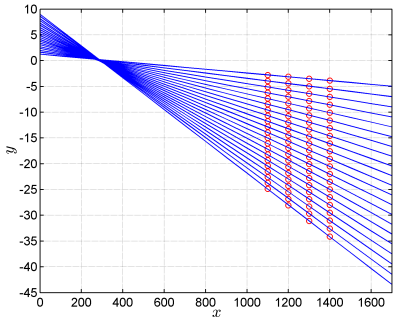

Fig. 4. Origin of the turbulent shear layer for VIC4

A. *Influence of the outflow condition*

In this section, different outflow conditions are studied on the first domain (extended up to $x = 2500$). The truly self-similarity region goes from $x \simeq 1000$ to $x \simeq 1400$ for all computations. Fig. 5 shows the velocity profile for the VIC4 simulation computed with the appropriate scaling $\eta = y/(x - x_0)$, where $x_0 = 280$ is the origin of the self-similar turbulent shear-layer. The curves are indeed the same for all x-stations.

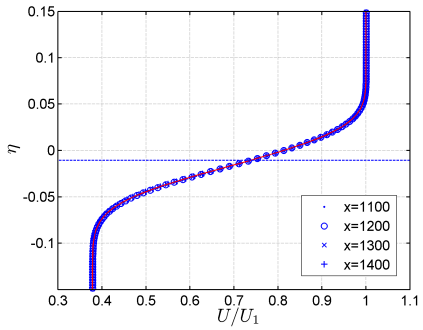

Fig. 5. Velocity profiles at different x-stations for VIC4. Position of the dividing streamline (dotted line)

The good collapse of the data indicates an inviscid (and turbulent) scaling law in the self-similar region. It follows that the thicknesses $\theta(x)$ or $\delta_w(x)$, also grow linearly. Fig. 6 shows them for the VIC4 simulation. The linear fits of the curves in the self-similar turbulent region are also plotted. Only the slopes of the curves are approximated, the origin of the line is set at the origin x_0. At a first glance, the outflow condition seems to greatly interfere with the results at the end of the domain, the simulation on the largest domain will show that this is due to another phenomenon.

Fig. 7 shows the dividing streamline $y^\bullet$ at different x-stations obtained by Eq. (7) and the few other streamlines obtained from the mean flow (U,V). Even tough the outflow condition influences the results downstream, it will be demonstrated that it does not influence significatively the results in the self-similar region of the turbulent shear-layer.

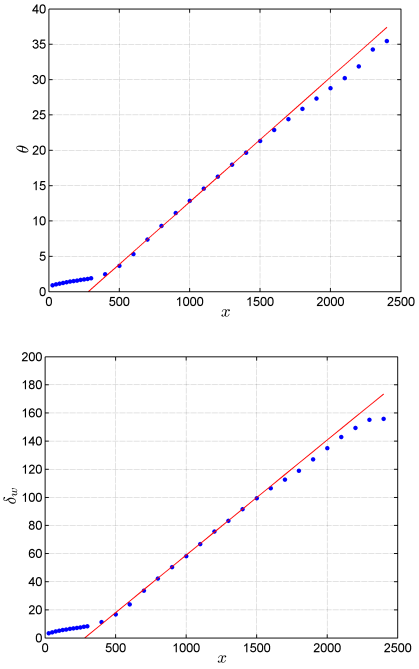

Fig. 6. Momentum thickness and vorticity thickness and their linear fits (solid line) for VIC4.

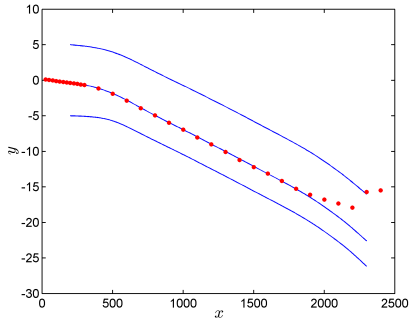

Fig. 7. Dividing streamline for VIC4. The solid lines correspond to three streamlines of the mean flow.

The analysis of the self-similarity on the turbulent region for the different computations gives the results in Table I. The values obtained show an excellent agreement, meaning the results in the self-similar region are not significatively dependent of the parameters of the outflow condition.

	x_0	$d\theta/dx$	$d\delta_w/dx$	$-dy^\bullet/dx$
VIC1	280	0.0177	0.0812	$9.67\ 10^{-}3$
VIC2	300	0.0179	0.0829	$9.68\ 10^{-}3$
VIC3	275	0.0178	0.0836	$1.01\ 10^{-}2$
VIC4	280	0.0176	0.0838	$9.79\ 10^{-}3$

TABLE I
COMPARISON BETWEEN THE DIFFERENT SIMULATIONS

B. Results on an extended domain

A computation on a domain extended up to $x = 3500$ (VIC5) is done to validate the results of the simulations described above. The parameters of the outflow condition are taken the same as those of the simulation VIC4.

The analysis of the self-similarity of the velocity and of the Reynolds stress highlights the existence of three different self-similarity regions (a, b and c), each with its virtual origin. The different self-similarity regions can be seen distinctly on the plots of the growing rates, see Fig. 8. Futhermore, the third region appears to have the same growth rate as that of the first one, see Table II. This means that the second, intermediate, region could be a transition region between the two others.

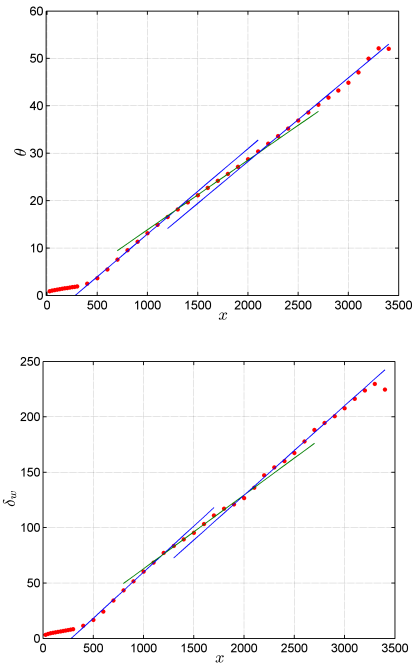

Fig. 8. Momentum thickness, vorticity thickness and their linear fits for the extended domain VIC5.

	x_0	$d\theta/dx$	$-dy^\bullet/dx$
Region 1	280	0.0839	$9.69\ 10^{-3}$
Region 2	50	0.0664	$9.65\ 10^{-3}$
Region 3	400	0.0806	$1.16\ 10^{-2}$

TABLE II
COMPARISON BETWEEN THE SELF-SIMILAR REGIONS FOR VIC5.

Fig. 9 shows the dividing streamline at different x-stations and the linear fits in the turbulent region. It is seen that the slope of the dividing streamline is roughly the same in the first and the second regions and that it increases in the third one.

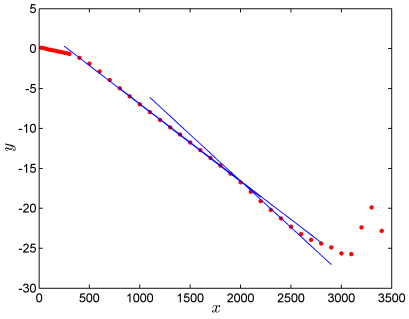

Fig. 9. Dividing streamline for VIC5.

Table III compares the results obtained on the extended domain with those obtained on the shorter one. It confirms that the results are indeed similar in the first self-similarity region. this also confirms that the first set of simulations (VIC1 to VIC4) was indeed a valid one. In Fig 10, the momentum thickness

	x_0	$d\theta/dx$	$d\delta_w/dx$	$-dy^\bullet/dx$
VIC5	280	0.0177	0.0812	$9.67\ 10^{-3}$
VIC4	280	0.0176	0.0838	$9.79\ 10^{-3}$

TABLE III
COMPARISON BETWEEN THE RESULTS OF THE SIMULATIONS ON THE TWO DOMAINS

obtained in the shorter domain simulation (VIC4) is also overlayed to the linear fits obtained in the extended domain simulation (VIC5). Notice that the second region, was in fact already visible in the results of the VIC4 simulation. Hence, it should not be attributed to an artificial influence of the outflow condition, as was first proposed.

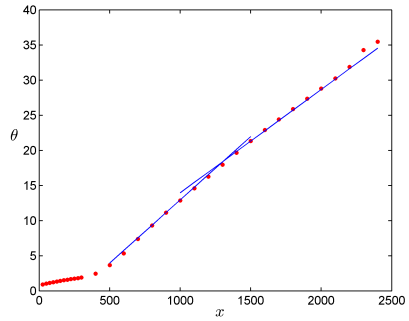

Fig. 10. Momentum thickness for VIC4 and the linear fits of VIC5 (solid lines).

IV. Conclusion

Several outflow conditions of the computation have been tested, showing that there was no significant influence on the results in the turbulent self-similar region. The results obtained on the extended domain have validated those on the shortest. They have also unveiled the possibility of multiple self-similar regions in such 2-D turbulence. To definitively confirm the existence of those regions, a simulation on a larger domain would be necessary. It would also allow to see if this phenomenon is repetitive. Exciting the shear-layer with a white noise at the inflow condition could also further confirm that the values obtained so farfor of the growing rates are "robust" (i.e., that they are insenstive to the white noise).

References

[1] Cocle R., Winckelmans G. and Daeninck G., *Combining the vortex-in-cell and parallel fast multipole methods for efficient domain decomposition simulation*, J. Comput. Phys. 227(2008) 9092-9120.

[2] Thirifay F., *Simulation of non-reactive and reactive shear flows using lagrangian particle methods*, PhD. thesis, 2006.

[3] Brown G. and Roshko A., *On Density Effects and Large Structures in Turbulent Mixing Layers*, J. Fluid Mech. 1974; 64:775-816.

Proceedings of the 8th National Congress on Theoretical and Applied Mechanics, May 28-29, Brussels, Belgium.

Smoke propagation in buildings : a simulation toolbox

S. Datoussaïd[1], S. Brohez[2], D. Lalisse[1], T. Capron
[1]Department of Civil Engineering, Faculté Polytechnique de Mons
Rue du Joncquois 53, 7000 Mons - Belgium
[2]Department of Chemical Engineering, Faculté Polytechnique de Mons
Rue de l'Epargne 56, 7000 Mons - Belgium
email: selim.datoussaid@fpms.ac.be, sylvain.brohez@fpms.ac.be, damien.lalisse@fpms.ac.be

Abstract— **As a process, fire can take many forms, all of which involve chemical reaction between combustible species and oxygen from the air. Properly harnessed, it provides great benefit as a source of power and heat to meet our industrial and domestic needs, but, unchecked, it can cause untold material damage and human suffering. In real terms, the direct fire losses may not have increased significantly over the past two decades, but the holding action has been bought by a substantial increase in other associated costs, namely improving the technical capability of the fire service and the adoption of more sophisticaded fire protection systems [1]. Further advances in combating wildfire are based on a fundamental approach which can be applied at the design stage rather than relying on fire incidents to draw attention to inherent fire hazards. Such approach requires a detailed understanding of the fire behaviour from an engineering standpoint. The substantial majority of fire fatalities can be attributed to the inhalation of smoke and toxic gases [8]. While many of these individuals may have been overcome by combustion products while asleep, a large number are found at points remote from the fire, perhaps attempting to effect their escape. So, life safety systems in buildings should incorporate means of protecting the occupants from smoke as they make their way to safety. For this to be achieved, the behaviour and movement of smoke within the building must be understood.**

Keywords— **fire, smoke, buildings**

I. Introduction

THE present paper is focused on the smoke propagation in buildings during a fire [5], [6]. The main assumption of the present work deals with the initiation of flaming combustion and the spread of flame : we consider that the compartment is in a fully developed fire regime [2]. The present parper describes the smoke movement in multiple interconnected spaces. In practice, a model with two zones is considered in each room connected with the compartment in fire : the upper zone is a smoke layer and the bottom zone is composed of fresh air. Each zone is defined by physic parameters such as temperature, density, pressure and chemical components. By writing the equilibrium equations of mass tranfer and energy, all the parameters can be calculated during the simulation. So, the smoke layer is growing until an opening is reached. Then the smoke is filling the adjacent room. The smoke layer in this room is growing until an other window is reached.
Thanks to the knowledge of the chemical components in the smoke and its temperature, the visibility and the toxicity of the smoke can be estimated.

II. Assumptions

The fire has been confined in a closed room without forced ventilation. Connections with adjacent rooms are made by rectangular openings. A two-zones approach is used to analysed the transfers between the smoke layer and the fresh air. Each zone is characterized by its pressure, density, volume and temperature.

The fire is modeled as a source point. Part of the produced energy coming from the flames is transfered by radiation; the rest of the energy is directly transfered to the smoke zone. Both zones transfer energy by convection with the inner walls.

The model is based on transfer of mass and energy between the zones in the adjacent rooms. The radiative and convection transfer modes are well-known and, for that reason, are not described in this paper. However, the combustion model and the flux in the openings are showed hereafter.

III. Combustion model

The main parameter for characterizing the power of the fire is the *heat released rate Q*. It can be estimed through the fire load of the building. If we consider a burning material with a heat of combustion ΔH_c, the rate of fuel involved during the fire is given by :

$$\dot{N}_c = \frac{Q}{\Delta H_c} \tag{1}$$

For a given burning material, the chemical reactions involving the oxidation of hydrocarbons produce water vapour and carbon dioxide, but also carbon monoxide gas and solid carbon as soot particles in the flames or in the smoke. So the heat of combustion ΔH_c refers to a complex

combination of complete and partial calorific values that take into account the lack of oxygen during the fire in a closed room.
Usually the production of chemical entities during an incomplete combustion should be given as assumptions of the model. In our approach, the production of the soot particles, the monoxide carbon, the monoxide nitrogen and the cinanide, is estimated through the research works of Tewarson [7]. He has shown the correlation between the production of chemical entities and the venting condition (that it means the available oxygen). Such correlation is based on experimental tests made on the main burning materials of the room. The figure 1 gives an example for the combustion of the pyridine. A description of such correlations can been found in [7].

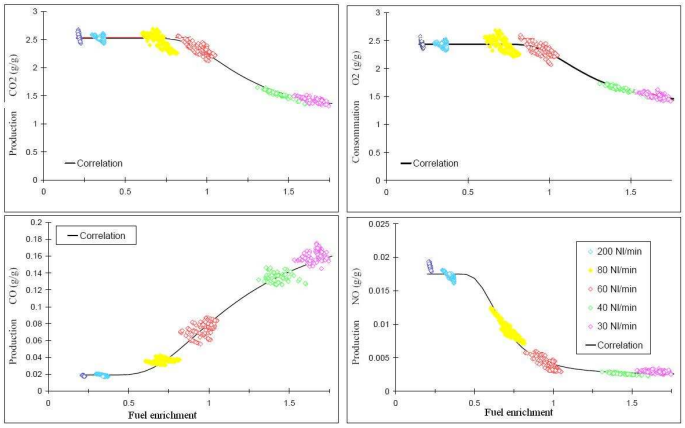

Fig. 1. Production of chemical entities according to the venting condition.

IV. Flow across openings

Several flows are taken into account according the kind of openings. Doors and windows are vertical openings where the air flow is mainly horizontal. Stairs and ceiling outlets are horizontal openings where the air flow is mainly vertical. Long corridors and tunnels are particular openings; so are mechanical ventilation systems. Thoses are not considered in the present paper. Moreover, such system is turn off by the automatic detection.

Air and smoke flows across the vertical openings are calculated by the Bernouilli law taken into account the difference of pressure in the adjacent zones. The flow across the horizontal openings is generally turbulent due to the difference of density of the gas in the two zones (turbulence appairs when the denser fluid is above the lighter one).

A. Vertical openings

The velocity of the fluid v crossing an opening depends on the difference of pressure ΔP and a throw coefficient C_d. The relation may be written as :

$$v = C_d \left(\frac{2\Delta P}{\rho} \right) \tag{2}$$

A common value for C_d is 0.7.
Of course, the difference of pressure linearly depends on the height. Moreover, the density of the gas depends on the zone but, at the boundary, the pressure of each zone remains equal. So the profile of pression at the vertical opening is chequered as shown on figure 2. The pressure is given by the relation :

$$P_i(z) = P_{i0} - g\rho_i(z - z_{i0}) \tag{3}$$

where P_{i0} refers to the pressure at the reference level z_{i0} in the zone i; g is the gravity acceleration and ρ the volumic mass.
The neutral planes are calculated by resolving the equality of pressure in the horizontaly adjacent zones. When the profile of pression is known, equation 2 is applied to get the profile of the flow velocity. So the mass tranfer between the rooms can be calculated.

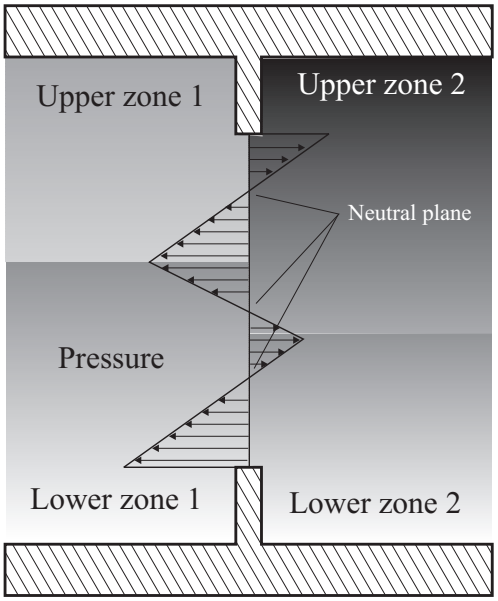

Fig. 2. Pressure distribution along a vertical opening.

B. Horizontal openings

In this case, the motion of the gas across the opening is due to, on one hand the difference of pressure and, on the other hand, the difference of density. It is common to considered the two phenomena distinctely in such a way

the flow is given by the summation :

$$V = V(\Delta P) + V_{EX} \tag{4}$$

The term $V(\Delta P)$ is due to the difference of pressure and may be calculated from the equation (2) with an uniform profile of pressure. The second terme V_{EX} is due to the difference of density between the top and bottom fluids. Mercer and Thompson have made several trial about that kind of problems and they have given empiric expression of the flow for different kind of appertures [8]. In the case of a rectangular opening A_v, they have given the following expression :

$$V_{EX} = V_{EX,max}(1 - \frac{|\delta P|}{|\Delta P_F|}) \tag{5}$$

$$V_{EX,max} = 0.1 \left[\frac{2g\Delta\rho A_v^{5/2}}{(\rho_{TOP} + \rho_{BOTTOM})} \right]^{1/2} \tag{6}$$

$$\Delta P_F = C_d^2 g \Delta\rho \frac{D^5}{2A_v^2} \tag{7}$$

D is the greater length of the rectangular opening; TOP and $BOTTOM$ refer to the fluids above an below the opening respectively.

V. Mass and energy conservation

The transfers between the two zones and between the adjacent rooms are regulated by the conservation of the mass and of the energy. So we should write the balance for each zone in each room.

For the lower zone, the transfers of gas depend on the fresh air entering and throwing out and on the air carrying away with the plume :

$$\frac{dN_l}{dt} = \dot{N}_{in,l} - \dot{N}_{out,l} - \dot{N}_{plume} \tag{8}$$

N refers to the moles. Several models have been proposed to estimate the plume debit. Generally, the model proposed by McCaffrey [8] is used but, for this preliminary studies, the plume debit is not calculated and is assumed to be constant. As the gas are ideal, we may rewrite the latest equation as :

$$\frac{dV_l}{dt} = \left[(\dot{N}_{in,l} - \dot{N}_{out,l} - \dot{N}_{plume}) \frac{R}{P_l} T_l^2 + V_l \frac{dT_l}{dt} \right] \frac{1}{T_l} \tag{9}$$

So the height of the zone can be estimated through the mass transfer, the temperature and the pressure.
For the upper zone, the same balance may be written but the debit of fuel is added. We consider in the present paper the combustion of pyridine that produces 9 chemical species (CO_2, CO, C, H_2O, O_2, N_2, HCN, NO, residue from combustion).

$$\frac{dV_u}{dt} = \left[(\dot{N}_{in,u} - \dot{N}_{out,u} + \dot{N}_{plume} + N_{fuel} \left(\sum_{i=1}^{9} f_i \right)) \frac{R}{P_u} T_u^2 + V_u \frac{dT_u}{dt} \right] \frac{1}{T_u} \tag{10}$$

Moreover, the total volume of the room remains constant.

$$V_u + V_l = V_{room} \tag{11}$$

The equations (9), (10) and (11) give the balance of mass for the whole room. Such equations may be written for all the rooms. In addition, the fraction of each chemical species is taken into account by the relations below, respectively for the upper and lower zone :

$$\dot{N}_{in,l} f_{in,l,i} - \dot{N}_{out,l} f_{out,l,i} - \dot{N}_{plume} f_{l,i} = \frac{P_l}{R} \frac{d\left(\frac{V_l f_{l,i}}{T_l}\right)}{dt} \tag{12}$$

$$\dot{N}_{in,u} f_{in,u,i} - \dot{N}_{out,u} f_{out,u,i} + \dot{N}_{plume} f_{u,i} + N_{fuel} f_i = \frac{P_u}{R} \frac{d\left(\frac{V_u f_{u,i}}{T_u}\right)}{dt} \tag{13}$$

$$f_{l,i} + f_{u,i} = f_i \tag{14}$$

In our case where 9 chemical species are considered, 27 equations per room are added.

The balance of energy is written for each zone taking into account on one hand the energy of the tranfering gas and, on the other hand the convection and the radiation with the solid surfaces. The energy of the gas is well described by its enthalpy. So the equilibrium equations of the upper and lower zone are :

$$\frac{N_l h_l}{dt} = q_l + \dot{N}_{in,l} h_{in,l} - \dot{N}_{out,l} h_{out,l} - \dot{N}_{plume} h_l \tag{15}$$

$$\frac{N_u h_u}{dt} = q_u + \dot{N}_{in,u} h_{in,u} - \dot{N}_{out,u} h_{out,u} + \dot{N}_{plume} h_u + \dot{N}_{fuel} h_{fuel} \tag{16}$$

where h refers to the enthalpy. It may be calculated according the temperature of the gas and its chemical composition. The tranfers of energy with the walls, the floor and the ceiling are mainly coming from radiation and convection. For the radiation mode, we make the assumption that the transfer only concerns the upper zone with the smoke. In practice, the lower zone is mainly composed of fresh air that remains transparent. The solid surfaces and the smoke are considered as *grey* so that the emissivity doesn't depend on the frequency of the radiation. As the fire is modeled as a point source, it can only produce radiations but cannot receive them. The emissivity factor for the surfaces

in contact with the smoke is 0.9 because they are covered by soot particles. For the other surfaces, the value of 0.6 is recommended. The emissivity of the smoke is calculated taken into account the contribution of the carbon dioxide, the water vapour and the soot particles.

The convection transfer mode is natural. Several empirical relations have been establish for the convection with a vertical surface. In this case, the temperature of the wall has to be taken into account. So the transfer of heat by conduction into the walls has to be taken into account too.

VI. Resolution

The finite difference method is used to resolve the system of differential equations. The data of the problem are the inner geometry of the building, especially the openings between the rooms and the characteristics of the building materials. The localization of the fire and its power is given. The unknows refer to two zones in each rooms : temperature, pressure, volume (or thickness of the gas), chemical components of the gas. In our case, we consider 9 chemical species.

VII. Example of results

Two adjacent rooms of $4.9\,m$ long, $4.0\,m$ wide and $4.0\,m$ height are considered. The openings are identical ($2.5\,m$ height and $1.0\,m$ wide). The solid surfaces are made of concrete. The fire occurs in room 1.

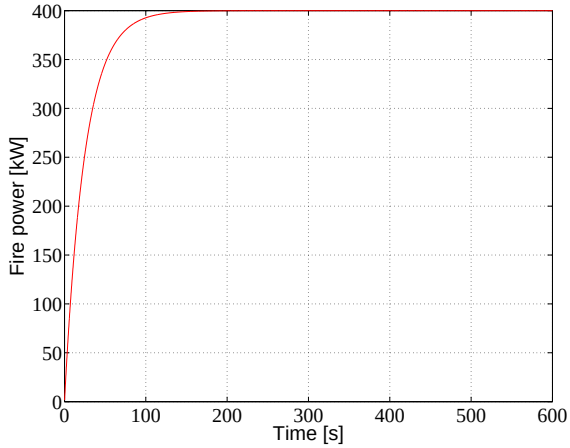

Fig. 3. Fire power

The figure 3 shows the imposed power of the fire. The temperatures reached in the zones are showed on the figure 4. The temperature of the ajdacent room remains constant since the smoke hasn't reached the opening. At time $t = 16.4\,s$, the smoke is entering in the room (fig.5) and the temperature is increasing in the upper zone of room 2.

During the simulation, the production of chemical species is monitoring. For example, the figure 6 shows

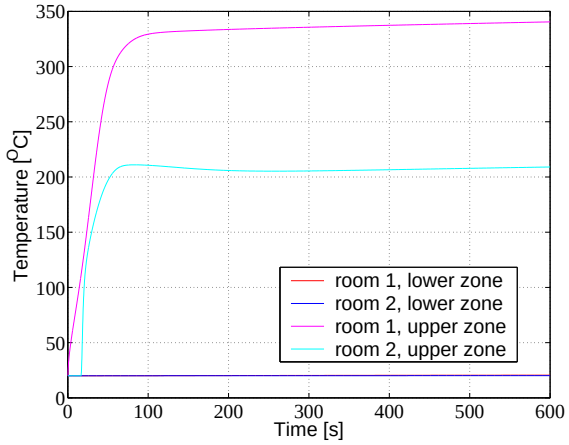

Fig. 4. Temperature of the zones in the two rooms

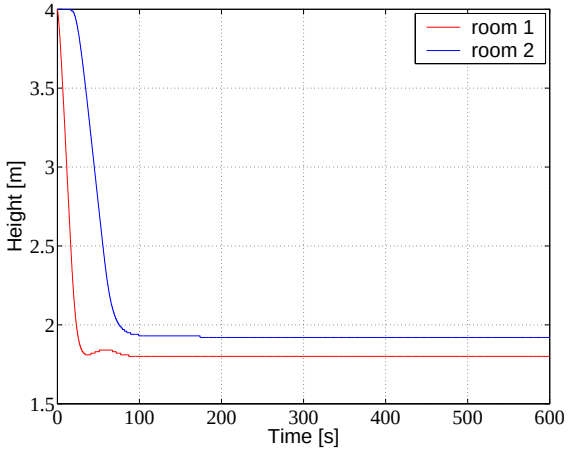

Fig. 5. Height of the smoke in the rooms

the quantity of carbon dioxide in the zones.

VIII. Conclusion

The present paper is focused on the smoke propagation in buildings during a fire. The main assumption of the present work deals with the initiation of flaming combustion and the spread of flame : we consider that the compartment is in a fully developed fire regime. The present parper describes the smoke movement in multiple interconnected spaces. In practice, a model with two zones is considered in each rooms connected with the compartment in fire : the upper zone is a smoke layer and the bottom zone is composed of fresh air. Each zone is defined by physic parameters such as temperature, density, pressure and chemical components. By writing the equilibrium equations of mass tranfer and energy, all the parameters can be calculated during the simulation.

Further progresses may be done. It concerns the model of the fire itself. A more sophisticated model of fire has already been considered but it is not included in the present

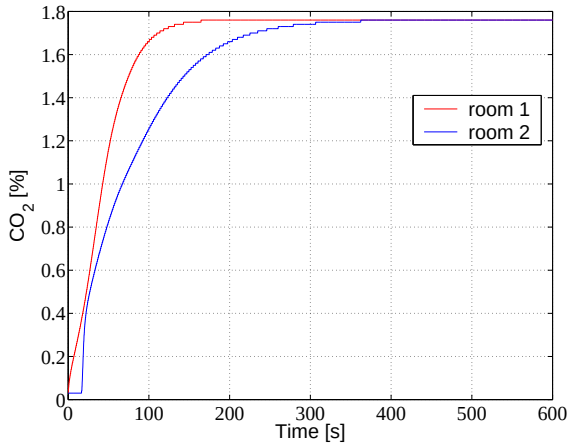

Fig. 6. CO_2 concentration in the rooms

approach because of its complexity [5]. Moreover, a better model of the ceiling jet and the fresh air carried away with the plume should be taken into account. However the present approach gives accurate results enough to quantify the propagation of the smoke in the building and its toxicity.

REFERENCES

[1] D. Rasbash, G. Ramachandran, B. Kandola, J. Watts et M. Law, *Evaluation of fire safety* , Wiley, 2004

[2] M. L. Janssens, *An Introduction to Mathematical Fire Modeling*, Southwest Research Institute, TECHNOMIC publishing co. inc, 2000

[3] Walter W. Jones, Richard D. Peacock, Glenn P. Forney et Paul A. Reneke, *CFAST Consolidated Model of Fire Growth and Smoke Transport (Version 6), Technical Reference Guide* , NIST Special Publication 1026, December 2005, http://www.nist.gov

[4] Walter W. Jones, Richard D. Peacock, Glenn P. Forney et Paul A. Reneke, *CFAST Consolidated Model of Fire Growth and Smoke Transport (Version 6), Users Guide* , NIST Special Publication 1041, December 2005, http://www.nist.gov

[5] Gaetan Parmentier, *Simulation dun incendie dans un compartiment ventilation naturelle* , travail de fin dtude, FPMs, 2006-2007

[6] Geoffrey Cambier , *Simulation dincendie de substances chimiques dans un compartiment ventilation naturelle* , travail de fin dtude, FPMs, 2002-2003

[7] S. Brohez, *Etude des feux de substances chimiques en milieu confin* , Thse de doctorat en science applique, FPMs, 2002

[8] D. Drysdale, *An introduction to fire dynamics - 2d edition*, Wiley 1998

Proceedings of the 8th National Congress on Theoretical and Applied Mechanics, May 28-29, Brussels, Belgium.

Fluid-Structure Interaction Algorithm for the Simulation of a Bileaflet Prosthetic Heart Valve

Sebastiaan Annerel, Joris Degroote, Jan Vierendeels
Department of Flow, Heat and Combustion Mechanics, Ghent University
Sint-Pietersnieuwstraat 41, 9000 Ghent – Belgium
email: Sebastiaan.Annerel@UGent.be, Joris.Degroote@UGent.be, Jan.Vierendeels@UGent.be

Abstract: **This paper describes an algorithm with two degrees of freedom that is used to simulate the dynamics of a rigid bileaflet prosthetic heart valve using fluid-structure interaction. The motion of each valve leaflet is calculated separately, taking into account their mutual interaction. The developed algorithm is implemented in FLUENT and is tested for a 2D bileaflet valve in an asymmetric geometry.**

Keywords: **FSI, bileaflet heart valve, algorithm**

I. Introduction

When simulating bileaflet heart valves, the motion of the fluid, the movement of the leaflet walls and their interaction need to be taken into account. This can be done by fluid-structure interaction. A description of FSI methods for bileaflet heart valves can be found in [4].
In previous work [1, 2], an FSI algorithm with one degree of freedom was developed, which implies that the two leaflets perform the same motion. This limitation is discussable, especially when the surrounding geometry is asymmetric. In this paper, an algorithm with two degrees of freedom is presented and tested.

The paper is organized as follows. First, we derive and analyze the algorithm and its implementation in FLUENT. Subsequently, the algorithm is illustrated and tested by a 2D case of a bileaflet valve in an asymmetric geometry.

II. Theoretical analysis and FSI algorithm

The FSI algorithm is based on the ALE approach, which implies that the grid follows the motion of the structure and subsequently needs an update. Because this exact motion is a priori unknown, a coupling algorithm is necessary.

The flow diagram of the algorithm is visualized in Figure 1. The implementation in FLUENT is done by journal files and UDFs. For each subiteration, the journal file updates the mesh, solves the Navier-Stokes equations and reads the data file of the time step. It solves the flow part of the problem.
The UDFs, on the other hand, simulate the structural part. They perform calculations with the obtained flow solution in order to check convergence and to set the motion parameters for each subiteration. They interact with and steer the actions of the journal file and thus performing FSI.
Next, the steps of the flow diagram are discussed into detail.

A. Valve mechanics

A bileaflet heart valve is modeled as a rigid casing wherein two separate rigid leaflets can rotate around their axis. Because the position of each leaflet is solely determined by its opening angle, the bileaflet valve has two degrees of freedom.

The movement of a rigid leaflet is governed by the equilibrium between the moment around its hinge and the product of its angular acceleration with its moment of inertia:

$$M = I \cdot \ddot{\theta} \tag{1}$$

For two leaflets, this gives the following two equations with M_i, I_i and $\ddot{\theta}_i$ representing respectively the moment, the moment of inertia and the angular acceleration of leaflet i around its rotation axis:

$$\begin{cases} M_1 = I_1 \cdot \ddot{\theta}_1 \\ M_2 = I_2 \cdot \ddot{\theta}_2 \end{cases} \tag{2}$$

When a frictionless hinge is supposed, the moment acting on the leaflet is the pressure (and viscous) moment.

In [1] is shown that an implicit coupling algorithm is necessary. Even within the subiterations of each time step, implicitness between the subiterations is needed to obtain fast convergence. Therefore, in each subiteration $k+1$ of a time step $n+1$, eq. (2) is linearized as follows, taking into account the mutual interaction between the leaflets:

$$\begin{cases} M_1^{n+1,k} + \dfrac{\partial M_1}{\partial \ddot{\theta}_1}\left(\ddot{\theta}_1^{n+1,k+1} - \ddot{\theta}_1^{n+1,k}\right) + \dfrac{\partial M_1}{\partial \ddot{\theta}_2}\left(\ddot{\theta}_2^{n+1,k+1} - \ddot{\theta}_2^{n+1,k}\right) = I_1 \cdot \ddot{\theta}_1^{n+1,k+1} \\ M_2^{n+1,k} + \dfrac{\partial M_2}{\partial \ddot{\theta}_1}\left(\ddot{\theta}_1^{n+1,k+1} - \ddot{\theta}_1^{n+1,k}\right) + \dfrac{\partial M_2}{\partial \ddot{\theta}_2}\left(\ddot{\theta}_2^{n+1,k+1} - \ddot{\theta}_2^{n+1,k}\right) = I_2 \cdot \ddot{\theta}_2^{n+1,k+1} \end{cases} \tag{3}$$

These equations can be rearranged as follows :

$$\begin{cases} M_1^{n+1,k} - \dfrac{\partial M_1}{\partial \ddot{\theta}_1}\ddot{\theta}_1^{n+1,k} - \dfrac{\partial M_1}{\partial \ddot{\theta}_2}\ddot{\theta}_2^{n+1,k} = I_1 \cdot \ddot{\theta}_1^{n+1,k+1} - \dfrac{\partial M_1}{\partial \ddot{\theta}_1}\ddot{\theta}_1^{n+1,k+1} - \dfrac{\partial M_1}{\partial \ddot{\theta}_2}\ddot{\theta}_2^{n+1,k+1} \\ M_2^{n+1,k} - \dfrac{\partial M_2}{\partial \ddot{\theta}_1}\ddot{\theta}_1^{n+1,k} - \dfrac{\partial M_2}{\partial \ddot{\theta}_2}\ddot{\theta}_2^{n+1,k} = I_2 \cdot \ddot{\theta}_2^{n+1,k+1} - \dfrac{\partial M_2}{\partial \ddot{\theta}_1}\ddot{\theta}_1^{n+1,k+1} - \dfrac{\partial M_2}{\partial \ddot{\theta}_2}\ddot{\theta}_2^{n+1,k+1} \end{cases} \tag{4}$$

Which gives in matrix notation:

$$\begin{bmatrix} M_1^{n+1,k} - \dfrac{\partial M_1}{\partial \ddot{\theta}_1}\ddot{\theta}_1^{n+1,k} - \dfrac{\partial M_1}{\partial \ddot{\theta}_2}\ddot{\theta}_2^{n+1,k} \\ M_2^{n+1,k} - \dfrac{\partial M_2}{\partial \ddot{\theta}_1}\ddot{\theta}_1^{n+1,k} - \dfrac{\partial M_2}{\partial \ddot{\theta}_2}\ddot{\theta}_2^{n+1,k} \end{bmatrix} = \begin{bmatrix} I_1 - \dfrac{\partial M_1}{\partial \ddot{\theta}_1} & -\dfrac{\partial M_1}{\partial \ddot{\theta}_2} \\ -\dfrac{\partial M_2}{\partial \ddot{\theta}_1} & I_2 - \dfrac{\partial M_2}{\partial \ddot{\theta}_2} \end{bmatrix} \cdot \begin{bmatrix} \ddot{\theta}_1^{n+1,k+1} \\ \ddot{\theta}_2^{n+1,k+1} \end{bmatrix} \tag{5}$$

or

$$\left[M\right]^{n+1,k} = \left[\Delta\right] \cdot \left[\ddot{\Theta}\right]^{n+1,k+1} \tag{6}$$

Thus, the matrix $\left[\ddot{\Theta}\right]^{n+1,k+1}$ contains the angular accelerations on time step $n+1$ and subiteration $k+1$. The matrix $[\Delta]$ is composed of the moments of inertia and the derivatives of the moments with respect to angular acceleration (i.e. the Jacobian). Matrix $[M]^{n+1,k}$ consists of all the remaining factors (in time step $n+1$ and subiteration k).

For a well-posed problem, the matrix [Δ] is nonsingular. So the previous equation can be rewritten as:

$$\left[\ddot{\Theta}\right]^{n+1,k+1} = \left[\Delta\right]^{-1} \cdot \left[M\right]^{n+1,k} \tag{7}$$

B. Estimating the Jacobian and calculating the valve motion

In order to solve eq. (7) and calculate the angular accelerations of the new subiteration, the Jacobian has to be known. However, when a black box flow solver is used, the derivatives of the moments with respect to the angular acceleration are approximated by finite differences. Therefore, three subiterations are needed within each time step. In the first and second subiteration (k=0 and k=1) a small perturbation δ is given to each of the angular accelerations, while keeping the other one fixed. In the third subiteration (k=2) no perturbation is given at all. For each subiteration the moments acting on the leaflets are calculated and stored, which gives in summary:

$$\begin{aligned}
k=0 \Rightarrow & \begin{cases} \ddot{\theta}_1^{n+1,k=0} = \ddot{\theta}_1^{n} + \delta \\ \ddot{\theta}_2^{n+1,k=0} = \ddot{\theta}_2^{n} \end{cases} \Rightarrow \begin{cases} M_1^{n+1,k=0} \\ M_2^{n+1,k=0} \end{cases} \\
k=1 \Rightarrow & \begin{cases} \ddot{\theta}_1^{n+1,k=1} = \ddot{\theta}_1^{n} \\ \ddot{\theta}_2^{n+1,k=1} = \ddot{\theta}_2^{n} + \delta \end{cases} \Rightarrow \begin{cases} M_1^{n+1,k=1} \\ M_2^{n+1,k=1} \end{cases} \\
k=2 \Rightarrow & \begin{cases} \ddot{\theta}_1^{n+1,k=2} = \ddot{\theta}_1^{n} \\ \ddot{\theta}_2^{n+1,k=2} = \ddot{\theta}_2^{n} \end{cases} \Rightarrow \begin{cases} M_1^{n+1,k=2} \\ M_2^{n+1,k=2} \end{cases}
\end{aligned} \tag{8}$$

The derivatives can now be estimated as follows: (i,j=1,2)

$$\frac{\partial M_i}{\partial \ddot{\theta}_j} \approx \frac{\Delta M_i}{\Delta \ddot{\theta}_j} \tag{9}$$

which gives for each component of the Jacobian:

$$\begin{aligned}
\frac{\partial M_1}{\partial \ddot{\theta}_1} &\approx \frac{\Delta M_1}{\Delta \ddot{\theta}_1} = \frac{M_1^{n+1,k=0} - M_1^{n+1,k=2}}{\ddot{\theta}_1^{n+1,k=0} - \ddot{\theta}_1^{n+1,k=2}} = \frac{M_1^{n+1,k=0} - M_1^{n+1,k=2}}{\delta} \\
\frac{\partial M_1}{\partial \ddot{\theta}_2} &\approx \frac{\Delta M_1}{\Delta \ddot{\theta}_2} = \frac{M_1^{n+1,k=1} - M_1^{n+1,k=2}}{\ddot{\theta}_2^{n+1,k=1} - \ddot{\theta}_2^{n+1,k=2}} = \frac{M_1^{n+1,k=1} - M_1^{n+1,k=2}}{\delta} \\
\frac{\partial M_2}{\partial \ddot{\theta}_1} &\approx \frac{\Delta M_2}{\Delta \ddot{\theta}_1} = \frac{M_2^{n+1,k=0} - M_2^{n+1,k=2}}{\ddot{\theta}_1^{n+1,k=0} - \ddot{\theta}_1^{n+1,k=2}} = \frac{M_2^{n+1,k=0} - M_2^{n+1,k=2}}{\delta} \\
\frac{\partial M_2}{\partial \ddot{\theta}_2} &\approx \frac{\Delta M_2}{\Delta \ddot{\theta}_2} = \frac{M_2^{n+1,k=1} - M_2^{n+1,k=2}}{\ddot{\theta}_2^{n+1,k=1} - \ddot{\theta}_2^{n+1,k=2}} = \frac{M_2^{n+1,k=1} - M_2^{n+1,k=2}}{\delta}
\end{aligned} \tag{10}$$

For the following subiterations (k>2) the angular accelerations can now be calculated by eq. (7), until the convergence criterion is satisfied. For each leaflet i, this convergence criterion is given by:

$$\left| M_i^{n+1,k+1} - I_i \cdot \ddot{\theta}_i^{n+1,k+1} \right| < \varepsilon \tag{11}$$

The convergence threshold ε is set at one percent of $M_i^{n+1,k+1}$:

$$\varepsilon = \frac{M_i^{n+1,k+1}}{100} \tag{12}$$

When the convergence criterion is satisfied, the geometry and data of the time step is stored and the next time step is initiated.

When going to a new time step, the initial angular accelerations are estimated based on a quadratic extrapolation of the accelerations from previous time steps. This estimation of the initial value will result in faster convergence.

From the angular acceleration obtained from eq. (7), the angular velocity and position of each leaflet on the time level $t + \Delta t$ is calculated using a time-integration scheme. In [1] is shown that a backward Euler scheme is preferred for strongly FSI coupling:

$$\begin{aligned}
\dot{\theta}_i^{n+1,k+1} &= \dot{\theta}_i^{n} + \Delta t \cdot \ddot{\theta}_i^{n+1,k+1} \\
\theta_i^{n+1,k+1} &= \theta_i^{n} + \Delta t \cdot \dot{\theta}_i^{n} + \Delta t^2 \cdot \ddot{\theta}_i^{n+1,k+1}
\end{aligned} \tag{15}$$

C. Behavior in fully opened / fully closed position

The angular position of a leaflet is restricted by a maximum (fully closed) and a minimum angle (fully opened). In reality, this is usually done by a physical blocking mechanism incorporated in the design of the hinges.

These limitations can be modeled by setting the position equal to the restriction and recalculating the angular velocity and acceleration. This is done as follows. When the calculated position of a leaflet exceeds its limitations, i.e. $\theta_i^{n+1,k+1} < \theta_{\min}$ or $\theta_i^{n+1,k+1} > \theta_{\max}$, then the position is set equal to this limit, i.e. $\theta_i^{n+1,k+1} = \theta_{\min}$ or $\theta_i^{n+1,k+1} = \theta_{\max}$. In order to move exactly to the limited position in the time step, the angular velocity $\dot{\theta}_i^{n+1,k+1}$ and acceleration $\ddot{\theta}_i^{n+1,k+1}$ needs to be recalculated (using the backward Euler scheme):

$$\begin{aligned}
\theta_i^{n+1,k+1} &= \theta_{\min} \text{ or } \theta_{\max} \\
\dot{\theta}_i^{n+1,k+1} &= \frac{\theta_i^{n+1,k+1} - \theta_i^{n}}{\Delta t} \\
\ddot{\theta}_i^{n+1,k+1} &= \frac{\dot{\theta}_i^{n+1,k+1} - \dot{\theta}_i^{n}}{\Delta t}
\end{aligned} \tag{16}$$

The previously described convergence criterion must be changed when the position is limited. The convergence no longer has to depend on the absolute value of the subtraction $\left(M_i^{n+1,k+1} - I_i \cdot \ddot{\theta}_i^{n+1,k+1} \right)$, but merely on its sign. This can be understood by adding to the momentum equation the reaction moment of the blocking mechanism exerted on the leaflets, i.e. M_i^r:

$$M_i^r + M_i^{n+1,k+1} = I_i \cdot \ddot{\theta}_i^{n+1,k+1} \tag{17}$$

or

$$M_i^r = -\left(M_i^{n+1,k+1} - I_i \cdot \ddot{\theta}_i^{n+1,k+1} \right) \tag{18}$$

In order to sustain contact between the leaflet and the blocking mechanism, this reaction moment will be either negative or positive (depending on the case: $\theta_{\min}$ or $\theta_{\max}$). As convergence criterion, this sign is checked.

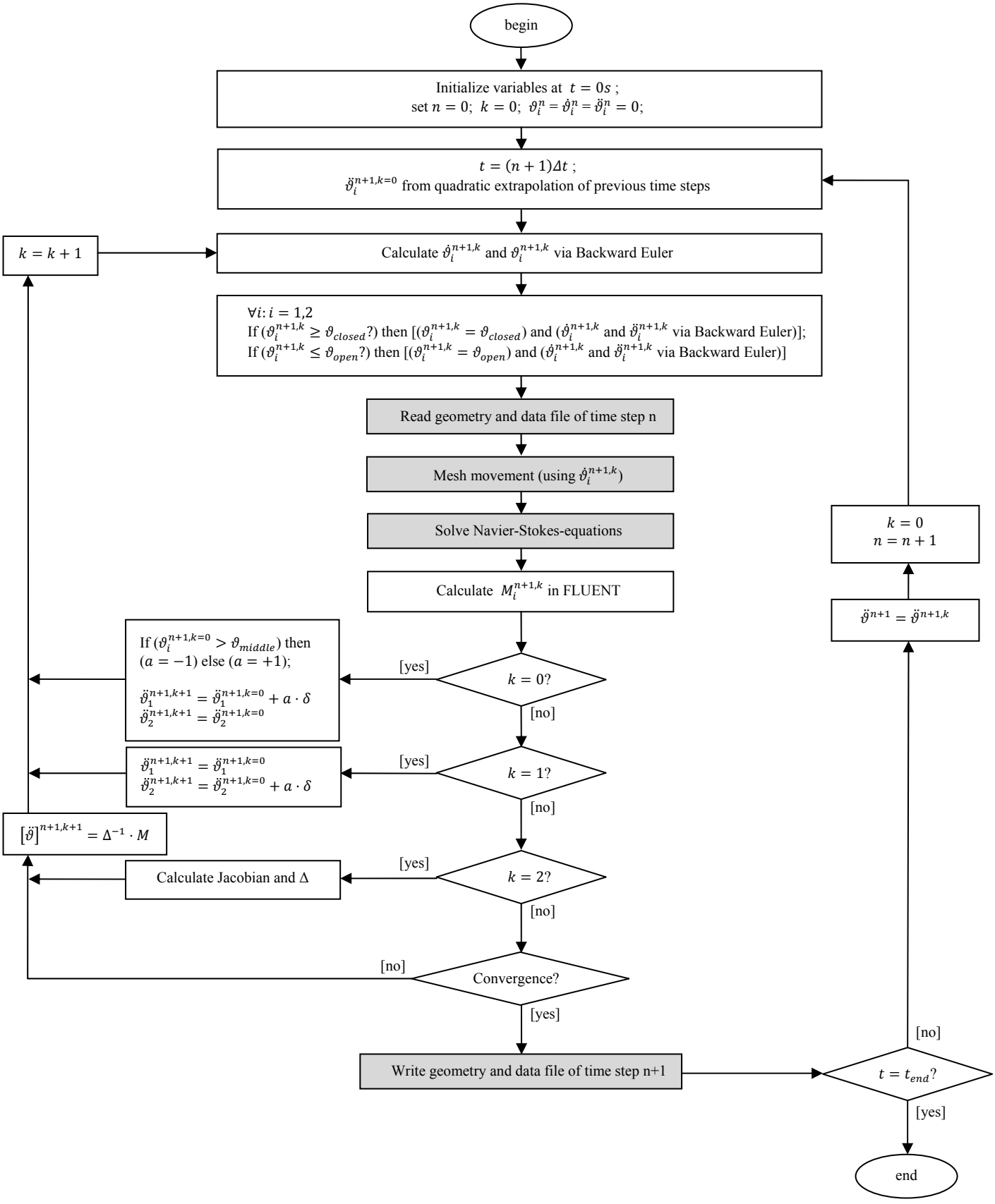

Fig. 1. Flow diagram of the implicit FSI coupling algorithm with two degrees of freedom, implemented in FLUENT. n = time step, k = subiteration step. Shaded: software executed using generated journal file. Unshaded: functions executed using compiled UDFs.

III. Results

This algorithm is implemented in FLUENT and tested for a 2D model of a bileaflet heart valve.
This 2D geometry is derived from a 3D model of a bileaflet aortic valve in a tube with solid walls and Valsalva sinuses, as depicted in Figure 2.a. The used aortic heart valve is a simplified model of the ATS Open Pivot Standard Heart Valve with size 25mm. The orifice inner diameter measures 20.8mm. The geometry of the Valsalva sinuses is based on [3]. The presence of these sinuses gives an asymmetric geometry downstream of the valve. Such asymmetry will result in a different motion for each valve leaflet and therefore it is an effective test for the algorithm.
Through this 3D model, a longitudinal 2D section was made perpendicular to the leaflet rotation axis (Figure 2.b).

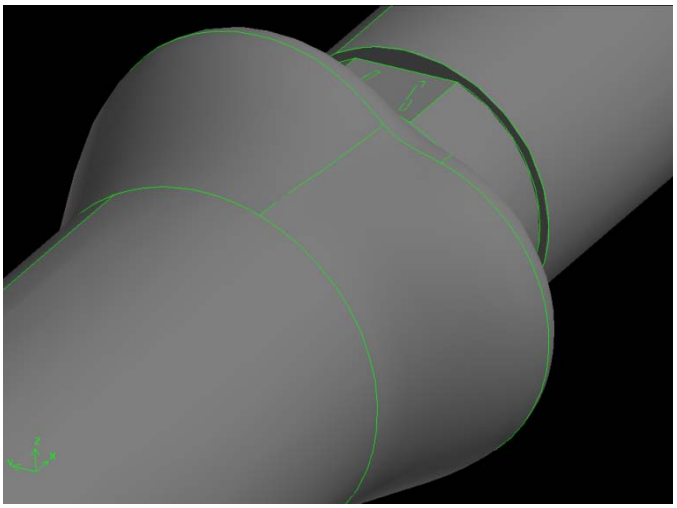

Fig. 2.a. View of the 3D model with Valsalva Sinuses.

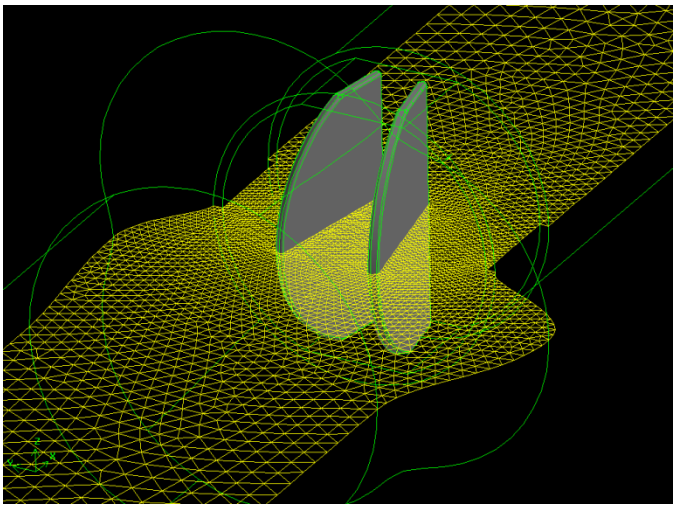

Fig. 2.b. In the 3D model a 2D longitudinal section was made.

In GAMBIT, the fluid domain is partitioned into a deforming and a non-deforming zone. The deforming grid is laid in the rotation zone of the leaflets, as illustrated in Figure 3.a. So, if applicable, it is updated in FLUENT using dynamic remeshing and spring smoothing. The non-deforming grid, however, is fixed during the subsequent time steps. Interior edges link the non-deforming and deforming zones. The geometry was meshed with triangular cells (Figure 3.b).

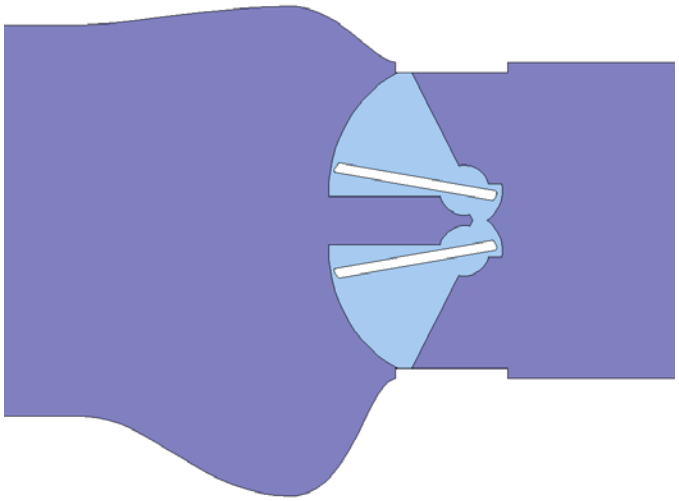

Fig. 3.a. The geometry is subdivided into a deforming (*light blue*) and a non-deforming zone (*dark blue*).

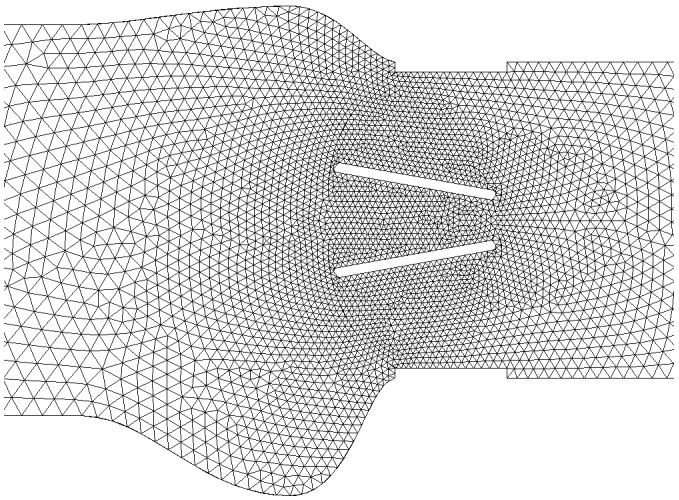

Fig. 3.b. The final grid is composed of triangular cells.

This 2D grid is subsequently imported into FLUENT and the case is set up. Velocity and pressure profiles are applied at resp. inlet (at the right) and outlet (at the left) boundaries. The velocity profile is visualized in Figure 4 and corresponds to the aortic flow pulse used in [2]. Water was chosen as the working fluid. A no-slip condition was applied to the walls.

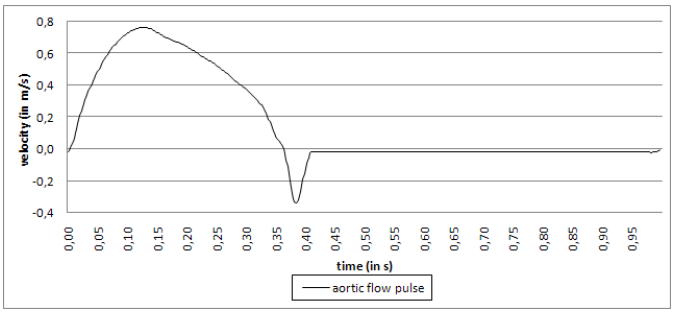

Fig. 4. Inlet aortic velocity-time pattern of one time cycle

The solution process shows that the algorithm is stable. For each time step, it reaches convergence within a few subiterations.

Figure 5 gives the resulting angular position of the upper and the lower leaflet as function of time. The fully opened position refers to 0º and the closing of the leaflets is restricted to 53.4º. The results clearly show the difference in motion between the leaflets. Although the upper leaflet closes much faster than the lower one, it opens at a slightly slower pace. It can be understood that the geometrical asymmetry triggers this asynchrony.

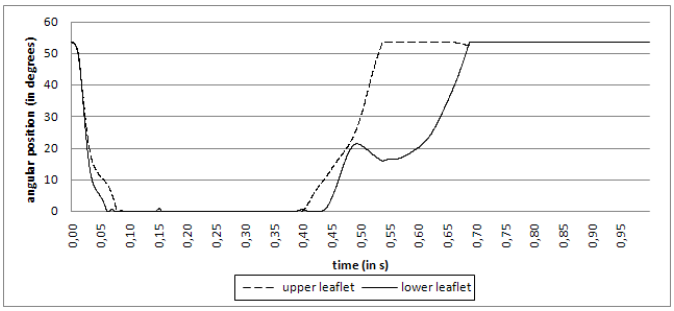

Fig. 5. Angular position of upper and lower leaflet in one time cycle

IV. Conclusions

An implicit FSI coupling algorithm for two degrees of freedom is presented in this paper and used to simulate the (asynchronous) motion of each leaflet of a bileaflet valve, taking into account their mutual influence.

The algorithm is successfully tested and implemented for a 2D case. The grid domain is subdivided into a deforming and a non-deforming zone. Hence, when the leaflets move and the mesh must be updated, only the deforming zone needs modification. This will lower the computational effort.

An FSI algorithm with one degree of freedom implies that the two leaflets are forced to perform the same motion. This paper shows that great asymmetry in the geometry can result in great differences in leaflet motion. In such cases, an algorithm with two degrees of freedom is preferred.

Acknowledgements

Sebastiaan Annerel is funded by a BOF-grant (Special Research Fund) from Ghent University Association.

References

[1] J. Vierendeels, K. Dumont, E. Dick and P. Verdonck, *Analysis and Stabilization of Fluid-Structure Interaction Algorithm for Rigid-Body Motion,* AIAA Journal, Vol. 43, No. 12, pp. 2549-2557, December 2005.

[2] K. Dumont, J. Vierendeels, R. Kaminsky, G. Van Nooten, P. Verdonck, D. Bluestein, *Comparison of the hemodynamic and thrombogenic performance of two bileaflet mechanical heart valves using a CFD/FSI model*, Journal of Biomechanical Engineering-Transactions of the Asme, pp. 558-565, 2007.

[3] H. Reul, A. Vahlbruch, M. Giersiepen, Th. Schmitz-Rode, V. Hirtz and S. Effert, *The geometry of the aortic root in health, at valve disease and after valve replacement,* J. Biomechanics, Vol. 23, No. 2, pp. 181-191, 1990.

[4] F. Sotiropoulos, I. Borazjani, *A review of state-of-the-art numerical methods for simulating flow through mechanical heart valves*, Med Biol Eng Comput, Vol. 47, No.3, pp. 245-256, 2009.

Proceedings of the 8th National Congress on Theoretical and Applied Mechanics, May 28-29, Brussels, Belgium.

Study of the Effects of Geometrical Parameters on the Performance of Cyclone Separators

Khairy Elsayed, Chris Lacor
Vrije Universiteit Brussel, Department of Mechanical Engineering, Research Group Fluid Mechanics and Thermodynamics, Pleinlaan 2, B-1050 Brussels, Belgium
Tel.: +32 26 29 2395; Fax.: +32 26 29 2880
Email: khairy.elsayed@vub.ac.be, chris.lacor@vub.ac.be

ABSTRACT

Different Mathematical models for cyclone separators with a tangential inlet were used to estimate the effect of geometrical parameters on the pressure drop and cut-off size. A prediction model for the pressure drop and cut-off diameter was obtained based on the response surface methodology by means of a statistical software. The results show that the vortex finder diameter, the inlet height, the inlet width, and the total cyclone height play an important role in influencing the cyclone performance. Different mathematical models were used in this study. Nearly all led to the same conclusions. For more understanding of the effect of the geometrical parameters on the flow field of cyclone separators, Large Eddy Simulations are performed for six test cases.

I. Introduction

Cyclones are widely used for removing industrial dust from air or process gases. They are the most frequently encountered type of gas-solid separator in industry. The primary advantages of cyclones are economy, simplicity in construction and ability to operate at high temperature and pressures. The principle of cyclone separation is simple, where the gasdust mixture enters from the inlet section. Then, the cylindrical body induces a spinning(swirl), vertical flow pattern to the gas–dust mixture. Centrifugal force separates the dust from the gas stream; the dust travels to the walls of the cylinder and down the conical section to the dust outlet. The gas exits through the vortex finder from the top. In order to describe the cyclone performance (pressure drop and collection efficiency) there are three approaches: Mathematical models, Experimental Investigation, and Computational Fluid Dynamics (CFD). The cyclone performance is affected by several parameters,Viz.: cyclone geometry (dimensions, shape of inlet section, number of inlets and vortex finder shape), inlet velocity (volume flow rate), dust mass loading, surface roughness.

This study is based on a cone cyclone with a tangential inlet cylinder, where seven geometrical parameters affect the flow field and performance, Viz.

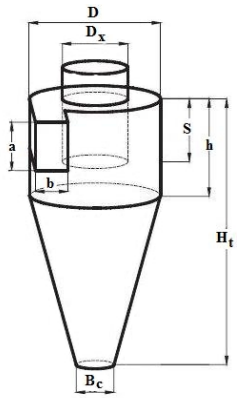

Fig. 1. Schematic diagram for cyclone separator

1. The inlet height, a
2. The inlet width, b
3. The vortex finder diameter, D_x
4. The vortex finder length, s
5. The dust outlet diameter, B_c
6. The cylindrical part height,h
7. The total cyclone height, H_t

as shown in Fig. I where D is the cyclone diameter

First the most important geometrical parameters were determined using mathematical modeling and statistical analysis, secondly, the effects of these factors were analyzed computationally using Large Eddy Simulation (LES).

II. MATHEMATICAL MODELS

During the past 50 years, interest in particle collection and pressure theories has steadily increased [1]. For estimation of pressure drop the following models were used

- Stairmand Model(1949) [2]
- Barth Model(1956) [3]
- Core Model presented by Lewellen (1971) [4]
- Shepherd and Lapple (1940) [5]
- Casal and Martinez-Bent (1983) [6]
- Empirical Correlation presented by Ramachandran

et al. (1991)[7]

To estimate the cut-off particle diameter the following two models were used

- Barth (1956) [3]
- Iozia and Leith (1989) [8]

A. Barth Model for Pressure Drop and Collection Efficiency

In 1956 Barth proposed a simple model based on force balance(classified as one of the Equilibrium-Orbit Models). This model enables to obtain the cut-off size and the pressure drop values.

A.1 Estimation of pressure drop

Barth subdivided the pressure drop into three contributions:

1. the inlet loss (this loss could be avoided by good design [3]).
2. the loss in the cyclone body.
3. the loss in the vortex finder.

The pressure drop in the cyclone body can be estimated from,

$$\Delta P_{body} = \frac{\rho v_x^2}{2}\frac{D_x}{D}\left(\frac{1}{\left(\frac{v_x}{v_{\theta CS}} - \frac{H_t - S}{0.5 D_x} f\right)^2} - \left(\frac{v_{\theta Cs}}{v_x}\right)^2\right) \tag{1}$$

where $v_{\theta CS}$ is the tangential velocity at the control surface CS, Fig. 2

$$v_{\theta CS} = \frac{\pi R_{in} R_x v_x}{a\ b\alpha + H_{CS}\pi f R_{in}} \tag{2}$$

where f is the friction factor (f=0.05), R_x is the vortex finder radius $R_x = D_x/2$, v_x is the mean axial velocity in the vortex finder $v_x = Q/(\pi R_x^2)$ where Q is the volume flow rate and H_{CS} is the height of the control surface extending from the bottom of the vortex finder to the cyclone bottom, see Fig. 2. R_{in} is the radial position of the center of the inlet (as shown in Fig.(3)), for a slot inlet $R_{in} = R - b/2$, where b is the inlet width and $R = D/2$ is the cyclone radius.

In a cyclone with a slot type of rectangular inlet, the inlet jet is compressed against the wall, resulting in a decrease in the area available for the incoming flow and an increase in the velocity. Barth accounted for this by introducing α, which is defined as the ratio of the moment-of-momentum of the gas in the inlet and the gas flowing along the wall, see Fig.(3). Barth introduced following formula to calculate α,

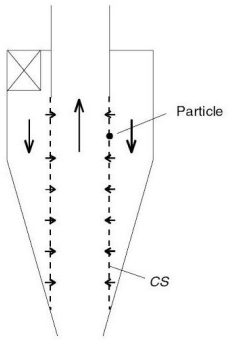

Fig. 2. The control surface concept in Barth model.

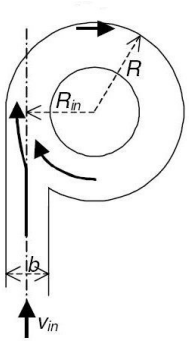

Fig. 3. Inlet flow pattern for slot inlet.

$$\alpha = 1 - 0.4\left(\frac{b}{R}\right)^{0.5} \tag{3}$$

The pressure drop in the vortex finder can be estimated using a semi- empirical approach as ,

$$\Delta P_x = (0.5\rho v_x^2)\left(\left(\frac{v_{\theta CS}}{v_x}\right)^2 + K\left(\frac{v_{\theta CS}}{v_x}\right)^{\frac{4}{3}}\right) \tag{4}$$

where K is the vortex finder entrance factor (K = 4.4). The total pressure drop $\Delta P = \Delta P_{body} + \Delta P_x$ can be made dimensionless using the average inlet velocity $v_{in} = \frac{Q}{ab}$ leading to the so-called Euler number based on the area average inlet velocity Eu_{in}.

$$Eu_{in} = \frac{\Delta P}{0.5\rho v_{in}^2} \tag{5}$$

A.2 Estimation of cut-off diameter

As mentioned above Barth's model is based on an "Equilibrium-orbit model". This model considers the imaginary cylindrical surface CS that is formed by continuing the vortex finder wall to the bottom of the cyclone Fig. 2. It is based on the force balance of a particle that is rotating in CS at radius R_x. The outward directed centrifugal force is balanced against

the inward drag caused by the gas flowing through surface CS and into the inner part of the vortex.

Large particles are therefore "centrifuged" out to the cyclone wall, (because centrifugal force > drag force so it will move outside of CS), and small particles are dragged in and escape out via the vortex finder.

The particle size for which the two forces balance -*the particles that orbit in equilibrium in* CS-is taken as the cyclone's x_{50} or cut-off size; it is the particle size that stands a 50–50 chance of being captured.

This particle size is of fundamental importance and is a measure of the intrinsic separation capability of the cyclone. Here, all the gas velocity components are assumed constant over CS for the computation of the equilibrium-orbit size.

Barth introduced the following formula to calculate the cut-off size x_{50},

$$x_{50} = \sqrt{\frac{v_{rCS}\, 9\, \mu_g\, D_x}{\rho_p\, v_{\theta CS}^2}} \tag{6}$$

where v_{rCS} is the uniform radial gas velocity in the surface of CS given by:

$$v_{rCS} = \frac{Q}{\pi D_x H_{CS}} \tag{7}$$

The following expression obtained from trigonometry relations can be used to calculate H_{CS}

$$\begin{aligned} H_{CS} &= \frac{(R-R_x)(H-h)}{R-(\frac{B_c}{2})} + (h-S) \quad \text{if } B_c > D_x \\ &= (H-S) \qquad\qquad\qquad\qquad \text{if } B_c \leq D_x \end{aligned} \tag{8}$$

III. Design of Experiment (Sensitivity analysis)

The usual method to optimizing any investigation set-up is to adjust one parameter at a time, keeping all others constant, until the optimum working conditions are found. Adjusting one parameter at a time is necessarily time consuming, and may not reveal all interactions between the parameters. In order to fully describe the response and interactions of any complex system a multivariate parametric study must be conducted.

A. Response surface methodology

Response Surface Methodology (RSM) is a powerful statistical analysis technique which is well suited to modeling complex multivariate processes, in applications where a response is influenced by several variables and the objective is to optimize this response. Box and Wilson first introduced the theory of RSM in 1951 ([11]), and RSM today is the most commonly used method of process optimization . Using RSM one may model and predict the effect of individual experimental parameters on a defined response output, as well as locating any interactions between the experimental parameters which otherwise may have been overlooked. RSM has been employed extensively in the field of engineering and manufacturing where many parameters are involved in a process.

In order to conduct any RSM analysis one must first design the experiment, identify the experimental parameters to adjust, and define the process response to be optimized. Once the experiment has been conducted and the recorded data tabulated, RSM analysis software models the data and attempts to fit a second-order polynomial to this data.

It is assumed that the performance of a cyclone is affected by seven geometrical factors, Viz.a/D, b/D, D_x/D, S/D, h/D, and H_t/D, while the values of other parameters affecting the cyclone performance are held constant, (gas density and viscosity, particle density, inlet velocity, mass loading, friction factor, cyclone diameter).

To study the effect of the seven geometrical parameters on the pressure drop and cut-off size, a full factorial design of experiment would require $2187(3^7)$ experiments, assuming three values for each parameter.

A more suitable design with a limited number of points can be done using Box-Behnken designs which are experimental designs for response surface methodology, devised by Box and Behnken in 1960 [12]. This set-up results in a Box-Behnken design of seven factors demanding only 64 calculations

The values of Euler numbers and cut-off diameters for the 64 designs are calculated with the mathematical models discussed before in Sec. II using VISUAL BASIC 6 code wrote by the authors. This is done in three steps, viz:

1. Construct the design using STATGRAPHICS and put these values in a file to read it by the Visual Basic 6 code.
2. calculate the values of Euler numbers and cut-off sizes using all mentioned models for cyclone performance
3. Analysis of the results using STATGRAPHICS

B. Analysis of the Result from Eu_{Barth}

The first step in analysis of response surface design is to determine which factors have a significant impact on the response variables. This is mostly done using a Pareto chart.The standardized Pareto chart for Barth's model for pressure drop is shown in Fig.4. It contains a bar for each effect, sorted from most significant to least significant parameter. The length of each bar is proportional to the standardized effect. A vertical line is drawn at the location of the 0.05 critical values for Student's t. Any bars that extend to the right of that line indicate effects that are statistically significant, For more details about statistical analysis refer to some statistical textbook e.g. [13].

From the Pareto chart Fig.4, the vortex finder diameter D_x, the inlet height a and the inlet width b appear to be the most significant factors affecting the pressure drop (Euler number).

Concerning correlation of variables, the following interactions seem to have an important effect: (1) the inlet width b and the vortex finder diameter D_x (i.e. BD). (2) the inlet height a and the vortex finder diameter D_x (i.e. AD). (3) the vortex finder diameter D_x with cyclone height H_t (i.e. DF).

The most significant effect is that of vortex finder diameter D_x with inverse relation with pressure drop. In general the ratio between the inlet area ($a \times b$) to the exit area ($\pi D_x^2/4$) has a large effect on pressure drop [10].

Fig. 5 shows the main effect of each parameter, leading to the same conclusion concerning the most significant geometrical parameters. Also it is clear from Fig.5 that the inlet height a is linearly related to the pressure drop. The effect of changing the inlet width b on the pressure drop is the most important at small values of b as shown in Fig. 5. The effect of H_t is small but its interaction with D_x denoted by DF in the Pareto chart, has a significant effect on the pressure drop. The remaining variables (B_c, h, S) have a weak effect on the pressure drop as shown in the Pareto chart, Fig. 4 and the main effect plot given in Fig.5.

Fig. 5 leads to the conclusion that changing D_x has a high effect on the pressure drop, with a very rapid decrease in the pressure drop when increasing D_x up to $D_x \approx 0.625$ after which the relation becomes direct. This may be explained as follows: although the pressure loss in the vortex finder decreases with increasing the vortex finder diameter, like the case of viscous flow in a pipe, the pressure drop in the cyclone body instead will increase due to the decrease of the flow area just after the flow entrance from the inlet

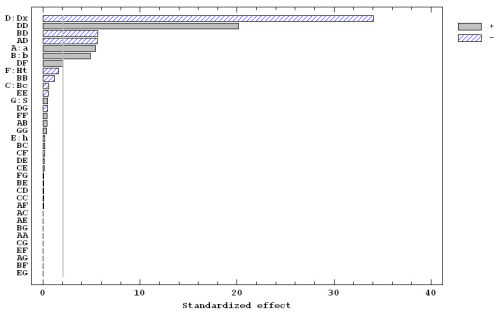

Fig. 4. The Pareto chart for Eu_{Barth}

region. This analysis indicates the large contribution of the pressure loss in the vortex finder to the total pressure drop (the pressure loss at the entrance, the pressure loss in the cyclone body, and the pressure loss in the vortex finder).

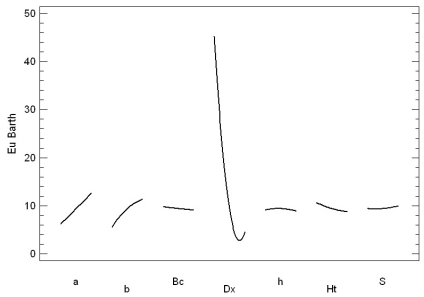

Fig. 5. The main effects plot for Eu_{Barth}

There are strong interactions between b and D_x. (denoted by BD in the Pareto chart Fig.4, a and D_x, (denoted by AD), and between D_x and H_t (denoted by DF). There is a negligible interaction between a and b (denoted by AB), and no interaction between a and H_t (denoted by AF), b and H_t (denoted by BF) as shown in the Pareto chart Fig. 4.

Fig. 6(a) shows the response surface plot of the effect of a and b on the pressure drop. The lowest pressure drop occurs at low values of a and b.The response surface of the effect of a and D_x is shown in Fig. 6(b) where the lowest pressure drop occurs at high values of a and D_x.

The correlated effect of b and D_x on the pressure drop is highly negative as shown in the Pareto chart Fig. 4 and Fig. 6(c) which indicates that at small values of D_x there is nearly no interaction between b and D_x. Also the interaction effect increases as D_x increases up to a point where $D_x \approx 0.625$ at which point there is nearly no interaction between b and D_x. The effect of H_t on the pressure drop is also very small but it comes into picture due to its strong interaction with D_x as shown in Fig. 4 and Fig. 6 which shows a change in the trend of the effect of H_t on pressure

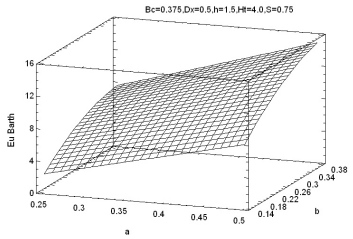

(a) The effect of a and b

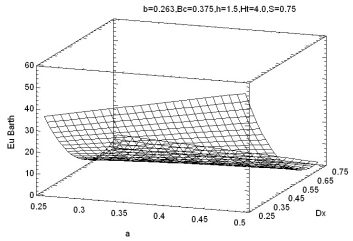

(b) The effect of a and D_x

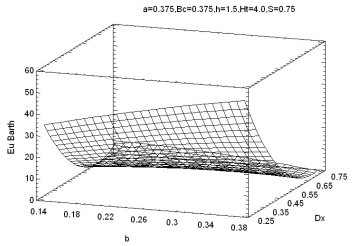

(c) The effect of b and D_x

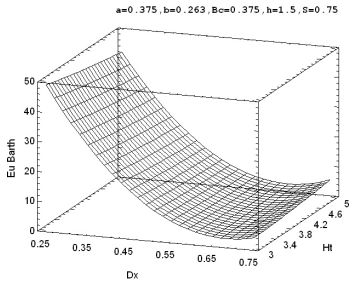

(d) The effect of D_x and H_t

Fig. 6. Response Surface Plots for Eu_{Barth}

drop.

For high D_x the pressure drop increases with increasing H_t (the pressure drop in this case remains low) while for low D_x there is an inverse relation between H_t and pressure drop (the value of pressure drop is also higher), so the best choice is therefore low H_t and high D_x.

This is also confirmed in the response surface plot given in Fig. 6(d).

C. Analysis of the Result from $X_{50_{Barth}}$

The previous section focussed on the optimum design to minimize the pressure drop in detail. This section will focus on the optimum design to minimize the cut-off size.

From the Pareto chart shown in Fig. 7, the most

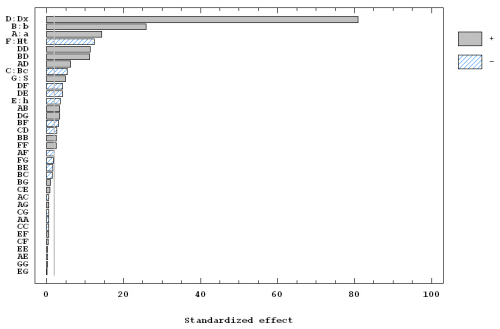

Fig. 7. The Pareto chart for $X_{50_{Barth}}$

significant effects are the vortex finder diameter D_x, the inlet width b , and the inlet height a.

This is similar as when analyzing Eu_{Barth}, however in this case the cyclone height H_t appears also to be a main factor affecting the cyclone efficiency (cut-off size). The interactions between the variables inlet width b and vortex finder diameter D_x (i.e. BD) , and inlet height a and vortex finder diameter D_x (i.e. AD) seem very prominent for the cyclone efficiency.

Actually all geometry parameters affect cut-off size but, the most significant effect is that of the vortex finder diameter D_x which has a direct relation with cut-off size. All parameters significantly affecting the pressure drop also affect the cyclone efficiency. Also the cyclone height H_t effect is significant in the study of the cut-off size with an inverse relation. The effect of most effective parameters is similar as for pressure drop. Exceptions are that the inlet height a gives a direct linear relation with high gradient Fig.8. The effect of changing inlet width b on cut-off size will be significant with nearly a linear relation as shown in Fig. 8. The main effect of H_t is significant with an inverse relation, while the change of other factors (B_c, h, S) have less effect on the cut-off size as shown from the Pareto chart, Fig. 7 and Main effect plot, Fig. 8 respectively.

It is clear from Fig. 8 that changing D_x has a high effect on pressure drop with very rapid increase in cut-off size with increasing of D_x so the value of cut-off size may be nearly four times its value at small values of D_x.

Fig. 9(a) shows the response surface plot for the effect of a and b on the cut-off size, where the lowest values of cut-off size occur at low values of a and b (as the case of pressure drop).

The response surface for the effect of a and D_x is shown in Fig. 9(b) where the lowest value for cut-off size occurs at low value of D_x whatever the value of a, and the effect of b and D_x is nearly the same as shown

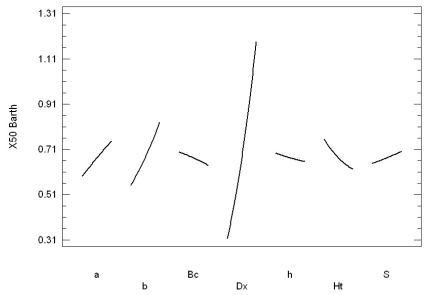

Fig. 8. Main effects plot for $X_{50_{Barth}}$

from Fig. 9(c) which was clear from the interaction plot .

The effect of H_t and D_x on the cut-off size is given in Fig. 6(d) and the shape of the surface shown is due to the direct relation between D_x with cut-off size and the inverse relation of H_t with it. From the figure it is observed that higher values of cut-off size occur at low values of H_t and high value of D_x, and lower values of cut-off size exist at high values of H_t and low value of D_x.

The reason of direct relation between increasing both inlet and exit cross sectional areas with cut off size is that: when these areas increased, the swirl intensity decreased; consequently the amount of particles thrown out to the cyclone wall due to centrifugal forces decreased, i.e. cut-off size increased. The effect of cone height on the cut-off size is significant as follow: however h has a small impact on the cut-off size, H_t has a large impact on it,. Also as cone height increases, the particle radial velocity decreases which prevent collected particles from reenter again the flow and escape; consequently the cut-off size decreased.

D. Optimization of the Result from Eu_{Barth} and $X_{50_{Barth}}$

From the previous analysis it is observed that the optimal values for the geometrical parameters that minimize the pressure drop are different from the values that minimize the cut-off size. As a result an optimization for the geometrical parameters values is needed.

Table I depicts the optimum values of the geometrical parameters that minimize the values of pressure drop and cut-off size. The table also gives the geometrical parameter values that result in worst performance.

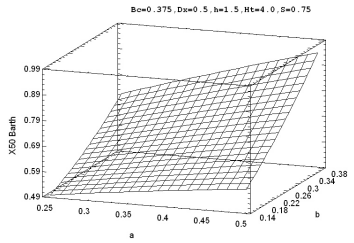

(a) The effect of a and b

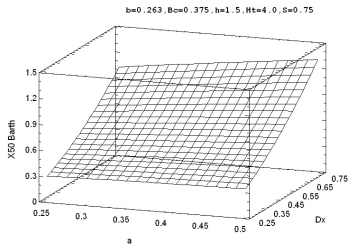

(b) The effect of a and D_x

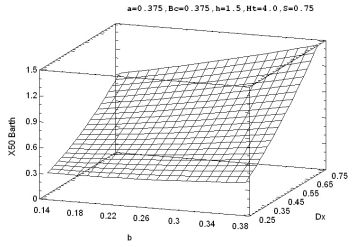

(c) The effect of b and D_x

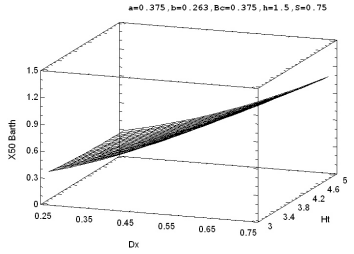

(d) The effect of D_x and H_t

Fig. 9. Response surface plots for $X_{50_{Barth}}$

IV. Computational Study using Reynolds Stress Turbulence Models (RSTM)

The conventional method of predicting the flow field and the collection efficiency of cyclone separator is experimental or via mathematical models. Recently application of computational fluid dynamics (CFD) for the numerical calculation of the gas flow field in a cyclone is becoming more popular [15]. One of the first CFD simulations was done by Griffiths and Boysan[16] who found that CFD simulations are able to predict the salient features of the fluid dynamics of cyclone separator, and this method of analysis is almost certainly less expensive than experiment, and represents a cost-effective route for design optimization.

To understand the effect of the geometrical pa-

rameters on the flow field of a cyclone separator six test cases are simulated computationally via FLUENT with Large Eddy Simulation. The details of the values of the geometrical parameters are given in table I.

V. Results and discussion from CFD simulation

A. The pressure field

The contour plots for static pressure for the six cyclones presented in table II show that the static pressure decreases radially from wall to center, with a negative pressure zone appearing in the forced vortex region (central region due to high swirling velocity). Some particles can therefore escape if they enter this zone. The pressure gradient is the largest along radial direction as there exists a highly intensified forced vortex, while the gradient in axial direction is small. The flow in the cyclone is not antisymmetric, as shown near the cone tip (due to one inlet section).

Two vortical motions exist: one moving down (outer vortex) and the other moving up (inner vortex). Both are clear in case of minimum pressure drop. Also a large region of negative pressure exists at the central region of all cyclones.

The maximum value for static pressure is that for the case of maximum pressure drop, which has the smallest vortex finder diameter. A "Vena-Contracta" phenomenon exists at the entrance of the vortex finder which causes excessive pressure drop. Also the inner vortex is very narrow, so the flow in the majority of the cyclone space is at very low velocity and consequently low swirl which affects the collection efficiency.

The pressure contours for the case of maximum pressure drop, min. cut-off size and optimum design are rather similar from three aspects: (1) the majority of the flow is at high static pressure. (2) there is a narrow low pressure region. (3) a Vena-Contracta phenomenon exists at the entrance of the vortex finder.

The pressure contours for the case of minimum pressure drop, which has the largest vortex finder diameter, show that: (1) the flow field in the cyclone is not symmetric. (2) the low pressure zone is very wide. (3) the inner vortex touches the cone walls which decreases the collection efficiency considerably as some collected particles can reenter the flow field due to high swirl velocity existing in the inner vortex, and then escape from the vortex finder.

For the case of minimum cut-off size the pressure drop is somewhat less than that for maximum pressure drop, but as the cut-off size is inversely proportional to the vortex finder diameter D_x, so here the vortex finder diameter D_x is small also but the inner vortex surface (CS in Barth's model) is nearly equal the vortex finder diameter D_x, and here again the negative pressure region is very narrow and contained inside the vortex finder.

For the case of maximum cut-off size, the pressure drop value is better than that for the cases of maximum pressure drop and minimum cut-off size as is clear from the contour values. Here the pressure contours are nearly similar to the case of minimum pressure drop, but here the inner vortex touches the cone surface which is harmful for cyclone performance; also still the pressure drop is larger than that for the case of minimum pressure drop.

The flow field of the optimum design case is in between that for the cases for minimum pressure drop and minimum cut-off size, with a longer cone to enhance collection efficiency and a moderate value of the vortex finder diameter D_x to optimize the pressure drop and the cut-off size. The inner vortex is nearly cylindrical and does not touch the cone surface.

For the worst design case the pressure drop is less than that for the maximum pressure drop but more than its value for all other cases. This case has the shortest cone height. The flow field has a wide region with nearly stagnant flow, also the negative pressure region extend throughout the cyclone from dust outlet till the gas outlet.

The dynamic pressure is the largest at the interface between the forced vortex and the quasi-free vortex zone. The distribution of the dynamic pressure is asymmetrical due to the asymmetry of the tangential velocity (because the cyclone has only one gas inlet, the axis of the vortex does not coincide with the axis of the geometry of the cyclone) as is clear from the contour plots for the case of minimum pressure drop .

The highest value of dynamic pressure occurs for the case of maximum pressure drop due to the high velocity spot existing in the vortex finder, while the majority of the flow field has small dynamic pressure values. Also the dynamic pressure distribution is more symmetrical than that of the minimum pressure drop case.

For the cases of minimum pressure drop and that of maximum cut-off size there is a spot of high dynamic pressure at the lip of the vortex finder due to high velocity; also the asymmetry of the flow field is very clear.

The dynamic pressure distribution for the case of minimum cut-off size and that for the optimum performance looks very similar; this can be explained by

the nearly equal values vortex finder diameter and cyclone height.

The dynamic pressure distribution for the case of maximum cut-off size is different than that for other cases as it has a larger vortex finder diameter and a short cyclone height; also the flow field near the vortex finder lip is completely chaotic due to the large vortex finder diameter. There is a spot all around the lip due to flow acceleration between the cyclone wall and the vortex finder wall.

The case of optimum design is in between that for the minimum pressure drop case and that for minimum cut-off size with a longer cyclone to enhance collection efficiency. The case of worst design is in between that for the maximum pressure drop and the maximum cut-off size with nearly the same values for a, b, H_t, s.

In the flow field for the case of worst design, the region of high static pressure is exactly the same region of low dynamic pressure. i.e. the majority of the flow field has a small velocity (swirl) which leads to low collection efficiency, while the velocity increase considerably via the vortex finder with large energy losses at the entrance of the vortex finder (entrance loss in viscous flow).

B. The tangential velocity

The tangential velocity distribution is similar to the dynamic pressure distribution meaning that the tangential velocity is the dominant velocity component in the cyclone separator. The value of the tangential velocity equals zero on the wall and the center of the flow field. The high speed gas enters the inlet and is accelerated up to $1.5 \sim 2.0$ times the inlet velocity (13.5 m/s). Then the velocity decreases as the gas spins down along the wall. Before it goes below the vortex finder, the gas flow collides with the follow-up flow and forms a chaotic flow close to the vortex finder outside wall. The gas velocity decreases sharply after that, this is the main cause of the short-circuiting flow and often results in a higher pressure drop (the same phenomenon was analyzed in previous work e.g. [17]).

Comparing the values of the tangential velocity for all cases, the maximum value occurs in the case of maximum pressure drop, where the maximum tangential velocity is five times the inlet velocity. There is a discrepancy of the tangential velocity patterns exist in the obtained results as follow. For the case of minimum pressure drop, there is a central cylinder with zero tangential velocity, while the majority of the cyclone have nearly the same value as tangential velocity is considerably low this means also low collection efficiency.

For the case of maximum pressure drop the tangential velocity values are very high, the flow field can be subdivided into several region according to the values of tangential velocity: (a) very high values at the inlet of the vortex finder. (b) very low values at the cyclone center and around the vortex finder far away from the inlet zone. (c) high values regions in a cylinder with diameter larger than the vortex finder diameter, so the inner vortex touches the cone wall and consequently a decrease in collection efficiency occurs as some particles which were already collected can reenter the ascending flow region. (d) Moderate values in the remaining region of the cyclone. A vena-Contracta phenomenon exists at the entrance of the vortex finder.

For minimum cut-off size, the cyclone becomes longer than that of the maximum pressure drop case; in addition the central cylinder of low velocity becomes twisted. Here the maximum velocity decreases to half the value of the maximum pressure drop case.

For the case of maximum cut-off size the tangential velocity is small and the flow field is chaotic. The flow with high tangential velocity touches the cone wall leading to a decrease of collection efficiency.

For the case of optimum design the flow field pattern is in between that for minimum cut-off size and minimum pressure drop, the geometrical parameter values are also in between. The maximum tangential velocity is larger than that for minimum pressure drop and less than that for minimum cut-off size. The flow field for the worst design case shows a very high velocity (four times the inlet velocity) but here the vortex finder is small and the cyclone is short. The majority of the flow field has high values (three times the inlet velocity).

C. The axial velocity

The maximum upward axial velocity occurs in the case of maximum pressure drop (eight times the inlet velocity value). In the case of minimum pressure drop the axial velocity values in the entire cyclone are nearly close. The axial velocity distribution for the cases of maximum pressure drop, minimum cut-off size, optimum design and worst design is nearly similar where three categories of values are distinctive: (a) a high axial velocity spot inside the vortex finder. (b) moderate axial velocity values in the vortex finder extend upto the zone underneath. (c) low axial velocity values in the remainder of the cyclone. The axial velocity distribution for the case of maximum cut-off size is similar to that for the case of minimum

pressure drop where the majority of the flow field has moderate values while a high axial velocity spot exists at the vortex finder inlet.

Conclusion and future work

All the geometrical parameters in the cyclone separator affect its performance, so to determine geometrical parameters which are the most significant a statistical analysis based on the response surface methodology (RSM) are performed with the aid of robust mathematical models to calculate the values for the pressure drop and cut-off size. The most significant geometrical parameters are the vortex finder diameter (the outlet cross sectional area), the inlet height and width (the inlet cross sectional area) and the cyclone height. In general, small values of the inlet area and high values of cyclone height (cone height) enhance the cyclone performance (low pressure drop and small cut-off size) but increasing D_x will decrease the pressure drop and increase the cut-off size so its value should be optimized to have the best performance as given by table I. LES investigations were performed on six extreme cases obtained from the statistical analysis to understand the effect of these geometrical parameters on the flow field pattern. All mathematical models used in this study gave the same conclusion especially about the significance of D_x, a, and b on the cyclone performance.As a conclusion from the present study only four geometrical parameters are significant, so a systematic CFD study for their impact on the flow field and performance is required.

TABLE I
Critical values of geometrical parameters

Factor	a	b	B_c	D_x	h	H_t	s	Eu	x_{50}
Min. value	0.25	0.15	0.25	0.25	1.00	3.00	0.500	-	-
Center value	0.38	0.26	0.38	0.50	1.50	4.00	0.750	-	-
Max. value	0.50	0.38	0.50	0.75	2.00	5.000	1.000	-	-
Min. Δp	0.38	0.38	0.38	0.75	1.99	3.990	0.749	0.0	1.37
Max. Δp	0.50	0.36	0.25	0.25	1.37	3.107	0.971	65.6	0.53
Min. x_{50}	0.50	0.15	0.25	0.25	1.01	4.395	0.811	43.1	0.25
Max. x_{50}	0.50	0.37	0.31	0.74	1.01	3.138	1.000	0.0	1.92
Optimum design	0.30	0.18	0.25	0.26	1.02	4.799	0.814	30.6	0.28
Worst design	0.47	0.38	0.26	0.32	1.25	3.011	1.000	47.1	0.70

References

[1] Zhao, B. and Su, Y., 2006. Particle collection theory for cyclone separators: Summary and comparison. Particle & Particle Systems Characterization 23, 484–488.

[2] Stairmand, C. J., 1949. Pressure drop in cyclone separator. Engineering 168,pp. 409-412.

[3] Barth, W., 1956. Design and layout of the cyclone separator on the basis of new investigations. Brennstoff-Warme-Kraft, Vol. 8, No. 4, 1956, pp. 1-9.

[4] Lewellen, W. S.,1971. A review of confined vortex flows. NASA CR-1772.

[5] Shepherd, C. B. and Lapple, C. E., 1940. Flow pattern and pressure drop in cyclone dust collectors cyclone without intel vane. Industrial & Engineering Chemistry, Vol.32 No. 9, pp 12461248

[6] Casal, J. and Martnez-Benet, J. M., 1983. A better way to calculate cyclone pressure drop. Chemical Engineering, Vol.90, No.2,pp. 99-100.

[7] Ramachandran, G., Leith, D., Dirgo, J., Feldman, H., 1991. Cyclone optimization based on a new empirical model for pressure drop. Aerosol Science and Technology 15, 135–148.

[8] Iozia, D. L., Leith, D., 1989. Effect of cyclone dimensions on gas flow pattern and collection efficiency. Aerosol Science and Technology 10, 491–500.

[9] Altmeyer, S., Mathieu, V., Jullemier, S., Contal, P., Midoux, N., Rode, S., Leclerc, J.P., 2004. Comparison of different models of cyclone prediction performance for various operating conditions using a general software. Chemical Engineering and Processing 43, 511–522.

[10] Hoffmann, A. C. and Stein, L. E., 2008. Gas Cyclones and Swirl Tubes Principle, Design and Operation, 2nd Edition. Springer.

[11] Wikipedia, 2008. Response surface methodology.

[12] Wikipedia, 2008. Box-Behnken designs.

[13] Antony, J., 2003. Design of Experiments for Engineers and Scientists. Butterworth-Heinemann.

[14] Polhemus, N. W., 2005. How to perform an optimization experiment using statgraphics centurion. Http://www.sigmaplus.fr/telecharg/StatG/howto9.pdf.

[15] Wang, B., Xu, D., Chu, K., Yu, A., 2006. Numerical study of gas-solid flow in a cyclone separator. Applied Mathematical Modelling 30, 1326-1342.

[16] Griffiths, W. D. and Boysan, F., 1996. Computational fluid dynamics (cfd) and empirical modelling of the performance of a number of cyclone samplers. Journal of Aerosol Science 27, 281–304.

[17] Xiang and R. B., Lee, K. W., 2005. Numerical study of flow field in cyclones of different height. Chemical Engineering and Processing 44,pp. 877-883.

TABLE II
THE TIME-AVERAGED CONTOUR PLOTS FOR THE SIX CYCLONES USING LES

Case	Min. pressure drop	Max. pressure drop	Min. cut-off size	Max. cut-off size	Optimum design	Worst design
The static pressure [Pa]	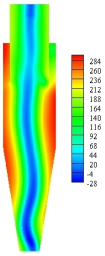	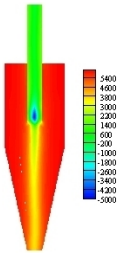	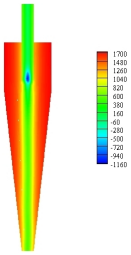	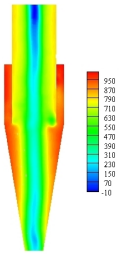	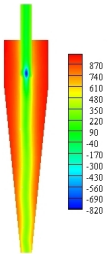	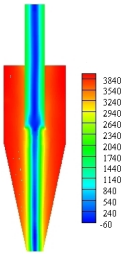
The dynamic pressure [Pa]	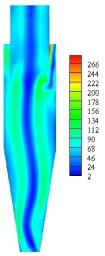	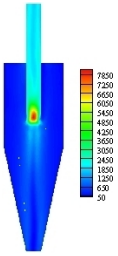	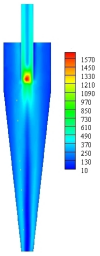	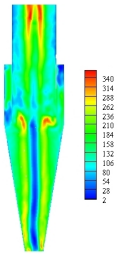	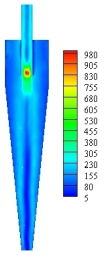	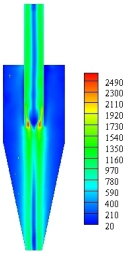
The tangential velocity [m/s]	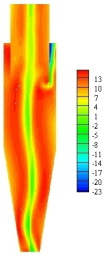	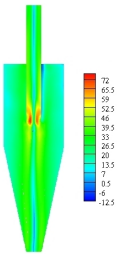	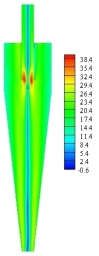	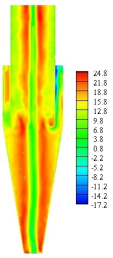	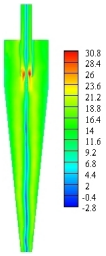	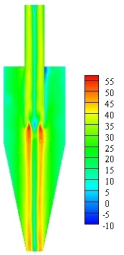
The axial velocity [m/s]	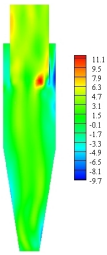	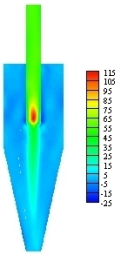	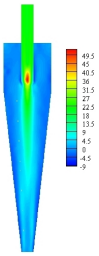	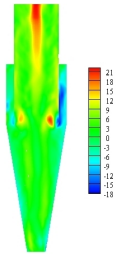	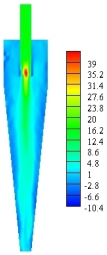	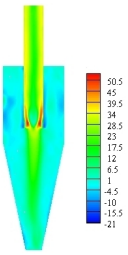
The velocity magnitude [m/s]	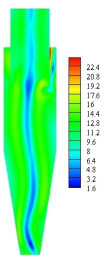	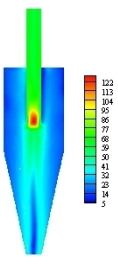	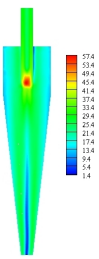	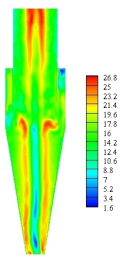	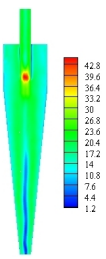	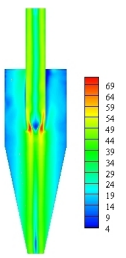

Proceedings of the 8th National Congress on Theoretical and Applied Mechanics, May 28-29, Brussels, Belgium.

A Deployable Mast for Kinematic Architecture

N. De Temmerman[1], M. Mollaert[1], L. De Laet[1], C. Henrotay[1], A. Paduart[1], L. Guldentops[1], T. Van Mele[1], W. Debacker[1]
[1]Vrije Universiteit Brussel – Department of Architectonic Engineering Sciences
Pleinlaan 2 – 1050 Brussel

niels.de.temmerman@vub.ac.be

Abstract: **Proposed here is a concept for a deployable mast with angulated scissor units, for use in adaptable temporary architectural constructions. The adaptable structure serves as a tower or truss-like mast for a temporary tensile surface structure and doubles up as an active element during the erection process. The mast consists of scissor-like elements (SLE's) which are an effective way of introducing a single D.O.F.(degree of freedom) mechanism into a structure, providing it with the necessary kinematic properties for transforming from a compact state to a larger, expanded state. The scissor units used here are not comprised of straight bars, but rather consist of angulated elements, i.e. bars having a kink angle. Although primarily intended for radially deployable closed loop structures, it is shown in this paper that angulated elements can also prove valuable for use in a linear three-dimensional scissor geometry.**

Keywords: **Deployable structures, transformable structures, adaptable architecture, angulated scissor elements, kinetic architecture**

I. Introduction

An innovative concept for a deployable hyperboloid mast with angulated scissor elements is presented. The scissor structure is a central vertical linear element, used to hold up several anticlastic membrane canopies at their high points. The question was raised whether it would be possible to design such a deployable mast for a temporary tensile structure and to use it as an active element during the erection process. In addition, the pantographic mast allows visitors to access several platforms to enjoy the views, under or above the different membrane elements. The proposed concept is a transformable version of the static concept shown in Figure 1.

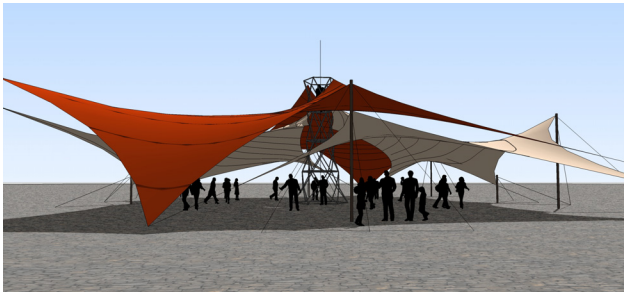

Figure 1: Mobile structure with membrane surfaces and arranged around a demountable central tower (© The Nomad Concept)

The original (undeployable) mast (or tower) consists of several modules which are assembled and dismantled on-site by stacking them vertically, for which a lifting device is needed. After assembly the membrane would have to be attached to the top, after which the pre-tension in the membrane can be introduced.

By making the mast deployable, all connections can be made on ground level, while the mechanism is in its undeployed, compact state, therefore eliminating the need for additional lifting equipment. After connections between the membrane elements and the mast have been made, the mechanism is deployed until the required height is reached and the membrane elements become tensioned. The mast could be deployed to such an extent that a sufficient amount of pre-tension is introduced in the membrane, ensuring the ability to withstand external loads. Since the mast is basically a mechanism, additional bracing is needed after full deployment to turn it into a load-bearing structure. To illustrate the concept, the simplest incarnation of the concept is used throughout the paper: a mast of triangular shape. But it must be noted that the concept is valid for any n-sided polygon. The extensive formulas for obtaining the geometry based on architectural design parameters [1] have been omitted for clarity.

II. Geometry

A. Dimensions

The deployable mast is horizontally divided in several modules, which are closed-loop configurations of identical hoberman's units or otherwise called angulated SLE's. Figure 2 shows an example of a mast with - in this case - triangular modules, of which three are stacked vertically.

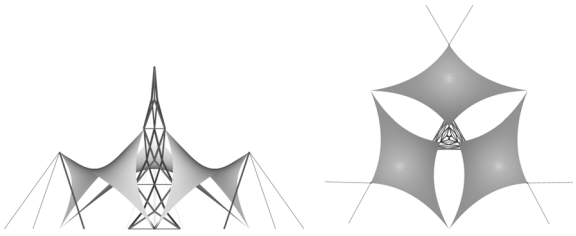

Figure 2: Side elevation and top view of the structure showing the three tensile surfaces arranged radially around the central mast

The mast is 8.5 m high and 2.7 m wide, while the tensile surfaces are identical and measure 10 m along their longest

diagonal. The top of the second module, at which the membrane elements are attached, is located at 5.2 metres above ground level. The other high point of the membranes is held 4 m above ground by additional masts.

B.Angulated elements vs. polar elements

It could be argued that a mast with a broad base and a narrow top can equally be built with polar units with decreasing size as they are located nearer to the top. In Figure 3 two linkages – one with angulated elements, another with polar units - are shown, with identical height and width, but with varying number of units U and different bar lengths. Using the angulated elements offers an advantage: while the linkage with angulated elements is built from only 3 SLE's with 11 hinges and nodes, the equivalent polar mechanism needs 8 units with 26 connections to reach a similar deployed geometry. The effect that the angulated elements have on the modules is that, during deployment, the top of a module becomes narrower than its base. The radius of the top of a certain module becomes equal to the radius of the base of the next, higher located module. This means that the narrowing effect is enhanced and passed on through the mechanism, from module to module, from bottom to top.

Linkage with angulated SLE's:	Equivalent linkage with polar SLE's:
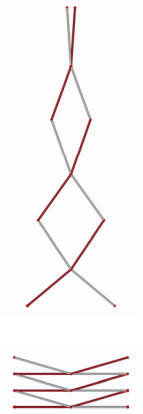	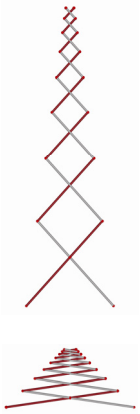
Number of SLE's: n=3 Number of hinges and end nodes: 11	Number of SLE's: n=8 Number of hinges and end nodes: 26

Figure 3: Comparison between a linkage with angulated SLE's and its conventional polar equivalent

The dimensions of the individual bars of the scissor units are such, that the horizontal projection of b is equal to a, as shown in Figure 4.

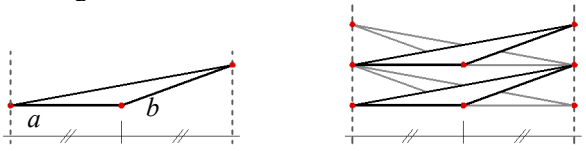

Figure 4: Imposed condition on the length of the semi-bars a and *b (a<b)*, in order to make the linkage foldable along the vertical axis

The most important parameters are the kink angle β of the angulated element and the deployment angle θ, as depicted in Figure 5. The relationship between a and b, as shown in Figure 4, leads to a hyperbolic shape for the mast. By satisfying alternative relationships between a and b, a simpler, prismoid shape for the mast can be obtained, with a simpler kinematic behaviour, as later will be explained.

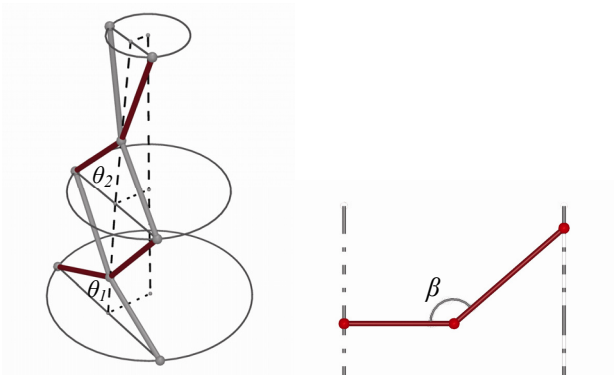

Figure 5: Most important parameters used for describing the geometry and the deployment

For a full and exhaustive description of all relevant design parameters and a comprehensive geometric design method, drawn up from the designer's point of view, the reader is referred to [1].

III. Transformation

A.Compacting for transport

The imaginary vertical axes connecting the end nodes of the bars can act as fold lines, used to further flatten the linkage. Therefore, the modules are 'cut open' along one fold line, after which the whole can be flatly folded for easier transport. Such a fold sequence is shown in Figure 6, which depicts the simplest possible structure: the one with a triangular base. This way of further compacting is presented as an option and could be ignored, on the condition that the dimensions in the undeployed state are kept reasonable.

	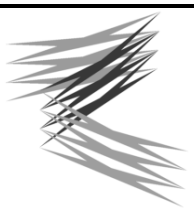
Step 1 (Compacted for transport)	Step 2
	
Step 3	Step 4 (ready to deploy)

Figure 6: Initial unfolding of the compacted linkage (transport) to its polygonal form (ready to deploy)

B.Deployment

The deployment sequence of the tower is presented in Figure 7, showing a top view and a side elevation for each stage. Stage 5 is the most compacted state, while stage 10 illustrates the fully deployed state. The maximum deployment is reached when the upper end nodes of the top module meet in one point.

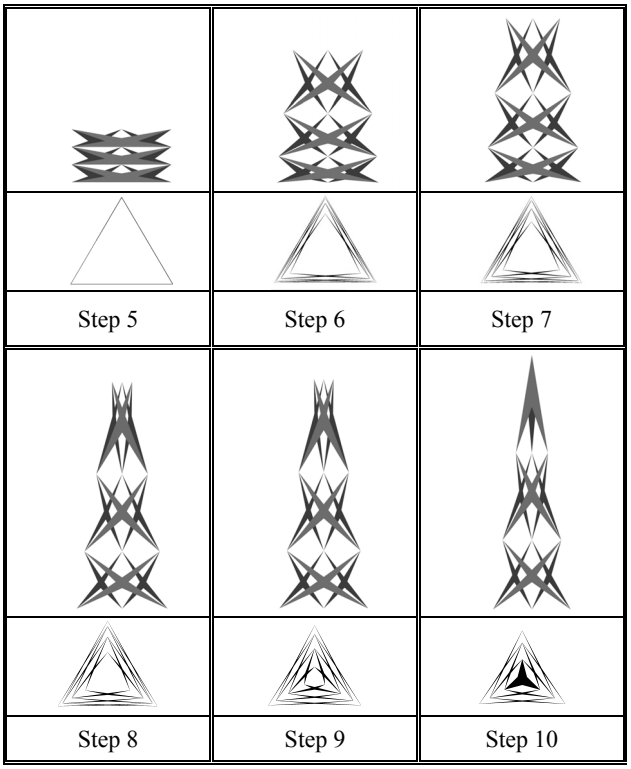

Figure 7: Six stages in the deployment of a triangular mast: elevation and top view

A short description is given of how the erection process could be executed, as shown in Figure 8:

- A: the tower is in its undeployed form. The membrane elements are attached to the nodes of the mechanism and fixed by their low points to the ground
- B: As the tower gradually deploys, the membranes are raised. When sufficient height is achieved, the additional masts are inserted and gradually put in their right location. Then, the cables fixing the secondary masts to the ground are brought under tension.
- C: Finally, the tower is slightly deployed further to add pre-tension in the membrane. Then, the tower is fixed to the ground by pinned supports and additional horizontal ties (cables or struts) can be inserted at the appropriate level.

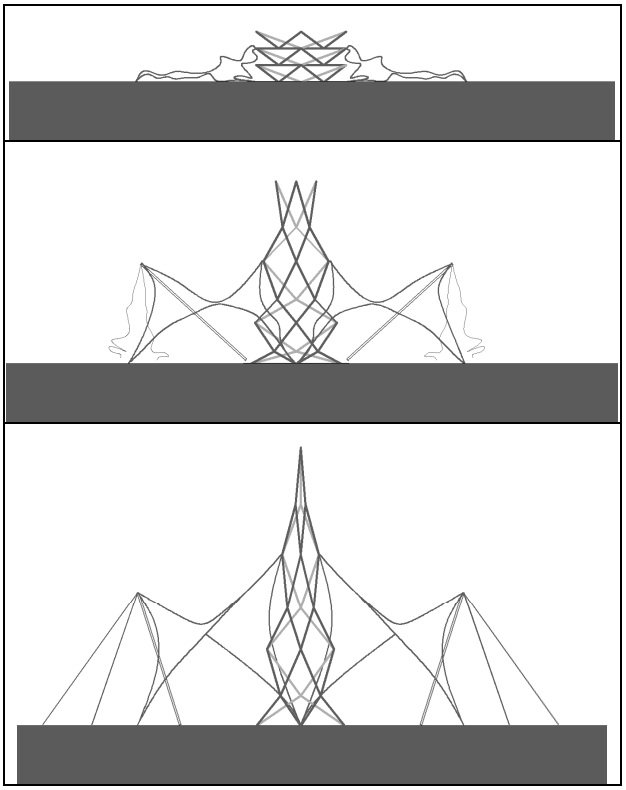

Figure 8: Deployment sequence (A, B and C) for the tower with the membrane elements attached

After deployment horizontal ties are added to enhance structural stiffness. Several solutions are possible: cable ties could be used, which are already present before deployment and are shortened as the structure deploys and becomes narrower. Struts could be added afterwards to brace the structure. An active cable can run over appropriately chosen nodes along a path and can be shortened to aid in the deployment.

C.Influence of parameters

Minimal changes in the design values can have a profound effect on the overall geometry. The parameters with the strongest impact on the geometry are the kink angle β (as shown in Figure 5) and, logically, the number of stacked modules n in the linkage. Figure 9 shows the undeployed and fully deployed position for three different configurations with specific values for β of 135°, 150° and 165°. All configurations have the same edge length. As β increases, the overall height of the deployed configuration also increases, while the radius of the footprint decreases.

The biggest impact however is noticeable in the undeployed configuration. By increasing β from 135° to 165°, the height in the stacked position is reduced to a third. So blunter kink angles lead to linkages which are more compact – easier transportable - in their undeployed state.

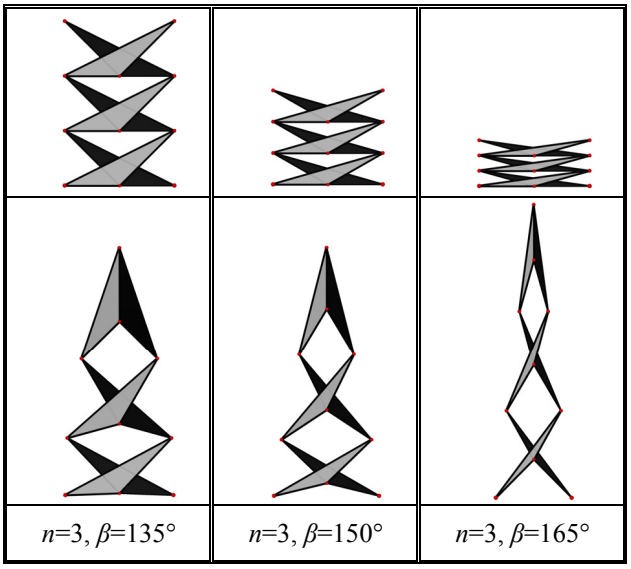

Figure 9: Illustration of the influence of the apex angle β on the geometry of a linkage with angulated SLE's with three modules (n=3) in the undeployed (top) and fully deployed configuration (below)

The top module in the linkage is the determining factor for the deployment range. Units with sharp kink angles tend to quickly reach their maximal deployment, therefore halting the deployment of the remaining modules. So if a substantial expansion in height is desired, it would be a better option to choose a blunt kink angle in combination with a higher number of modules: the blunt kink angle makes the undeployed configuration more compact in height and increases the deployment interval (0 to θ_{max}). A choice will have to be made concerning the optimal number of modules that will suit the design, taking all relevant parameters into consideration.

IV. Kinematic Behaviour

Figure 10 shows a schematic representation of an undeployed and an intermediate deployment position of the same linkage. As the deployment progresses, the angulated SLE's of each module tilt inward at the top. The dotted lines are imaginary fold lines around which mobility has to be allowed in order to complete the deployment. Through connection of the end nodes, each scissor unit can be represented by a trapezoid, of which the contour changes constantly during deployment. Between quadrilaterals ABDC and CDFE and between CDFE and EFHG there is a relative rotation which causes them not to remain coplanar

The joints connecting the end nodes of the units will have to take into account all aspects of this mobility. In Figure 11 and Figure 12 a proposal for such a joint is pictured, showing the seven rotational degrees of freedom needed for the deployment, as well as for the linkage to be compactly folded.

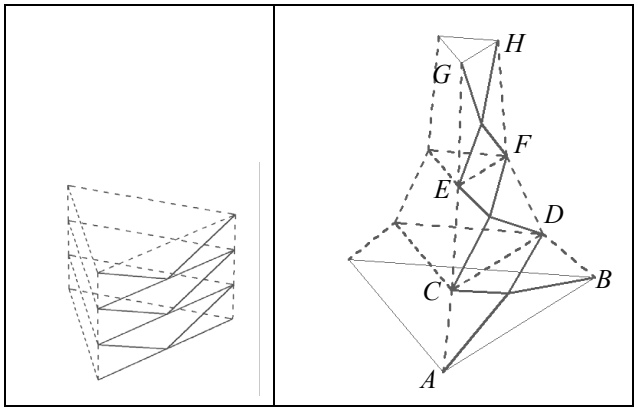

Figure 10: A schematic representation of the relative rotations of the quadrilaterals around imaginary fold axes during deployment

In order for the mechanism to be usable as a structure, the mobility will have to be constrained. To analyse the mobility of the system, an equivalent hinged plate model is presented in Figure 13. which represents the linkage with the rotational degree of freedom of the scissor linkage removed. After removal of this D.O.F. the remaining mobility determines to what extent constraints have to be added. Due to triangulation of the modules, there is no additional mobility which means it is basically a single D.O.F.-mechanism. Therefore, it is sufficient to constrain the movement of the rotational degree of freedom of the scissor units. As usual, fixing two appropriately chosen nodes is enough to remove the rotational D.O.F from the scissor linkage. But for using the tower as a load bearing structure, all three lower nodes have to be fixed to the ground by pinned supports. Additionally, it has been found through preliminary structural analyses, that horizontal ties - cables or struts - between the nodes greatly improve structural performance and lead to much smaller sections for the individual bars, thus enhancing the weight/height ratio [1].

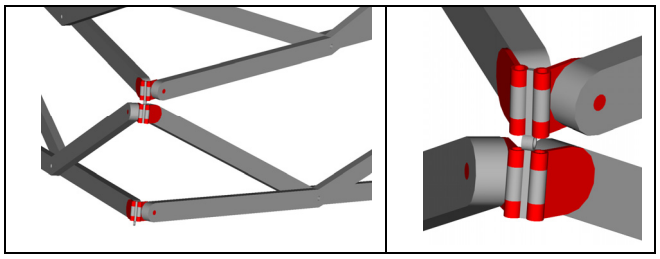

Figure 11: Kinematic joint connecting the angulated elements at their end nodes

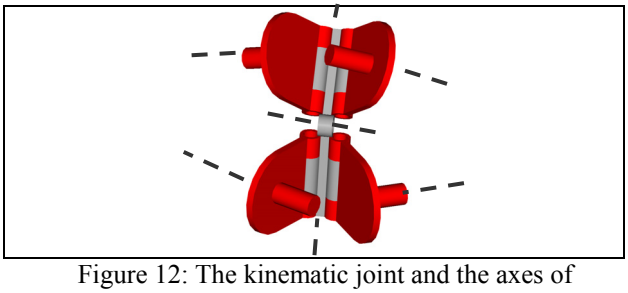

Figure 12: The kinematic joint and the axes of revolution for the seven rotational degrees of freedom

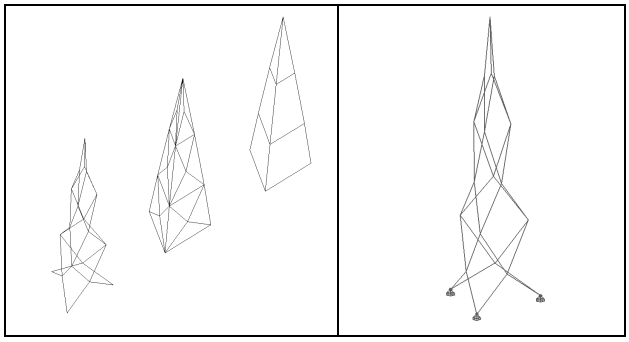

Figure 13: The scissor linkage in its deployed state and its equivalent hinged plate structure for mobility analysis (left) – Fixing the structure by pinned supports (right)

V. Simplified Geometry

The scissor linkage in the previously described geometry has in its undeployed state a prismatic shape and all angulated elements per vertical row (or lateral face of the prism) are coplanar. During deployment, however, the shape gradually changes into a hyperboloid, which means that the angulated elements per vertical row are no longer coplanar, i.e. they experience relative rotation, as can be seen in the triangular example of Figure 14 (left). As a consequence, the articulated hinges (Figure 12) will have to allow an extra rotational D.O.F around the horizontal axes between modules to cope with this movement, which adds to the complexity of the joint design.

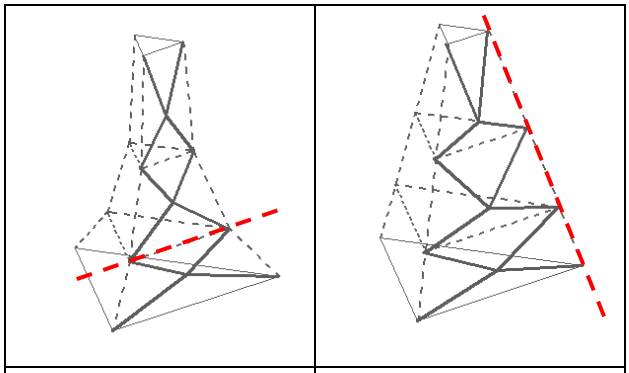

Figure 14: Difference in geometry between the hyperboloid and the prismoid version

The described deployment behaviour is caused by the particular geometry of the angulated elements, which consist of two differently sized semi-bars *a* and *b*, turning the angulated elements non-symmetrical. The overall geometry of this solution shall be referred to as *hyperboloid*.

Now, an alternative concept is proposed, which is similar in setup to the hyperboloid version, but has simplified joints for interconnecting the modules. If the angulated elements within a vertical row can be kept coplanar, then the hinges between modules would not have to allow an extra rotational D.O.F. around the horizontal axes between modules, effectively decreasing the mechanical complexity. Also, the end nodes of the angulated elements remain collinear, as shown in the triangular example of Figure 14 (right). The effect on the overall shape is that it resembles a prism before, during and after deployment. More precisely, such a shape is known in geometry as a *prismoid.*

This particular prismoid geometry can only be achieved if symmetrical angulated elements are used, i.e. elements with identical semi-lengths.

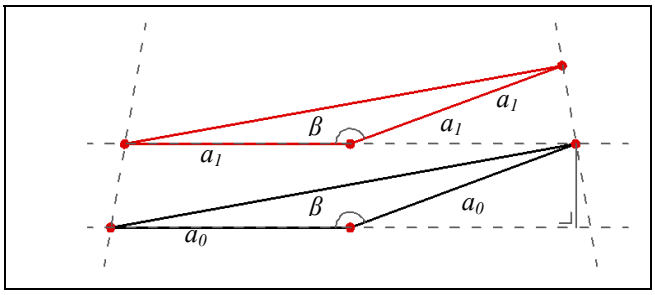

Figure 15: Symmetrical and non-identical angulated elements result in a fully compactable configuration: *prismoid solution*

Furthermore, an extra condition is imposed on the scissor geometry, as Figure 15 shows. The angulated elements become smaller near the top and their geometry is such that their lower end nodes and intermediate hinge are collinear in the undeployed position. This configuration ensures the highest degree of compactness.

The relationship between the lengths of semi-bars of consecutive angulated elements can be derived. The length of the semi-bar a_1 can be expressed in terms of a_0 as follows:

$$a_1 = a_0 \cos(\pi - \beta) \qquad (1)$$

With the kink angle β and the length of the semi-bar of the bottom most angulated element a_0 chosen as design parameters, the length semi-bar of the n^{th} element can be written as:

$$a_n = a_0 (\cos(\pi - \beta))^n \qquad (2)$$

To illustrate what happens during deployment, Figure 16 shows the corresponding closed loop structure which uses the same vertical linkage, but arranged radially in a common plane. The planar linkage is depicted in three consecutive stages - undeployed, partially deployed and fully deployed. During deployment, a constant angle (marked by the red intersecting lines), is subtended by each vertical linkage. This characteristic is precisely what makes the design of radially deployable closed loop structures possible [3].

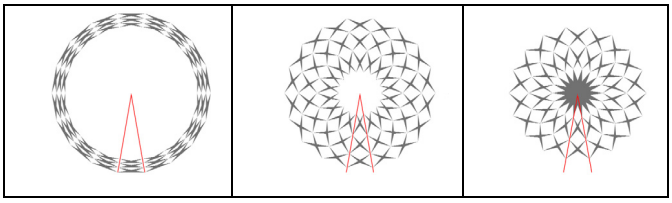

Figure 16: Three consecutive stages of the corresponding planar closed-loop structure

Figure 17 shows a three-dimensional model of a triangular prismoid tower in three deployment stages.

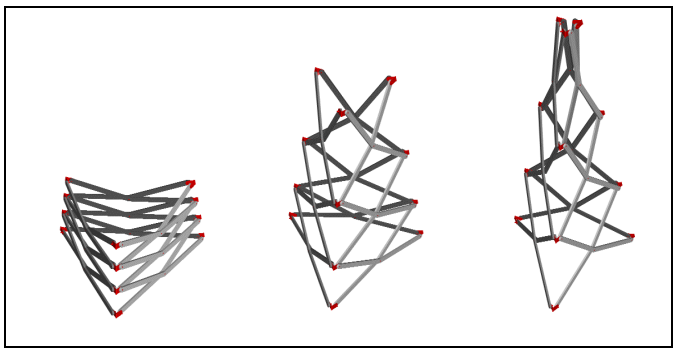

Figure 17: Perspective view of the deployment of a triangular prismoid tower

The simplified solution for the articulated hinge - which connects four bars at once - is shown in Figure 18.

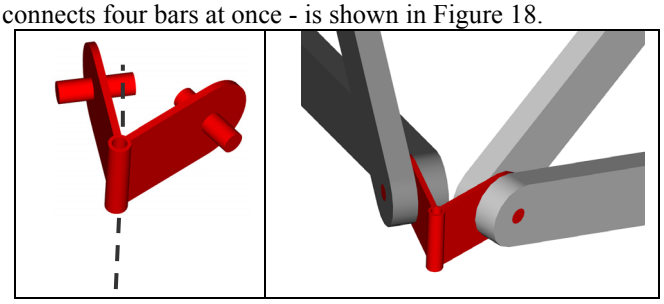

Figure 18: Detailed view of the simplified hinge connecting four scissor bars

In Figure 13, an equivalent hinged-plate structure for the hyperboloid geometry was introduced, which has shown that the only D.O.F. in the system is the rotational D.O.F. of the scissors. When the same method is applied to the prismoid solution, it can be seen that this holds no longer true. It can be concluded that the prismoid solution is – apart from the triangular geometry – a multiple D.O.F.-mechanism [1]. To turn the mechanism into a structure, and therefore removing all D.O.F.'s, all lower nodes are fixed to the ground by pinned supports.

VI. From Model to Realisation

A.1/20 scale model

In order to evaluate whether the obtained kinematic behaviour of the hyperboloid mechanism is indeed the desired one, a detailed working model has been constructed, as shown in Figure 19. This 1/20 scale model with triangular section allows the same D.O.F.'s as the full scale original and demonstrates, as expected, a single kinematic D.O.F.

Figure 19: Deployment of the 1/20 detailed scale model

B.1/2 scale model

The kinematic behaviour of the simplified prismoid solution has been verified by means of a ½ scale model, resulting in a 4 m high mast, as shown in Figure 20. Laminated wood was used for the angulated elements and steel for the connections. A cable-pulley system driven by an electric winch is used for the deployment.

Figure 20: Compacted and deployed state of the proof-of-concept scale model

VII. Summary

In this chapter, a novel idea has been put forward for a deployable hyperboloid mast or tower, used for the deployment of a membrane canopy, without the need for additional lifting equipment. Angulated elements are of great use in the design of all kinds of radially retractable roof structures [3]. This concept has shown that these elements can be used in a slightly different way, i.e. in a linear mechanism. The two-fold purpose of the mast, namely holding up the membrane elements in the deployed position and serving as an active element during the erection process, has been demonstrated. It has been found that the proposed linear structure offers an advantage over existing solutions: using angulated elements instead of polar units for the same deployed geometry, has lead to a significant reduction of the number of scissor members and connections.

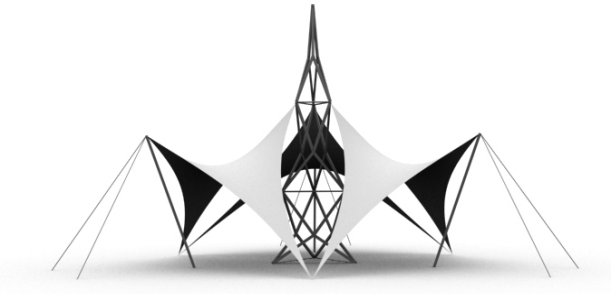

Figure 21: Rendered image of the concept : a triangular actuated mast for temporary tensile surface structures

Further, an alternative shape, called a prismoid geometry, has been proposed. This has proven to be a simpler solution

compared to the hyperboloid geometry in terms of kinematic behaviour, therefore allowing the use of greatly simplified joints. Through the use of an equivalent hinged-plate model, the mobility of both the hyperboloid and prismoid geometry has been assessed. It was found that the hyperboloid configuration is always, regardless of the polygonal shape, a one-degree-of-freedom mechanism. The prismoid solution, on the other hand, is always, apart from the triangular geometry, a multiple-D.O.F.- mechanism.

The proposed concept has made innovative use of angulated scissor elements in an original application (Figure 21). Although the concept has been proven to work, more detailed analysis, including structural design of the joints, is needed.

VIII. References

[1] De Temmerman*, N., Design and Analysis of Deployable Bar Structures for Mobile Architectural Applications,* PhD-dissertation, Vrije Universiteit Brussel, Brussel, 2007

[2] Hoberman, C., *Reversibly Expandable Doubly-Curved Truss Structure,* United States Patent No. 4942700, 1990

[3] Jensen, F., *Concepts for Retractable Roof Structures*. PhD-dissertation, University of Cambridge, Cambridge, 2004

Proceedings of the 8th National Congress on Theoretical and Applied Mechanics, May 28-29, Brussels, Belgium.

Future Giant Segmented Mirrors : Scale Effects in Active Optics and the Use of Composites in ELTs Structures

Renaud Bastaits[1], Gonçalo Rodrigues[1], Bilal Mokrani[1], André Preumont[1]
[1]Active Structures Laboratory, Université Libre de Bruxelles 50 Avenue F.D. Roosevelt, 1050 Bruxelles
email: rbastait@ulb.ac.be, goncalo.rodrigues@ulb.ac.be, bmokrani@ulb.ac.be, andre.preumont@ulb.ac.be

Abstract— **This paper is concerned with the extrapolation of the active optics of current 10-meter class telescopes (Keck, VLT) to the next generation of 30m to 40m Extremely Large Telescopes (ELT), and future, even larger ones. It describes how the various factors affecting the structural response and the control-structure interaction are influenced by the size of the telescope. Using the scaling laws for the natural frequencies and the structural response on the one hand, and the control requirements on the other hand, the paper shows how orders of magnitude can be estimated without resorting to complicated analysis. One especially important aspect for larger telescopes is that the joint increase of the control bandwidth and the reduction of their resonance frequencies will make them substantially more sensitive to control-structure interaction than smaller ones.**

Keywords— active optics, ELT, control-structure interaction, scale effects

I. Introduction

FIGURE 1 shows the primary mirrors (M1) of the largest optical telescopes [1], the existing ones: Hubble Space Telescope (HST), ESO's VLT at Paranal and Keck in Hawaï, and the future ones under design: The James Webb Space Telescope (JWST) and the two Extremely Large Telescopes (ELT), the American TMT [2] and the European E-ELT [3], due to be built within the next decade. There are plans to build even larger ones with a primary mirror close to 100m in a more distant future (OWL). All future large telescopes will be segmented. Note that the size of the earth-based telescopes is one order of magnitude larger than the space telescopes. Note also that there seems to be a huge gap between the largest existing segmented telescope (Keck) and the future ones. The gap is so big that one can reasonably wonder if the past experience with Keck is sufficient to warrant a sound design and optimum operation of the future ELTs. Table 1 gives more data on Keck and the future E-ELT. Figure 2 shows a view of the primary mirror of E-ELT [4,5]; it consists of 984 aspherical segments, each of them equipped with 6 edge sensors and 3 two-stage position actuators.

As the size of the telescopes increases, they become increasingly sensitive to external disturbances such as thermal gradients, gravity and wind, and also to internal disturbances from support equipments such as pumps, cryocoolers, fans, etc.... As a result, their shape stability relies more and more on active control means: the control system involves larger loop gains, and therefore a significantly larger bandwidth. At the same time, the natural frequency of future ELTs is expected to be substantially lower than any operating telescopes (Table 1). So far, the classical method for minimizing control-structure interaction relies on having a wide separation between the lowest resonance frequency and the control bandwidth [6,7]. However, the joint effect of increasing the control bandwidth and reducing the natural frequency of the structure, and the very low inherent damping of welded steel structures, poses unprecedented challenges to the design of new giant telescopes and calls for innovative ways to alleviate control-structure interaction and avoid control instability.

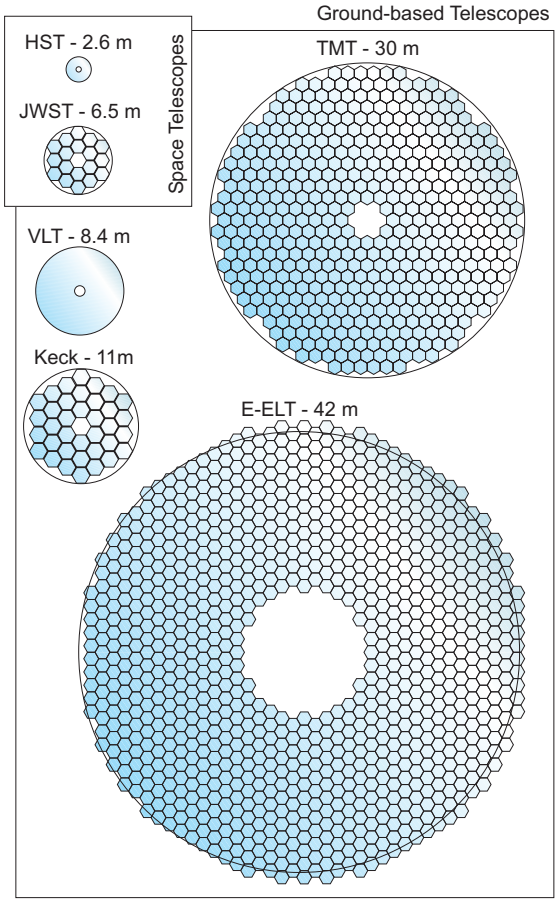

Fig. 1. Primary mirrors (M1) of current and future optical and infrared telescopes.

	Keck	E-ELT
M1 diameter: D	11 m	42 m
Segment size	1.8 m	1.4 m
Collecting Area	76 m^2	1250 m^2
# Segments: N	36	984
# Actuators	108	2952
# Edge Sensors	168	5604
$f_{segment}$ (+ Whiffle Tree)	25 Hz	$\sim$60 Hz
f_1 (M_1)	$\sim$10 Hz	$\sim$2.5 Hz
f_2 (M_2)	$\sim$5 Hz	$\sim$1-2 Hz
Adaptive Optics # d.o.f.($S \simeq 0.5$)	$\sim$ 1000	$\sim$ 12000
Tube and mount mass	$\sim$110 t	$\sim$2000 t

TABLE I
KECK VS E-ELT

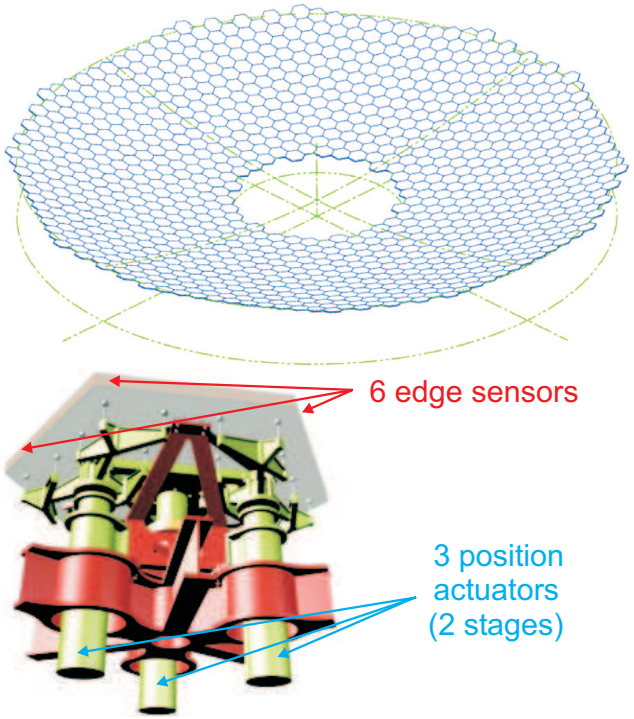

Fig. 2. Primary mirror (M1) of the future E-ELT telescope; it consists of 984 segments, each of them equipped with 6 edge sensors and 3 two-stage position actuators.

This paper is organized as follows: section 2 briefly describes the control architecture of large telescopes and large segmented primary mirrors; the subsequent sections discuss scaling laws for truss supported segmented mirrors: section 3 considers the deflection under gravity, section 4 examines the first resonance frequency, section 5 the control bandwidth, section 6 illustrates the control-structure interaction and section 7 analyzes the response to wind gusts; section 8 summarizes the results and highlights the most relevant design parameters.

II. CONTROL ARCHITECTURE

Figure 3, describes the temporal and spatial frequency distribution of the various layers of the control system involved in the wavefront correction of a large telescope [9]; the spatial frequency is expressed in terms of Zernike modes. The amplitude involved in the adaptive optics is generally small, typically a few microns. Our discussion is focused on M1; the amplitudes to be corrected by the active optics are much larger than this [7]; in Keck, the gravity disturbances are managed first with feedforward control (from a look-up table) and the feedback is only required to compensate the residual error.

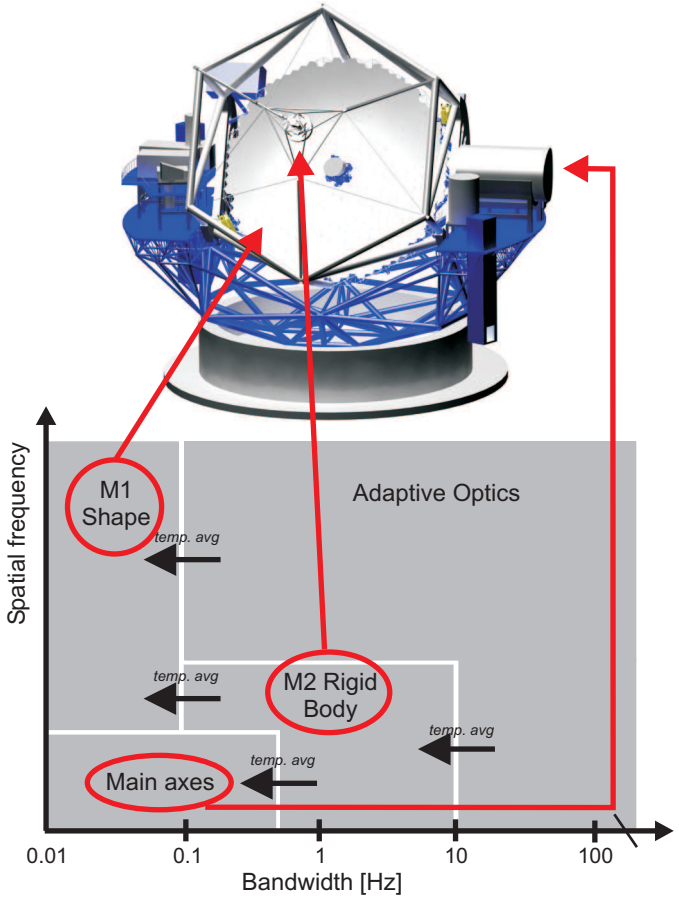

Fig. 3. Temporal and spatial frequency distribution of the various control layers of a large telescope (adapted from [9]).

The co-phasing strategy of segmented mirrors is illustrated in Fig.4; m is the mass of the segment, k and c refer to the stiffness and damping of the whiffle tree, m_a, k_a, c_a and Fa describe the position actuators (free actuator displacement: $a = F_a/k_a$). The resonance frequencies of the supporting truss are f_i. For E-ELT, the local modes of the segments are one order of magnitude larger than the

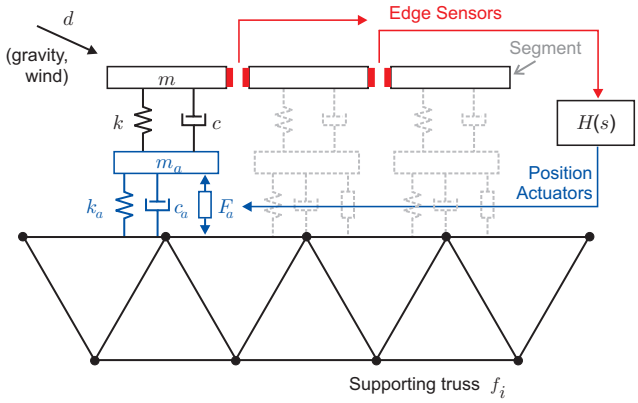

Fig. 4. Co-phasing strategy of segmented mirrors. Every segment is equipped with 3 position actuators.

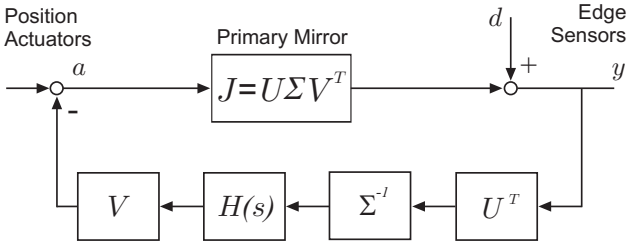

Fig. 5. Block diagram of the co-phasing control system (the Σ^{-1} block is limited to the non-zero singular values).

first mode of the supporting structure (Table 1). Every segment is provided with three position actuators and six edge sensors measuring the displacement of the segment with respect to its six neighbors. The quasi-static relationship between the actuator displacements a and the edge sensor output y is

$$y = Ja \tag{1}$$

where J is the Jacobian of the segmented mirror. Upon performing a singular value decomposition (SVD):

$$J = U\Sigma V^T \tag{2}$$

where the column of U are the orthonormalized sensor modes, the column of V are the orthonormalized actuator modes, and Σ contains the singular values on its diagonal. The pseudo-inverse of the Jacobian J^+ is readily obtained by

$$J^+ = V\Sigma^{-1}U^T \tag{3}$$

The control system assumes that the supporting truss is rigid and works according to Fig.5 [10], where the Σ^{-1} block is limited to the non-zero singular values and the set of filters $H(s)$ provide (hopefully) adequate disturbance rejection and stability margins. Note that piston, tilt and defocus are unobservable from ideal edge sensors and must be taken care of by other sensors.

The global deformations of the supporting truss, either static due to gravity, or the lowest vibration modes, introduce optical aberrations. The details of these aberrations depend on the exact boundary conditions of the supporting truss, but they tend to be dominantly in the lowest optical modes such as defocus and astigmatism; precisely those which are not, or only weakly observable from the edge sensors [they correspond to the lowest singular values in the decomposition (2)]. This is illustrated in Fig.6 on an hypothetical free flying truss structure supporting segmented mirrors (space telescope). For this free-free boundary conditions, the first vibration mode is mostly astigmatism. The figure also shows the Point Spread Function (PSF) corresponding to the largest circular aperture inside the mirror, resulting from a vibration amplitude of $\lambda/2$ peak to valley (250 nm in this case).

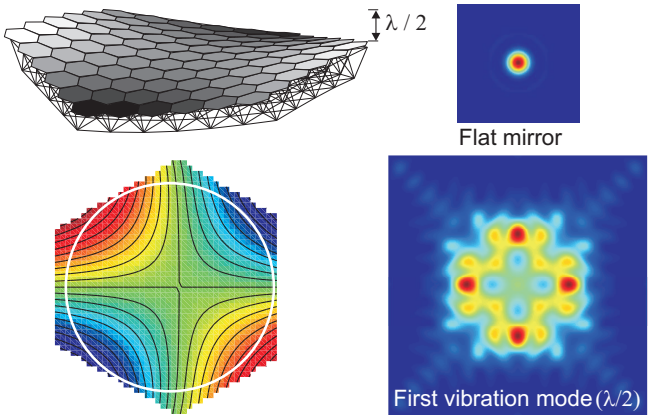

Fig. 6. First vibration mode of a free flying truss supporting a flat segmented mirror. The diameter of the segments is d=2m. The first mode is essentially astigmatism. The figure also shows the PSF corresponding to the largest circular aperture inside the mirror, when it is flat and when the vibration amplitude is $\lambda/2$ (peak to valley).

In order to be able to compensate for the deflection of the supporting truss, the set of edge sensors must be supplemented by a Shack-Hartman sensor (or another) measuring the normal to the segment (one normal by segment). In fact, the Shack-Hartman array does not measure the normal to the segments, but rather the normal to the wavefront, in which the atmospheric turbulence appears as noise, and must be filtered out as well as possible. This leads to the control architecture of Fig.7. The control objective is to bring the wavefront distortion back to a level

within the stroke of the adaptive optics, i.e. less than a few microns. The following sections discuss some scaling laws for truss supported segmented mirrors.

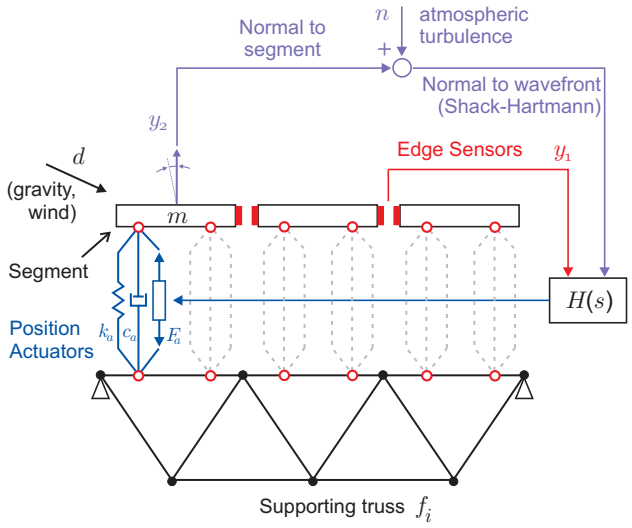

Fig. 7. Active optics control flow for large segmented mirrors.

III. Static Deflection under Gravity

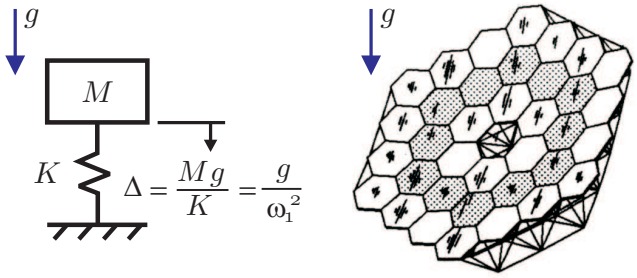

Fig. 8. The static deflection under gravity scales according to $\Delta \propto f_1^{-2}$.

A spring mass system subjected to gravity (Fig.8) undergoes a deflection $\Delta = Mg = K = g/\omega_1^2$. More generally, for given boundary conditions, the gravity-induced deflection of a truss structure scales according to

$$\Delta \propto f_1^{-2} \tag{4}$$

where f_1 is the lowest natural frequency of the structure. Referring to Table 1, this means that the primary mirror of E-ELT will undergo gravity disturbances 16 times larger than Keck; the control gains will have to be increased accordingly.

IV. First Resonance Frequency

The foregoing section has shown the central role played by the first natural frequency in the static deflection. It is

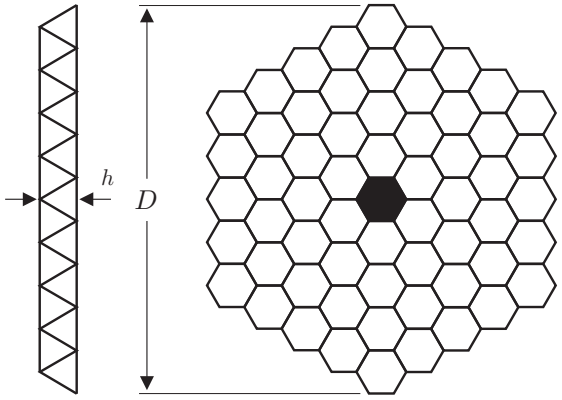

Fig. 9. Geometry of the truss supported reflector.

interesting to investigate the scaling law for the first natural frequency of a truss supported segmented reflector. According to [11,12], the first natural frequency of a free flying truss follows

$$f_1 \sim \frac{0.852}{D}\left(\frac{h}{D}\right)\sqrt{\eta \cdot \frac{E}{\rho}} \tag{5}$$

where η is the structural mass fraction

$$\eta = \frac{\text{Truss Mass}}{\text{Truss Mass + Reflector Mass}} \tag{6}$$

(using lighter reflectors increases η). In Equ.(5), h and D are respectively the thickness and the diameter of the supporting truss (Fig.9); E is the Young modulus and ρ the material density of the truss. The coefficient 0.852 refers to the free-free boundary conditions, but this result also applies to other boundary conditions with another coefficient. For a given family of telescopes, the ratio h/D is fixed and $f_1 \propto D^{-1}$ (this fits the data of table 1). Equation (5) shows clearly the advantage of building the supporting truss with a material of high specific modulus E/ρ. Table 2 compares the mechanical properties of traditional structural materials for telescope structures (steel and aluminum) with carbon fiber reinforced composites (CFRP) [13]. Observe that the latter have a specific modulus 4 times larger than either steel or aluminum, which doubles the natural frequency f_1 if everything else is equal. As a side effect, the outstanding thermal stability of CFRP is worth noting; the thermal expansion coefficient α of CFRP given in Table 2 is the minimum value; it can be tailored to a large extent. Let us now examine the impact of the foregoing discussion on the active optics control system.

V. Control Bandwidth

At present, the active optics controllers do not include a real-time dynamic model of the support structure; the

	E (GPa)	ρ (g/cm^3)	E/ρ	α ($10^{-6}\,^oC^{-1}$)
Steel	210	7.8	27	12
Al	70	2.7	26	23
CFRP	180/230	1.5/1.6	120/140	-0.2/0.1

TABLE II
MECHANICAL AND THERMAL EXPANSION PROPERTIES OF STEEL, ALUMINIUM (AL) AND CARBON FIBER REINFORCED PLASTICS (CFRP)

control system assumes that the support truss is rigid and that the input-output relationship is fully described by the Jacobian (Fig.5). In this section, we examine the impact of the scaling laws for the static deflection and the natural frequency f_1 on the control bandwidth of the gravity compensation.

Figure 10 shows the open-loop transfer function $|GH|$ of an hypothetical controller for gravity compensation; the decay rate has been assumed of -20 dB/decade in the vicinity of crossover, consistent with [6,7].[1]. The lower curve has been drawn with a bandwidth equal to that of VLT, f_c = 0.03 Hz ([14],p.332)[2]; the corresponding amplitude at the earth rotation frequency (1.16 10^{-5} Hz) is 68 dB.

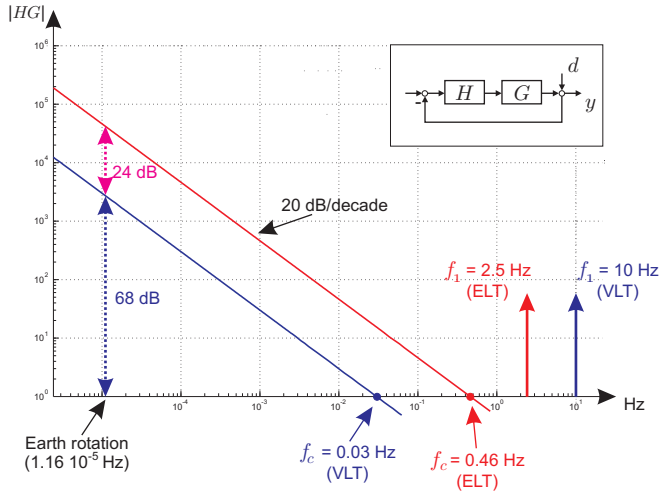

Fig. 10. Comparison of the control bandwidth of the gravity compensation of VLT and ELT.

The disturbance rejection is governed by the sensitivity function $S(f)$ (e.g.[16]):

$$\frac{y}{d} = S(f) = \frac{1}{1+GH} \tag{7}$$

which means that 68 dB reduces a static deformation of 110 μm to 40 nm.

[1]This gives a phase margin of 90^o

[2]The control approach for the active optics of VLT is based on [15]

From the previous section and the data from Table 1, the gravity deformations of a telescope of the ELT class are likely to be 16 times larger than those of a current 10-meter class telescope such as VLT or Keck[3]. Thus, achieving the same accuracy on the controlled shape will require that the disturbance rejection, and therefore $|GH|$ be 16 times larger (+24 dB); with the same decay rate, this corresponds to the upper curve in Fig.10, and increases the bandwidth from f_c = 0.03 Hz to f_c = 0.46 Hz. Note that, at the same time, following our scaling laws, the first natural frequency of the support structure has been reduced from f_1 = 10 Hz for VLT to $f_1 \simeq$ 2.5 Hz for E-ELT.

More sophisticated controllers will be able to achieve a steeper decay rate than s^{-1}; if the average roll-off rate within the bandwidth follows s^{-a}, the loop gain $|GH(f)|$ at the frequency f is related to the bandwidth by

$$|GH(f)| = (f_c/f)^a$$

Thus, if the loop gain at the earth rotation frequency is to be scaled according to f_1^{-2} , this means that the controller bandwidth must be scaled according to

$$f_c \propto f_1^{-2/a} \tag{8}$$

VI. CONTROL-STRUCTURE INTERACTION

Control-structure interaction is well known to people dealing with flexible structures; it occurs when the control bandwidth f_c and the frequencies of the flexible modes f_i become close to each other; it depends strongly on the frequency ratio f_i/f_c and also on the modal gain (measuring the capacity of a mode to be excited by the control) and the damping ratio ξ_i. In Keck, the critical mode for control-structure interaction turned out to be a local mode of the segment and whiffle tree near 25 Hz [7]. The segments of ELT have been designed to be stiffer (Table 1) to alleviate this problem, but the joint effect of the increase of the bandwidth and the reduction of the natural frequencies deserves a careful attention; according to Fig.10, the ratio f_1/f_c is reduced from about 300 for VLT to about 5 for ELT. With a more general controller, the frequency ratio f_i/f_c scales according to

$$\frac{f_1}{f_c} \propto f_1^{1+2/a} \tag{9}$$

where a is the average decay rate (expressed in number of poles) within the bandwidth (0 < a < 2).

[3]Even if a feedforward control is used, it is reasonnable to assume that the same fraction of the deflection will be corrected by the feedback loop

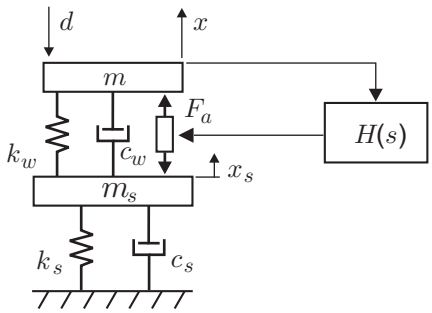

Fig. 11. Position control of a two-mass system. k_w refers to the whiffle tree and k_s to the support structure. Model used to study the control-structure interaction by reducing k_s.

The control-structure interaction can be illustrated with the two-mass model of Fig.11, which is a simplified version of Fig.7; m is the mass of a segment and the subscripts w and s refer to the whiffle tree and the support structure, respectively; the damping ratio is assumed the same for all modes. The control objective is to keep the segment position x fixed in spite of the low frequency disturbance d applied to it, and the controller is (integral plus low-pass filter):

$$H(s) = \frac{g}{s}\frac{1}{1+\tau s} \tag{10}$$

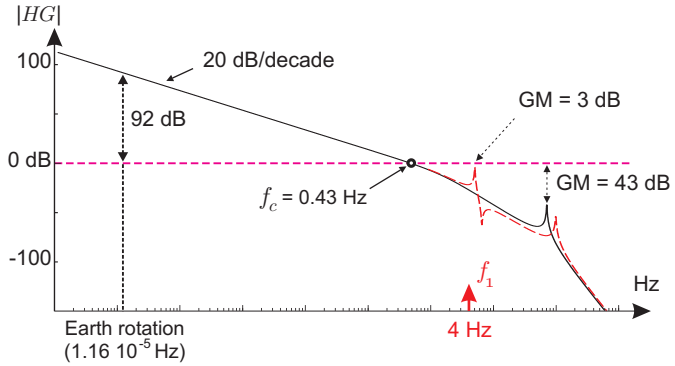

Fig. 12. Position control of a two-mass system. Open loop transfer function for a rigid support (full line) and when the first resonance is reduced to 4Hz (dashed line).

Figure 12 shows the open-loop transfer function for the system of Fig.11 for a rigid support, and when the first resonance is reduced to $f_1 = 4$ Hz. Figure 13 shows the evolution of the gain margin GM as a function of the frequency ratio f_1/f_c for various values of the damping ratio ξ; the figure has been obtained by reducing gradually the stiffness k_s. These results are consistent with those obtained with a much bigger model involving 91 segments [17].

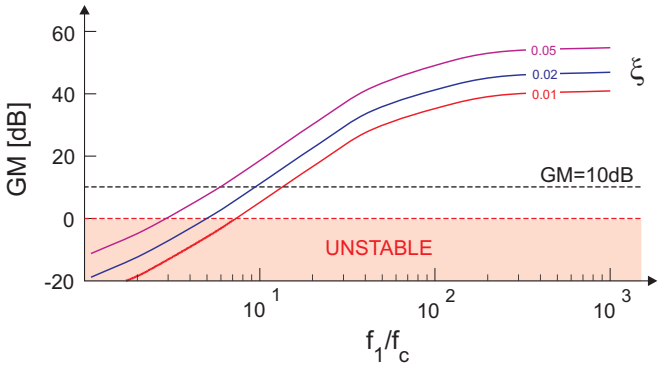

Fig. 13. Position control of a two-mass system. Evolution of the gain margin with the frequency ratio f_1/f_c, for various values of the structural damping ξ.

VII. Wind Response

The wind response of a large telescope is a very complicated problem which has already received a lot of attention [18,19,20]. The wind loads depend strongly on the design of the enclosure and the mirror orientation. The primary mirror may act as a lifting surface or respond like a bluff body; the reality is probably a mix of two, and there may be a strong coupling between the primary mirror and the secondary mirror. In this section, we only consider the scale effect of the along-wind response of a bluff body subjected to turbulent wind gusts according to the approach classically used in wind engineering [21,22,23].

In this study, we assume that the turbulent wind force is distributed according to Davenport's spectrum [21]; its power spectral density $\Phi(f)$ has the shape of Fig.14(a), which is such that the flexible modes of the structures are in the tail of the distribution, where it behaves according to

$$\Phi(f) \propto f^{-5/3} \tag{11}$$

(other power laws are met in the literature: f^{-2} or $f^{-7/3}$, but this is only of minor importance for our discussion). The structural response consists of a large quasi-static contribution and a dynamic (resonant) response. Due to the decaying shape of (11), the resonant response is generally dominated by the first mode, Fig.14(b). One can also observe that the quasi-static response will be attenuated by the controller while the resonant response which is beyond the control bandwidth is amplified by the sensitivity, Fig.14(c). The amplification at resonance of the controlled response corresponds to a reduced damping $\xi^* = \xi/S(f_1)$ where $S(f_1)$ is the sensitivity at the resonance frequency f_1. Comparing the cumulative RMS response with and without control, one sees that, with control, the resonant

part becomes the largest contributor to the RMS response, Fig.14(d).

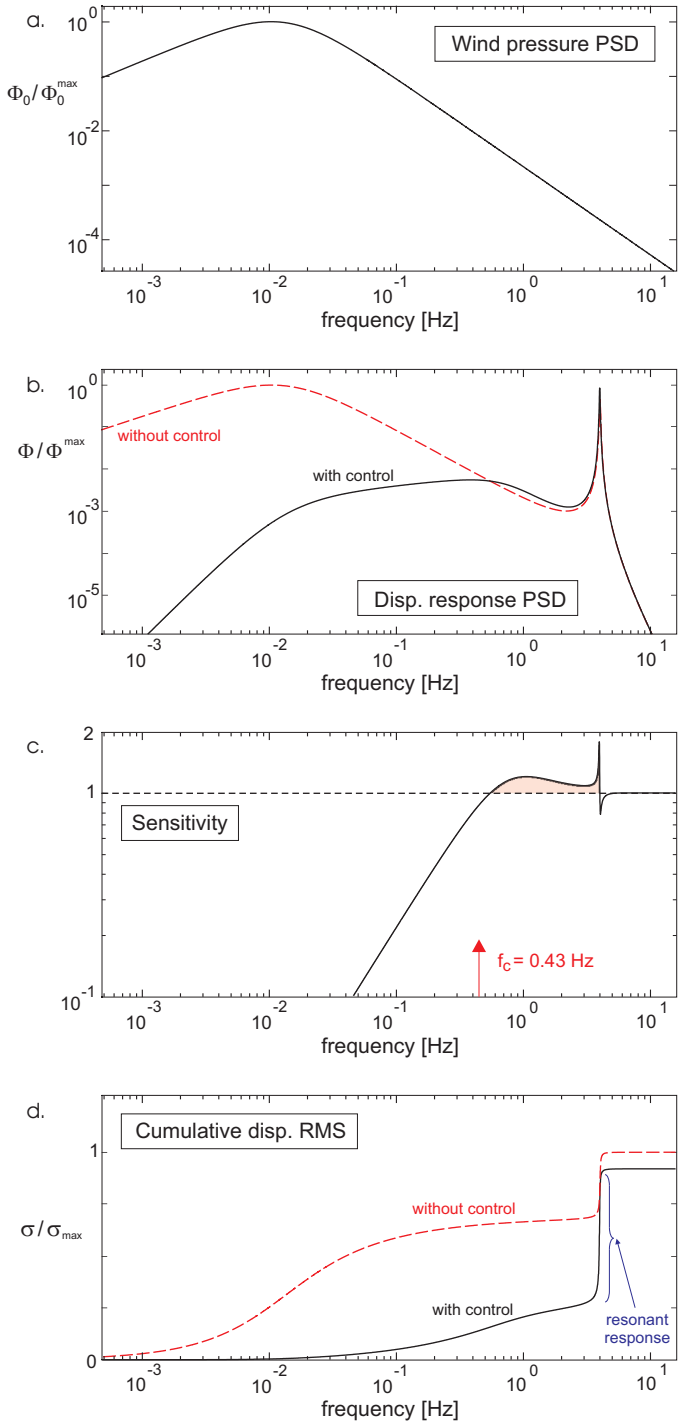

Fig. 14. (a) Davenport's turbulent wind spectrum, normalized to its maximum. (b) Structural response to turbulent wind, with and without control (normalized to its maximum). (c) Sensitivity function; the first resonance belongs to the frequency range with a significant amplification. (d) Cumulative RMS response $[\int_0^f \Phi(\nu)d\nu]^{1/2}$ (normalized to its maximum); the resonant response is amplified by the control.

The random response of a structure to a point force with random amplitude of power spectral density (PSD) $\Phi_0(f)$ can be evaluated by

$$\Phi(f) = \Phi_0(f)|H(f)|^2 \tag{12}$$

where $H(f)$ is the frequency response function (FRF) between the excitation and the response. If the structural response is dominated by a single mode, the FRF is essentially that of a single degree of freedom oscillator of mass m equal to the mass of the mode, frequency f_1 and damping ξ. When the resonant response dominates, the mean square (MS) value can be approximated by the so-called white noise approximation, where $\Phi_0(f) \simeq \Phi_0(f_1)$. (e.g. see [24], p.76 or [25], p. 80); this leads to

$$\sigma^2 = \int_0^\infty \Phi(f)df \propto \frac{\Phi_0(f_1)}{m^2\xi f_1^3} \propto \frac{1}{m^2\xi f_1^{14/3}} \tag{13}$$

where Equ.(11) has been used.

The foregoing result assumes a point force excitation, representative of a global mode being excited by the pressure field on one segment. If one looks at the global response, one has to consider the correlation between the excitations acting at different points on the telescope; according to Davenport's model, the spatial coherence follows

$$C(\Delta z), f) = exp\left(\frac{-fc|\Delta z|}{u_{10}}\right) \tag{14}$$

where c is a correlation constant, $c \cong 7$, u_{10} is the mean wind reference velocity, f is the frequency and Δz is the vertical separation between two points. The correlation length is therefore $\delta \sim u_{10}/fc$. Setting $u_{10} \simeq 10$ m/s as an order of magnitude, and $f = f_1 \simeq 2.5$ Hz, one sees that the correlation length is typically lower than the size of one segment. One can therefore assume that the forces acting on the various segments are statistically independent, leading to a global response

$$\sigma^2 = \frac{N}{m^2\xi f_1^{14/3}} \tag{15}$$

where N is the number of segments. Using the data given earlier, we know that the natural frequency scales as $f_1 \propto D^{-1}$, N scales as $N \propto D^2$ and the mass of the telescope tube and mount scales between D^2 and D^3 ([14], p.79). Assuming $m \propto D^{5/2}$ as an average, one gets

$$\sigma^2 = D^{5/3}\xi^{-1} \tag{16}$$

This result is based on general theory of wind engineering and random vibration and on the scaling laws discussed previously for telescopes of the same family; it is very crude and does not take into account specific features of the telescope and the skill of the wind engineers in the design of the telescope enclosure, but it probably gives orders of magnitude.

VIII. Summary and conclusion

This study has been devoted to the extrapolation of the active optics of current 10-meter class telescopes (Keck, VLT) to the next generation of 30 m to 40 m Extremely Large Telescopes (ELT), and possibly future ones. The various aspects of the structural response and the control-structure interaction affected by the size of the telescope have been considered and orders of magnitude have been estimated. Based on crude analysis, the following results have been obtained:

The *static deflection under gravity* scales as

$$\Delta \propto f_1^{-2} \tag{17}$$

The *first resonance frequency* f_1 varies according to

$$f_1 \propto D^{-1}\sqrt{\frac{E}{\rho}} \tag{18}$$

where D is the diameter of M1 and E/ρ is the specific modulus of the structural material.

The *control bandwidth* f_c of the gravity compensation system follows

$$f_c \propto f_1^{-2/a} \tag{19}$$

where a is the average decay rate (number of poles) within the bandwidth ($0 < a < 2$).

The *RMS response to wind gust* scales as

$$\sigma = D^{5/6}\xi^{-1/2} \tag{20}$$

which is roughly proportional to D. It must be kept in mind, however, that because the resonant response occurs in the frequency range with the highest sensitivity, a reduction of ξ due to control-structure interaction must be considered.

The parameters governing the *control-structure interaction* are the damping ξ and the frequency ratio f_1/f_c which scales according to

$$\frac{f_1}{f_c} \propto f_1^{1+2/a} \tag{21}$$

Once the diameter D has been fixed, there are only 3 free parameters[4]: the specific modulus of the structural material, E/ρ, the structural damping ξ and the average decay rate a within the control bandwidth, which depends on the control system design. The use of CFRP instead of metallic structures has a potential for doubling f_1; various options for damping actively truss structures with active struts or cable networks are discussed in [26].

Acknowledgments

The authors wish to thank the anonymous reviewers for their numerous comments which have been very helpful in improving this text. Gonçalo Rodrigues thanks Fundação para a Ciência e a Tecnologia (FCT), Portugal, for his PhD grant SFRH/BD/ 21732/2005, and Renaud Bastaits thanks Fonds National de la Recherche Scientifique (FNRS), Belgium, for his FRIA PhD grant FC76554.

References

[1] Wilson R. N., *Reflecting Telescope Optics I and II*, Springer-Verlag, 1999.

[2] Nelson, J., Sanders G., The status of the Thirty Meter Telescope project, In *Ground-based and Airborne Telescopes II* - SPIE 7012 (2008), Larry M. Stepp, Ed.

[3] Gilmozzi, R., Spyromilio, J., The 42m European ELT: status, In *Ground-based and Air- borne Telescopes II* - SPIE 7012 (2008), Larry M. Stepp, Ed.

[4] Dimmler, M., E-ELT Programme: M1 Control Strategies, E-TRE-ESO-449-0211, Issue 1, April 2008.

[5] Dimmler, M., Erm, T., Bauvir, B., Sedghi, B., Bonnet, H., Muller, & Wallander, A., E-ELT Primary Mirror Control System, In *Ground-based and Airborne Telescopes II* - SPIE 7012 (2008), Larry M. Stepp, Ed.

[6] Aubrun, J.N., Lorell, K.R., Mast, T.S. & Nelson, J.E., Dynamic Analysis of the Actively Controlled Segmented Mirror of the W.M. Keck Ten-Meter Telescope, *IEEE Control Systems Magazine*, 3-10, December 1987.

[7] Aubrun, J.N., Lorell, K.R., Havas & T.W., Henninger, W.C., Performance Analysis of the Segment Alignment Control System for the Ten-Meter Telescope, *Automatica*, Vol.24, No 4, 437-453, 1988.

[8] European Southern Observatory, *The VLT White Book*, ESO, 1998.

[9] Angeli, G.Z., Cho, M.K., Whorton, M.S., Active optics and architecture for a giant segmented mirror telescope, in *Future Giant Telescopes* (Angel, and Gilmozzi, eds.), 2002. Proc. SPIE 4840, Paper No. 4840-22, pages 129-139.

[10] Chanan, G. MacMartin, D.G., Nelson, J., & Mast, T., Control and alignment of segmented-mirror telescopes: matrices, modes, and

[4] for a family of telescopes, the ratio h/D ay be regarded as fixed.

error propagation, *Applied Optics*, Vol.43, No 6, 1223-1232, Feb. 2004.

[11] Lake, M.S., Peterson, L.D. & Levine, M.B., Rationale for Defining Structural Require- ments for Large Space Telescopes, *AIAA Journal of Spacecraft and Rockets*, Vol.39, No 5, September-October, 2002.

[12] Lake, M.S., Peterson, L.D. & Mikulas, M.M., Space Structures on the Back of an envelope: John Hedgepeth's Design Approach, *AIAA Journal of Spacecraft and Rockets*, Vol.43, No 6, November-December, 2006.

[13] Agarwal, B.D. & Broutman, L.J., *Analysis and Performance of Fiber Composites*, Wiley, 2nd Ed., 1990.

[14] Bely, P.Y. (Editor), *The Design and Construction of Large Optical Telescopes*, Springer, 2003.

[15] Wilson, R., N., Franza, F., and Noethe, L., Active Optics I: A system for optimizing the optical quality and reducing the costs of large telescopes, *Journal of Modern Optics*, 34, 4 (1987), 485-509.

[16] Franklin, G.F., Powell, J.D., Emani-Naemi, A., *Feedback Control of Dynamic Systems*, Addison-Wesley, 1986.

[17] Bastaits, R., Rodrigues, G., Mokrani, B. & Preumont, A., Active Optics of Large Segmented Mirrors: Dynamics and Control, submitted for publication in *AIAA Journal of Guidance, Control and Dynamics*, 2009.

[18] Padin, S., Wind-induced deformations in a segmented mirror, *Applied Optics*, Vol.41, No 13, 2381-2389, May 2002.

[19] Padin, S., Davison, W., Model of image degradation due to wind buffeting on an extremely large telescope, *Applied Optics*, Vol.43, No 3, 592-600, Jan. 2004.

[20] MacMynowski, D., Vogiatzis, K., Angeli, G.Z., Fitzsimmons, J. & Nelson, J., *Applied Optics*, Vol.45, No 30, 7912-7923, 0ct. 2006.

[21] Davenport, A.G., The application of statistical concepts to the wind loading of structures, *Proc. Inst. Civ. Eng.*, Vol.19, 449-471, Aug. 1961.

[22] Scanlan, R.H. & Simiu, E., *Wind Effects on Structures*, Wiley, 1996.

[23] Blevins, *Flow-Induced Vibration*, 2nd Edition, Krieger, 1990.

[24] Crandall, S.H. & Mark, W.D., *Random Vibration in Mechanical Systems*, Academic Press, 1963.

[25] Preumont, A., *Random Vibration and Spectral Analysis*, Kluwer, 1994.

[26] Preumont, A., *Vibration Control of Active Structures, An Introduction*, 2nd Edition, Kluwer, 2002.

Proceedings of the 8th National Congress on Theoretical and Applied Mechanics, May 28-29, Brussels, Belgium.

Mechanisms for Deployable Tensairity Structures

ir. arch. Lars De Laet[1], Prof. Marijke Mollaert[1], dr. Rolf Luchsinger[2],
dr. ir. arch. Niels De Temmerman[1], ir. Laurent Guldentops[1]
[1]æ-lab (Research Group for Architectural Engineering)
Department of Architectural Engineering, Vrije Universiteit Brussel
Pleinlaan 2, 1050 Brussels - Belgium
[2]Head of Center, Empa - Center for Synergetic Structures
Überlandstrasse 129, Dübendorf, CH-8600, Switzerland
email: lars.de.laet@vub.ac.be, marijke.mollaert@vub.ac.be, rolf.luchsinger@empa.ch,
niels.de.temmerman@vub.ac.be, laurent.guldentops@vub.ac.be

Abstract— **Tensairity is a new lightweight structural concept. It is a synergetic combination of struts and cables stabilized by a membrane, which is inflated by low pressurized air. The outcome of this interaction between the different elements is a structure with the load bearing capacity of conventional steel girders and the low weight of an air beam. The innovative concept Tensairity provides moreover features few conventional structures have, such as a fast assembling/dismantling, and a compact storage and transport volume. This technology has obvious a great potential for temporary and mobile architectural applications. However, improvements and adaptations to the structural concept have to be identified to make the Tensairity concept suitable for deployable applications. After all, a basic Tensairity girder can not be folded or rolled together without disassembling the different parts it is constituted of. A foldable Tensairity structure is developed and investigated experimentally in this research. The influence on this promising mechanism called the foldable truss of different parameters such as the amount of hinges and the presence of pretensioned cables, is studied and discussed. The results are summarized and will then provide the basis for further research for a proposal of an optimised deployment mechanism for the deployable Tensairity structure.**

Keywords— **Tensairity structure, Deployable, Inflatable, Foldable**

I. Introduction

A. The structural concept Tensairity

INFLATABLE structures have been used by engineers and architects since several decades. These structures offer lightweight solutions with a relatively high structural efficiency and provide features no other type of structure has, such as collapsibility, translucency, and a variety of shapes that can be produced. The assembling and dismantling of inflatable structures is fast by simple inflation and deflation, and the transport and storage volume are minimal. In spite of these exceptional properties, one of the major drawbacks of inflatable structures is their limited load bearing capacity. Significant loads can only be carried with high pressures in the structure which leads to very high fabric tensions that can only be supported by expensive fabrics. Air tightness, pressure management and safety become with increasing pressure a serious issue. High pressure inflatable structures are therefore generally not suitable and desirable for civil applications.

The problem of the limited load bearing capacity of pneumatic structures is solved by the new structural concept Tensairity. This is a synergetic combination of a low pressure air beam (typical pressures for Tensairity are in order of 100 mbar) and traditional building elements such as cables and struts (Figure 1). The tension and compression elements are physically separated by the air inflated beam, which when inflated pretensions the tension element and stabilizes the compression element against buckling. Due to this subtle interaction between the elements, a basic Tensairity structure has the load bearing capacity of conventional steel girders, combined with most of the properties of a simple air beam (low weight, fast set- up) [1].

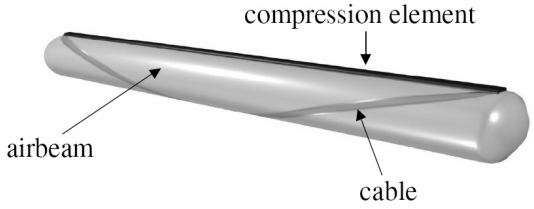

Fig. 1. A basic Tensairity beam

Since the structural principle of Tensairity is quite recent, the technology is still fully in development and a lot of efforts are made to investigate and understand these synergetic structures. Nevertheless, a number of remarkable Tensairity structures such as a roof over a parking garage or a skier bridge have recently been realized (Figure 2 and 3).

The innovative concept Tensairity provides features few conventional structures have, such as a fast assembling/dismantling, and a compact storage and transport volume. This technology has obvious a great potential

Fig. 2. Parking garage in Montreux

Fig. 3. Skiers bridge in Lanselevillard

for temporary and mobile architectural applications. However, while the air beam is easily deployed by inflation, the development of deployable Tensairity structures can be quite a challenge. The compression element of the Tensairity structure possesses some bending stiffness and must be tightly connected with the hull (in order to maintain its buckling-free behaviour). Thus, the basic Tensairity girder cannot be folded or rolled together when deflated.

B. Deployable Tensairity Structure

A Tensairity structure which can be folded or rolled together when deflated to a compact configuration without disassembling the different components it is constituted of is called a deployable Tensairity structure. The deployment of such a structure is initiated by increasing the inner pressure of the air beam. Once a reasonable pre-stress is achieved in the membrane due to this inner pressure, the structure is in its fully deployed state and is able to bear loads like a Tensairity structure with a continuous and stiff compression element.

Different types of solutions for a foldable compression element can be identified. Using a compression element with low bending stiffness in deflated state is one solution. This way, the structure can be rolled or packed together as a whole when no internal overpressure is present. Such a solution is called a flexible compression element and has already been investigated and discussed by the author in [2]. Various proposals, such as separate wooden segments, chains, hydraulic hoses etc., have been analyzed and evaluated by means of experiments on scale models (figure 4).

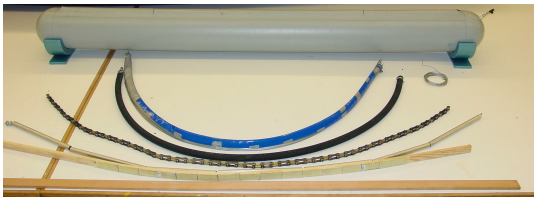

Fig. 4. Flexible compression element: overview of investigated proposals

Another solution for a deployable compression element is a mechanism of bars. This paper presents the development and experimentally investigation of such a bar mechanism, called the foldable Tensairity truss structure. The influence of different parameters on the kinematic and load bearing behaviour (such as the amount of hinges and the presence of pretensioned cables), is studied and discussed. The results are summarized and will then provide the basis for further research for a proposal of an optimised deployment mechanism for the deployable Tensairity structure.

II. Foldable Tensairity truss

Inspired by the foldable trusses from Calatravas PhD [3], Luchsinger et al. [4] developed a foldable truss system as kinetic mechanism for a deployable Tensairity structure. The foldable truss Calatrava investigated is a conventional truss where the horizontal tension and compression bars are divided in two and reconnected with an intermediate hinge (figure 5). This way, the truss becomes a mechanism. Calatrava used a vertical bar to lock the mechanism in deployed configuration and thus stabilize the system. Luchsinger et al. adjusted the system for using it in a Tensairity structure by replacing the vertical bars with (pretensioned) cables (figure 6). The diagonals can be included or excluded. The compression and tension bars are in the deployable Tensairity structure continuously attached with the hull, and this way, the truss is stable when the air beam is fully inflated.

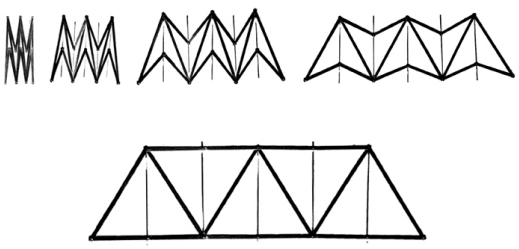

Fig. 5. Foldable truss by Calatrava [3]

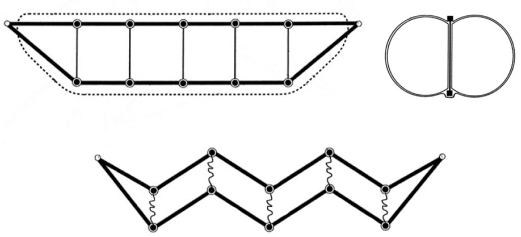

Fig. 6. Foldable truss for tensairity beam by Luchsinger et al. [4]

One of the objectives of this research is to improve and optimize the system proposed by Luchsinger et al. Therefore, the foldable truss is evaluated by investigating its structural behaviour in the inflated state. These results are described in the sections below and will provide the basis for further research for a proposal of an optimised deployment mechanism for the deployable Tensairity structure.

A. *Experimental investigation - setup*

A deployable Tensairity beam was investigated experimentally. The studied model is two meter long and the maximum height in the middle of the beam is 0.20m. The air beam is composed of two layers. An outer PU coated polyester fabric carries the tension forces caused by the air pressure and surrounds two internal bags made of thin PU foil that keeps the structure airtight. These internal bags are positioned adjacent to each other in the longitudinal direction. This way, elements connecting the compression and tension side of the beam can be placed between the two bags (figure 6). The internal pressure of these bags varies during the experiments; depending on the investigated case, a pressure of 75, 100 or 125 mbars was chosen. The cables and bars used are made of steel and the bars have a rectangular cross section (10mm x 6 mm). The compression and tension elements are connected with the fabric by means of pockets. Holes are made in the pockets and fabric to connect upper and lower side of the beam by cables or struts.

The two meter long statically determined deployable Tensairity beam is supported by a stiff steel frame. The loads are applied by means of weights in the upper or lower hinges, depending on the load case. The loads were applied in steps of 1kg. The deflections of the beam are measured in ten points, distributed evenly at the upper and lower side of the beam (figure 7). The load bearing behaviour of the deployable Tensairity structure is studied during the experiments by measuring the deflections of the structure under different load cases. Three different load cases were applied during the experiments: a point load in the middle of the upper compression element, a distributed load (point loads on all the upper hinges), and an asymmetric load (point loads on half of the upper hinges).
Various configurations are tested in order to reveal the influence of the different parameters on the load bearing behaviour, such as the amount of hinges and the presence of pretensioned cables that connect the upper and lower hinges. The investigated configurations are illustrated in figure 8. The configurations 1 and 2 have different amount of hinges. Cases 3 till 12 have the same steel structure (mechanism), but a different arrangement of cables (dotted lines) or diagonal bars (lines). Configuration 4 has the same arrangement as 3, but the cables are shorter which results in a higher pretension in the cable in inflated state.

Fig. 7. Set-up for load-deflection experiments on scale model

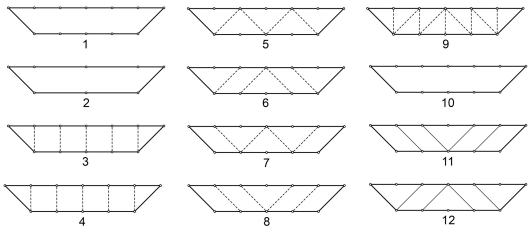

Fig. 8. Investigated configurations

B. *Results*

- Load cycles

When the deployable Tensairity beam is loaded, the fabric adapts to the new load condition during the first load cycle. The load-displacement responses of the second and third load cycle are almost identical (figure 9). The deflections of the third cycle are noted. The Tensairity girder also shows a pronounced hysteresis indicating energy dissipation. This hysteresis has to be attributed to the air beam, since the aluminum chords of the Tensairity girder have an elastic behavior. It can result from the fabric or from energy dissipation into the compressed air. The details behind the hysteresis are not yet understood and are subject of further studies. It is in any case an interesting aspect regarding the dynamic properties and damping behavior of

Tensairity girders. More information on this matter can be found in [5].

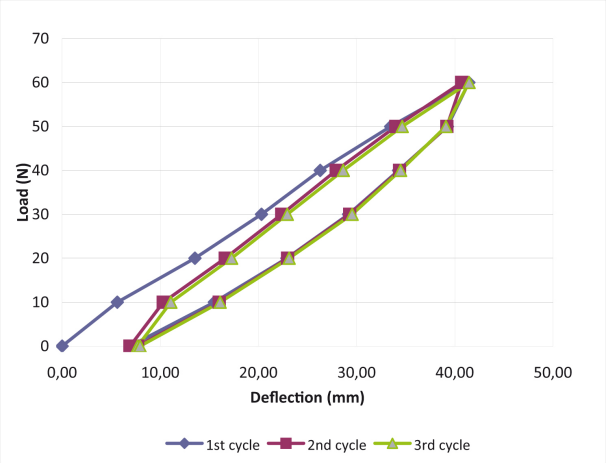

Fig. 9. Load-displacement response of three load cycles

- Influence of internal pressure

The internal pressure of the beam was varied during the experiments. The deflections of various configurations were measured with an internal pressure of 75, 100 and 125 mbars. The results reveal the influence of the internal pressure of Tensairity beams on the load-bearing behaviour. There can be concluded that the stiffness of the structure is increased with increasing pressure. After all, a higher pressure and thus a more pretensioned membrane leads to a more constant spacing between tension and compression element. Moreover, the friction between the pocket and the compression element increases with higher pressure values, which results in a stiffer structure.

- Influence of load case and point(s) of application

It is evident that the displacement of the beam along its length is dependent of the load case. However, unlike conventional structures, the deflection of a Tensairity beam is not similar when the load is applied on the upper or lower side of the beam (figure 10). A larger displacement arises at the side where the load is applied, which indicates the load transfer between upper and lower chord by means of tensioned fabric as explained in [6].

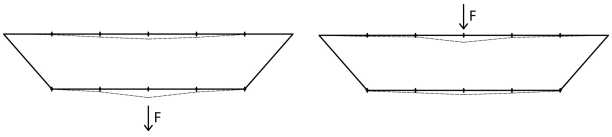

Fig. 10. Different deflection when the load is applied on the upper or lower side of the beam.

- Influence of (number of) hinges

The load-displacement response of case 1 and 2 for a distributed load is investigated and illustrated in figure 11. The central displacement at the tension chord is given on the X-axis, the Y-axis represents the applied load. Both configurations have quite similar deflections under the same load and thus similar stiffness, despite the different number of hinges. The presence and influence of the middle hinge on the stiffness is thus much greater than that of the other hinges. These conclusions are valid for all three investigated load cases.

- Influence of configuration of pre-stressed cables that connect the hinges on compression and tension side

Figure 11 shows the load-displacement diagram under distributed load of the different deployable Tensairity beam configurations (at the third load cycle). Figure 12 represents the deflection of the upper strut of all investigated configurations. It can be seen that the configuration of internal cables has an influence on the load-bearing behaviour, since every case has a different stiffness. Case 1, the configuration without any internal cable shows the biggest deflection; case 6 is the stiffest configuration. It is remarkable that the deflections under a point load and an asymmetric load are analogue; the ranking of the different cases is the same. Current research is analysing these results thoroughly to identify the load-transfer between the different elements of the Tensairity structure and to determine what the most optimal configuration is.

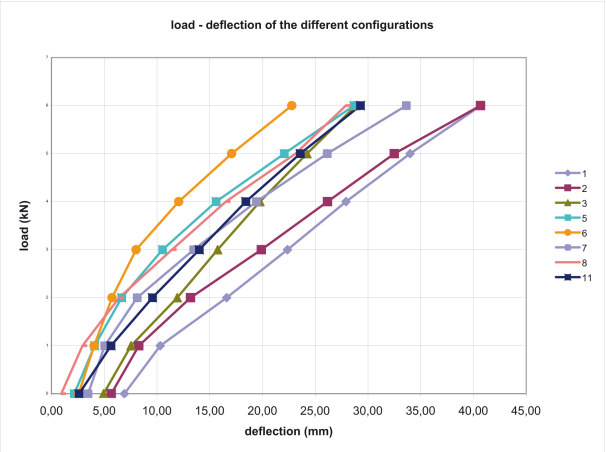

Fig. 11. Load-displacement in the middle of compression chord for the various configurations

C. Optimization of the shape

Not only the internal pressure and the configurations of internal prestressed cables influence the stiffness of the structure. Also the form of a Tensairity structure can be altered to change the stiffness. The cylindrical Tensairity beam consisting of a single linear compression element and two spiraled cables (figure 1) is the simplest one, but, as it turns out, not the most efficient one. Research

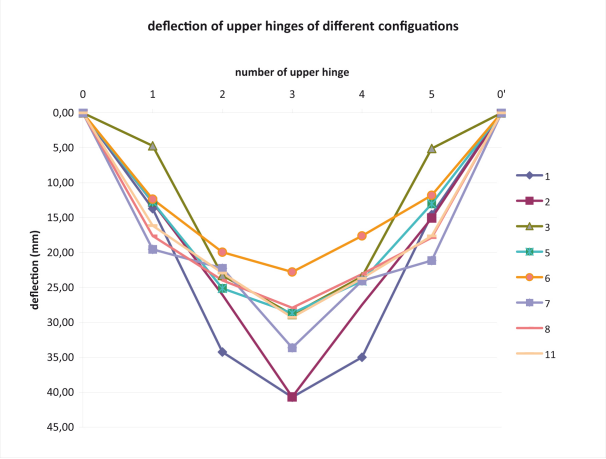

Fig. 12. Final (scaled) position of hinges of various configurations at maximal load

pointed out, by means of theoretical and numerical results, that shapes with a curved compression element (spindle shapes) are more efficient than the cylindrical [7]. Figure 13 shows an evaluation of different shapes by means of a load-deflection graph. Consequently, efforts are currently made to develop a deployable spindle shaped Tensairity structure.

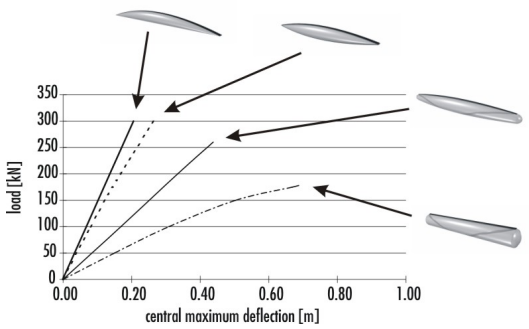

Fig. 13. Evaluation of different shapes by means of load-deflection graph [7]

III. Conclusions

Identifying suitable deployment mechanisms for Tensairity structures will widen the range of applications where these lightweight structures will be used, especially as structural efficient solution for temporary and mobile constructions. The exploration and analysis of ideas for deployable systems by means of experiments on scale models is the recommended method to evaluate proposals and gain understanding of the influence of different parameters.

By investigating the foldable truss system, there could be revealed that the stiffness of the foldable truss system is not influenced very much by a higher amount of hinges in the compression and tension chords. The arrangement of cables on the other hand has an influence on the stiffness of the deployable Tensairity beam, just like the pretension in the cables. The overall shape of the Tensairity beam also has an influence on the stiffness of the structure. Structures with a curved compression element, like the spindle shaped structure, show to be promising and are currently under investigation.

These results will provide the basis for a proposal of an optimised deployment mechanism for the deployable Tensairity structure. The challenge is now to improve the promising proposals by making them more efficient. An in-depth investigation on the kinematic aspects of the deployable Tensairity beam, like the hinges and the folding of the membrane, is as well an important task of current and future research.

Acknowledgments

This research is funded by the Research Foundation Flanders (FWO-Vlaanderen).

References

[1] Luchsinger, R. H., et al., *The new structural concept Tensairity: Basic principles.*, in A. Zingoni (ed.), Proceedings of the Second International Conference on Structural Engineering, Mechanics and Computation. Lisse (The Netherlands): A.A. Balkema/Swets Zeitlinger, 2004.

[2] De Laet, L. et al., *Deployable Tensairity Structures*, in J. Salinas (ed.), Proceedings of the International Symposium on New materials and technologies, new designs and innovations: International Association for Shell and Spatial Structures, Acapulco (Mexico), 2008.

[3] Calatrava, S., *Zur Faltbarkeit von Fachwerken*, PhD Dissertation 6870, ETH Zrich, 1981.

[4] Luchsinger, R. H., *Patent: Collapsible Pneumatically Stabilised Supports*, EP1861567.

[5] Luchsinger, R. H., and Crettol, R., *The role of fabrics in Tensairity.*, Proceedings of the International Symposium on New Perspectives for Shell and Spatial Structures: International Association for Shell and Spatial Structures, Beijing (China), 2006.

[6] Luchsinger, R. H., and Crettol, R., *Experimental and Numerical Study of Spindle Shaped Tensairity Girders.*, International Journal of Space Structures, 21(3), 2006, pp. 119-130.

[7] Pedretti, A. et al., *The new structural concept Tensairity: FE-modeling and applications.*, in A. Zingoni (ed.), Proceedings of the Second International Conference on Structural Engineering, Mechanics and Computation. Lisse (The Netherlands): A.A. Balkema/Swets Zeitlinger, 2004.

Optimisation at conceptual design stage with morphological indicators: pros and cons

T. Vandenbergh[1], W. P. De Wilde[2]
[1]Vrije Universiteit Brussel – Department of Mechanics of Materials and Construction
Pleinlaan 2 – 1050 Brussel
[2]Vrije Universiteit Brussel – Department of Mechanics of Materials and Constructions
Pleinlaan 2 – 1050 Brussel
email: tvdbergh@vub.ac.be, pdwilde@vub.ac.be

Abstract: **Within the framework of sustainable development one strives for structures with a minimum volume of material. At conceptual design stage a clear hierarchy among the different structural topologies can be established with Morphological Indicators (MI). This paper gives a review of the MI-theory, in which only resistance and element buckling are considered during the optimisation process. This approach often results in solutions with problematic stiffness behaviour, yielding important additional volume in the final project. The second part illustrates the applicability limits of the method if additional design criteria are considered, through the example of an axially loaded truss column. MI enables the designer to distinguish a design for strength from a design for stiffness problem. In the first case, the actual MI-theory offers an efficient structural optimisation tool at conceptual design stage. In the latter, alternative optimisation methods should be used.**

Keywords: **conceptual design, morphological indicators, design for strength, design for stiffness, fully stressed**

I. INTRODUCTION

Conceptual design, along with problem identification and analysis, make up the initial stage of the structural design process. Problem analysis transforms the often vague statement of a design task into a set of design requirements. Conceptual design encompasses the generation of concepts and integration into system-level solutions, leading to a relatively detailed design [1].

The assessment of structural performance is, mainly at present time, the result of late finite element analysis processes (FEA) which remain computationally expensive, limiting their use to the analysis of a limited number of design alternatives. But, in the conceptual design stage, the quality depends on the comprehension and on the exploration of the design space [2].

During the conceptual design stage, an engineer or architect creates the general outline of a structure. In this phase a few solutions are selected out of the many possibilities because of their adaptedness to the most important requirements. More specifically, in the context of morphological indicators, one seeks structures with minimum volume. A good conceptual design will then yield a solution (topology and geometry) that will not (or slightly) change its relative superiority to other solutions when more detailed design calculations are performed. Hence it is very important to assess the possible impact or necessity of detailed calculations such as (global) buckling, dynamics, weight of connections, second order effects among others. If the context of the situation allows the use of the indicator of volume in its simplest form, a larger topological/geometrical solution space can be browsed for. This viewpoint can be expressed as follows: one should always optimise structures with a minimum number of variables as long as the detailed analysis will not alter the efficiency of the structure considerably.

A. Morphological Indicators

Morphological Indicators are design tools allowing the optimisation of structures at the stage of conceptual design using a limited set of parameters [3]. The indicator of volume W allows the comparison of the volume of material used for different structural systems.

$$W = \frac{\sigma V}{FL} \tag{1}$$

It is the volume of an isomorphic structure with unit span L, with at least one section dimensioned at its unit allowable stress σ, subjected to a system of loads with unit resultant F.

The displacement indicator Δ compares the displacement of different structural systems.

$$\Delta = \frac{E\delta}{\sigma L} \tag{2}$$

It is the maximum displacement of an isomorphic structure with unit span L in a material with unit Young's modulus E, with at least one section dimensioned on its unit allowable stress σ, subjected to a system loads with unit resultant F.

In the European design prestandards [4] the normative constraints on static displacements are expressed as an upper limit on δ/L. δ is the maximum total displacement of the structure and L the span of the structure. This constraint can be translated to an upper limit on the displacement indicator, Δ. Imposing an upper value on δ/L results in imposing an upper value on Δ. However the constraint on Δ becomes material dependant. The larger the proportion of Young's modulus over the allowable stress, the larger the allowable value of Δ and the less severe the constraint

$$\Delta < \Delta_{\lim} = \frac{E}{\sigma}\left(\frac{\delta}{L}\right)_{\lim} \tag{3}$$

The analytical expressions of both W and Δ have been established by Samyn [3], [6] and Latteur [5] for trusses, beams, arches, cables, cable stayed structures, masts and frames subjected to a limited number of (simple) load cases and supports. For statically determinate structures those MI are only function of the geometrical slenderness L/H (length divided by the height of a rectangle that frames the structure). Instabilities, self weight and second order effects are neglected. Efficiency curves depicting the geometrical slenderness with respect to the minimum volume material can be established (Fig. 1).

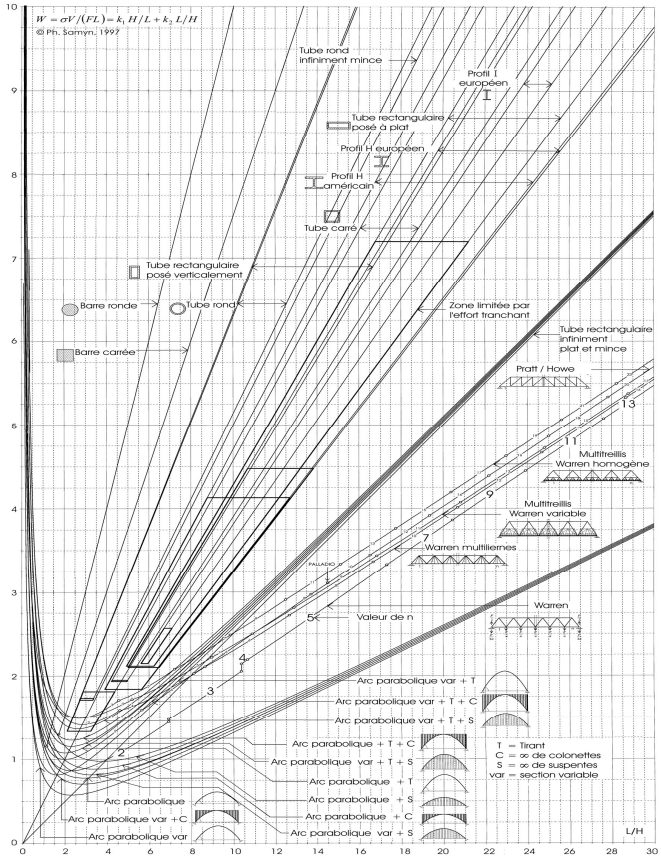

Fig. 1. Indicator of volume as a function of the slenderness for classical structural typologies, neglecting buckling. [6]

This figure allows the comparison between different structural typologies and topologies with a reduced number of variables. For classic truss topologies (Warren, Howe, Pratt, etc.) W and Δ only depend on the number of panels and the geometrical slenderness. In a more general way, one can conclude that those MI only depend on the proportion of the rectangle in which the structure is inscribed and on the shape/topology (i.e. how this rectangle is filled). Those results are based on a fully stressed[1] design of statically determinate structures and for a dominant load case (in this case a uniformly distributed vertical load).

[1] In which every element works at its allowable stress level under at least one of the given load conditions

The buckling indicator Ψ developed by Latteur [5] takes buckling in individual elements into account.

$$\Psi = \frac{\mu\sigma L}{\sqrt{qEF}} \tag{4}$$

This factor gives an indication for the buckling tendency of the compression elements in a structure with span L, composed of bars with a form factor $q = I/\Omega^2$ (Fig. 2) (with I the second moment of inertia and Ω the section area) in a material with Young's modulus E, with at least one section dimensioned on its allowable stress σ, subjected to a system of load with total resultant F. μ is the proportion of the buckling length of the compression bars over their geometrical length (which depends on the connection type).

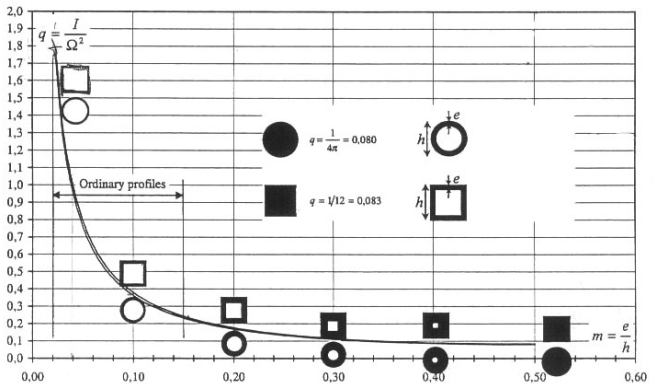

Fig. 2. Form factor of double axis symmetric square and circular profile [5].

This contribution modifies the element sizing. It implies the use of one extra parameter (Ψ), but increases the precision of the optimisation process. It enables the evaluation of the extra necessary volume of material to avoid buckling. Moreover, it affects the optimal solution. For example: the higher the value of the buckling indicator, the higher the optimal slenderness and number of panels for trusses.

The definition of the indicator of buckling clearly demonstrates that the buckling sensitivity depends on the span-load ration ($L/\sqrt{F}$). This quantity is defined as the structural index [7]. This index illustrates that morphological indicators are dimensionless but depend upon scale effects.

II. Problem Statement

Recent research [8] shows that not only the volume (indicator of volume W) and the maximal static displacement (indicator of displacement Δ) can be predicted at conceptual design stage, but other fundamental structural characteristics as well. Van Steirteghem [8] provides a method to evaluate the first natural eigenfrequency of a structure, introducing the indicator of fundamental eigenfrequency

$$\Theta = 2\pi f \sqrt{\frac{z^* \sigma L}{gE}} \tag{5}$$

This indicator represents the first natural frequency of a structure with a unit length L composed of members working at a unit stress σ and with a unit elastic modulus E, for which the ratio of the co-vibrating load to the total load is equal to $z^* = 1$ in Serviceability Limit State[2]. Moreover, this indicator depends on the same variables as the indicator of volume and displacement. This finding is confirmed by validation of trusses [9].

To avoid resonance the eigenfrequency should not fall within the frequencies interval excited by the external loads $[f_{\min}, f_{\max}]$. Those excitation frequencies define problem related limits on the value of the indicator of fundamental eigenfrequency

$$\Theta \notin \left[\Theta_{\min} = 2\pi f_{\min} \sqrt{\frac{z^* \sigma L}{gE}}; \Theta_{\max} = 2\pi f_{\max} \sqrt{\frac{z^* \sigma L}{gE}} \right] \tag{6}$$

The studies performed in [10] and [11] shows that the global planar stability of truss arches can be evaluated by means of the indicator of global planar stability

$$\Lambda_{cr} = \frac{F_{cr} \sigma}{FE} \tag{7}$$

It is the critical global planar buckling load of an isomorphic structure in a material with unit Young's modulus E, with at least one section of every element dimensioned at its unit allowable stress σ, subjected to a system of loads with unit resultant F. Again, detailed analysis demonstrates that Λ_{cr} only depends on the same variables as the indicator of volume, no additional or different variables are necessary. The planar stability of the structures is guaranteed if the critical global buckling load exceeds the applied load

$$F_{cr} > F \Leftrightarrow \Lambda_{cr} > \Lambda_{cr,\lim} = \frac{\sigma}{E} \tag{8}$$

Hence it is possible to assess the strength, the stiffness and the planar stability of a truss arch at conceptual design stage on the basis of a limited number of variables. This essential advantage of MI can be combined with powerful search algorithms, which enables the comparison of a large number of structural morphologies, within a relatively short calculation time ([13], [14] and [15]).

Nevertheless, there is an implicit restriction on the use of the morphological indictors as optimisation tool. If all of above mentioned stiffness constraints are met, the volume indicator offers a very efficient objective function for volume minimization. However, if at least one of the stiffness constraints is violated, the designer can only modify the input variables to stiffen the structure: the slenderness, the shape and the topology. The section distribution or sizing cannot be altered since fixed by the assumption of a fully stressed design (in which every element works at its allowable stress level under at least one of the given load conditions).

The use of MI bases its user-friendly/efficient approach by exploring only two of the three possible optimisation branches:

- sizing: to fix the dimensions (cross section and second moment of inertia) of each element
- shape optimisation: the global form of the structure (dimensions and node configuration)
- topological optimisation: the way of connecting the different nodes

The use of MI considers implicitly fully stressed design as being the optimal sizing and therefore does not further explore the first branch. The optimisation process is carried out on the shape and topology. In case only strength and element buckling are the dimensioning design criteria, this is a correct working method. When one of the stiffness constraints is not met, this assumption is no longer valid. The use of fully to stressed design does not allow an alternative sizing and can therefore lead to unacceptable results.

III. Example of Applicability Limits

The simple 2D-example shown in Fig. 3 illustrates the limit of optimisation with MI. Assume a truss column of the K-type (fixed geometry), charged by two identical vertical point loads, $F/2$, at the column tops (Fig. 3). A slenderness $L/H = 40$[3] and a buckling indicator $\psi = 30$ are imposed. (Note that the type of used profile is implicitly considered by the value and the definition of the buckling indicator.) The vertical bars are hinged to the central elements but also have a pinned connection with the adjacent verticals. Since the construction is statically determinate, every section can be modified without altering the load distribution path. The choice of the number of panels (1 to 10) and the section distribution are free and will be optimized. Only planar (in)stability is considered.

A. Calculation assumptions

In accordance to the European design prestandards [16], the bar imperfections do not have to be considered in the global analysis of frame structures if the bars are only axially loaded, which is the case in this paper. Furthermore, the bar imperfections due to the effect of initial imperfections and residual fabrication (welding or forming) stresses, should only be considered for the analysis on bar level. The use of the

[2] As defined in [12]

[3] This slenderness can lead to low angles between the different elements, though the European design standards [18] proscribe minimal angles of 30° for direct connections between tubular elements. But with an appropriate pinned-joint design low angles can be reached.

buckling indicator covers those imperfections by considering design curve d, as described in Latteur [5].

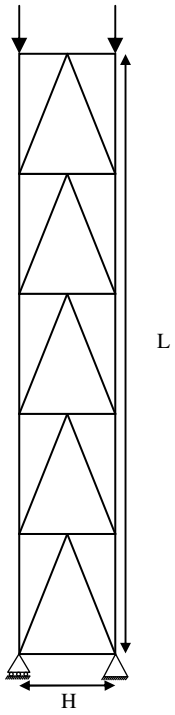

Fig. 3. Truss column of K-type: five panels and hinged connections.

The values of the critical buckling load are obtained by using a second order FE-analysis (elastic and geometrical stiffness matrices), which takes shear effects into account. An analytically solved example from Timoshenko [17] has been introduced in order to validate the used FE (Fig. 4).

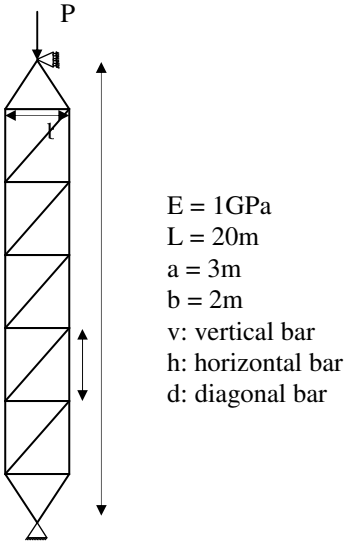

Fig. 4. Axially loaded statically determined truss column [16].

The differences in critical buckling load between the theoretical values of Timoshenko [17] and the numerical values do not exceed 5.7% (Table1), which is far less than the predicted impact of shear effects. This result demonstrates that shear effects are considered and confirms the calculation of the buckling load, performed by the FE used in the numerical example below.

Table 1. Relative difference for critical buckling load obtained by Timoshenko [16] and by a Finite Element Method (FEM).

I_d (m^4) [b]	A_d (m^2) [c]	A_h (m^2) [c]	A_v (m^2) [c]	$P_{crit,Timoshenko}$ (N)	P_{FEM} (N)	Relative difference (%)
10^{-4}	0.5	0.3	10^{-2}	$2.193*10^5$ [a]	$2.194*10^5$ [1]	0.02
10^{-4}	$0.5*10^{-1}$	$0.3*10^{-1}$	10^{-2}	$2.193*10^5$ [a]	$2.194*10^5$ [1]	0.02
10^{-4}	$0.5*10^{-2}$	$0.3*10^{-2}$	10^{-2}	$2.193*10^5$ [a]	$2.194*10^5$ [1]	0.02
10^{-4}	$0.5*10^{-3}$	$0.3*10^{-3}$	10^{-2}	$2.193*10^5$ [a]	$2.194*10^5$ [1]	0.02
10^{-4}	$0.5*10^{-4}$	$0.3*10^{-4}$	10^{-2}	9.77810^3	$1.033*10^4$	5.65
10^{-4}	$0.5*10^{-5}$	$0.3*10^{-5}$	10^{-2}	$9.954*10^2$	$1.044*10^3$	4.89
10^{-4}	$0.5*10^{-6}$	$0.3*10^{-6}$	10^{-2}	$9.972*10$	$1.045*10^2$	4.80
10^{-4}	$0.5*10^{-7}$	$0.3*10^{-7}$	10^{-2}	9.973	$1.048*10$	5.07

[a] Buckling of a vertical bar element
[b] I: second order inertia moment
[c] A: cross section

B.Results

If one only considers the resistance criterion, fully stressed design yields the optimal solution. The vertical elements are loaded axially; the central elements are not loaded. Hence, the central elements do not need material, resulting in a volume indicator which is independent of the number of panels

$$W = \frac{\sigma V}{FL} = \frac{\sigma}{FL}\sum_{i}^{verticals} V_i = 2.\frac{\sigma}{FL}\left(\frac{LF}{2\sigma}\right) = 1 \qquad (9)$$

When bar buckling is considered, the sections should be increased (the central elements remain unloaded). The indicator of volume becomes dependent of the number of panels and the buckling indicator

$$W = \frac{1}{2}\left(1+\sqrt{1+\frac{8\Psi^2}{\pi^2 n^2}}\right) \qquad (10)$$

The more panels, the lower the buckling length of the verticals, resulting in a lower indicator of volume. A lower buckling indicator also implies a lower necessary volume. For an extreme large number of panels and a very low buckling indicator, the indicator of volume tends to 1, which is the under limit given by the resistance criterion

$$\lim_{\substack{n\to\infty \\ \Psi\to 0}} W = \lim_{\substack{n\to\infty \\ \Psi\to 0}} \frac{1}{2}\left(1+\sqrt{1+\frac{8\Psi^2}{\pi^2 n^2}}\right) = 1 \qquad (11)$$

When the global planar stability is taken into account, one immediately notices that the previous solution is composed of a set of hinged connected bars on two vertical lines. This structure is a mechanism and has therefore a global planar stability indicator of 0. In this example one of the three stiffness constraints is not satisfied ($\Lambda_{cr} < \Lambda_{cr,\lim}$). The modification of the input variables, maintaining a section distribution based on the fully stressed design always result in a mechanism. Hence fully stressed design is of no use.

A possible solution is to introduce one extra variable α, which represents the section ratio from the central elements with respect to the vertical elements. This implies a first additional degree of freedom for the sizing optimisation, since the section of central elements can be optimised independently of the verticals. Fig. 5 and Fig. 6 show respectively the indicator of global planar stability and the indicator of volume as a function of α for different number of panels n. In this example a realistic value (ψ=30) for the buckling indicator is assumed.

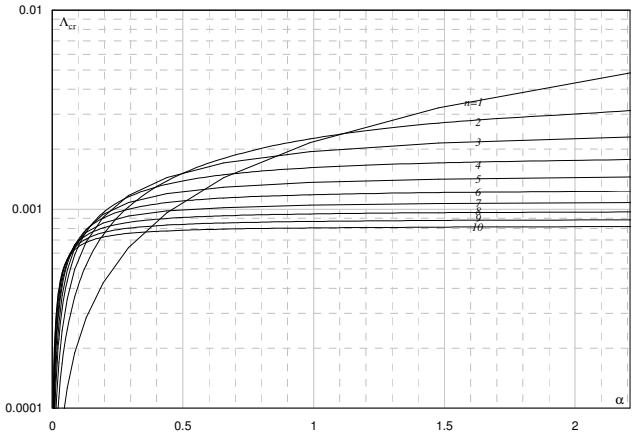

Fig. 5. Indicator of global planar stability as a function of α for different number of panels (K-type truss column, $L/H = 40, \psi = 30$).

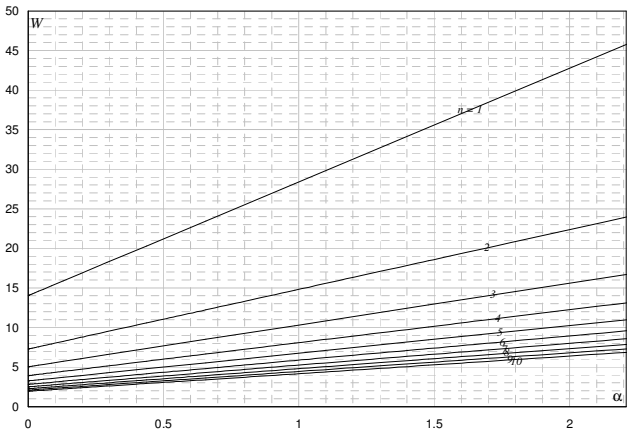

Fig. 6. Indicator of volume as a function of α for different number of panels (K-type truss column, $L/H = 40, \psi = 30$).

The global planar stability indicator needs to exceed the critical value of σ/E in order to guarantee global planar stability. If the structure is unstable, the stress level is decreased from σ to $\beta\sigma$ ($\beta < 1$). This global stress level reduction does not affect the relative section distribution, since it increases every bar section with the same proportionality. Fig. 7 shows the corresponding value of the volume indicator for a column with $E/\sigma = 100$ ($\Lambda_{crit,\lim} = 0{,}01$). Again a buckling indicator of 30 is assumed.

For a given slenderness, buckling indicator and limit value of the global planar stability indicator, one can find the couples of optimal values for the number of panels and α. The higher α, the higher the necessary volume and the lower the corresponding optimal number of panels. The lightest solution is given by a column with ten panels and $\alpha = 0{,}1548$ ($W = 32{,}61$). As mentioned above, the fully stressed solution ($\alpha = 0$) always results in a unstable column or $W = \infty$.

A further step to free cross-section sizing is performed by allowing different section ratio's for the horizontal (α_h) and the diagonal (α_d) central elements. Two degrees of freedom for sizing are introduced and the optimum is not longer found by exhaustive searching, but with a genetic algorithm. The optimum yields $\alpha_h = 0{,}1548, \alpha_d = 0{,}1548$ en $n = 10$ ($W = 32{,}61$). This extra variable does not result in a volume gain. This example illustrates that additional sizing parameters do not always necessarily lead to a more optimal solution.

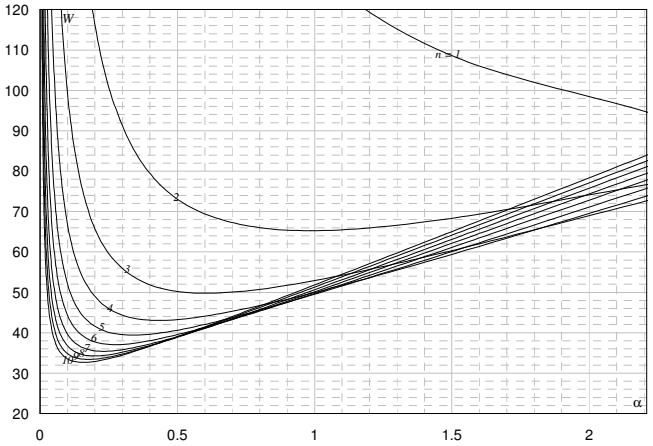

Fig. 7. Volume indicator of planar stable truss column as a function of α for different number of panels. (K-type, $L/H = 40, \psi = 30$ en $\sigma/E = 0{,}01$).

Finally, the comparison can be made with the truss column in which every section is sized individually (free sizing). The number of variables increases to the number of panels and the section of every bar element. A genetic algorithm allows to fix the minimum indicator of volume on ten panels, with $W = 26{,}64$. This approach represents a volume gain of twenty percent compared to the single-degree-of-freedom solution for sizing. The main disadvantage is the dependency of a very large number of variables, which annihilates the benefits of using the volume indicator instead of the volume and implies much higher calculation times. Fig. 8 gives an idea of the corresponding section distributions.

This example illustrates that fully stressed design does not always represent the best/lightest sizing method, if other design constraints are considered (here global stability). This

conclusion is also valid for other design criteria (dynamics, static displacements, etc.) and other structures (arches, trusses, etc.).

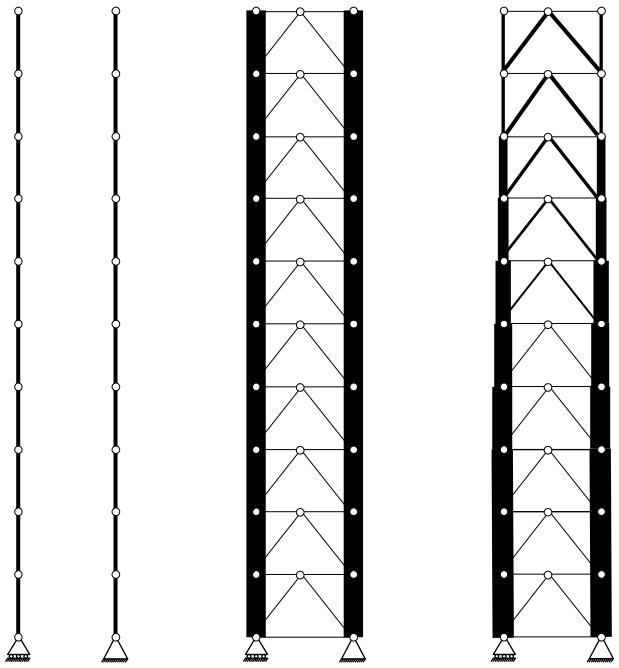

Fig. 8. Section distribution and corresponding volume indicator of optimal truss columns with increasing sizing freedom, considering global planar instability (K-type, $L/H = 40, \psi = 30$ en $\sigma/E = 0{,}01$).

IV. Conclusion

In structural optimisation one can state that if at least one of the stiffness constraints (acceptable static displacements, global stability and absence of resonance) is not met, fully stressed design does not guarantee the most efficient solution. Hence, up to now, morphological indicators are used to offer a very performing conceptual optimisation tool in a design for strength approach. In design for stiffness one needs different optimisation techniques and/or to accept that every additional non fully stressed section stands for an additional input variable to optimize. Analysis of the indicator of displacement, the indicator of first eigenfrequency and the indicator of global planar stability proves that even at the stage of conceptual design one can determine whether design for stiffness or design for strength is the designing parameter (Fig. 9).

To summarize, one can state that the power of the morphological indicators, which are dependent on a limited number of design variables, follows from the fixed sizing. However, the downside of the medal is that sizing represents one of the fundamental optimisation branches, which should be used in design for stiffness problems. Though, the evaluation of the morphological indicators discussed in this paper enables to determine whether one has to deal with such a design for stiffness problem or not.

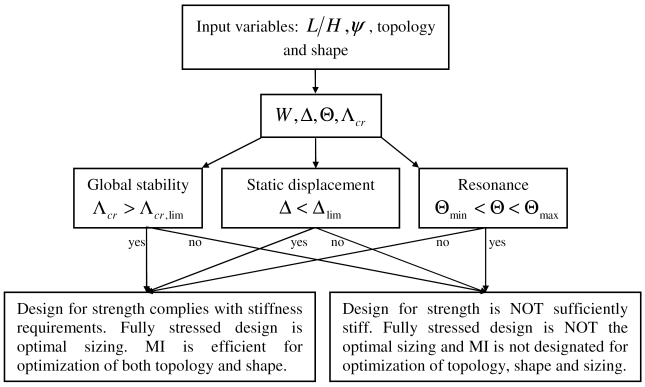

Fig. 9. Flowchart for the use of morphological indicators at conceptual design stage.

Acknowledgments

The authors want to thank the Institute for the Promotion of Innovation through Science and Technology in Flanders (IWT Vlaanderen), which funds this research.

References

[1] Kroll E, Condoor S, Jansson *DG., Innovative Conceptual Design – Theory and Application of Parameter Analysis*, Great Britain: Cambridge University, 2001.

[2] Yannou B, Hamdi A, Landel E., *Une stratégie de modélisation conceptuelle pour la prise en compte de performances vibro-acoustiques en préconception d'un berceau automobile*. Paris, France: Mécanique & industries (Méc. ind.), Elsevier, (ISSN 1296-2139), 2000.

[3] Samyn P., *Etude Comparée du Volume et du déplacement de Structures Isostatiques Bidimensionnelles sous Charges Verticales entre Deux Appuis. Vers un outil d'évaluation de prédimensionnement des structures (Tome 1 à 4)*, PhD Thesis. Belgium: Université de Liège, 1999.

[4] Eurocode - *Design of steel structures Part 1-1: General rules and rules for buildings (Belgian application document)*. European Prestandard NBN ENV 1993-1-1:1992, (section 4) 49-52.

[5] Latteur P., *Optimisation et Prédimensionnement des Treillis, Arcs, Poutres et Câbles sur Base d'Indicateurs Morphologiques (Tome 1 à 4)*, PhD Thesis, Belgium, Vrije Universiteit Brussel, 2000.

[6] Samyn P., *Etude de la morphologie des structures à l'aide des indicateurs de volume et de déplacement*, Belgium, Académie Royale de Belgique, Classes des Sciences, 2004.

[7] Shanley FR., Weight–*strength analysis of aircraft structures (2nd ed.)*. New York, Dover Publications, Inc., 1960.

[8] Van Steirteghem J., *A Contribution to the Optimisation of Structures Using Morphological Indicators: (In)Stability and Dynamics*, PhD Thesis, Belgium, Vrije Universiteit Brussel, 2005.

[9] T. Vandenbergh, B. Verbeeck and W.P. De Wilde, Dynamical analysis and optimisation of statically determinate trusses at conceptual design stage, in *Proceedings for the ECCOMAS Thematic Conference (COMPDYN 2007) on Computational Methods in Structural Dynamics and Earthquake Engineering,* M. Papadrakakis, D.C. Charmpis, N.D. Lagaros and Y. Tsompanakis, (Editors), p253, 2007.

[10] T. Vandenbergh, W.P. De Wilde, P. Latteur and L. Vantomme, Optimisation of Statically Determinate Trusses Considering Planar Instabilities at Conceptual Design Stage, in *Proceedings for the Third International Congress dedicated to the "art, science and practice of structural engineering" (Structural Engineers World Congress)*, p141, 2007.

[11] Vantomme L., *Uitbreiding van de theorie van de morfologische indicatoren naar het specifiek geval van de parabolische vakwerkboog: ontwerprichtlijnen en –strategie*, Master Thesis, Belgium, Vrije Universiteit Brussel, 2007.

[12] Eurocode - *Basis of structural design. European Standard NBN EN 1990: 2002*, (section 3) 27-29.

[13] Verbeeck B, De Wilde W P, Samyn P, Van Steirteghem J. *High Performance Structures and Materials* (conference held in Ancona, Italy): The Use of Genetic Algortihms and Morphological Indicators in the Optimisation of 2D Trusses, Southampton, UK: Brebbia CA, De Wilde WP (ed), WIT Press; 2004; 571-577.

[14] Verbeeck B, De Wilde WP, Samyn P, Van Steirteghem J. *High Performance Structures and Materials* (conference held in Skiathos, Greece) The Need of Numerical Techniques for the Optimisation of Structures Using Morphological Indicators. Southampton, UK: Hernandez S, Brebbia CA (ed), WIT Press; 2005; 65-72.

[15] T. Vandenbergh, B. Verbeeck, W.P. De Wilde and P. Latteur, The Use of Morphological Indicators and Genetic Algorithms in Structural Optimisation Considering Stiffness Constraints, in *Proceedings of The Eighth International Conference on Computational Structures Technology*, B.H.V. Topping, G. Montero and R. Montenegro, (Editors), Civil-Comp Press, Stirlingshire, United Kingdom, paper 201, 2006.

[16] Eurocode - *Design of steel structures Part 1-1: General rules and rules for buildings (Belgian application document)*, European Prestandard NBN ENV 1993-1-1:1992, (5.2.4) 61-64.

[17] Timoshenko S P, Gere J M., *Theory of elastic stability (2nd ed.)*, New York: McGraw-Hill Book Company, Inc., 1961, 132-137.

[18] Eurocode – *Design of steel structures Part 1-8: Design of joints. European Standard NBN EN 1993-1-8: 2005*, (7.1.2) 101.

Proceedings of the 8th National Congress on Theoretical and Applied Mechanics, May 28-29, Brussels, Belgium.

A coupled two-scale computational approach for quasi-brittle out-of-plane structural failure

Benoît C.N. Mercatoris[1], Thierry J. Massart[1]
[1]Department of Building, Architecture and Town Planning, Université Libre de Bruxelles
Avenue F.D. Roosevelt 50 CP 194/2, 1050 Brussels - Belgium
email: bmercato@batir.ulb.ac.be,thmassar@batir.ulb.ac.be

Abstract— **This contribution discusses the formulation of a two-scale computational framework for flexural failure in masonry shells. The heterogeneous nature of masonry coupled to its periodic stacking of quasi-brittle constituents leads to preferential damage patterns. Their influence can be incorporated in structural computations using computational homogenisation concepts. The ingredients needed to couple the structural and constituents scales are introduced for the case of damaging materials, and a coupled two-scale framework for masonry shells is outlined. This procedure allows incorporating naturally the anisotropic damaging effects of the masonry material degradation. The contribution will illustrate the two-scale results by comparing them to full fine scale models for in-plane failure and out-of-plane failure.**

Keywords— **Structural analysis, Multi-scale discontinuities, Multi-scale detection, Periodic homogenisation, Failure, Fine scale comparison.**

I. Introduction

THE formulation of macroscopic constitutive laws for the behaviour of masonry is a complex task, due to its strongly heterogeneous microstructure which considerably influences its overall mechanical behaviour. Due to the quasi-brittle nature of its constituents, this results in initial and damage-induced (evolving) anisotropy properties, accompanied with localisation of damage. In its structural use, such a material may be subjected to cracking, leading to localisation of damage at both the structural and fine scales. Closed-form laws have therefore been developed for equivalent anisotropic media for elastic and cracking behaviour, see [1], later applied for the modelling of plate failure, see [2]. The use of such models in the cracking regime is however impeded by their costly and cumbersome identification. As a complementary approach to closed-form constitutive relations, the multi-scale computational strategies aim at solving this issue by deducing a homogenised response at the structural scale from a representative volume element (RVE), based on constituents properties and averaging theorems.

II. Computational homogenisation

Computational homogenisation approaches allow to identify homogenised continuum properties from the constituents constitutive behaviour of a heterogeneous mesostructure. This allows the set up of nested computational procedures in which, in each (macroscopic) point of the structural scale discretisation, a sample of the mesostructure is used to determine the material response. For this purpose the local macroscopic strain measure is applied in an average sense to the mesostructure and the resulting mesostructural stresses are determined numerically. The averaging of these mesostructural stresses and the condensation of the mesostructural tangent stiffness to the homogenised tangent stiffness then furnish the macroscopic material response associated with the macroscopic point. The definition of such a nested scheme essentially requires the definition of four ingredients: (i) a fine scale constitutive description for the constituents, (ii) the definition of a representative mesostructural sample, (iii) the choice of a coarse scale representation, and (iv) the set-up of scale transitions linking structural and fine scale quantities.

III. Two-scale framework for out-of-plane failure

In order to incorporate damage localisation effects at both the structural and fine scales, this approach has to be adapted, by carefully selecting the above-mentioned features. In particular, both the fine and coarse scale descriptions have to deal with localisation of damage, and the scale transition procedure should be adapted accordingly. For in-plane loaded structures, in which both fine and coarse scale descriptions follow similar kinematical assumptions, these adaptations have been proposed recently with different methodologies in [3], [4]. This approach can be extended to shell formulations, where higher order kinematical quantities such as curvatures appear at the structural scale. This requires adaptations within the structural scale description as well as in the scale transitions.

A. Non-linear periodic homogenisation of masonry shell behaviour

A scale transition for homogenisation towards a Kirchhoff-Love shell behaviour was recently proposed in [5]. Based on a periodicity assumption (see Figure 1 for

the case of masonry), a strain-periodic displacement field may be imposed under the form

$$\left\{ \begin{array}{rcl} u_\alpha(\vec{x}) & = & E_{\alpha\beta}x_\beta + \chi_{\alpha\beta}x_\beta x_3 + u^p_\alpha(\vec{x}) \\ u_3(\vec{x}) & = & -\frac{1}{2}\chi_{\alpha\beta}x_\alpha x_\beta + u^p_3(\vec{x}) \end{array} \right. \quad (1)$$

where $\vec{u}^p$ is a periodic fluctuation such that $\vec{u}^p(\vec{x}+\vec{V}^\alpha) = \vec{u}^p(\vec{x})$ and where $\alpha,\beta = 1,2$, see [6] and [5]. The strain measures associated with a shell kinematical description can then be expressed in terms of the controlling degrees of freedom depicted in Figure 1. The constituents inside the unit cell may be modelled using any closed-form formulation. The simplest representation for mortar joints consists in cohesive zones equipped with a Mohr-Coulomb criterion. The bricks are assumed to exhibit a linear elastic behaviour. As a result, the response of a coarse scale point under any loading program may be computed.

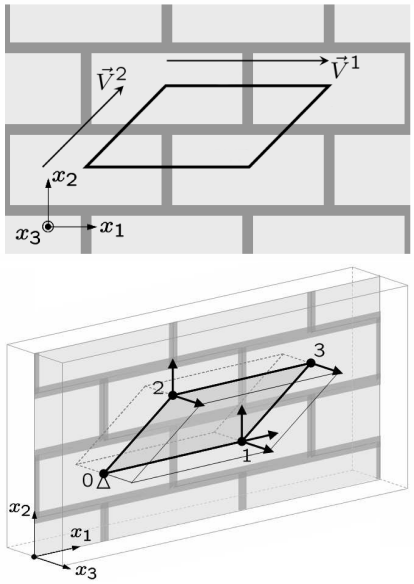

Fig. 1. Periodic masonry structure (top) and controlling degrees of freedom (bottom), see [5].

B. Localisation detection at the structural scale

Any localisation enhancement at the coarse scale to represent failure requires a criterion to detect localisation and to determine its orientation. However, in a computational homogenisation procedure, the macroscopic material response is not postulated a priori but rather computed from the material laws introduced at the microstructural level. This criterion should then be based on computationally homogenised results, the only information available characterising the average material behaviour. The detection of the structural scale localisation can be based on the acoustic tensor concept extended to the shell description, see [7]. This tensor has to be constructed based on the homogenised stiffness such that the localisation detection takes into account the coupling of flexural and membrane effects. It can be shown, see [8], that such a procedure allows to extract mesostructurally motivated average localisation orientations, based on the non positive definiteness of this tensor, for various coupled flexural-membrane loading paths, see Figure 2 for illustration.

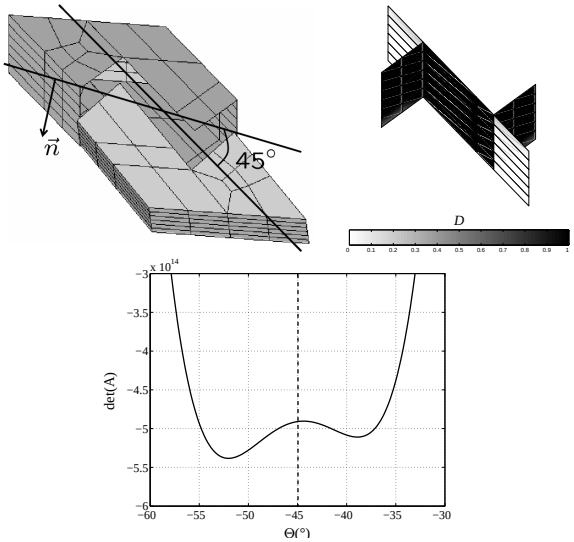

Fig. 2. Out-of-plane stair-case bending failure at 45° (brick shape factor of 0.5): Deformed shape of the unit cell (top-left), joint damage distribution (top-right) and related acoustic tensor determinant spectrum (bottom): non positive values indicate orientation for potential localisation.

C. Incorporation of a strong discontinuity at the structural scale

The structural scale problem is solved using the finite element method and using an embedded strong discontinuity model in which the behaviour of the discontinuity is obtained from fine scale computations. Once structural localisation is detected, the coarse scale displacement field is enriched by a strong discontinuity, in the spirit of [9]. A displacement jump $\vec{\xi}_u$ and a rotation jump $\vec{\xi}_\theta$ are introduced along a discontinuity line Γ_d, the orientation of which is deduced from the acoustic tensor-based criterion. These jumps are added to the regular continuous part of the displacement and rotation fields according to

$$\left\{ \begin{array}{rcl} \vec{u}_e & = & \vec{u} + \Psi_u \vec{\xi}_u \\ \vec{\vartheta}_e & = & \vec{\vartheta} + \Psi_\vartheta \vec{\xi}_\vartheta \end{array} \right. \quad (2)$$

where Ψ_u and Ψ_ϑ represents a set of functions exhibiting a unit jump along the discontinuity line. The enhanced generalised strain tensors (membrane deformation tensor and curvature tensor) are obtained by differentiating the

enhanced displacement and rotation fields, which leads to

$$\begin{cases} \mathbf{E_e} = (\vec{\nabla}\vec{\mathbf{u}}_\mathbf{e})^{\text{sym}} = \mathbf{E}(\vec{\mathbf{u}}) + \mathbf{G_E}(\vec{\xi}_\mathbf{u}) + (\vec{\xi}_\mathbf{u}\,\vec{\mathbf{n}})^{\text{sym}}\,\delta_\mathbf{d} \\ \chi_e = (\vec{\nabla}\vec{\vartheta}_e)^{\text{sym}} = \chi(\vec{\vartheta}) + \mathbf{G}_\chi(\vec{\xi}_\vartheta) + (\vec{\xi}_\vartheta\,\vec{\mathbf{n}})^{\text{sym}}\,\delta_\mathbf{d} \end{cases} \quad (3)$$

where $\mathbf{E}(\vec{\mathbf{u}})$ and $\chi(\vec{\vartheta})$ are the generalised strain tensors based on classical kinematics, $\mathbf{G_E}(\vec{\xi}_\mathbf{u})$ and $\mathbf{G}_\chi(\vec{\xi}_\vartheta)$ are a set of strain operators associated to the displacement and rotation jumps, and δ_d is the Dirac function centered on the discontinuity line, see [9].

In order to determine the additional displacement jump field, the weak form of equilibrium is solved together with a weak continuity condition on the stress along the discontinuity line:

$$\begin{cases} \int_{\Gamma_d} \left(\vec{N}_d - \mathbf{N}\cdot\vec{\mathbf{n}}\right) \mathrm{d}\Gamma_\mathrm{d} &= 0 \\ \int_{\Gamma_d} \left(\vec{M}_d - \mathbf{M}\cdot\vec{\mathbf{n}}\right) \mathrm{d}\Gamma_\mathrm{d} &= 0 \end{cases} \quad (4)$$

where $\vec{N}_d$ and $\vec{M}_d$ are the generalised stress vectors across the discontinuity, $\mathbf{N}$ and $\mathbf{M}$ are the generalised stress tensors (normal effort tensor and bending moment tensor) in the bulk, surrounding the discontinuity, and $\vec{n}$ is the normal to the discontinuity line Γ_d. A material response which links the generalised stress vectors to the displacement and rotation jumps is required to drive the discontinuity and reads

$$\begin{cases} \delta\vec{N}_d &= {}^2\mathbf{C}_\mathbf{d}^{\text{mm}} \cdot \delta\vec{\xi}_\mathbf{u} + {}^2\mathbf{C}_\mathbf{d}^{\text{mb}} \cdot \delta\vec{\xi}_\vartheta \\ \delta\vec{M}_d &= {}^2\mathbf{C}_\mathbf{d}^{\text{bm}} \cdot \delta\vec{\xi}_\mathbf{u} + {}^2\mathbf{C}_\mathbf{d}^{\text{bb}} \cdot \delta\vec{\xi}_\vartheta \end{cases} \quad (5)$$

where ${}^2\mathbf{C}_\mathbf{d}^{\text{ij}}$ are the discontinuity tangent stiffness tensors. Once the embedded discontinuity is introduced, the bulk of the element is assumed to unload elastically from the state reached at that point.

D. Upscaling localising behaviour towards the coarse scale discontinuity

In the present contribution, contrary to the approach proposed by [9] where the material behaviour is defined by closed-form laws, both the bulk and discontinuity material behaviours are deduced from fine scale unit cell computations. A material secant stiffness is extracted from the unit cell in which the structural localisation has just been detected in order to compute the elastic unloading of the bulk. The material behaviour of the discontinuity, described by Equation (5) at the coarse scale, must be extracted from the fine scale description by means of an enhanced upscaling procedure. A further damaging unit cell is used for this purpose, which will be denoted in the sequel as Localising Volume Element (LVE).

The extraction of the coarse scale discontinuity response requires the definition of average generalised strain tensors $\mathbf{E}^{\text{LVE}}$ and χ^{LVE} to be applied on the LVE from the coarse scale displacement and rotation jumps; as well as the evaluation of $\vec{N}_d$, $\vec{M}_d$ and ${}^2\mathbf{C}_\mathbf{d}^{\text{ij}}$ from the results of the LVE computation. An approximate energy consistency argument is used in order to build a relationship between the displacement and rotation jump vectors $\vec{\xi}_u$ and $\vec{\xi}_\vartheta$, and the average generalised strain tensors $\mathbf{E}^{\text{LVE}}$ and χ^{LVE}, see [10] for the in-plane case.

IV. Comparison of multi-scale and fine scale results on structural examples

The proposed multi-scale scheme was implemented using parallel computation. Two structural computations are performed and the results are compared to a fine scale computation used as a reference in order to challenge the periodicity and scale separation assumptions of the computational homogenisation procedure. The considered cases are the in-plane confined shearing and the out-of-plane bed-joint cracking of a masonry wall. The results comparison is based both on the overall response of the wall and on the obtained failure mode.

A. In-plane confined shearing of a masonry wall

An in-plane case is illustrated in details in [10]. It consists of a planar masonry wall of dimensions $2220 \times 2160 \times 98\,\text{mm}^3$, with bricks of dimensions $120 \times 60 \times 98\,\text{mm}^3$ stacked according to a running bond pattern. The loading is applied in two phases. In the first phase, the wall is compressed by prescribing a uniform vertical displacement of the top boundary. In the second loading phase, the vertical displacement of the top boundary is kept fixed and a horizontal shearing displacement is prescribed on the top right corner of the wall. The load-displacement response of the second loading phase is depicted in Figure 3. To illustrate the global failure mechanisms, the deformed configurations at the peak load are depicted in Figure 4 for the both full fine scale and multi-scale computations.

B. Out-of-plane bed-joint cracking of a masonry wall

The capacities of the proposed approach can also be shown for the out-of-plane behaviour by means of a structural computation. The case of bed-joint out-of-plane failure mode propagation is considered on a rectangular masonry shell simply supported on the two opposite edges parallel to the bed-joint. The wall is loaded by prescribing the vertical displacement of two points at the middle of only one free edge. The overall response of the wall is depicted in Figure 5 for both the full fine scale and multi-scale models. The deformed configuration in the softening regime is shown in Figure 6 for the both computations. Furthermore, the structural response of the masonry shell is drawn for different values of the mortar joint fracture

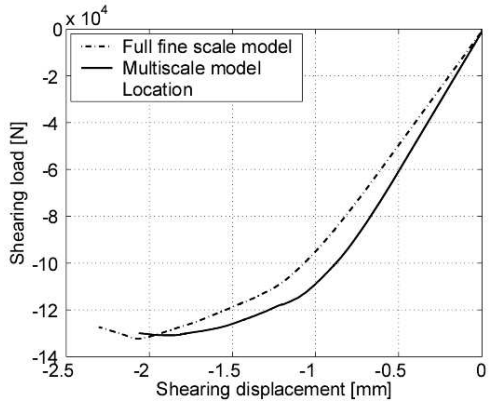

Fig. 3. In-plane confined shearing wall test. Comparison of the load-displacement reponses for full fine scale modelling (dashed line) and multiscale simulation (solid line).

energy in order to show that the mesostructural material parameters are properly upscaled. This case also allows to show that the appearance of membrane-flexural couplings due to the different tensile and compressive strengths of the damaging joints is well incorporated in the homogenisation procedure and in the localisation analyses.

V. Conclusions

It was shown that the multi-scale modelling yields results in good agreement with respect to complete fine scale computations results for both the limit load and the failure mode. The multi-scale methodology proves to be a valuable tool for the investigation of masonry structures. In particular, it allows to account for the strong coupling between the structural response and the underlying mesostructural features of the material. Specific enhancements are however needed in order to account properly for the consequences of the quasi-brittle nature of the constituents. Localisation is detected and treated in this contribution at both the mesoscopic and macroscopic scales by means of an enhanced scale transition.

Acknowledgments

References

[1] P.B. Lourenço, R. de Borst, J.G. Rots, *A plane stress softening plasticity model for orthotropic materials*, International Journal for Numerical Methods in Engineering, **40(21)**, 4033–4057, 1997.

[2] P.B. Lourenço, *Anisotropic softening model for masonry plates and shells*, Journal of Structural Engineering ASCE, **126(9)**, 1008–1016, 2000.

[3] T.J. Massart, R.H.J. Peerlings, M.G.D. Geers, *An enhanced multi-scale approach for masonry wall computations with localization of damage*, International Journal for Numerical Methods in Engineering, **69**, 1022–1059, 2007.

[4] T. Belytschko, S. Loehnert, J.H. Song, *Multiscale aggregating discontinuities: A method for circumventing loss of material stability*, International Journal for Numerical Methods in Engineering, **73**, 869–894, 2008.

[5] M. Mistler, A. Anthoine, C. Butenweg, *In-plane and out-of-plane homogenisation of masonry*, Computers & Structures, **85**, 1321–1330, 2007.

[6] A. Anthoine, *Derivation of the in-plane elastic characteristics of masonry through homogenization theory*, International Journal of Solids and Structures, **32(2)**, 137–163, 1995.

[7] J. Makowski, H. Stumpf, *Strain localization in stress-resultant theory of shells*, Mechanics Research Communications, **25(4)**, 455–465, 1998.

[8] B.C.N. Mercatoris, P. Bouillard, T.J. Massart, *Multi-scale detection of failure in planar masonry thin shells using computational homogenisation*, Engineering Fracture Mechanics, **76(4)**, 479–499, 2009.

[9] F. Armero, D. Ehrlich, *Finite element methods for the multi-scale modeling of softening hinge lines in plates at failure*, Computer Methods in Applied Mechanics and Engineering, **195**, 1283–1324, 2006.

[10] B.C.N. Mercatoris, T.J. Massart, *Assessment of periodic homogenisation-based multiscale computational schemes for quasi-brittle structural failure*, International Journal for Multiscale Computational Engineering, (In Press).

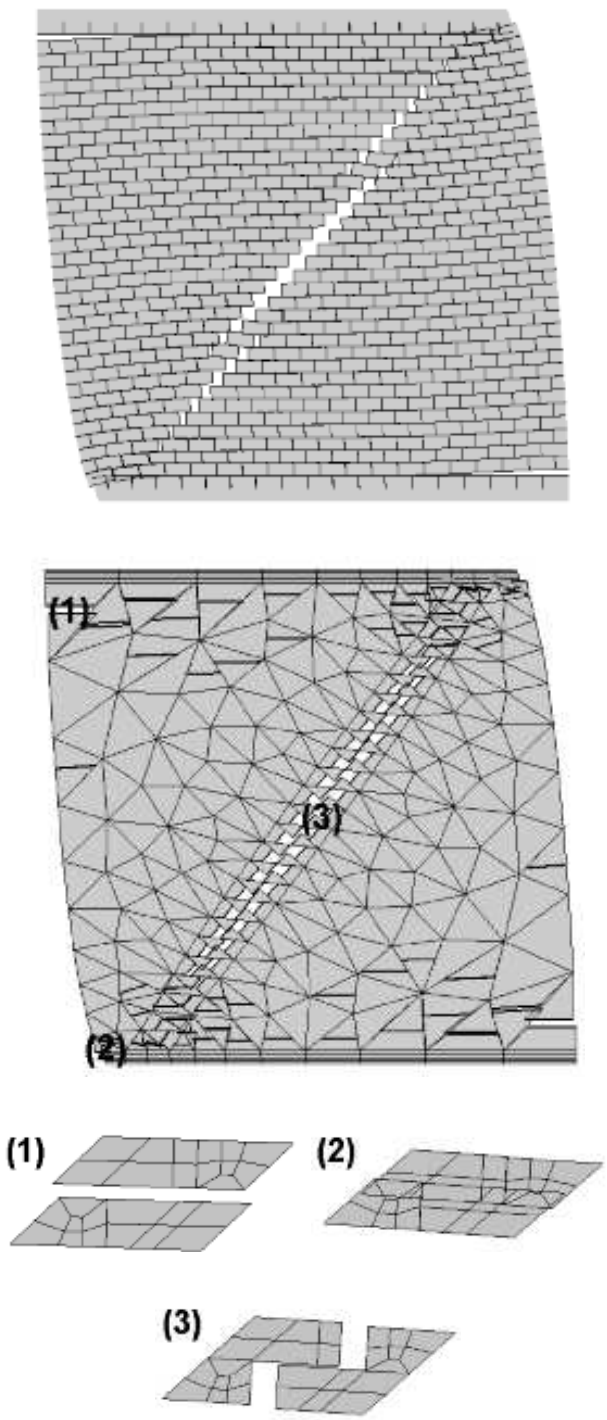

Fig. 4. Deformed configuration at the peak of the in-plane confined shearing load-displacement response of the wall (the displacements of the wall are magnified by a factor of 200): (top) deformed configuration of the complete fine scale computation, (centre) deformed configuration of the multi-scale computation and (bottom) related deformed unit cells (the displacements of the cells are magnified by a factor of 50).

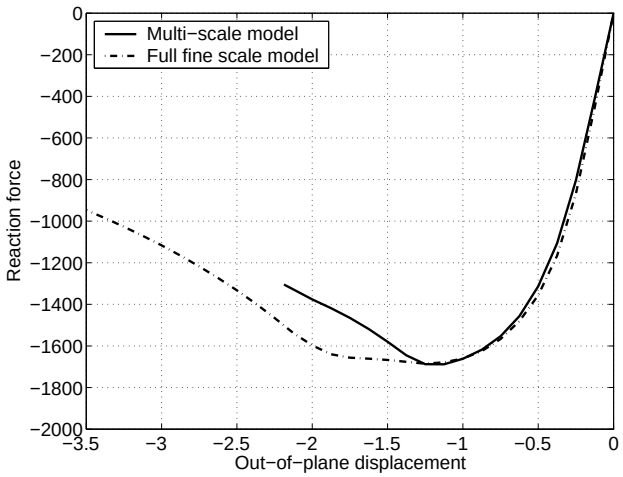

Fig. 5. Out-of-plane bed-joint cracking test. Comparison of the torque-rotation reponses for full fine scale modelling (dashed line) and multi-scale simulation (solid line).

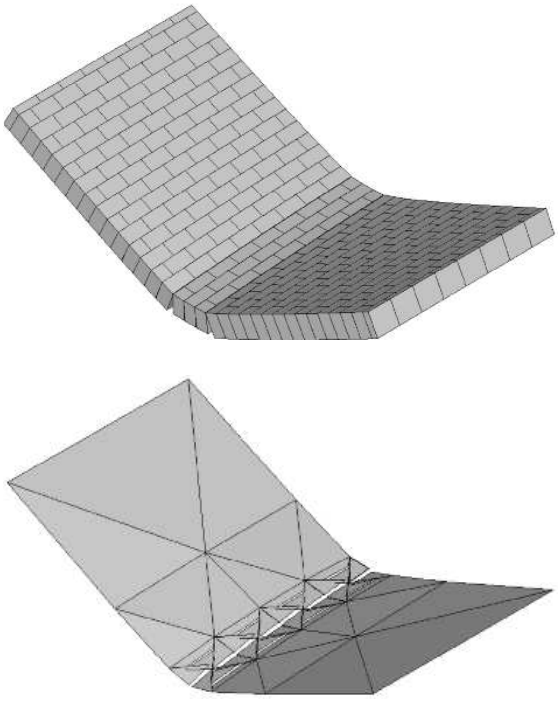

Fig. 6. Deformed configuration in the softening regime of the response of the wall (the displacements of the wall are magnified by a factor of 200): (top) deformed configuration of the complete fine scale computation and (bottom) deformed configuration of the multi-scale computation.

Degradation models for reliability estimation and mean residual lifetime

Christophe Letot[1], Pierre Dehombreux[1]
[1]Service de Génie Mécanique & Pôle Risques, Faculté Polytechnique de Mons
53 Rue du Joncquois, 7000 Mons - Belgique
email : christophe.letot@umons.ac.be, pierre.dehombreux@umons.ac.be,

Abstract—**This paper discusses the interest of some degradation models and measurements in order to improve the reliability assessment of an equipment. Classical methods used to estimate the reliability are based on a set of failure times on which a reliability model is fitted. Usual models are exponential, Weibull and lognormal laws. If an equipment is subjected to a degradation process on which a threshold may be fixed, it is useful to track this degradation to retrieve the health state of the system at some time points. From the set of degradation points, a degradation model may be fitted. This degradation model is then used to predict the failure time. The interest of this approach is that no failure is needed to retrieve the reliability information. Moreover it allows the estimation of the mean residual lifetime of the equipment as the degradation curve may be extrapolated to its critical threshold.**

Keywords— **reliability, mean residual lifetime, degradation, physical model**

I. Introduction and Reviewing

MEAN residual lifetime (MRL) may be predicted according to three approaches (figure 1).

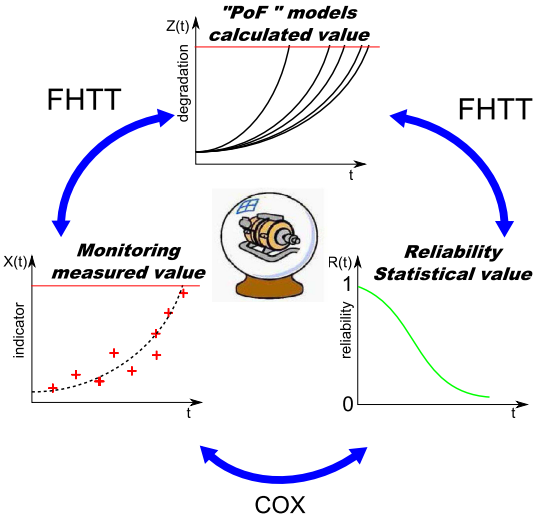

Fig. 1. The three approaches to estimates MRL and their links

The first method considers Physics-of-Failures (PoF) models for which the degradation law is supposed to be known. It consists of studying the effects of dispersion on some parameters of the law. The second method (condition monitoring) supposes that a degradation measurement may be tracked with time (this could be a crack size, a loss of efficiency in a gas turbine, a vibration measurement,...) ; based on the degradation data, this approach fits a degradation law. The last approach is the statistical reliability study based on the collection of failure times.

Improving the reliability estimation with degradation information may be achieved by linking the reliability approach with either the monitoring approach (if the degradation may be tracked) or either with the Physics-of-Failures approach.

- The first link is achieved by using a proportionnal hazard model developped by Cox [2]. The Cox model is mainly used in the fields of medecine or maintenance to study the influence of covariate data on different subjects. The expression of this model is composed of a base risk function which is corrected by a term that includes the covariates. The main difficulty for the Cox model is the estimation of the parameters when the covariates are time dependant.
- The second method is achieved by using First Hitting Threshold Time (FHTT) models [3]. The goal of this method is to determine the time of reaching a critical threshold for stochastic degradation curves.

FHTT models may be also used with monitored data as illustrated in figure 1. In this paper, we will focus our work on the FHTT approach applied to PoF models.
FHTT models have been already used in various applications. Whitmore [4] used such models in a survival analysis study. Van Noortwijk [5] used a gamma FHTT process to represent a loss of resistance for a dike. Lawless [6] also used a gamma FHTT process to model the evolution of cracks. Lee and Whitmore [3] summarized the recent advancements for FHTT models. Maintenance decision policies based on the FHTT theory are presented in [12] and [13].

II. Background information

A. Reliability notions

Reliability (R) is the ability of a system or component to perform its required functions under stated conditions for a specified period of time. Reliability is measured by a probability value that decreases as time goes on. If T is a stochastic failure time of an equipment, the mathematical

expression of its reliability is :

$$R(t) = P(T > t) \tag{1}$$

The complementary function of the reliability is the failure function (F). The failure function represents the repartition of failure times for a set of identical equipements that have been tested. The failure function is thus used to fit a reliability model on failure data.

$$F(t) = 1 - R(t) = 1 - P(T > t) = P(T < t) \tag{2}$$

The repartition of failure times may be represented by the density function (f). The density function is the derivative of the failure function.

$$f(t) = \frac{dF(t)}{dt} = -\frac{dR(t)}{dt} \tag{3}$$

From the above equations we define the failure rate (h) as to be the ratio of the density function by the reliability function. It indicates the risk of failure at time t according that the equipment has already survived until t.

$$h(t) = \frac{f(t)}{R(t)} \tag{4}$$

B. Reliability models

From a set of failure times, we may fit a reliability model. Usual models are :

- **Exponential**

$$R(t) = \exp(-\lambda t) \tag{5}$$

λ is the scale parameter. Exponential models have a constant failure rate and are memoryless. They are well suited when the failures occur randomly.

- **Lognormal**

$$R(t) = \Phi_{nor}(\frac{\ln(t) - \mu}{\sigma}) \tag{6}$$

μ is the mean parameter and σ is the standard deviation. Lognormal models allows to get only positive failure times by the logarithmic transformation of time.

- **Weibull law**

$$R(t) = \exp(-(\frac{t - \gamma}{\eta})^{\beta}) \tag{7}$$

η is the scale parameter, β is the shape parameter and γ is the location parameter (usually γ = 0). Weibull models are well suited for most cases as they are quite flexible with both parameters η and β. They are mainly used for components that undergo some degradation.

C. Model fitting

From a collection of N failure data, a non parametric failure function ($\hat{F}$) may be calculated. There are several methods to get this function. The basic idea is to sort the failure times by ascending order and to count the number (i) of failures occured after each time inspection. Here are some examples :

- **Kaplan-Meier**

$$\hat{F}(t_i) = \frac{i}{N} \tag{8}$$

This basic formulation presents the disadvantage of having a probability equal to 1 for the last observed failure time.

- **Product limit (or medium rank)**

$$\hat{F}(t_i) = \frac{i}{N + 1} \tag{9}$$

The denominator is increased by one to solve the problem of having a probability = 1 for the last observed failure time.

- **Rank adjust (or median rank)**

$$\hat{F}(t_i) = \left(1 + \frac{N - i + 1}{i} F_{0.50,k,l}\right)^{-1} \tag{10}$$

where $F_{0.50,k,l}$ is the Fisher-Snedecor distribution with $k = 2(N - i + 1)$ and $l = 2i$ degrés de liberté. An approached formulation may be used :

$$\hat{F}(t_i) = \frac{i - 0.3}{N + 0.4} \tag{11}$$

From this non parametric failure function $\hat{F}(t_i)$ we can adjust a reliability model. The methods to fit these models are :

- **Regression methods**
  It consists of linearising the failure function to obtain the form $Y = AX + B$.

  Example for the weibull law :

$$\ln\left(\ln\left(\frac{1}{1 - \hat{F}(t)}\right)\right) = \beta \ln(t) - \beta \ln(\eta) \tag{12}$$

Identifying the parameters, we obtain

$$\begin{cases} \beta = A \\ \eta = \exp(\frac{-B}{\beta}) \end{cases} \tag{13}$$

- **Maximum likelihood methods**
  This method consists of finding the parameters of the law that maximize the likelihood to find back the failure times. The likelihood function has the form [7] :

$$L(p) = \prod_{i=1}^{n} f(t_i|p) \tag{14}$$

Using the logarithmic transformation, the parameters that maximize the likelihood are found by taking the partial derivative for each parameter.

$$\frac{\delta \ln L(p_1, ..., p_k)}{\delta p_i} = 0 \ ; \ \ i = 1, ..., k \tag{15}$$

Example for the exponential law :

$$L(\lambda, t_i) = \prod_{i=1}^{n} \lambda \exp(-\lambda t_i) \tag{16}$$

$$\frac{\delta \ln(\lambda, t_i)}{\delta \lambda} = \sum_{i=1}^{n} \left(\frac{1}{\lambda} - t_i \right) = 0 \tag{17}$$

$$\frac{1}{\lambda} = \frac{1}{n} \sum_{i=1}^{n} t_i \tag{18}$$

III. FHTT APPROACH AND MEAN REMAINING USEFUL LIFE

First Hitting Threshold Time models are composed by :

- A stochastic degradation function $Z(t)$ that represents the evolution of a degradation process (physical wear, chemical corrosion, a loss of quality or performance)
- A critical threshold z_c that corresponds to the failure of the equipment or the process (critical stress, size of cracks, critical limit of performance,...)

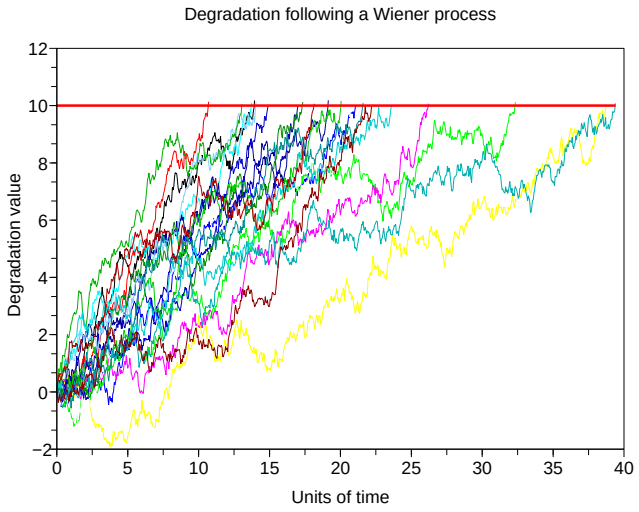

Fig. 2. Example of Gaussian stochastic degradation curves for 20 items

From the above statements, the first hitting time (T_c) to reach the critical threshold is :

$$T_c = \inf\{t|Z(t) \geq z_c\} \tag{19}$$

This formulation involves that we observed a truncated stochastic process as we do not take care of the evolution of the process when it goes beyond the threshold. For each item, the observed field is thus a random interval $[0, T_{ci}]$ as at time T_{ci} the failure occurs for item i (and $Z(T_{ci}) = z_{ci}$). Choosing a stochastic degradation model is function of the nature of the observed process and available data. Indeed for a process that mainly undergoes shocks without any loss of degradation between two consecutive shocks, a gamma model of the degradation is well suited.
The equation 19 may be linked to the reliability :

$$R(t) = P(T_c > t) \tag{20}$$

$$Z(T_c) = z_c \Leftrightarrow T_c = Z^{-1}(z_c) \tag{21}$$

$$R(t) = P(Z^{-1}(z_c) > t) \tag{22}$$

For example, if we consider the following degradation process :

$$Z(t) = Z(0) + mt + \sigma W(t) \tag{23}$$

with :

m the mean trend and σ the drift, W(t) is a Wiener process caracterised by :

- W(0) = 0 ;
- W(t) is a continuous function respect to time ;

- W(t) has independant steps according to W(t)-W(s) = N(0,t-s).

$Z(t)$ is thus a Gaussian degradation process with a linear trend. An example of degradation curves following this process is showed in figure 3 with the following parameters $m = 0.5$, $\sigma = \sqrt{0.5}$, $z_c = 10$ and a step increment of 0.1 units of time. One can proove that the failure times are distributed according to an inverse Gaussian law with density function [14] :

$$f(t, z_c, \sigma, m) = \frac{z_c}{\sqrt{2\pi}\sigma} t^{-3/2} \exp\left[-\frac{(z_c - mt)}{2\sigma^2 t}\right] \quad (24)$$

If the degradation relationship $Z(t)$ is continuous respect to time, we can define a damage index DI at time t_i by :

$$\mathrm{DI}(t_i) = \frac{Z(t_i) - Z(t_0)}{Z(T_c) - Z(t_0)} \quad (25)$$

The mean residual lifetime at time t (MRL(t)) may be obtained from the reliability information by [8] :

$$\mathrm{MRL}(t) = \frac{\int_t^\infty R(t)dt}{R(t)} \quad (26)$$

At t=0, we obtain the mean time to failure (MTTF) :

$$\mathrm{MRL}(0) = \frac{\int_0^\infty R(t)dt}{R(0)} = \frac{\int_0^\infty R(t)dt}{1} = \mathrm{MTTF} \quad (27)$$

The figure 4 presents the evolution of the mean residual life obtained from the failure rate function respect to time for a modified Weibull extension distribution with a reliability function [9] :

$$R(t) = \exp\left[\eta \left(1 - \exp\left(\frac{\mathrm{t}}{\alpha}\right)^\beta\right)\right] \quad (28)$$

The figure 5 shows a comparison of the mean residual life function obtained by eq. 26.

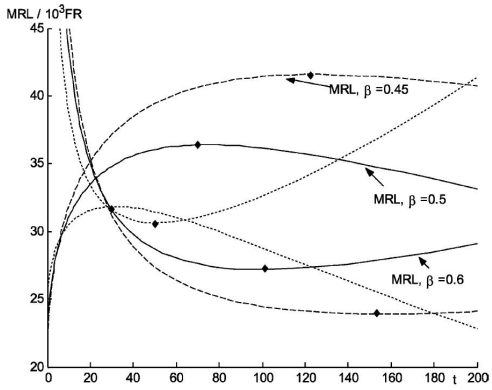

Fig. 3. MRL(t) and FR(t) for a Weibull extension distribution (α = 100, η = 2) [9]

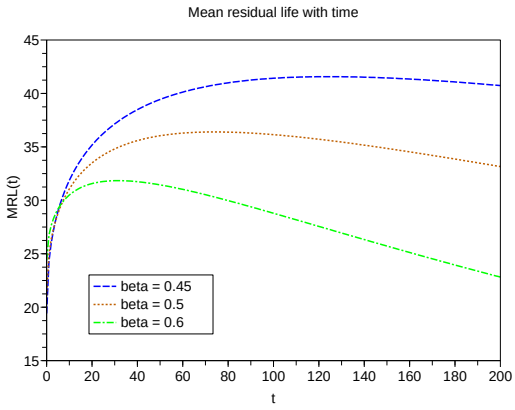

Fig. 4. MRL(t) for a Weibull extension distribution (α = 100, η = 2) by eq. 26

IV. Theoritical illustrations

This approach is applied to two examples. The first one considers the evolution of crack growth according to Paris law. The second one considers the degradation of electrical resistances according to an Arrhenius type formulation and its consequences on the output voltage threshold.

A. Paris degradation law

The first application concerns the crack growth for mechanical equipments. The degradation model is the simplified Paris relationship [10] which links the evolution of a crack size a with the number of cycles N by :

$$\frac{da}{dN} = C\ \Delta K^m \quad (29)$$

with $\Delta K = K_{max} - K_{min}$. K is the stress intensity factor ($\mathrm{MPa}\sqrt{\mathrm{m}}$). This factor may have various forms depending of the shape function $F(a)$:

$$K = \sigma\ \sqrt{\pi a}\ F(a) \quad (30)$$

For this example we consider $F(a) = 1$.

$$\Delta K = (\sigma_{max} - \sigma_{min})\ \sqrt{\pi\ a} \quad (31)$$

The sollicitation is supposed to be composed of tensile strength and compressive strength with $\sigma_{mean} = 0$. σ_{min} corresponds to compressive strength and is fixed to 0 as a compressive strength tends to close the crack.

$$\Delta K = \sigma\ \sqrt{\pi a} \quad (32)$$

with $\sigma = \sigma_{max}$ and

$$\frac{da}{dN} = C\ \sigma^m\ (\pi\ a)^{m/2} \quad (33)$$

$$\frac{1}{dN} = \frac{C\ \sigma^m\ (\pi\ a)^{m/2}}{da} \quad (34)$$

$$N_c = \int_{a_0}^{a_c} (C\ \sigma^m\ (\pi\ a)^{m/2})^{-1} da \tag{35}$$

$$N_c = \frac{1}{C\ \sigma^m\ \pi^{m/2}} \int_{a_0}^{a_c} a^{-m/2} da \tag{36}$$

$$N_c = \frac{a_c^{-(m/2)+1} - a_0^{-(m/2)+1}}{(-(m/2)+1)\ (C\ \sigma^m\ \pi^{m/2})} \tag{37}$$

Thus the number of cycles to critical failure (N_c) may be calculated by the above equation if we know the parameters. For example :

- $a_0 = 0.001$ m
- $a_c = 0.08$ m
- $\sigma = 100$ MPa
- $m = 3$
- $C = 5.28\ 10^{-12} \frac{\text{m}}{\text{cycle}} (\text{MPa}\sqrt{\text{m}})^{-m}$

We obtain $N_c = 1.91\ 10^6$ cycles

Then we introduce some dispersion on the parameter C according to a Weibull law distribution. The scale parameter is equal to the nominal value of C $\eta_C = 5.28\ 10^{-12} \frac{\text{m}}{\text{cycle}} (\text{MPa}\sqrt{\text{m}})^{-m}$ while the shape parameter is arbitrary fixed to $\beta_C = 40$ to represent the dispersion.

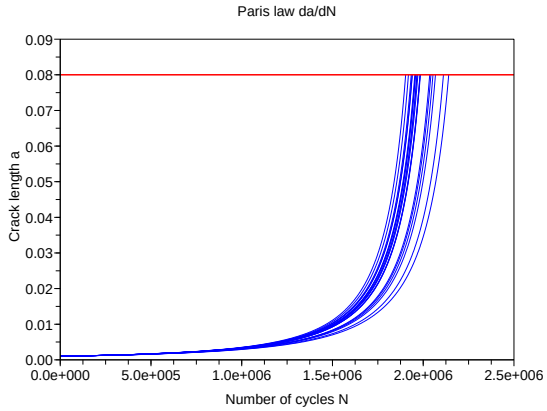

Fig. 5. Paris degradation curves da/dN

The figure 6 represents the evolution of the crack size a with the number of cycles N for 20 items with the above parameters ($a_0, a_c, \sigma, m, C \approx \text{Weibull}(\beta_C, \eta_C)$).

The reliability function may be expressed by :

$$R(N) = P(N_c > N) \tag{38}$$

$$R(N) = P\left(\frac{a_c^{-(m/2)+1} - a_0^{-(m/2)+1}}{(-(m/2)+1)\ (C\ \sigma^m\ \pi^{m/2})} > N\right) \tag{39}$$

$$R(N) = P\left(C < \frac{a_c^{-(m/2)+1} - a_0^{-(m/2)+1}}{(-(m/2)+1)\ (\sigma^m\ \pi^{m/2})\ N}\right) \tag{40}$$

and the failure function by :

$$F(N) = 1 - R(N) \tag{41}$$

C is a stochastic value following a Weibull distribution $W(\beta_c, \eta_c)$:

$$P(C < u) = 1 - \exp(-(\frac{u}{\eta_c})^{\beta_c}) \tag{42}$$

So the reliability function $R(N)$ is :

$$1 - \exp\left(-\left(\frac{a_c^{-(m/2)+1} - a_0^{-(m/2)+1}}{(-(m/2)+1)\ (\sigma^m\ \pi^{m/2})\ N\ \eta_C}\right)^{\beta_C}\right) \tag{43}$$

Simulations have been achieved on 500 items. Results are presented on the figure 7. The red stair curve is the non parametric failure function obtained by the product limit (PL) approach on simulated failure times (eq. 9). The long dash dot cyan curve is a Weibull model adjusted from the non parametric failure function by the regression method (eq. 12). The dash blue curve is a lognormal model also fitted on the non parametric failure function by regression. The dot brown curve is a Weibull model fitted by the maximum likelihood estimation (MLE) method. Finally the dash dot green curve is the predicted failure function from eq. 41 and eq. 43.

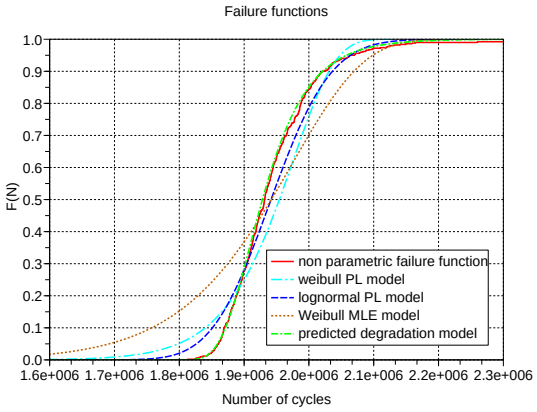

Fig. 6. Failure function for different reliability models

The predicted degradation model best fits the non parametric failure function. The weibull PL model fits the data with a correlation factor of 80% while the lognormal model fits the data with a correlation factor of 94% (table I).

The reliability obtained by the predicted degradation model allows us to predict the mean residual lifetime for a given damage index. For a DI = 0.5 we can find the mean number of cycles N_i corresponding to this DI by eq. 25.

$$\text{DI}(N_i) = \frac{a(N_i) - a(0)}{a(N_c) - a(0)} \tag{44}$$

$$0.5 = \frac{a(N_i) - 0.001}{0.08 - 0.001} \tag{45}$$

We find that the mean crack length $a(N_i)$ for DI = 0.5 is 0.0405 m. The mean number of cycles N_i may be obtained by eq. 37

$$N_i = \frac{a(N_i)^{-(m/2)+1} - a(0)^{-(m/2)+1}}{(-(m/2)+1)\,(C\,\sigma^m\,\pi^{m/2})} \tag{46}$$

We find $N_i = 1.813$ Mcycles. Finally eq. 26 gives us the mean residual lifetime.

$$\text{MRL}(1.813 \text{ Mcycles}) = \frac{\int_{1.813 \text{ Mcycles}}^{\infty} R(t)dt}{R(1.813 \text{ Mcycles})} \tag{47}$$

The MRL for an observed DI = 0.5 before the crack reaches the threshold worth 126334 cycles.

TABLE I
RESULTS OBTAINED FOR THE 4 RELIABILITY MODELS

Model	scale	shape	correlation	MRL(1.813 Mcycles)
Weibull PL	1.977 Mcycles	31.24	75%	0.143 Mcycles
Lognormal PL	14.48 cycles	0.037	90%	0.138 Mcycles
Weibull MLE	1.979 Mcycles	18.87	-6455	0.155 Mcycles
Degradation	————	40	99%	0.126 Mcycles

We can see that the degradation reliability model is the pessimistic model for the MRL calculation.

B. Electrical resistance degradation

This second example concerns the increase of electrical resistance values over time [11]. For an electrical system, this increase of resistance values will have an effect of the output voltage. It is well known that the inital value of resistances may differs by some percentages of the nominal value. The goal is to determine the impact of this initial dispersion on the evolution of the output voltage. Lets consider the following basic electric diagram (figure 8).

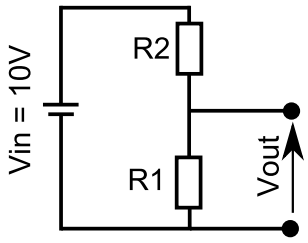

Fig. 7. Electrical diagram

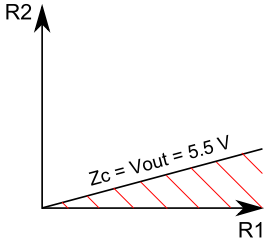

Fig. 8. Failure : V_{out} > 5.5 V

The link between the input voltage and the output voltage is

$$V_{out}(t) = \frac{R_1(t)}{(R_1(t) + R_2(t))}\,V_{in} \tag{48}$$

We consider the input voltage $V_{in} = 10$ V fixed in time. Nominal initial values for R_{01} and R_{02} are both fixed to $5\ \Omega$ and supposed to be affected by the same dispersion. The expected initial nominal value for V_{out} is thus equal to 5 V. The maximum output voltage allowed is fixed to 5.5 V. A weibull distribution is chosen to consider some dispersions on the initial values of the resistances.

$$P(R_{01}, R_{02} < X) = 1 - \exp\left(-\left(\frac{X}{\eta}\right)^{\beta}\right) \tag{49}$$

η = 5 Ω corresponds to the expected initial value and β is fixed to 40 to have a dispersion on $R_{01,2}$ that ranges from $[4, 5.5[$ with a high probability.

Resistances values will degrade over time due to temperature effect. This is known as the resistance drift $\frac{\Delta R}{R}$ and can be modelized by an Arrhenius type formulation.

$$\frac{\Delta R(t)}{R_0} = \frac{R(t) - R_0}{R_0} = \alpha\ t \exp\left(-\frac{E_a}{k\,T}\right) \tag{50}$$

where :

- E_a is the activation energy = 0.9 eV.
- α is the pre-exponential constant. α_{R1} = 1.624 10^{13} Ω/time unit and α_{R2} = 1.624 10^{12} Ω/time unit.
- k is the Boltzmann's constant = 8.6 $10^{(-5)}$ eV/K.
- T the temperature = 293 K.

Equation 50 may be transformed in

$$R(t) = R_0\ \left(1 + \alpha\ t \exp\left(\frac{-E_a}{k\,T}\right)\right) \tag{51}$$

Subsituting the parameters by their values we have :

$$\begin{cases} R_1(t) = R_{10}\ (1 + 0.005\ t) \\ R_2(t) = R_{20}\ (1 + 0.0005\ t) \end{cases} \tag{52}$$

First of all we will established the mathematical relationship that gives the failure time (= time from which $V_{out} > 5.5V$). From equation 48, introducing the ratio $R1(t)/R2(t) = A(t)$:

$$V_{out}(t) = \frac{R1(t)/R2(t)}{((R1(t)/R2(t)) + 1)}\,V_{in} \tag{53}$$

$$V_{out}(t) = \frac{A(t)}{(A(t) + 1)}\,V_{in} \tag{54}$$

At T_c The threshold $V_{max} = 5.5V$ is reached

$$V_{out}(T_c) = \frac{\frac{R_{10}\ (1+0.005T_c)}{R_{20}\ (1+0.0005T_c)}}{(\frac{R_{10}\ (1+0.005T_c)}{R_{20}\ (1+0.0005T_c)} + 1)}\ V_{in} = V_{max} \quad (55)$$

Isolating T_c, we obtain :

$$T_c = \frac{\frac{R_{10}}{R_{20}} + 1 - \frac{R_{10}}{R_{20}}\frac{V_{in}}{V_{max}}}{0.005(\frac{R_{10}}{R_{20}}\frac{V_{in}}{V_{max}} - \frac{R_{10}}{R_{20}} - 0.1)} \quad (56)$$

$R_{10}/R_{20} = A_0$ being the initial ratio of the resistances,

$$T_c = \frac{A_0\ (1 - \frac{V_{in}}{V_{max}}) + 1}{0.005\ (A_0(\frac{V_{in}}{V_{max}} - 1) - 0.1)} \quad (57)$$

Equation 57 allows to predict the failure times by the knowledge of the initial values of $R_{01,2}$ and the ratio V_{in}/V_{max}. Table II shows a comparison between simulated times and predicted times with equation 57 for 10 items.

TABLE II
SIMULATED AND PREDICTED TIMES COMPARISON

n^o	Tsimul	Tpred
1	41.6	41.53
2	58.4	58.34
3	59.0	58.87
4	56.4	56.15
5	56.0	55.80
6	51.2	50.97
7	49.0	48.73
8	57.6	57.37
9	46.2	45.87
10	63.8	63.76

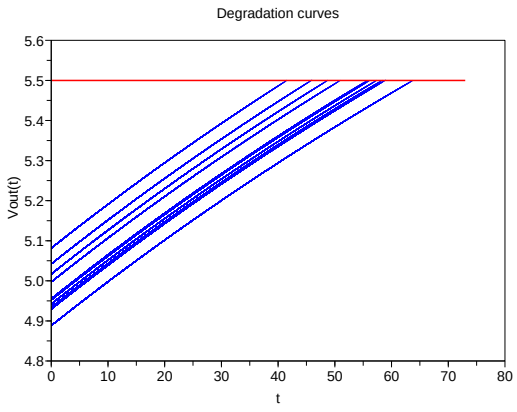

Fig. 9. Degradation curves from random initial values of resistances

The reliability function may be also predicted as well.

$$R(t) = P(T_c > t) \quad (58)$$

$$P\left(\frac{A_0\ (1 - \frac{V_{in}}{V_{max}}) + 1}{0.005\ (A_0\ (\frac{V_{in}}{V_{max}} - 1) - 0.1)}\ > t\right) \quad (59)$$

Isolating the factor A_0 in the left hand term :

$$P\left(A_0\ < \frac{1 + 0.0005t}{(\frac{V_{in}}{V_{max}} - 1)(1 + 0.005t)}\right) \quad (60)$$

Remembering that the initial values of resistances R_{01} and R_{02} are distributed according to a Weibull law with shape parameter $\beta = 40$ and scale parameter $\eta = 5$, the ratio of the initial resistances A_0 is distributed according to a Weibull law with shape parameter $\beta_A = 40$ and a scale parameter $\eta_A = R_{01}/R_{02}$. A_0 is a stochastic value following a Weibull distribution $W(\beta_{A_0}, \eta_{A_0})$

$$P(A_0\ < u) = 1 - \exp\left(-\left(\frac{u}{\eta_A}\right)^{\beta_A}\right) \quad (61)$$

Thus equation 60 becomes :

$$R(t) = 1 - \exp\left(-\left(\frac{1 + 0.0005\ t}{(\frac{V_{in}}{V_{max}} - 1)(1 + 0.005\ t)\ \eta_A}\right)^{\beta_A}\right) \quad (62)$$

Equation 62 is different from usual Weibull expressions as the time factor also appears at the denominator. Simulations have been achieved on 500 items (figure 11). The red stair curve is the non parametric failure function obtained by the product limit approach on simulated failure times (eq. 9). The dash blue curve is a Weibull model adjusted from the non parametric failure function by the regression method (eq. 12). The dot yellow curve is a lognormal model also fitted on the non parametric failure function by regression. The dash dot green curve is the predicted failure function from eq. 62.

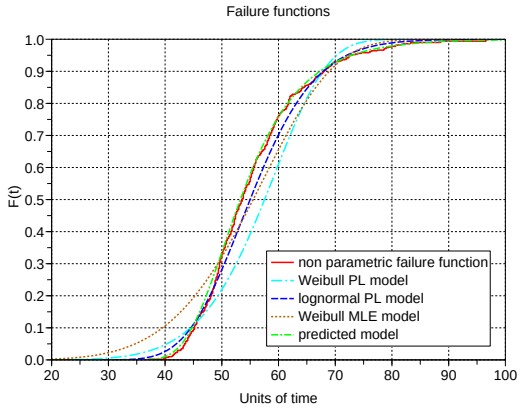

Fig. 10. Failures functions for different models

We can see that the predicted model best fits the data. For the adjusted models, the lognormal model has a better correlation factor (98%) than the weibull law (87%) (table III).

Residual lifetime estimation from a damage index is obtained as follow. For a DI = 0.5, we can find the mean time t_i corresponding to this DI by eq. 25.

$$\text{DI}(t_i) = \frac{V_{out}(t_i) - V_{out}(t_0)}{V_{out}(t_c) - V_{out}(t_0)} \tag{63}$$

$$\text{DI}(t_i) = \frac{V_{out}(t_i) - 5}{5.5 - 5} \tag{64}$$

We obtain $V_{out}(t_i) = 5.25$ V. By eq. 57 we obtain the time t_i corresponding to the DI = 0.5

$$t_i = \frac{A_0\ (1 - \frac{V_{in}}{V_{out(t_i)}}) + 1}{0.005\ (A_0(\frac{V_{in}}{V_{out(t_i)}} - 1) - 0.1)} \tag{65}$$

We find $t_i = 23.67$ units of time (UT) and finally eq. 26 gives us the expected mean remaining useful life at time t_i

$$\text{MRL}(23.67UT) = \frac{\int_{23.67UT}^{\infty} R(t)dt}{R(23.67UT)} \tag{66}$$

The MRL at time $t_i = 23.67$ for the device to reach the voltage threshold of 5.5 V worth 31.32 UT.

TABLE III
RESULTS OBTAINED FOR THE 4 RELIABILITY MODELS

Model	scale	shape	correlation	MRL(23.67)
Weibull PL	60.5 UT	7.32	86%	33.1 UT
Lognormal PL	4 UT	0.16 UT	98%	31.53 UT
Weibull MLE	59.3 UT	5.55	-1874	31.32 UT
Degradation	———	40	99%	31.32 UT

Once again, we see that the degradation reliability model is the pessimistic model for the MRL calculation.

V. CONCLUSION

This paper discussed the interest of having the knowledge of the degradation process for a device to retrieve the reliability. We focused on theoretical examples that showed that the predicted model of the reliability best fits the simulated failure times. From the reliability model based on the degradation process, the estimation of mean remaining useful life may then be achieved. The calculation of the MRL for the different reliability models showed that the degradation model is the pessimistic one for both applications.

Future works for this research consists of applying the FHTT theory to experimental degradation data and to establish a maintenance decision rule based on degradation reliability models.

REFERENCES

[1] Byington, Kalgren, *Prognostic Techniques and Critical Data Elements for Avionics*, Prognostics and Health Management for Electronics Workshop University of Maryland, 2004.

[2] Cox, *Regression Models and Life Tables (with Discussion)*, Journal of the Royal Statistical Society, Series B 34 :187-220, 2000.

[3] Mei-Ling Ting Lee, G.A. Whitmore, *Threshold regression for survival analysis : Modeling event times by a stochastic process reaching a boundary*, Statistical Science,4 :501-513,2006.

[4] G.A. Whitmore, *Assessing lung cancer risk in railroad workers using a first hitting time regression model* , Environmetrics 15(5) : 501-512, 2004.

[5] J.M. Van Noortwijk, *Gamma processes for time-dependant reliability of structures*, 2000.

[6] Jerry Lawless, *Covariates and random effects in a gamma process model with application to degradation and failure*, Lifetime data Analysis,10 :213-227,2004.

[7] O. Basile, P. Dehombreux, F. Riane, *Evaluation of the uncertainty affecting reliability models* Journal of Quality and Maintenance Engineering, Vol. 13, No 2, 2007.

[8] Peter J. Smith, *Analyse of failure and survival data*, Texts in Statistical Science, Chapman & Hall/CRC 2002

[9] M. Xie, T.N. Goh, Y. Tang, *On changing points of mean residual life and failure rate function for some generalized Weibull distributions*, Reliability Engineering and System Safety , 84, 293-299, Elsevier, 2004.

[10] R. Jones, L. Molent, S. Pitt, *Similitude and the Paris crack growth law*, International Journal of Fatigue 30, 1873-1880, 2008

[11] Johannes Adrianus Van Den Bogaard *Product lifecycle optimization using dynamic degradation models*, Thesis, Technische Universiteit Eindhoven 2005

[12] A. Grall, M. Fouladirad, *Maintenance decision rule with embedded online Bayesian change detection for gradually non-stationary deteriorating systems*, Proc. IMechE Vol. 222, 2008.

[13] Estelle Deloux, *Politiques de maintenance conditionnelle pour un systeme à dégradation continue soumis à un environnement stressant*, Thesis, École Nationale Supérieure des Techniques Industrielles et des Mines de Nantes, 2008.

[14] Mikhail Nikulin & al. *Statistique des essais accélérés*, Lavoisier, Paris, 2007.

A numerical study on the axial crushing response of pultruded tubes under blast load

D.A. Kakogiannis[1], D. Van Hemelrjick[1], J. Van Ackeren[1], J. Wastiels[1], S. Palanivelu[2], W. Van Paepegem[2], J. Vantomme[3]
[1] Department of Mechanics of Materials and Constructions, Vrije Universiteit Brussel
Pleinlaan 2, 1050 Brussels – Belgium
[2] Department of Materials Science and Engineering, Ghent University
Sint-Pietersnieuwstraaat 41, 9000 Gent – Belgium
[3] Civil and Material Engineering Department/Royal Military Academy
Renaissancelaan 30, B-1000, Brussels – Belgium

email: Dimitrios.Kakogiannis@vub.ac.be

I. Introduction

The increasing interest on safety and crashworthiness in structures leads to additional design requirements in any application where high energy absorption is required, one of which is the protection of civil structures under blast loading. Structures often are protected by claddings made from ductile materials absorbing energy because of plastic deformation [1]. Also composite unidirectional reinforced tubular sections are considered as effective energy absorbers due to the failure mechanism which increases the energy absorption capacity of the structure. In the present paper is studied the failure mechanism of a circular composite tube with corrugated edge under blast load.

II. Numerical Modeling

One type of pultruded circular composite tubes was used for the present study. The matrix was polyvinylester reinforced unidirectionally with glass fibers. The length of the specimens was 100mm the outer diameter 25.4mm and inner 21.3mm. The triggering was a corrugated pattern of 45^o at the edge of the tube. It was measured the transmitted impulse and the crushing distance of the tubes after the blast for masses from 5gr to 21gr C4 studying the effect of various stand off distances from the steel disk.

The numerical models were made in LS-DYNA 971 code. Two layers of Belyscko-Tsay quadrilateral elements were used, which were located at the mid-plane of one half of the thickness of the tube.

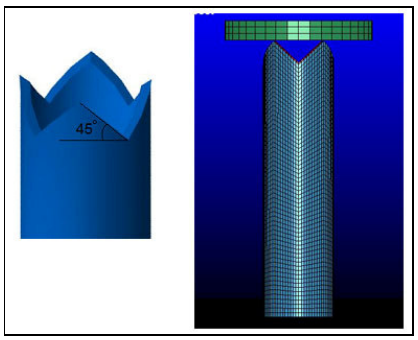

Fig. 1. Pultruded tube with triggering.

A contact algorithm was used to tie the two layers between them accounting both normal and shear forces in the interface. The constitutive material model with the criterion of Chang–Chang was used which is a modification of Hashin's failure criterion [2, 3]. The steel disk that was attached on the top of the tube was modelled as elastic and was accelerated with the algorithm for blast load that is implemented in LS-DYNA 971 code.

Acknowledgements

The financial support of FWO Research Foundation Flanders and the support from BISRU(Blast Impact and Survivability Research Unit) from Cape Town University is gratefully acknowledged.

References

[1] D. Karagiozova, G. N. Nurick, S. Chung Kim Yuen, *Energy absorption of aluminium alloy circular and square tubes under an axial explosive load*, Thin-Walled Structures, Vol.43 pp 956-982, 2005.

[2] Haipeng Han, Farid Taheri, Neil Pegg, You Lu, *A numerical study on the axial crushing responseof hybrid pultruded and ±45^o braided tubes*, Composite Structures 80 (2007) 253–264.

[3] *Ls-Dyna Keyword User's Manual*, V971, LSTC, Livemore, CA, 2007.

Proceedings of the 8th National Congress on Theoretical and Applied Mechanics, May 28-29, Brussels, Belgium.

Micromechanical damage modeling of elastoplastic composites with misaligned short fibers

Slim Kammoun[1], Issam Doghri[1], Laurent Delannay[1]
[1]Université Catholique de Louvain, Center for Systems Engineering and Applied Mechanics (CESAME), 4, Av. G.Lemaître, B-1348 Louvain-la-Neuve, Belgium.
email: slim.kammoun@uclouvain.be, issam.doghri@uclouvain.be, laurent.delannay@uclouvain.be

Abstract

A MICROMECHANICAL damage modeling approach is presented to predict the overall elastoplastic behavior and damage evolution in short fiber reinforced composite materials. The matrix is considered as elastoplastic and the fibers are elastic. The practical use of the approach is for thermoplastic matrix reinforced with short glass fibers. There exist several approaches to failure modeling. In a previous work [1] [2], we mainly investigated a rather new one, the so-called First Pseudograin Failure method (**FPGF**). By analogy to First Ply Failure for laminated composites, the representative volume element (**RVE**) is considered as a set of pseudograins that fail and affect progressively the stiffness of the RVE up to total failure. Each pseudograin is a two-phase composite with aligned inclusions. The overall stiffness of the composite is predicted with a two-step homogenization procedure (figure 1). In the first step, the pseudograins are homogenized individually (e.g. Mori-Tanaka scheme [3]). The second step consists in the homogenization of homogenized pseudograins. To predict rupture of each pseudograin, failure criteria - commonly used for laminates- are combined with the model. In this work, we present a new version of FPGF model in which failure criteria are replaced by an anisotropic damage model. For each pseudograin, damage is described by two variables d_l and d_t which represent, respectively, damage in the fibers direction and in the transverse one . d_l takes into account damage due to fibers breakage and fiber/matrix debonding. d_t represents damage induced by matrix cracking (figure 2). The two damage variables are governed by Weibull-type functions. Model parameters are identified rigorously from available experimental data. The model is implemented in the finite element code ABAQUS coupled to the DIGIMAT composite materials software and results are compared with experimental curves.

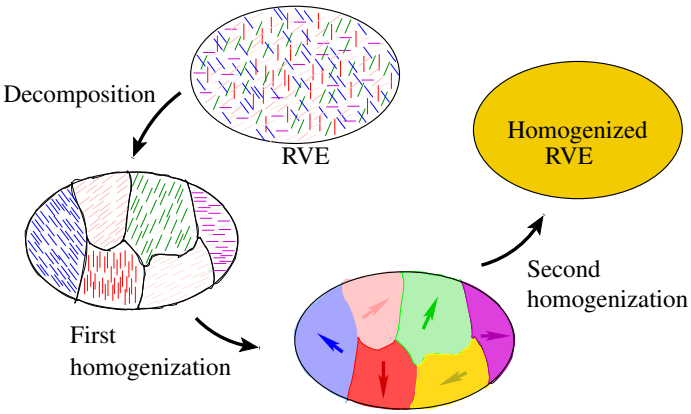

Fig. 1. Two-step homogenization procedure.

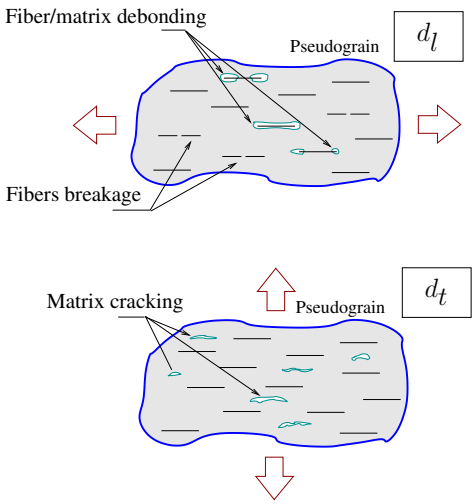

Fig. 2. Damage variables at the pseudograin level.

Acknowledgments

We gratefully acknowledge the support of the following initiative and institution: Région Wallonne through DAMOFIP project and **e-Xstream** engineering SA (Available from: http://www.e-xstream.com). First author thanks Laurence Brassart for her help to implement the model.

References

[1] Slim Kammoun, Issam Doghri, Laurent Delannay, *Micromechanical modeling of the progressive failure of composites with misaligned inclusions.*, Euromediterranean Symposium on Advances in Geomaterials and Structures Second edition Hammamet, 2008 (P 307-313).
[2] Slim Kammoun, Issam Doghri, Laurent Delannay, *Micromechanical modeling of the progressive failure of elasto-viscoplastic matrix-based composites with misaligned elastic fibers.*, Advanced COmputational Methods in ENgineering (ACOMEN) -Liège, 2008.
[3] Mori T., Tanaka K., *Average stress in matrix and average elastic energy of materials with misfitting inclusions.*, Acta Matall 21 (1973) 571-574.

An investigation of the mechanical behaviour of carbon epoxy cross ply cruciform specimens under biaxial loading

A. Makris, C. Ramault, D. Van Hemelrijck
Department of Mechanics of Materials and Constructions, Vrije Universiteit Brussel
1050 Brussels, Belgium
amakris@vub.ac.be

E. Lamkanfi, W. Van Paepegem
Department of Mechanical Construction and Production, Ghent University
9000 Ghent, Belgium

Abstract: **In the present study carbon epoxy cruciform type specimens with a cross ply lay up, were biaxially and uniaxially loaded in their plane using four independent servo-hydraulic actuators. Four different biaxial loading ratios were investigated while the applied load was quasi-static. A comparison between experimental observations for the strain evolution of the biaxially loaded central section of the specimen coming from digital image correlation measurements (DIC) and a three dimensional finite element damage model (FEDM) will be shown. Furthermore the failure loads coming from the load shells of the machine were straightforward compared with the output of the FEDM.**

Keywords: **Biaxially loaded, Digital Image Correlation (DIC), Finite Element Damage Model (FEDM)**

INTRODUCTION

The lack of reliable multiaxial or even biaxial experimental data to validate failure theories is the critical step in the evolution and a most efficient usage of composite materials [1]. Due to the complex anisotropic behaviour of composite materials more advanced experimental testing is needed. The current practice of using uniaxial test results to predict failure for multiaxial stress states seems inadequate. To study the mechanical behaviour of fibre reinforced polymeric matrix composite laminates under static and cyclic in-plane complex stress states a horizontal biaxial loading frame and a special cruciform type specimen have been developed. The reliability of the experimental failure data depends a lot on the proper design of the cruciform specimen and in the accuracy of the measurements [2]. The specimen should fulfil some requirements as failure must occur mainly in the biaxially loaded centre and the strain distribution should also be uniform. Smits et.al. [3] proposed a geometry to satisfy these requirements. In the present study the evolution of the strain of the biaxially loaded central section of the common used cruciform geometry [4,5] was experimentally and numerically investigated. Furthermore a progressive damage modelling (PDM) [6,7] technique was applied using the commercial finite element software 'Ansys' in order to simulate the biaxial mechanical test.

A) Experimental part

A1. Plane biaxial test bench for cruciform specimens

The biaxial test rig, see Fig.1, developed at VUB has a capacity of 100kN in each perpendicular direction, but only in tension, limiting the experimental results to the first quadrant of the two-dimensional stress space. This type of machine is often used in order to actualize mechanical biaxial tests of composite materials or metals [8-10]. As no cylinders with hydrostatic bearing were used, failure or slip in one arm of the specimen will result in sudden radial forces which could seriously damage the servo-hydraulic cylinders and load cells. To prevent this, hinges were used to connect the specimen to the load cells and the servo-hydraulic cylinders to the test frame. Using four hinges in each loading direction results in an unstable situation in compression and consequently only tension loads can be applied. The stroke of the cylinders is 150mm. The loading may be static or dynamic up to a frequency of 20Hz. Each cylinder is independently controlled and any type of loading waveform, including spectral sequences of variable amplitude, can be efficiently introduced using the dedicated software and control system.

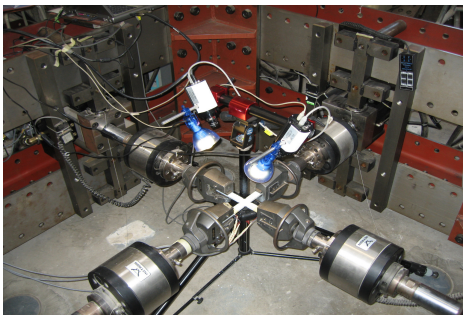

Fig.1. Plane biaxial test device for testing cruciform specimens.

A2. Cruciform specimen and mechanical properties of the UD material

The specimens tested were manufactured using carbon UD SE84 prepreg material. The lay up used for this study was $[(90/0)_2$, $(0/90)_2]_{sym}$ and the thickness of each lamina was 0.28mm. This gives a total nominal thickness of 4.48 mm for the arms of the cruciform specimen and of 2.24 mm for the

biaxially loaded zone where one group of $[(90/0)_2]$ was milled away at each side of the specimen, see Figure 2a. A special speckle pattern was also applied on the surface of the specimen in order to actualize accurate measurements using the Digital Image Correlation Technique, see Figure 2b.

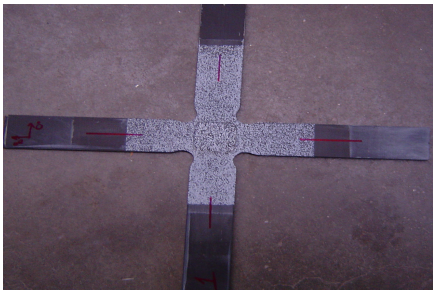

Fig 2a. Cruciform geometry.

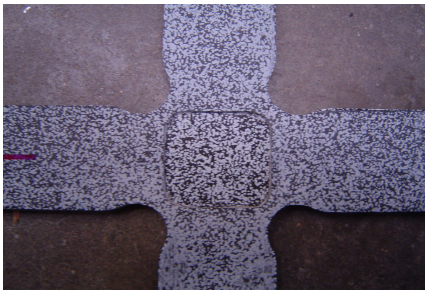

Fig 2b. Applied special speckle pattern.

In order to obtain the elastic properties and strength of the UD material, mechanical tests were realized. For the uniaxial properties (E_1, E_2, ν_{12}...), rectangular coupons were tested under tension or compression while for the shear properties v-notched specimens were selected. In table 1 the elastic properties of the UD SE84 material can be found. These properties together with the strength of the lamina, see table 2, were used as basic input for the FEDM.

Table 1.
Elastic properties of the UD SE84 carbon lamina.

	E_1 [GPa]	E_2 [GPa]	E_3 [GPa]	G_{12} [GPa]	G_{23} [GPa]	G_{13} [GPa]	ν_{12} -	ν_{23} -	ν_{13} -
average	124.3	8.14	7.8	4.49	2.44	3.93	0.32	0.32	0.32

where ‘123’ is the fiber coordinate system, ‘1’ is the fiber direction, ‘2’ is the direction transverse to the fibers and ‘3 is the direction through thickness.

Table 2.
Strength of the UD SE84 carbon lamina.

	X_T [MPa]	X_C [MPa]	Y_T [MPa]	Y_C [MPa]	Z_T [MPa]	Z_C [MPa]	S_{12} [MPa]	S_{23} [MPa]	S_{13} [MPa]
average	2751	1180	25	165	42	165	106.9	35.21	97.87

where X_T, X_C are the tensile and compressive strength longitudinal to the fibers, Y_T, Y_C are the tensile and compressive strength transverse to the fibers normal to ‘13’ plane, Z_T, Z_C are the tensile and compressive strength transverse to the fibers normal to ‘12’ plane and Sij, i,j=1,2,3, is the shear strength of the lamina.

A3. Strain measurements using Digital Image Correlation technique

To be able to study the symmetry of the strains and the occurring shear strains experimentally, full field methods are necessary. Strain measurements using a strain gage or extensometer are not sufficient because both give an average value of the deformation along their gauge length and sometimes fail earlier than the specimen.

The strain field of glass epoxy specimens of the same geometry under uniaxial or biaxial loading conditions was in a previous study extensively investigated [2]. There due to the complexity of the specimen's geometry different measurement techniques (Strain gages, Digital Image Correlation (DIC) and Electronic Speckle pattern Interferometry (ESPI) techniques were used combined or separately) were applied to investigate strain concentrations and finally obtain the valid strain field of the zone of interest.

In the present study Digital Image Correlation Technique (DICT) was used to follow the strain evolution of the areas of interest. DICT is an experimental technique, which offers the possibility to determine in-plane and out of plane displacement and deformation fields of the surface of objects under any kind of loading, based on a comparison between images taken at different load steps. By deriving the displacement field the desirable strain field is obtained.

In the present study four different load ratios (Fx/Fy) were applied on cruciform specimens (three different biaxial cases 1/1, 2/1, 3/1 and a uniaxial case 1/0) and for each ratio average two specimens were tested in tension until total failure, see Figure 3a. Biaxial testing of cruciform specimens was performed using load control of the machine with a constant load speed of 5kN/min and uniaxial testing of them by displacement control with a displacement rate of 1mm/min. Below is also presented the failure envelope for the cross-ply cruciform laminate in strain space from measurements coming from the geometrical centre of the central section, see Figure 3b.

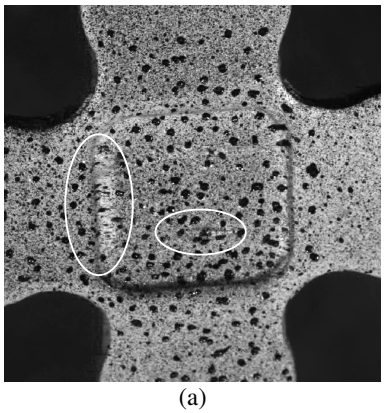

(a)

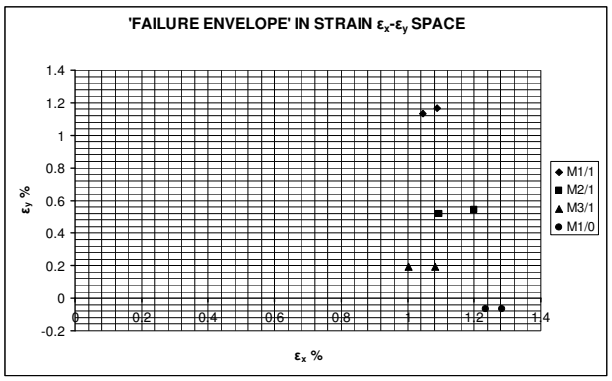

(b)

Figure 3. (a) A specimen under 80% of the total failure load (3/1 load case), marked are local damaged areas, (b) Failure envelope of the cross ply laminate.

B) Numerical Part

B.1 Progressive damage modelling

A three dimensional finite element model was developed using the commercial software 'Ansys' in order to compare with the experimental observations. The model is using a progressive damage scenario. Progressive damage modelling (PDM) technique has four basic steps, (i) stress analysis of the structure, (ii) failure analysis in an element basis, (iii) degradation of the properties of the failed elements and (iv) application of a total failure criterion. The procedure stops when the total failure occurs which means that the structure cannot take any additional load. Below is briefly described how each step of the method was used in order to simulate the testing of the cruciform specimen.

Stress analysis was done by using 'Ansys' solver

Failure analysis:

Six different failure modes are considered namely, matrix tensile and compressive cracking, fibre tensile and compressive cracking, and delamination in tension and compression. These failure modes represent basic failure modes of the composite materials. For the detection of the failure modes, a set of 3-D stress-based polynomial failure criteria is used. Specifically, Hashin-type failure criteria [11] are used for detecting the failure modes of the matrix, the fibre compressive mode and delamination, while for detecting the fibre tensile mode, the Maximum Stress was used. The specific set of failure criteria has been proposed in [12, 13], in which it has been successfully used for analysing failure of composite bolted joints subjected to tensile loading.

Degradation:

The material properties degradation is performed in an element basis. That means that each time a specific failure mode is satisfied for an element then its material elastic properties are being degradated properly according to degradation rules. Details about the nature of these rules can be found in [12, 14, and 15]. The proposed degradation

scenario was extended in this study, by means that the second time that the same failure criterion is satisfied in a specific element, the material properties of it are being degradated close to zero (and not to zero, to avoid numerical instabilities). Three different degradation factors are used for matrix failure, fiber failure and delamination failure.

Total failure:

The total failure criterion declares when the structure cannot take any additional load. It depends on the nature of the problem what can be considered as total failure. In this study total failure is achieved when the displacement of an edge node of an arm of the specimen exceeds a predefined value (ex. 20mm). It can be also shown as a sudden change of the slope of the Load –displacement graph. Below the Load-Displacement graph is plotted for the uniaxial case from the FEDM and from the experimental data see Figure 4.

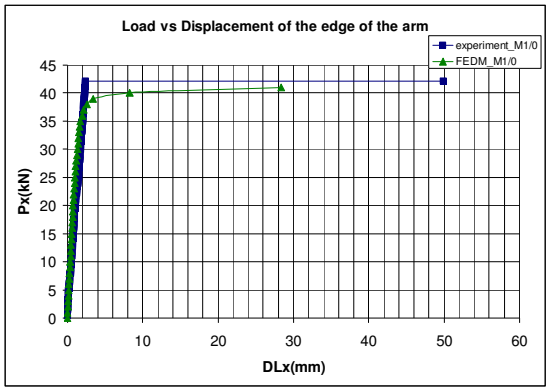

Figure 4. Load – displacement graph for the edge of the specimen

B.2 Flowchart of the model

A computer program has been created using 'ANSYS' FE code [16] in order to implement the progressive damage technique and simulate the mechanical testing of the cruciform specimen. The geometry of the specimen was parametrically built which allowed modifications of the dimensions easily to be done. An important feature of the program is that the steps of failure analysis and material property degradation have been programmed in a separate subroutine. This adjustment gives the ability to choose failure criteria and degradation rules according to the specific case studied. The program is explained by the flowchart shown in Fig. 5 and involves the following steps: (i) creation of the 3-D model by giving as input the material properties, the geometry of the examined configuration, the boundary conditions, the initial load and the load step, (ii) performing stress analysis using 'Ansys' solver to calculate the stresses, (iii) check for final failure (iv) performing failure analysis by applying the failure criteria, (v) check for failures; if no failure is predicted, the applied load is increased by a pre-defined increment and the program returns to stress analysis; if a mode of failure is predicted the program continues to the next step, (vi) degradation of material properties increase load and return to stress analysis.

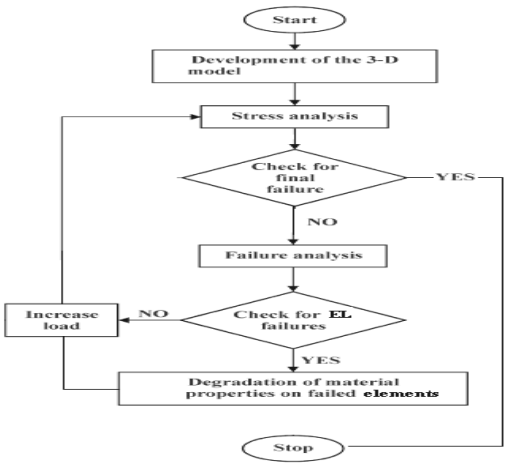

Figure 5. Flowchart of the Finite Element Damage Model

B.3 Cruciform modelling using solid elements

For the 3d modeling of the specimen 'solid46' element type [17] was selected. 'Solid46' is an 8-node layered solid element, designed to model layered thick shells or solids, with three degrees of freedom at each node: translations in the nodal x, y, and z directions. For the cruciform modeling through thickness one element corresponds to one layer, see fig. 6.

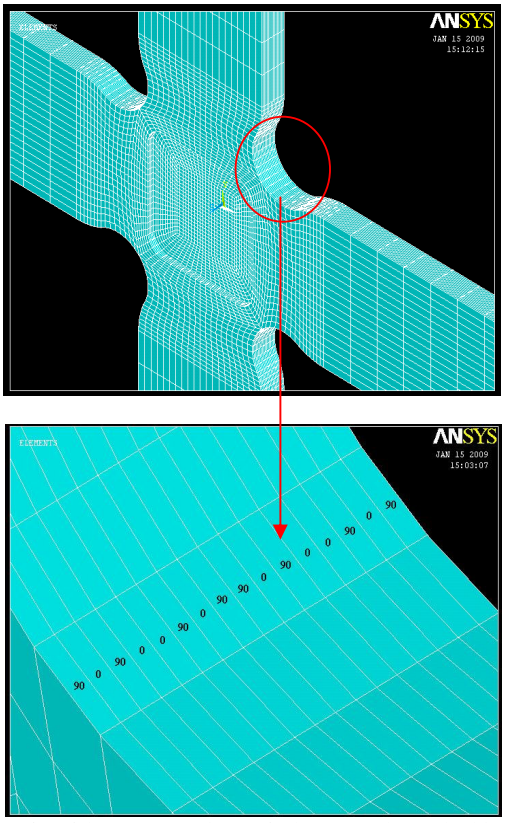

Figure 6. 16 layers meaning 16 elements through thickness or 1 element/layer

C) Comparison between FEDM and DIC observations

Below, table 3, are compared the failure loads as measured from the load shells of the biaxial machine with the output failure loads from the finite element program. The variation of the results was from 2% to 6%.

Table 3. Failure loads

BIAXIAL RATIO	EXPERIMENTS		FEDM		FEDM vs EXPERIMENTS
	Failure Fx (kN)	Failure Fy (kN)	Failure Fx (kN)	Failure Fy (kN)	variation %
M1/1	42.10	42.16	43.00	43.00	2.09
M1/1b	40.50	40.71	43.00	43.00	5.81
M2/1	44.41	22.21	42.00	21.00	5.75
M2/1b	42.35	21.17	42.00	21.00	0.82
M3/1	37.78	12.59	40.00	13.33	5.54
M3/1b	37.57	12.52	40.00	13.33	6.08
M1/0	42.14	0.00	41.00	0.00	2.77
M1/0b	42.40	0.00	41.00	0.00	3.41

Below, figure 7, are presented the load strain graphs from the four loading cases, for both FEDM and from the DICT measurements, from the centre of the specimen. Strain is plotted for both directions (e_{xx}, e_{yy}) and the in-plane shear strain e_{xy} as well. For all the loading cases the shear is negligible and there is a good correlation between measurements and the FEDM.

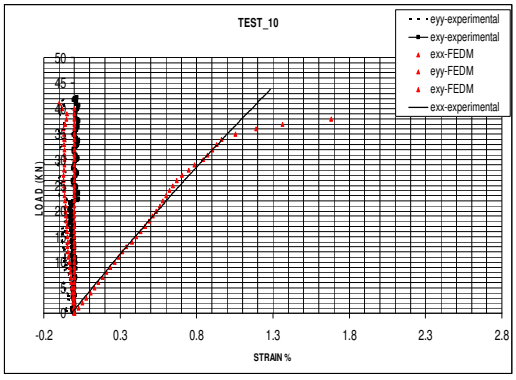

(a)

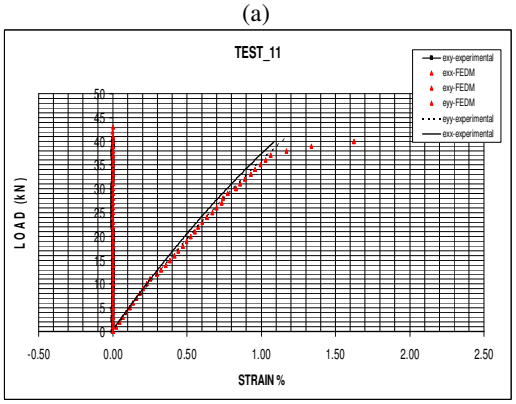

(b)

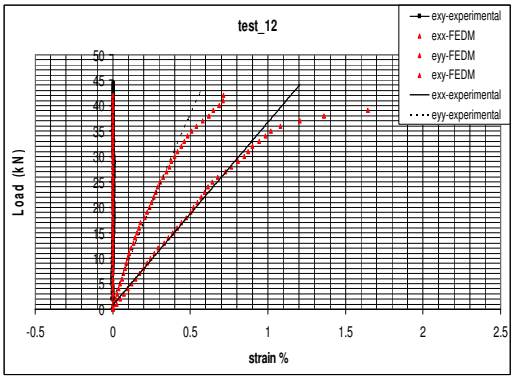

(c)

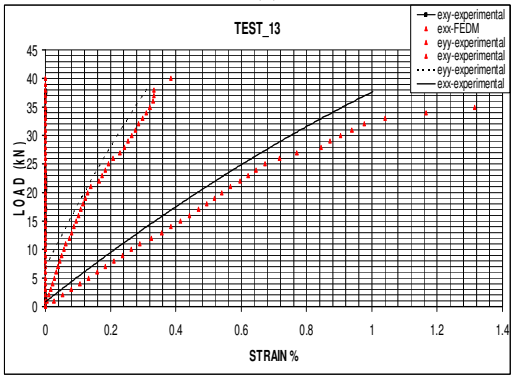

(d)

Figure 7. A comparison between DIC measurements and the FEDM for the load-strain graphs for the four loading cases.

A quantitative as well qualitative comparison between the first principal strain distribution coming from the DIC measurements and the finite element program is shown in Figure 8. The data are plotted for 50% of the total failure of each loading case.

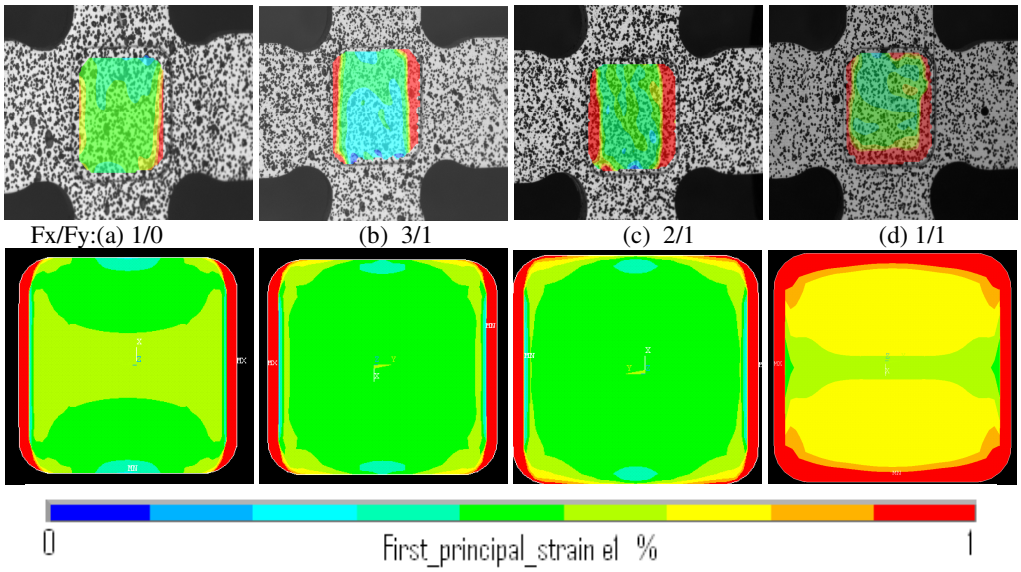

Figure 8. First principal strain for the four load cases i) measured using DICT (above) ii) calculated and presented for the central biaxially loaded section from the FEDM (below).

Conclusion/Future

The finite element model with the progressive damage scenario implemented showed good correlation with the experimental observations coming from the DIC measurements and the data from the load shells of the machine. The variation for the failure loads coming from the FEDM and the experiments is kept between 2-6 %. Moreover there is a good match, quantitative and qualitative, concerning the strain field of the central biaxially loaded section.

An optimization of the cruciform specimen using a shell finite element model and a gradient optimization technique has been done. There as optimization objective is used the uniformity of the central strain field and the concentration of the damage in the central biaxially loaded section. The 3d model which is presented here and proved to produce reliable results will be used as a simulation tool of the experiment in order to 'fast' evaluate the outputs of the optimization method before manufacturing and testing real specimens.

References

[1] Hinton MJ, Kaddour AS, Soden PD. Failure Criteria in Fibre Reinforced Polymer Composites: The World-Wide Failure Exercise, A Composite Science and Technology Compendium: Elsevier, 2004

[2] D. Van Hemelrijck, C. Ramault, A. Makris, E. Lamkanfi, W. Van Paepegem, D.Lecompte, "Biaxial testing of fibre reinforced composite laminates", Proceedings of the institution of mechanical engineers, part L: Journal of Materials: Design and Applications,Vol. 222, Issue L4, 2008, pp 231-239.

[3] Smits A., Van Hemelrijck D., Philippidis T.P. and Cardon A., "Design of a cruciform specimen for biaxial testing of fibre reinforced composite laminates", Composites Science & Technology, 2006:66(7-8):964-975.

[4] Yu Y, Wan M, Wu XD, Design of a cruciform biaxial tensile specimen for limit strain analysis by FEM, *Journal of materials Processing Technology*, vol 123, 67-70, 2002

[5] Welsh JS, Adams DF, An experimental investigation of the biaxial strength of IM6/3501-6 carbon epoxy cross ply laminates using cruciform specimens, *Composites Part A*, vol 33, 829-839, 2002

[6] Chang FK, Chang KY. A progressive damage model for laminated composites containing stress concentrations. J Comp Mater 1987;21: 834–55.

[7] Tan SC. A progressive failure model for composite laminates containing openings. J
Comp Mater 1991; 25:556–77.

[8]Boehler JP, Demmerle S, Koss S. A new direct biaxial testing machine for anisotropic materials. Exp Mech 1994; 34(1): 1-9.

[9]Welsh JS, Adams DF. Development of an electromechanical triaxial test facility for composite materials. Exp Mech 2000; 40(3): 312-320.

[10]Makinde A, Thibodeau L, Neale KW. Development of an apparatus for biaxial testing using cruciform specimens. Exp Mech 1992; 32(2): 138-144.

[11]Hashin Z. Failure criteria for unidirectional fibre composites. J Appl Mech 1980; 47:329–34.

[12]Camanho PP, Matthews FL. A progressive damage model for mechanically fastened joints in composite laminates. J Comp Mater 2000; 33:906–27.

[13]Camanho PP, Matthews FL. Stress analysis and strength prediction of mechanically fastened joints in FRP: a review. Comp, Part A 1997; 28A:529–47.

[14]K.I. Tserpes, P. Papanikos, G. Labeas, Sp. Pantelakis, Fatigue damage accumulation and residual strength assessment of CFRP laminates, Comp. Struct. 63 (2) (2004) 219– 230.

[15] P. Papanikos , K.I. Tserpes , G. Labeas , Sp. Pantelakis Progressive damage modelling of bonded composite repairs Theoretical and Applied Fracture Mechanics 43 (2005) 189–198

[16]ANSYS Users Manual, Version 6, Swanson Analysis Systems, Inc., 2002. 198 P. Papanikos et al. / Theoretical and Applied Fracture Mechanics 43 (2005) 189–198

[17]Taylor, R. L., Beresford, P. J., and Wilson, E. L., "A Non-Conforming Element for Stress Analysis", International Journal for Numerical Methods in Engineering, Vol. 10, pp. 1211-1219 (1976).

Proceedings of the 8th National Congress on Theoretical and Applied Mechanics, May 28-29, Brussels, Belgium.

Conjugate Heat Transfer in a Turbine Blade Internal Cooling Channel

Coletti, F.[1], Scialanga, M.[1], Arts, T.[1]
[1] von Karman Institute for Fluid Dynamics – Turbomachinery and Propulsion Department,
Chaussée de Waterloo 72, 1640 Rhode-Saint-Gènese – Belgium
email: coletti@vki.ac.be, scialang@vki.ac.be, arts@vki.ac.be

Abstract: **The present contribution is devoted to the experimental study of the conjugate heat transfer in a turbine blade cooling cavity located near the trailing edge. The cooling scheme is characterized by a trapezoidal cross-section, one rib-roughened wall and slots along two opposite walls. The Reynolds number, defined at the inlet of the test section, is set at 67500 for all the experiments. Uniform heat flux is imposed along the outer side of the rib-roughened wall. The measurements are carried out using two different ribbed walls, one in stainless steel and the other one in ceramoplastic, with thermal conductivities of 16 and 1 $Wm^{-1}K^{-1}$ respectively. Highly resolved distributions of temperature over the rib-roughened wall are obtained by means of infrared thermography. The impact of the conduction through the wall on the solid-fluid convection is demonstrated comparing the present results with purely convective experiments carried out on the same configuration. Attention is drawn on the effect of the solid-fluid conductivity ratio.**

Keywords: **internal cooling, trailing edge, conjugate heat transfer, infrared thermography.**

I. INTRODUCTION

Modern gas turbine engines use active cooling in key components of the turbine to prevent failure under the extreme operating conditions they face. There are two primary mechanisms to accomplish this, film cooling and internal forced convection cooling. In internal cooling, the air flowing through the passages is bled from the high pressure compressor, bypassing the combustor, and enters through the root of the blade. The coolant is then ejected at the blade tip, through trailing edge cooling slots or through surface film cooling holes. In modern turbine blades, there are up to seven sets of cooling passages, one each for the leading and trailing edges and the others for mid-chord passages.

The cooling passages are extremely complex, including turns, section variations, and substantial roughness in the form of ribs, pins or dimples. These devices enhance the cooling effectiveness by augmenting convective heat transfer and turbulence transport coefficients, besides increasing the surface area for convective heat transfer. The best schemes provide high cooling effectiveness with minimal coolant mass flow rates and pressure drop penalties.

An inaccurate knowledge of the internal passage heat transfer rate is a major factor in the uncertainty of turbine blade life-time prediction, resulting in less efficient internal cooling channel design. The analysis of the heat transfer distribution over the cooling channel surfaces is crucial to ensure that the maximum temperatures stay below material limits, and to calculate thermal stresses.

Reviews of mechanisms and performance of heat transfer augmentation techniques were presented by Han et al. [1]. In standard rib-roughened channels the coolant usually flows along the main channel axis. In addition, internal forced convection cooling shows its maximum effectiveness when coupled with impingement cooling. The coolant bleeds through parallel cavities via rows of holes through a dividing wall; jet arrays are produced and achieve a large heat transfer enhancement in the impingement regions. Applications of this method to ribbed cavities were demonstrated, among others, by Akella and Han [2] and Taslim et al. [3]. These authors particularly underlined the influence of the relative position of the turbulators and the holes and the rib height to hole diameter ratio.

The cross-section of an internal cooling channel varies depending on its location: the cavity near the leading edge mostly exhibits a triangular cross-section, while channels near the trailing edge can be triangular or trapezoidal. Cooling the trailing edge represent an especially challenging task, since the aerodynamic requirement of high slenderness is conflicting with the need of integrating internal cooling cavities. Cunha et al. [4] presented analytical models for representative trailing edge configurations and compared performances. To the authors' best knowledge, the first case resembling the geometry investigated in the present paper was presented by Taslim et al. [5].

All the papers above, as most of the experimental or numerical works available in literature, consider artificial thermal boundary conditions imposed at the solid-fluid interface: either the temperature (Dirichlet boundary condition) or the heat flux (Neumann boundary condition), or the heat transfer coefficient (Robin boundary condition) are specified at the solid-fluid interface. In the engine, of course, none of the above is respected. The only constraint is the interface continuity of temperature and heat flux, as it results from the coupled convective and conductive heat transfer modes. The latter is referred as conjugate (or fourth type) thermal boundary condition. If a truly realistic prediction of the metal temperature is sought, a conjugate solution of the conduction-convection problem is required, both in laboratory experiences and in numerical simulations.

A number of contributions on conjugate heat transfer are presented in literature, since the early work by Perelman [6], who first formulated the problem, and Luikov et al. [7], who provided the first analytical solution for a flat plate in convective-conductive regime. In more recent publications, the conjugate effects were extensively investigated in the field of electronic components, e.g. in Fedorov et al. [8]. Also in

turbomachinery, most of the contributions are numerically oriented, as those of Bohn and coworkers [9, 10], Heselhaus [11], and Amaral et al. [12] and Verstraete et al. [13]. Few papers deal with the conjugate investigation of rib-roughened channels, as the numerical efforts of Webb and Ramadhyani [14], Young and Vafai [15] and Iaccarino et al. [16], and the experimental investigations of Fedrizzi and Arts [17] and Agostini and Arts [18]. There are very scarce examples of experimental studies stressing the influence of the thermal conductivity of the solid, as done by Martiny [19] who extensively investigated an effusion cooling plate, using two different materials.

The present investigation addresses the experimental study of the conjugate heat transfer in a turbine blade cooling cavity located near the trailing edge, The investigated geometries and Reynolds number are representative of today's engine development technology. The measurements are performed on a model machined at a scale of about 25:1. The cooling scheme is characterized by a trapezoidal cross-section, one rib-roughened wall and slots along two opposite walls. This configuration was first investigated by Armellini et al. [20] and Coletti et al. [21, 22]; high resolution aerodynamic and purely convective heat transfer distributions, obtained imposing uniform heat flux at the solid-fluid interface, were presented. In the present contribution the heat flux is imposed at the outer side of he ribbed wall, and the influence of the conduction through the solid is investigated for two differently conductive materials.

II. Theoretical Background

A. Description of the heat transfer process

In order to obtain useful information from an experimental or numerical investigation on a model simulating a real device, an invariant descriptor of the heat transfer process should be available, i.e. the measured descriptor should be transportable from the investigated model to the field, in any geometrically similar situation (Moffat, [23]).

Among possible descriptors of the heat transfer process, the most common choice is the heat transfer coefficient, defined by Newton's law:

$$h = \frac{q_w}{\left(T_w - T_f\right)} \tag{1}$$

where q_w is the wall-normal heat flux, T_w is the wall temperature and T_f is the bulk flow temperature. Very often h is presented in terms of the adimensional Nusselt number:

$$Nu = \frac{hD_h}{k_f} \tag{2}$$

It must be noticed that the classic heat transfer coefficient definition is meaningful only for situations where either uniform wall temperature or uniform heat flux is imposed at the solid-fluid interface. Abrupt changes of the thermal boundary condition would force the heat transfer to $+\infty$ or $-\infty$ (Kays and Crawford, [24]).

However, substituting the bulk flow temperature T_f with the adiabatic wall temperature T_{ad}, i.e. the temperature of the local surface element when there is no heat transfer from it to the flow, the definition of the heat transfer coefficient can be made independent from the thermal boundary condition, provided the heat transfer is purely convective.

The conjugate heat transfer mode introduces an additional complexity, since no constraint is forced at the wall, apart from thermal equilibrium and heat flux continuity. Therefore the flux released to the flow by a surface element at a given temperature will be determined not only by the flow field, but also by the conduction through the wall.

B. Dimensional analysis

To understand the role of the various physical variables, it is useful to perform a dimensional analysis. The approach of the Buckingham Pi Theorem is followed.

In conjugate heat transfer, as in most heat transfer problems, four fundamentals units are to be considered: mass, length, time and temperature. Nine physical variables appear to play a role:

$$D, u, \rho, \mu, c_P, k_f, k_w, \theta, q_w$$

which are respectively: geometrical length scale, flow velocity, density, dynamic viscosity, specific heat capacity and thermal conductivity of the fluid, thermal conductivity of the solid, temperature driving force (T_w-T_f) and wall heat flux. Some considerations are to be made about the list of variables above: since in the present investigation the channel volume and the wall thickness are scaled with the same ratio, one geometrical variable is sufficient; the fluid temperature is preferred to the adiabatic wall temperature, as in the present case flow velocities are low, and mild heat flux and temperature changes at the wall are anticipated; finally, since the heat flux at the solid-fluid interface is related in deterministic manner to the uniform heat flux imposed at the outer side of the wall, q_0, the latter will be used. As one can see, the heat transfer coefficient has not been defined for the moment.

The conjugate heat transfer process can be described by an equation such as:

$$F_1(D, u, \rho, \mu, c_P, k_f, k_w, \theta, q_w) = 0 \tag{3}$$

According to the Buckingham Pi Theorem the number of adimensional parameter describing the phenomenon is equal to the number of physical quantities minus the number of fundamental units [25], so eq. 3 can be rearranged as:

$$F_2(\Pi_1, \Pi_2, \Pi_3, \Pi_4, \Pi_5) = 0 \tag{4}$$

where Π_i are the five adimensional parameters.
By means of the recurring sets method and proper choice of the variables, the following adimensional groups are derived:

$$\mathrm{Re} = \frac{\rho u D}{\mu} \tag{5}$$

$$\mathrm{Pr} = \frac{\mu c_P}{k_f} \tag{6}$$

$$Ec = \frac{u^2}{c_P \theta} \tag{7}$$

$$K = \frac{k_w}{k_f} \tag{8}$$

$$\Theta = \frac{k_f \theta}{q_0 D} \tag{9}$$

The first three groups are the well known Reynolds number, Prandtl number and Eckert number. The latter is a measure of the viscous dissipation in the flow, and can therefore be neglected in the present application. K is the solid-to-fluid thermal conductivity ratio, while Θ is the adimensional wall temperature. Equation 4 can now be written as:

$$F_2(\mathrm{Re}, \mathrm{Pr}, Ec, K, \Theta) = 0 \tag{10}$$

which can be made explicit for Θ:

$$\Theta = F_3(\mathrm{Re}, \mathrm{Pr}, Ec, K) \tag{11}$$

Hence, provided that Re, Pr and K are matched between engine conditions and laboratory environment, and neglecting Ec, distributions of Θ measured in the magnified model can be applied to the real internal cooling cavity of the airfoil. The defined adimensional wall temperature is therefore a first candidate as adimensional invariant descriptor of the conjugate heat transfer problem in object.

A similar reasoning can be followed if the usual heat transfer coefficient is defined. The wall heat flux becomes then redundant and the constitutive equation is:

$$G_1(D, u, \rho, \mu, c_P, k_f, k_w, \theta, h) = 0 \tag{12}$$

The adimensional analysis results in:

$$G_2(\mathrm{Re}, \mathrm{Pr}, Ec, K, Nu) = 0 \tag{13}$$

which can be made explicit for Nu:

$$Nu = G_3(\mathrm{Re}, \mathrm{Pr}, Ec, K) \tag{14}$$

If Re, Pr and K are respected, also the Nusselt number appears to be an invariant descriptor of the conjugate heat transfer phenomenon. It is remarkable that the last dimensional analysis gives the same set of adimensional groups as derived for pure convection, Schlichting [26], with the addition of the conductivity ratio K. The results from the present analysis are in fact similar to what was summarized for conjugate heat transfer by Shah and London [27], who instead use the Peclet number, which is of negligible interest here since thermal diffusion in the flow is neglected.

C. Comparison between heat transfer descriptors

Both Θ and Nu are transportable from laboratory experiments to the engine environment. Since in the present situation, as we must see, a constant fluid temperature is assumed, the adimensional temperature contains only one unknown quantity, the wall temperature. On the other hand, as pointed out by Faghri and Sparrow [28], the Nusselt number is somehow an inconvenient parameter to describe conjugate heat transfer, since it expresses the ratio of two unknowns, heat flux and temperature at the wall.

When measured, both groups can be used to validate conjugate heat transfer calculations. However, to retrieve Nu from temperature measurements one needs to solve the conduction through the wall (direct measurement of temperature and heat flux at the same location is usually not a viable solution). On the other hand, wall temperature measurements are sufficient to evaluate Θ.

Nevertheless, solving the conduction through the wall may provide important insights on the heat transfer process, as the heat flow pattern within the solid is retrieved.

Finally, when comparing results from the conjugate mode with purely convective quantities for the same configuration, as it is attempted in the present paper, the use of the Nusselt number (almost universally adopted in convection) is certainly convenient. We will show however that the impact of conduction on the convective heat transfer can be assessed also observing the adimensional wall temperature.

III. Experimental Set-up

The measurement campaign is conducted on a large scale model reproducing a trailing edge cooling channel of a modern turbine blade (Fig. 1). It consists of two adjacent trapezoidal cavities: the first one, the inlet channel, simulates the passage before the trailing edge and has a hydraulic diameter $D_{h,inlet}$ = 81.4 mm; the second one is the trailing edge cavity under investigation. The two passages are connected by a number of racetrack shaped slots with a hydraulic diameter $D_{h,mid}$ = 21.9 mm (mid-wall slots), through which coolant jets are flowing; the axes of the mid-wall slots are sloped with an angle close to 30 degrees with respect to the horizontal direction, in such a way that the crossing jets impinge on the rib-roughened wall of the trailing edge cavity. These slots present an aspect ratio AR_{mid} about 0.5 and their length is about twice their hydraulic diameter. In the rib-roughened configuration the bottom wall is equipped with squared cross-section ribs. These obstacles are inclined at 30 degrees with respect to the main axis of the channel (y-direction), their pitch is 7.5 rib heights and they present a mean blockage ratio of 0.3.

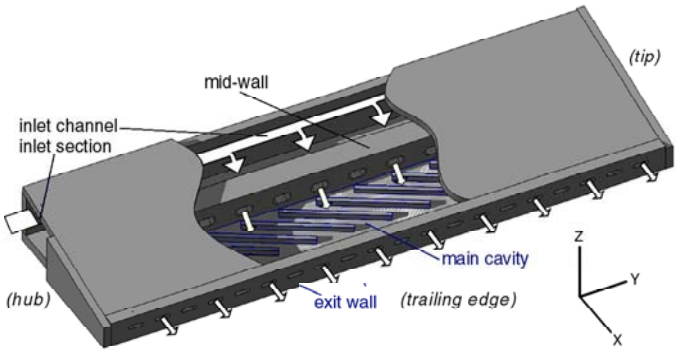

Fig. 1. Test section

The flow exits the channel through a number of horizontal racetrack shaped slots with an hydraulic diameter $D_{h,exit}$ = 11.7 mm, their aspect ratio AR_{exit} is almost 0.2 and their length is about twice their hydraulic diameter.

The test section is machined out of Plexiglas, except for the central part of the rib-roughened wall, which is of stainless steel (AISI 304) or ceramoplastic (Mykroy-Mycalex). The thermal conductivities of these two materials are listed in Tab. I.

The geometrical periodicity of the channel in the *y*-direction allows considering the investigated area to be representative of most of the test section, as demonstrated in former works by the aerodynamic [20] and convective results [21]. This justifies the choice of concentrating the experimental effort in this central area.

The experimental set-up is sketched in Fig. 2. The air flow is regulated by an upstream centrifugal blower, which discharges it through a 9 kW heat exchanger and then into a settling chamber. The latter is connected to the test section via an inlet channel, as long as the test section itself.

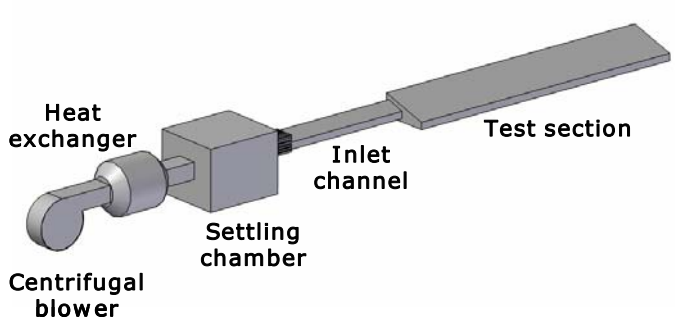

Fig. 2. Experimental set-up.

The operating conditions are monitored in the inlet section by static pressure taps, a traversing Pitot probe and a K-type thermocouple. All experiments are conducted at a fixed Reynolds number equal to 67500, based on the inlet section hydraulic diameter. In order to check pressure drop and mass flow distributions across the various slots, static pressure taps are drilled in each mid-wall and exit slot. The average Reynolds number of the crossing jets is equal to 18500. The outlet conditions are quantified by means of a Pitot probe and a K-type thermocouple traversing downstream the exit slots.

TABLE I

THERMAL CONDUTIVITIES OF THE MATERIALS USED FOR THE RIB-ROUGHENEND WALL

Material	Grade	k [$Wm^{-1}K^{-1}$] @ 300 K
Stainless steel	AISI 304	15.6
Ceramoplastic	Mykroy-Mycalex	1.15

IV. EXPERIMENTAL PROCEDURE

A. Calibration and measurement

Figure 3 schematically displays the configuration used during the experimental campaign. A uniform heat flux boundary condition is generated by dissipating DC power into a thin Inconel foil glued to the bottom side of the rib-roughened wall. The heat losses are minimized by placing strongly insulating foam underneath the heating foil. The losses evaluation is obtained by means of several K-type thermocouples. The wall temperature is measured via infra-red thermography.

The geometry of the ribbed wall prevents from acquiring a single thermogram of the whole investigated surface. Three separate IR images are grabbed and the temperature distribution over a single periodical domain is reconstructed. The domain consists of one rib and the adjacent floor.

Due to the large scale of the model, an optical window (Germanium or other IR-transparent materials) would have been very expensive. A transparent polyethylene film was used instead. Since the channel works above atmospheric pressure, the film is slightly deformed during the tests. A system of movable bars hinged to the Plexiglas smooth wall is exploited to minimize the film deflection, without impeding the optical access. Maximum film deflection is estimated to be 3 mm, and its influence is considered negligible for the development of the flow pattern.

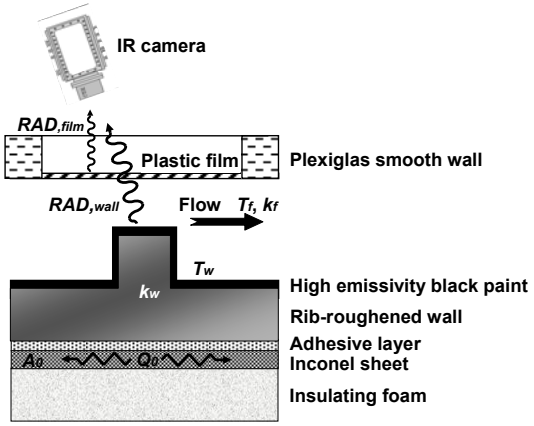

Fig. 3. Infra-red thermography scheme

An in-situ, pixel-by-pixel calibration of the IR camera is performed. Using the heat exchanger, the air is brought at a

given temperature level (controlled by a thermocouple in the inlet section). The target surface is streamlined by the air flow until isothermal conditions are achieved along its surface. The temperature of the wall is checked by 8 K-type thermocouples drilled in the slab up to 0.5 mm from the wet surface, at locations far enough from the investigated domain, not to alter the heat conduction through the wall. Once the isothermal condition is achieved, a thermogram of the surface is acquired. The procedure is repeated for several temperature levels, and the data points are fitted with a second order polynomial: for each pixel a calibration curve is obtained, correlating the object signal recorded by the IR sensor with the wall temperature (Fig. 4). When the calibration is completed, the heater is switched off and the heat flux is imposed via the Inconel foil. Once the steady state is reached, ten thermograms are grabbed within a few seconds and averaged, in order to reduce noise due to ambient radiation. The target surface is painted with high emissivity black paint from Mankiewicz GmbH.

The radiation emitted by the polyethylene film during the calibration is accounted for. When the film is streamlined by the heated air, its temperature gets higher than during the measurement. In a separate experiment, the film temperature is varied by means of a heat gun, while keeping constant the wall temperature: the variation of the object signal is correlated to the film temperature, for different wall temperature. The relation turns out to be approximately linear, with a proportionality coefficient only slightly varying for different wall temperatures.

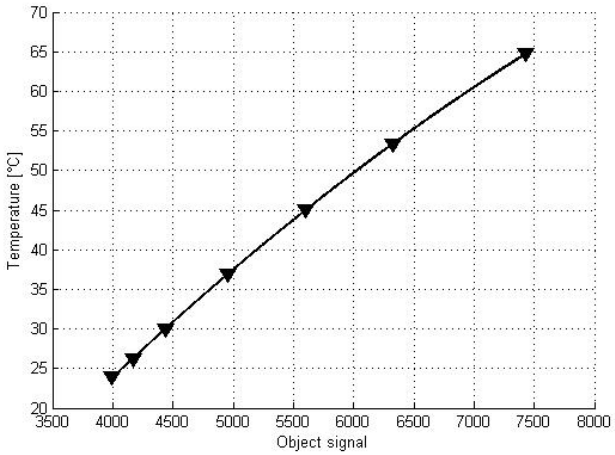

Fig. 4. Example of local (pixel-wise) calibration curve

B. Presentation of the heat transfer results

The heat transfer performance is quantified in terms of the adimensional temperature:

$$\Theta = \frac{A_0 k_f (T_w - T_f)}{Q_0 D_{h,mid}} \qquad (15)$$

where $Q_0 = VI$ is the heat flux produced by dissipating the current I due to the potential V, and A_0 is the area across which V is established. T_f is assumed to be equal to the flow temperature at the inlet section, given that the flow temperature rise across the heated section is modest.

In order to obtain heat transfer coefficient (and Nusselt number) distributions, the local wall-normal heat flux is required, which in turn implies solving the conduction in the solid. The problem can be tackled solving the Fourier equation of conduction in a three-dimensional domain representing a single ribbed domain (Fig. 5) by means of a commercial FEM solver: the measured wall temperature is imposed on the top side (ribbed surface) and the experimentally applied heat flux on the bottom side. Adiabatic and periodic wall conditions on the lateral sides are considered to be realistic. However, the values of heat flux computed on the rib-roughened wall proved to be dramatically sensitive to the imposed wall temperature: the unavoidable noise and the error associated to the uncertainty results in large over- and under-shoots in the computed derivative of the wall temperature, even when the domain is discretized with a highly refined grid. Non-physical negative values of wall heat flux appear in regions where weak heat transfer rates are expected.

Because of the lack of a realistic estimate of the Nusselt number, the choice of Θ as heat transfer descriptor is forced. The adimensional temperature distribution obtained in the model will hold in the engine environment only if all the other important adimensional parameters, Pr, Re and K, are matched. The Prandtl number is a property of the fluid, while the imposed Reynolds number is representative of a real blade cooling channel. As for the solid-fluid conductivity ratio, the values of K for a real cooled blade in operating conditions are compared in Tab. II with those obtained in the present study. The former is estimated considering Nimonic 105 (at 1250 K) as blade material and air (at 1050 K) as coolant flow. As seen, neither stainless steel nor ceramoplastic provide the correct value of the conductivity ratio. Nevertheless, as they bound a range which contains the proper value, they can be regarded as extreme conditions.

In order to properly match K, a material with conductivity about 10 $W/m^{-1}K^{-1}$ at ambient temperature should be used.

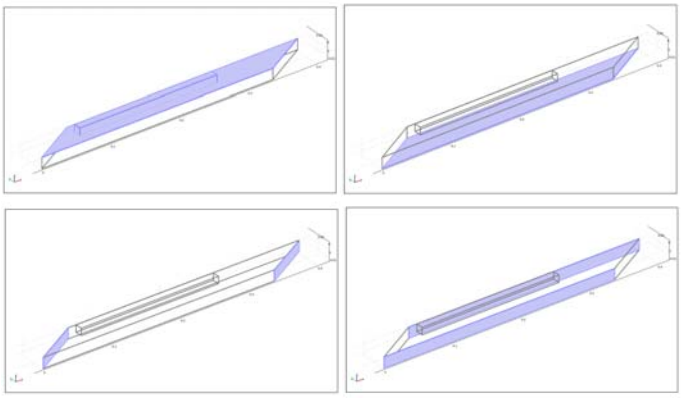

Fig. 5. Numerical domain with thermal boundary conditions imposed on the highlighted surfaces: measured temperature

(top left), Joule heat flux (top right), zero heat flux (bottom left), periodicity (bottom right).

Few materials fit this requirement, and it is interesting to notice that Ni-based superalloys used for blading are among these materials. More generally, the thermal conductivities of air and the one of superalloys present parallel temperature dependence. This circumstance leads to the following appealing conclusion: if a real blade is used to perform conjugate heat transfer investigations at a temperature level different from the real operating conditions, the conductivity ratio is naturally matched. The weak temperature dependence of K for Nimonic–air coupling is illustrated in Fig. 6

TABLE II

THERMAL CONDUTIVITIES RATIO IN ENGINE CONDITION AND IN LABORATORY CONDITIONS EMPLOYING DIFFERENT MATERIALS

Environment	**Solid**	**Fluid**	***K* [-]**
Engine	Nimonic 105 @1250 K	Air @1050K	375
Laboratory	AISI 304 @320K	Air @300K	600
Laboratory	Mykroy-Mycalex @320K	Air @300K	44
Laboratory	Nimonic 105 @320K	Air @300K	388

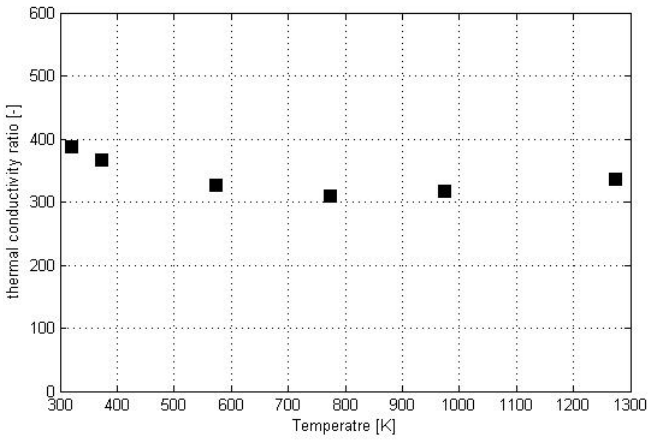

Fig. 6. Temperature variation of thermal conductivity ratio for Nimonic-air coupling.

C. Uncertainty analysis

The uncertainty associated to the adimensional temperature mainly depends on the wall temperature measured and on the evaluation of the imposed heat flux. Uncertainties of 0.15 K are associated to the temperature measurements by means of thermocouples. The heat flux generated by Joule effect is measured with an uncertainty of 4%. The conductive loss is less than $0.01Q_0$, which results in a conservative estimation of 5% for the uncertainty on Q_0.

The main error sources for the wall temperature measurements are (i) the non perfect isothermal condition achieved during calibration and (ii) the uncertainty on the plastic film temperature. During calibration, the wall temperature uniformity varies by +/-0.7 K. Moreover, temperature variations of +/-1 K are possible along the plastic film which, given the influence of the window temperature, may result in additional error of +/- 0.2 K for the wall temperature.

Typical magnitudes of the measured quantities are 1200 W for the heat flux and 20 K for wall-coolant temperature difference, resulting in relative experimental uncertainty of 9 % on Θ. This estimation is based on a 95% confidence interval and is determined following the approach of Kline and McClintock [29].

V. RESULTS AND DISCUSSION

In the present section results of the conjugate heat transfer investigation performed on the rib-roughened wall are presented in terms of adimensional temperature for the two different materials used, namely stainless steel and ceramoplastic. Before presenting and discussing the results of the heat transfer measurements, it is worth summarizing briefly the mean flow model deduced in a former work (Fig. 7). The jet coming from slot *i* mainly impinges on rib *i*, but part of it also reaches rib *i+1* and rib *i+2*. The flow impinging on rib *i* is partially deflected toward the mid-wall and partially toward rib *i+1*. In both cases the streamlines are lead to an upward motion and impinge on the upper wall.

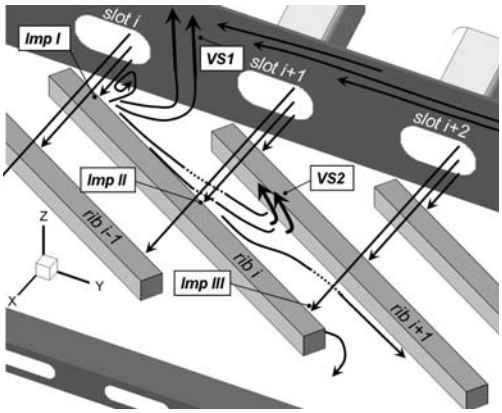

Fig. 7. Mean flow model in the main cavity, [20].

A. Stainless steel rib-roughened wall

Contour plots of the adimensional temperature Θ_{conj} on the stainless steel rib-roughened wall are displayed in Fig. 8. The subscript "conj" indicates that the distribution results from the conjugate regime, a distinction that will be useful later on.

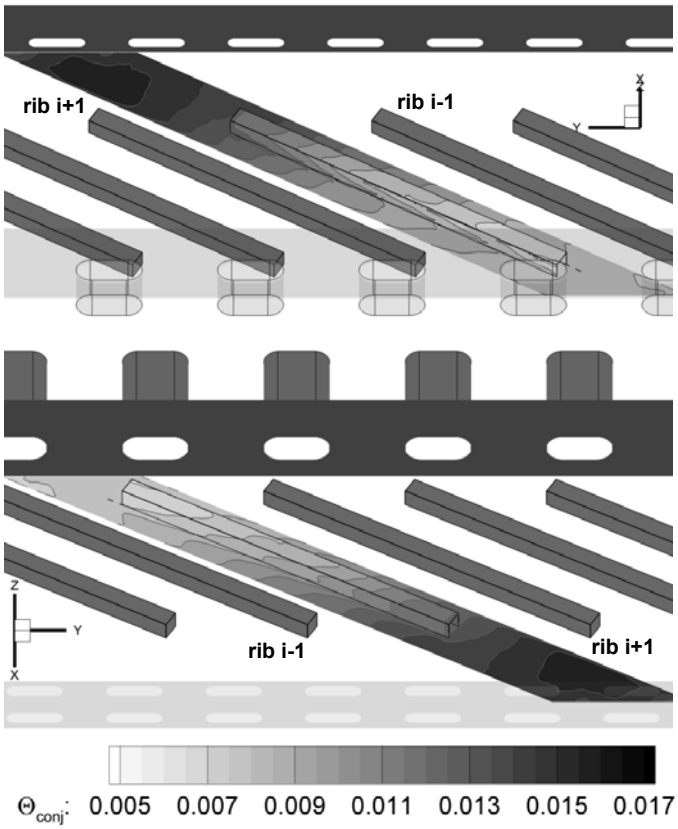

Fig. 8. Adimensional temperature distribution along stainless steel rib-roughened wall: impingement side view (upper) and exit side view (lower)

The main feature of the Θ_{conj} distribution is the temperature gradient distinctly aligned with the jet axis (*x*-direction): the cooling appears much more effective in the vicinity of the mid-wall, especially (and obviously), at the first impingement, on the rib edge as well as on the adjacent floor region. To identify the second and third impingements, however much weaker, a temperature profile is extracted along the top side of rib *i*, at 0.3 rib height from the impingement side (see Fig. 11). As one can see, Θ_{conj} shows a minimum where the first impingement is produced; further the temperature profile shows an inflection in correspondence of the second impingement; about the rib far end, where the third and weakest impingement occurs, the trend of Θ_{conj} shows a knee. Nearby the exit wall, semicircular patterns appear in between each pair of exit slots, consistent with evidences of impingements produced at the exit wall shown by Armellini et al. [20] and Coletti et al. [21].

As the adimensional temperature cannot be rigorously defined in a purely convective regime, a direct comparison between the present results and the convective heat transfer distributions presented by Coletti et al. [21, 22] is not possible. Nevertheless the impact of the conjugate heat transfer may be assessed by means of a simple "numerical experiment": referring to the computational domain in Fig. 5, the convective heat transfer coefficient distribution is imposed as thermal boundary condition along the ribbed surface, while the level of

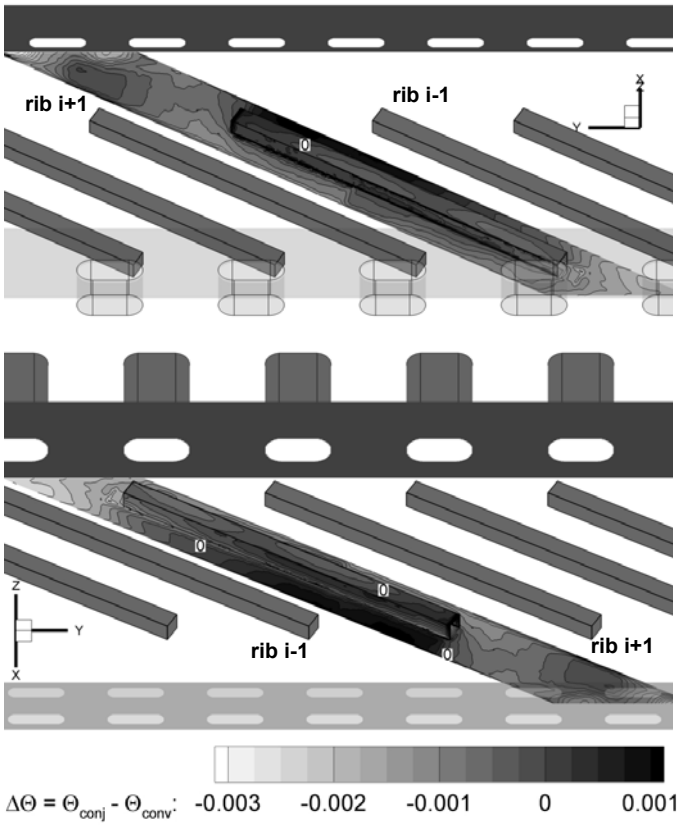

Fig. 9. Conjugate-convective adimensional temperature difference along stainless steel rib-roughened wall: impingement side view (upper) and exit side view (lower)

heat flux applied during the conjugate experiments is imposed at the bottom side. Thermal conductivity is set constant and equal to the one of AISI 304. The solution of the conduction through the wall (obtained using COMSOL Multiphysics®) is more stable in this case, as enforcing a Robin condition is less problematic than imposing a Dirichlet condition. The computed "convective" wall temperature is not realistic: it results in fact from the assumption that the local convective heat transfer coefficient measured in pure convection holds in conjugate regime too. The difference between Θ_{conj} and Θ_{conv} (the computed "convective" wall temperature adimensionalized in the same manner) represents the error made in estimating the wall temperature if the convective heat transfer coefficient distribution is applied to the conjugate problem.

Fig. 9 presents plots of the adimensional temperature difference $\Delta\Theta = \Theta_{conj} - \Theta_{conv}$ over the ribbed surface. In the regions where such difference is positive (negative), applying the purely convective heat transfer coefficient distributions leads to an underestimation (overestimation) of the wall temperature, i.e. an overestimation (underestimation) of the local cooling performance. It appears that the areas of impingement, on the rib tip and in between the exit slots, i.e.

where the cooling is maximally effective, are also the regions where the cooling performance is

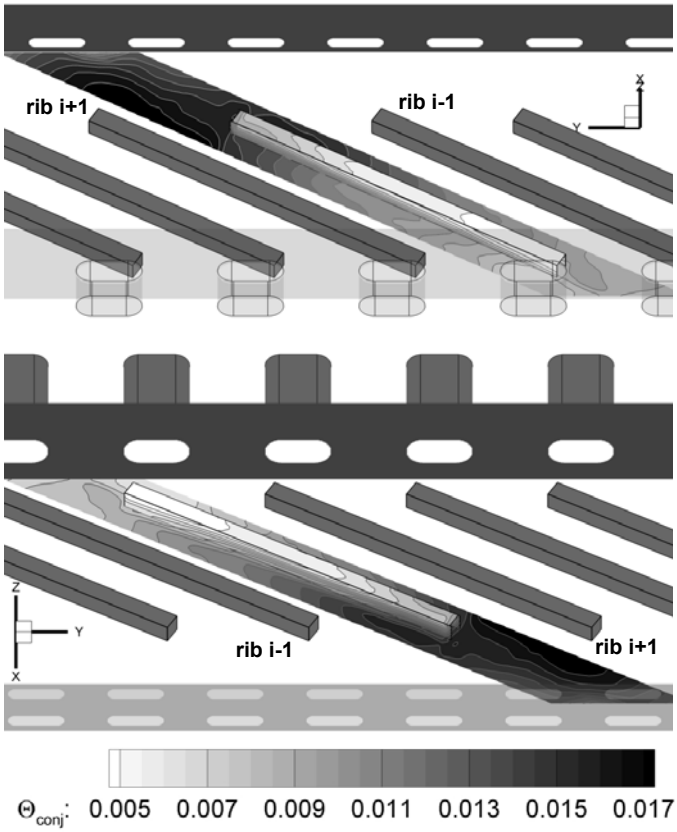

Fig. 9. Conjugate-convective adimensional temperature difference along ceramoplastic rib-roughened wall: impingement side view (upper) and exit side view (lower)

between the exit slots. The effect of the impingement on the rib surface is best visualized when an

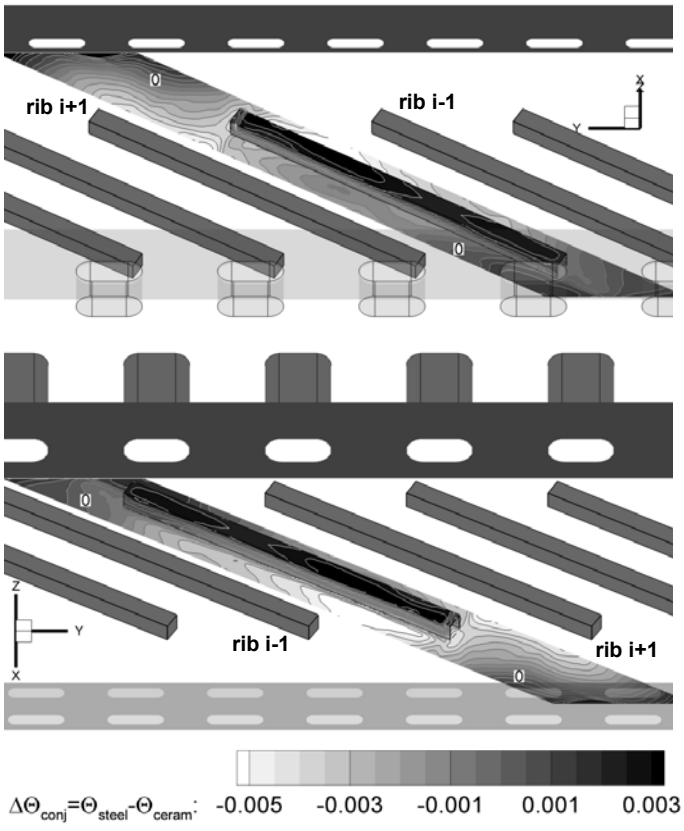

Fig. 10. Adimensional temperature difference between stainless steel and ceramoplastic rib-roughened wall: impingement side view (upper) and exit side view (lower)

underestimated, and vice versa. One could therefore infer that, with respect to the convective heat transfer coefficient, the conjugate heat transfer coefficient distribution would present higher unbalance between efficiently cooled and poorly cooled regions. The latter conclusion must be regarded as speculation until trustworthy heat transfer coefficient distributions are obtained in conjugate regime.

From a quantitative point of view, a maximum absolute deviation of $\Delta\Theta$ = 0.003 is found. In terms of real wall temperature on the experimental model, this corresponds to about 3 K, which is largely beyond the measurement uncertainty. As discussed above, transfering Θ distributions obtained in the model to the engine conditions is not licit, since the conductivity ratio in the experiments is different from the real one.

B. Ceramoplastic rib-roughened wall

Figure 9 displays local distributions of the adimensional temperature Θ_{conj} on the ceramoplastic rib-roughened wall. The trend is similar to what displayed along the stainless steel wall: the wall temperature increases as approaching the exit wall, with the exception of the semicircular patterns in adimensional wall temperature profile is extracted along the rib top side, 0.3 rib height away from the impingement side (Fig. 11): the effect of the three impingements is apparent. From the same picture it is also evident that the rib top side is cooled more efficiently for the ceramoplastic wall than for the stainless steel wall. Vice versa, regions which are poorly cooled, as the floor downstream of the rib, shows even higher temperature levels in the ceramoplastic model. This general behavior is clearly visible in Fig. 10, which displays the local

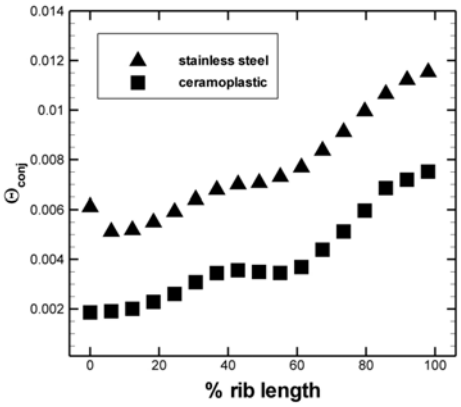

Fig. 11. Adimensional temperature profile extracted along the rib top side, 0.3 rib height from the side facing the impingement

difference between the adimensional temperature along the stainless steel and the ceramoplastic walls. The phenomenon was predictable, as in the stainless steel the temperature differences are better smoothed because of the higher conduction.

VI. CONCLUSIONS

A ribbed trailing edge cooling channel with slots along two opposite lateral walls is characterized in terms of conjugate heat transfer performance through infra-red thermography. Local adimensional temperature distributions are obtained on the rib-roughened bottom wall, including the rib surface. Heat transfer distributions previously obtained on the same configuration in purely convective regime stand as term of comparison.

An adimensional analysis is performed in order to state correctly the problem and identify the appropriate descriptors of the conjugate heat transfer phenomenon. The major conclusions of this analysis can be summarized as follows:

- Both the Nusselt number and the adimensional wall temperature are candidate as invariant descriptors of the phenomenon, the second being far more convenient to evaluate.

- If a realistic temperature (or heat transfer coefficient) distribution is to be obtained experimentally, the solid-fluid thermal conductivity ratio needs to be matched between laboratory experience and engine reality. This requirement is naturally accomplished if realistic Ni-based superalloys are used, no matter what the temperature level is.

As for the cooling scheme in object, the main outcomes of the experimental campaign are:

- The adimensional temperature pattern is strongly affected by the impingements on the rib by the crossing jets. In general, the temperature gradient is distinctly directed from the mid-wall to the exit wall.

- Applying the purely convective heat transfer coefficient distribution as Robin boundary condition would lead to an underestimation of the wall temperature in the poorly cooled regions, and vice versa to a temperature overestimation in the effectively cooled regions.

- A decrease in the conductivity ratio leads to an increase in temperature unbalance between effectively cooled and ineffectively cooled areas, due to the augmented thermal resistance.

REFERENCES

[1] Han, J. C., Dutta, S., and Ekkad, S., 2000, "Gas Turbine Heat Transfer and Cooling Technology". Taylor and Francis, New York.

[2] Akella, K., and Han, J. C., 1999, "Impingement Coolingin Rotating Two-Pass Rectangular Channels With Ribbed Walls". J. of Thermophysics and Heat Transfer, 13(3), pp. 364–371.

[3] Taslim, M. E., Bakhtari, K., and Liu, H., 2003. "Experimental and Numerical Investigation of Impingement on a Rib-Roughened Leading Edge Wall". J. of Turbomachinery, 125(4), pp. 682–691.

[4] Cunha, F. J., Dahmer, M. T., and Chyu, M. K., 2006, "Analysis of Airfoil Trailing Edge Heat Transfer and its Significance in Thermal-Mechanical Design and Durability". J. of Turbomachinery, 128(4), pp. 738–746.

[5] Taslim, M. E., Li, T., and Spring, D., 1998, "Measurements of Heat Transfer Coefficients in Rib-Roughened Trailing-Edge Cavities With Crossover Jets". ASME Paper No 98-GT-435.

[6] Perelman, T.L., 1961, "On Conjugated Problems of Heat Transfer", International J. of Heat and Mass Transfer, 3(4), pp. 293-304.

[7] A. V. Luikov, V. A. Aleksashenko, and A. A. Aleksashenko, 1971, "Analytical Methods of Solution of Conjugated Problems in Convective Heat Transfer," International Journal of Heat and Mass Transfer, vol. 14(8), pp. 1047–1056.

[8] Fedorov, A.G. & Viskanta, R., 2000, "Three Dimensional Conjugate heat Transfer in the Microchannel Heat Sink for Electronic Packaging", International J. of Heat and Mass Transfer, 43(3), pp. 399-415.

[9] Bohn, D., Heuer, T., Kusterer, K., 2005, "Conjugate Flow and Heat Transfer Investigation of a Turbo Charger", J. Eng. Gas Turbines Power 127(3), pp. 663-669.

[10] Bohn, D., Ren, J., Kusterer, K., 2005, "Cooling Performance of the Steam-Cooled Vane in a Steam Turbine Cascade", ASME Paper No GT2005-68148.

[11] Heselhaus, A., 1998, "A Hybrid Coupling Scheme and Stability Analysis for Coupled Solid/Fluid Turbine Blade Temperature Calculations" ASME Paper No. 98-GT-88.

[12] Amaral, S., Verstraete, T., Van den Braembussche, R. A., Arts, T., 2008, "Design and Optimization of the Internal Cooling Channels of a HP Turbine Blade — Part I, Methodology", ASME Paper No. GT2008-51077.

[13] Verstraete, T., Amaral, S., Van den Braembussche, R. A., Arts, T., 2008, "Design and Optimization of the Internal Cooling Channels of a HP Turbine Blade — Part II, Optimization", ASME Paper No. GT2008-51080.

[14] Webb, B. W., Ramadhyani, S., 1985. "Conjugate Heat Transfer in a Channel With Staggered Ribs", International J. of Heat and Mass Transfer, 28(9), pp. 1679-1687.

[15] Young, T. J., Vafai, K., 1998, "Convective Cooling of a Heated Obstacle in a Channel", International J. of Heat and Mass Transfer, 41, pp.3131-3148.

[16] Iaccarino, G.; Ooi, A., Durbin, P.A., Behnia, M., 2002, "Conjugate heat transfer prediction in two-dimensional ribbed passages", International J. of Heat and Fluid Flow, 23, pp. 340-345.

[17] Fedrizzi, R. and Arts, T., 2004, "Investigation of the conjugate conductive-convective thermal behavior of a rib-roughened internal cooling channel", ASME Paper No. GT2004-53046.

[18] Agostini, F., and Arts, T., 2005, "Investigation of the conjugate conductive-convective thermal behavior of a rib-roughened internal cooling channel", ASME Paper No. GT2005-68166.

[19] Martiny, M., 1998, "Wärmeübergang in effusionsgekühlten Flammrohrwänden", Ph.D. Thesis, University of Karlsruhe.

[20] Armellini, A., Coletti, F., Arts, T., and Scholtes, C., 2008, "Aero-Thermal Investigation of a Rib-Roughened Trailing Edge ChannelWith Crossing-Jets - Part I: Flow Field Analysis". ASME Paper No 08-GT-50694.

[21] Coletti, F., Armellini, A., Arts, T., and Scholtes, C., 2008, "Aero-Thermal Investigation of a Rib-Roughened Trailing Edge ChannelWith Crossing-Jets - Part I: Flow Field Analysis". ASME Paper No 08-GT-50695.

[22] Coletti, F., Facchinetti, E., Arts, T., 2009 "Effect of Inclined Ribs on the Aero-Thermal Performance of a Trailing Edge Cooling Cavity With Crossing Jets", 8th European Turbomachinery Conference, Graz, Austria.

[23] Moffat, R. J., 1998, "What's New in Convective Heat Transfer", International J. of Heat and Fluid Flow, 19, pp. 90-101.

[24] Kays, W., Crawford, M., 1993, "Convective Heat and Mass Transfer", McGraw-Hill.

[25] Buckingham, E., 1914, *Phys. Rev*, vol. 4, pag. 345.

[26] Schlichting, H., Gersten, K., Mayes, C., Krause, E., 2000, “Boundary Layer Theory”, Springer.
[27] Shah, R. K., and London, A. L., 1978, “Laminar Flow Forced Convection in Ducts”, Academic Press.
[28] Faghri, M., and Sparrow, E. M., 1980, “Simultaneous Wall and Fluid Axial Conduction in Laminar Pipe-Flow Heat Transfer”, J. of Heat Transfer, 102, pp. 58-63.
[29] Kline, S. J., and McClintok, F. A., 1953, “Describing Uncertainties in Single Sample Experiments”, Mechanical Engineering Journal, 75(1), pp. 3–8.

Droplet internal recirculation measurement by micro-PIV

M. R. Vetrano[1] , F. Lebeau[2], J. van Beeck[1] and M. Riethmuller[1]

[1] von Karman Institute for Fluid Dynamics, Chaussée de Waterloo 72, B-1640, Rhode-Saint-Genèse
[2] Faculté Universitaire des Sciences Agronomiques de Gembloux -UMC, 2 passage des déportés, 5030 Gembloux

email: vetrano@ki.ac.be, lebeau.f@fsagx.ac.be, vanbeeck@vki.ac.be, riethmuller@vki.ac.be

Abstract: **In this communication measurements by micro-PIV of the flow within a jet resulting from a capillary tube with piezoelectric control are carried out. The flow rate of the jet is adjusted by means of a pushing syringe system. Sub-micrometric fluorescent particles are employed in low concentration as seeding in order to have good signal to noise ratios and the ensemble averaging method is used to increase the height of the correlation peaks. To use the ensemble averaging method several couples of frames taken in the same conditions are needed. Stroboscopy is used to achieve this require. Moreover changing the delay of stroboscopy all the jetting phenomenon can be analyzed in detail. The effect of the optical aberrations occurred during the micro-PIV acquisitions is analyzed.**

Keywords: Droplets, micro-PIV.

I. Introduction

The micro-PIV consists in an extension of the standard Particle Image Velocimetry technique to the study of flows at micrometric scale. This technique has been presented the first time by Santiago et al. at the end of nineties [1] [2]. In his first tests, Santiago where using 300 nm fluorescent particles to observe an Hele-Shaw flow around a cylindrical obstacle of 30 μm diameter, then measurement in rectangular micro-channel have been performed. Many other studies have been conducted to analyze the advantages and the disadvantages of the micro-PIV technique. Problems related to the depth of measurements or to the seeding low concentration are nowadays pretty solved [3] [4].

Up to now the largest interest have been done on the research of micro-flow dynamics in channels possessing a rectangular section. Nevertheless micro-PIV could be used to evaluate the dynamics of micro-flows of different shapes as velocity field inside micro-droplets or flows in cylindrical channels. In this paper one of this applications, namely the measurements of flow field inside a droplet during its formation through the breakup of a liquid jet is described.

This communication is structured in five sections. The first one concerns the introduction to the micro-fluidics and to the micro-PIV technique. The second chapter describes in details the micro-PIV measurement technique, its advantages and its limitations. The introduction of the "ensemble average" concept will be also given. The third chapter is related to optical aberration problems encountered during the experiment, namely problems of astigmatism and of deformation of measurement plane. The fourth and fifth chapters concern respectively the experimental conditions and the measurement results. The paper ends with the conclusion, the perspectives and the future plans.

II. The measurement technique

In this section the micro-PIV measurement technique is detailed described with its advantages and its limitations.

A. Optical configuration

The micro-PIV technique can be viewed as a standard PIV in which the measurement plane is not defined anymore by a laser sheet but by the measurement plane of an epifluorescent microscope system. The seeding used is very often constituted by polyester sub-micron fluorescent particle possessing a Stoke shift larger than 40 nm. A simplified sketch of the optical configuration of a micro-PIV system is shown on Figure 1.

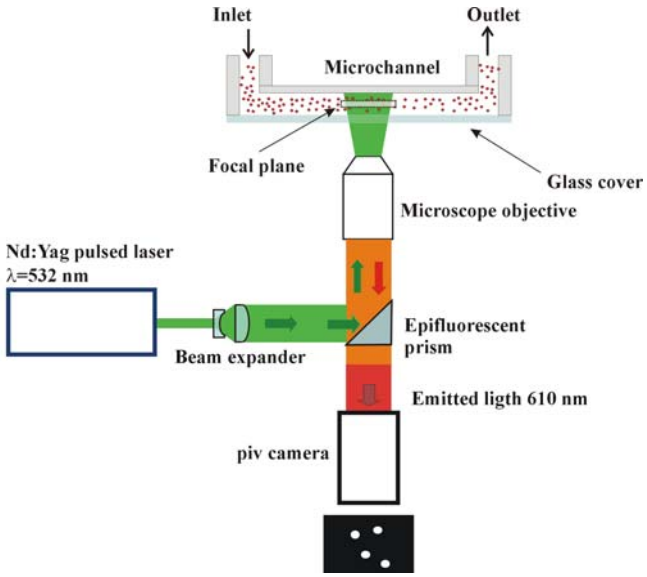

Figure 1: Sketch of the optical configuration for a micro-PIV system

A Nd-Yag pulsed laser beam, with a wavelength of λ=532 nm, is enlarged by a system of lenses and directed, through an epifluorescent prism and a microscope objective.

The light coming out of the objective illuminates a specified volume of a micro-channel in which liquid seeded with fluorescent particles is flowing.

The particles are excited by the laser light and emit in a different spectral band (see Figure 2).

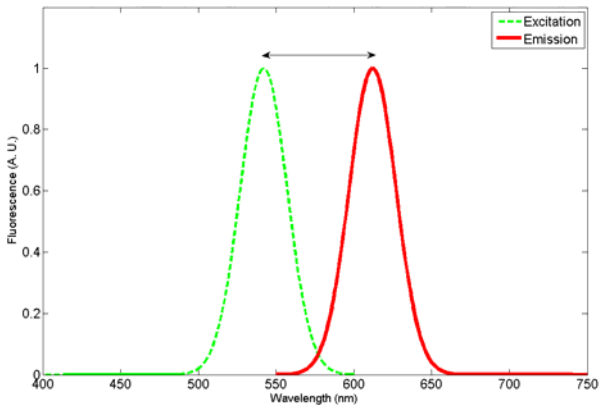

Figure 2 : Example Stoke shift

The light emitted is collected by the microscope objective, passes through an epifluorescent prism and is directed on a synchronized PIV camera that acquire the particle images.

B.Depth of field and particle concentration

The main difference between a standard PIV optical configuration and a micro – PIV one is that the measurement plane is not defined by a laser sheet but a full volume of seeded flow is illuminated and a measurement plane is defined by the optical configuration. Due to this particular configuration the signal-to-noise ratio for instantaneous velocity field measurement is low if some precautions are not taken into account. Indeed particles out of measurement plane still emit light that is collected by the microscope but not cross-correlated. Studies show that one of the ways to reduce this problem is to use low concentration of particles or to reduce the channel depth [3]. Unfortunately this decrease of particles concentration is at the source of the fact that the number of particles present in the correlation window. Since the flows encountered in micro-fluidics are in general laminar and either steady or periodic it is not necessary to measure the instantaneous velocity field but the mean flow field is sufficient.

C.Ensemble average

The ensemble average method has been introduced by Meinhart et al. [4]. It is based on the consideration that, differently from the image average method, the peak correlation function was constituted only by the correlation function of cross-correlated images. This method indeed calculates the average correlation function as the sum of the correlation function of the single cross correlated images :

$$\begin{aligned}\overline{R}_{AB}(s) &= \overline{\iint A(X)B(X+s)\cdot d^2X} = \\ &= \iint \overline{A(X)B(X+s)\cdot d^2X} = \\ &= \iint \sum_{i=1}^{N_{av}} A_i B_i \cdot d^2X \ ,\end{aligned} \qquad (1)$$

where N_{av} is the number of correlation function used for the average.

The correlation function is strongly improved by the averaged ensemble method, as can be seen on Figure 3.

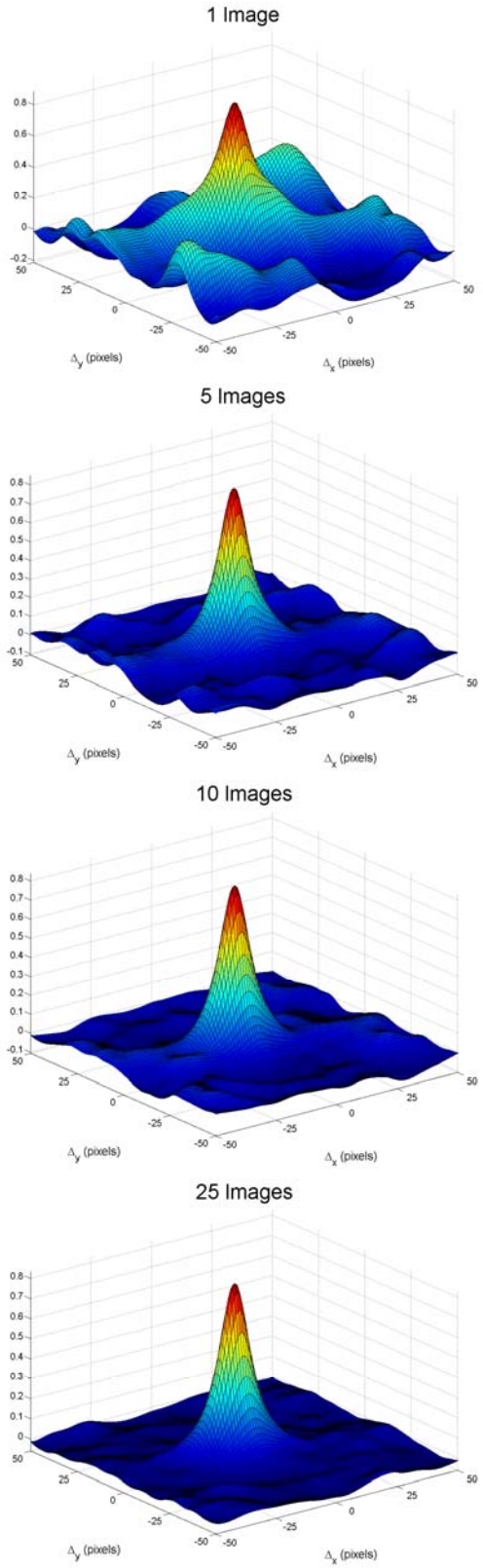

Figure 3: Signal to noise ratio improvement by means of the correlation peak ensemble average.

III. Optical aberration

In an experimental configuration as the one under analysis optical aberrations may play a significant role since they can affect the position and shape of the particle images and then the velocity field. In this paper the two main optical aberration experienced during the tests are analyzed, namely the astigmatism and the measurement plane deformation.

A. Astigmatism

Astigmatism occurs when a lens (in this case the droplet which behaves as a lens) does not present a symmetrical front to the incident light rays. Indeed two planes can be defined as tangential (containing the object and the axis of symmetry) and the sagittal plane perpendicular to the tangential plane. This two planes form their foci at two different distances form the lens.So, in the presence of astigmatism, an off-axis point appears as a sharp line oriented along the sagittal and tangential plane (see Figure 4). In between these two foci, a round but "blurry" image is formed. This is called circle of least confusion. This plane often represents the best compromise image location in a system with astigmatism.

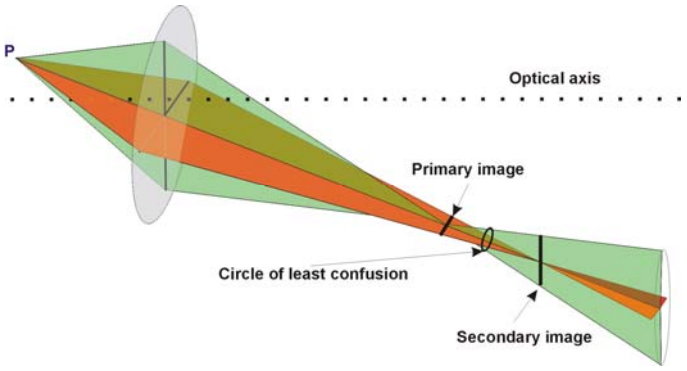

Figure 4: Schematic drawing of the astigmatic aberration. The primary image is corresponding to the

The astigmatism is clearly present in the droplets images as can be seen in Figure 5.

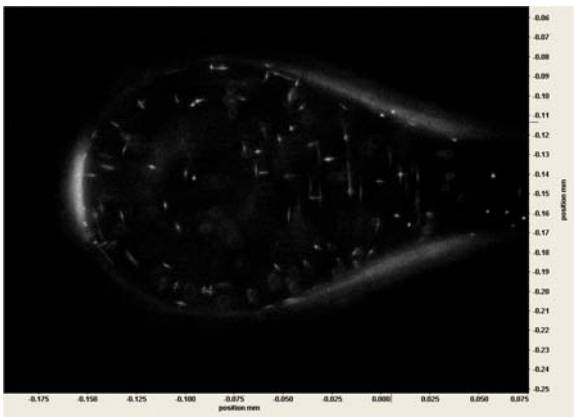

Figure 5: Image of a detaching drop at 40xMagnification. The horizontal and vertical strips are images of the particles distorted by astigmatic aberration.

This astigmatism cannot be corrected in the experimental configuration, nevertheless test have been performed to evaluate the possibility of using the cross correlation method on lines instead of points.

These tests show that, unless the interrogation window become smaller than the line, the cross correlation remains good and is suitable to contribute to the ensemble average.

B. Measurement plane deformation

In a typical microPIV configuration the measurement plane is defined by the focal plane of the microscope. If this focal plane is sited inside a curved transparent object it can be deformed as it was passing through a lens.

Geometric optics calculations have been made in order to calculate such a deformation. In Figure 6 an example of focal plane distortion due to the passage of the light rays inside the droplet is shown.

This example corresponds to the deformation of a 20X microscope objective plane due to the passage through a water droplet (real refractive index n=1.33) of 100 μm diameter. The objective aperture is equal to 0.3 and the working distance is 7.3 mm and a depth of field of DOF=8.65 μm.

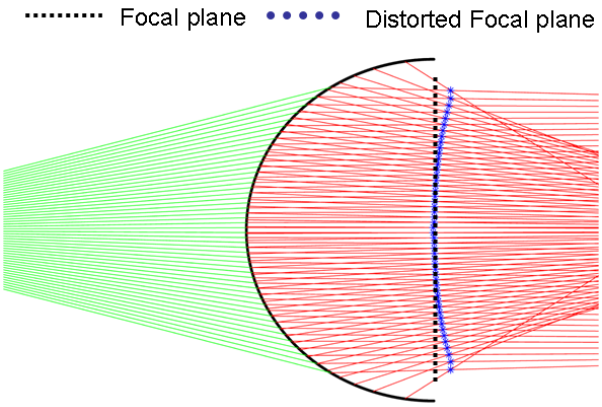

Figure 6 : Example of focal plane deformation due to the passage of the light rays through a droplet.

In this conditions the deformed plane differs from the straight one of about Δ=8 μm, then in this case, being Δ less than the DOF the plane deformation does not affect the measurements.

Moreover one has to consider that, as discussed in the Paragraph II.B, the measurement plane thickness is always larger than the objective DOF. It can also be observed that the difference between the deformed plane and the straight one decreases with the droplet diameter.

The plane deformation has to be calculated every time experiments as the one presented in this paper are conducted. One of the future works based on this consideration will be to find a law capable to define if the deformation of the objective plane affects the measurements on the basis of the optical configuration, droplet curvature and relative refractive index.

IV. Experimental conditions

A 70 microns capillary tube driven by an annular piezoelectric element has been used to generate liquid droplets in air (non confined flow). The signal used to drive the piezoelectric element is sinusoidal with a frequency of 8 kHz. A mixture of 30% glycerin and 0% water is used as testing fluid. This liquid has been seeded with fluorescent tracer particles possessing a mean size of 0.86 µm.

In Figure 7 a picture of the capillary tube under the microscope objective is shown.

Figure 7: Image of the piezoelectric capillary tube.

The methodology used to perform the measurements is the following. A pushing syringe system is used to drive the flow at constant flow rate into de capillary tube. The piezoelectric element is driven by a sinusoidal wave at frequency f_c. To perform the image acquisition, two synchronized signals are generated by an analog output card.

The first signal is amplified to drive the piezoelectric control. The second one is used to trigger the PIV laser system. The trigger signal frequency is less than 5 Hz to be compatible to the PIV camera maximum acquisition rate.

The trigger signal is chosen to perform a stroboscopic sequence of n1 acquisition to cover a piezoelectric control signal cycle.

As a result, a sequence of images with regular phase shift is obtained. The same signal sequence is repeated n_2 times successively to get n_2 synchronized repetitions for each phase step (n_1 x n_2 being limited by the maximum number of images taken from the PIV camera). In such a way the breakup of the liquid jet coming out from the nozzle can be divided in several time steps up to the droplet formation. This technique allows the analysis of the droplet generation event in time. In Figure 8 an example of micro-PIV image obtained during the experiments is shown.

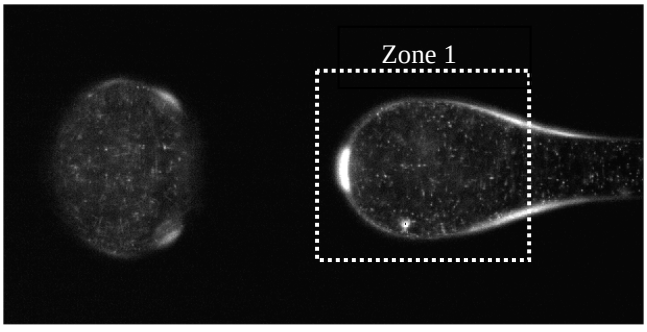

Figure 8: Example of micro-PIV image.

The liquid flow rate is monitored during the experiment in and kept to a constant value

A. Post-processing

The micro-PIV image post processing is done using the ensemble average method with a minimum of 4 couples of images. A dynamic mask, automatically detecting the liquid borders, is used to mask the zones of the image in which the liquid is absent.

The velocity of the jet at the exit of the capillary tube is measured by micro-PIV and compared with the one obtained by the ratio between the liquid flow rate and the capillary tube section. The value obtained is subtracted to the velocity field of the liquid jet, measured by micro-PIV, in order to obtain the internal movements of the fluid (relative motion).

The window size used for the cross-correlation is kept quite large in order to do not affect the measurement by the presence of the strips created by the astigmatism (Paragraph III.A.).

V. Results

In this section some of the most important results obtained during the measurement campaign are shown. These results concern the flow velocity measurement inside a detaching droplet, the possibility to perform velocity measurements in different planes of the detaching droplet and a first attempt to validate such measurements.

A. Internal velocity measurement

In Figure 9 the internal velocity pattern of a detaching droplet, corresponding to the Zone 1 of Figure 5 is presented. One can see hot there are two recirculations on the border of the drop (red zones in which the velocity become positive). These recirculations correspond to the stretching of the liquid jet which will give place to a liquid detachment and then to the droplet formation.

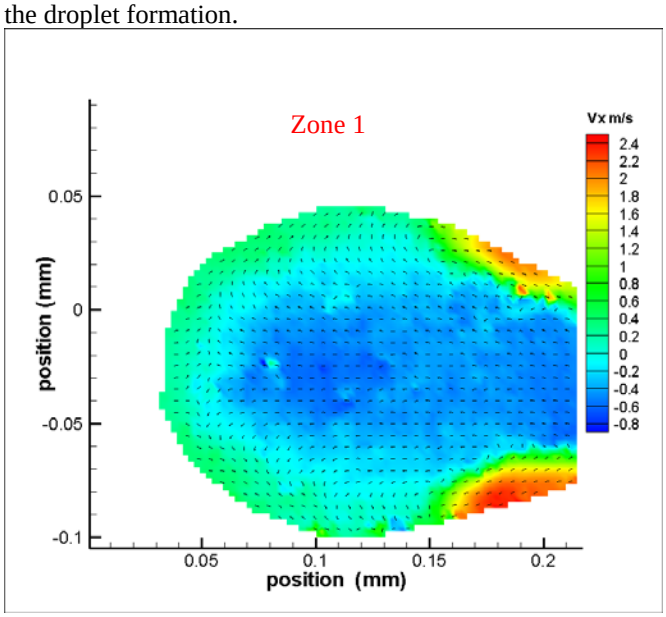

Figure 9 : Relative velocity pattern corresponding to Zone 1 of Figure 8.

Measurements of the detaching droplet can be also performed in different planes as Figure 10 shows. This, providing that the measurement plane deformation is not affecting the measurement, could give the possibility to retrieve from a series of 2D velocity patterns a 3D one.

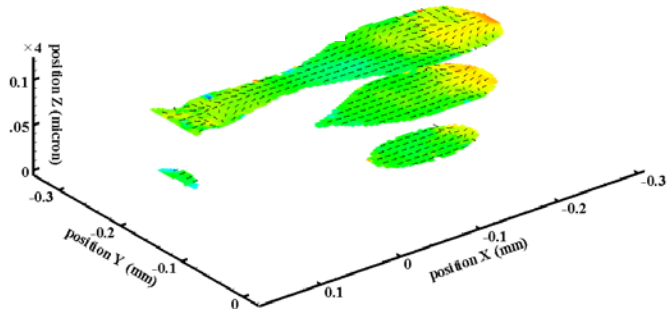

Figure 10: Micro-PIV measurement in different planes of a detaching droplet

The micro-PIV measurements performed have been roughly validated comparing the evolution of the mean flow rate in a fixed point of an image frame with the impulse signal which is given to the piezoelectric capillary tube.

This comparison is shown in Figure 11, where the sinusoidal shape of the input signal is retrieved.

The mean flow rate calculated by means of micro-PIV velocities and the one imposed differs of about 8%. This is due to statistic error performed during the flow rate measurement using the pushing syringe system. On the other hand also the detection of the drop contour, which is essential for the calculation of the flow rate by means of micro-PIV velocities is very delicate and can affect the results.

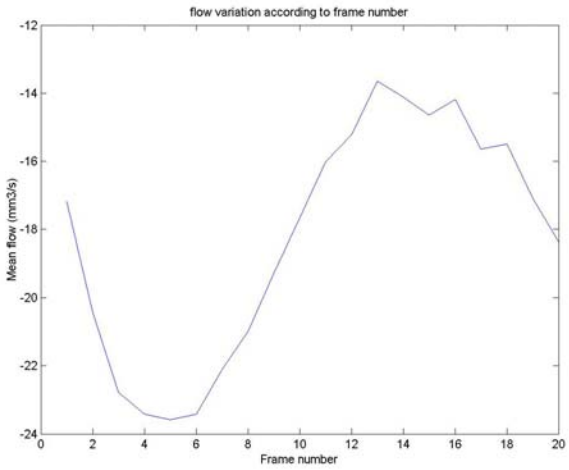

Figure 11: Mean flow variation in a fixed position of the frame

VI. Conclusions

In this paper it has been shown that, even in presence of optical aberrations it is possible to measure the flow field inside a droplet during its detachment from a capillary piezoelectric tube. These measurements have been roughly validate comparing the mean flow-rate measured by micro-PIV to the one imposed by the pushing syringe system. This measurement campaign is largely promising and gives many perspectives. New tests are planned to see the effect of fluid viscosity on the internal droplet flow field and non-isothermal tests are also envisaged.

References

[1] J. G. Santiago, S. T. Wereley, C. D. Meinhart, D. J. Beebe and R. J. Adrian, “A micro particle image velocimetry system”, Exp. Fluids 13, 105-116 (1998)

[2] C. D. Meinhart, S. T. Werely and J. G. Santiago, “PIV measurement of a microchannel flow”, Exp. Fluids 27, 414-419 (1999)

[3] C. D. Meinhart, S. T. Werely and M. H. B. Gray, “Volume illumination for two-dimensional particle image velocimetry”, Meas. Sci. Technol. 11, 809-814 (2000)

[4] C. D. Meinhart, S. T. Werely and J. G. Santiago , “A PIV algorithm for Estimating time-averaged velocity fields” Journals of fluid engineering, 122 285-289 (2000)

Proceedings of the 8th National Congress on Theoretical and Applied Mechanics, May 28-29, Brussels, Belgium.

One pixel resolution temporal profilometry technique using a multimedia LCD projector

Bart Ribbens[1,2], Steve Vanlanduit[2], Dirk Dom[1], Patrick Guillaume[2]
[1]Department of Applied Engineering and Technology, Artesis University College of Antwerp
Paardenmarkt 92, 2000 Antwerp - Belgium
[2]Acoustics & Vibration Research Group, Department of Mechanical Engineering, Vrije Universiteit Brussel
Pleinlaan 2, 1050 Brussels - Belgium
email: bart.ribbens@artesis.be, steve.vanlanduit@vub.ac.be, dirk.dom@artesis.be, patrick.guillaume@vub.ac.be

Abstract—**Profilometry is widely used as a control method in automation systems or for scanning and converting real objects into 3 dimensional models. Different techniques using grids and lasers can be found in literature. The available techniques can be divided into two main categories: temporal and spatial profilometry [1][2][3]. Most setups are based on the spatial phase unwrapping method in which there is only need for one or a few images. The problem when using this class of unwrapping algorithms is that discontinuities in the model are difficult to measure.**
In this paper a temporal method is proposed in which a LCD projector is used in combination with an industrial camera. The proposed technique has a high accuracy and is insensitive to variable light conditions.

Keywords— **profilometry, dimensional metrology, fringe processing**

I. Introduction

PROFILOMETRY techniques can be divided into two main categories: Spatial and temporal profilometry. Both techniques have advantages and disadvantages, so for each application and scale, a technique has to be chosen. Because sinusoidal gratings are used, phase unwrapping techniques can be used to calculate the height of an object. One of the biggest problems of the spatial phase unwrapping technique is that the detection of large steps is impossible or very difficult. In the temporal techniques more images are needed which can result in higher calculation times. In the spatial profilometry one or a few images are used to make a quantitative measurement of the shape of a surface. If a fringe pattern is projected, the phase can be obtained by different demodulation techniques like the isotropic Fourier demodulation[5] and the spatial asynchronous demodulation[6].
After the phase is known at every pixel in the image, the phase can be unwrapped. The phase can be unwrapped using different unwrapping techniques[7][8][9]. Also Moiré techniques[10] can be used to make a quantitative measurement of a 3-D shape.
Because computers become faster and camera's cheaper, the temporal techniques become more interesting. In this paper a one pixel resolution profilometry technique is proposed based on a varying frequency. Objects of 200 mm can easily be scanned by using a multimedia beamer so no expensive projection equipment is needed. The setup (fig.1) is also very easy and there is no need for extra optics.

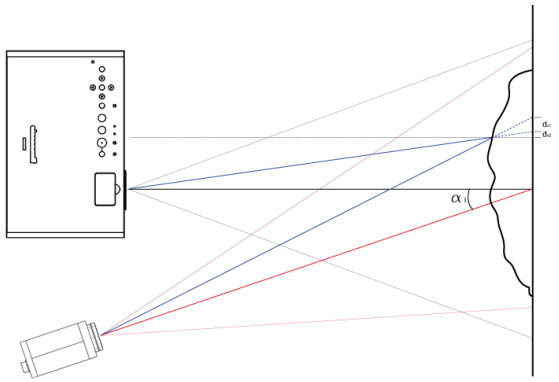

Fig. 1. Setup

Assume that a sinusoidal fringe pattern with frequency f_X in the X direction is projected onto an object with a height distribution given by $h(x,y)$. If an image is acquired, the intensity can be written as

$$i(x,y) = r(x,y)(1+\cos\{2\pi f_X[x+h(x,y)\tan\alpha]\},$$

where $r(x,y)$ is the reflectance of the object and α is the angle between the camera and the LCD projector. By estimating the phase modulation $\varphi(x,y)$ of the carrier frequency f_X from the intensity image $i(x,y)$, one can obtain the height $h(x,y)$:

$$h(x,y) = \frac{\varphi(x,y)}{2\pi f_X \tan\alpha}$$

.

II. Development of projection software

Projecting fringe patterns with varying frequency (fig. 2, 3) can be done in different ways. In the proposed method the fringes are generated with a computer. For the projection a Philips LC434199 LCD projector with a maximum refresh rate of 120 frames per second (FPS) is used. This beamer is connected to a computer with a nVidia PX9500GT graphics card with 512 Mb of video RAM. A

good graphics card is needed in our setup because every frame that is projected has to be different. When using a card with less video memory, the projection software is running on a lower speed than the frequency of the beamer which sometimes gives a fringe pattern that is projected twice. This phenomenon lowers the accuracy of the proposed method. The speed is also depending on the type of processor you have. The faster the CPU, the faster the software can be.

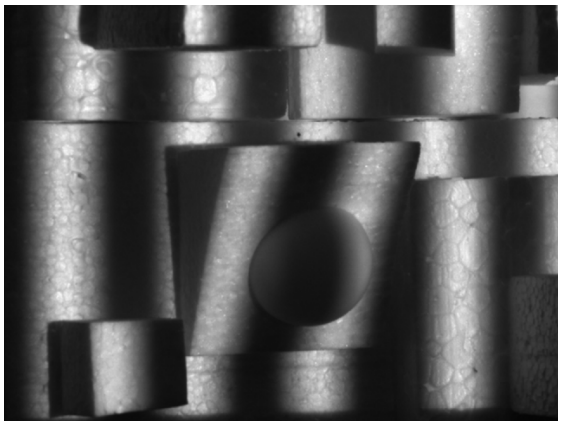

Fig. 2. Fringe pattern with low frequency

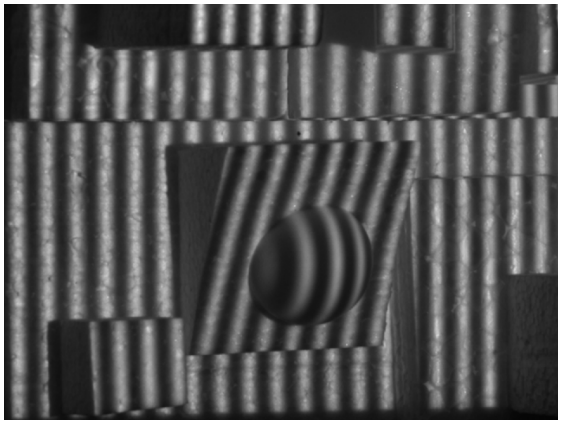

Fig. 3. Fringe pattern with high frequency

Because projecting fringes with a standard mathematical program like Matlab cannot give you 60 FPS, specific software is written in Visual Basic .NET. It is obvious that printing lines on the screen using the normal programming language is also slow. The reason is that the software sends every pixel seperately to the graphics card. All the calculations in this case are done by the CPU of the computer. This also slows down extremely the other programs that are running on the computer.
The speed of a standard fringe projecting program written in VB.NET is compareable to the visualisation speed of Matlab. When the time needed to calculate and build an image that has to be projected on the screen is higher than the refreshing time, incomplete projections will appear.

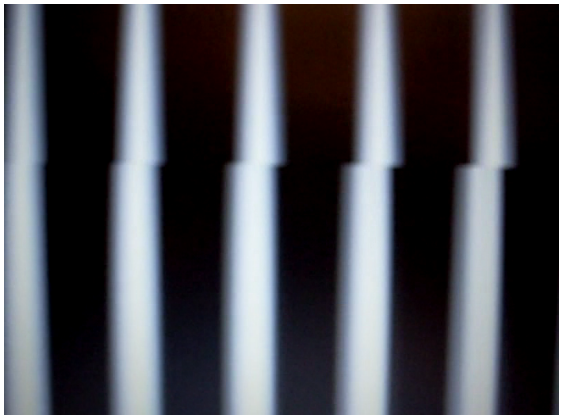

Fig. 4. Uncomplete fringe projection (Matlab)

To make the projection software faster, there is the option to program in Direct3D or OpenGL. Because OpenGL is supported by nearly every operating system (Windows, Mac OSX, Linux, ...) this cross-platform API is used.
To easily use the OpenGL commands in VB.NET, a framework had to be chosen. The software written for the validation of the proposed technique is based on the TAO framework. This framework is completely free and it gives the programmer the opportunity to write very fast programs to visualise two or three dimensional images.

An extra important parameter in this proposed method is that the best results can be obtained by using a graphics card in which the OpenGL refreshing rate is locked. This means that the card is not generating more projections than the screen or beamer can visualise. The reason is that calculating something that can not be seen is a waste of computational time.
In our setup, this setting is a given, because our software will only run at the speed of the beamer. This means that there will never be projected twice the same fringe pattern on the screen. Also every fringe pattern that is programmed will appear on the screen.
When the refresh rate of the beamer is 60Hz, the program will generate 60 FPS and if the refresh rate is 75Hz, the program will also run on 75Hz. The faster the beamer, the faster the system can work as long as the computer can create the fringes fast enough.

III. Method to trigger the camera

It is important to take the images with a camera in a certain period of the projection cycle (fig. 5). The projection cycle includes horizontal and a vertical synchronization signals sent by the two trigger cables inside the VGA cable.
The projection cycle starts with a vertical synchronization

pulse (table I). Then the horizontal synchronization signal is used to build up all the image lines. Every time a horizontal sync is sent, a new image line will be drawn on the screen. After all the lines are built, the screen (projection) is stable for a certain time. When a new cycle has to begin, a vertical synchronization signal is sent.

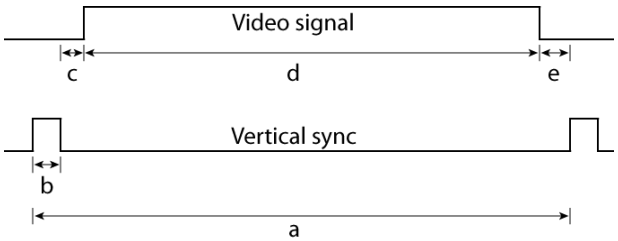

Fig. 5. VGA timing: (a) Total frame time, (b) vertical sync length, (c) back porch, (d) active video time and (e) front porche

TABLE I
VERTICAL SYNCHRONIZATION TIMING

Horizontal pixels	1024	1024
Vertical scan lines	768	768
Vertical scan polarity	Neg	Neg
Vertical Frequency	60Hz	75Hz
a - Total frame time	16,67 ms	13,33 ms
b - Sync length	0,12 ms	0,05 ms
c - Back porch	0,60 ms	0,47 ms
d - Active video time	15,88 ms	12,79 ms
e - Front porch	0,06 ms	0,02 ms

For the setup the shield is removed in the middle of the VGA cable and the vertical synchronization cable is cut. Also the trigger ground cable is cut when the shield is removed. The next step is soldering the cables together again with a new trigger cable. After isolating the cables, the shield has to be replaced in its original position and also soldered again. When this step is not done properly, it is possible that there arise some standing waves, which makes the cable not work anymore. Also a lot of noise can appear when the shield is not fixed properly.
When using the self-made VGA cable for triggering the camera, the trigger will still arise on the wrong moment. This is because the camera is triggered to take a shot at the moment the screen is building up. This gives images where half the screen is refreshed and half the screen is still the old image (fig. 6). This problem can be solved by using a trigger delay, programmable in the camera. In the software of Allied Vision Technology delivered with the camera, a delay of for example 4000 μs can be set which gives the certainty that the image that is taken is perfectly stable.
By using this technique a bad image will never appear which gives the possibility to shoot perfect frames at a speed of 75 FPS, which is the maximum refresh rate used in the tests. Since the AVT Pike 32C camera can handle 120 frames per second the limiting factor is still the beamer in combination with the graphics card.

Fig. 6. Example of bad timing

IV. PROPOSED PROFILOMETRY TECHNIQUE

The technique proposed in this paper is based on the estimation of a frequency using a fast fourier transform. Each measurement starts with the projection of sinusoidal fringes with a varying frequency on a surface. The projection software projects the fringes with a fixed phase on the left of the screen. By increasing the number of fringes, more fringes will pass on the right side than on the left side of the object. This results in a different frequency for every vertical line in the temporal domain. This property is used to calculate the height of the object. When the fringe density is higher, the contrast between the highest and the lowest gray value will be smaller. This phenomena is shown in figure 7.
A camera, placed at an angle α to the beamer (fig. 1), records all the projected fringes and the images are stored on the hard disk. After all the images are taken, for every pixel the FFT has to be calculated. By doing this, the frequency can easily be obtained for each pixel of the camera. One of the advantages of this proposed technique is that when there is a problem with some pixels, this only results in a local fault. The results of the pixels around the local fault will not be influenced.
When the FFT in each pixel is known, an estimation algorithm is needed to find the base frequency. Because the images contain noise and the projected sinus waves are never perfect, a lot of leakage, harmonics and noise will

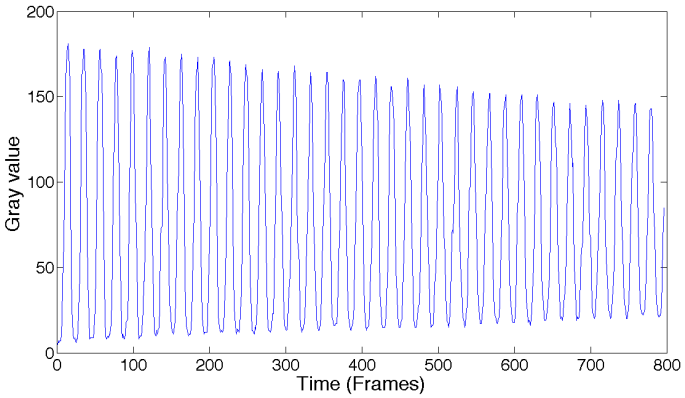

Fig. 7. Gray value of one pixel in the time domain

appear in the FFT plot (fig.8). When simply detecting the highest frequency, only an accuracy of 15-20 mm can be obtained when scanning objects as large as the ones used as validation and with a comparable setup.

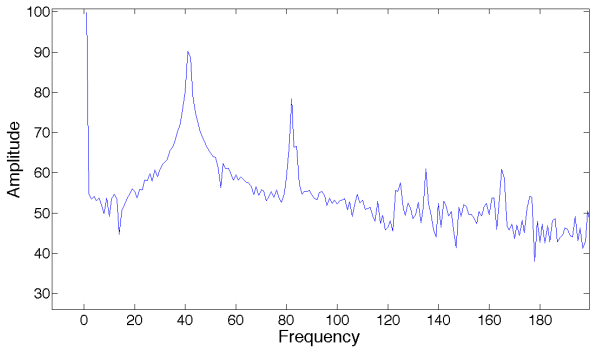

Fig. 8. Detail of FFT of one pixel in time domain

Because the frequency has to be estimated in each pixel, a fast and accurate method has to be used. In this method it is necessary to assume that the frequency of the fringes is increasing with a constant speed so the signal is periodic. A very fast FFT based technique is described in [4]. The method estimates the parameters of a sinusoid based on the complex amplitudes of the FFT lines with the highest amplitude.

V. Camera calibration

In the setup a high quality camera lens with a C-mount thread is used. The lens is tested with a camera calibration toolbox, but because the lens gives nearly no radial distortion, the pictures obtained by the camera are not compensated by the parameters found with the toolbox.

But in the technique, proposed in this paper, another type of calibration is used. Before scanning an object, a flat surface is scanned and the frequency differences are calculated (fig. 9). This gives a good reference for further measurements. When an object is scanned and the estimated frequencies are calculated, the results are diminished with the results of the reference scan. This gives a compensation for all the local distortions and for the different angles between the projection of the beamer and the camera. By using this method not all the angles have to be calculated and interpolated to obtain the shape of an object.

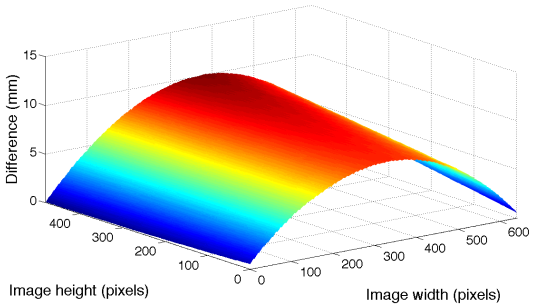

Fig. 9. Compensated reference plane

Nevertheless, two parameters have to be measured as accurately as possible: The angle between the camera and the beamer and the amount of pixels used to represent one millimeter. To validate the proposed technique using different angles, the setup is screwed on a plate with holes on certain positions, where the angle between the camera and the beamer is known. This setup can easily be made with a CNC machine. By using a special ground plate, no more angles have to be measured. For the best results it is still possible to measure some known objects and change the angle slightly untill the system is fully calibrated. For the validations published in this paper an angle of 13.49mm and 17,81 degrees is used.

The other parameter that is critical to calculate the real height of an object is the pixel/mm ratio. There are two methods to find how much pixels are used to represent one millimeter. Because the size of the CCD of the camera and the lens is known, the ratio can be calculated by measuring the distance of the camera to the reference plane. Because it is difficult to measure the distance, a camera calibration method is used.

A printed paper with eight squares (fig. 10) is fixed on the reference plane. This background is used for all the validation experiments. The two squares in each corner give a perfectly detectable corner in the point where they touch each other. The distance between the crossings of the squares is known.

When a white screen is projected on the reference plane, a high quality image an be taken. By using a method that is based on the Harris corner detection algorithm[11], the corner extraction can be done with a subpixel accuracy. When the distance between the squares is known in pixels

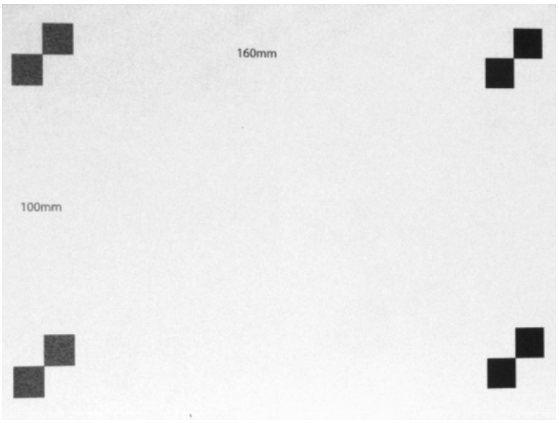

Fig. 10. Camera calibration image

the conversion factor can be calculated.

The calibration technique used in this paper results in an easy equation to calculate the real height of each pixel captured by the camera.

$$H_{mm} = \frac{\frac{f_{estimated}}{\Delta f_{ref_{estimated}}} \cdot \frac{W_{camera}}{R_{px\_mm}}}{\tan(\alpha)}$$

H_{mm} = Real height of the object in mm.
$f_{estimated}$ = Estimated frequency of the object
$\Delta f_{ref_{estimated}}$ = Maximum of the estimated frequency of the reference plane - Minimum of estimated frequency of the reference plane
W_{camera} = Width of camera in pixels (here 640)
R_{px_mm} = pixel/mm ratio

VI. Validation results

A. Scanning a block

For the first part of the validation of the proposed technique, a block of expanded polystyrene with a thickness of 42,5 mm is used. Since it is low quality expanded polystyrene, the surface is not perfectly flat. The reason the validation is done with a block of expanded polystyrene, is the very bright white color.
The camera now is able to measure nearly perfect black and white lines, so the 8 bit grayscale is nearly completely used. When using a darker object, like the pyramid in the second validation experiment, a large part of the grayscale cannot be used. Even when the color influences the measurements, the accuracy stays the same.
Because there can exist an offset by replacing the reference plane with the object that has to be measured, the background of the object is also measured. This results in a straight forward compensation of the shape heights.
The numerical results of the scan of a simple block can be found in table II and the visual result in figure 11.

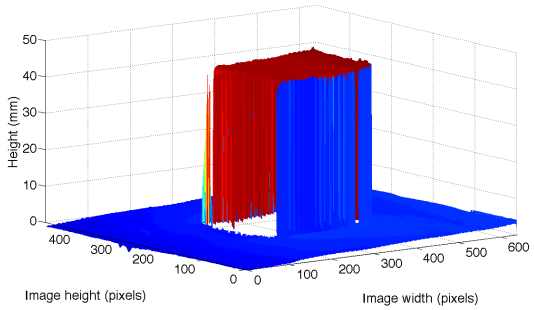

Fig. 11. Result of scanned block

TABLE II
BLOCK

Measurement	Mechanical (mm)	Optical (mm)	Std (mm)
M1 - R1	42,50	42,463	0,178
M1 - R2	42,50	42,431	0,190
M2 - R1	42,50	42,501	0,195
M2 - R2	42,50	42,505	0,182
M3 - R1	42,50	42,504	0,165
M3 - R2	42,50	42,441	0,170

M1: Block measurement 1
R1: Reference measurement 1
Mechanical: Height measured with a ruler, accuracy 0,05mm
Optical: Height calculated with proposed technique
Std: Average standard deviation of the block

B. Scanning a pyramid

For the second part of the validation a self-made pyramid is used (fig. 12). This material has a light gray/brown color, but the accuracy of the proposed technique is not influenced by this color. As long as the color is not too close to black, the methods works with a constant accuracy. The result (table III) shows that a good accuracy can be obtained using this proposed technique, but improvements are still possible.

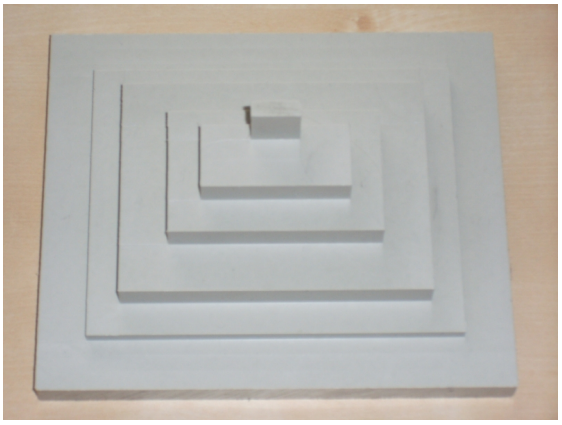

Fig. 12. Pyramid

TABLE III
PYRAMID - LEFT SCANNING

Zone	Mech. (mm)	Optical (mm)	Std (mm)
0 (gnd)	0		
1	10,30	10,192	0,266
2	14,70	14,501	0,164
3	24,80	24,438	0,184
4	34,80	34,325	0,169
5	44,80	44,327	0,362
6	60,00	60,608	0,478
7	44,70	44,633	0,443
8	34,70	34,392	0,184
9	24,70	24,312	0,245
10	14,80	14,569	0,175
11	10,15	10,199	0,216
12 (gnd)	0		

M1: Block measurement 1
R1: Reference measurement 1
Mechanical: Height measured with a ruler, accuracy 0,05mm
Optical: Height calculated with proposed technique
Std: Average standard deviation of the block

VII. CONCLUSIONS

This proposed temporal profilometry technique only uses a LCD beamer and an industrial camera for the measurement of an unknown shape, which makes the setup cheap and easy. The algorithm, needed for the extraction of the height, is based on the projection of a sinusoidal grating with varying frequencies. The gray values obtained by the camera can be evaluated by the FFT estimation algorithm which gives much better results than using a straightforward estimation of the frequency. The conversion to a real world scale model is done by using a geometric calculation.

The technique proposed in this paper, in which each pixel of the camera only represents $0,25mm$, has a height accuracy of $100\mu m$ for a block with a certain height. When measuring an object with a lot of discontinuities, the resolution is $500\mu m$. The tests also show that the color has no influence on the accuracy of the technique as long as the color of the object is not nearly black. This is an important difference compared to a lot of phase unwrapping techniques described in literature.

Furthermore, the validation tests give an indication that the method still can be improved by improving the fringe projection so that the amplitude of the projected sine wave is constant over time.

REFERENCES

[1] J. M. Huntley, H. Saldner *Temporal phase-unwrapping algrithm for automated interferogram analysis*, Applied Optics 32, 3047-3052, 1993.

[2] Lars Paulsson, *Temporal phase unwrapping applied to wavelength-scanning interferometry*, Applied Optics 39, 3285-3288, 2000.

[3] Mitsuo Takeda, Quan Gu, Masaya Kinoshita, Hideaki Takai, and Yosuke Takahashi *Frequency-multiplex Fourier-transform profilometry: a single-shot three-dimensional shape measurement of objects with large height discontinuities and/or surface isolations*, Applied Optics 36, 5347-5354, 1997.

[4] H. Renders, J. Schoukens, G. Vilain *High-Accuracy Spectrum Analysis of Sampled Discrete Frequency Signals by Analytical Leakage Compensation*, IEEE Transactions on Instrumentation and Measurement 33 ,287-292, 1984.

[5] Mitsuo Takeda, Kazuhiro Mutoh *Fourier transform profilometry for the automatic measurement of 3-D object shapes*, Applied Optics 22, 3977-3982, 1983.

[6] J. A. Gomez Pedrero, J. A. Quiroga, M. Servn *Asynchronous phase demodulation algorithm for temporal evaluation of fringe patterns with spatial carrier*, Journal of Modern Optics 51, 97109, 2004.

[7] Thomas J. Flynn *Two-dimensional phase unwrapping with minimum weighted discontinuity*, J. Opt. Soc. Am. A 14, 2692-2701, 1997.

[8] D. C. Ghiglia, M. D. Pritt *Two-Dimensional Phase Unwrapping: Theory, Algorithms, and Software*, Wiley, 1998.

[9] M. D. Pritt *Phase unwrapping by means of multigrid techniques for interferometric SAR*, IEEE Transactions on Geoscience and Remote Sensing 34, 728-38, 1996.

[10] Jan A. N. Buytaert, Joris J. J. Dirckx *Moiré profilometry using liquid crystals for projection and demodulation*, Opt. Express 16, 179-193, 2008.

[11] C. Harris, M. Stephens *A combined corner and edge detection*, In Proceedings of The Fourth Alvey Vision Conference, 147-151, 1988.

Proceedings of the 8th National Congress
on Theoretical and Applied Mechanics,
May 28-29, Brussels, Belgium.

Study of large deformation phenomena in SPIF using an in-process DIC technique

Ioannis Vasilakos[1], Jun Gu[1], Bachir Belkassem[1], Hugo Sol[1], Johan Verbet[2], Joost Duflou[2]
[1]Department of materials and constructions, Vrije Universiteit Brussel
Pleinlaan 2, 1050 Brussels – Belgium
[2]Department of mechanical engineering, Katholieke Universiteit Leuven
Celestijnenlaan 300B Leuven – Belgium
email: ivasilak@vub.ac.be, jungu@vub.ac.be, bachir.belkassen@vub.ac.be, hugos@vub.ac.be,
Johan.Verbet@mech.kuleuven.be, Joost.Duflou@mech.kuleuven.be

I. ABSTRACT

Single point incremental forming (SPIF) is a promising new production technique in which a metal sheet is formed stepwise by a spherical tool. However, the technique still shows some particularities. It is observed that the final geometry of a SPIF part can deviate significantly from the programmed tool path. As illustrated in this paper, elastic springback is only to a minor extent responsible for this phenomenon. The goal of the presented paper is to illustrate the gradual emergence of unintended deviations as measured by means of a Digital Image Correlation (DIC) technique. Two CCD cameras were used to take the necessary in-process images. The mechanism of deformation in function of the forming depth is documented and discussed.

II. INTRODUCTION

Single point incremental forming (SPIF) is a promising sheet metal forming process for rapid prototyping applications and for small quantity productions. The SPIF process is based on the tool path followed by a CNC controlled spherical tool. The process thanks its flexibility to the fact that SPIF, in contrast with other forming techniques, doesn't require a dedicated die to operate. As a result, the lead-time can be low and tooling costs can be avoided [1, 2]. Despite the many advantages of the SPIF process, a remaining drawback of the technique is the lack of accuracy of the obtained final parts. To overcome this problem, it is necessary to carefully study the occurring states of stress during SPIF. This is not an easy task, since large plastic strains occur and hence accurate material models are required in numerical simulations. These material models must also be able to predict spring back effects and residual stresses. Both phenomena are considered as possible candidates to explain deviations from the desired final geometry. Springback effects are observed in a material point at many stages: after the tool has passed, new vertical step increment, when the work piece is released from the clamped boundary conditions and finally when the work piece is trimmed. Several parameters affect the process mechanics in SPIF. These parameters can be divided in three categories:

1. Process parameters (tool diameter, incremental step size between two successive loops, tool rotation speed, use of lubricant).
2. Material parameters (strain hardening, anisotropy, yield behaviour, Young modulus).
3. Parameters related to the design of the part (blank thickness, geometry, including steepness of the component surfaces).

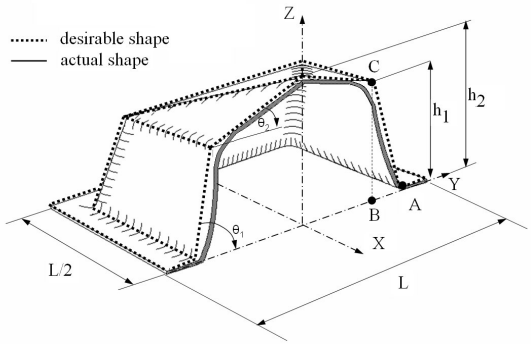

Fig. 1. The cross-section at coordinates (0, y, z)

All the above mentioned parameters can have a possible influence on the deviation of the final geometry from the designed one [3, 4].
The purpose of this study is to investigate the deformation phenomena in the SPIF process of a two angle- pyramid (see Figure 1). This paper is focused on the in-process tracing of six selected points during SPIF in terms of displacement and spring back. Possible reasons for the occurring shape deviation of the two-angle-pyramid, the evolution of the displacements and thickness distribution on the formed pyramid are studied.

III. DIMENSIONAL MEASUREMENTS

Measurement system
A laser-line scanner with an accuracy of ± 15 μm was used to measure the actual shape of the SPIF made two-angle-pyramids. The scanned point cloud was mapped onto the CAD model using a best fit method. The point cloud was then compared to the CAD model and the deviations between them were plotted.

Measured thickness distribution for the two-angle-pyramid
The cross section (in the x = 0 plane) of the two-angle-pyramid is chosen since a big shape deviation was observed there (see Figure. 1). The measurement of the thickness was performed by subtracting the measured external and internal geometry of the pyramid. In total 373357 points were scanned for the determination of the thickness distribution. The identification of the thickness along the chosen section was obtained by extracting the points characterised by x=0. The dimensions and geometrical values of the designed two-angle-pyramid are given in table I.

TABLE I

L (mm)	h_1(mm)	h_2(mm)	θ_1(°)	θ_2(°)
225	60	90	65	30

The measured geometry and thickness profile of the two-angle pyramid in the selected cross section are plotted in Figure 2.
Assuming that only in-plane strains occur, the sine law can be used as a first estimate for the final thickness of the part at zone AC (T_{AC}) based on the original thickness of the zone AB (T_{AB}) and the wall angle θ1. It has experimentally been verified that the process follows this law [5] with a tendency to over-form slightly [6].

$$T_{(CB)} = T_{(AB)} \sin(90 - a) \quad (1)$$

IV. Working Principle Of DIC

A DIC measurement procedure (Figure 3) consists of taking a sequence of pictures from an object surface with two charged coupled device (CCD) cameras. Each CCD camera uses a 1392 x 1040 pixel sensor. The DIC system requires an arbitrary speckle pattern that is either sprayed or painted onto the object surface or provided by the texture of the specimen itself.
The concept on which the software is based is that the distribution of grey scale values in a subset of the picture taken at the reference state corresponds to the distribution of grey values of the same subset of the picture taken at a processed state from the specimen. By tracking the subsets in each successive image, the relative displacement of the surface of interest is obtained. In a next step, the resulting strains can then be calculated. In the used set up, two cameras are used to measure both the in- and out of plane displacements of the specimen's surface [4].

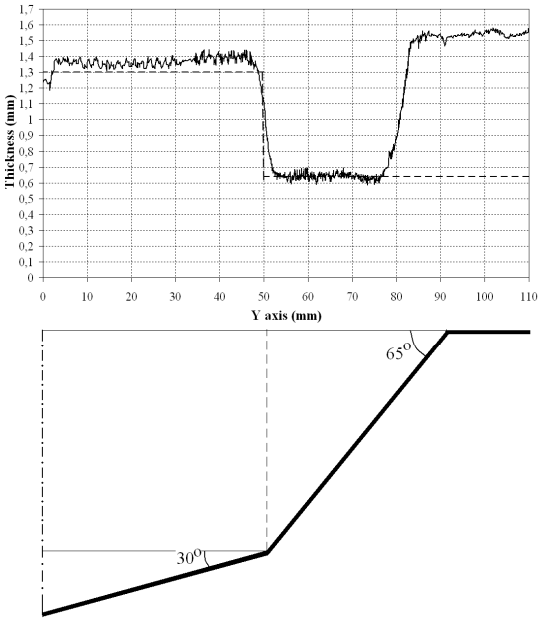

Fig.2. Thickness distribution in the cross-section (0,y,z) compared with the sine law.

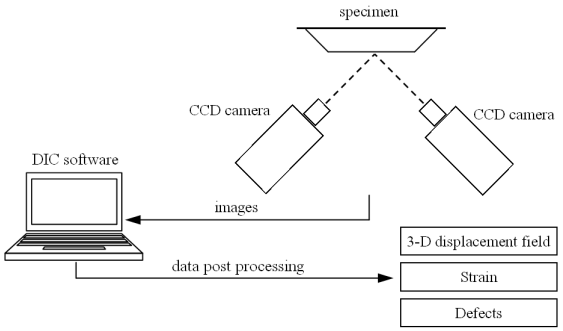

Fig.3. Working principle of DIC

V. DIC-SPIF In Process Measurements

A stiff three-axis CNC milling machine was used as the platform for the SPIF process. A cylindrical stylus with a 10 mm diameter spherical head was mounted on the horizontal axis of the machine. An aluminum alloy AA3003 sheet with a thickness of 1.5 mm was considered in this study. A blank with dimensions of 225x225 mm was supported on a four-sided steel fixture and clamped rigidly to this fixture with a backing plate with aperture dimensions of 182 x 182 mm. The whole fixture was mounted vertically on the working table of the horizontal milling machine so that the blank was perpendicular to the stylus. During the forming process, the tool traveled with a certain feed rate and only the material available inside of the orifice of the backing plate could be deformed by the tool. After traveling the entire path of one contour, the tool moved deeper in a stepwise fashion to follow the next contour. This process was repeated until the desired depth was reached.
Two CCD cameras are installed on the bench of the milling machine, and focussed on the outside of the two-angle-pyramid. In this way, it was possible to take a sequence of pictures during the SPIF process. In the present study, a two-angle-pyramid was formed and the process was stopped at a depth of 90 mm (the depth of 60 mm for the 65° pyramid, an additional depth of 30 mm for the 30° pyramid). The step size was chosen to be 1 mm. Continuous lubrication was used between the tool and the blank during the process. The DIC experiment was performed in several steps:

1. A speckle pattern was painted on the outer surface of the cone. After a state of the art 3D calibration, the system was ready for the in-process measurement of the displacement field.
2. After the reference picture was taken from the undeformed blank, low feed rate processing at 500 mm/min and a rotational speed of 50rpm. The pictures were captured at a 4Hz frequency throughout the entire SPIF process.

VI. DIC Results & Discussions

Database and accuracy
Six material points defining a planar section were selected on the sheet metal (see figure. 4a). The used DIC system has an accuracy of 0.1 pixel. The experimentally measured profile of the pyramid and the displacement evolution of the selected material points starting from the undeformed blank are plotted in figure 4b.

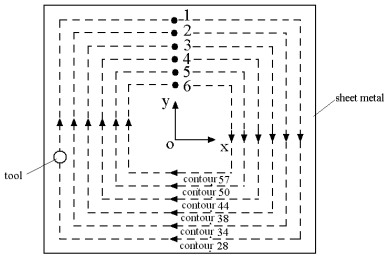

Fig.4a. Diagram of the six selected points

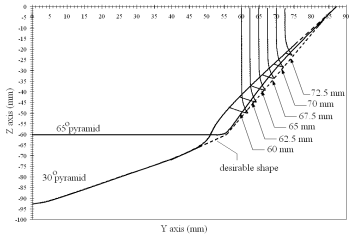

Fig.4b. Displacement evolution

Total displacement

One of the material points, point 6, is selected for detailed discussion of the displacement evolution recorded by DIC through the total SPIF process.

The displacement evolution of point 6 (with the coordinate of (0, 60, 0) in the undeformed sheet) is plotted as a function of time in figure 5. Three regions are distinguished.

1. *Region I (AB)*: The tool started to work far from this point. As the tool came closer to the material point, the displacement of the point increased. At that moment the material point was situated in the unformed area of the two-angle-pyramid, and maintained its elastic material properties. The displacement curve shows a stepwise evolution. Every step corresponds to the total displacement of the material point, during one contour. The total number of steps is equal to that of the contours.
2. *Region II (BC)*: The tool is now very close to the selected point. The material point is severely plastically deformed due to the high stress levels induced in the vicinity of the tool path. The 65^o part of the pyramid formation is finished at the end of *region II*.
3. *Region III (CD)*: The tool has passed the material point and started to form the 30^o part of the pyramid. The material point was situated in the deformed area. As the distance between the tool and the material point increases, the displacement value of the observed material point started to reduce, which caused an increasing shape deviation for this material point.

The deviation of the material points in z- axis can be defined as the difference between the maximum displacement and the final displacement.

$$deviation = max.\ displacement - final\ displacement \quad (2)$$

In order to visualize the three regions discussed above on the surface of the two-angle-pyramid, three images are selected.

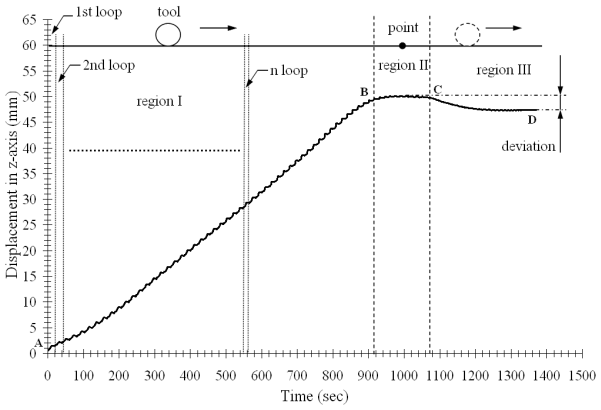

Fig.5. Total displacement in the z-axis of material point 6 during two-angle-pyramid forming

During the final stage of *Region II* and in *Region III* (see figure 6), the tool finished the first pyramid and was forming the second pyramid. It is noticed that part of the deviation is emerging during the final contours of the forming of the 65^o pyramid, another part is caused by the forming of the second pyramid with 30^o. In addition, the value of the displacement of the material point reduced quickly during the early stage of forming the second pyramid. The displacement gradually converges to a stable level towards the end of the process.

The total displacements in z-axis of the six material points were investigated in a similar way. The displacement of the evolution in Region II is different for every point (See fig. 7). The farther the selected point is from the centre point of the pyramid (0, 0, 0), the broader the region II is. This is because, for instance, material point 1 is the first point which reached the deformed area of the material during SPIF process. When this material point is deformed, its displacement in z-axis tends to be stabilized.

The final deviations of these points at the end of the two-angle pyramid are not equal. The final deviation of the six selected points versus to their thicknesses is presented in figure 8. Thickness does not affect the deviation of the points from their desired position.

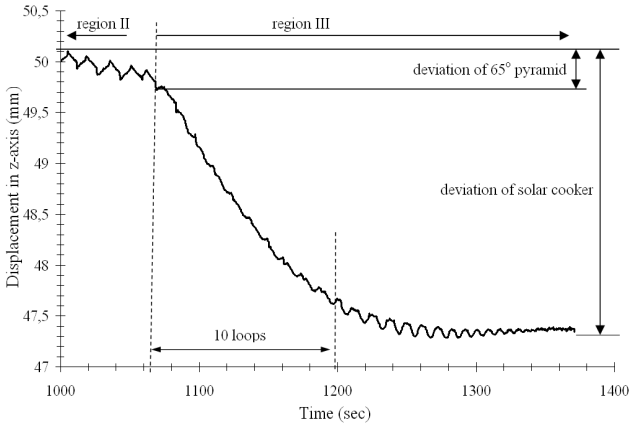

Fig.6. The displacement evolution on 6th point in region III

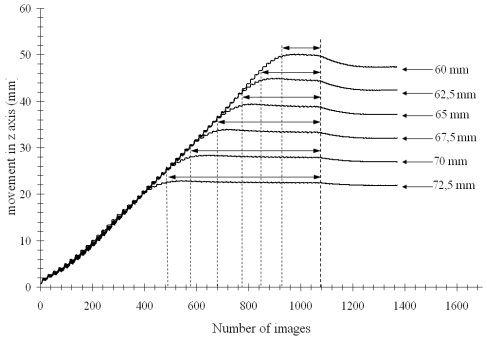

Fig.7. Displacement in z-axis for six selected points

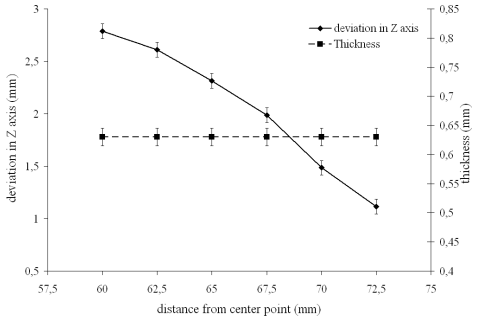

Fig.8. Deviation in z-axis of the six selected points

Springback

During the forming process as the tool was moving in one contour, it is noticed that the selected point is deformed in the z-axis direction and afterwards returns to a specific value of displacement. A specific evolution of the displacement is extracted on material point 1 when the tool was passing there (see Figure 10). It is found that:

1. $t_1 < t < t_{contact}$. The tool was approaching the material point. The displacement of the selected point in z axis slightly increases.
2. $t = t_{contact}$. The tool was in contact with the selected point. The displacement reached its maximum value.
3. $t_{contact} < t < t_2$. The tool was departing from the selected point. The displacement decreases gradually due to material spring back and remained at a final value at the end of the contour.

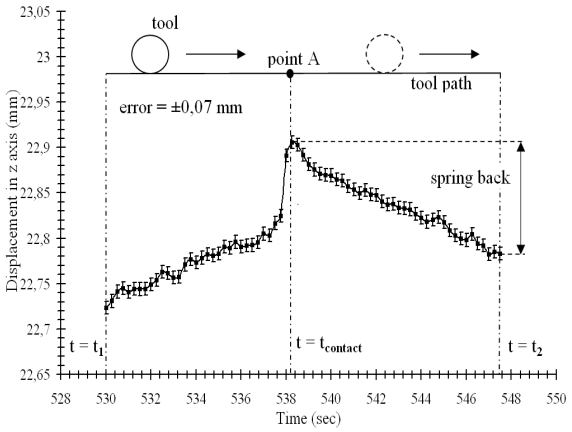

Fig.10. The displacement evolution of the material point during the tool transit.

VII. CONCLUSIONS

The evolution of the displacements and the spring back phenomena on specific material points were studied in detail. Several conclusions were exported during the study of this paper

1. Elastic spring back as occurring immediately after a tool transit is only responsible for a minor fraction of the total geometrical error.
2. Deformations occur mainly after direct contact with the tool and are built up gradually over multiple contours.
3. Deformations caused by equal angle processing are limited while slope changes induce large deviations with decreasing impact in function of the distance from the slope change location.
4. The relation between the thickness distribution and the shape deviation based on six selected material points was investigated. It appeared that the shape deviation is independent on the thickness at those selected points (see fig.8).

According to the observation made in the frame of this paper, adaptive tool path strategies based on in-process observations can not be affective in a single pass strategy.

ACKNOWLEDGEMENTS

The authors would like to acknowledge the financial support from the Flemish Institute of fundamental Sciences (FWO) and from the Institute for the Promotion of Innovation by Science and Technology in Flanders (IWT).

REFERENCES

[1] P.A.F. Martins, N. Bay, M. Skjoedt, M.B. Silva: *Theory of single point incremental forming,* CIRP Annals – manufacturing technology 57 (2008) 247-252.

[2] J.R Duflou, J. Verbert, B. Belkassem, J. Gu, H. Sol: *Process window enhancement for single point incremental forming through multi-step toolpaths,* CIRP Annals – manufacturing technology 57 (2008) 253-256.

[3] F. Micari, G. Amprogio, L. filice: *Shape and dimensional accuracy in single point incremental forming: state of the art and future trends,* Journal of materials processing technology 191 (2007) 390-395.

[4] S. He, J. Gu, H. Sol, A. Van Bael, P. Van Houtte, Y. Tunckol, J. Duflou: *Determination of strain in incremental sheet forming process*, Key Engineering Materials, 344 (2007) 503-510.

[5] S. Matsubara: *A computer numerically controlled dieless incremental forming of a sheet metal,* Journal of engineering manufacture 215/7 (2001) 959-966.

[6] D. Young, J. Jeswiet: *Wall thickness variations in single point incremental forming,* Journal of engineering manufacture 18/11 (2004) 1453-1459

Proceedings of the 8th National Congress on Theoretical and Applied Mechanics, May 28-29, Brussels, Belgium.

Experimental investigation of scaling laws for mechanical fatigue behaviour

Brecht Van Hooreweder, Paul Sas, Rene Boonen, David Moens, Filip De Coninck
Department of Mechanical Engineering, Katholieke Universiteit Leuven
Celestijnenlaan 300b, 3001 Heverlee – Belgium
email: brecht.vanhooreweder@mech.kuleuven.be

Abstract: ***This paper deals with the use of scaling laws for mechanical fatigue behaviour. It focuses on the development of a multi-axial test rig for testing selective laser sintered components.***

Keywords: Mechanical fatigue, Size effects, Scaling laws, Selective laser sintering, Non destructive inspection

I. INTRODUCTION

The physics of fatigue have been well known for over 100 years. However, correct application of this knowledge still holds challenges [1]. One of these challenges is to accurately predict the fatigue life of large mechanical components under alternating load.

Different types of fatigue analysis can be used to tackle this problem. A number of analytical and numerical calculation techniques exist to determine the expected fatigue life in an early stage of the development process [2][3]. These techniques are based on test results from standardized fatigue experiments. Different parameters are used to take deviations from these standardized conditions (size, loading, surface quality, plasticity, …) into account [4][5].

Due to the large amount and the complexity of the parameters that influence the fatigue phenomenon, the accuracy of analytical and numerical calculation techniques to predict the fatigue life of a multi-axial loaded mechanical component is in practice often unsatisfactory. Fatigue tests on the original component yield more accurate results, but impose an expensive and time consuming test setup, especially for large components [6].

This research focuses on the determination of the fatigue life of large mechanical components by means of fatigue experiments on smaller scale models under dynamic excitation. To accomplish this, appropriate scaling laws are needed to extrapolate the fatigue life of the scale models to the fatigue life of the original component.

II. SCALING LAWS FOR DURABILITY ANALYSIS

A. Advantages

Fatigue testing on small scale models has clear advantages compared to fatigue tests on full scale prototypes. Developing the test setup requires less time and space. Moreover, producing the scale models can be done with a limited amount of time and material and applying the (smaller) loads requires less energy. Also the mass of the test object is lower. This leads to an increased natural frequency of the test specimen which allows testing at higher cycle frequencies without any danger for resonance to occur.

Many of these advantages can also be found in wind tunnel testing, where scale models have been used for many years [7]. Small models of planes, buildings or cars are tested at increased wind speeds to obtain the same Reynolds number as in real life conditions. Afterwards, the measured aerodynamic drag can be extrapolated and the aerodynamic properties of the full scale structure can be determined in a fast and economical way.

B. Size effects

The effects of the size of a component on its fatigue life are generally annotated as “size effects” [6]. In contrast to the quite straightforward and frequently used scaling laws in aerodynamics, the fatigue phenomenon does not lend itself that easily for this purpose. Starting from 1939, some studies have be undertaken to analyze size effects in metals [8] [9][10]. As a result, it has been shown that under fully reversed rotational bending, test specimens with a large diameter experience a shorter fatigue life than specimens with a small diameter [11][12]. Two factors dominate this effect:

1) Variability in material properties

It is a well known fact that at microscale every material is inhomogeneous and anisotropic. Small mechanical defects are always present and distributed randomly throughout the material [13]. For rotational bending, the mechanical defects at the surface of the test specimen are most critical because of the maximum stresses acting there. These defects are often caused during a machining process and can be seen as stress raisers. Since fatigue failure is a weak link mechanism, one can understand that a larger diameter implies a higher probability for a ‘weak link’ to occur. Consequently, crack initiation is more likely to start, followed by crack growth and final fracture.

This local variation in strength is more pronounced in fatigue testing then in plastic deformation. This is due to the fact that fatigue failure arises from failure of the weakest element, while plastic properties are determined by the average behaviour of a large number of elements.

2) Stress gradient

When a test specimen is subjected to rotating bending, a stress gradient exists between the maximum stress at the surface layer and the minimum stress at the neutral line. Specimens with increased diameter that are subjected to the same maximum stress will experience a steeper gradient as can be

seen in Fig.1. As a result, the volume subjected to >90% of the maximum stress (V90%) is larger for the specimen with increased diameter (Fig.1). Assuming this critical volume to be the driving force for fatigue failure, it can be understood that a larger diameter implies a shorter fatigue life [14].

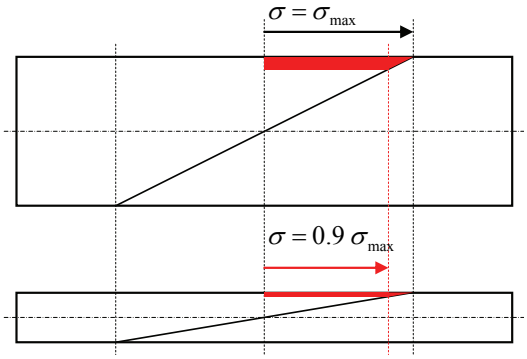

Fig.1 Stress gradient and critical volume

This theory, which was developed by Kugel in 1961, is also known as the critical volume concept [15]. Fatigue experiments on steel under alternating loading from Kloos [16] and Sonsino [17] indicated a clear relation between the endurance limit (S_e) and the critical volume ($V_{90\%}$). In this formula $S_{e,r}$ and $V_{90\%,r}$ represent the known endurance limit and critical volume from a reference specimen. For any component one can determine $V_{90\%}$ and thus calculate the component's endurance limit using:

$$\frac{S_e}{S_{e,r}} \leq \left(\frac{V_{90\%,r}}{V_{90\%}} \right)^{0.05} \quad if \quad D_{specimen} \leq 30mm$$

The influence of the stress gradient on the fatigue life also explains the more profound size effect when loading in rotating bending in comparison with alternating loading in tension. The results from rotating beam and cyclic tension experiments on 37Cr4 steel from Kloos illustrate this (Fig.2).

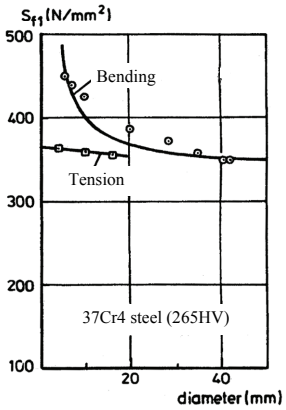

Fig.2 Size effect for alternating bending and tension [16]

C. Influencing factors

There are a number of parameters that influence the fatigue properties of a material. Fig.3 gives an overview.

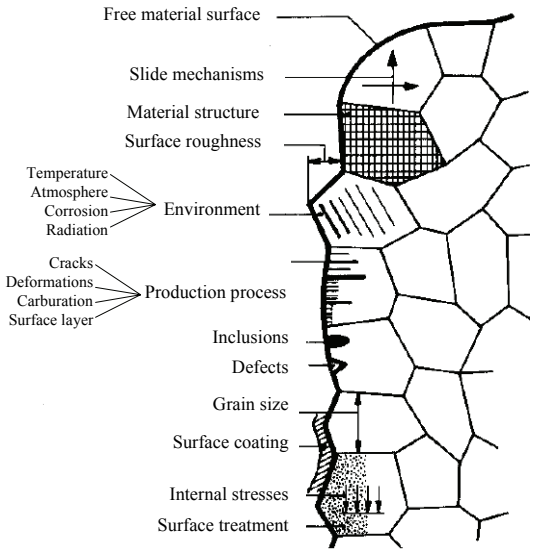

Fig.3 Some fatigue influencing factors

It is often very difficult to distinguish between these factors [18]. That is one of the main reasons why research on the pure effect of geometric size on the fatigue properties of metals is extremely difficult. To obtain a uniformly scaled geometry the surface roughness has to change. This can only be done using different production parameters, leading to different residual stresses in the surface layer and just below. Since this is the most critical region for crack nucleation to occur, the scaling of surface roughness most be done with high precision while keeping in mind the consequences.

Also temperature plays an important role. Small specimens, having a greater surface/volume ratio, can dissipate heat more easily than large specimens. High temperatures can result in transformations in the material structure and facilitate plastic deformation in the crack zone. Generally, this effect depends to a great extent on the used material and the applied temperature range.

Another important factor is the frequency of the applied load. The fatigue properties of metals are usually found to be independent of the testing frequency up to 250Hz [6]. However, if a large test specimen is tested at low frequency to avoid high temperatures, corrosion can play a more prominent role then in a small test specimen tested at a higher frequency.

Furthermore, the test setup itself needs to be capable of clamping test specimens of different size without introducing secondary bending or alignment errors. The actual amount by which the loading axis of a test setup deviates from the axis of the test specimen is characteristic of the test setup itself and independent of the test piece. Therefore, the secondary bending stress imposed on the test piece as a result of non-axiality of load may be considerably larger for small then for large test pieces.

III. Experimental Validation of Scaling Laws

In order to gain more insight in scale effects for the fatigue behaviour of steel and plastic, an experimental test setup will be developed based on the well known rotating bar bending test setup (Fig.4) invented by Wöhler in 1850. The four point bending principle implies a constant bending moment between the load bearings. Letting the motor run results in alternating tension and compression stresses in the surface layer of the test specimen.

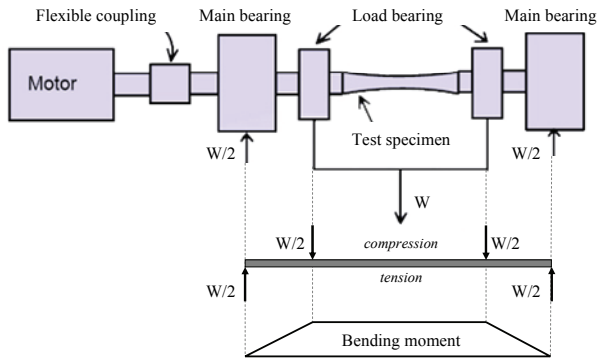

Fig.4 Rotating bar bending test setup

This test setup has a number of advantages. First of all it is standardized (DIN 50113 and ISO 1143) [19], which allows a large number of existing test results to be used for validation purposes. Furthermore, only relatively cheap, conventional parts are needed to develop the structure. Also, the test frequency can easily reach up to 9000rpm (150Hz).

However, none of the commercial test rigs allows for clamping of specimens with a large range of diameters. Therefore, the authors want to develop a multi-axial test rig, combining alternating bending forces with torsional loads, for test specimens with test section diameters (d) between 5 and 20mm.

Combining bending and torsion can be done in two ways: electro-mechanically (i) and mechanically (ii). In both cases it is desirable that some form of power circulation is provided [20]. The first method involves the installation of a generator at the free end of the main shaft of the test rig. By changing the electrical load, the amplitude and fluctuation of the torsional stresses in the test specimen can be adjusted. It is also possible to create a closed loop system and to supply the generated electricity back to the motor. The second method is presented in Fig.5.

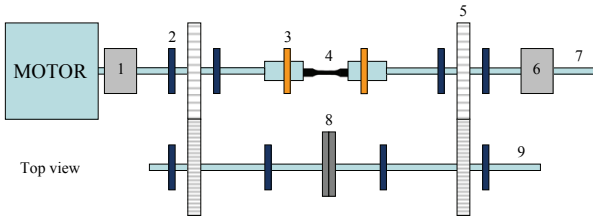

Fig.5 Combining bending and torsion

This test rig includes a flexible coupling (1), support bearings (2), load bearings (3), test specimen (4), two gear sets (5), cycle counter (6), rigid (7) and flexible (9) shaft and a special type of indexing head (8). Before starting the test, the user uses two lever arms to introduce torque in the flexible shaft by turning the two discs of the indexing head relatively to each other. Due to the closed transmission loop, the test specimen experiences a constant amount of shear stress which can be measured with strain gauges. It needs to be emphasized that macroplasticity must be avoided in any component of the transmission loop in order to avoid a change in torque and shear stresses. Furthermore it is clear that this method does not provide the means of combining cyclic bending with cyclic torsion. Only a constant mean shear stress can be superimposed on the cyclic bending load. In addition one could notice that the motor only needs to provide the power equal to the power losses in the closed transmission loop.

A. Selective laser sintered components

Past research projects have indicated that it is extremely difficult to prepare geometrically similar specimens of increasing diameter which have the same metallurgical structure and residual stress distribution throughout the cross section [8][21]. Therefore, the authors will primary focus on the testing of plastic selective laser sintered components at different scales.

Laser sintering is an additive fabrication process in which layers of preheated powder are spread and laser radiation is used to sinter selected areas of this powder (Fig.6) [22]. Starting from CAD data, very complex components can be build up layer by layer within a few hours. This production process makes it possible to manufacture test specimens at different scales more easily. However, various process parameters such as laser power, beam speed, delay time, cooling time, build orientation and layer thickness need to be precisely controlled so that all the components experience the same influencing factors [23][24].

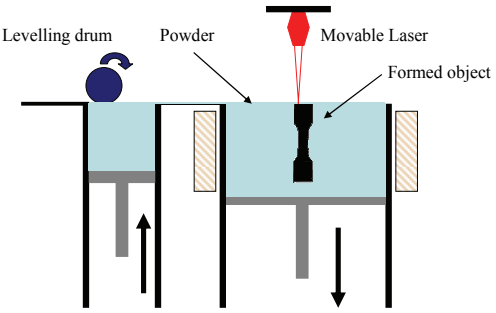

Fig.6 Selective laser sintering

Although this research focuses on the scale effects itself, selective laser sintered components are increasingly being used for functional purposes in medical and automotive applications. Unfortunately, knowledge of the fatigue properties of these sintered materials is very limited and accurate fatigue life predictions are therefore not possible. The results of this research project will help to gain some insight in the fatigue behaviour of sintered products.

B. Test Specimens

The design of the test specimen should be such that failure occurs only in the test section (L_c). For tangentially blending fillets this implies $D \geq d \times (1.5)^{0.5}$, $r \geq (8 \times d)$ and $L_c \geq (2.5 \times d)$ according to ASTM E466 [25] which is more conservative then the DIN or ISO standards for rotating bending [19].

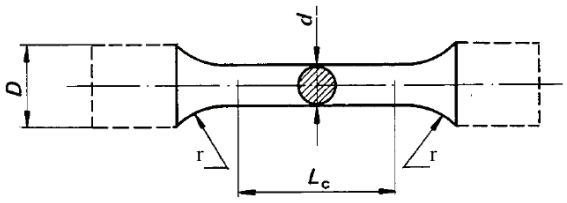

Fig.7 Test specimen geometry

According to ASTM E739 [26] regarding stress-life testing, a minimum of 12 to 24 specimens need to be tested for reliable fatigue data. For the purpose of this research, 20 specimens will be tested at each scale. In order to reach a replication between 75 and 88%, 5 stress levels will be used to deduce the SN-curve for specimens at a particular scale.

C. Non destructive inspection

Fatigue life can be split into a crack initiation and a crack propagation period as indicated in Fig.8. The first mechanism can be seen as a surface phenomenon, while crack propagation depends more on the bulk properties of the material [5]. It may be noted that the initiation period covers a significant part of the fatigue life for most materials.

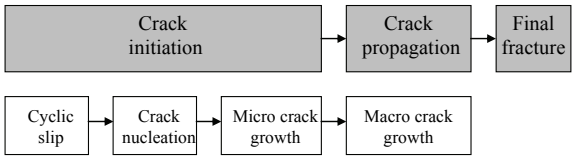

Fig.8 Fatigue failure process

The transition point between initiation and propagation depends highly on the material tested and is very difficult to find. In order to be able to distinguish between these two failure types and gain more understanding about the failure mechanism in general, a non-destructive inspection (NDI) technique will be used.

The acoustic emission (AE) technique has been successfully used in the past for locating and monitoring fatigue cracks in steel, plastic and composite components [27][28]. The technique is based on the fact that almost any material emits acoustic energy when stressed. This elastic strain energy is released from a number of causes such as plastic deformation, the sliding of grain boundaries over one another, from inclusions cracking and from crack growth [29]. A piezoelectric element converts these mechanical vibrations into electrical signals which are then filtered, amplified and related to the accumulation of damage occurring in the component under investigation. A major advantage is the possibility of continuous monitoring. Therefore, AE is suited for real-time non-destructive inspection in the previously prescribed multi-axial test rig. However, there are some points of attention regarding the combination of rotating machinery and AE techniques. First of all – since it's not possible to mount the sensors directly on the test specimen – the only suitable places for the sensors are the load bearings (Fig.5). Also, the detectability of AE events depends solely upon whether or not the amplitude of the event exceeds the ambient noise in the detection system. The vibrations of the motor, the bearings and the gears will disturb the signals resulting from the fatigue mechanism itself. Furthermore, because the most important emission events are random and unrepeated, signal averaging is not an option [30]. Only when these secondary vibrations can be controlled, one can focus on the signal resulting from fatigue damage. Since AE has been used in the past for condition monitoring of rotating machinery [31], this seems to be a challenging but promising research objective.

Another possibility for non-destructive inspection is the use of an optical microscope, equipped with DIC (differential interference contrast) and a CCD (charged coupled device) camera. This apparatus can be used for real-time monitoring of the growth of surface slip bands [32]. Because fatigue is an irreversible process, it is also possible to interrupt the fatigue test at certain stages and evaluate the cumulative damage.

IV. Conclusion

More profound knowledge of size effects in fatigue behaviour can lead to the development of inexpensive test rigs to determine the fatigue life of large components. Experiments can be done by using smaller scale models and afterwards, the results from these tests can be extrapolated by using appropriate scaling laws. However, because of the various influencing factors, scale effects in fatigue are difficult to analyse. Also the production of geometrically similar test specimens at different scales which have the same metallurgical structure and residual stress distribution is complicated. Therefore, plastic selective laser sintered components at different scales will be tested using a multi-axial test rig. Also non destructive inspection techniques will be used to gain more insight in the fatigue phenomena when testing at different scales.

Acknowledgements

This research is financed by a project of the Institute for the Promotion of Innovation through Science and Technology in Flanders (IWT Vlaanderen) in association with Flanders 'Drive.

References

[1] Darell F. Socie, *Fatigue made easy: Historical Introduction*, University of Illinois at Urbana-Champaign, 2002.

[2] FKM-guideline, *Analytical Strength Assessment of Components in Mechanical Engineering*, VDMA, 5th revised edition, 2003.

[3] MSC Fatigue User manual, nCode International Ltd. Sheffield UK, 2003.

[4] Bernd Bertsche, *Reliability in Automotive and Mechanical Engineering*, Springer, 2002.

[5] J. Schijve, *Fatigue of Structures and Materials*, Kluwer Academic Publishers, 2009.

[6] E. Zahavi and V. Torbilo, *Fatigue Design: Life Expectancy of Machine Parts*, CRC-press, 1996.

[7] K. Pettersson, A. Rizzi, *Aerodynamic scaling to free flight conditions: Past and present*. Progress in Aerospace Sciences 44, 295-313, 2008.

[8] W. Weibull, *Fatigue testing and analysis of results*. Pergamon Press, 1961.

[9] Findley WN, *An explanation of size effect in fatigue of metals*. J Mech Engng Sci; 14:424-5, 1972.

[10] Morkovin D. and Moore, H.f. *Third progress report on the effect of size of specimen on fatigue strength of three types of steel*, Proc. Amer. Soc. Test. Mater. 44, 137-158, 1944.

[11] O.J. Horger, *Fatigue characteristics of large sections*, American Society of Metals, 1953.

[12] Hatanaka H, Shimizu S, Nagae A. *Size effect on rotating bending fatigue in steels*. Null JSME, 26:1288-95, 1983.

[13] Mc Clintock F.A., *The statistical theory of size and shape effects in fatigue*, ASME Paper No.55, 1955.

[14] Phillips G.E. and Heywood R.B. *The size effect in Fatigue of plain and notched steel specimens loaded under reversed direct stress.* Proc. Instn. Mech. Engrs., 176, 113, London, 1951.

[15] Kugel, R. *A relation between theoretical stress concentration factor and fatigue notch factor deduced from the concept of highly stressed volume*. ASTM Proc. 61, 732-748, 1961.

[16] Kloos, K.H. *Grösseneinfluss und dauerfestikeitsengeschaften under besondered berücksichtigung optimierter oberflächenbehaundlung*. Werkstofftechnik 12, 134-142, 1981.

[17] Sonsino, C.M. *Zur bewertung des schwingfestikeitsverhaltens von bauteilen mit hilfe örtlicher beanspruchen*. Konstruction 45, 25-33, 1993.

[18] L. Yung-Li, P. Jwo, H. Richard, *Fatigue Testing and Analysis: Theory and Practice*. Amsterdam, Elsevier, 2005.

[19] ISO 1143 and DIN 50113 standard, *Rotating bar bending Fatigue Testing.*

[20] D.H. Wright, *Testing automotive materials and components*. SAE International, 1993.

[21] American society for metals. *Metals handbook: Mechanical testing, 9th ed.* - Metals Park (Ohio), 1985

[22] L. Lü, J. Fuh; Y.S. Wong, *Laser-induced materials and processes for rapid prototyping*. Kluwer Academic Publishers, London, 2001.

[23] P. K. Jain, P.M. Pandey, P.V.M. Rao, *Effect of delay time on part strength in selective laser sintering*. Int. J. Adv. Manuf. Tech, 2008.

[24] P. Marcelis, *Control of selective laser sintering and selective laser melting processes.* PhD thesis, K.U.Leuven, Belgium, 2007.

[25] ASTM E466 – 96 standard, *Conducting force controlled constant amplitude axial fatigue test of metallic materials*.

[26] ASTM E739 – 91 standard, *Statistical analysis of SN and EN Fatigue Data.*

[27] M.E. Biancolini, C. Brutti, G. Paparo, A. Zanini, *Fatigue cracks nucleation on steel, acoustic emission and fractal analysis.* International Journal on Fatigue 28, 1820-1825, 2006.

[28] D. Van Hemelrijck, A. anastassopoulos. *Non destructive testing*. Rotterdam, 1996.

[29] R. Halmshaw. *Non destructive testing*. Hodder Headline, London, 1995.

[30] K.J. Marsh, R.A. Smith, R.O. Ritchie, *Fatigue crack measurement: Techniques and applications.* Engineering materials advisory service, London, 1991.

[31] S.C. Kerkyras. *The use of acoustic emission as a condition monitoring tool of rotating and reciprocating machinery*. Emerging Technologies in NDT, Rotterdam, 2000.

[32] G.F. Miscow, P.E.V. de Miranda, T.A. Netto, J.C.R. Plácido, *Techniques to characterize fatigue behaviour of full size drill pipes and small scale samples*. International Journal of Fatigue 26, 575-584, 2004.

Proceedings of the 8th National Congress
on Theoretical and Applied Mechanics,
May 28-29, Brussels, Belgium.

Time-accurate numerical simulations of transitional flows

Jan G. Wissink
Brunel University - School of Engineering and Design
Kingston Lane - Uxbridge, UB8 3PH, UK
e-mail: jan.wissink@brunel.ac.uk

Transitional flows are ubiquitous. Examples range from internal flows such as in Osborne Reynolds' famous experiment – in which he studied the instability of Poiseuille flow in a pipe - to external flows such as the flow over airfoils. For transition to occur an unstable laminar flow needs to be disturbed. The larger the disturbance is, the quicker the flow will undergo transition. A recent repeat of Reynolds' experiment, using the original apparatus, showed an earlier onset of transition which was attributed to the increased traffic load on the nearby streets.

Over the years, transitional boundary layer flows have received much attention. Transition to turbulence is sometimes triggered explicitly in order to avoid downstream boundary layer separation, which may adversely affect the aerodynamical properties of an airfoil and could lead to stall or mechanical failure. Basically, three types of boundary layer transition can be observed:

1) Natural transition - through the triggering of Tollmien-Schlichting waves that evolve into Λ-vortices in the downstream direction. Farther downstream, the Λ-vortices become unstable and turn into turbulent spots that grow and eventually merge to form a fully turbulent boundary layer downstream. An example of this type of transition can be found in the boundary layer flow over wind turbine blades.
2) In by-pass transition one or more stages of the natural transition scenario are by-passed. Typical examples of by-pass transition can be found in the flow over low-pressure (LP) turbine blades, where relatively strong free-stream fluctuations tend to trigger low-speed streaks in the laminar boundary layer. These streaks (which are small, negative jets) may undergo transition through a Kelvin-Helmholtz (KH) instability and eventually form turbulent spots.
3) Separation-induced transition may occur naturally in flow over LP compressor blades. It is characterized by the formation of a laminar separation bubble. As the flow separates, it usually undergoes a KH instability leading to a roll-up of the separated boundary layer. Inside the roll turbulence is generated by the triggering of elliptical instabilities. Farther downstream, the flow may re-attach to form a fully turbulent boundary layer.

In modern jet engines the LP turbine supplies power to the fan and, sometimes, the first compressor stages. Recent increases in fan diameters require a higher work-output from the LP turbine at reduced rotational speed. Typically, an LP turbine is relatively heavy since it consists of several stages, while its efficiency strongly influences fuel consumption. Hence, even small improvements have a significant effect. The periodic unsteadiness induced by rotor–stator interaction and the low Reynolds number are characteristic for flow in an LP turbine. Both phenomena directly affect blade boundary layer transition, the tendency to separation, heat transfer and flow losses. Separation of the boundary layer along a turbine blade changes the aerodynamical properties of a blade and might eventually cause mechanical failure. Free-stream fluctuations and incoming wakes, generated by the upstream row of blades, can be employed to passively control this boundary layer separation. As the level of external fluctuations is too high for natural transition to occur, by-pass transition is very common and, sometimes, also separation-induced transition can be found.

Because of the relatively low Reynolds numbers, recent increases in computational power have made it possible to perform highly-resolved, time-accurate numerical simulations of flows over model LP turbine and compressor blades. The time-accurate numerical simulations aim to improve the understanding of the complicated interaction of both periodic and uniformly distributed external fluctuations with the blade boundary layer. At first, the periodic suppression of a laminar separation bubble on the suction surface of a LP turbine blade by periodically impinging wakes is studied in great detail. A KH instability is found to be triggered by the large-scale periodic movement of the wake. Further transition to turbulence – triggered by small-scale, three-dimensional free-stream fluctuations - is found to take place inside the KH rolls. Along the pressure surface a distinctive pattern of streamwise longitudinal vortical structures is found to form by the stretching of the wake's vortical structures by the main flow.
Separation bubbles can be affected by the occurrence of by-pass transition upstream of the location of separation. This will be illustrated by further simulations of flow around a LP compressor blade: The impinging wakes periodically trigger turbulent spots that move downstream and locally suppress separation. Once the turbulent spot has passed, after a transient period the separation bubble is found to recover.

Proceedings of the 8th National Congress on Theoretical and Applied Mechanics, May 28-29, Brussels, Belgium.

Designing intelligent products: the next revolution in virtual engineering

Herman Van der Auweraer, Jan Anthonis, Jan Leuridan
LMS International
Interleuvenlaan 68, B-3001 Leuven - Belgium
e-mail: herman.vanderauweraer@lmsintl.com

Abstract: **The increasing use of heterogeneous technologies to realize product functions and the growing contribution of electronic and mechatronic content to the product value require rethinking the product design and engineering processes. An approach is presented based on virtual and physical prototype testing. A first element is the development of more realistic multi-disciplinary simulation models based on the integration between 3D geometry-based models and 1D multi-physics system-theoretic models. A second aspect is the support of controls engineering through the use of more representative "Plant" models, allowing to synchronize the mechanical and controls development cycles. Embedding control laws furthermore paves the way to Model-In-the-Loop (MIL) and Software-In-the-Loop (SIL) concepts. By linking the virtual models to hardware systems on a physical test-bench, Hardware in the Loop testing (HIL) is made possible. The discussion focuses on the car industry including typical examples in vehicle performance engineering.**

Keywords: **multidisciplinary design, mechatronics, simulation**

I. Introduction

Product innovation managers face continuously increasing challenges with respect to their product portfolio. The traditional demands for improved performance, time-to-market and competitive price setting are strained by requirements related to product branding, personalization and ecological, safety and legislation aspects. This leads to increasingly complex, "intelligent", products relying on active components and implemented by heterogeneous technologies.

To enable this evolution, it is mandatory that the product development approach itself evolves. Integrated design and engineering methods based on physical and virtual testing have become key enablers in the product design process. Extending these to support the current product innovation challenges is hence a topic of major research initiatives.

The key engineering challenges that need to be addressed to develop such "intelligent" products are the inherent multidisciplinarity and the integration of control system concepts in the product. This requires the corresponding test and simulation methodologies to extend beyond the traditional CAD-driven approach and support the use of system and functional models crossing the boundaries of disciplines and integrating systems engineering with control engineering. It requires adopting methodologies crossing the classical Test and Simulation boundaries, leading to new physical and virtual testing paradigms such as Software-in-the-Loop and Hardware-in-the-Loop. These concepts are illustrated by vehicle design engineering case studies, demonstrating the use of 3D and 1D system and control models in applications such as vehicle chassis and powertrain design.

II. Automotive industry challenges

The automotive industry represents a significant part of the economic activity, in Europe and globally. Common drivers are the improvement of customer satisfaction (performance, personalization, safety, comfort, brand values,…) and the adherence to increasingly strict environmental and safety regulations, while at the same time reducing design and manufacturing costs and reducing the time to market. The product evolution is dominated by pushing the envelope on these conflicting demands.

A major evolution currently taking place in this industry is the increase of the electronic and mechatronic content in vehicles. Several studies forecast that the related increase to the vehicle value may well become up to 40% by 2010 and that up to 80% of the automotive innovation will come from intelligent systems [1-4]. This of course relates in part to entertainment and telematics systems, but also to the use of many control systems applied to powertrain, chassis and body engineering [5-7]. One example is the optimization of performance, economy and emissions with engine and transmission controls to realize "green" driving through energy regeneration, automatic start/stop and smart driving control. Another example is the realization of "safe" driving, through the application of ABS and ESP systems for vehicle dynamics control, but also through the adoption of numerous Advanced Driver Assistance Systems (ADAS) such as for lane following, active cruise control, object detection etc. (Fig. 1).

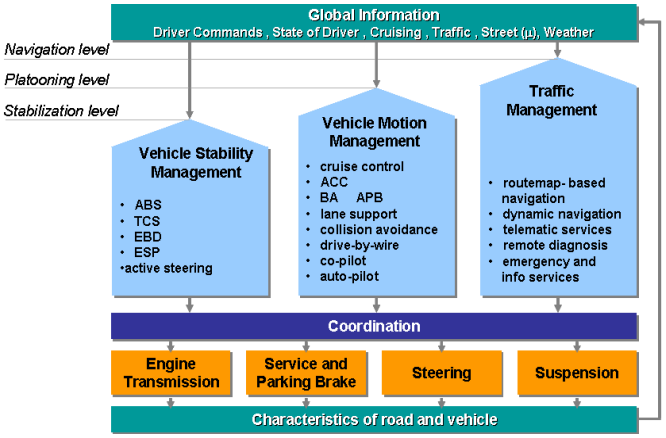

Figure 1: Vehicle safety intelligent systems

And every vehicle design has ultimately to aim for best customer experience, e.g. by optimizing through control systems ride comfort and handling behaviour and driveability, or by adoption of active systems to control brand sound.

This evolution will however not only impact the vehicle product content itself, but also the way vehicle developers (OEM) will cooperate with suppliers in new business models, offering new opportunities for full subsystem responsibility. It will also impact the way the design and development process itself has to change to enable widespread market introduction in standard vehicles [2, 4, 8, 9].

As a consequence, innovative solutions have lately been introduced for communication and entertainment, engine control and active safety. To a large extent, these innovations however remain on the level of add-on systems and a major need exists to integrate all functionality on the vehicle level through a systems approach. Configuration and performance optimization, system integration, control, component, subsystem and system-level validation of the intelligent systems must be an intrinsic part of the standard vehicle engineering process, just as this is today the case for the structural, vibro-acoustic and kinematic design. This is the goal for Intelligent Vehicle Systems Design Engineering.

III. ENGINEERING CHALLENGES FOR INTELLIGENT VEHICLE SYSTEMS

In an intelligent system, the mechanical, electrical, thermal… components of a product are connected through sensors and actuators with controllers that define the overall functioning of the product. The engineering of such an intelligent system hence requires the combination of multi-physics systems development (mechanical, thermal, fluids, electrical…), including the development of sensors and actuators, with controls engineering. The intersection of all these disciplines is referred to as mechatronics engineering.

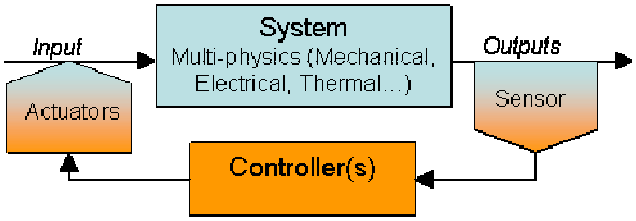

Figure 2: Generic intelligent system model

The performance engineering of products with intelligent systems mandates simulation and test solutions that are capable to analyze and optimize the performance of such a product, taking into account (1) the interactions of components and subsystems in the product, each possibly with different physics representations (mechanical, thermal, fluids…) and (2) working as "active" systems, with sensors and actuators, and interconnected to controllers. (Fig. 2)

This requires the combined simulation of multi-physics systems and the controls, e.g. simulating vehicle dynamics with ESP controls. This is also why related test systems must have an interface to vehicle networks (CAN, Flexray), where the status on the control systems is available. For example, to test the drivability of a vehicle with active suspension controls, one needs to measure vibrations of the driveline, and simultaneously the status of the active suspension controls from the CAN bus as the vibrations will depend on the working of the mechanical components and on the controller; any interpretation of the test data is meaningless unless one knows what the controller was doing at the same time.

As Fig. 3 illustrates, the engineering of intelligent systems requires the application of two interconnected "V-shaped" developments: one focusing on the multi-physics system engineering (like the mechanical and electrical components of an electrically powered steering system, including sensors and actuators); and one focused on the controls engineering, the control logic, the software and realization of the control hardware and embedded software.

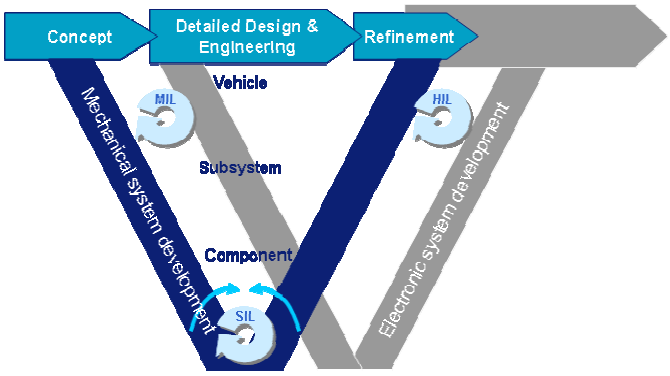

Figure 3: Double-V process for mechatronic systems

Fig. 4 shows for the example of engine design, how models of various abstractions are used at the various design levels, including 0-D requirement models, 1-D functional and physics models down to 3-D detailed design models. Testing takes place at the level of components using HIL testbenches while full vehicle integration tests provide the validation in integrated and operational conditions.

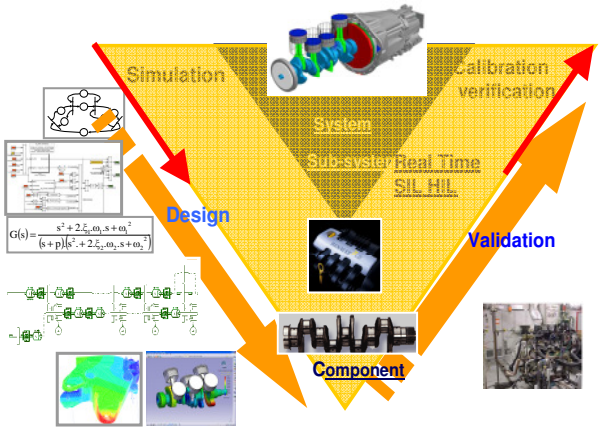

Figure 4: V-process for an engine system

Up to present this process is however very little integrated, with a clearly separated mechanic and electronic design cycle and hence failing to address the need for integrated and maximally frontloaded system modeling. The challenge in this

process is to enable a Multi-Functional System Mock-Up that can be used throughout the complete design process, based on a scalable and inter-operable simulation approach, including target setting, concept system engineering, functional simulation, 3D detailed simulation and test validation. Some further comments on the various challenges follow below.

A. Multi-physics system modelling, simulation and validation

To engineer intelligent systems, there is an expanded need for multi-physics system modeling, simulation and validation.

For example, the performance engineering of an electrical assisted steering system requires a combination of mechanical and electrical system modeling. A brake system requires mechanic, hydraulic and electric system models. An engine requires models for combustion, kinematics, dynamics, structural analysis, including specialized models for bearings. An important challenge is to extend the capabilities for multi-physics system simulation from component and subsystem level, to full system level, where more types of physical behaviour need to be taken into account.

Multi-physics system modeling, simulation and validation will also need to handle an increasing diversity and complexity of sensors and actuators that are used in intelligent systems; and to take into account the environment in which the intelligent system will operate. For example, to simulate the working of an active cruise control in a vehicle, one needs the modeling of driving scenarios including traffic (like approaching vehicles), the modeling of the functioning of the radar that is used as sensor for traffic, and the integration with vehicle dynamics. When additionally combined with vision systems (cameras), one needs the simulation of driving scenarios in a virtual environment with high realism, to simulate for example the functioning of the vision system for operation in different weather conditions (rain, fog…) or light conditions (day, night…), so as to properly validate the functioning of the vision system, and how it will interact with the vehicle dynamics.

Interaction and integration between heterogeneously modeled components and (sub)systems is a prerequisite which requires flexible and open simulation platforms. The approach must be a scalable one, starting from "frontloaded" conceptual and functional descriptions where models of increasing complexity can be added when the design cycle proceeds and more detailed knowledge (e.g. in terms of 3D models) is built up, leading to hybrid approaches combining 1D and 3D models for those parts where each model is best suited.

Mechanical and electrical/electronic system models must be integrated as soon as possible in the design process, enabling to reduce or even eliminate the divide between the 2 V-cycles.

An important, but uncharted domain is furthermore the development of test-based solutions for multi-physics system characterization just as they exist in the 3D field. Parameter identification, model validation and updating and developing hybrid models will enable exploiting the unique combination of test and simulation to advance multi-physics simulation.

A clear requirement hence exists to stepping up the capability for multi-physics system simulation, to respond to a critical need in the industry to accelerate product development of intelligent systems through an integrated, multifunctional system mock-up approach (Fig.5).

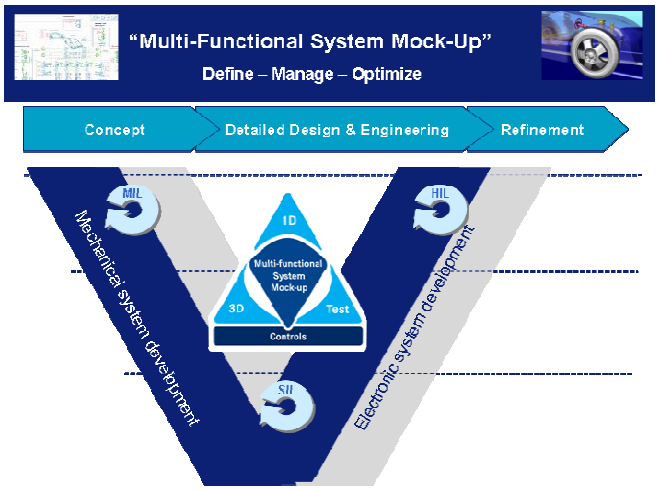

Figure 5: Multi-Functional System Mock-Up

B.Connecting multi-physics system engineering to controls engineering

Basically, two interconnection objectives can be distinguished: one is to perform systems engineering based on the multi-physics "plant" model, including the application (and hence representation of) control (Fig. 6a); the other is to perform control engineering, including the model of the systems "plant" model (Fig. 6b).

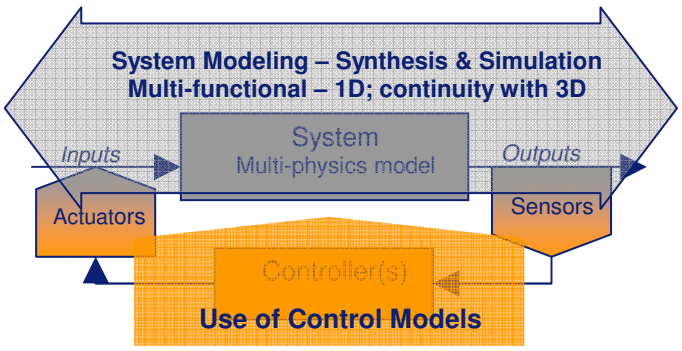

Figure 6a: Systems engineering with control models

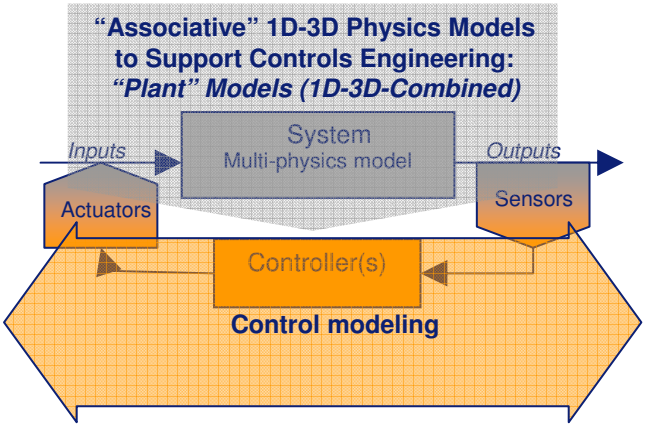

Figure 6b: Control engineering with systems models

The first objective for example serves the purpose of configuration design or concept evaluation studies or the optimization of the mechanical system design taking into account the presence of control and certain control laws (or even systems). The second objective is then oriented to the development of the optimal control logic, the development and verification of control hardware, control libraries and embedded software up to the validation and calibration of the control system on the ECU (Fig. 7).

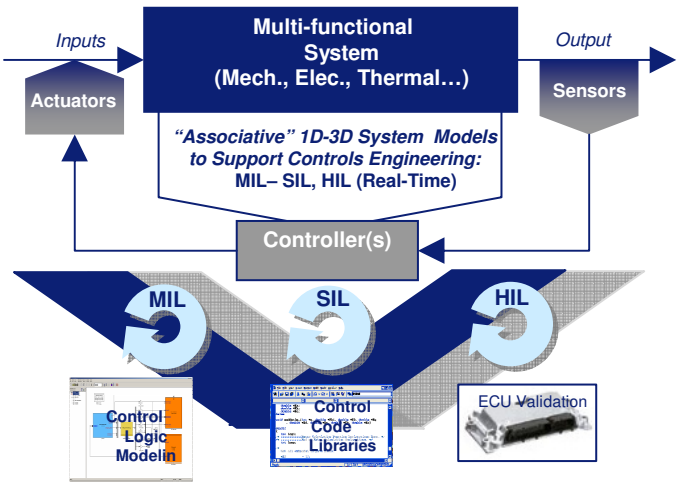

Figure 7: Associative 1D-3D models

All these stages of control engineering require interaction with multi-physics system engineering. One can distinguish the following phases:

(1) The combination of the multi-physics simulation model with this of the controller, to enable the design of the control logic and the performance engineering of the intelligent system. This is referred to as **"Model-in-the-Loop" (MIL)**. The simulation is "off-line", i.e. there is no requirement for Real-Time.

Different approaches exist. One may embed state equations with a description of the plant system (e.g. MBS or 1-D model) into these of the control (or vice versa) to enable the use of one solver, or adopt a true co-simulation approach where each system part runs its own solver. Figure 8 shows a summary of various approaches for the case of an MBS and a CACE (Computer Aided Control Engineering) model.

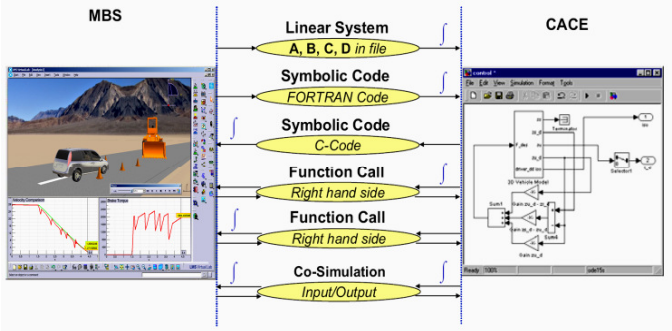

Figure 8: Co-simulation approaches

Alternatively, or in combination with above approaches, a reduction of the plant model (e.g. an FE or complex, even non-linear MBS model) into a description compatible with the controller model (e.g. state-space formulation) may be required. Model reduction is a well established field, covering a large spectrum of techniques. The reduction step mostly achieves its goals at expense of the full observability and/or controllability of the physical phenomena, leading to a macroscopic 'equivalence' but loosing direct insight in the microscopic observation domain. The challenge is to develop model compression methodologies that allow maintaining a relation with the physical meaning of model parameters

Such co-simulation and model reduction approaches are used both for MIL applications for systems engineering and for control logic engineering.

(2) The next step is the development and optimization of the "embedded" control software. This needs also to be done in context of the functioning of the multi-physics system to be controlled. This is referred to as "Software-in-the-Loop" (SIL). Where some of this can be done in off-line simulation (provided software libraries of the controller are available), the final optimization needs to take into account the working of the software in real-time, requiring real-time capable multi-physics simulation models.

(3) The final testing and calibration of the controller software and hardware, requires the controller to be connected to a multi-physics simulation model of the components, subsystems or system, in a dedicated computing environment that is referred to as "Hardware-in-the-Loop" (HIL); of course, this requires real-time capable simulation models.

From the SIL and HIL problem definition, it is obvious that one of the critical problems in running multi-physics models in a control context is their affordability in real-time, requiring to identify the best trade-off between model compression and real-time affordability. It also requires deriving criteria for assessing accuracy and reliability of real-time models in a run-time environment.

Of particular importance to the in-vehicle application is to map the process of real time systems and embedded software to the AUTOSAR standard. Defining a platform independent development approach is key to make best profit of technology development. Hardware platforms for embedded system modelling and development must hence comply with industry standards such as the AUTOSAR platform which is gaining large consensus.

Also for testing intelligent systems new challenges emerge, by providing testing systems that have the most complete interfacing to vehicle networks and standards (CAN now, but tomorrow, FlexRAY and others), so as to enable best measurement and analysis of a product performance in the context of the operation of the controller(s).

IV. CASE: VEHICLE DYNAMICS CO-SIMULATION

This case shows the integration between system and control simulations for vehicle ABS (Anti-lock Braking System)

evaluation. Multi-attribute models are developed to optimize and balance vehicle performances such as handling and road noise. The typically optimized parameters are hardpoint locations as well as suspension bushing stiffness values [10-12].

Such a multibody simulation (MBS) vehicle model, made in LMS Virtual.Lab Motion, was then used in a co-simulation approach with MATLAB/Simulink to develop control algorithms for active safety purposes [13]. Benefit is made of the capability of each package to use own integration algorithms tuned on purpose for the typical problems faced with it. This also offers the engineers to implement and tune the control algorithms without losing the complexity of the complete virtual prototype. Figures 9 and 10 show part of the MBS model (front axle), the ABS control model and some simulation results.

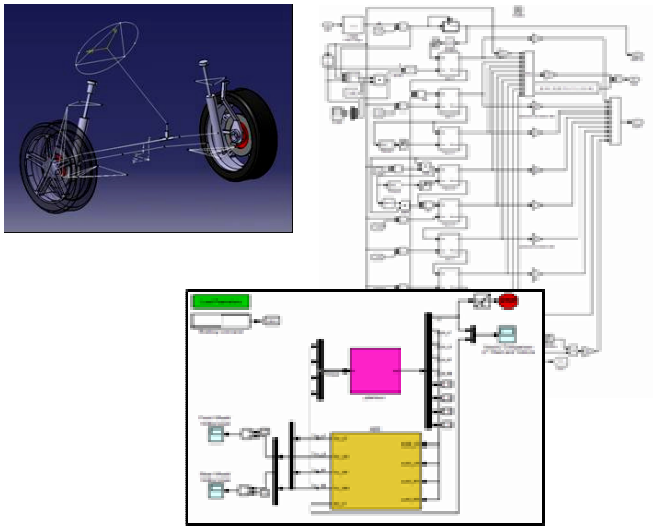

Figure 9: ABS-chassis system co-simulation model

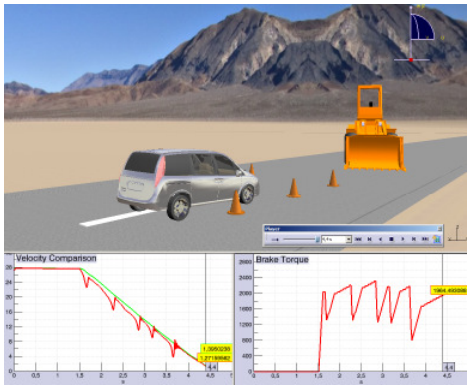

Figure 10: ABS-chassis co-simulation results

A VDC (Vehicle Dynamics Control) system is used to control the lateral dynamics of the vehicle, especially at the scenarios with larger lateral acceleration, lower road friction. One typical way of control in VDC is to use ABS to generate braking torque, independently for the 4 wheels according to the inputs of sensors for steering wheel angle, yaw rate, lateral accelerations, etc. and the drivers command regarding desired vehicle behaviour. Figure 11 shows the VDC data flow within the closed vehicle system control loop.

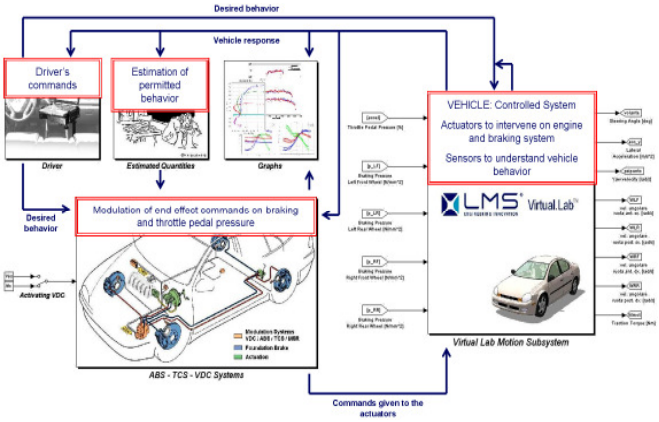

Figure 11: VDC model and data flow

Two ISO standard maneuvers were adopted during the simulations, Step Steer (ISO 7401) and Double Lane Change (ISO 3881), with VDC on and off. Figure 12 shows the resulting path of the vehicle with/without VDC under a step steer maneuver, clearly showing the difference between the lateral displacement responses.

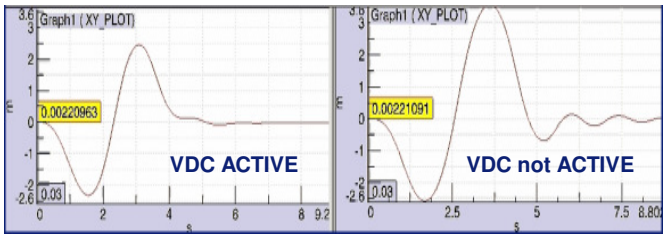

Figure 12: Steep Steer Trajectory (VDC On/off)

Figure 13 shows the results of the yaw rate of the vehicle with/without VDC system. The obvious improvement in yaw rate response shows the effect of VDC on lateral dynamics of the vehicle. In particular, a greater effect is observed after a certain period of time when VDC system suppresses effectively the transient yaw vibration due to the impulse at the steering wheel.

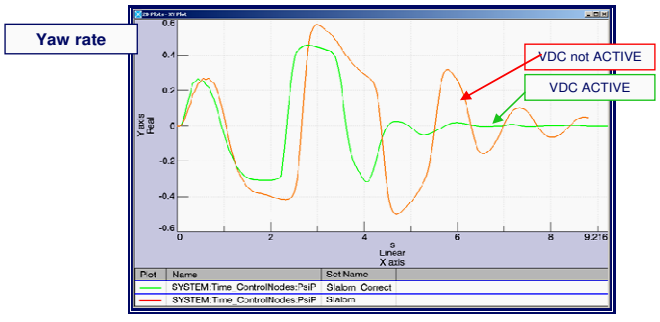

Figure 13: Yaw Rate (VDC On/Off)

V. CASE: MECHATRONIC OPTIMIZATION OF AN ACTIVE DAMPER

The design of an active suspension is more than the design of a control law. The control law will steer actuators that interact with the chassis of the vehicle and the measured response of the vehicle will affect the new computed values of the controller. Therefore in order to optimize the active

damper, the chassis dynamics and the control law need to be taken into account [14, 15].

The active damper, to be manufactured by Tenneco, is a hydraulic type, consisting of a hydraulic single rod cylinder, two valves and a pump [16]. The objective is to optimize the cylinder and rod diameters, the pump flow and the characteristics of the valves with respect to energy consumption while meeting some comfort and ride and handling performance criteria.

The optimization is performed in two stages. (Fig. 14) Theoretically, and regardless of physical feasibility, every desired performance can be achieved provided that sufficient energy is pumped into the system. Therefore, in a first stage, the set of active dampers is determined that can meet the desired performance. In the second stage, the damper parameters that deliver the lowest power consumption are selected from the set of the first stage. In this way, the damper is obtained with lowest power consumption while meeting the performance criteria with respect to comfort and ride and handling.

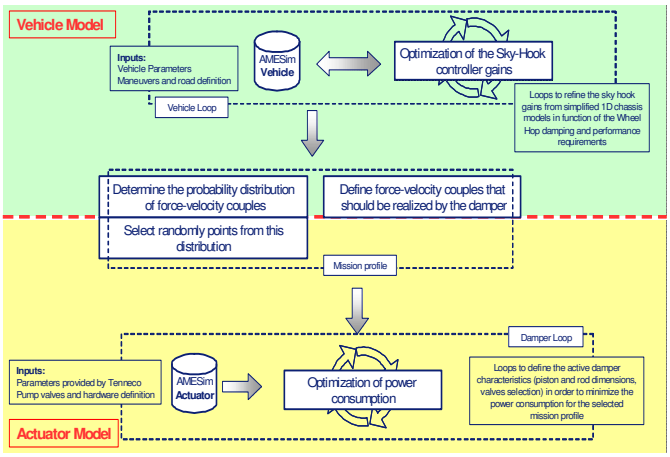

Figure 14: Active damper simulation approach

The split in the two stages is possible because of the control structure designed by Tenneco. The controller consists of a master controller which is a kind of sky-hook control algorithm that processes inputs from accelerometer, suspension deflection, steering, throttle and braking data into the desired forces that need to be applied by the active dampers to the four corners of the car (approach similar to [17]). Distributed control, the so- called actuator management, ensures that the requested forces are generated by the active shock absorber.

A behaviour model, implemented in LMS Imagine.Lab, is used in the first stage of the optimization (Fig. 15). It consists of a 15 degrees of freedom car model, power train and braking system, front and rear suspension including the elasto-kinematics and tires (Pacejka model). Instead of implementing the active shock absorbers in the model, the forces computed by the controller are immediately fed into the suspension. In this way, perfect actuator behaviour is assumed. The master controller is tuned such that the desired performance is met. Once the master controller is tuned, force-velocity couples are calculated to determine the set of damper parameters that can realize the required performance.

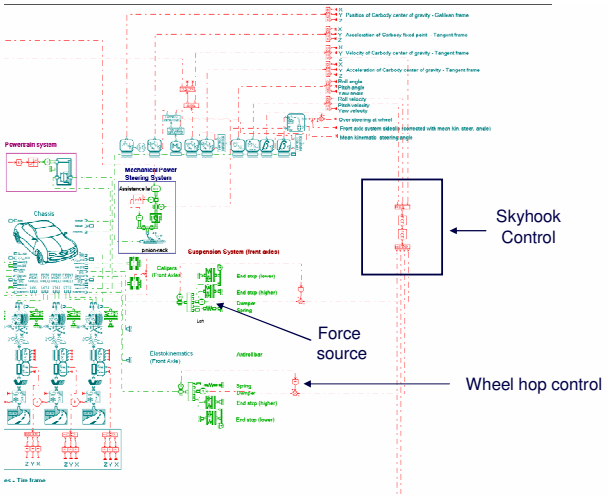

Figure 15: Active suspension 1D model

The second stage consists of a detailed model of the damper, built with the hydraulic component design library in LMS Imagine.Lab (Fig 16). Using force-velocity couples from the most occurring road profiles, the optimal damper parameters with respect to energy consumption are selected. The optimization is a mixed integer problem, involving a discrete parameter set, solved with Optimus. Three valve families are available. Within a family the course of the valve characteristics is similar. Therefore, each valve can be represented by a basic characteristic and some scaling parameter. The optimization delivers the piston and rod diameter, the maximum pump flow and the selected valve characteristics.

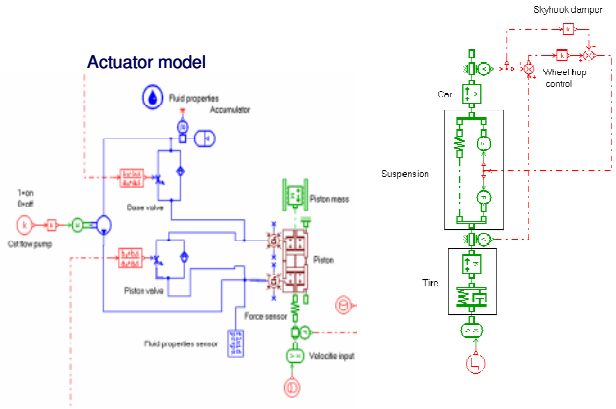

Figure 16: Damper 1D Imagine.Lab model (left) and simplified Z-translation model (right)

After the optimization, a power consumption reduction of 50 % was realized with respect to the initial configuration.

VI. CASE: HIL TESTING OF A PASSIVE DAMPER

A car is a complex system of individual components that interact with each other. Therefore, the performance of the component should be assessed within the environment it is placed in. This can be performed within a complete virtual environment or in a prototype. In the context of upfront engineering, an evaluation in a combined virtual environment with physical components, the so-called Hardware in the Loop

(HIL) can be beneficial. A typical scenario can be a supplier that must validate the performance of a component in a car while no car prototype is available yet. In the present work, the component to be tested is a passive shock absorber.

The HIL process consists of several stages. First a model of the environment of the component needs to be synthesized. In this case, this is the car, from which one shock absorber is removed. The car model is implemented in LMS Imagine.Lab and consists of a 15 degrees of freedom chassis equipped with front and rear suspension. Pacejka tire models, simplified braking and power train system are included (Fig. 17). Steering angles and road profiles can be specified by the user. This model is converted to a real-time environment and run using the real-time solver.

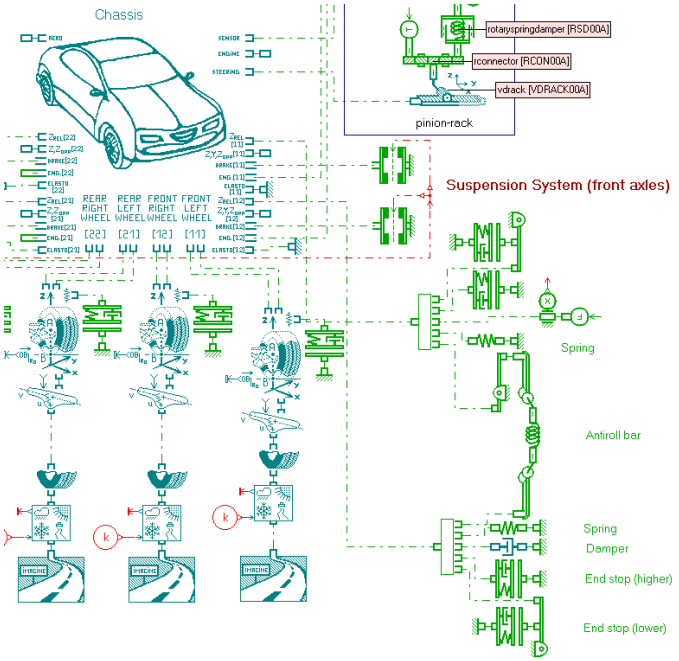

Figure 17: LMS Imagine.Lab vehicle model

As the model needs to interact with the physical world, the timing of in- and outputs should correspond to the real world. At the sample interval, the model and the component in the physical world exchange information. This means that the simulation of the model for the next sample interval should be completed within this interval. To achieve this, a deterministic solver is selected, in this case a fixed step size solver. A critical issue is selecting the time step such that the model converges and the required accuracy of the variables of interest is achieved.

This selection is also related to the specific hardware platform (computer or DSP) on which the real time model will run. In case the timing can not be achieved, model simplifications must be made. For this project, the elasto-kinematics of the vehicle have been removed and the sample interval was set to 1.2ms. The hardware to run the model is a Pentium M 1.4 GHz with 1GByte cash in PC/ 104 plus format from Kontron. The model is run in a Debian Linux environment patched by RTAI to make it real-time.

In order to transmit the computed loads from the model to the damper, an electro-dynamic actuator is applied. To realize the requested loads, an actuator control system needs to be designed. An important issue is the selection of the output variable of the model. In case of the damper, this can be the displacement/velocity or the force. It is generally known that a displacement loop has a lower bandwidth than a force control loop but on the other hand, a position control loop is much more robust and easy to stabilize than a position control loop. In this case, a position control loop is selected, providing good signal following characteristics up to 10 Hz.

Finally, the response of the system, the force, needs to be measured and fed into the model. This creates a closed loop system. Because of non-ideal behaviour of the actuator, instabilities may occur. Therefore an additional stabilizing control loop is installed. Figure 18 shows an overview of the HIL test setup.

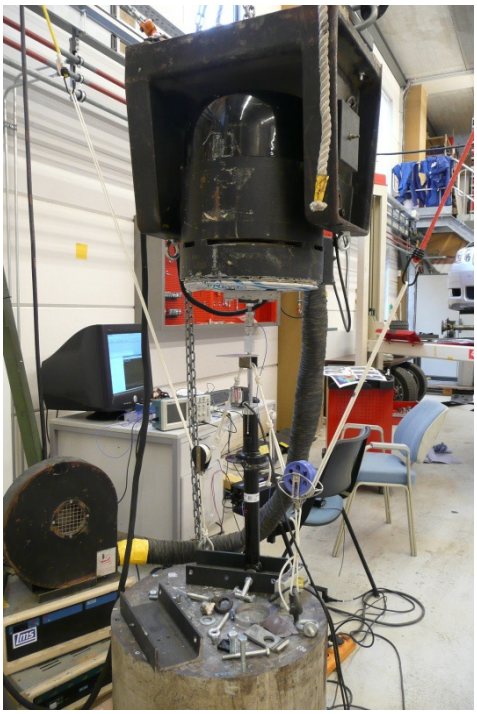

Figure 18: Damper HIL test setup

Based on the choices made, the HIL system is able to validate the shock absorber up to 10 Hz. It is clear that during the design of a HIL, several decisions need to be made that determine the final performance.

VII. CASE: MOTORCYCLE DYNAMICS MODELING

This example concerns the modeling of a motorcycle-driver system in view of accident dynamics analysis as performed as part of the EC funded research project MYMOSA [18]. Unlike cars, where most of the developed active control systems are based on simplified dynamic models, the unstable nature of 2-wheeled vehicles makes them more difficult to analyze for control purposes. In this way, the role of the rider model is fundamental to properly evaluate the active systems performance at the design stage [18-21].

As shown in Figure 19, the developed motorcycle model is composed of six rigid bodies: the front wheel, the lower part of the fork, the upper part of the fork (including the

handlebars), the front frame (including the engine and the fuel tank), the swinging arm and the rear wheel.

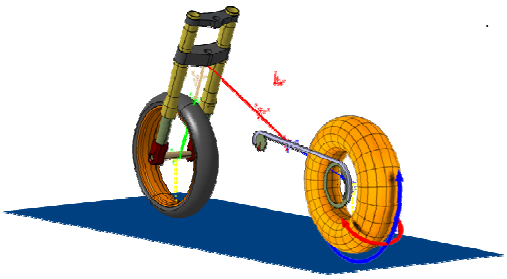

Figure 19: Multibody motorcycle model

For this study, the rider was considered rigidly attached to the front frame. This means that the only action that the rider exerts to control the direction of the motorcycle is a torque on the handlebars. This approach is valid for the most common manoeuvres. However, an MBS rider model will be considered in the future for more advanced simulations taking into account the movements of the rider. Figure 20 shows the 1D integrated control-motorcycle model including the driver control (Simulink).

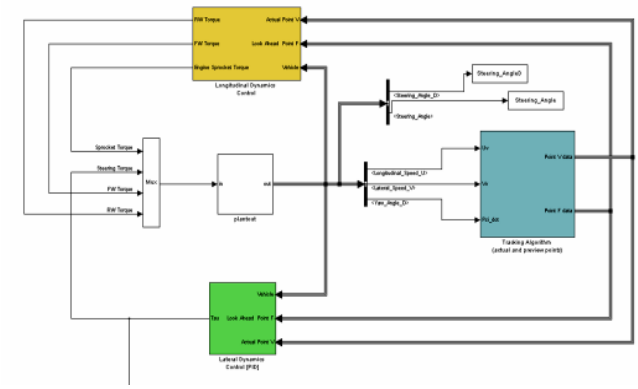

Figure 20: Integrated control model

This model is composed of four main blocks. The tracking algorithm provides all the information about the track and the relative position of the motorcycle with respect to it. The plant block represents the MBS model and is the interface between Simulink and LMS Virtual.Lab Motion. Finally, the rider model is implemented as two control blocks which stabilize the lateral and longitudinal dynamics of the motorcycle. Figure 21 presents the closed-loop results for a double lane change at high speed (22m/s).

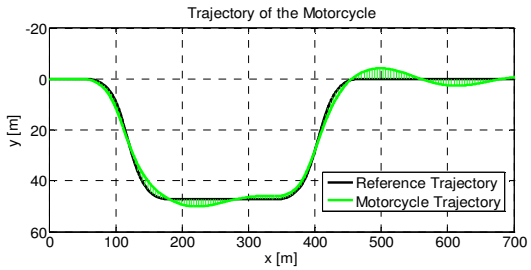

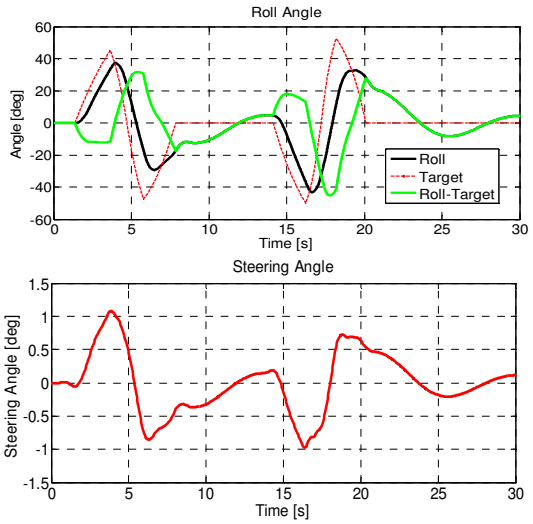

Figure 21: Closed-loop driving results

As shown in the upper result, the trajectory followed by the motorcycle matches the reference quite well. In the middle plot, one can observe how the roll angle of the motorcycle tends to follow the target angle. It is worth noting that both curves would only coincide in steady-state conditions. Finally, the steering angle is shown in the lower result, where the two lane changes are clearly distinguished. First the angle increases until it reaches 1 degree and then it decreases to -0.85. The inverse cycle is repeated for the second lane change.

VIII. CASE: ACTIVE NOISE CONTROL

Multifunctional or active materials can be used as sensor and/or actuators, which, when coupled to a control system, form intelligent structures. These structures generate an added value in their application, reducing costs and the space required for their implementation and by increasing the simplicity and number of elements necessary in the system.

The modeling problem basically consists of relating the large-size 3D, frequency domain (FE, BE-based) vibro-acoustic and structural models for the vehicle structure and structural components, interior vehicle cavities and exterior propagation field, with models of smart material sensors and actuators and a time domain control model (Fig. 22).

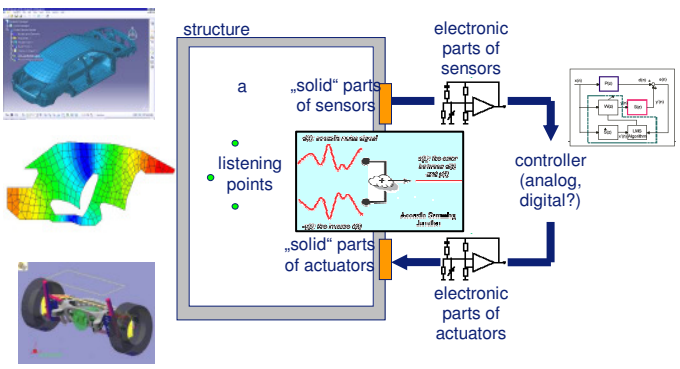

Figure 22: Active noise control system approach

The main applied approach for the structural part is this of model reduction, allowing to incorporate the reduced model as a plant model in the controller simulation. Sensors and actuators are often represented by 1D models for their functional performance, while the added mass and stiffness are accounted in the 3D FE models. The acoustic propagation can be related to the structural outputs by means of an Acoustic Transfer Vector approach. An application to the active firewall control of a vehicle-like test setup with piezo-patches is shown in Figure 23.

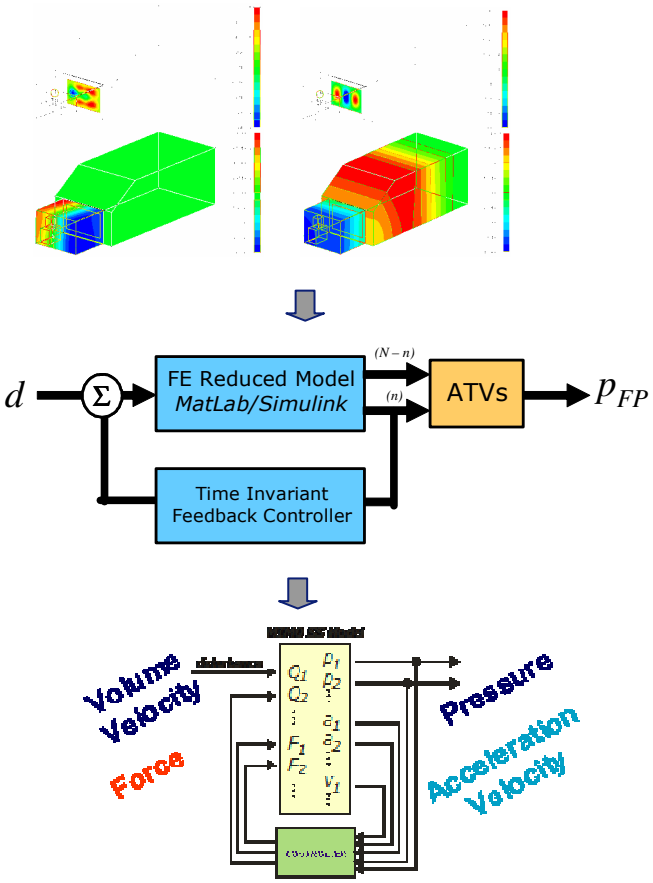

Figure 23: Active firewall mechatronics model

An extensive discussion can be found in [22-25].

IX. FUNCTIONAL SYSTEM MOCK-UP – THE MODELISAR PROJECT

It is in the context of the clear need for powerful intelligent systems simulation tools that the European ITEA2 collaborative research project MODELISAR has been defined [26]. MODELISAR will provide solutions enabling the integrated design, test and management of automotive systems. It defines a new open Functional Mockup Interface (FMI) to support co-simulation between multi-physics system modeling (such as in particular Modelica [27]) and AUTOSAR [28] for embedded control software generation (Fig. 24). System simulation models and AUTOSAR code may then be concurrently simulated within a Hardware-in-the Loop, Software-in–the-Loop, or Model-in-the-loop environment.

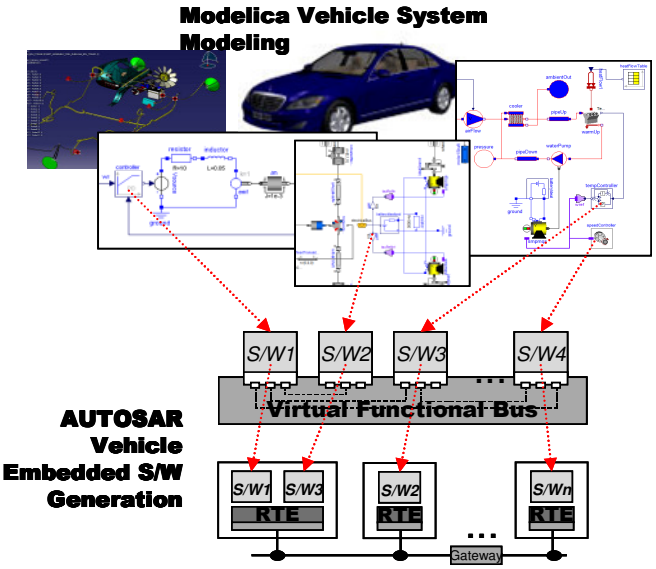

Figure 24: MODELISAR Multi-functional system mock-up

It is the objective of this project to develop the modelling technology enabling to address vehicle co-simulation with a single and scalable approach, including enhancing 3D and 1D modeling technology and confer its real-time capability. The technology research includes extensions to the model formulation, to embed behavioural modeling and procedures to derive these elements from component-based models, as well as dedicated optimization of the solver and integration strategy.

To prove the validity of these concepts, the technology will be implemented in the form of a real-time executable software code, and applied in the various tasks of development of a vehicle embedded system and control application, up to actual implementation level on a dedicated hardware platform that will be built on purpose to validate a number of use case scenarios. Use cases target some of the most real-time critical automotive and aerospace applications ranging from embedded systems, vehicle dynamics, control, (e.g. semi-active suspension, ESP, etc.) and engine and powertrain control. The latter applications are essential to make a next step in efficiency improvement and emission control and will form the basis for new generations of propulsions systems and vehicle concepts [29-33].

CONCLUSION

The performance engineering of intelligent vehicle systems mandates simulation and test methods that are capable to simulate, analyze and optimize the performance of such a product, taking into account the interaction of many subsystems and working as active systems with sensors, actuators and interconnections to controllers.

The key of any hereto applicable virtual testing approach is the combined simulation of multi-physics systems and the controls. The actual integration between system models and control models depends on the purpose of the analysis, being systems engineering or controller design and optimization. Depending on the phase of the design process, Model-in-the-Loop, Software-in-the-Loop and Hardware-in-the-Loop

approaches can be distinguished, each with their own rationale for model integration, real-time performance and hardware connection.

To make this process effective and efficient, a scalable multi-physics and control integration approach is proposed, based on a seamless integration of 3D, 1D and control models, and paving the way to a Multi-functional System Mock-up paradigm.

ACKNOWLEDGEMENTS

The presented research is conducted in the context of a coordinated research effort for the development of design engineering solutions for intelligent system. This programme is partially funded through a number of research projects such as ITEA2 project Modelisar and Flanders Drive projects Hybrid Drive, ReVAS (Research Vehicle for Active Safety) and InAst (Integrated Active Safety Technology), supported by IWT Vlaanderen and the Marie Curie projects SIMVIA2, MYMOSA, and VECOM, co-financed by the European Commission.

The authors also acknowledge the contribution of Mr. Nicolas Alborello, trainee from INSA Toulouse, Dr. Leopoldo de Oliveira from K.U.Leuven and the Marie Curie fellows Marco Gubitosa, Ondrej Marek and David Moreno Giner.

REFERENCES

[1] Anil Valsan, “Trends, Technology Roadmaps and Strategic Market Analysis of Vehicle Safety Systems in Europe”, International Automotive Electronics Congress, Oct. 24, 2006, Paris (F)

[2] McKinsey's Automotive & Assembly Practice, HAWK 2015 - Knowledge-based changes in the automotive value chain, McKinsey, 2004

[3] JSAE, The automobile in the Year 2030, Society of Automotive Engineers of Japan, 2007

[4] System Design: New Product Development for Mechatronics, Aberdeen Group, www.aberdeen.com

[5] C. Laurgeau, “Present and future of intelligent transportation systems”, Proc. ICAT 2008, Int. Conf. on Automotive Technologies, Nov. 13-14, 2008, Istanbul (TR)

[6] A. Vahidi et al., Research advances in intelligent collision avoidance and adaptive cruise control, IEEE Trans. Intell. Transp. Syst., 4(3), 143-153

[7] European Commission, “Towards Europe-wide Safer, Cleaner and Efficient Mobility: The First Intelligent Car Report”, Communication from the Commission to the European Parliament, the Council, the European Economic and Social Committee and the Committee of the Regions, COM(2007) 541, 17.09.2007

[8] Terry Costlow, “Managing Software Growth”, Automotive Engineering International, Nov. 20, 2008

[9] H. Van der Auweraer, A. Vecchio, B. Peeters, S. Dom, P. Mas, (2008), “Hybrid Testing in Aerospace and Ground Vehicle Development”, in “Hybrid Simulation: Theory, Implementation and Applications”, p.203-214, Editors S. Mettupalayam and V. Saouma

[10] P. Kvasnicka, G. Prokop, A. Rettinger, H. Stahl, “Comprehensive Approach to the Chassis Control Development”, SAE Paper 2006-01-1280, Proc. SAE 2006 World Congress & Exhibition, April 3-6, 2006, Cobo Center, Detroit, MI, USA

[11] W.C. Prescott, J.A. Laughlin, “Implementation and Usage of Design Sensitivity Analysis in Multibody Dynamics Software”, Proc. Eccomas, Thematic Conference on Multibody Dynamics, Milan, Italy, June 2007

[12] M. Gubitosa, J. De Cuyper, V. Cibrario, “Optimized Design Method of Vehicle Suspension Systems using a Reverse Engineering Approach”, Paper IMECE2008-66623, Proc. IMECE2008, Nov. 2-6, 2008, Boston (MA-USA)

[13] J. De Cuyper, M. Gubitosa, J. Kang, G. Lethé, M. Furmann, D. Kading, “Vehicle Dynamics Control – A Case Study in LMS Virtual.Lab Motion”, Proc. 4th Asian Conference on Multibody Dynamics 2008, Aug. 20-23, 2008, Seogwipo-city, Korea

[14] M. Alirand, E. Botelle, J. Sau, "Modeling A Force Control Actuator for Semi Active Car Dampers- Basics”, 16th IAVSD Symposium, Dynamics of Vehicles on Roads and Tracks, Aug 29-Sept-03 1999, Pretoria (SA)

[15] Y. He, J. McPhee, “Multidisciplinary design optimization of mechatronic vehicles with active suspensions”, Journal of Sound and Vibration, 283 (2005) 217–241

[16] C. Lauwerys, J. Swevers, P. Sas, “Robust linear control of an active suspension on a quarter car test-rig”, Control Engineering Practice 13 (2005) 577–586

[17] J. Swevers, C. Lauwerys, B. Vandersmissen, M. Maes, K. Reybrouck, P. Sas A model-free control structure for the on-line tuning of the semi-active suspension of a passenger car, Mechanical Systems and Signal Processing 21 (2007) 1422–1436

[18] http://www.mymosa.eu/

[19] Vittore Cossalter and Roberto Lot, A Motorcycle Multi-Body Model for Real Time Simulations Based on the Natural Coordinates Approach, Vehicle System Dynamics, 2002, Vol. 37, No. 6, pp. 423-447

[20] E. Botellee, M. Lebrun, “Environment for Conceptual Design of Motorcycles using AMESim, Proc. 2-nd Int. Conf. on Development and Trends of Motorcycles, June 12-13, 2003, Munich (DE)

[21] D. Moreno Giner, C. Brenna, I. Symeonidis, G. Kavadarlic, “MYMOSA – Towards the Simulation of Realistic Motorcycle Manoeuvres by Coupling Multibody and Control Techniques”, Paper IMECE2008-67297, Proc. IMECE2008, Nov. 2-6, 2008, Boston (MA-USA)

[22] L.P.R. de Oliveira, K. Janssens, P. Gajdatsy, H. Van der Auweraer, P.S. Varoto, P. Sas, W. Desmet, (2008), “Active sound quality control of engine induced cavity noise”, Mechanical Systems and Signal Processing, 23 (2009) 476– 488

[23] H. Van der Auweraer, K. Janssens, L. de Oliveira, M. da Silva, W. Desmet, (2007), “Virtual Prototyping for Sound Quality Design of Automobiles”, Sound and Vibration, Vol. 41, No.4, Apr. 2007, pp 26-31.

[24] H. Van der Auweraer, P. Mas, P. Segaert, L. de Oliveira, M. da Silva, W. Desmet, (2007), “CAE-based Design of Active Noise Control Solutions”, SAE Paper 2007-26-032, Proc. SIAT 2007, Pune (India), 17-20 Jan. 2007.

[25] http://www.smart-structures.eu/

[26] F. Bichet (ed), “MODELISAR, From System Modeling to S/W running on the Vehicle”, ITEA2 Full Project Proposal, 2007

[27] http://www.modelica.org/

[28] http://www.autosar.org/find02_07.php

[29] F. Syed, R. Nallapa, D. Ramaswamy, SAE Paper 2007-01-0274, “Integrated Modeling Environment for Detailed Algorithm Design, Simulation and Code Generation”, Proc. SAE World Congress & Exhibition, April 2007, Detroit (MI-USA)

[30] B. Saerens, E. Van den Bulck, J. Swevers, M. Diehl, “Model Predictive Control of Automotive Powertrains - First Experimental Results”, Proc. 47th IEEE Conference on Decision and Control, Dec. 9-11, 2008, Cancun, Mexico

[31] D. Ramaswamy, R. McGee, S. Sivashankar, A, Deshpande, J. Allen, K. Rzemien, “Walt Stuart A Case Study in Hardware-In-the-Loop Testing: Development of an ECU for a Hybrid Electric Vehicle”, SAE Paper 2004-01-0303, Proc. SAE 2004 World Congress & Exhibition, March 2004, Detroit (MI-USA)

[32] A. Lynn, E. Smid, M. Eshragi, N. Caldwell, D. Woody, “Modeling Hydraulic Regenerative Hybrid Vehicles Using AMESim and Matlab/Simulink”, Proceedings of SPIE, Enabling technologies for simulation science. Conference No9, Orlando FL, USA, (2005), vol. 5805, pp. 24-40

[33] H. Nuglisch, H. Dupont, “Global Vehicle System Simulation as Basis for an Analysis of Vehicle Energy Consumption”, Proc. 4th Braunschweig Symposium on Hybrid Vehicles and Energy Management, Feb. 14-15, 2007, Braunschweig (DE)

Proceedings of the 8th National Congress
on Theoretical and Applied Mechanics,
May 28-29, Brussels, Belgium.

Embedded Reduced Order Models for Thermal and Fluid Simulations

Brian T. Helenbrook
Clarkson University, Department of Mechanical and Aeronautical Engineering
Potsdam, NY 1399-5725
email: helenbrk@clarkson.edu@

Abstract

Reduced order modeling is the process of generating low-dimensional models for infinite dimensional systems. A common application of reduced order modeling is to fluid flow. A fluid flow has an infinite range of flow states that can exist. However, in a typical fluids problem only a small range of those flow states is exhibited. To take advantage of this fact a tool like the proper orthogonal decomposition can be used. The proper orthogonal decomposition finds the smallest set of orthogonal functions (or POD modes) that can accurately represent the range of flow states. The governing equations for the flow can then be compressed onto the space of states described by those functions using weighted integral methods. This then results in a low dimensional model. In this talk we investigate the performance of such reduced order models, and propose the concept of embedding these models into larger flow simulations. The purpose of embedding is to use POD modes in flow locations where the flow behavior is low-dimensional while in regions where the flow is higher-dimensional to use normal simulation techniques. As an example, in dilute particle laden flow, the near region of the particles is typically low dimensional while the large scale flow can be turbulent and strongly affected by geometry and inlet conditions. Reduced order models can be generated for the flow around the particle and coupled to the large scale flow simulation allowing fast and accurate computations of particle laden flow.

A unifying formulation for discontinuous high-order methods in CFD

Z.J. Wang
Department of Aerospace Engineering and CFD Center
Iowa State University
Ames, Iowa 50011, U.S.A.

Recently a new high-order formulation for 1D conservation laws was developed by Huynh based on the idea of "flux reconstruction". The formulation was capable of unifying several popular methods including the discontinuous Galerkin, staggered grid multi-domain method, or the spectral difference/spectral volume methods into a single family. The extension of the method to quadrilateral and hexahedral elements is straightforward. In an attempt to extend the method to other element types such as triangular, tetrahedral or prismatic elements, the idea of "flux reconstruction" is generalized into a "lifting collocation penalty" approach. With a judicious selection of solution points and flux points, the approach can be made simple and efficient to implement for mixed grids, and for high-order curved boundaries. In addition, the formulation includes the discontinuous Galerkin, spectral volume and spectral difference methods as special cases. Several test problems in both 2D and 3D will be presented to demonstrate the capability of the method.

References

1. F. Bassi and S. Rebay, High-order accurate discontinuous finite element solution of the 2D Euler equations, J. Comput. Phys. 138, 251-285 (1997).
2. B. Cockburn and C.-W. Shu, TVB Runge-Kutta local projection discontinuous Galerkin finite element method for conservation laws II: general framework, Mathematics of Computation 52, 411-435 (1989).
3. H.T. Huynh, A flux reconstruction approach to high-order schemes including discontinuous Galerkin methods, AIAA Paper 2007-4079.
4. D.A. Kopriva and J.H. Kolias, A conservative staggered-grid Chebyshev multidomain method for compressible flows, J. Comput. Phys. 125, 244 (1996).
5. Y. Liu, M. Vinokur, and Z.J. Wang, "Discontinuous Spectral Difference Method for Conservation Laws on Unstructured Grids," Journal of Computational Physics Vol. 216, pp. 780-801 (2006).
6. Z.J. Wang, Spectral (Finite) volume method for conservation laws on unstructured grids: basic formulation, J. Comput. Phys. Vol. 178, pp. 210-251, 2002.
7. Z.J. Wang and H. Gao, "A Unifying Lifting Collocation Penalty Formulation for the Euler Equations on Mixed Grids," AIAA-2009-401.

Proceedings of the 8th National Congress on Theoretical and Applied Mechanics, May 28-29, Brussels, Belgium.

Mathematical modeling of bone regeneration during fracture healing

L. Geris[1], J. Vander Sloten[1], H. Van Oosterwyck[1]
[1]Division of Biomechanics and Engineering Design, Department of Mechanical Engineering, K.U.Leuven
Celestijnenlaan 300C (2419), 3001 Leuven – Belgium
email: liesbet.geris@kuleuven.be, jos.vandersloten@kuleuven.be, hans.vanoosterwyck@kuleuven.be

I. Introduction

Over the last decade, mathematical modeling has found its way to the field of bone regeneration research (as reviewed in [1]). At first, simple mechanoregulatory models were proposed linking the nature and magnitude of mechanical stimuli to the cell fate. In general, high stresses and strains give rise to the development of cartilage or fibrous tissue whereas bone can only be formed in areas of low mechanical stimulation. Gradually, more emphasis was laid on the biology steering the process of bone regeneration and bioregulatory models were developed where only biological cues, such as growth factors or the presence of vascularization determine the outcome of the regeneration process. Finally, a third category of mathematical models, mechanobioregulatory models, emerged combining the effects of both mechanical and biological stimuli on the regeneration process.

The authors have contributed to these developments by proposing both a bioregulatory model [2] and, based on that, a mechanobioregulatory model [3]. The novelty of these models lies in their special attention for the importance of angiogenesis (i.e. formation of blood vessels) on the regeneration process. These models were used to simulate normal and impaired healing situations and to design novel treatment strategies for the latter. The results have been successfully corroborated by comparison with several *in vivo* experiments in rodents.

II. Materials and Methods

The bioregulatory model describes the spatiotemporal evolution of the concentrations/densities of the main cell, tissue and growth factor types involved in the regeneration process. These concentrations can change due to migration, differentiation, proliferation, decay etc. This is mathematically described by means of continuum scale partial differential equations of the taxis-diffusion-reaction type. This system was implemented using a custom finite volumes code, paying special attention to the model's requirements of mass conservation and non-negativity of the variables [4].

The influence of mechanics was introduced in the bioregulatory models by changing the parameter values of certain processes depending on the local mechanical stimulus after every loading step. For example, the proliferation rate of osteoblasts (bone forming cells) was enhanced for a certain range of fluid flow velocities [5] (tissues were modeled to be biphasic).

III. Results

Figure 1 shows an example of how these models can be used in bone regeneration research. Fig 1a shows the result of an overloaded fracture where no bone is formed and the entire regeneration zone is filled with soft tissue. Simulating treatment of this impaired healing situation by placing a fixator that removes the overload (Fig 1b), predicts the recapitulation of angiogenesis followed by the formation of bone in the regeneration zone. Another treatment strategy that was investigated is the administration of osteogenic growth factors at the moment of stabilization. Again, recapitulation of the healing process is observed, albeit with a slightly different healing pattern.

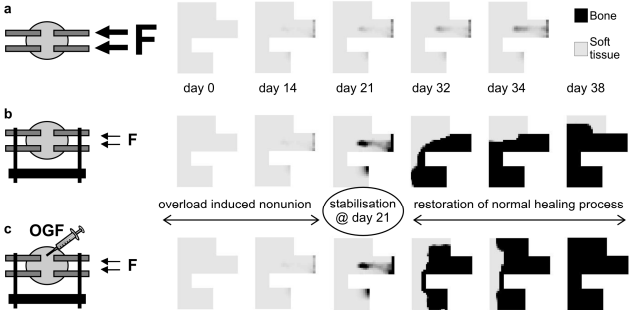

Fig. 1. Overload induced impaired healing and potential treatment strategies. Due to symmetry reasons, only one quarter of the regeneration zone is shown on the right.

IV. Conclusions

The developed mathematical framework is such that it easily allows for the investigation of additional mechanical stimuli and for additional biological processes to be made dependent on these stimuli. It thereby allows for both the investigation of experimentally testable hypotheses on the regeneration process itself and for the design of clinically relevant treatment strategies for impaired healing situations.

Acknowledgements

LG is a postdoctoral research fellow of FWO Flanders.

References

[1] L. Geris, J. Vander Sloten, H. Van Oosterwyck, In silico biology of bone modeling and remodeling – regeneration. *Phil Trans Roy Soc A*, accepted for publication, 2009.

[2] L. Geris, A. Gerisch, J. Vander Sloten, R. Weiner, H. Van Oosterwyck, Angiogenesis in bone fracture healing: a bioregulatory model, *J Theor Biol*, 251(1), 137-158, 2008.

[3] L. Geris, J. Vander Sloten, H. Van Oosterwyck, An integrated mathematical modelling framework for the study of bone fracture healing, *J Biomech*, 41(S1), 107, 2008.

[4] A. Gerisch, L. Geris, A finite volume spatial discretisation for taxis-diffusion-reaction systems with axi-symmetry: application to fracture healing. *In Advances in Mathematical Modeling of Biological Systems*, *Volume I*, Eds. A. Deutsch, L. Brusch, H. Byrne, G. de Vries and H.-P. Herzel, Birkhäuser, Boston, 2007, pp 303-316, ISBN 0-8176-4557-8.

[5] I. Owan, D.B. Burr, C.H. Turner, J. Qiu, Y. Tu, J.E. Onyia, R.L. Duncan, Mechanotransduction in bone: osteoblasts are more responsive to fluid force than mechanical strain. *Am J Phys*, 273:810-815, 1997

The iCub Humanoid – Design, Development and Operation

Professor D G Caldwell
Director, Italian Institute of Technology, Genoa, 16163,Italy.
Email: Darwin.Caldwell@iit.it

Abstract

The development of greater understanding of human cognition is currently an active area of research within both
i). neuroscience, where the goal is to develop greater understanding of the mechanisms of the human brain, and
ii). robotics where the aim is to develop robots with human-like cognitive capacities.

The EU funded "RobotCub" project hypothesises that cognitive development requires physical embodiment – without the capacity to interact with the world, intelligence will at best be abstract and disconnected from the world. To test this concept, "Robotcub" has developed a child-like humanoid robot – the iCub.

The iCub aims to replicate both the physical and cognitive abilities of an 18 month to 3 ½ year old child. To ensure that this interaction is as accurate as possible the robot must be a faithful representation of the infant inspiration. As a result the 'baby' robot, stands 100cm tall, fits within the general size and shape of a child, weighs less than 23 kg and has 69 d.o.f.

This presentation will concentrate on the mechatronic design of the iCub. It will explore the specification process, planning, and development, particularly concentrating on the legs, waist and hands. We will also consider possible future directions for the design of the iCub and other humanoids.